



Irasema Alcántara-Ayala
Željko Arbanas
David Huntley
Kazuo Konagai
Snježana Mihalić Arbanas
Matjaž Mikoš

Maneesha V. Ramesh
Kyoji Sassa
Shinji Sassa
Huiming Tang
Binod Tiwari
Editors

Progress in Landslide Research and Technology Volume 2 Issue 2, 2023



OPEN ACCESS

Progress in Landslide Research and Technology

The Open Access book series of the International Consortium on Landslides (ICL) aims to be the common platform for the publication of recent progress in landslide research and technology for practical applications and the benefit of society contributing to the Kyoto Landslide Commitment 2020, which is expected to continue up to 2030 and even beyond for the global promotion of understanding and reducing landslide disaster risk as well as the 2030 Agenda Sustainable Development Goals. The contributions include original and review articles, case studies, activity reports and teaching tools for the promotion of understanding and reducing landslide disaster risks.

Irasema Alcántara-Ayala • Željko Arbanas •
David Huntley • Kazuo Konagai •
Snježana Mihalić Arbanas • Matjaž Mikoš •
Maneesha V. Ramesh • Kyoji Sassa •
Shinji Sassa • Huiming Tang • Binod Tiwari
Editors

Progress in Landslide Research and Technology, Volume 2 Issue 2, 2023

Editors

Irasema Alcántara-Ayala
Institute of Geography
Natl Autonomous University of Mexico
Ciudad De Mexico, Estado de México
Mexico

Željko Arbanas
Faculty of Civil Engineering
University of Rijeka
Rijeka, Croatia

David Huntley
Geological Survey of Canada
Vancouver, BC, Canada

Kazuo Konagai
International Consortium on Landslides
Kyoto, Japan

Snježana Mihalić Arbanas
Fac. Mining, Geology and Petroleum Eng.
University of Zagreb
Zagreb, Croatia

Matjaž Mikoš
Faculty of Civil & Geodetic Engineering
University of Ljubljana
Ljubljana, Slovenia

Maneesha V. Ramesh
Amrita Cent. for Wireless Networks, App.
Amrita School of Sustainable Development
Amritapuri, India

Kyoji Sassa
International Consortium on Landslides
Kyoto, Japan

Shinji Sassa
National Institute of Maritime,
Port and Aviation Technology
Port and Airport Research Institute
Yokosuka, Japan

Huiming Tang
Engineering Faculty
China University of Geoscience
Wuhan, China

Binod Tiwari
Civil & Environmental Engineering
California State University, Fullerton
Fullerton, CA, USA



ISSN 2731-3794 ISSN 2731-3808 (electronic)
Progress in Landslide Research and Technology
ISBN 978-3-031-44295-7 ISBN 978-3-031-44296-4 (eBook)
<https://doi.org/10.1007/978-3-031-44296-4>

This work contains media enhancements, which are displayed with a “play” icon. Material in the print book can be viewed on a mobile device by downloading the Springer Nature “More Media” app available in the major app stores. The media enhancements in the online version of the work can be accessed directly by authorized users.

© International Consortium on Landslides 2023. This book is an open access publication.

Open Access This book is licensed under the terms of the Creative Commons Attribution 4.0 International License (<http://creativecommons.org/licenses/by/4.0/>), which permits use, sharing, adaptation, distribution and reproduction in any medium or format, as long as you give appropriate credit to the original author(s) and the source, provide a link to the Creative Commons license and indicate if changes were made.

The images or other third party material in this book are included in the book's Creative Commons license, unless indicated otherwise in a credit line to the material. If material is not included in the book's Creative Commons license and your intended use is not permitted by statutory regulation or exceeds the permitted use, you will need to obtain permission directly from the copyright holder.

The use of general descriptive names, registered names, trademarks, service marks, etc. in this publication does not imply, even in the absence of a specific statement, that such names are exempt from the relevant protective laws and regulations and therefore free for general use.

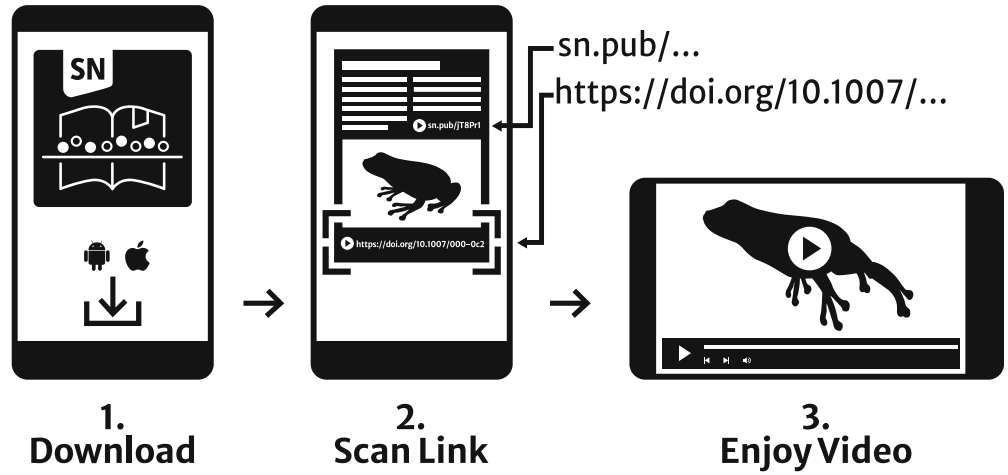
The publisher, the authors, and the editors are safe to assume that the advice and information in this book are believed to be true and accurate at the date of publication. Neither the publisher nor the authors or the editors give a warranty, expressed or implied, with respect to the material contained herein or for any errors or omissions that may have been made. The publisher remains neutral with regard to jurisdictional claims in published maps and institutional affiliations.

Cover illustration: In the Thompson River valley, south-central British Columbia, Canada, thick (>100 m) accumulations of glacial lake sediments, tills, and outwash have a complex history of sudden rapid translational failure and liquefaction in the past, and slower rotational slumping along toe slopes, head scarps, and tributary channels at present. (Photograph taken by Drew Rotheram-Clarke)

This Springer imprint is published by the registered company Springer Nature Switzerland AG
The registered company address is: Gewerbestrasse 11, 6330 Cham, Switzerland

Paper in this product is recyclable.

Springer Nature More Media App



Support: customerservice@springernature.com

Editorial Board of the Book Series

Editor-in-Chief

Kyoji Sassa, International Consortium on Landslides, Japan

Assistant Editors-in-Chief

Kazuo Konagai, International Consortium on Landslides, Japan

Binod Tiwari, California State University, Fullerton, USA

Željko Arbanas, University of Rijeka, Croatia

Editors

Biljana Abolmasov, University of Belgrade, Republic of Serbia

Beena Ajmera, Iowa State University, USA

Irasema Alcántara-Ayala, National Autonomous University of Mexico, Mexico

Netra Prakash Bhandary, Ehime University, Japan

Sabatino Cuomo, University of Salerno, Italy

Yasser Elshayeb, Cairo University, Egypt

Xuanmei Fan, Chengdu University of Technology, China

Faisal Fathani, University of Gadjah Mada, Indonesia

Louis Ge, National Taiwan University, Chinese Taipei

Ivan Gratchev, Griffith University, Australia

David Huntley, Geological Survey of Canada, Canada

Snježana Mihalić-Arbanas, University of Zagreb, Croatia

Matjaž Mikoš, University of Ljubljana, Slovenia

Maneesha Ramesh, Amrita University, India

Paola Reichenbach, Research Institute for Geo-Hydrological Protection, CNR, Italy

Shinji Sassa, Port and Airport Research Institute, Japan

Josef Stemberk, Institute of Rock Structure and Mechanics, CAS, Czech Republic

Alexander Strom, Geodynamic Research Center, Russia

Huiming Tang, China University of Geosciences, Wuhan, China

David Tappin, British Geological Survey, UK

Veronica Tofani, University of Florence, Italy

Vít Vilímek, Charles University, Czech Republic

Fawu Wang, Tongji University, China

Wei Shan, Northeast Forestry University, China

KLC2020 Managing Committee

Kyoji Sassa (Chairman), Secretary General, Secretariat of the Kyoto Landslide Commitment 2020

Kaoru Takara, Managing Director, Secretariat of the Kyoto Landslide Commitment 2020

Matjaž Mikoš, Chair of the Global Promotion Committee of the International Programme on Landslides and Kyoto Landslide Commitment 2020

Qunli Han, Co-chair of the Global Promotion Committee of the International Programme on Landslides and Kyoto Landslide Commitment 2020

Nicola Casagli, President of the International Consortium on Landslides

Peter Bobrowsky, Immediate past President of the International Consortium on Landslides

Advisory Members for KLC2020

Abou Amani, Director, Division of Water Sciences, Secretary, Intergovernmental Hydrological Programme (IHP), UNESCO

Soichiro Yasukawa, Programme specialist, Coordinator for Disaster Risk Reduction and Resilience, UNESCO

Daniel Lebel, Director General, Geological Survey of Canada, Natural Resources Canada, Canada

John Ludden, President of the International Union of Geological Sciences (IUGS)

John LaBrecque, Chair of IUGG GeoRisk Commission, Center for Space Research, University of Texas at Austin, USA

Rafiq Azzam, President of the International Association for the Engineering Geology and the Environment (IAEG)

Paolo Canuti, past President of the International Consortium on Landslides (ICL), Italy

Sálvano Briceño, First chair of the Global Promotion Committee of the International Programme on Landslides

Badaoui Rouhban, Chair of the KLC2020 Launching Session and Moderator of ISDR-ICL Sendai Landslide Partnerships 2015–2025 Session of 3rd WCDRR in 2015

KLC2020 Official Promoters

Host Organization

International Consortium on Landslides (ICL)/Nicola Casagli

Public Sectors: KLC2020 Official Promoters-Public

International Unions/Associations, Governmental Organizations, Universities and Research Institutes

The International Union of Geological Sciences (IUGS)/John Ludden

The International Union of Geodesy and Geophysics (IUGG)/Kathy Whaler

The International Association for the Engineering Geology and the Environment/Rafiq Azzam

International Geosynthetics Society (IGS)/John Kraus

Geological Survey of Canada, Natural Resources Canada, Canada/Daniel Lebel

Faculty of Civil and Geodetic Engineering, University of Ljubljana, Slovenia/Matjaž Mikoš

China University of Geosciences, Wuhan, China/Huiming Tang

Department of Civil Engineering, National Taiwan University, Chinese Taipei/Shang-Hsien Hsien
Institute of Rock Structure and Mechanics, the Czech Academy of Sciences/Josef Stemberk
Institute of Cold Regions Science and Engineering, Northeast Forestry University, China/Wei Shan

Private Sectors: KLC2020 Official Promoters-Private

Companies and Corporation

Marui & Co., Ltd, Japan, Nippon Koei Co., Ltd, Japan, Ellegi srl, Italy
Chuo Kaihatsu Corporation, Japan, Godai Corporation, Japan
Kiso-Jiban Consultants Co., Ltd, Japan, Kokusai Kogyo Co., Ltd., Japan, OSASI Technos, Inc., Japan

Standing Editors for KLC2020 Book Series

Kyoji Sassa, International Consortium on Landslides, Kyoto, Japan
Kazuo Konagai, International Consortium on Landslides, Kyoto, Japan
Binod Tiwari, California State University, Fullerton, USA
Željko Arbanas, University of Rijeka, Croatia
Paola Reichenbach, Research Institute for Geo-Hydrological Protection, CNR, Italy
Shinji Sassa, Port and Airport Research Institute, Yokosuka, Japan
Fawu Wang, Tongji University, Shanghai, China
Khang Dang, VNU University of Science, Vietnam National University, Vietnam
Beena Ajmera, Iowa State University, USA

Editorial Office

Secretariat of the Kyoto Landslide Commitment 2020 International Consortium on Landslides (ICL)
138-1 Tanaka-Asukai cho, Sakyo-ku, Kyoto 606-8226, Japan E-mail: klc2020@landslides.org

Global Promotion Committee of the International Programme on Landslides and Kyoto Landslide Commitment 2020

A Commitment to the Sendai Framework and the Sustainable Development Goals

Chair

Matjaž Mikoš (Faculty of Civil and Geodetic Engineering, University of Ljubljana)

Co-chairs

Qunli Han (Integrated Research on Disaster Risk, IRDR)

Soichiro Yasukawa (Programme Specialist on Disaster Risk Reduction, UNESCO, Paris)

Hiroshi Kitazato (Treasurer of IUGS)

John LaBrecque (Chair of IUGG GeoRisk Commission)

Secretary

Kyoji Sassa (IPL World Centre, Director)

Members of the IPL-KLC Global Promotion Committee

ICL Full Members

Geotechnical Engineering Office, Hong Kong, China; UNESCO Chair for the Prevention and the Sustainable Management of Geo-hydrological Hazards—University of Florence, Italy; Faculty of Civil and Geodetic Engineering, University of Ljubljana (ULFGG), Slovenia; and other members (total 61 members from 30 countries/regions).

ICL Supporting Organizations

UNESCO, UNDRR, WMO, FAO, UNU, ISC, WFEO, IUGS, IUGG, Government of Japan (CAO, MEXT, MAFF, MLIT)

KLC2020 Official Promoters

Host Organization

International Consortium on Landslides (ICL)/Nicola Casagli

Public Sectors: KLC2020 Official Promoters—Public

- The International Union of Geological Sciences (IUGS)/John Ludden
- The International Union of Geodesy and Geophysics (IUGG)/Kathy Whaler
- The International Association for the Engineering Geology and the Environment (IAEG)/Rafiq Azzam
- International Geosynthetics Society (IGS)/John Kraus
- Geological Survey of Canada, Natural Resources Canada, Canada/Daniel Lebel
- Faculty of Civil and Geodetic Engineering, University of Ljubljana, Slovenia/Matjaž Mikoš
- China University of Geosciences, Wuhan, China/Huiming Tang
- Department of Civil Engineering, National Taiwan University, Chinese Taipei/Shang-Hsien Hsien

- Institute of Rock Structure and Mechanics, the Czech Academy of Sciences/Josef Stemberk
- Institute of Cold Regions Science and Engineering, Northeast Forestry University, China/
Wei Shan

Private Sectors: KLC2020 Official Promoters—Private

- Marui & Co., Ltd, Japan
- Nippon Koei Co., Ltd, Japan
- Ellegi srl, Italy
- Chuo Kaihatsu Corporation, Japan
- Godai Kaihatsu Corporation, Japan
- Kiso-Jiban Consultants Co., Ltd, Japan
- Kokusai Kogyo Co., Ltd., Japan
- OSASI Technos, Inc., Japan

IPL World Centre

IPL World Centre (IWC) was established in 2006 by the Tokyo Action Plan to serve, as it does, as the secretariat of IPL, GPC/IPL, and the UNITWIN UNESCO-KU-ICL Programme. IWC also serves as the secretariat of KLC2020. IWC is a part of the legal body (NPO-ICL registered in Kyoto, Japan) of ICL. The Council of the IWC consists of advisors from the Ministry of Education, Sports, Science and Technology, Ministry of Agriculture, Forestry and Fisheries, Ministry of Land, Infrastructure and Tourism of the Government of Japan, UNESCO, and of members from ICL Headquarters, chairs of GPC/IPL-KLC, presidents, and officers of ICL.

Secretariat of GPC/IPL-KLC

Secretary

Kyoji Sassa

International Consortium on Landslides

138-1 Tanaka-Asukai cho, Sakyo-ku, Kyoto 606-8226, Japan

Tel: +81 (75) 723 0640

Fax: +81 (75) 950 0910

E-mail: klc2020@landslides.org

URL: <https://www.landslides.org/>

Contents

Part I ICL Landslide Lesson

Advancements in Shear Strength Interpretation, Testing, and Use for Landslide Analysis	3
Binod Tiwari and Beena Ajmera	
Rock Avalanches in the Tibetan Plateau of China	55
Yufeng Wang, Qiangong Cheng, Qiwen Lin, Anwen Shi, Jie Ming, Zhiyi Feng, and Zhang Song	

Part II Original Articles

Landslide Susceptibility Zonation Using GIS-Based Frequency Ratio Approach in the Kulon Progo Mountains Area, Indonesia	115
Egy Erzagian, Wahyu Wilopo, and Teuku Faisal Fathani	
Physically-Based Regional Landslide Forecasting Modelling: Model Set-up and Validation	127
Veronica Tofani, Elena Benedetta Masi, and Guglielmo Rossi	
Consequence: Frequency Matrix as a Tool to Assess Landslides Risk	137
Michel Jaboyedoff	
Do not Let Your Guard Down: Landslide Exposure and Local Awareness in Mexico	155
Ricardo J. Garnica-Peña and Irasema Alcántara-Ayala	
Landslides in Higher Education Curricula and Beyond	167
Matjaž Mikoš	
Community Scale Landslide Resilience: A Citizen-Science Approach	183
Maneesha Vinodini Ramesh, Hemalatha Thirugnanam, Nitin Kumar Mohanan, Balmukund Singh, Harichandana C Ekkirala, and Ramesh Guntha	
Remedial Measures Impact on Slope Stability and Landslide Occurrence in Small-Scale Slope Physical Model in 1 g Conditions	197
Željko Arbanas, Josip Peranić, Vedran Jagodnik, Martina Vivoda Prodan, and Nina Čeh	
Surficial Geology and Geomorphology of the North Slide, Thompson River Valley, British Columbia, Canada: Application of Fundamental Geoscience Information to Interpretations of Geospatial Monitoring Results	221
David Huntley, Drew Rotheram-Clarke, Kelvin Sattler, and David Elwood	

High Resolution Numerical Weather Simulation for Orographic Precipitation as an Accurate Early Warning Tool for Landslide Vulnerable Terrains	239
H. A. A. I. S. Bandara and Ryo Onishi	
Climate Change as Modifier of Landslide Susceptibility: Case Study in Davao Oriental, Philippines	247
Mary Antonette A. Beroya-Eitner, May Celine T. M. Vicente, Julie Mae B. Dado, Marion Roel S. Dimain, Joel T. Maquiling, and Faye Abigail T. Cruz	
Fractal-Based Evaluation of the Spatial Relationship Between Conditioning Factors and the Distribution of Landslides (a Case Study in Tinh Tuc, Cao Bang Province, Vietnam)	259
Binh Van Duong, Igor K. Fomenko, and Kien Trung Nguyen	
Procedure of Data Processing for the Improvement of Failure Time Prediction of a Landslide Based on the Velocity and Acceleration of the Displacement	269
Imaya Ariyaratna and Katsuo Sasahara	
Numerical Analysis of the Effect of Rainfall on the Stability of Sandstone-Covered Mudstone Cutting Slopes	285
Ying Guo, Yating Du, Wei Shan, and Chengcheng Zhang	
Part III Review Articles	
Post-formation Behavior of Hattian Landslide Dam and Post-breaching Situation	299
Ahsan Sattar and Kazuo Konagai	
Investigation of Debris Flow Impact Mechanisms and Designs	311
Charles W. W. Ng, Sunil Poudyal, Haiming Liu, Aastha Bhatta, W. A. Roanga K. De Silva, and Zhenyang Jia	
A Review of the Disaster Risk Assessment Perspectives	323
Dayan Munasinghe, Terrance Fernando, Kaushal Keraminiyage, and Asiri Karunawardena	
Part IV IPL Projects, World Centres of Excellence on Landslide Risk Reduction, and Kyoto Landslide Commitment 2020	
Application of LAND-SUITE for Landslide Susceptibility Modelling Using Different Mapping Units: A Case Study in Croatia	343
Sanja Bernat Gazibara, Marko Sinčić, Mauro Rossi, Paola Reichenbach, Martin Krkač, Hrvoje Lukačić, Petra Jagodnik, Gabrijela Šarić, and Snježana Mihalić Arbanas	
An Integrated Approach to Landslides Risk Management for Local and National Authorities	355
Biljana Abolmasov, Miloš Marjanović, Uroš Đurić, and Jelka Krušić	
Assessing Landslide Hazard in the High City of Antananarivo, Madagascar (UNESCO Tentative Site)	361
William Frodella, Daniele Spizzichino, Giacomo Lazzeri, Claudio Margottini, Veronica Tofani, and Nicola Casagli	

Part V ICL Landslide Teaching Tools

Teaching Tool for LS-Tsunami	375
Khang Dang, Kyoji Sassa, and Doan Huy Loi	

Part VI Technical Notes and Case Studies

CLiRtheRoads: An Integrated Approach to Landslide Risk Management on Roads in Serbia	403
Biljana Abolmasov, Ranka Stanković, Miloš Marjanović, Nikola Vulović, and Uroš Đurić	

Part VII World Landslide Reports

Rock Slope Instabilities Affecting the AIUla Archaeological Sites (KSA)	413
José Ignacio Gallego, Claudio Margottini, Ingrid Perissé Valero, Daniele Spizzichino, Tommaso Beni, Daniela Boldini, Francesca Bonometti, Nicola Casagli, Riccardo Castellanza, Giovanni Battista Crosta, Paolo Frattini, William Frodella, Giovanni Gigli, Edoardo Lusini, Serena Rigamonti, Giulia Rusconi, and Lorenzo Vitrano	
Refugees' Perception of Landslide Disasters: Insights from the Rohingya Camps in Cox's Bazar, Bangladesh	431
A. S. M. Maksud Kamal, Anika Samm-A, Bayes Ahmed, and Peter Sammonds	
KLC2020 Official Promoters	441
Geological Survey of Canada, Natural Resources Canada	443
Faculty of Civil and Geodetic Engineering, University of Ljubljana	447
China University of Geosciences, Wuhan	451
Department of Civil Engineering, National Taiwan University	457
Institute of Cold Regions Science and Engineering, Northeast Forestry University	461
Marui & Co. Ltd.	463
Nippon Koei Co., Ltd., Geohazard Management Division	467
Ellegi Srl	471
Chuo Kaihatsu Corporation	475
Godai Kaihatsu Corporation	479
Kiso-Jiban Consultants Co. Ltd	483
Kokusai Kogyo Co. Ltd	485
OSASI Technos, Inc.	489
List of ICL Members	493
Index	497

Part I

ICL Landslide Lesson



Advancements in Shear Strength Interpretation, Testing, and Use for Landslide Analysis

Binod Tiwari and Beena Ajmera

Abstract

Landslides are devastating natural disasters that result in loss of life, property damage, and community disruption. They have global impacts, causing fatalities and economic losses, particularly in mountainous regions near densely populated areas. Landslides can be caused by natural factors, including water saturation from heavy rainfall, snowmelt, and changes in groundwater levels, as well as seismic activity such as earthquakes and volcanic eruptions. Human activities, such as altering drainage patterns, destabilizing slopes, and removing vegetation, also contribute to landslides. Construction and development on slopes, over-steepening, and improper land management practices can further increase the risk of landslides. A key component in understanding the stability of slopes will be knowledge of the shear strength of the soils involved. However, to do so, it will be necessary to understand the various measuring methods of shear strength, loading conditions, and other parameters. Different methods and tests are employed to determine the shear strength of soil, depending on the specific conditions and objectives. Direct shear tests are often utilized to measure peak and fully softened shear strengths. Triaxial tests, on the other hand, are suitable for assessing both peak and fully softened shear strengths under drained or undrained conditions. Generally, the ring shear device is preferred for measurements of the residual shear strengths. However, multiple reversal direct shear tests and specifically modified direct shear tests as well as triaxial tests have also been utilized for this purpose. The cyclic simple shear test is recommended as an effective technique for replicating

in-situ conditions to investigate the cyclic resistance and post-cyclic shear strengths of soils. Several correlations have been developed in the literature to estimate various shear strengths, including the fully softened and residual shear strengths of soil, as summarized in this paper. These correlations utilize parameters such as the liquid limit, plasticity index, mineralogy, clay fraction, and effective normal stress. The undrained shear strength of over-consolidated soils can be captured with the use of the Stress History and Normalized Soil Engineering Properties (SHANSEP) method. Extending this approach with the use of the normalized undrained strength ratio can result in two correlations that can capture the undrained shear strength. The paper also presents correlations for the true and base friction angles to estimate the shear strength using Hvorslev's theory. This allows for a departure from the use of the cohesion intercept and friction angle in the Mohr-Coulomb failure envelope, both of which are dependent on the over-consolidation ratio. The power function effectively represents the cyclic strength curves in soils with the curve fitting parameters a and b defining their shape and position. A correlation between the normalized undrained strength ratio and post-cyclic effective stress ratio to assess the undrained shear strength after cyclic loading was also introduced. This correlation was shown to also capture the effects of excess pore pressure dissipation and reductions in shear strength induced by a second cyclic load.

Keywords

Landslides · Shear strength · Soil testing · Slope stability · Residual shear strength · Fully softened shear strength

B. Tiwari (✉)

Department of Civil and Environmental Engineering, California State University, Fullerton, CA, USA
e-mail: btiwari@fullerton.edu

B. Ajmera

Department of Civil, Construction and Environmental Engineering, Iowa State University, Ames, IA, USA
e-mail: bajmera@iastate.edu

© The Author(s) 2023

I. Alcántara-Ayala et al. (eds.), *Progress in Landslide Research and Technology, Volume 2 Issue 2, 2023*, Progress in Landslide Research and Technology, https://doi.org/10.1007/978-3-031-44296-4_1

1 Background

Landslides are natural disasters that can have catastrophic consequences, causing loss of life, immense property damage, and disrupting communities. They are characterized by the rapid movement of soil, rock, and debris down slopes and have the potential for far-reaching impacts on both human and natural environments. Understanding the severity of landslides and their implications is essential for implementing proactive measures to mitigate risks and enhance resilience in vulnerable areas.

Landslides caused approximately 11,500 fatalities per year between 2004 and 2016 worldwide (United Nations Office for Disaster Risk Reduction, UNDRR 2019). It is important to note that the number of fatalities can vary greatly depending on the severity and location of the landslide, as shown in Fig. 1. This figure shows that the risk of deaths from landslides increases in highly mountainous regions in proximity to dense neighborhoods. In particular, Fig. 1 shows that

the highest mortality risks appear in Asia near the Himalayas and in South America by the Andes. Some examples of disastrous landslides in the past decade are provided in Table 1. In addition, to the location of the failure, the table also provides some information about the volume of material involved and the number of fatalities caused.

In addition to the fatalities, landslides can cause extensive damage to buildings, roads, and other infrastructure. The economic impact can be significant. For example, in the United States, landslides cost an average of \$1–2 billion annually in direct costs and indirect economic losses (USGS 2022). Figure 2 shows the total economic damages resulting from landslides around the world in 2004, 2010, and 2016. As seen, the cost can be much higher in countries with less developed infrastructure and limited resources for disaster response and recovery.

Other impacts by landslides cannot be captured quantitatively. For example, landslides can have long-lasting effects on the environment. They can alter landscapes, destroy

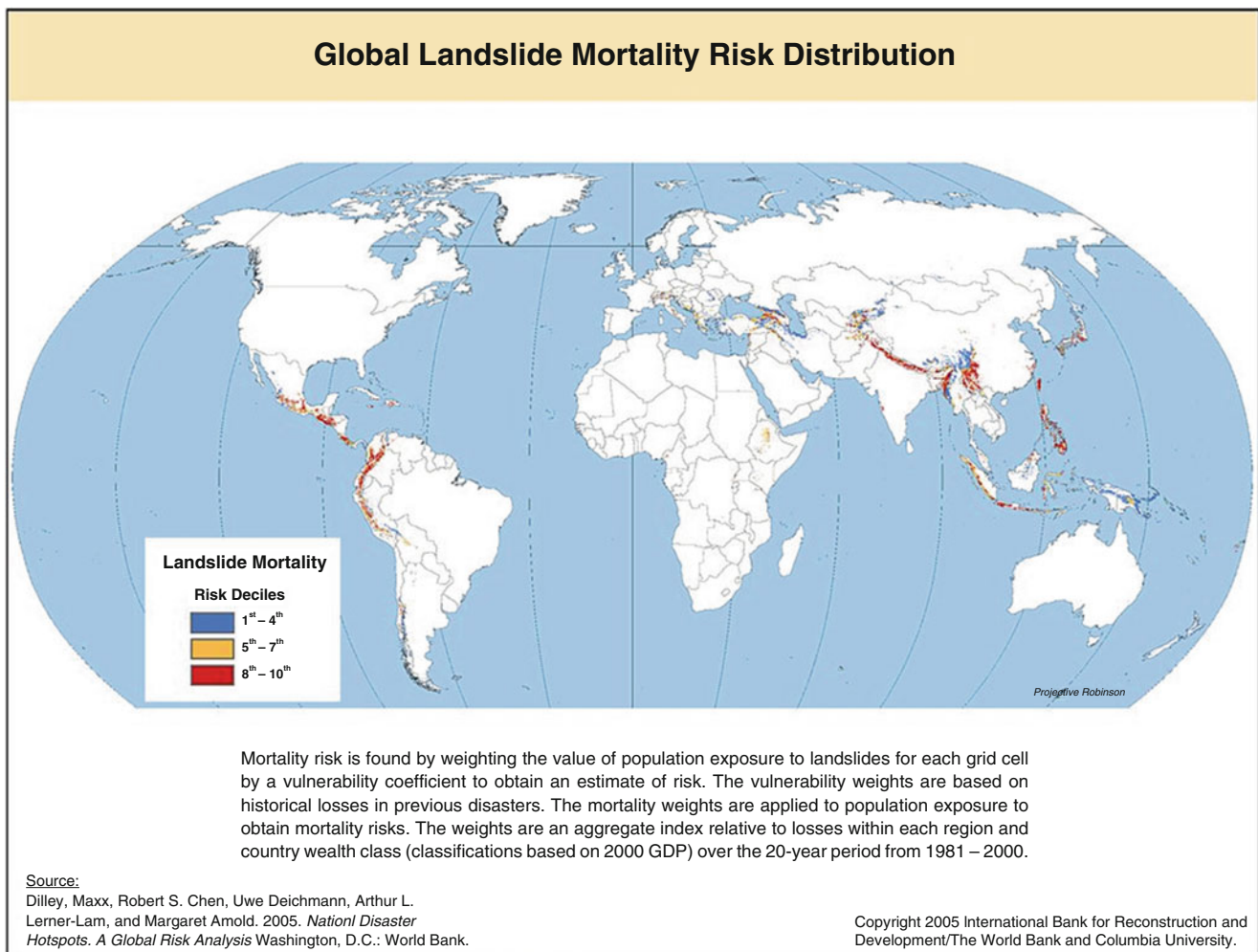


Fig. 1 Mortality risk from landslides (Source: Ritchie et al. 2022)

Table 1 Selected disastrous landslide events in recent history

Name/Location	Date of Failure	Fatalities	Reference(s)
Tumbi quarry landslide, Papua New Guinea (5.956°S, 142.789°E)	January 24, 2012	60	Robbins et al. (2012)
Bingham canyon mine landslide (40.523°N, 112.151°W)	April 10, 2013	0	NASA Earth Observatory (2022) and Hilbert et al. (2014)
Oso mudslide (48.283°N, 121.847°W)	March 22, 2014	43	Wartman et al. (2016)
Abe Berek landslide, Argo District, Afghanistan	May 2, 2014	2700	Zhang et al. (2015)
West Salt Creek landslide (39.167°N, 107.848°W)	May 25, 2014	3	Coe et al. (2015)
Malin landslide (19.161°N, 73.688°E)	July 30, 2014	160	Ering and Sivakumar Babu (2016)
Sunkoshi blockage, Sindhupalchok District, Nepal	August 2, 2014	156	Shrestha and Nakagawa (2016)
Hiroshima landslides, Hiroshima prefecture, Japan	August 20, 2014	74	Fukuoka et al. (2015)
Hpakant jade mine disaster, Hpakant, Myanmar	November 21, 2015	114	Lin et al. (2021)
Shenzhen landslide, Shenzhen, China	December 20, 2015	73	Yang et al. (2017)
Chitan hydropower landslide, Tianing, southeastern China	May 8, 2016	36	Zhang et al. (2019)
Aranayake landslide, Aranayake, Sri Lanka	May 17, 2016	127	Tan et al. (2020)
Mocoa landslide (1.15°N, 76.648°W)	April 2, 2017	316	Cheng et al. (2018)
Karrat Fjord landslide (71.535°N, 53.213°W)	June 17, 2017	4	Gauthier et al. (2017)
Xinmo landslide (32.067°N, 103.65°E)	June 24, 2017	10	Fan et al. (2017)
Montecito mudslide, Montecito, California	January 9, 2018	20	Tiwari et al. (2020a, b)
Hpakant jade mine disaster, Hpakant, Myanmar	July 2, 2020	175	Lin et al. (2021)
Pettimudi landslide (10.163°N, 77.013°E)	August 7, 2020	66	Achu et al. (2020)
Atami debris flow, Shizuoka, Japan	July 3, 2021	27	Zhang et al. (2022)
Manipur landslide, Noney District, Manipur, India	June 30, 2022	58	Baruah et al. (2023)

vegetation, and disrupt ecosystems. The sediment and debris carried by landslides can also affect rivers and streams, leading to water pollution and affecting aquatic habitats. The disturbance they cause to communities can lead to the displacement of residents, loss of livelihoods, and social and economic instability. Infrastructure damage can hamper transportation, communication, and access to essential services, affecting the overall well-being of the impacted areas.

2 Causes of Landslides

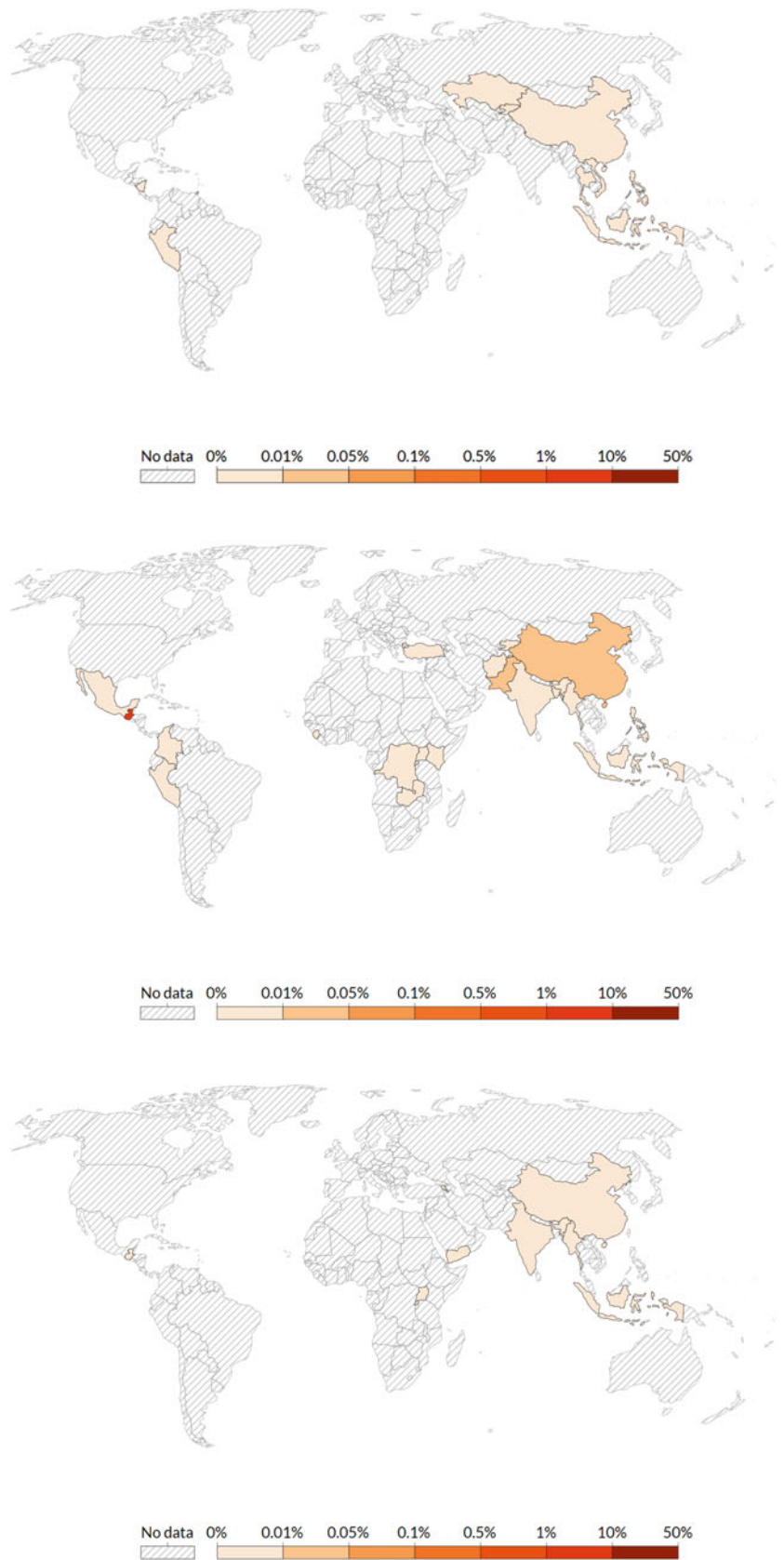
Landslides can be attributed to two main categories of causes: natural factors and those influenced by human activities. In certain instances, landslides may arise from a combination of both factors, either exacerbating their occurrence or contributing to their initiation.

Landslides are often initiated by the saturation of slopes due to the infiltration of water. This saturation process can be triggered by various elements, such as heavy rainfall, snowmelt, fluctuations in groundwater levels, and changes in

surface water near coastal areas, earth dams, lakes, reservoirs, canals, and rivers. The connection between landslides and floods is tightly intertwined as both are influenced by precipitation, runoff, and the saturation of soil by water. Floods can contribute to landslides by eroding stream and river banks and saturating slopes through overland flow. On the other hand, landslides can lead to flooding when displaced rocks and debris obstruct water pathways, causing water to accumulate. Moreover, the debris from landslides can impede natural water channels, diverting the flow and resulting in localized erosion and flood-like conditions. Landslides can also have additional consequences, including the potential to generate tsunamis, cause reservoirs to overflow, and reduce the capacity of these reservoirs to store water. Steep slopes affected by wildfires are particularly susceptible to landslides due to a combination of factors, including the loss of vegetation due to burning, changes in soil chemistry, and subsequent saturation of slopes from various water sources.

The occurrence of earthquakes significantly increases the likelihood of landslides due to multiple factors. The seismic shaking itself can directly trigger landslides, while

Fig. 2 Economic damages as a percent of the gross domestic product (GDP) in (top) 2004, (middle) 2010, and (bottom) 2016 (Source: Ritchie et al. 2022)



susceptible sediment layers may undergo liquefaction, and soil materials can experience dilation caused by the shaking, facilitating rapid water infiltration. Another significant hazard is the formation of landslide dams in streams and rivers downstream of steep slopes. These dams occur when the earthquake dislodges rocks and soil, obstructing the natural flow of water and causing it to accumulate behind the dam, leading to upstream flooding. However, due to their inherent instability, these landslide dams can undergo rapid or gradual erosion, eventually failing catastrophically and releasing the stored water suddenly with severe downstream damages and impacts.

Volcanic activity can trigger devastating landslides, such as volcanic debris flows (lahars), where melted snow mixes with rock, soil, ash, and water, rapidly descending steep volcano slopes and causing widespread destruction. These events can also lead to the collapse of volcanic structures, resulting in rockslides, landslides, and debris avalanches, with the potential to generate submarine landslides and tsunamis.

Human expansion onto new land and the development of residential areas, towns, and cities is another primary contributor to the occurrence of landslides. Activities such as altering drainage patterns, destabilizing slopes, and removing vegetation are common human-induced factors that can initiate landslides. Over-steepening slopes through excavation and excessive loading can also lead to slope instability.

Additionally, human activities like irrigation, landscaping, reservoir management, leaking pipes, and improper excavation or grading on slopes can trigger landslides, even in previously stable areas.

3 Planning and Design of Landslide Stabilization Works

To understand the mechanics involved in the landslide process and design appropriate prevention (or control) measures, slope stability analysis is performed. The methods of slope stability analysis could be simple equations that can be solved in available spreadsheets to complex equations that require robust numerical analysis platforms. Regardless of the method used, common parameters needed for the analyses include slope geometry/topography, potential depth of the sliding surface, location of the groundwater table, soil density, external forces causing destabilization, and shear strength properties of soil.

Shown in Fig. 3 is a photograph of the Portuguese Bend Landslide, among the largest active landslides in the USA. This landslide is located near Los Angeles in California. We use very simple to complicated equations to plan and/or design stabilizing measures for such landslides. To initiate any slope stability analysis, we need to first obtain the cross-sectional details of the landslides that include the ground



Fig. 3 Picture of Portuguese Bend Landslide, among the largest active landslides in USA

surface, groundwater table, and sliding surface profiles of the landslide. The ground surface profile is obtained from the topographical map/survey. Groundwater surface profiles can be obtained from groundwater surveys through boreholes. The sliding surface profile is obtained from borehole profile information.

Shown in Eq. 1 is a simplest formula to calculate stability of the slope, using the cross-sectional details explained in Fig. 4. The entire slope is divided into a number of vertical slices and stability calculations are performed for each slice and later summed up. In Eq. 1, F is factor of safety of slope, L_n is the length of the sliding surface, W_n is weight of the slice, α is angle of inclination of the sliding plane, F_h is horizontal components of all external forces, u_n is pore water pressure at the sliding surface, and c and ϕ are the shear strength parameters (cohesion intercept and internal friction angle, respectively), which will be described in more detail in the subsequent sections.

$$F = \frac{\sum_{n=1}^{n=p} (c' \Delta L_n + ((W_n \cos \alpha_n - F_h \sin \alpha - u_n \Delta L_n) \tan \phi'))}{\sum_{n=1}^{n=p} W_n \sin \alpha_n + F_h \cos \alpha} \quad (1)$$

4 Brief Overview of Shear Strengths

The shear strength of soils plays a critical role in slope stability analyses. It is vital to evaluate the potential for slope failures and to determine the appropriate measures to mitigate risks. The internal resistance of a soil to a shearing force is known as the shear strength of soil. This resistance is jointly developed because of the friction between soil particles and the work that is required to cause changes in volume of the soil. Both the friction between individual grains of the soil mass, or the grain-grain friction, and the interlocking of the grains will contribute to the first component of the resistance. On the other hand, electromagnetic attraction between the soil particles and the effects of over-consolidation will result in the development of the second component of the resistance. As expected, factors that affect either or both of the components of the resistance will result in changes to the shear strength of soil. Some notable factors that will strongly influence the shear strength include the density (or void ratio), the overburden pressure (or confining stress), grain shape and roughness and stress history.

To clearly illustrate the shearing behavior of soil and its strength, it is important to understand the soil formation process. Soils are formed through the weathering of rocks. As such mineralogical composition of the soil will depend on the parent rocks. Let's take an example of a soil layer formed through sedimentation of soil particles that were transported

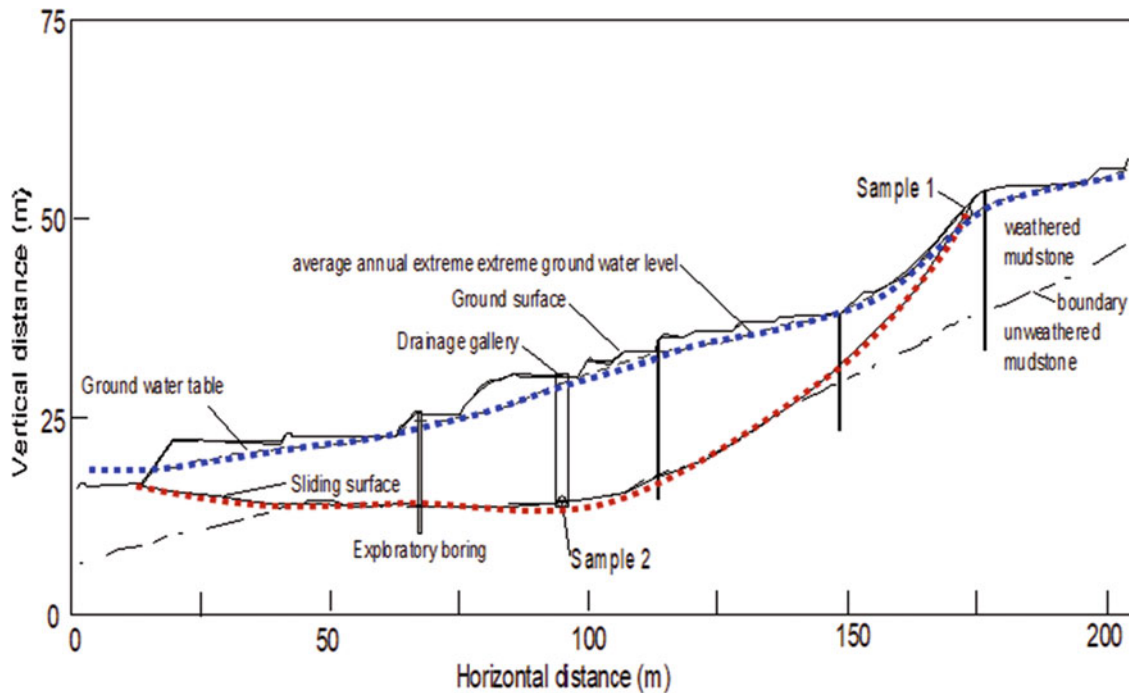


Fig. 4 A typical cross-section of a landslide area in Japan

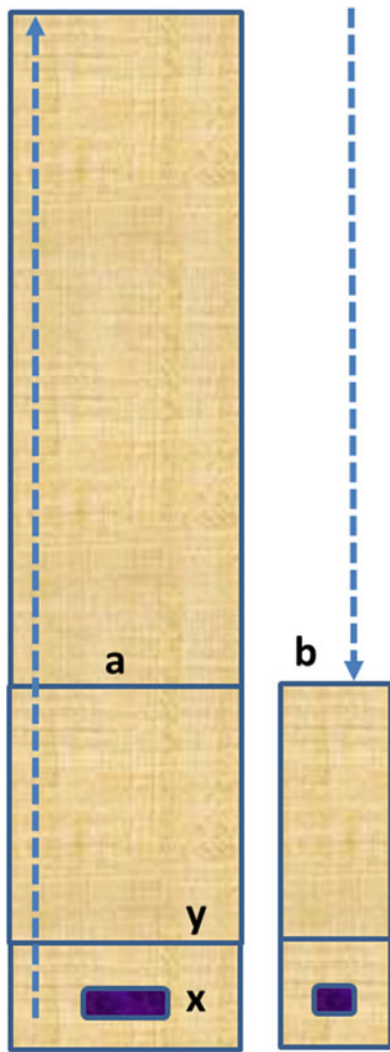


Fig. 5 (Left) Soil sedimentation process; (right) loss of soil due to various natural causes

down by the water bodies. As these particles sediment and accumulate, they create soil layers at the bank of the water body, as presented in Fig. 5. Upward arrow in left image in Fig. 5 shows that the soil is continuously filled up as the sedimentation process continues. However, the top layer of the soil is also lost during erosion and landslide processes, as shown by the downward arrow in right image in Fig. 5.

The mechanism how soil density changes with an increase in soil depth and the effect on its shear strength is presented in Fig. 6. Effective normal stress is the overburden pressure acting on the soil element at any location, which is sum of the unit weight of soil mass multiplied by the corresponding depth of each layer minus any pore water pressure acting the soil element (unit weight of water multiplied by the depth of water above the soil element). Void ratio is calculated as the volume of void space in the soil mass divided by the total volume of only the solid soil components. With an increase in

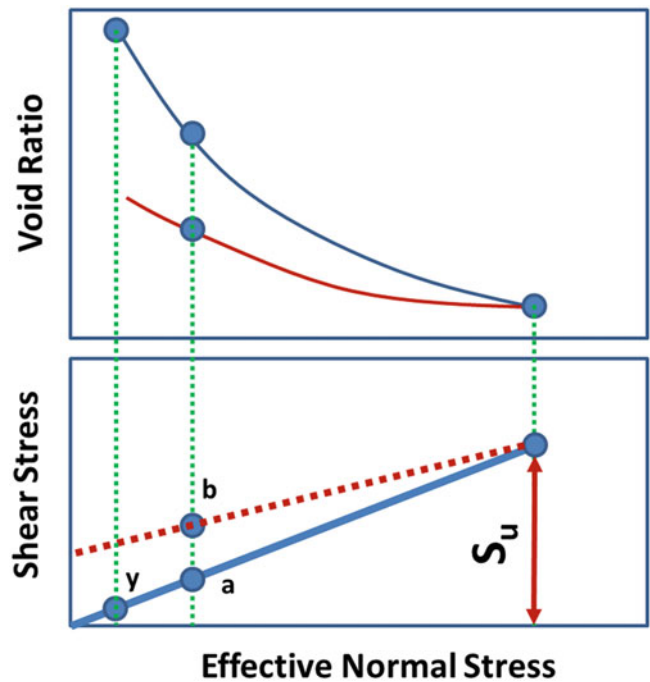
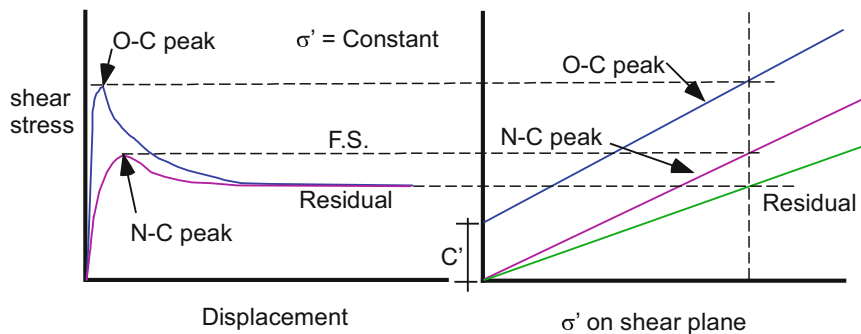


Fig. 6 Void ratio and shear strength variation in soils with effective normal stress

the height of sedimentation, effective normal stress increases and that will cause a reduction in the volume of void space by squeezing the air or water filling the pore spaces out. As such, the void ratio of soil element decreases with an increase in soil sedimentation depth or the effective normal stress, as presented in Fig. 6. Let's consider soil element *x* in Fig. 5. With an increase in effective normal stress on *x* as the sedimentation depths increase to the level *y*, level *a* and the top surface, the void ratio decreases logarithmically. Shear strength of the soil also increases linearly with the increase in the effective normal stress, as presented in Fig. 6. When a certain depth of the same soil mass is lost due to various natural phenomenon such as erosion or landslides, the effective normal stress decreases and the corresponding void ratio of the soil increases. However, the void ratio of soil element at *x* does not rebound back to the original void ratio observed during the sedimentation process. Slope of the rebound (or swelling) curve is around one fourth to one sixth of the slope of the original (or virgin) curve. As such, soil already at *x*, overburdened with the depth up to point *b* (after the loss of soil depth) in Fig. 5 has higher density and shear strength than it was under the condition presented at point *a* although the total overburden depth is the same. Soil element at depth *x* under the overburden pressure due to soil depth presented at point *a* and *b* are called normally consolidated and over-consolidated soils, respectively. In other words, normally consolidated soils (soil at point *x* during sedimentation process shown on the left side in Fig. 5) does not experience

Fig. 7 Shear stress—shear displacement (left) and shear stress—normal stress (right) relationship for over-consolidated and normally consolidated soils



effective normal stress more than the current effective normal stress, while the over-consolidated soils (soil at point x shown on the right side in Fig. 5) has experienced higher effective normal stresses in the past compared to the current effective normal stress. For the same effective normal stress, over-consolidated soils exhibit higher shear strengths than the normally consolidated soils, as shown in Fig. 6. Shear strength of the soil is generally denoted as S_u in geotechnical engineering practice and it has a significant role in stability of the slopes.

When we take a soil sample from location x on the right side of Fig. 5, confine it in a container, apply a certain amount of vertical stress and then apply horizontal stress incrementally to increase the horizontal displacement along a shearing plane, horizontal stress required to obtain certain displacement increases consistently up to a peak value. At that point, the soil starts rupturing and it will require less horizontal stress to deform the soil further. The required horizontal stress become constant at certain amount of soil displacement. This shear stress is called residual shear stress. This shear stress—shear displacement relationship is presented in Fig. 7. If we take the soil from location x at left side of Fig. 5 and follow the same experiment, we obtain similar behavior. However, the magnitude of peak shear stress is much less than that observed for the soil from the right side, although the residual shear stress remains the same. That is mainly due to the over-consolidation effect explained earlier and illustrated in Fig. 6. If we completely remold the soil sample from location x at the right side of Fig. 5 and repeat the experiment, the shear stress—shear displacement curve will follow the trend observed for the soil at location x collected from right side of Fig. 5. If we repeat the experiments by increasing the amount of effective normal stress (σ'), shear stress required for the over-consolidated peak, normally consolidated peak, and residual shear stress conditions also increase corresponding to the increase in normal stress, as presented in Fig. 7.

Materials were found to rupture because of a combination of applied normal and shear stresses (Mohr 1900). Mohr's work resulted in a relationship that expressed the shear stress at failure (or shear strength) as a function of the applied

normal stress and resulted in a curved failure envelope. Coulomb (1776) noted that it was sufficient to estimate the shear stress on a failure plane (τ) to be linearly related to the normal stress (σ). This resulted in the Mohr-Coulomb failure criteria, as defined by Eq. 2 and represented by the straight lines on the right side of Fig. 7. In Eq. 2, c represents the cohesion intercept and ϕ is the internal friction angle. The soil mass will not fail if the combination of the normal and shear stresses falls below the Mohr-Coulomb failure envelope. However, the soil mass fails if this combination plots above the envelope.

$$\tau = c + \sigma \tan \phi \quad (2)$$

The Mohr-Coulomb failure criteria is applicable for both drained and undrained loading conditions. Under drained loading conditions, loads are applied on a soil mass a rate sufficiently slow to ensure that no excess pore pressures are induced. Drained loading conditions result when loads in the field are applied very slowly or when the loads applied are present on the soil mass for a sufficiently long duration to ensure that all excess pore pressures that were generated have been allowed to dissipate. On the other hand, when loads are applied rapidly such that the generated excess pore pressures cannot dissipate, undrained loading conditions will prevail. While Eq. 2 is applicable for undrained (or also called total) conditions, the Mohr-Coulomb failure criteria is expressed in terms of Eq. 3 for the drained (or also called effective) conditions. In Eq. 3, σ' is the effective normal stress acting on the soil mass, which can be computed as the difference between the total normal stress and pore pressure (u). The shear strength parameters are the effective stress cohesion (c') (Fig. 7) and the effective (drained) angle of internal friction (ϕ).

$$\tau = c' + \sigma' \tan \phi' = c' + (\sigma - u) \tan \phi' \quad (3)$$

Soils will exhibit different behaviors during various stages of the shearing process, which will affect their shear

strengths. It will be necessary to select the appropriate shear strength when performing stability analyses or designing mitigation strategies. At beginning of the shearing process, the soil mass will exhibit nearly elastic behavior. After this initial stage, the soil will reach its peak shear strength (Fig. 7) or the maximum shear resistance that can be developed because of interparticle friction and interlocking. With continued shearing, the relationship between the shear stress and shear displacement will show a point of inflection corresponding to a post-peak strength loss (Fig. 7). This was stated to correspond to the fully softened shear strength by Duncan et al. (2011) and indicates that the soil is at its critical state. Peak shear strength of soils is the maximum shear strength at its natural state. In general, if the (fine-grained) soil in the field is in a over-consolidated state, it will exhibit both a cohesion intercept and internal friction angle when it is sheared in the drained condition under varying effective normal stresses and failure envelope is generated. The cohesion component is mainly due to over-consolidation and diagenesis during the formation process. Normally consolidated soils do not exhibit a cohesion intercept.

The fully softened shear strength was first identified by Skempton (1970) when changes in the water content were observed to cause a softening of the soil mass. Skempton (1970) further noted that this softening results in a reduction of the shear strength of the soil mass to a strength corresponding to when the soil is in its critical state. In this condition, additional shear displacements do not occur in the soil mass as the water content continues to fluctuate. Furthermore, Skempton (1970) found that the peak shear strength parameters of a normally consolidated clay are numerically equal to the fully softened shear strength parameters. Peak shear strength of the soil at location x in left side of Fig. 5, presented as the lower peak in Fig. 7, is the fully softened shear strength of soil at location x , which is irrespective of the over-consolidation state.

Continued shearing of the soil mass for large amounts of displacement will cause a reorientation of the particles. In particular, these particles will become aligned with the direction of shearing. When the long axis of clay particles becomes aligned with the shearing direction, it results in the formation of polished slickenslide surfaces. Under these conditions, the shear strength will result in a constant minimum value or the residual shear strength (Fig. 7).

Until now, an implicit focus on the paper has been on the static shear strengths. However, the application of cyclic loads, such as those induced by earthquakes, blasting, wave action, machine vibrations, etc., affects the shearing resistance of the soil mass. In particular, the resistance of the soil mass during the application of the cyclic loads and the available resistance after cyclic loads will both be necessary to

evaluate the stability of slopes under seismic loading as well as post-earthquake slope stability analyses.

Cyclic resistance, or the ability of a soil mass to withstand cyclic loading, is typically represented with the use of cyclic strength curves. Cyclic strength curves are obtained by plotting the number of cycles required to reach a particular failure criterion against a measure of the severity of the cyclic loading. Failure criteria are typically associated with a level of strain induced in the soil mass, but can also correspond to specific conditions like liquefaction or a particular pore pressure ratio. The severity of the cyclic loading is typically expressed in terms of a cyclic stress ratio (CSR), which is equal to ratio of the amplitude of the cyclic shear stress to the overburden pressure. Like with the Mohr-Coulomb failure envelope, the soil mass will not fail if the combination of the number of cycles of the cyclic load and the applied cyclic stress ratio plot below the cyclic strength curve. However, it will fail if this combination plots above the cyclic strength curve.

The application of cyclic loads will typically occur under undrained conditions. That is, the loads induced by the earthquake, for example, are so rapidly applied that excess pore pressures generated will not have sufficient time to dissipate. Furthermore, the undrained shear strength typically available in the soil mass after cyclic loading (or the post-cyclic undrained shear strength) will not be equal to the undrained shear strength before the application of the cyclic loads. Thus, knowledge of the post-cyclic undrained shear strength of the soil mass will also be necessary in the evaluation of the stability of slopes.

Ajmera and Tiwari (2021) summarized the soil properties required to perform slope stability analyses. In particular, they noted the different properties needed for stability calculations associated with the end of the construction, during multistage loading and over the long term. Furthermore, these properties were discussed for both free-draining and impermeable materials. For free-draining layers, regardless of whether the analyses are performed for the end of construction, multistage loading or long-term conditions, the same information is needed. Specifically, for these materials, the total unit weights should be used, external water pressures and internal pore pressures from steady state seepage analyses should be included and effective shear strength parameters should be used.

For the impermeable layers, the properties will vary depending on the condition being analyzed. In particular,

- End of construction: The total unit weight should be used. External water pressures will be included, but the internal pore pressures should not be. The total shear strength parameters should be utilized.
- Multistage loading: Like the end of construction, the total unit weights should be used, while external water

pressures are incorporated and internal pore pressures are not. However, the shear strength will be represented by the undrained cohesion.

- Long term: Similar to free-draining layers, the total unit weights will be used. Steady state seepage analyses should be used to determine the external water pressures and internal pore pressures, both of which will be incorporated into the analyses. For this condition, the effective shear strength parameters should be used.

In general, peak shear strength of soil is used to evaluate the stability of an intact slope/ground (although it is rare to get a perfectly intact slope). Fully softened shear strength is used if the slope exhibits cracks/fissures but has not been slid in the past (or first-time potential slides), while residual shear strength is used for reactivated slopes/slides, stiff fissured clays (or slopes having brittle clay materials) that exhibit progressive failure mechanism. Cyclic (or post-cyclic) shear strength parameters are used to evaluate seismic (or post-cyclic) stability of the slopes. The subsequent sections will discuss about how those different shear strength parameters are measured in the laboratory or are estimated if laboratory measurements are not possible or available. Estimating these soil properties with easily measurable soil parameters are advantageous when sufficient soil samples to run the shear tests or shear test devices are not available.

5 Shear Strength Measurements

Several methods and tests are available in order to measure the shear strength of soil. The selection of the measurement method will depend on a number of factors including the type of soil, the shear strength(s) needed in the design or analyses, and the field conditions and expected mode(s) of failure. This paper will provide a short summary of several of these methods and tests.

5.1 Direct Shear Tests

Direct shear tests are commonly used to measure the shear strengths of soils under drained conditions because they are widely available, are easy to run and to interpret, and are relatively quick. However, in a direct shear test, the shear strength is always measured on the horizontal shearing plane. This plane may not be the weakest potentially resulting in an overestimate of the shear strength. Additionally, as the sample is sheared, the displacement causes a reduction in the cross-sectional area. Direct shear tests have been used to measure the peak, fully softened and residual shear strengths of a soil mass although it is not ideal to measure the residual

shear strength of soil with the direct shear device. Figure 8 shows the photographs of typical direct shear devices available in practice.

To conduct direct shear tests, it is necessary to either obtain an undisturbed sample from the field or to use remolded samples. Remolded samples may be natural samples that have been reconstituted or be samples prepared in the laboratory, as Tiwari and Ajmera (2011) did using dry clay minerals. Samples may be saturated, dry or prepared to some desired moisture content. Undisturbed samples may need to be trimmed to the dimensions associated with the specifications and requirements of the direct shear device available for the testing. It will be necessary to record the dimensions and weight of the sample before the testing procedures commence.

Once the sample is placed in the direct shear box, the assembly should be placed in the apparatus. If the sample is saturated, the sample will be submerged in a water bath in the assembly to ensure that it remains saturated during the entire testing process. However, when testing dry or moist samples, the water bath will not be necessary. After the direct shear box has been placed in the apparatus and the displacement and load transducers have been assembled, the test will commence with a consolidation (or vertical compression) phase. During the direct shear test, it will be necessary to measure the horizontal and vertical displacements and the shear force requiring the use of at least two displacement sensors, such as dial gauges or LVDTs, and one load sensor, such as a proving ring or load cell.

In the consolidation phase, a vertical load representing the normal stress is applied to the soil sample. This is achieved by placing weights on a loading arm or a pneumatic system. Figure 8 contains images of two direct shear systems: one applies a normal stress with the placement of weights (top image in Fig. 8) and the other uses a pneumatic system (bottom image in Fig. 8). The normal stress may need to be applied in increments allowing sufficient time between the increments for pore pressures to dissipate to ensure that the sample is capable of sustaining the next normal stress without sample extrusion.

ASTM D3080/D3080M (2011) provides details about the specifications for a direct shear test along with some specifics about conducting a direct shear test. Tiwari and Ajmera (2011) provided a detailed description of the methods they adapted to measure the fully softened shear strength. In particular, they prepared their samples by mixing dry powdered minerals with sufficient distilled water to achieve an initial moisture content equal to the liquid limit of the soil mass. This mixture was allowed to hydrate before it was transformed into a slurry using a batch mixer. The slurry was, then, evenly placed in the direct shear box using a vinyl cake decoration bag with a metal tip. To consolidate the slurry, incremental pressures were applied with real-time



Fig. 8 Pictures of direct shear devices that apply normal stress using (top) weights placed on loading arm and (bottom) pneumatic system

consolidation observations made using an automated data acquisition system integrated with the direct shear device. The shearing stage commenced after the primary consolidation at the desired normal stress was completed and was allowed to continue until the fully softened shear strength (or peak of the normally consolidated samples) was reached. It is recommended that at least four tests be conducted at different normal stresses to determine the friction angle and cohesion for the soil mass.

Logarithm of time versus displacement graphs are used to monitor the dissipation of excess pore pressures that were generated due to the application of the normal stress on the soil mass. An example of this graph is shown in Fig. 9, which captures the three stages of deformation. The first stage

corresponds to initial compression. This is usually a result of preloading occurring during the sample preparation process and the placement of the top platen on the sample. Primary consolidation occurs during the second stage. During this stage, the applied loads are gradually transferred from the pore water to the soil skeleton as the pressurized water exits the soil mass. The third stage is secondary compression. Deformation observed in this stage is a result of the plastic readjustment of the soil fabric. Each increment of the consolidation phase of a direct shear test is usually maintained until the primary consolidation is complete.

When the primary consolidation is complete under the target normal stress, a horizontal force will be applied at a constant rate. The rate should be selected to be slow enough to ensure that pore pressures generated during the shearing process dissipate when the failure of the sample occurs. The vertical displacement versus logarithm of time graph from Fig. 9 can be used to compute the shearing rate. In particular, the time to failure (t_f) is computed using Eq. 4, in which t_{50} is the time required for the specimen to achieve 50% consolidation under the maximum normal stress. Equation 5 is then used to compute the shearing rate (R_d) with knowledge of the expected horizontal displacement at failure (d_f). This is in alignment with the recommendations in ASTM D3080/D3080M.

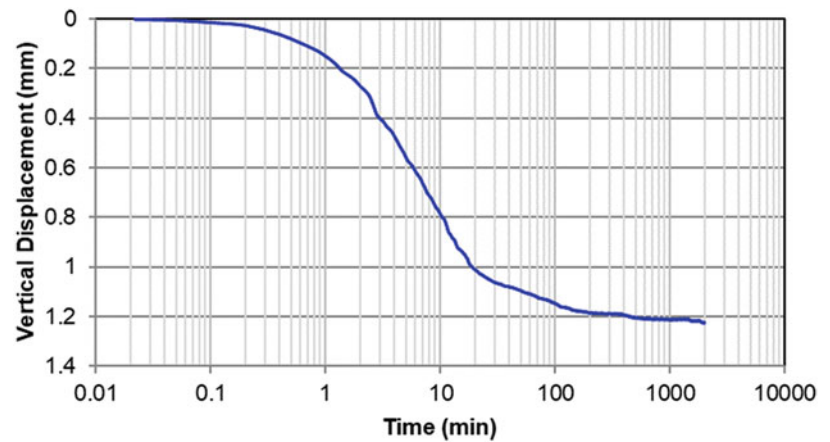
$$t_f = 50t_{50} \quad (4)$$

$$R_d = \frac{d_f}{t_f} \quad (5)$$

During the shearing process, the horizontal displacement, vertical displacement and applied shear force should be measured and recorded. The shearing process continues until the shear strength (peak or fully softened) is obtained or for a maximum deformation of 10% of the height of the sample (ASTM D3080/D3080M). The data collected is used to develop horizontal displacement versus shear stress and horizontal displacement versus vertical stress graphs, like the examples provided in Figs. 10 and 11. The shear stress can be computed by taking the quotient of the applied shear force with the area of the sample.

The differences in the behavior of normally consolidated and over-consolidated clays can be seen Figs. 10 and 11. Specifically, over-consolidated soils will tend to exhibit a clear peak in the shear stress versus horizontal displacement. After the peak strength is achieved, these soils will show a reduction in the shear stress with continued horizontal shearing. Furthermore, over-consolidated soils will tend to exhibit dilative tendencies, in that the volume of the soil mass will increase as the sample is sheared. On the other hand, normally consolidated soils will tend to be contractive in nature

Fig. 9 Example of logarithm of time versus vertical displacement curve obtained during consolidation



illustrated by an increase in the vertical displacement with horizontal displacement (Fig. 11).

The peak or fully softened shear strength can be obtained from Fig. 10. When this shear strength is plotted against the normal stress for each test conducted, it will be possible to obtain the Mohr-Coulomb failure envelope as shown in Fig. 12. The y-intercept of the best-fit line through the data will yield the cohesion intercept. The cohesion intercept of normally consolidated soils should be zero. The inclination of this line from the horizontal will give the friction angle.

The direct shear device has also been used to measure the residual shear strength with the customized test process developed as outlined in Meehan et al. (2011). Some other authors have also presented the residual shear strengths of soils they tested using a multiple reversal direct shear testing. In doing so, they have sheared their samples to the displacement limit on the device and returned back the specimen to the starting position by reversing the loading. The soil specimen is once again sheared to the maximum displacement allowed by the direct shear device at the shearing rate slow enough to maintain the drained loading condition. This process is repeated until the residual shear strength is obtained. However, such multiple reversal direct shear tests are not recommended to obtain the residual shear strengths. It is

recommended to obtain the residual shear strength of soils using the ring shear device. As with the peak and fully softened shear strength measurements, it is recommended that at least four direct shear tests be conducted to determine the parameters associated with the residual shear strength.

5.2 Triaxial Tests

Another commonly available soil testing system is the triaxial device. Triaxial tests represent the field situation better than the direct shear device. However, the test procedures are more complicated and more expensive compared to the direct shear tests. The peak and fully softened shear strengths have both been frequently measured with the use of consolidated drained (CD) and consolidated undrained (CU) triaxial tests. It should be noted that triaxial tests will be difficult to perform on soft samples or on samples at low confining pressures. Furthermore, CD testing of low permeability clays may be lengthy in duration due to the amount of time required to back pressure saturate the sample as well as the required strain rate to ensure dissipation of pore pressures generated during the shearing process. The time required for

Fig. 10 Shear stress versus horizontal displacement graphs for normally and over-consolidated samples

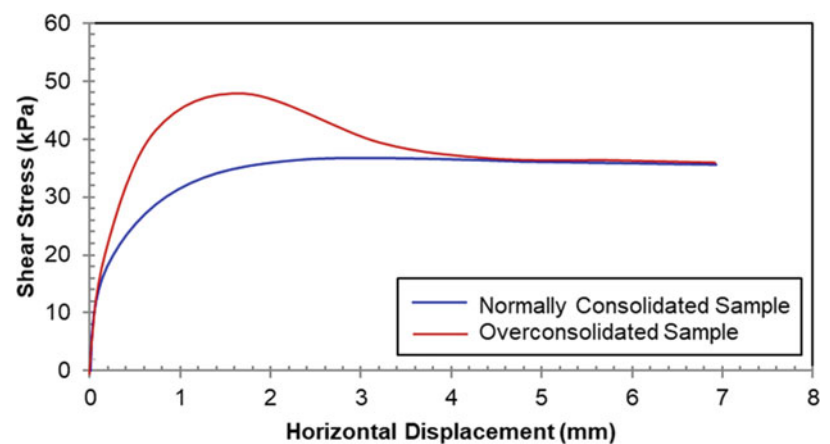
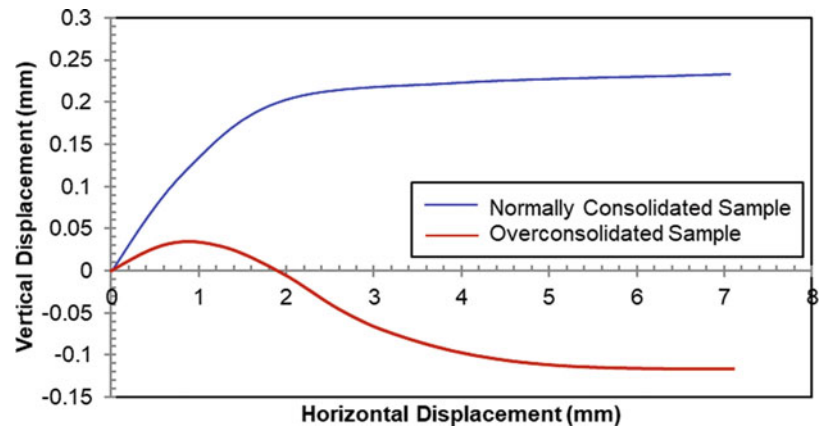


Fig. 11 Vertical displacement versus horizontal displacement graphs for normally and over-consolidated samples



back pressure saturation will also be a concern when conducting CU triaxial tests on such low permeability soils.

ASTM D7181 (2020) contains the specifications for CD triaxial tests. In addition, it also summarizes the procedures followed to conduct these tests. Typically, CD triaxial tests will require cylindrical soil samples with heights that are at least double the diameter. The sample is then sandwiched between two porous stones encompassed in a thin rubber membrane, as presented in Fig. 13. The assembly is placed within a water-filled cylindrical chamber and the pressure of the water in the chamber is increased in order to apply a cell (or confining) pressure on the sample (Fig. 14).

After the sample is mounted, back pressure saturation is used to saturate the sample. In this process, back pressure is applied to the sample as water is forced into the voids within the soil mass resulting in a displacement of the air (or other gasses) present. The water pressure must be carefully controlled to ensure that the sample is not damaged during the saturation process. The saturation is verified with the use of Skempton’s pore pressure coefficient or B-value. This value is a measure of the changes in pore pressure that result due an increase in the cell pressure. If the sample is saturated, the B-value will be close to one. Lower B-values will indicate that the void spaces are filled with both water and air and

thus, the sample is not saturated. Typically, the sample is said to be saturated if the B-value is greater than 0.95, but in some cases, lower B-values may also be accepted.

Once the sample has been saturated, it will be consolidated by increasing the pressure of water in the chamber to the required confining pressure. The completion of the primary consolidation is monitored using real-time data collected and recorded by an attached computer system. At this point, the sample will be sheared at a rate slow enough to ensure drained loading conditions. Termination of the shearing process typically coincides with the measurement of the peak deviator stress or the application of 20% axial strain. The axial strain criterion results from the maximum allowed deformation in the soil sample before the applied deviatoric stresses become eccentric in nature. The process is repeated for at least three, preferably four, samples to allow for the determination of shear strength parameters.

The procedures for conducting CU triaxial tests are nearly identical to those described above for the CD triaxial test. They can be found described within ASTM D4767 (2020). There are some major differences between the CD and CU triaxial tests. The biggest is that the drainage valve is closed during the shearing process in a CU triaxial test. In contrast, during the CD triaxial test, this valve is left open allowing

Fig. 12 Examples of Mohr-Coulomb failure envelopes

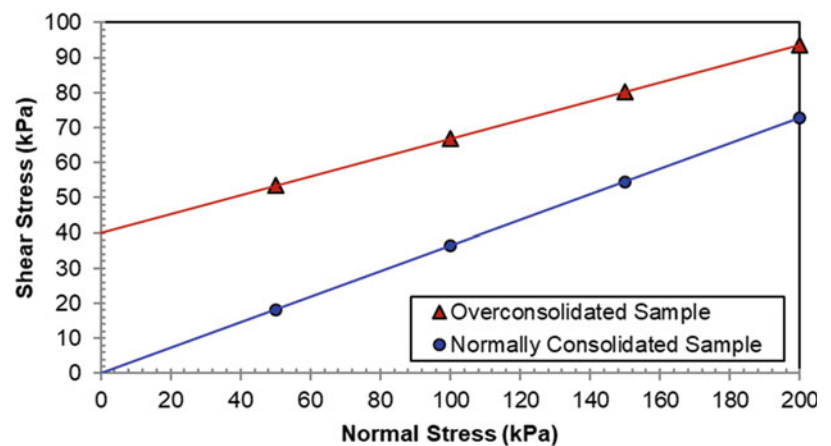
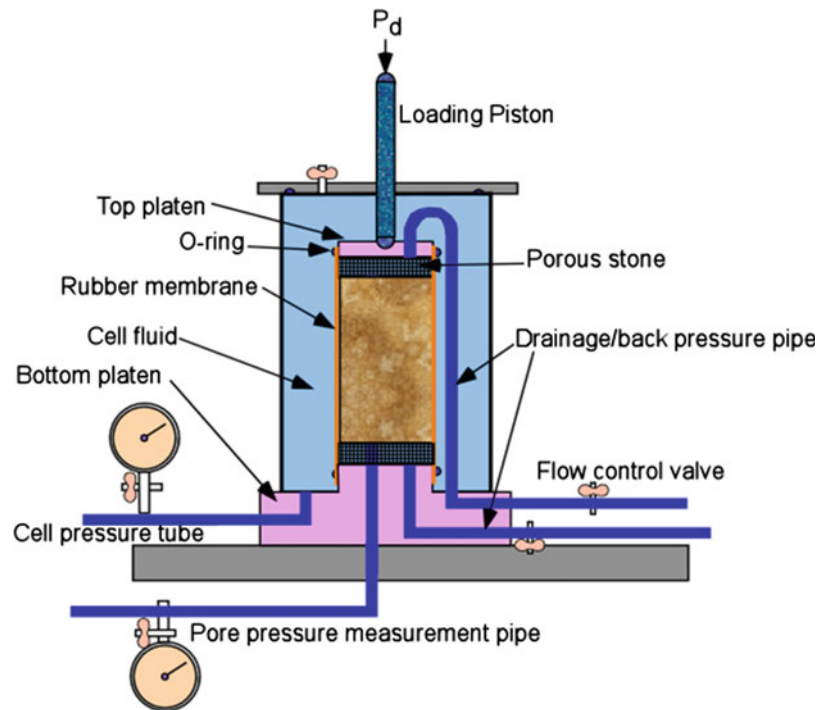




Fig. 13 A triaxial test sample assembly

volume change to occur (or the pressurized pore water to drain out). These changes in the volume are measured by collecting the drained pore water from the sample. However, since the valve is closed in the CU triaxial test, volume change is not possible and pore pressures will be generated with the soil mass, instead. Instead of measuring the volume change, the CU triaxial test will measure the pore pressures generated. Finally, since volume change is not allowed in a CU triaxial test, the test can be conducted at a faster rate than CD triaxial tests, which must allow sufficient time during the shearing process for excess pore pressures to dissipate and the resulting volume change to occur. Thus, CD triaxial tests are typically conducted at shearing rates that are about eight

Fig. 14 Illustration of a triaxial testing mechanism



to ten times slower than the shearing rates used in CU triaxial tests.

Data related to the axial deformation, cell pressure (σ_3') and deviator force are recorded during the shearing process. In the CD triaxial test, the change in the volume of the sample is also recorded, whereas, the pore pressure is recorded in the CU triaxial test. Since volume change is permitted in the CD triaxial test, the cross-sectional area of the sample will not remain constant over the duration of the shearing process. The area (A) can be computed using Eq. 6. In Eq. 6, A_c is the initial cross-sectional area of the sample, ϵ_a is the axial strain and ϵ_v is the volumetric strain. The axial and volumetric strains can be computed using Eqs. 7 and 8 as ratios of the axial deformation (ΔL) to the original length (L) and the change in volume (ΔV) to the original volume (V), respectively.

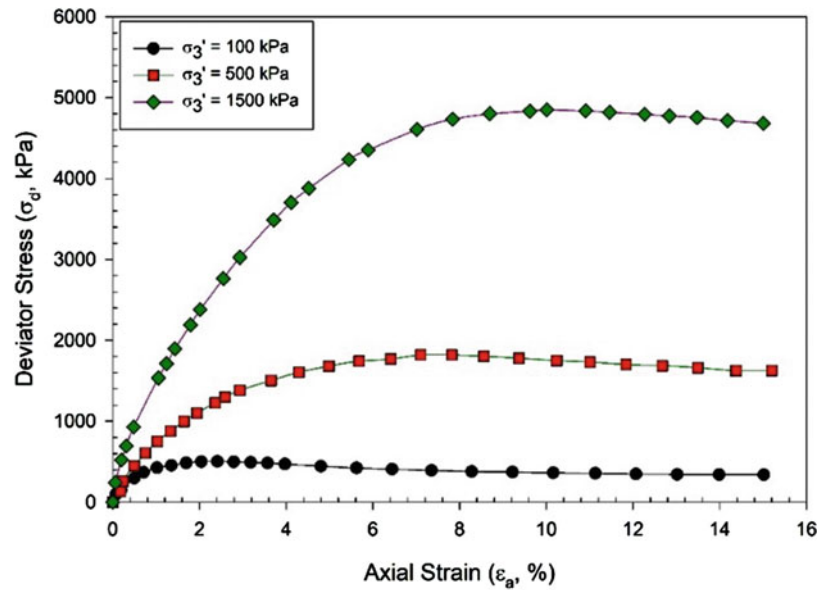
$$A = \frac{A_c(1 - \epsilon_v)}{1 - \epsilon_a} \quad (6)$$

$$\epsilon_a = \frac{\Delta L}{L} \quad (7)$$

$$\epsilon_v = \frac{\Delta V}{V} \quad (8)$$

The area from Eq. 6 and the deviator force (P_d) will make it possible to determine the deviator stress (σ_d) from Eq. 9. An example of the variation of this deviator stress with axial strain is shown in Fig. 15. Figure 16 contains an example of

Fig. 15 Example of deviator stress versus axial strain graphs obtained from CD triaxial tests



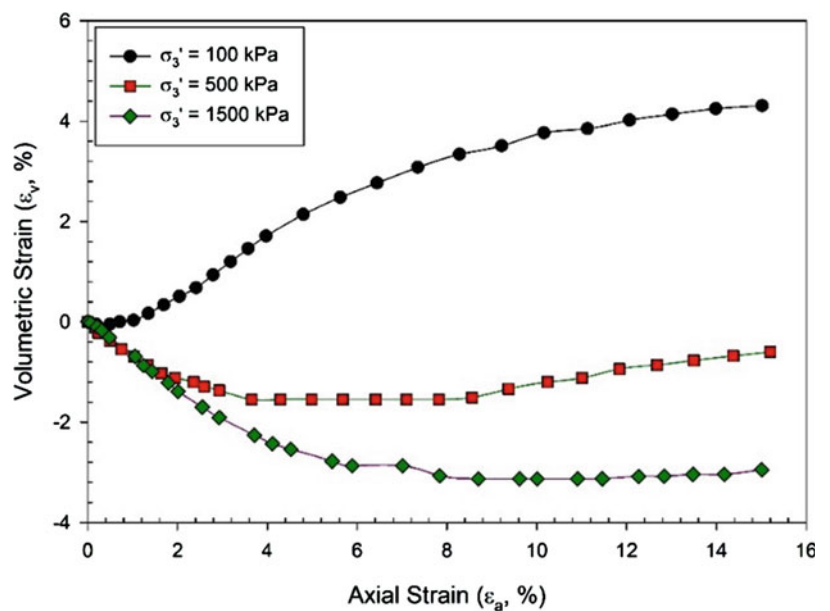
the corresponding volumetric strains with axial strains. The trends in Figs. 15 and 16 will be similar to the shear stress versus horizontal displacement and vertical displacement versus horizontal displacement graphs obtained from a direct shear test. Specifically, normally consolidated samples will tend to exhibit plateau in the deviator stress and compressive volume change behavior. This is similar to that shown for the sample tested under a confining pressure of 1500 kPa in Figs. 15 and 16. On the other hand, over-consolidated samples will have a clear peak followed by strain softening behavior (that is, a reduction in the deviator stress with an increase in the axial strain). The volume change behavior will be dilative indicating an increase in the volume of the sample. When the sample in Figs. 15 and 16 was tested under a

confining pressure of 1000 kPa, it exhibited behavior typical of over-consolidated soils.

$$\sigma_d = \frac{P_d}{A} \tag{9}$$

The deviator stress at failure can be used to compute the effective axial stress at failure (σ₁') as shown in Eq. 10. The axial stress at failure and the corresponding confining pressure represent the normal stresses on the vertical and horizontal planes of the soil element tested allowing for the construction of a Mohr's circle. Such Mohr's circles will then be constructed for each CD triaxial test conducted. An

Fig. 16 Example of volumetric strain versus axial strain graphs obtained from cd triaxial tests



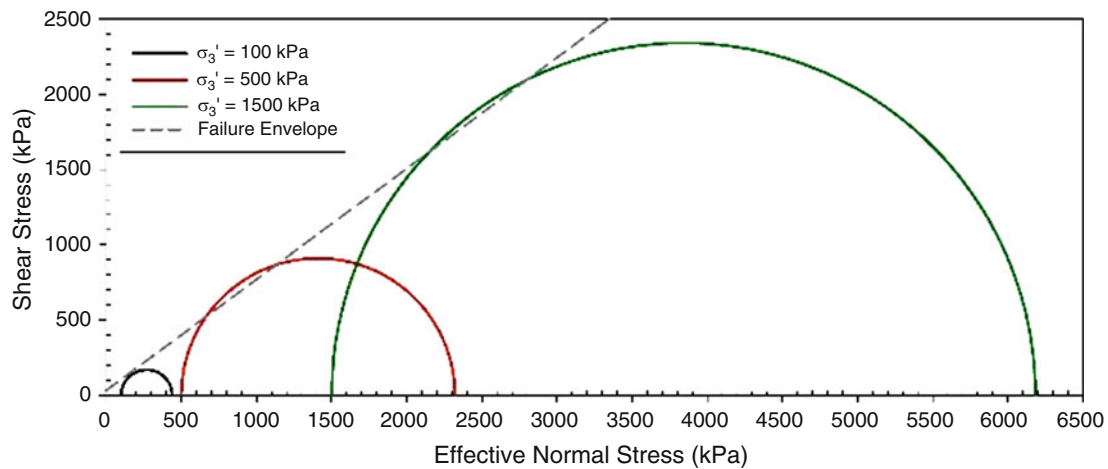


Fig. 17 Example of deviator stress versus axial strain graphs obtained from CD triaxial tests

example is shown in Fig. 17. The best-fit line tangent to these Mohr's circles will be the Mohr-Coulomb failure envelope, whose intercept will be equal to the effective cohesion and the slope can be used to compute the effective friction angle.

$$\sigma_1' = \sigma_3' + \sigma_d \quad (10)$$

The procedures for reducing the data from the CU triaxial test is similar to that described above for the CU triaxial test. However, since volume change is not permitted during the shearing process, the pore pressure generated in the sample is recorded in lieu of the volume change. Thus, the CU triaxial test will allow for the determination of both the total and effective shear strength parameters. The cross-sectional area of the sample at any point in the shearing process can be computed using Eqs. 6 and 7. It should be noted that since volume change is not permitted, the volumetric strain will be equal to zero. Equation 9 can then be used to determine the deviator stress.

Figure 18 presents an example of the deviator stress (Fig. 18 top) and pore pressure (Fig. 18 bottom) versus axial strain graphs obtained from a series of CU triaxial tests. In an over-consolidated soil, the curve for the deviator stress versus axial strain would be expected to display a peak similar to those trends shown in Figs. 10 and 15 for the direct shear and CD triaxial tests, respectively. Furthermore, negative pore pressures could be expected to develop in the sample as it tended to exhibit dilatative tendencies.

The total confining pressure (σ_3) will be equal to the cell pressure applied on the sample at the end of the consolidation phase (or at the instant that the shearing process commenced). The effective confining pressure (σ_3') can be computed as the difference between the total confining pressure and pore pressure (u) recorded, as shown in Eq. 11. Equations 10

and 12 are then used to compute the effective and total axial stresses, respectively.

$$\sigma_3' = \sigma_3 - u \quad (11)$$

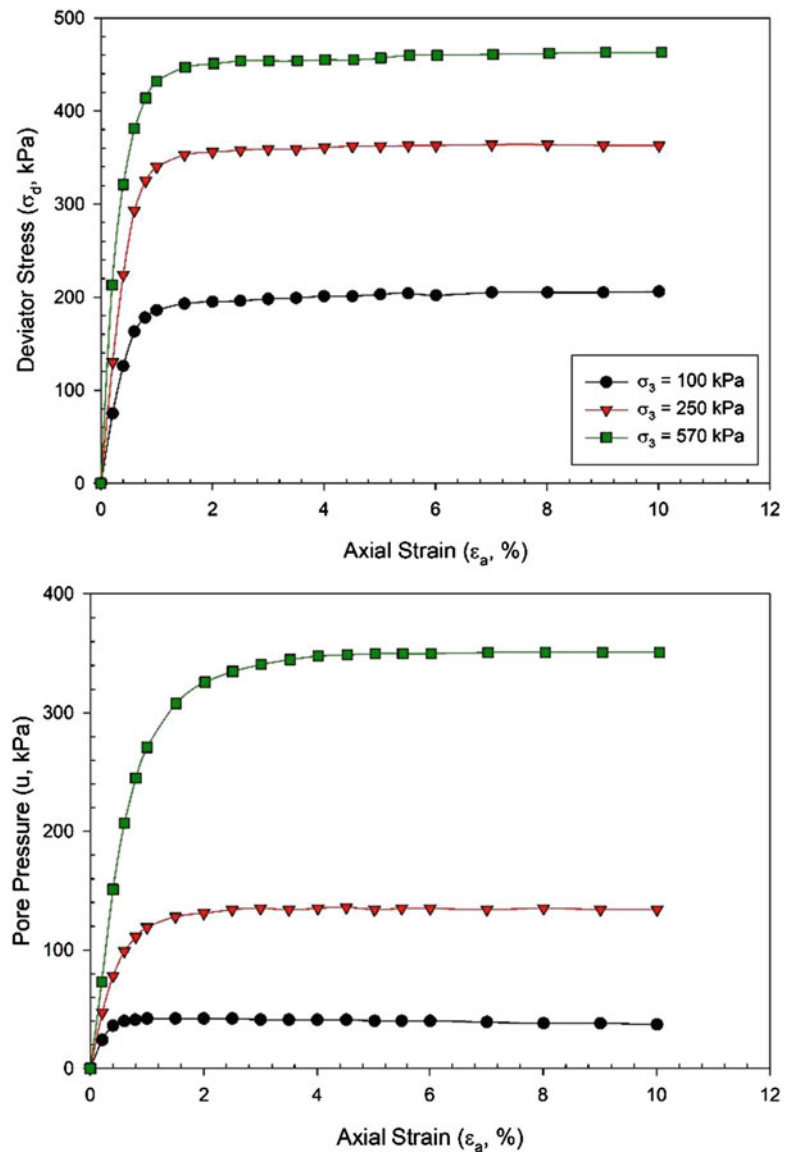
$$\sigma_1 = \sigma_3 + \sigma_d \quad (12)$$

The total and effective confining and axial stresses at failure will provide the information necessary to draw the respective Mohr's circles at failure. This is illustrated with the example in Fig. 19. As with the CD triaxial test, a best-fit line drawn tangent to the effective stress Mohr's circles will facilitate the measurement of the effective cohesion intercept and the effective friction angle. Similarly, the best-fit line tangent to the total stress Mohr's circle will indicate the corresponding undrained shear strength parameters.

Meehan et al. (2011) used triaxial tests to measure the residual shear strength of samples using polished slickenside surfaces. To do so, they constructed a special mold to be used during the sample preparation that would prevent significant disturbance. This mold allowed the sample to be cut using a wire and polished to form slickenside surfaces. Some figures of the process are provided in Fig. 20. In their study, Meehan et al. (2011) constructed the mold to have a failure plane inclined at 55° from the horizontal based on the expected residual friction angle for the soils they were testing. To create the polished surface, they sheared both parts of the sample for a total displacement of approximately 2 m along a frosted glass. The sample was then reassembled and placed in a triaxial cell in order to measure the residual shear strengths.

The shear strengths measured in a triaxial test can be significantly affected by the end-platen restraints (Meehan et al. 2011; Bishop and Henkel 1962; Barden and McDermott 1965; Chandler 1966; Skempton and Petley 1967).

Fig. 18 Example results from CU triaxial test for (top) deviator stress versus axial strain and (bottom) pore pressure versus axial strain



Specifications to conduct triaxial compression tests using a free top platen on specimens that will fail in a single plane shearing mechanism were provided by Bishop and Henkel (1962) and adapted by Skempton and Petley (1967) and Chandler (1966). A free end approach was presented by Barden and McDermott (1965). In this approach, a greased membrane was used. The membrane allowed the ends of the specimen to expand radially, while permitting the specimen to experience a small amount of lateral movement during the shearing process. Meehan et al. (2011) used a both ends free platen approach in their study. This approach minimized the effect of lateral platen restraint while the sample was sheared along a single plane.

To use the both ends free approach, Meehan et al. (2011) constructed special base and top platens that permitted unrestrained lateral movement of the specimen during the

shearing process. Figures 21 and 22 contain schematics and pictures of the triaxial test device set-up used. As seen from these figures, free lateral movement was permitted by placing ball bearings in a thin vacuum grease. They opted to use 3.2 mm diameter steel ball bearings placing seventy of them in each of the top and bottom platens. Their system resembles that utilized by Bishop and Henkel (1962), who used rollers. The use of ball bearings allows for unrestrained movement in any horizontal direction. In addition, the system used by Meehan et al. (2011) has a free base.

5.3 Direct Simple Shear Tests

Direct simple shear tests have been used to measure the peak and fully softened shear strengths. This device offers several

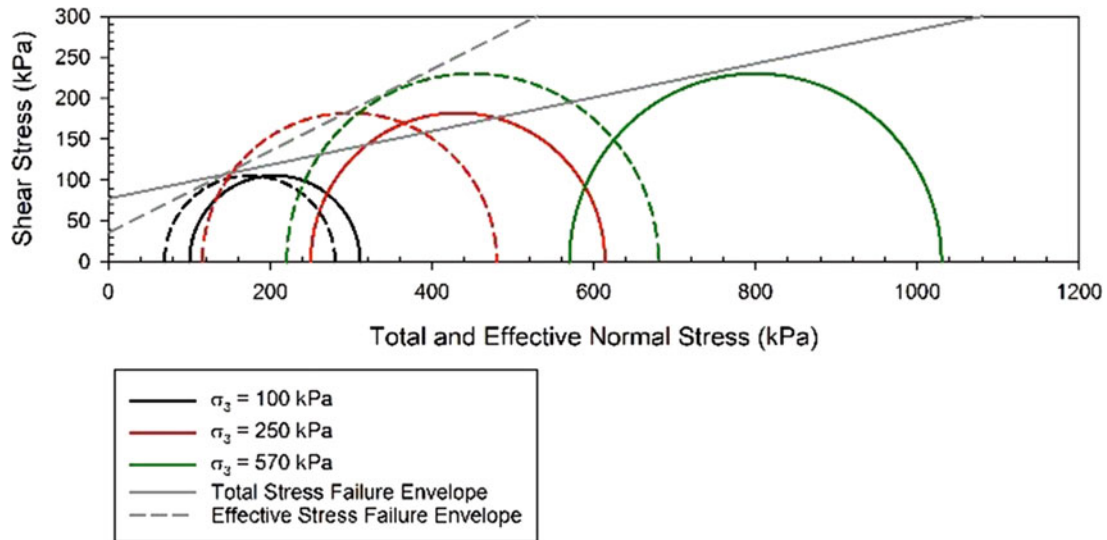


Fig. 19 Example of Mohr's circles and failure envelopes obtained from CU triaxial tests

advantages compared to the direct shear and triaxial tests. Similar to the direct shear apparatus, the test setup is relatively straightforward. However, in direct simple shear tests, the sample is allowed to fail along its weakest plane. Furthermore, the cross-sectional area remains constant throughout the shearing process. This provides results that are more accurate. Additionally, simple shear tests require smaller soil samples than triaxial testing, resulting in shorter consolidation times. It is important to note that commercial availability of this device is currently limited.

The direct simple shear tests are conducted following the guidelines outlined in ASTM D6528 (2017). Tiwari and Ajmera (2014) conducted tests on ten different soil samples using the direct simple shear apparatus. The procedures used in their study closely resemble those described by Tiwari and Ajmera (2011) for direct shear testing of similar soil samples. Fig. 23 shows the simple shear device used by Tiwari and Ajmera (2011) and samples prior and after shearing. In the direct simple shear tests performed by Tiwari and Ajmera (2014), the soil sample is carefully placed within a rubber

Fig. 20 Images of (a) specialized mold, (b) sample cut by a wire, (c) polishing process and (d) slickenside surfaces created (Source: Meehan et al. 2011)

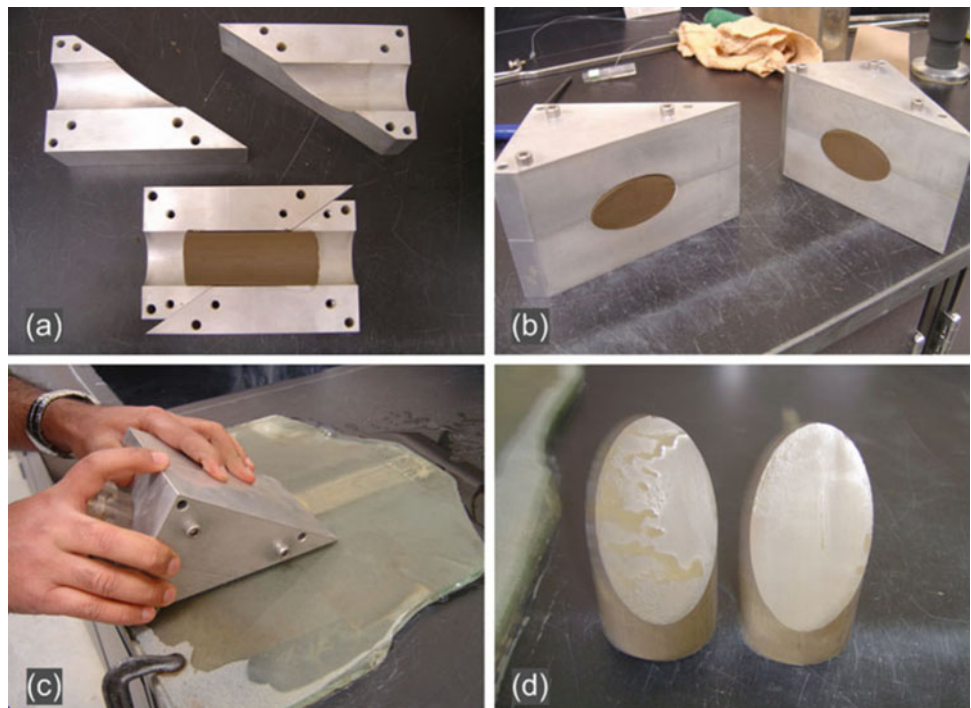


Fig. 21 Both ends free triaxial test set-up schematic from Meehan et al. (2011) (a) before and (b) after shearing

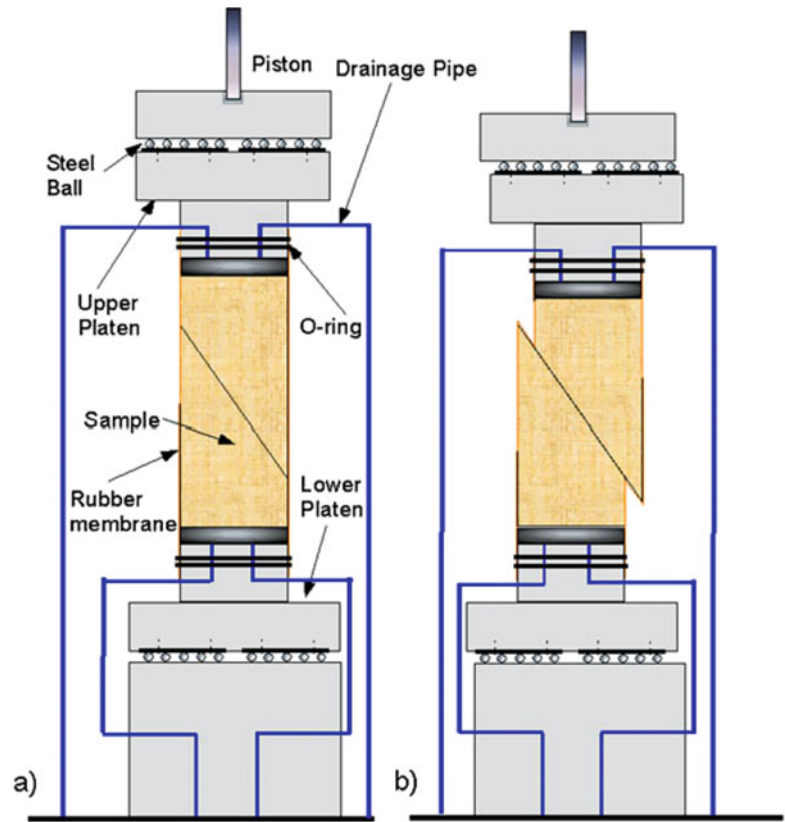
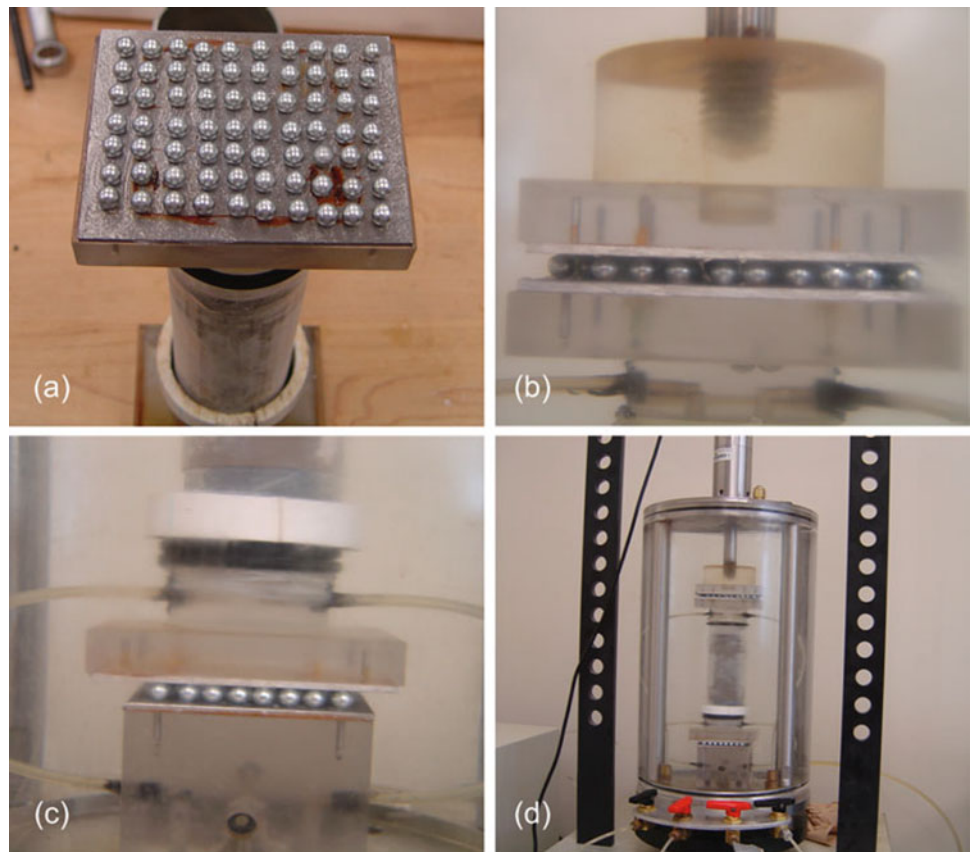


Fig. 22 Pictures of the both ends free triaxial system from Meehan et al. (2011). (a) placement of ball bearings on a platen, (b) connection of top platen with triaxial device, (c) connection of the bottom platen with triaxial device and (d) entire set-up



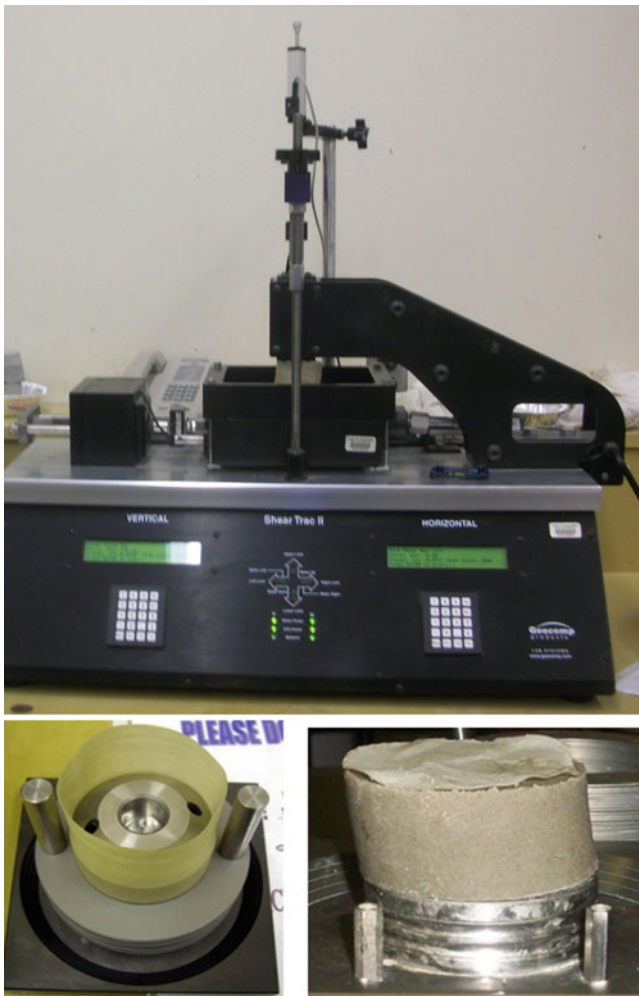


Fig. 23 (top) a typical simple shear device, (bottom left) sample preparation and (bottom right) sample after the shearing process is completed

membrane and positioned inside a stack of Teflon® rings. In other simple shear apparatuses, the sample may be laterally confined by a wire mesh. Subsequently, this assembly is securely placed into the direct simple shear box, where the consolidation process takes place. This consolidation process may be designed to occur incrementally. After the sample is subjected to the desired normal stress and the primary consolidation is complete, shearing of the sample is induced by applying a shear force at a desired strain rate. The shearing phase is conducted under undrained conditions. By maintaining undrained conditions, any changes in the pore water pressure are captured and considered in the analysis. Per ASTM D6528, the shearing process is continued until the peak shear strength is obtained or for a maximum of shear strain of 25%.

During shearing phase of the direct simple shear test, the sensors on the device will record the horizontal displacement (Δx) along with the normal (P) and shear (T) forces. In the data reduction, this information is used to compute the shear

strain (γ), the effective normal stress (σ'), pore pressure (u) and shear stress (τ) on the sample. To do so, Eqs. 13 to 16, respectively, are utilized. In these equations, σ'_c is the consolidation pressure. As noted before, constant volume is maintained during the shearing phase of a direct simple shear test. Thus, the changes in the effective normal stress are found to be equivalent to the pore pressure developed in the sample (Airey and Wood 1987; Bjerrum and Landva 1966, and Dyvik et al. 1987).

$$\gamma = \frac{\Delta x}{H} \quad (13)$$

$$\sigma' = \frac{P}{A} \quad (14)$$

$$u = \sigma'_c - \sigma' \quad (15)$$

$$\tau = \frac{T}{A} \quad (16)$$

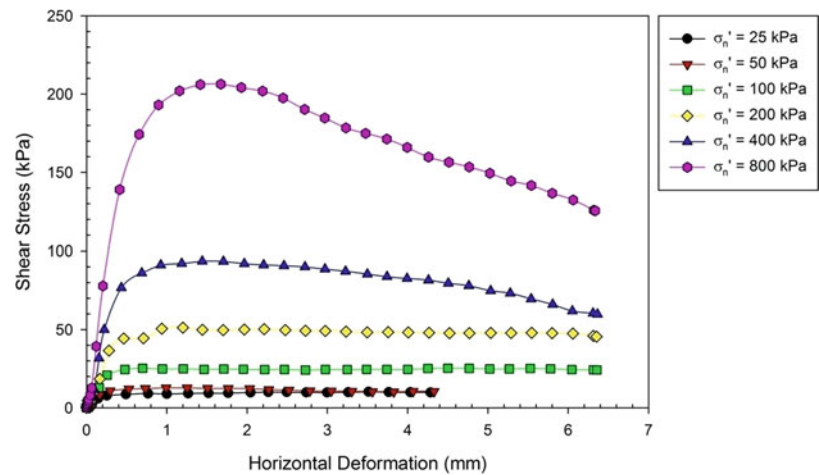
Using the parameters measured from the direct shear test, stress-strain curves and pore pressure versus strain curves should be prepared for each sample tested. Figure 24 contains an example of the shear strain versus shear stress curves obtained from a series of direct simple shear tests, while Fig. 25 contains the corresponding shear strain versus pore pressure curves. These figures correspond to normally consolidated samples and thus, result in the compressive tendencies in the pore pressure that is generated during the shearing process. Figure 26 provide an example of the results obtained from a series of direct simple shear test conducted on samples at different over-consolidation ratios.

The maximum shear stress in Figs. 24 and 26 correspond to the shear strength of the sample. When this shear strength is plotted against the corresponding consolidation pressure, the Mohr-Coulomb envelope associated with total stress is obtained. On the other hand, when the corresponding effective normal is used instead of the consolidation pressure, the Mohr-Coulomb failure envelope obtained allows for the determination of the effective shear strength parameters. An example of the total and effective stress Mohr-Coulomb envelopes is shown in Fig. 27. As before, the y-intercept will indicate the cohesion intercept, while the slope of the line can be used to compute the friction angle for the total and effective stress conditions.

5.4 Ring Shear Tests

The ring shear device has emerged as the preferred technique for quantifying residual shear strength due to its unique ability to continuously shear samples in a single direction

Fig. 24 Example of the shear stress versus shear strain curves obtained from simple shear tests conducted on normally consolidated samples



while maintaining a consistent cross-sectional area (Watry and Lade 2000). In particular, researchers, such as Bishop et al. (1971), have emphasized that only the torsional or ring shear test can genuinely replicate residual conditions within laboratory settings. Similarly, Lupini et al. (1981) asserted that the ring shear device offers the most precise measurement of residual shear strength, minimizing any potential ambiguities. In fact, Hawkins and Privett (1985) concluded that ring shear tests exhibit superior repeatability compared to alternative methods. However, it is worth noting that the non-uniform distribution of stress across the annular samples used in these tests poses a potential challenge.

The development of the ring shear device for assessing residual strength has been extensively documented in various publications, including the works of Bromhead et al. (1999), Hvorselv (1939), and Boucek (1977). The initial development of the ring shear test is credited to Arthur Casagrande and was later reported by Hvorselv (1939) according to Harris and Watson (1997). Bishop et al. (1971) introduced a specific type of ring shear device capable of measuring residual shear strength under large displacements. To expedite drainage, LaGatta (1970) and Bromhead (1979)

incorporated smaller, thinner samples into their designs. While Stark and Eid (1994) proposed additional modifications, it has been argued by Bromhead et al. (1999) that these alterations deviated from the device's intended simplicity and user-friendly nature. Anayi et al. (1989) further suggested modifications to the Bromhead ring shear device advocating for doubled sample thickness and changes to the torque arm shape to accommodate larger samples. Steward and Cripps (1983), Hawkins and Privett (1985), Stark and Eid (1993), and Dewhurst et al. (1996) also proposed their own modifications to the ring shear device.

As a result of the parallel development of different ring shear devices (Fig. 28), each variation presents distinct advantages and disadvantages. For instance, the design presented by Bishop et al. (1971) allows for adjustable gaps between the top and bottom rings, thereby facilitating the testing of wet specimens. Shearing occurs at the mid-height of the sample in this particular device. Conversely, the device predominantly developed by Bromhead (1979) shears the soil samples in close proximity to the upper platen. Notably, this design enables the achievement of the residual condition at smaller strain levels.

Fig. 25 Example of the pore pressure versus shear strain curves obtained from simple shear tests conducted on normally consolidated samples

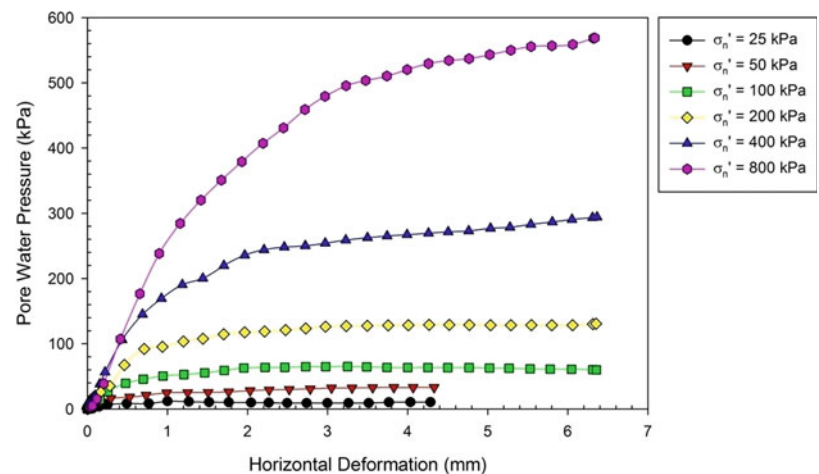
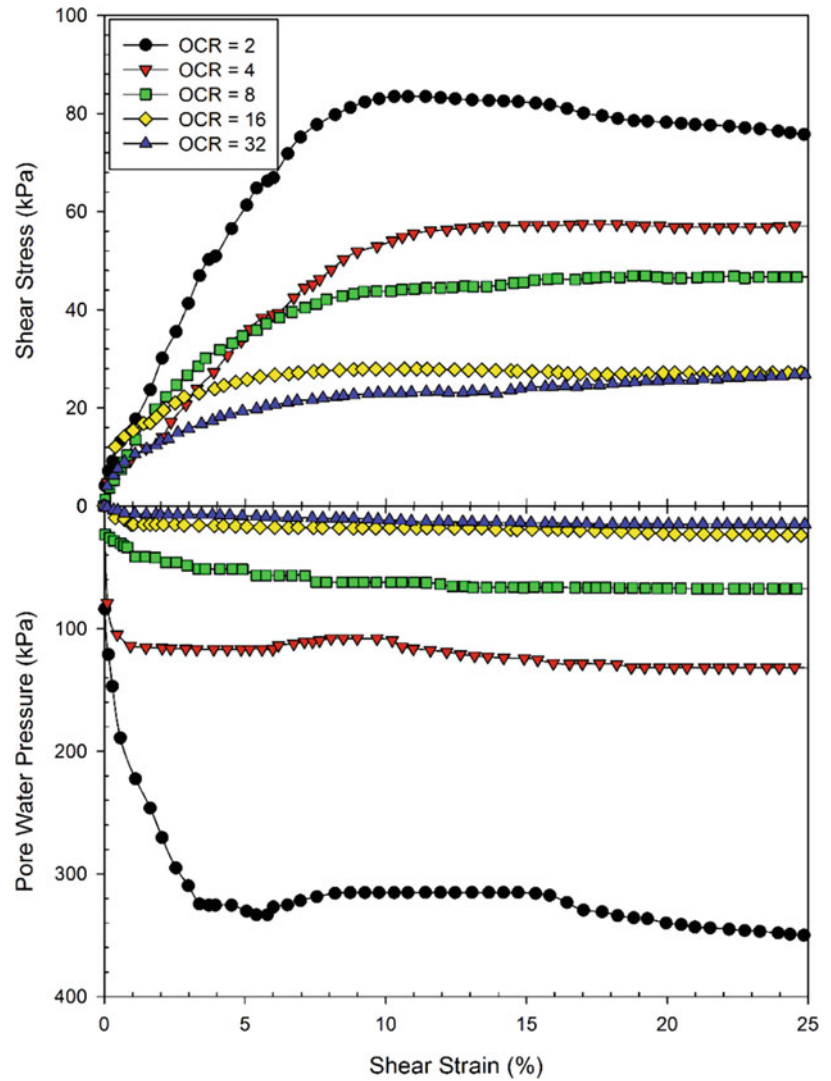


Fig. 26 Example of the shear stress-shear strain and pore pressure versus shear strain curves obtained from simple shear tests conducted on over-consolidated samples with a pre-consolidation pressure of 1200 kPa (Source: Ajmera et al. 2018, with permission from ASCE)



Data collection during the shear phase of the ring shear test consists of measurements of the axial deformation, torque angle (θ) and shear force. The horizontal displacement (Δx) is then computed using Eq. 17, where r_{avg} is the average radius of the sample found using Eq. 18 as the average of the internal (r_i) and external (r_o) radii of the annular sample. Next, the shear stress is computed using Eq. 19 as a function of the shear force, the average radius and the polar moment of inertia (J). The polar moment of inertia of an annular sample

can be computed from Eq. 20. These results are used to develop horizontal displacement versus shear stress and axial deformation versus horizontal deformation curves.

$$\Delta x = \frac{\pi(r_{avg})(\theta)}{180^\circ} \tag{17}$$

Fig. 27 Example total and effective stress Mohr-Coulomb failure envelopes from simple shear tests

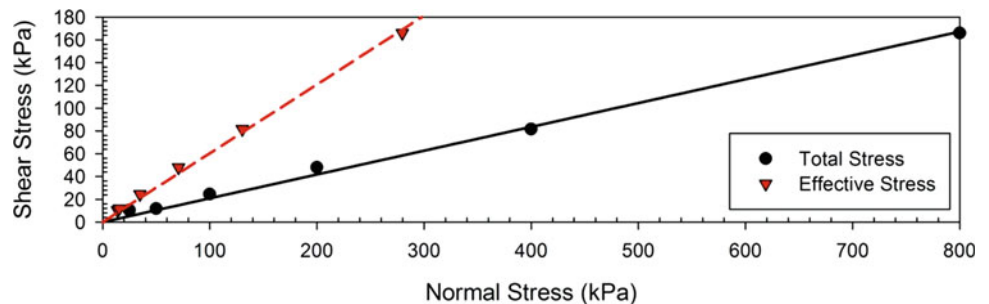




Fig. 28 Different types of ring shear devices available in practice

$$r_{avg} = \frac{r_o + r_i}{2} \quad (18)$$

$$\tau = \frac{Tr_{avg}}{J} \quad (19)$$

$$J = \frac{\pi(r_o^4 - r_i^4)}{2} \quad (20)$$

Figure 29 shows an example of the horizontal displacement versus shear stress obtained from ring shear tests. The residual shear strengths obtained at large displacements from these curves are used to plot a Mohr-Coulomb failure envelope. A typical Mohr-Coulomb envelope from the ring shear test is shown in Fig. 30.

ASTM D6467 (2013) provides detailed procedures for conducting ring shear tests to measure the residual shear strength of cohesive soils. Multiple methods can be employed, involving different normal stresses, to establish the failure envelope and determine the shear strength parameters. In their study, Tiwari and Marui (2004) examined three testing methods for the ring shear device: separate tests for each normal stress as well as a multistage ring shear test with increasing or decreasing loads. Although the residual friction angle remained consistent across the testing methods, variations were observed in the cohesion intercept. Tiwari and Marui (2004) underscored the advantages of employing a multistage ring shear test, including enhanced consistency by employing the same sample for all normal stresses and reduced sample volume requirements in comparison to that required to conduct separate ring shear tests. These benefits corroborated the findings of Bromhead (1992) and Harris and Watson (1997).

Tiwari and Marui (2005) provided detailed procedures for conducting ring shear tests to measure the residual shear strength, which are briefly summarized here. The study utilized a ring shear device based on the Imperial College and Norwegian Geotechnical Institute (NGI) model. This device was originally described by Bishop et al. (1971). Several modifications were made to the device to enhance its functionality including the ability to accommodate larger sample sizes, transparent outer rings for external observation of the soil sample during shearing, a wide range of shearing rates, and a pore-water measurement system at the shearing plane. For their experiments, natural soil samples passing through a 2 mm sieve or soil mixtures were mixed with distilled water to achieve a water content close to the liquid limit (Tiwari and Marui 2005). These samples were then loaded into the ring shear device and compacted. Consolidation was carried out incrementally until more than 95% consolidation was achieved at each step. After determining the residual shear strength at the highest of the desired normal stresses, Tiwari and Marui (2005) employed the reducing

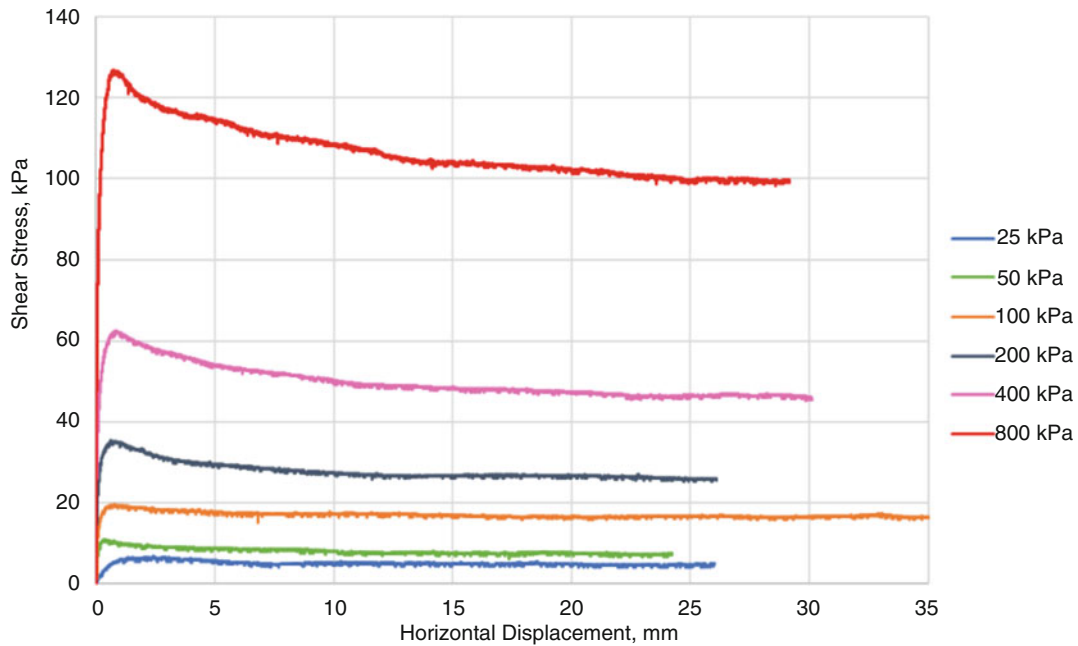


Fig. 29 Shear stress versus horizontal displacement curve examples from ring shear tests (Source: Tiwari et al. 2020a, b, with permission from ASCE)

load multistage ring shear testing method to measure the residual shear strengths at lower normal stresses. This method is described in detail in Bromhead (1992) and Tiwari and Marui (2004).

5.5 Cyclic Simple Shear Tests

The cyclic simple shear test was found to be most suitable for replicating the in-situ cyclic stresses caused by ground shaking, by several researchers including Seed and Peacock (1971), Finn et al. (1971), Silver et al. (1976), Vucetic (1988), and Song et al. (2004). Based on these findings, the cyclic simple shear apparatus is recommended to capture the cyclic and post-cyclic response of soils. Ajmera et al. (2017, 2019) used a cyclic simple shear device that confines the soil specimen in a stack of Teflon®-rings and a latex membrane

to conduct testing on a number of laboratory prepared and natural samples.

In their study, Ajmera et al. (2017, 2019) used sample preparation procedures identical to those previously described by Tiwari and Ajmera (2011, 2014) to conduct direct shear and simple shear tests, respectively. In particular, Ajmera et al. (2017, 2019) prepared their laboratory samples by mixing dry mineral powders in the appropriate proportions based on their dry weight, followed by the addition of de-aired distilled water to achieve a liquidity index of one. The mixtures were allowed to hydrate for a minimum of 24 h. Each specimen was then placed in the cyclic simple shear apparatus, where the specimens underwent incremental consolidation under at-rest conditions. In each increment, the stress was doubled after each completion of primary consolidation until a target normal stress was reached (Ajmera et al. 2017, 2019).

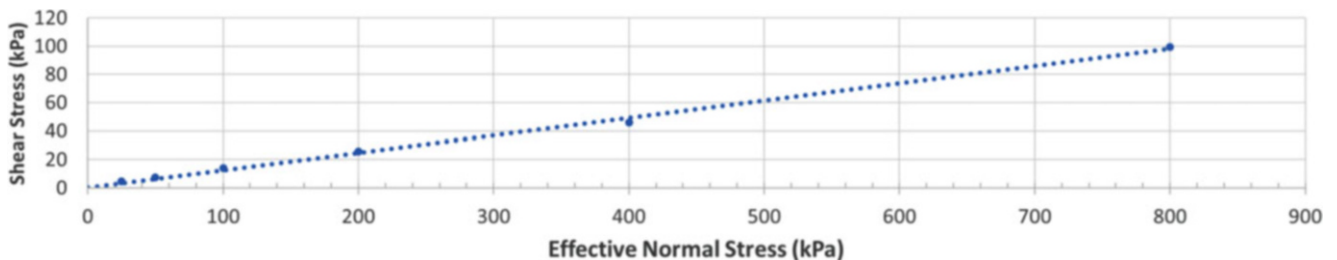


Fig. 30 Example of the Mohr-Coulomb failure envelope for the residual shear strength (Source: Tiwari et al. 2020a, b, with permission from ASCE)

Following primary consolidation at the target normal stress, the specimens were subjected to stress-controlled cyclic loading while maintaining constant volume. In Ajmera et al. (2017, 2019), a sinusoidal wave form with a frequency of 0.5 Hz was applied to generate the cyclic stresses, consistent with recommendations in the literature. The amplitude of the cyclic load was determined by the cyclic stress ratio (CSR). The cyclic stress ratio represents the ratio of the amplitude of the cyclic stress to the vertical consolidation stress. This definition aligns with the one used by Bray and Sancio (2006). Cyclic loading was continued until the specimen experienced a double amplitude shear strain of 10%. If the desired strain level was not reached within 500 cycles, the cyclic phase of the test was terminated. The termination criteria Ajmera et al. (2017, 2019) adapted is similar to the recommendations in the ASTM D5311/D5311M (2013).

During the cyclic loading phase, time series data related to the horizontal (Δx) and vertical (Δy) displacements along with the vertical (P) and shear (T) forces is recorded. The frequency (f) and time (t) data is used to calculate the number of cycles (N) using Eq. 21. Furthermore, since the frequency and period (T) of a cyclic load are interrelated, the relationship between the time data and the period is also presented in Eq. 21. Equations 13 to 16 are used to compute the shear strain, effective normal stress, pore pressure and shear stress, respectively, during the cyclic loading phase of the test.

$$N = tf = \frac{t}{T} \quad (21)$$

Stress and pore pressure behavior during the cyclic phase of a cyclic simple shear test is shown in Fig. 31. The example

in Fig. 31 is for a sample that was subjected to a cyclic stress ratio of 0.141. The corresponding stress-strain hysteresis loops for this sample are presented in Fig. 32. In this figure, the double amplitude shear strain or the difference between the shear strain at the peak and trough of the cyclic load, was less than 10%. This resulted in the application of 500 cycles of loading as Fig. 31 illustrated. The curve labeled effective normal stress depicts the variation in the effective normal stress over the duration of the cyclic loading, which is shown with the curve labeled applied cyclic stress. The pore pressure curve was then back-calculated. These results can be used to compute the double amplitude shear strain developed in each cycle and with the use of interpolation, it will be possible to determine the number of cycles required to reach a targeted level of shear strain in the sample.

Based on the guidelines presented by Andersen et al. (1976) and Brown et al. (1977), a subsequent phase of undrained strain-controlled static loading was initiated immediately after the completion of the cyclic loading phase in the study performed by Ajmera et al. (2019). In this phase, the top platen was kept fixed while the bottom platen was horizontally displaced at a constant rate of 5% per hour. This loading rate adhered to the recommendations specified in ASTM D6528 and aimed to determine the undrained shear strength of the specimen after it has experienced cyclic loading (or the post-cyclic undrained shear strength). The data reduction procedures will be identical to those described previously for the direct simple shear tests. As such, they are not re-produced here.

Ajmera et al. (2021) recognized that soils in-situ are typical subjected to multiple cyclic loading events instead of a single event, as assumed by Ajmera et al. (2017, 2019). That

Fig. 31 Example of stress and pore pressure behavior of sample during the cyclic simple shear test

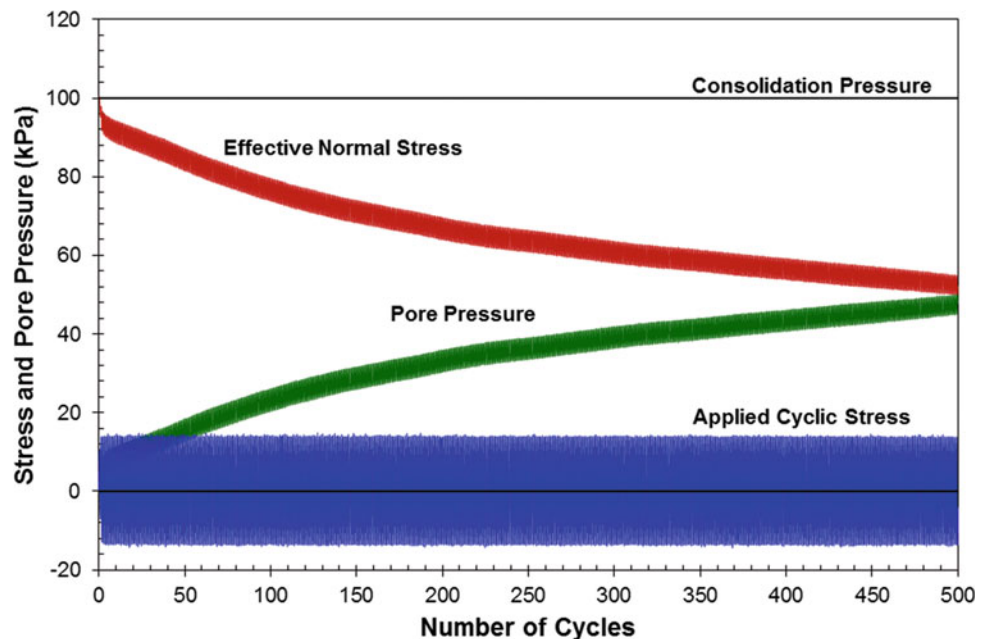
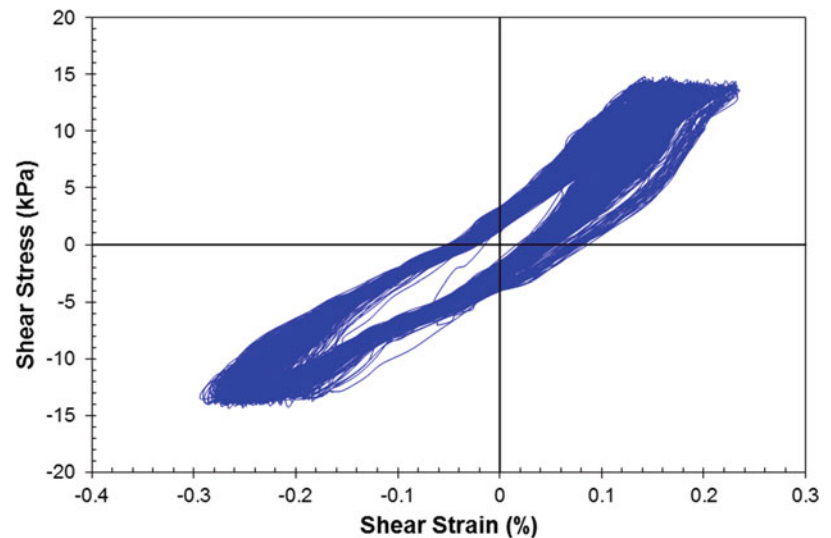


Fig. 32 Stress-strain hysteresis loops from the cyclic phase of a cyclic simple shear test



is, in an earthquake, the soil mass would be subjected to a number of foreshocks, the main shock, and several aftershocks over a short duration. Ajmera et al. (2021) noted that this sequential occurrence of seismic events has the potential to intensify the degradation of soil strength, possibly leading to subsequent failures or even more severe consequences. Thus, they conducted cyclic simple shear tests following the sample and testing procedures previously described (Ajmera et al. 2017, 2019), but rather than measuring the undrained shear strength immediately after the application of a cyclic load, their samples were subjected to another cyclic load. Different degrees of excess pore pressure dissipation were permitted between the two cyclic loading events. The second cyclic load also had a sinusoidal waveform with an amplitude determined by a second cyclic stress ratio and a frequency of 0.5 Hz. Like Ajmera et al. (2017, 2019), Ajmera et al. (2021) also terminated the cyclic loads when 10% double amplitude shear strains or 500 cycles of loading was obtained. The undrained shear strength was then measured using procedures identical to those described in Ajmera et al. (2019) immediately following the termination of the second cyclic loading phase.

5.6 Cyclic Triaxial Tests

While the cyclic simple shear test is the most representative of in-situ conditions during the application of cyclic loads, the cyclic triaxial test is more commonly used to determine the dynamic properties of soils. A picture of a cyclic triaxial test system is shown in Fig. 33, while a closer image of the sample set-up is provided in Fig. 34.

The procedures for conducting a cyclic triaxial test can be found in ASTM D5311/D5311M. Procedures described earlier for the CD and CU triaxial tests are the same as those

used to prepare, back-pressure saturate and consolidate the sample to the desired confining pressure in a cyclic triaxial test. However, after the completion of the primary consolidation, the sample will be subjected to a cyclic load to obtain the cyclic characteristics following which it may be sheared under static conditions to capture the post-cyclic behavior. Similar to the cyclic simple shear test, a sinusoidal wave form is typically used to apply the cyclic loads. However, while the amplitude is still expressed in terms of the cyclic stress ratio, this ratio is computed using Eq. 22, where $\sigma_{d,cyc}$ is the amplitude of the cyclic deviator stress applied. A number of different termination criteria exist in the literature to determine when to stop the application of the cyclic load. These criteria are often a combination of one or more of the following types of constraints: a minimum pore pressure ratio, a maximum single or double amplitude axial strain, or a maximum number of cycles of loading. The single amplitude axial strain is the maximum strain from the origin in either compression or extension during a single cycle, while the double

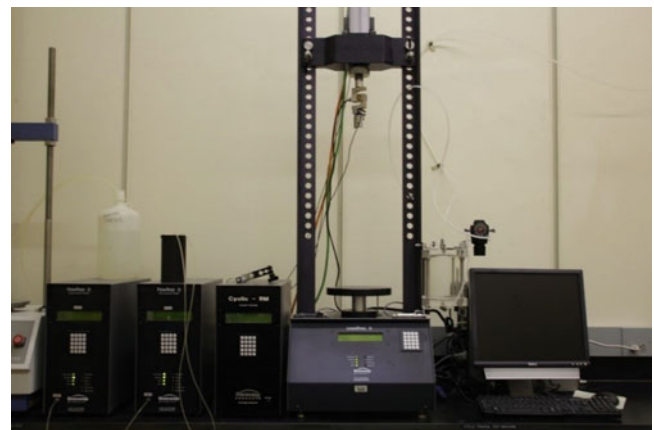


Fig. 33 Cyclic triaxial system

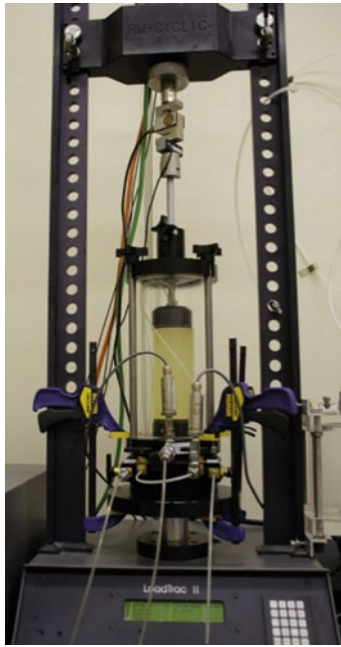


Fig. 34 Close-up picture of sample set-up in cyclic triaxial test

amplitude axial strain the difference between the maximum strain in compression and extension in a single cycle of load. The recommended termination criteria in ASTM D5311/D5311M are a maximum double amplitude axial strain of 20%, a maximum single amplitude axial strain of 20% in either compression or extension or a maximum of 500 cycles of loading.

$$CSR = \frac{\sigma_{d,cyc}}{2\sigma'_3} \quad (22)$$

Data pertinent to the axial deformation, pore pressure and deviator force is recorded during the cyclic phase of a cyclic triaxial test. Equations 6, 7 and 9 presented previously can be used to compute the corresponding stresses and strains during the test. If the sample is subjected to axial compression after the application of the cyclic loads to obtain the post-cyclic shear strength and behavior, the data reduction will be identical to that described previously for the CU triaxial test.

6 Correlations Methods to Obtain Soil Shear Strengths

The best way to obtain the shear strength parameters for slope stability analyses using the appropriate soil testing procedures explained in previous section. However, it is not always possible to obtain enough soil samples or soil testing devices to perform those tests. In such situations, if we obtain soil samples from appropriate depths even in small quantities

that are enough for index property testing (e.g. hydrometer analysis, liquid limit tests, plastic limit tests, and x-ray diffraction), we can indirectly estimate pertinent shear strengths through various correlations with these properties. Some of those correlation methods are explained in the following sections.

6.1 Fully Softened Shear Strength

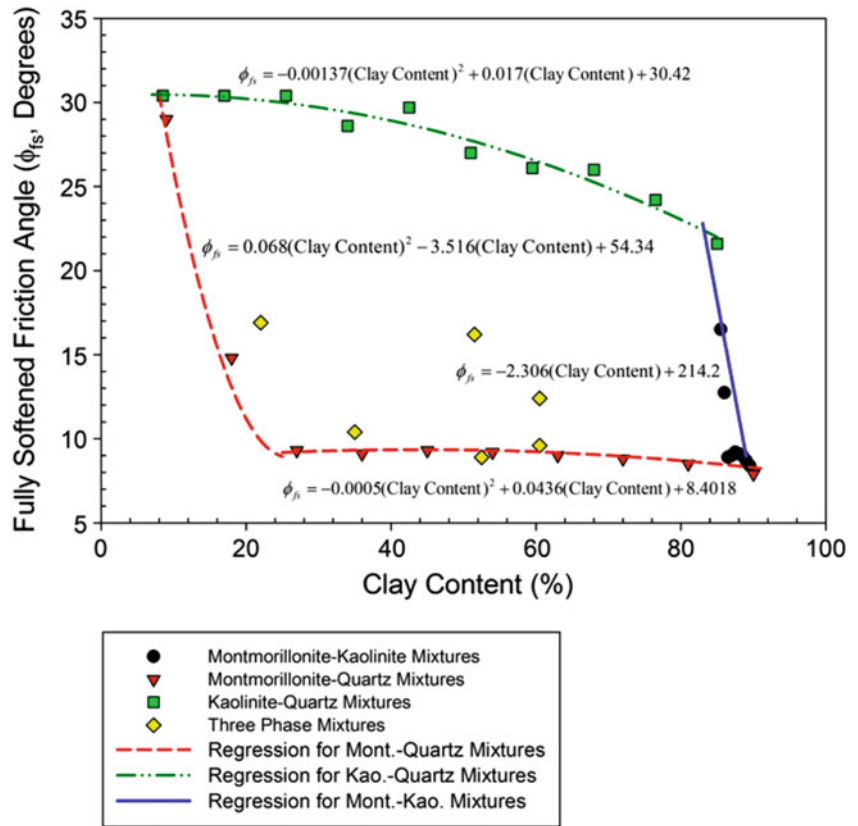
Correlations to estimate the fully softened shear strength have appeared in the literature since 1970. In particular, the correlations in the literature have used the following parameters to develop relationships to estimate the fully softened shear strengths:

- Plasticity index (Ladd et al. 1977; Moon 1984; and Mesri and Abdel-Ghaffar 1993; Castellanos and Brandon 2013)
- Plasticity index and mineralogy (Tiwari and Ajmera 2011, 2015)
- Liquid limit and clay fraction (Saleh and Wright 2005)
- Liquid limit and effective normal stress (Wright 2005)
- Liquid limit and mineralogy (Tiwari and Ajmera 2011, 2015)
- Liquid limit, clay fraction and effective normal stress (Eid 1996; Stark et al. 2005; Stark and Hussain 2015)
- Clay fraction and mineralogy (Tiwari and Ajmera 2011)
- Mineralogy (Tiwari and Ajmera 2011)
- Combinations of various parameters (Eid and Rabie 2016; Castellanos et al. 2016; Castellanos and Brandon 2019; Stark and Fernandez 2019).

In their comprehensive study, Tiwari and Ajmera (2011) conducted an extensive analysis of thirty-six laboratory-prepared soil samples using the direct shear testing. These samples were prepared by blending different proportions of clay minerals, particularly montmorillonite and kaolinite, with ground quartz. The primary objective of their research was to establish correlations between the fully softened shear strength, clay content, and mineralogical composition of the soils.

Tiwari and Ajmera (2011) presented several correlations in their study. Figure 35 shows the relationship they developed between the clay content, mineralogy, and the fully softened shear strength. This figure illustrated the importance of considering the clay mineralogy in estimating the fully softened shear strength. Specifically, Fig. 35 shows the significant differences, at a constant clay content, between the fully softened friction angles with mixtures of kaolinite with quartz having significantly higher strengths than the mixtures of montmorillonite with quartz. They also explored the correlation between the fully softened friction angle and the liquid limit, taking into account the specific clay mineralogy.

Fig. 35 Correlation to estimate the fully softened friction angle as a function of clay content and mineralogy proposed by Tiwari and Ajmera (2011)



This relationship, depicted in Fig. 36, offers a useful tool for estimating the fully softened friction angle based on the liquid limit of a given soil sample. Furthermore, the relationships are significantly better than those previously presented by Wright et al. (2007) and Stark et al. (2005).

In addition to the liquid limit, Tiwari and Ajmera (2011) investigated the correlation between the fully softened

friction angle and the plasticity index. They found that the relationship with the plasticity index could be generalized across different mineralogical compositions. Their proposed relationship is shown in Fig. 37. A unique contribution from the work conducted by Tiwari and Ajmera (2011) was the examination of the fully softened shear strength in terms of the clay mineralogy. They introduced a triangular correlation

Fig. 36 Correlation to estimate the fully softened friction angle as a function of the liquid limit and clay mineralogy proposed by Tiwari and Ajmera (2011)

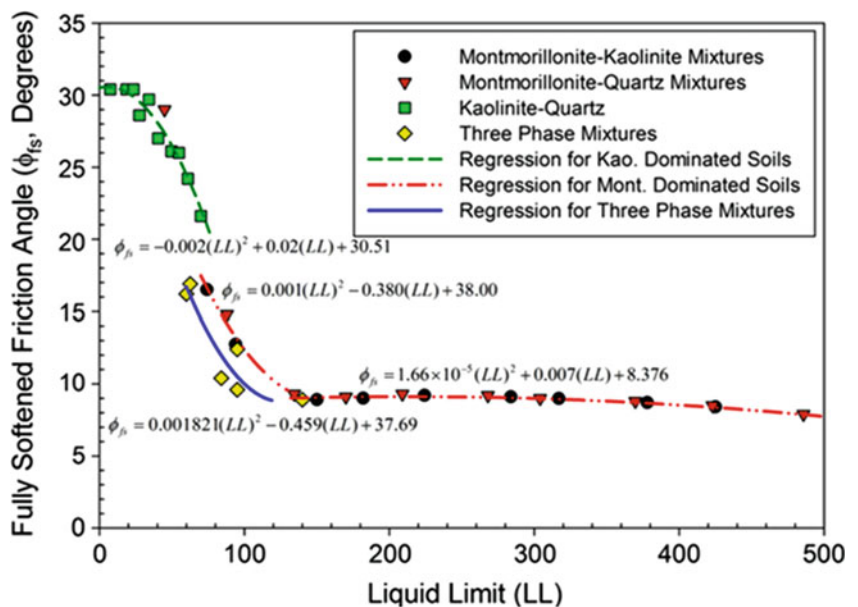
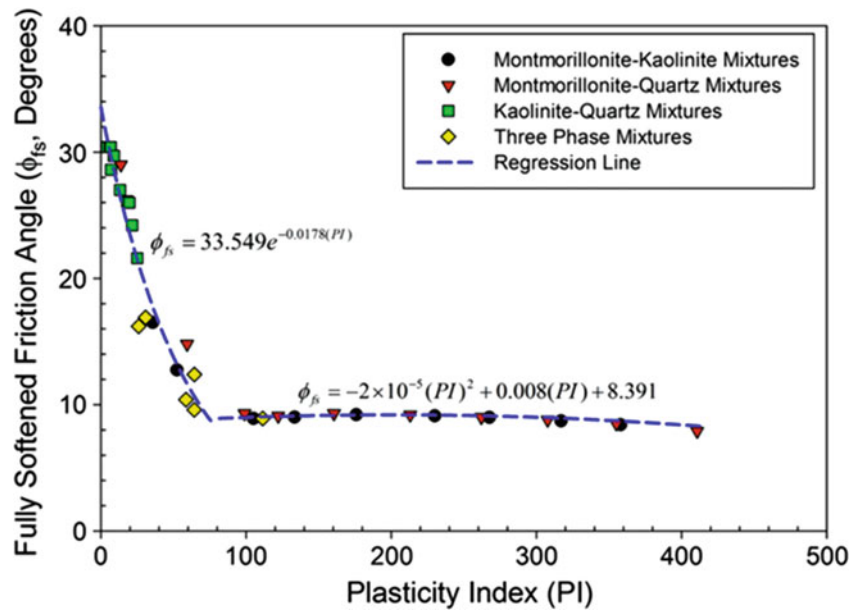


Fig. 37 Correlation proposed by Tiwari and Ajmera (2011) to estimate the fully softened shear strength as a function of plasticity index



chart, as shown in Fig. 38, which enables the estimation of the fully softened friction angle based on the percentages of clay minerals present in the soil mass. Figure 38 further demonstrated the strong control of clay mineralogy on the fully softened shear strength. Specifically, at low kaolinite contents, the fully softened friction angle was found to only vary slightly, while at higher kaolinite contents, the fully softened friction angle was sensitive to the amount of kaolinite present in the soil mass. On the other hand, when the montmorillonite content was high, the quantity of

montmorillonite present did not significantly influence the fully softened friction angle, while strong dependency of the fully softened friction angle on the amount of montmorillonite was noted in soils with low montmorillonite contents.

To validate the proposed correlations, Tiwari and Ajmera (2011) compared their estimated values with results obtained from over eighty natural soils. They discovered that their estimates, derived from Figs. 36 and 37, had an acceptable margin of error within 25% when compared to the measured values. Furthermore, the estimates based on the triangular

Fig. 38 Proposed triangular correlation chart in Tiwari and Ajmera for the fully softened friction angle in terms of clay mineralogy

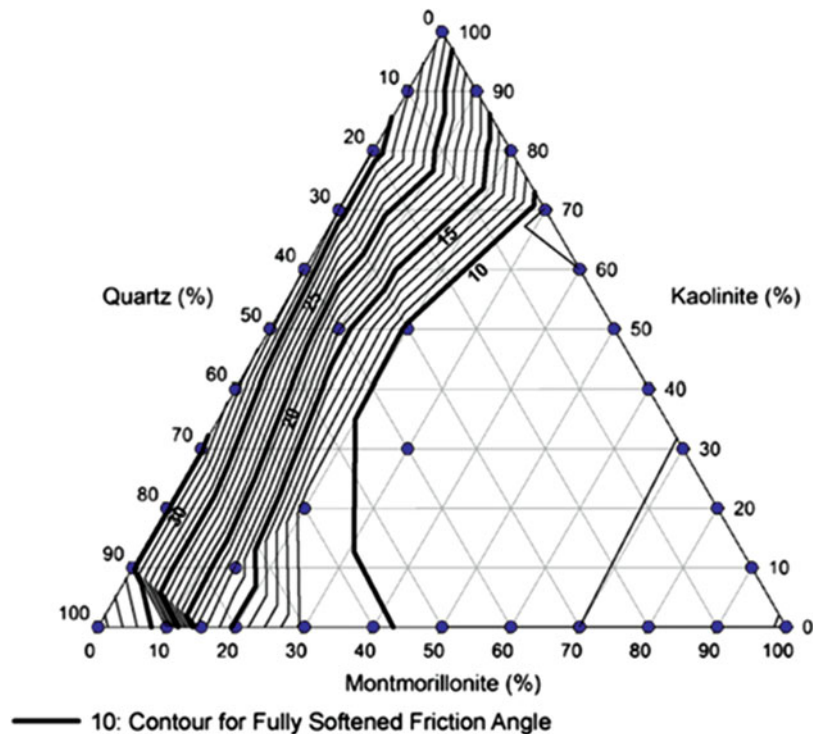
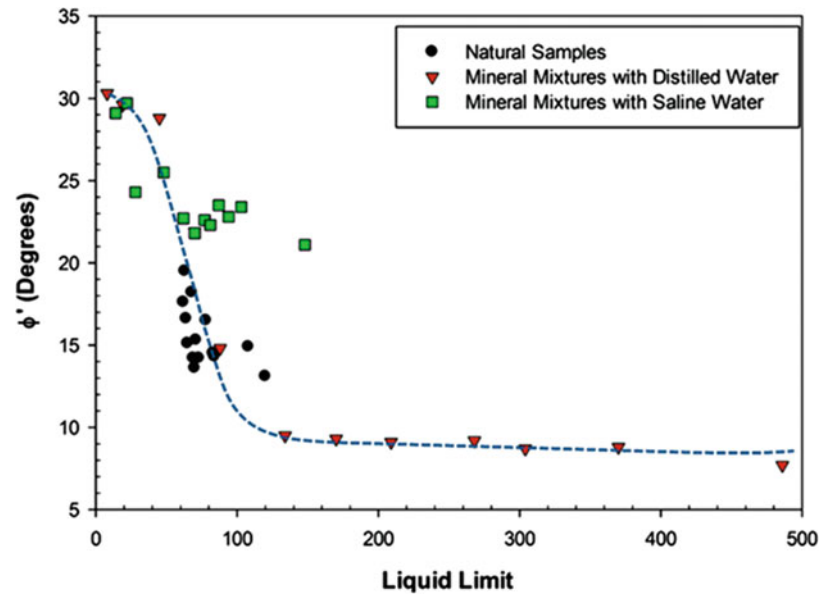


Fig. 39 Correlation proposed by Tiwari and Ajmera (2015) to estimate the fully softened shear strength as a function of liquid limit and pore fluid fluids (with permission from ASCE)



correlation chart demonstrated an even higher accuracy with deviations of less than 15%.

Tiwari and Ajmera (2014) delved into the impact of pore fluid chemistry on the fully softened friction angle of soils. They conducted a comprehensive analysis and developed unified correlations to estimate the fully softened friction angle for two scenarios: soils with distilled water and soils with saline water as the pore fluid. In Tiwari and Ajmera (2014), saline water was prepared to be a solution of sodium chloride with a 0.5 M concentration.

From the results obtained, Tiwari and Ajmera (2014) developed a number of correlations to estimate the fully softened shear strength for the different pore fluids they tested. Some of these are re-produced in this paper. Figure 39 illustrates the relationship between the fully softened friction

angle and the liquid limit, specifically for soils with distilled water as the pore fluid as well as those with saline water as the pore fluid. Similarly, Fig. 40 depicts the correlation between the fully softened friction angle and the plasticity index for those soils with both of the pore fluids examined by Tiwari and Ajmera (2014). Both Figs. 39 and 40 illustrated that the fully softened friction angle remained nearly constant at liquid limits greater than 150 and plasticity indices greater than 100, respectively. Under these conditions, the montmorillonite present in the soil mass may be dominating the behavior and thus, the strength available.

Tiwari and Ajmera (2015) presented correlations, as shown in Figs. 41 and 42, that establish the relationship between the ratio of the fully softened friction angle with saline water as the pore fluid to the fully softened friction

Fig. 40 Correlation proposed by Tiwari and Ajmera (2015) to estimate the fully softened shear strength as a function of plasticity index and pore fluid fluids

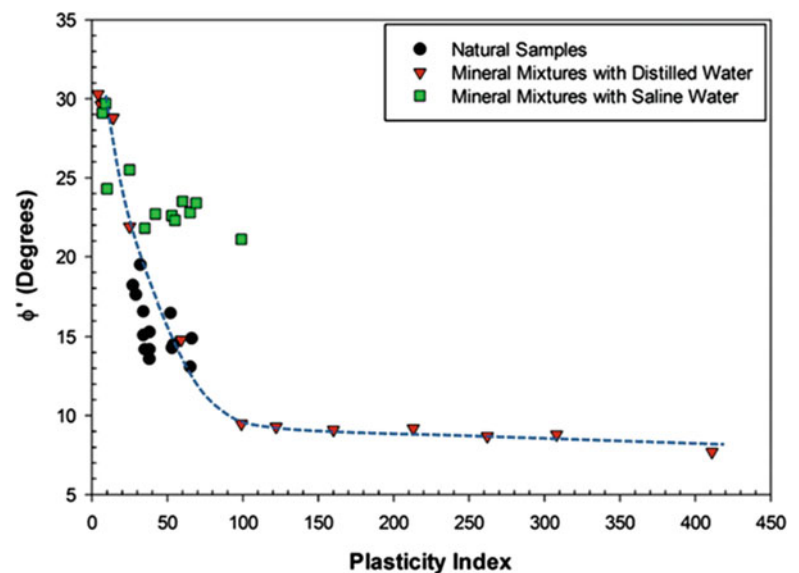
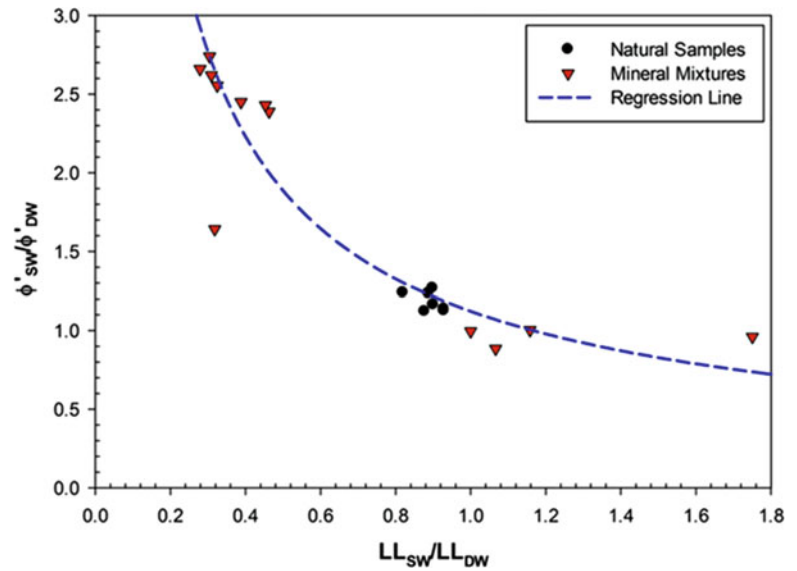


Fig. 41 Correlation proposed by Tiwari and Ajmera (2015) to estimate the ratio of the fully softened friction angle with saline water as the pore fluid to the fully softened friction angle with distilled water as a function of the same ratio for the liquid limits (with permission from ASCE)



angle with distilled water as the pore fluid. These ratios are determined based on the corresponding ratios of the liquid limits and plasticity indices for the respective pore fluids. Figures 41 and 42 demonstrated that the differences in the fully softened shear strength that resulted when different pore fluids were present could be attributed to the effects of the pore fluids on the plasticity characteristics of the soil mass.

6.2 Residual Shear Strength

A number of correlations to estimate the residual shear strength are available in the literature. These correlations are related to a variety of different parameters including the following:

- Clay fraction (Skempton 1964; Lupini et al. 1981; and Tika and Hutchinson 1999)
- Liquid limit (Cancelli 1977; Mesri and Cepeda-Diaz 1986; and Stark and Eid 1997)
- Liquid limit and mineralogy (Tiwari and Marui 2003; and Tiwari and Marui 2005)
- Liquid limit, clay fraction and effective normal stress (Stark and Eid 1994; Eid 1996; Stark and Hussain 2015; Eid et al. 2016; and Tiwari and Marui 2005)
- Plasticity index (Voight 1973; Kanji 1974; Kanji and Wolle 1977; Gibo 1985; Borden and Putrich 1986; Müller-Vonmoss and Løken 1989; Tiwari and Marui 2005; and Toyota et al. 2009)
- Plasticity index and effective normal stress (Hawkins and Privett 1985)

Fig. 42 Correlation proposed by Tiwari and Ajmera (2015) to estimate the ratio of the fully softened friction angle with saline water as the pore fluid to the fully softened friction angle with distilled water as a function of the same ratio for the plasticity indices (with permission from ASCE)

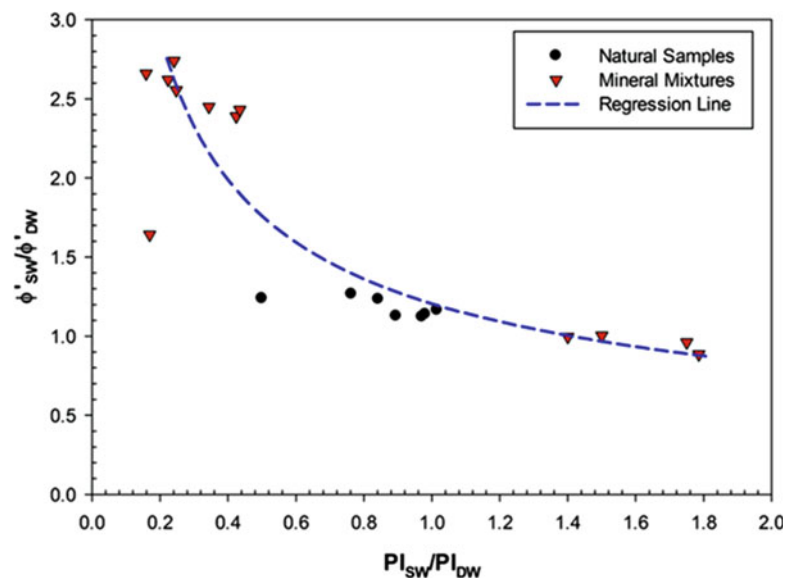
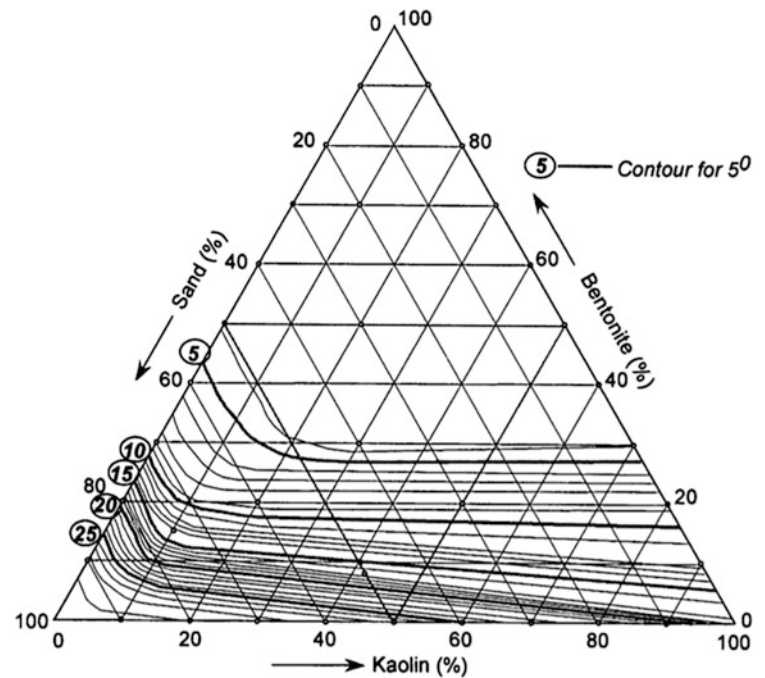


Fig. 43 Tiwari and Marui (2003) proposed triangular correlation chart for the residual friction angle



- Plasticity index and mineralogy (Tiwari and Marui 2003; and Tiwari and Marui 2005)
- Plasticity index, clay fraction and effective normal stress (Eid et al. 2016)
- Mineralogy (Müller-Vonmoss and Løken 1989; Tiwari and Marui 2005; and Tiwari and Marui 2003)
- Various combinations of a numerous factors (Collotta et al. 1989)

Tiwari and Marui (2003) conducted a comprehensive study involving ring shear tests on mixtures of bentonite, kaolin, and Toyoura sand. Their research shed light on the influence of clay mineralogy on the residual friction angles of these soil materials. In addition to their experimental conclusions, Tiwari and Marui (2003) went further and provided practical correlations to estimate the residual friction angle based on the mineralogical composition of the soil mass. They devised a triangular correlation chart, depicted in Fig. 43, which serves as a useful tool for estimating the residual friction angle by considering the specific clay minerals present in the soil. Tiwari and Marui (2003) noted that the effect of kaolin on the residual friction angle was significant when less than 10% kaolin was present beyond which the effect was negligible. They further concluded that for soils with more than 50% sand and 30% bentonite, the residual friction angle was nearly constant at 3.7° regardless of the amount of kaolin present in the soil mass.

The correlations illustrated in Figs. 44 and 45 were introduced by Tiwari and Marui (2003). They enable the estimation of the residual friction angle using the liquid limit and plasticity index, respectively. These correlations

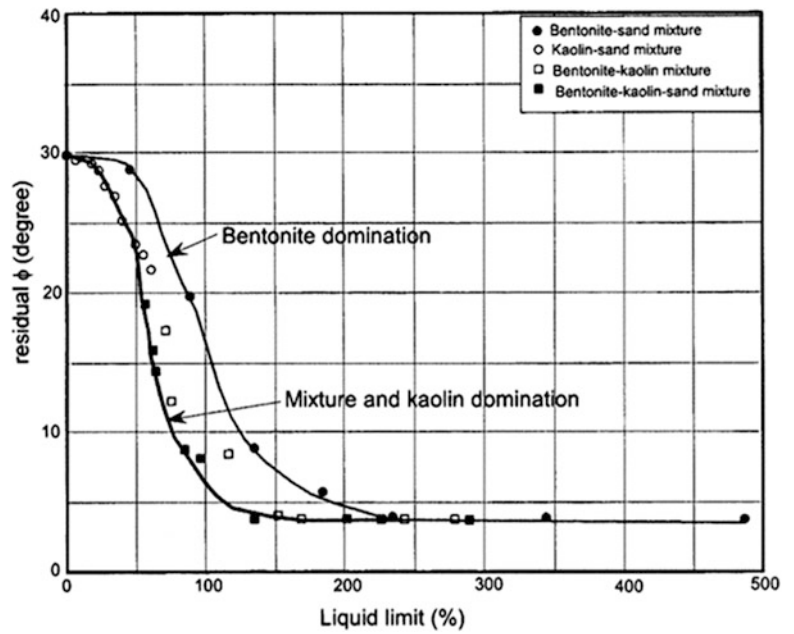
take into account the mineralogical composition of the soil mass highlighting the significance of clay mineralogy in determining the residual friction angle. Figures 44 and 45 demonstrated that the residual friction angle of soils with kaolin was greater than that of soils containing bentonite, even though both samples had the same liquid limit or plasticity index. However, when the liquid limit or plasticity index was greater than 200, the residual friction angle was at a minimum value of 3.7° .

In their research, Tiwari and Marui (2005) critically assessed the correlation proposed by Stark and Eid (1994) for estimating the residual friction angle. They discovered that this correlation, which relied on parameters such as clay fraction, liquid limit, and effective normal stress, had a tendency to significantly overestimate the residual friction angle, sometimes by up to five times. Moreover, Tiwari and Marui (2005) emphasized that the Stark and Eid (1994) correlation was limited in its applicability, being valid only for certain mineral types and failing to provide accurate estimates for a broader range of soils.

Tiwari and Marui (2005) introduced Fig. 46, which contains a correlation between the residual friction angle and both the clay fraction and mineralogical composition of the soil mass. The figure revealed significant variations in the residual friction angle, exceeding 20° in some cases, depending on the clay mineralogy at the same clay content. This further supports their observations of the correlations presented by Stark and Eid (1994), as previously summarized.

Figure 47 contains the correlation presented by Tiwari and Marui (2005) to estimate the residual friction angle based the

Fig. 44 Proposed correlation by Tiwari and Marui (2003) for the residual friction angle as a function of the liquid limit and clay mineralogy



liquid limit. They noted that the correlations presented by Stark and Eid (1994) tended to overestimate the residual friction angle for soils with liquid limits greater than 200. However, the relationship in Fig. 47 could reasonably estimate the residual shear strength for all of the natural samples they tested along with over 70% of the results for the natural samples available in the literature. A relationship to estimate the residual friction angle from the plasticity index, as proposed by Tiwari and Marui (2005), is depicted in Fig. 48. As with the correlation in Fig. 47, the relationship in Fig. 48 was able to estimate the residual shear strength of natural samples with good accuracy. In particular, Fig. 48 shows that the

majority of the results from the natural samples were located at the lower bound of the correlation curves developed by Tiwari and Marui (2005).

Tiwari and Marui (2005) also prepared a triangular correlation chart, as shown in Fig. 49a, with contours providing a method to estimate the residual friction angle by considering the clay mineralogy in the soil mass. They divided the triangular correlation chart into seven zones (Fig. 49b) that could capture the variation in the residual friction angle with respect to the amount of the various clay minerals (Fig. 49c). The majority of the natural samples they tested were found to fall into zones A and B.

Fig. 45 Proposed correlation by Tiwari and Marui (2003) for the residual friction angle as a function of the plasticity index and clay mineralogy

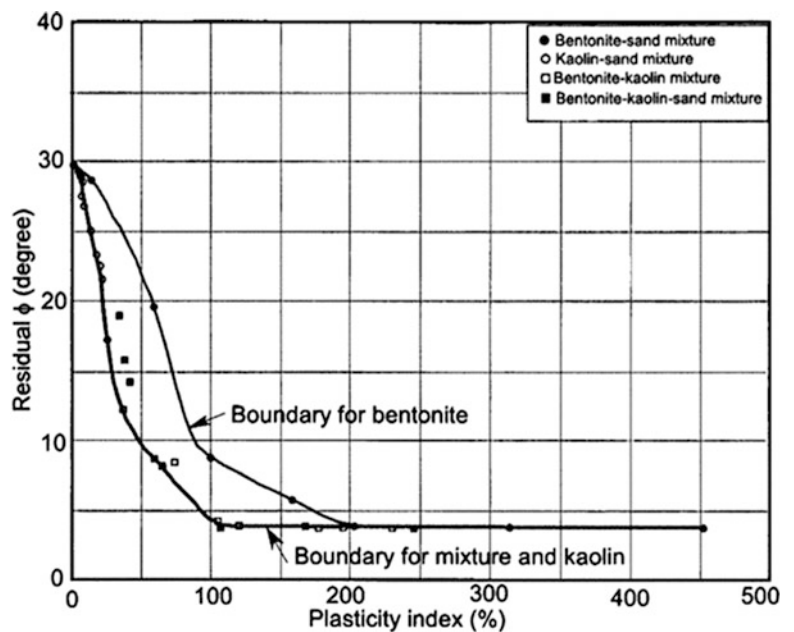
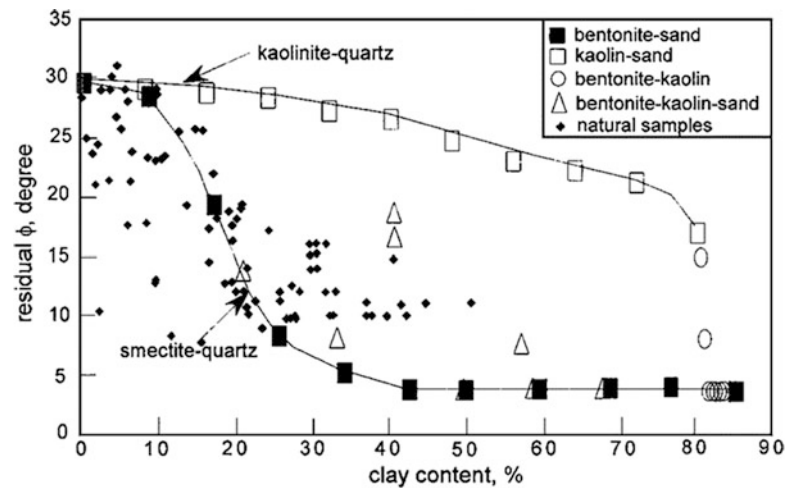


Fig. 46 Correlation proposed by Tiwari and Marui (2005) to estimate for the residual friction angle as a function of the clay content and mineralogy (with permission from ASCE)



6.3 Undrained Shear Strengths of Over-Consolidated Clays

The Stress History and Normalized Soil Engineering Properties (SHANSEP) method, introduced by Ladd and Foott (1974) and further developed by Ladd et al. (1977), provides a means to assess the impact of the over-consolidation ratio on the undrained shear strength in soils. The undrained shear strength is estimated using the undrained strength ratio, which is defined as the ratio of the undrained shear strength to the effective vertical stress. This method takes into account the influence of the over-consolidation ratio. By analyzing the relationship between the undrained strength ratio and the over-consolidation ratio, SHANSEP allows for the estimation of undrained shear strength under different stress conditions.

Ajmera et al. (2016) extended the SHANSEP method by computing the normalized undrained strength ratio. This was calculated by normalizing the undrained strength ratio at a given over-consolidation ratio to the undrained strength ratio at an over-consolidation ratio of unity (or that for a normally consolidated soil). By doing so, Ajmera et al. (2018)

presented two relationships between the normalized undrained strength ratio and the over-consolidation ratio for fine-grained soils. These relationships are shown in Fig. 50. At a constant over-consolidation ratio, the normalized undrained strength ratio for the mixtures of montmorillonite with quartz is higher than that of mixtures of kaolinite with quartz.

In Eqs. (2) and (3), the shear strength parameters of a soil mass are significantly influenced by its stress history. When dealing with normally consolidated clays, the cohesion intercept is typically assumed to be zero. In contrast, over-consolidated clays typically exhibit a non-zero cohesion intercept. In such soils, the magnitude of the cohesion intercept generally increases with an increase in the over-consolidation ratio. The friction angle also varies between normally consolidated and over-consolidated specimens of the same soil. Hvorslev (1960) emphasized that the cohesion intercept and the friction angle in Eqs. (2) and (3) are not indicative of the actual soil properties but rather act as mathematical tools for determining shear strength. According to Hvorslev (1960), the shear strength of clays is influenced by two fundamental parameters: the true friction angle (ϕ_e) and

Fig. 47 Correlation proposed by Tiwari and Marui (2005) to estimate for the residual friction angle as a function of the liquid limit and mineralogy (with permission from ASCE)

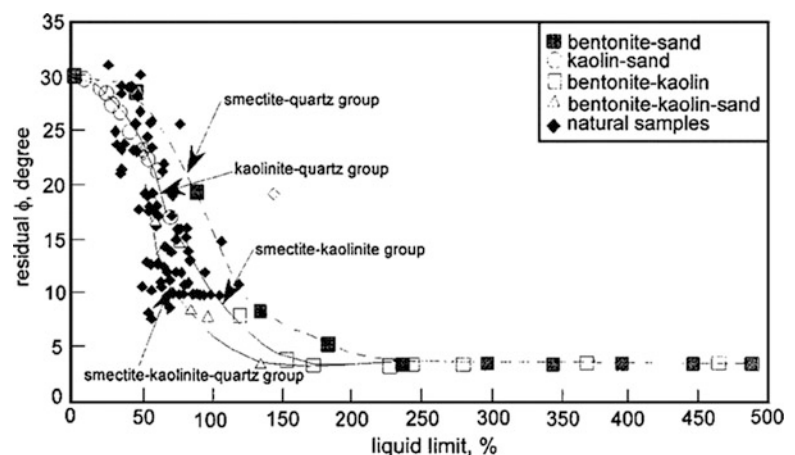
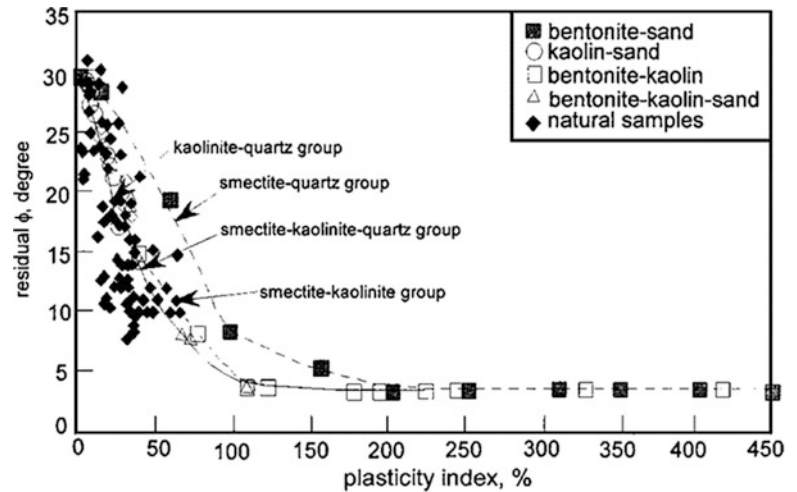


Fig. 48 Correlation proposed by Tiwari and Marui (2005) to estimate for the residual friction angle as a function of the plasticity index and mineralogy (with permission from ASCE)



the base friction angle (ϕ_c). These parameters remain unchanged regardless of the over-consolidation ratio.

With knowledge of the equivalent pre-consolidation pressure (σ_{pe}), the shear strength of the soil can be determined using Eq. 23. In the case of normally consolidated soils, the equivalent pre-consolidation pressure will be equivalent to the effective vertical stress. However, for over-consolidated soils, the equivalent pre-consolidation pressure corresponds to the effective vertical stress that would result in the same void ratio if the soil were normally consolidated.

$$\tau = \sigma_{pe} \tan \phi_c + \sigma' \tan \phi_e \tag{23}$$

Tiwari et al. (2022) presented the correlations in Figs. 51 and 52 to estimate the true and base friction angles, respectively, from the plasticity index. They pointed out that the true friction angle did not heavily dependent on the mineralogical composition of the soil mass. Furthermore, Tiwari et al. (2022) found that the true friction angle was nearly constant at 10° in soils with plasticity indices greater than 80. On the other hand, the base friction angle was heavily dependent on the clay minerals present, as illustrated in Fig. 52. An increase in the plasticity index is found to cause an increase in the base friction angle in the mixtures of kaolinite with quartz, while it was constant at 2° in the mixtures of montmorillonite with quartz.

6.4 Cyclic Shear Strength

The power function was found to be a good representative of the cyclic strength curves of soils by Ishihara et al. (1980) and Ajmera et al. (2017). In particular, Eq. 24, establishes a relationship between the CSR and the number of cycles (N) required to achieve a specific failure criteria using two

curve fitting parameters a and b. These parameters play a crucial role in defining the shape and position of the cyclic strength curves. Specifically, the curve fitting parameter a primarily influences the vertical position of the cyclic strength curve, while the parameter b controls the slope or inclination of the curve.

$$CSR = aN^{-b} \tag{24}$$

Ajmera et al. (2017) presented correlations that allowed for the curve fitting parameters a and b to be estimated with knowledge of the liquid limit or plasticity index. These correlations are depicted in Figs. 53, 54, 55, and 56. Their results indicated that an increase in liquid limit generally leads to an increase in the value of a, indicating an increase in cyclic resistance for soils with liquid limits below 100 (Fig. 53). However, for soils with liquid limits above 100, the value of a decreases, implying a decrease in cyclic resistance. Similarly, Fig. 54 shows that as the plasticity index increases, the value of a generally increases for soils plasticity indices below 60 beyond which the value of a decreases with increasing plasticity index. Ajmera et al. (2017) attributed the increase in cyclic resistance to the formation of a clay matrix around quartz particles. It should be noted that these results are based on normally consolidated samples and thus, the observed trends may vary in over-consolidated soils.

From Figs. 55 and 56, Ajmera et al. (2017) clearly demonstrate the contrasting behavior of cyclic resistance between two different clay minerals used in the mixtures they tested. For soils containing kaolinite, b increases with both liquid limit and plasticity index, indicating a steeper cyclic strength curve as the plasticity index rises. In contrast, for soils with montmorillonite, b decreases with increasing liquid limit and

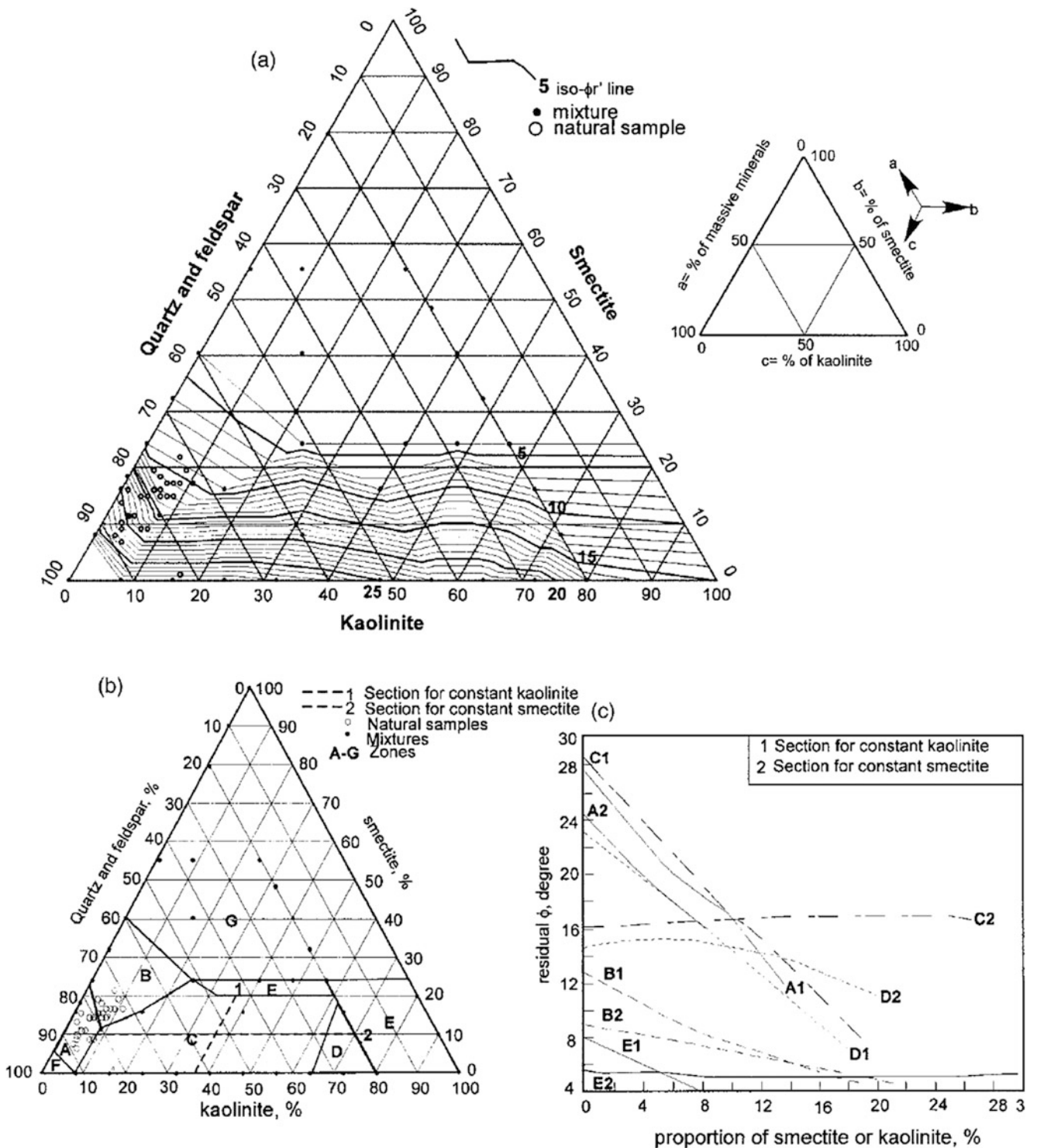


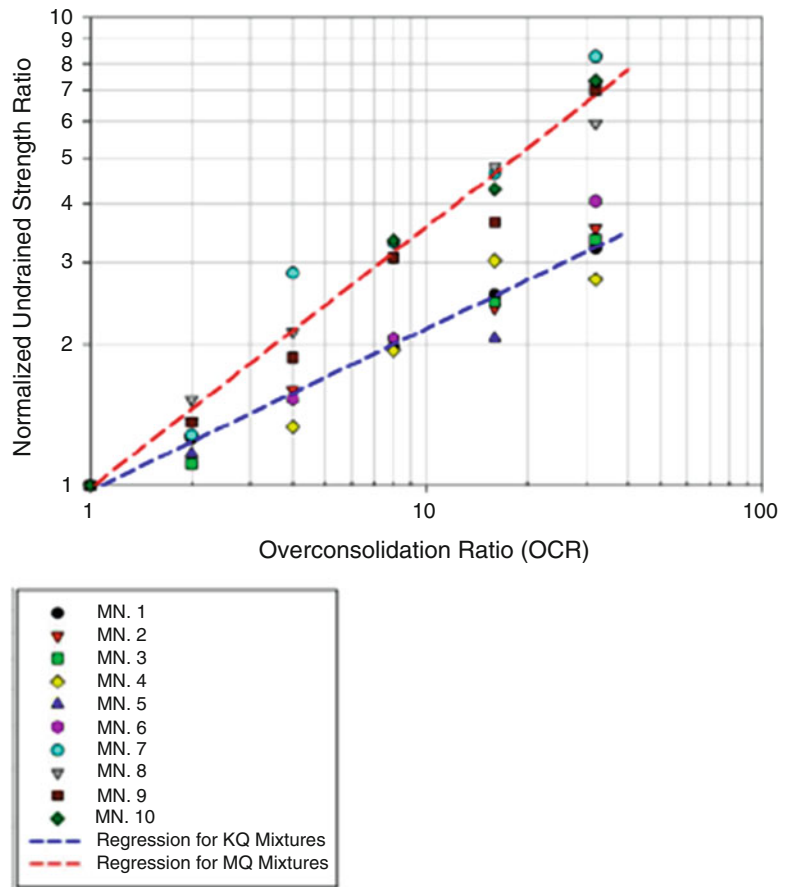
Fig. 49 (a) Triangular correlation chart for residual friction angle by Tiwari and Marui (2005), (b) zones used to illustrate effects of clay minerals and (c) effects of single clay mineral in each zone (with permission from ASCE)

plasticity index, suggesting flatter cyclic strength curves with higher plasticity indices.

When two sets of cyclic loads are applied on a sample, the cyclic resistance available during the second cyclic event is

dependent on the degree to which excess pore pressures generated from the first cyclic load are allowed to dissipate before the second cyclic load is applied. Ajmera et al. (2021) presented relationships containing the cyclic strength curves

Fig. 50 Correlation between normalized undrained strength ratio with over-consolidation ratio from Ajmera et al. (2018) (with permission from ASCE)



for a second cyclic load for kaolinite samples. Figure 57 illustrates that an increase in the degree of pore pressure dissipation results in an increase in the cyclic resistance, as depicted by an upward shift in the cyclic strength curves.

6.5 Post-Cyclic Undrained Shear Strength

Ajmera et al. (2019) provided a number of correlations to estimate the undrained shear strength after cyclic loading, defined as the post-cyclic undrained shear strength. However,

Fig. 51 Correlation from Tiwari et al. (2022) for the true friction angle with respect to the plasticity index (with permission from ASCE)

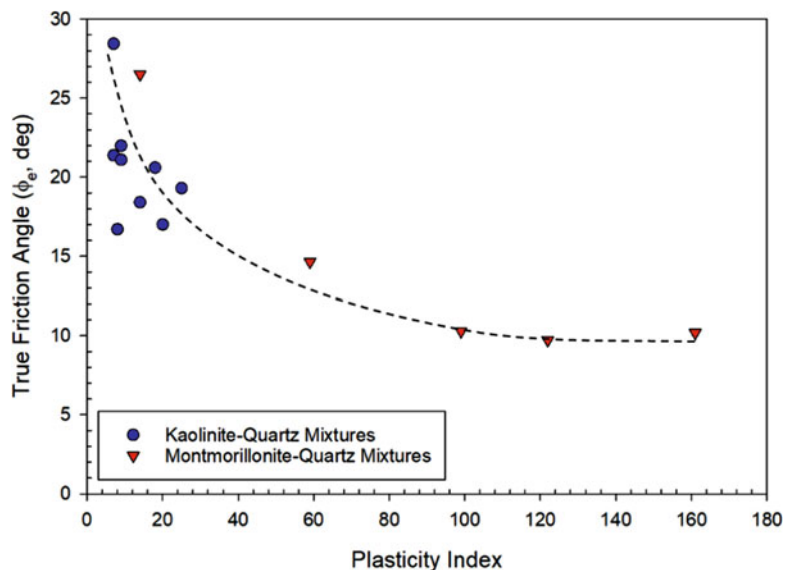
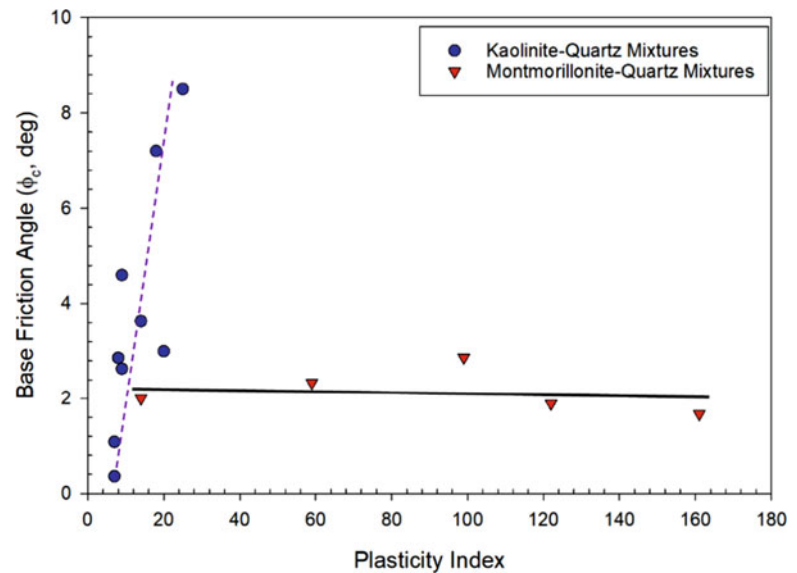


Fig. 52 Correlation from Tiwari et al. (2022) for the base friction angle with respect to the plasticity index (with permission from ASCE)



in their correlations, this shear strength was typically normalized by the effective vertical stress prior to cyclic loading to obtain the post-cyclic undrained strength ratio. One of the correlations Ajmera et al. (2019) developed between the post-cyclic undrained strength ratio and the plasticity index is shown in Fig. 58. This figure shows that for soils with plasticity indices less than 50, an increase in the post-cyclic undrained strength ratio occurred with an increase in the plasticity index. On the other hand, when the soils had a plasticity index greater than 50, the post-cyclic undrained strength ratio decreased with an increase in the plasticity index.

Figure 59 contains the correlation that Ajmera et al. (2019) proposed between the post-cyclic undrained strength ratio and the pore pressure ratio. The pore pressure ratio is computed as the ratio of the excess pore pressure generated during cyclic loading to the effective normal stress

immediately prior to the application of the cyclic load. Like Fig. 58, there is a substantial scatter around the correlation proposed. However, Ajmera et al. (2019) highlighted that this relationship indicates that an increase in the pore pressure ratio would correspond to a reduction in the post-cyclic undrained strength ratio.

A correlation between the degradation ratio and the plasticity index was also provided by Ajmera et al. (2019). The degradation ratio is ratio of the post-cyclic undrained shear strength to the static undrained shear strength. It serves as a measure of the amount of reduction in the undrained shear strength that resulted from the cyclic loading. The correlation developed by Ajmera et al. (2019) is provided in Fig. 60. In soils containing kaolinite as the clay mineral, Fig. 60 indicates that the degradation ratio rises as the plasticity index (PI) increases. However, the impact of the cyclic stress ratio on the degradation ratio was found to be negligible.

Fig. 53 Correlation proposed by Ajmera et al. (2017) to estimate curve fitting parameter a as a function of the liquid limit

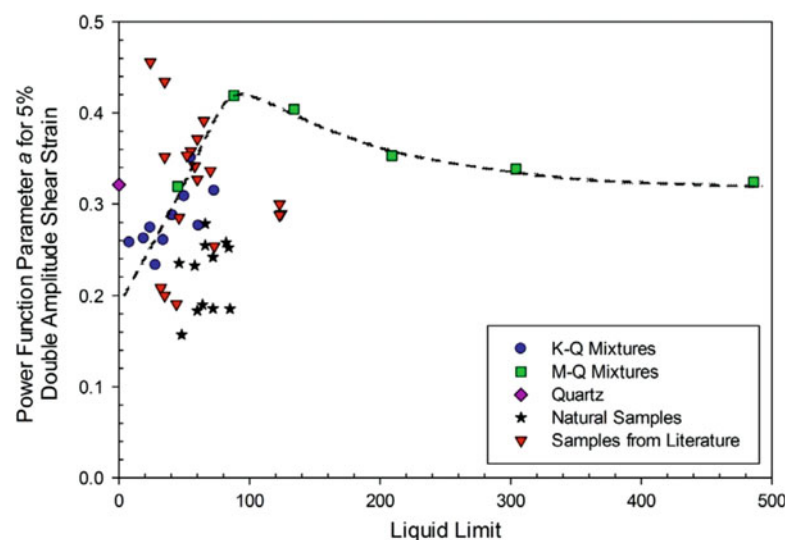
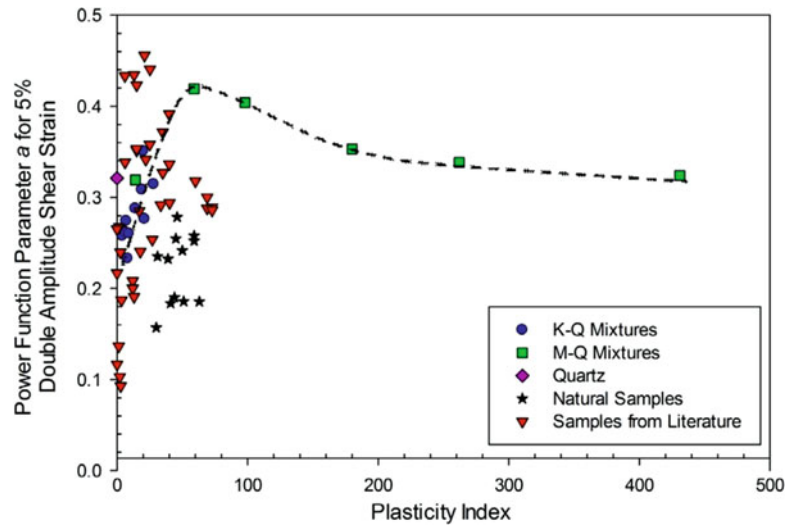


Fig. 54 Correlation proposed by Ajmera et al. (2017) to estimate curve fitting parameter a as a function of the plasticity index



Conversely, in soils where montmorillonite is the clay mineral, the degradation ratio is influenced by the cyclic stress ratio. As the cyclic stress ratio increases, there is a corresponding decrease in the degradation ratio.

Ajmera et al. (2019) calculated the normalized undrained strength ratio and the post-cyclic effective stress ratio for the samples they tested. The normalized undrained strength ratio is an extension of the parameter first proposed by Ajmera et al. (2016). In Ajmera et al. (2019), the normalized undrained strength ratio (Norm. USR) was obtained when the post-cyclic undrained strength ratio was normalized by the undrained strength ratio. In other words, the normalized undrained strength ratio is calculated using Eq. 25. In this equation, s_u is the undrained shear strength, σ' is the effective normal stress, and the addition of the subscript “pc” indicates the values correspond to the post-cyclic conditions (that is, the conditions immediately following the application of a cyclic load). The post-cyclic effective stress ratio (PC-ESR)

is ratio of the consolidation pressure (or effective stress prior to the application of a cyclic load) to the post-cyclic effective stress, as shown in Eq. 26. It can also be computed with knowledge of the pore pressure ratio (r_u) or the ratio of the excess pore pressure generated during cyclic loading to the consolidation pressure. The formula to do so is also provided in Eq. 26.

$$Normalized\ USR = \frac{s_{u,pc}/\sigma'_{pc}}{s_u/\sigma'_c} \tag{25}$$

$$PC - ESR = \frac{\sigma'_c}{\sigma'_{pc}} = \frac{1}{1 - r_u} \tag{26}$$

Ajmera et al. (2019) proposed the correlation, as presented in Fig. 61, between the normalized undrained strength ratio and the post-cyclic effective stress ratio. Figure 61 illustrates

Fig. 55 Correlation proposed by Ajmera et al. (2017) to estimate curve fitting parameter b as a function of the liquid limit

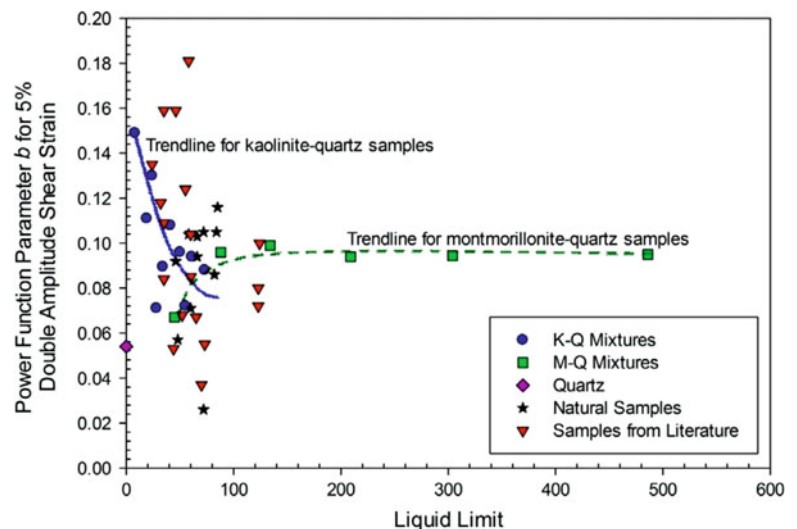
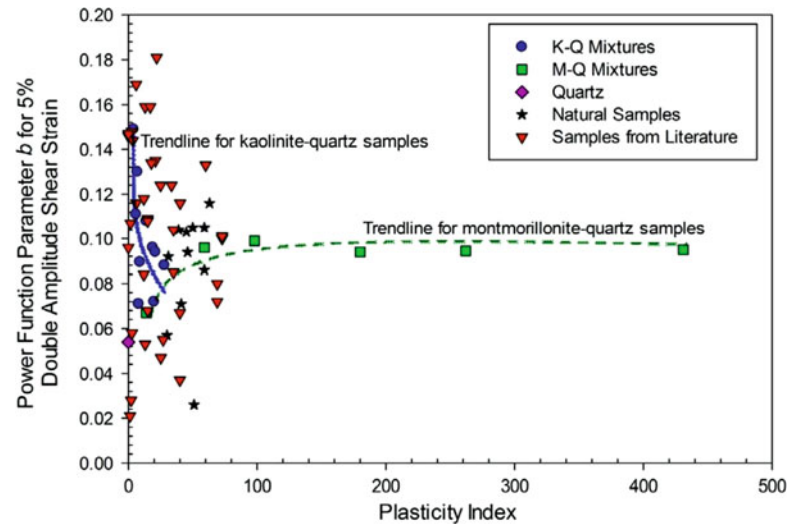


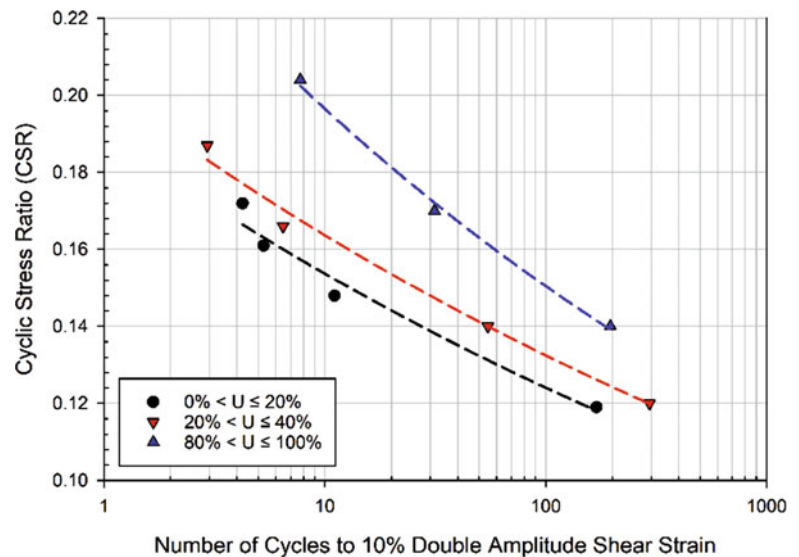
Fig. 56 Correlation proposed by Ajmera et al. (2017) to estimate curve fitting parameter b as a function of the plasticity index



an intriguing trend: as the post-cyclic effective stress ratio increases, the normalized undrained strength ratio also exhibits a corresponding increase. At a post-cyclic effective stress ratio value of one, the normalized undrained strength remains at one, indicating no reduction in shear strength. However, as the post-cyclic effective stress ratio rises, reaching around 20, the normalized undrained strength climbs to approximately 10.

The correlation in Fig. 61 was shown to be capable of capturing the post-cyclic undrained shear strength of soils subjected to two sets of cyclic loads in Ajmera et al. (2021). This is illustrated in Fig. 62, in which the post-cyclic effective stress ratio was calculated immediately after the end of the second cyclic load. Thus, the relationship, originally developed by Ajmera et al. (2019), is able to capture the effects of excess pore pressure dissipation between cyclic loads and any additional reductions in undrained shear strength induced by the second cyclic load.

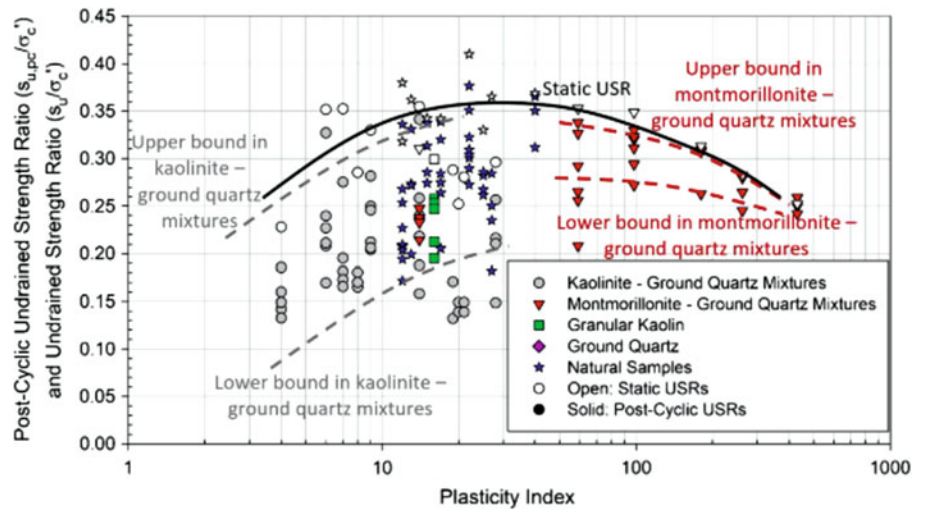
Fig. 57 Cyclic strength curves for kaolinite samples during a second cyclic load



6.6 Various Other Correlations

Only Stark et al. (2005) and Tiwari and Ajmera (2011) explored the relationships between the fully softened and residual friction angles. However, the correlations presented by Stark et al. (2005) contain significant scatter and hence, will not be discussed. Tiwari and Ajmera (2011) primarily focused on investigating the fully softened shear strength of soils but also provided insights into the relationship between the residual and fully softened friction angles. The residual friction angles used in their analysis were derived from the work of Tiwari and Marui (2005). In their findings, presented in Figs. 63 and 64, the authors proposed new relationships that describe the difference between fully softened and residual friction angles based on the liquid limit and plasticity index, respectively. Tiwari and Ajmera (2011) further introduced normalized relationships for the difference between fully softened and residual friction angles,

Fig. 58 Correlation to estimate post-cyclic undrained shear strength with the use of the plasticity index developed by Ajmera et al. (2019) (with permission from ASCE)



individually normalized by the respective angles. Figures 65, 66, 67, and 68 depict these relationships with respect to the liquid limit and plasticity indices of the soil samples.

7 Example of Shear Strength Estimation with Correlation Methods

In this section, we will demonstrate a few examples on how to estimate shear strength parameters of two soil samples collected from different locations and having different soil mineralogical dominations as illustrated by their activity values.

Soil A

Liquid limit = 60, Plasticity index = 20, Clay Fraction = 22%, Effective vertical stress at sampling location = 100 kPa, Initial void ratio (e_0) = 0.88, Over-

consolidation ratio = 8, Compression index (C_c) = 0.28, and Recompression index (C_r) = 0.05.

Soil B

Liquid limit = 80, Plasticity index = 40, Clay Fraction = 13.0%, Effective vertical stress at the sampling location = 100 kPa, Initial void ratio = 1.30, Overconsolidation ratio = 2, Compression index = 0.43, and Recompression index = 0.08.

After an earthquake, excess pore pressures are generated in both of those soils. The pore pressure ratios immediately after the earthquake event are estimated to be equal to 0.59 for Soil A and 0.18 for Soil B. If this information is not available, the pore excess pore pressure generated from an earthquake (Δu) can be calculated using Eq. 27 from Davis and Berrill (1982). In this equation, R is the distance from the earthquake epicenter to the location of the soil element expressed in meters, N_1 is the blow counts from a standard

Fig. 59 Correlation between post-cyclic undrained strength ratio and the pore pressure ratio from Ajmera et al. (2019) (with permission from ASCE)

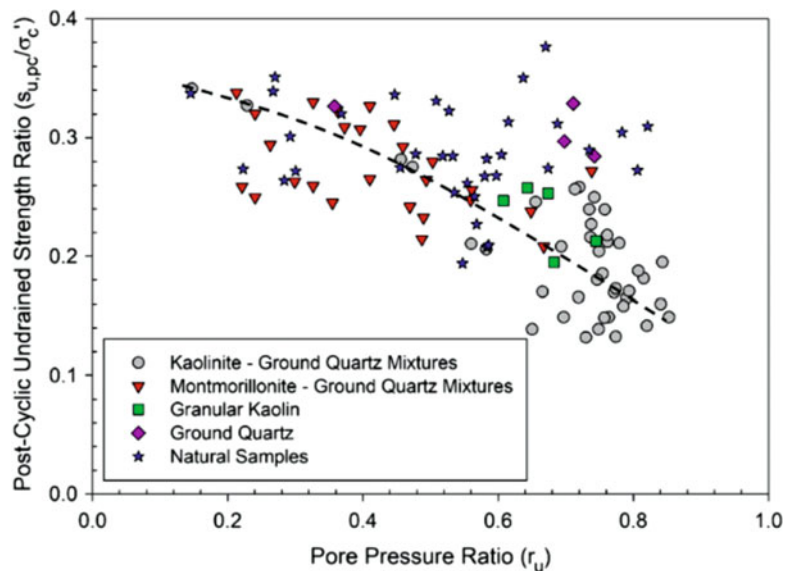
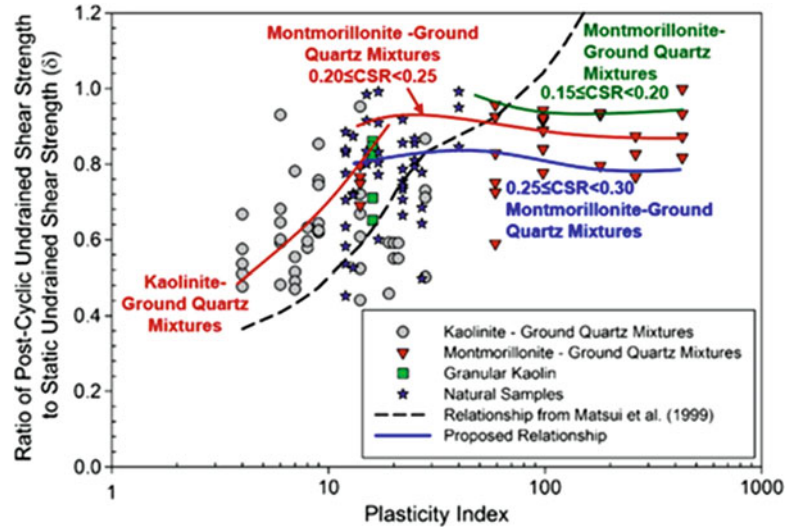


Fig. 60 Correlation between degradation ratio and plasticity index developed by Ajmera et al. (2019) (with permission from ASCE)



penetration test corrected to an overburden pressure of 1 tsf (96 kPa), and M is the magnitude of the earthquake. Both Δu and σ_v' should be expressed in kPa in Eq. 27.

During a standard penetration test, a split-spoon sampler is driven into the ground using a standard number of blows with a hammer. The resistance offered by the soil to the penetration of the sampler is recorded as the N -value (N). However, the N -value obtained is influenced by the overburden pressure or stress applied to the soil at the specific test depth. To account for this influence and allow for better comparisons between different depths and locations, the N -value is commonly corrected to a standard reference pressure of 1 tsf (96 kPa) using Eq. 28, in which σ_v' should be in kPa.

$$\Delta u = \frac{450}{R^2 N_1^2 \sqrt{\sigma_v'}} 10^{1.5M} \quad (27)$$

$$N_1 = N \sqrt{\frac{100}{\sigma_v'}} \quad (28)$$

If the soil samples have activity (Eq. 29) values higher than 2–3, they are expansive soils and are montmorillonitic in nature. If the soil samples have activities less than 0.8–1.0, they are considered as kaolinitic or illitic soils.

Fig. 61 Correlation proposed by Ajmera et al. (2019) to estimate the post-cyclic undrained shear strength in terms of the normalized undrained strength ratio as a function of the post-cyclic effective stress ratio (with permission from ASCE)

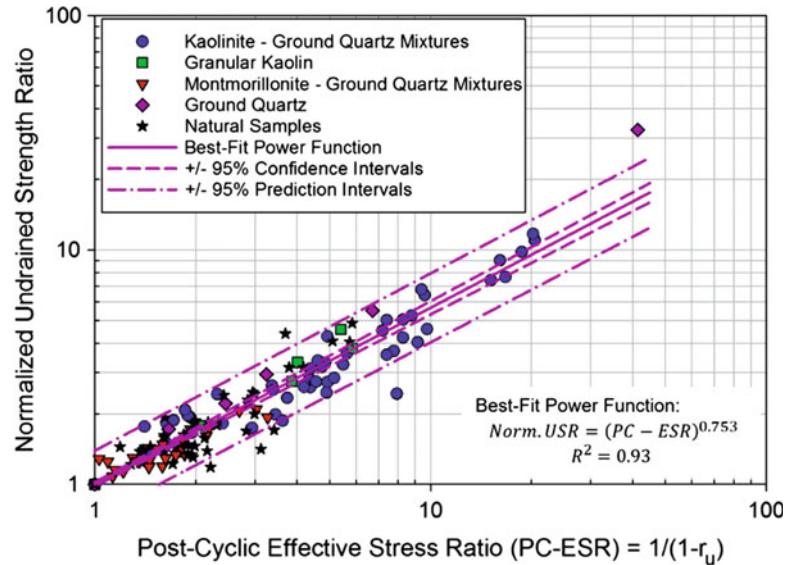
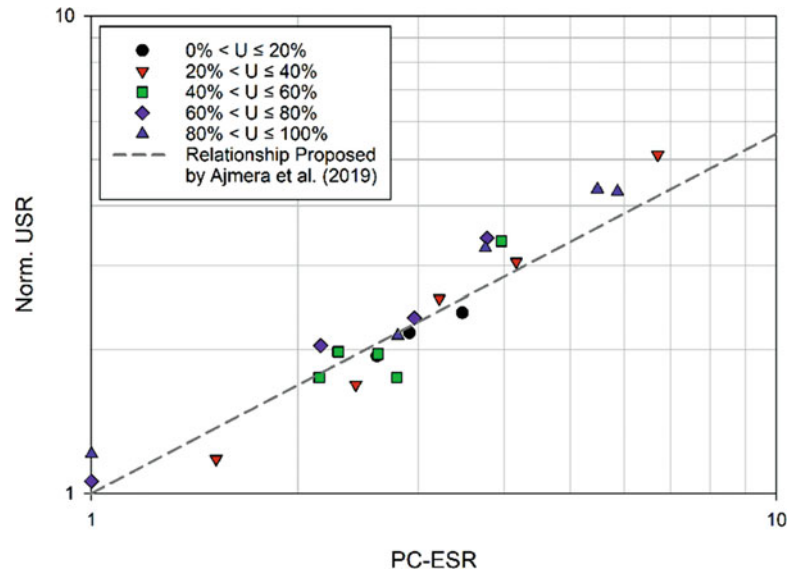


Fig. 62 Use of the correlation from Ajmera et al. (2019) to estimate the normalized undrained strength ratio from the post-cyclic effective stress ratio



Soil A: 23°
Soil B: 16°

$$\text{Activity of soil} = (\text{Plasticity Index} / \text{Clay Fraction}) \quad (29)$$

For Soil A, Activity = (20/22) = 0.91 [Kaolinitic]
For soil B, Activity = (40/13) = 3.1 [Montmorillinitic]

Fully Softened Shear Strength

From Fig. 36, the fully softened friction angle is calculated as follows:

Soil A: 24°
Soil B: 16°

From Fig. 37, the fully softened friction angle is calculated as follows:

Residual Shear Strength

From the central line in Fig. 47, the residual friction angle is calculated as follows:

Soil A: 20°
Soil B: 14°

From the central line in Fig. 48, the fully softened friction angle can be calculated as follows:

Soil A: 20°
Soil B: 14°

Fig. 63 Correlation from Tiwari and Ajmera (2011) between the differences in the fully softened and residual friction angles as a function of the liquid limit

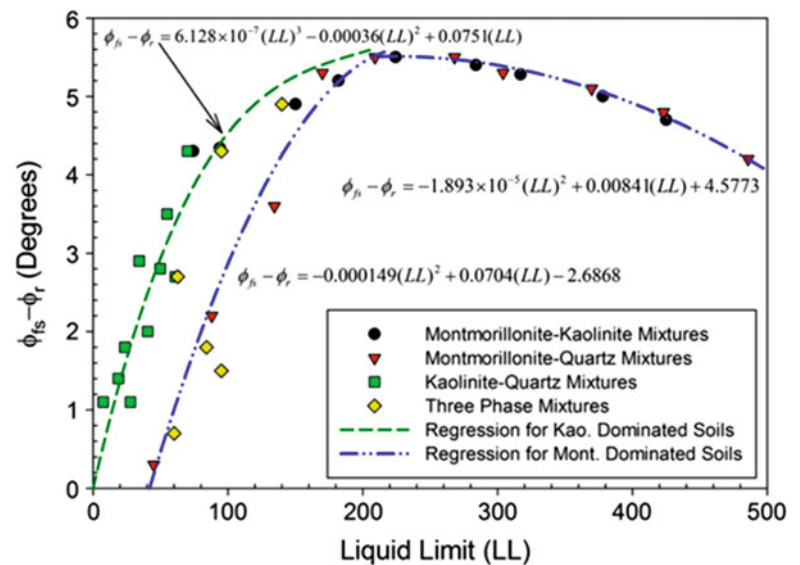
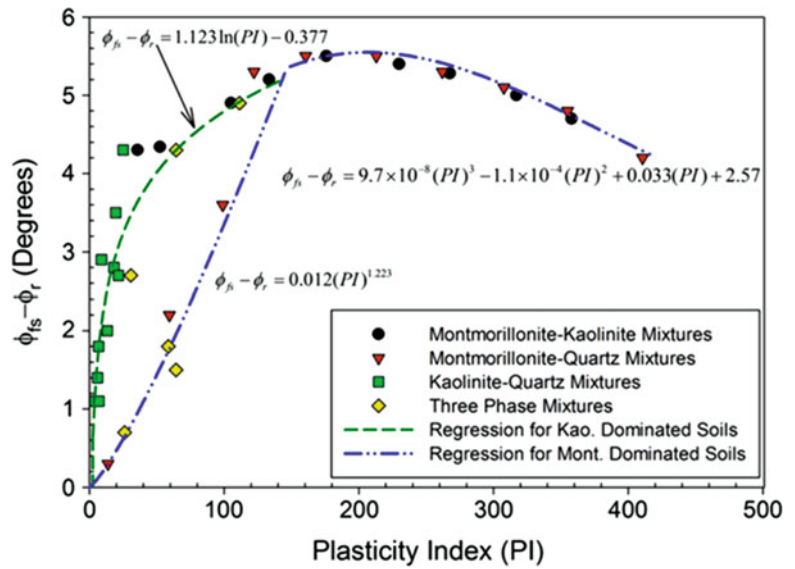


Fig. 64 Correlation from Tiwari and Ajmera (2011) between the differences in the fully softened and residual friction angles as a function of the plasticity index



Let's consider the average friction angles obtained from two methods.

Soil A: Fully Softened Friction Angle: 23.5°
Residual Friction Angle: 20°

Soil B: Fully Softened Friction Angle: 16°
Residual Friction Angle: 14°

Soil A:

Fully Softened shear strength: $100 \tan 23.5^\circ = 43.5 \text{ kPa}$.
Residual shear strength: $100 \tan 20^\circ = 36.4 \text{ kPa}$.

Soil B:

Fully Softened shear strength: $100 \tan 16^\circ = 28.7 \text{ kPa}$.
Residual shear strength: $100 \tan 14^\circ = 24.9 \text{ kPa}$.

Using the true and base friction angle, the fully softened shear strengths for these two soils could be estimated from

the correlations presented by Tiwari et al. (2022) in Figs. 51 and 52. To obtain the fully softened shear strength, the equivalent pre-consolidation pressure will be equal to the effective vertical stress. Thus,

Soil A: $\phi_e = 19^\circ$ and $\phi_c = 7^\circ$

$$\tau = \sigma_{pe} \tan \phi_c + \sigma' \tan \phi_e$$

$$\tau = 100 \tan 7 + 400 \tan 19 = 44.7 \text{ kPa}$$

Soil B: $\phi_e = 15^\circ$ and $\phi_c = 2^\circ$

$$\tau = 100 \tan 2 + 100 \tan 15 = 30.2 \text{ kPa}$$

Values obtained from both methods are very close.

Fig. 65 Correlation from Tiwari and Ajmera (2011) between the differences in the fully softened and residual friction angles normalized by the fully softened friction angle as a function of the liquid limit

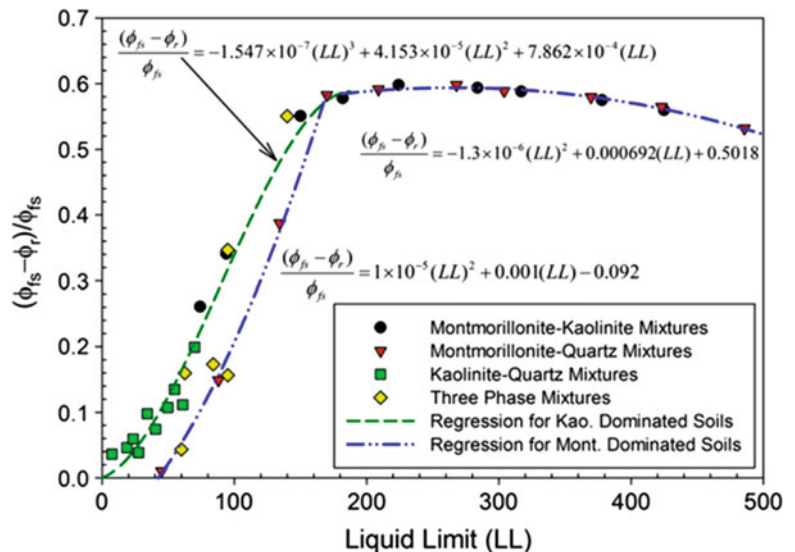
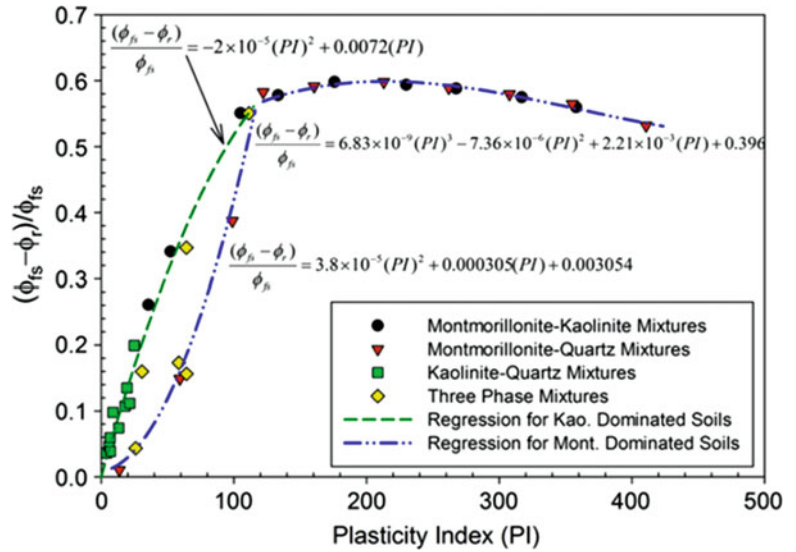


Fig. 66 Correlation from Tiwari and Ajmera (2011) between the differences in the fully softened and residual friction angles normalized by the fully softened friction angle as a function of the plasticity index



Peak Shear Strength

Soil A: The soil with an over-consolidation ratio of 8 and an effective vertical stress of 100 kPa will have a pre-consolidation pressure (σ'_p) of:

$$e_p = 0.88 - 0.05 \log\left(\frac{800}{100}\right) = 0.835$$

Where, e_p is the void ratio of the sample at the pre-consolidation pressure.

$$\sigma'_p = OCR \times \sigma' = 8(100) = 800 \text{ kPa.}$$

$$\text{Now, } C_c = \frac{(e_o - e_p)}{\log\left(\frac{\sigma'_p}{\sigma'_{pe}}\right)}$$

Using the compression and recompression indices, the equivalent pre-consolidation pressure is found as follows:

$$0.28 = \frac{0.88 - 0.835}{\log\left(\frac{800}{\sigma'_{pe}}\right)}$$

$$C_r = \frac{e_o - e_p}{\log\left(\frac{\sigma'_p}{\sigma'}\right)}$$

$$\text{Thus, } \sigma'_{pe} = 552.6 \text{ kPa}$$

$$\text{So, } e_p = e_o - C_r \log\left(\frac{\sigma'_p}{\sigma'}\right)$$

Fig. 67 Correlation from Tiwari and Ajmera (2011) between the differences in the fully softened and residual friction angles normalized by the residual friction angle as a function of the liquid limit

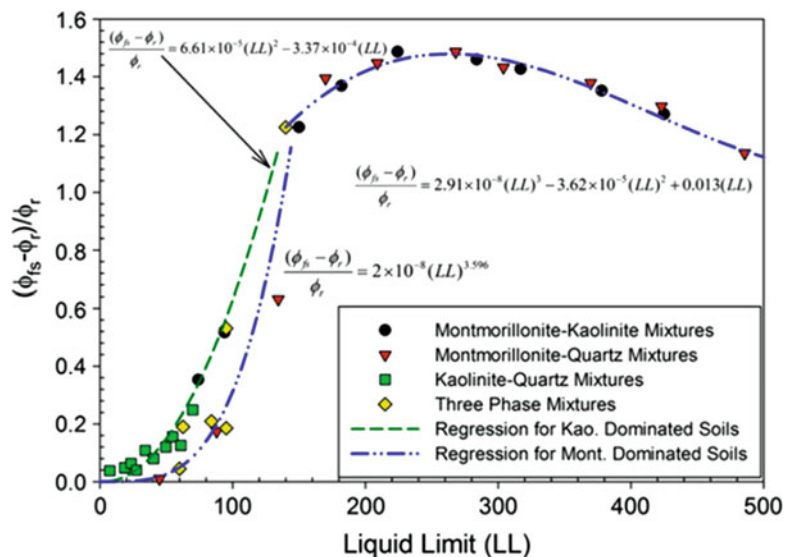
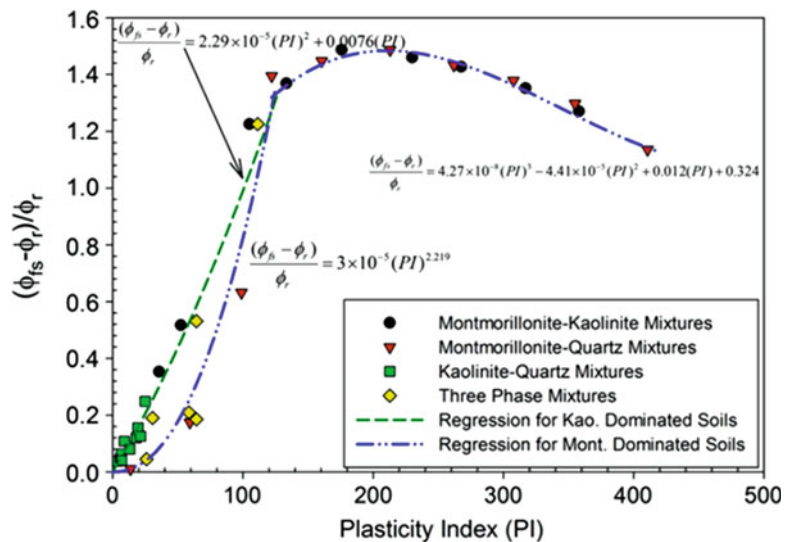


Fig. 68 Correlation from Tiwari and Ajmera (2011) between the differences in the fully softened and residual friction angles normalized by the residual friction angle as a function of the plasticity index



As estimated before, $\phi_e = 19^\circ$ and $\phi_c = 7^\circ$. Thus, the peak shear strength is:

$$\tau = 552.6 \tan 7 + 100 \tan 19 = 102.3 \text{ kPa}$$

$$\text{Soil B : } \sigma'_p = 2(100) = 200 \text{ kPa}$$

$$e_p = 1.30 - 0.08 \log\left(\frac{200}{100}\right) = 1.28$$

$$0.43 = \frac{1.3 - 1.28}{\log\left(\frac{200}{\sigma'_{pe}}\right)}$$

$$\sigma'_{pe} = 63.3 \text{ kPa}$$

As calculated above, $\phi_e = 15^\circ$ and $\phi_c = 2^\circ$. Thus, the peak shear strength will be equal to:

$$\tau = 63.3 \tan 2 + 100 \tan 15 = 29.0 \text{ kPa}$$

From Fig. 50, the normalized undrained strength ratio from a central line can be found to be:

Soil A: 2.7

Soil B: 1.1

Using Fig. 58, the static undrained strength ratios for the normally consolidated consolidations will be:

Soil A: 0.37

Soil B: 0.33

Thus, the peak shear strength can be calculated as:

$$\text{Soil A : } USR_{OCR=8} = Norm.USR \times \frac{S_u}{\sigma'_c}$$

$$USR_{OCR=8} = 2.7(0.37) = 1.00$$

$$\tau = 1.00(100) = 100 \text{ kPa}$$

$$\text{Soil B : } USR_{OCR=2} = 1.1(0.33) = 0.36$$

$$\tau = 0.33(100) = 33 \text{ kPa}$$

Both methods yield similar peak shear strengths.

Cyclic Strength Curves and Post-Cyclic Undrained Shear Strength

The relationship in Fig. 54 would indicate that Soil A has a power function parameter a of 0.28, while that for Soil B is 0.38. Using the correlation in Fig. 56, the power function parameter b can be found to be 0.087 and 0.085 for Soils A and B, respectively. Thus, the cyclic strength curves corresponding to 5% double amplitude shear strain can be drawn using Eq. 24. Specifically, the power functions are going to be:

$$\text{Soil A : } CSR = 0.28N_5^{-0.087}$$

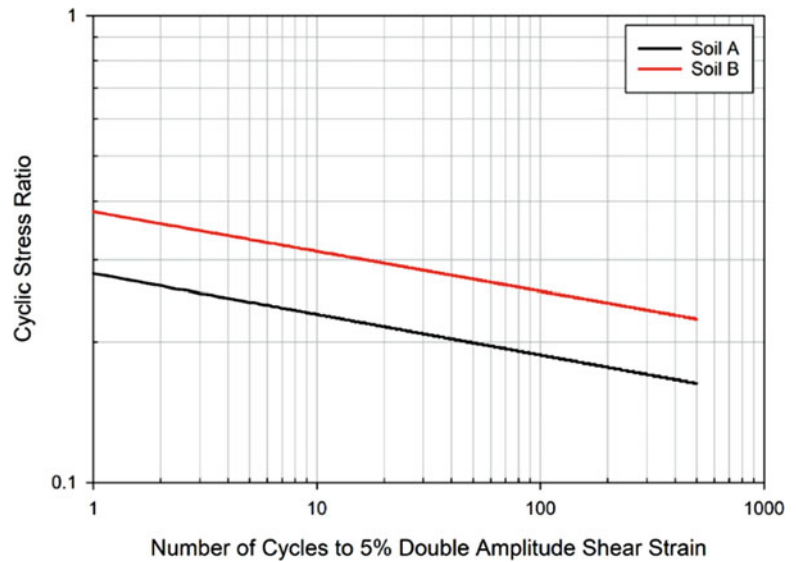
$$\text{Soil B : } CSR = 0.38N_5^{-0.085}$$

The corresponding cyclic strength curves obtained when these equations are plotted are shown in Fig. 69.

The following process can be used to determine the post-cyclic effective stress ratio.

Using Eq. 26, the post-cyclic effective stress ratios would be:

Fig. 69 Cyclic strength curves for hypothetical Soils A and B



Soil A: $PC - ESR = \frac{1}{1-r_u} = \frac{1}{1-0.59} = 2.42$
 Soil B: $PC - ESR = \frac{1}{1-0.18} = 1.23$

Thus, from the correlation presented in Fig. 61,

Soil A: $Norm. USR = (PC - ESR)^{0.753}$
 $Norm. USR = 2.42^{0.753} = 1.94$
 Soil B: $Norm. USR = 1.17^{0.753} = 1.17$

If the undrained strength ratio of both of these two soils prior to the cyclic loads were 0.36, then the post-cyclic undrained strength ratio would be equal to:

Soil A: $\frac{s_{u,pc}}{\sigma_{pc}} = Norm. USR \times USR$
 $\frac{s_{u,pc}}{\sigma_{pc}} = 1.94 \times 0.36 = 0.70$
 Soil B: $\frac{s_{u,pc}}{\sigma_{pc}} = 1.17 \times 0.36 = 0.42$

Now, $\sigma'_{pc} = \sigma' - u = \sigma'(1 - r_u)$. Thus, the effective vertical stress immediately following the application of the cyclic loading is:

Soil A: $\sigma'_{pc} = 400(1 - 0.59) = 164 \text{ kPa}$
 Soil B: $\sigma'_{pc} = 50(1 - 0.18) = 41 \text{ kPa}$

Using this, the post-cyclic undrained shear strength can be calculated as:

Soil A: $s_{u, pc} = 0.70(164) = 114.8 \text{ kPa}$
 Soil B: $s_{u, pc} = 0.42(41) = 17.22 \text{ kPa}$.

These results indicate that there was a degradation in the undrained shear strength since the static undrained shear strengths were:

Soil A: $s_u = 0.36(400) = 144 \text{ kPa}$
 Soil B: $s_u = 0.36(50) = 18 \text{ kPa}$.

The degradations ratios associated with these two soils are:

Soil A: $\delta = \frac{s_{u,pc}}{s_u} = \frac{114.8}{144} = 0.80$
 Soil B: $\delta = \frac{17.22}{18} = 0.96$

Degradation ratios indicate that Soil A experienced a 20% reduction in shear strength as a result of the cyclic loading. On the other hand, the cyclic loading only caused a 4% reduction in the shear strength in Soil B.

Using the relationship in Fig. 60, the degradation ratios would be:

Soil A: 0.84
 Soil B: 0.94

These values are similar to those obtained above using the other method.

8 Summary and Recommendations

Landslides pose catastrophic consequences, resulting in loss of life, property damage, and disruption of communities. Natural factors like heavy rainfall, snowmelt, and groundwater fluctuations induce water saturation, triggering landslides. Earthquakes heighten landslide risks through shaking, liquefaction, and the formation of landslide dams that can lead to flooding. Volcanic activity also contributes to devastating landslides, such as volcanic debris flows and structural collapses. Furthermore, human activities like altering drainage patterns, destabilizing slopes, and removing vegetation

exacerbate landslide occurrences. The effects of landslides are also exacerbated in various regions. For example, mountainous regions face higher mortality risks, while countries with limited resources experience greater economic losses. Furthermore, these natural disasters have far-reaching environmental and societal impacts, including landscape alteration, vegetation destruction, ecosystem disruption, and water pollution from sediment and debris. Landslides displace residents, jeopardize livelihoods, and instigate social and economic instability. Infrastructure damage impedes transportation, communication, and access to vital services. Understanding landslides is pivotal for implementing proactive measures that mitigate risks and enhance resilience, safeguarding the well-being of communities.

The shear strength of soils is a crucial factor in analyzing slope stability and implementing measures to mitigate risks. Shear strength refers to the internal resistance of soil to shearing forces, which is influenced by factors such as friction between soil particles, interlocking of grains, electromagnetic attraction, over-consolidation effects, density, overburden pressure, grain shape, roughness, and stress history. During shearing, soils exhibit different behaviors, including elastic behavior, peak shear strength, post-peak strength loss, and fully softened shear strength. The fully softened shear strength occurs when changes in water content cause a reduction in shear strength as the soil approaches its critical state. Continued shearing can lead to particle reorientation and the formation of polished slickenside surfaces, resulting in the residual shear strength. The shear strength of soil is typically represented using the Mohr-Coulomb failure criteria.

In addition to shear strength parameters under static conditions, the resistance of soil to cyclic loads is essential for slope stability analysis in seismic regions. Cyclic strength curves, representing the number of cycles to failure against cyclic stress ratio, provide information on the ability of a soil mass to withstand cyclic loading. Furthermore, knowledge of the post-cyclic undrained shear strength is also necessary to evaluate slope stability after cyclic loading. Different soil properties are required for stability analysis depending on conditions, including end-of-construction, multistage loading, and long-term analysis, as well as for free-draining and impermeable materials. The recommended parameters of each of these conditions and types of soils were summarized in this paper.

Direct shear tests are commonly used to measure the shear strengths of soils under drained conditions. These tests are widely available, easy to run and interpret, and relatively quick. However, the shear strength is always measured on the horizontal shearing plane, which may not be the weakest plane and can result in an overestimate of the shear strength. Direct shear tests can measure the peak, fully softened, and residual shear strengths of soil. ASTM D3080/D3080M

provides details and specifications for conducting direct shear tests.

Triaxial tests are another commonly used method for measuring shear strength. These tests can measure both peak and fully softened shear strengths using consolidated drained (CD) and consolidated undrained (CU) triaxial tests. CD testing of low permeability clays may be time-consuming due to back pressure saturation requirements. ASTM D7181 provides specifications for CD triaxial tests, while ASTM D4767 outlines procedures for CU triaxial tests.

Ring shear tests have emerged as the preferred method for quantifying residual shear strength. These tests allow continuous shearing of samples in a single direction while maintaining a consistent cross-sectional area, closely replicating residual conditions. The non-uniform stress distribution across annular samples used in ring shear tests can pose challenges. Different variations of the ring shear device have been developed, each with its own advantages and disadvantages. ASTM D6467 provides detailed procedures for conducting ring shear tests to measure the residual shear strength of cohesive soils.

Direct simple shear tests offer advantages compared to direct shear and triaxial tests. They allow the sample to fail along its weakest plane while the cross-sectional area remains constant throughout the shearing process. These tests require smaller soil samples and shorter consolidation times. However, the commercial availability of direct simple shear devices is currently limited. ASTM D6528 provides guidelines for conducting direct simple shear tests.

A number of correlations for the fully softened shear strength are available in the literature. The key ones were summarized in this paper. These correlations provided insights into the impact of clay mineralogy. In particular, it was seen that significant differences in the fully softened friction angles between different clay mineral mixtures existed, even at a constant clay content. Furthermore, the correlations between the fully softened friction angle and the plasticity index or the liquid limit should be utilized in practice. If mineralogical compositions are not available, soil activity information should be used to identify whether the soil is montmorillinitic or kaolinitic (or illitic) from a mineralogical point of view.

The impact of pore fluid chemistry on fully softened shear strength was also presented in this paper. Correlations developed for soils with different pore fluids make it possible to estimate the fully softened friction angle in terms of the plasticity index or the liquid limit. Additionally, variations in the fully softened friction angle observed in soils with different pore fluid chemistries could be attributed to the impacts of these pore fluids on the plasticity characteristics of the soil mass.

Tiwari and Marui (2003) conducted a comprehensive study on the influence of clay mineralogy on residual friction

angles. They found that the presence of kaolin had a significant effect on the residual friction angle, particularly when kaolin content was less than 10%. However, for soils with high sand and bentonite content, the residual friction angle remained nearly constant regardless of kaolin content.

The correlations based on liquid limit and plasticity index developed by Tiwari and Marui (2005) take into account the mineralogical composition of the soil mass. They showed that the residual friction angle of soils with kaolin was higher than that of soils containing bentonite, even with similar liquid limits or plasticity indices. They also noted that for soils with liquid limits or plasticity indices exceeding 200, the residual friction angle reached a minimum value of 3.7° .

The SHANSEP method allows for the estimation of undrained shear strength considering the over-consolidation ratio. This method was extended by Ajmera et al. (2018) with the introduction of the normalized undrained strength ratio. They revealed that mixtures of montmorillonite with quartz have higher ratios than mixtures of kaolinite with quartz.

The shear strength parameters in the Mohr-Coulomb failure criteria are influenced by stress history, with over-consolidated clays showing a non-zero cohesion intercept and varying friction angles. Tiwari et al. (2022) provided correlations to estimate the true and base friction angles from the plasticity index, finding that the true friction angle remained constant at 10° for soils with high plasticity indices, while the base friction angle varied with clay mineral composition. In the mixtures of montmorillonite-quartz, the base friction angle could be taken to be constant at a value of 2° .

Correlations presented by Ajmera et al. (2017) allow for the estimation of the curve fitting parameters a and b based on liquid limit or plasticity index to calculate the cyclic resistance of a soil mass. Increasing liquid limit generally increases the value of a for soils with liquid limits below 100 indicating higher cyclic resistance. However, for liquid limits above 100, a decreases. The behavior of parameter b varies with clay mineral type. For kaolinite, b increases with liquid limit and plasticity index, while for montmorillonite, b decreases. Dissipation of excess pore pressure between cyclic loads influences cyclic resistance, with increased dissipation leading to higher cyclic resistance.

Ajmera et al. (2019) provided correlations to estimate the post-cyclic undrained shear strength and introduced the normalized undrained strength ratio. The normalized undrained strength ratio is calculated by normalizing the post-cyclic undrained strength ratio by the undrained strength ratio. As the post-cyclic effective stress ratio increases, the normalized undrained strength ratio also increases. This correlation was found to capture the post-cyclic undrained shear strength after two sets of cyclic loads and thus, could consider the dissipation of excess pore pressure and the effects of the second cyclic load.

References

- Achu AL, Joseph S, Aju CD, Mathai J (2020) Preliminary analysis of a catastrophic landslide event on 6 august 2020 at Pettimudi, Kerala state, India. *Landslides* 18:1459–1463
- Airey DW, Wood DM (1987) An evaluation of direct simple shear tests on clay. *Géotechnique* 37(1):25–35
- Ajmera B, Tiwari B, Pantha K (2016) Mineralogical effect on idealized, normalized strength curves for over-consolidated clays. *Proceedings of the Geotechnical and Structural Engineering Congress 2016: 1532–1539*
- Ajmera B, Tiwari B (2021) Recent advances in the methods of slope stability and deformation analyses. In: *Understanding and reducing landslide disaster risk, WLF2020, ICL contribution to landslide disaster risk reduction, vol 4*, pp 81–108
- Ajmera B, Brandon T, Tiwari B (2017) Influence of index properties on shape of cyclic strength curve for clay-silt mixtures. *Soil Dyn Earthq Eng* 102:46–55
- Ajmera B, Brandon T, Tiwari B (2019) Characterization of the reduction in undrained shear strength in fine-grained soils due to cyclic loading. *J Geotech Geoenviron* 145(5):04019017
- Ajmera B, Tiwari B, Al-Behadili M (2018) Effect of normalization on developing shansep based undrained shear strengths of fine-grained Soils. In: *Proceedings of the 2018 International Foundations Conference and Equipment Expo, vol 295. Geotechnical Special Publication*, pp 229–236
- Ajmera B, Tiwari B, Iqbal MS, Meeks T (2021) Experimental evaluation of shear strength fluctuations of clayey soils due to multiple cyclic loads. In: *Proceedings of the 20th International Conference on Soil Mechanics and Geotechnical Engineering, vol 2*, pp 9–14
- Anayi JT, Boyce JR, Rogers CDF (1989) Modified Bromhead ring shear apparatus. *Geotech Test J* 12(2):171–173
- Andersen KH, Brown SF, Foss J, Pool JH, Rosenbrand WF (1976) Effect of cyclic loading on clay behaviour. *Norw Geotech Inst Publ* 113:1–6
- ASTM D3080/3080M (2011) Standard test method for direct shear test of soils under consolidated drained conditions. *ASTM International*
- ASTM D4767 (2020) Standard test method for consolidated undrained triaxial compression test for cohesive soils. *ASTM International*
- ASTM D5311/D5311 (2013) Standard test method for load controlled cyclic triaxial strength of soil. *ASTM International*
- ASTM D6467 (2013) Standard test method for torsional ring shear test to determine drained residual shear strength of cohesive soils. *ASTM International*
- ASTM D6528 (2017) Standard test method for consolidated undrained direct simple shear testing of fine grain soils. *ASTM International*
- ASTM D7181 (2020) Standard test method for consolidated drained Triaxial compression test for soils. *ASTM International*
- Barden L, McDermott RJW (1965) Use of free ends in Triaxial testing of clays. *J Soil Mech Found Div* 91(6):1–23
- Baruah S, Dey C, Sanoujam M (2023) Preliminary account on the 20th June 2022 Tupul, Manipur landslide of Northeast India. *Landslides*:1–6
- Bishop AW, Henkel DJ (1962) *The measurement of soil properties*. Edward Arnold Publishers
- Bishop AW, Green GE, Garga VK, Andersen A, Brown JD (1971) A new ring shear apparatus and its application to the measurement of residual strength. *Géotechnique* 21:273–328
- Bjerrum L, Landva A (1966) Direct simple-shear tests on a Norwegian quick clay. *Géotechnique* 16(1):1–20
- Borden RH, Putrich SF (1986) Drained-strength parameters from direct shear tests for slope stability analyses in Overconsolidated fissured residual soils. *Transp Res Rec* 1089:102–113

- Boucek B (1977) Ring shear tests on clay, vol 3. Publication of the Institute for Foundation Engineering, Soil Mechanics, Rock Mechanics, and Water Ways Construction, pp 7–41
- Bray JD, Sancio RB (2006) Assessment of the liquefaction susceptibility of fine-grained soil during the Loma Prieta earthquake. *J Geotech Geoenviron* 132(9):1165–1177
- Bromhead EN (1979) A simple ring shear apparatus. *Ground Eng* 12(5): 40–44
- Bromhead EN (1992) *Stability of slopes*, 2nd edn. Surrey University Press
- Bromhead EN, Harris AJ, Ibsen ML (1999) Statistical variability of ring shear test results on a shear zone in London clay. In: *Proceedings of the International Symposium on Slope Stability Engineering*, vol 2, pp 1109–1114
- Brown SF, Andersen KH, McElvaney J (1977) The effect of drainage on cyclic loading of clay. In: *Proceedings of the 9th International Conference on Soil Mechanics and Foundation Engineering*, vol 2, pp 195–200
- Cancelli A (1977) Residual shear strength and stability analysis of a landslide in fissured Overconsolidated clays. *Bull Int Assoc Eng Geol* 16:193–197
- Castellanos BA, Brandon TL (2013) A comparison between the shear strength measured with direct shear and triaxial devices on undisturbed and remolded soils. In: *Proceedings of the 18th International Conference on Soil Mechanics and Geotechnical Engineering*, pp 317–320
- Castellanos BA, Brandon TL (2019) Fully softened shear strength: application, measurement, and correlations. In: *Geotechnical Engineering in the XXI Century: Lessons Learned and Future Challenges*
- Castellanos BA, Brandon TL, Vanden Berge DR (2016) Correlations for fully softened shear strength parameters. *Geotech Test J* 39(4): 568–581
- Chandler RJ (1966) The measurement of residual strength in Triaxial compression. *Géotechnique* 16(3):181–186
- Cheng D, Cui Y, Su F, Jia Y, Choi CE (2018) The characteristics of the Mocoa compound disaster event, Colombia. *Landslides* 15:1223–1232
- Coe JA, Baum RL, Allstadt K, Kochevar BF, Schmitt RG, Morgan ML, White JL, Stratton BT, Hayashi TA, Kean JW (2015) Forensic Analysis of the May 2014 West Salt Creek Rock Avalanche in Western Colorado. In: *AGU Fall Meeting Abstracts*, NH34A-07
- Collotta T, Cantoni R, Pavesi U, Ruberl E, Moretti PC (1989) A correlation between residual friction angle, gradation and the index properties of cohesive soils. *Géotechnique* 39(2):343–346
- Coulomb CB (1776) *Essai sur une application des regles de Maximums et Minimums à quelques Problèmes de Statique, relatifs à l'Architecture*. *Memoires de Mathematique et de Physique*, à l'Academie Royale des Sciences 3(38)
- Davis RO, Berrill JB (1982) Energy dissipation and seismic liquefaction in sands. *Earthq Eng Struct Dyn* 10(1):59–68
- Dewhurst DN, Clennell MB, Brown KM, Westbrook G, K. (1996) Fabric and hydraulic conductivity of sheared clays. *Géotechnique* 46(4):761–768
- Duncan JM, Brandon TL, Vanden Berge DR (2011) *Report of The Workshop on Shear Strength for Stability of Slopes in Highly Plastic Clays*. Center for Geotechnical Practice and Research, CGPR Report #67, Virginia Polytechnic Institute and State University
- Dyvik R, Berre T, Lacasse S, Raadim B (1987) Comparison of truly undrained and constant drained simple shear tests. *Géotechnique* 37: 3–10
- Eid HT (1996) *Drained shear strength of stiff clays for slope stability analyses.* Ph.D. Dissertation., University of Illinois at Urbana-Champaign
- Eid HT, Rabie KH (2016) Fully softened shear strength for soil slope stability analyses. *Int J Geomech* 17(1):04016023 1-10
- Eid HT, Rabie KH, Wijewickreme D (2016) Drained residual shear strength at effective Normal stresses relevant to soil slope stability analyses. *Eng Geol* 204:94–107
- Ering P, Sivakumar Babu GL (2016) Probabilistic Back analysis of rainfall induced landslide—a case study of Malin landslide, India. *Eng Geol* 208:154–164
- Fan C, Xu Q, Scaringi G, Dai L, Li W, Dong X, Zhu X, Pei X, Dai K, Havenith H-B (2017) Failure mechanism and kinematics of the deadly June 24th 2017 Xinmo landslide, Maoxian, Sichuan, China. *Landslides* 14(6):2129–2146
- Finn WDL, Pickering DJ, Bransby PL (1971) Sand liquefaction in Triaxial and simple shear Tests. *J Soil Mech Found Div* 97(4): 639–659
- Fukuoka H, Sassa K, Wang C (2015) August 2014 Hiroshima landslide disaster and its societal impact. In: *EGU General Assembly Conference Abstracts*, vol 6691
- Gauthier D, Anderson SA, Fritz HM, Giachetti T (2017) Karrat Fjord (Greenland) Tsunamiogenic landslide of 17 June 2017: initial 3D observations. *Landslides* 15:327–332
- Gibo S (1985) The ring shear behavior and residual strength. In: *Proceedings of the 4th International Conference and Field Workshop on Landslides*, pp 283–288
- Harris AJ, Watson PDJ (1997) Optimal procedure for the ring shear test. *Ground Eng*:26–28
- Hawkins AB, Privett KD (1985) Measurement and use of residual shear strength of cohesive soils. *Ground Eng*:22–29
- Hilbert G, Ekström G, Stark CP (2014) Dynamics of the Bingham canyon mine landslides from seismic signal analysis. *Geophys Res Lett* 41:4535–4541
- Hvorselv MJ (1939) Torsion shear tests and their place in the determination of the shearing resistance of soils. *Ground Eng* 18(8):22–29
- Hvorslev MJ (1960) Physical components of the shear strength of saturated clays. In: *Proceedings of the Shear Strength Conference*, pp 169–273
- Ishihara K, Troncoso J, Kawase Y, Takahashi Y (1980) Cyclic strength characteristics of tailings materials. *Soils Found* 20(4):127–142
- Kanji MA (1974) The relationship between drained friction angles and Atterberg limits of natural soils. *Géotechnique* 24(4):671–674
- Kanji MA, Wolle CM (1977) Residual strength—new testing and microstructure. In: *Proceedings of the 9th International Conference on Soil Mechanics*, vol 1, pp 153–154
- Ladd CC, Foott R (1974) New design procedure for stability of soft clays. *J Geotech Eng* 100(7):763–786
- Ladd CC, Foott R, Ishihara K, Schlosser F, Poulos HG (1977) Stress-deformation and strength characteristics. In: *Proceedings of the 9th International Conference on Soil Mechanics and Foundation Engineering*, pp 421–494
- LaGatta DP (1970) Residual strength of clays and clay-shales by rotation shear tests. *Harvard Soil Mechanics Series* 86
- Lin YN, Park E, Wang Y, Quek YP, Lim J, Alcantara E, Loc HH (2021) The 2020 Hpakant jade mine disaster, Myanmar: a multi-sensor investigation for slope failure. *ISPRS J Photogramm Remote Sens* 177:291–305
- Lupini JF, Skinner AE, Vaughan PR (1981) The drained residual strength of cohesive soils. *Géotechnique* 31(2):181–213
- Meehan CL, Tiwari B, Brandon TL, Duncan JM (2011) Triaxial shear testing of polished Slickensided surfaces. *Landslides* 8:449–458
- Mesri G, Abdel-Ghaffar MEM (1993) Cohesion intercept in effective stress-stability analysis. *J Geotech Eng* 119(8):1229–1249
- Mesri G, Cepeda-Diaz AF (1986) Residual shear strength of clays and shales. *Géotechnique* 36(2):269–274
- Mohr O (1900) Welche Umstände Bedinge die Elastizitätsgrenze und den Bruch eines Materiales? *Zeitschrift des Vereines Deutscher Ingenieure* 44(1524–1530):1572–1577

- Moon AT (1984) Effective shear strength parameters for stiff fissured clays. In: Proceedings of the 4th Australia-New Zealand Conference on Geomechanics, pp 107–111
- Müller-Vonmoss M, Løken T (1989) The shearing behavior of clays. *Appl Clay Sci* 4:125–141
- NASA Earth Observatory (2022) Sizing up the landslide at bingham canyon mine. NASA Earth Observatory. Retrieved from: <https://earthobservatory.nasa.gov/images/81364/sizing-up-the-landslide-at-bingham-canyon-mine>
- Ritchie H, Rosado P, Roser M (2022) Natural disasters. *OurWorldInData.org*. Retrieved from: <https://ourworldindata.org/natural-disasters>
- Robbins JC, Petterson MG, Mylne K, Espi JO (2012) Tumbi landslide, Papua New Guinea: rainfall induced? *Landslides* 10:673–684
- Saleh AA, Wright SG (2005) Shear strength correlations and remedial measure guidelines for long-term stability of slopes constructed of highly plastic clay soils. Center for Transportation Research, University of Texas at Austin
- Seed HB, Peacock WH (1971) Test procedures for measuring soil liquefaction characteristics. *J Soil Mech Found Div* 97(8): 1099–1119
- Shrestha BB, Nakagawa H (2016) Hazard assessment of the formation and failure of the Sunkoshi landslide dam in Nepal. *Nat Hazards* 82: 2029–2049
- Silver ML, Chan CK, Ladd RS, Lee KL, Tiedemann DA, Townsend FC, Valera JE, Wilson JH (1976) Cyclic Triaxial strength of standard test sand. *J Geotech Eng Div* 102(5):511–523
- Skempton AW (1964) Long-term stability of clay slopes. *Géotechnique* 14(2):77–102
- Skempton AW (1970) First-time slides in over-consolidated clays. *Géotechnique* 20(3):320–324
- Skempton AW, Petley DJ (1967) The strength along structural discontinuities in stiff clays. *Geotechnical Conference*:29–46
- Song B, Yasuhara K, Santoshi M (2004) Direct simple shear testing of post-cyclic degradation in stiffness of nonplastic silt. *ASTM Geotechnical Test J* 27(6):1–7
- Stark TD, Eid HT (1993) Modified Bromhead ring shear apparatus. *Geotech Test J* 16(1):100–107
- Stark TD, Eid HT (1994) Drained residual strength of cohesive soils. *J Geotech Eng* 120(5):856–871
- Stark TD, Eid HT (1997) Slope stability analyses in stiff fissured clays. *J Geotech Geoenviron* 123(4):335–343
- Stark TD, Fernandez R (2019) Fully softened shear strength measurement and correlations. *Geotech Test J* 43:20190124
- Stark TD, Hussain M (2015) Empirical correlations: drained shear strength for slope stability analyses. *J Geotech Geoenviron* 139(6): 853–862
- Stark TD, Choi H, McCone S (2005) Drained shear strength parameters for analysis of landslides. *J Geotech Geoenviron* 131(5):575–588
- Steward HE, Cripps JC (1983) Some engineering implications of chemical weathering of pyritic shale. *Q J Eng Geol* 16:281–289
- Tan Q, Sassa K, Dang K, Konagai K, Karunawardena A, Bandara RMS, Tang H, Soto G (2020) Estimation of the past and future landslide hazards in the neighboring slopes of the 2016 Aranayake landslide, Sri Lanka. *Landslides* 17:1727–1738
- Tika TE, Hutchinson JN (1999) Ring shear tests on soil from the vaiont landslide slip surface. *Géotechnique* 49(1):59–74
- Tiwari B, Ajmera B (2011) A new correlation relating the shear strength of reconstituted soil to the proportions of clay minerals and plasticity characteristics. *Appl Clay Sci* 53(1):48–57
- Tiwari B, Ajmera B (2014) Curvature of failure envelopes for normally consolidated clays. In: Proceedings of the Third World Landslide Forum—Landslide Science for a Safer Geo-environment, vol 2, pp 117–122
- Tiwari B, Ajmera B (2015) Reduction in fully softened shear strength of natural clays with NaCl leaching and its effect on slope stability. *J Geotech Geoenviron* 141(1):04014086 1-10
- Tiwari B, Marui H (2003) Estimation of residual shear strength for bentonite-kaolin-Toyouura sand mixture. *J Jpn Landslide Soc* 40(2): 124–133
- Tiwari B, Marui H (2004) Objective oriented multistage ring shear test for shear strength of landslide soil. *J Geotech Geoenviron* 130(2): 217–222
- Tiwari B, Marui H (2005) A new method for the correlation of residual shear strength of the soil with mineralogical composition. *J Geotech Geoenviron* 131(9):1139–1150
- Tiwari B, Ajmera B, Al-Behadili M, Mohammed M (2022) True and base friction angles of clays. In: Proceedings of GeoCongress 2022, Geotechnical Special Publication, vol 333, pp 56–64
- Tiwari B, Ajmera B, Gonzalez A, Sonbol H (2020a) Impact of wildfire on triggering mudslides—a case study of the 2018 Montecito debris flows. In: Proceedings of Geo-Congress 2020, Geotechnical Special Publication, vol 316, pp 40–49
- Tiwari B, Padgett J, Ajmera B, Bieda A (2020b) Effect of mineralogical composition and pore water chemistry on shearing rate dependent residual shear strength of soil. In: Proceedings of Geo-Congress 2020, Geotechnical Special Publication, vol 317, pp 332–340
- Toyota H, Nakamura K, Sugimoto M, Sakai N (2009) Ring shear tests to evaluate strength parameters in various Remoulded soils. *Géotechnique* 59(8):649–659
- UNDRR (2019) Global assessment report on disaster risk reduction 2019. United Nations Office for Disaster Risk Reduction
- Voight B (1973) Correlation between Atterberg plasticity limits and residual shear strength of natural soils. *Géotechnique* 23(2):265–267
- Vucetic M (1988) Normalized behavior of offshore clay under uniform cyclic loading. *Can Geotech J* 25:33–41
- Wartman J, Montgomery DR, Anderson SA, Keaton JR, Benoit J, dela Chapelle, J. and Gilbert, R. (2016) The 22 march 2014 Oso landslide, Washington, USA. *Geomorphology* 253:275–288
- Watry SM, Lade PV (2000) Residual shear strengths of bentonites on Palos Verdes Peninsula, California. *Proceedings of Geo-Denver* 2000:323–342
- Wright SG (2005) Evaluation of soil shear strengths for slope and Retaining Wall stability analyses with emphasis on high plasticity clays.,” Report No. FHWA/TC-06/5-1874-01-1., Federal Highway Administration
- Wright SG, Zornberg JG, Aguetant E (2007) The fully softened shear strength of high plasticity clays.,” Research Report FHWA/TX-07/0-5202-3., University of Texas at Austin
- Yang H, Xia J, Thompson JR, Flower RJ (2017) Urban construction and demolition waste and landfill failure in Shenzhen, China. *Waste Manag* 63:393–396
- Zhang J, Gurung DR, Liu R, Murthy MSR, Su F (2015) Abe Berek landslide and landslide susceptibility assessment in Badakhshan Province, Afghanistan. *Landslides* 12:597–609
- Zhang S, Wang F, Li R (2022) First insight into the catastrophic Atami debris flow induced by a rain gush on 3 July 2021 in Shizuoka, Japan. *Landslides* 19(2):527–532
- Zhang Y, Chen N, Liu M, Wang T, Deng M, Wu K, Khanal BR (2019) Debris flows originating from colluvium deposits in hollow regions during a heavy storm process in Taining, southeastern China. *Landslides* 17:335–347

Open Access This chapter is licensed under the terms of the Creative Commons Attribution 4.0 International License (<http://creativecommons.org/licenses/by/4.0/>), which permits use, sharing, adaptation, distribution and reproduction in any medium or format, as long as you give appropriate credit to the original author(s) and the source, provide a link to the Creative Commons license and indicate if changes were made.

The images or other third party material in this chapter are included in the chapter's Creative Commons license, unless indicated otherwise in a credit line to the material. If material is not included in the chapter's Creative Commons license and your intended use is not permitted by statutory regulation or exceeds the permitted use, you will need to obtain permission directly from the copyright holder.





Rock Avalanches in the Tibetan Plateau of China

Yufeng Wang, Qiangong Cheng, Qiwen Lin, Anwen Shi, Jie Ming, Zhiyi Feng, and Zhang Song

Abstract

China is a country with high mountainous areas widely distributed, which is characterized by high reliefs, intensive tectonic activity, fragile ecological environments, etc. Under such particular background, rock avalanches, as one of the most threatening geological disasters in the high mountainous regions, have drawn much scientific interest because of their sudden occurrence, huge volumes ($>10^6 \text{ m}^3$), high velocities ($>20 \text{ m/s}$), and extremely low *Fahrböschung* (typically 0.1 to 0.3) with destructive disasters caused. Focusing on the Tibetan Plateau of China, spatial distribution of rock avalanches in its certain area was conducted, hoping to provide insights into the controlling factors of rock avalanches' formation. Furthermore, several typical rock avalanches were investigated in detail based on remote sensing analysis, mapping of fixed wing unmanned aerial vehicle and detailed field investigations. It is reached that *toreva* blocks, transverse and longitudinal ridges, ridges separated by conjugate troughs, and hummocks are common and widely distributed surficial landforms in rock avalanche deposits, which usually display in a clear sequential distribution. In the cross-section, a series of internal sedimentary structures, including jigsaw structures, inner shear zones, diapiric structures, convoluted laminations, faults, etc., were identified. Based on these detailed geological features, the possible emplacement processes and mechanisms are discussed to provide insights into the extremely high mobility of rock avalanches.

Keywords

China · Rock avalanche · Spatial distribution · Surficial landforms · Internal sedimentary · Emplacement mechanism

1 Introduction

In the past 20 years, the occurrence of rock avalanches has significantly increased due to the effects of climate warming, frequent seismic activities, glacier retreat, and increasing human activities in mountainous areas, which has attracted increasing scientific attention due to their ability to produce catastrophic effects (Dunning et al. 2007; Catane et al. 2008; Sun et al. 2011; Huang et al. 2012; Barth 2014; Fan et al. 2017; Strom and Abdrakhmatov 2018; Zhu et al. 2019; Friele et al. 2020). Controlled by their large volumes ($>1 \times 10^6 \text{ m}^3$), extremely high velocities ($>20 \text{ m/s}$) and long runouts ($>1 \text{ km}$), such geological events often affect human activities and property suddenly without warning, and can cause disasters (Legros 2002; Evans et al. 2007; Hewitt et al. 2008; Guthrie et al. 2012; Pudasaini and Miller 2013; Delaney and Evans 2014; Lucas et al. 2014; Ostermann and Sanders 2017; Zhang et al. 2020). A typical example of such disaster is the Nevados Huascarán ice-rock avalanche, which occurred in the Peruvian Andes on 31 May 1970. The detached masses fragmented greatly in propagation and transformed into a debris avalanche with a volume and average velocity of up to 10^8 m^3 and 77.8 m/s , respectively, which buried the whole Yungay city in the downstream and killed over 18,000 people (Plafker and Ericksen 1978). Another typical example is the Chamoli ice-rock avalanche occurred in 7 February 2021 in India. The area where the Chamoli ice-rock avalanche occurred is situated in the Himalayan orogeny of the Tibetan Plateau. In this case, $\sim 23 \times 10^6 \text{ m}^3$ of the detached ice and rock travelled downstream rapidly along the Rontigad valley and fragmented intensively. When it arrived at the Rishi Ganga valley, it

Y. Wang · Q. Cheng (✉) · Q. Lin · A. Shi · J. Ming · Z. Feng
Department of Engineering Geology, Southwest Jiaotong University,
Chengdu, China
e-mail: wangyufeng@home.swjtu.edu.cn; chengqiangong@swjtu.edu.cn;
linqiwen@my.swjtu.edu.cn; shianwen@my.swjtu.edu.cn;
mingjie@my.swjtu.edu.cn; Zhiyifeng@my.swjtu.edu.cn

Z. Song
China Railway Eryuan Engineering Group Co.ltd, Chengdou, China

formed a short-lived landslide dam 46 m thick and 800 m long. After then, the dam failed with a flood disaster chain formed, causing the damages of two hydropower stations and influencing many people, with the economic losses being over 15 billion rupees (Kropáček et al. 2021).

To illustrate the hypermobility of rock avalanches, some hypotheses have been proposed, such as air cushion (Shreve 1968), frictional-thermal related mechanisms (Habib 1975; He et al. 2015; Wang et al. 2017; Hu et al. 2019), acoustic fluidization (Melosh 1978; Johnson et al. 2016), entrainment (Hung and Evans 2004; Iverson and Ouyang 2015; Aaron and McDougall 2019), dynamic fragmentation (Davies and McSaveney 2009), and self-excited vibration (Wang et al. 2015). Moreover, important research efforts focusing on field investigations (Weidinger et al. 2014; Iverson et al. 2015; Dufresne et al. 2016; Wang et al. 2018; Dufresne and Geertsema 2020; Shi et al. 2023), laboratory experiments (Iverson et al. 2004; Shea and van Wyk de Vries 2008; Manzella and Labiouse 2013; Iverson 2015; Wang et al. 2016; Pudasaini and Jaboyedoff 2020), and numerical simulations (Pudasaini and Hutter 2007; Cagnoli and Piersanti 2015; Mergili et al. 2018) have also been conducted to gain better understanding of the hypermobility of rock avalanches. However, due to the destructive capacity of rock avalanches, it is still hard to obtain effective geological evidences during the high speed movement of rock avalanches. The kinematics and dynamics of rock avalanches are still unclear and need further study.

In China, the proportion of mountainous areas in the total area of the country is up to 69% with rock avalanches commonly developed. It is reported that the number of rock avalanches occurred in 2001–2020 is up to 74 only in the western mountainous area with more than 4000 people being killed and the direct economic losses being up to tens of billions RMB. The west mountainous areas in China is one part of the Tibetan Plateau, which is the largest area with high mountainous morphologies developed with most rock avalanches occurred in this region. Therefore, considering the particularity of the geological environment of the Tibetan Plateau in China and the common distribution of rock avalanches, we focused on this area with a series of rock avalanches being studied in the past 10 years. Based on our previous works, the Himalayan Mountains of the Tibetan Plateau in China was firstly selected as a studied area with the spatial distribution of rock avalanches is presented. Then, several typical rock avalanches in the Tibetan Plateau of China were introduced in detail, hoping to provide enough field evidence that could be used in further analogue and numerical modeling of rock avalanches.

2 Geological Setting of the Studied Area

The studied area is situated in the Tibetan Plateau. For the Tibetan Plateau, it is one the youngest and highest mountainous region in the world, which is featured by a wide variety of geologies, geomorphologies, and climates. For the evolution of the Tibetan Plateau, it is formed at ~55 Ma resulted by the intensive and ongoing plate collision of India with Eurasia. Under the control of its special geological background, it is a natural laboratory for the study of major geological disasters, such as huge rockslides, rock avalanches, ice-rock avalanches, and is attracting more and more scientific attention. The data of global positioning system (GPS) indicates that convergence is still lasted in the Tibetan Plateau with numerous earthquakes being generated (Larson et al. 1999; Tapponnier et al. 2001; Zhang et al. 2004). In the past 100 years, 36 events with $M_s > 7$ have been reported by Advanced National Seismic System (Fig. 1).

As shown in Fig. 1, the Tibetan Plateau is characterized by diverse and complex patterns of active fault systems comprising predominate block bounding faults and internal faults, accommodating the continuous deformation of India-Eurasia collision (Yin and Harrison 2000; Tapponnier et al. 2001; Yin 2010). The southwestern margin of the study area is defined by the ~2400 km Himalaya frontal thrust, which lies along the south range front of the Himalayas. This fault accommodates the underthrusting of the Indian Plate beneath Tibet (Elliott et al. 2016; Whipple et al. 2016). The eastern margin of the Tibetan Plateau is marked by the 500 km, NE-SW-trending Longmen Shan thrust belt, which is dominated by thrust faults and thrust-related fold structures (Lin et al. 2014). In the north, the active left-slip Altyn Tagh fault system extending over 2000 km links the strike-slip Haiyuan fault in the east and the NW-SE-trending Pamir thrust belt in the northwest, defining the northern boundary of the Tibetan Plateau (Yin 2010). In Plateau's interior, a series of large thrust faults and strike-slip faults trend EW to NW-SE, demarcating the boundary between large basins and ranges (e.g., Kunlun fault, Altyn Tagh fault, Haiyuan fault, Xianshuihe fault, etc.). Furthermore, a set of normal fault system are well-developed in the southern Tibet, which are attributed to the ongoing movement of roughly EW extension (Yin 2000; Blisniuk et al. 2001). These fault systems remain active and are associated with the continuous thickening and widespread viscous flow of the crust and mantle of the entire Tibetan Plateau, and time-dependent, localized shear between coherent lithospheric blocks (Yin 2010).

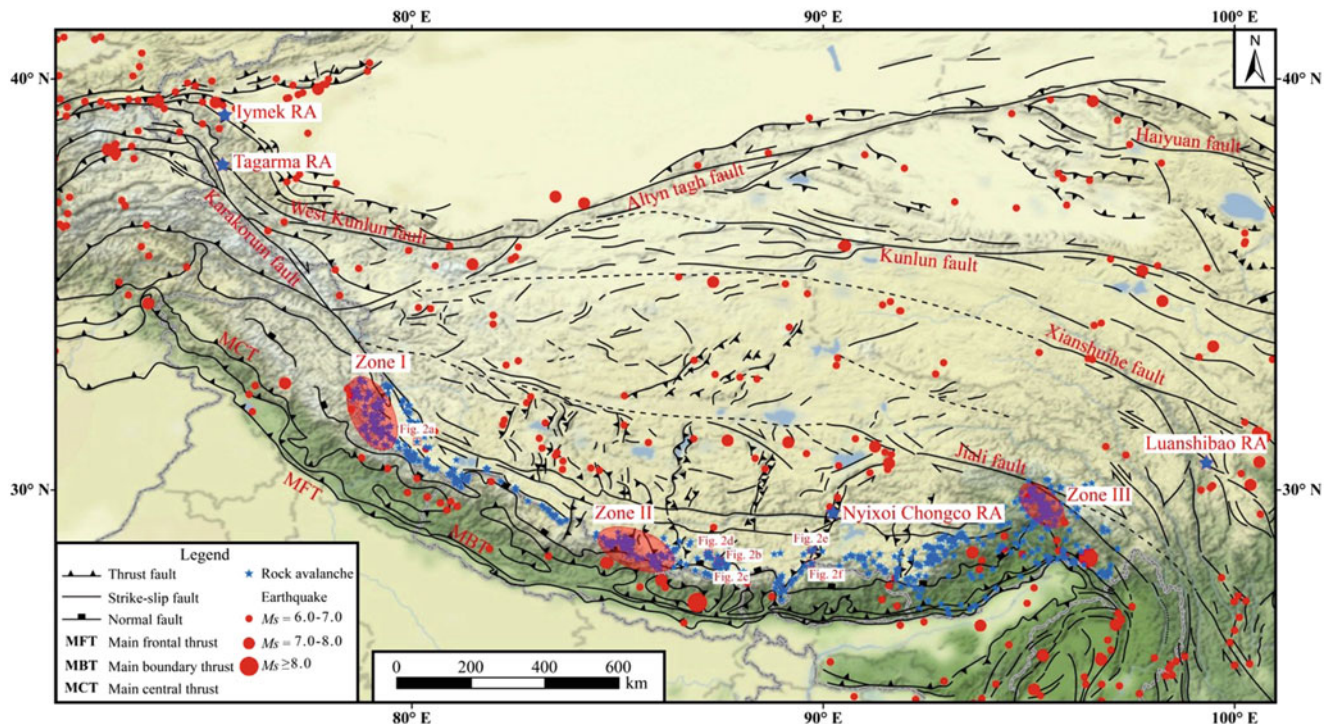


Fig. 1 Geological map of the Tibetan Plateau with strong earthquakes being marked

3 Distribution of Rock Avalanches in the Study Area

Owing to the effects of intense tectonic activities and long-term weathering, intensely fractured bedrocks are widely distributed with high topographic reliefs developed, which are thought to be particularly favorable for the generation of catastrophic bedrock landslides. Many giant rock avalanches have been reported in this area and are increasingly attracting researchers' attention (Yuan et al. 2013; Weidinger et al. 2014; Reznichenko et al. 2017; Strom and Abdrakhmatov 2018; Wang et al. 2018, 2019a, b, 2020). Focusing on the Tibetan Plateau area in China, study on the spatial distribution of rock avalanches in the Himalayan Range is firstly conducted. Then, further studies on the characteristics of some typical rock avalanches were conducted based on our previous remote sensing and field investigations.

3.1 Spatial Distribution of Rock Avalanches in the Himalayan Range, China

The Himalayan Range is situated in the place where the Indian Plate and Eurasian Plate meet, which is characterized by high relief, intensive tectonic activity, intensive river erosion, strong glaciation, etc. (Whipple et al. 2016;

Schwanghart et al. 2018; Soret et al. 2021). As the south margin of the Tibetan Plateau, the Himalayan Range is distributed in several countries with some distributed in China. Under the control of the special geological environment, rock avalanches are highly developed in this area. So, take the Himalayan Range in China as the studied area, the spatial distribution of rock avalanches is analyzed. Here, only the rock avalanches with their accumulated areas being over $\geq 0.2 \text{ km}^2$ are interpreted. Through remote sensing interpretation and field investigations, the total number of rock avalanches identified in the Himalayan Range of China is up to 772 with their spatial distribution being marked in Fig. 1. According to the equation proposed by Larsen et al. (2010), the volumes of these identified rock avalanches were calculated.

$$V = \alpha * A^\gamma \quad (1)$$

Where, $\log \alpha = -0.836 \pm 0.015$, $\gamma = 1.332 \pm 0.005$, V represents the volume of rock avalanche, and A represents the accumulated area of avalanche mass. Through calculation, it is reached that the number of rock avalanches with volumes $\geq 1 \times 10^7 \text{ m}^3$ is up to 485, occupying 34.5% of total number.

As shown in Fig. 1, the distribution of rock avalanches in the study area is extremely uneven in space depending on the geological environment. Figure 2 show several rock

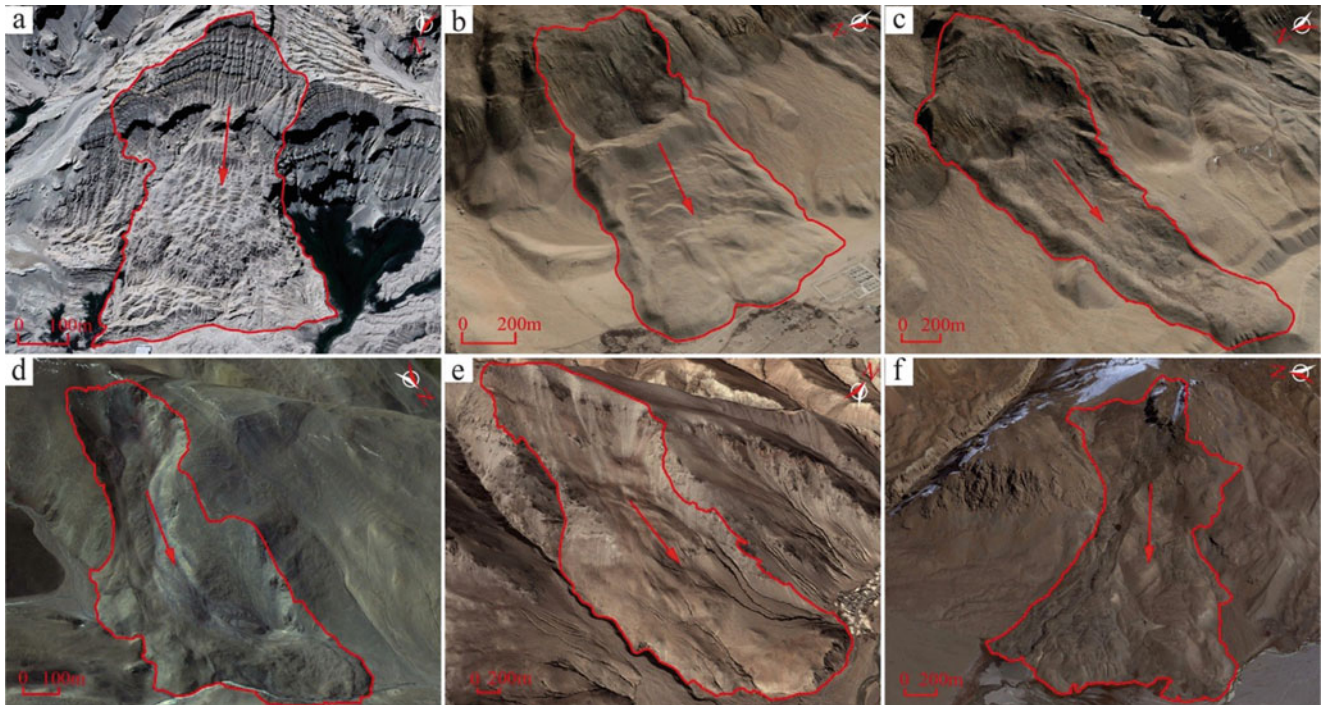


Fig. 2 Remote sensing images of several rock avalanches occurred in the Himalayan Range

avalanches developed in the Himalayan Range. From the images of these rock avalanches, it also can be seen that different morphologies and landforms can be observed among them, which indicates that varying pregnant geological environments are also contributed to varying deposited characteristics of rock avalanches. Taking the Zhada rock avalanche (Fig. 2a) as an example, its bedrock in the source area is weakly consolidated conglomerate, fine conglomerate mixed with sandstone of Tuolin Formation in Neogene. The orientation of the stratum in this case is nearly horizontal with a series of steep fissures developed in the source area. Under the control of the steep fissure and nearly horizontal stratum, the avalanche displays a relatively larger width and shorter runoff. In the deposit, the original stratigraphy is well preserved with a series of minor scarps generated. For the cases shown in Fig. 2b and c, the lithology of their source area bedrock is same. However, they present some different deposited features. To learn the possible influence of geological environments on the generation of rock avalanches in the study region, a primary study on the relationships between rock avalanches with elevation, slope angle, slope orientation, lithology, fault, river system and glaciers are analyzed here. The following results were derived primarily.

1. From east to west, there are three densely distributed areas for rock avalanches generated in the Himalayan Range, which are the western high mountainous area belong to the Ali region (Zone I), the area within the north-south rift

zone (Zone II) and the area around the Yarlung-Zangbo suture belt (Zone III). From north to south, it can be seen that the density of rock avalanches in the high Himalayan zone is relatively high.

2. Under the control of altitude, most of rock avalanches are distributed in the elevation of 4000–6000 m, which are usually the upstream areas of rivers or seasonal ice and snow covered areas. In the area of the eastern Himalayan tectonic syntaxis, the elevations of most rock avalanches range from 1000–3500 m, which is different from other places, indicating that other factors instead of elevation should be more contribute to the generation of rock avalanches here.
3. In the Himalayas, slopes with the angle ranging from 20° to 50° are most commonly distributed, which is corresponding to the distribution of deep mountainous canyons and glacial erosion valleys. In such environment, the preferred angles of slopes with rock avalanches occurred range from 20–40° mainly.
4. Under the influences of rainfall, sunlight and temperature, etc., the density of rock avalanches generated on the slopes facing SW and S is obviously higher than that on the N and NW facing slopes. Meanwhile, the number of rock avalanches generated on the slopes facing SW-S and N-NE is relatively higher than slopes facing other directions, which should have a certain relationship between the N-NE principal stress direction generated due to collision between the Indian and Eurasian Plates.

5. For the control of lithology, the formations consisting of relative hard rocks interbedded with weak interlayers are the preferred strata for rock avalanches occurrence. For such formations, the appearance of the weak layers is the controlling zone for rock avalanches generation. The number of rock avalanches generated in hard rock formations is in the second place. Meanwhile, it is noticed that the slope angles are steeper in the areas composed of relative hard rocks. This indicates that such lithology usually form relatively steep slopes, which provides preferred topography condition for the generation of rock avalanches.
6. The distribution of rock avalanches presents a good correlation with the extensions of major faults. Under the control of the major fault systems, i.e., the main central thrust, north-south rifts, southern Tibet detachment system and the Yarlung-Zangbo suture zone, rock avalanches present a striped distribution in plan-view. The closer the distance away from fault, the more the number of rock avalanches formed.
7. For rock avalanches generated in the areas influenced by glaciers, the slope angle (20–50°), elevation and volume of rock avalanches are relatively higher than for those in non-glaciated areas. Meanwhile, in the glaciated areas, rock avalanches are commonly developed on the slopes facing N, W and NW. Conversely, rock avalanches generated in the non-glacial areas are mainly formed on the slopes facing S and SW. This indicates an obvious control of glacier on the generation of rock avalanches.

Through a comparison of different factors on the spatial distribution of rock avalanches in the Himalayas of China, we primary reached that the fault systems should be the most significant factor for the generation of rock avalanches. In the high Himalaya region of China, the role of glacier should be the second factor, which intensively influences the stability of the bedrocks in the source areas through the effects of unloading caused by glacier retreat and freeze-thaw cycles. For the non-glacial areas, lithology should be the second key factor, which determines the slope steepness and, thus, its stability.

3.2 Locations of the Typical Rock Avalanches

To learn the characteristics of rock avalanches developed in the Tibetan Plateau of China, several typical cases are presented for further investigation, i.e., the Luanshibao rock avalanche, Nyixoi Chongco rock avalanche, Tagarma rock avalanche and Iymek rock avalanche. As shown in Fig. 1, they are distributed in different areas of the Tibetan Plateau with the Luanshibao rock avalanche in the Sichuan West Plateau, Nyixoi Chongco rock avalanche in the South Tibet

detachment system, and Tagarma and Iymek rock avalanches in the Pamir-western Himalayan syntaxis. Focusing on the deposited characteristics of these typical cases, their deposited characteristics are described in detail, hoping to provide more geological evidences for the study of rock avalanches. Figure 3 shows the remote images of the studied cases.

4 Characteristics of Typical Rock Avalanche Deposits

As indicated by the deposited characteristics along the travelling paths of rock avalanches, the detached masses commonly display very significant mobility and propagate like fluid. Along their travelling paths, sequential distributions of a series of landforms and internal structures indicating fluid-like motion are commonly observed, which show typical planar zonation and vertical gradation (Dufresne et al. 2016; Strom and Abdrakhmatov 2018; Wang et al. 2018, 2019a, 2020; Mitchell et al. 2020).

According to the spatial distributions of landforms and internal structures, rock avalanche deposits can be divided into three zones in plan-view from proximal to distal areas: the source area, the transition zone and the accumulation zone (Dufresne et al. 2016; Wang et al. 2018). The source area usually has the armchair shape with a steep bedrock scarp in the upper part and a relatively gentle slope in the lower part. Sometimes, small amount of rock avalanche deposits covers the relatively gentle section. The transition zone where the sliding mass rapidly propagates is often narrow and long in plan-view. In the transition zone, large-scale torea blocks are typically displayed, which are characterized by a relatively flat top surface and a steep scarp facing downstream. Additionally, longitudinal ridges and linear structures are common being formed by the rapid movement of rock avalanche debris. The accumulation zone is the main area where most of rock avalanche mass deposited. In plan-view, the deposits of rock avalanches often have lobate or fan-like shape. Margins of the accumulation zone are characterized by raised rims that are also called levees, and distal ridges. There are also trimlines left by moving debris along the travelling path. The frontal margins of most rock avalanches are often present in fingering deposit (digitate fronts). On the top surfaces of the deposits in the accumulation zones, clear longitudinal ridges with longitudinal groove-like troughs, transverse wave-like ridges, hummocks or conical hills, en echelon crevasse-like ridges, and X-shaped (fish scale-like) landforms with both ridges and troughs often form (Strom and Abdrakhmatov 2018; Wang et al. 2018, 2019a, 2020).

In the cross-section, the most typical deposited feature of rock avalanche deposits is inverse grading (Fig. 4). According to its vertical grain size distribution, the deposit

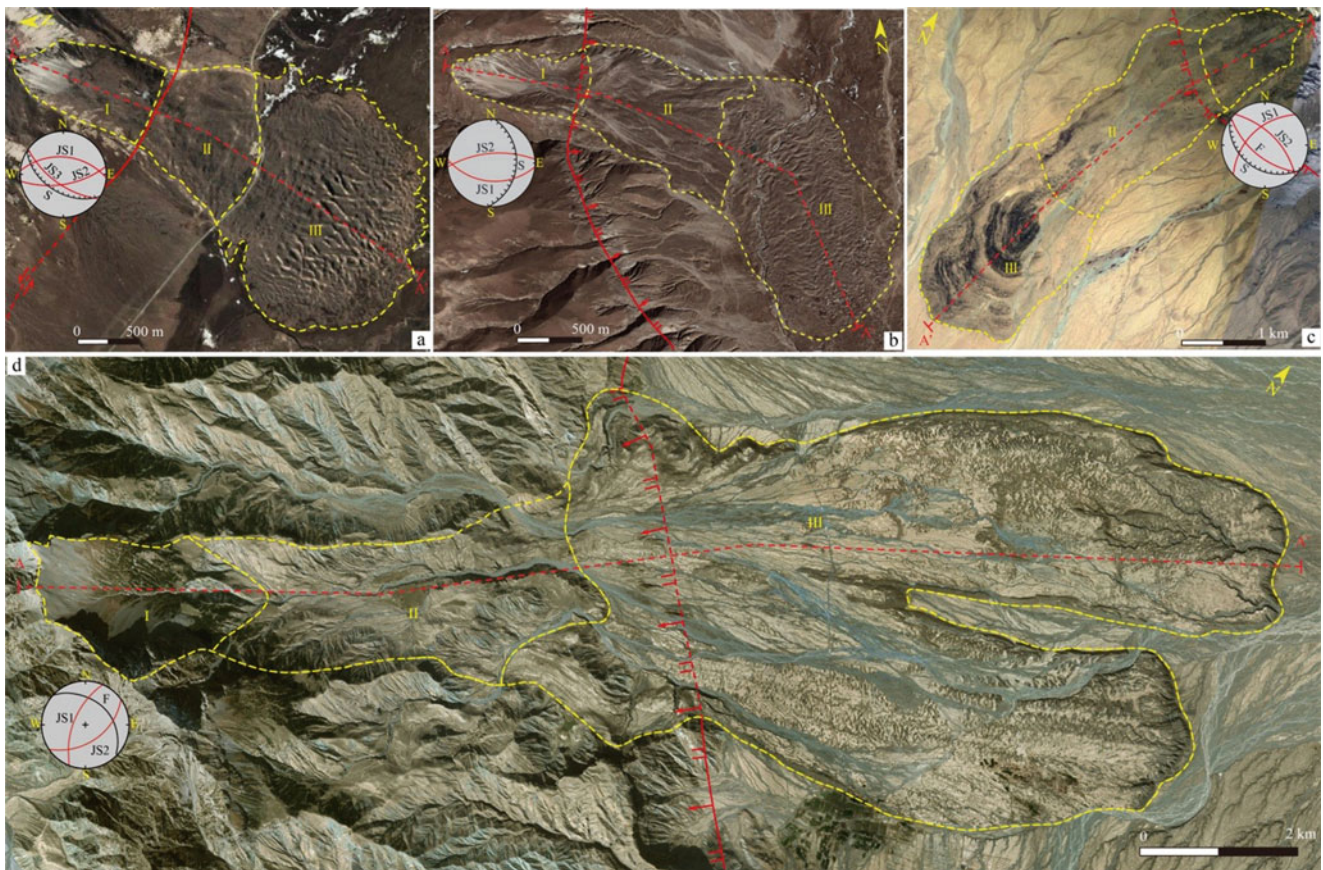


Fig. 3 Typical rock avalanches distributed in the Tibetan Plateau, China (a: Luanshibao rock avalanche; b: Nyixoi Chongco rock avalanche; c: Tagarma rock avalanche; d: Iymek rock avalanche)

can be divided into three facies from top to bottom: carapace facies, body facies and basal facies (Dufresne et al. 2016; Strom and Abdrakhmatov 2018; Wang et al. 2019a, 2020). The main difference among these facies is their grain size distribution. The carapace facies is defined as an assemblage of large and angular interlocking blocks concentrated near the surface of a rock avalanche deposit and is the coarsest unit in a rock avalanche deposit (Dunning 2006; Davies and McSaveney 2009; McColl and Davies 2011; Dufresne et al. 2016). Fine particles seldom occur in the carapace facies, and thus this facies is mainly clast-supported. Body facies usually forms the main part of rock avalanche deposits. This facies shows a wide range of grain sizes from fine particles of several millimeters (mm) to coarse clasts of tens of centimeters (cm). Sometimes, blocks larger than 1 m also can be seen in the body facies. The body facies shows a matrix-supported structure with coarse clasts being surrounded by large amount of fine particles. The basal facies is the bottom part of a rock avalanche deposit as shown in Fig. 4. As the direct contact zone with the substrate, the basal facies is highly fragmented and mainly composed of fine

particles of mm scale or even finer particles due to intense interaction between the sliding mass and substrate.

In addition to above mentioned landforms and deposit facies, some other characteristics are also commonly observed in rock avalanche deposits, such as preserved stratigraphic sequence, jigsaw structure, multi-layered internal shear zones, etc. At the bottom of rock avalanche deposits, a series of basal deformation structures formed by intensive interaction between the sliding mass and substrate can also be observed, such as basal shear zones with folds, faults, diapiric structures, wedge intrusion, and sand dykes, etc. The variations of the grain size distribution and internal structures revealed in rock avalanche deposits from carapace facies to basal facies indicate the occurrence of different interactions among particles with varying depth. On the other hand, it also indicates the occurrence of different deformation processes and dynamic fragmentation with depth. All of these geological evidences revealed along rock avalanche paths are key insights in revealing the kinematics and dynamics of rock avalanches. In the following, detailed studies on the four cases are conducted.

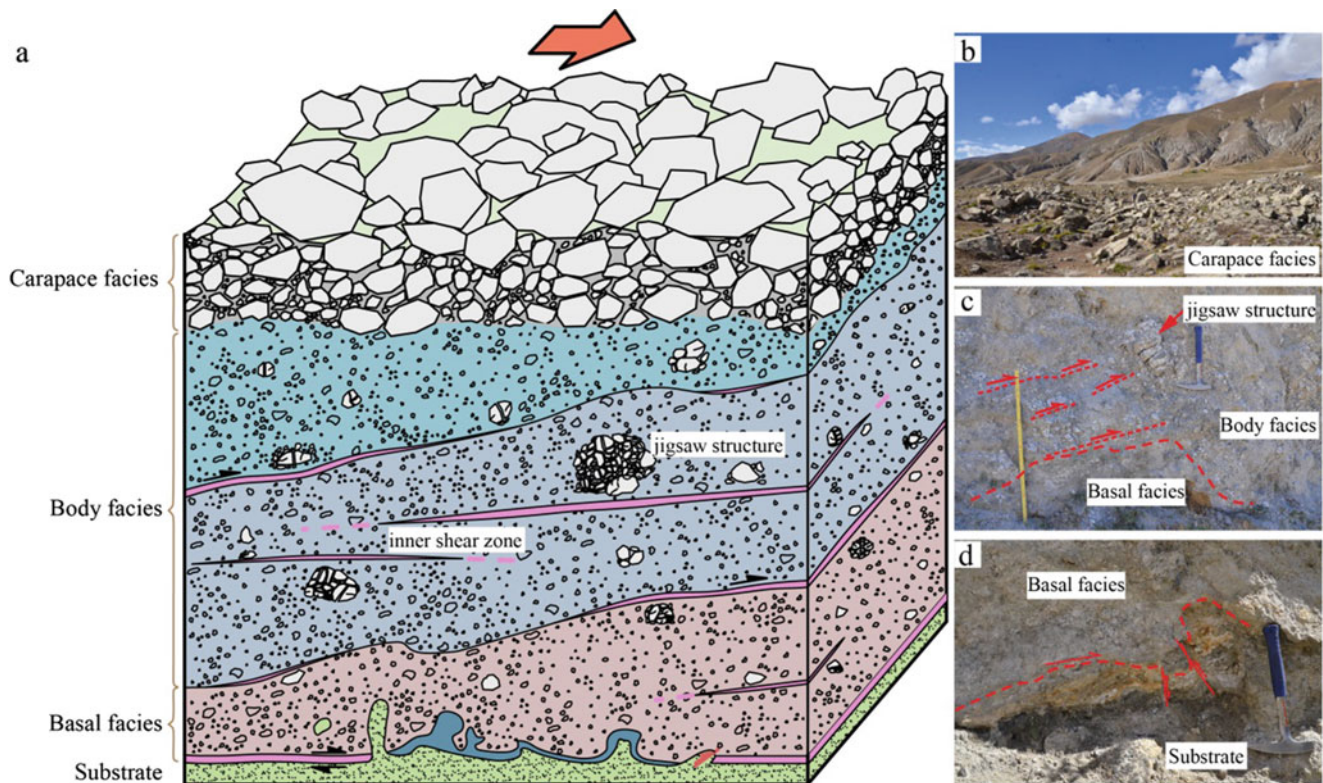


Fig. 4 Conceptual models of the vertical structures of typical rock avalanches (Referred on Weidinger et al. (2014) and Dufresne et al. (2016))

4.1 Luanshibao Rock Avalanche

4.1.1 Geological Setting and General Features of the Luanshibao Rock Avalanche

The Luanshibao rock avalanche is situated in the Maoyaba basin, Litang County, Sichuan Province, China. This is regionally part of the Sichuan West Plateau. As shown in Fig. 5, the Sichuan West Plateau is on the eastern margin of the Tibetan Plateau. Due to the intensive collision between the Indian and Eurasian plates, the Sichuan West Plateau is characterized by complex geologic structures with numerous faults and folds generated. The main fault belts formed in the West Plateau include the Jinshajiang fault system (F1), Litang-Dewu fault system (F2), Xianshuihe fault system (F3), Anninghe fault system (F4), and Longmenshan thrust belt (F5) as exhibited in Fig. 5. It is reported that all of these fault belts are still active with strong earthquakes recorded in history (Tang and Han 1993; Yin and Harrison 2000). The strongest earthquake recorded in history is the Wenchuan earthquake occurred in 2008 along the Longmenshan thrust belt with abundant geological disasters (Dai et al. 2011).

As shown in Fig. 5, the 385-km-long Litang-Dewu fault system (F2) is very active among these fault belts with 3 strong historical earthquakes ($M > 7$) being recorded. Xu et al. (2005) reported that F2 had an average sinistral slip rate

of 4.0 ± 1.0 mm/a and a reverse slip rate being 0.1–1.8 mm/a over the past 14 ka. From west to east, F2 is further divided into four subsidiary faults that are Chalong-Maoyaba fault (F2-1), Litang-Dewu fault (F2-2), Czhong fault (F2-3), and Mula fault (F2-4). The subsidiary fault F2-1 passes through the Maoyaba basin where the Luanshibao rock avalanche occurred as exhibited in Fig. 5. In history, two strong earthquakes with $M > 7$ ever occurred along this fault. The latest one is the M_s 7.3 Litang earthquake, which occurred on May 25, 1948, and caused a 70-km-long surface rupture (Tang and Han 1993). The high-level of activity along this fault system during the Quaternary contributed to the formation of the Maoyaba basin (Tang and Han 1993).

Figure 6 shows the geological setting of the Maoyaba basin, where the Luanshibao rock avalanche had occurred. For the bedrock of the studied area, there are the appearances of the Upper Triassic strata of the Qugasi (T_{3q}), Tumugou (T_{3t}), Lanashan (T_{3l}), and Lamaya (T_{3lm}) formations and intrusive rocks ($\gamma\delta_5^{1-d}$, $\eta\gamma_5^{1-d}$, $\gamma\beta_5^{1-d}$, and $\delta\alpha_5^{1-c}$) coeval with the Triassic Period (257–205 Ma). Within the basin, the Quaternary deposits, consisting of Upper Pleistocene lacustrine facies (Q_p^l) and alluvial-fluvial facies ($Q_p^{al} - Q_p^{pl}$) and Holocene alluvial facies (Q_h^{al}), accumulated (Tang and Han 1993).

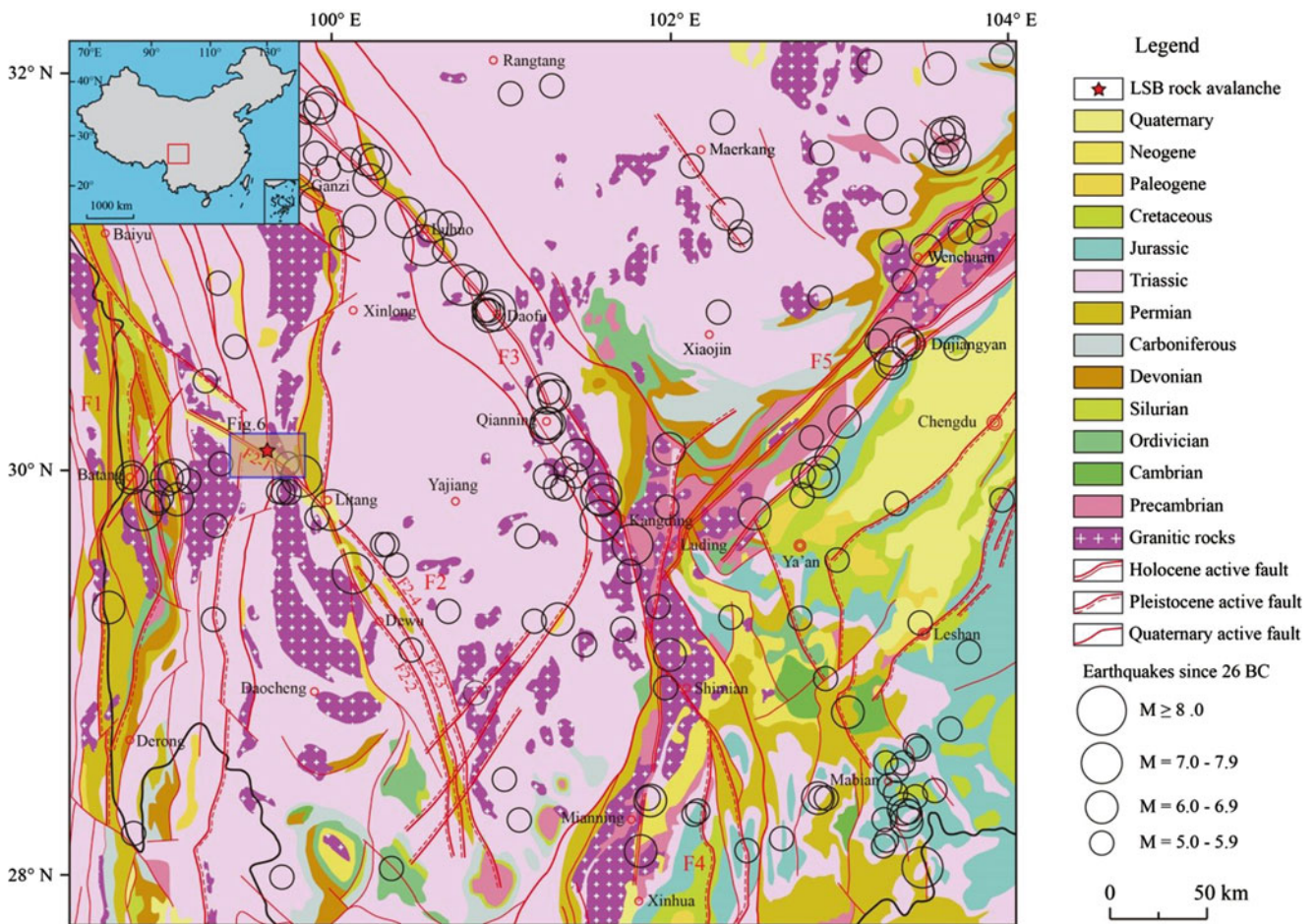


Fig. 5 Simplified geological map showing major faults and earthquake activity on the Sichuan West Plateau, China

As shown in Fig. 3a, the Luanshibao rock avalanche detached from a steep slope of the Maoyaba basin northern margin. The horizontal distance and vertical drop from the head of the scarp to the toe of the avalanche deposit is 4.1 km and 821 m, respectively, yielding a fahrböschung (the ratio of the height of the highest point on the main scarp (H) to the horizontal projection of distance from this point to the tip of a rock avalanche (L) (Heim 1932)) of 0.2. This low value indicates an extremely high mobility of this rock avalanche (Cruden and Varnes 1996; Lucas et al. 2014). In plan-view, the accumulated area of the avalanche deposit is up to 4.4 km², and the estimated total volumes of the detached rock mass and accumulated debris are 39–47 × 10⁶ m³ and 64–94 × 10⁶ m³, respectively (Guo et al. 2016).

Fig. 7 shows one longitudinal profile of the avalanche with its position being marked in Fig. 4a. As shown in Fig. 7, F2–1 is located at the toe of the source area. Bounded by F2–1, the avalanche source area ranges in elevation from 4275 to 4931 m above sea level (a.s.l.) and locates on the NE hanging wall of the fault. The bedrock in this area is composed of granodiorite and biotite granite of Triassic Maohuoshan

intrusion rock ($\gamma\delta_5^{1-d}$) mainly. Due to the effects of tectonic events and long-term weathering, the bedrock has been intensely fractured with three sets of preferred joints (Fig. 4a). The dip directions and dip angles of these joint sets are 0–10/40–50° (JS1), 165–175/60–70° (JS2), and 200–250/60–70° (JS3). The rest part of the avalanche is distributed in the SW footwall with the elevation ranging from 4110 to 4290 m a.s.l. For this area, the slope angle is relatively low. And the farther away from the source area, the lower the slope angle is. The substrate of this part is composed of Quaternary alluvial-fluvial facies ($Q_p^{al}-Q_p^{pl}$).

4.1.2 Sedimentary Features of the Avalanche Deposit

(1) Plan zonation and landforms

In plan-view, the Luanshibao rock avalanche is present in a tongue shape (Fig. 8a). On the surface of the deposit, prominent well-developed morphologies, including torea blocks, transverse and longitudinal ridges, large ridges separated by conjugate troughs, and hummocks, are spatially distributed

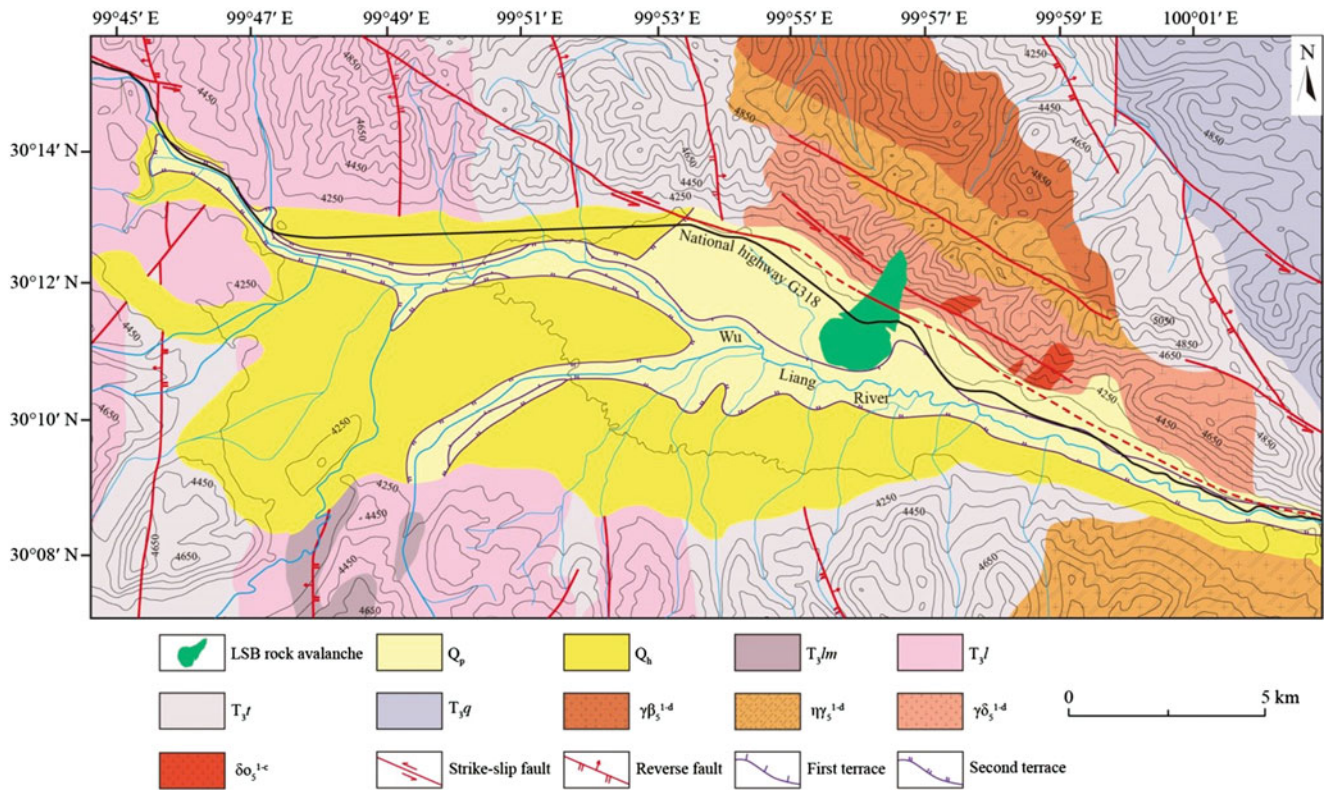


Fig. 6 Geological setting of the Maoyaba basin where the Luanshibao rock avalanche had occurred

from the proximal to the distal areas. Such regularly spatial distribution of so many landforms in one avalanche is rare seen in most reported rock avalanches. Here, the toveba blocks are associated with a massive portion composed of highly fragmented rock mass with a short runout and a steep

downward slope-parallel scarp, which is located within or proximal to the source area. The observed ridges feature length-to-width ratios generally greater than 2 and heights larger than 5 m. The lineaments are characterized by length-to-width ratios greater than 2 and heights less than 5 m.

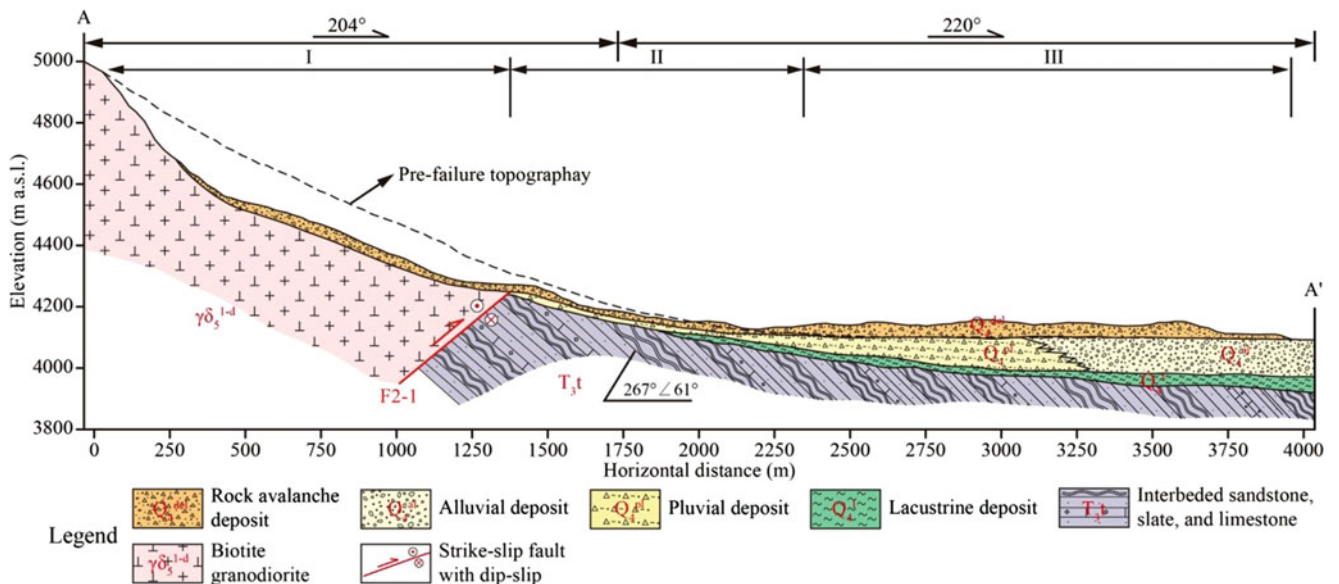


Fig. 7 Longitudinal profile of the Luanshibao rock avalanche

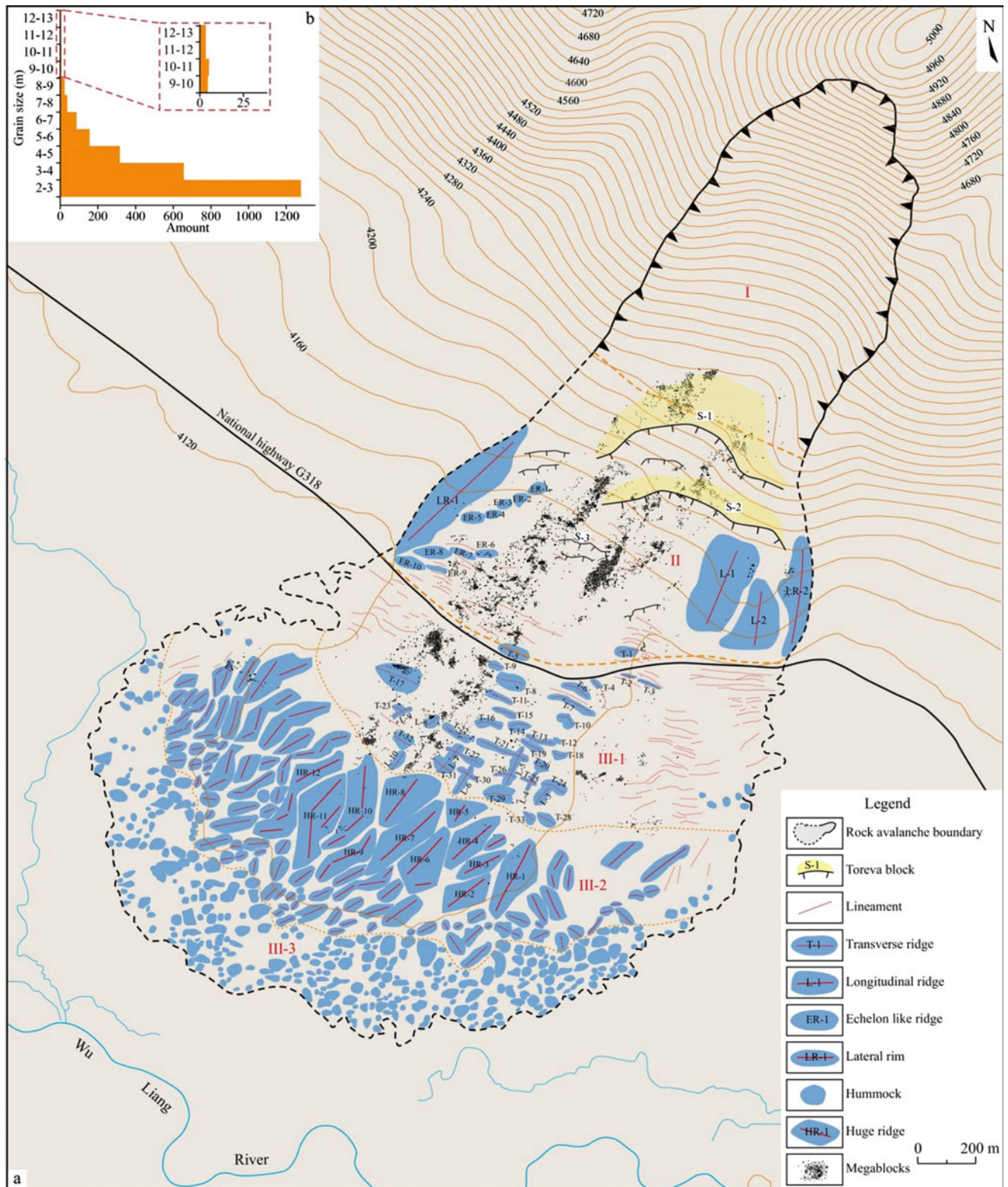


Fig. 8 Sketch of the Luanshibao rock avalanche (a) with statistics of huge blocks on the top surface (b)

Hummocks are defined as a landform with a length-to-width ratio of 1–2 (Dufresne and Davies 2009).

According to the sequential distribution of these surface morphologies along the travelling path, it can be divided into three zones in plan-view that are: the source area (I), the transition zone (II), and the accumulation zone (III). In the following, detailed descriptions of the morphologies in each zone are given to explain the rock avalanche transport dynamics.

a) Source area (I)

The source area, ranging from 4275 to 4931 m a.s.l., displays a U-shape in plan-view. This zone is characterized by a steep well-exposed scarp and a relatively gentle section with talus accumulation. The maximum longitudinal length and width of the source area are approximately 1500 m and 700 m, respectively (Fig. 3a). For the steep exposed part, its average slope is 35° with a relatively plain surface. Controlling by the preferred joint sets shown in Fig. 4a, the exposed scarp is characterized by a blocky and intensively fractured structure. For the lower relatively gentle section, its average slope angle is 20° and was partially covered by avalanche debris and post-avalanche talus.

b) Transition zone (II)

For the transition zone, two typical landforms are well developed—toreva blocks and longitudinal ridges (Fig. 8a). As shown in Fig. 9a, two notable toreva blocks were generated next to the source area, i.e., the Level-1 (S-1) and Level-2 (S-2) toreva blocks. The S-1 toreva block ranges from 4200 to 4280 m a.s.l. and present a maximum length and width of 450 m and 150 m, respectively. In plan-view, it presents a crescent shape with its top surface inclined slightly upstream (Fig. 9b). The frontal edge of the S-1 toreva block displays a steep dipping escarpment with a maximum vertical difference of up to 65 m (Fig. 9c). In the transverse direction, the elevation of the S-1 toreva block decreases from left to right (Figs. 9a and c). Next to the S-1 toreva block is the S-2 toreva block ranging in elevation from 4175 to 4200 m a.s.l. In plan-view, the S-2 toreva block is also crescent shaped (Figs. 9a and d), with a relatively smaller size compared with the S-1 toreva block. The S-2 toreva block features a relatively gentler escarpment along its downward side (Fig. 9a). Unlike the undulating topography of the rear part of the transition zone, its frontal part is relatively flat, with several small-scale escarpments and minor lineaments sparsely distributed in the central area. The orientations of these landforms are nearly perpendicular to the main sliding direction of the rock avalanche. Among these features, the largest is the S-3 toreva block with a 10-m-high downward escarpment (Fig. 10a).

The second prominent features in zone II are two large longitudinal ridges (L-1 and L-2) in the frontal part of zone II (Fig. 8a), which are 280–340 m long and 150–180 m wide. In plan-view, they are oval in shape and oriented N10–25°E, nearly parallel to the main sliding direction of the rock avalanche (Fig. 8a). Another interesting feature is the display of two large lateral rims (LR-1 and LR-2) that stand approximately 20 m above the original topography along the left and right margins of this zone. Figures 10b and c are photographs of the accumulated features of both lateral rims captured during the field investigation. Additionally, a series of small-scale en echelon-like ridges adjacent to the right margin of zone II were also observed. The NE-SW orientations of the en echelon-like ridges are oblique to the main sliding direction of the rock avalanche, indicating the existence of lateral spreading near the right margin of the sliding mass.

c) Accumulation zone (III)

As shown in Fig. 8a, different landforms are well developed in the accumulation zone and present sequential distribution. According to the spatial distribution of landforms in zone III, it can be further divided into three sub-zones, i.e., sub-zone III-1 with transverse and longitudinal ridges, sub-zone III-2 with large ridges separated by conjugate troughs and sub-zone III-3 with hummocks.

For sub-zone III-1, gradual changes are observed from the rear to the front. Transverse ridges are present in the rear part, and criss-crossing transverse and longitudinal ridges are present in the front part (Fig. 8a). According to the statistics, the number of prominent transverse ridges formed in the rear part is up to 18. They are mainly concentrated in the central area of sub-zone III-1 (Fig. 8a). These transverse ridges emerge 5–20 m above their surroundings. Figure 11 shows several transverse ridges photographed from different orientations. As shown in Fig. 11, the top surfaces of these transverse ridges are relatively flat with huge blocks mainly concentrated in the upstream slope.

Greatly different from the landforms present in the rear part of sub-zone III-1, a criss-crossing feature composed of transverse and longitudinal ridges is present in the front part with good continuity present (Fig. 12). Here, these criss-crossing ridges are 20–50 m wide and 30–150 m long. Differing slightly from the relief of the transverse ridges in the rear part of sub-zone III-1, these criss-crossing ridges stand 10–20 m above their surroundings. Due to the presence of these criss-crossing ridges, approximately rectangular depressions were observed in this sub-zone. Figure 12e is the photo of one depression taken during the field investigation.

To quantify the preferred direction of these ridges, statistics of their orientations were conducted with the results being graphed in Fig. 13. The orientations of the transverse

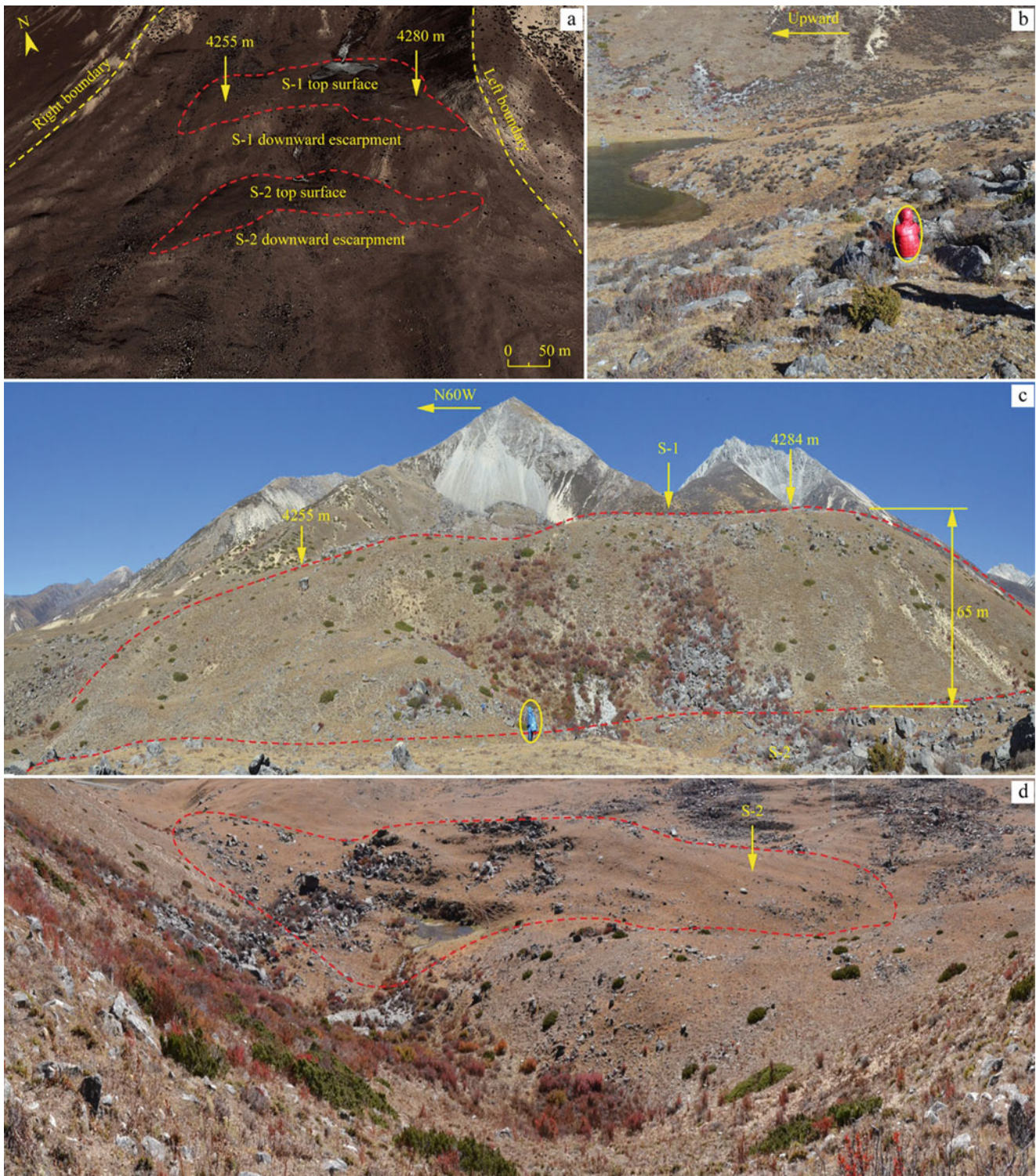


Fig. 9 Extension of the tovera blocks in the transition zone of the Luanshibao rock avalanche

ridges range from N55°W to N80°W mainly (Fig. 13a), nearly perpendicular to the sliding direction of the detached mass in this section. The longitudinal ridges are mainly parallel to the sliding direction of the detached mass, with

strikes of 30–40° (Fig. 13b, including the L-1 and L-2 ridges in the transition zone).

Next to sub-zone III-1, large ridges separated by conjugate troughs form sub-zone III-2. As shown in Fig. 8a, greatly

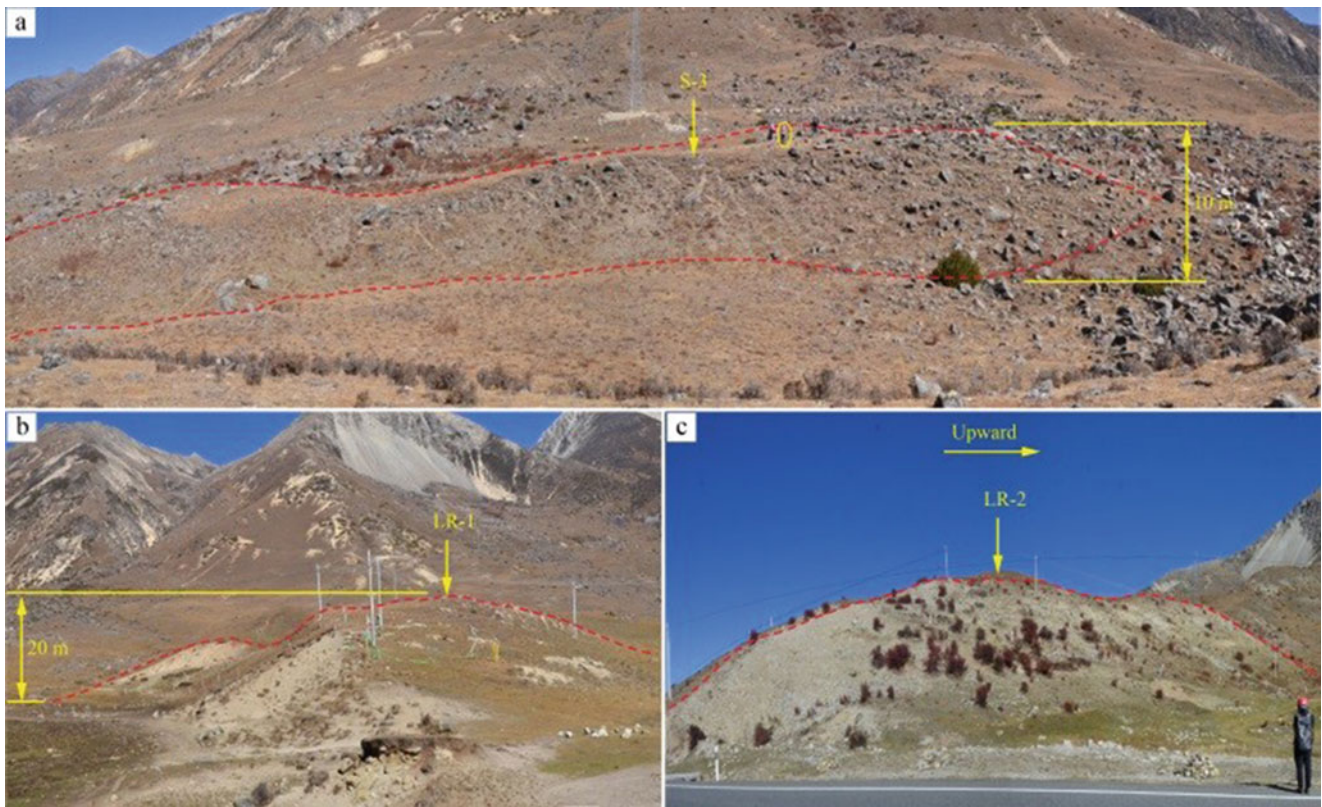


Fig. 10 Extensions of S-3 toeva block (a) and both lateral ridges (b-c)

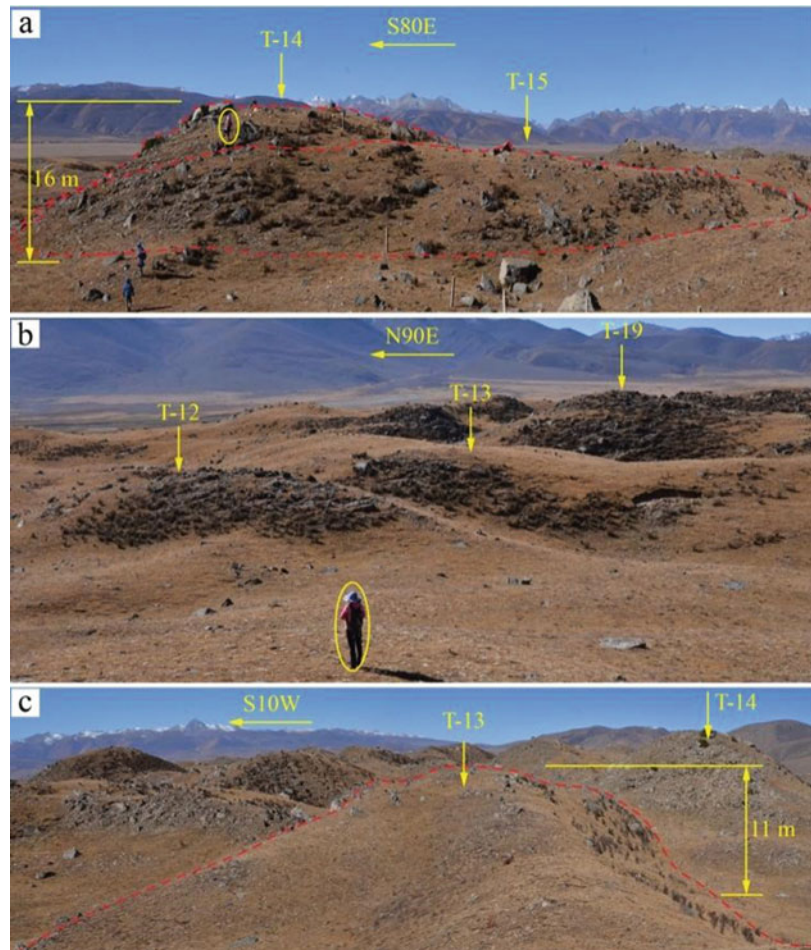
different from the display of the landforms in sub-zone III-1, a series of well-developed large ridges are well developed in sub-zone III-2. Figure 14a shows an enlarged view of the extension of the conjugated ridges in this subzone. As exhibited in Fig. 14a, large ridges in this sub-zone have the parallelogram or rhomboid shape mainly. Closer to the longitudinal central line, larger the accumulated ridge is. Among these large ridges, there are deep conjugate troughs (e.g., CT-1 to CT-17 in Fig. 14a), which contributes to the formation of these parallelogram shaped ridges. Ridges in sub-zone III-2 range from 110–280 m in length and from 40–100 m in width mainly. The elevation difference between the ridges and the troughs is 15–20 m. Figure 14b-d shows three large ridges photographed during the field investigation.

Furthermore, statistics on the orientations of some of the large ridges and the deep troughs are plotted in Fig. 15. The large ridges are mainly oriented 20–40°, nearly parallel to the sliding direction of the detached mass in this section. The deep troughs have two sets of preferred orientations, i.e., 0–20° and 50–70°. With increasing distance from the longitudinal centre line of sub-zone III-2, the dimensions of the ridges and troughs decrease markedly and become difficult to recognize. Moreover, another interesting morphology in sub-zone III-2 is the presence of minor undulating topography on the top surfaces of the large ridges, as exhibited in

Fig. 14b-d. This feature is similar to waves in water, with a series of alternating peaks and troughs. The orientation of the undulating topography is perpendicular to the longitudinal axes of the ridges.

In the frontal part of zone III, it is an area characterized by a series of hummocks, i.e., sub-zone III-3. This sub-zone is the distal depositional area of the Luanshibao rock avalanche and is dominated by a series of small-scale, roughly circular or circular hummocks (Fig. 8a). These hummocks are 15 to 40 m in diameter and stand approximately 5–12 m above their surroundings (Fig. 16a-b). The largest hummock is the one labelled with the red dashed line in Fig. 16a. The length and width of this hummock are 45 m and 39 m, respectively, and they raise 12 m above the surrounding. In plan-view, the hummocks in sub-zone III-3 present a sparsely distributed pattern and decrease in sizes and in height-to-width ratios with increasing distance from the proximal to the distal and marginal areas. Another striking feature in sub-zone III-3 is the presence of a steep frontal edge of the deposited mass (Fig. 16c-d). It was measured that the vertical difference between the frontal edge of the deposited mass and the surface of the river is greater than 2 m. In some sections, the height of the frontal edge of the deposited mass even reaches 5.6 m.

Fig. 11 Extensions of transverse ridges in the rear part of sub-zone III-1 in the Luanshibao rock avalanche



(2) Internal deposited features

In addition to these surficial features, some typical internal deposited structures were also observed in the deposit. The first interesting feature is the layout of the carapace facies with many huge blocks (Figs. 8a and 17). In plan-view, the amount of megablocks accumulated in the right part of the rock avalanche deposit is obviously higher than that in the left part (Fig. 8a). Most of blocks are concentrated in the depressions in the right-hand parts of zone II and sub-zone III-1.

In vertical profile, this facies is usually clast-supported with large voids. Most blocks retain the original source stratigraphy without mixing and are featured by irregular angular shapes with very sharp edges and well-developed fractures. Jigsaw structures are observed in some megablocks (Fig. 17e). On the surfaces of some megablocks, step fractures (e.g., SF in Fig. 17d and f) were common observed, indicating the occurrence of brittle fracturing during debris motion (Wang et al. 2015). The measurements of the long-axis orientations of some megablocks revealed that the orientations of most of megablocks are slightly oblique to

the rock avalanche travel direction. To quantify the block size distributions on the top surface of the carapace facies, blocks with long axes of ≥ 2 m were sampled and counted based on our field investigations and remote sensing images. Figure 8b shows the statistical results plotted in a frequency distribution histogram. As shown in Fig. 8b, the number of blocks with long axes of ≥ 2 m counted in the Luanshibao rock avalanches is up to 2521. For the distribution of blocks, megablocks with long-axes of 2 to 3 m are the most common. The largest megablock is 12.5 m long and is located in zone II.

Other prominent features revealed in the Luanshibao rock avalanche deposits are the inverse grading and jigsaw structures (Wang et al. 2018; Zeng et al. 2019). During field investigation, exposures of 0.6 to 10 m in height were observed in the deposit, allowing us to examine the internal structure of its upper portion. Figure 18 shows several profiles taken during our field investigation. In the deposit, coarse-grained clast-supported breccia and blocks with a fine-grained matrix are universally distributed. The clasts are angular, with little or no rounding by abrasion. Similar to the textures of the megablocks (Fig. 17e), jigsaw structures

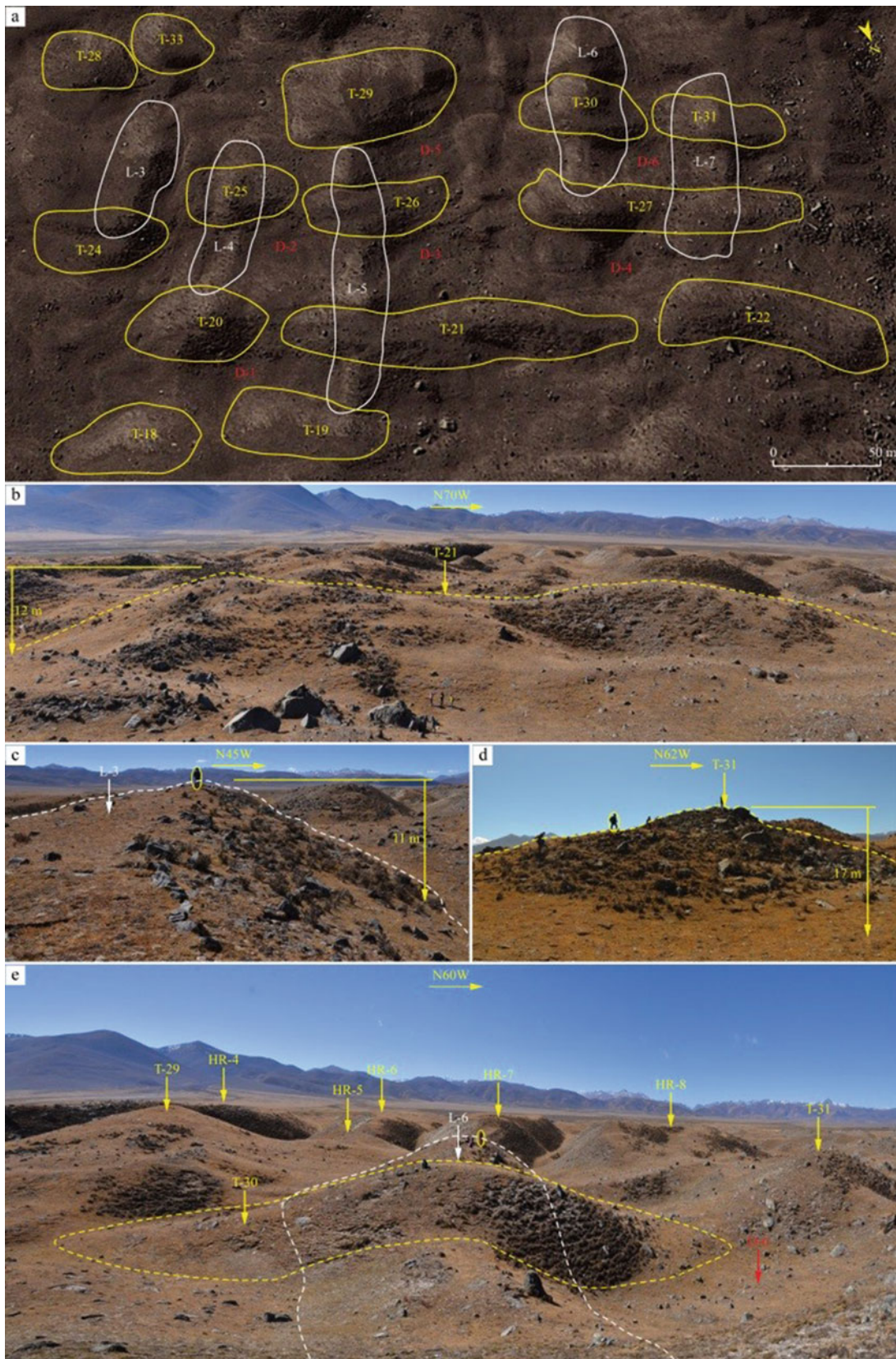


Fig. 12 Extensions of criss-crossing ridges in the frontal part of sub-zone III-1 in the Luanshibao rock avalanche

Fig. 13 Rose diagrams of the transverse (a) and longitudinal (b) ridges in sub-zone III-1 of the Luanshibao rock avalanche with the red arrow indicating the main propagated direction

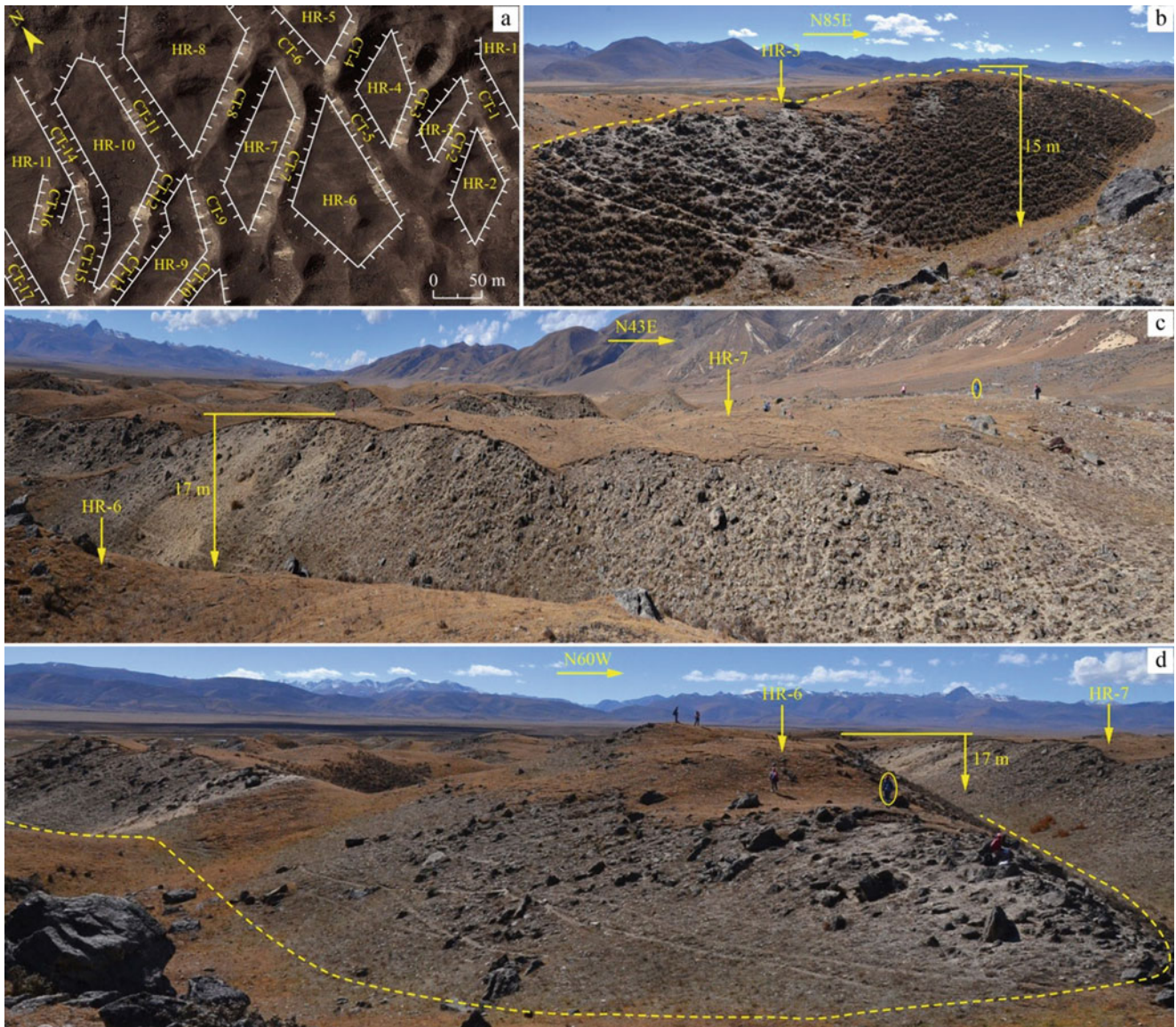
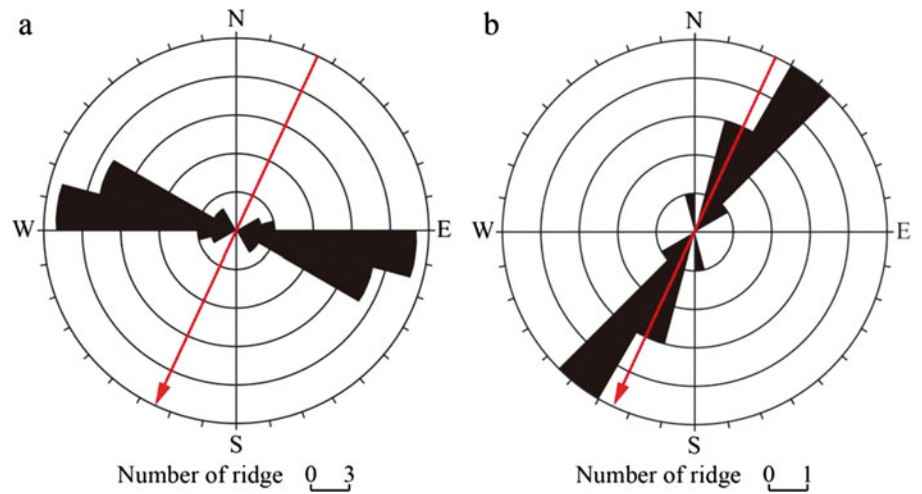


Fig. 14 Extensions of parallelogram shaped ridges in sub-zone III-2 in the Luanshibao rock avalanche

Fig. 15 Rose diagrams of ridges and troughs in sub-zone III-2 of the Luanshibao rock avalanche

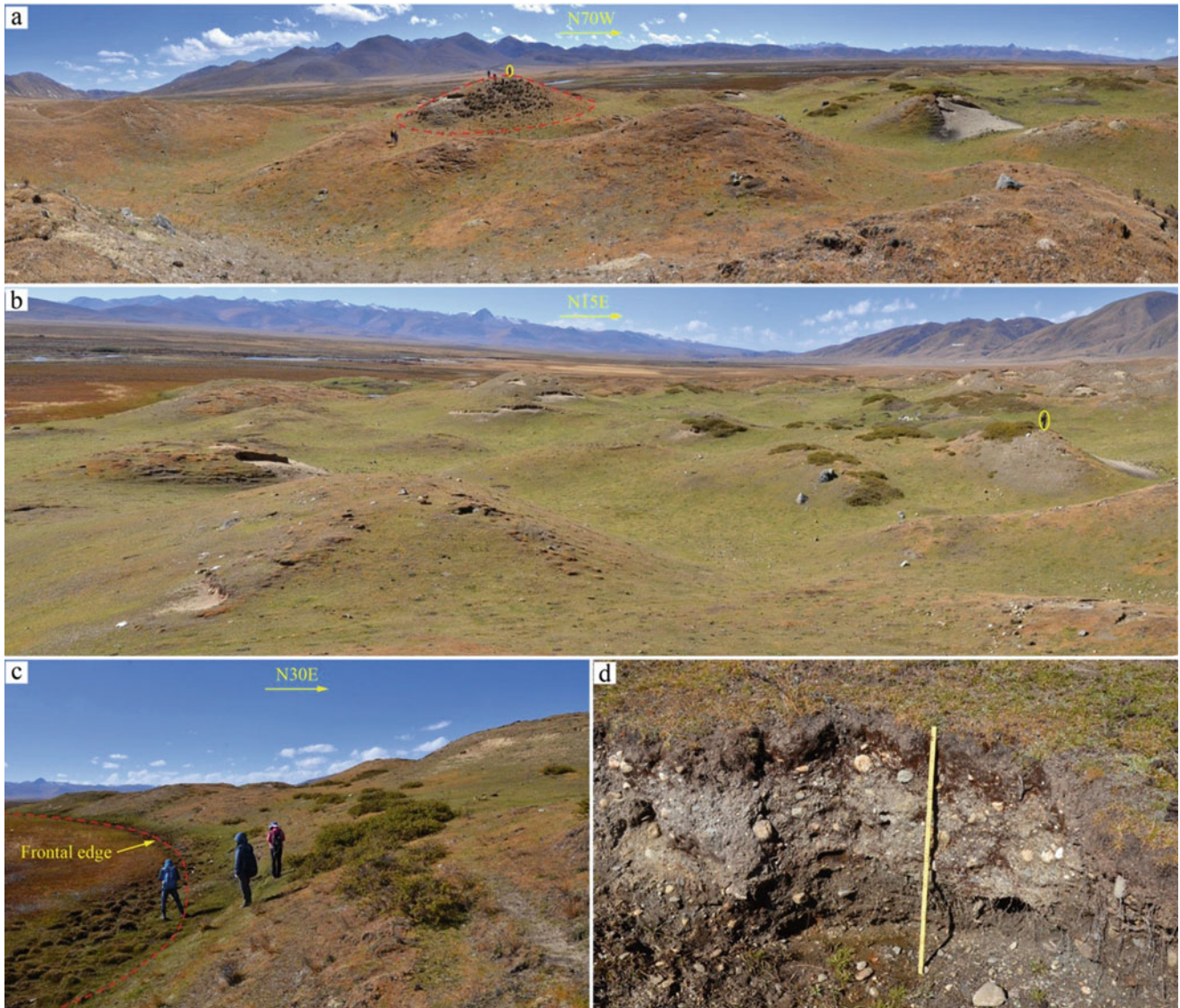
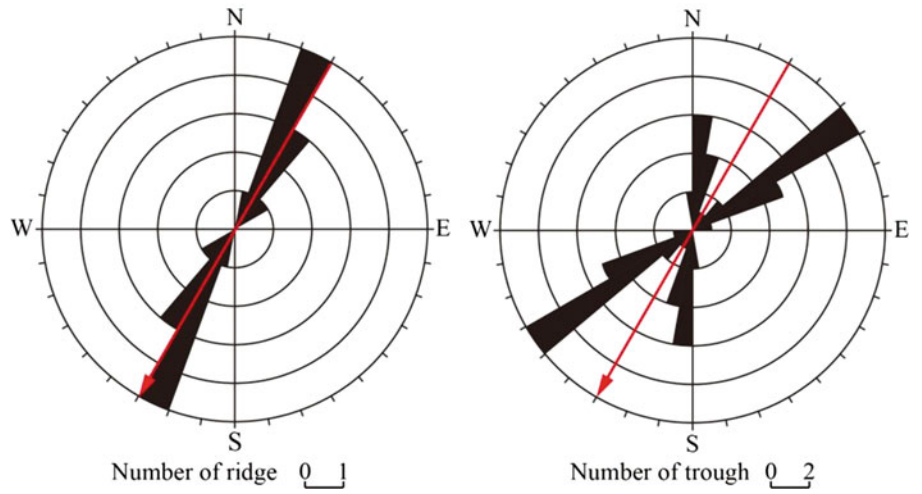


Fig. 16 Hummocks (a-b) and frontal edge (c-d) of the Luanshibao rock avalanche

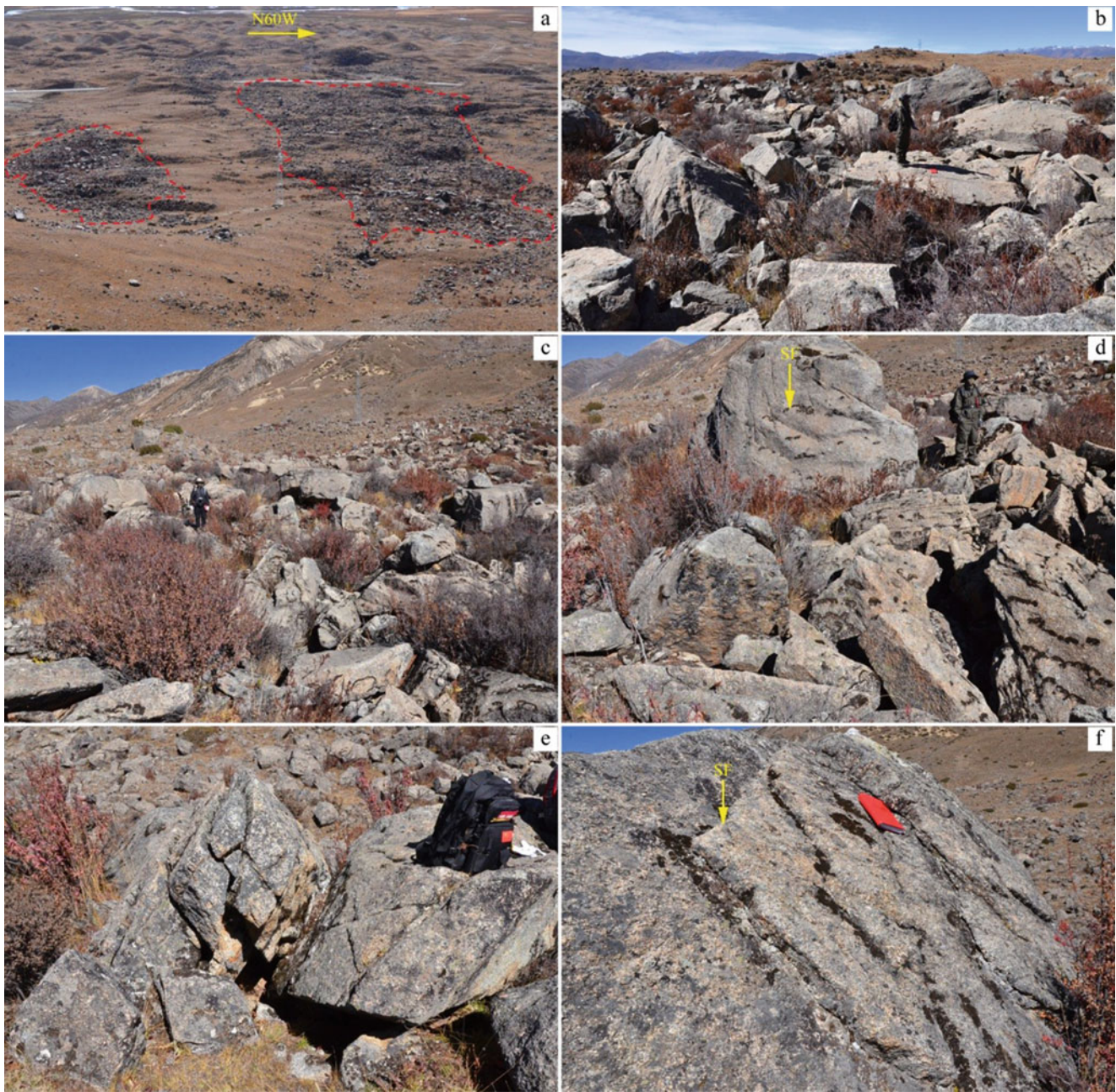


Fig. 17 Distribution of blocks in the carapace facies of the Luanshibao rock avalanche

are also observed in some excavated cross sections (Fig. 18), indicating a low disturbance in the propagation of the avalanche mass.

4.2 Nyixoi Chongco Rock Avalanche

4.2.1 Geological Setting and General Features of the Nyixoi Chongco Rock Avalanche

The Nyixoi Chongco rock avalanche is situated in the Angang graben, Nimu County, Tibetan Autonomous Region,

China. The Angang graben belongs to the Yadong-Gulu rift, which is one of the North-South (N-S) trending rifts in the South Tibet detachment system (Fig. 19). The South Tibet detachment system, as one of the main structures formed by the Indian-Eurasia collision, is composed of 7 nearly parallel N-S rifts, which were initiated 8–23 Ma ago. Among them, the Yadong-Gulu rift is the youngest one in the Lhasa Terrane with its central segment being initiated 5 to 8 Ma ago. This young rift is characterized by intense tectonic activity with strong historical earthquakes (Harrison et al. 1995; Chung et al. 2005; Zhang et al. 2013). The latest strong M_s

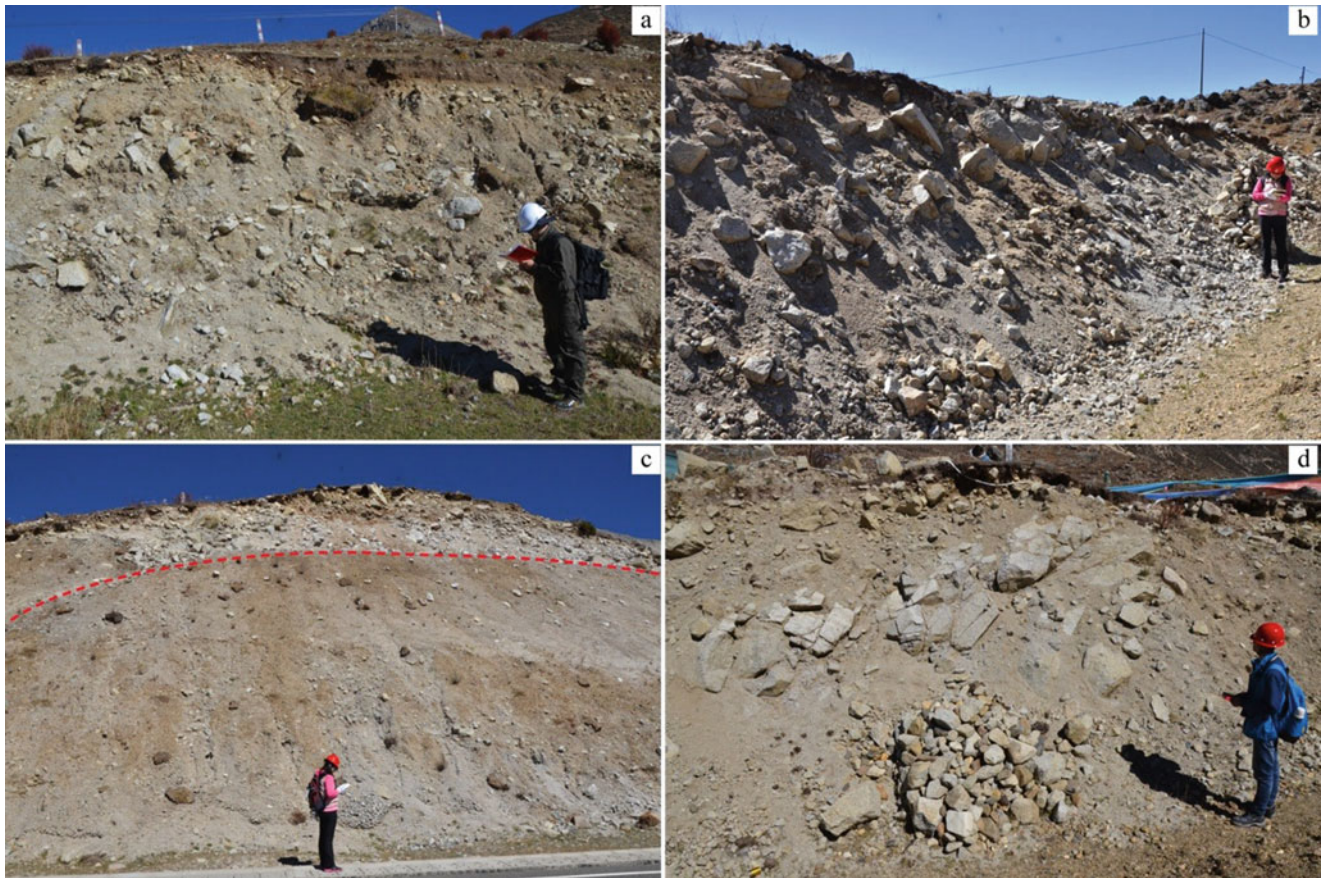


Fig. 18 Vertical profiles revealed in the Luanshibao rock avalanche

6.3 Angang earthquake occurred in this area in 1992. Furthermore, Wu et al. (2015) conducted a series of OSL and ^{14}C dating on samples collected from the western main boundary fault of the Angang graben and concluded that the latest prehistoric strong earthquake in this area should occur about 2.2 ka ago with its M_w being over 7.0.

Under the effect of historical tectonic activities, the Yadong-Gulu rift is associated with an asymmetrical normal fault system was generated with its width being 30–40 km. The Angang graben is bounded from west and east by normal faults and the western one is more developed, with a series of preserved fault triangular facets, fault scarps, and fracture zones of bedrocks, suggesting that it is an active fault with frequent, strong earthquakes. The Angang Graben is a typical half-graben situated in the central segment of the Yadong-Gulu rift, which is 3–4 km wide and 22–24 km long. It presents a generally steeper and higher relief in its western than its eastern flank, and is characterized by rugged alpine topography due to strong erosion.

As shown in Fig. 20, the Nyixoi Chongco rock avalanche is located on the west flank of the Angang graben. The bedrock in the studied area is the Paleogene monzonitic granite (E_2Kd), which is distributed in the footwall of the

Yadong-Gulu rift mainly. The hanging wall is covered by Pleistocene deposit (Q_p), and Holocene alluvial (Q_h^{al}) and colluvial-pluvial (Q_h^{col+pl}) deposits mainly.

In plan-view, the Nyixoi Chongco rock avalanche has an elongated tongue shape (Fig. 20). Due to topographic confinement, the movement direction of the Nyixoi Chongco rock avalanche presents an obvious turn of $\sim 50^\circ$ toward southeast from the transition zone to the accumulation zone. The runout of the Nyixoi Chongco rock avalanche was ~ 4600 m with a vertical drop height of ~ 885 m, and thus the $F_{arb} \sim 0.19$, indicating an extremely high mobility of the avalanche mass (Cruden and Varnes 1996; Lucas et al. 2014). Through reconstruction of the topography of the source area, volume of the detached mass was assessed as $\sim 0.28 \times 10^8 \text{ m}^3$ with a maximum thickness of rock avalanche deposit ~ 50 m (Wang et al. 2020). Along the N-S extension of the rift, the Xuqu River is well-developed with some vertical profiles of the avalanche deposits being revealed, which provides opportunity for the study of its internal features.

Figure 21 is a longitudinal profile of the avalanche with its position being marked in Fig. 4b. Bounded by the normal fault, the avalanche source area ranges in elevation from 4270

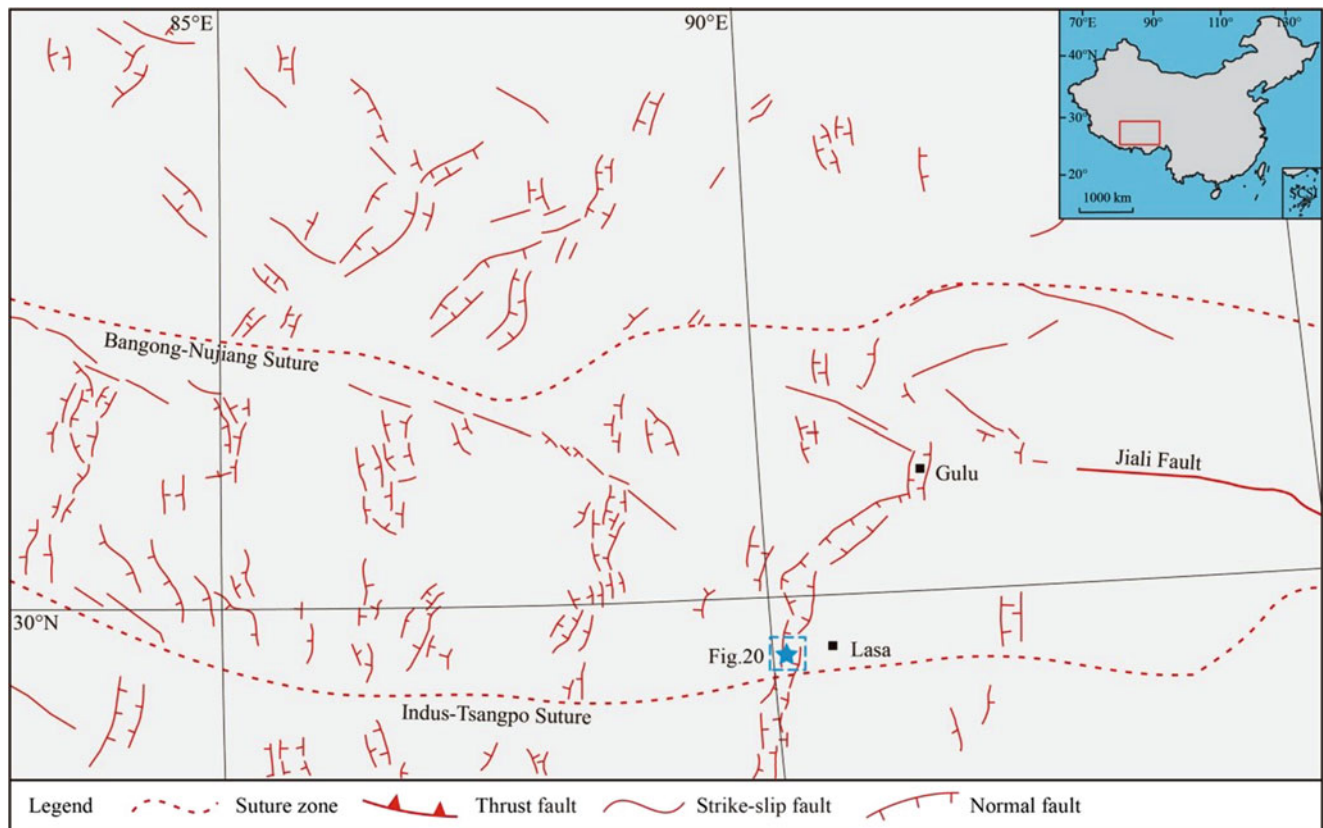


Fig. 19 Regional geological setting of the Angang graben

to 4850 m a.s.l. and locates on the footwall of the fault, giving a height difference of 580 m. The bedrock in this area is mainly composed of biotite monzonitic granite belonging to the Konglangdong formation of the Eocene (E_2Kd). Due to the effects of tectonic events and long-term weathering, the bedrock has been intensely fractured with two sets of preferred joints generated (Fig. 4b). The dip directions and dip angles of these joint sets are $180\text{--}190^\circ/40\text{--}50^\circ$ (JS1) and $350\text{--}360^\circ/60\text{--}70^\circ$ (JS2), respectively, controlling the wedge failure of the rock mass in the source area. In the hanging wall, it is the distribution of the rest part of the avalanche with the elevation ranging from 3965 to 4270 m a.s.l. For this area, the slope angle is relatively low. And the farther away from the source area, the lower the slope angle is. The substrate of this part is composed of Quaternary colluvial-diluvial (Q_4^{col} - Q_4^{dl}) and alluvial deposits (Q_4^{al}).

4.2.2 Sedimentary Features of the Avalanche Deposit

(1) Plan zonation and landforms

As exhibited in Fig. 22, a series of landforms are sequentially distributed along the travelling path of the Nyixoi Chongco rock avalanche, including torea blocks, longitudinal ridges, transverse ridges, en echelon ridges and hummocks.

According to the spatial distribution of these landforms, the Nyixoi Chongco rock avalanche can be divided into three zones from proximal to distal part: the source area (I), the transition zone (II), and the accumulation zone (III). Field investigation reveals that scarps with heights over 15 m developed in the frontal part of the transition zone, which formed the natural boundary between the transition zone and the accumulation zone. Since the source area presents a steep topography, the transition zone and the accumulation zone present relatively gentle topography with mean slope of $\sim 10^\circ$ and $< 2^\circ$, respectively. Due to post-rock avalanche erosion by the Xuqu River, the section of the avalanche deposit is revealed, which provides precious geological evidences for studies on the internal sedimentary characteristics and the rock avalanche deposit-substrate interactions.

a) Source area (I)

The source area of the Nyixoi Chongco rock avalanche is located on the footwall of the boundary normal fault developed in the west flank of Angang graben. Similar to the Luanshibao rock avalanche, its source area also displays a U-shape in plan-view. As exhibited in Fig. 21, this area is also characterized by a steep well-exposed scarp and a relatively gentle section with talus accumulated. Bedrock in the

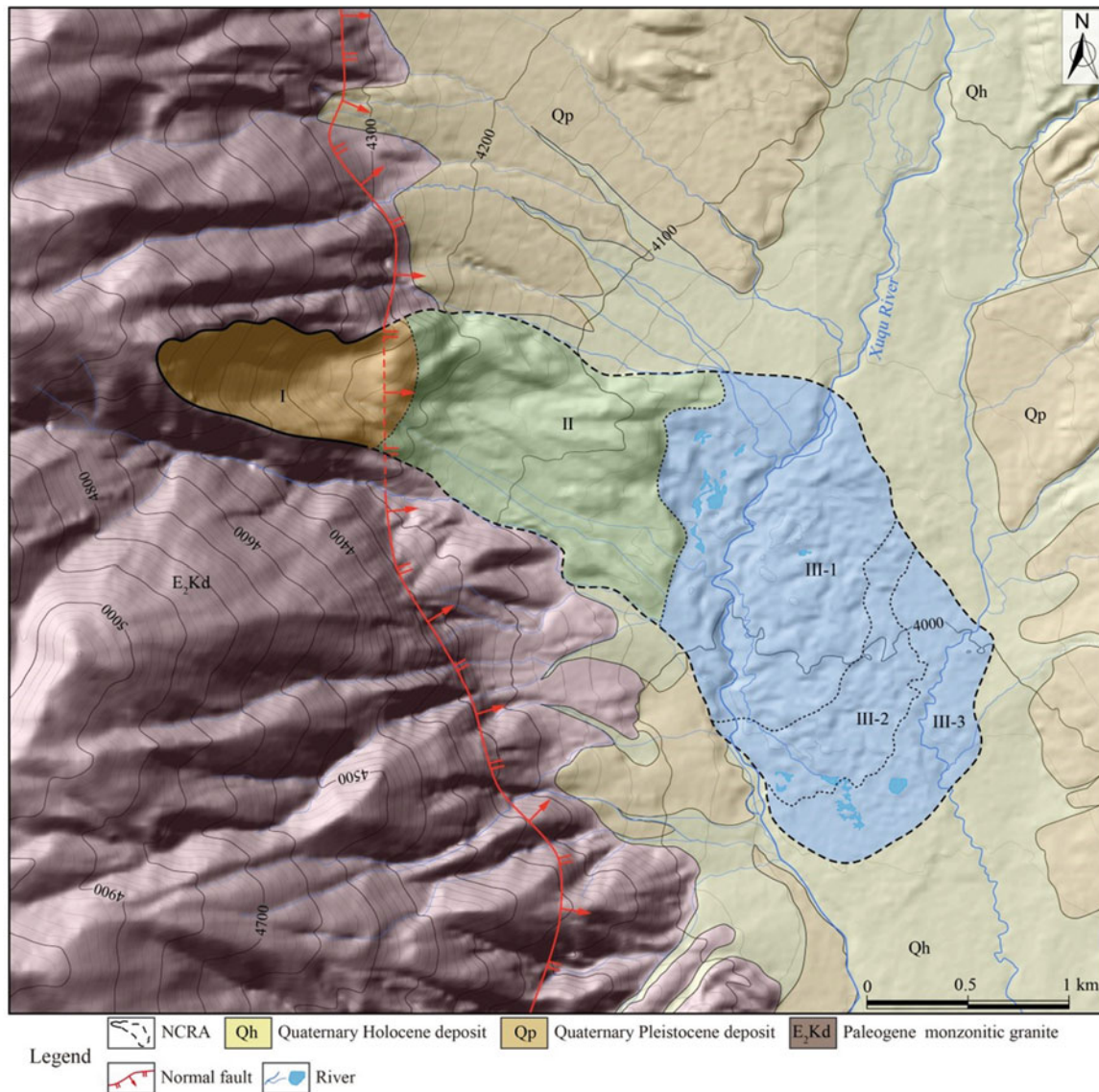


Fig. 20 Geological setting of the studied area where the Nyixoi Chongco rock avalanche is situated

source area was highly fractured due to cut of those discontinuities with wedge failure developed in the source area.

b) Transition zone (II)

The transition zone is characterized by large toveva blocks (S-1 and S-2) and large longitudinal ridges (LR) from its rear area to its frontal area as exhibited in Fig. 22. In plan-view, the S-1 toveva block is 270 m long and 100 m wide with 90 m high frontal steep escarpment (Fig. 23a). Next to S-1, it is the display of S-2 toveva block, which is 700 m in length. The height of its frontal escarpment is about 65 m as exhibited in Fig. 22b. Compared to the escarpment of S-1, the slope angle of the frontal escarpment of S-2 is relatively lower. On the top

surfaces of both toveva blocks, numerous blocks are distributed (Fig. 23c), with some displaying jigsaw structures.

Next to both toveva blocks, it is the extensions of longitudinal ridges (LR) as shown in Fig. 22. Due to the erosion of surficial runoff, the deposited landform in the right part of zone II has been changed. So, only the landforms deposited in the middle and left part of zone II were investigated in detail during our field survey. Figure 24a shows the extension of the longitudinal ridges in zone II. It can be seen that the lengths of the longitudinal ridges all exceed 590 m, with the aspect ratio > 100 . In plan-view, L-1 is in a long strip shape with its length and width being ~ 1000 m and ~ 120 m, respectively. L-2 presents a fan-shape from the narrow proximal to relative wide distal part with its length being ~ 750 m.

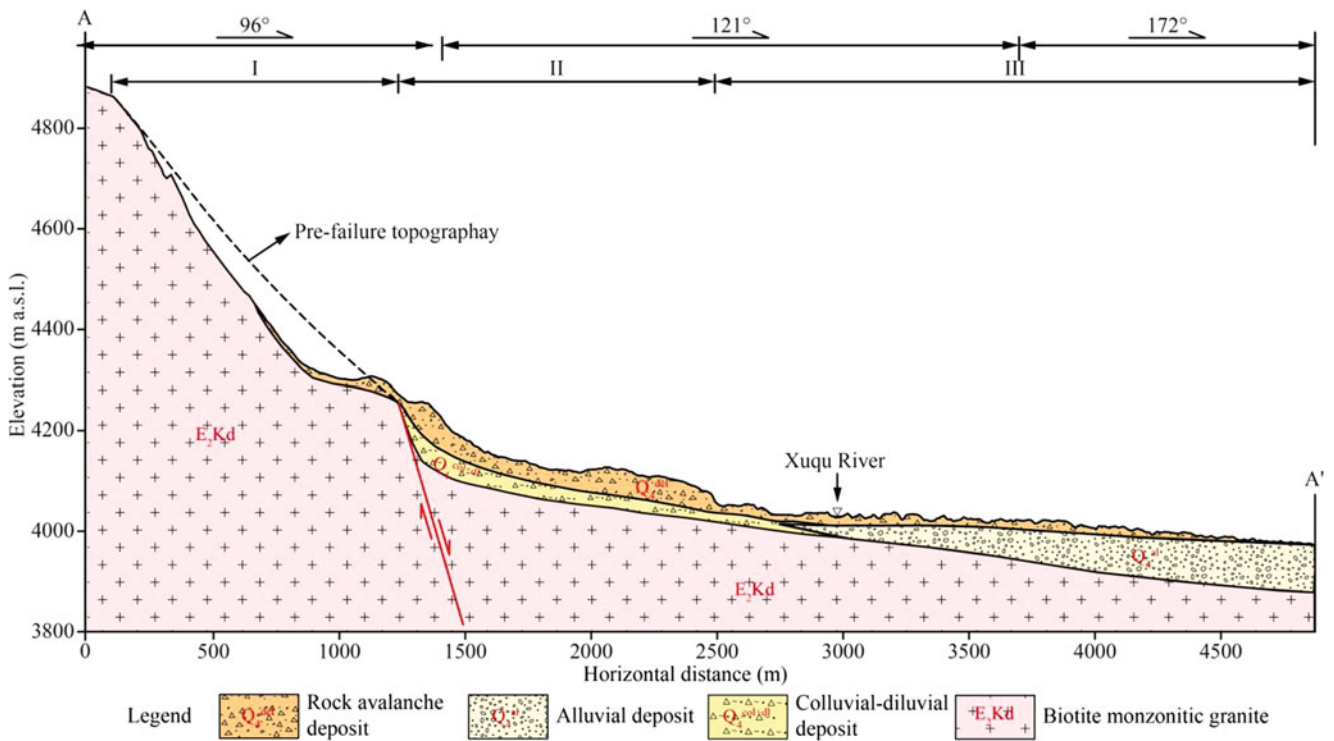


Fig. 21 Longitudinal profile of the Nyixoi Chongco rock avalanche with different scales in vertical and horizontal axes

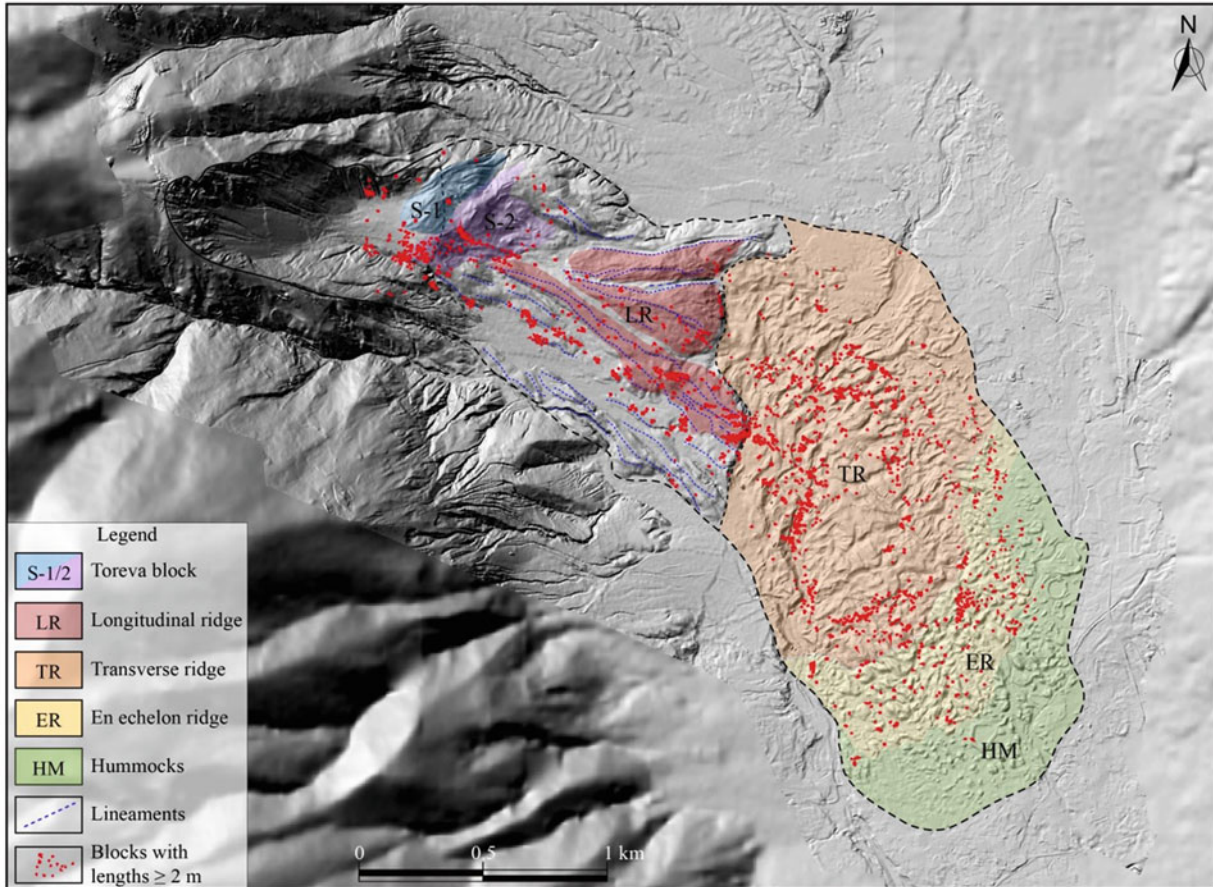


Fig. 22 Shaded relief map of the Nyixoi Chongco rock avalanche with the main landforms marked

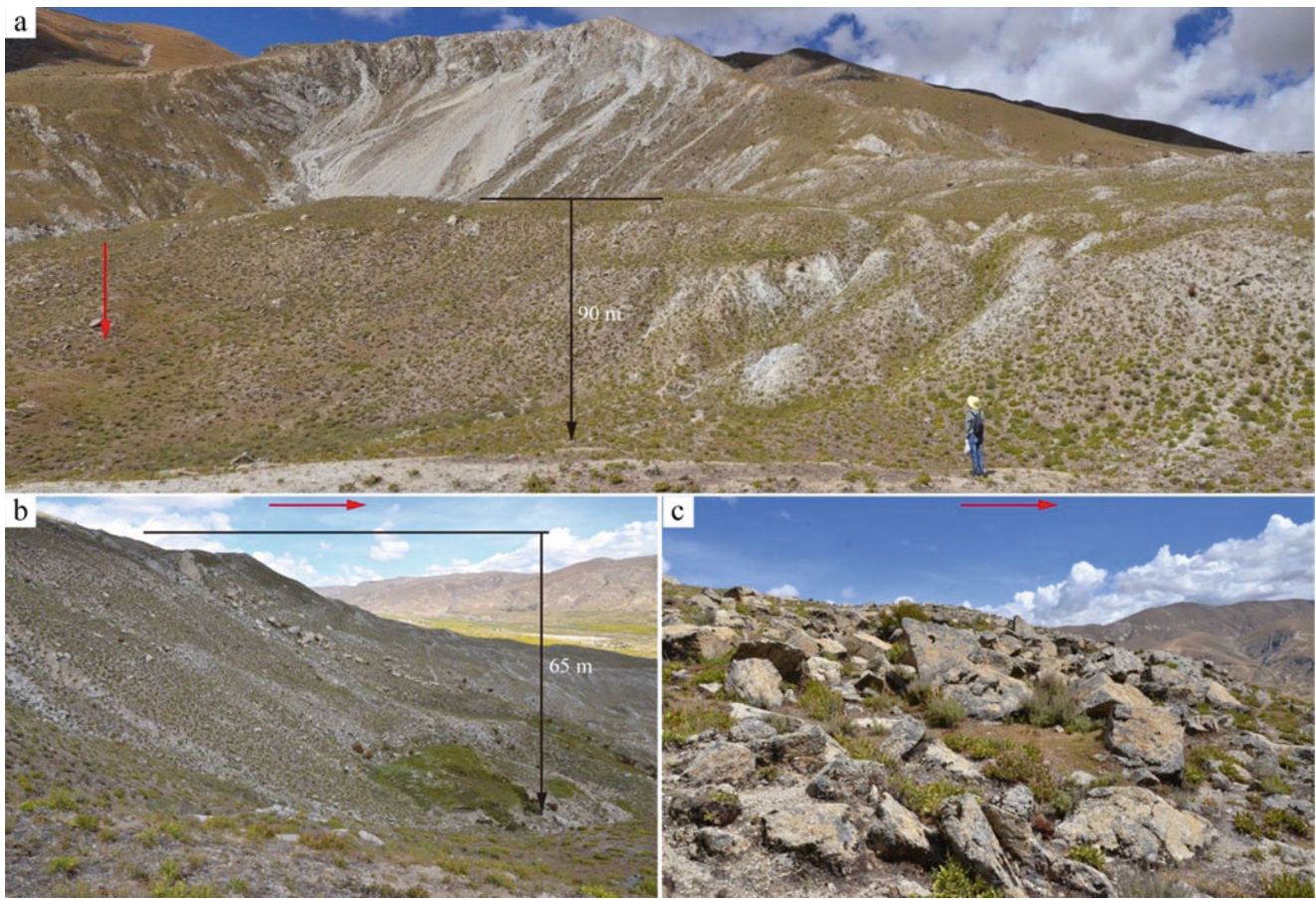


Fig. 23 Toreva blocks in the transition zone of the Nyixoi Chongco rock avalanche (**a**: S-1 toreva block; **b**: S-2 toreva block; **c**: distribution of blocks on the top surface of S-2; the red arrow indicates the movement direction of the sliding mass)

L-3 displays an oval shape with its length and width being ~ 590 m and ~ 100 m, respectively. The orientation of the ridges is $100\text{--}120^\circ$, which are nearly parallel to the main moving direction of the avalanche mass. Besides these longitudinal ridges, another interesting landform was observed during our field survey, which is the distribution of numerous secondary en echelon-arranged ridges distributed on the surfaces of the longitudinal ridges (Fig. 24b-c). The secondary ridges formed an acute angle with the main ridges.

c) Accumulation zone (III)

For the accumulation zone, transverse ridges, en echelon-arranged ridges, and hummocks of various sizes are sequentially developed and well-preserved. According to the spatial distribution of these landforms from the proximal to distal area of zone III, it can be further divided into three sub-zones, which are sub-zone III-1 with transverse ridges (TR) and secondary shear faulting, sub-zone III-2 with en echelon ridges (ER), and sub-zone III-3 with hummocks (HM) (Fig. 22).

The sub-zone III-1 with transverse ridges and secondary shear faulting starts from the turning part of the avalanche and comprises the main part of zone III (Fig. 22). In the rear part of this sub-zone, the transverse ridges are 30–60 m long, 15–30 m wide, and 20–30 m high. Figure 25a-b shows the extension of some transverse ridges in this sub-zone. Huge transverse ridges with length > 100 m are distributed locally. The aspect ratio of transverse ridges in this sub-zone is 2–3, with large transverse troughs developed between adjacent ridges. The ridges along with the troughs formed the ridge-trough coupled landforms (Fig. 25b). The main trend of the transverse ridges is $40\text{--}70^\circ$, which is nearly perpendicular to the movement direction of the avalanche mass. In the frontal part of sub-zone III-1, the scales of transverse ridges increase slightly with most ridges ranging from 20–70 m in length and even > 100 m (Fig. 22). Meanwhile, the width of transverse ridges in this part is also larger, especially for those near the central line of the avalanche, whose width exceeds 70 m. Another interesting feature observed in the frontal part of sub-zone TR is the extensions of the secondary shear faulting on the surfaces of several large transverse ridges near the center line of the avalanche. As shown in Fig. 25c, a large

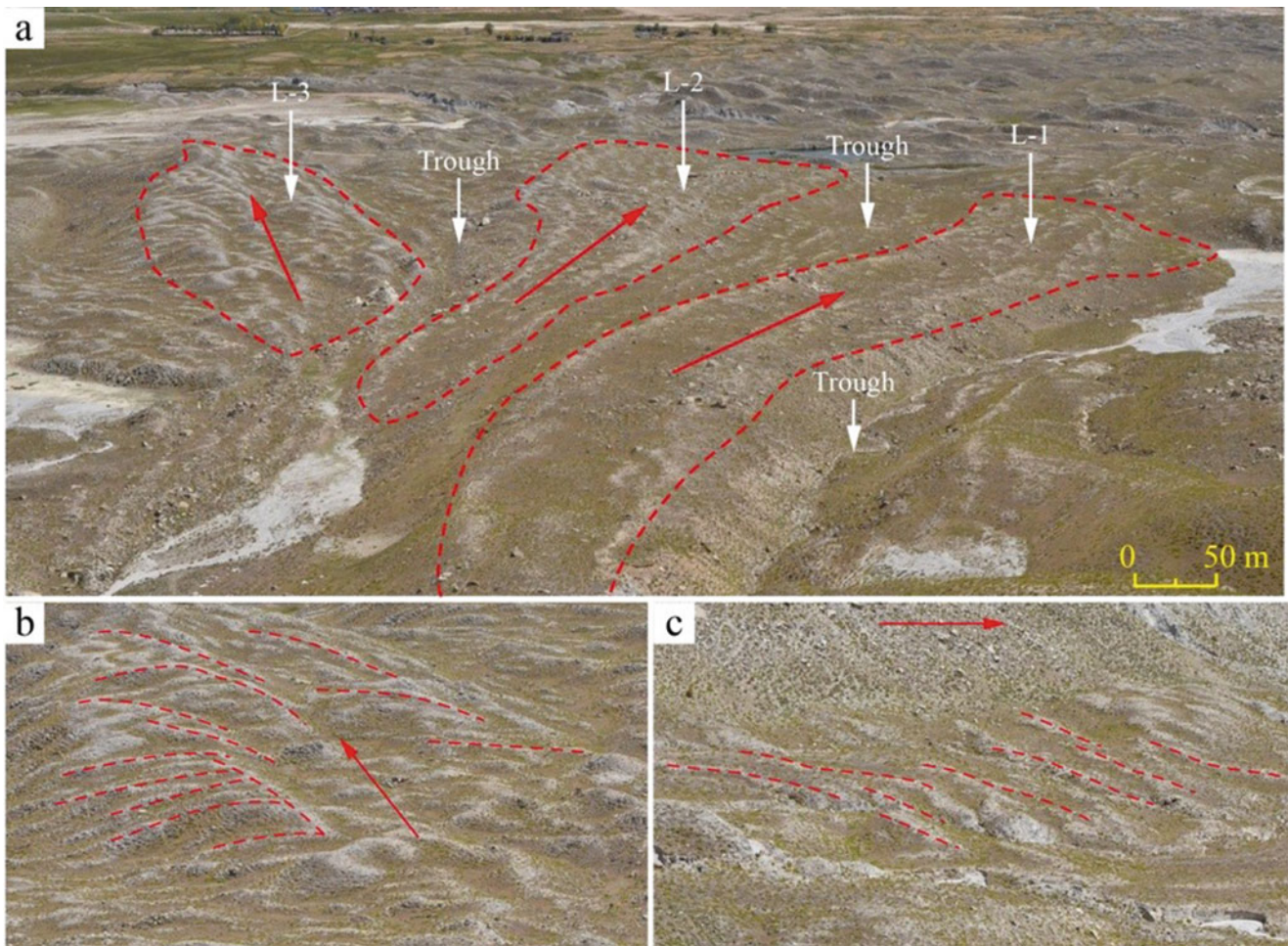


Fig. 24 Longitudinal ridges in the transition zone of the Nyixoi Chongco rock avalanche

transverse ridge has been cut and separated into 5 parts by several dextral secondary shear faulting. Such landform has also been reported in previous studies (Shea and van Wyk de Vries 2008; Paguican et al. 2014; Longchamp et al. 2016).

Next to sub-zone III-1, there is a sub-zone III-2 with en echelon ridges (ER). In this sub-zone, these en echelon ridges have relatively smaller sizes in 10–60 m long, 10–20 m wide, and 20–30 m high (Fig. 22). Figure 25d shows one set of the en echelon ridges in this sub-zone with their main trends being 30–40° and 310–320°, respectively, forming an acute angle with the movement direction of the sliding mass. In this sub-zone, the scales of ridges are smaller than that of sub-zone III-1.

Similar to the Luanshibao rock avalanche, the frontal part of the Nyixoi Chongco rock avalanche is a sub-zone III-3 with multiple hummocks (HM). As shown in Fig. 22, this sub-zone is composed mainly of a series of small-scaled hummocks with their maximum diameters of 10–50 m and heights of 5–12 m, respectively. Figure 24e shows the extension of several hummocks in this sub-zone, which are present

in nearly circular shapes. On the top surface of hummocks in this sub-zone, there is almost no blocks. Hummocks in sub-zone III-3 are distributed without main trend.

(2) Internal deposited features

Apart from these landforms as described above, some typical internal deposited features were also observed. The first prominent feature is the carapace facies with numerous huge blocks (Figs. 22 and 26). As indicated by the red points (representing blocks >2 m in long axes) marked in Fig. 22, megablocks are commonly distributed along the sliding path. It is obvious that megablocks are distributed with spatial heterogeneity, as the number of megablocks on the slope of transverse ridges is much larger than on the back of the slope. Furthermore, the main orientation of the majority of megablocks (Fig. 26a-c) is nearly parallel to the main trend of the transverse ridges (i.e., perpendicular to the movement direction of the avalanche). Among these megablocks, jigsaw

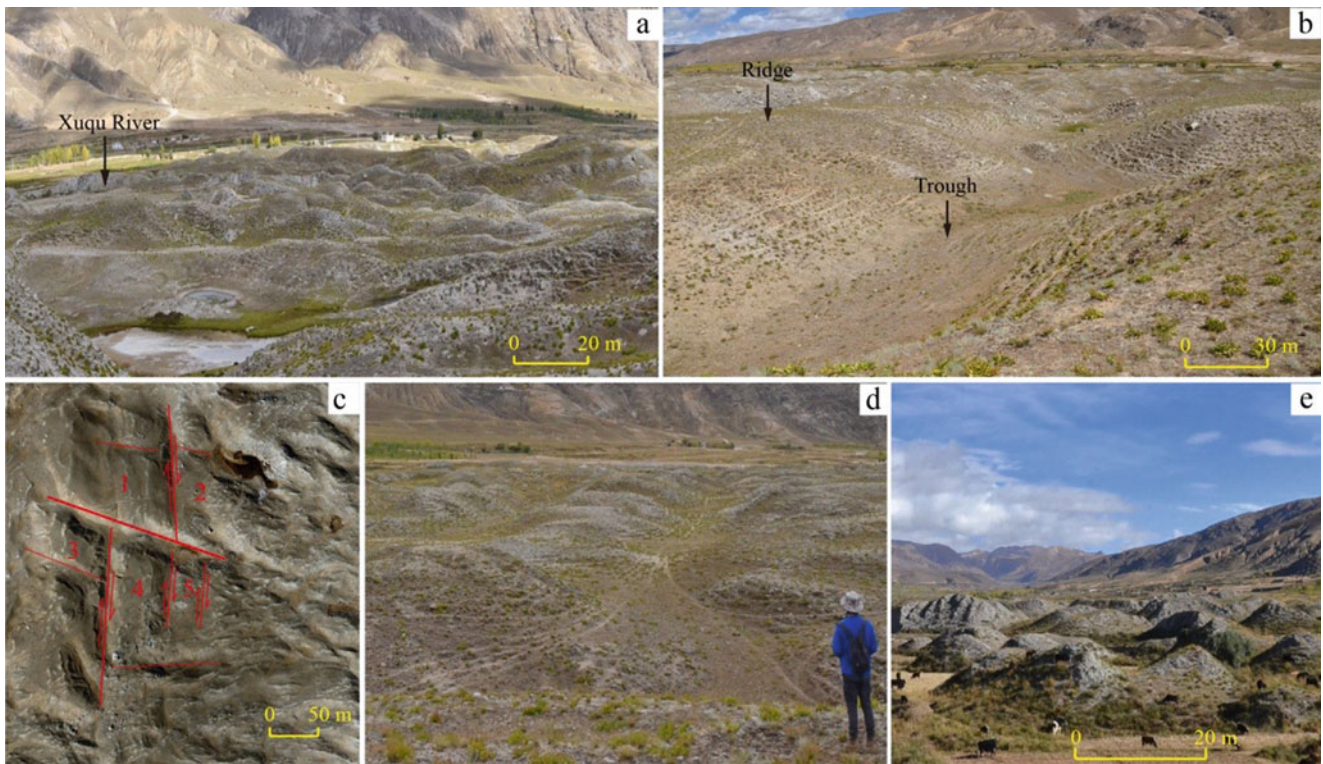


Fig. 25 Surficial topography in the accumulation zone of the Nyixoi Chongco rock avalanche (**a-b**: the transverse ridge-trough coupled topography present in the sub-zone TR; **c**: secondary shear faulting on

the surfaces of transverse ridges in the sub-zone TR; **d**: en echelon ridges in sub-zone ER; **e**: hummocks in sub-zone HM)

structures are commonly observed along the travelling path (Fig. 26d-f).

As described above, well-preserved outcrops were revealed due to post-avalanche river erosion, which provides invaluable geological evidences for the study of rock

avalanche emplacement. Figure 27a shows that the Nyixoi Chongco rock avalanche deposit is inversely graded with the carapace facies, the body facies, and the basal facies being sequential present from the top to the bottom. The carapace facies consists of angular blocks with size mainly ranging

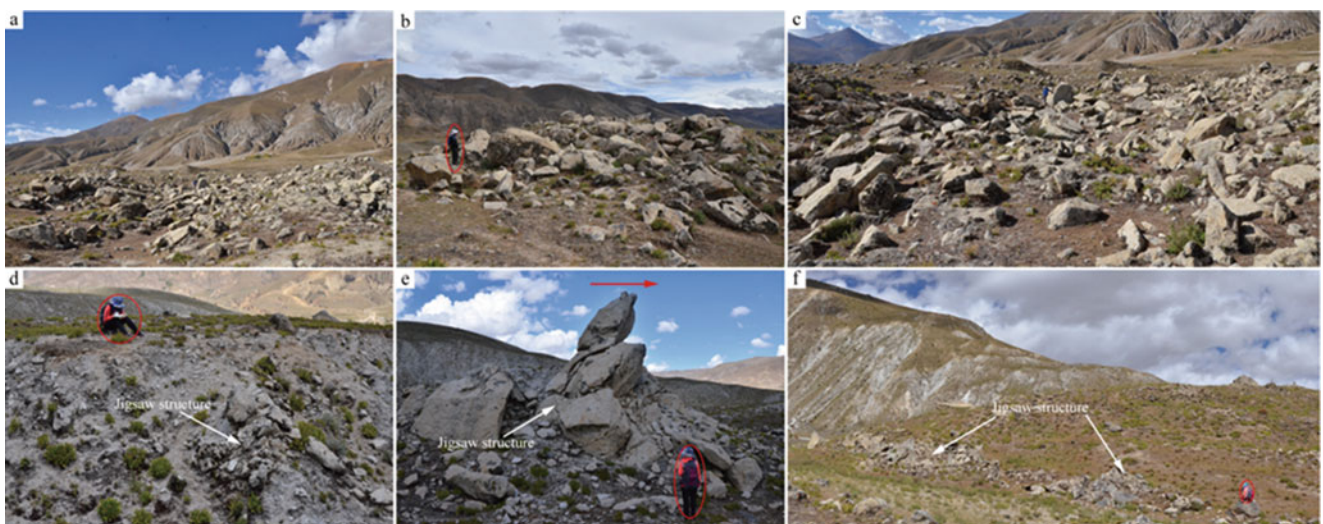


Fig. 26 Surficial features of the carapace faices of the Nyixoi Chongco rock avalanche (The movement direction of the rock avalanche is shown as the red arrow)

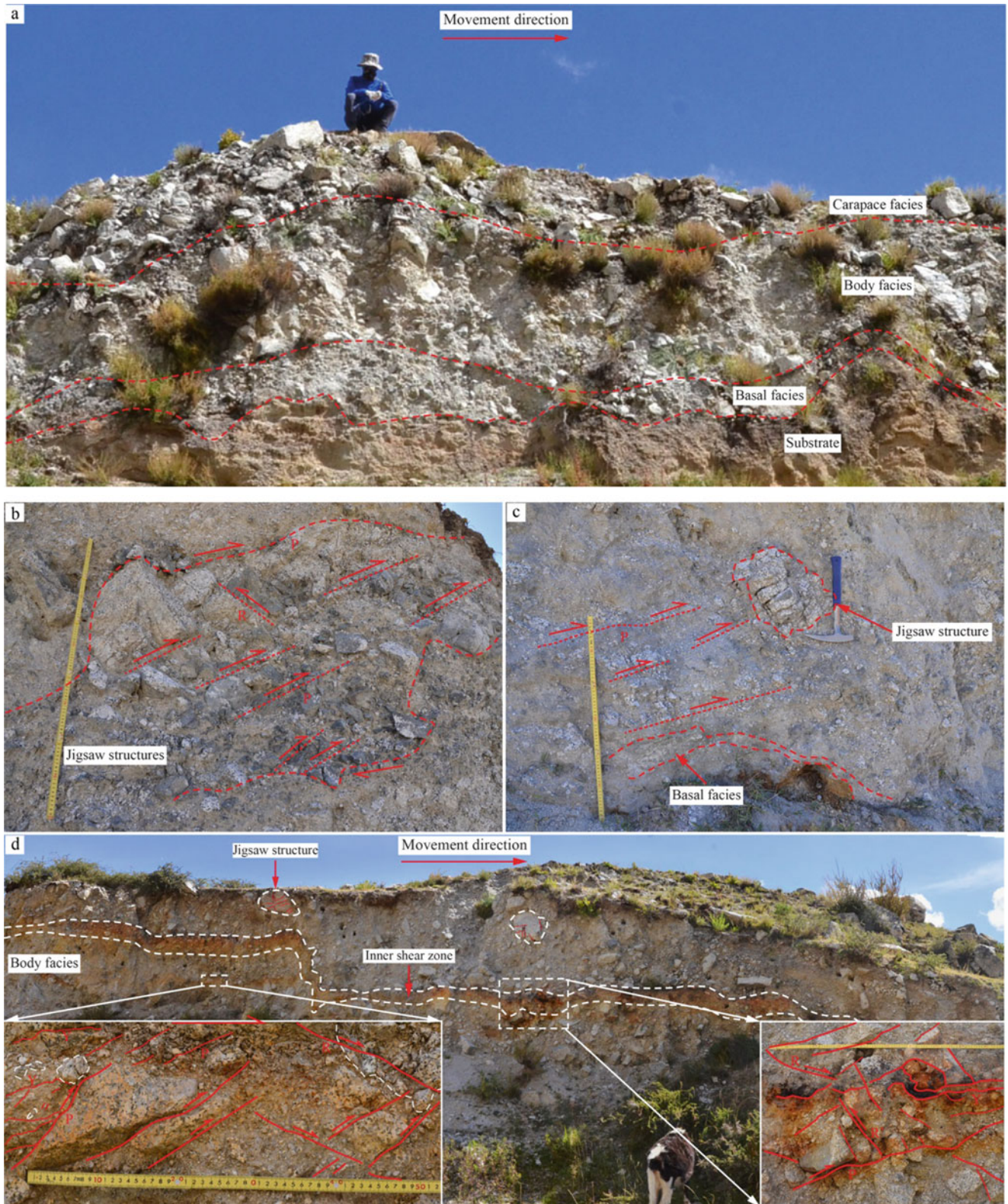


Fig. 27 Sedimentary features of the Nyixoi Chongco rock avalanche

from a dozen of centimeters to several meters. Small amount of fine particles fill the pores among blocks as matrix. Thus, the carapace facies is characterized by a clast-supported structure. The body facies contains fewer blocks yet it is composed of clasts with size ranging from several millimeters to a dozen of centimeters mainly. Clasts in the body facies are also angular and poorly rounded. In some outcrops, jigsaw structures are commonly observed in the body facies (Fig. 27b-d), indicating that the original shape of clasts was preserved after fracturing with the fragments did not separating apart or just dislocated minor. In the areas with jigsaw structures appeared, directional arrangements of fragmented clasts can be observed as exhibited in Fig. 27b-c. In one outcrop, z-shaped inner shear band was observed (Fig. 27d). The color of the inner shear band is tangerine, which is significantly different from the color of the main deposits. Grain size in this band is finer than the main deposits. Locally, even black clay scale grains are present in the inner shear band. Another interesting feature as revealed by some outcrops is the appearance of shear structures. As shown in the outcrops of Fig. 27b-d, three preferred sets of shear structures in varying scales, i.e., R shear, P shear and Y shear, can be observed, indicating the internal shearing mode in the emplacement of the avalanche mass.

The basal facies is the direct contact zone with the substrate. Due to the intense interaction between the sliding mass and substrate, the mean grain size in this facies is finest compared with the carapace facies and the body facies. For this facies, it consists of fine particles <2 mm with a small number of clasts mainly. Along the contact line between the basal facies and substrate, preferred alignment of clasts were observed (Fig. 28a-b and d-e), indicating the relative direction of movement of the sliding mass over the substrate. In the Nyixoi Chongco rock avalanche, the eroded depth has exceeded the thickness of the avalanche with the interaction morphology between the avalanche mass and substrate being well revealed as shown in Fig. 28. The substrate of the Nyixoi Chongco rock avalanche is a layer of alluvial deposits consisting of silty and clayey particles (finer than the rock avalanche particles) mainly, which is classified as a soft substrate (Shi et al. 2023). Under the control of such relatively soft substrate, a series of diapiric structures with varying size and morphology were generated along the interface of the basal facies and substrate (Fig. 28). For these diapiric structures, their upstream slopes and the downstream slopes are asymmetric with the downstream slopes being steeper. In some outcrops, vertical fold and recumbent fold were even generated, indicating an intensive interaction between the avalanche mass and substrate (Fig. 28g, l-m). With the generation of such structures, their original layer sequences are still well-preserved, indicating low disturbance and mixing during formation. Consisting with the preservation of the

layer sequence, the boundary between the avalanche mass and substrate is sharp without obvious mixing, which also indicates a low disturbance between the basal facies and the substrate during the avalanche propagation.

4.3 Tagarma Rock Avalanche

4.3.1 Geological Setting and General Features of the Tagarma Rock Avalanche

Tagarma rock avalanche is located in the Tarim Basin, south of Muztag Ata peak in the Eastern Pamir (Fig. 29). This region is in the northwestern part of the Himalayan convergence zone formed as a result of continuous collision of the Indian-Eurasian plates initiated about 55 Ma ago. For the western tectonic knot, it is one of the regions in the Tibetan Plateau experiencing the strongest tectonic stresses and exhibiting the fastest uplift and denudation rates (Robinson et al. 2004). To date, the convergence zone remains ongoing deformation with an uplift rate of 1.5 ± 0.5 mm/yr. and a shortening rate of 20–25 mm/yr. (Bufe et al. 2017). Such intensive deformation has been promoting to the striking topography, active tectonics and high seismicity in this range (Arrowsmith and Strecker 1999; Cowgill 2010; Strom 2010). Under the effect of historical intensive tectonic activities, a series of fault systems with different scales and kinematics have been generated as shown in Fig. 29. Northward, it reaches the Pamir Arc tectonic belt, and southward, extends to the Nanga Parbat-Haramush massif.

Among these fault systems, the Kongur Shan normal fault is the main fault system going across the studied area (Fig. 29), which is a well-known extensional system and was formed in the late Cenozoic due to the exhumation of the Muztagh Ata gneiss dome. The extension of this fault is approximately 250 km with its overall strike being NNW and the dip angle ranging from 55° to 75° . It is reported that this fault zone began to generate at 7–8 Ma and remains active as a Holocene active fault. The latest strong earthquake recorded in this region is the 1895 Tashkurgan earthquake with magnitude of M_w 7.0 (Seong et al. 2009).

Fig. 30 shows the geological setting of the Muztag Ata peak region, where the Tagarma rock avalanche occurred. The bedrock is composed of Paleoproterozoic gneiss (Pt₁B), Paleogene monzonitic granite ($\eta\gamma$ E), Triassic monzonitic granite ($\eta\gamma$ T), and Triassic Quartz diorite ($\delta\sigma$ T). The basin is filled by the Upper Pleistocene glacial deposits (Q_p^{gl}), glaciofluvial outwash deposits (Q_p^{fgl}), and alluvial-diluvial deposits (Q_p^{pal}), and Holocene alluvial facies (Q_h^{al}), alluvial-diluvial deposits (Q_h^{pal}), glacial deposits (Q_h^{gl}) and fluvial deposits (Q_h^{fl}). Due to different geological processes, the Quaternary landscapes in this region have undergone significant erosion and alteration. Divided by the Kongur Shan normal fault, bedrocks in this studied area appears in the

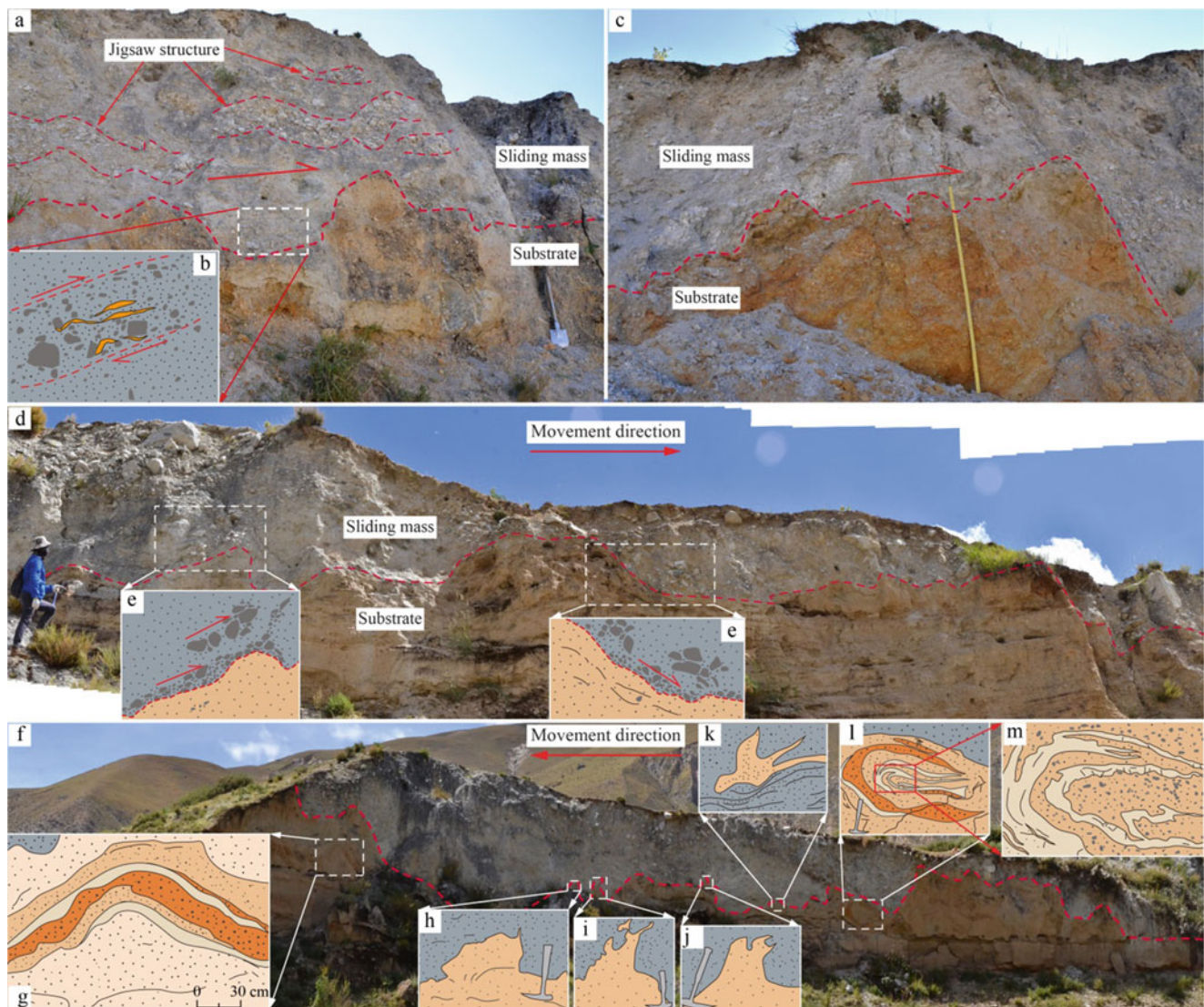


Fig. 28 Diapiric structures generated along the avalanche mass and substrate of the Nyixoi Chongco rock avalanche

footwall mainly with the hanging wall being covered by Quaternary deposits mainly as exhibited in Fig. 30. The footwall belongs to the Muztagh Ata gneiss dome, characterized by high relief. Gneiss underwent medium- to high-grade metamorphism during the Paleoproterozoic Era. The Tagarma rock avalanche was just one case originated from the gneiss dome. The highest peak in the area is Muztagh Ata, which stands at an elevation of 7509 m a.s.l. For the hanging wall, it is featured by gentle slopes, with the Tagarma intermontane basin formed in the downstream.

For the climate of this area, it falls within the domain of mid-latitude westerlies and too far to be affected by Indian summer monsoon. So, its climate is characterized by cold and aridity, with an average annual precipitation of 76 mm and temperature of 3.6 °C (Sun et al. 2006; Seong et al. 2009).

The Muztagh Ata peak is covered by glacier as shown in Fig. 30.

As shown in Fig. 30, the Tagarma rock avalanche was detached from a steep southwestern slope of the Muztagh Ata peak (38° 4' 33" N, 75° 10' 57" E). The source area is a high mountainous ridge with an extremely steep frontal slope on the footwall of the Kongur Shan normal fault (Fig. 31), and is composed of the Paleoproterozoic gneiss (Pt₁B). The gneiss exhibits well-developed foliations (F) and dips to the southwest at an angle of 60°. As a result of historical tectonic activities and weathering, two sets of joint structures with attitudes about 315°∠50° (JS1) and 60°∠70° (JS2) dissect the bedrock (Fig. 4c). The travel path on the hanging wall presents a relatively flat terrain in contrast to the steep source area, mainly composed of Quaternary glaciofluvial outwash

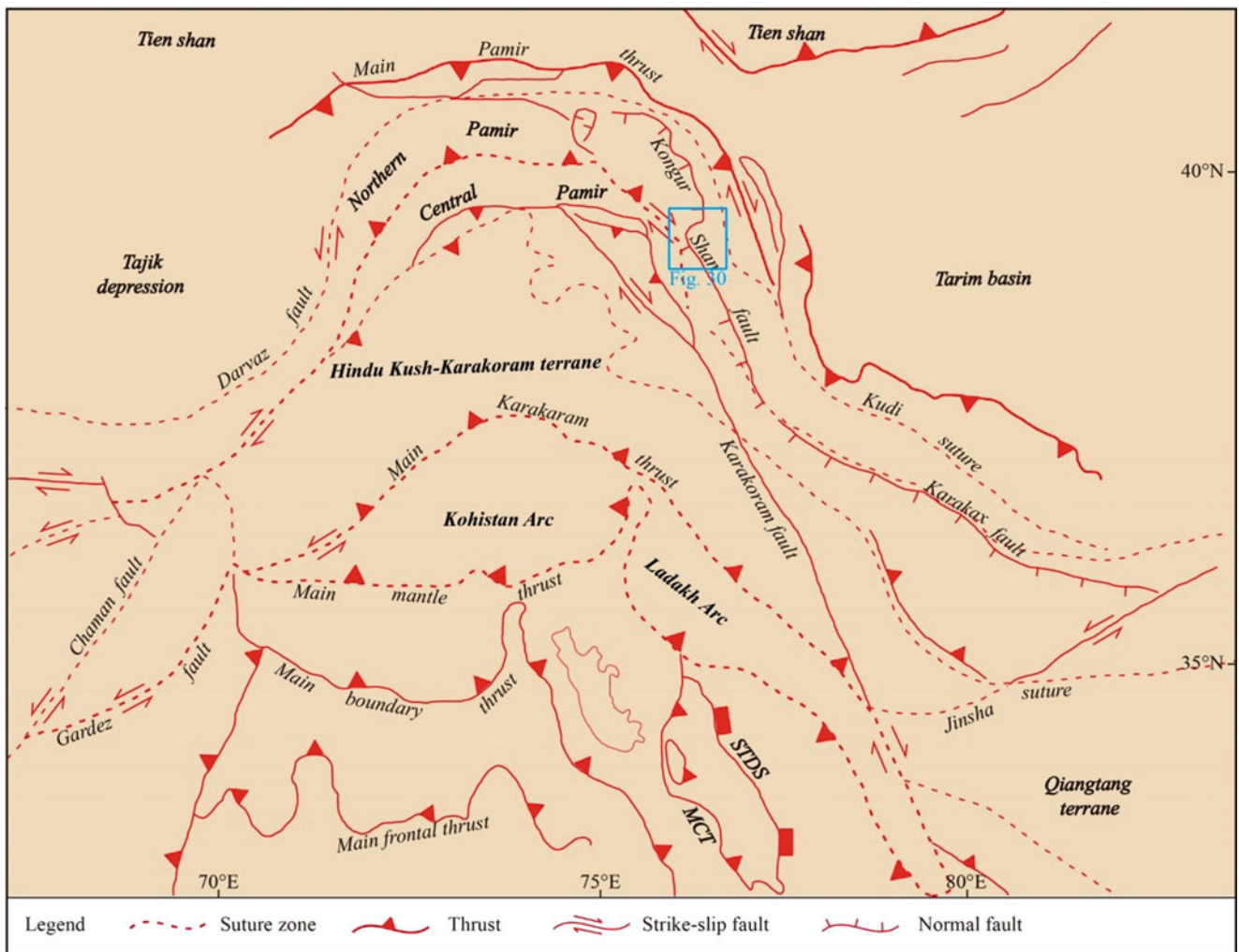


Fig. 29 Regional geological setting of the Pamir-western Himalayan syntaxis region

deposits (Qp^{gl}) (Fig. 31b). By ^{10}Be dating of gneiss boulders sampled from the avalanche deposits, Yuan et al. (2013) reached that this event should occur approximately 6.8 ka B.P. Based on an analysis of the fault activity and climatic environment of the study region, Zhu et al. (2019) proposed that the Tagarma rock slope was stable under natural conditions through a discrete element modeling and most likely was triggered by a paleoseismic event. The mean annual rainfall of this region is only 76 mm, which is too low to trigger a landslide as large as the Tagarma rock avalanche. Glaciers have accumulated only in the high-elevation areas, and no evidence of freeze-thaw process has been found in the source area. Thus, we also agree that the Tagarma rock avalanche was a single event triggered by a strong earthquake (Wang et al. 2020).

In plan-view, the Tagarma rock avalanche deposited in an elongated tongue shape (Fig. 31a). The horizontal distance (L) and vertical drop (H) from the head of the scarp to the toe

of the avalanche deposit is 5430 m and 1510 m, respectively, giving rise to a *fahrböschung* value (H/L; Heim 1932) of 0.28. This low value indicates a hypermobility of the rock avalanche (Cruden and Varnes 1996; Lucas et al. 2014). The accumulated area of the avalanche deposit is up to 6.15 km². With the help of a fixed-wing unmanned aerial vehicle (UAV), high-resolution aerial images of the Tagarma rock avalanche were captured in July 2018, and its high-resolution DEM model was built. Based on the high-resolution DEM data, the pre-avalanche topography of the Tagarma rock avalanche was reconstructed utilizing the Topo to Raster tool in ArcMap 10.7 software (ESRI). Additionally, through a comparison of the pre- and post-avalanche topographies, it has been determined that the detached rock mass and the deposit have approximate volumes of 0.96×10^8 m³ and 1.1×10^8 m³, respectively. As such, the coefficient of dilatation for this landslide is calculated to be 1.15.

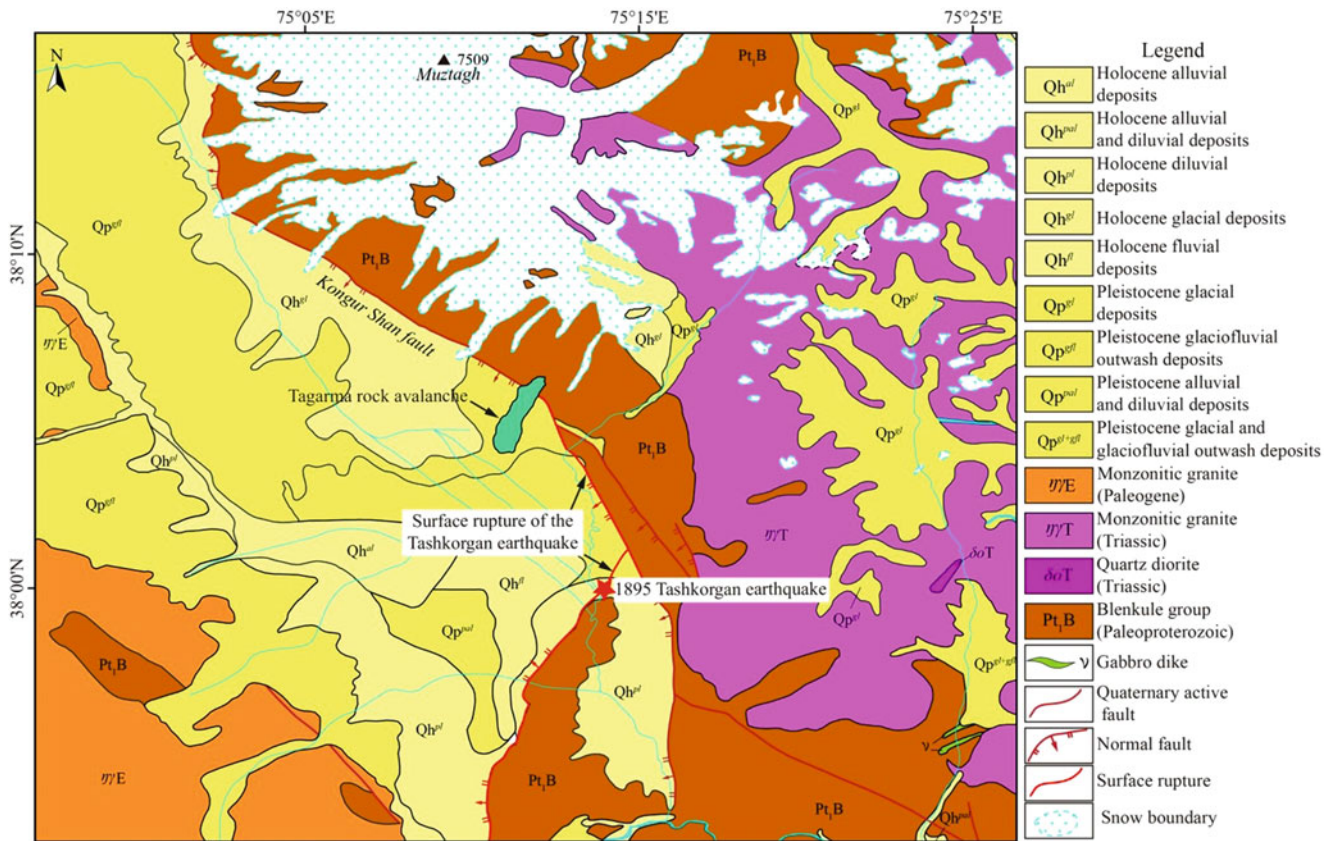


Fig. 30 Geological setting of the studied area where the Tagarma rock avalanche occurred

The debris tongue of this avalanche has a sharp and steep distal edge that exceeds 50 m in height, which is like to lava flows, surpasses the majority of rock avalanches with comparable flat travel paths (Evans et al. 2007; Dufresne et al. 2010; Basharat et al. 2012; Charrière et al. 2016; Wang et al. 2018, 2019a, b). Due to the arid climate, vegetation is rare along the avalanche path, and only two gullies resulting from upstream glacial meltwater were observed. In contrast to sediments on the left side of the source area that have been altered by gullies, landforms unaffected by such features are well-preserved on the surface of this region from proximal to distal locations. Owing to the dry climatic conditions prevalent in the research region, blocks manifest negligible levels of weathering. Furthermore, some well-preserved outcrops exposed by gully erosion were revealed, which is advantage for the study of the avalanche propagation.

4.3.2 Sedimentary Features of the Avalanche Deposit

(1) Plan zonation and landforms

As described above, high resolution images of the rock avalanche were obtained by UAV with the resolution of the aerial images being approximately 0.1 m, which was high

enough for observing the landforms of the avalanche deposit. Figure 32 is the shaded relief map of the avalanche derived from these images. As shown in Fig. 32, the spatial distributions of landforms along the travelling path can be highlighted and are easier to observe. From Fig. 32, it can be seen that an array of prominent topographic features emerge on the deposit surface, including toreva block, lateral levees, arc-shaped transverse ridges and linear longitudinal structures from proximal to distal areas. Based on the spatial distribution of these landforms, the avalanche can be divided into three zones: the source area (I), transition zone (II), and accumulation zone (III). In the following, the landforms of each zone are described in detail based on the analysis of these maps and field investigations.

a) Source area (I)

The source area, situated at the footwall of the Kongur Shan normal fault, ranges in elevation from 4010 to 4791 m a.s.l. The fault approximately intersects with the toe of the rupture surface of the rock avalanche. In plan-view, the source area has the U-shape with its maximum length and width being 1250 m and 780 m, respectively. As shown in Fig. 33a, the source area is composed of an upper steep well-exposed scarp

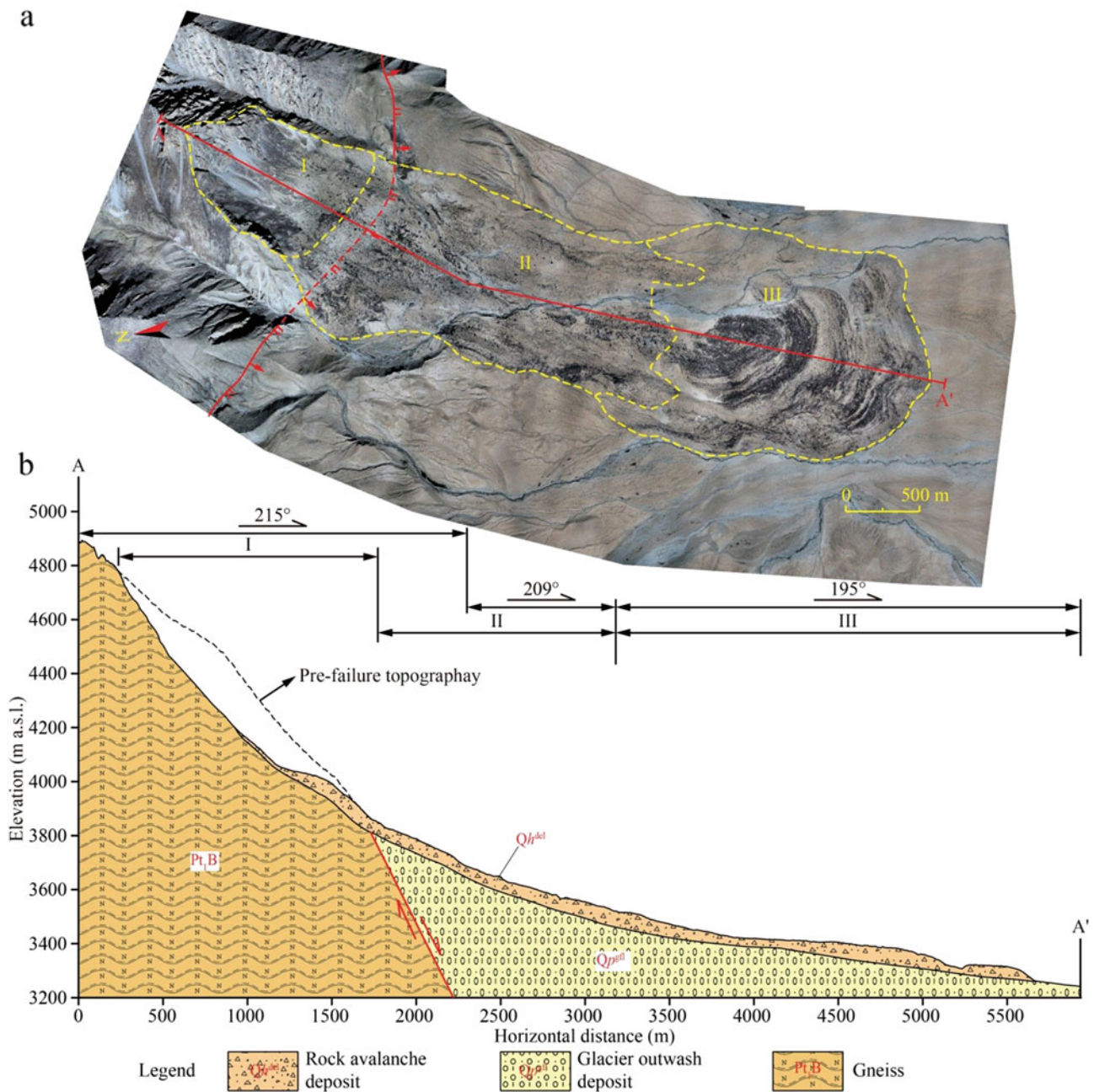


Fig. 31 Remote image (a) and longitudinal profile (b) of the Tagarma rock avalanche

(I-1) and a relatively gentle section with talus accumulation (I-2). For the steep exposed part (I-1), its average slope is over 50° with the preferred joint sets being seen clearly (Fig. 33a). Cutting by the preferred joint sets, the exposed scarp is characterized by a blocky and intensively fractured structure. For the lower relatively gentle section (I-2), its average slope angle is lower than 30° and was covered by avalanche debris and post-avalanche talus.

b) Transition zone (II)

As exhibited in Fig. 31a, a gully sourced from the glacier in the upstream goes across the transition zone, which destroyed the surficial features of zone II greatly. So, only the toreva block near to the source area and both lateral levees are still well-preserved. Figure 33b shows the extension of the toreva block taken during the field survey. It can be seen that the top surface of the toreva block is relatively flat with some huge

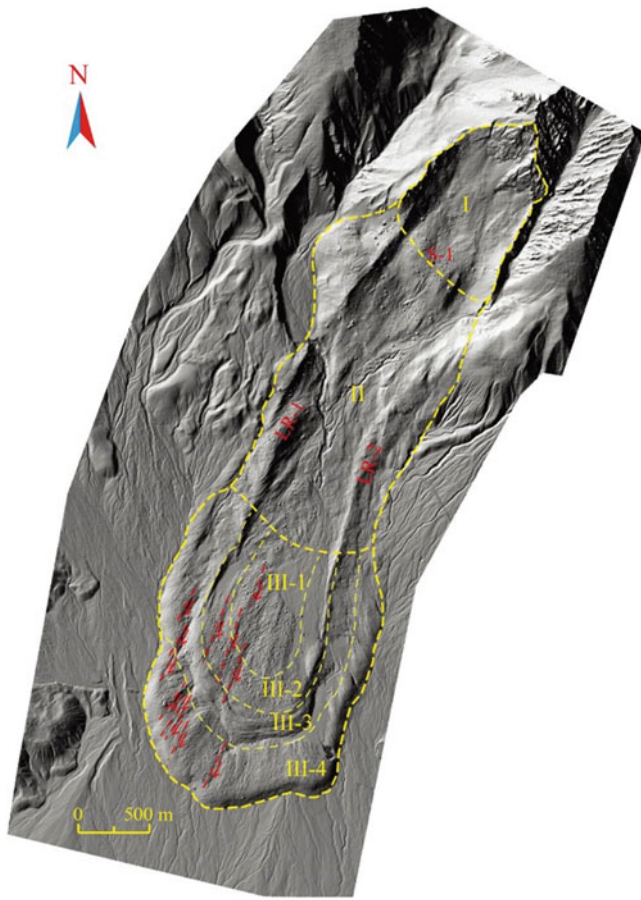


Fig. 32 Shaded relief map of the Tagarma rock avalanche

blocks distributed. It is measured that the width of the toveva block is up to 572 m with the height of its frontal escarpment being up to 150 m. As exhibited in Fig. 33b, a well-preserved outcrop of the toveva block is revealed with an intact rock mass intersected by three sets of structures being observed. The orientations of joint sets in the intact rock mass are $315^{\circ}/40^{\circ}$ (JS1'), $60^{\circ}/75^{\circ}$ (JS2') and $220^{\circ}/55^{\circ}$ (F'), respectively, which is similar to that of the bedrock in the source area. This indicates that the detached mass should be slightly fragmented and has a minimal disturbance when it reached the rear part of the transition zone.

In addition to the toveva block, the second prominent feature in the transition zone is the extension of both large lateral levees (LR-1 and LR-2). Figure 33c show the extension of the right lateral levee (LR-1). The LR-1 spans a length of roughly 1600 m and is elevated approximately 60 m above its surroundings. The length and width of LR-2 are 2000 m and 40 m, respectively. On the top surfaces of both lateral ridges, there is a widespread distribution of boulders as exhibited in Fig. 33c.

c) Accumulation zone (III)

Compared with the transition zone, the landforms in the accumulation zone are slightly eroded and relatively well-preserved. As exhibited in Fig. 31a, the most typical surficial feature in zone III is a sequential distribution of arc-shaped transverse ridges with convex sides facing forward. Unlike linear transverse ridges observed in other rock avalanches described herein, those of the Tagarma rock avalanche exhibit curvature. This provides an ideal condition for a meticulous study of the characteristics of arc-shaped transverse ridges.

From Fig. 31a, it can be seen that megablocks within zone III exhibit alternate dense and sparse concentrations as runout increases. According to the variations in megablock concentrations and topographies in this zone, zone III can be further divided into four distinct sub-zones, namely III-1, III-2, III-3 and III-4 (Fig. 34a). In these sub-zones, the transverse ridges exhibit a stepped distribution in the longitudinal direction, featuring enormous and steep steps. Figures 34c-d are photos of the frontal escarpment of the transverse ridges with their locations being marked by yellow squares in Fig. 34a. Height of the steep step that forms the frontal edge of sub-zones III-3 and III-4 is greater than 30 m and.

Corresponding to the layout of these arc-shaped transverse ridges, another notable characteristic observed in zone III is the directional distribution pattern of megablocks along the arc-shaped transverse ridges. To give a direct impression of the spatial extensions of blocks in this zone and accurately assess the distributed regularity of blocks on the top surface of each arc-shaped transverse ridge, 11 sites as highlighted by red squares in Fig. 33a were selected for statistical analysis of the preferred extensions of blocks with varying location. For each site, its size is $50 \times 50 \text{ m}^2$. The rose diagrams shown in Fig. 33b depict the preferred orientations of blocks corresponding to the 11 sites. For each site, only boulders with the side length $> 1 \text{ m}$ were counted. And a total of 3676 blocks were analyzed, with roughly 300 blocks of $l > 1 \text{ m}$ in each site. As indicated in Fig. 33b, blocks in the three sites within sub-zone III-1 (i.e., No. 1', No. 2', and No. 3') exhibit a predominant orientation of approximately N. Additionally, a secondary preferential orientation towards $\text{N}85^{\circ}\text{W}$ can be observed for the blocks in site No. 3'. For blocks in sites No. 4' and No. 5' in sub-zone III-2, their preferred orientations are $310\text{--}330^{\circ}$ and $270\text{--}280^{\circ}$, respectively. For blocks in sites No. 6' and No. 9' in sub-zones III-3 and III-4, their preferred orientations are $300\text{--}330^{\circ}$. For blocks in site No. 10', the preferred orientation is $270\text{--}280^{\circ}$, which is same to that of blocks in No. 5' in sub-zone III-2. The preferred orientation of blocks in No. 11' is $50\text{--}60^{\circ}$. From the

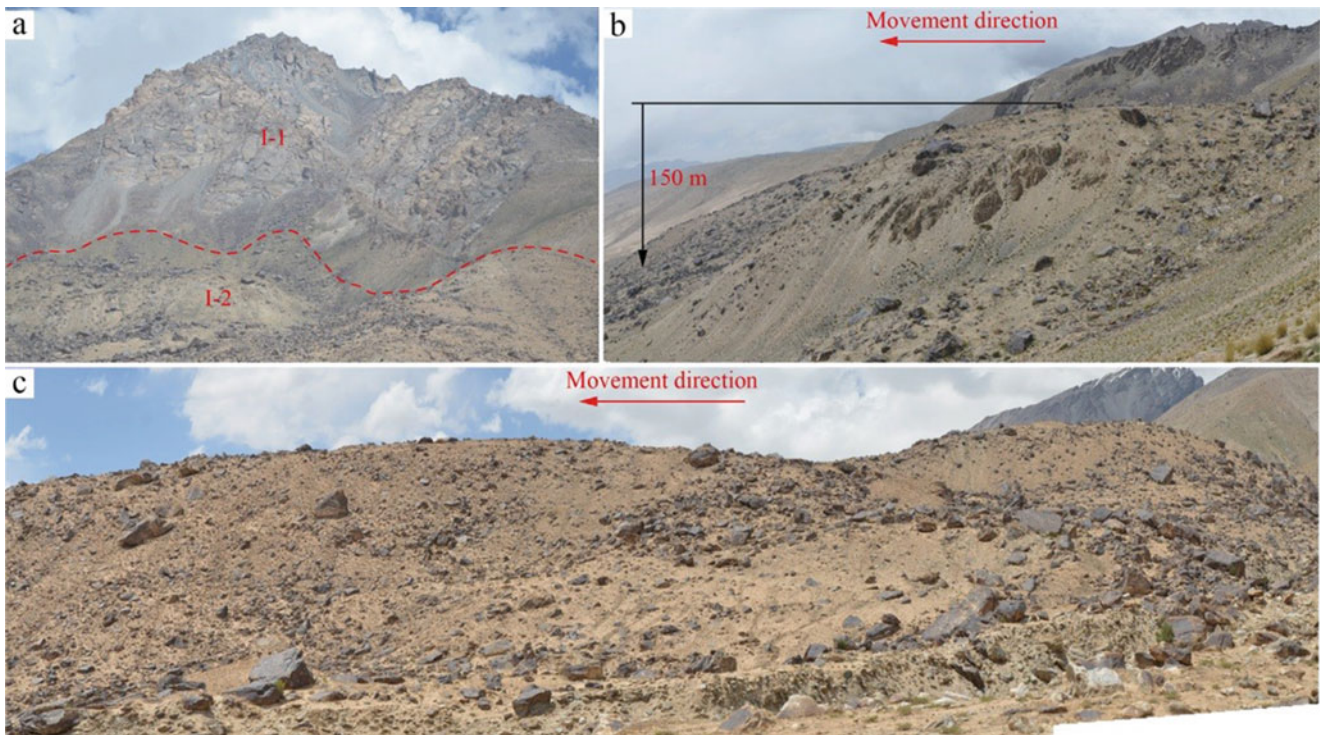


Fig. 33 Photos showing the extension of the source area (a), toreva block (b) and right lateral ridge (c) of the Tagarma rock avalanche

extensions of blocks in each site, it can be reached that most of blocks are aligned tangentially to the trajectories of the arc-shaped transverse ridges, except sites No. 2', No. 7' and No. 8'.

As exhibited in Fig. 32, the third prominent feature of zone III is the extension of the linear longitudinal structures as highlighted by the red dashed lines in the shaded relief map of the Tagarma rock avalanche. In plan-view, these linear longitudinal structures display a feature of dextral shearing.

(2) Internal deposited features

Apart from these landforms as described above, some typical internal deposited structures were also observed in the deposit. The first prominent feature is the layout of the carapace facies with many huge blocks (Figs. 35a-f). As exhibited in Figs. 35a-g, directional alignment of megablocks is evident along the entire travelling path. Clusters of superimposed megablocks exhibiting varying degrees of fragmentation are widely distributed in the carapace facies, forming what is known as an imbricate structure. And jigsaw structures were commonly observed. Based on the distribution of these megablocks, a conceptual model to illustrate how the distribution of these clusters changes with increasing runout is reached (Fig. 35g). For the avalanche mass accumulated at the rear edge of the transition zone, it displays

a very low disturbance with a typical jigsaw structure can be observed in the profile of the toreva block (Fig. 35b). The orientation relationship of its internal three sets of structures essentially inherits the bedrock orientations in the source area, with only a minor degree of rotation during movement. As the runout increases, the detached rockmass undergoes further fragmentation, which is controlled by internal foliation and two sets of structures. This results in the formation of these slab-like megablocks that are several dozen meters in length. The contact surface is formed due to control exerted by internal foliation, and these megablocks are distributed in a superimposed relationship facing upstream (Fig. 35c, e-f) or downstream (Fig. 35c-d).

In addition to the alignment of megablocks in the carapace facies, several typical internal sedimentary characteristics were also observed within the deposit. The first prominent feature is the inverse grading as exhibited in Fig. 36a. As shown in Fig. 36b, the carapace facies is mainly composed of angular blocks. To quantify the grain size distribution of the deposit, one sampling location of the carapace facies was selected for grain size analysis. It is reached that the content of blocks ≥ 10 mm in length is over 60%. Similar to the directional alignment of megablocks observed on the top surface of the accumulation zone, the orientation of megablocks can also be observed in profile, either upstream or downstream. The body facies contains nearly 80% of the deposit with its grain size ranging from mm to dozens of cm

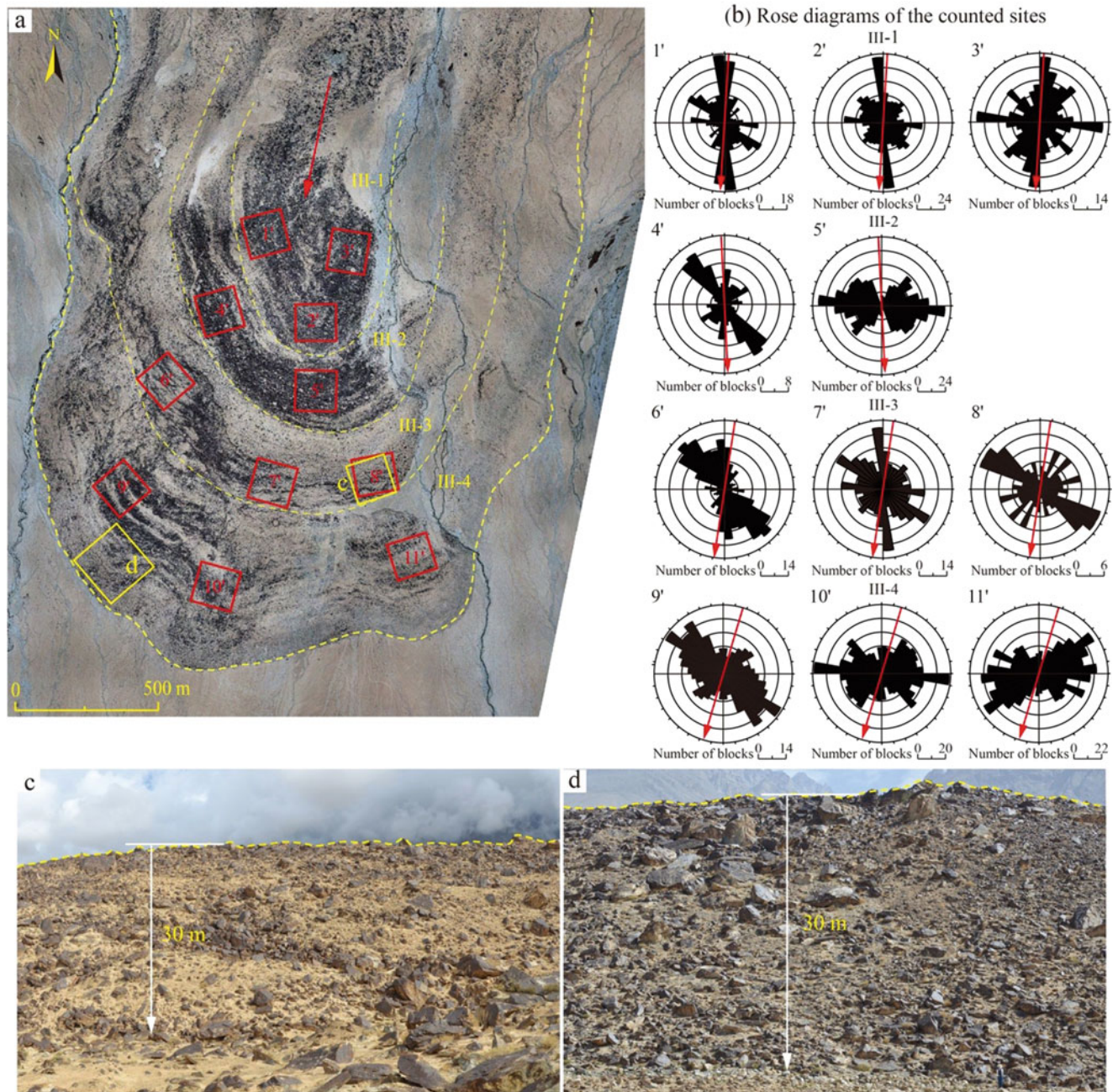


Fig. 34 Enlarged view of the accumulation zone (a) with rose diagrams of the counted sites (b), and two enlarged views of the stepped slopes in zone III (c-d)

(Fig. 36c). The basal facies is primarily supported by a matrix with a relatively high content of angular and irregular fine-grained clasts (Fig. 36d). As the lowest zone of the avalanche mass, it exhibits the highest degree of fragmentation with its particle size being significantly smaller than that of the body facies and carapace facies. The content of particles < 1 mm in size is over 40%, which is significantly greater than that in the body facies. Furthermore, the majority of the coarse fragments within the sediment exhibit a slab-like morphology

with their upper surface oriented downstream and their inclination direction aligned with the propagation vector of the avalanche mass.

The substrate beneath the basal facies is composed of well-rounded pebbles and boulders, which are distinctly different from the avalanche mass (Fig. 36a). These clasts were deposited in directional arrangements either upstream or downstream (Fig. 36e-f), indicating the existence of pushing and squeezing effect from the avalanche mass. Cracks and

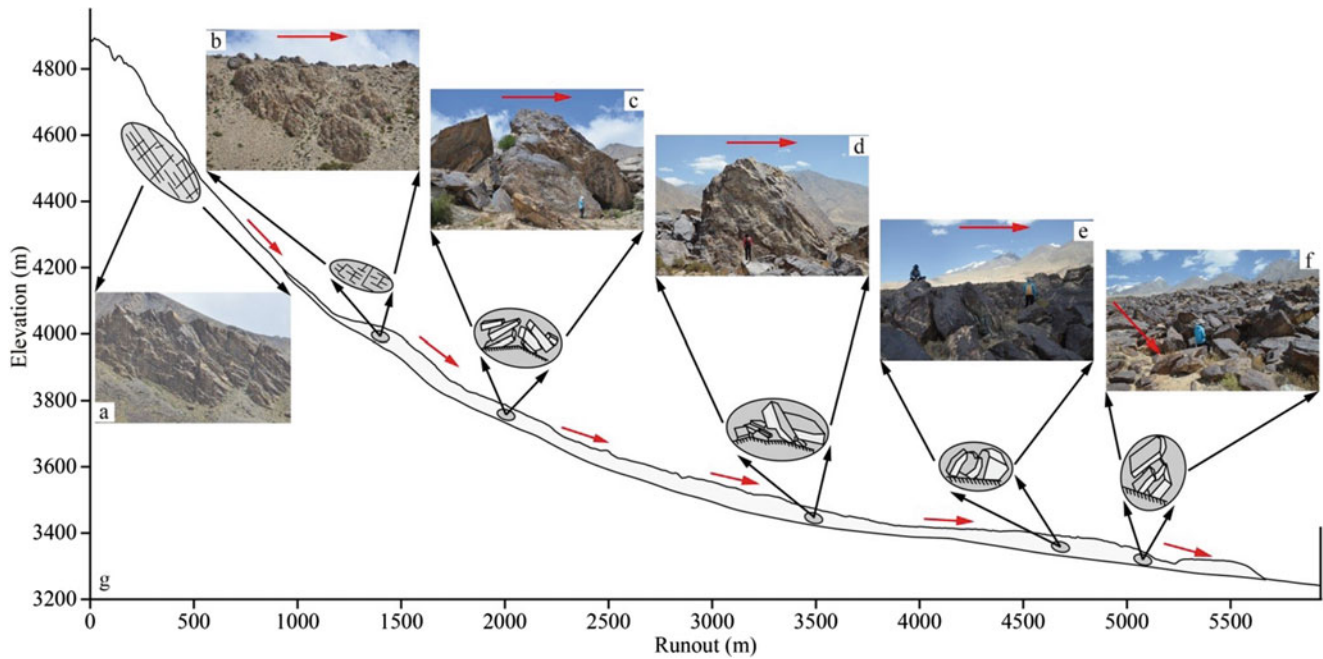


Fig. 35 Photos showing the extension of megablocks along the travelling path and corresponding conceptual model with the red arrow indicating the movement direction

fissures are commonly developed in the well-aligned boulders and pebbles in the substrate (Fig. 36g-h), which is consistent with the findings of Dufresne et al. (2010) and suggests strong interactions between the avalanche mass and substrate. In addition to these features, another interesting phenomenon was also observed during the field investigation. That is the extension of a nearly horizontal boundary between the basal and substrate with minimal mixing observed, which is obvious different from that observed in the Nyixoi Chongco rock avalanche.

4.4 Iymek Rock Avalanche

4.4.1 Geological Setting and General Features of the Iymek Rock Avalanche

The gigantic Iymek rock avalanche is the longest rock avalanche reported in China at present (Shi et al. 2023). It is located in the eastern foot of Pamir (Fig. 37a). As shown in Fig. 37b, an arcuate thrust belt comprising a series of actively seismogenic thrust faults dipping to south are well-developed along the margin of Pamir, i.e., the main Pamir thrust. It demarcates the boundary between the Pamir and the Tarim basin (Fu et al. 2011; Chevalier et al. 2011, 2015). This fault system, characterized by intensive tectonic activity, is the source zone of strong earthquakes with high magnitude (Arrowsmith and Strecker 1999; Zubovich et al. 2010; Fan et al. 1994; Strecker et al. 2003; Ischuk et al. 2013).

The Main Pamir Thrust passing across the IRA deposits, is a ~ 1000 km long, seismogenic, and segmented reverse fault with low angle dipping to southwest and defines the northeast boundary of the Pamir (Figs. 37b and 38a). GPS data suggest the Main Pamir Thrust remains tectonically active and the uphill rate along it reach up to 6 mm year^{-1} in the Alai valley. Controlled by the Main Pamir Thrust, the hanging wall is composed of bedrock mainly, including the Upper Cretaceous (K_2), Upper Carboniferous to Lower Permian (C_3-P_1), Carboniferous (C), Lower Palaeozoic (Pz_1) sedimentary and metamorphic rocks and Permian granite (γ_4^3). In the footwall is the Tarim basin, representing a gentle piedmont basin filled with Upper Pleistocene to Holocene alluvial and diluvial deposits (Q_{3-4}^{al-pl}), Middle Pleistocene alluvial deposit (Q_2^{al}) and Pliocene to Lower Pleistocene deposit (N_2-Q_1).

In terms of the climatic environment, this range is located in the innermost part of the continent surrounded by high mountains, making it extreme dry. It belongs to an extremely continental climate with mean annual precipitation less than 100 mm/yr . In mountainous region immediately behind the Iymek rock avalanche, the Quaternary glaciation and deglaciation occurred repeatedly and left abundant peculiar landforms, such as regular curvilinear form, evenly truncated spurs, and wide infilled floor (Liu et al. 2014; Strom and Abdrakhmatov 2018). However, there are no signatures related to glaciation or deglaciation on both sides of the Iymek and adjoining valleys.

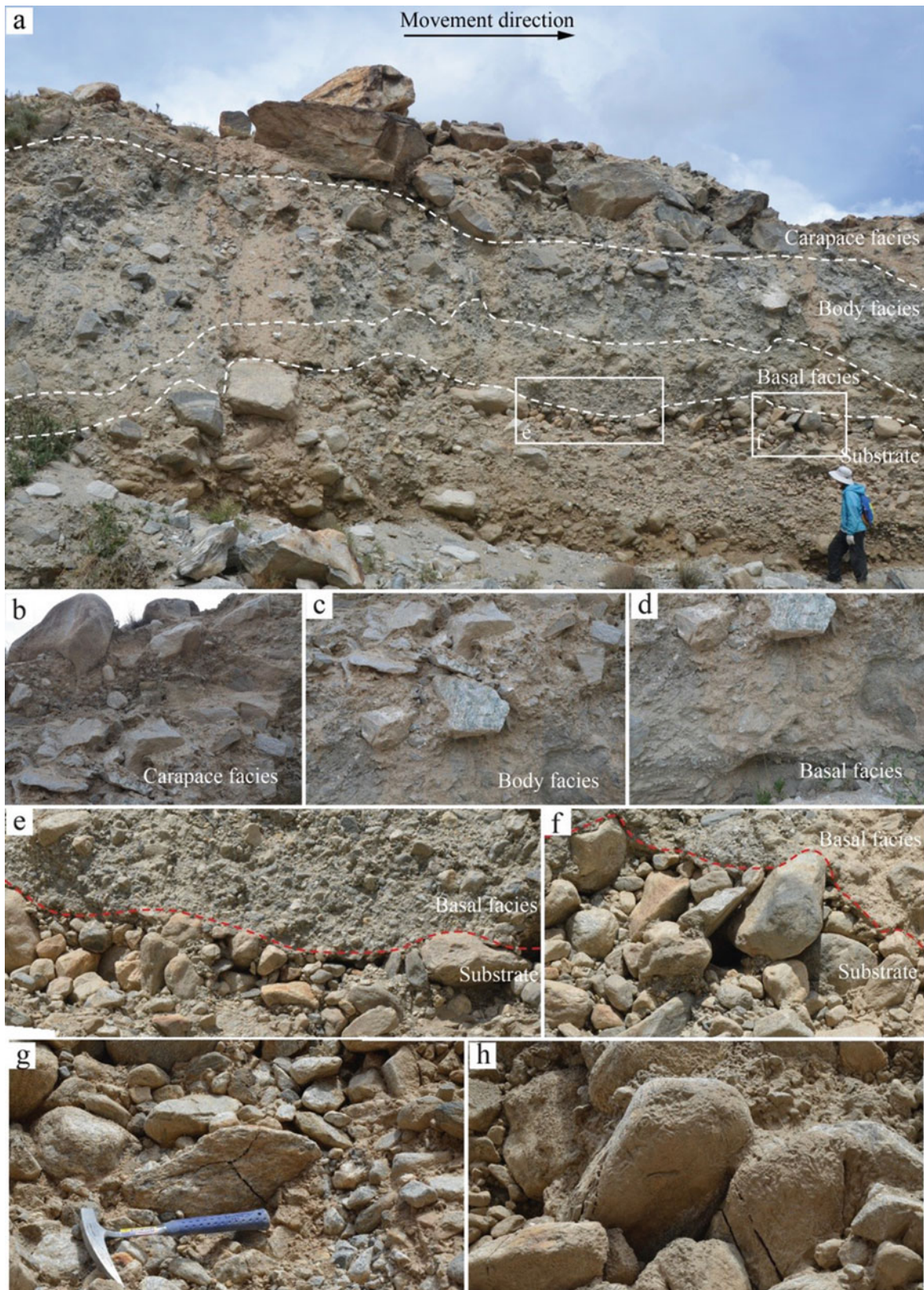


Fig. 36 Photos showing the inverse grading of the deposit and substrate layout

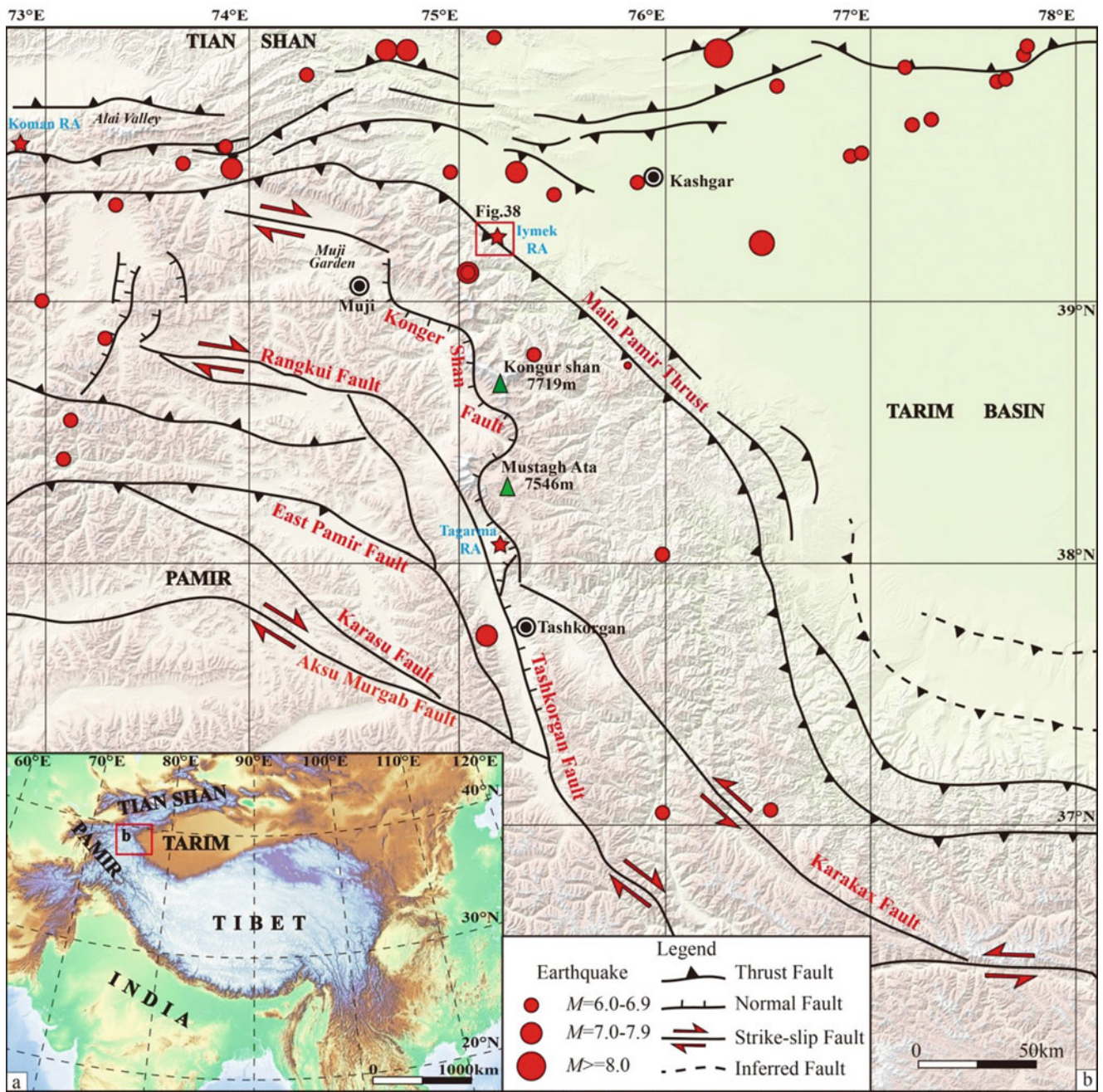


Fig. 37 Location of the Iymek rock avalanche and regional geological setting

As shown in Fig. 38b, the Iymek peak is composed of the meta-sedimentary rocks with different degrees of metamorphism formed in the lower Palaeozoic Era, including chlorite schists, marbles and intercalated metamorphic conglomerates. The anclinal bedrocks develop centimetric foliations (F) dipping to southwest at 15–40° and are dissected by two sets of joints with attitudes 113°∠60° (JS1) and 325°∠45° (JS2), respectively (Fig. 4d). Such nearly

orthogonal discontinuities are particularly responsible for a wedge failure.

The Iymek rock avalanche detached from the steep Iymek peak most likely triggered by strong earthquake along the Main Pamir Thrust ~7.1 ka ago (Yuan et al. 2013; Shi et al. 2023). After detaching from the source area, the huge mass travelled downward rapidly along the laterally confined valley and deposited onto a gentle basin terrain as an

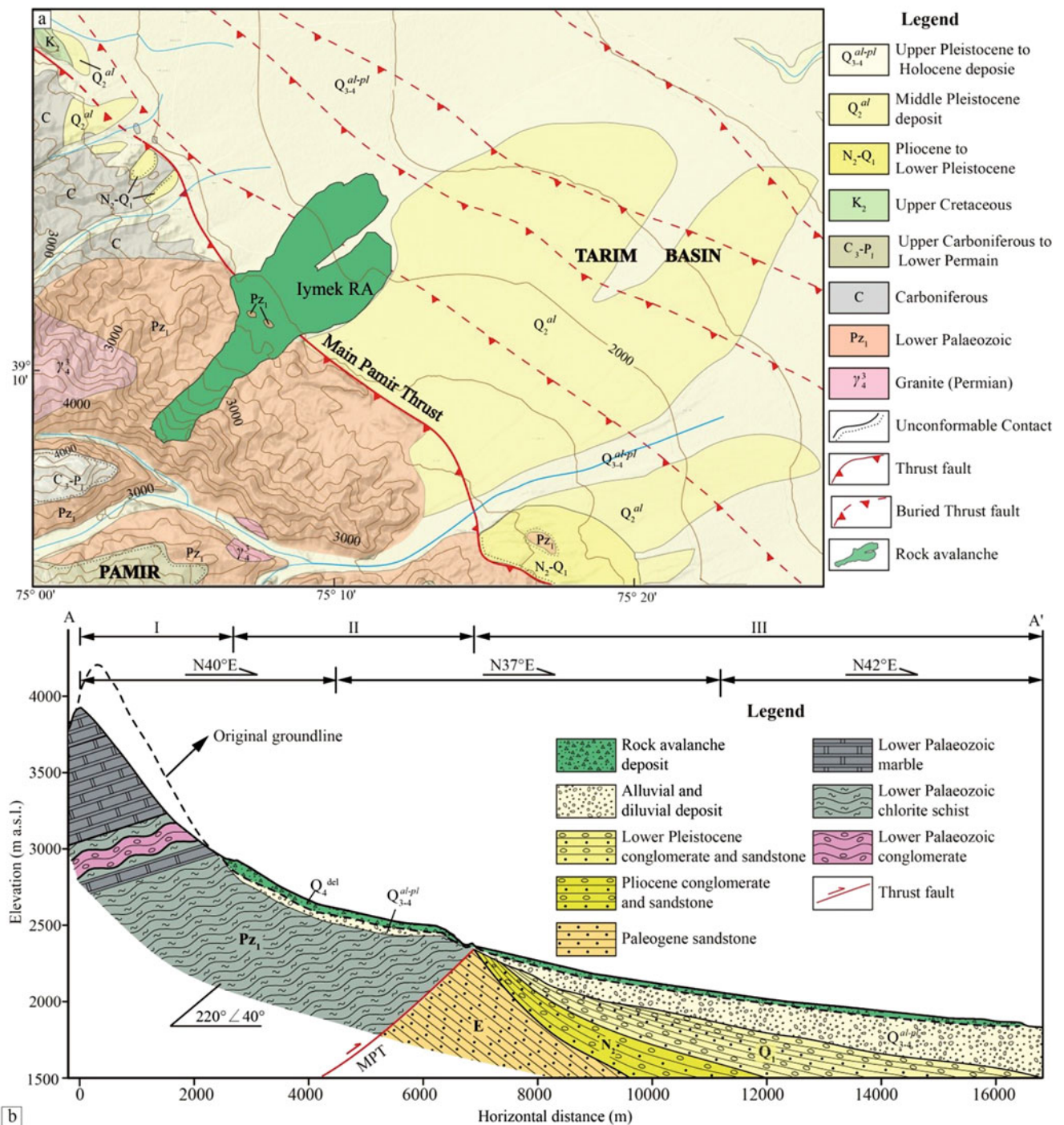


Fig. 38 Geological setting of the Iymek rock avalanche (a) with a longitudinal profile of A-A' (b)

asymmetrically elongated sheet (Fig. 39a). In plan-view, the depositional sheet is surrounded by bulging distal edges and raised margins, making the avalanche deposit clearly distinguished from adjacent alluvial deposits (Fig. 39a). From the current head to the toe, the drop height of the avalanche is 2135 m and the travelled distance is 16.3 km, which correspond to an apparent friction coefficient of 0.13. The covered

area is over 48.0 km² with varying deposited thickness. It is measured that the thickest depth is over 90 m distributed in the valley section and the thinnest depth is ~10 m in the middle part of the deposit sheet. Through topography reconstruction, it is reached that the detached volume and the depositional volume of the Iymek rock avalanche are

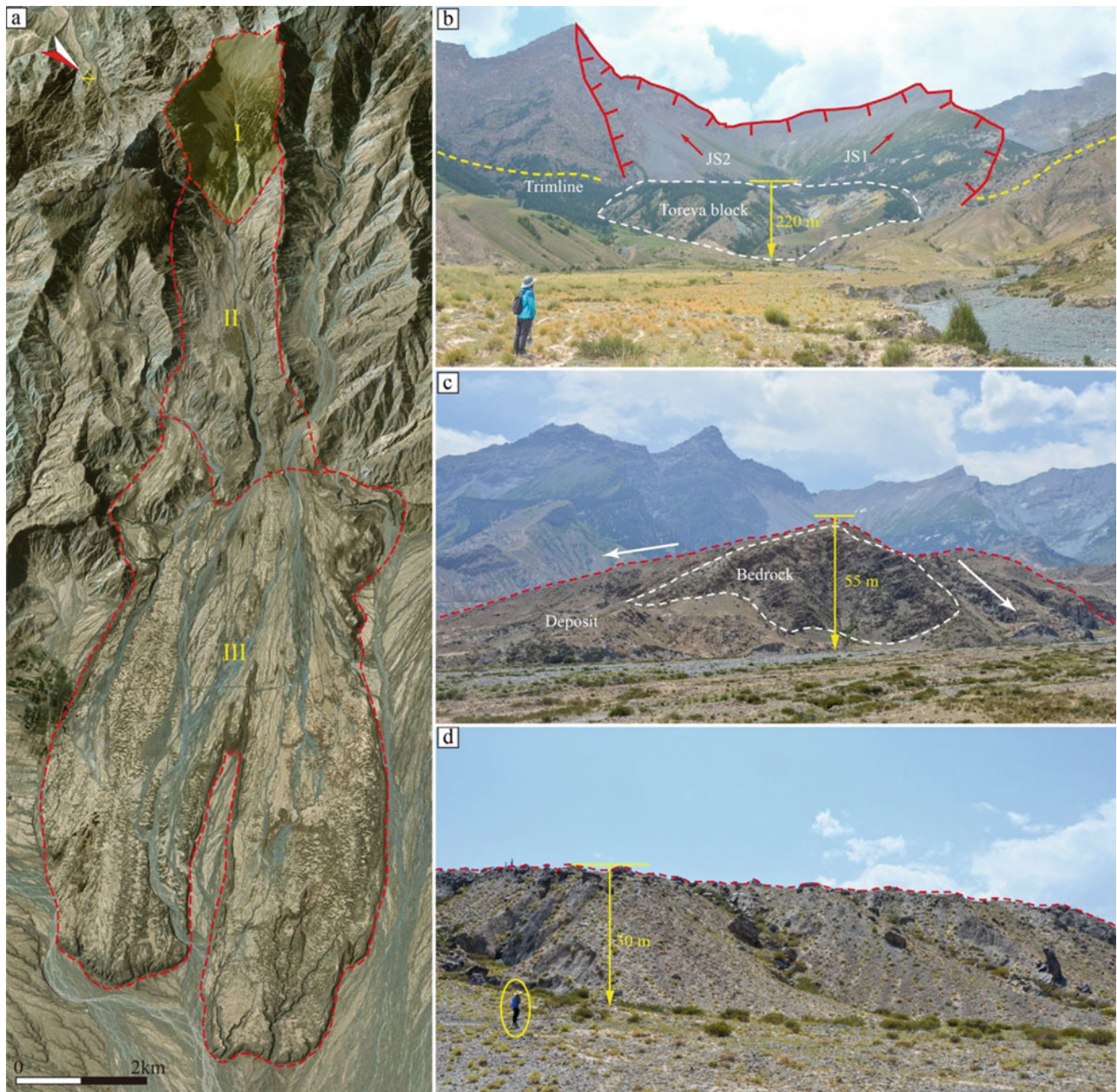


Fig. 39 Remote sensing image showing three zones of the Iymek rock avalanche (I: the source area; II: the transition zone; III: the accumulation zone) (a) and enlarged views of the stepped slopes dividing the three zones (b-d)

$\sim 0.98 \text{ km}^3$ and 1.37 km^3 , respectively, yielding a dilatation coefficient of 1.39 (Shi et al. 2023).

Figure 38b shows one longitudinal profile of the avalanche with its position being marked in Fig. 4d. From Fig. 38b, it can be seen that the Main Pamir Thrust is located along the boundary of the transition zone and accumulation zone, which is also a terrain rapid change zone. Bounded by the Main Pamir Thrust, the avalanche source area and transition zone are mainly composed of marble, chlorite schist and conglomerate of Lower Palaeozoic. Due to the effects of

tectonic events and long-term weathering, the bedrock has been intensely fractured with preferred joints developed (Fig. 4d). The accumulation zone is at the NE footwall. For this area, the slope angle is relatively low. And the farther away from the source area, the lower the slope angle is. The substrate of this part is composed of Quaternary alluvial-fluvial facies (Q_{3-4}^{al-pl}).

The arid climate allows the huge deposit sheet to be well-preserved. Subsequent river erosion yields a series of well-exposed outcrops with thickness more than 80 meters,

providing a good opportunity to learn the internal characteristics of the deposit. This catastrophic emplacement leaves a splendid legacy bearing tremendous volume, well-preserved landforms, as well as spectacular exposures, which provide an excellent laboratory for studying rock avalanches.

4.4.2 Sedimentary Features of the Avalanche Deposit

(1) Plan zonation and landforms

As exhibited in Fig. 39a, the Iymek rock avalanche presents an elongated tongue with two branches at its frontal part. On the surface of the deposit, prominent well-developed landforms, including toreva blocks, transverse and longitudinal ridges, and hummocks, are distributed from the proximal to the distal areas. Based on geomorphological and depositional characteristics, three zones can be recognised from the scarp to the distal edge (Fig. 38a): the source area (I), the transition zone (II), and the accumulation zone (III).

a) Source area (I)

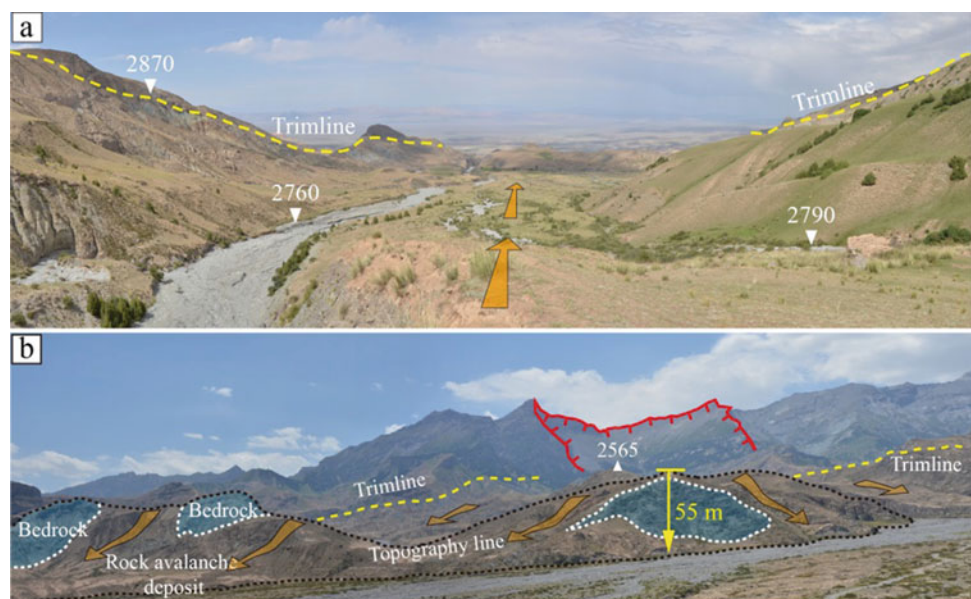
The source area of the deep-seated Iymek rock avalanche features a V-shaped scar (Fig. 39b). The source area scar is 3.0 km long, and 1.7 km wide with its elevation ranging from 2800 to 3980 m a.s.l. Through reconstructing of the pre-avalanche topography, it is derived that the original altitude of the Iymek peak was up to 4225 m a.s.l., higher than present altitude. The main scarp of the detached wedge is behind the original ridge crest, shaving the summit peak about 250 m. The southeast-facing scarp is a nearly planar surface reflecting the light of sun.

b) Transition zone (II)

For the transition zone, the first prominent landform is the display of a large toreva block at the base of the source area. As the prominent landform near the source area, it consists of one or more faulted blocks that have slid down a little distance without disintegration and covers the toe of rupture surface. The diamond-shaped toreva block has a relatively gentle platform with a length of ~900 m in the movement direction, a maximum width of 800 m, and a vertical height of 220 m (Fig. 39b). A well-exposed outcrop reveal its internal structures efficiently, which indicates that the toreva block is composed of undisintegrated host rock mass, i.e., the grey marble overlying on the green schists bearing continuous, undistorted original foliations.

The second typical feature of the transition zone is a well-confined valley topography in the downstream, which has a length and width of 4.0–4.8 km and 2.0 km, respectively (Fig. 40a). The open valley bottom provides the avalanche mass propagation along laterally confined valley that gradually widens downstream. Along both lateral boundaries, a pair of parallel trimlines composed of the avalanche masses adhering to the lateral bedrock ridges can be observed. The continuous trimlines extend 4 km along both valley sides and stand 100 m above the current deposit surface. Trimlines indicate the original thickness of rapidly moving debris passing here during rock avalanche motion. At end of the transition zone, complex terrain consisted of several pre-existing rocky hills as the throat of the passage lead to the moving mass split into several streams along the channels (Fig. 40b). Although most of them are covered by avalanche materials, three isolated rocky islands formed by in-situ bedrock can be identified. Figure 39c shows one profile of the in-situ island

Fig. 40 Panorama of the transition zone comprising well-confined valley topography and trimlines (a), and its frontal complex terrain (b)



photographed during field survey. The right one forms a 55 m high steep downward escarpment comprising of metamorphic conglomerates mainly.

c) Accumulation zone (III)

In the accumulation zone, the sheet is composed of two asymmetrically elongated lobes. On a low-angle (3–4°) basin surface, the left lobe extends 9 km with a width of 2.5 km and the right lobe extends 7 km with a width of 2.7 km in the 45–50° direction. Each lobe is surrounded by relatively steep lateral levees and bulging distal fronts with heights of nearly 30 m (Fig. 39d). The steep frontal rim is

similar to the steep frontal rim of the Tagarma rock avalanche. Figure 41 shows an enlarged view of the accumulation zone. From Fig. 41, it can be seen that the surficial landform in zone III is a classical wave-like topography akin to other large rock avalanches, including flowbands, hummocks, as well as longitudinal and transverse ridges. According to the spatial distribution of these landforms, zone III can be further divided into six sub-zones as exhibited in Fig. 41.

The proximal area of zone III is characterized by a series of elongated flowbands and longitudinal ridges (the sub-zone III-P). As shown in Fig. 41, the flowbands commonly extend several hundred meters to thousand meters toward the

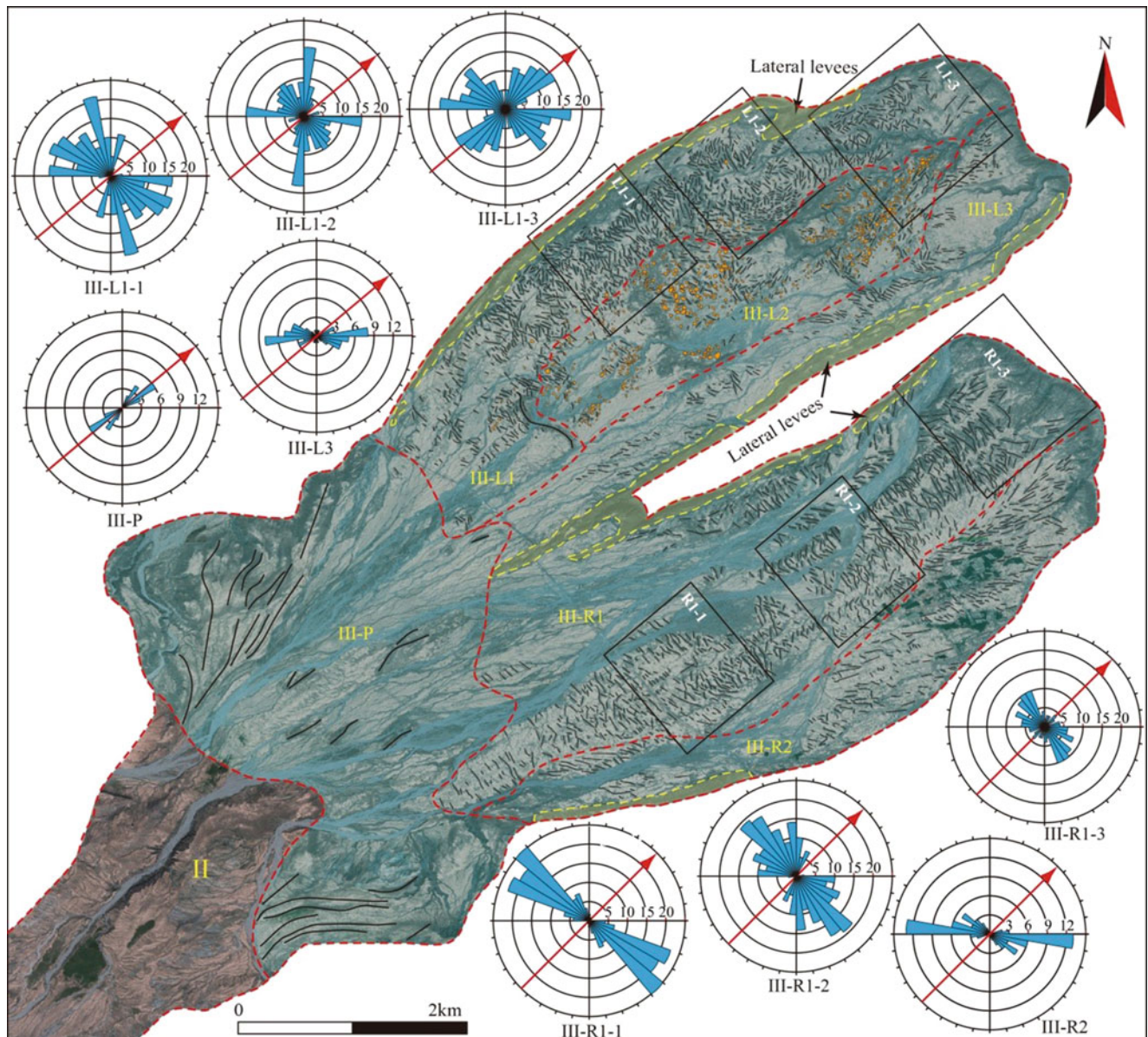


Fig. 41 Enlarged view of the accumulation zone with the six sub-zones being marked and corresponding rose diagrams of ridge directions in each sub-zone. The ridges and hummocks are marked by the block short lines and the orange circles, respectively



Fig. 42 Morphological features in sub-zone III-P. (a) Flowbands on the right side with their corresponding satellite image (b). (c) Flowbands on the left side. (d) Longitudinal ridges with their corresponding satellite image (e)

movement direction and align with parallel longitudinal grooves. Close to the margins of both lateral sides of sub-zone III-P, a series of sub-parallel flowbands are well continuous, and can be traced up to 1.0 km with widths of 30 to 100 m. Especially, the flowbands on the right side extend more than 1.0 km and display a flexural shape to accommodate the flow-like motion of the avalanche mass (Fig. 42a-b). The right side flowbands consist of block clusters and are separated by areas lacking large blocks.

The left side flowbands are relatively straight directed less than 30° , diverging from the main rock avalanche direction (45°) and deflecting to the left lateral margin, suggesting the local moving direction during rock avalanche propagation. Furthermore, some flowbands split into sub-parallel multiple bands (Fig. 41c). In the central part of sub-zone III-P, several longitudinal ridges stand tens meters above the adjacent alluvial deposit (Fig. 41d-e). These ridges stretch hundreds of meters with a preferred orientation of $40\text{--}50^\circ$, parallel to

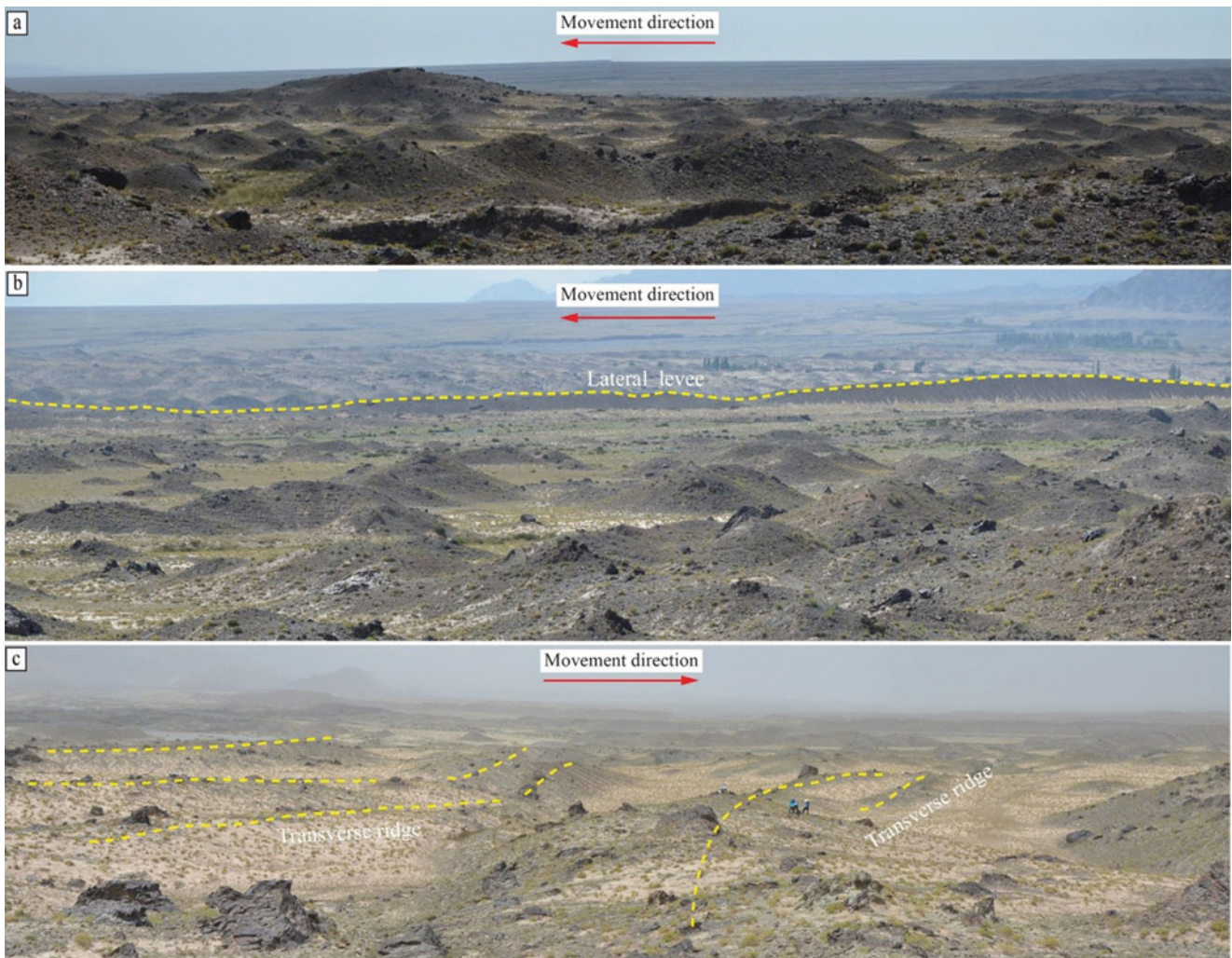


Fig. 43 Photographs exhibiting the deposited feature of the ridges in sub-zones III-L1 (a-b) and III-R1 (c)

the moving direction of the avalanche mass. In terms of interior, ridges consist of intensively fragmented marble clasts, rather than of large (> 1 m) block aggregations.

Next to the sub-zone III-P with longitudinal landforms distributed, there are series of conjugate ridges in the left lobe, named as sub-zone III-L1. In this sub-zone, undulating topography like water waves is the most general landform (Fig. 43a-b). With the increase of runout, the scales and preferred orientations of ridges slightly change with three preferential directions. To quantify the preferred extensions of ridges in sub-zone III-L1, three areas L1-1, L1-2, and L1-3 were selected for statistical analysis with corresponding rose diagrams being graphed (Fig. 41). We found that the conjugate ridges in the III-L1-1 area strike $160\text{--}170^\circ$ and $90\text{--}100^\circ$, respectively, oblique to the avalanche mass main movement direction. The angle between the both preferred sets of conjugate ridges is 60° . In addition, a set of ridges oriented at $110\text{--}130^\circ$ are also well-developed in this part. In

the area of III-L1-2, the X-conjugate ridges are still the prevailing ridges with their preferred extensions being of $90\text{--}100^\circ$ and $180\text{--}190^\circ$, respectively. With a further increase of runout, the ridges apparently present two different prevailing orientations with one being slightly parallel to the main moving direction and another being mainly oriented at $90\text{--}130^\circ$ oblique to the main moving direction.

In the right lobe (the sub-zone III-R1), series of transverse ridges are distributed next to the sub-zone III-P. Similar to sub-zone III-L1, undulating topography like water waves is also the most general landform in sub-zone III-R1, although their shapes and scales are different. In sub-zone III-R1, it is mainly featured by a series of transverse ridges and associated depressions (Fig. 43c). The surfaces of these transverse ridges are covered by fragmented clasts and blocks. Spatially, these transverse ridges extend 50 to 370 m in length with the width and height ranging from 20 to 50 m and 2 to 10 m, respectively. The wavelengths between

adjacent transverse ridges or grooves are 20 to 80 m, with the mean value of 50 m. To clarify the spatial orientation of these ridges, three areas named R1-1, R1-2, and R1-3 were selected for statistical analysis with the corresponding rose diagrams being graphed (Fig. 41). The preferred orientation of the transverse ridges in sub-zone III-R1 is 130–150°, which is perpendicular to the avalanche mass main moving direction (45°). Additionally, it is noticed that the scale and density of the transverse ridges in sub-zone III-R1 varies with runout. In the central area of sub-zone III-R1, the transverse ridges are distributed relatively uniformly and have approximately equal wavelength. As the runout increases, the transverse ridges appear to be denser with their widths being larger and the adjacent grooves being shallower, so that it is difficult to distinguish individual ridges in the distal area.

In addition to the distribution of the landforms in sub-zones III-L1 and III-R1, another prominent feature is the oblique ridges along the marginal areas in both lobes (Fig. 41), named as sub-zones III-L3 and III-R2. In both sub-zones, the oblique ridges are well extended with an echelon alignment featured by dextral shear dislocations. These ridges can maximally stretch for about 400 m long and about 10–50 m wide. From the rose diagrams of

subzones III-L3 and III-R2 (Fig. 41), it can be reached that the prevailing orientation of these oblique ridges is about East in both areas and oblique to the main moving direction (45°).

Besides, there are multiple hummocks in the medial area of the left lobe, which is named as sub-zone III-L2. In plan-view, over 1000 hummocks can be identified (Fig. 41), which is also a diagnostic morphologic feature reported at other rock avalanches. These hummocks are featured by regular or irregular circular cones and circular to elliptical shapes in plan-view. They commonly range from 10 m to 50 m in diameter and raise 2–10 m above adjacent deposit surface (Fig. 44a-b). A typical example shown Fig. 44b is a circular hummock that has a height of 4.3 m with a diameter of 14 m and consists of intensively fragmented clasts rather than large blocks. The distribution of hummocks is relatively non-uniform. Some stand alone, while others distributed closely and separated by shallow grooves, forming a large hummock or ridge.

The last significant feature in zone III is the extensions of the lateral levees in each lobe, which comprise the sheet margins in the accumulation zone (Fig. 41). A pairs of levees along the left lobe are of good continuity and well-preserved. The left levee of the left lobe extends 6.2 km with a width of

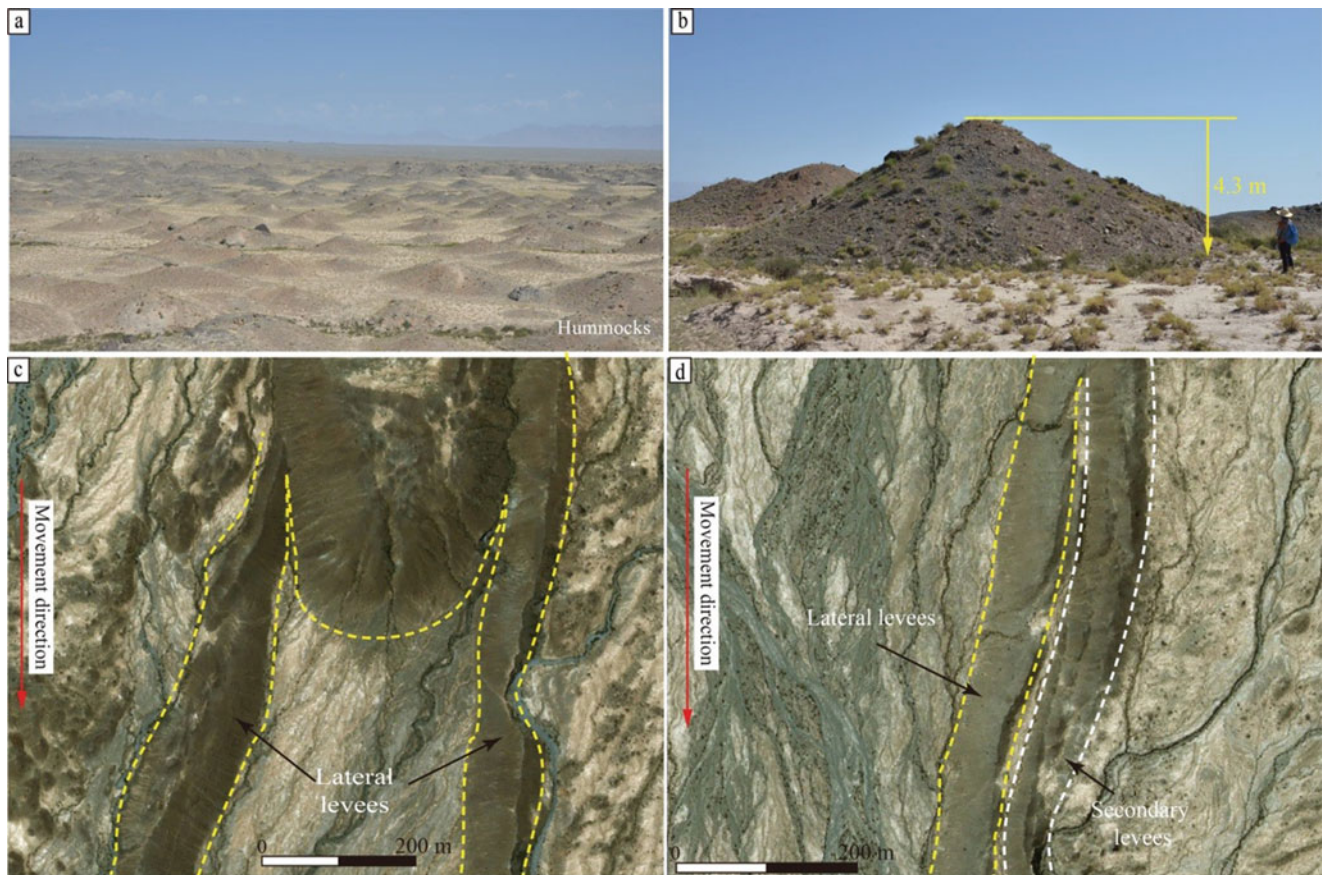


Fig. 44 Photographs of hummocks in sub-zone III-L2 (a-b) and lateral levees in zone III (c-d)

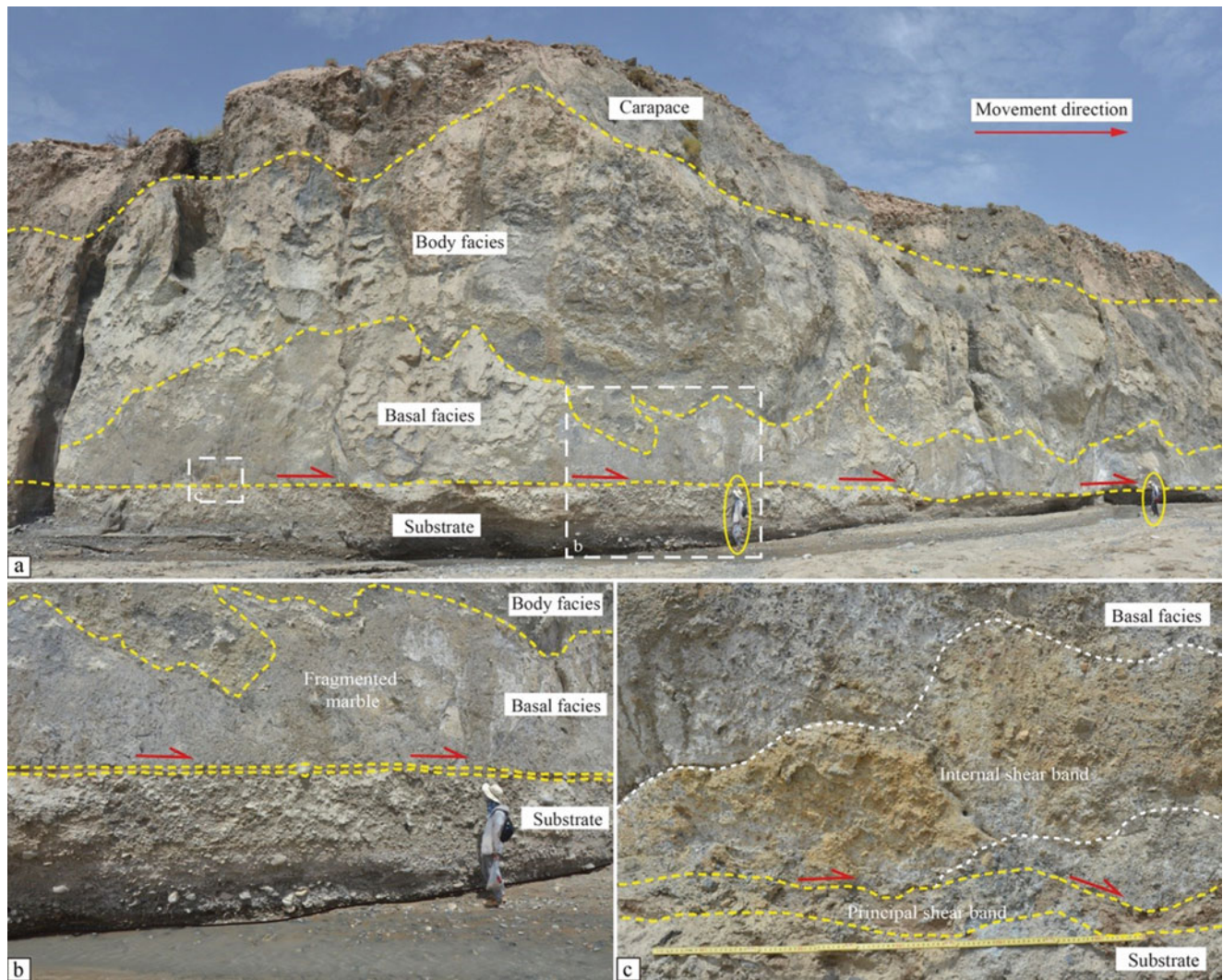


Fig. 45 Three facies of the Iymek rock avalanche deposit in accumulation zone (a) with both close-up views to show the interaction features between the basal facies and underlying substrate (b-c)

60–110 m and rises from 20–30 m above the outer side terrain. The right levee extends straightly 5.8 km with width of 80–100. Interestingly, a secondary levee with a width of about 50–60 m, with the overlapping on the inside of the primary right levee is observed, forming a multiple sub-parallel levee (Fig. 44c-d). By contrast, in the right lobe, its left levee extending 3.6 km is discontinuous and broken into several segments because of subsequent erosion. The right levee segment remains only 1.5 km in the proximal area and the counterpart completely disappeared in the distal area due to intensive erosion. These levees are higher than the undulating depositional terrain surrounding them.

(2) Internal deposited features

As shown in Fig. 45a, the Iymek rock avalanche deposit also can be generalized into three facies from the top to bottom,

i.e., the carapace facies, body facies, and basal facies, forming a classical inverse grading.

a) Carapace facies

For the carapace facies, large blocks with preserved original foliations are widely distributed on the surface (Fig. 46a-c). Directional alignment of blocks can also be observed in the Iymek rock avalanche deposit. And the foliated surfaces of most blocks are facing upstream or downstream (Fig. 46b-c), which is similar to the Tagarma rock avalanche. Through a statistical analysis on the grain size distribution of the surficial blocks, it is reached that the block size distribution of the carapace facies presents a wide span from several centimeters to the maximum up to 10 m (Fig. 46a-c). In outcrops, this facies predominantly consist of poorly sorted coarse clasts (Fig. 46d-e). Irregular angular clasts bearing very sharp edges



Fig. 46 Representative carapace facies comprising large blocks. (a) A panorama of the blocky surface of the deposit. (b-c) Surficial blocks preserved their original foliations. (d-e) Internal structures of the carapace facies

interlock with each other, resulting in a clast-supported structure. In some outcrops, jigsaw structures with original foliations being preserved can be observed (Fig. 46e). For these jigsaw fractured blocks, they experienced disintegration, but did not separate and were commonly immersed in fragmented smaller clasts.

b) Body facies

Underlying the carapace facies, it is the layout of the body facies, which constitutes the main part of rock avalanche deposits. As shown in Fig. 45a, the body facies of the Lymeck rock avalanche deposit is mainly composed of clasts

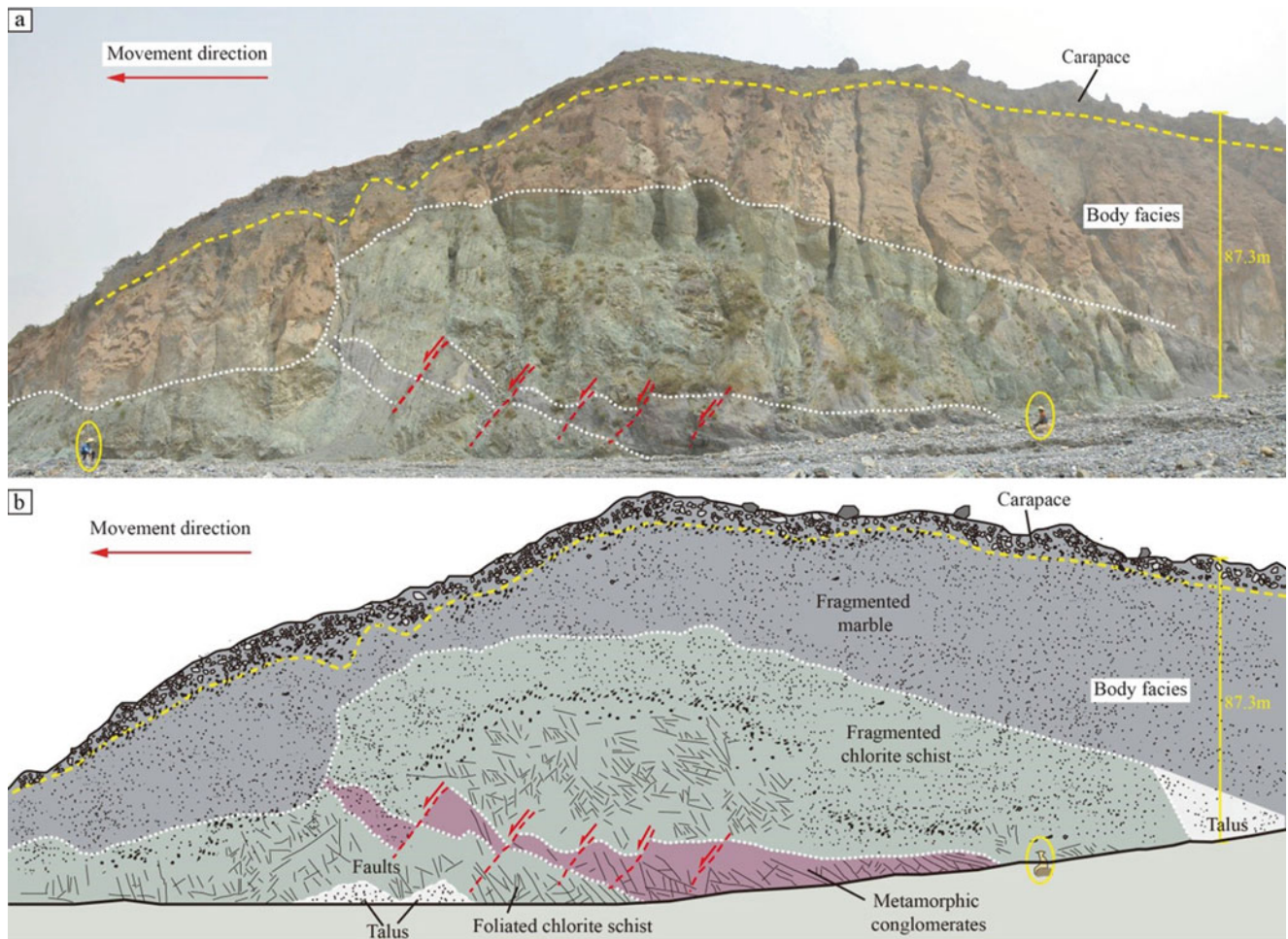


Fig. 47 Typical outcrop in the transition zone shows the preserved original bedrock stratigraphy and faults. In the schematic representations, the colour grey, green, and red represent the marble breccia, chlorite schist breccia and metamorphic conglomerate breccia, respectively

ranging from ultrafine powders to decametric blocks, implying an intensive but heterogeneous fragmentation. Those blocks include isolated jigsaw-fractured clasts and large isolated blocks, which still preserve their original foliations and are commonly surrounded by fine-grained matrix with a matrix-supported structure.

In the body facies, some different landslide-tectonic structures are also well developed. The first one is the preserved initial stratigraphy. As exhibited in Figs. 47a and 48a, preservation of original stratigraphic sequence composed of grey marble layer overlying green chlorite schist layer can be observed commonly throughout the Iymek rock avalanche deposit from the transition zone to accumulation zone, although the avalanche mass has experienced long runout and has been fragmented completely. Figure 47 shows an ~87 m high outcrop in the transition zone. For this outcrop, the upper part of the body facies is fragmented marble with the underlying material being fragmented chlorite schist. Both of them consist of the body facies with a clear boundary

between them, indicating a low disturbance and mixing in the body facies. In the underlying chlorite schist layer, the original rock mass structure without distortion can also be observed, indicating a low disturbance of the fragmented mass. Additionally, a purple-red metamorphic conglomerates layer about 3–4 m thick sandwiched in the schist layers can be observed. In the fragmented chlorite schist, some small-scaled normal faults were generated. Similar to the outcrop shown in Figs. 47 and 48a shows another outcrop with preserved original stratigraphy in the body facies, which is at the proximal area of the accumulation zone. As the runout further increases, the underlying chlorite schist layer is invisible due to the limited erosion depth. Figure 48b-c is both enlarged views to show the contact relationships between both fragmented layers in the body facies. It can be seen that although the avalanche mass displays an increasing fragmentation with travelled distance in the accumulation zone, the contact surface between the fragmented marble

layer and green schist layer is still well-defined without intensive internal mixing.

The second typical feature in the body facies should be the appearances of a series small-scaled normal and reverse faults as revealed by outcrops in the deposit from the transition zone to the accumulation zone. As shown in the outcrop in the transition zone (Fig. 47), several high-angle normal faults dipping to the avalanche movement direction that dislocated the metamorphic conglomerate layer are well developed. In the outcrop of the accumulation zone (Fig. 48a), several small-scaled normal faults interspersed in the body facies were also observed, which were truncated by a large low-angle thrust fault. Figure 48d-e shows enlarged views of the fault system. The combined relationship of these faults is an important geological evidence, indicating the direction of relative movement of material in the body facies. Beneath the thrust fault, a narrow wedge along the movement direction consisting of chlorite schist clasts inserted into the marble matrix and tapers off (Fig. 48e). In the distal area, numerous faults also can be identified. Compared with the transition zone, these faults have relatively smaller length but are distributed densely, and have complex interrelation. For instance, an outcrop belonging to the transverse ridge displays a set of normal and reverse faults interlace with each other and dislocate the internal layers and shear bands (Fig. 49a).

The third prominent feature in the body facies throughout the avalanche deposit is the distribution of narrow internal shear bands composed of highly pulverized ultrafine grains. Most of shear bands have thicknesses of centimetres and are subhorizontal with little undulations. The colour of the internal shear bands is obviously different from adjacent materials, which is easy to be identified (Fig. 49). As shown in Fig. 49a, a series of internal shear bands are well generated that are displaced by a number of moderately dipping normal faults and divided into several segments. These shear bands feature undulated bands bearing thin trailing vein or present an elongated lens shape (Fig. 49b). Additionally, some shear bands display complex structures like a flame or irregularly contorted appearance, implying an intensive shearing (Fig. 49d).

The last and key deposited feature observed in the body facies should be the presence of a spectacular flame-like structure. This structure consists of an array of undulated shear bands with upward-pointing cusps, which was exposed on a cross-section of a lateral levee (Fig. 50). As the enlarged view in Fig. 50b indicated, fragmented marble matrix is interspersed with fragmented chlorite schist material, but their boundary is still sharp without intense mixing. Some clast aggregations with lenticle shapes are immersed in the fine-grained matrix (Fig. 50d). In addition, some small shear-induced flame bands with light orange colour is immersed in the pulverized marble facies, which is only several

centimetres thick and extends for about 2 m (Fig. 50e). Its appearance is intensively contorted and displays an irregularly undulated boundary, tapering off gradually towards the lateral margin. This is one of the important findings reached in this rock avalanche, which provides geological evidences to reveal the formation mechanism of lateral levees.

c) Basal facies

Beneath the body facies, at rock avalanche deposits base is the basal facies, directly interacting with substrate (Fig. 51). This facies consists of the finest grains with millimetre-sized matrix compared with overlying deposit materials, implying more intensive fragmentation and pulverization due to significant shearing under overburden. From the outcrops where the substrate is exposed, it can be seen that the contact between the basal facies and substrate is considerably sharp without obvious mixing. Principal shear bands at the bottom of the avalanche deposit, characterised by well continuous, relatively planar extension and traced for several hundred meters in outcrops, can be observed, forming a distinct boundary between the deposit and substrate. Typical shear bands rooted in the basal facies (Fig. 45c) occasionally can be observed and presents a light orange colour. Additionally, structures of clastic dikes and diapiric structures due to avalanche-substrate interaction can be observed in the basal facies (Fig. 51a). An irregular wedge of diapiric intrusion squeezed into the overlying basal facies and resulted in the deformation of adjacent materials (Fig. 51a). In this outcrop, pulverised avalanche material is mainly less than 2 cm and presents a layer-like texture that curved extremely to form convoluted laminations, making the diapiric structure like an asymmetric thrusting fold. However, the axial plane is opposite to the moving direction of the avalanche mass. Different from the basal facies, the underlying substrate mainly consists of pebbles and gravels ranging from 2 to 10 cm in size, which are much coarser than the avalanche basal facies materials (Fig. 51b). These pebbles present original sedimentary features, characterized by a compact distribution with oblique long axis and a good cemented status.

In the basal facies, there is another interesting feature, which provides geological evidence for the role of liquefaction in rock avalanche propagation. There are some clastic dikes generated in an outcrop near the frontal area of the accumulation zone. These spectacular clastic dikes are related to substrate liquefaction at the accumulation zone (Fig. 52). In the exposures, these clastic dikes root from the substrate (Fig. 52) and extend vertically into the overlying rock avalanche deposit with the maximum height being up to 8 m and several centimetres to 2 m in width. They commonly display elongated wedge shapes and taper off from the bottom to top. In vertical, they display continuous extension without any

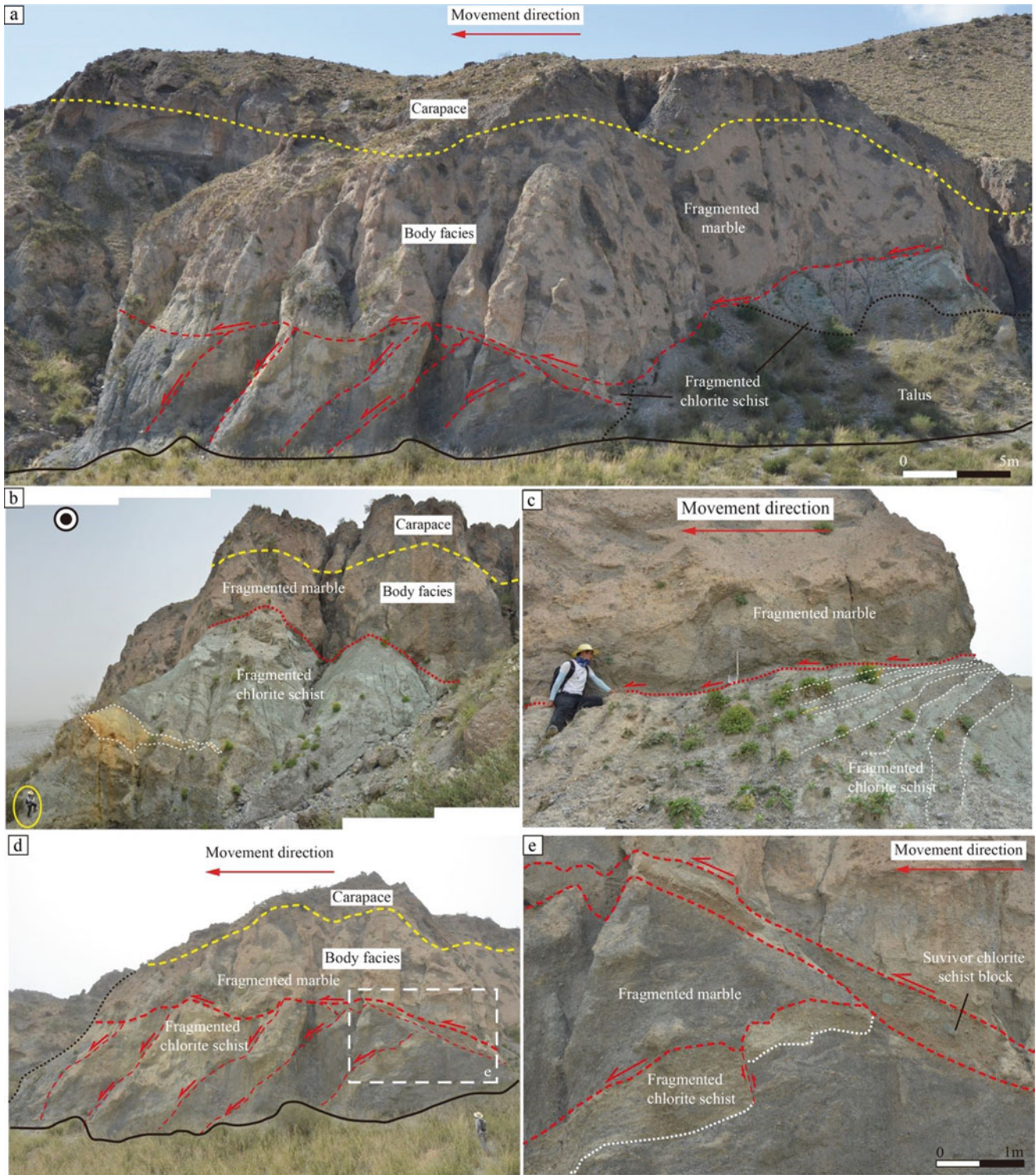


Fig. 48 Preserved original stratigraphy in the proximal area of the accumulation zone. A layer of green fragmented chlorite schist breccia was sandwiched by grey fragmented marble breccia

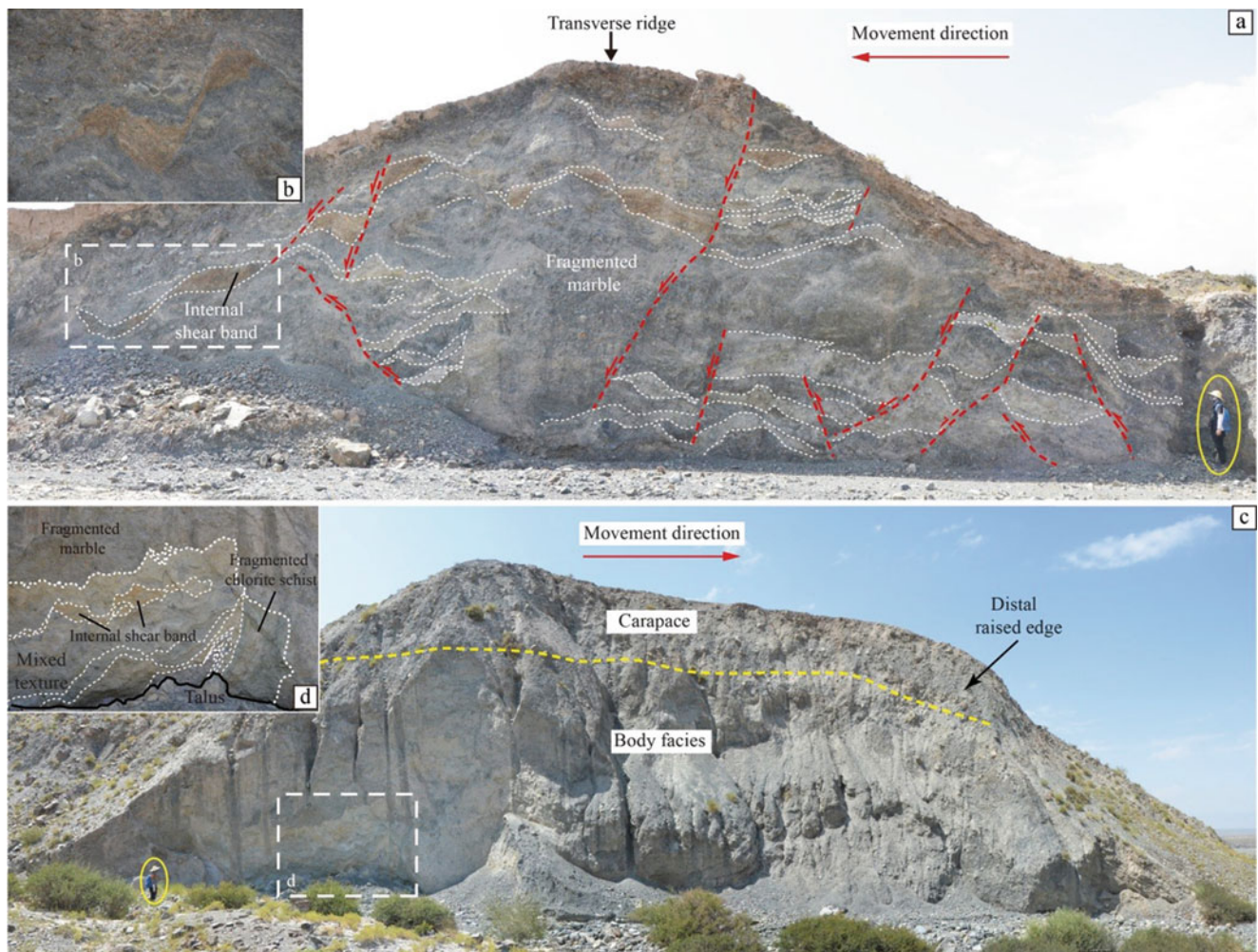


Fig. 49 Extension of faults developed in the frontal area of the accumulation zone with internal shear bands

trace of being cut by the moving avalanche mass. In contrast, some subhorizontal shear bands within the avalanche deposit were separated and dislocated by the clastic dikes (Fig. 52d–g). These clastic dikes consist of fine grains that are mixtures of clays and sands with high circularity, and present relatively homogenous internal textures, suggesting a source of substrate. Diameters of gravels are 1–2 cm with the largest being up to 4 cm, and fine-grained sands replaced gravels with the height increasing. Furthermore, some clastic dikes exhibit well-organized internal structures indicating flow-like motion. For instance, a clastic dike that is 8 meters high and 2.5 meters wide displays a series of upward arched lineations inclined at angles of 30 to 50° relative to both clastic dike walls (Fig. 52e). Due to fine grains aligned regularly within the dikes, a similar clastic dike comprising a series of oblique and repeated laminations that are in inclined contact with the dike walls at a high angle was also observed in another outcrop (Fig. 52f). The existence of the dikes indicates that liquefaction occurred in the substrate when the avalanche

mass arrived. As indicated by the relationship between the avalanche mass and dikes, it can be deduced that the avalanche mass was dislocated by the dikes with the dikes not being disturbed. This indicates that the dikes should be generated during the final accumulation stage of the avalanche mass, rather than during the propagation process.

5 Discussion

Take the area of the Himalayan range in China as an studied area, the spatial distribution of rock avalanches in the studied area is conducted with the controlling factors on the generation of rock avalanches being primarily analyzed. Furthermore, several typical rock avalanches that occurred in the Tibetan Plateau, demonstrating excellent landforms and internal deposition features, are introduced in detail, hoping to provide more geological evidences insight on rock avalanche kinematics. With these studies, it can be reached that

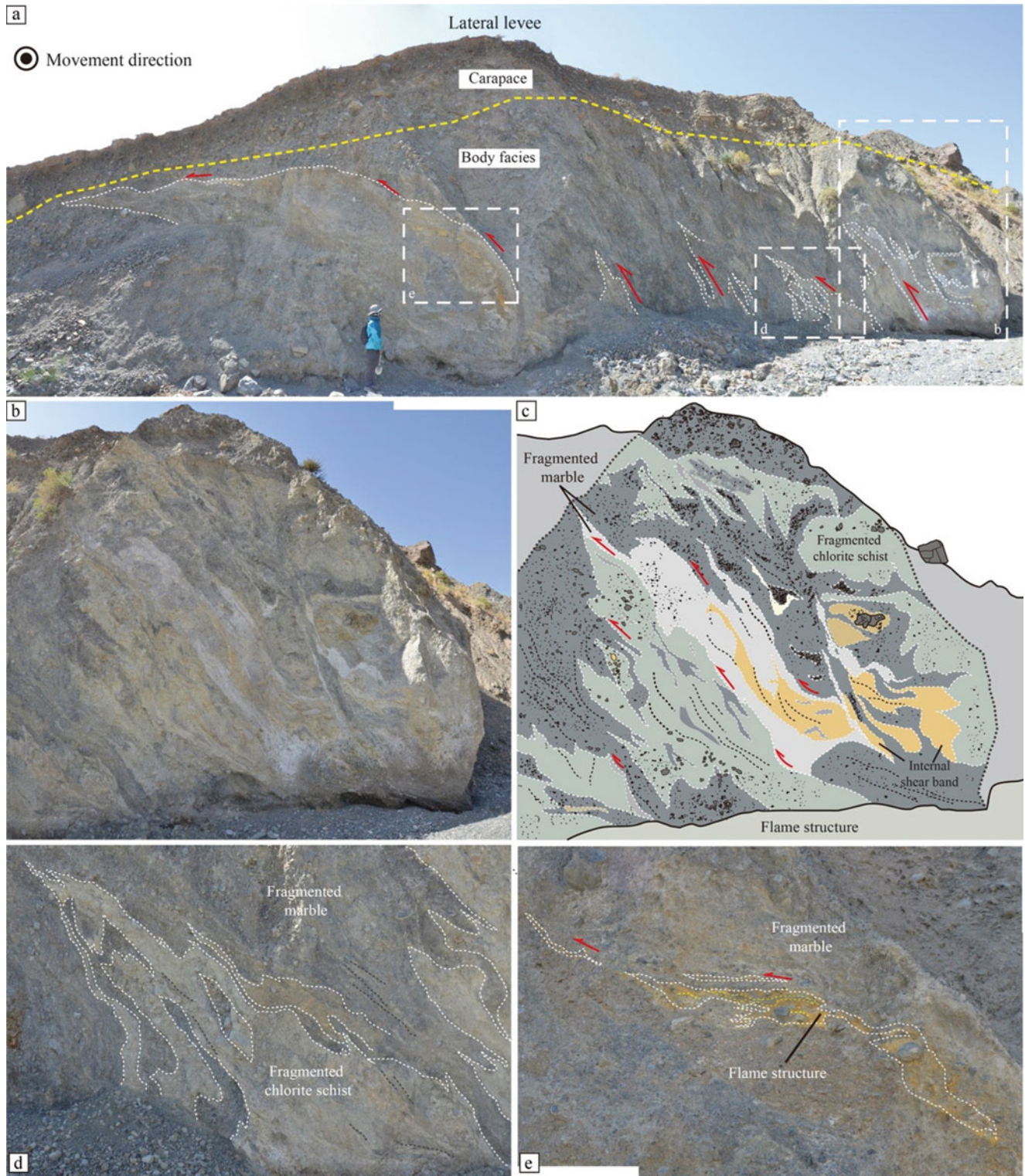


Fig. 50 Rolled flame structures within the lateral levee (a) with enlarged views of internal structures (b, d-e) and their schematic representations (c)

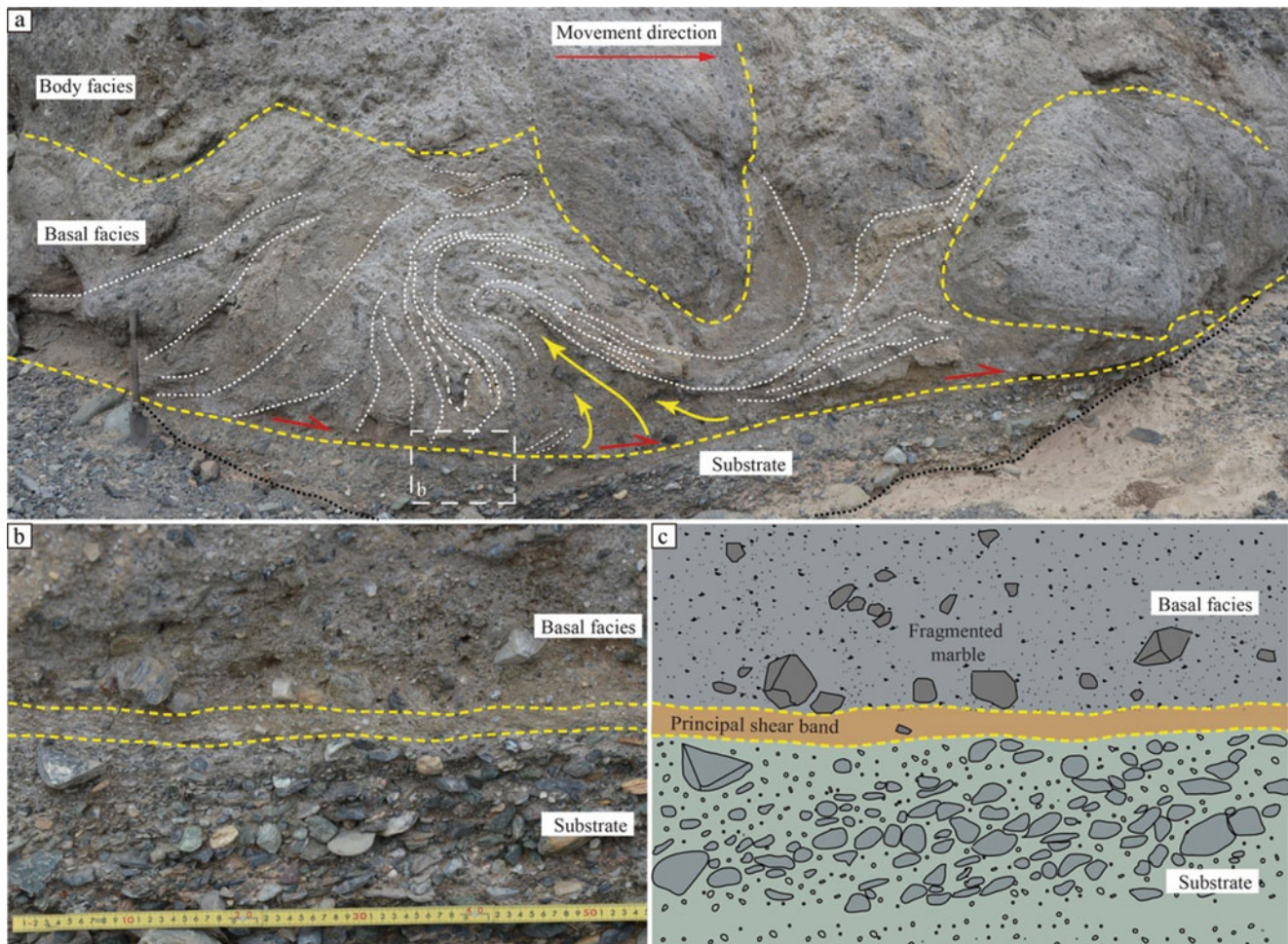


Fig. 51 Diapiric structure in the basal facies (a) with enlarged view showing the contact form between the basal facies and substrate (b-c)

active fault has a prominent role in the predetermining and occurrence of rock avalanches. Controlled by faults, the source areas of rock avalanches are commonly located on steep bedrock slopes with well-developed structures. The transition and accumulation zones are usually located on the rest fault wall with Quaternary deposits distributed along the travelling path. For the Quaternary deposits, they may be fine-grained fluvial materials, which can be classified as a relatively soft substrate like the Luanshibao and Nyixoi Chongco rock avalanches. Sometimes, they are composed of coarse-grained materials sourced from diluvial or fluviglacial processes, which can be classified as a relatively hard substrate like at the Tagarma and Iymek rock avalanches. Through detailed studies on the deposited features of the four typical cases in the Tibet Plateau, similar landforms are observed in their transition zone, such as torea blocks with steep frontal escarpments and longitudinal ridges. Different deposited features also can be observed along their accumulation zones due to variations in substrate conditions.

As argued in previous studies (Andrade and van Wyk de Vries 2010; Thompson et al. 2010; Strom 2010; Johnson et al. 2012; Paguican et al. 2014; Longchamp et al. 2016; Wang et al. 2018, 2019a, b, 2020), torea blocks are usually products of a rapid stretching process, which commonly distributes in the rear part of the transition zone, especially at the toe of the source area. Next to the distribution of torea blocks, it is usually the distribution of longitudinal landforms, which is attributed to an extensional stress status in propagation with a sinistral or dextral shearing occurred along the lateral margins (Valderrama et al. 2016; Wang et al. 2018). Through a comparison of the four cases, it can be reached that material conditions of the substrate have little influence on the generation of landforms in the transition zone.

For the generation of transverse ridges, it is generally the products of compression in the deceleration process of avalanche masses (Nicoletti and Parise 1996; Shea and van Wyk de Vries 2008; Dufresne and Davies 2009; Ostermann et al. 2012; Paguican et al. 2014; Yoshida 2014; Charrière et al.

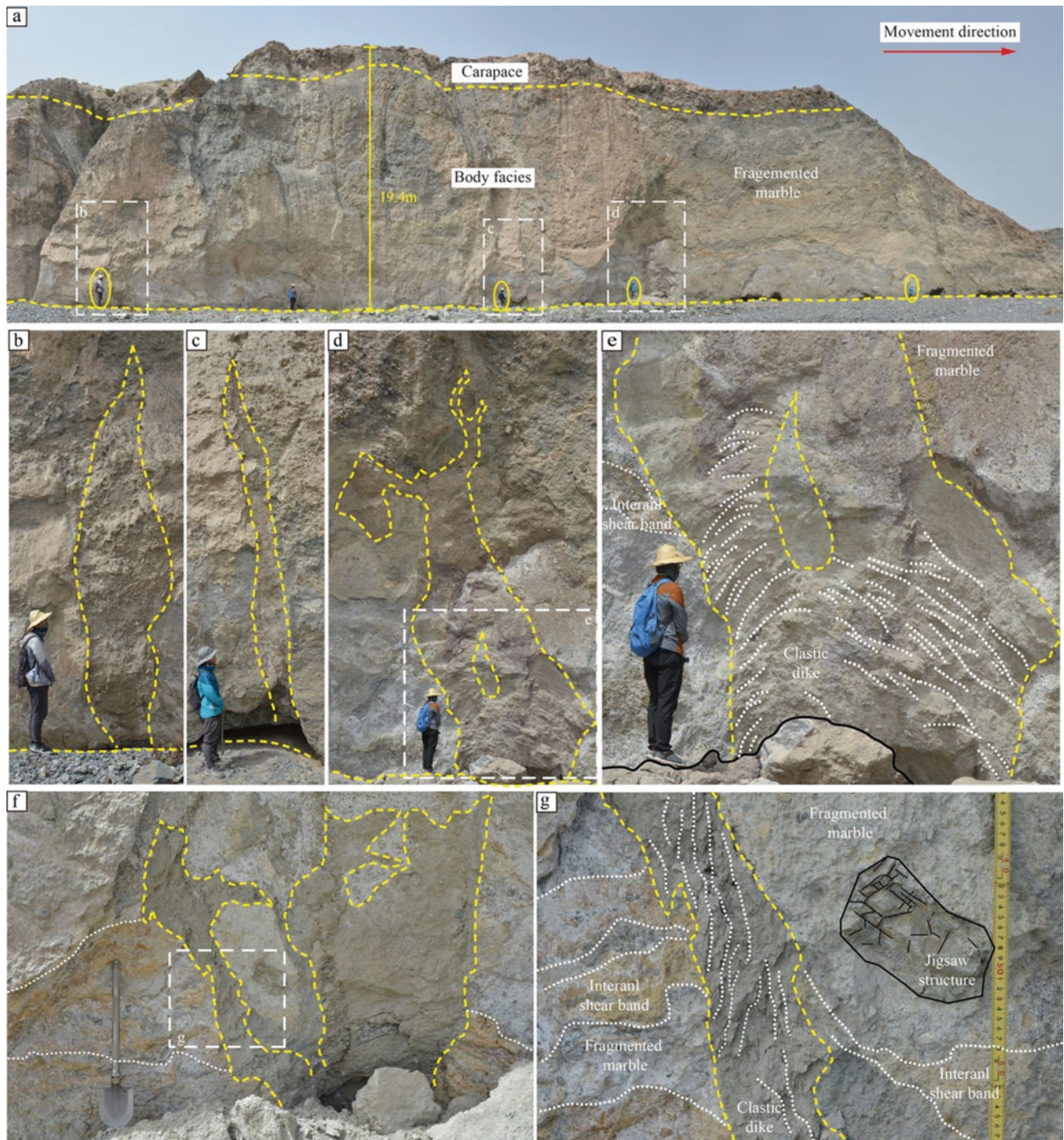


Fig. 52 Outcrops (a, f) with enlarged views of typical clastic dikes (b-e, g)

2016). For the occurrence of the rapid deceleration process, it is resulted by the gradually slowing down of the slope of the travelling path. With the slowing down of the travelling path slope, the basal friction will increase, which is disadvantage for the propagation of the avalanche mass. As described above, slope angles of the accumulation zones of the

Luanshibao and Nyixoi Chongco rock avalanches are both less than 2°. Yoshida (2014) argued that gentler travelling path can result in the reduction of down-sliding force and the increase of basal friction, which is disadvantageous for the emplacement of avalanche masses. In the deceleration process, different emplacement forms should occur under the

influence of different substrate conditions. For the Luanshibao and Nyixoi Chongco rock avalanches with soft substrates, the increase of basal friction was relatively low and the avalanche masses still kept relatively high mobility. Lateral spreading increases obviously due to the low lateral resistance of a soft substrate. With the occurrence of lateral spreading, a series of small-scaled hummocks will be generated. And a relative thin sheet will form with its frontal leading edge usually being several meters only. Greatly different from the Luanshibao and Nyixoi Chongco rock avalanches with soft substrates, the Tagarma and Iymek rock avalanches featured by hard substrates have steep and high frontal leading edges with the thickness being up to tens of meters. Meanwhile, the degree of lateral spreading is limited and there is almost no distribution of hummocks. Through a comparison of volume, it can be seen that the volume of the Tagarma rock avalanche is similar to that of the Luanshibao and Nyixoi Chongco rock avalanches, but they have different deposited features. This indicates that volume should not be the key role for the difference of the deposited features of the rock avalanches with different substrates. A comparison of the landforms and internal deposited structures of these rock avalanches indicates that the detached mass generally displays a rapid extensional movement in the transition zone. In the accumulation zone, the avalanche should display a rapid deceleration process with intensive compression in the condition of a hard substrate. When the substrate is soft, the avalanche should display a combination of longitudinal deceleration and lateral spreading in unconfined conditions.

In addition to the differential movement of rock avalanches under different substrate conditions, a series of other sheared structures can be observed in rock avalanche deposits, such as jigsaw structures, preserved original stratigraphy sequence, aligned distribution of clasts, etc. These are geological evidences of a laminar-like flow movement. Furthermore, geological evidences for the generation of lateral levees are observed in the Iymek rock avalanche, which indicates that the formation of lateral levees should be resulted from a lateral bulldozing process instead of a sorting process typical of granular flows. In the frontal area of the accumulation, the liquefaction phenomenon is also observed with the avalanche mass being dislocated, which indicated that the liquefied dikes should be generated at the final moment and have no contribution to the high mobility of the rock avalanche.

6 Conclusion

Rock avalanches, as one of the most threatening geological processes in mountainous regions, commonly cause tremendous threat to life. With this study, the sedimentary structures

of four typical rock avalanches are analyzed in detail with the following conclusions being reached.

1. Through a comparison of different factors on the spatial distribution of rock avalanches in the Himalayas of China, we primarily reached that the fault systems should be the most significant factor for their generation. For the non-glacial areas, the role of glacier should be the second factor, which intensively influences the stability of the bedrocks in the source areas. For the non-glacial areas, lithology should be the second key factor, which determines the slope steepness and, thus, its stability.
2. In rock avalanche deposits, some features such as jigsaw structures, preserved original stratigraphy sequence, aligned distribution of clasts are commonly developed, indicating a low disturbance of the avalanche mass in propagation. Hence, it is proposed that the propagation of rock avalanches should be a rapid motion similar to a laminar flow.
3. After detaching from the source area, the rock avalanche mass exhibits an extension-dominated sliding process in the transition zone. When it arrives at the accumulation zone, it fails into a compression-dominated sliding process. If the substrate is composed of soft material like water-rich fluvial deposits, a rapid radial spreading process will appear in unconfined conditions at the frontal edge due to the rapid decrease of basal friction with a relatively thin deposited sheet being formed. If the substrate is composed of hard material like dry diluvial or fluvio-glacial deposits, the moving mass will display a steep and thick leading edge due to a high increase of basal friction before motion halts.
4. The finding of the rolling flame structures within the raised lateral levees of the Iymek rock avalanche is the helpful geological evidence for the exploration of the formation mechanisms of lateral levee. With this evidence, it is reached that the formation of the lateral levees is associated with a lateral bulldozing movement of the avalanche mass instead of a complex mechanism related to grain self-segregation. In this process, the rear materials continuously push and plough the front decelerated materials aside, resulting in the formation of these outward extended flame-like shear bands.
5. The appearance of the clastic dikes in the Iymek rock avalanche suggests that the occurrence of substrate liquefaction should be caused by the high-energy shearing during emplacement. But, the localized liquefaction of the substrate is not a contributor for the high mobility of the Iymek rock avalanche. It is only a product of the strong interaction between the sliding mass and the substrate during the final accumulated stage.

Acknowledgments This work was supported by the National Natural Science Foundation of China [grant numbers U2244229, 42177131 and 42207203]. The authors declare that they have no conflict of interests. The data presented in this paper are available on request from the corresponding author.

References

- Aaron J, Mcdougall S (2019) Rock avalanche mobility: the role of path material. *Eng Geol* 257:105126
- Andrade SD, van Wyk de Vries B (2010) Structural analysis of the early stages of catastrophic stratovolcano flank-collapse using analogue models. *Bull Volcanol* 72:771–789
- Arrowsmith JR, Strecker MR (1999) Seismotectonic range-front segmentation and mountain-belt growth in the Pamir-alai region, Kyrgyzstan (India-Eurasia collision zone). *Geol Soc Am Bull* 111(11):1665–1683
- Barth NC (2014) The Cascade rock avalanche: implications of a very large alpine Fault-triggered failure, New Zealand. *Landslides* 11(3):327–341
- Basharat M, Rohn J, Ehret D, Baig MS (2012) Lithological and structural control of Hattian Bala rock avalanche triggered by the Kashmir earthquake 2005, sub-Himalayas, northern Pakistan. *J Earth Sci* 23:213–224
- Blisniuk PM, Hacker BR, Glodny J, Ratschbacher L, Bi S, Wu Z, McWilliams MO, Calvert A (2001) Normal faulting in Central Tibet since at least 13.5 Myr ago. *Nature* 412(6847):628–632
- Bufe A, Bekaert DPS, Hussain E, Bookhagen B, Burbank DW, Thompson JJA, Chen J, Li T, Liu LT, Gan WJ (2017) Temporal changes in rock uplift rates of folds in the foreland of the Tian Shan and the Pamir from geodetic and geologic data. *Geophys Res Lett* 44(21):10977–10987
- Cagnoli B, Piersanti A (2015) Grain size and flow volume effects on granular flow mobility in numerical simulations: 3-D discrete element modeling of flows of angular rock fragments. *J Geophys Res Solid Earth* 120(4):2350–2366
- Catane SG, Cabria HB, Zarco MAH, Saturay RM Jr, Mirasol-Robert AA (2008) The 17 February 2006 Guinsaogon rock slide-debris avalanche, Southern Leyte, Philippines: deposit characteristics and failure mechanism. *Bull Eng Geol Environ* 67:305–320
- Charrière M, Humair F, Froese C, Jaboyedoff M, Pedrazzini A, Longchamp C (2016) From the source area to the deposit: collapse, fragmentation, and propagation of the Frank slide. *Geol Soc Am Bull* 128(1–2):332–351
- Chevalier ML, Li HB, Pan JW, Pei JL, Wu FY, Xu W, Sun ZM, Liu DL (2011) Fast slip-rate along the northern end of the Karakorum fault system, western Tibet. *Geophys Res Lett* 38(22)
- Chevalier ML, Pan JW, Li HB, Liu DL, Wang M (2015) Quantification of both normal and right-lateral late quaternary activity along the Kongur Shan extensional system, Chinese Pamir. *Terra Nova* 27(5):379–391
- Chung SL, Chu MF, Zhang YQ, Xie YW, Lo CH, Lee TY, Lan CY, Li XH, Zhang Q, Wang YZ (2005) Tibetan tectonic evolution inferred from spatial and temporal variations in post-collisional magmatism. *Earth Sci Rev* 68(3–4):173–196
- Cowgill E (2010) Cenozoic right-slip faulting along the eastern margin of the Pamir salient, northwestern China. *Geol Soc Am Bull* 122(1–2):145–161
- Cruden DM, Varnes DJ (1996) Landslide types and processes. In: Turner AK, Schuster RL (eds) *Landslides: investigation and mitigation*, special report 247. National Academy Press, Washington, pp 36–75
- Dai FC, Xu C, Yao X, Xu L, Tu XB, Gong QM (2011) Spatial distribution of landslides triggered by the 2008 Ms 8.0 Wenchuan earthquake, China. *J Asian Earth Sci* 40(4):883–895
- Davies TR, McSaveney MJ (2009) The role of rock fragmentation in the motion of large landslides. *Eng Geol* 109(1–2):67–79
- Delaney KB, Evans SG (2014) The 1997 Mount Munday landslide (British Columbia) and the behaviour of rock avalanches on glacier surfaces. *Landslides* 11(6):1019–1036
- Dufresne A, Davies TR (2009) Longitudinal ridges in mass movement deposits. *Geomorphology* 105(3–4):171–181
- Dufresne A, Davies TR, McSaveney MJ (2010) Influence of runout-path material on emplacement of the round top rock avalanche, New Zealand. *Earth Surface Process and Landforms* 35(2):190–201
- Dufresne A, Bsmeier A, Prager C (2016) Sedimentology of rock avalanche deposits—case study and review. *Earth Sci Rev* 163:234–259
- Dufresne A, Geertsema IM (2020) Rock slide–debris avalanches: flow transformation and hummock formation, examples from British Columbia. *Landslides* 17:15–32
- Dunning SA (2006). (Special Issue) The grain size distribution of rock-avalanche deposits in valley-confined settings. *Ital J Eng Geol Environ* 1:117–121
- Dunning SA, Mitchell WA, Rosser NJ, Petley DN (2007) The Hattian Bala rock avalanche and associated landslides triggered by the Kashmir earthquake of 8 October 2005. *Eng Geol* 93:130–144
- Elliott JR, Jolivet R, Gonzalez PJ, Avouac JP, Hollingsworth J, Searle MP, Stevens VL (2016) Himalayan megathrust geometry and relation to topography revealed by the Gorkha earthquake. *Nat Geosci* 9(2):174–180
- Evans SG, Guthrie RH, Roberts NJ, Bishop NF (2007) The disastrous 17 February 2006 rockslide-debris avalanche on Leyte Island, Philippines: a catastrophic landslide in tropical. *Nat Hazards Earth Syst Sci* 7(1):89–101
- Fan G, Ni JF, Wallace TC (1994) Active tectonics of the Pamirs and Karakorum. *J Geophys Res* 99(B4):7131–7160
- Fan XM, Xu Q, Scaringi G, Dai LX, Li WL, Dong XJ, Zhu X, Pei XJ, Dai KR, Havenith HB (2017) Failure mechanism and kinematics of the deadly June 24th 2017 Xinmo landslide, Maoxian, Sichuan, China. *Landslides* 14(6):2129–2146
- Friele P, Millard TH, Mitchell A, Allstadt KE, Menounos B, Geertsema M, Clague JJ (2020) Observations on the may 2019 Joffre peak landslides, British Columbia. *Landslides* 17:913–930
- Fu B, Ninomiya Y, Guo J. Slip partitioning in the northeast Pamir-Tian Shan convergence zone. *Tectonophysics*, 2011, 483(3–4):344–364, 364
- Guo CB, Zhang YS, Montgomery DR, Du YB, Zhang GZ, Wang SF (2016) How unusual is the long-runout of the earthquake-triggered Giant Luanshibao landslide, Tibetan plateau, China? *Geomorphology* 259:145–154
- Guthrie RH, Friele P, Allstadt K, Roberts N, Evans SG, Delaney KB, Roche D, Clague JJ, Jakob M (2012) The 6 august 2010 mount meager rock slide-debris flow, Coast Mountains, British Columbia: characteristics, dynamics, and implications for hazard and risk assessment. *Nat Hazards Earth Syst Sci* 12(5):1277–1294
- Habib P (1975) Production of gaseous pore pressure during rock slides. *Rock Mech Rock Eng* 7(4):193–197
- Harrison TM, Copeland P, Kidd WSF, Lovera OM (1995) Activation of the Nyainqentanghla shear zone: implications for uplift of the southern Tibetan plateau. *Tectonics* 14(3):658–676
- He SM, Liu W, Wang J (2015) Dynamic simulation of landslide based on thermo-poro-elastic approach. *Comput Geosci* 75:24–32
- Heim A (1932) *Landslides and human lives*. Bitech Publishers, Vancouver
- Hewitt K, Clague JJ, Orwin JF (2008) Legacies of catastrophic rock slope failures in mountain landscapes. *Earth-Science Review* 87(1–2):1–38

- Hu W, Huang RQ, Mcsaveney M, Yao L, Xu Q, Feng MS, Zhang XH (2019) Superheated steam, hot CO₂ and dynamic recrystallization from frictional heat jointly lubricated a giant landslide: field and experimental evidence. *Earth Planet Sci Lett* 510:85–93
- Huang RQ, Pei XJ, Fan XM, Zhang WF, Li SG, Li BL (2012) The characteristics and failure mechanism of the largest landslide triggered by the Wenchuan earthquake, may 12, 2008, China. *Landslides* 9(1):131–142
- Hungr O, Evans SG (2004) Entrainment of debris in rock avalanches: an analysis of a long run-out mechanism. *Geol Soc Am Bull* 116(9–10): 1240–1252
- Ischuk A, Bendick R, Rybin A, Molnar P, Zubovich AV (2013) Kinematics of the Pamir and Hindu Kush regions from GPS geodesy. *Geophys Res Lett* 118(5):2408–2416
- Iverson RM, Ouyang CJ (2015) Entrainment of bed material by earth-surface mass flows: review and reformulation of depth-integrated theory. *Rev Geophys* 53(1):27–58
- Iverson RM (2015) Scaling and design of landslide and debris-flow experiments. *Geomorphology* 244:9–20
- Iverson RM, Logan M, Denlinger RP (2004) Granular avalanches across irregular three-dimensional terrain: 2. Experimental tests. *J Geophys Res Earth Surf* 109(F1)
- Iverson RM, George DL, Allstadt K, Reid ME, Collins BD, Vallance JW, Schilling SP, Godt JW, Cannon CM, Magirl CS, Baum RL, Coe JA, Schulz WH, Bower JB (2015) Landslide mobility and hazards: implications of the 2014 Oso disaster. *Earth Planet Sci Lett* 412:197–208
- Kropáček J, Vilímek V, Mehrishi P (2021) A preliminary assessment of the Chamoli rock and ice avalanche in the Indian Himalayas by remote sensing. *Landslides* 18(10):3489–3497
- Johnson BC, Campbell CS, Melosh HJ (2016) The reduction of friction in long runout landslides as an emergent phenomenon. *J Geophys Res Earth* 121(5):881–889
- Johnson CG, Kokelaar BP, Iverson RM, Logan M, LaHusen RG, Gray JMT (2012) Grain-size segregation and levee formation in geophysical mass flows. *J Geophys Res Earth* 117:F01032
- Larson KM, Roland B, Bilham R, Freymueller JT (1999) Kinematics of the India-Eurasia collision zone from GPS measurements. *J Geophys Res Solid Earth* 104(B1):1077–1093
- Larsen IJ, Montgomery DR, Korup O (2010) Landslide erosion controlled by hillslope material. *Nat Geosci* 3(4):247–251
- Legros F (2002) The mobility of long-runout landslides. *Eng Geol* 63: 301–331
- Lin A, Rao G, Yan B (2014) Structural analysis of the right-lateral strike-slip Qingchuan fault, northeastern segment of the Longmen Shan thrust belt, Central China. *J Struct Geol* 68:227–244
- Liu X, Herzsuh U, Wang Y, Kuhn G, Yu Z (2014) Glacier fluctuations of Muztagh Ata and temperature changes during the late Holocene in westernmost Tibetan plateau, based on glaciolacustrine sediment records. *Geophys Res Lett* 41(17): 6265–6273
- Longchamp C, Abellan A, Jaboyedoff M, Manzella I (2016) 3-D models and structural analysis of rock avalanches: the study of the deformation process to better understand the propagation mechanism. *Earth Surf Dyn* 4(3):743–755
- Lucas A, Mangeney A, Ampuero JP (2014) Frictional velocity-weakening in landslides on earth and on other planetary bodies. *Nat Commun* 5(1):3417
- Manzella I, Labiouse V (2013) Empirical and analytical analyses of laboratory granular flows to investigate rock avalanche propagation. *Landslides* 10(1):23–36
- Melosh HJ (1978) Acoustic fluidization. *Am Sci* 71(B13):158–168
- Mergili M, Frank B, Fischer JT, Huggel C, Pudasainia SP (2018) Computational experiments on the 1962 and 1970 landslide events at Huascarán (Peru) with lavaflow: lessons learned for predictive mass flow simulations. *Geomorphology* 322:15–28
- Mitchell A, Mcdougall S, Aaron J, Brideau MA (2020) Rock avalanche-generated sediment mass flows: definitions and Hazard. *Front Earth Sci* 8:543937
- McColl ST, Davies TR (2011) Evidence for a rock-avalanche origin for ‘the hillocks’ “moraine”, Otago, New Zealand. *Geomorphology* 127(3–4):216–224
- Nicoletti PG, Parise M (1996) Geomorphology and kinematics of the Conturrana rockslide-debris flow (NW Sicily). *Earth Surf Process Landf* 21:875–892
- Ostermann M, Sanders D (2017) The Brenner pass rock avalanche cluster suggests a close relation between long-term slope deformation (DSGSDs and translational rock slides) and catastrophic failure. *Geomorphology* 289:44–59
- Ostermann M, Sanders D, Ivy-Ochs S, Alfimov V, Rockenschaub M, Romer A (2012) Early Holocene (8.6 ka) rock avalanche deposits, Obereberg valley (eastern Alps): landform interpretation and kinematics of rapid mass movement. *Geomorphology* 171-172:83–93
- Paguican EMR, Wyk V, de Vries B, Lagmay AFM (2014) Hummocks: how they form and how they evolve in rockslide-debris avalanches. *Landslides* 11(1):67–80
- Plafker G, Ericksen GE (1978) Nevados Huascarán avalanches, Peru. In: Voight B (ed) *Rockslides and avalanches*. Elsevier, Amsterdam, pp 277–314
- Pudasaini SP, Hutter K (2007) *Avalanche dynamics: dynamics of rapid flows of dense granular avalanches*. Springer, Verlag Berlin Heidelberg, pp 1–602
- Pudasaini SP, Jaboyedoff M (2020) A general analytical model for superelevation in landslide. *Landslides* 17(6):1377–1392
- Pudasaini SP, Miller SA (2013) The hypermobility of huge landslides and avalanches. *Eng Geol* 157:124–132
- Reznichenko NV, Andrews GR, Geater RE, Strom A (2017) Multiple origins of large hummock deposits in Alai Valley, northern Pamir: implications for palaeoclimate reconstructions. *Geomorphology* 285:347–362
- Robinson AC, Yin A, Manning CE, Harrison MT, Zhang SH, Wang XF (2004) Tectonic evolution of the northeastern Pamir: constraints from the northern portion of the Cenozoic Kongur Shan extensional system, western China. *Geol Soc Am Bull* 116(7–8):953–973
- Schwanghart W, Ryan M, Korup O (2018) Topographic and seismic constraints on the vulnerability of Himalayan hydropower. *Geophys Res Lett* 45(17):8985–8992
- Seong YB, Owen LA, Yi C, Finkel RC, Schoenbohm L (2009) Geomorphology of anomalously high glaciated mountains at the northwestern end of Tibet: Muztagh Ata and Kongur Shan. *Geomorphology* 103(2):227–250
- Shea T, van Wyk de Vries B (2008) Structural analysis and analogue modeling of the kinematics and dynamics of rockslide avalanches. *Geosphere* 4(4):657–686
- Shi AW, Wang YF, Cheng QG, Lin QW, Li TH, Wünnemann B (2023) The largest rock avalanche in China at Iymek, eastern Pamir, and its spectacular emplacement landscape. *Geomorphology* 421:108521
- Shreve RL (1968) Leakage and fluidization in air-layer lubricated avalanches. *Geol Soc Am Bull* 79(5):653–658
- Soret M, Larson K P, Cottle J, Ali A. How Himalayan collision stems from subduction. *Geology*, 2021, 49(8): 894–898
- Strecker MR, Hilley GE, Arrowsmith JR, Coutand I (2003) Differential structural and geomorphic mountain-front evolution in an active continental collision zone: the northwest Pamir, southern Kyrgyzstan. *Geol Soc Am Bull* 115(2):166–181
- Strom A (2010) Landslide dams in Central Asia region. *Landslides—Journal of the Japan Landslide Society* 47(6):309–324
- Strom A, Abdrakhmatov K (2018) *Rockslides and rock avalanches of Central Asia*. Elsevier, Netherlands, pp 1–424
- Sun BG, Mao WY, Feng YR (2006) Study on the change of air temperature, precipitation and runoff volume in the Yarkant river basin. *Arid Zone Res* 23(2):203–209. (In Chinese)

- Sun P, Zhang YS, Shi JS, Chen LW (2011) Analysis on the dynamical process of Donghekou rockslide-debris flow triggered by 5.12 Wenchuan earthquake. *J Mt Sci* 8(2):140–148
- Tang RC, Han WB (1993) Active faults and earthquake in Sichuan Province. Earthquake Publish Company, Beijing (In Chinese)
- Tapponnier P, Xu ZQ, Roger F, Meyer B, Arnaud N, Wittlinger G, Yang JS (2001) Oblique stepwise rise and growth of the Tibetan plateau. *Science* 294(5547):1671–1677
- Thompson N, Bennett MR, Petford N (2010) Development of characteristic volcanic debris avalanche deposit structures: new insight from distinct element simulations. *J Volcanol Geotherm Res* 192(3–4):191–200
- Valderrama P, Roche O, Samaniego P, van Wyk de Vries B, Bernard K, Marino J (2016) Dynamic implications of ridges on a debris avalanche deposit at Tutupaca volcano (southern Peru). *Bull Volcanol* 78(2):14
- Wang YF, Cheng QG, Zhu Q (2015) Surface microscopic examination of quartz grains from rock avalanche basal facies. *Can Geotech J* 52(2):167–181
- Wang YF, Xu Q, Cheng QG, Li Y, Luo ZX (2016) Spreading and deposit characteristics of a rapid dry granular avalanche across 3D topography: experimental study. *Rock Mech Rock Eng* 49(11):1–22
- Wang YF, Dong JJ, Cheng QG (2017) Velocity-dependent frictional weakening of large rock avalanche basal facies: implications for rock avalanche hypermobility? *J Geophys Res Solid Earth* 122(3):1648–1676
- Wang YF, Cheng QG, Lin QW, Li K, Yang HF (2018) Insights into the kinematics and dynamics of the Luanshibao rock avalanche (Tibetan plateau, China) based on its complex surface landforms. *Geomorphology* 317:170–183
- Wang YF, Cheng QG, Shi AW, Yuan YQ, Yin BM, Qiu YH (2019a) Sedimentary deformation structures in the Nyixoi Chongco rock avalanche: implications on rock avalanche transport mechanisms. *Landslides* 16(3):523–532
- Wang YF, Cheng QG, Shi AW, Yuan YQ, Qiu YH, Yin BM (2019b) Characteristics and transport mechanism of the Nyixoi Chongco rock avalanche on the Tibetan plateau, China. *Geomorphology* 343:92–105
- Wang YF, Cheng QG, Yuan YQ, Wang J, Qiu YH, Yin BM, Shi AW, Guo ZW (2020) Emplacement mechanisms of the Tagarma rock avalanche on the Pamir-western Himalayan syntaxis of the Tibet plateau, China. *Landslides* 17(3):527–542
- Weidinger JT, Korup O, Munack H, Altenberger U, Dunning SA, Tippelt G, Lottermoser W (2014) Giant rockslides from the inside. *Earth Planet Sci Lett* 389:62–73
- Whipple K, Shirzaei M, Hodges KV, Arrowsmith JR (2016) Active shortening within the Himalayan orogenic wedge implied by the 2015 Gorkha earthquake. *Nat Geosci* 9(9):711–716
- Wu ZH, Ye PS, Wang CM, Zhang KQ, Zhao H, Zheng YG, Yin JH, Li HH (2015) The relics, ages and significance of prehistoric large earthquakes in the Angang graben in the South Tibet. *Earth Science-Journal of China University of Geosciences* 40(10):1621–1642
- Xu XW, Wen XZ, Yu GH, Zheng R, Luo H, Zheng B (2005) Average slip rate, earthquake rupturing segmentation and recurrence behavior on the Litang fault zone, western Sichuan Province, China. *Science in China series (D)*. *Earth Sci* 48(8):1183–1196
- Yin A (2000) Mode of Cenozoic east-west extension in Tibet suggesting a common origin of rifts in Asia during the Indo-Asian collision. *J Geophys Res Solid Earth* 105(B9):21745–21759
- Yin A, Harrison TM (2000) Geologic evolution of the Himalayan-Tibetan orogeny. *Annu Rev Earth Planet Sci* 28(1):211–280
- Yin A (2010) Cenozoic tectonic evolution of Asia: a preliminary synthesis. *Tectonophysics* 488(1–4):293–325
- Yoshida H (2014) Hummock alignment in Japanese volcanic debris avalanches controlled by pre-avalanche slope of depositional area. *Geomorphology* 223:67–80
- Yuan ZD, Chen J, Owen LA, Hedrick KA, Caffee MW, Li WQ, Schoenbohm LM, Robinson AC (2013) Nature and timing of large landslides within an active orogen, eastern Pamir, China. *Geomorphology* 182:49–65
- Zeng QL, Zhang LQ, Davies T, Yuan GX, Xue XY, Wei RQ, Yin QF, Liao LY (2019) Morphology and inner structure of Luanshibao rock avalanche in Litang, China and its implications for long runout mechanisms. *Eng Geol* 260(8):105216
- Zhang PZ, Shen Z, Wang M, Gan WJ, Bürgmann R, Molnar P, Wang Q, Niu ZJ, Sun JZ, Wu JC, Hanrong S, You XZ (2004) Continuous deformation of the Tibetan plateau from global positioning system data. *Geology* 32(9):809–812
- Zhang YB, Xing AG, Jin KP, Zhuang Y, Bilal M, Xu SM, Zhu YQ (2020) Investigation and dynamic analyses of rockslide-induced debris avalanche in Shuicheng, Guizhou, China. *Landslides* 17:2189–2203
- Zhang Z, Chen Y, Yuan X, Tian X, Klempner SL, Xu T, Bai Z, Zhang H, Wu J, Teng J (2013) Normal faulting from simple shear rifting in South Tibet, using evidence from passive seismic profiling across the Yadong-Gulu rift. *Tectonophysics* 606:178–186
- Zhu YX, Dai FC, Yao X, Tu XB, Shi XS (2019) Field investigation and numerical simulation of the seismic triggering mechanism of the Tahman landslide in eastern Pamir. Northwest China. *Bull Eng Geol Environ* 78(8):5795–5809
- Zubovich AV, Wang XQ, Scherba YG, Schelochkov GG, Reilinger R, Reigber C, Mosienko OI, Molnar P, Michajljow W, Makarov VI, Li J, Kuzikov SI, Herring TA, Hamburger MW, Hager BH, Dang YM, Bragin VD, Beisenbaev RT (2010) GPS velocity field for the Tien Shan and surrounding regions. *Tectonics* 29(6):TC6014

Open Access This chapter is licensed under the terms of the Creative Commons Attribution 4.0 International License (<http://creativecommons.org/licenses/by/4.0/>), which permits use, sharing, adaptation, distribution and reproduction in any medium or format, as long as you give appropriate credit to the original author(s) and the source, provide a link to the Creative Commons license and indicate if changes were made.

The images or other third party material in this chapter are included in the chapter's Creative Commons license, unless indicated otherwise in a credit line to the material. If material is not included in the chapter's Creative Commons license and your intended use is not permitted by statutory regulation or exceeds the permitted use, you will need to obtain permission directly from the copyright holder.



Part II

Original Articles



Landslide Susceptibility Zonation Using GIS-Based Frequency Ratio Approach in the Kulon Progo Mountains Area, Indonesia

Egy Erzagian, Wahyu Wilopo, and Teuku Faisal Fathani

Abstract

Landslides cause many casualties, environmental damage, property losses, and psychological impacts. Landslides frequently occur in the Kulon Progo Mountains area of Indonesia and are especially triggered by high-intensity rainfall between November and March. Research on landslide susceptibility in the Kulon Progo Mountains area can be a relevant tool to prevent or reduce the risk of landslide potential. Therefore, this research aims to develop a landslide susceptibility map using the frequency ratio (FR) method. Controlling factors, namely, elevation, slope, aspect, lithology, lineament density, distance from streams, distance from roads, land use, and rainfall, were combined with landslide data to develop a landslide susceptibility map by GIS software. Seven hundred and forty-four landslide data points were acquired from field surveys, Google Earth image interpretation, and the Regional Disaster Management Agency (BPBD) of the Kulon Progo, Purworejo, and Magelang regencies. Landslide data were randomly selected for map modeling (80%) and validation (20%). The FR analysis shows that the research area can be classified into four landslide susceptibility zones based on the LSI value: low (LSI 4.05–7.85), moderate (LSI 7.86–9.85), high (LSI 9.86–12.81), and very high (LSI 12.82–19.46). The landslide susceptibility map was validated using the area under the curve (AUC) method, resulting in a success rate of 80.1% and a predictive rate of 81.3%.

Keywords

Landslide susceptibility · Frequency ratio · GIS analysis

1 Introduction

The Kulon Progo Mountains form a mountainous area in the southern part of Java Island, Indonesia. Tectonic processes and volcanic activities that formed the Kulon Progo Mountains area have occurred from the Tertiary to the Quaternary (Widagdo et al. 2018a, b). The Kulon Progo Mountains are generally composed of weathered and altered volcanic rocks that form a thick layer of soil with clay minerals. This weathered rock and thick soil layer is prone to landslides (Fookes et al. 2005).

Landslides are generally controlled by several factors, such as slope, lithology, geological structure, hydrological conditions, land use, and rainfall (Skilodimou et al. 2018; Conforti and Ietto 2020; Mersha and Meten 2020). Landslide activity in the Kulon Progo Mountains increases yearly, especially the activity triggered by high-intensity rainfall, for example, the Cempaka tropical cyclone in 2017–2018. The Regional Disaster Management Agency reported 744 landslide events in the period of 2015–2020. Landslides in the Kulon Progo Mountains area have caused numerous casualties, environmental damage, property losses, and psychological impacts. Therefore, landslide susceptibility maps of the Kulon Progo Mountains provide an important tool to prevent or reduce landslide risk. In addition, landslide susceptibility maps can be used by decision-makers for land use planning, landslide prevention, monitoring, and mitigation actions.

The purpose of this research is to develop a landslide susceptibility map. This research uses data on the distribution of landslide occurrence points and factors controlling landslides, such as elevation, slope, aspect, lithology, lineament density, distance from streams, distance from roads,

E. Erzagian · W. Wilopo (✉)
Department of Geological Engineering, Universitas Gadjah Mada,
Yogyakarta, Indonesia
e-mail: egy Erzagian@mail.ugm.ac.id; wilopo_w@ugm.ac.id

T. F. Fathani
Department of Civil and Environmental Engineering, Universitas
Gadjah Mada, Yogyakarta, Indonesia
e-mail: tfathani@ugm.ac.id

land use, and rainfall, to identify the landslide susceptibility zones.

2 Research Area

The research area is the Kulon Progo Mountains, which were geomorphologically formed as a Tertiary volcanic product (Widagdo et al. 2018a, b). This area includes two provinces: the Special Region of Yogyakarta and Central Java. It consists of 3 regencies, namely, Kulon Progo, Purworejo, and Magelang, and 12 subdistricts, which are Bagelen, Bener, Borobudur, Girimulyo, Kalibawang, Kaligesing, Kokap, Loano, Pengasih, Purworejo, Salaman, and Samigaluh (Fig. 1). The area is geographically located from 110°02'11.14"E to 110°16'02.30"E and 7°33'01.16"S to 7°52'08.02"S and covers an area of approximately 533.43 km².

The area has elevations between 19 and 976 masl. The morphology comprises a steeply sloping area with a height of up to 976 masl, a moderately sloping area with a lower elevation, and a gently sloping area with a low elevation. In the area, streams have flow directions of NW–SE on the west slope, SE–NW on the east slope, SW–NE on the north slope, and NE–SW on the south slope. The area is regionally composed of Tertiary–Quaternary volcanic and intrusive rocks, especially the Kebo-Butak Formation and andesite intrusion. The stratigraphy of the Kulon Progo Mountains area from oldest to youngest (Rahardjo et al. 1995) is as follows:

1. The Nanggulan Formation (Teon), the oldest rock formation, consists of sandstones with intercalations of lignite, sandy marl, claystone with limonite concretions, intercalations of marl and limestone, sandstone, and tuff. The formation age is Eocene–Oligocene.

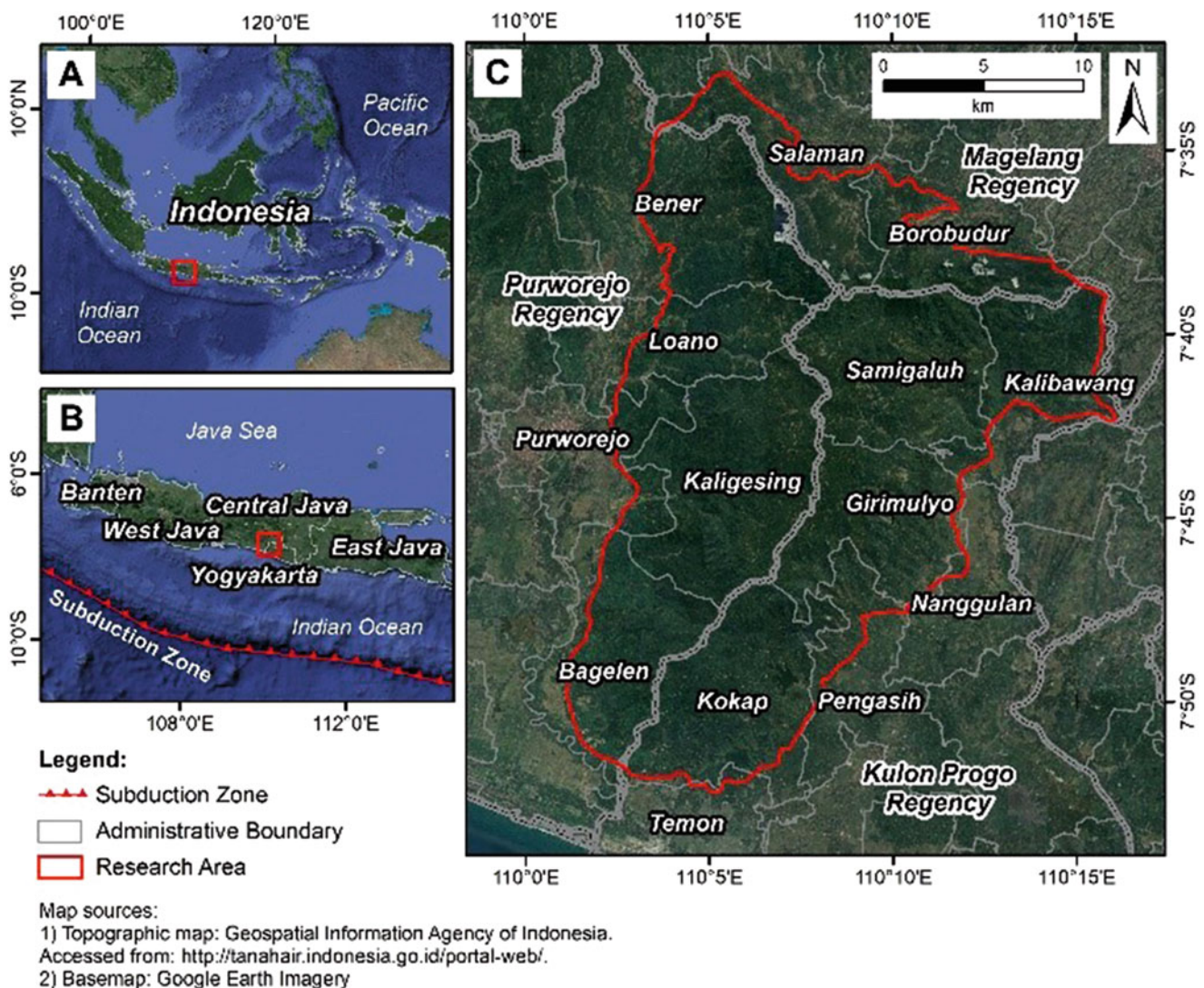


Fig. 1 (a) Map of Indonesia; (b) map of Java Island; and (c) research area

2. The Kebo-Butak Formation (Tm_{ok}) is unconformably deposited above the Nanggulan Formation. This formation consists of andesitic breccia, tuff, lapilli tuff, agglomerates, and intercalations of andesitic lava flows. The formation age is Oligocene–Miocene.
3. Intrusive rocks break through to the bottom of the Kebo-Butak Formation. The intrusive rocks consist of an andesite intrusion (a) and a dacite intrusion (da). The rock age is Miocene.
4. The Jonggrangan Formation (Tm_j) is unconformably deposited above the Kebo-Butak Formation. This formation is exposed in the middle of the Kulon Progo Mountains. It consists of conglomerate, tuffaceous marl, carbonate sandstone, and claystone with lignite at the bottom, while layered limestone and coral limestone make up the top. The formation age is early Miocene–middle Miocene.
5. The Sentolo Formation (Tm_{ps}) is conformably deposited and has an interfingering contact with the Jonggrangan Formation. This formation consists of limestone and marl sandstone. The formation age is middle Miocene–Pliocene.
6. Young volcanic deposits of Merapi Volcano (Qm_i) are unconformably deposited above the Sentolo Formation. This formation comprises undifferentiated tuff, ash, breccia, agglomerate, and lava flows. The formation age is the Pleistocene.
7. The alluvium and colluvium (Qa) consist of gravel, sand, silt, and clay along large rivers and coastal plains. The colluvium (Qc) consists of unsorted debris from the Kebo-Butak Formation.

3 Methodology

Landslides may reoccur under similar circumstances as previous landslides, so it is necessary to identify potential landslides by determining the factors that control them (Lee and Talib 2005). The analysis of the landslide susceptibility map is carried out using the frequency ratio (FR) method and the overlay process using GIS. The FR method is one of the statistical methods used in mapping landslide susceptibility using two variables (Mersha and Meten 2020). In this study, 80% of landslide occurrence points are used to analyze landslide susceptibility maps, while 20% are used for validation.

The landslide susceptibility map used in the frequency ratio method is based on the relationship between the landslide distribution and each controlling factor. The landslide-controlling factors in this study are elevation, slope, aspect, lithology, lineament density, distance from streams, distance from roads, land use, and rainfall. Each landslide-controlling factor is classified into several categories and then integrated

with the distribution of landslide occurrence points. The *FR* for each category is obtained through statistical calculations, as shown in Eq. 1 (Tazik et al. 2014).

The FR map for each landslide-controlling factor is processed using GIS tools by setting the FR value. The calculated FR value shows the correlation degree between landslides and certain factor classes (Rasyid et al. 2016; Mersha and Meten 2020). An FR value equal to 1 is the average value for the occurrence of movement for a specific factor. $FR > 1$ indicates a high potential for landslides, while $FR < 1$ indicates a low potential.

$$FR = \frac{D_i}{A_i} \frac{\sum_{i=1}^N D_i}{\sum_{i=1}^N A_i} \quad (1)$$

where.

FR: Frequency ratio of each class for a certain factor (*i*)

D_i: Number of landslide points for a certain factor (*i*)

A_i: Area of a class for a certain factor (*i*)

N: Number of factors

The overlay process combines several maps of landslide-controlling factors. All the *FR* values on each controlling factor map are summed to derive the landslide susceptibility index (*LSI*) value, as shown in Eq. 2 (Tazik et al. 2014).

$$LSI = FR_1 + FR_2 + FR_3 + \dots + FR_N \quad (2)$$

Using the Jenks natural breaks method, the landslide susceptibility map is classified based on the *LSI* value. The Jenks natural breaks method produces a map that can be interpreted by showing the spatial probability of future landslides ranging from very low to very high landslide susceptibility (Adition et al. 2018).

The landslide susceptibility map validation is carried out using the area under the curve (AUC) method by making both success and predictive rate curves (Lee and Talib 2005; Mersha and Meten 2020). The success rate on the AUC indicates the accuracy and quality of the resulting map developed based on modeling data, while the AUC prediction rate explains the capacity of the suggested map to predict the landslide susceptibility (Yalcin and Bulut 2007).

4 Dataset and Analysis

The collected data in this study consist of the distribution of landslide events and controlling factors processed using GIS. Nine landslide factors, including elevation, slope, aspect,

Table 1 Research dataset

Data	Data Source	Usage
Digital elevation model (DEM)	DEMNAS with 8.23 m × 8.23 m grid resolution (Geospatial Information Agency of Indonesia 2023)	Elevation, slope, aspect, stream, lineament
Geological map	Geological map of the Yogyakarta Sheet, Java, the scale of 1:100,000 (Rahardjo et al. 1995)	Lithology and lineament
Geological structure map	Lineament's interpretation and geological structure maps of the Kulon Progo mountains area (Rahardjo et al. 1995; Widagdo et al. 2018a, b)	Lineament
Road distribution	Road map scale of 1:25,000 (Geospatial Information Agency of Indonesia (2015–2019))	Road
Land use map	Land use map scale of 1:25,000 (Geospatial Information Agency of Indonesia (2015–2019))	Land use
Rainfall data	Rainfall data reported in the 2011–2020 period for each regency (Central Bureau of Statistics of Kulon Progo 2021; Central Bureau of Statistics of Purworejo 2021; Central Bureau of Statistics of Magelang 2021)	Rainfall
Landslide database	Rotational landslide event summary data from each regency (regional disaster management agency)	Landslide events
Satellite imagery	Google earth satellite imagery	Landslide events

lithology, lineament density, distance from streams, distance from roads, land use, and rainfall, are used in this research. Table 1 shows the data sources used to analyze landslide susceptibility maps.

Landslide events are verified and added via Google Earth satellite image interpretation (Fig. 2). Rotational and translational slides are the dominant types of landslides. The number of landslides in the research area is 744 points, where 595 points (80% of the total landslide events) are used as modeling data to prepare landslide susceptibility maps and 149 points (20% of the total landslide events) are used to validate the landslide susceptibility map. Landslide events for modeling and validation are randomly selected.

An elevation, a part of morphology, is formed by a combination of tectonic activity, erosion-weathering processes, and climatic effects (Ilija and Tsangaratos 2016). Elevations contribute indirectly to landslide events. The elevation map (Fig. 3a) was generated from DEM analysis and divided into five classes, i.e., 0–200 masl, 201–400 masl, 401–600 masl, 601–800 masl, and 801–1000 masl.

An aspect indicates the slope's direction and affects the slope's exposure to sunlight, wind direction, degree of saturation, and discontinuity conditions (Psomiadis et al. 2020; Mersha and Meten 2020). The aspect map (Fig. 3b) is generated from DEM data and divided into ten classes, i.e., flat (–1), north (0–22.5), northeast (22.5–67.5), east (67.5–112.5), southeast (112.5–157.5), south (157.5–202.5), southwest (202.5–247.5), west (247.5–292.5), northwest (292.5–337.5), and north (337.5–360).

A slope, as a geomorphological component, significantly contributes to landslides. The potential increases due to the greater driving force on steep slope conditions. The slope data are obtained from digital elevation model (DEM) analysis with an 8.23 × 8.23 m grid resolution. The slope map from

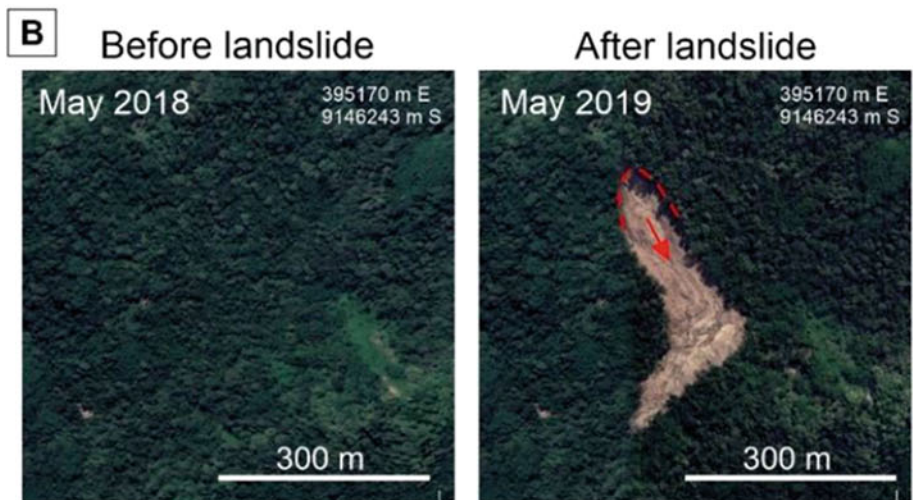
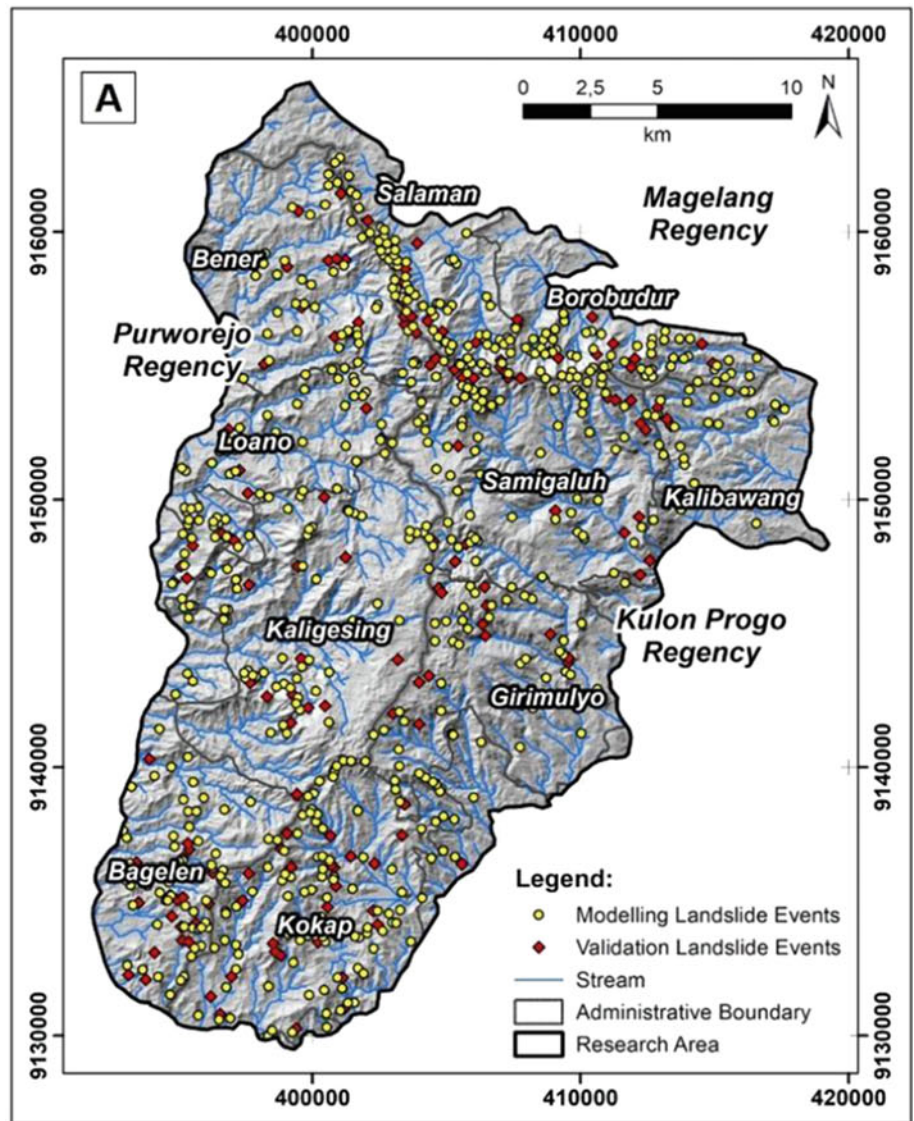
the DEM analysis is divided into four slope categories, i.e., 0°–15°, 16°–25°, 26°–35°, and 36°–57°, as shown in Fig. 3c.

Landslides commonly occur on slopes composed of weathered rock and residual soil with a thick layer and contain clay minerals (Fookes et al. 2005). Lithological data are obtained from the Geological Map of the Yogyakarta Sheet (Rahardjo et al. 1995). The lithologic map is divided into seven units based on rock formations, i.e., the Nanggulan Formation, Kebo-Butak Formation, intrusive rocks, Jonggrangan Formation, Sentolo Formation, young volcanic deposits of Merapi, and alluvium–colluvium deposits, as shown in Fig. 3d. The field survey shows that almost all the rocks are weathered and intrusive rocks. This is probably due to the dense geological structures that speed up the weathering process.

Lineaments generally indicate fractures, discontinuities, and shear zones that can contribute to landslides (Sarkar and Kanungo 2004). The lineament data are obtained from digital elevation model (DEM) analysis by considering secondary data, including geological maps developed by previous researchers, lineament interpretation, and geological structure maps. The lineament density is analyzed using the kernel density function in GIS. The lineament density map of the geological structure is classified into four categories, i.e., 0.31–1.45 km/km², 1.46–2.05 km/km², 2.06–2.55 km/km², and 2.56–3.58 km/km² (Fig. 3e).

The distance from streams is one of the factors that can indicate landslides and associated erosion processes to describe slope changes. The distance from streams is generated using the buffering function in GIS analysis. Stream data are obtained from watershed analysis using a DEM with a 200 × 200 m threshold and verified by the 1:25,000 scale topographic map. The distance from streams map (Fig. 3f) is categorized into four categories, i.e., <100 meters, 100–200 meters, 200–400 meters, and >400 meters.

Fig. 2 (a) Landslide event distribution map; (b) verification based on Google Earth image interpretation



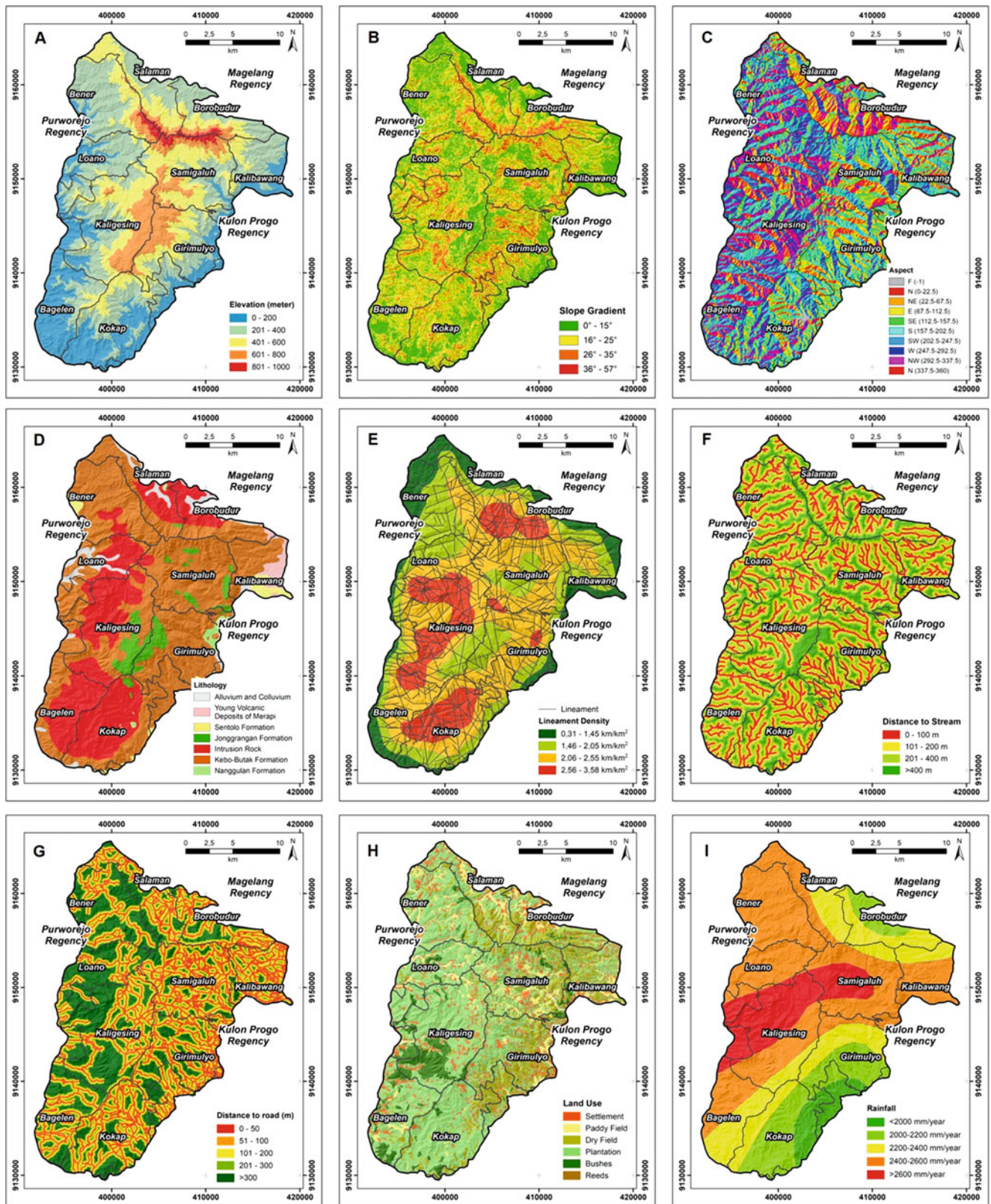


Fig. 3 Landslide-controlling factor maps: (a) elevation; (b) slope; (c) aspect; (d) lithology; (e) lineament density; (f) distance from streams; (g) distance from roads; (h) land use, and (i) rainfall

Road construction is closely related to vegetation removal and excavation, which can form steep slopes (Psomiadis et al. 2020). The road network in the study area, which consists of main roads and local roads, is one of the factors that can affect landslides. The road distance map (Fig. 3g) was developed from the buffer zone of the road network without including footpaths and divided into five classes, namely 0–50 m, 51–100 m, 101–200 m, 201–300 m, and > 300 m.

Land use has significant control over erosion and deposition. Land use, such as vegetation or plant residues, can withstand raindrops, increase infiltration, reduce runoff velocity, and increase water flow capacity (Akgün and Türk 2011). Land use with sparse vegetation generally shows faster erosion and slope conditions prone to landslides (Yalcin and Bulut 2007). The land use map (Fig. 3h) is classified into six land use types, i.e., settlements, paddy fields, dry fields, plantations, bushes, and reeds. Land use types are digitized from the 1:25,000 scale topographic map.

Rainfall intensity is one of the major triggers for landslides that can directly impact settlements (Haque et al. 2019). Prolonged and high-intensity rainfall generally triggers landslides because it can increase hydrostatic and pore water pressure below the surface. Rainfall data are obtained from rainfall data reports from the Kulon Progo, Purworejo, and Magelang regencies in the 2011–2020 period. Landslide occurrence distribution data are obtained from the Regional Disaster Management Agency (BPBD) of each regency. The rainfall data that were used have a longer period than the available landslide data. More accurate results can be obtained with a longer period of hydrological data. The annual rainfall intensity data for 10 years (2010–2019) are obtained from 12 nearby rainfall stations. The annual rainfall average value is 2409 mm/year, with a range of data of 1786–3021 mm/year. The rainfall map is analyzed using GIS interpolation with the kriging method based on the average annual rainfall data of each station. The rainfall map (Fig. 3i) is divided into five categories, i.e., <2000 mm/year, 2000–2200 mm/year, 2200–2400 mm/year, 2400–2600 mm/year, and > 2600 mm/year.

5 Result & Discussion

The results of the FR calculation show that the landslide susceptibility level is higher as the degree of the slope increases. The landslide-controlling factor, with $FR > 1$, mainly shows a high frequency of landslides, while $FR < 1$ shows a lower frequency. The 801–1000 masl elevation has the highest FR value, significantly influencing landslide events, while the lowest FR value is the 0–200 masl elevation. The slope with angles of $>15^\circ$ has a significant contribution to landslides. The highest FR value for the slope factor is the slope with angles of 36° – 57° , while the lowest is in the

slope with angles of 0° – 15° . In terms of aspect, the FR value of the north class (0–22.5) has the highest FR value, followed by north (337.5–360) and northeast (22.5–67.5). The lowest FR value for aspect is the flat category (–1).

In terms of lithology, Kebo-Butak Formation causes significant landslides in the research area, followed by intrusive rocks (andesite and dacite), the Jonggrangan Formation, and Nanggulan Formation. Kebo-Butak Formation generally undergoes weathering and alteration to form a thick layer of soil and is prone to landslides. A low number of landslide occurrences is found in alluvium deposits, colluvium deposits, the young volcanic deposits of Merapi Volcano, and the Sentolo Formation. The lineament density of 2.56–3.58 km/km² has the highest FR value and greatly contributes to landslides. A lineament is a weak plane that can indicate geological structures (such as joints and faults) or cracks, accelerate the weathering process, and allow water to infiltrate the slope. In general, the number of landslides increases as the lineament density increases. For the distance from streams, a distance from the river of >400 m significantly contributes to landslides, while a distance from the river of <100 m has a minor contribution. This result shows that the stream does not significantly control landslide occurrences.

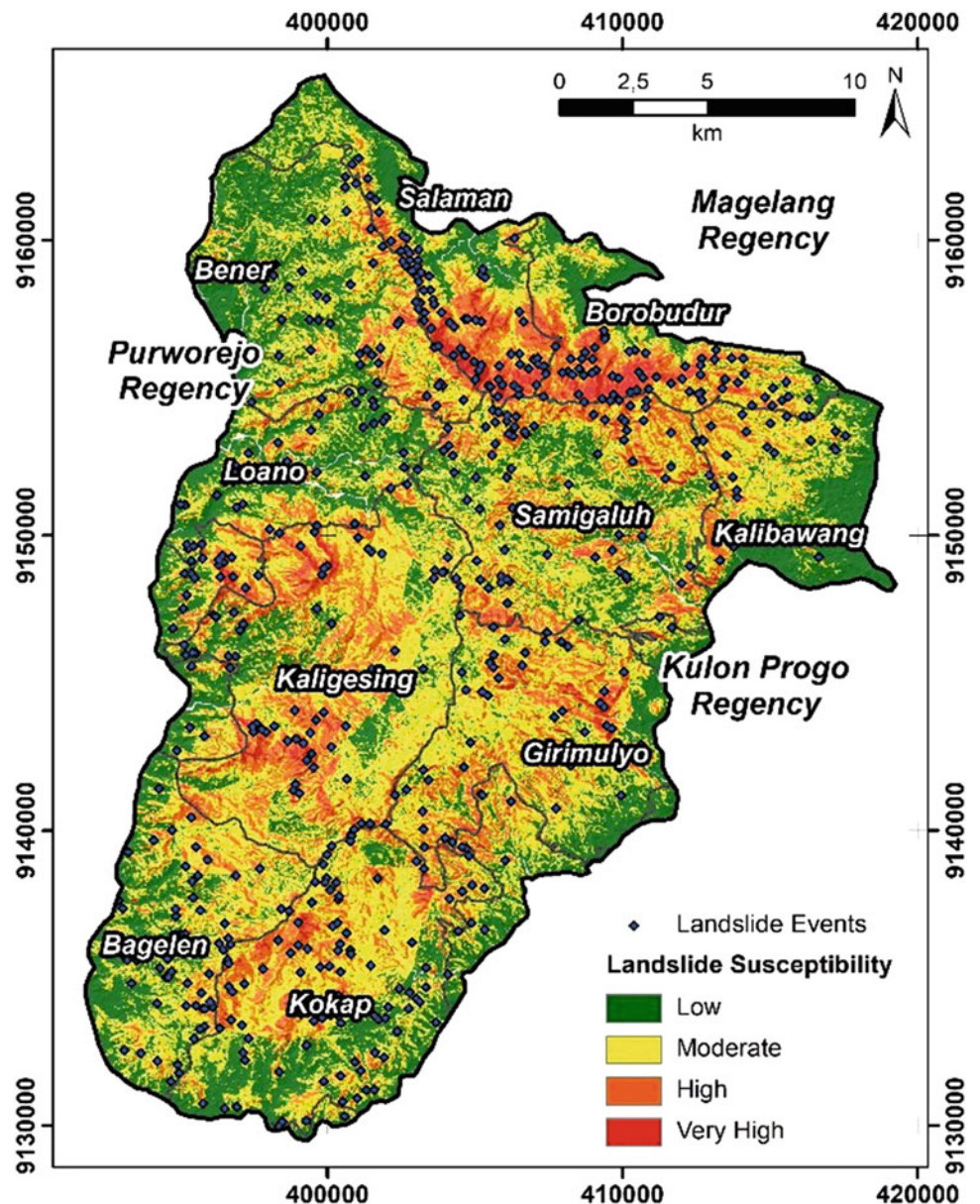
For land use, frequent landslides are usually influenced by reeds, bushes, and dry fields. Areas with reeds, bushes, and dry fields usually have sparse vegetation, and consequently, erosion occurs more quickly, and the areas are thus prone to landslides. The results of the FR calculation show that the frequency of landslides increases as the intensity of rainfall increases. A rainfall of 2200–2400 mm/year significantly contributes to landslides.

The *LSI* values are arranged as *LSI* maps and classified into ten categories to determine the FR validation. The *FR* values for each landslide-controlling factor are summed and overlaid in GIS processing to produce the *LSI* value. The *LSI* value calculated through this analysis can describe the level of landslide susceptibility. The *LSI* value has a range of 4.05–19.46.

Using the Jenks natural breaks method, the reclassification of *LSI* values produces four landslide susceptibility zones. This method is a standard method that is commonly used and has a high level of reliability (North 2009). The four landslide susceptibility zones in the research area are low (*LSI* 4.05–7.85), moderate (*LSI* 7.86–9.85), high (*LSI* 9.86–12.81), and very high (*LSI* 12.82–19.46).

- (a) The low landslide susceptibility zone (*LSI* 4.05–7.85) has an area of approximately 172.51 km² (32,34% of the total area). This zone is on a plain and sloping area adjacent to the Kulon Progo Mountains. The total number of landslides in this zone is 28 points; therefore, the landslide density is 0.162 per km².

Fig. 4 Landslide susceptibility map of the research area



- (b) The moderate landslide susceptibility zone (LSI 7.86–9.85) has an area of 219.39 km² (41.13% of the total area). The total number of landslides in this zone is 163 points. The landslide density in this zone is 0.742 per km². In general, an intermediate landslide susceptibility zone can be found in almost all areas of the Kulon Progo Mountains, especially in the Girimulyo, Kokap, Loano, and Bagelen areas.
- (c) The high landslide susceptibility zone (LSI 9.86–12.81) has an area of 118.94 km² (22.30% of the total area). This zone can be found in almost all areas of the Kulon Progo Mountains and is mainly concentrated in the Kokap, Kaligesing, Samigaluh, Kalibawang, Salaman, and Borobudur subdistricts. The total number of landslides in these areas is the highest, with 396 landslides, resulting in a density of 3.32 per km².

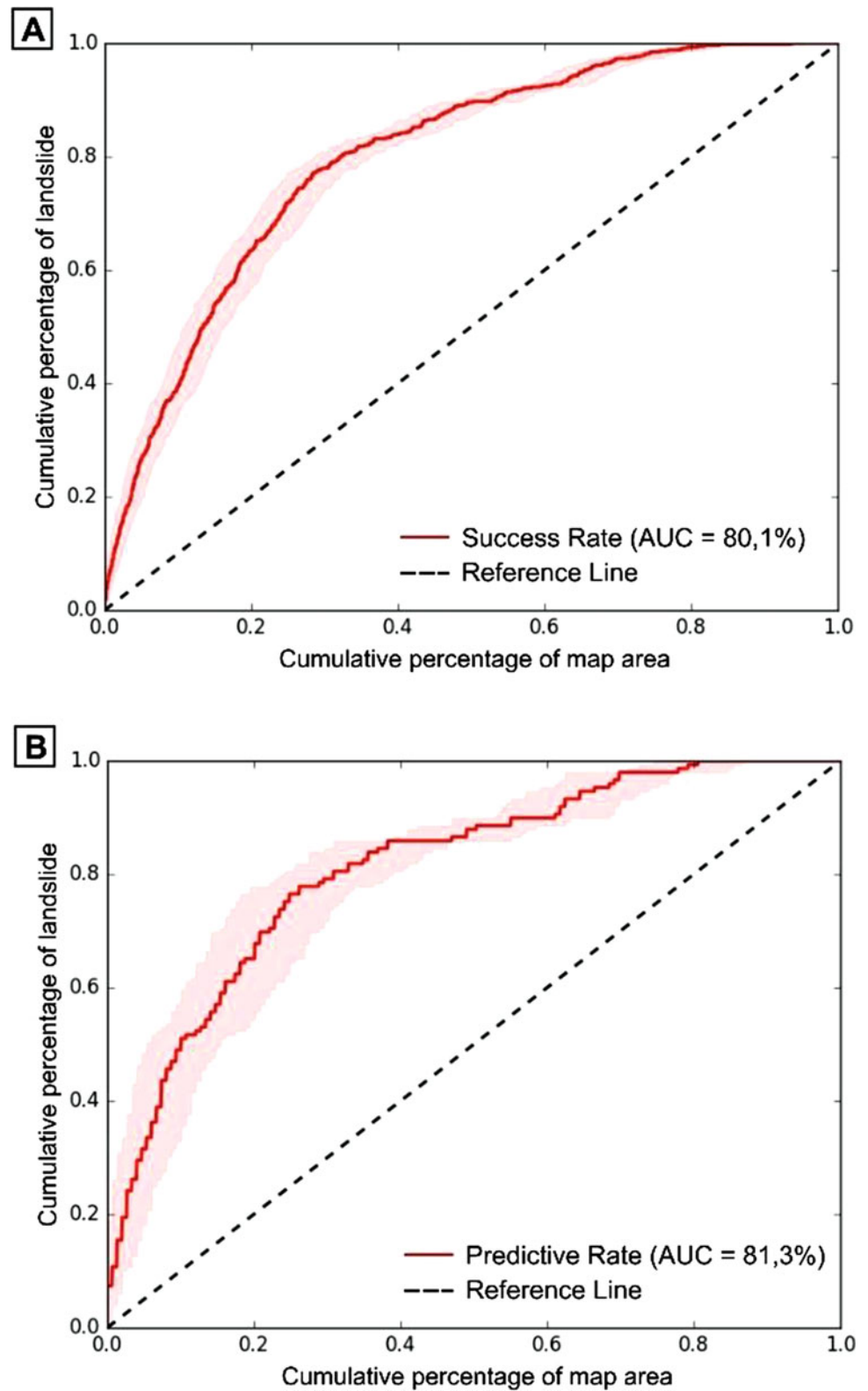
The very high landslide susceptibility zone (LSI 12.82–19.46) has an area of 22.59 km² (4.23% of the total area). The total number of landslides in this zone is 207, with a density of 6.90 per km². Most of the hills with steep slopes comprise this zone, mainly concentrated in Samigaluh, Bener, Salaman, and Borobudur subdistricts (Fig. 4 and Table 2).

Elevation, slope, aspect, lineament density, and rainfall significantly contribute to the high and very high susceptibility zones. In addition, the high and very high susceptibility zones are also located mainly in weathered intrusive rocks and bushes. Most of the landslides occurred in the high susceptibility zone; however, the densest landslides occurred in the very high-susceptibility zone. The AUC method was used to validate the success and prediction rates of the landslide susceptibility map. Figure 5 shows the graphic of the

Table 2 Classes and the FR calculation for each landslide-controlling factor

Factor	Class	A_i (km ²)	$\sum A_i$ (km ²)	D_i	$\sum D_i$	FR
Elevation	0–200 masl	120.11	533.43	89	595	0.66
	201–400 masl	212.14		211		0.89
	401–600 masl	123.62		174		1.26
	601–800 masl	68.45		121		1.58
	801–1000 masl	9.11		38		3.74
Slope	0°–15°	213.9	533.43	0	595	0.00
	16°–25°	217.32		210		0.87
	26°–35°	93.41		314		3.01
	36°–57°	9.07		71		7.02
Aspect	F (–1)	11.48	533.43	4	595	0.31
	N (0–22.5)	30.85		70		2.03
	NE (22.5–67.5)	65.74		106		1.45
	E (67.5–112.5)	60.18		89		1.33
	SE (112.5–157.5)	64.63		63		0.87
	S (157.5–202.5)	75.51		62		0.74
	SW (202.5–247.5)	74.69		57		0.68
	W (247.5–292.5)	60.98		43		0.63
	NW (292.5–337.5)	60.81		50		0.74
	N (337.5–360)	28.56		51		1.60
Lithology	Alluvium and colluvium	19.72	533.43	5	595	0.23
	Young volcanic deposits of Merapi	7.84		1		0.11
	Sentolo formation	9.66		1		0.09
	Jonggrangan formation	25.30		20		0.71
	Intrusive rocks	155.11		177		1.02
	Kebo-Butak formation	311.88		390		1.12
	Nanggulan formation	3.92		1		0.23
Lineament density	0.31–1.45 km/km ²	65.18	533.43	28	595	0.39
	1.46–2.05 km/km ²	152.4		126		0.74
	2.06–2.55 km/km ²	219.01		187		0.77
	2.56–3.58 km/km ²	96.84		255		2.36
Distance from streams	<100 meter	129.38	533.43	110	595	0.76
	100–200 meter	120.86		127		0.94
	200–400 meter	188.35		212		1.01
	>400 meter	94.84		146		1.38
Distance from roads	0–50 meter	108.29	533.43	129	595	1.07
	51–100 meter	84.6		73		0.77
	101–200 meter	117.9		104		0.79
	201–300 meter	71.24		76		0.96
	>300 meter	151.4		130		0.77
Land use	Settlements	54.34	533.43	26	595	0.43
	Paddy fields	36.83		12		0.29
	Dry fields	91.93		167		1.63
	Plantations	311.41		321		0.92
	Bushes	37.64		67		1.60
	Reeds	1.28		3		2.10
Rainfall	<2000 mm/year	27.53	533.43	24	595	0.78
	2000–2200 mm/year	75.69		79		0.94
	2200–2400 mm/year	118.04		182		1.38
	2400–2600 mm/year	234.35		242		0.93
	>2600 mm/year	77.82		68		0.78

Fig. 5 (a) Success rate and (b) predictive rate curve for landslide susceptibility map validation



success and predictive rate curves, with the cumulative percentage of landslides on the x-axis and the cumulative percentage of map area on the y-axis. The validation value of the landslide susceptibility map is obtained from the calculation

of the area under the curve. As a result, the success rate of the landslide susceptibility map is 80.1%, and the prediction rate is 81.30%. The validation values show very good results. This result is better than the previous research (Erzagian

et al. 2023), which only had a success rate of 76.62% and a prediction rate of 75.34% using six controlling factor parameters. Development of landslide susceptibility map using more parameters will increase the accuracy of the map.

6 Conclusion

Landslide susceptibility mapping using the FR method in the Kulon Progo Mountains area, Indonesia, resulted in four landslide susceptibility zones, i.e., low, moderate, high, and very high. A high elevation, north-facing aspect, steep slope, high lineament density, and high rainfall intensity significantly control the high-susceptibility zones. More than half of the study area has high- and very high-susceptibility zones in the weathered intrusive rock unit and bushes. Very high landslide susceptibility zones can be found in the Kaligesing, Girimulyo, Samigaluh, Kalibawang, Bener, Salaman, and Borobudur subdistricts. The landslide susceptibility map developed with the FR method has a success rate of 80.1% and a prediction rate of 81.30%, which can be categorized as a good result. The landslide susceptibility map can be used as basic information for land use planning and mitigation by the local government.

Acknowledgments We would like to thank the Regional Disaster Management Agencies (BPBD) of Kulon Progo Regency, Purworejo Regency, and Magelang Regency for their help in obtaining the landslide data.

References

- Arditian A, Kubota T, Shinohara Y (2018) Comparison of GIS-based landslide susceptibility models using frequency ratio, logistic regression, and artificial neural network in a tertiary region of Ambon, Indonesia. *Geomorphology* 318:101–111. <https://doi.org/10.1016/j.geomorph.2018.06.006>
- Akgün A, Türk N (2011) Mapping erosion susceptibility by a multivariate statistical method: a case study from the Ayvalık region, NW Turkey. *Comput Geosci* 37(9):1515–1524
- Central Bureau of Statistics of Kulon Progo (2021). <https://kulonprogokab.bps.go.id/publication.html>
- Central Bureau of Statistics of Magelang (2021). <https://magelangkab.bps.go.id/publication.html>
- Central Bureau of Statistics of Purworejo (2021). <https://purworejokab.bps.go.id/publication.html>
- Conforti M, Ietto F (2020) Influence of tectonics and morphometric features on the landslide distribution: a case study from the Mesima Basin (Calabria, South Italy). *J Earth Sci* 31(2):393–409. <https://doi.org/10.1007/s12583-019-1231-z>
- Erzagian E, Wilopo W, Fathani TF (2023) Landslide susceptibility mapping using frequency ratio method in Kulon Progo Mountains area, Indonesia. *AIP Conference Proceedings* 2598:070004. <https://doi.org/10.1063/5.0127478>
- Fookes PG, Lee EM, Milligan GC, Press CRC (2005) *Geomorphology for engineers*: Scotland. Whittles Publishing, Dunbeath, pp 329–337
- Geospatial Information Agency of Indonesia (2015–2019) Indonesia's digital topographic map. Bogor, West Java. <http://tanahair.indonesia.go.id/portal-web/>
- Geospatial Information Agency of Indonesia (2023) DEMNAS. <https://tanahair.indonesia.go.id/demnas/>
- Haque U, Da Silva PF, Devoli G, Pilz J, Zhao B, Khaloua A, Glass GE (2019) The human cost of global warming: deadly landslides and their triggers (1995–2014). *Sci Total Environ* 682:673–684. <https://doi.org/10.1016/j.scitotenv.2019.03.415>
- Iliia I, Tsangaratos P (2016) Applying weight of evidence method and sensitivity analysis to produce a landslide susceptibility map. *Landslides* 13:379–397
- Lee S, Talib JA (2005) Probabilistic landslide susceptibility and factor effect analysis. *Environ Geol* 47:982–990. <https://doi.org/10.1007/s00254-005-1228-z>
- Mersha T, Meten M (2020) GIS-based landslide susceptibility mapping and assessment using bivariate statistical methods in Simada area, northwestern Ethiopia. *Geoenvironmental Disasters* 7(1):1–22. <https://doi.org/10.1186/s40677-020-00155-x>
- North MA (2009) A method for implementing a statistically significant number of data classes in the Jenks algorithm. In: Sixth International Conference on Fuzzy Systems and Knowledge Discovery, vol 2009, Tianjin, China, pp 35–38. <https://doi.org/10.1109/FSKD.2009.319>
- Psomiadis E, Papazachariou A, Soulis KX, Alexiou DS, Charalampopoulos I (2020) Landslide mapping and susceptibility assessment using geospatial analysis and earth observation data. *Land* 9(5):133
- Rahardjo W, Sukandarrumidi, Rosidi HMD (1995) Geological map of the Yogyakarta sheet, Java, scale 1:100,000, Geological Survey of Indonesia, Indonesian Ministry of Energy and Mineral Resources
- Rasyid AR, Bhandary NP, Yatabe R (2016) Performance of frequency ratio and logistic regression model in creating GIS based landslides susceptibility map at Lompobattang Mountain, Indonesia *Geoenviron Disasters* 3:19. <https://doi.org/10.1186/s40677-016-0053-x>
- Sarkar S, Kanungo DP (2004) An integrated approach for landslide susceptibility mapping using remote sensing and GIS. *Photogramm Eng Remote Sens* 70(5):617–625. <https://doi.org/10.14358/PERS.70.5.617>
- Skilodimou HD, Bathrellos GD, Koskeridou E, Soukis K, Rozos D (2018) Physical and anthropogenic factors related to landslide activity in the northern Peloponnese, Greece. *Land* 7(3):85. <https://doi.org/10.3390/land7030085>
- Tazik E, Jahantab Z, Bakhtiari M, Rezaei A, Alavipanah SK (2014) Landslide susceptibility mapping by combining the three methods fuzzy logic, frequency ratio and analytical hierarchy process in Dozain basin. *The International Archives of Photogrammetry, Remote Sensing and Spatial Information Sciences* 40(2):267–272. <https://doi.org/10.5194/isprsarchives-XL-2-W3-267-2014>
- Widagdo A, Pramumijoyo S, Harijoko A (2018a) Morphotectono-volcanic of tertiary volcanic rock in Kulon Progo mountains area, Yogyakarta-Indonesia. In *IOP Conf.Series: earth and environmental science* (Vol. 212, No. 1, p. 012051): IOP Publishing. <https://doi.org/10.1088/1755-1315/212/1/012052>
- Widagdo A, Pramumijoyo S, Harijoko A, Setiyanto A (2018b) Fault lineaments control on disaster potentials in Kulon Progo Mountains area-Central Java-Indonesia. In *MATEC Web of Conferences* Vol. 229 No. 03008: EDP Sciences
- Yalcin A, Bulut F (2007) Landslide susceptibility mapping using GIS and digital photogrammetric techniques: a case study from Ardesen (NE-Turkey). *Nat Hazards* 41(1):201–226. <https://doi.org/10.1007/s11069-006-9030-0>

Open Access This chapter is licensed under the terms of the Creative Commons Attribution 4.0 International License (<http://creativecommons.org/licenses/by/4.0/>), which permits use, sharing, adaptation, distribution and reproduction in any medium or format, as long as you give appropriate credit to the original author(s) and the source, provide a link to the Creative Commons license and indicate if changes were made.

The images or other third party material in this chapter are included in the chapter's Creative Commons license, unless indicated otherwise in a credit line to the material. If material is not included in the chapter's Creative Commons license and your intended use is not permitted by statutory regulation or exceeds the permitted use, you will need to obtain permission directly from the copyright holder.





Physically-Based Regional Landslide Forecasting Modelling: Model Set-up and Validation

Veronica Tofani, Elena Benedetta Masi, and Guglielmo Rossi

Abstract

In this work, the High REsolution Slope Stability Simulator (HIRESSS) model was applied to predict the occurrence of shallow landslides on a regional scale. HIRESSS is a physically based distributed slope stability simulator for analyzing the occurrence of shallow landslides during a rainfall event. The modeling software consists of two parts: hydrological and a geotechnical. The hydrological model is based on an analytical solution of an approximated form of the Richards equation, while the geotechnical stability model is based on an infinite slope model that accounts for unsaturated soil conditions. The model was applied in the Aosta Valley region, located in the northwest of the Alpine chain. The Aosta Valley is highly susceptible to landslides, especially shallow, rapid landslides and rockfalls. The geotechnical and hydrological characteristics of the slopes were recorded in two field measurement campaigns at 12 measurement points. To account for the effects of vegetation on landslides the soil reinforcement due to the presence of roots was also taken into account. The model was applied in back analysis for an event that affected the Aosta Valley in 2009, triggering several fast shallow landslides. In this work the model setup and the validation of the model outcomes are described.

Keywords

Shallow landslides · Landslide prediction · Numerical modeling · Geotechnical characterization · Valle d'Aosta region

V. Tofani (✉) · E. B. Masi

Department of Earth Sciences, University of Florence, Florence, Italy
e-mail: veronica.tofani@unifi.it; elenabenedetta.masi@unifi.it

G. Rossi

Civil Protection Center, University of Florence, Florence, Italy
e-mail: guglielmo.rossi@unifi.it

1 Introduction

Shallow landslides are often harbingers of an impending major debris flow. They usually begin as shallow mass movements, involving only a few tens of cubic meters of terrain, but can develop into rapid mass movements that take on characteristics of debris flows and avalanches (Masi et al. 2023). Shallow landslides are triggered by intense rainfall, and multiple and diffuse landslides are often triggered in the region affected by the rainfall.

There are two approaches for predicting shallow landslides at the regional scale: (a) the use of precipitation thresholds based on statistical analysis of rainfall and landslides, and (b) the use of physically based deterministic models (Salvatici et al. 2018). The first category of models is based on a statistical approach by searching for functional relationships between triggering factors (such as precipitation intensity/duration) and actual events in a given area to define warning thresholds. The second category includes the physically based approaches that combine hydrological models and slope stability analysis to predict hazard areas. The stability model is usually based on the infinite slope model. Soil moisture dynamics are usually based on a modified version of the steady-state wetness index (Arnone et al. 2011) or an approximation of the Richards equation (Baum et al. 2002; Simoni et al. 2008). Such models typically provide slope stability assessments based on the factor of safety (FS) (e.g., Baum et al. 2002). While the former approach is currently used primarily at the regional scale (Aleotti 2004; Martelloni et al. 2012; Lagomarsino et al. 2013), the latter approach is more commonly applied at the slope or catchment scale (Pack et al. 2001; Baum et al. 2002, 2010; Lu and Godt 2008; Simoni et al. 2008; Arnone et al. 2011; Salciarini et al. 2017; Park et al. 2013; Rossi et al. 2013). The insufficient knowledge of the spatial distribution of hydrological and geotechnical parameters caused by the extreme heterogeneity and inherent variability of the soil at large scales (Tofani et al. 2017) means that the application of

physically based models is generally avoided at regional scales. Conversely, physically based models allow spatial and temporal prediction of landslide occurrence with high accuracy, producing accurate hazard maps that can aid in landslide risk assessment and management (Salvatici et al. 2018).

Insufficient knowledge of the spatial distribution of hydrological and geotechnical parameters caused by the extreme heterogeneity and inherent variability of soil properties at large scales hinders the application of physically based models at regional scales.

The uncertainty related to hydrological and geotechnical parameters (such as cohesion, internal friction angle, and hydraulic conductivity) can be overcome using a probabilistic approach, supported by the combined use of Monte Carlo simulations. In this case, the output is a distributed probability of failure, i.e., the probability of having the factor of safety below a defined threshold (usually one).

The interpretation of the results is already problematic, since a calibration and validation procedure must be taken into account to define the value of the failure probability for distinguishing between stable and unstable pixels and, in view of possible application purposes, to transform the probabilistic results into warnings related to larger spatial units (e.g., catchments or warning zones). In order to provide reliable results to stakeholders involved in hazard management, it might be advisable to reaggregate across spatial units (e.g., catchments, slope units, and municipalities) and temporal units—a strategy followed by much work focused on operational applications of slope stability models. In particular, for spatial aggregation of probabilistic results, a calibration procedure must be performed to define how many pixels (over a value of failure probability to be defined) are required to consider a spatial unit unstable.

In this work, we apply the physically based HIRESSS (HIgh REsolution Slope Stability Simulator) model (Rossi et al. 2013) in the eastern portion of the Aosta Valley region (Italy), in order to test the capacity of the model to forecast the occurrence of shallow landslides at the regional scale. In particular, the HIRESSS code will be tested in back-analysis, modelling a rainfall event that has occurred in 2009 and that triggered several shallow landslides in the study area. The specific objectives of the study are: (i) model set-up, (ii) analysis and validation of the model outcome.

2 HIRESSS Model and Study Area

2.1 HIRESSS Model

The HIRESSS model (Rossi et al. 2013) is composed of two different modules—hydrological and geotechnical. The hydrological model receives the rainfall data as dynamical

input and provides the pressure head as a perturbation to the geotechnical model, that provides results in terms of failure probabilities. The structure of the software is inspired by the work of Iverson (Iverson 2000) also used in the TRIGRS software. The hydrological model is based on an analytical solution of an approximated form of Richards equation under the wet condition hypothesis, and it is introduced as a modelled form of hydraulic diffusivity. The geotechnical model is based on an infinite slope model that considers the unsaturated conditions. During the stability analysis, the proposed model considers the increase in strength and cohesion due to matric suction in unsaturated soil due to negative pressure head. Moreover, the soil mass variation on partially saturated soil caused by the water infiltration is modelled. The model then provides for Monte Carlo simulations to manage the typical geotechnical parameters uncertainty. The Monte Carlo simulation manages a probability distribution of the input parameter, and the ending results of the simulator are slope failure probabilities. Applications of HIRESSS in different geological-geomorphological contexts and soil typologies have been presented in Rossi et al. 2013; Tofani et al. 2017; Salvatici et al. 2018; Cuomo et al. 2021.

The HIRESSS model needs the following spatially distributed input data: slope gradient, effective cohesion, root cohesion, friction angle, dry unit weight, soil thickness, hydraulic conductivity, initial soil saturation, soil water retention curves, and rainfall intensity.

HIRESSS considers the effect of the root reinforcement to the stability of slopes. The root reinforcement was modelled as a component of the total cohesion of soil (e.g., Operstein and Frydman 2000; Giadrossich et al. 2010). Original FS (factor of safety) equations (Rossi et al. 2013) were modified considering the root reinforcement (Masi et al. 2023).

The HIRESSS model has several features that make it suitable for landslide prediction at regional scale and an important tool for early warning such as (i) the capability of computing the factor of safety at each time step and not only at the end of the rainfall event; (ii) the variable-depth computation of slope stability; (iii) high processing speed even for extensive area analysis; (iv) high spatial and temporal resolution.

2.2 Study Area

The Valle d'Aosta region (3200 km²) is part of the alpine chain, passing through the principal Europe-vergent Austroalpine-Penninic structural domain of the Western Alps. The geomorphology of the study area is characterized by steep slopes and valleys shaped by glaciers. The glacial modelling is shown in the U-shape of the Lys and Ayas valleys, and the erosive depositional forms found in the Ayas Valley. The three valleys' watercourses, the Lys

Creek, the Evançon Creek, and the Dora Baltea River, contributed to the glacial deposits modelling with the formation of alluvial fans.

The region is very prone to landslides due to the high steepness of slopes and abundant mean annual precipitation (800–900 mm/y during the decade 2000–2009): rockfalls, deep-seated gravitational slope deformations, rocks avalanches, debris avalanches, debris flows, and debris slides are the main mass movements to which the area is subjected.

As typical in alpine valleys, the study area has a prevalence of highly vegetated areas, while human settlement distribution is located at the valley bottom. The land cover is prevalently represented by forest, natural grassland, and rocky outcrops with little or no vegetation (Fig. 1).

The HIRESSS model has been tested in a portion of the Valle d’Aosta region, the eastern part called “alert zone B” by the regional civil protection authorities. The area is characterized by three main valleys: Champorcher Valley, Gressoney or Lys Valley, and Ayas Valley. The first is located on the right side of the Dora Baltea catchment and represents the southern part of the study area. The second and third valleys show a north–south orientation and are delimited to the north by Monte Rosa Massif (4527 m a.s.l.) and to south by the Dora Baltea River.

This area has been affected in 2009 by an intense rainfall event. In particular between the 26 and the 28 of April 2009 highly intense rainfall and snowfall had fallen in the Alert zone B causing multiple landslides (9 landslides of different types in the Alert zone B were reported, 26 landslides in the Region) with a maximum of rainfall of 268 mm in three days was recorded by on the meteorological station in the area.

3 Data Collection and Preparation

The input parameters can be divided in two classes: the static data and the dynamical data. Static data are geotechnical and morphological parameters while dynamical data are represented by the hourly rainfall intensity.

The HIRESSS input is in raster, which means that point data and parameters have to be adequately spatially distributed. In this application the spatial resolution was 10 m.

The soil parameters were derived from the in situ and laboratory geotechnical tests and analysis.

3.1 Static Data

The slope gradient was calculated from the a DEM with a resolution of 10 m. Effective cohesion, friction angle, hydraulic conductivity, effective porosity, and dry unit weight were obtained and spatialized according to lithology. The soil parameters were derived from the in situ and laboratory geotechnical tests and analysis.

In particular, the properties of slope deposits were determined by in situ and laboratory measurements (Bicocchi et al. 2016; Tofani et al. 2017) at 12 survey points.

Location of survey points and results of the measurements are reported in Fig. 1 and Table 1 respectively.

Details about data collection from the in-situ surveys to the laboratory analyses and methods of data elaboration to product input maps had been reported in Salvatici et al. (2018).

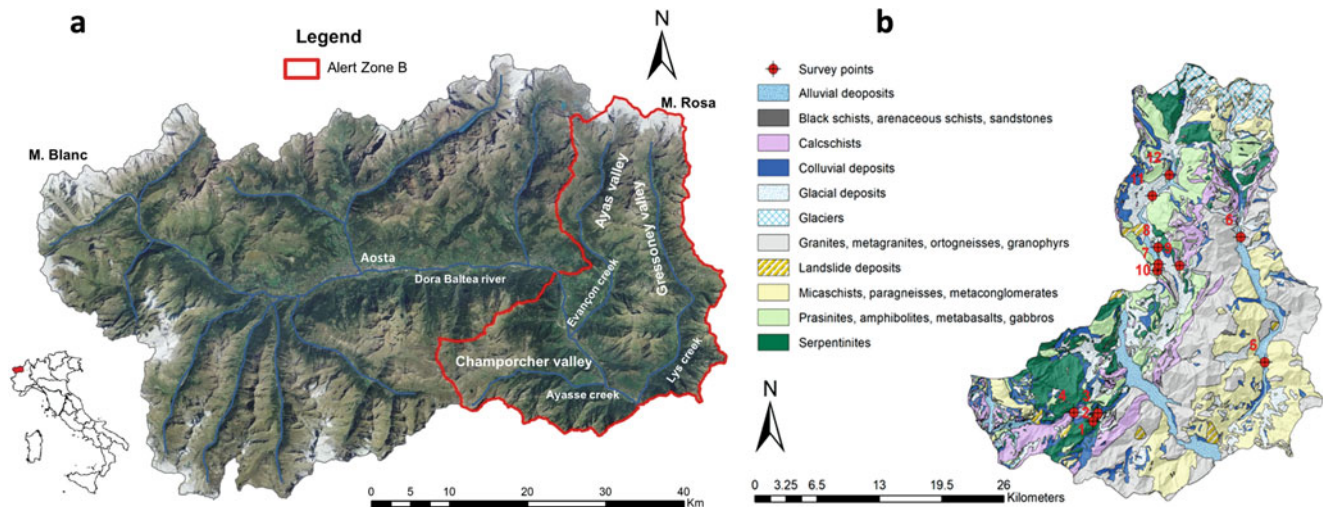


Fig. 1 (a) Aosta valley in the northwest Italy and alert zone B in red, (b) Lithology and survey points, modified from Salvatici et al. 2018 and Masi et al. 2023

Table 1 Geotechnical parameters of each lithological class as input for the HIRESSES model

Lithological classes	Soil Type	ϕ' (°)	c' (Pa)	γ_d (kN m^{-3})	n (%)	k_s (m s^{-1})	h_b (mH_2O)	q_r	λ
Calcareous schist	Sand with gravelly silt	31	1000	16.5	39	1.1E-05	0.1466	0.041	0.322
Alluvial deposits	Sand with gravel and silt	26	1000	14.0	46	3.0E-06	0.1466	0.041	0.322
Glacial deposits	Sand with silty gravel	31	1000	15.3	41	2.7E-06	0.1466	0.041	0.322
Colluvial deposits	Sand with silty gravel	25	1000	13.7	47	2.5E-06	0.1466	0.041	0.322
Granites	Sandy gravel	30	1000	17.6	32	4.0E-06	0.1466	0.041	0.322
Mica schists	Sandy silty gravel	30	1000	17.7	32	6.0E-06	0.1466	0.041	0.322
Pietre Verdi	Gravel with silty sand	32	1000	16.3	37	4.6E-06	0.1466	0.041	0.322

Root cohesion variation map had been elaborated using for the plant species distribution the land use map Corine Land Cover 2012. Values adopted for the simulations varies from 0.1 to 19 kPa.

3.2 Dynamic Data

The dynamic data consist of the precipitation intensities read by the model to calculate the soil saturation and consequently the matrix suction and pressure head of each pixel for each time step. The initial distribution of soil saturation can be provided to the model if available. Otherwise, it is possible to insert an initial soil saturation of zero for each pixel of the area, the model starts at zero and, through the hydrological equations on which it is based, calculates the soil saturation for each time step. It is worth noting that zero soil saturation is not realistic even for very permeable coarse soils, especially under the climatic conditions of the study areas. Therefore, it is important to have sufficient backward extension of precipitation data with respect to a given time period of interest for the simulation to ensure that the saturation conditions reconstructed by the hydrological model are hardly affected by the notional initial soil saturation (Masi et al. 2023).

In the study area of the Valle d'Aosta, the hourly rainfall data from 27 rain gauges were available. The rainfall data had been elaborated applying the Thiessen polygon methodology (Rhynsburger 1973) modified to consider catchment basins to spatialize the data set and generate the raster maps (Salvatici et al. 2018). The periods of rainfall considered to perform the stability simulations is from 02/04/2009 to 30/04/2009.

Between April 26 and 28, 2009, the VdA region experienced intense rainfall that particularly affected the southeastern areas and caused numerous landslides.

The Lillianes Granges weather station recorded 268 mm of cumulative rainfall over the three days, 208 mm of which fell on April 27 alone (Fig. 2).

4 HIRESSES Simulation and Analysis of the Results

The HIRESSES input data were entered into the HIRESSES model to obtain hourly or daily maps of the landslide occurrence.

4.1 Monte Carlo Simulations

A study on the preferable number of Monte Carlo iterations had been performed. The Monte Carlo iterations performed by HIRESSES to manage the spatial uncertainty of the input parameters is a fundamental aspect of the forecasting procedure, the setting of which strongly affects the resulting failures probabilities. The higher the number of iterations, the higher the reliability of the forecasts. On the other hand, a higher number of iterations considerably slows down the processing calculations, so that the question here is finding the best compromise between processing time and reliability of the results (Masi et al. 2023).

To determine an appropriate number of iterations in the context of the present study, four simulations of the Valle d'Aosta 2009 event were performed with the same input values of the parameters but with different numbers of iterations (10, 100, 1000, 10000 shoots). The simulation results were then compared considering the number of unstable pixels calculated in the three cases for the same days of the event and the processing times (Fig. 3). The caution value of 1.2 for the safety factor and 80% for the failure probability (FP) were chosen as the threshold values for the instability of a pixel. The threshold of 80% was chosen based on previous HIRESSES applications (Rossi et al. 2013; Salvatici et al. 2018).

The difference between the 10- simulation and the 100- simulation resulted in about 100000 fewer unstable pixels for the latter, while there was an average difference of 25000 pixels between the 100s simulation and the 1000s simulations

Fig. 2 Intensity and cumulative rainfall per day from for second till 30th of April 2009. Daily and cumulative rainfall referring to the whole area had been calculated as mean values of the data registered by the 27 rain gauges

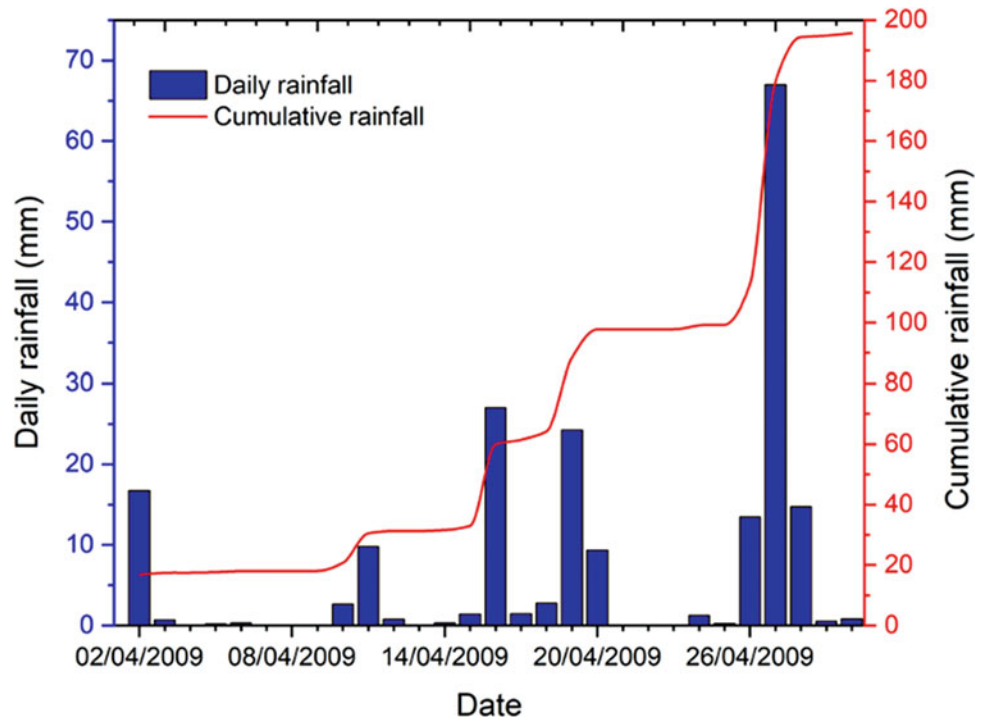
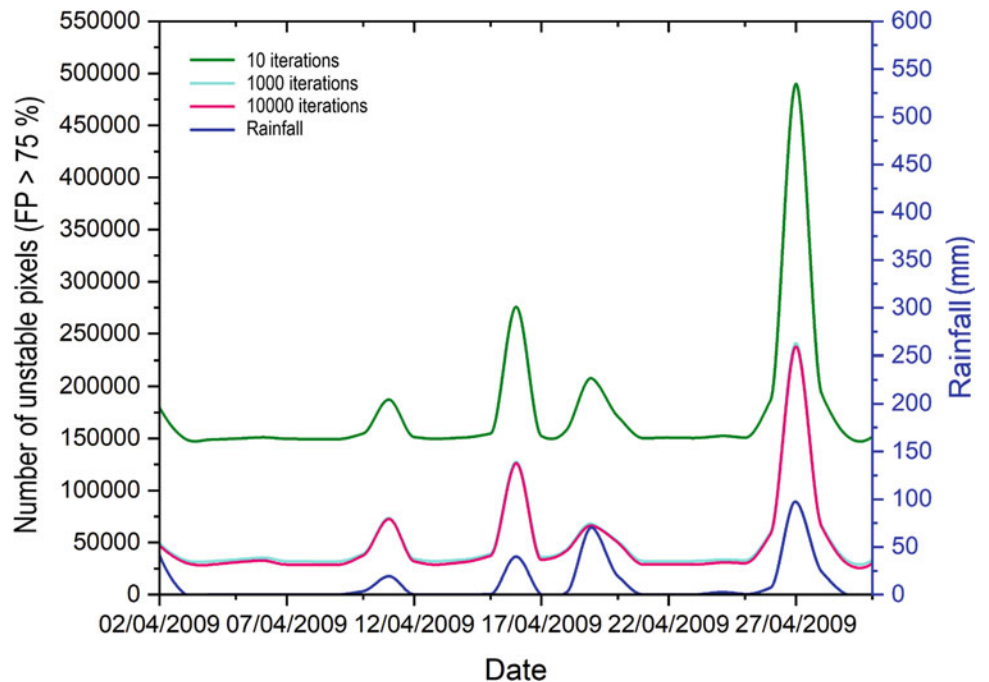


Fig. 3 Results of simulations with a different number of Monte Carlo iterations. Colored curves represent trend of unstable pixels (resulting having a daily max failure probability higher than 80%) (modified from Masi et al. 2023)



(again, the simulation obtained by a higher number of iterations had fewer unstable pixels). In contrast, the differences between the 1000 simulation and the 10000 simulation were so small that they can be considered negligible, while they represent a significant difference in terms of

processing time. The 1000 simulation took 2346 min (39 h), while the 10000 simulation took 21039 min (350 h). The convergence of the results and the quite different processing times led to the choice of 1000 iterations for the successive simulations.

4.2 Analysis of the Model Output and Validation

The simulation of the 2009 event was carried out at 1000 Monte Carlo iterations with a resolution of $10\text{ m} \times 10\text{ m}$.

To validate the model outcomes the inventory, comprise 9 landslides, recorded as points or instability areas.

The HIRESSS output selected for validation is the 24-hr map of failure probabilities for the day of April 27 (Fig. 4). The 24-h step was preferred over the 1-h step in view of the fact that the temporal localization of occurred events rarely achieves such accuracy. Within the range of three days on which the disruptions are reported (April 26-28), the day of April 27 was selected, during which the most intense precipitation peaks were recorded.

The study area was subdivided into sub-basins (Fig. 5) whose dimensions were set in order to be able to contain the average size of the typical shallow landslides in the area and at the same time not to be too large.

The shapefile produced and selected for the purpose of spatial aggregation is characterized by sub-basins whose most downstream node collects the flow of at least 3000

pixels, this threshold allowed to obtain spatial units whose average size is equal to 0.37 km^2 .

Finally, the spatial units were superimposed on the polygons of the rain gauges in the area in order to exclude sub-basins that were within the polygons for which rainfall data for the period April 2-30, 2009 are not available (due to temporary malfunctions of the data collection systems some rain gauges may not present continuous rainfall data), since the landslide triggering probabilities calculated by HIRESSS for these areas are for obvious reasons unreliable.

In order to carry out the calibration procedure and to identify how many pixels are necessary to define a spatial unit unstable three different combination of threshold of failure probability and number of pixels have been defined; 80%/250 pixels, 80%/300 pixels, 80%/350 pixels.

The final stage of the test related to the spatial aggregation of the outputs consisted of validating the different pairings of pixel number/probability threshold by spatial comparison of the spatial units identified as unstable according to the different combinations and the location of the actual landslide events resulting in the construction of the contingency table (data related to correct alarms, missed alarms, false alarms, correct non-alarms) (Table 2).

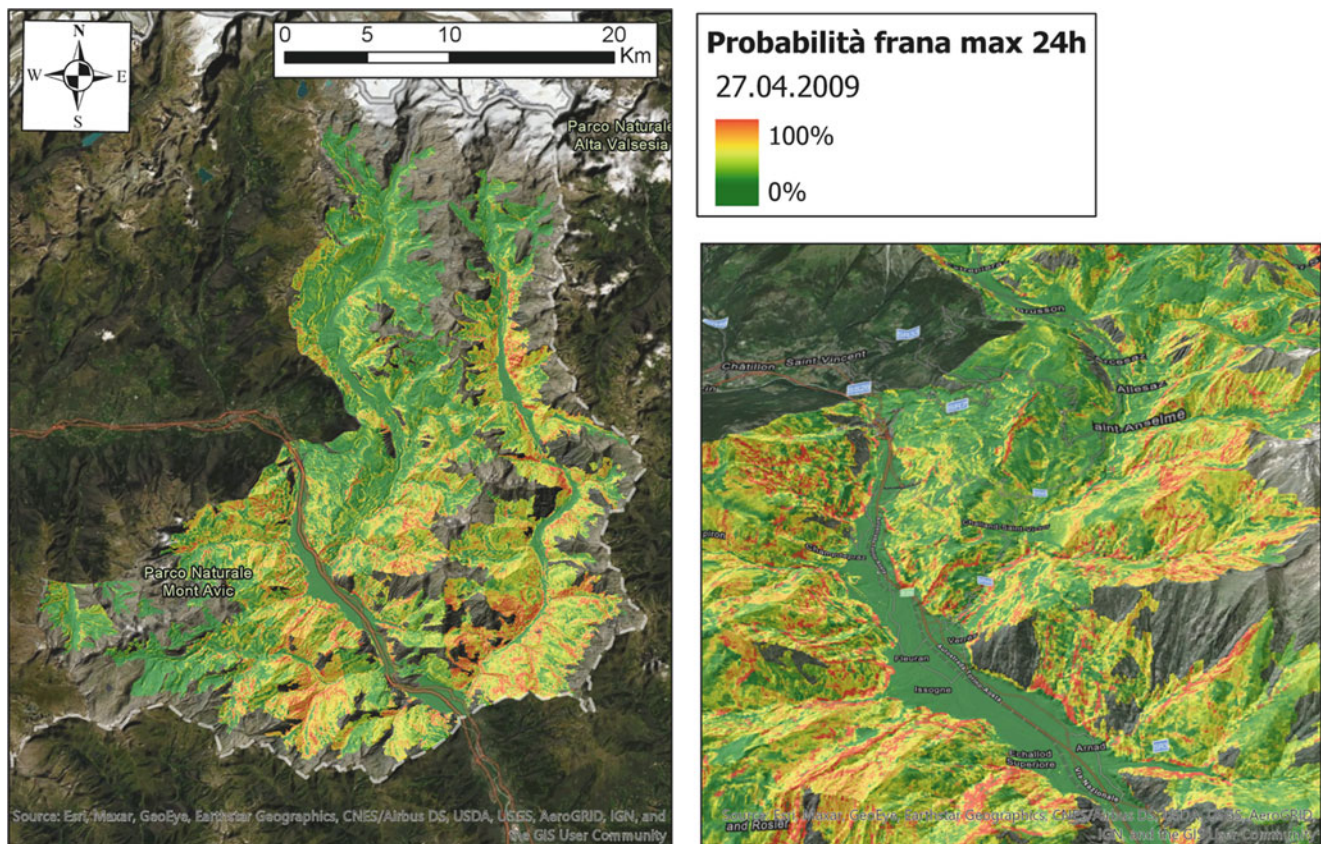
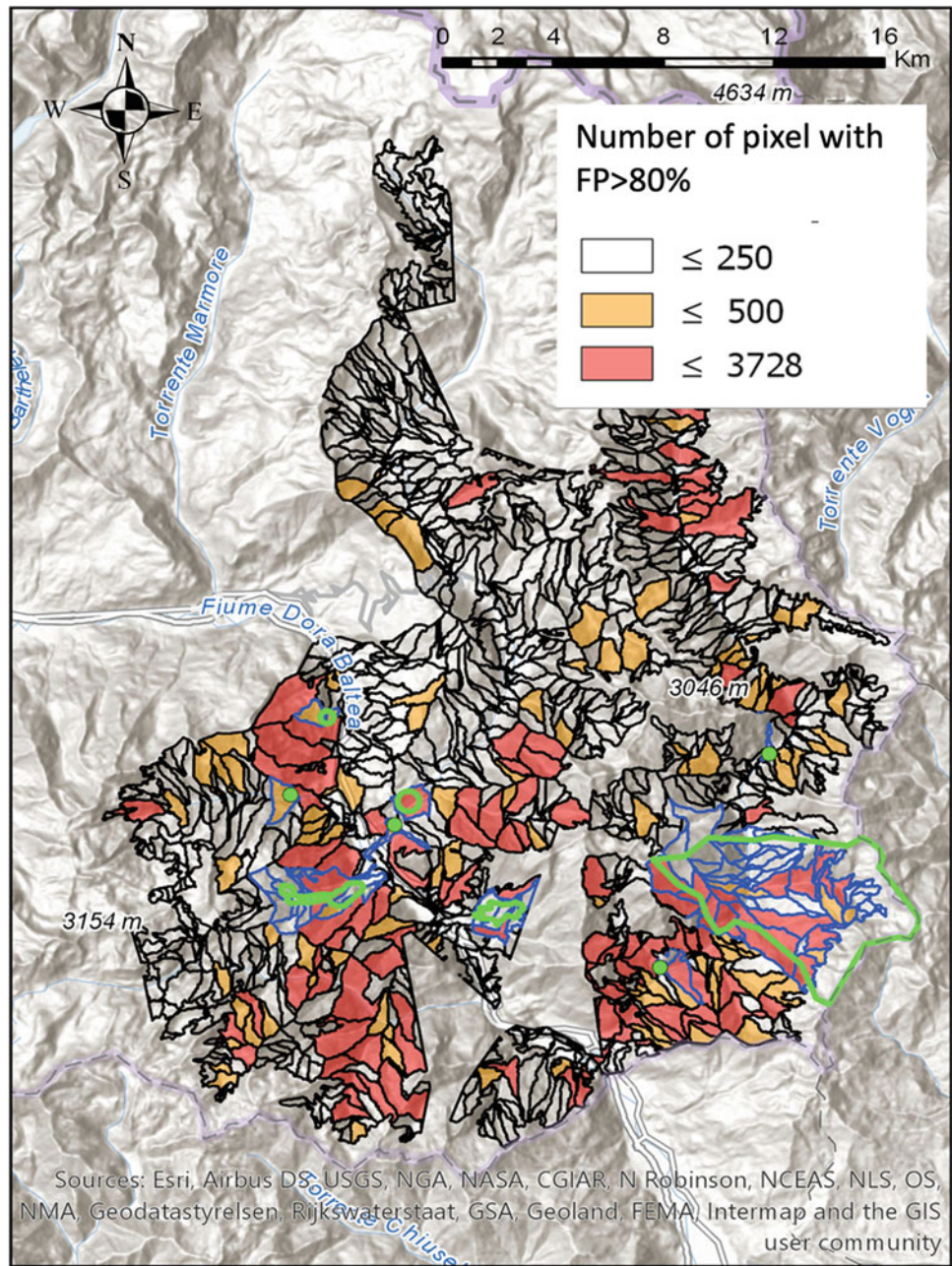


Fig. 4 HIRESSS 24-hr map of failure probabilities for the day of April 27

Fig. 5 Spatial units with more than 250 pixels with failure probability equal to 80%. Green points and areas are landslides, black lines are spatial units



The combination that returned the highest value of correct alarms was the one that predicted the value of 250 pixels with failure probability greater than 80% as the threshold of instability, with 88.9% true positives the modeling in this case was able to predict 8 landslides out of the 9 recorded in reality. At the same time this combination produced the highest value of

false alarms, which was 13.9% in this case. The lowest value of false alarms was found for the 80%/350 pixel pairing, a combination that also, however, produced the lowest value of correct alarms, with 66.7% true positives such aggregation allowed the modeling to detect 6 out of 9 landslides.

Table 2 Contingency matrix for the validation of the model results. *TP* true positive, *FN* false negative, *TN* true negative, *FPs* false positive

Failure probability/ Number of pixels	TP	FN	TN	FP
80/250	88.9%	11.1%	86.1%	13.9%
80/300	77.8%	22.8%	88.6%	11.4%
80/350	66.7%	33.3%	89.9%	10.1%

It is worth noticing that the distribution of the landslide events recorded and used for validation are all located near the most important infrastructures in the area: this leads to the hypothesis that the landslide database used lacks all those events that although they occurred (during the three days investigated April 26–28) were not recorded because they occurred in more remote areas and therefore were not intercepted. This hypothesis could likely be the cause of the values of correct and false alarms found, which while good do not match the potential of the modeling procedure using HIRESSES and aggregation that have been verified in other contexts.

5 Conclusion

The HIRESSES code (a physically based distributed slope stability simulator for analyzing shallow landslide triggering conditions in real time and over large areas) was applied to the eastern sector of the Aosta Valley region in order to test its capability to forecast shallow landslides at the regional scale. The model was applied in back analysis for an event occurred in 2009.

In order to run the model two campaigns of on-site measurements and laboratory experiments were performed at 12 survey points. The data collected contributed to the generation of an input map of parameters for the HIRESSES model according to lithological classes. The effect of vegetation on slope stability in terms of root reinforcement was also taken into account, based on the plant species distribution and literature values of root cohesion, to produce a map of root reinforcement of the study area.

The outcomes of the model are daily failure probability maps with a spatial resolution of 10 m. The HIRESSES code incorporates the Monte Carlo simulation in order to take into account the uncertainty of input parameters.

The test on the number of Monte Carlo iterations showed that the best compromise between the accuracy of the results and the time required for HIRESSES to conclude the processing is represented by the value of 1000 iterations: in fact, requiring the model to perform this number of iterations gives results not dissimilar to those obtainable through 10000 iterations but in a considerably shorter time.

The aggregation procedure was applied and validated with reference to the event of intense rainfall that occurred in alert area B between April 26 and 28, 2009 on HIRESSES model outputs obtained through 1000-iterations simulation. The procedure involved classifying spatial units according to different thresholds of number of pixels contained within their perimeter having model-calculated failure probabilities greater than 80%.

The best result between high value of correct alarms (TP) and low value of false alarms (FP) produced by the

aggregation procedure was obtained with the combination probability of triggering 80%/250 pixels within the 2009 event (24h output of April 27, 2009) with 88.9% and 13.9% respectively.

The application has also highlighted some drawbacks that are mainly related to the validation of the model performance. In particular, a satisfactory validation of the model is only possible if a complete event database of landslides with spatial and temporal resolution equal to the HIRESSES model resolutions is available.

Acknowledgments This research has been carried out in the framework of a research agreement between the Civil Protection Center of the University of Florence and Aosta Valley regional administration. The authors are grateful to Ascanio Rosi, Michele D'ambrosio, Carlo Tacconi Stefanelli and Pietro Vannocci for their help in the field work and laboratory analysis.

References

- Aleotti P (2004) A warning system for rainfall-induced shallow failures. *Eng Geol* 73:247–265. <https://doi.org/10.1016/j.enggeo.2004.01.007>
- Amone E, Noto L, Lepore C, Bras R (2011) Physically-based and distributed approach to analyze rainfall-triggered landslides at watershed scale. *Geomorphology* 133:121–131
- Baum RL, Godt JW, Savage WZ (2010) Estimating the timing and location of shallow rainfall-induced landslides using a model for transient unsaturated infiltration. *J Geophys Res* 118:1999–1999. <https://doi.org/10.1029/2009JF001321>
- Baum RL, Savage W, Godt J (2002) Trigrs: a fortran program for transient rainfall infiltration and gridbased regional slopestability analysis. Open-file Report, US Geological Survey, 2002
- Biococchi G, D'Ambrosio M, Rossi G, Rosi A, Tacconi-Stefanelli C, Segoni S, Nocentini M, Vannocci P, Tofani V, Casagli N, Catani F (2016) Shear strength and permeability in situ measures to improve landslide forecasting models: a case study in the eastern Tuscany (Central Italy). In book: landslides and engineered slopes. Experience, theory and practice, 419–424. <https://doi.org/10.1201/b21520-42>
- Cuomo S, Masi EB, Tofani V, Moscariello M, Rossi G, Matano F (2021) Multiseasonal probabilistic slope stability analysis of a large area of unsaturated pyroclastic soils. *Landslides* 18(4): 1259–1274. <https://doi.org/10.1007/s10346-020-01561-w>
- Giadrossich F, Guastini E, Preti F, Vannocci P (2010) Metodologie sperimentali per l'esecuzione di prove di taglio diretto su terre rinforzate con radici. *Experimental methodologies for the direct shear tests on soils reinforced by roots. Geol Tecnica Ambientale* 4:5–12
- Iverson RM (2000) Landslide triggering by rain infiltration. *Water Resour Res* 36(7):1897–1910. <https://doi.org/10.1029/2000WR900090>
- Lagamarsino D, Segoni S, Fanti R, Catani F (2013) Updating and tuning a regional-scale landslide early warning system. *Landslides* 10(1): 91–97
- Lu N, Godt J (2008) Infinite slope stability under steady unsaturated seepage conditions. *Water Resour Res* 44:11
- Martelloni G, Segoni S, Fanti R, Catani F (2012) Rainfall thresholds for the forecasting of landslide occurrence at regional scale. *Landslides* 9(485–495):485–495. <https://doi.org/10.1007/s10346-011-0308-2>

- Masi EB, Tofani V, Rossi G, Cuomo S, Wu W, Salciarini D, Caporali E, Catani F (2023) Effects of roots cohesion on regional distributed slope stability modelling. *Catena* 222:106853. <https://doi.org/10.1016/j.catena.2022.106853>
- Operstein V, Frydman S (2000) The influence of vegetation on soil strength. *Proceedings of the Institution of Civil Engineers-Ground Improvement* 4(2):81–89
- Pack R, Tarboton D, Goodwin C (2001) Assessing terrain stability in a GIS using SINMAP. In: 15th Annual GIS Conference, GIS, 2001
- Park HJ, Lee JH, Woo I (2013) Assessment of rainfall-induced shallow landslide susceptibility using a GIS-based probabilistic approach. *Eng Geol* 161:1–15
- Rhynsburger D (1973) Analytic delineation of Thiessen polygons. *Geogr Anal* 5(2):133–144. <https://doi.org/10.1111/j.1538-4632.1973.tb01003.x>
- Rossi G, Catani F, Leoni L, Segoni S, Tofani V (2013) HIRESSS: a physically based slope stability simulator for HPC applications. *Nat Hazards Earth Syst Sci* 13:151–166
- Salciarini D, Fanelli G, Tamagnini C (2017) A probabilistic model for rainfall-induced shallow landslide prediction at the regional scale. *Landslides* 14:1731–1746
- Salvatici T, Tofani V, Rossi G, D'Ambrosio M, Tacconi Stefanelli C, Masi EB, Rosi A, Pazzi V, Vannocci P, Petrolo M, Catani F, Ratto S, Stevenin H, Casagli N (2018) Regional physically based landslide early warning modelling: soil parameterisation and validation of the results. *Nat Hazards Earth Syst Sci* 18:1919–1935. <https://doi.org/10.5194/nhess-18-1919-2018>
- Simoni S, Zanotti F, Bertoldi G, Rigon R (2008) Modelling the probability of occurrence of shallow landslides and channelized debris flows using geotop-fs. *Hydrol Process* 22:532–545
- Tofani V, Biccocchi G, Rossi G, Segoni S, D'Ambrosio M, Casagli N, Catani N (2017) Soil characterization for shallow landslides modeling: a case study in the northern Apennines (Central Italy). *Landslides* 14:755–770. <https://doi.org/10.1007/s10346-017-0809-8>

Open Access This chapter is licensed under the terms of the Creative Commons Attribution 4.0 International License (<http://creativecommons.org/licenses/by/4.0/>), which permits use, sharing, adaptation, distribution and reproduction in any medium or format, as long as you give appropriate credit to the original author(s) and the source, provide a link to the Creative Commons license and indicate if changes were made.

The images or other third party material in this chapter are included in the chapter's Creative Commons license, unless indicated otherwise in a credit line to the material. If material is not included in the chapter's Creative Commons license and your intended use is not permitted by statutory regulation or exceeds the permitted use, you will need to obtain permission directly from the copyright holder.



Consequence: Frequency Matrix as a Tool to Assess Landslides Risk

Michel Jaboyedoff

Abstract

Since F-N curves have been proposed, the use of consequences-frequency matrices (CFM) has been extensively used in several domains and in risk and hazard analysis. It represents a common framework for many applications, including project management and decision-making. CFM are diagrams which possess consequence and frequency classes on the axes. They permit to classify risks and hazards based on expert knowledge with limited quantitative data. In this paper, we propose to present the main characteristics of such tools. The semi-quantitative approaches are privileged, numbers must be attached to the limit of classes, in order to avoid erroneous uses. Comparison with F-N curve is addressed. It appears that giving probabilities to all classes is a way to introduce uncertainties and to get exceedance curves. The use of triangular probability distribution functions to describe the belonging to classes is a possibility coupled with a Bayesian approach. A short example is provided.

Keywords

Risk matrix · Consequences · Frequency · Landslides

1 Introduction

Because of the complexity of risk systems, it is not always possible to quantify fully the variables involved in the calculation, since many aspects are not fully quantifiable. However, in most cases, risk analysis is essential for decision-making (Van Westen and Greiving 2017), especially when the ins and outs are not well known. Methodologies have been developed to fulfil these gaps, since the nineties, notably by the NASA space shuttle program (Haimes 2009): “Risk

M. Jaboyedoff (✉)

Risk-group-ISTE, Institute of Earth Sciences, Faculté des géosciences et de l’environnement, University of Lausanne, Vaud, Switzerland
e-mail: michel.jaboyedoff@unil.ch

filtering, ranking and management” (RFRM). To rank the risk events and scenarios, these methods may use the so-called “risk matrix” displaying frequency (λ) or hazard (H) or probability versus consequences (Co), divided in classes for each axis. These consequences-frequency matrices (CFM) are diagrams representing consequence and frequency on x and y axes respectively, which are usually divided into classes. The CFM are often used and presented in textbooks (e.g., Ale 2009) as a tool for assessing and comparing different situations for objects at risk. The results are the possibility to rank and compare risk situations by classes of consequences (Co) and hazard level (H). Such approaches have been developed earlier in the industry production sector (Gillet 1985), and are used nowadays in administrations, army operations (Armée Suisse 2012) or material acquisition (DOD 2006), project management (Raydugin 2012), epidemic assessment in the EU (ECDC 2011) or at the world level (WHO 2020), evaluating risks related to corporate risk profile (TBCS 2011), commercial acquisitions (DOD 2006), natural risks (OFPP 2013) and also in insurances (ZHA 2013).

Since CFMs are a discrete version of F-N or f-N curves, where F if the frequency of events with the number of deaths equal or greater than N (f-N is the non-cumulative version), which are continuous in values, they have been extensively used in several domains, they are both probability consequences diagrams (PCDS) (Ale et al. 2015). But one of the drawbacks of F-N curves is the risk acceptability limits, which is not well established for F-N and f-N, and therefore for CFM. The F-N approaches are nowadays used in landslide hazard and risk assessment (Dai et al. 2002; Fell et al. 2008) and matrices are often cited but not so much used (Dai et al. 2002; Lacasse and Nadim 2009). The principles are the same, but CFM allow the analysis of scenarios that are often impossible to solve by detailed investigations with the limited resources of the project (Pasman and Vrijling 2003). They permit classifying risks based on expert knowledge with limited quantitative data or more quantitative approach.

But they are often misused and not well applied, because it must be a semi-quantitative approach, and some simple rules are not well followed. Furthermore, they are often not used to visualize the evolution of risk with time or mitigation, or to represent uncertainty, etc. except a few examples (Wang et al. 2014; Macciotta et al. 2020). It seems that some codification must be addressed to make CFM more relevant to risk analysis. The classes that are used must be established in a clear way, and the question of frequency or/and probability must be well treated. The question of the uncertainty is raised, one of the proposed solutions is to estimate the belonging to all classes. Here we intend to raise some questions and problems that are partially solvable if some further information about the scales of frequencies and consequences is given, because we do not claim to be exhaustive, it is a first step towards a better use.

2 The Main Principle of Matrix Use

The CFM techniques aim at providing risk assessment for ranking different type of dangers (UK-CO 2017), or specific case study by answering the questions (Haimés 2009): *What can go wrong? What are their consequences and likelihood?* On the side of the industries and insurances the following procedure for risk filtering, ranking and management (RFRM) is used (Krause et al. 1995; Haimés 2009):

1. Scope definitions: what are the problems?
2. Creation of a group of experts concerned by each level of the analyzed risky system.
3. Hazard identification, i.e., identification of potential events and their scenarios
4. Risk filtering and ranking in several sub-stages which implies to establish frequency (probability) and impact classes and their corresponding limits (in loop with point 5)
 - 4.1 Use decision trees to select for Co and H
 - 4.2 Place in risk matrix
5. Establish a ranking.
6. Risk management, including the quantification of the potential risk reduction, which necessitate the understanding of causes and effects.
7. Finalization of decision-making process
8. Refinement of the process with the feedback

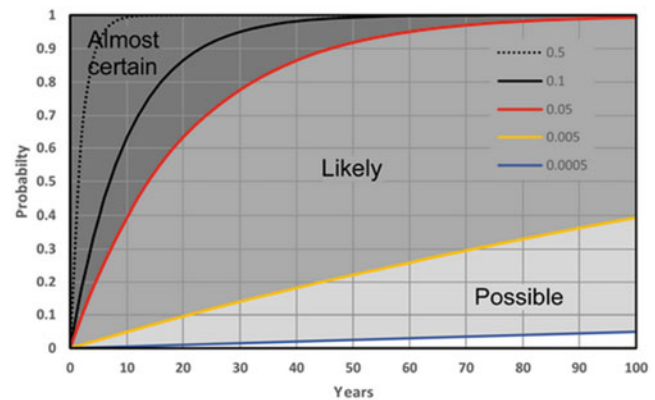


Fig. 1 Verbal terms for the potentiality of at least one event occurs within a period assuming frequency limits corresponding to $T = 2, 10, 20, 200, 2000$ years (after AGS 2007)

3 The Conceptual Background

Risk can be defined in different ways, for ISO (2009) it is defined as “The effect of uncertainty on objectives”, in the landslide community it is a “*measure of the probability and severity of an adverse effect to life, health, properties, or the environment, Risk = Hazard × Potential Worth of Loss*” (Fell et al. 2005), and hazard is defined as “*probability that a particular danger (threat) occurs within a given period of time*” (Fell et al. 2005). But this poses a problem, since risk units is “*an annual loss of property’s value*” (Fell et al. 2005), because there is no time dependence in the above formula, especially such as debris-flows or rockfall occurs more than once in a year. But the link between frequency ($\lambda_i(M_i)$) of random events of magnitude M_i or larger, which is the inverse of the return period ($T_i = 1/\lambda_i$), and the probability P_i there is at least one event during a period Δt is given by the Poisson law (Corominas et al. 2014) (Fig. 1):

$$P_i(n \geq 1, \Delta t) = 1 - e^{-\lambda \Delta t}$$

It means that it is equivalent to use λ or P and Δt , but the consequence is that the risk for a single scenario i of magnitude M_i for an object E located at the position X can be presented in two ways.

The first have a unit of loss per unit of time:

$$R(E, X) = \lambda(M_i) P(X|M_i) Exp(E, X) V(I(X, M_i)) W(E)$$

Where $P(X|M_i)$ is the probability of propagation at the location X of an event of magnitude M_i , $Exp(E, X)$ the exposure

or probability of presence of the object E, $V(I(X, M_i))$ the vulnerability of the object for the intensity I at the location X knowing M_i and $W(E)$ the value of the object or number of people affected. The hazard at the location X with an intensity I is given by $\lambda_i(X) = H(X| M_i) = \lambda(M_i) P(X| M_i)$. For simplification, the intensity I is known based on M_i , but H can also directly include the intensity.

The second way it is to use the probability P of a period, usually 1 year ($\Delta t = 1$), and the consequence C, i.e.:

$$P(X, M_i) = 1 - e^{-\lambda_i(X)\Delta t} \text{ and } Co(E, X, M_i) = Exp(E, X) V(I(X, M_i)) W(E)$$

In case of multiple events with reconstruction, the use of Poisson law for $n = 1, 2, \dots, n$ maybe used, if significant. The matrix usually represents Co versus P or H, but if P is used the period must be indicated, which is often omitted. For small frequency the $P \approx \lambda$, there is less than 2% difference for the annual probability $\lambda\Delta t = 1/T > 25$. To perform a full risk calculation class of magnitude must be used and formally an integration or a summation must be performed over M_i , X, (implicitly λ_i) and E.

In landslide community the matrix is often used to qualify a unique situation, and do not consider cumulative incremental risk as it can be made in F-N curves, but F-N curves can be represented as points in f-N curve for a specific event, but then the limits of risk acceptability and tolerability may be changed. The F-N is based on the same principle that the frequency f or H, it uses the concept of societal risk, i.e. the potential loss of life of N or more people with a frequency F (Jonkman et al. 2003), N was in the original version a dose of exposition to radioactivity (Farmer 1967) but it can be applied to human life as well for economic loss (Fell and Hartford 1997) or any consequences (Ale et al. 2015).

4 Example of Risk Matrix

Examples of risk matrix are numerous. As an example, the the UK cabinet office (2017), published a risk matrix (Fig. 2), for UK, comparing the different natural hazards, pandemics, major accidents, and social risks (they use societal which does not correspond to the landslide risk terminology). It is clear that climate and environmental related risk and pandemics are classified as the higher risk for the UK. For landslide the matrix developed by Porter and Morgenstern (2013) is very useful, because it provides in addition order of magnitudes of frequency and the different type of impacts for Health and Safety, Environment, Social & Cultural (Fig. 3). It underlined that the likelihood categories must be kept constant, but the consequences can be scaled depending on the

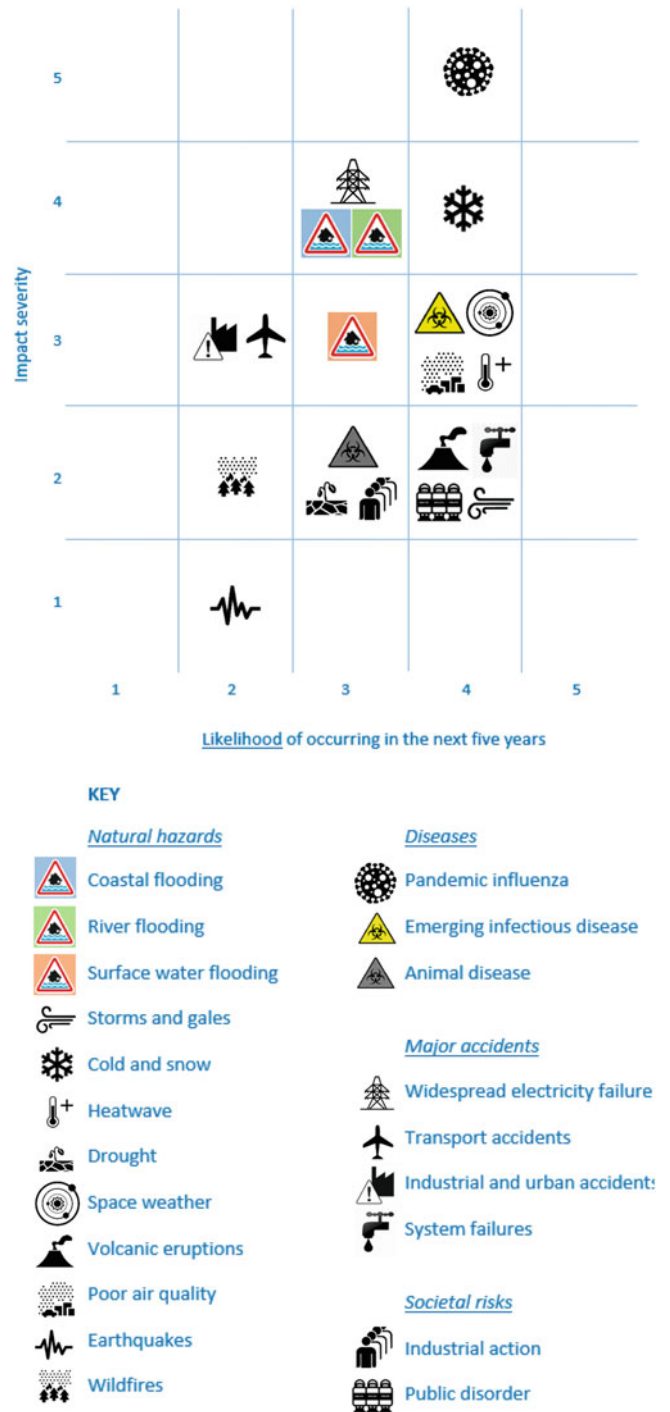


Fig. 2 Summary by the UK Cabinet Office to represent the hazards, diseases, accidents, and social risks in a likelihood (probability) impact severity risk matrix (from UK-CO 2017)

purpose, for instance the size of a company and the risk of bankruptcy (Porter and Morgenstern 2013).

Multi-hazard Risk Evaluation Matrix (SAMPLE)												
For the Qualitative Assessment of Natural Hazards												
				Risk Evaluation and Response								
				VH	Very High	Risk is imminent; short-term risk reduction required; long-term risk reduction plan must be developed and implemented						
				H	High	Risk is unacceptable; long-term risk reduction plan must be developed and implemented in a reasonable time frame. Planning should begin immediately						
				M	Moderate	Risk may be tolerable; more detailed review required; reduce risk to As Low As Reasonably Practicable (ALARP)						
				L	Low	Risk is tolerable; continue to monitor and reduce risk to As Low As Reasonably Practicable (ALARP)						
Partial Risk (annual probability)			VL	Very Low	Risk is broadly acceptable; no further review or risk reduction required							
Likelihood Descriptions	Indices		Probability Range									
Event typically occurs at least once per year	F	Almost certain	>0.9	M	H	H	VH	VH	VH			
Event typically occurs every few years	E	Very Likely	0.1 to 0.9	L	M	H	H	VH	VH			
Event expected to occur every 10 to 100 years	D	Likely	0.01 to 0.1	L	L	M	H	H	VH			
Event expected to occur every 100 to 1,000 years	C	Possible	0.001 to 0.01	VL	L	L	M	H	H			
Event expected to occur every 1,000 to 10,000 years	B	Unlikely	0.0001 to 0.001	VL	VL	L	L	M	H			
Event is possible but expected to occur less than once every 10,000 years	A	Very Unlikely	<0.0001	VL	VL	VL	L	L	M			
Description of expected negative outcome (Consequence)	Indices			1	2	3	4	5	6			
				Incidental	Minor	Moderate	Major	Severe	Catastrophic			
	Health and Safety	No impact	Slight impact; recoverable within days	Minor injury or personal hardship; recoverable within days or weeks	Serious injury or personal hardship; recoverable within weeks or months	Fatality or serious personal long-term hardship	Multiple fatalities					
	Environment	Insignificant	Localized short-term impact; recovery within days or weeks	Localized long-term impact; recoverable within weeks or months	Widespread long-term impact; recoverable within months or years	Widespread impact; not recoverable within the lifetime of the project	Irreparable loss of a species					
	Social & Cultural	Negligible impact	Slight impact to social & cultural values; recoverable within days or weeks	Moderate impact to social & cultural values; recoverable within weeks or months	Significant impact to social & cultural values; recoverable within months or years	Partial loss of social & cultural values; not recoverable within the lifetime of the project	Complete loss of social & cultural values					
	Economic	Negligible; no business interruption	<\$10,000 business	<\$100,000 business	<\$1M business	<\$10M business	>\$10M business					

Fig. 3 Example of risk matrix designed by BGC company and proposed to geological survey of Canada Sample Qualitative Risk Evaluation Matrix (from Porter and Morgenstern 2013)

5 Issues Linked to the Use of Matrix

5.1 Scale and Verbal Terms

The use of scales to enter in the matrix is important, they are usually not numerical, but often annual probabilities are given for indication, like for AGS (2007) the verbal terms used to qualify the hazard is based on the frequency, but they named the frequency annual probability which is confusing (Ale et al. 2015) (Fig. 1). As mentioned in the RFRM the limits of acceptability in PCDS can be chosen depending on the situation and the experts' opinions or can be fixed based on quantitative values as for F-N curves using criteria at the

level of a country (Pasman and Vrijling 2003) or a region (Fell and Hartford 1997).

The studies about verbal terms quantifications show a large variability for different terms assessing the probabilities (Fig. 4). Several surveys about terms showed that the difference in probability on average between the terms "unlikely" and "likely" is of 60% from ~20% to ~70%, with a ratio varying approximately from 5 to 3.5, which is far from one order of magnitude (Fig. 4). For industrial project limits of the classes of probability can be below 0.1% for very low 10% for low, above 50% for high and 90% for very high (Raydugin 2012), which correspond to annual frequency 0.001, 0.11, 0.69, and 2.3 events per year respectively, but if it used for the life of the industry let say 30 years it must be divided by 30 ($3.34 \cdot 10^{-5}$, 0.0035, 0.023, 0.077 or in terms

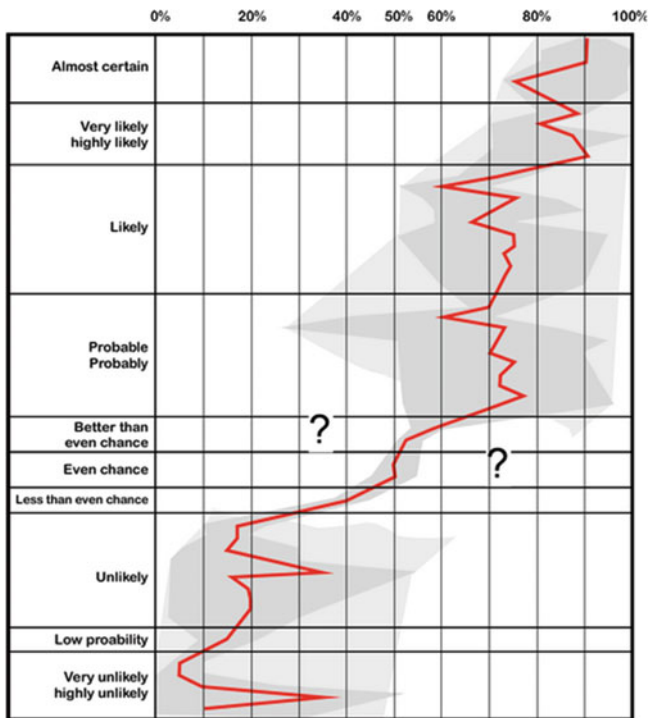


Fig. 4 Results of various surveys of verbal terms with average (red line) and variability (grey zone) and the envelope of the data using light grey, showing the very large variability (modified from Barnes 2016)

of T: $\sim 3 \cdot 10^4$, 285, 43, 13) because $\lambda = -\ln(1 - P)/\Delta t$ which appears as more relevant. For military actions, the yardstick probabilities are very high, 5% is remote chance and 20% highly unlikely (Defence Intelligence 2023).

The above considerations show the variability of interpretation. For landslides the comparison of the annual frequency used for the matrix in Australia (AGS 2007) and the

Canadian one (Porter and Morgenstern 2013), the second being inspired by the first one (Fig. 1, Table 1). There is a shift in the value and variability in the terms, but the order of magnitude of events are similar and likely starts at 100 to 200 years return period, which indicates for those adverse conditions will probably occur during the life of the infrastructure or the building (AGS 2007).

The scales of the damages are very close as expected, in addition comparison with values for industries, the numbers are similar. Gillet (1985) proposed to compare the estimated hazard with standardized frequencies of occurrence and their associated expected losses like shown in the last two columns of Table 2, if it is higher or if the uncertainty is too high, then the risk reduction must be considered.

5.1.1 The Classes of Consequences and Frequency or Probability

As underlined above if the verbal terms are used, they must be attached to some numbers or explanation (Table 1) to make them more reliable, since the verbal alone can be very vague. To choose the membership to a class of consequences or frequency, several strategies can be used. It can be based on a set of indicators with weight which provide a value for one or for both scales as for geotechnical and geomorphic indicators used for quick clays risk analysis (Lacasse and Nadim 2009) (Fig. 5).

The decision trees are standard tools to analyze risk or hazard (Leroueil and Locat 1998; Haimes 2009; Lacasse et al. 2008). They can be used to provide the class values for one or both axes. It is preferable to use dichotomic branches as proposed for pandemic (ECDC 2011), because it is easier to decide. For instance, the frequencies or return periods (T_i) can be deduced by the process below, which

Table 1 Comparison of the frequency scale of the risk matrix from Australia and Canada, for the Canadian “almost certain” correspond to the event typically occurs at least once per year (scales taken from AGS 2007 and Porter and Morgenstern 2013)

Frequency	Porter and Morgenstern (2013)	AGS (2007)	Limits
10^{-6}	Very unlikely	Barely credible	5×10^{-6}
10^{-5}		Rare	5×10^{-5}
10^{-4}	Unlikely	Unlikely	5×10^{-4}
0.001		Possible	0.005
0.010	Likely	Likely	0.05
0.10		Almost certain	
0.10	Very likely		
0.90			
0.90	Almost certain		
1.0			
1.0			

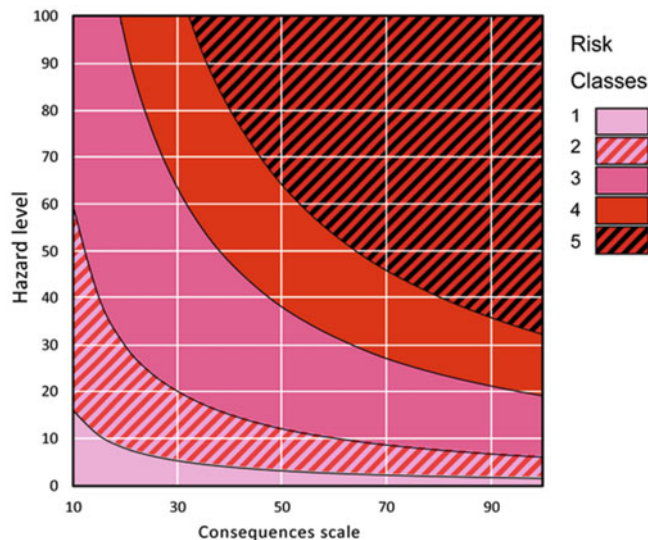


Fig. 5 Continuous scale risk matrix or PCDS example using indicators leading to create relative risk classes in a consequence-(hazard) susceptibility diagram (based on the criteria of Lacasse and Nadim 2009)

depend on the climate and the environment, thus no values are given:

1. Are any signs of landslide activity present?

- (a) In the scree/talus slope or in the landslide deposits
- (b) Within the slope
 - (i) Scar clearly visible
 - (ii) Displacements

• **If YES → proceed to point 2, if NO go to point 4**

2. Can recent landslide activity be observed?

- (a) In the scree or in the deposits
 - (i) Fresh traces are visible
- (b) Within the slope
 - (i) Scar (fresh)
 - (ii) Active displacement (measurable)

• **If NO → proceed to point 3, if YES the frequency can be assumed to be less than T_1 years.**

3. Are the traces of landslide activity apparently unchanged but still clear?

- (a) In the scree or in the deposits
 - (i) Recent traces are not visible
- (b) Within the slope

- (i) Scar (no trace of activity)
- (ii) Displacement traces clearly visible

• **If YES the frequency can be assumed between T_1 and T_2 years, and if NO go to point 4.**

4. Are the traces not obvious?

- (a) Presence of old vegetation
- (b) Smoothed topography

• **If YES the frequency can be larger than T_3 years, and if NO it can be estimated larger than T_2 years but less than T_3 years.**

For the consequences scale, it is also possible to perform a decision tree to set the classes, as for instance for a landslide threatening a road (Fig. 6).

Another possibility is to ask to the expert to set the probability of belong to all the classes of the scale, as proposed by Vengeon et al. (2001), for which the frequency is set by an array of probability—delay for failure of landslides. Such an approach can be used for consequences and frequency as well (Table 2).

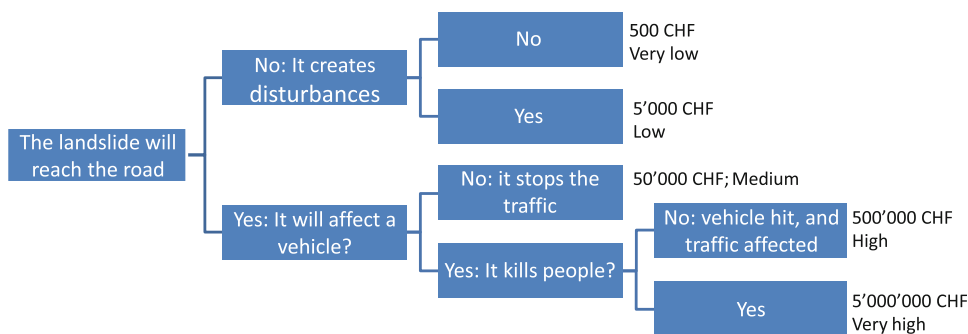
5.2 Setting the Risk Limits for Risk Matrix and F-N Curves

CFMs suffer some weaknesses. The risk scale (colours) is often not consistent (Cox Jr. 2008), because for instance, a point at the corner of a class can belong to 3 different risk classes, then in that case by changing by one unity each axes the difference can be of 2 class levels. In principle the classes of risk have to respect as much as possible the principle that the isorisk limits are hyperbolas, i.e., $H = R/Co$. Let us make an analogy with F-N diagram which can be considered as numerical “matrix”. In case of aversion to risks (φ), the limits must be adapted as it is the case for F-N diagram for floods in the Netherlands $\varphi = 2$, where N is the consequence:

$$F = \frac{R}{N^\varphi}$$

As a consequence, the CFM integrating aversion, in a 5×5 matrix, using simply two relative scales numbered from 1 (very low) to 5 (very high), it is possible to create 4 risk classes without triple points based on $\lambda \times Co$ providing a risk scale going from 1 to 25, but using the same risk scale the

Fig. 6 Decision tree to deduce the consequences levels for the Pont Bourquin landslide in Switzerland (see below for more explanations)



second and third risk class must be merged because the range of value goes from 1 to 125 and the high risk limits move to 25 (Fig. 7).

F-N diagrams are cumulative, but some authors tend to use non-cumulative f-N curve as did Farmer (1967) originally (Ale et al. 2015), this raises a question: does the F-N limits must be the integral of f-N (Ale et al. 2015)? When creating risk classes for probability consequences diagrams, the classes limits must be set up depending on one or the other assumption. In addition, they must be set designed on which domain it applies, i.e., population, region, country, object infrastructures, etc. The limits are usually not defined by the law so as mentioned above the rules must be set by a group or expert or using a true participative approach (Mereu et al. 2007). In the Netherland the F-N criterion for unacceptability are based on the risk for the whole population considering the industrial hazard is at 10^{-6} and for the sum of incremental risks to 10^{-5} , then assuming that $F(\geq N) \times N^2 < 10^{-3}$ for $N \geq 10$ (Pasman and Vrijling 2003).

This process highlights the significance of considering the specific domain it is being applied to. In the context of Hong Kong, the current approach involves utilizing the land area as a basis (Hung and Wong 2007). However, it is worth noting that this may not be the most optimal choice, as the F-N is dependent on the number of people affected. Therefore, in principle, it would be preferable to establish the individual risk threshold multiplied by the population concerned to get the threshold for one death. The selection of the aversion

parameter, i.e., the slope of the limit, should be made with consideration of cultural factors. As shown for the Netherlands the reasoning can be more sophisticated, based on observed F-N curve for various hazards. This way to think must be kept in mind when fixing matrix risk classes.

Another issue is the individual risk (IR), because matrix can be used for specific activity, as we have seen the limit for army, industry or voluntary dangerous activity the threshold must be adapted and can be defined as follow (Pasman and Vrijling 2003): $IR = \beta \times 10^{-3}$, where β is the policy factor, assuming the following values 100 for voluntary or exceptional professional activity (rescuing, military, etc.), 1 with self-determination assuming a direct benefit and 0.01 for facing involuntary hazard.

As final remarks, if you add people in the system then or if the territory is extended, shall the line of acceptance changes? Yes, if the individual risk is kept and no if an improvement is requested. f-N is problematic, because it corresponds to an incremental risk, so depending on how many threats are considered the limits will change. This depends on the ratio of the importance of the considered threats versus the others.

5.3 Uncertainty

Because of the fuzziness of human appreciation, uncertainty must be added. There are several ways to add it as it is distributed in more than one class the estimation of F and

Table 2 Comparison of scales for damages, the last column is the relationship between frequency and costs in industries which are the basis for risk analysis for industries after Gillet (1985). The costs have been for 2023 considering inflation and exchange with US\$ for CAD and £

Terms (AGS 2007)	Damages cost to the property value	Terms (Porter and Morgenstern 2013)	Value	Terms (Gillet 1985)	Frequency of occurrence	Expected loss value
Insignificant	0.50%	Minor	<\$ 12'000	Minor	1	<\$ 7000
Minor	5%	Moderate	<\$ 120'000	Appreciable	0.1	<\$ 70'000
Medium	20%	Major	<\$ 1'200'000	Major	0.01	<\$ 700'000
Major	60%	Severe	<\$ 12'000'000	Severe	0.001	<\$ 7'000'000
Catastrophic	200%	Catastrophic	≥ \$ 12'000'000	Total destruction	0.0001	≥\$ 7'000'000

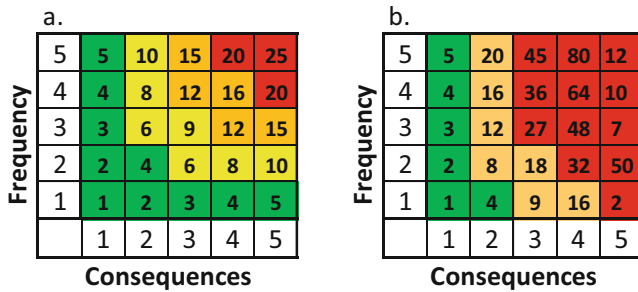


Fig. 7 Example of 5 × 5 risk matrices a. with a hyperbola risk scale, 4 classes (a) and with aversion and only 3 classes (b)

Co. The use of minimum, maximum and average can be used to assess the uncertainty. In fact, the belonging to all classes can also be assessed (see below).

5.4 Risk Reduction

The risk matrices are very useful to visualize the risk reduction scenario, especially in a qualitative way, because it can represent the paths (arrows) of the different option of risk scenarios (Solheim, et al. 2005). In addition, it allows to input the risks that can be induced by the changes created by a mitigation. In industrial material sciences, such representations are used (Cowles et al. 2012).

For instance, the flood management can create fuse plug spillway in protective dike (Schmocker et al. 2013), to force the flood in less at-risk areas. In the case of rockfall, dikes or nets, can make local authorities confident and let new construction behind protective measures, which, in fact, can increase the risks (Farvacque et al. 2019). When the risk matrices are used for representing risk reduction, they must include the questions about the potential consequences (Fig. 8).

5.5 Representing the Cascading Effect

It means that a rule must be added to the use of risk matrix, which to consider and represent the cascading effect (Gill and Malamud 2016) of protecting an area. The cascading effects are important nowadays, especially in the context of climate change. In the case of Natech (Risks from Natural Hazards at Hazardous Installations) the use of matrices can be very useful to show the consequences of a natural disaster (Girgin et al. 2019).

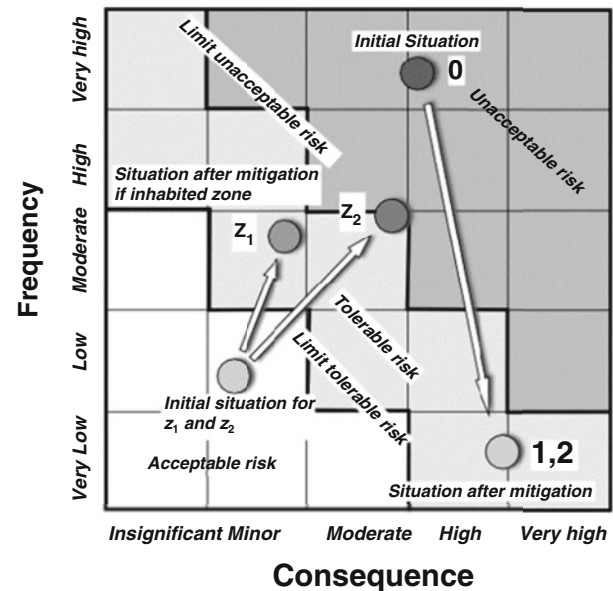
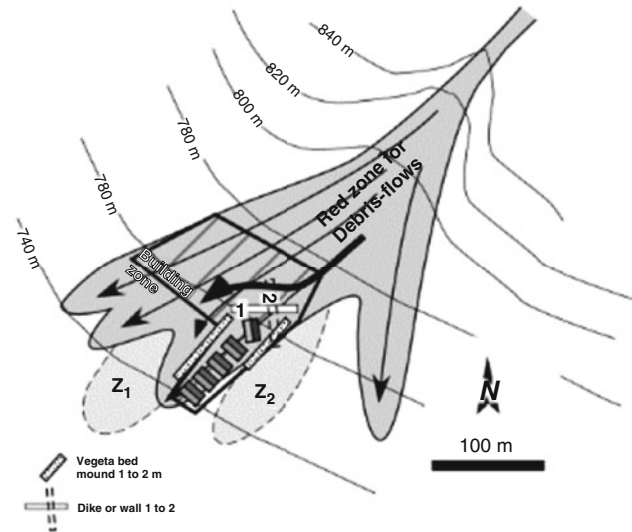


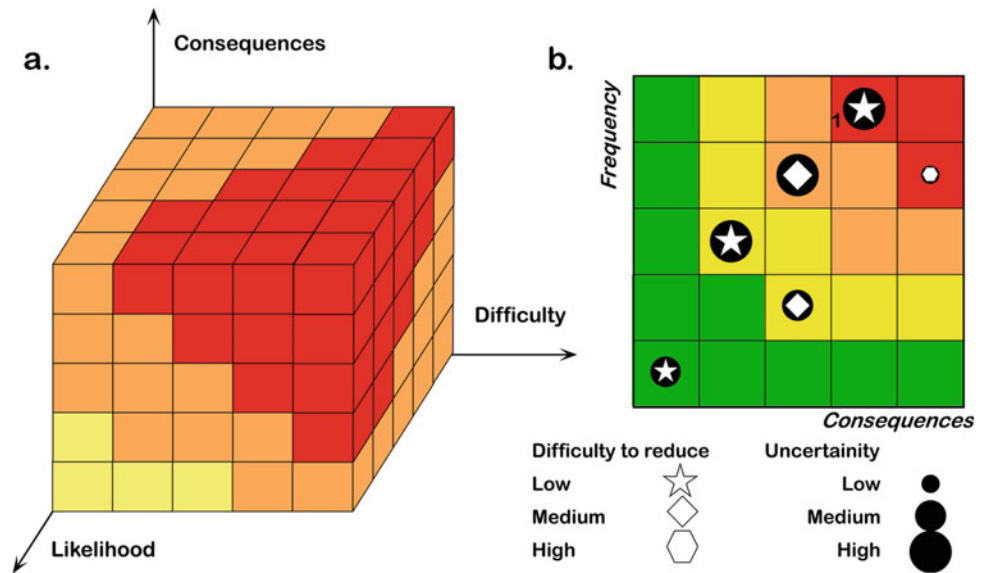
Fig. 8 Example of potential building area in a high hazard area and illustration of the proposed solutions. CFM is used to represent the degree of risk. The scope of tolerable risk (light grey) is between the limits of tolerance and of acceptability (modified after Jaboyedoff et al. 2014)

5.6 Adding Dimensions

Frequency and consequences are not the only parameters that can be considered, some other parameters can be added such as:

- Difficulty to reduce risk (Zhang et al. 2016).
- Uncertainty (Gillet 1985).
- The difficulty is to detect (Martinez-Marquez et al. 2020) or characterize the hazard.
- Etc.

Fig. 9 (a) example of 3D matrix including difficulties with a scale inspired from Zhang et al. (2016) and (b) conceptual example of a 4-dimensional matrix including difficulty to reduce and uncertainty



If 3 variables are used, frequency, consequences and a third one among the previous ones, a 3D matrix can be used or a matrix using different symbol shape and size can provide 4D information for instance (Fig. 9).

5.7 Cumulative Versus Non-cumulative Scale

F-N graphs are in cumulative form, but even if it is cumulative, it is non-exhaustive looking at the risk level, so therefore the frequency is calibrated on incremental risks, normally dedicated to one type of hazard and their consequences. The scales for risk matrix are semi-quantitative or qualitative, but they must follow the same principle as F-N or f-N.

In most of the case, the risk matrices are non-cumulative because it allows to compare different situations or type of risks. But a semiquantitative approach may allow a cumulative approach, or, as we will see in an example below, each scenario represented by a class of the matrix must be qualified.

5.7.1 An Example Ambiguous Use of Matrix

In Switzerland the assessment of hazard level uses a matrix representing the return period or frequency and the intensity (Raetzo et al. 2002). It is in fact a sort of risk matrix because intensity levels are related to some resistance of objects which is called “danger”. The matrix is a 3 × 3 matrix, and the axes are inverted, and the frequency scale is inverted (Fig. 10a). It contains issues like a triple point (7), three half classes and when looking at the transposition in an intensity—frequency the scale appear to be very refined even if it seems possible to get the frequencies by the investigation (Fig. 10b). Considering the question of what the probabilities attached to the limit high (30 years), medium (100 years) and low (300 years) are, respectively, for a 1-year

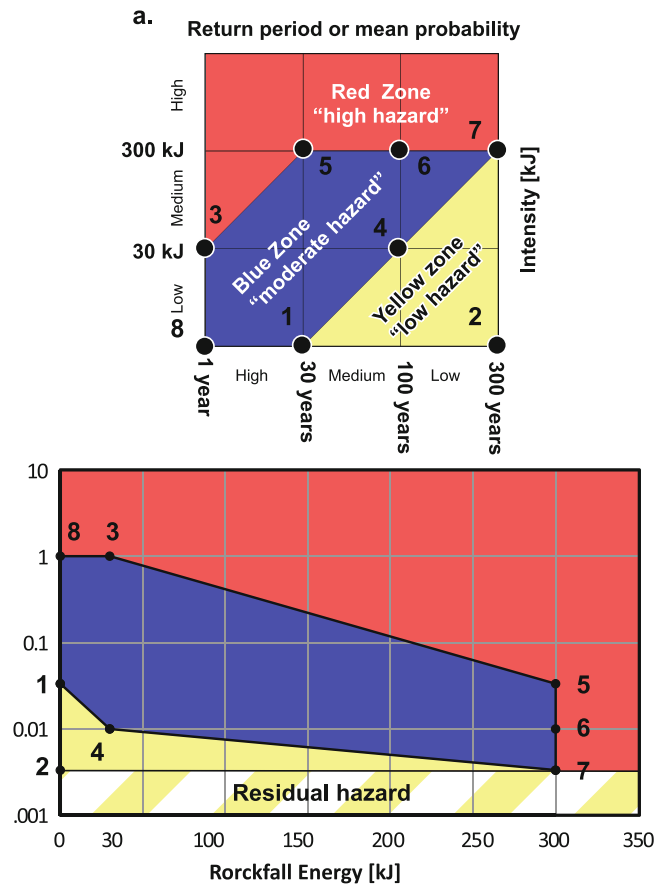


Fig. 10 (a) Hazard Swiss matrix for rockfall (after Raetzo et al. 2002) and (b) corresponding Energy (linear)—frequency (log) diagram

are 3.28%, 1.00% and 0.33%, which is very close and difficult to discriminate, uncertainty is necessary to assess in a such case, especially for verbal appreciations, but such a

scale can be relevant on the field by looking at the traces of rockfall for instance, but it must be kept in mind that has a high uncertainty. Nowadays in Switzerland scenario must be assessed for all return periods (OFEV 2016), but the principle of the matrix is still used.

6 Summaries of the Recommendations

Following the above observations and findings, we can make a non-exhaustive list of elements to consider when creating risk matrices:

- Usually, CFM includes relative scales based on verbal terms, but they must be attached to numbers or description of frequency and consequences scales.
- The risk classes scale must follow rules such classes multiplication $R_{ij} = \lambda_i \times Co_j$, or they can be adapted on purpose with justification or considering aversion.
 - The matrix must be preferentially equal or larger than 4×4 matrix.
 - No triple points must appear.
- The uses for decision trees are very useful for choosing the classes on both axes.
- When using F-N concept, the strategy must be clearly defined, and the limits must be adapted considering the population and the individual risk threshold, this must be described. In the case of not using such a strategy, this must be clearly stated.
- Risk matrices are an excellent tool to represent risk reduction paths.
- The matrix can be used for any type of consequences.
- The cascading events can be represented by such matrix, but the conditions leading so such situations must be clearly described and the probability and frequency estimation correctly assessed.
- The use of cumulative version must consider that depending on the extent of the treats considered, the threshold can change, because usually for one threat it is 10^{-2} times the individual risk for involuntary risk, because it is incremental it is one risk among others. It is the way to use F-N curves but for matrix it is not recommended.
- The uncertainty must be assessed.
- The dimension of the matrix can exceed 2, especially by adding uncertainty and difficulty to reduce risk.

The risk matrix as well as the F-N or F-Consequence graphs provide a framework for risk assessment, which is very useful for representing, communicating, and teaching.

7 Example of Integration of Assessment for all Classes

In the following lines, an example of CFM is given related to an update of the risk assessment of Pont Bourquin landslide (Switzerland) (Jaboyedoff et al. 2009, 2014). The goal is to evaluate all the probabilities of a 5×5 risk matrix classes. The method uses CFM by developing point 4 of the above-mentioned RFRM process, including part of the points 3 to 5. It uses a Bayesian approach to estimate the belonging to classes of frequency and consequences based on prior probabilities provided by experts (here the expert is the author to set the example), the likelihood being based on triangular distribution. The probabilities to belong to a class of risk are calculated by the multiplication of both probabilities to belong to frequency and consequences.

Similar attempts were performed for technical system by Krause et al. (1995) introducing uncertainty in the input data by using fuzzy logic: the classes are fuzzified by applying a membership function to the classes of frequencies and consequences, we replaced fuzzy logic by Bayesian approach.

8 Method

8.1 The Belonging to a Class and its Uncertainty

Uncertainties are involved when experts are providing their opinions about the belonging to a class of events, which can be named “very low, low, medium, high, very high” referring frequencies and consequences. As for the fuzzy logic framework (Zadeh 1975), the class belonging is not unique and there exists a probability of belonging to the other classes. It means that when an expert attributes an event to a class it also implies a “membership” to other neighboring classes. Instead of using the fuzzy logic terminology as “membership”, it is preferred to use the likelihood $P(C_j | CE_i)$ of the attribution to a class CE_i by an expert to be distributed to neighboring classes C_j .

The prior probability to belong to each class is equivalent to ask to experts an estimation of the uncertainty empirically. It can be decided by a group of experts, or an expert can give

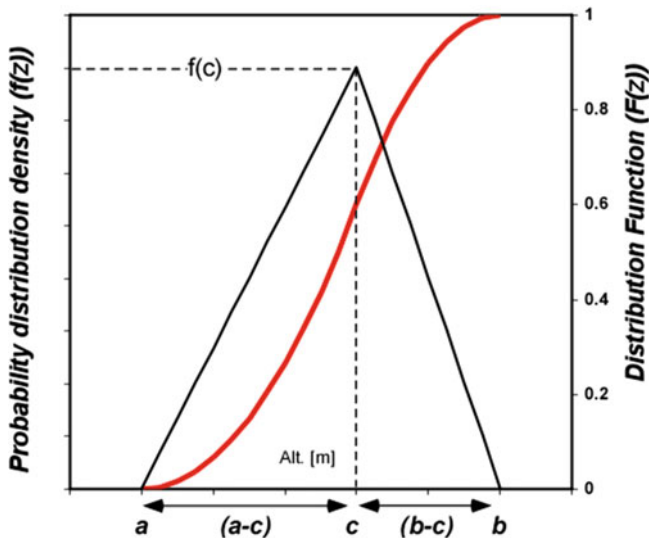


Fig. 11 Parameter defining triangular distributions

his definition of belonging to a class. This can be a direct way to introduce the uncertainty, but we try to go a bit further here.

Formally, if a class has a lower limit l_j and upper limit l_{j+1} and if the distribution of the weights from a class chosen by an expert CE_i to the others using a scale of value x is given by $f(x)dx$, then the likelihood or weight to belong effectively to the class C_j is given by (Jaboyedoff et al. 2014):

$$P(C_j|CE_i) = \int_{l_j}^{l_{j+1}} f(x)dx \quad (1)$$

The function $f(x)$ can be of any type, and they are chosen by using for instance the variance, the mean, etc. Here, we will use the triangular distribution (Kotz and van Drop 2004; Haimes 2009) (Fig. 11):

$$F(x) = \begin{cases} 0 & \text{for } x < a \\ \frac{(x-a)^2}{(c-a)(b-a)} & \text{for } a \leq x \leq c \\ 1 - \frac{(b-x)^2}{(b-c)(b-a)} & \text{for } c < x \leq b \\ 1 & \text{for } x > b \end{cases} \quad (2)$$

Where $F(x)$ is the cumulative distribution function (CDF) of $f(x)$ ($F(x) = \int f(x)dx$), and the domain $[a, b]$ corresponds to non-zero $f(x)$ and c is the x value of the maximum of $f(x)$.

8.2 Classes Definitions

Such triangular density function (pdf) is often used to represent expert uncertainty (Vose 2008). It presents the advantage

to ask expert simple questions to define the distribution (Jaboyedoff et al. 2014):

- What do you consider as the lower possible value (a) for an event (frequency, intensity, impacts, etc.), classified in the class C_j ?
- What do you consider as the upper possible value (b) for an event (frequency, intensity, damage, etc.), classified in the class C_j ?

Here, we will consider that the maximum of $f(x)$, i.e., $f(c)$ is located at the central value of a class considered by the expert as the most probable, but for the lower and the upper classes the choice is different, and other solutions can be chosen.

8.3 The Expert Assessment for a Specific Event

For most of the matrix approaches (Haimes 2009), all the possible events (Ev) have to be listed. Each event corresponds to a process that can lead to different scenarios for consequence and frequency.

The classes and their associated distribution definitions are independent of the events. An expert has its own interpretation of a potential event Ev that can lead to different scenarios of consequences and frequency independently. The expert may give, for each scenario, a weight to each class of consequences, and this is also applicable for frequencies scenarios. Therefore, all couples of frequencies-consequences (Co) related to an event Ev (λ, Co) must be distributed following the potential scenarios. For instance, as proposed by Vengeon et al. (2001), the frequency can be set first by an array of probability or weight—delay (return period or frequency) or more generally relative classes of probability. Then, the weight (probability) must be normalized to 1 and distributed among the respective belonging to the other classes, i.e., $P(CE_i)$ the expert weight distribution for one event (prior probability) (Fig. 12a). This is also performed for the impact. Using the Bayesian theory, the probabilities of a class C $P(C)$ of a frequency $P_\lambda(C_i)$ or an consequence $P_{Co}(C_j)$ of classes λ, Co respectively are given by (Jaboyedoff et al. 2014):

$$\begin{bmatrix} P(C_1|CE_1) & \dots & P(C_1|CE_n) \\ \vdots & \ddots & \vdots \\ P(C_n|CE_1) & \dots & P(C_n|CE_n) \end{bmatrix} \begin{bmatrix} P(CE_1) \\ \vdots \\ P(CE_n) \end{bmatrix} = \begin{bmatrix} P(C_1) \\ \vdots \\ P(C_n) \end{bmatrix} \quad (3)$$

By introducing values for the limits, it is then possible to provide exceedance curves for consequence or return period (Fig. 12b).

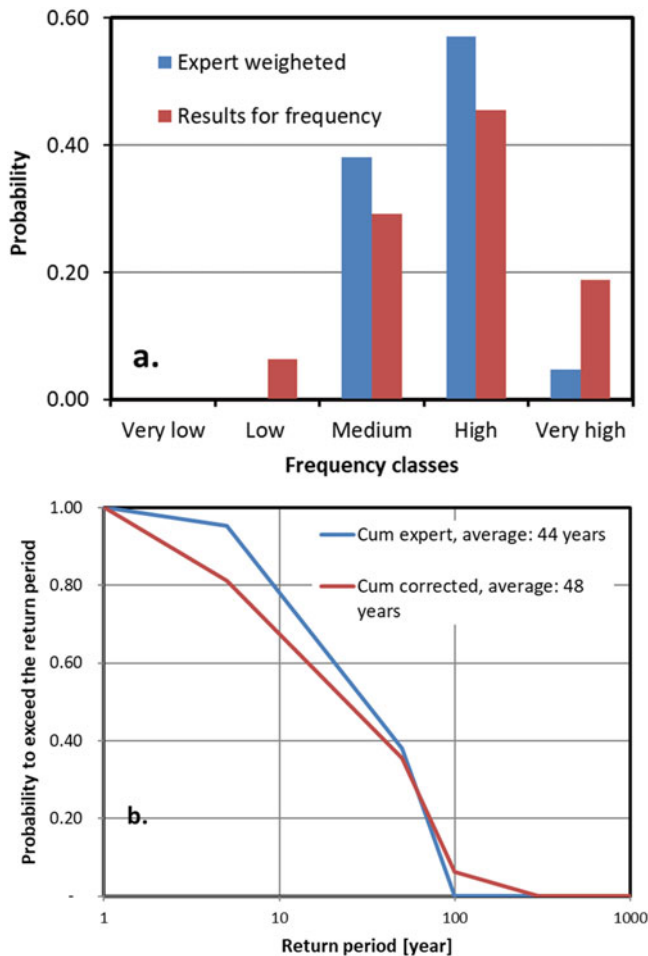


Fig. 12 (a) histogram of the probabilities $P(CE_j)$ (blue) for the frequencies given by the expert and $P(C_i)$ (red) the corrected one by Bayesian approach. (b) resulting curve of exceedance using the class limit (see below for these limits)

8.4 The Matrix Construction

The different probabilities for classes for frequencies $P_\lambda(C_i)$ and consequences $P_{Co}(C_j)$ can be multiplied to get a matrix of probability of each matrix element ($P(C_{ij})$) is given by element (Fig. 13):

$$P(C_{ij}) = P_f(C_i) \times P_{Co}(C_j) \text{ with } \sum P(C_{ij}) = 1 \quad (4)$$

where each element of the risk matrix corresponds to scenarios defined by the frequency and the consequences, the two scales are considered implicitly independent. This allows to obtain an exceedance curve of risk level that is attributed to each element in two ways. In the first case, for each amount of money the average frequency is calculated:

$$\lambda_j = \sum_{i=1}^n P(C_{ij}) \times \lambda_i \quad (5)$$

Where λ_i are the frequency for each frequency class. In the second case, the class values 1 to 5 with 5 being the highest of both scales are multiplied, going from 1 to 25. The annual risk can be calculated and frequency of exceedance of each Co_j is obtained by cumulating the frequencies of the frequency classes, and the risk classes can also be presented in terms of probability to exceed each risk classes.

8.5 The Example of a Particular Unstable Mass of Pont Bourquin Landslide

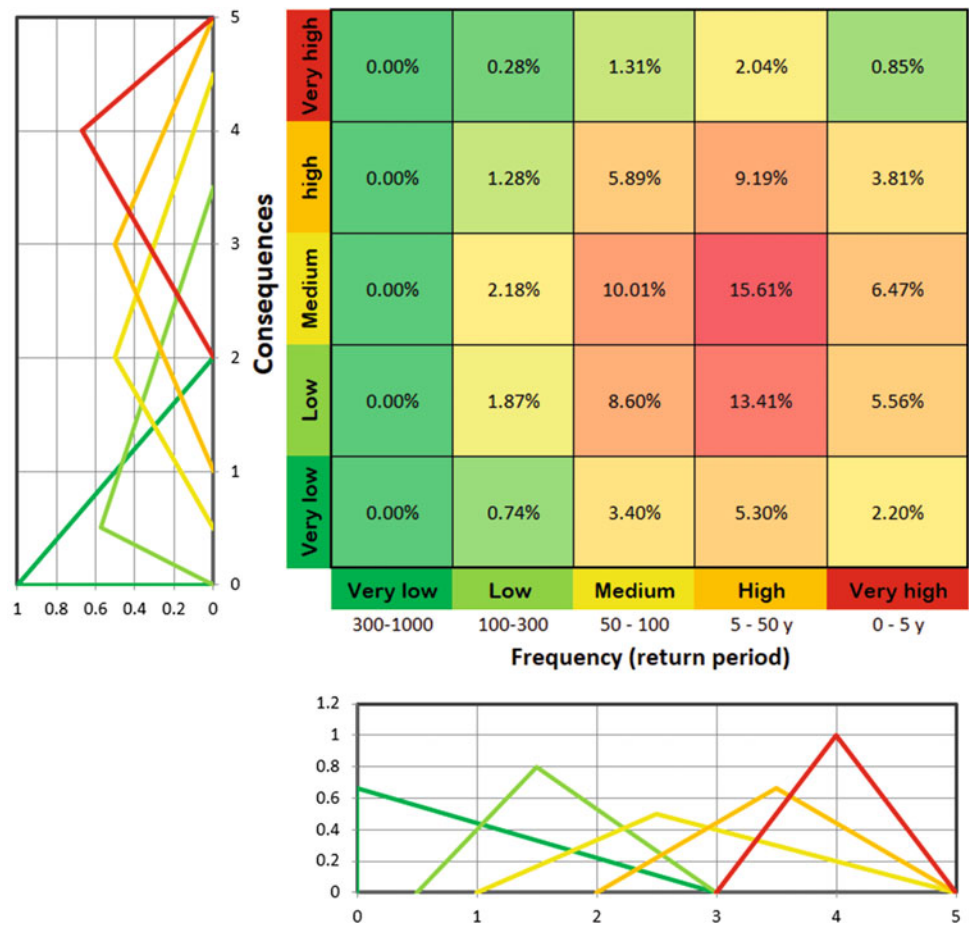
The example below is partially taken from Jaboyedoff et al. (2014) using a new assessment since no major event occurred and considering the new situation.

8.5.1 Landslide Settings

Pont Bourquin Landslide (PBL) is located in the Swiss Prealps, close to Les Diablerets, Switzerland (Jaboyedoff et al. 2009) (Fig. 14). First, evidence of gravitational deformation activity can be observed on aerial photos taken in the late sixties. This activity gradually developed until 2004. The first large slope displacements happened in 2006, when movements up to 80 cm occurred on the head scarp. Subsequently, a mudflow reached the road just below the landslide on fifth of July 2007 and another flow destroyed the forest at the toe of the slide in August 2010. For this second event, we were able to demonstrate the drop of surface shear wave seismic velocity at a depth of 9–11 m a few days before the collapse (Mainsant et al. 2012). Afterwards, remedial works were carried out, including a trunk-framed box at the toe of the instability and gullies on the mass body to evacuate surface waters. However, the landslide body is still moving, with velocities like the former ones.

Nowadays, the landslide is still active, and three zones are particularly threatening. In the present example, we will assess the risk for one of these potential source areas. It is approximately 5000 m³ material that is detached on the north-eastern part of the landslide. The displacement is observable by visual inspection of the back scarp, sudden reactivation failure of this compartment and a fast propagation toward the road is expected. A detailed description of the situation is not the goal of this paper, therefore, we will simply present an example illustrating the general framework of the method.

Fig. 13 Example of matrix showing the proximity of each element of the matrix and the distribution function used to calculate the likelihood $P(C_j | CE_i)$ of both axes



8.5.2 The Classes and Scales

To create the limits of classes for the frequencies or return periods we use a modified version of the Swiss danger matrix (Lateltin 1997): Very low (300–1000 years), Low (100–300 years), Medium (50–100 years), High (5–50 years) and Very high (0–5 years), the average is used as the frequency for the classes.

The classes of consequences have been designed depending on the considered scenario. We used five million CHF as the worst-case scenario, which corresponds, according to the willingness-to-pay value generally used in Switzerland, to the death of one person (Fig. 6). Each class is one order of magnitude different from its neighbors.

8.5.3 Setting the Prior Probabilities

Prior probabilities have been set using the Eq. [1] and $P_{\lambda}(C_i)$ from Fig. 12 and the triangular distributions shown in Fig. 11. For very low frequencies, looking at the likelihood functions in Fig. 13 shown below the matrix, the error of attribution can be quite high towards the higher frequencies, while for the very high frequencies they are distributed symmetrically between the two highest classes. The intermediate classes are distributed nearly symmetrically over neighboring classes.

The first question is whether or not the landslide will reach to the road after a sudden reactivation failure, considering up to the possibility of killing one person in a vehicle. The weights $P_{Co}(CE_j)$ were sat at 1.9%, 19.2%, 57.7%, 19.2%, 1.9% respectively for the classes very low, low, medium, high and very high, used with the values indicted in Fig. 6. The vertical distributions in Fig. 13 are used for the likelihood functions used to calculate the probability to belong to a class. Please note that not all hazard sources have been considered here (Fig. 14).

8.5.4 Results

The use of prior probability to correct expert assessment (Fig. 12a) implies that the average return period changes from 44 to 48 years, which is limited by construction (Fig. 12). The curve of exceedance shows that the corrected probability to be below 5 years is around 20%, whereas it is 5% for the original value (expert opinion), and to exceed 100 years goes from zero to 6% (Fig. 12b). The exceedances of the consequences per event (Fig. 15) show first that the average value of corrected costs (344,000.—CHF) is increased by more than 50% more than double the non-corrected value (222,000.- CHF). The probability to



Fig. 14 The location of the unstable zone on the landslide (white dashed line) and the national road that can be affected

exceed 50,000.—CHF decreases from 80% to 60% but are very similar for high values.

We can extract the curve of exceedance for the risk level divided in five classes from 1 to 25 (5×5) in 5 equal classes (Fig. 16). This shows that there is around 5% chance to be in the very high-risk class and 50% to be lower than medium risk. It is also possible to obtain the annual risk:

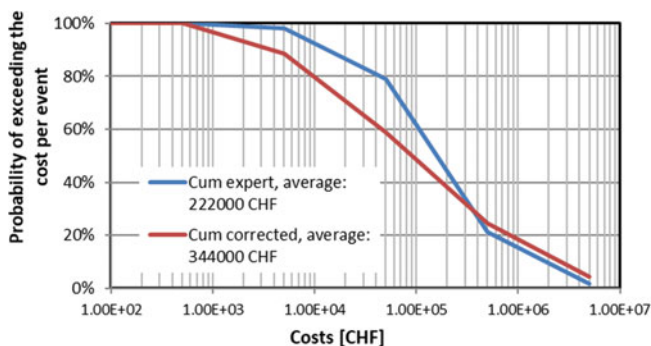


Fig. 15 Curve of exceedance of the cost per event, using the limit of the classes for both corrected and uncorrected probabilities

$$R = \sum_{j=1}^m \sum_{i=1}^n P(C_{ij}) \times \lambda_i \times Co_j \quad (6)$$

which is around 33,000.- CHF/year.

Using Eq. 5, an exceedance curve can also be obtained (Fig. 17) by summing the frequency of decreasing damage levels, which indicate the frequency of 4.3×10^{-3} (or on average every 230 years) to reach five million CHF, 5.7×10^{-2} (or on average every 18 years) to be over 50,000.- CHF and 8.5×10^{-2} (or on average every 12 years) to overpass 5000.- CHF.

9 Discussion and Conclusion

The use of CFMs must follow certain rules, the use of numbers for the classe's delimitations is important to avoid misunderstanding since the verbal qualification are often fuzzy. If the numbers are used, it enables extracting semi-quantitative risk estimation as well as the curve of exceedance. The limits must be fixed depending on the case study and the domain on which it applies as for F-N diagram.

The example tries to demonstrate that if it is possible to give a probability of belonging to all classes of a risk matrix, it provides a more reliable results which can be delivered in different forms and integrate fully uncertainty that is expressed by the exceedance curves. This approach allows to avoid most of the problems linked to the use of CFM.

The fact that the experts must give two times their opinions, first for the likelihood (the scale fuzziness), and second for the prior probability (weight for each class) is a way to introduce uncertainty, which is often lacking in the risk matrix approach. The expert can be separated in two groups, for the likelihood it can be fixed by regulation, for instance. The use of Bayesian approach is also easier than fuzzy logic. Here we used the concept of having only an estimation by the expert of the PDFs for categories of consequences and of frequency belonging. But another solution would have to give a PDFs for the frequency classes of each consequence level. It allows to extend the domain of hazard and consequences that are often not considered by experts. In addition, it does not only give one result, but also gives exceedance curves.

The results obtained from a more classical risk analysis was greater than the one analyzed here (Limousin 2013), it gave 278'000.- CHF/year for 3 unstable masses. But since nearly 10 years no large event occurred, which has the consequence to lower the expert hazard assessment. Nevertheless, there are several remaining problems:

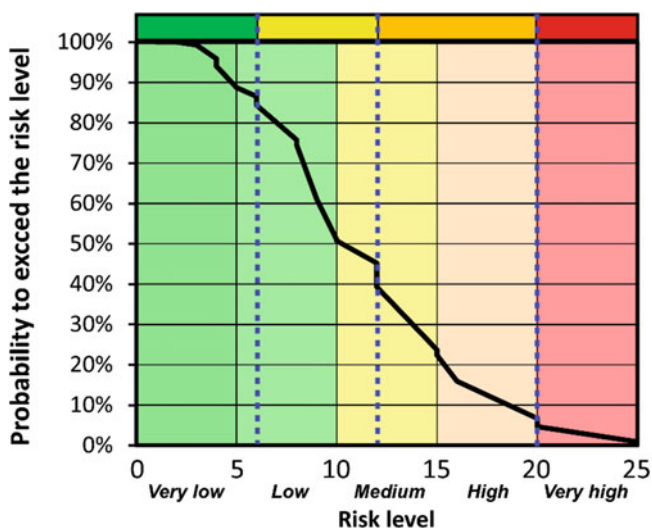


Fig. 16 Curve of exceedance for risk levels divided in 5 categories derive from the numbers of Fig. 7a and the limit in blue represents the four classes shown in Fig. 7a with the colours displayed on the top of the graph

- The discretization of the value by classes which are not equal in width raises the problem of non-linearity and singular points at the limits of the classes. This must be further explored, especially using other PDFs or CDFs such as power law or exponential.
- The way to calculate the risk and its distribution must be explored further, because the solution proposed is not unique.
- The extension of the classes to infinite and to zero is a problem, the question is if the limits of classes are used for the return period or frequency or if the average of limits is used are chosen the problem are different. The sum of CFM probability matrix is equal to one.

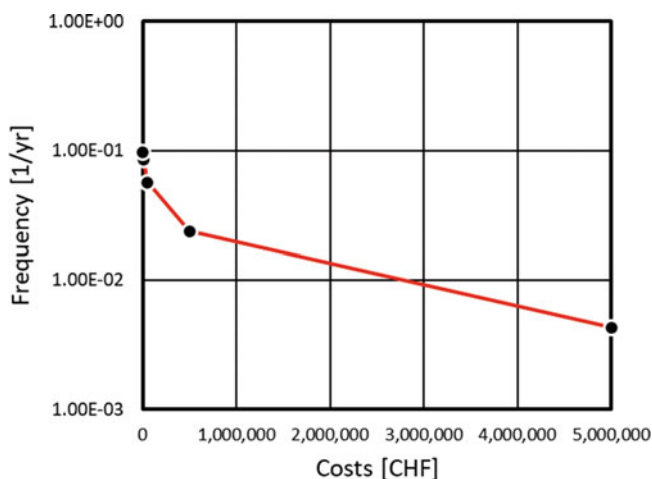


Fig. 17 Exceedance curves for consequences

It is clear from above that risk matrix can integrate the risk reduction or the difficulty to reduce it along with the uncertainty. The use of PDF estimate is also a tool to see at which level to act, i.e., reducing high impact event or small impact event or both, such an approach permits to discriminate the solutions. In addition, we experienced in lectures that the use of risk matrix is a good way to promote collective work in a classroom and to address several different types of risks.

We think that the present method improves some of the weaknesses of the matrix approach that can greatly support decision-making or may help for communicating in a better way the risks.

Acknowledgement The author would like to thank all the members of the risk team, in particular P. Limousin, at ISTE, UNIL for their great support and Prof. M. Kanevski who suggested us to use Bayesian approach. I also warmly thank Prof. J. Locat for his comments and corrections. Part of this research was funded by the European Commission within the Marie Curie Research and Training Network ‘CHANGES (led by C. Van Westen): Changing Hydrometeorological Risks as Analysed by a New Generation of European Scientists’ (2011-2014, Grant No. 263953) under seventh framework program.

References

AGS (Australian Geomechanics Society) (2007) Sub-committee on landslide risk management, a National Landslide Risk Management Framework for Australia. *Aust Geomech* 42:1–36

Ale B (2009) Risk: an introduction: the concepts of risk, danger and chance. Routledge, Taylor and Francis Group, p 134

Ale B, Burnap P, Slater D (2015) On the origin of PCDS–(probability consequence diagrams). *Saf Sci* 72:229–239. <https://doi.org/10.1016/j.ssci.2014.09.003>

Armée Suisse (2012) Sécurité intégrale, p. 153, Retrived April 2023. https://www.vtg.admin.ch/content/vtg-internet/fr/service/info_trp_sicherheit/_jcr_content/contentPar/tabs_copy/items/downloads/tabPar/downloadlist/downloadItems/190_1472734389467.download/52_059_f.pdf

Barnes A (2016) Making Intelligence analysis more intelligent: using numeric probabilities. *Intell National Secur* 31:327–344. <https://doi.org/10.1080/02684527.2014.994955>

Corominas J, van Westen C, Frattini P, Cascini L, Malet JP, Fotopoulou S, Catani F, Van Den Eeckhaut M, Mavrouli O, Agliardi F, Pitolakis K, Winter MG, Pastor M, Ferlisi S, Tofani V, Hervás J, Smith JT (2014) Recommendations for the quantitative analysis of landslide risk. *Bull Eng Geol Environ* 73(2):209–263

Cowles B, Backman D, Dutton R (2012) Verification and validation of ICME methods and models for aerospace applications. *Integr Mater Manuf Innov* 1:3–18. <https://doi.org/10.1186/2193-9772-1-2>

Cox LA Jr (2008) W’at’s wrong with risk matrices? *Risk Anal* 28:497–512

Dai FC, Lee CF, Ngai YY (2002) Landslide risk assessment and management: an overview. *Eng Geol* 64(1):65–87

Defence Intelligence (2023) Defence Intelligence–communicating probability. <https://www.gov.uk/government/news/defence-intelligence-communicating-probability>. Accessed February 2023

DOD (2006) Risk management guide for DOD acquisition, 6th Edition (Version 1.0), ADA470492, p. 34

- ECDC (2011) European Centre for disease prevention and control: operational guidance on rapid risk assessment methodology. Stockholm, ECDC, 68
- Farmer FR (1967) Siting criteria—a new approach. Containment and Siting of Nuclear Power Plants. Proceedings of a Symposium on the Containment and Siting of Nuclear Power Plants
- Farvacque M, Lopez-Saez J, Corona C, Toe D, Bourrier F, Eckert N (2019) How is rockfall risk impacted by land-use and land-cover changes? Insights from the French Alps. *Glob Planet Chang* 174: 138–152. <https://doi.org/10.1016/j.gloplacha.2019.01.009>
- Fell R, Hartford D (1997) Landslide risk management. In: *Landslide risk assessment*. Routledge, pp 51–109
- Fell R, Ho KK, Lacasse S, Leroi E (2005) A framework for landslide risk assessment and management. In: *Landslide risk management*. CRC Press, pp 13–36
- Fell R, Corominas J, Bonnard C, Cascini L, Leroi E, Savage WZ (2008) Guidelines for landslide susceptibility, hazard and risk zoning for land use planning. *Eng Geol* 102(3):85–98
- Gill JC, Malamud BD (2016) Hazard interactions and interaction networks (cascades) within multi-hazard methodologies. *Earth Syst Dynam* 7:659–679. <https://doi.org/10.5194/esd-7-659-2016>
- Gillet JE (1985) Rapid ranking of process Hazard. *Process Eng* 66:19–22
- Girgin S, Necci A, Krausmann E (2019) Dealing with cascading multi-hazard risks in national risk assessment: the case of Natech accidents. *Int J Disaster Risk Reduct* 35:101072. <https://doi.org/10.1016/j.ijdrr.2019.101072>
- Haimes YY (2009) Risk Modeling, Assessment, and Management, 3rd edn. John Wiley & Sons, p 1009
- Hung O, Wong HN (2007) Landslide risk acceptability criteria: are F–N plots objective? *Geotech News* 25:47–50
- ISO (2009) Risk management—principles and guidelines. ISO 31000:24
- Jaboyedoff M, Loye A, Oppikofer T, Pedrazzini A, Güelli Pons M, Locat J (2009) Earth-flow in a complex geological environment: the example of Pont Bourquin, les Diablerets (Western Switzerland). In: Malet J-P, Remaître A, Bogaard T (eds) *Landslide processes*, pp 131–137
- Jaboyedoff M, Aye Z, Derron MH, Nicolet P, Olyazadeh R (2014) Using the consequence–frequency matrix to reduce the risk: examples and teaching. *Int. Conf. on the Analysis and Management of Changing Risk for natural hazards—CHANGES project*, Padova Italy. p. 9
- Jonkman SN, van Gelder PHAJM, Vrijling JK (2003) An overview of quantitative risk measures for loss of life and economic damage. *J Hazard Mater* 99:1–30. [https://doi.org/10.1016/S0304-3894\(02\)00283-2](https://doi.org/10.1016/S0304-3894(02)00283-2)
- Kotz S, van Drop JR (2004) Beyond Beta: other continuous families of distributions with bounded support and applications. *World Scientific*, p 289
- Krause J-P, Mock R, Gheorghe AD (1995) Assessment of risks from technical systems: integrating fuzzy logic into the Zurich Hazard analysis method. *Int J Environ Res Public Health (IJEP)* 5(2–3): 278–296
- Lacasse S, Nadim F (2009) Landslide risk assessment and mitigation strategy. In: Sassa K, Canuti P (eds) *Landslides—disaster risk reduction*. Springer, Berlin Heidelberg, Berlin, Heidelberg, pp 31–61
- Lacasse S, Eidsvik U, Nadim F, Høeg K, Blikra LH (2008) Event Tree analysis of Åknes rock slide hazard. IV Geohazards Québec, 4th Canadian Conf. on Geohazards. 551–557
- Lateltin O (1997) Prise en compte des dangers dus aux mouvements de terrain dans le cadre des activités ‘e l’aménagement du territoire. *Recommandations, OFEFP*, 42
- Leroueil S, Locat J (1998) Slope movements: geotechnical characterisation, risk assessment and mitigation. *Proc. 11th Danube-European Conf. Soil Mech. Geotech. Eng., Porec, Croatia*, 95–106. Also published in *proc. 8th congress Int. Assoc. Eng. Geology, Vancouver, 933-944, Balkema, Rotterdam*
- Limousin P (2013) De la caractérisation du sol, à l’étude de propagation et des risques: Les cas du glissement de Pont Bourquin. *Univ. Lausanne Master Thesis*, p. 100
- Macciotta R, Gräpel C, Keegan T, Duxbury J, Skirrow R (2020) Quantitative risk assessment of rock slope instabilities that threaten a highway near Canmore, Alberta, Canada: managing risk calculation uncertainty in practice. *Can Geotech J* 57(3):337–353
- Mainsant G, Larose E, Brönnimann C, Jongmans D, Michoud C, Jaboyedoff M (2012) Ambient seismic noise monitoring of a clay landslide: toward failure prediction. *JGR-ES* 117, F01030:12. <https://doi.org/10.1029/2011JF002159>
- Martinez-Marquez D, Terhaer K, Scheinmann P, Mirmajafizadeh A, Carty CP, Stewart RA (2020) Quality by design for industry translation: three-dimensional risk assessment failure mode, effects, and criticality analysis for additively manufactured patient-specific implants. *Engg Rep* 2:e12113. <https://doi.org/10.1002/eng2.12113>
- Mereu A, Sardu C, Minerba L, Sotgiu A, Contu P (2007) Evidence based public health policy and practice: participative risk communication in an industrial village in Sardinia. *J Epidemiol Community Health*(1979-) 61:122–127
- OFEV (2016) Protection contre les dangers dus aux mouvements de terrain. Aide à l’exécution concernant la gestion des dangers dus aux glissements de terrain, aux chutes de pierres et aux coulées de boue. Office fédéral de l’environnement, Berne L’environnement pratique 1608:98
- OFPP (2013) Aide-mémoire KATAPLAN.- Analyse et prévention des dangers et préparation aux situations d’urgence. Office fédéral de la protection de la population, p. 55
- Pasman HJ, Vrijling JK (2003) Social risk assessment of large technical systems. In: *Human Factors and Ergonomics in Manufacturing & Service Industries*, vol 13, pp 305–316. <https://doi.org/10.1002/hfm.10046>
- Porter M, Morgenstern N (2013) Landslide risk evaluation—canadian technical guidelines and best practices related to landslides: a national initiative for loss reduction; geological survey of Canada. *Open File* 7312:21. <https://doi.org/10.4095/292234>
- Raetzo H, Lateltin O, Bollinger D, Tripet J (2002) Hazard assessment in Switzerland—codes of practice for mass movements. *Bull Eng Geol Environ* 61:263–268. <https://doi.org/10.1007/s10064-002-0163-4>
- Raydugin Y (2012) Consistent application of risk Management for Selection of engineering design options in mega-projects. *Int J Risk Conting Manag (IJRCM)* 1:44–55. <https://doi.org/10.4018/ijrcm.2012100104>
- Schmocker L, Höck E, Mayor PA, Weitbrecht V (2013) Hydraulic model study of the fuse plug spillway at Hagneck Canal, Switzerland. *J Hydraul Eng* 139:894–904. [https://doi.org/10.1061/\(ASCE\)HY.1943-7900.0000733](https://doi.org/10.1061/(ASCE)HY.1943-7900.0000733)
- Solheim A, Bhasin R, De Blasio FV, Blikra LH, Boyle S, Braathen A, Dehls J, Elverhøi A, Eitzelmüller B, Glimsdal S (2005) International Centre for Geohazards (ICG): Assessment, prevention and mitigation of geohazards. *Nor J Geol* 85:45-62. *Norsk Geologisk Forening*.
- TBCS (Treasury Board of Canada Secretariat) (2011) Guide to corporate risk profiles. Retrieved in April 2023. <https://www.canada.ca/en/treasury-board-secretariat/corporate/risk-management/corporate-risk-profiles.html>
- UK-CO (Cabinet Office) (2017) National risk register of civil emergencies. Retrieved from https://assets.publishing.service.gov.uk/government/uploads/system/uploads/attachment_data/file/644968/UK_National_Risk_Register_2017.pdf
- Vengeon JM, Hantz D, Dussauge C (2001) Prédicibilité des éboulements roc eux: approche probabiliste par combinaisons d’études historiques et géomécaniques. *Rev Fr Géotech* 95/96:143–154

- Vose D (2008) Risk analysis: a quantitative guide, 3rd edn. John Wiley & Sons, p 752
- Wang X, Frattini P, Crosta GB, Zhang L, Agliardi F, Lari S, Yang Z (2014) Uncertainty assessment in quantitative rockfall risk assessment. *Landslides* 11:711–722. <https://doi.org/10.1007/s10346-013-0447-8>
- Van Westen CJ, Greiving S (2017) Multi-hazard risk assessment and decision making, *Environmental hazards Methodologies for Risk Assessment and Management*. Dalezios, N. R. (ed.). IWA Publishing, PP 31-94.
- WHO, 2020. How to use WHO risk assessment and mitigation checklist for mass gatherings in the context of COVID-19. WHO/2019-nCoV/Mass_gathering_RAtool/20202, p. 4
- Zadeh LA (1975) The concept of a linguistic variable and its applications to approximate reasoning, part I. *Inf Sci* 8:199–249
- ZHA (2013) Methodology Zurich Hazard Analysis. www.zurich.com/riskengineering/global/services/strategic_risk_management/zha_services. Last Access 18 Apr 2013
- Zhang D, Han J, Song J, Yuan Y (2016) A risk assessment approach based on fuzzy 3D risk matrix for network device. In: 2016 2nd IEEE international conference on computer and communications (ICCC), pp 1106–1110

Open Access This chapter is licensed under the terms of the Creative Commons Attribution 4.0 International License (<http://creativecommons.org/licenses/by/4.0/>), which permits use, sharing, adaptation, distribution and reproduction in any medium or format, as long as you give appropriate credit to the original author(s) and the source, provide a link to the Creative Commons license and indicate if changes were made.

The images or other third party material in this chapter are included in the chapter's Creative Commons license, unless indicated otherwise in a credit line to the material. If material is not included in the chapter's Creative Commons license and your intended use is not permitted by statutory regulation or exceeds the permitted use, you will need to obtain permission directly from the copyright holder.





Do not Let Your Guard Down: Landslide Exposure and Local Awareness in Mexico

Ricardo J. Garnica-Peña and Irasema Alcántara-Ayala

Abstract

The International Consortium on Landslides, through the Sendai Partnerships 2015–2025 and the Kyoto Landslide Commitment 2020 for Global Promotion of Understanding and Reducing Landslide Disaster Risk, aims to support the implementation of the Sendai Framework for Disaster Risk Reduction. This involves various actions in which enhancing capacity building, knowledge transfer, and raising awareness are sought. One of the problems related to people's awareness of landslide disaster risk is their biased perception when landslides do not often occur in areas highly susceptible to such hazards. This study analyzes the expansion of the urban area of a community located in an area highly exposed to landslides. This was performed by producing high-resolution images and field observations using drones from 2007 to 2023. The spatiotemporal analysis indicates that in the last decade, landslides have not occurred. Therefore, recommendations are made to enhance landslide disaster risk awareness in a sustained manner.

Keywords

Landslide preparedness · Disaster risk awareness · Disaster risk reduction · Sustained policies · Risk perception · Risk communication

1 Introduction

The goal of the Sendai Framework for Disaster Risk Reduction is to “prevent new and reduce existing disaster risk through the implementation of integrated and inclusive economic, structural, legal, social, health, cultural, educational, environmental, technological, political and institutional

R. J. Garnica-Peña (✉) · I. Alcántara-Ayala
National Autonomous University of Mexico (UNAM), Institute of Geography, Mexico City, Mexico
e-mail: garnica@geografia.unam.mx; ialcantara@geografia.unam.mx

measures that prevent and reduce hazard exposure and vulnerability to disaster, increase preparedness for response and recovery, and thus strengthen resilience” (UNISDR 2015: 12). This should be achieved by implementing its four priorities for action: Priority (1) Understanding disaster risk; Priority (2) Strengthening disaster risk governance to manage disaster risk; Priority (3) Investing in disaster risk reduction for resilience; and Priority (4) Enhancing disaster preparedness for effective response and to “Build Back Better” in recovery, rehabilitation, and reconstruction. Although the Science and Technology Community plays a significant role in attaining all of them, by its nature, understanding disaster risk (Priority 1) is strongly associated with scientific commitment.

The accomplishment of this priority at the national and local levels requires that landslide experts promote, among other issues, “national strategies to strengthen public education and awareness in disaster risk reduction, including disaster risk information and knowledge, through campaigns, social media, and community mobilization, taking into account specific audiences and their needs” (UNISDR 2015: 15).

The success of this endeavor, especially regarding landslide disaster risk, relies on different strategies and initiatives, including the Sendai Partnerships 2015–2025 and the Kyoto Landslide Commitment 2020 for Global Promotion of Understanding and Reducing Landslide Disaster Risk (KLC2020). These undertakings promote landslide research and capacity building, including education for disaster risk reduction, especially in developing countries (Sassa 2015, 2016). Of particular relevance for this chapter is the priority Action 5 of the KLC2020, which seeks to enhance open communication within society through integrated research, capacity building, knowledge transfer, awareness raising, training, and educational activities to enable societies to develop effective policies and strategies for reducing landslide disaster risk, to strengthen their capacities for preventing hazards to develop into major disasters, and to

enhance the effectiveness and efficiency of relief programs (Sassa 2018, 2020).

In light of these concerns, this study focused on analyzing the expansion of the urban area of a district highly exposed to landslides in the municipality of Teziutlán, Puebla, and its relationship with the spatial-temporal distribution of this type of process. In the following sections, this chapter addresses the need to reinforce disaster risk landslide awareness on a continual basis. A broad reflection on landslide exposure and awareness is provided in section two, followed by a description of the studied area in sect. 3. Section 4 deals with the methodology. Results are provided in sect. 5 while concluding remarks are presented in sect. 6.

2 Landslide Exposure and Awareness

The terms *exposure* and *awareness* are key for understanding disaster risk. According to the Oxford dictionary, while exposure involves being in a place or situation without protection from something harmful or unpleasant, awareness means knowing something, knowing that something exists and is important.

Exposure has been defined by UNISDRR (2017) as the situation of people, infrastructure, housing, production capacities, and other tangible human assets located in hazard-prone areas. In other words, it involves the component of location given by specific geographic coordinates to represent the dimension of space and its constituents that can be potentially affected by a hazard, in this case, landslides. Therefore, the term reflects a specific itemization of humanness, socio-economic, material, cultural, and environmental assets that can be easily affected by hazards of diverse origins. Awareness of landslide exposure involves knowing that the potential occurrence of a landslide in a specific place is significant, and therefore information, knowledge, and actions must be developed.

Awareness of landslide disaster risk (i.e., Solana and Kilburn 2003) is strongly linked to people's perception of landslides (Alcántara-Ayala 2018). This topic is quite complex (Slovic 1987; Pidgeon et al. 1992) and needs to be properly addressed. However, although its analysis is beyond the scope of this chapter, it can be said that the perception of risk involves the explanations that people construct and conceive of understanding the dynamics of the complex interactions that give rise to risk; in other words, the latent or potential condition for one or several disasters to occur. These explanations are based on experiences (Barnett and Breakwell 2001), beliefs (Aucote et al. 2010), social and cultural frameworks, gender (Gustafson 1998), feelings, and needs (see Hernández-Moreno and Alcántara-Ayala 2017; Alcántara-Ayala and Moreno 2016).

Quite often, people reject the possibility of a disaster being repeated. The myth of personal invulnerability (Joffe and Joffé 1999) also plays a role in disaster risk perception and, thus, awareness. This involves recognizing the presence of a situation that can be regarded as a risk. Still, if it occurs, it is believed to impact somebody else, such as neighbors or people from another city, but those at risk are safe. This idea of avoiding acceptance (Finlay and Fell 1997) leads to a lack of awareness and preparedness, increasing vulnerability and disaster risk.

Furthermore, disaster risk perception is also associated with understanding the spatial and temporal dimensions of the hazards, in this case, landslides.

The problems of enacting a single long-term future associated with disaster risk management involve perceptions of people's at-risk and quotidian priorities. While daily security and subsistence are in people's minds, the occurrence of landslides is, by no effect, a priority. Nonetheless, understanding landslide disaster risk in areas exposed to this type of hazard requires continuous raising of awareness, particularly when no disasters have occurred.

How people measure time concerning the occurrence of disasters is very complex and deserves in-depth study. Based on field observations in provincial areas, it is recognized that the future is often measured based on personal, family, and collective interest events. Patronal festivities and local traditions are eagerly awaited, where medicinal artisans work with celebrants to forget the problems of reality, including those derived from disaster risk.

3 Studied Area

Teziutlán is in the northeast of Puebla province, in the Central East part of Mexico (Fig. 1). It has a population of 103,583. It comprises 32 localities, of which 62,849 people live in the municipal capital and the rest in towns of various sizes (INEGI 2021). Historically, this area has endured several disasters associated with rainfall-induced landslides that result from the combination of high-susceptible lithology and increasing exposure of vulnerable communities (Alcantara-Ayala 2004). Pyroclastic deposits generated from the Caldera de Los Humeros, along with overlaying sedimentary and metamorphic rocks, are the most critical lithological units susceptible to landsliding (Murillo-García et al. 2019).

The most severe landslide-associated disaster in this region occurred in October 1999. Dozens of landslides affected Teziutlán, where more than one hundred people lost their lives, and the economic impact was very high. Diverse investigations have documented various aspects of this disaster and the ingredients of landslide disaster risk in the municipality (Alcántara-Ayala et al. 2017, 2018). These



Fig. 1 Location of the studied area

include understanding hazards (Garnica-Peña and Alcántara-Ayala 2017), vulnerability, exposure (Garnica-Peña et al. 2021a, b), and different mechanisms to reduce landslide disaster risk (Alcántara-Ayala and Moreno 2016).

In Teziutlán, disasters associated with landslides triggered by rainfall (Alcantara-Ayala 2004) continue to be viewed as an external, exogenous event during which the population plays no role other than cooperating during the response. Therefore, in addition to past efforts, there is a clear need to raise sustained mechanisms of landslide disaster risk awareness at the local level, at the time people at risk are embedded in activities that capture their interest, regardless of their nature.

4 Methodology

The analysis is based on material collected from 2007 to 2023. A methodology combining the analysis of an available orthophoto from the National Institute of Statistics and Geography and images produced by Unmanned Aerial Vehicles (UAVs) was adopted to distinguish between the occurrence

of rainfall-triggered landslides and the effects of the expansion of the urban area (Fig. 2).

4.1 Aerial Survey Using UAVs

A couple of flights were made in the study area. The mobile application, Map Pilot Pro, was used in both cases. In this application, the area to be flown was defined, and parameters such as the flight height above the ground were established (which defined, together with the size of the image, the resolution of the acquired images), superimposition or frontal and lateral overlap, and movement speed of the equipment. Due to the size of the surface, it was necessary to use four batteries on each mission to cover the full area at the established height.

Sometimes, in mountain zones with dense vegetation, a lack of information or coverage of ground conditions results when flights are carried out in only one direction. To avoid data gaps in aerial photography, UAV missions consisted of lines in a North-South and East-West direction to successfully cover the entire study area. DJI Phantom 4 Pro equipment, consisting of a camera with a 1" sensor and 20-megapixels effective resolution, was used for these missions. It also had an average autonomy of 20 min per battery.

Once the images were acquired, they were processed in the Bentley ContextCapture software to obtain various products such as orthophotos, point clouds, digital surface models (DSM), and three-dimensional triangular mesh models. For this study, only photographic mosaics were used. The processing consisted of the following stages: (a) define the control points (ground control points), mooring points (tie points), and scale points were first defined; (b) aerial triangulation was undertaken; (c) a 3D mesh was then generated; and lastly, (d) orthophotos and digital surface models were created.

For the flight carried out in April 2017 with the Phantom 4 Pro equipment, the Map Pilot Pro application (Maps Made Easy©) was used. The flight had a W-E direction, at 150 m above the ground, with an 80% frontal and 80% lateral overlap. Additionally, an N-S flight was carried out, with a height above the ground of 150 m and an 80% frontal and 80% lateral overlap. The number of photos acquired was 739, and the orthophoto was generated at 9 cm-resolution.

The Map Pilot Pro application (Maps Made Easy©) was used for the flight carried out in February 2023. The W-E and N-E flights were carried out 100 m above the ground, with a frontal and lateral overlap of 80%. Some 1866 photos were acquired. Additionally, the FPVCameraforDJI application was used with a Point of Interest (POI) flight mode to take oblique shots. Flight 1 was carried out at 50 and 60 m above the ground, with a radius of 55 m and 70 m and an inclination

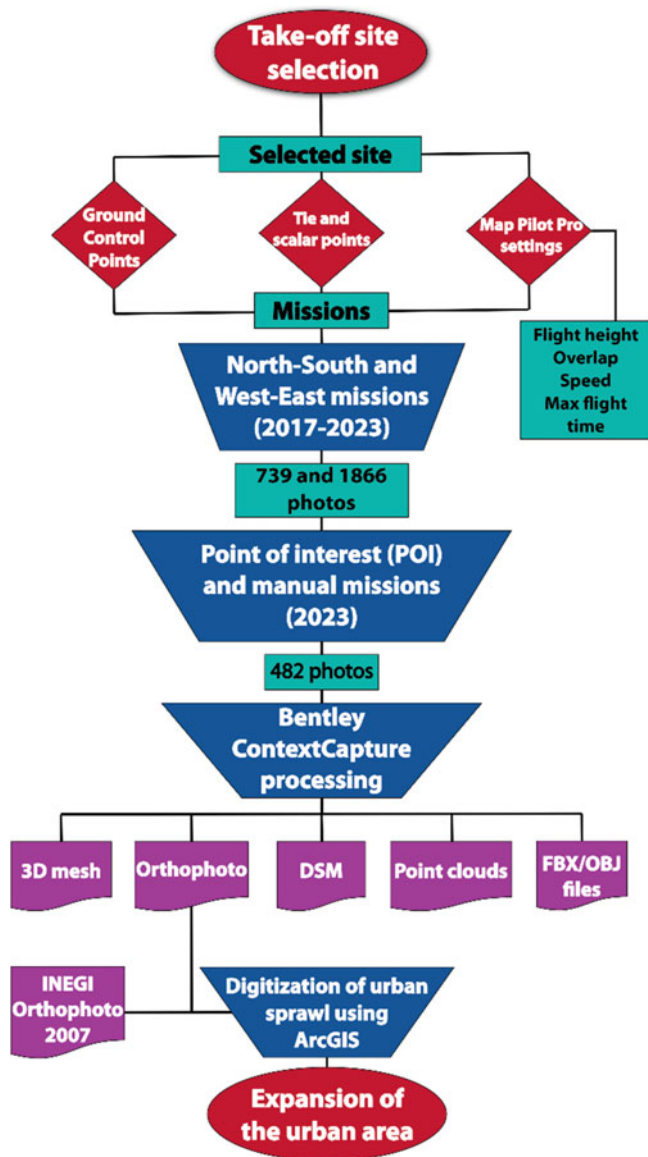


Fig. 2 Strategy for the analysis of the expansion of the urban area

of 36 to 42 degrees. Flight 2 was carried out at 65 m and 70 m, with a radius of 75 m and 85 m and an inclination of 35 to 40 degrees. The third flight was flown at 55 m and 65 m, with a radius of 55 m and 70 m, and an inclination of 36 degrees. A total of 288 photos were acquired. Likewise, an additional manual flight was carried out to capture oblique shots every 3 seconds in the most exposed areas of the houses, through which 194 photos were acquired. The generated orthophoto had a resolution of 6 cm.

4.2 Expansion of the Urban Area

The expansion of the urban area was delimited directly from the images for the orthophotos produced for 2017 and 2023.

Using ESRI ArcGIS 10.8 software, three polygon vector layers were created, one for each revised date. In the edition of layers, the urbanized areas were delimited, and modified surfaces were calculated for each of the dates. It should be noted that it was not possible to carry out this action for older images. This was because the low spatial resolution did not allow us to differentiate and identify, in detail, the urban and the rural limits. For this reason, the 2007 orthophoto was prepared by INEGI, which had a resolution of 50 cm per pixel.

4.3 Rainfall Series

Monthly rainfall information for the Teziutlán rain gauge from 1991 to 2022 was extracted from two databases of the National Water Commission. However, the information from the years 1995 and 2003 was incomplete.

5 Results

UAVs have been widely used, especially during the last decade, to analyze the diverse aspects of landslide disaster risk, especially those characterizing landslide hazards (Garnica-Peña and Alcántara-Ayala 2021). Following such an approach, it is possible to identify the expansion of the urban area of Juárez, Ávila Camacho, and Lindavista neighborhoods.

Although the original plan was to analyze a longer period, the quality of available images of the research area is not good enough to compare with information derived from the high-resolution images recently obtained using UAVs.

According to the analysis, the study area has a surface of 313,522 m², of which one-third is currently built. The built area in 2007 was 98,906; a decade later, in 2017, it had only increased by 2,636 m². However, in the following 5 years, it expanded to 7,537 m² (Table 1).

Despite the lack of land-use planning implementation, the steep terrain greatly limits urban area expansion (Fig. 3). However, in some cases, this takes place vertically, increasing the load of the already landslide susceptible slopes.

The entire municipality has been developed without considering disaster risk management (Fig. 4). Even before the landslides of 1999, the occurrence of diverse disaster episodes called for the attention of regional and local authorities to consider incorporating the existing potential impact of hazards into policymaking

However, the lack of coordination and accountability mechanisms at the subnational and national levels substantially limits progress in the municipalities and at-risk localities. Teziutlán has not been the exception. Efforts are

Table 1 Expansion of the Urban Area

Urbanized area	Surface m ²	Hectares
Study area surface	313,522.4	31.35
Built area (total)	109,080.4	10.91
Built area 2007	98,906.3	9.89
Built area 2017	2636.8	0.26
Built area 2023	7537.3	0.76

heterogeneous regarding the local authorities' particular interests.

Using the landslide inventory developed by Murillo-García and Alcántara-Ayala (2017), it is possible to identify the number of landslides in the area of interest. Accordingly, based on field observation and analyzing aerial photos and satellite images, 33 movements are recognized in an area of 17,649.9 m². Likewise, 3 landslides are identified as occurring in 1942, one in 1974, and 27 during the disaster of October 1999 (Table 2).

The consequences of the 1999 disaster were particularly severe, and temporarily enhanced the preoccupation of the inhabitants and Civil Protection authorities. In 2013, two

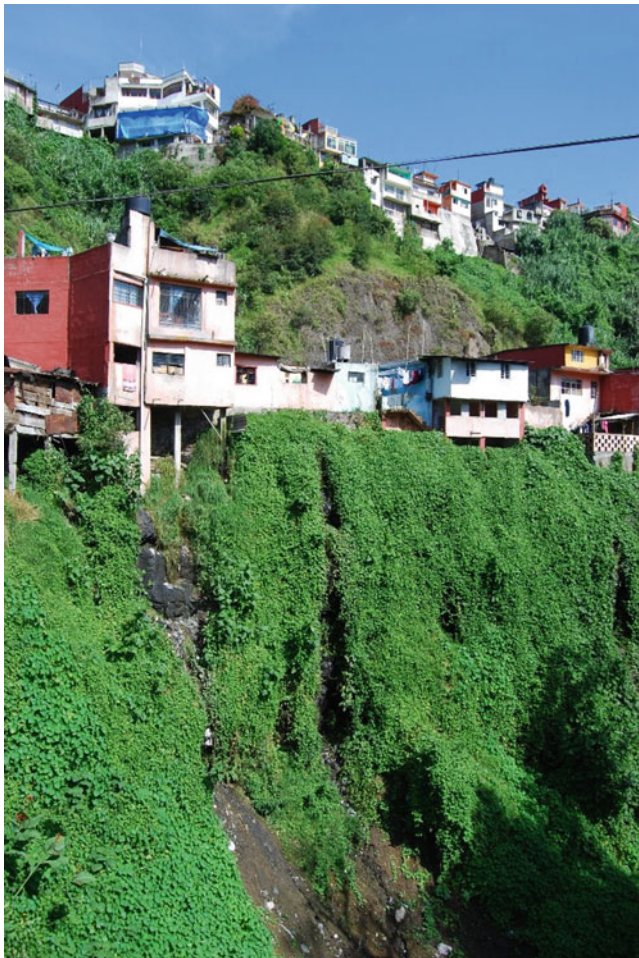


Fig. 3 Dwellings developed on landslide susceptible areas of Teziutlán municipality, Puebla, México

additional landslides were induced by rainfall. Since no casualties were involved, this episode was not a strong reminder of the 1999 events and, most importantly, what can take place in the future (Table 2).

The spatial distribution of landslides in 2007 and their impact on inhabited dwellings are represented in Fig. 5. Now distinguishable is the development of houses on steep slopes, susceptible to landslides, expanding towards the bottom of the ravine.

Figure 5 also shows the coalescence of two landslide deposits in the lower part of the ravine and their marginal impact on the community. Although a high percentage of the inhabited areas are not severely affected by the instability of the slopes, it is evident that some landslide crowns extend under the lower parts of the buildings. This has severe implications because of possible landslide reactivation.

There was little population growth over the next decade and limited urban encroachment (Fig. 7). This slower evolution could be linked to the development of housing areas in other areas of the municipal head booming over the 2007-2017 period.

However, the dwellings constructed in the Juárez neighborhood are developed in areas with active landslides. In the Ávila Camacho area, houses and landslides are encroaching on the bottom of the ravine (Fig. 6). In contrast, those in Lindavista continue to increase the load on the slopes with vertical constructions.

It is important to mention that at the community level, for example, the Juárez neighborhood possesses a well-functioning local committee that solves societal problems through their community efforts. Unfortunately, landslides are of concern in most places only when landslides have occurred in the recent past (Fig. 7).

The expansion of the urban area in Teziutlán has responded to the need to house people who immigrate from adjacent areas to work in the maquila, which is the main activity of the municipality. This leads to the creation of built landscapes of a mixed nature, in which the use of different materials with heterogeneous quality and resistance are used (Fig. 8).

A larger area of urban development was identified in the analyzed image of 2023 (Fig. 9). Regardless of the previously recognized character of instability of the hillslopes, a vegetated slope in the Juárez neighborhood already affected by landslides is being transformed into an infrastructure zone.



Fig. 4 Images of the expansion of the urban area of the municipality of Teziutlán, Puebla, and the research area in 1956 and 2017

This involves the construction of three buildings, presumably for housing (Fig. 10). To a much lesser degree, small dwellings have been built in the north-eastern sector of the Linda vista neighborhood and the southwestern portion of Ávila Camacho (see Fig. 9).

Development of the urban space in Teziutlán takes place without considering territorial planning and even less integrated disaster risk management. While the collective memory of authorities regarding past disasters associated with rainfall-induced landslides are easily erased by economic interests and profits, community memory is often shaped by risk perceptions on which pressing issues concerning livelihoods, essential needs, and quotidian problems prevail over landslide disaster risk awareness and preparedness.

According to the available rainfall series, 2013, 2010, 1999, 2017, and 1949 recorded the maximum annual

precipitation amounts in descending order. These corresponded to 2733.20, 2020.60, 1983.30, 1958.50, and 1949 mm of rain, respectively. The maximum monthly precipitation occurred in September in all years, and together with the precipitation of October, it amounted to 1146.50, 738, 942.5, 942.8, and 802.5 mm, correspondingly CONAGUA n.d.).

Indeed, rainfall threshold analysis requires more detailed and complete information. Nonetheless, from Fig. 11, it can be observed that the year 2013 was the wettest of the last three decades. After that year, no more landslides occurred. Thus, communities are inclined to neglect the understanding and remembrance of the causality of disasters they have suffered in the past. Therefore, it is suggested that beyond highly technical efforts to evaluate landslide disaster risk, a sound program of landslide disaster risk awareness should be put in place permanently to raise the consciousness of people

Table 2 Temporal distribution of the number of landslides in the research area

Landslides	Number	Area m ²
Number of landslides (total)	33	17,649.9
Number of landslides 1942	3	1975.8
Number of landslides 1974	1	228.7
Number of landslides 1999	27	15,021.8
Number of landslides 2013	2	423.6

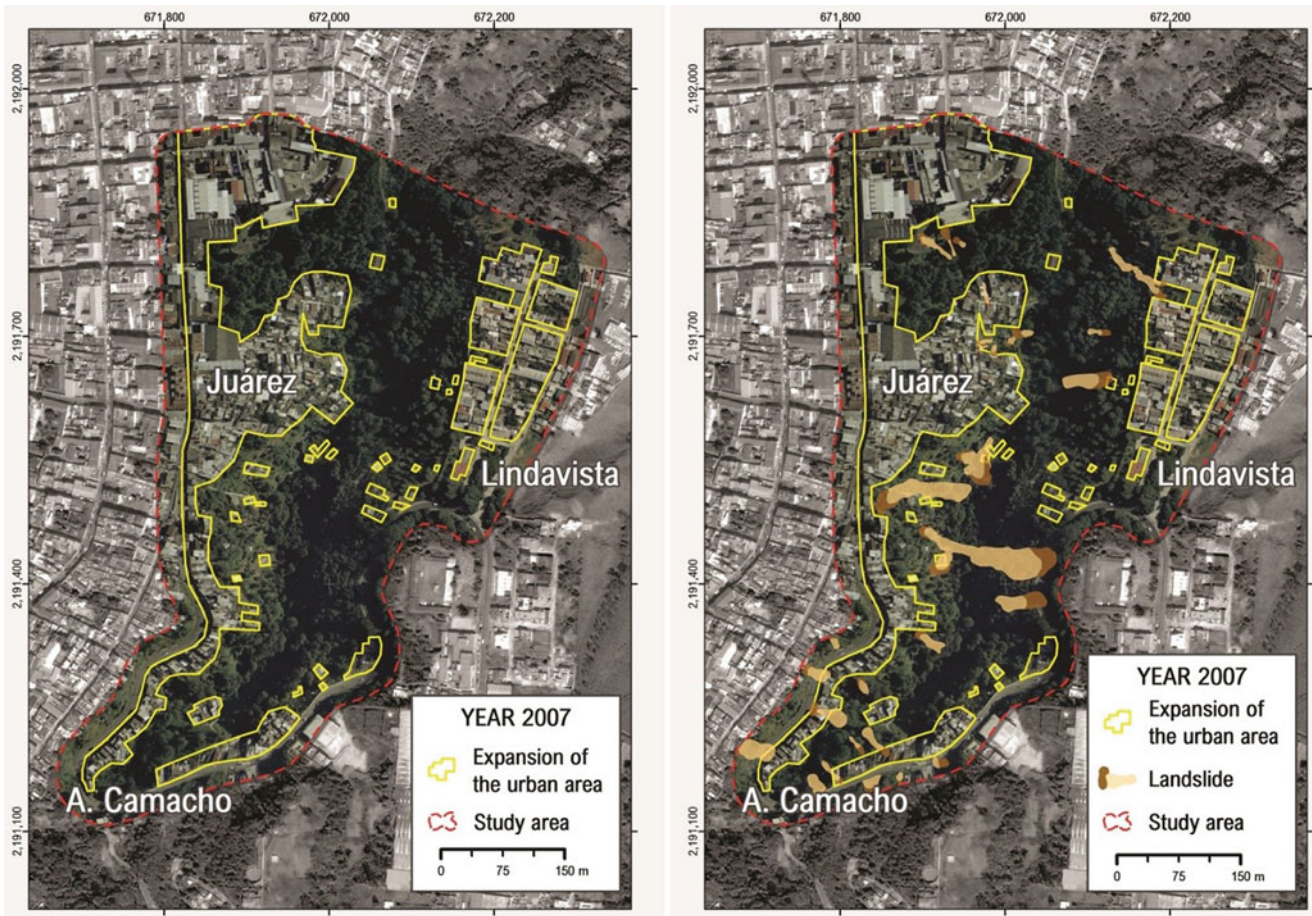


Fig. 5 Expansion of the urban area and spatial distribution of landslides on the inhabited dwellings in 2007

at risk about the importance of working together and the necessity to avoid the construction of new risks.



Fig. 6 Housing continues to be built, moving toward the bottom of the ravines, lacking proper drainage systems

6 Concluding Remarks

The skewed expansion of urban areas and the potential impacts of climate change (Adler et al. 2022) are among the most significant controls of landslide risk in Teziutlán, Puebla, México; a mountain zone highly susceptible to hill-slope instability. This condition requires the significant involvement of authorities and communities in order to understand and address landslide disaster risk. The latter is strongly linked to the perception of risk.

Landslide disaster risk perception plays a key role, not only in terms of behavior, but as a basic element to improve community awareness and preparedness of authorities oriented toward disaster risk management (Landeros-Mugica et al. 2016). This goes hand-in-hand with risk communication as a process in which, starting from their original perceptions,



Fig. 7 Expansion of the urban area and spatial distribution of landslides on the inhabited dwellings in 2017

it is possible to lead people to an adequate perception and to become aware of the risk involved.



Fig. 8 Built landscapes of a mixed nature have been constructed for immigrants who work for the maquila

Landslide disaster risk awareness requires significant efforts since it is closely related to people's perception of risk. Consequently, it is important to design strategies to raise awareness and sustain such educational attempts over time.

Although exploratory in nature, the analysis carried out in the paper provides insights and recommendations to support landslide disaster risk awareness by suggesting future actions at the local level. A key recommendation is to implement a landslide disaster risk awareness program during the main festivities and traditional gatherings organized in the municipality. Likewise, education and religious institutions, along with places of work and transport, should incorporate spaces for information dissemination. There are several challenges attached to this type of initiative, including the difficulty of landslides occurring through time, in other words, not only during the rainfall season but throughout the year.

Likewise, programs and content should be directed to each population group, and when possible, they should include education programs at all levels. Finally, we recognize that only with this kind of radical effort can science and

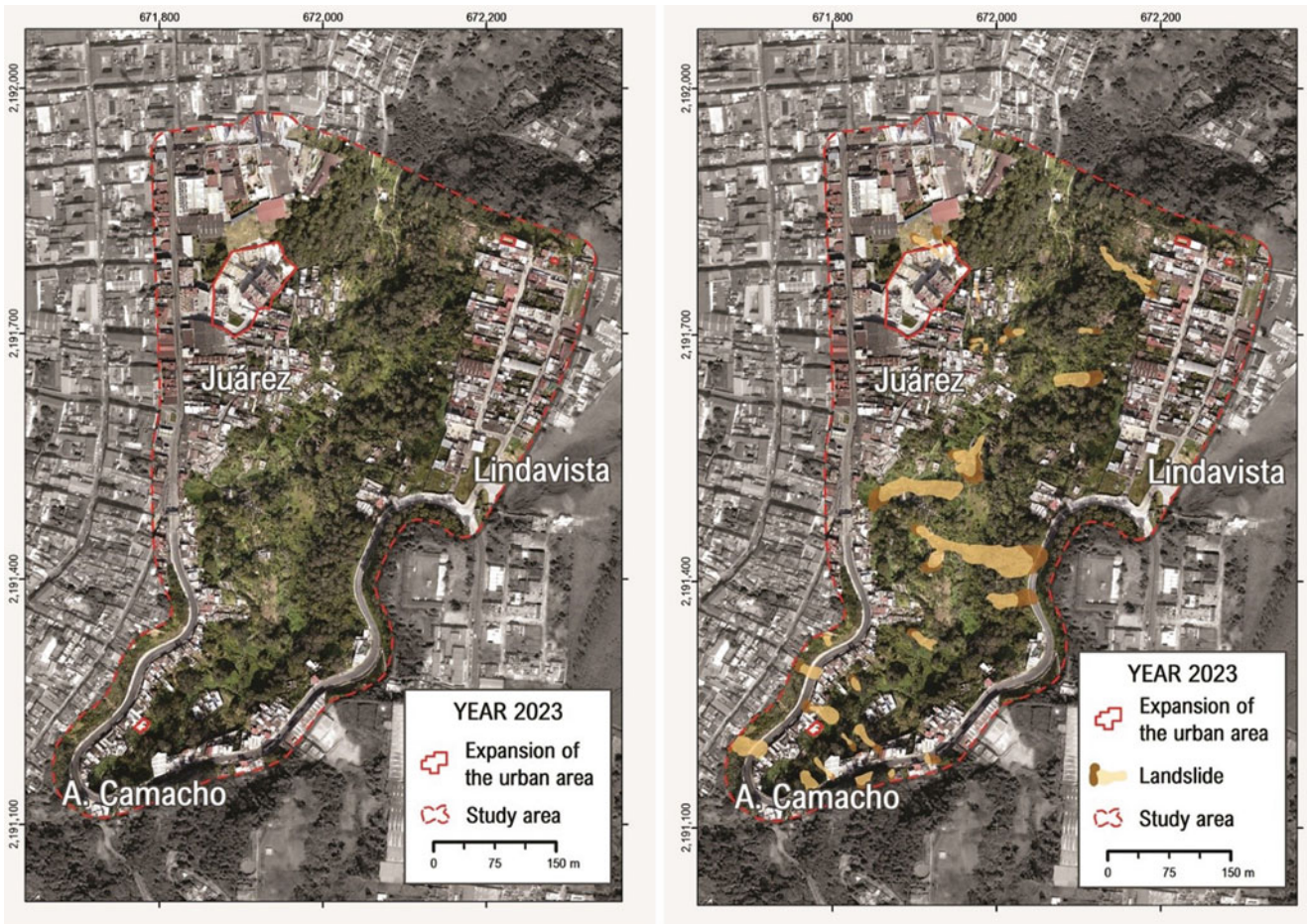
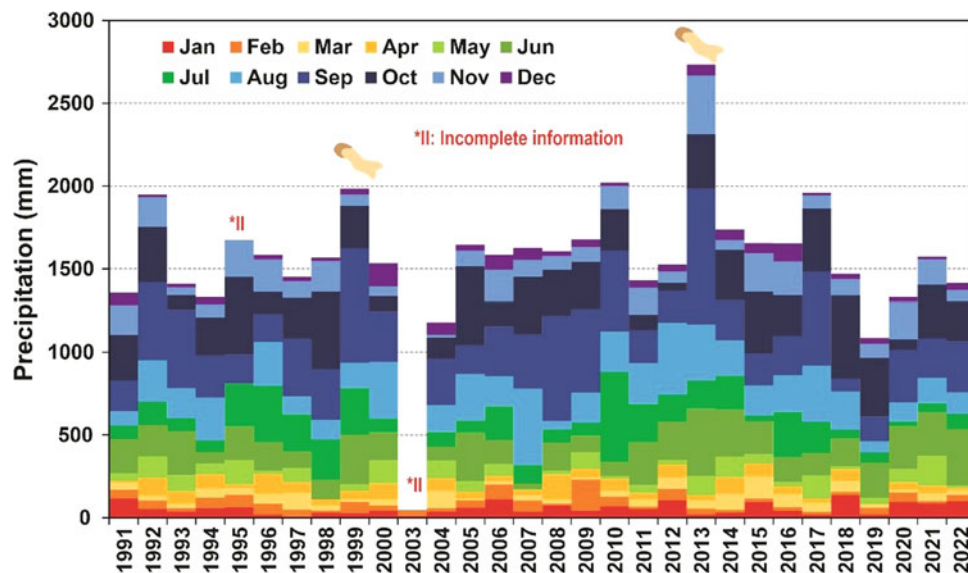


Fig. 9 Expansion of the urban area and spatial distribution of landslides on the inhabited dwellings in 2023



Fig. 10 New buildings constructed in areas highly susceptible to landslides in the Juárez neighborhood, 2023

Fig. 11 Monthly precipitation data at the Teziutlán, Puebla rain gauge, from 1991 to 2022 (Source: adapted from CONAGUA n.d.)



technology be intertwined with a solid commitment to the betterment of society (Alcántara-Ayala and Sassa 2021).

Acknowledgments We sincerely thank DGAPA-UNAM, who provided financial support to conduct landslide risk research through Project PAPIIT IN300823. Thanks are also to the paper's reviewers, whose comments and suggestions helped improve the manuscript.

References

- Adler C, Bhatt I, Huggel C, Muccione V, Prakash A, Alcántara-Ayala I et al (2022) Cross-chapter paper 5: mountains. In: Pörtner HO, Roberts DC et al (eds) IPCC [Intergovernmental Panel on Climate Change]. Climate change 2022: impacts, adaptation, and vulnerability. Contribution of working group II to the sixth assessment report of the intergovernmental panel on climate change. Cambridge University Press
- Alcántara-Ayala I (2004) Hazard assessment of rainfall-induced landsliding in Mexico. *Geomorphology* 61(1–2):19–40
- Alcántara-Ayala I (2018) TXT-tool 4.052-1.1: landslide risk perception. *Landslide dynamics: ISDR-ICL landslide interactive teaching tools: volume 2: testing, risk management and country practices*, 555–568
- Alcántara-Ayala I, Moreno AR (2016) Landslide risk perception and communication for disaster risk management in mountain areas of developing countries: a Mexican foretaste. *J Mt Sci* 1, 13, 12:2079–2093
- Alcántara-Ayala I, Garnica-Peña RJ, Coll-Hurtado A, de Gutiérrez MacGregor MT (Eds.) (2017) *Inestabilidad de Laderas en Teziutlán, Puebla. Factores inductores del riesgo (Landslides in Teziutlán, Puebla. Disaster Risk Drivers)*, Institute of Geography, UNAM, 223 pp. In Spanish
- Alcántara-Ayala I, Garnica-Peña RJ, Murillo-García FG, Salazar-Oropeza MO, Méndez-Martínez A, Coll-Hurtado A (2018) Landslide disaster risk awareness in Mexico: community access to mapping at local scale. *Landslides* 15(8):1691–1704
- Alcántara-Ayala I, Sassa K (2021) Contribution of the international consortium on landslides to the implementation of the Sendai framework for disaster risk reduction: engraining to the science and technology roadmap. *Landslides* 18:21–29
- Aucote HM, Miner A, Dahlhaus P (2010) Rockfalls: predicting high-risk behaviours from beliefs. *Disaster Prev Manag* 19:20–31
- Barnett J, Breakwell GM (2001) Risk perception and experience: hazard personality profiles and individual differences. *Risk Anal* 21:171–178
- CONAGUA (n.d.) Información Estadística Climatológica, <https://smn.conagua.gob.mx/es/climatologia/> In Spanish
- Finlay PJ, Fell R (1997) Landslides: risk perception and acceptance. *Can Geotech J* 34:169–188
- Garnica-Peña RJ, Alcántara-Ayala I (2017) Landslide synchronic evaluation by using unmanned aerial vehicles (UAV): some insights on disaster risk in Teziutlán, Puebla, México. In: *Advancing culture of living with landslides*, vol 2, pp 209–218
- Garnica-Peña RJ, Alcántara-Ayala I (2021) The use of UAVs for landslide disaster risk research and disaster risk management: a literature review. *J Mt Sci* 18(2):482–498
- Garnica-Peña RJ, Cardón-Idelfonso G, and Alcántara-Ayala I. (2021a). Landslide exposure community-based mapping: a first encounter in a small rural locality of Mexico. *Understanding and reducing landslide disaster risk: volume 1 Sendai landslide partnerships and Kyoto landslide commitment* 5th, 559–566
- Garnica-Peña RJ, García-Marroquin G, and Alcántara-Ayala I. (2021b) On the use of UAVs for landslide exposure of households: La Gloria Neighbourhood, Teziutlán, Puebla. *Understanding and reducing landslide disaster risk: volume 2 from mapping to Hazard and risk zonation* 5th, 457–466
- Gustafson PE (1998) Gender differences in risk perception: theoretical and methodological perspectives. *Risk Anal* 18:805–811
- Hernández-Moreno G, Alcántara-Ayala I (2017) Landslide risk perception in Mexico: a research gate into public awareness and knowledge. *Landslides* 14:351–371
- INEGI (2021) Censo de Población y Vivienda 2020—Cuestionario Básico (population and housing census 2020—basic questionnaire). Available at <https://www.gob.mx/inec/documentos/resultados-del-censo-de-poblacion-y-vivienda-2020-inegi> in Spanish
- Joffe H, Joffé H (1999) *Risk and 'the Other'*. Cambridge University Press
- Landeros-Mugica K, Urbina-Soria J, Alcántara-Ayala I (2016) The good, the bad and the ugly: on the interactions among experience, exposure and commitment with reference to landslide risk perception in México. *Nat Hazards* 1(80):1515–1537

- Murillo-García F, Alcántara-Ayala I (2017) Landslide inventory, Teziutlán municipality, Puebla, México (1942–2015). *J Maps* 13(2):767–776
- Murillo-García FG, Steger S, Alcántara-Ayala I (2019) Landslide susceptibility: a statistically-based assessment on a depositional pyroclastic ramp. *J Mt Sci* 16(3):561–580
- Pidgeon N, Hood C, Jones D, Turner B, Gibson R (1992) Risk perception. In G. Royal Society Study (Ed.). *Risk: analysis, perception, and management*. London, pp. 89–134
- Sassa K (2015) ISDR-ICL Sendai partnerships 2015–2025 for global promotion of understanding and reducing landslide. *Landslides* 12(4):631–640
- Sassa K (2016) Implementation of the ISDR-ICL Sendai partnerships 2015–2025 for global promotion of understanding and reducing landslide disaster risk. *Landslides* 13(2):211–214
- Sassa K (2018) Zero draft of the Kyoto 2020 commitment for global promotion of understanding and reducing landslide disaster risk. *Landslides* 15(3):389–392
- Sassa K (2020) Launching session of the Kyoto landslide commitment 2020. *Landslides* 17(8):1743–1744
- Slovic P (1987) Perception of risk. *Science* 236:280–285
- Solana MC, Kilburn CRJ (2003) Public awareness of landslide hazards: the Barranco de Tirajana, gran Canaria, Spain. *Geomorphology* 54: 39–48
- UNISDR (United Nations International Strategy for Disaster Reduction) (2015) Sendai framework for disaster risk reduction 2015–2030. UNISDR, Geneva
- UNISDR (2017) Report of the open-ended intergovernmental expert working group on indicators and terminology relating to disaster risk reduction. UNISDR, Geneva

Open Access This chapter is licensed under the terms of the Creative Commons Attribution 4.0 International License (<http://creativecommons.org/licenses/by/4.0/>), which permits use, sharing, adaptation, distribution and reproduction in any medium or format, as long as you give appropriate credit to the original author(s) and the source, provide a link to the Creative Commons license and indicate if changes were made.

The images or other third party material in this chapter are included in the chapter's Creative Commons license, unless indicated otherwise in a credit line to the material. If material is not included in the chapter's Creative Commons license and your intended use is not permitted by statutory regulation or exceeds the permitted use, you will need to obtain permission directly from the copyright holder.





Landslides in Higher Education Curricula and Beyond

Matjaž Mikoš

Abstract

Education is a human right and plays a decisive role in capacity building from the pre-school level to professional, under-, and postgraduate university study programmes in higher education institutions and beyond, such as summer schools or as a part of lifelong education for a general audience. It gives us a profession or helps the general population and diverse stakeholders (e.g., policy and decision makers) increase society's resilience against natural hazards, such as landslides. Thus, education finds a principal place also in numerous international documents accepted by the UN organizations.

The article looks at education as a topic of international strategic documents on disaster risk reduction. It uses diverse web tools and databases to assess worldwide efforts in teaching/education on landslides and their disaster risk reduction at higher education levels and beyond. The focus is on the higher education study programmes offering courses on slope stability and landslide mitigation. This topic is widely covered by study programmes in the field of disaster risk management and classical study programmes in civil, geological, geotechnical engineering, as well as in geology and geography. The second cycle covers the landslide topic, i. e. master study programmes and university programmes are prevailing. There is an apparent lack of academic programmes offered as blended programmes or distance learning programmes in disaster risk reduction, including landslide risk. Certificates and diploma levels prevail among academic programmes offered as online courses or continuing education.

The web search found a few (summer) schools dedicated to landslide topics and a variety of other open-access material that can be used for education and capacity

building, such as blogs, databases, teaching tools, presentations, or video lectures.

The International Consortium on Landslides might offer collected information in this article on its web pages under the topic "Educational tools" and then open it up to their members and landslide community to contribute to the content by sending links to elsewhere freely available educational material in landslide disaster risk reduction.

Keywords

Disaster Risk Reduction · Higher education · Landslides · MOOCs · Summer schools · Sustainable Development Goals · University curricula

1 Introduction

1.1 General Views on Higher Education

Article 26 of the United Nations Universal Declaration of Human Rights (UDHR) states "Everyone has the right to education. Education shall be free, at least in the elementary and fundamental stages. Elementary education shall be compulsory. Technical and professional education shall be made generally available and higher education shall be equally accessible to all on the basis of merit." (UN 1948).

The Sendai Framework for Disaster Risk Reduction 2015–2030 (UNDRR Preventionweb 2015) supports education as one of the strategic tools for its implementation. The term "culture of prevention and education" is used.

For the SFW "Priority 1: Understanding disaster risk", at the national and local levels, it is important to (UNDRR Preventionweb 2015; 24(g); 24(l)):

- To build the knowledge of government officials at all levels, civil society, communities and volunteers, as well as the private sector, through sharing experiences, lessons

M. Mikoš (✉)

University of Ljubljana, UNESCO Chair on Water-related Disaster Risk Reduction, Ljubljana, Slovenia
e-mail: matjaz.mikos@fgg.uni-lj.si

© The Author(s) 2023

I. Alcántara-Ayala et al. (eds.), *Progress in Landslide Research and Technology, Volume 2 Issue 2, 2023*, Progress in Landslide Research and Technology, https://doi.org/10.1007/978-3-031-44296-4_7

167

learned, good practices and training and education on disaster risk reduction, including the use of existing training and education mechanisms and peer learning;

- To promote the incorporation of disaster risk knowledge, including disaster prevention, mitigation, preparedness, response, recovery, and rehabilitation, in formal and non-formal education, as well as in civic education at all levels, as well as in professional education and training;

Understandably, landslides are not mentioned in these documents separately from other disasters and are covered under the more general topic of disaster risk reduction.

The Global Alliance for Disaster Risk Reduction & Resilience in the Education Sector (GADRRRES) is a multi-stakeholder platform comprised of UN Agencies, International Non-Governmental Agencies, other leading humanitarian and development organizations, and similar regional alliances, advocating for and supporting child rights, resilience, and sustainability in the education sector. In 2022, the “Comprehensive School Safety Framework 2022–2030—for Child Rights and Resilience in the Education Sector” was published (GADRRRES 2022). The framework provides a comprehensive approach to resilience and safety from all hazards (including landslide/rockslide, debris or mud-flow and glacial lake outbursts) and all risks confronting education and child protection sector populations, systems, and programs. It supports access, quality, and management strategies in the education sector.

Recently, UNESCO published a new social contract under the motto “Futures for Education”—a global initiative to reimagine how knowledge and learning can shape the future of humanity and the planet (UNESCO 2021). The report stresses the need for quality education throughout life (lifelong learning) and asks universities and other higher education institutions to be active in every aspect of building a new social contract for education. The topic of landslides, landslide research and technology, and landslide disaster risk reduction is clearly an education topic that must incorporate reinvented higher education goals, such as inter and intra-disciplinarity, lifelong learning approach, or programme diversity and flexible learning pathways (UNESCO 2022a).

Education is also strongly integrated into the IHP-IX Strategic Plan of the Intergovernmental Hydrological Programme (UNESCO IHP) entitled “Science for a Water Secure World in a Changing Environment” (UNESCO 2022b). This Ninth Phase of the UNESCO IHP is running in the period 2022–2029, sets one of five Performance Indicators (PI) as PI 2: The number of Member States with enhanced water informal, formal, and non-formal education at all levels, and as one five Priority Areas (PA) as PA 2: Water education in the Fourth Industrial Revolution including Sustainability (UNESCO 2022b). This document lists

among the challenges and opportunities also water security as the capacity of a population to ensure efficient protection of life and property against water-related hazards such as floods, landslides, land subsidence, and droughts.

The International Consortium on Landslides (ICL) accepted the Final Draft of the Kyoto 2020 Commitment for Global Promotion of Understanding and Reducing Landslide Disaster Risk which was signed by the first signatories in September 2019 (Sassa 2019). This commitment supports the implementation, follow-up, and review of the Sendai Framework 2015–2030, the UN 2030 Agenda for Sustainable Development, the New Urban Agenda, and the Paris Climate Agreement as it addresses the adverse effects of climate change.

The text of KLC2020 is available on the ICL web (ICL 2023b). Among the accepted 10 priority actions, Action 5 deals with: “The promotion of open communication with local governments and society through integrated research, capacity building, knowledge transfer, awareness-raising, training, and educational activities, to enable societies and local communities to develop effective policies and strategies for reducing landslide disaster risk, to strengthen their capacities for preventing hazards from developing into major disasters, and to enhance the effectiveness and efficiency of relief programs.” (ICL 2023b).

1.2 The Focus of this Article

The research questions in this article were: (i) assess the importance of higher education on specific landslides in selected international strategic documents on disaster risk reduction, and (ii) assess the worldwide efforts in teaching/educating on landslides and their disaster risk reduction in higher education curricula and beyond—in a more open education forms that are also offered by the International Consortium on Landslides.

2 Materials and Methods

The United Nations Office for Disaster Risk Reduction (UNDRR) Prevention web pages offer among other educational resources also, a list of academic programmes in disaster risk reduction (UNDRR 2022a, b). The platform offers 300+ academic programmes in the field of disaster risk management, at the following levels: bachelor, master’s, certificate/diploma, and doctorate, and of the following types: blended programme, continuing education, distance learning, online courses, and academic programmes.

When searching for master studies around the world, web pages of the FindAUniversity, Sheffield, UK, and their search platform “FindAMaster”, launched in 2004, were used

(FindAUniversity 2023). The platform is a directory of nearly 25,000 master's degrees and postgraduate qualifications at universities around the world—it includes Master's degree programmes, including part-time, distance learning, Master of Arts (MA), Master of Science (MSc), MBA (Master of Business Administration), Master of Research (MRes), and Master by Research (MPhil) programmes as well as other postgraduate study opportunities.

Another tool applied was the Studyportal (2023), offering 200,000+ courses at 3750+ educational institutes across 110 countries. The offered portals for each of the three Bologna cycle study programs: Bachelor degrees (www.bachelorsportal.com, 105,000+ Bachelors), Master degrees (www.mastersportal.com, 85,000+ Masters), and Ph.D. degrees (www.phdportal.com, 6000+ PhDs). Study programmes at each portal can be searched in 18 fields, such as Engineering & Technology, or Natural Sciences & Mathematics.

Furthermore, Google Search was performed using keywords: university, higher education, landslides, disaster risk control, certificate, certified.

Finally, we search the Web of Science (Clarivate Analytics 2023) using the keywords “summer school” AND “landslide”. Also, the web portal for summer schools in Europe (www.summerschoolsineroupe.eu) was tried to find landslide disaster risk reduction events.

3 Results and Discussion

3.1 Background Studies on Landslides and Study Programmes

Searching the SCOPUS and Web of Science databases for published studies on study programmes or courses regarding slope stability or landslides (mass movements, debris flows) revealed only a few published studies on this topic.

Bæverfjord and Thakur (2008) reported on two quick clay slides in Norway, and how these two case studies have impacted the teaching at the Norwegian University of Technology and Science (NTNU), Trondheim, Norway, provided by the Geotechnical Group at NTNU—mainly in the form of the International Master programme in Geotechnics and Geohazards.

Ozkazanc and Yuksel (2015) acknowledged the need for disaster mitigation education by determining the level of disaster awareness of students of Gazi University Faculty of Architecture, City and Regional Planning in Turkey.

Munoz et al. (2020) analyzed school safety and disaster education in South America (Brazil, Colombia) and the Caribbean (Cuba, the Dominican Republic, Jamaica, and Puerto Rico) in order to increase understanding of natural hazards and disaster preparedness.

Lo Presti (2013) reported on the intrinsic advantages and possible drawbacks of an inductive teaching approach at the University of Pisa (Italy) in the master course in Civil Engineering of Infrastructures, teaching a class on “slope stability” on the basis of a real case study. A later study reported on three-year experiences with this teaching approach (Giusti and Lo Presti 2015). Dewi (2020) on the other hand, stresses that combining fieldwork and research was possible to gain geography students' understanding of disaster risk reduction in the school community especially in disaster-prone areas such as Central Java, Indonesia. Ranglund et al. (2018) report on student gaming and active scenario building using different platforms during a Bachelor in Crisis Management and Communication course at The Inland Norway University of Applied Sciences. A virtual town was programmed in which different bad things happen, among them landslides. The students' reactions were very positive. These studies stress the importance of studying landslide disaster risk reduction in real cases, and it would be of great importance to have detailed databases on such landslide cases around the world so that educators can select appropriate cases and use them in the curriculum.

The need to incorporate natural hazards mitigation and strategies into engineering study programmes was not studied much in periodicals; two studies deal with civil engineering curriculum (Perdomo and Pando 2014; Cross and Kaklamanos 2017). Another recently published study looked at physics education students at Tadulako University in Indonesia, and their understanding on the environmental concept of landsliding (Hatibe et al. 2020). Similarly, a study by Labibah et al. (2020) aimed to find out the role of integrated landslide disaster education in physics subject viewed from high school student's preparedness in Kulon Progo, Yogyakarta in Indonesia, and concluded that it is very crucial to be implemented in learning and teaching activities using integrated learning model to raise disaster preparedness and students' science knowledge.

Guo et al. (2020) realized that landslide hazard education to the public could enhance their awareness of disaster risk. Since current disaster education is mainly aimed at students and ambulance personnel, where education methods focus on textbook teaching and professional training, there is a lack of effective communication channels between educators and the public. Hence, they proposed a visual representation method of landslide hazards, focusing on the combination of dynamic and static visual representation frameworks. This study stresses the potential of technologies such as augmented reality and visualization techniques in disaster risk dialogue and teaching natural hazards.

Sezgin and Cirak (2021) studied the role of Massive Open Online Courses (MOOC) in engineering education using an exploratory systematic review of peer-reviewed literature. Their study's findings indicate that online virtual labs, social

networks, flipped classroom strategy, active learning, small private online courses, and motivation are the key lodestar topics in “MOOCs in engineering education research” and engineering education researchers mostly employ practice-based and quantitative research approaches. Looking at Web of Science and using the search “MOOC AND disaster” in Topic (title, abstract, author keywords, Keywords Plus), yielded only 3 results, using the search “MOOC AND landslide*” yielded no hits whatsoever.

3.2 Academic Programmes in Disaster Risk Management

Using the PreventionWeb platform, over 300+ academic programmes were retrieved from the database—the details on the level and type of these programmes are given in Table 1.

Most academic programmes in disaster risk management are university programmes, among online courses certificates and diploma, are the most frequent levels; the same is true for continuing education. Not many academic programmes are offered as Ph.D. (Doctor of Philosophy), i.e., doctoral studies in disaster risk reduction. There is still much free room for distance learning courses and online courses of disaster risk reduction; this is also true for landslide disaster risk reduction.

3.3 University Study Programs in Disaster Risk Reduction & Management

Using FindAMaster platform, in total 35 master’s degrees were found as of February 2023 in disaster risk reduction. The offered degrees are from Master of Science (MSc), Master of Arts (MA), and Master of Research (MRes), over Postgraduate Certificates (PG Cert) to Postgraduate Diploma (PG Dip). The search results are presented in Table 2. Using the same platform again, 14 master’s degrees and 1 Ph.D. degree were found as of February 2023 in the field of landslide(s). The search results are presented in Table 3.

Using the Studyportals (2023) and searching for master’s degrees, within the discipline “Applied Sciences & Professions” and in the field of “Emergency & Disaster Management”, there are 202 master’s degrees—131 degrees were offered as on-campus learning, 89 degrees as on-line learning, and 10 as blended learning (several options for each degree were possible). Out of 202 degrees, 93 are offered in North America, 63 in Europe, 24 in Oceania, 19 in Asia, only 3 in Africa, and none in South America. In Table 4, selected master’s degrees out of 202 degrees listed in the Master portal are presented with links to the study programmes description. Comparably, using the Bachelor portal and the PhD portal, for the field of “Emergency & Disaster Management”, there are 148 bachelor’s degrees offered (110 in the North America, and 30 in Europe, and a few elsewhere), and only 3 PhD degrees.

Using the Google search for academic programmes, some results are presented in Table 5. Among other institutions, the University of Geneva offers a Specialization Certificate for the Assessment and Management of Geological and Climate Related Risk with a stand-alone Landslide Risk module (UG 2023). This module addresses landslide risk assessment: description and characterization and mechanisms of slope movements, such as landslide, rock instabilities, and debris flows are discussed; an overview of hazard, risk assessment and mapping are provided, including empirical and modeling approaches; finally protective measures are discussed. University of Twente offers a Master of Science programme in Geo-information Science and Earth Observation with eight specializations, including Natural Hazards and Disaster Risk Reduction (UT 2023).

The Massive Open Online Courses (MOCCs), invented in 2008 as a distance education tool, were widely introduced into education and distance learning in 2012. They are online teaching form reaching large numbers of students and are to be distinguished from traditional face-to-face classroom teaching. MOCCs that were found on the web using Google search and are related/covering topics on slope stability and landslides are presented in Table 6. Quite some courses are available for free of different levels (no prior knowledge necessary), can be absolved after enrolling before flexible

Table 1 Academic programmes found as of early February 2023 in the PreventionWeb platform in disaster risk reduction (UNDRR 2022b)

Academic programme type	Academic programme level			
	Bachelor	Certificate/Diploma	Masters	Doctorate
Blended programmes	1	3	7	0
Continuing education	1	15	1	0
Distance learning	3	7	2	0
Online courses	1	19	8	0
University programmes	36	58	115	24

Table 2 The selected master's degrees in disaster risk reduction as of early February 2023, using the FindAMaster platform (www.findamasters.com), sorted by the institution name

University	Title of the program	Source
Bournemouth university	MSc—Disaster management	https://www.findamasters.com/masters-degrees/course/msc-disaster-management/?i21d4134c50143
Coventry University	MSc—Disaster management and resilience	https://www.findamasters.com/masters-degrees/course/disaster-management-and-resilience-msc/?i49d2694c2601
	PGCert—Disaster, risk and resilience	https://www.findamasters.com/masters-degrees/course/disaster-risk-and-resilience-pgcert/?i49d2694c65862
Durham University	MA—Climate, risk & society	https://www.findamasters.com/masters-degrees/course/ma-climate-risk-and-society/?i67d5259c17271
	MA—Environmental Hazards & Risk	https://www.findamasters.com/masters-degrees/course/ma-environmental-hazards-and-risk/?i67d5259c69422
	MSc—Climate, risk & society	https://www.findamasters.com/masters-degrees/course/msc-climate-risk-and-society/?i67d5259c69421
	MSc—Environmental Hazards & Risk	https://www.findamasters.com/masters-degrees/course/msc-environmental-hazards-and-risk/?i67d5259c69423
Loughborough University	MSc—Flood modelling and management	https://www.findamasters.com/masters-degrees/course/msc-flood-modelling-and-management/?i153d6593c66891
Northumbria University, Newcastle	MSc—Disaster management and sustainable development	https://www.findamasters.com/masters-degrees/course/msc-disaster-management-and-sustainable-development-1-year-full-time/?i180d8389c60164
TATA Institute of Social Sciences, Mumbai	MA / MSc—Disaster management	https://www.findamasters.com/masters-degrees/course/master-of-arts-master-of-science-disaster-management-mumbai-campus/?i3729d8877c69517
University of Manchester	MSc—International disaster management	https://www.findamasters.com/masters-degrees/course/msc-international-disaster-management/?i332d4473c28896
	MSc—International disaster management and humanitarian response	https://www.findamasters.com/masters-degrees/course/msc-international-disaster-management-and-humanitarian-response/?i332d4473c61743
University College London (UCL)	MSc / PG dip—Earthquake engineering with disaster management	https://www.findamasters.com/masters-degrees/course/earthquake-engineering-with-disaster-management-msc-pg-dip/?i274d1826c20036
	MSc / PG dip—Engineering for international development	https://www.findamasters.com/masters-degrees/course/engineering-for-international-development-msc-pg-dip/?i274d1826c35277
	MSc / PG cert—Space risks & disaster reduction	https://www.findamasters.com/masters-degrees/course/space-risks-and-disaster-reduction-msc-pg-cert/?i274d1844c45247
	MRes—risk and disaster reduction	https://www.findamasters.com/masters-degrees/course/risk-and-disaster-reduction-mres/?i274d8712c24436
	MSc / PG dip—Risk, disaster and resilience	https://www.findamasters.com/masters-degrees/course/risk-disaster-and-resilience-msc-pg-dip/?i274d8712c40321
University of Bristol	MSc—Earthquake engineering and infrastructure resilience	https://www.findamasters.com/masters-degrees/course/earthquake-engineering-and-infrastructure-resilience-msc/?i287d6200c48844
University of Derby	MSc—Intelligence, security and disaster management	https://www.findamasters.com/masters-degrees/course/intelligence-security-and-disaster-management-msc/?i295d3397c50014
University of Twente	MSc—Geo-information science and earth observation	https://www.findamasters.com/masters-degrees/course/geo-information-science-and-earth-observation-msc/?i754d8913c70327
Van Hall Larenstein, University of Applied Sciences	MSc—Management of Development—Specialisation disaster risk management	https://www.findamasters.com/masters-degrees/course/master-of-management-of-development-msc-specialisation-disaster-risk-management/?i962d6062c22679

deadlines, following its own pace, and allow even getting a certificate for reasonable money after a successful completion of the course.

3.4 Selected Summer Schools on Landslides

A search in January 2023 in the Web of Science Core Collection (Clarivate Analytics 2023) using a search combination

“summer schools” AND “landslide” yield only 7 hits, among those the following ones presented below.

- One-week Innsbruck Summer School of Alpine Research 2015 on close-range sensing techniques in Alpine terrain in Obergurgl, Austria, by an international team from several universities and research centers (Rutzinger et al. 2018). Of the applicants, a group of 40 early career researchers was selected with interest in about ten types

Table 3 The Master and PhD degrees covering the topic of landslides as of early February 2023, using the FindAMaster platform (www.findmasters.com) and Keystone Masterstudies platform (www.masterstudies.com), sorted by the institution name

University	Title of the program	Source
Aberdeen University, UK	MSc—Advanced mechanical engineering	https://www.findmasters.com/masters-degrees/course/advanced-mechanical-engineering-msc/?i2d4439c46741
Cardiff University, UK	MSc—Environmental hazards	https://www.findmasters.com/masters-degrees/course/environmental-hazards-msc/?i33d2698c59177
Durham University, UK	MA—Environmental Hazards & Risk	https://www.findmasters.com/masters-degrees/course/ma-environmental-hazards-and-risk/?i67d5259c69422
	MSc—Environmental Hazards & Risk	https://www.findmasters.com/masters-degrees/course/msc-environmental-hazards-and-risk/?i67d5259c69423
Hong Kong University of Science and Technology, China	MPhil—Civil engineering	https://www.findmasters.com/masters-degrees/course/master-of-philosophy-in-civil-engineering/?i1175d8726c66299
Massey University, New Zealand	MSc—Geography	https://www.findmasters.com/masters-degrees/course/msc-environmental-hazards-and-risk/?i67d5259c69423
Newcastle University, UK	MPhil—Civil engineering (water resources)	https://www.findmasters.com/masters-degrees/course/civil-engineering-water-resources-mphil/?i177d7800c9419
University College London (UCL), UK	MSc—Geophysical hazards	https://www.findmasters.com/masters-degrees/course/geophysical-hazards-msc/?i274d1839c20112
Université Côte d’Azur, France	MSc—Environmental hazards and risk management	https://www.findmasters.com/masters-degrees/course/msc-in-environmental-hazards-and-risk-management/?i336d8370c62864
University of Otago, New Zealand	MAppSc—Applied geology	https://www.findmasters.com/masters-degrees/course/master-of-applied-geology-mappsc/?i653d6470c58949
	MSc—Geology	https://www.findmasters.com/masters-degrees/course/master-of-geology-msc/?i653d6470c58981
University of Padua, Italy	Water and geological risk engineering	https://www.findmasters.com/masters-degrees/course/water-and-geological-risk-engineering/?i1283d7794c63814
University of Pavia, Italy	MSc—Environmental engineering—Reach: REsilience to climAte CHange effects	https://www.findmasters.com/masters-degrees/course/environmental-engineering-curriculum-in-reach-resilience-to-climate-change-effects/?i1940d8374c68290
	MSc—Civil engineering for mitigation of risk from natural hazards	https://www.masterstudies.com/Master-degree-in-Civil-Engineering-for-Mitigation-of-Risk-from-Natural-Hazards/Italy/Uni-Pavia/
University of Plymouth, UK	ResM—Geological sciences	https://www.findmasters.com/masters-degrees/course/resm-geological-sciences/?i341d764c63976
University of Portsmouth, UK	PhD—Environment, geography and geosciences	https://www.findmasters.com/masters-degrees/course/environment-geography-and-geosciences-distance-learning-phd/?i343d750c65336
	MSc—Geological and environmental hazards	https://www.findmasters.com/masters-degrees/course/geological-and-environmental-hazards-msc/?i343d750c492

of specialized surveying tools, i. e. laser scanners, a remotely piloted aircraft system, a thermal camera, a backpack mobile mapping system, and different grade photogrammetric equipment.

- The Geoinformatics Building Technology and Research Centre, Department of Civil Engineering, Chitkara University, Himachal Pradesh organized a “Natural Resource Database Management System—Department of Science and Technology (NRDMS—DST) sponsored 21-day Summer School on Geospatial Technologies (Level 2) Mountain Disaster Management—Landslide” from 9 to 29th May 2019 (Prakasam et al. 2022). The theme of the training programme was “Landslide Disaster Management and Modelling through various geospatial technologies, hands-on approach, and field training”. Participants from

various backgrounds, such as researchers, academicians, scientists, administrative staff, NDMA & NDRF officers, have been selected to attend the summer school. The training programme mainly focused on various aspects of landslides, such as vulnerability and risk assessment, slope stability assessment and stabilization measures, field techniques for collecting data, and high-resolution 2D and 3D modelling.

- A Summer School on “Landslides and Slope Stability Analysis in Rwanda” took place in 2022 at Rwanda Polytechnic—College of Musanze (Rwanda) (Valentino et al. 2023). The Summer School was organized by the hosting institution (Rwanda Polytechnic—College of Musanze) in cooperation with the University of Parma (Italy), Rwanda Water Resources Board (RWB), and

Table 4 The selected master's degrees in emergency & Disaster Management as of early February 2023, using the Master portal platform (www.mastersportal.com), sorted by the institution name

University	Title of the program	Source
Georgetown University, Washington D.C, USA	Master—International emergency and disaster management	https://www.mastersportal.com/studies/363581/international-emergency-and-disaster-management.html
National Taiwan University, Taipei, Taiwan	MSc—Disaster risk reduction and resilience	https://www.mastersportal.com/studies/367568/disaster-risk-reduction-and-resilience.html
University College London, London, United Kingdom	MSc—Risk and disaster science	https://www.mastersportal.com/studies/270375/risk-and-disaster-science.html
	MSc—Risk, disaster and resilience	https://www.mastersportal.com/studies/41933/risk-disaster-and-resilience.html
	MSc—Risk and disaster reduction	https://www.mastersportal.com/studies/41598/risk-and-disaster-reduction.html
University of Canterbury, Christchurch, New Zealand	Master—Disaster, risk and resilience	https://www.mastersportal.com/studies/320283/disaster-risk-and-resilience.html
University of Manchester, Manchester, United Kingdom	MSc—International disaster management	https://www.mastersportal.com/studies/72553/international-disaster-management.html
University of Newcastle, New South Wales, Australia	Graduate certificate—Disaster risk reduction	https://www.mastersportal.com/studies/299561/graduate-certificate-in-disaster-risk-reduction.html
York University, Toronto, Canada	Master—Disaster and emergency management	https://www.mastersportal.com/studies/91066/disaster-and-emergency-management.html

Table 5 The master's degrees that offer courses on slope stability and landslides as of early February 2023, using the Google search platform (www.google.com), sorted by the institution name

University	Title of the program	Course on Landslides	Source
EPFL, Lausanne, Switzerland	MSc—Civil engineering	CIVIL-530 slope stability	https://edu.epfl.ch/coursebook/en/slope-stability-CIVIL-530
National Graduate Institute for Policy Studies (GRIPS), Tokyo, Japan	Master – Disaster management	Control measures for Landslide & Debris Flow	https://www.grips.ac.jp/en/education/inter_programs/disaster/
Norwegian University of Science and Technology (NTNU), Norway	MSc—Geotechnics and Geohazards & MSc—Geotechnology	TGB4290 landslides	https://www.ntnu.edu/studies/courses/TGB4290
		TBA5150 Geohazards and risk	https://www.ntnu.edu/studies/courses/TBA5150
University of Geneva, Switzerland	Specialisation certificate for the assessment and Management of Geological and Climate Related risk	Landslide risk module	https://www.unige.ch/sciences/terre/CERG-C/training/terrain/
University of Calgary, Alberta, Canada	MSc—Civil engineering	ENCI 675 landslides and slope stability	https://contacts.ucalgary.ca/info/enci/courses/f21/ENCI675
University of Genoa, Italy	MSc—Engineering for natural risk management	94,641 landslide hazards	https://corsi.unige.it/en/off.f/2021/ins/51119
University of Pavia, Italy	MSc—Civil Engineering for Mitigation of Risk from Natural Hazards	GEO05 landslide hazard and risk	http://civrisk.unipv.it/hyris/landslide-hazard-and-risk-2/
University of Pennsylvania, USA	MSc—Applied geoscience	GEOL 672690 Landslides	https://www.lps.upenn.edu/courses/landslides/2021a
University of Twente, Netherlands	MSc—Geo-information science and earth observation	Data-driven Hazard modelling Disaster risk management Physically-based Hazard modelling	https://studyguide.itc.nl/m-geo/all-courses/201800282/data-driven-hazard-modelling https://studyguide.itc.nl/m-geo/all-courses/201800304/disaster-risk-management https://studyguide.itc.nl/m-geo/all-courses/201800289/physically-based-hazard-modelling
University of Wisconsin—Madison, USA	Interdisciplinary professional program	Slope stability and landslides	https://interpro.wisc.edu/courses/slope-stability-and-landslides/
Western University, Ontario, Canada	MSc—Civil and environmental engineering	CEE9621a landslides and slope stability	https://www.eng.uwo.ca/civil/graduate/current_students/graduate_courses/CEE-9621a-2020-outline.pdf

Table 6 The Massive Open Online Courses (MOOCs) also covering topics on slope stability and landslides as of mid-February 2023, using the Google search platform (www.google.com), sorted by the institution name

Institution	Title of the MOOC	Source
EO4GEO alliance & ISPRA, Italy	Landslide affecting cultural heritage sites—Roman Thermae of Baia	http://www.eo4geo.eu/training-actions/eo4geo-mooc/
École Polytechnique Fédérale de Lausanne (EPFL), Lausanne, Switzerland	A resilient future: Science and technology for disaster risk reduction	https://www.edx.org/course/a-resilient-future-science-and-technology-for-disa
Hong Kong University of Science and Technology (HKUST), China	Slope engineering—understanding landslides using slope engineering concepts.	https://www.hkmooc.hk/courses/HKUST+CIVIL-slope
GEOMAR Helmholtz Centre for Ocean Research, Kiel & Kiel University, Germany	One planet—One ocean: From science to solutions—Part on 5.3 submarine landslides and tsunamis	https://www.edx.org/course/one-planet-one-ocean
TH Köln—University of Applied Sciences, Germany—regional climate and disaster resilience e-learning platform	EDRR001: Disasters and ecosystems: Resilience in a changing climate	https://courses.adpc.net/courses/course-v1:CNRD+EDRR001+2017_T1/about
University of Alaska, Fairbanks, USA	Synthetic aperture radar: Foundations	https://www.edx.org/course/sar-foundations
University of Alaska, Fairbanks, USA	Synthetic aperture radar: Hazards	https://www.edx.org/course/sar-hazards
University of Alaska, Fairbanks, USA	Synthetic aperture radar: Ecosystems	https://www.edx.org/course/sar-ecosystems
University of Alaska, Fairbanks, USA	Professional certificate in SAR: Applications	https://www.edx.org/professional-certificate/alaskax-synthetic-aperture-radar-sar-applications
University of Pittsburgh, USA	Disaster preparedness	https://www.coursera.org/learn/disaster-preparedness
UN Environment Programme (UNEP) & Partnerships for Environment and Disaster Risk Reduction (PEDRR)	Certificate course on nature-based solutions (NbS) for disaster and climate resilience	https://pedrr.org/mooc
UN Office for Outer Space Affairs (UNOOSA) & Centre for Space Science & Technology Education in Asia and the Pacific (CSSTEAP)	Geospatial applications for disaster risk management	https://www.preventionweb.net/news/mooc-geospatial-applications-disaster-risk-management

Rwanda Transport Development Agency (RTDA) in the framework of the Erasmus + EnRHed project (<https://enrhed-erasmusplus.com/>) (Petrella et al. 2022).

The EnRHed project (“Enhancement of Rwandan Higher Education in strategic fields for sustainable growth”) was co-funded by the European Commission and is coordinated by the University of Parma. Among the strategic fields for sustainable development, this project deals with “Environmental protection, safety, and management.” In this domain, the topic of landslides plays a fundamental role, especially referring to the Rwandan context. It was the first time such a kind of Summer School on slope stability analysis took place in Rwanda. Besides the organizing institutions, the Summer School was supported by many other sponsors, like ICL—International Consortium on Landslides, AIGeo—Italian Association of Physical Geography and Geomorphology, IAH Italian Chapter—International Association of Hydrogeologists, Rocscience Inc., and the University of Parma.

Also search in abstracts, titles and keywords in the SCOPUS database using terms “summer school”, “landslide”, “debris flow”, and “mass movement” revealed no new hits compared to the Web of Science database.

Nevertheless, summer schools are popular forms of training, especially for post-graduate (master) and doctoral (Ph.D. and post-doc) students and young researchers in general. In July 2016, a post-graduate training school on landslides and other geological hazards in active volcanic environments was offered in the Azores, Portugal (<https://formose2016.wixsite.com/formose2016>). In 2019, a summer school was organised in NE Italy for early-career scientists on historic and prehistoric landslides in the northern Italian Alps with implications for new hazard maps in mountainous areas. In July 2024, as a forerunner to the 14th International Symposium on Landslides to be held in Chambéry, France (<https://www.isl2024.com/>), a short summer school is offered on an overview of the fundamentals of slope engineering.

3.5 Landslide-Related Capacity Building Examples

There are a few international summer schools closely related to landslide research and mitigation worth being mentioned specifically. The first one is a summer school in Europe, and the other two are organized in Asia. It follows a list of more than a dozen landslide-related capacity-building cases—among others the ICL initiative for a landslide school network, ICL Teaching Tools, ICP/IPL World Report on Landslides, and further educational materials (blogs, portals, platforms, databases, lectures).

3.6 Case 1: The International School on Landslide Risk Assessment and Mitigation (LARAM)

The International School on “LAndslide Risk Assessment and Mitigation” (LARAM, <http://www.laram.unisa.it>), was founded in 2005 as a pioneering didactic and research initiative of the Geotechnical Engineering Group of the University of Salerno (Cascini et al. 2012). The main activity of LARAM is a yearly 2-week School for Ph.D. students and Young Doctors. The main objectives of LARAM are to develop high educational interdisciplinary programs for assessing, forecasting, and mitigating landslide risk at different scales and to promote the creation of training programs aimed at solving real landslide risk problems using the most advanced theories and methodologies in the fields of geotechnical engineering, geomechanics, geology, physical geography, mathematical modelling, monitoring, GIS techniques, risk management, and other relevant topics. Other initiatives include shorter courses, scientific sessions and workshops, research projects and other dissemination activities (Cascini et al. 2021).

Since 2006, 11 editions were held in Salerno, Italy, 3 editions were held in Chengdu, China. More details on the number and geographical distribution of the students selected to participate in the LARAM doctoral school are reported in Cascini et al. (2018). Over 200 Universities provided the doctoral school with 591 Ph.D. students from 2006 to 2018 (Cascini et al. 2019). In 2020, the LARAM school went online (Cascini et al. 2020), and in 2021, the LARAM school was announced on the Landslide Blog (AGU 2021), and in 2022 on the PreventionWeb pages (UNDRR 2022c).

3.7 Case 2: Kokomerem Summer School on Rockslides and Related Phenomena in the Kokomeren River Valley (Kyrgyzstan)

ICL Annual Summer School on Rockslides and Related Phenomena in Kyrgyzstan (Strom 2014) started in 2006 (Strom and Abdrakhmatov 2009, 2013), being supported by the IPL Projects M111, M126 and finally C106-2 (Mikoš et al. 2023). The schools are running ever since 2006, being interrupted only by COVID-19 pandemic (Strom and Abdrakhmatov 2013, 2015a, b, 2018, 2019, 2023).

This training course aims to familiarize students and young landslide researchers with various types of large-scale bedrock landslides (rockslides), with geological factors favorable for their origin and with their primary and secondary effects such as river damming and subsequent outburst floods.

3.8 Case 3: The International Research Association on Large Landslides (iRALL) School

The International Research Association on Large Landslides (iRALL; <http://irall.skjlgp.cdut.edu.cn/index.htm>) was founded in 2015. Its secretariat is located at the State Key Laboratory of Geohazard Prevention and Geoenvironment Protection, Chengdu University of Technology, China. The school was established in 2016 and offers annually high-level courses, focusing on the investigation, analysis, and management of large landslides for Ph.D. students and postdocs from all over the world, with international experts on the research of large landslides as teaching staff. The last edition of iRALL School 2022 offered 4 days introductory courses, cutting-edge progress, and software training. The topics covered landslide hazard identification, earthquake induced landslide mechanism, rainfall induced landslide hydrological control, large-scale debris flow mechanism, glacial hazards, remote sensing, and numerical simulation technology in the application of landslide hazards.

3.9 Case 4: ICL Landslide School Network

In 2011, the International Consortium on Landslides, Kyoto, Japan, initiated a proposal for the ICL Landslide School Network (Karnawati and Yin 2011) as an ICL contribution to worldwide efforts for effective landslide risk reduction. A special 3-page guideline for this network was prepared (ICL 2010) as the network starting point. In 2012, the proposal for the network was upgraded to the ICL Capacity Development Network, coordinated by the University Gadjah Mada, Indonesia (ICL 2012). The last progress report published on

the ICL web pages is from 2018 (<https://www.landslides.org/projects/icl-networks/>).

3.10 Case 5: ICL Landslide Teaching Tools

In 2013, International Consortium on Landslides (ICL) has decided to compile a collection of landslide teaching tools (Sassa et al. 2013) to provide teaching materials to ICL members and other landslide teaching entities to assist in the education of university students, local government officers, staff in nongovernmental organizations, and the public. The teaching toolbox contains five parts (He et al. 2014): (1) mapping and site prediction; (2) monitoring and early warning; (3) testing and numerical simulation; (4) risk management; and (5) country practices and case studies. The teaching toolbox contains three types of tools: (1) TXT tools consisting of original texts with figures; (2) PDF tools consisting of already published reference papers, manuals, guidelines, and others; and (3) PPT tools consisting of PowerPoint® files made for lectures.

In 2018, the ICL published the second and quite expanded edition of its landslides teaching tools, providing numerous teaching tools from a variety of international organizations and institutes, and it included guidelines for monitoring, modeling, and capacity development in:

- Volume 1 on fundamentals, mapping, and monitoring (Sassa et al. 2018a), and in
- Volume 2 on testing, risk management, and country practices (Sassa et al. 2018b)

Since the introduction of the ICL open-access book series “Progress in Landslide Research and Technology” (P-LRT) (Sassa 2021b), articles on teaching tools are published in this book series. In P-LRT Volume 1 Issue 1 an article on the software LS-RAPID presenting its manual and video tutorials was published (Ajmera et al. 2023). In P-LRT Volume 1 Issue 2 an article was published on undrained dynamic loading ring shear testing with video (Loi et al. 2023), and an article how to reach remotely the vegetation works to protect slopes against mass wasting by using video materials as a case study in Bhutan (Hirota et al. 2023). In P-LRT Volume 2 Issue 1, an article on the application of LAND-SUITE for zonation of landslide susceptibility in Spain (this volume), and an article on landslide and soil erosion inventory mapping based on high-resolution remote sensing data as a case study in Croatia will be published (this volume). All ICL landslide teaching tools are useful teaching materials for summer schools or higher education curriculum focused on landslide disaster risk reduction.

3.11 Case 6: ICL/IPL World Report on Landslides

The International Consortium on Landslides (ICL) and International Program on Landslides (IPL) created web data base and web cooperation platform for sharing information about landslide case studies in the global landslide community. The idea of World Report on Landslides (WRL) was initiated in 2010, and rules for web publication were defined in 2014 (Abolmasov et al. 2017). This activity was a ICL and IPL contribution to the Sendai Partnership 2015–2030 for Global Promotion of Understanding and Reducing Landslide Disaster Risk (Sassa 2015), and to the Sendai Framework for Disaster Risk Reduction 2015-2030 (UNDRR PreventionWeb 2015).

This platform is still not as active as it might be for the benefit of the world landslide community, also for educators to use it in courses on slope stability and landslides. The advantage of this platform is that it gives an opportunity to publish on the web a very detailed case study with all technical details of a landslide.

3.12 Case 7: UNDRR PreventionWeb Platform

The United Nations Office for Disaster Risk Reduction (UNDRR) offers the PreventionWeb (www.preventionweb.net), the collaborative global knowledge sharing platform for disaster risk reduction and resilience. The site offers a range of knowledge products and services to facilitate the work of DRR professionals. The PreventionWeb features content that helps DRR stakeholders better understand disaster risk and learn from implementing DRR strategies, policies, and measures. There is freely available educational material, for the search on “landslide(s)” with 762 results as of February 2023 (417 news, 247 publications, and 64 events).

The PreventionWeb platform lists academic programmes across the world which offer education on all levels (including bachelor, master, diploma, etc.) related to disaster risk reduction.

Under the topic “Educational materials”, the PreventionWeb platform also offers a variety of children’s books, textbooks, lesson plans, activities, games, and online resources on disaster prevention and school safety—from pre-school and kindergarten level to secondary schools.

3.13 Case 8: United States Geological Survey (USGS) Web Sources

The United States Geological Survey (USGS; <https://www.usgs.gov/>) offers a variety of web tools that can be used for educational purposes in the field of natural hazards, including

for landslide disaster risk reduction and capacity building. There is a short overview of some of the useful tools:

- Global Earthquake-Triggered Ground Failure Inventory Database that includes repository of Earthquake-Triggered Ground-Failure Inventories Web Application (interactive map) and An Open Repository of Earthquake-Triggered Ground-Failure Inventories (data) (USGS 2023a).
- Comprehensive Global Database of Earthquake-Induced Landslide Events and Their Impacts (ver. 2.0, February 2022; Seal et al. 2022; USGS 2023b).
- USGS Public Lecture Series (USGS 2023c) that offer virtual attendance using live streaming of the public lecture over the MSTeams® platform.

3.14 Case 9: NASA Models and Datasets

With actionable Earth observations, the NASA Earth Science Applied Sciences Program empowers communities across the world to find solutions to the challenges they face every day (<https://appliedsciences.nasa.gov/>). One of the projects on this web platform is entitled “Enabling Landslide Disaster Risk Reduction and Response throughout the disaster life cycle with a multi-scale toolbox” (NASA 2023a). This project is a part of NASA landslide research and is advancing landslide hazard assessment and forecasting using machine learning models, satellite data, model products, and post-event information that describes where landslides have taken place. This project provides the only open-source, continually updating model of rainfall-triggered landslide hazards available in near real-time across most of the world.

The global Landslide Hazard Assessment for Situational Awareness (LHASA) model was developed by NASA that combines Global Precipitation Model (GPM; <https://gpm.nasa.gov/>) near real-time precipitation data with a global susceptibility map to generate estimates of where and when rainfall-triggered landslides are likely to occur around the world (NASA 2023b). Information on landslide reports is available on the Cooperative Open Online Landslide Repository (COOLR; <https://gpm.nasa.gov/landslides/>), which combines data from NASA’s Global Landslide Catalog, other landslide inventories and contributions from citizen scientists via the [Landslide Reporter Application](https://maps.nccs.nasa.gov/apps/landslide_reporter/) (https://maps.nccs.nasa.gov/apps/landslide_reporter/).

3.15 Case 10: The Landslide Blog in AGU Blogosphere

The American Geophysical Union (AGU) hosts so-called Blogosphere (<https://blogs.agu.org/>) with numerous blogs,

among them the Landslide Blog (<https://blogs.agu.org/landslideblog/>) run by David Petley of the University of Hull, UK. The Landslide Blog provides commentary and analysis of landslide events occurring worldwide, including the landslides themselves, the latest research, and conferences and meetings.

3.16 Case 11: BeSafeNet Platform

The BeSafeNet initiative, starting in 2003 and promoted by the EUR-OPA Major Hazards Agreement of the Council of Europe, has as a main aim, to better protect people from hazards through better informing them on the causes and the consequences of natural and technological hazards (Micallef et al. 2014). This web platform “BE-SAFE-NET” is a tool for promoting risk culture among populations, focusing on teachers to prepare material for elementary school students (BeSafeNet 2023), also covers natural hazards’ topic on landslides (<https://besafenet.net/hazards/landslides/>)—the page was prepared by CERG—European Centre on Geomorphological Hazards from Strasbourg, France (Maquaire et al. 2009).

3.17 Case 12: The International Society for Rock Mechanics and Rock Engineering (ISRM) Course

The ISRM course on "Prevention methods for Landslides in Rock Masses" is now available in open access (ISRM 2023). The course has four parts, with a total of 24 lectures:

- Part A—Understanding landslides in rock mass (four lectures)
- Part B—Methods for quantifying rock mass (eight lectures)
- Part C—Methods for landslide potential of rock mass (five lectures)
- Part D—Measures for preventing landslides in rock mass (seven lectures)

3.18 Case 13: The LARIMIT Portal

The LaRiMiT (Landslide Risk Mitigation Toolbox; <https://www.larimit.com/>) is an Expert-Based Landslide Mitigation Portal assisting users of identifying cost-effective structural landslide risk mitigation options (Uzielli et al. 2017). It is a technical tool for quick selection of landslide risk mitigation measures, but is not intended to replace detailed, site-specific technical investigations, and as much it is a valuable tool for educational purposes. The toolbox was initially developed

within the framework of the European Union 7th Framework Programme project “SafeLand—Living with landslide risk in Europe: Assessment, effects of global change, and risk management strategies” and further developed by the Norwegian Geotechnical Institute (Kalsnes and Capobianco 2019).

3.19 Case 14: Humanitarian Library

The Humanitarian Library was launched in 2013, and is the only inter-agency, inter-sector, crowd-sourced, and community-moderated platform in the humanitarian space (<https://www.humanitarian.org/>). Among its resources, channels and events, there are 75 hits as of March 2023 related to landslides: 70 resources and five collections. One of the five collections is entitled “Landslide Mitigation and Disaster Risk Management—Case Studies and Good Practice” (Humanitarian Library 2023), it was last updated in 2020 and encompassed eight documents.

3.20 Case 15: The VISUS Methodology

UNESCO is actively engaged in empowering schools and their communities to identify the hazards they are exposed to, map their vulnerabilities and capacities, and enhance school safety. To do so, UNESCO promotes a multi-hazard school safety assessment methodology, namely VISUS (Visual Inspection for Defining Safety Upgrading Strategies) (Grimaz and Malisan 2020). Developed by the UNESCO Chair on Intersectoral Safety for Disaster Risk Reduction and Resilience, SPRINT-Lab, University of Udine, Italy, the methodology provides decision-makers with tools and information, allowing them to make science-based decisions on where and how to invest their available resources for enhancing school safety. The VISUS methodology, which has a strong component in capacity building for decision-makers, technical staff, and universities, has been successfully tested in seven mostly developing countries (UNESCO 2023).

3.21 Case 16: The Twinkl Platform

The Twinkl platform (<https://www.twinkl.co.uk/>) offers free educational materials for parents and young students below 18 years of age, on a variety of topics, including natural hazards.

4 Conclusions

The importance of education for landslide disaster risk reduction is clear and unequivocal. The education for natural disaster risk reduction should start as early as possible, even

in the kindergarten (preschool) level and should be offered as a life-long education topic for wider society. The topic of landslide disaster risk reduction in all its variety and depth comes to complete coverage in the curricula of higher education institutions. This topic is widely covered in undergraduate and graduate study programmes in engineering (geotechnical engineering, geological engineering, civil engineering, . . .), but also in science programmes (geology, geography, . . .) and social sciences programmes (risk management, disaster management, resilience, risk dialogue . . .). The topic is mainly covered as a constituent part of more general courses, and to a lesser extent, as courses on slope stability and landslides. This is why summer schools on landslide disaster risk reduction are welcome to offer students an opportunity to deepen their understanding and knowledge in this topic, coming from various disciplines. They make it possible to have an inter-disciplinary milieu, and to stimulate cross-sectoral thinking that is important to understand landslides as socio-technical complex system that needs cross-sectoral approach and systems thinking, quite often supported by critical and innovative thinking.

The article gives a short overview of some (selected) courses and study programmes worldwide offering knowledge and competencies for landslide disaster risk reduction. There are though many more higher education study programmes not covered in this overview, as there are thousands of universities around the world. With respect to summer schools on landslides, the overview is more complete, as the offer is not so extensive.

The worldwide landslide community is invited to support efforts for society resilience against landslides by intensifying their efforts for capacity building in parallel to their research activities. For the International Consortium on Landslides (ICL 2023a), the KLC 2020 Commitment for Global Promotion of Understanding and Reducing Landslide Disaster Risk (Sassa 2021a), is a standing support and reminder to be active (also) in the field of capacity building, not only through research, but also education.

The ICL activities, not only in research, but also in capacity building for society resilience, is supporting the implementation of the ninth phase of the UNESCO Intergovernmental Hydrological Programme (IHP-IX) 2022–2029 (UNESCO 2022b).

Acknowledgments This article resulted from the capacity-building activities of the UNESCO Chair on Water-related Disaster Risk Reduction at the University of Ljubljana (2020–2024), and of the World Centre of Excellence on Landslide Risk Reduction (2020–2023) at the Faculty of Civil and Geodetic Engineering, University of Ljubljana. The author would like to acknowledge the financial support of Slovenian Research Agency by core funding P2–0180, and of the University of Ljubljana from the Development Fund for the activities of the UNESCO Chair on Water-related Disaster Risk Reduction (WRDRR).

References

- Abolmasov B, Fathani TF, Liu KF, Sassa K (2017) Progress of the world report on landslides. In: Sassa K, Mikoš M, Yin Y (eds) *Advancing culture of living with landslides*. WLF 2017. Springer, Cham. https://doi.org/10.1007/978-3-319-59469-9_18
- AGU (2021) The LARAM 2021 school. The Landslide Blog. American Geophysical Union. Washington D.C., USA. Available at: <https://blogs.agu.org/landslideblog/2021/05/14/laram/>. Accessed 12 Feb 2023
- Ajmera B, Ahari HE, Loi DH, Setiawan H, Dang K, Sassa K (2023) LS-RAPID manual with video tutorials. In: Sassa K, Konagai K, Tiwari B, Arbanas Ž, Sassa S (eds) *Progress in landslide research and technology*, Volume 1 Issue 1, 2022. Springer, Cham, pp 343–406. https://doi.org/10.1007/978-3-031-16898-7_26
- Bæverfjord MG, Thakur V (2008) Landslides in education: the Verdal and Rissa landslides. In: *Proceedings of the 6th International Conference on Case Histories in Geotechnical Engineering*, Arlington, USA. Vol. 1, p. 8. <https://scholarsmine.mst.edu/icchge/7icchge/session09/6>
- BeSafeNet (2023) EUR-OPA major hazards agreement. <https://besafenet.net/>. Accessed 31 Jan 2023
- Cascini L, Sorbino G, Calvello M, Cuomo S (2012) The LARAM School: teaching “landslide risk assessment and mitigation” to PhD students. *SFGE 2012, Proc. Conf. on Shaking the Foundations of Geo-engineering Education*, Galway, Ireland, pp. 211–218
- Cascini L, Calvello M, Cuomo S (2018) LARAM School 2018: the doctoral school on “landslide risk assessment and mitigation”. *Landslides* 15(7):1445–1447. <https://doi.org/10.1007/s10346-018-1006-0>
- Cascini L, Calvello M, Cuomo S, Jaboyedoff M, Peduto D (2019) LARAM school 2019: the yearly doctoral school on “Landslide risk assessment and mitigation”. *Landslides* 16(2):1419–1421. <https://doi.org/10.1007/s10346-019-01193-9>
- Cascini L, Calvello M, Cuomo S, Peduto D, Moscariello M, Nicodemo G, Pecorano G (2020) LARAM school 2020 goes online: the 15th doctoral school on “Landslide risk assessment and mitigation”. *Landslides* 17:1997–1999. <https://doi.org/10.1007/s10346-020-01456-w>
- Cascini L, Calvello M, Cuomo S (2021) LARAM school: an ongoing experience. In: Sassa K, Mikoš M, Sassa S, Bobrowsky PT, Takara K, Dang K (eds) *Understanding and reducing landslide disaster risk*. WLF 2020. ICL contribution to landslide disaster risk reduction. Springer, Cham, pp 251–257. <https://doi.org/10.1007/978-3-030-60196-6>
- Clarivate Analytics (2023) Web of science core collection. <https://www.webofscience.com/wos/woscc/basic-search>. Accessed 20 Jan 2023
- Cross TC, Kaklamanos J (2017) Incorporating natural disasters into the undergraduate civil engineering curriculum a case study of hurricane Katrina and the Oso landslide. In: Awotona A (ed) *Planning for community-based disaster resilience worldwide: learning from case studies in six continents*. Routledge, pp 121–133
- Dewi RP (2020) Fieldwork and research impact on learning of disaster risk reduction. *Univ J Educ Res* 8(8):3718–3724. <https://doi.org/10.13189/ujer.2020.080852>
- FindAUniversity (2023) The postgraduate experts. FindAUniversity Ltd, Sheffield, UK. <https://www.findauniversity.com/>. Accessed: 8 February 2023
- Guo Y, Zhu J, Fu L, Li W, Zheng Q, Zhao Y, Wu S (2020) A visual representation method for landslide disaster visualization for public education. *Journal of Wuhan University (Information Science Edition)* 45(09)
- Hatibe A, Salam A, Gustina S (2020) An analysis of the understanding of physical education students on the environmental physical concept in landslide matter. *J Phys Conf Ser* 1760(1):012047. <https://doi.org/10.1088/1742-6596/1760/1/012047>
- He B, Sassa K, McSaveney M, Nagai O (2014) Development of ICL landslide teaching tools. *Landslides* 11(1):153–159. <https://doi.org/10.1007/s10346-013-0460-y>
- Hirota K, Suganuma Y, Iwasaki T, Kuwano T (2023) How to teach remotely the vegetation works to protect slopes against mass wasting: a case of using video materials in Bhutan. In: Alcántara-Ayala I, Arbanas Ž, Huntley D, Konagai K, Mikoš M, Sassa K, Sassa S, Tang H, Tiwari B (eds) *Progress in landslide research and technology*, Volume 1 Issue 2, 2022. Springer, Cham, pp 361–370. https://doi.org/10.1007/978-3-031-18471-0_26
- GADRRRES (2022) Comprehensive school safety framework 2022–2030—for child rights and resilience in the education sector. Global Alliance for disaster risk reduction & resilience in the education sector, p. 26. Available at: <https://gadrrres.net/comprehensive-school-safety-framework/#CSS-Framework>. Accessed 12 Feb 2023
- Giusti I, Lo Presti D (2015) An example of teaching slope stability from true case histories: three year experience. In: 2015 International Conference on Interactive Collaborative Learning (ICL), Florence, Italy. 1059–1064. doi:<https://doi.org/10.1109/ICL.2015.7318178>
- Grimaz S, Malisan P (2020) Multi-hazard visual inspection for defining safety upgrading strategies of learning facilities at territorial level: VISUS methodology. *Int J Disaster Risk Reduct* 44:101435. <https://doi.org/10.1016/j.ijdrr.2019.101435>
- Humanitarian Library (2023) Landslide mitigation and disaster risk management—case studies and good practice. Humanitarian Library. Shelter Centre, Satigny-Geneva, Switzerland. Available at: <https://www.humanitarianlibrary.org/collection/landslide-mitigation-and-disaster-risk-management-case-studies-and-good-practice>. Accessed 23 Mar 2023
- ICL (2010) Guideline of landslide school network. <https://icl.iplhq.org/landslide-school-network/>. Accessed 20 Jan 2023
- ICL (2012) ICL capacity development network. http://www.landslides.org/wp-content/uploads/pdfipl/2012/12/2.-Proposal_LCN-LSN_Karnawati.pdf. Accessed 20 Jan 2023
- ICL (2023a) International consortium on landslides. <https://www.landslides.org/>. Accessed 28 Jan 2023
- ICL (2023b) International consortium on landslides. Kyoto 2020 Commitment. <https://www.landslides.org/ipl-info/2020-landslide-kyoto-commitment/>. Accessed 26 Jan 2023
- ISRM (2023) Prof. Zhong-qi Quentin YUE’s course on prevention methods for landslides in rock masses. International Society for Rock Mechanics and Rock Engineering, ISRM secretariat, Lisbon, Portugal. Available at: <https://isrm.net/page/show/1525>. Accessed 12 Feb 2023
- Kalsnes B, Capobianco V (2019) Nature-based solutions—landslides safety measures. *Klima 2050 report* 16. Centre for Research-based Innovation (SFI), Trondheim, Norway. p. 52. <https://www.sintefbok.no/book/download/1234>. Accessed 24 Feb 2023
- Karnawati D, Yin Y (2011) How to develop the landslide school network for strengthening regional activities and capacity development for risk preparedness. Round Table Discussion, IPL-ICL Session in Global Platform 2011. https://www.preventionweb.net/files/globalplatform/entry_presentation~landslideschoolnetwork.pdf. Accessed 28 Jan 2023
- Labibah UN, Kuswanto H, Susiyanti (2020) Integrated landslide disaster education in physics subject viewed from high school students preparedness in Kulon Progo, Yogyakarta. *J Phys Conf Ser* 1440:012026. <https://iopscience.iop.org/article/10.1088/1742-6596/1440/1/012026>. Accessed 11 Mar 2023
- Lo Presti D (2013) An example of teaching slope stability from true case histories. In: 7th International Conference on Case Histories in Geotechnical Engineering, Chicago, USA. <https://scholarsmine.mst.edu/icchge/7icchge/session01/4>

- Loi DH, Jayakody SHS, Sassa K (2023) Teaching tool “undrained dynamic loading ring shear testing with video”. In: Alcántara-Ayala I, Arbanas Ž, Huntley D, Konagai K, Mikoš M, Sassa K, Sassa S, Tang H, Tiwari B (eds) *Progress in landslide research and technology*, Volume 1 Issue 2, 2022. Springer, Cham, pp 325–359. https://doi.org/10.1007/978-3-031-18471-0_25
- Maquaire O, Malet J-P, Castaldini D, von Elverfeldt K, Pla F, Soldati, Greco R, Pasuto A (2009) The BE-SAFE-NET website: a tool for the education on landslides. In: Malet J-P, Remaitre A, Bogaard T (Eds.): *Landslide processes. From geomorphologic mapping to dynamic modelling. Proceedings of the International Conference on Landslide Processes: from geomorphologic mapping to dynamic modeling*, 6–7 February 2009, Strasbourg, France. pp. 321–326. <https://hal.science/hal-00533774>. Accessed 31 Jan 2023
- Micallef A, Alexandrou A, Gerosimou G, Castaldini D, Papadopoulos M, Pla F, Poyarkov V (2014) Public awareness on natural and technological hazards as a key for safety: the BeSafeNet initiative contribution. International conference “analysis and Management of Changing Risks for natural hazards”, 18–19 November 2014, Padua, Italy. pp. CP8-1–CP8-6. <https://core.ac.uk/download/54007472.pdf>. Accessed 31 Jan 2023
- Mikoš M, Sassa K, Han Q (2023) International Programme on landslides—a short overview of its historical development. In: Sassa K, Konagai K, Tiwari B, Arbanas Ž, Sassa S (eds) *Progress in landslide research and technology*, Volume 1 Issue 1, 2022. Springer, Cham, pp 45–62. https://doi.org/10.1007/978-3-031-16898-7_3
- Munoz VA, Carby B, Abella EC, Cardona OD, LopezMarrero T, Marchezini V, Meyreles L, Olivato D, Trajber R, Wisner B (2020) Success, innovation and challenge: school safety and disaster education in South America and the Caribbean. *International Journal of Disaster Risk Reduction* 44:101395. <https://doi.org/10.1016/j.ijdrr.2019.101395>
- NASA (2023a) Enabling landslide disaster risk reduction and response throughout the disaster life cycle with a multi-scale toolbox. National Aeronautics and Space Administration, Earth Science Division. <https://appliedsciences.nasa.gov/what-we-do/projects/enabling-landslide-disaster-risk-reduction-and-response-throughout-disaster>. Accessed 23 Mar 2023
- NASA (2023b) Modeling and reporting landslides. NASA Global Precipitation Measurements. National Aeronautics and Space Administration. <https://gpm.nasa.gov/applications/landslides/#rainfalltriggeredlandslides>. Accessed 23 Mar 2023
- Ozkazanc S, Yuksel UD (2015) Evaluation of disaster awareness and sensitivity level of higher education students. *Procedia Soc Behav Sci* 197:745–753. <https://doi.org/10.1016/j.sbspro.2015.07.168>
- Perdomo JL, Pando MA (2014) Using information technology to incorporate natural hazards and mitigation strategies in the civil engineering curriculum. *J Prof Issues Eng Educ Pract* 140(1):04013004. [https://doi.org/10.1061/\(ASCE\)EI.1943-5541.0000175](https://doi.org/10.1061/(ASCE)EI.1943-5541.0000175)
- Petrella E, Chelli A, Valentino R (2022) High-level training on the topic of landslides and slope stability in Rwanda. *Acque Sotterranee—Italian Journal of Groundwater* 11(3):67–69
- Prakasam C, Aravinth R, Saravanan R (2022) Report on NRDMS: DST sponsored 21-day (level 2) Summer School on mountain disaster management: landslide from 9 to 29th may 2019. *Natl Acad Sci Lett* 45:95–103. <https://doi.org/10.1007/s40009-021-01068-5>
- Ranglund OJ, Have H, Venemyr GO, Vold T, Braun R (2018) Gaming and scenario building: a student active approach to learning. In: *12th European Conference on Games-based Learning*, 526–531
- Rutzinger M, Höfle B, Lindenbergh R, Oude Elberink S, Pirotti F, Sailer R, Scaioni M, Stötter J, Wujanz D (2018) Close-range sensing techniques in alpine terrain. *ISPRS Annals of the Photogrammetry, Remote Sensing and Spatial Information Sciences*, Volume III-6, 2016 XXIII ISPRS Congress, 12–19 July 2016. Czech Republic, Prague, pp 15–22
- Sassa K (2015) ISDR-ICL Sendai partnerships 2015–2025 for global promotion of understanding and reducing landslide disaster risk. *Landslides* 12:631–640. <https://doi.org/10.1007/s10346-015-0586-1>
- Sassa K (2019) The fifth world landslide forum and the final draft of the Kyoto 2020 commitment. *Landslides* 16(2):201–211. <https://doi.org/10.1007/s10346-018-01133-z>
- Sassa K (2021a) The Kyoto landslide commitment 2020: launched. *Landslides* 18(1):5–20. <https://doi.org/10.1007/s10346-020-01575-4>
- Sassa K (2021b) New open access book series “Progress in landslide research and technology”. *Landslides* 18(11):3509–3512. <https://doi.org/10.1007/s10346-021-01759-6>
- Sassa K, He B, McSaveney M, Nagai O (2013) *ICL landslide teaching tools*. ICL Press, p. 405
- Sassa K, Guzzetti F, Yamagishi H, Arbanas Ž, Casagli N, McSaveney M, Khang KH (2018a) *Landslide dynamics: ISDR-ICL landslide interactive teaching tools*. In: Volume 1: Fundamentals, mapping and monitoring. Springer, Cham, p 604. <https://doi.org/10.1007/978-3-319-57774-6>
- Sassa K, Tiwari B, Liu K-F, McSaveney M, Strom A, Setiawan H (2018b) *Landslide dynamics: ISDR-ICL landslide interactive teaching tools*. In: Testing, risk management and country practices, vol 2. Springer, Cham, p 836. <https://doi.org/10.1007/978-3-319-57777-7>
- Seal DM, Jessee AN, Hamburger MW, Dills CW, Allstadt KE (2022) Comprehensive global database of earthquake-induced landslide events and their impacts (ver. 2.0, February 2022). U.S. Geological Survey data release. Available at: <https://doi.org/10.5066/P9RG3MBE>. Accessed 8 Feb 2023
- Strom A (2014) Rockslides and rock avalanches in the Kokomeren River valley (Kyrgyz Tien Shan). In: Mihalić Arbanas S, Arbanas Ž (eds) *Landslide and flood hazard assessment*. Faculty of Mining, Geology and Petroleum Engineering, University of Zagreb and Faculty of Civil Engineering, University of Rijeka, pp 245–250
- Strom A, Abdrakhmatov K (2009) International Summer School on rockslides and related phenomena in the Kokomeren River valley, Tien Shan, Kyrgyzstan. In: Sassa K, Canuti P (eds) *Landslides—disaster risk reduction*. Springer, Berlin Heidelberg, pp 223–227. https://doi.org/10.1007/978-3-540-69970-5_12
- Strom A, Abdrakhmatov K (2013) International Summer School on rockslides and related phenomena in the Kokomeren River basin, Kyrgyzstan. In: Sassa K, Rouhban B, Briceño S, McSaveney M, He B (eds) *Landslides: global risk preparedness*. Springer, Berlin Heidelberg, pp 85–94. https://doi.org/10.1007/978-3-642-22087-6_6
- Strom A, Abdrakhmatov K (2015a) International summer school on rockslides and related phenomena in the Kokomeren River valley (Kyrgyzstan). *Landslides* 12(3):625–626. <https://doi.org/10.1007/s10346-015-0581-6>
- Strom A, Abdrakhmatov K (2015b) 2016 International Summer School on rockslides and related phenomena in the Kokomeren River valley (Kyrgyzstan). *Landslides* 12(6):1233–1234. <https://doi.org/10.1007/s10346-015-0655-5>
- Strom A, Abdrakhmatov K (2018) 2018 International Summer School on rockslides and related phenomena in the Kokomeren River valley (Kyrgyzstan). *Landslides* 15(1):181–182. <https://doi.org/10.1007/s10346-017-0930-8>
- Strom A, Abdrakhmatov K (2019) 2019 International Summer School on rockslides and related phenomena in the Kokomeren River valley (Kyrgyzstan). *Landslides* 16(5):1055–1057. <https://doi.org/10.1007/s10346-019-01173-z>
- Strom A, Abdrakhmatov K (2023) 2023 International Summer School on rockslides and related phenomena in the Kokomeren River basin (Kyrgyzstan) (ICL Kokomeren Summer School). *Landslides* 20: 875–876. <https://doi.org/10.1007/s10346-023-02033-7>

- Studyportals (2023) Studyportals B.V., Eindhoven, the Netherlands. <https://studyportals.com/>. Accessed 8 Feb 2023
- Sezgin S, Cirak NS (2021) The role of MOOCs in engineering education: an exploratory systematic review of peer-reviewed literature. *Comput Appl Eng Educ* 29(4):950–968. <https://doi.org/10.1002/cae.22350>
- UG (2023) CERG-C Specialisation Certificate for the assessment and management of geological and climate related risk–The Landslide Risk Module. <https://www.unige.ch/sciences/terre/CERG-C/training/terrain/>. Accessed: 29 January 2023]
- UN (1948) Universal declaration of human rights. <https://documents-dds-ny.un.org/doc/RESOLUTION/GEN/NR0/043/88/PDF/NR004388.pdf?OpenElement>. Accessed 28 Jan 2023
- UNDRR PreventionWeb (2015) Sendai framework for disaster risk reduction 2015–2030. United Nations Office for Disaster Risk Reduction, Geneva. Available at: https://www.preventionweb.net/files/43291_sendaiframeworkfordrren.pdf. Accessed 28 Jan 2023
- UNDRR PreventionWeb (2022a) Academic Programme. United Nations Office for Disaster Risk Reduction, Geneva. Available at: <https://www.preventionweb.net/resource-type/academic-programme>. Accessed 2 Feb 2022
- UNDRR PreventionWeb (2022b) Certificate of advanced studies in disaster risk reduction. United Nations Office for Disaster Risk Reduction, Geneva. Available at: <https://www.preventionweb.net/resource/certificate-fUNESCOadvanced-studies-disaster-risk-reduction>. Accessed 28 Oct 2022
- UNDRR PreventionWeb (2022c) LARAM school 2022 hybrid: doctoral school on “landslide risk assessment and mitigation”. United Nations Office for Disaster Risk Reduction, Geneva. Available at: <https://www.preventionweb.net/event/laram-school-2022-hybrid-doctoral-school-landslide-risk-assessment-and-mitigation>. Accessed 12 Feb 2023
- UNESCO (2021) Reimagining our futures together–A new social contract for education. 188. <https://unesdoc.unesco.org/ark:/48223/pf0000379707>. Accessed 28 Jan 2023
- UNESCO (2022a) Beyond limits–new ways to reinvent higher education. Roadmap proposed for the 3rd world higher education conference WHEC2022 | 18-20 may 2022, working document. 40p. UNESCO, Paris. Available at: <https://cdn.eventsbase.com/www.whec2022.org/uploads/users/699058/uploads/69c2df623079c3845e236c56ba2d7a8aa21b3d75489e28c7910226f24f7989aec7aae05a23f31fae4587aeb4be088f99dccd.6282b2a95281d.pdf>. Accessed 31 Jan 2023
- UNESCO (2022b) IHP-IX: strategic plan of the intergovernmental hydrological Programme: science for a water secure world in a changing environment, ninth phase 2022–2029. UNESCO, Paris, p 51. <https://unesdoc.unesco.org/ark:/48223/pf0000381318>. Accessed 9 Feb 2023
- UNESCO (2023) School safety assessment: VISUS methodology. UNESCO, Geneva. Available at: <https://en.unesco.org/disaster-risk-reduction/education-school-safety/visus>. Accessed 7 Feb 2023
- USGS (2023a) Global earthquake-triggered ground failure inventory database. United States geological survey. Available at: <https://www.usgs.gov/programs/landslide-hazards/science/global-earthquake-triggered-ground-failure-inventory-database>. Accessed 9 Feb 2023
- USGS (2023b) Comprehensive global database of earthquake-induced landslide events and their impacts (ver. 2.0, February 2022). United States Geological Survey. Available at: <https://www.usgs.gov/data/comprehensive-global-database-earthquake-induced-landslide-events-and-their-impacts-ver-20>. Accessed 9 Feb 2023
- USGS (2023c) Public lecture series. United States geological survey. Available at: <https://www.usgs.gov/public-lecture-series>. Accessed 9 Feb 2023
- UT (2023) Master geo-information and earth observation. University of Twente, Netherlands. Available at: <https://www.itc.nl/education/studyfinder/geo-information-science-earth-observation/>. Accessed 12 Feb 2023
- Uzielli M, Choi JC, Kalsnes BG (2017) A web-based landslide risk mitigation portal. In: Mikoš M, Arbanas Ž, Yin Y, Sassa K (eds) *Advancing culture of living with landslides*. WLF 2017. Springer, Cham, pp 431–438. https://doi.org/10.1007/978-3-319-53487-9_50
- Valentino R, Chelli A, Petrella E (2023) Training on the topic of landslides and slope stability in Rwanda: a Summer School in the framework of the Erasmus + EnRHed project. *Landslides* 20(1): 223–228. <https://doi.org/10.1007/s10346-022-01999-0>

Open Access This chapter is licensed under the terms of the Creative Commons Attribution 4.0 International License (<http://creativecommons.org/licenses/by/4.0/>), which permits use, sharing, adaptation, distribution and reproduction in any medium or format, as long as you give appropriate credit to the original author(s) and the source, provide a link to the Creative Commons license and indicate if changes were made.

The images or other third party material in this chapter are included in the chapter's Creative Commons license, unless indicated otherwise in a credit line to the material. If material is not included in the chapter's Creative Commons license and your intended use is not permitted by statutory regulation or exceeds the permitted use, you will need to obtain permission directly from the copyright holder.





Community Scale Landslide Resilience: A Citizen-Science Approach

Maneesha Vinodini Ramesh, Hemalatha Thirugnanam, Nitin Kumar Mohanan, Balmukund Singh, Harichandana C Ekkirala, and Ramesh Guntha

Abstract

Building landslide resilience at a community scale is the most effective way to protect people against landslides. But building resilience at a community scale can become difficult, given the large spatial scale spanned by locations vulnerable to landslides and the number of communities that might get affected. So, in this chapter, we discuss how to build community-scale landslide resilience using a citizen-science approach. The potential of citizen-science approaches for building landslide resilience at the community level is immense, given that the citizens become resources to build resilience. Yet challenges exist in this approach as novel tools and operationalizing methods are seldom found in the literature. Therefore, this chapter examines the requirements, solutions, and dimensions of landslide resilience and presents a framework to strengthen community-scale resilience. The framework addresses how citizens can be engaged before, during, and after a disaster. This chapter also presents a few example tools used to operationalize this theoretical framework, such as Landslide tracker mobile app, Amritakripa mobile app, social media data analysis, and community involvement. It also examines the difficulties found while applying the citizen science approach in two case study locations in India: Munnar in the Western Ghats and Chandmari in Sikkim. This chapter and the case study can help policymakers, community leaders, change makers, administrative officials, and researchers in disaster management.

Keywords

Landslide · Community resilience · Citizen science

1 Introduction

Landslides are among the most devastating disasters we can observe on hilly terrains. The spatial and temporal scale associated with landslides can destroy or disperse otherwise flourishing communities on these hilly terrains. Interventions in the form of mitigation measures (Sujatha et al. 2023) and early warning systems (Fathani et al. 2023) are effective tools and can protect communities against landslides. But various factors, such as economic, social, and physical, hinder the adoption of these interventions in poor or vulnerable communities. To translate these vulnerable communities into sustainable and resilient communities, adopting an improved and novel approach to building landslide resilience requires equal participation of all entities, including community citizens (Anderson and Holcombe 2013).

Landslides affected an estimated 4.8 million people and caused more than 18,000 deaths from 1998–2017 globally (Turner 2018). Rising global temperatures due to climate change are expected to trigger more landslides, especially in mountainous areas with extreme rainfall events, snowfall, and glacial melts (Disaster Management 2018; IMD 2018). Additionally, landslides as part of multi-hazard events are becoming a noticeable concern. As per EM-DAT database, the year 2022 witnessed 387 environmental disasters worldwide, an increase from the decadal average of 370 from 2002 to 2021 (CRED <https://reliefweb.int/report/world/2022-disasters-numbers>). More and more landslides are seen as part of multi-hazard events such as floods, storms, earthquakes, etc. Thus, traditional approaches to disaster management, such as establishing disaster management agencies, building the capacity of rescue forces, etc., are becoming increasingly ineffective. Global prominence has

M. V. Ramesh · H. Thirugnanam (✉) · N. K. Mohanan · B. Singh · H. C. Ekkirala · R. Guntha
Center for Wireless Networks and Applications (WNA), Amrita School for Sustainable Futures, Amrita Vishwa Vidyapeetham, Amritapuri, India
e-mail: maneesha@amrita.edu; hemalathat@am.amrita.edu; nitinkm@am.amrita.edu; balmukundsingh@am.amrita.edu; amidids20008@am.students.amrita.edu; rameshg@am.amrita.edu

been placed on building resilience to climate change and its associated risks, such as landslides.

However, there is a gap between available scientific knowledge and the adoption of technological interventions by people at the community scale, where people are most vulnerable. This may stem from a lack of fundamental resources in the at-risk communities, including knowledge and expertise, financial support, governance support, effective policies, and pathways to access these interventions. Oftentimes the technological interventions themselves lack the co-design and participatory rural appraisal techniques needed to understand the challenges and needs of specific communities for whom it is designed. Hence to design suitable and easy-to-adopt interventions that are driven by the voice of the people, we need to adopt new approaches that are driven by the citizens. This calls for a close multi-stakeholder partnership between civil protection officials, academicians, and community members to create a novel citizen-science approach toward building landslide-resilient communities, as will be discussed in this book chapter.

This book chapter explores existing interventions that enhance the advancement of climate resilience using citizen-centric approaches in fields of hazard inventory and landslide hazard and risk assessments, illustrated through two case studies from India. The requirements and solutions for achieving economic, social, physical, institutional, and environmental resilience are discussed. The chapter finally proposes some key requirements for achieving a landslide-resilient community throughout the disaster management cycle of pre, post, and during a disaster.

2 Related Works

2.1 Review of the Existing Citizen Science Approach

Citizen science is “Scientific knowledge cogeneration by members of the general public, in collaboration with professional scientists and scientific institutions” (Haklay 2013; Haklay et al. 2021). There have been growing global citizen science associations in recent years owing to the development of new tools and artificial intelligence-based algorithms (Can et al. 2019). Other advantages of the citizen’s approach are increased democratic engagement, public awareness, and involvement in current social challenges (Cieslik et al. 2019). Numerous research articles have used multimedia resources in terms of photos, videos, chats, dialogs, etc., from social media, news, and other open information platforms as sources for data for their research (Kocaman et al. 2018; See et al. 2016; Silvertown 2009). Recent developments in computational technologies can extract useful scientific inputs from these data sources

generated by the citizens (Kocaman and Gokceoglu 2019a, b). These approaches are referred to as citizen science. They are useful for landslide studies where people living or working in landslide areas can act like human sensors and deciphers of local information (See et al. 2016). Several volunteer organizations trained by scientific institutions have been introduced in vulnerable places to aid in the quick and cost-effective collection of geodata (Goodchild 2007; Rohan et al. 2020).

Major challenges in using this approach are low accuracy of data, lack of standard terminology, language barriers, uncertainties led by missing data, reduced reliability of the information, and hence special techniques are required to decipher useful information (Goodchild 2007). These factors may drastically affect the regional landslide assessments (Kocaman et al. 2018). As a result, the development of data quality assessment and validation strategies has become a new venue of research in disaster management (Kocaman and Gokceoglu 2019a, b; Gu et al. 2015; Juang et al. 2019). In other words, the focus has been on bringing aspects of geodata such as categorizations based on location, participant type, medium of data collection, type of data, etc., so that reliability can be assessed and assured for developing the Landslide monitoring applications and data collections. (Parajuli and Shakya 2019; See et al. 2016; Can et al. 2020; Rohan et al. 2020). Other developments are in the field of developing efficient tools for volunteers to enable them to provide data and observations on landslides, i.e., NASA landslide reporter; Landslip Landslide tracker (Hariharan and Guntha 2021), runout distance assessments, store them in cloud servers and dynamically display on GIS-based interfaces. In other reviews, published earlier, the emphasis is on the categorization of citizen-science-based tools useful for different parts of disaster management (Kocaman et al. 2018; Kocaman and Gokceoglu 2019a, b). Traditionally evolved local practices are at times more insightful (Dekens 2007; Hiwasaki et al. 2014). However, the contribution of citizen sciences is also subject to geographical location, the technological know-how of the citizens, motivation, and participation behaviors (Franceschinis et al. 2020; Gaventa and Barrett 2010).

A vital aspect of accurate landslide forecasting and modeling is access to a comprehensive and well-maintained hazard inventory (Landslide Reporter 2019). Capturing landslide hazard date, time, location, the magnitude of impact, and the trigger is a necessity recognized by many in the landslide scientific community. However, maintaining such a database is a tremendous challenge for single-hazard events, which is further complicated in multi-hazard events. Specifically for multi-hazard events, the time interval between each hazard is essential to forecast potential risk increases. In lieu of this, the UK NERC/FCDO funded LANDSLIP project ‘Landslide multi-hazard risk assessment,

preparedness and early warning in South Asia' (<http://www.landslip.org/>) also attempted to create a web and mobile App that allows for crowd-sourced information to create a landslide hazard inventory including information on the trigger, damage assessment and type of landslides.

3 Citizen Science Approach

3.1 Requirements, Solutions, and Dimension of Landslide Resilience

Community resilience against landslides has multiple dimensions associated with Economic, Social, Physical, Institutional, and Environmental resilience. Requirements, solutions, and association with the above dimensions for achieving landslide-resilient communities are enumerated below:

1. Comprehensive landslide risk assessment: A comprehensive assessment of landslide risk is essential for identifying areas susceptible to landslides and implementing policies to restrict further development in these fragile locations. These measures help in building the physical and environmental resilience of the community (Ramesh et al. 2023; Rohan et al. 2021; Wadhawan et al. 2020)
2. Land-use planning and zoning: Following a landslide risk assessment, proper land-use planning and zoning can help to prevent development in areas that are susceptible to landslides and protect the community from the impacts of landslides, resulting in establishing physical, economic, and environmental resilience of the community.
3. Building codes and standards: Developing building codes and standards that consider landslide risk can help ensure that buildings are constructed to withstand potential landslide hazards such as sinking or creep movements. These activities would help in bringing in physical resilience.
4. Early warning systems: Early warning systems (EWS) can help to alert residents to the potential for landslides and give them enough time to evacuate or take other protective/preventive measures. In the long term, the instrumentation output of EWS can help in planning and implementing landslide mitigation measures and hence help bring in physical and environmental resilience. (Thirugnanam et al. 2022)
5. Education and awareness: Educating the community about the risks associated with landslides and their exposure level will help improve the community's risk perception. Additionally, providing them with information on how to prepare for and respond to landslides as a community, as opposed to individuals, is very important for building the community's social resilience.

6. Community involvement, Coordination, and collaboration: Effective coordination and collaboration between government agencies, community organizations, and community members, are essential for implementing landslide risk reduction measures and building a resilient community. Moreover, a changemaker or community leader who works in tandem with organizations such as the Disaster Management Agency (DMA), Disaster Response Forces (DRF), and Non-Governmental Agencies (NGOs) can help strengthen the institutional resilience of the community.

4 Operationalization of the Citizen-Science Approach

Operationalization of the citizen-science approach is a complex task that involves coordination among the community members, collaboration with stakeholders, technical expertise, institutional capacity, supporting data, and access to resources and tools. The implementation of this approach within a framework and the use of various tools for implementation is discussed further in this section below.

4.1 Framework: Involving Citizens in Building Community-Scale Landslide Resilience

This section discusses a citizen-centric framework for establishing a landslide-resilient community at various stages of a disaster cycle (i.e., pre, during, and post-disaster). Figure 2 below depicts the framework for achieving a landslide-resilient community involving citizens. A further model is being adopted and operationalized at two case study areas in the Indian subcontinent, one in the Western Ghats (Munnar, Kerala) and another in the MCT zone of Himalaya (Chandmari, Sikkim). Munnar is a hill station in the Western Ghats, with an altitude of 1532 m, spanning an area of 187 km², and Munnar gram panchayat has a total of 32,029 inhabitants. (<https://en.wikipedia.org/wiki/Munnar>) Chandmari is a settlement in Sikkim Himalayas, with an altitude of 1786 m, spanning an area of 0.56 km² consisting of 1043 inhabitants.

(<https://geoiq.io/places/Chandmari/QcioAkbcFC>)

4.2 Pre-Disaster Measures

"Prevention is better than cure" research shows that a considerable amount of cost and time can be saved if the communities are prepared to face the disasters. To prepare, the communities need to be aware of their physical,

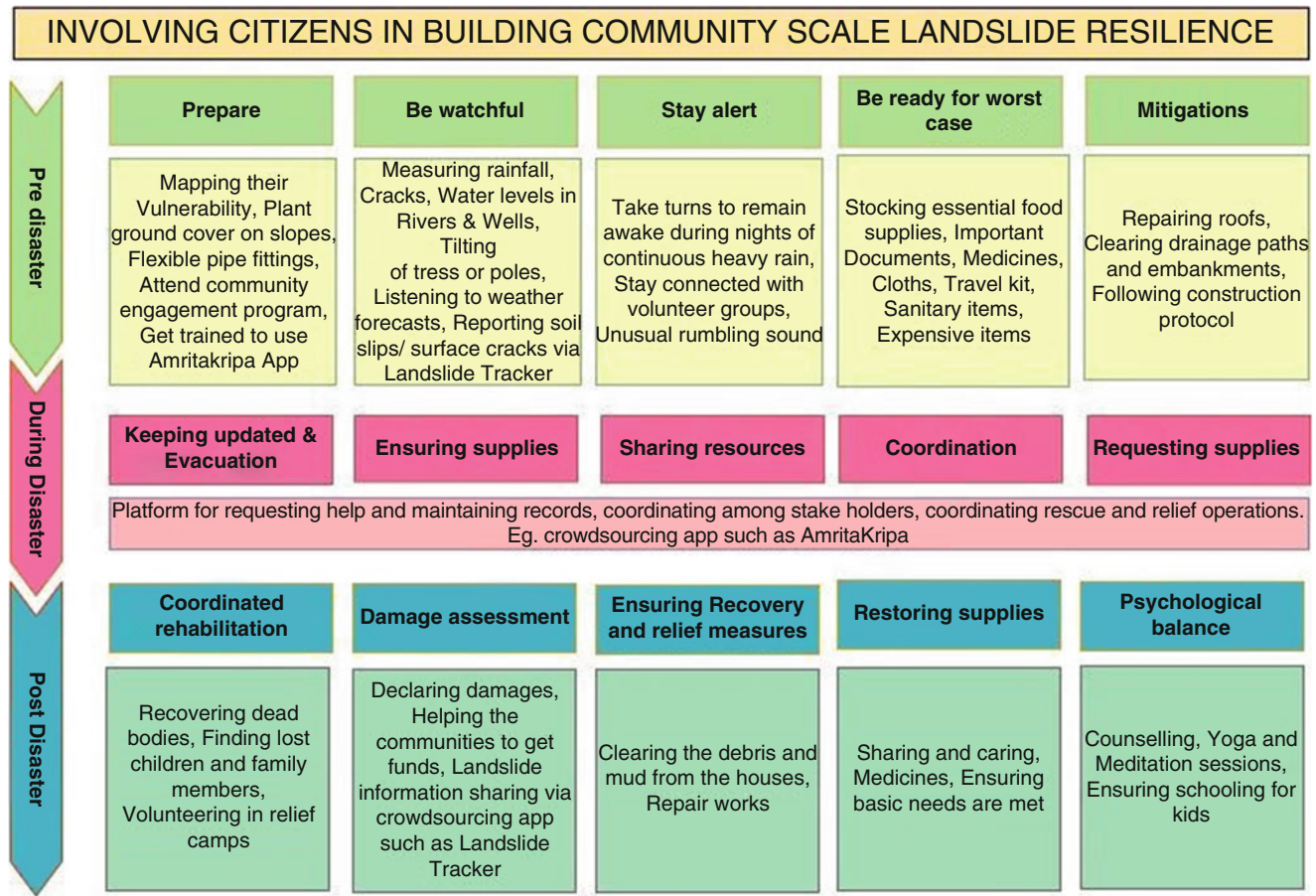


Fig. 1 Proposed framework for involving citizens in building community-scale landslide resilience

economic, or social vulnerabilities. Mapping them provides clarity to the community members, which can also help them to be watchful, stay alert, be ready for the worst case, and undertake possible mitigations to avoid the projected loss. Measures such as planting vegetation on a slope, blanketing the slope surface for soil erosion control, directing surface runoffs, using flexible pipes to avoid breaking up utility lines, repairing buildings, and avoiding water leakages can be very helpful in reducing the chance of a landslide and minimizes the damage during the onset of a landslide (Fig. 1).

During heavy rain, there are chances of power and network failures, and people may lose connectivity from the outside world and must remain on their own. During heavy rain, they must take turns remaining awake during the night and be prepared for the worst case. If they hear any unusual rumbling sound, they should alert others and evacuate the houses. Old-age family members, pregnant women, and children should be given special care during such times. Stocking essential supplies can help them feed their families when shops close or roads get blocked in remote areas. All families in the community should be trained to prepare a survival kit (also known as an emergency/disaster kit) that includes their

important documents, medicines, clothes, travel kits, sanitary items, non-perishable food items, and any other necessary items ready in bags so that as soon as the decision on evacuation is made, they can leave the place without further delay.

Organize community engagement programs with the assistance of disaster management experts from whom the community can get awareness about landslide precursors, do's and don'ts during disasters, emergency first aid measures, etc. During these engagements, the community becomes acquainted with tools and technologies such as crowd-sourced apps (Ex: Landslide Tracker App, AmritaKripa App), and others that can assist the community at various stages of the disaster. Moreover, these events help the community identify community champions and volunteers who can play vital roles during a disaster. Additionally, these community champions can take the knowledge of this training to various other individuals at the grassroots level of the community and transfer knowledge related to evacuation routes, safe grounds, and nearest relief camp locations. Such engagements will establish social resilience in the community.

During the monsoon season, the community must watch for rainfall, river water levels, and groundwater levels through wells. These are essential near real-time information on the hydrological triggers of landslides. Similarly, the tilting of trees can be indicative of creep movements. Surface slips may indicate subsidence, fault activation, and induced seismicity. However, the communities living in landslide-prone areas have learned to live with the disasters over time. Yet, assisting them with planned frameworks and tools can help them become more resilient, in light of climate change leading to an increasing number of yearly landslides.

4.3 During-Disaster Measures

Once the community receives the early warning for evacuation from the government, its priority would be to act quickly and move all its members to safe ground and then to the nearest relief camps. During the evacuation process, the community members have to ensure higher priority to vulnerable community members such as old aged, specially-abled, pregnant women, and children. Further, ensure to take the survival kits prepared during the pre-disaster period. This survival kit will help the community survive until relief materials reach various agencies.

Once the community is established temporarily in the relief camp, the next step is to ensure that all the community members are evacuated and that no one is left behind. Depending upon the available evacuation time and efficacy of the evacuation procedure, if some members couldn't evacuate, such members need to be identified during further search and rescue operations. Community leaders should coordinate these activities alongside the regional government agencies in charge of disaster management, such as the Disaster Relief Force (DRF) and the Disaster Management Agency (DMA). The community can utilize crowd-sourced tools, such as Amritakripa, social media platforms, etc., to coordinate these activities. The community also needs to ensure human rights protection during the disaster. This priority must be taken by the community leaders with support from the community. The community should also adjust and adapt to support the needs of the individuals on an equity basis.

4.4 Post-Disaster Measures

Depending on the scale and magnitude of the disaster, the damage to various infrastructures, utilities, and houses will vary. Hence, post-disaster management activities must be started by conducting a damage assessment. The outcome

to the damage assessment will be used to plan the further rehabilitation process and appeals to central govt agencies for financial aid. Often conducting a detailed damage assessment takes a lot of time and leads to delays in further processes. Still, with the aid of community leaders, it is possible to get rough damage estimates, using which central agencies can expedite the rehabilitation process.

The rehabilitation process has varying complexities associated with the financial/economic dimension. Though some citizens would have insurance benefits and could quickly bounce back, the community's poor/economically backward citizens would often rely on government relief funds, thereby extending the economic impact on their lives. Families with missing or deceased members would have to reshuffle their roles depending on their losses. For example, the loss of an income-producing member of the family would imply higher economic vulnerability. Hence, to resolve such issues, the community should actively engage with various govt and non-govt agencies to get benefits for vulnerable members of the community. The community can also set up self-help groups (SHGs) that can engage these people and generate income for them. These activities will help in the economic and social resilience of the community.

Apart from the short-term activities described above, the long-term activities during the post-disaster period will help ensure the community can build back better and make itself more resilient against future disasters. These aspects involve better policies, technological interventions, mitigation measures, etc., but these topics are beyond the scope of the citizen-science approach. They hence won't be covered in this book chapter.

5 Tools for Operationalization

5.1 Community Engagement

Citizen involvement in the design and development process helps build awareness and a sense of ownership, leading to resilience building. In Munnar, the community was made to get involved from the beginning of the deployment stages. Community engagement programs were established following the deployment to explain the capabilities and other features of the landslide early warning system. Community members and the individuals living close to the deployment site got involved in maintaining the system by providing access to water and other resources, changing batteries as needed, and alerting us about animal intrusion, damaged cables, etc. This way, the community took ownership of the system. The first step towards resilience is to increase the local community's awareness level of the potential hazards

their community is facing. Engaging the local community in pre-disaster drills to impart knowledge on proper evacuation routes and procedures. These drills would also help identify community leaders who can lead during such events. These drills would also help the community identify and recognize the vulnerable people in their community, such as the old aged, handicapped, people with special needs, etc., and be prepared to act during the limited time after warnings are issued.

5.2 Social Media Data Analysis

Social media has been used in disaster preparedness and management to strengthen situational awareness and improve emergency response. The common public can be informed of authoritative situational notifications by following official natural disaster management organizations on social media. We have used historical and real-time Twitter data to arrive at models that provide a spatiotemporal summary of the events related to “heavy rainfall before a landslide or a flood disaster.”. These precursor data are collated and evaluated, then the plausible occurrence of natural hazards that can be anticipated is identified using event detection algorithms. Due to the flooding of tweets during heavy rainfall and other disaster precursor conditions, government officials cannot decide when to take an event seriously because the information is not spatially and temporally quantified. This work helps the government authorities in decision-making and will provide situational awareness for the public (Fig. 2).

5.3 AmritaKripa Mobile App

AmritaKripa is a disaster relief platform where users can request help regarding evacuation, medicines, and supplies, and other groups of people can provide the supplies. It has been used extensively during the 2018 and 2019 Kerala (Guntha et al. 2020) floods, where citizens’ inputs and feedback have helped it to organically evolve and upgrade to make it more user-friendly, flexible, and effective for managing rescue and relief efforts during single or multi-hazard situations. The location-based app could locate the demand and supplies, summarize, and help coordinate the efforts. This was also supported by 24/7 call centers where people could report their needs and the availability of excess resources. The app has supported such as (a) Requests and Offers; (b) Types, subtypes, and attributes; (c) Summary. The app was supported by a 24/7 call center during the 2018 and 2019 Kerala extreme events as some people were not able to enter information into the app due to poor connectivity, lack of time, and training, however with the help of the call center this issue was taken care of.

5.4 Landslide Tracker Mobile App

The frequency of landslides on vulnerable hill slopes increases during the monsoon season. Data collection on vital variables is necessary to enhance disaster management due to the ever-increasing landslide incidences. Amrita has created a crowdsourcing-based application to facilitate real-time data collection, validation, summary, and distribution

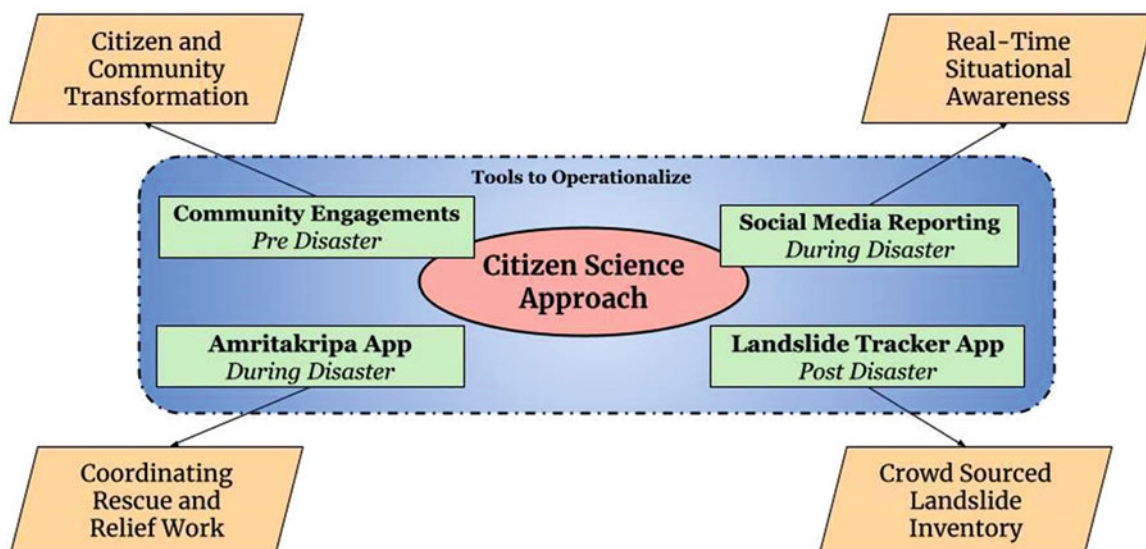


Fig. 2 Tools used in the operationalization of the citizen-science approach

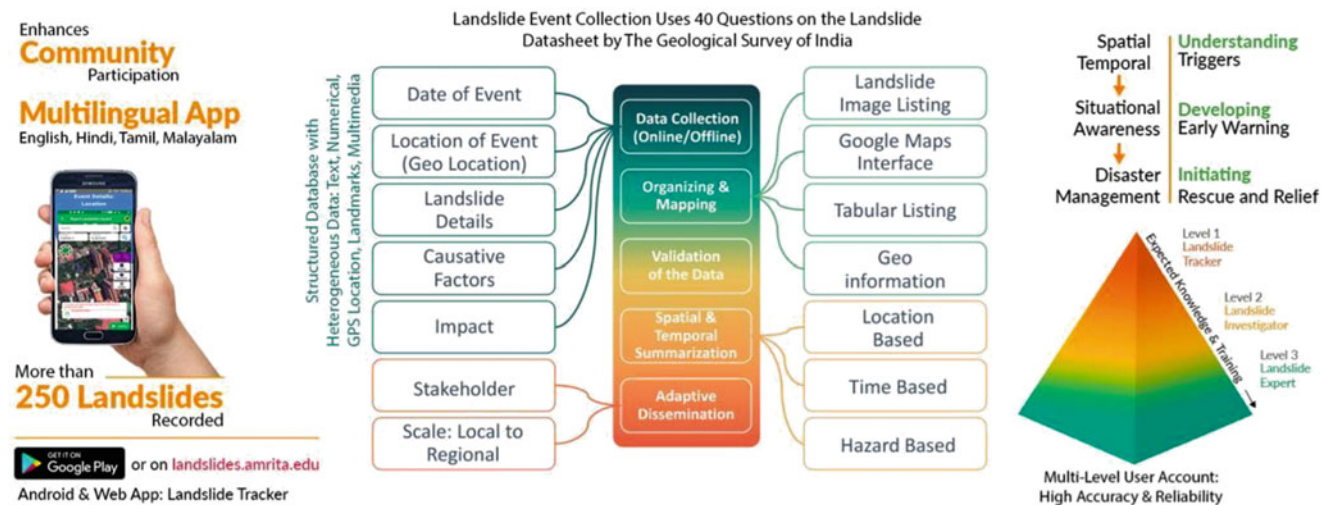


Fig. 3 Landslide tracker mobile App: A crowdsourced mobile app for ‘Spatial-temporal tracking of landslide events’

processes, as shown in Fig. 3. This software was created and developed by Amrita Vishwa Vidyapeetham as part of the LANDSLIP research project (<http://www.landslip.org/>). It is also freely accessible on Google Play Store.

It integrates heterogeneous data into a structural database, which includes numbers, text, GPS locations, landmarks, and photos. Using GPS location, date and time of occurrence, images, type, material, size, impact, area, geology, geomorphology, and comments, this geo-enabled approach aids in the real-time tracking of landslides. Additionally, it supports offline data entry. To guarantee the accuracy of landslide data, it also offers multiple-level user accounts based on their expert levels, such as Tracker, Investigator, and Expert. The occurrences have been recorded and tracked using innovative UI designs. All users have quick access to see the submitted landslides. The User can view entered landslides using the Google Maps interface, the tabular listing, or the landslide image listing. Date/Time and other filters can narrow down the landslides. The smartphone app uses brief papers and videos to raise awareness about the risk of landslides. It contains instructions for staying safe, taking pictures, mapping, and selecting data from various possibilities. The suggested methodology is unique because it improves community involvement, incorporates event data collecting, organization, geographical and temporal summarization, and validates landslip events and their impact. It locates, maps, and informs landslide incidents in real-time so that appropriate disaster management procedures can be started to lower the risk level. The training was given to the community to build resilience to landslides through community involvement and student involvement in technical and social elements. The training was provided on how to measure rainfall at people’s houses using the “Landslide Tracker” smartphone app (Guntha and Vinodini Ramesh 2021, April),

as well as how to map the precursors of landslides, such as fissures in structures and roadways, rising river levels, etc. The current gap between scientific ideas and their practical implications in society can be closed by using an integrated strategy of technically technical and socially social involvement.

6 Case Study: Implementation of Framework

As mentioned, the above framework has been implemented in two case study sites. The two-case study site description is given below:

- Munnar is situated in the Western Ghats region of the Indian peninsula. It is a hill station and a popular tourist destination, with more than 24,000 international and 780,000 domestic tourists. Extreme rainfall events influenced by South Asian monsoon, improper drainage, development of buildings, roads, slope modifications, etc., trigger frequent landslides yearly. The landslide potential is enhanced by three rivers that converge in Munnar, causing flooding. The communities and individuals living in Munnar face multiple challenges during monsoon season, threatening their security, livelihood, and life due to these landslides.
- Chandmari is situated in the MCT zone of the Himalayas in Sikkim state of India. It is also a hill station and a popular tourist destination. The population density of Chandmari is 1858 people per sq. km. The terrain, geology, and climatic setting of Chandmari make it prone to landslides. Chandmari sees numerous large to very small-scale surficial landslides every year. Apart from this



Fig. 4 Implementation of the proposed framework in the pre-disaster period. (a). Measuring rainfall using manual rain gauges by school children. (b). The intensification of rainfall is shown from the data collected by kids in Munnar. (c). Live-in labs students measuring the cross-section of the river in low flow time. This was useful for estimating river discharge (cross-section *height * velocity). (d).

Chandmari has also experienced cloud burst events in the past, and hence community resilience-based approach is more crucial.

The framework implementation in the case study area during the various phases of disaster is shown in Figs. 4, 5 and 6. The community's citizens are involved in various pre-disaster activities during the pre-disaster phase. Figure 4 shows

Locating and mapping the fresh surface slips. (e). A community engagement program is being conducted involving all the stakeholders. (f) Girl students are being trained to map their vulnerability. (g). Community champions are equipped to measure and monitor the discharge of rivers from a bridge of an already measured cross-section

images related to various pre-disaster activities undertaken in the case study locations: Munnar and Chandmari. Figure 4a shows the DIY rain gauge used by school children in the community to measure rainfall. Figure 4b shows the rainfall measurement records maintained by the children in the community. The figure shows that the daily cumulative rainfall in the month of June, which is the monsoon season, is increasing from June 13 onwards. Such rainfall quantified

information provides precise awareness to the community rather than perceiving it as qualitative information such as light or heavy rainfall. Figure 4c shows the community members measuring the cross-section and bathymetry of various streams before the onset of the monsoon season to estimate the water level rise in streams and to understand the discharge capability and its changes resulting from sedimentation. Figure 4d shows the community members recording a landslide in their locality using the Landslide Tracker app. Figure 4e shows the community engagement program organized by Amrita and the local panchayat officers, community leaders, police cops, firefighters, and community members attending this event. Figure 4f shows the youth members, especially school and college girls, involved in the discussion before the monsoon. Community champions are equipped to measure and monitor the discharge of rivers from a bridge of an already measured cross-section.

Figure 5 shows images of various activities during a landslide disaster undertaken in the case study locations: Munnar and Chandmari. Figure 5a shows a house that was damaged due to a landslide in 2018. Another catastrophic landslide happened near our deployment site in Munnar in August-2020. Figure 5b also shows another location of a big landslide event in Rajamala, Munnar, where the volunteers started coordinating the rescue and relief operations after the landslide. Figure 5c shows the combined effort by the community members to clear the drains during the monsoon for smooth passage of excess water, because excess water accumulated may lead to a rise in pore-water pressure, which could further lead to slips in the soil. Figure 5d shows community volunteers coordinating with the National Disaster Response Force (NDRF) team to rescue people. Figure 5e shows the Amrita Kripa Rescue app advertisement and 24 hr. operational call center during the 2018 Kerala multi-hazard event. Over 6000 users had installed Amrita Kripa mobile app and call center to request help, rescue, food supplies, medicines, essentials, etc., during the 2018 and 2019 Kerala multi-hazards, impacting more than 400,000 lives. There are several cases of lost children and missing parents, and they need to be identified. For modeling landslides and early warning, it is very important to maintain systemic inventories and records on recent landslides. Figure 5f is a picture while the Amrita volunteers were working on setting up a call center, receiving calls, updating the App, and supporting the ground teams to the location of the victims.

Figure 6 shows images related to various activities during the post-disaster period. Figure 6a shows the coordinated rehabilitation work in progress soon after the Rajamala landslide. There was massive destruction, roads were blocked, bridges were washed away, and tons of debris accumulated, which needed to be removed to smooth the transportation and utility lines. After the disaster hits an area, some houses are

fully damaged, whereas some are partially damaged. Usually, it takes a while for people to get back to normal life. They might repair and live in the same houses or get a new place to build houses. During such time they must spend time in the relief camps. Figure 6b. Shows the active community members from Munnar volunteering in relief camps, ensuring the food supplies for the affected people sheltered in the relief camps. Often during rescue and relief operations, negative social elements are also active. Figure 6c. Shows the screenshot for the landslide tracker app used for systemic landslide information sharing. Figure 6d. Shows the district administration distributing the relief amount to affected people. Figure 6e Shows a group of volunteers with a truck filled with food and essential supplies. Figure 6f shows a group of social scientists from Amrita interacting, and counseling the people of communities who lost their family members in the landslide. During a disaster, people might have to endure trauma and stress. They are survivors of the landslide. However, some may have lost their near and dear ones, faced injuries, and might be mentally ill post-disaster. There are cases where some children deny going to school, they fear water. During our study in Kerala, we have witnessed cases where people who have invested their entire savings in building their house, when the house was buried in a landslide, get into an acute depression stage and need help. Long-term counseling programs and other economic and social resilience measures must be Self-help groups.

7 Discussion

7.1 Practical Challenges & Implementation Gaps

Achieving landslide community resilience is a complex and multifaceted challenge that requires addressing various practical challenges. In general, the challenges include:

- **Unwillingness to relocate:** During our interviews, we found that few community members show a lack of willingness to relocate to safer locations despite being told by the officials that they reside at potential risk. The various factors for this generic unwillingness might be (i) due to emotional attachment to their homes and communities, (ii) due to concerns about losing their livelihoods, (iii) due to concern regarding access to services and amenities in the relocated place, (iv) due to lack of sufficient incentives from the govt such as financial compensations to set-up new infrastructure such as building house, fencing wall, etc. (v) due to trust deficits between the community members and the stakeholders, and (vi) general social anxiety in the community is also seen



Fig. 5 Implementation of the proposed framework during the disaster period. (a). Shows a landslide damaging a house. (b). Coordinated rescue and ensured supplies during relief operations by volunteers. (c). Community champions coordinate to clear the drains during the monsoon to smooth the passage of excess water. (d). Community volunteers coordinating along with the NDRF team are working to rescue people.

e) Shows advertising of the Amrita Kripa Rescue app and 24-hour operational call center where people could request help during the 2018 and 2019 Kerala multi-hazards. (f) Shows a group of Amrita volunteers working in the set-up, receiving calls, updating the App, and supporting the ground teams to the location of the victims

as relocations involving physically unrooting the entire community from its current location.

To address these challenges and implementation gaps, involving community members in the decision-making process, providing adequate support and incentives, and working closely with relevant government agencies,

NGOs, and other stakeholders is important. Effective communication and awareness-raising efforts can also help to build trust and understanding between community members and those responsible for implementing the relocation program. Finally, it's important to develop comprehensive and sustainable relocation plans that address the

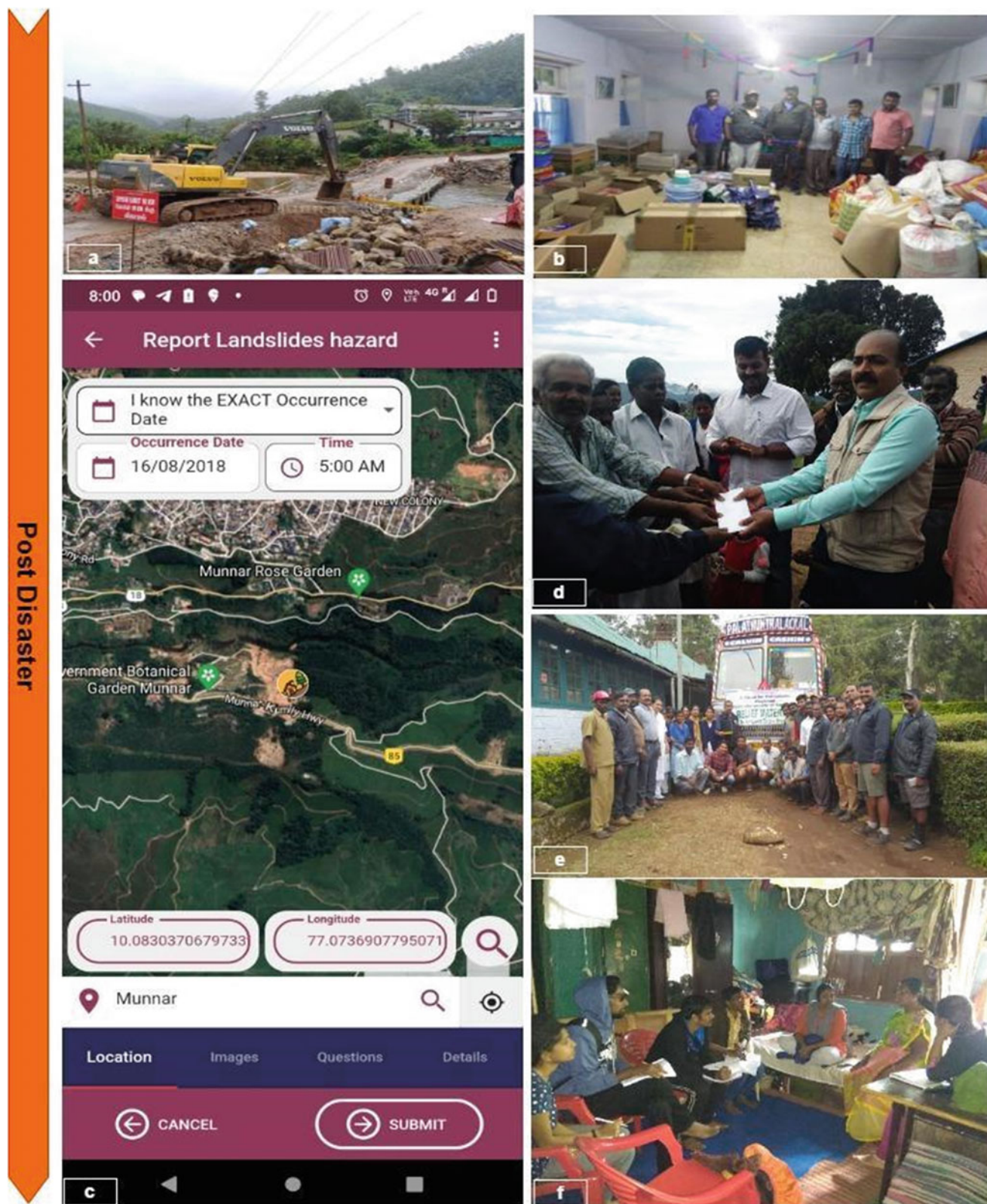


Fig. 6 Implementation of the proposed framework in the post-disaster period. (a). Shows the work in progress after the Rajamala landslide and coordinated rehabilitation. (b). Shows the active community members from Munnar volunteering in relief camps, ensuring the food supplies for the affected people sheltered in the relief camps. (c). Shows the screenshot for the landslide tracker app used for systemic landslide

information sharing. (d). Figures show that district administration distributes the relief amount to affected people. (e) shows a group of volunteers with a truck filled with food and essential supplies. (f). Fig shows a group from Amrita interacting, consoling, and counseling the people of communities who lost their family members in the landslide

needs and concerns of all stakeholders, including those being relocated and the broader community.

- **Non-transfer of indigenous knowledge:** The very fact that these vulnerable communities have survived in a landslide-prone area indicates strong indigenous knowledge regarding landslides. This knowledge includes ways to plan their settlements, building architectures, selection of crops that strengthen slope stability, rainwater management, locations of ephemeral drainages, etc. However, with increasing population and modernization, this indigenous knowledge about the risk and living in synchronization with nature is not efficiently transferred from generation to generation. This leads to weakening the coping capacity of the new generation. The protection of indigenous knowledge for landslide resilience faces several challenges, such as (i) lack of recognition and acknowledgment of the value of indigenous knowledge systems, (ii) many modern engineering approaches to landslide resilience tend to ignore or dismiss traditional knowledge and practices (iii) lack of younger generation's interest in understanding and appreciation of indigenous knowledge, (iv) lack of documentation and preservation of traditional knowledge, as most of it exist in oral form between the older generation, and (vi) finally lack of effective collaboration and communication between indigenous communities and modern scientific communities.
- **Lack of risk self-perception:** Individuals or communities often underestimate the potential risk of landslides in their area. This can occur due to a variety of factors, such as a lack of knowledge or awareness about the local geology and topography, a belief that past landslides were isolated incidents and unlikely to occur again, or a sense of complacency due to a lack of recent landslide events. However, this lack of proper landslide risk perception can be dangerous, leading to inadequate preparation and response measures in the event of an actual landslide. Thus, individuals and communities must be aware of the potential risks and take appropriate steps to mitigate them. Disaster education, awareness programmes, engagement in citizen-stakeholder dialogues, etc., can help raise the community's landslide risk self-perception.
- **Security issues in relief camps:** From our interviews in the study area, when people from different walks of life are in relief camps, there are cultural gaps, and inequity in terms of gender, age, race, caste, religion, etc., which may lead to dominance, cases of harassment, abuse, etc. This is one of the major hindrances to the people's willingness to evacuate to relief camps and temporary shelters.
- **Limited resources:** Building resilience to landslides requires significant resources, including financial, technical, and human resources. Getting approval and funding to

conduct such engagement programs is also a challenge. Many communities lack the necessary resources to implement and sustain resilience measures, hindering their efforts. The community leaders and NGOs having a rapport with the stakeholders can somewhat solve this practical challenge.

- **Community participation and ownership:** Community participation and ownership are critical for effective landslide community resilience; however, the practical challenges are (i) people living in landslide-vulnerable communities are usually from the lower middle class and depend on daily earnings; (ii) engaging communities can be challenging, particularly if they lack awareness or understanding of landslide risks. The practical challenge would be to make the individuals in the community understand the importance and their responsibility for the community's welfare.
- **Limited technical expertise:** Implementing landslide resilience measures often requires technical expertise in engineering, geology, and hydrology fields. Understanding landslide risk is a multidisciplinary challenge and requires integrating several domains of knowledge, which is very challenging. Many communities, particularly those in low-income countries, lack access to such expertise. Support from stakeholders, strong community leadership, and commitment to work for society can somewhat solve this limitation.
- **Data availability and quality:** Reliable data on landslide risks, vulnerabilities, and impacts are critical for effective resilience planning and implementation by stakeholders. However, data availability and quality can be a significant challenge in many landslide-prone areas, particularly in low-income countries.
- **Institutional capacity:** Effective landslide community resilience requires strong local, regional, and national institutional capacity. However, many institutions lack the resources, capacity, and political will to effectively address landslide risks.
- **Hurdles in outreach programs:** While conducting outreach programs, people frequently use the time to discuss other critical everyday issues that they want to transmit to the administration because officials of the administration are present. As a result, bringing the ordinance to the topic of disaster becomes difficult. However, smart moderation of the programs, effective communication skills, and support of local leadership should be sought in such situations.

Addressing these practical challenges requires a multi-stakeholder approach involving community members, government agencies, NGOs, and other leaders. Key strategies include building community awareness and participation,

improving technical capacity, enhancing data availability and quality, strengthening institutional capacity, and mobilizing resources to support resilience-building efforts.

8 Conclusion

The growing potential of citizen science with increased internet use is being utilized globally for extracting and validating essential information for landslide modeling and early warnings. This work discusses the gigantic potential of citizen-science techniques for establishing landslide resilience at the community level. It discusses implementing a proposed framework in the Indian context with two case study areas. This citizen-centric framework has been asserted at various stages of a disaster cycle, considering pre, during, and post-disaster time.

It also discusses the requirements, solutions, and dimensions of landslide resilience which went into developing effective disaster management tools, including Community Engagement, Social media data analysis, the Amrita Kripa mobile app, and the Landslide Tracker mobile app. They have been illustrated along with various practical challenges such as limited resources, limited technical expertise, and non-willingness of people to evacuate their houses experienced during the implication of the proposed approach.

Providing aids like training, awareness programs, co-design workshops, tools for mapping and sharing information, requesting supplies, and free medical camps could bridge the gaps and solve such challenges. Further effective communication skills, support of local leadership, community awareness programs, encouraging participation, improving technical capacity, enhancing data availability and quality, strengthening institutional capacity, and mobilizing resources to support resilience-building efforts are requisites. These practices can sustain the culture of keeping up the indigenous knowledge of local climate, local disasters, and resilient practices exercised in the community. Such frugal but quantitative measurements can transform and empower ordinary citizens into citizen scientists. The case study in this article can be useful for policy-makers, community leaders, change-makers, administrative officials, and researchers in disaster management. It can be implemented in other landslide-prone areas with minimal changes.

Acknowledgments The authors would like to express immense gratitude for the motivation and guidance provided by Dr. Sri. Mata Amritanandamayi Devi, the Chancellor of Amrita Vishwa Vidyapeetham. The authors are thankful to all the involved faculty and students of Amrita Vishwa Vidyapeetham for their valuable support and hard work during the EWS deployment and community engagement activities in Munnar and Sikkim which includes but not limited to Dr. Venkat Rangan, Vice Chancellor, Amrita Vishwa Vidyapeetham, Prof. Balaji Hariharan, Prof. Sudesh Kumar Wadawan,

Mr. Sudarshan V, Ms. Indukala P, Mr. Aravind H, Mr., Arun Kumar J, Mr. Deepak B, Dr. Rekha P, Mr. Tinu, Dr. Nirmala V, Kaushik R, Mr. Selvakumar G, and Mr. Dawa Lepcha. Special thanks to the community champions, the stakeholders, and government administrations for on-ground support. This work is a part of IPL/WCoE/Kyoto Commitment activities of the World Center of Excellence on Landslide Risk Reduction (WCoE 2017-2020; 2020-2023) “Enhancement of the existing Real-time Landslide Monitoring and Early Warning System in Western Ghats & Himalayas, India” conducted by Amrita Vishwa Vidyapeetham (Leader: Maneesha Vinodini Ramesh). Amrita Vishwa Vidyapeetham, Kollam, Kerala, funded this work under the project “Community Based Disaster Resilience through Landslide Early Warning System.”

References

- Anderson MG, Holcombe E (2013) Community-based landslide risk reduction: managing disasters in small steps. World Bank Publications
- Can R, Kocaman S, Gokceoglu C (2019) A convolutional neural network architecture for auto-detection of landslide photographs to assess citizen science and volunteered geographic information data quality. *ISPRS Int J Geo Inf* 8(7):300
- Can R, Kocaman S, Gokceoglu C (2020) Development of a Citsci and artificial intelligence supported Gis platform for landslide data collection, vol 43. *International Archives of The Photogrammetry, Remote Sensing & Spatial Information Sciences*. Cred <https://reliefweb.int/report/world/2022-disasters-numbers>
- Cieslik K, Shakya P, Uprety M, Dewulf A, Russell C, Clark J, Dhakal A (2019) Building resilience to chronic landslide hazard through citizen science. *Front Earth Sci* 7:278
- Dekens J (2007) Local knowledge for disaster preparedness: a literature review. *International Centre for Integrated Mountain Development (ICIMOD), Kathmandu*
- Disaster Management (2018) *International Archives of the Photogrammetry, Remote Sensing and Spatial Information Sciences*. 42, W4.
- Fathani TF, Karnawati D, Wilopo W, Setiawan H (2023) Strengthening the resilience by implementing a standard for landslide early warning systems. In: *Progress in landslide research and technology*, Vol 1. Springer International Publishing, Cham, pp 277–284
- Franceschinis C, Thiene M, Mattea S, Scarpa R (2020) Do information and citizens characteristics affect public acceptability of landslide protection measures? A latent class approach. *Handbook of Climate Services*:503–513
- Gaventa J, Barrett G (2010) So what difference does it make? Mapping the outcomes of citizen engagement. University of Sussex, Falmer. <https://geoiq.io/places/Chandmari/QcioAkbcFC>
- Goodchild M (2007) Citizens as sensors: the world of volunteered geography. *GeoJournal* 69:211–221
- Gu J, Wang Z, Kuen J, Ma L, Shahroudy A, Shuai B, Liu T, Wang X, Wang G, Cai J et al (2015) Recent advances in convolutional neural networks. *Pattern Recognition* 77
- Guntha R, Rao SN, Ramesh MV (2020) Deployment experiences with amrita Kripa: a user-friendly feature rich crowdsourced humanitarian application. *Procedia Computer Science* 171:302–311
- Guntha R, Vinodini Ramesh M (2021) Technical considerations for building a landslide tracker mobile app. In *EGU General Assembly Conference Abstracts* (pp. EGU21-6019)
- Haklay MM (2013) Neogeography and the delusion of democratisation. *Environ Plan A* 45:55–69. <https://doi.org/10.1068/a45184>
- Haklay MM, Dörler D, Heigl F, Manzoni M, Hecker S, Vohland K (2021) What is citizen science? The challenges of definition. *The science of citizen science*, 13

- Hariharan B, Guntha R (2021) Crowdsourced landslide tracking-lessons from field experiences of landslide tracker mobile app. In EGU General Assembly Conference Abstracts (pp. EGU21-12711)
- Hiwasaki L, Luna E, Shaw R (2014) Process for integrating local and indigenous knowledge with science for hydro-meteorological disaster risk reduction and climate change adaptation in coastal and small Island communities. *The International Journal of Disaster Risk Reduction* 10:15–27. <https://doi.org/10.1016/j.ijdrr.2014.07.007>
- IMD (2018). <https://sdma.kerala.gov.in/wp-content/uploads/2020/08/IMD-Monsoon-Extreme-Rainfall-2018.pdf>
- Juang CS, Stanley TA, Kirschbaum DB (2019) Using citizen science to expand the global map of landslides: introducing the cooperative open online landslide repository (COOLR). *PLoS One* 14(7): e0218657
- Kocaman S, Anbaroglu B, Gokceoglu C, Altan O (2018) A review on citizen science (CitSci) applications for disaster management, vol XLII-3/W4, pp 301–306
- Kocaman S, Gokceoglu C (2019a) CitSci as a new approach for landslide researches. *Intelligent Systems for Crisis Management: Gi4DM* 2018 11, 161-183
- Kocaman S, Gokceoglu C (2019b) A CitSci app for landslide data collection. *Landslides* 16:611–615
- Landslide Reporter (2019) Accessed 13 Apr 2019 https://www.nasa.gov/solve/landslide_reporter/
- Parajuli BP, Shakya P (2019, January) Empowering citizens about emerging technologies for resilience building to landslide risk reduction in mountainous rural parts of Nepal. *Geophysical Research Abstracts* 21
- Ramesh MV, Thirugnanam H, Singh B, Nitin Kumar M, Pullarkatt D (2023) Landslide early warning systems: requirements and solutions for disaster risk reduction—India. In: *Progress in Landslide Research and Technology*, Volume 1 Issue 2, 2022. Springer International Publishing, Cham, pp 259–286
- Rohan T, Wondolowski NA, Shelef E (2020) Landslide susceptibility analysis based on citizen reports to a 311 system. In *AGU Fall Meeting Abstracts* (Vol. 2020, pp. NH031-07)
- Rohan TJ, Wondolowski N, Shelef E (2021) Landslide susceptibility analysis based on citizen reports. *Earth Surf Process Landf* 46(4): 791–803
- Scott D, Barnett C (2009) Something in the air: civic science and contentious environmental politics in post-apartheid South Africa. *Geoforum* 40(3):373–382
- See L, Mooney P, Foody G, Bastin L, Comber A, Estima J, Fritz S, Kerle N, Jiang B, Laakso M, Liu HY, Milčinski G, Nikšič M, Painho M, Pódör A, Olteanu-Raimond AM, Rutzinger M (2016) Crowdsourcing, citizen science or volunteered geographic information? The current state of crowdsourced geographic information. *ISPRS Int J Geo Inf* 5:55
- Silvertown J (2009) A new dawn for CitSci. *Trends Eco Evol* 24:467–471
- Sujatha ER, Sudarsan JS, Nithiyantham S (2023) A review on sustainable reinforcing techniques to stabilize slopes against landslides. *Int J Environ Sci Technol*:1–10
- Thirugnanam H, Uhlemann S, Reghunadh R, Ramesh MV, Rangan VP (2022) Review of landslide monitoring techniques with IoT integration opportunities. *IEEE Journal of Selected Topics in Applied Earth Observations and Remote Sensing* 15:5317–5338
- Turner AK (2018) Social and environmental impacts of landslides. *Innovative Infrastructure Solutions* 3:1–25. <https://en.wikipedia.org/wiki/Munnar>
- Wadhawan SK, Singh B, Ramesh MV (2020) Causative factors of landslides 2019: case study in Malappuram and Wayanad districts of Kerala, India. *Landslides* 17:2689–2697

Open Access This chapter is licensed under the terms of the Creative Commons Attribution 4.0 International License (<http://creativecommons.org/licenses/by/4.0/>), which permits use, sharing, adaptation, distribution and reproduction in any medium or format, as long as you give appropriate credit to the original author(s) and the source, provide a link to the Creative Commons license and indicate if changes were made.

The images or other third party material in this chapter are included in the chapter's Creative Commons license, unless indicated otherwise in a credit line to the material. If material is not included in the chapter's Creative Commons license and your intended use is not permitted by statutory regulation or exceeds the permitted use, you will need to obtain permission directly from the copyright holder.





Remedial Measures Impact on Slope Stability and Landslide Occurrence in Small-Scale Slope Physical Model in 1 g Conditions

Željko Arbanas, Josip Peranić, Vedran Jagodnik, Martina Vivoda Prodan, and Nina Čeh

Abstract

Physical modelling of landslides by analysing the behaviour of small-scale landslide models subjected to artificial rainfall can be divided into modelling under 1 g conditions and under increased acceleration (n times gravity) in a centrifuge. Physical modelling of landslide initiation began in 1970s in Japan on scaled natural slope models and after initial experiences with field and laboratory research, the small-scale landslide modelling has found a wide application around the world in different aspects of landslide investigations, analysing different types of landslides, different types of slope materials and landslide movements. The main task of landslide physical modelling is research of initiation, motion and accumulation of fast flow-like slides caused by infiltration of surface water or by shaking on a shaking table. Studies that have included landslide mitigation measures into small-scale physical models are rare and have not established correlations with a behaviour of on-site mitigation constructions. This paper discusses the behaviour of small-scale slope models supported by remedial measures under artificial rain in 1 g loading conditions. Models of slope built of different materials, with and without applied remedial measures (gravity retaining wall, gabion wall, pile wall) were exposed to identical intensities of artificial rainfall. The results of the simulations indicated that the slopes supported by remedial measures retained stability of the slope in the same conditions in which the sandy slope collapsed, as well as under significantly prolonged precipitations. At the end of the simulations, significantly higher rainfall intensities were applied to the supported slopes, exceeding the infiltration capacity of the slope material and affecting surface runout. The combination

of surface erosion and saturation of superficial layer of a slope caused initiations of flow processes, while complete saturation of a slope when ground water level reached slope surface caused forming of a surface of rupture and consequently movements of the formed landslide body. The data obtained from the geodetic and geotechnical monitoring system enabled understanding of the overall process of rainfall infiltration and soil strength reduction to the development of the surface of rupture in a slope.

Keywords

Landslide · Small-scale model · 1 g · Remedial measure · Artificial rainfall · Monitoring

1 Introduction

Landslides are caused by exposure to hazardous motions of soil and rock down the slope (Cruden 1991) that threaten vulnerable human settlements in mountains, cities, along riverbanks, coasts and islands. An increase in the frequency and/or intensity of heavy rainfall caused by climate change, and shift in the location and periodicity of this rainfall due to changing climate significantly intensify the risk of landslides in some landslide prone areas. Although they are not frequent, strong earthquakes have potential to trigger rapid and long runout landslides. The combined effects of triggering factors including rainfall and earthquakes, can lead to greater impacts through disastrous landslides such as debris flows, rock falls and mega-slides. Landslides cause casualties and damage in the world every year: in the period between 2004 and 2016 landslides caused more than 4600 casualties and damage of more than 10 billion US\$ per year over the world with the probable growth of these values in coming years (Froude and Petley 2018).

The answers of scientists, engineers, and all others included in landslide risk reduction is in significant developing of landslide science in different fields from landslide

Ž. Arbanas (✉) · J. Peranić · V. Jagodnik · M. Vivoda Prodan · N. Čeh
Faculty of Civil Engineering, University of Rijeka, Rijeka, Croatia
e-mail: zeljko.arbanas@gradri.uniri.hr; josip.peranic@gradri.uniri.hr;
vedran.jagodnik@gradri.uniri.hr; martina.vivoda@gradri.uniri.hr; nina.cheh@gradri.uniri.hr

identification, mapping, and investigation; identification of landslide susceptibility, hazard, and risk; soil and rock testing; landslide modelling and simulation to landslide monitoring, mitigation, and remediation. Some of the answers are in different types of modelling of landslide related research. Landslide modelling for a long time was based on only numerical modelling techniques. Physical modelling of landslide analyzing small scale landslide models' behavior was started in 1970s and 1980s in Japan (Oka 1972; Kutara and Ishizuka 1982; Yagi et al. 1985; Yamaguchi et al. 1989) in natural slopes exposed to artificial rainfall. The laboratory experiments of landslide behavior in a scaled physical model (also called flume or flume test) started in 1980s and 1990s in Canada (Hunger and Morgenstern 1984), Japan (Yagi et al. 1985) and Australia (Eckersley 1990) under 1 g conditions. On the other hand, small-scale landslide modelling under increased acceleration (n times the gravity) was successfully developed using a centrifuge (e.g. Kimura 1991; Take et al. 2004; Liang et al. 2017).

After initial experiences with field and laboratory research, the small-scale landslide modelling has found a wide application around the world in different aspects of landslide investigations, analyzing different types of landslides (e.g., flows, slides, falls and toppling) as well as different types of materials (rock mass, sandy, silty, and clayey materials) and landslide movements. The main task of landslide physical modelling was research of initiation, motion and accumulation of fast flow-like slides caused by infiltration of surface water in a slope and fluidification (Peranić et al. 2022c). Small-scale landslide physical modelling was also oriented to the second most important triggering factor, i.e., earthquakes after 2005 (Hong et al. 2005; Wartman et al. 2005; Lin and Wang 2006).

Although the small-scale landslide physical models, modern monitoring techniques and different monitoring equipment enable good insight into initiation and development of modelled landslide, crucial issue is to establish relationships between small-scale, brief, idealized and by artificial boundary restricted model with the complex natural landslide process (Iverson 2015). These relationships are known as scaling or scaling laws and play a crucial role in small-scale model designing and interpretation of results. Successful scaling (of material parameters, model dimensions, boundary conditions, rainfall intensity and shaking parameters as triggering factors, measured movements, velocities, accelerations etc.) is a necessary precondition for realization of successful small-scale landslide modelling (Peranić et al. 2022c). The use of physical modeling in landslide research has been significantly increasing in recent years.

The research Project Physical modelling of landslide remediation constructions' behavior under static and seismic actions, funded by the Croatian Science Foundation, started in October 2018 at the Faculty of Civil Engineering,

University of Rijeka, Croatia. The main Project aim is modelling behavior of landslide remedial constructions in physical models of scaled landslides in static and seismic conditions (Arbanas et al. 2019, 2020). In this paper, the behavior of small-scale slope models supported by remedial measures under artificial rain in 1 g loading conditions will be presented and discussed. Models of slope built of different soil materials, with and without of applied remedial measures (gravity retaining wall, gabion wall, pile wall) were exposed to identical intensities of artificial rainfall. The results of conducted measurements form installed geodetic and geotechnical monitoring system enabled understanding of overall process of rainfall infiltration and soil strength reduction to the development of the slip surface in a slope.

2 Material and Methods

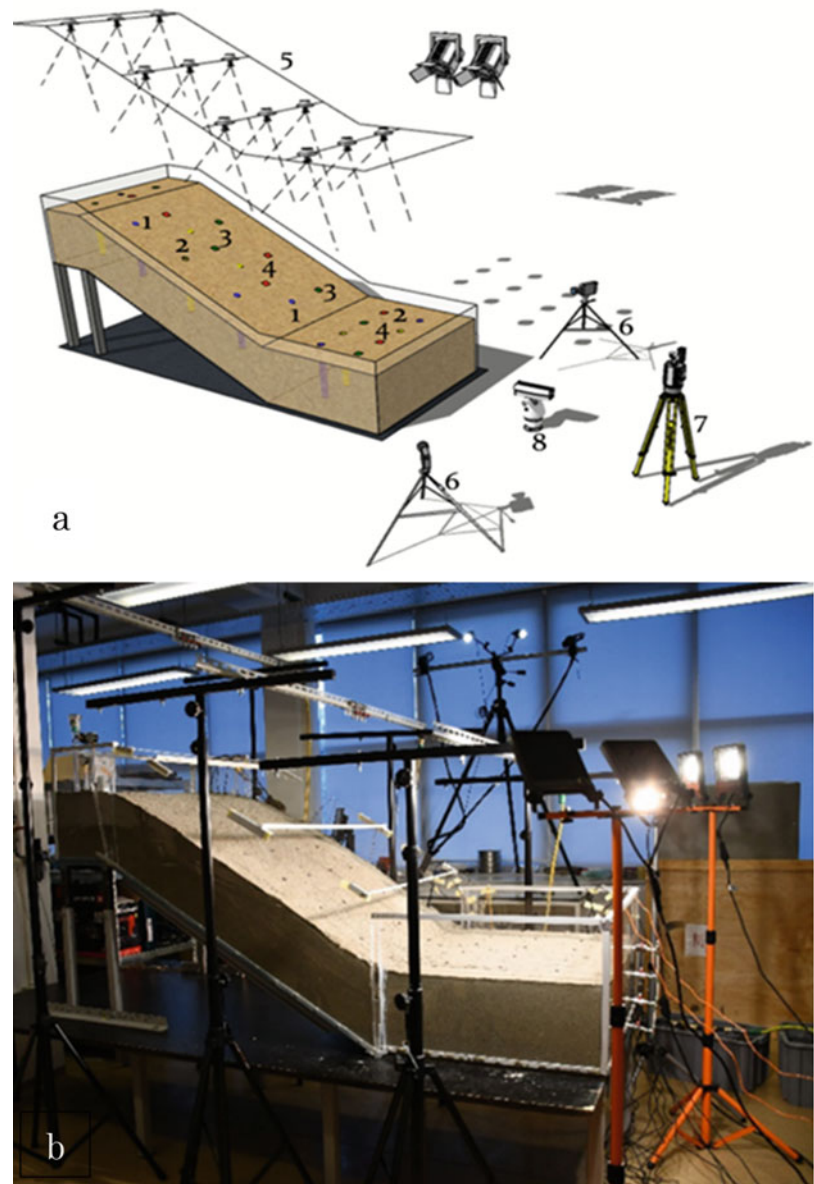
2.1 Physical Model

The physical model of a scaled slope was designed to enable initiation of a landslide caused by controlled artificial rainfall and equipped with adequate photogrammetric equipment and complex sensor network with ability to measure displacements, soil moisture and pore water pressures within a slope (Fig. 1) (Arbanas et al. 2020; Jagodnik et al. 2020). The dimensions of the model (flume) are 1.0 m (width) \times 2.3 m (length) \times 0.5 m (height). The maximum depth of a soil material in the slope was adopted to be 30 cm. Slope inclination of the model can be adjusted from 20° to 45°. To prevent possible sliding of the soil mass at the contact with the slope base, the geogrid mesh is fixed to the slope base to increase friction. The series of tests were carried out on slope inclinations of 30°, 35° and 40° with three different types of soil as slope material without and with applied different types of remedial measures (gravity retaining wall, gabion wall, pile wall).

2.2 Soil Material Properties

Three different soil materials with relatively simple behavior were selected to build the typical small-scale physical slope models: uniform sand (S) and sand-kaolin mixtures with 10% (SK10) and 15% (SK15) kaolin content. The fine-grained (0–1 mm) uniform Drava River sand was chosen as the base material to represent soil material in cohesionless slopes. The other materials were a mixture of the base sandy material with 10% and 15% by mass of industrial kaolin, representing the behavior of fine-grained, cohesive materials with low but stable present cohesion. Kaolin was chosen as a clay with low plasticity and a relatively well graded grain size distribution

Fig. 1 (a) Schematic view of the physical model with monitoring equipment: (1) tensiometers, (2) pore pressure transducers, (3) strain gauges, (4) accelerometers, (5) rainfall simulator (sprinkler system), (6) high speed cameras, (7) terrestrial laser scanner (TLS), (8) infrared camera; (b) photo of the physical model (Arbanas et al. 2020; Jagodnik et al. 2020)



curve and is not too sensitive to changes in water content (Arbanas et al. 2019; Peranić et al. 2022c).

The sand-kaolin mixtures were prepared by adding a predetermined amount of dry kaolin to dry sand (gravimetrically) and then mixing thoroughly with a laboratory mixer. During or before mixing, the amount of clean water was also poured into the soil mixture to achieve the desired initial soil moisture content. Once a homogeneous mixture was achieved, the material was placed in plastic bags, sealed and left to rest until the model was built (Vivoda Prodan et al. 2023). Grain size distribution curves were determined using a combination of sieving and sedimentation (hydrometer) analysis and are presented in Fig. 2.

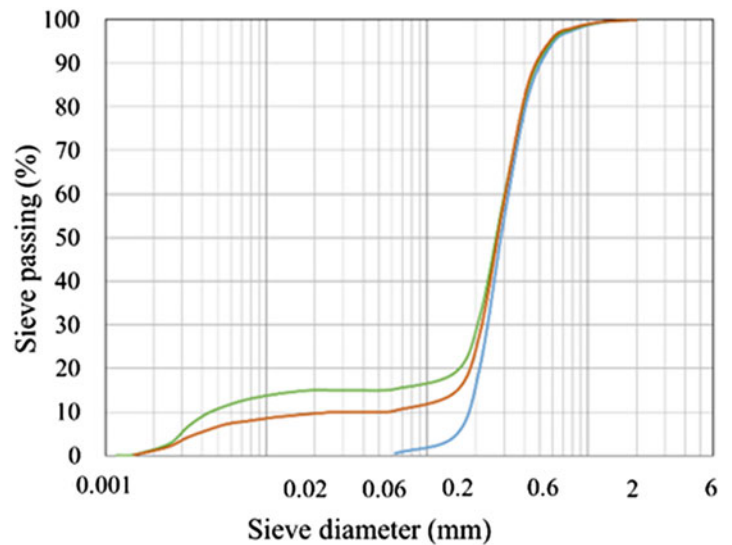
The Mohr-Coulomb strength parameters of the described materials—friction angle and cohesion were determined in a

direct shear device at low normal stresses like those in the small-scale slope model at the same relative density of 50%. Hydraulic conductivity was determined at the same conditions as in the slope model, using the falling head test in an oedometer and triaxial apparatus. The basic physical and mechanical properties of the described materials and the targeted initial conditions at the start of the tests are given in Table 1 (Arbanas et al. 2020; Jagodnik et al. 2020; Peranić et al. 2022c; Vivoda Prodan et al. 2023).

2.3 Monitoring Equipment

In all types of slope physical models, very important issue is use and installation of measuring equipment necessary to

Fig. 2 Grain size distribution curves of sand (S) (in blue), sand-kaolin mixtures with 10% of kaolin content (SK10) (in orange) and sand-kaolin mixtures with 15% of kaolin content (SK15) (in green) (Vivoda Prodan et al. 2023)



enable measuring of movement, deformation, oscillations, pressure, forces, moisture, and other parameters necessary to determine the behavior of the slope. The selection of the measuring techniques and equipment in the physical model follows the practice of monitoring systems established on real landslides. In this sense, the sensor systems used in physical models can be divided into geotechnical monitoring systems and geodetic monitoring systems (Mihalić Arbanas and Arbanas 2015), where geodetic systems are mostly based on modern photogrammetric techniques for multi-temporal landslide analysis (Zanutta et al. 2006; Scaioni et al. 2015; Cignetti et al. 2019). Modern photogrammetric techniques including Structure from Motion (*SfM*) techniques for multi-temporal landslide analysis represent the most important tools for measuring of movement (Bitelli et al. 2004),

acceleration and velocity of soil mass during sliding along artificial slopes in the physical models. Modern high-speed cameras enabled to provide stereo image sequences during sliding process, which is very important for investigation of very fast landslide occurrences (e.g., Akca 2013; Feng et al. 2016). Geotechnical monitoring in physical models is based on application of miniature sensors equivalent to in field used geotechnical monitoring equipment (Wieczorek and Snyder 2009). Different researchers established different monitoring systems using available types of sensors with adequate precision for scaled slope models (de Dios et al. 2009; Ooi et al. 2010; Wang et al. 2013; Ooi and Wang 2014; Lu et al. 2015).

The monitoring system established in a physical model followed the principles used in the observation of real landslides and consisted of a geotechnical and a geodetic

Table 1 The basic physical and mechanical properties of the sand and sand-kaolin mixtures built in the small-scale model and the initial conditions at the start of the tests

Parameter	Sand (S)	Sand-kaolin mixture	
		SK10	SK15
Specific gravity, G_s	2.70	2.69	2.67
Dry density, ρ_d (g/cm ³)	1.52	1.43	1.51
Total density, ρ_t (g/cm ³)	1.55	1.50	1.63
Effective particle size			
D_{10} (mm)	0.19	0.038	0.056
D_{60} (mm)	0.37	0.31	0.207
Uniformity coefficient, c_u	1.947	8.16	54.107
Minimum void ratio, e_{min}	0.641	0.647	0.544
Maximum void ratio, e_{max}	0.911	1.121	1.430
Hydraulic conductivity, k_s (m/s)	1E-05	6.78E-06	3.5E-06
Friction angle, ϕ (°)	33.5	32.5	32.4
Cohesion, c (kPa)	0	2.7	3.4
Initial porosity, n_i	0.44	0.469	0.434
Initial void ration, e_i	0.78	0.884	0.766
Initial relative density, D_{ri}	0.5	0.5	0.75
Initial water content, w_i (%)	2	5	8.1

monitoring system. The geotechnical monitoring system comprised of a complex network of miniature sensors equivalent to the geotechnical monitoring devices used in the field (Mihalić Arbanas and Arbanas 2015).

The ARAMIS system is an optical, noncontact 3D measurement system (GOM mbH, Braunschweig, Germany) that provides the entire workflow from taking measurements to analyzing data and presentation of the results. A set of two 4-megapixel and two 12-megapixel high-speed cameras were used for multi-temporal landslide analysis from captured stereo image sequences (Čeh et al. 2022). The system enables continuous monitoring of the 3D coordinates of reference points through all stages of the activity of scaled landslide models. The FARO Focus 3D X 130 (FARO Technologies Inc., Lake Mary, FL, USA) terrestrial laser scanner was used to capture the 3D model surface at high resolution before the start and at the end of the test.

The scanner uses phase-shift technology to accurately determine the relative 3D position of the scanned points, while reference points are used to overlap the scanned areas and define the relative coordinate system. A Nikon D500 camera (Nikon Inc., Melville, NY, USA) with an ultra-wide-angle Tokina AT-X 11–20 lens was used for the *SfM* photogrammetry survey of the physical models. This technology allows the creation of 3D models from multiple overlapping images taken at different triangulation angles.

The geotechnical monitoring system consisted of a complex network of miniature sensors connected to data loggers, enabling continuous data collection on soil moisture, positive pore-water pressures and soil suction, electrical conductivity, temperature, pressures, displacements, and accelerations (Pajalić et al. 2021; Peranić et al. 2022a).

Accurate observation of the hydromechanical response of small-scale slopes under controlled initial and boundary conditions provides necessary information on variables controlling the instability phenomena of rainfall-induced landslides. The development of a suitable sensor network for the test conditions and the selection of appropriate measurement techniques is the crucial step in the development of small-scale physical landslide models. There were several requirements that were considered during the selection of the measuring devices. Information on soil moisture content and the change in pore-water pressure (both positive and negative values) during rainfall infiltration had to be available at appropriate time intervals, depending on the experimental conditions. This requirement necessitated the use of digitized sensors and pressure transducers in combination with suitable data loggers with programmable data collection intervals. The additional important requirement to be considered was that the project envisaged testing a wide range of soils, from sand to clay. Therefore, the selected measurement equipment had to be able to cover a wide measurement range occurring in different soil textures, while ensuring sufficient precision

and resolution of the measured quantities, as well as the reasonable responsiveness and equilibration times depending on the tested soil type. Another consideration relates to data redundancy: data had to be collected simultaneously at several depths and along different profiles to obtain a complete picture of the temporal and spatial evolution of different variables during the experiment. Finally, the chosen monitoring equipment was intended to be used with both the small-scale physical landslide models for testing under static (rainfall) and seismic (earthquake) conditions (Peranić et al. 2022a). The detailed description of the selected and used sensors for monitoring the hydromechanical response of the slope model was provided by Peranić et al. (Peranić et al. 2022a) and Pajalić et al. (Pajalić et al. 2021).

2.4 Rainfall Simulator

The rainfall characteristics play a decisive role in rainfall-induced slope failures in small-scale physical slope models. The design of a rainfall simulator should meet specific requirements of the project and it was an important issue in the early stages of the platform's development. In particular: the ability to apply a wide range of rain intensities depending on the soil material tested and the specific objectives of the experiment, sufficient spatial uniformity of the simulated rainfall and the ability to change rainfall patterns and characteristics, the prevention of excessive erosion due to raindrop impact forces (which are closely related to raindrop diameter and impact velocity), the portability of the rainfall simulator, due to its possible use not only with the platform for testing under static conditions, but also under dynamic conditions, were the main considerations in the design and construction of the simulator (Peranić et al. 2022a).

Rainfall simulators are widely used tools to study hydrological processes such as interaction of rainfall with soil, soil erosion, surface runoff and infiltration (Lora et al. 2016a). Although it was possible to use some of the already developed rainfall simulators (Iserloh et al. 2012, 2013; Lora et al. 2016b), a new rainfall simulator was constructed as part of the project due to the lack of standard solutions.

The rainfall simulator developed through the project consists of three independent branches that delivered water from the main control block to the spray nozzles each equipped with four different axial-flow full-cone nozzles with a spray angle of 45° or 60°. Each branch has been placed at such a height that the water can reach the edges of the plexiglass sides without creating too much water on the edges or water coming out of the model. This solution covers a wide range of rainfall intensities, from less than 30 l/h/m² to more than 140 l/h/m² at the reference pressure of 2 bars. A wide range of rainfall intensities and the possibility to change the location of rainfall by opening or closing valves on each of



Fig. 3 Photo of one branch with four axial-flow full-cone spraying nozzles

the branches allows the modelling of different rainfall patterns and different rainfall intensities applied to the small-scale slope model (Arbanas et al. 2020). The main control block was connected to the water supply network, and consisted of the control units that regulated the rainfall simulator's work, such as water pressure regulators, manometers, flow measuring units, filters, etc. High-density polyethylene pipes conveyed the pressurized water from the control block to three sprinkler branches, which were adjustable in height and equipped with various spray nozzles, Figs. 2 and 3. The rainfall simulator was fully portable and could be easily dismantled and installed at any location with a water supply ensured (Peranić et al. 2022a).

2.5 Remedial Structures

Remedial measures chosen to be tested in this research are mostly selected as constructions that are commonly used in remediation of relatively small landslides and are usually applied at the foot of the slope. These constructions belong to the group of retaining structures, but partly also to the groups of slope geometry modifications and drainage (Popescu 2001; Mihalić Arbanas and Arbanas 2015). Three types of retaining structures are selected as most effective: a gravity wall in sandy material, a gabion wall in silty material (sand-kaolin mixture with 10% of kaolin content, SK10) and a pile wall in clayey material (sand-kaolin mixture with 15% of kaolin content, SK15). The first step in construction of remedial measures was selection of scale factor. It was decided that the scale factor in geometrical scale low would be 1:20, and all dimensions of the selected remedial measure were scaled to 1:20.

Considering the gravity retaining wall and the pile wall construction as remedial measures in the foot of a slope, which usually behave as rigid structures without or with

only very small internal deformations, 3D printing of elements of structures in scaled dimension using polylactic acid (PLA) material was selected to imitate remedial structures in real slopes. At the same time, the strength and deformability parameters of the material used for 3D printing are high enough to ensure rigid behavior of structures the without possibility of internal structure failure. Gabion wall structures are flexible structures that enable significant deformations of the overall structure, particular elements (filled gabion baskets) as well as along the contacts of the elements without losing the stability of the overall structure. Scaled gabion baskets are made of fiberglass netting, while the filling consists of gravel grains scaled in relation to the size of the stone blocks used in standard construction.

Gravity retaining model elements are 20.0 cm long and 26.0 cm high; the foundation is 6.0 deep and 9.0 cm wide, Fig. 4. The rear face of the wall is in the lower part inclined at 108° while the upper part is vertical. The elements are connected with vertical key-pin elements enabling articular connection between the individual elements in one unique wall construction. In the lower part of the wall, above the foundation, two lines of the drains are derived to ensure adequate drainage and avoid forming hydrostatic pressure above the foundation behind the wall.

The piles have 4.0 cm of outer and 3.0 cm of inner diameter, and a length of 32 cm (Fig. 5a). The piles are connected in elements of 3 piles, which are connected to the foundation beam (Fig. 5b) and head beam (Fig. 5c). The foundation beam is just an element that does not exist in field construction but is necessary to establish fixation in a base (e.g., bedrock in the field). The head beam is 6.0×6.0 cm and has 5.0 cm deep holes for the pile heads. The axial distance between piles is 6.5 cm. The base of the foundation beam is adjusted to the slope model inclination and 8.0 cm deep holes ensure the tightness of the pile bases. Head and foundation elements are connected with vertical key-pin elements

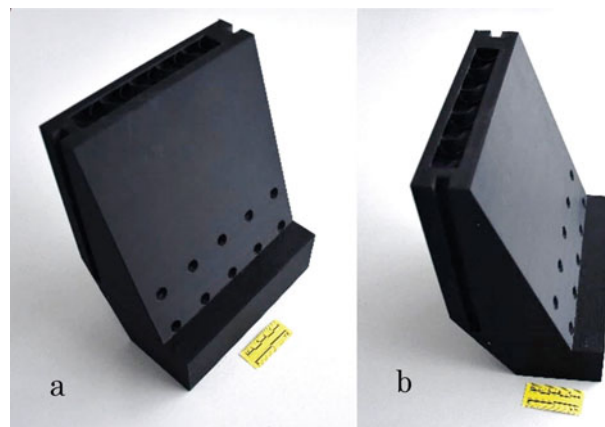


Fig. 4 Photo of gravity retaining model elements. (a) front view, (b) side view

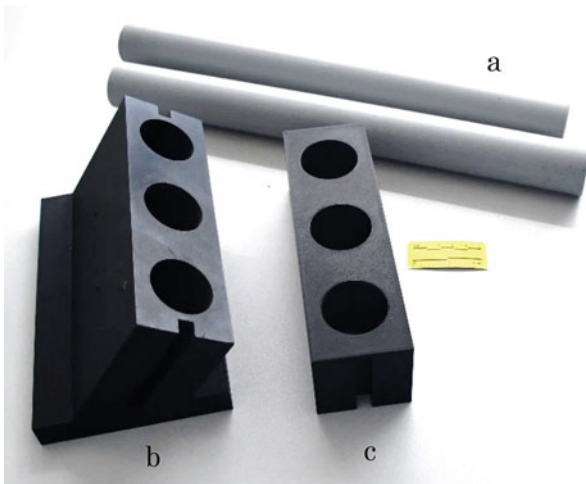


Fig. 5 Photo of pile wall elements. (a) piles, (b) foundation beam, (c) head beam

enabling articular connection between the individual elements in one unique pile wall construction.

Scaled gabion baskets made of fiberglass netting have dimensions of $5.0 \times 5.0 \times 10.0$ cm and the filling material is uniform gravel 0.4–0.8 mm, Fig. 6. The gabion baskets are tailored from one piece of net and fixed by hot gluing.

3 Construction of Slope Models

3.1 Construction of Slope Models without Remedial Measure

The previously described types of soil material (uniform sand (S) and sand-kaolin mixtures with 10% (SK10) and 15% (SK15) kaolin content) were built-in in the flume in five layers each 6 cm thick, up to a total height of 30 cm. To reach homogeneity of the material in the slope and relatively uniform conditions in built-up soil material, the model was built in three segments—lower (L), middle (M), and upper (U) part—building up the material from the foot to the top of the slope with compaction in each layer. To prevent possible sliding of the soil mass at the contact with the flume base, the geogrid mesh is fixed to the flume base to increase friction (Arbanas et al. 2020).

Each type of soil material was previously tested using standard Proctor test according to the American Society for Testing and Materials (ASTM) standards and the American Association of State Highway and Transportation Officials (AASHTO) standards to determine optimal moisture content and adequate dry density of the material. The used materials were pre-prepared at optimal water content (Table 1) and build-in by manual compaction using the undercompaction method (Ladd 1978). For each segment of the slope and each



Fig. 6 Photo of gabion model elements

layer, the necessary mass of a soil material was previously calculated and weighed to ensure that the required initial compaction has been achieved. Before placement of the next layer, the surface of the previous layer was raked and sprayed with water to maintain the initial moisture and achieve the best possible connection between soil material of each layer.

All sensors used in the tests inside the slope material were installed parallel to the soil layers after compaction of a layer was completed. The water-related sensors that were used in this research were TEROS 10 and TEROS 12 frequency-domain reflectometry-based soil moisture sensors which provided an indirect measurement of the volumetric water content of porous materials installed in all three tests, while the TEROS 31 mini tensiometers and the TEROS 21 maintenance-free matric potential sensor for measurement of soil water potential were used only in the tests with sand-kaolin mixtures. All sensors were manufactured by the METER Group AG (Munich, Germany) (Peranić et al. 2022b). The locations of the sensors were chosen as critical points for monitoring of the hydro-mechanical response of soil material in a slope model. The sensors were installed in the lower (L), middle (M) and upper (H) part of the slope, at different depths (6, 12, 18 and 24 cm) along the same profile to provide data at the same cross-section that enables validation and numerical analysis of the observed landslide initiation (Fig. 8) (Vivoda Prodan et al. 2023a).

3.2 Construction of Slope Model with Installation of Gravity Wall

In the test after construction of the sand slope in same conditions as in the test without remedial measures, installation of gravity retaining wall was completed following the

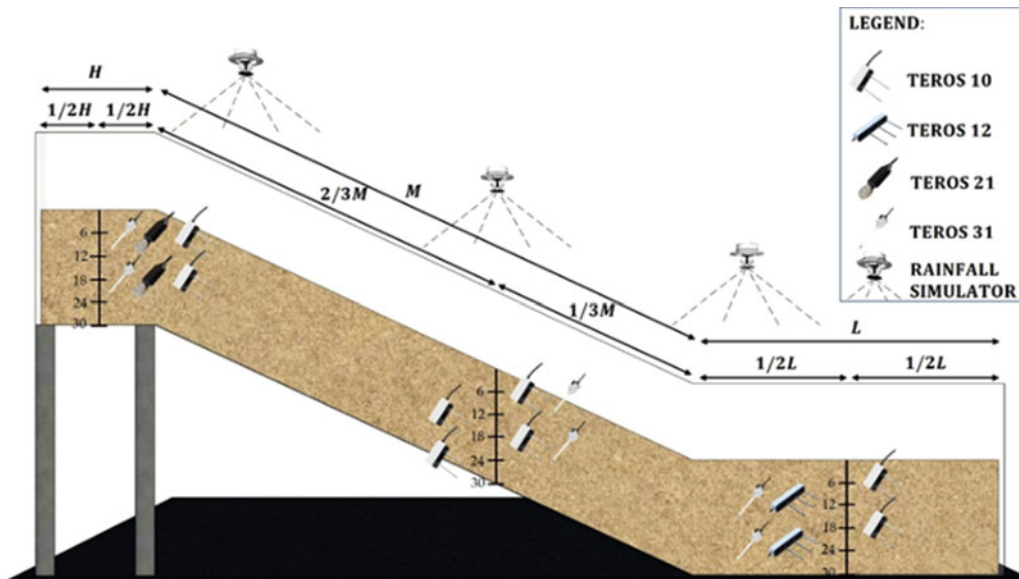


Fig. 7 Positions of the embedded water related sensors in the small-scale landslide model

sequence of works that is commonly carried out in a real slope. The gravity retaining wall was constructed from five 20.0 cm long 3D-printed elements described previously, interconnected by an articular connection. The height and other dimensions of the wall were based on geometrical similarity of 1:20. The material used for the backfill of the wall was gravel, the grain size distribution of which was determined from geometrical similarity with coarse crushed stone fill material 1:20 that is usually used as backfill material behind walls. According to the position in the slope, the strength parameters of this material have no importance, while the hydraulic conductivity is significantly higher than for sand in the slope and has no influence on the infiltration process (Arbanas et al. 2022a) (Fig. 7).

Additional impact of buttressing material is in increasing of vertical forces in the foot of the slope with consequently rise of soil strength in the zone as well as general decreasing of slope inclination.

When the model slope of sandy material (S) was built at the inclination of 35° , the foundation pit in the foot of the slope was excavated and additionally compacted, and the retaining gravity wall was lined (Fig. 8a, b, c). After installation of sensors at the rear face of the wall and laying geotextile, backfilling with gravel material was started (Fig. 8d, e). The slope was stepwise excavated to ensure adequate contact between the sandy slope and the gravel buttressing embankment (Fig. 8f, g). The gravel material was separated from the sandy material by a geotextile and compacted with a manual compactor (Fig. 8d to g). The

buttressing material was built-in to approximately two thirds of the height of the slope with an inclination of the surface of 1:1.5 (Fig. 8h).

3.3 Construction of Slope Model with Installation of Gabion Wall

In the test after construction of the silty slope (SK10) under the same conditions as in the test without remedial measures, installation of gabion retaining wall was completed following the order of works that is usually performed on a real slope. The gravity retaining wall was constructed from five previously described gabion boxes in 4 rows. The height and other dimensions of the wall were based on geometrical similarity of 1:20. The material used for the backfill of the wall was gravel with the grain size distribution determined from geometrical similarity with coarse crushed stone fill material 1:20 that is usually used as backfill material behind walls. According to the position in the slope, the strength parameters of this material are of no significance, while the hydraulic conductivity is significantly higher than for sand, allowing infiltration and vertical drainage to the level of the gabion wall foundation. As with the gravity wall, an additional effect of the buttressing material is in increasing vertical forces in the slope's foot area and the consequent increase in soil strength in the zone, as well as general decreasing of slope inclination.



Fig. 8 Installation of the gravity wall and buttressing embankment behind the wall into the prepared sandy slope: (a) excavated foundation pit and installed element of the gravity wall, (b) first wall element installed in the foundation pit, (c) a view at the partially installed wall in the foot of the slope, (d) excavation for backfill behind the wall with

installed sensors; geotextile is laid, (e) filling the gravel material behind the wall, (f) filled buttressing embankment behind the gravity wall along the slope, (g) a view at buttressing embankment behind the gravity wall, (h) model prepared for testing

When the 35° model slope from silty material (SK10) was built, the foundation pit in the foot of the slope was excavated, filled with 2.0 cm of gravelly material and additionally compacted (Fig. 9a), and the gabion boxes were built-in rows with regular overlapping (Fig. 9b to f). After installation of sensors and laying the geotextile, backfilling with gravel material was started (Fig. 9d to f). The slope was stepwise excavated to ensure adequate contact between the silty slope and gravel buttressing embankment (Fig. 9d to g). Gravel and silty material were separated by geotextile and compacted with a manual compactor (Fig. 9d to g). The buttressing material with a slope of 1:2 was built-in to approximately two thirds of the height of the slope (Fig. 9h).

3.4 Construction of Slope Model with Installation of Pile Wall

The installation of a pile wall in the slope model differs significantly from the installation of a gravity and gabion wall. While the installation of gravity and gabion wall models completely follows the order of works corresponding to those of a real slope, the installation of the pile wall and establishing of a small-scale slope model are carried out in parallel (Vivoda Prodan et al. 2023b). The first step is setting and fixing the foundation beam to the base of the model platform. The role of the foundation beam is to ensure the tightness of pile's bases for the future retaining the load of the sliding body due to the movements down the slope. The foundation beam was assembled from five previously described 3D-printed elements, Fig. 10a. The pile wall consists of 15 piles with 4 cm of outer diameter and at 6.5 cm of axial distance. The height (40 cm) and other dimensions of the pile wall and its elements were based on geometrical similarity of 1:20. After setting and fixing foundation beam, the first layer soil material was built in and compacted in all parts of the slope (L, M, H) and the model slope of clayey material (SK15) was built at the inclination of 35°. The following step was the installation of the piles into the foundation beam was, Fig. 10b, after which placement and compaction of the other four layers of slope clayey soil material was conducted, until the planned slope model surface, Fig. 10c, d. After the clay slope model was built, the buttressing counterfort of gravelly material is constructed in the front of the pile wall. The embankment is 20.0 cm tall, with a 10.0 cm wide crown and 1:1.5 inclined front slope, Fig. 10e. The material used for the backfill of the wall was gravel with granulometric composition determined from geometrical similarity with coarse crushed stone fill material 1:20 that is usually used as embankment fill materials. The gravel material in the counterfort was separated from the clayey material on the slope by geotextile and compacted with a manual compactor. This buttressing counterfort has two

roles: to hold on to the pile wall and to ensure faster drainage of water behind the pile wall. In real site, an additional role of this embankment is to provide a working plateau for heavy equipment for installation of piles.

Three trenches, 8.0 cm wide, 10.0 cm deep and 65.0 cm long (from the pile wall along the slope), were excavated behind the pile wall and filled with gravel material Fig. 10e, f. Gravel material in trenches was separated from clayey material in the slope by geotextile and compacted by a manual compactor. The main role of these trenches is to collect part of the surface water on the slope and enable faster drainage to the toe of the slope. The second role is to increase the resistance of the slope surface to erosion by surface outflow.

The next stage in slope construction is the installation of a head beam at the top of the piles and connecting the individual piles into a single construction, Fig. 10f, g. After the installation of the head beam, the space between it and the slope was filled and compacted with a manual compactor, Fig. 10g, h.

4 Testing and Results

4.1 Testing of Slope Models without Remedial Measures

The previous chapters have described the materials and methods used in small-scale landslide modelling in this research. Series of tests at the slopes of different materials (i.e., uniform sand (S) and sand-kaolin mixtures with 10% (SK10) and 15% (SK15) kaolin content) and different slope inclinations (30°, 35°, 40°) and different rainfall scenarios, but without installed remedial measures are conducted.

A very large volume of result data was collected from various sensors installed inside a slope (tensiometers, pore pressure sensors, accelerometers, MEMS, pressure cells), as well as surface displacements captured by the ARAMIS system, terrestrial LiDAR scanning and digital camera that enables in-depth analysis of the sliding triggering and initiation process inside the slope, and its evolution under different initial and rainfall conditions. A significant part of research and analyses were carried out considering and comparing the conditions present in the model at the moment of landslide initiation and the modes of further landslide development. The following analyses were carried out and published: initiation and development of a landslide in a slope of clear uniform sand (S) (Arbanas et al. 2020; Jagodnik et al. 2020; Pajalić et al. 2021); initiation of a sandy slope due to the rise of the groundwater level and hydraulic pathways and a reduction in the shear strength of the soil due to infiltration in small-scale slope model built in sandy (S) and silty (SK10) materials (Peranić et al. 2022a); comparison of the mechanism of rainfall induced landslides in small-scale models



Fig. 9 Installation of the gabion wall and buttressing embankment behind the wall in a prepared silty slope: (a) excavated foundation pit with compacted layer of gravel, (b) first row of gabion boxes installed in foundation pit, (c) second row of gabion boxes installed, (d) filled buttressing embankment behind the gravity wall separated from the

slope material with geotextile, (e) installed second row of gabion boxes, (f) filled buttressing embankment behind the gravity wall along the slope, (g) a view at the buttressing embankment behind the gabion wall, (h) model prepared for testing



Fig. 10 Installation of pile wall construction and buttressing counterfort in the front of the wall in clayey slope: (a) setting and fixing foundation beam to the model base, (b) installation of piles in foundation beam, (c) built in the soil layers in the slope, (d) base of buttressing

counterfort in the front of piles, (e) complete buttressing counterfort and excavated trenches (f) filled trenches and installed head beam, (g) a view at pile wall with embankment behind the head beam, (h) model prepared for testing

built of different materials (sandy (S), silty (SK10) and clayey (SK15)) (Vivoda Prodan et al. 2023a, b); comparison of landslide initiation in small-scale sandy (S) and clayey (SK15) slopes (Peranić et al. 2022c); comparison of the behavior of sandy (S) and clayey (SK15) slopes during rainfall in small-scale model (Arbanas et al. 2022b); and rainfall loss and erosion process in a small-scale slope (Bezák et al. 2022). In this chapter, these results will not be presented separately. Instead, results are used to highlight the impact of remedial measure constructions exposed to the same conditions as slopes built from the same material and exposed to same rainfall events without present remedial measure constructions.

4.2 Testing of Slope Model with Gravity Retaining Wall

After the slope models were built and the monitoring equipment installed in the slope, the slope models were exposed to artificial rainfall from three nozzles, one nozzle in each part of the slope—the upper (U), middle (M) and lower (L) part. The results of two tests are presented here: two models of a sandy (S) slope, with and without applied gravity retaining wall, were exposed to identical intensities of artificial rainfall. The course of the test developments is shown in Fig. 11. In both tests, the slopes were exposed to an initial rainfall intensity of 81.4 mm/h. The selection of rainfall intensity was based on infiltration conditions in a slope and the main requirement was that all rainwater at the point of contact on the model surface infiltrates without forming surface runoff. The applied intensities were at the upper precipitation values that can be infiltrated in a soil (Arbanas et al. 2022a).

After the initial establishment of a constant rainfall intensity and a stable infiltration process, both slope models were exposed to rainfall with a constant intensity for both slopes to allow similar rainfall conditions in a slope with and without a gravity retaining wall applied. The intensity of 81.4 mm/h was maintained for 56 min when the first crack occurred in the slope model without remedial measures applied (Test no. 2) and after the ground water level reached soil surface in the lower (L) part of the model, Fig. 12a. The constant groundwater level in the lower (L) part of the model was maintained until the end of the test and the nozzle above the lower part of the model was closed. During this period, the landslide in the slope without gravity wall applied developed retrogressively to the top of the slope (Fig. 12a, c, e), while in the slope with gravity wall applied there were no visible signs of landslide initiation in the form of development of cracks during this entire period.

When the retrogressive development of the landslide in the slope without gravity wall reached the top of the slope,

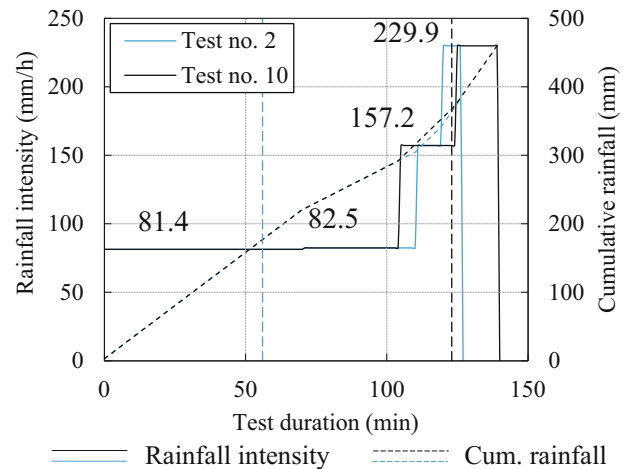


Fig. 11 Simulated rainfall during the test on the sandy slope without gravity wall (blue) and the test on the sandy slope with gravity wall applied in the foot of the slope (black). Vertical lines mark the times of the first crack evidence

the rainfall intensity was increased to 157.2 mm/h in the next 10 min, and finally increased to 229.9 mm/h until the final failure of the slope 128 min after the start of the test. A similar succession of rainfall was applied to the slope without a gravity wall, but there was no initiation of a landslide in a similar time period and with similar rainfall intensities (Fig. 11).

At the same time, under the same rainfall conditions, no sliding process in the slope with the retaining gravity wall applied occurred, indicating that the remedial measures applied with the gravity wall and the coarser backfill material behind the wall confirmed the intended role in maintaining the stability of the sandy slope (Test no. 10). The first cracks in the test on the slope with the gravity wall occurred in the 123rd min after the increase of rainfall intensity to 157.2 mm/h and it was completed after the 134th min with the opening of the nozzles in the upper part of the slope with an intensity of 229.9 mm/h, which was above the infiltration capacity of the sandy material.

After the application of a high rainfall intensity in the upper part of the slope (229.9 mm/h), higher than the infiltration capacity of the sandy material, there was a sudden development of the erosion process of the sandy material and a global instability of the slope occurred, which resulted in exceeding the bearing capacity of the soil under the retaining wall foundation, Fig. 12b, d, e. Although the retaining wall did not completely collapse and overturn, the horizontal displacement caused by the local failure below the retaining wall foundation and the horizontal soil compaction in the foot of the slope enabled a global collapse of the slope. The applied rainfall intensities that caused this global collapse are significantly high and, considering scaling relative to real slope sizes, represent rare extreme rainfall events.

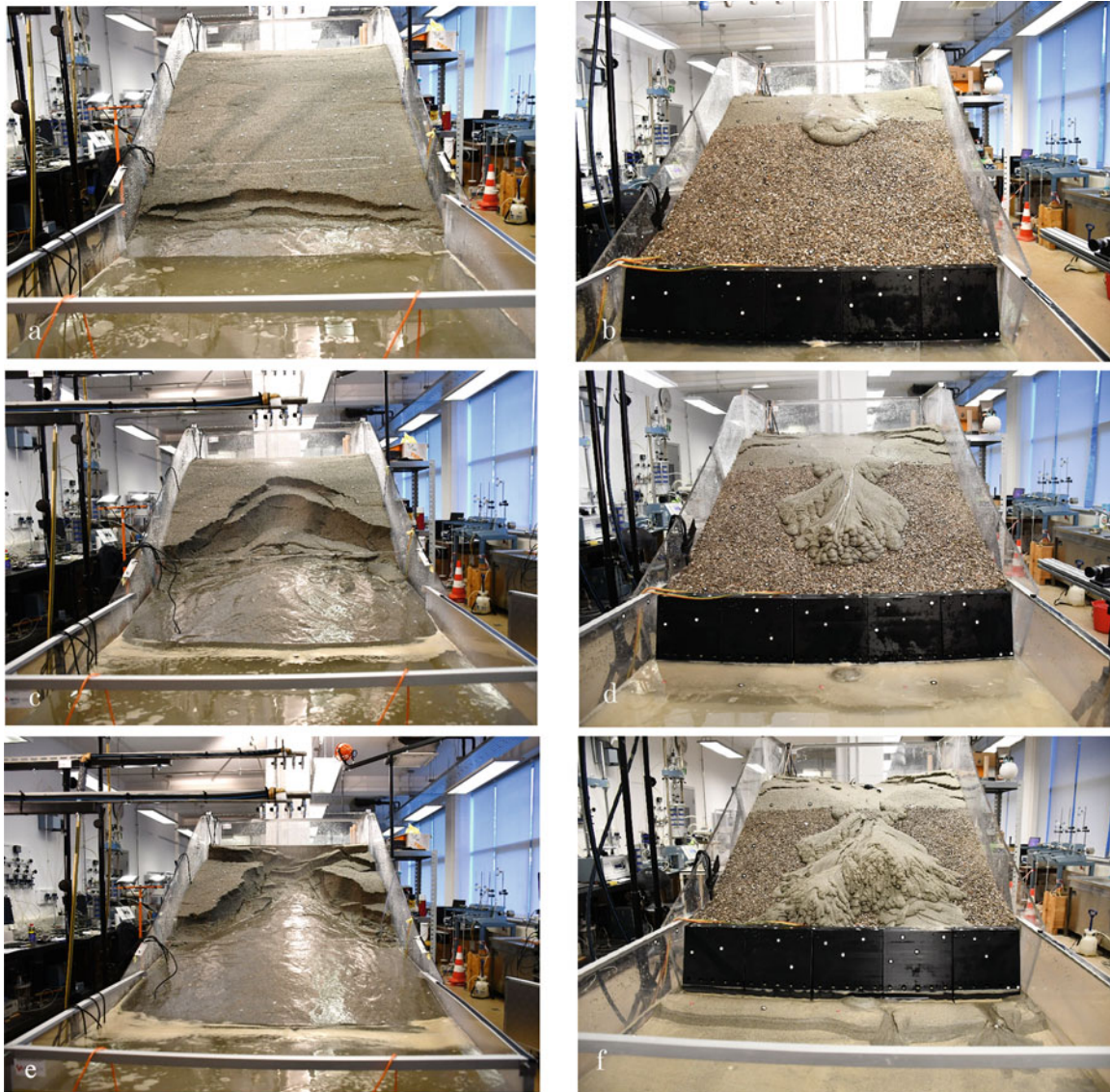


Fig. 12 Development of landslides in small-scale sandy slope without and with installed gravity retaining wall: (a) initial instability in the foot of the unsupported slope (62 min), (b) slope after the first cracks in the slope with retaining wall (129 min), (c) development of the landslide to the top of the unsupported slope (90 min), (d) development of the

landslide to the top and advancement of the debris flow on the slope with retaining wall (134 min), (e) landslide in the unsupported slope at the end of the test (134 min), (f) landslide and debris flow in the slope with retaining wall at the end of the test (155 min)

The superficial signs of landslide initiation that occurred and the reasons for their occurrence in the case of a slope without applied gravity wall can be explained by the results of continuous volumetric water content monitoring (Fig. 13). The process of landslide initiation and development was described by the volumetric water content increasing due to infiltration until saturation in the deepest part of the slope, forming the water table. As it becomes established, a flow down the slope begins, causing a rapid rise in the groundwater level in the lower part of the slope. This leads to a decrease in the soil shear strength with complete loss of matric suction,

failure and further retrogressive landslide development to the top of the slope (Peranić et al. 2022c), Fig. 12a, c, e.

In both tests, almost the same rainfall exposure conditions were achieved, and the monitoring devices were installed in the same positions on the slope to allow measurement of changes in volumetric water content. The sensors for measuring volumetric water content were installed at four different depths (6, 12, 18 and 24 cm below the slope surface) in the lower (L), middle (M) and upper (H) parts of the slope (Fig. 13). When analyzing the development of rainfall infiltration and the formation of a ground water level along the

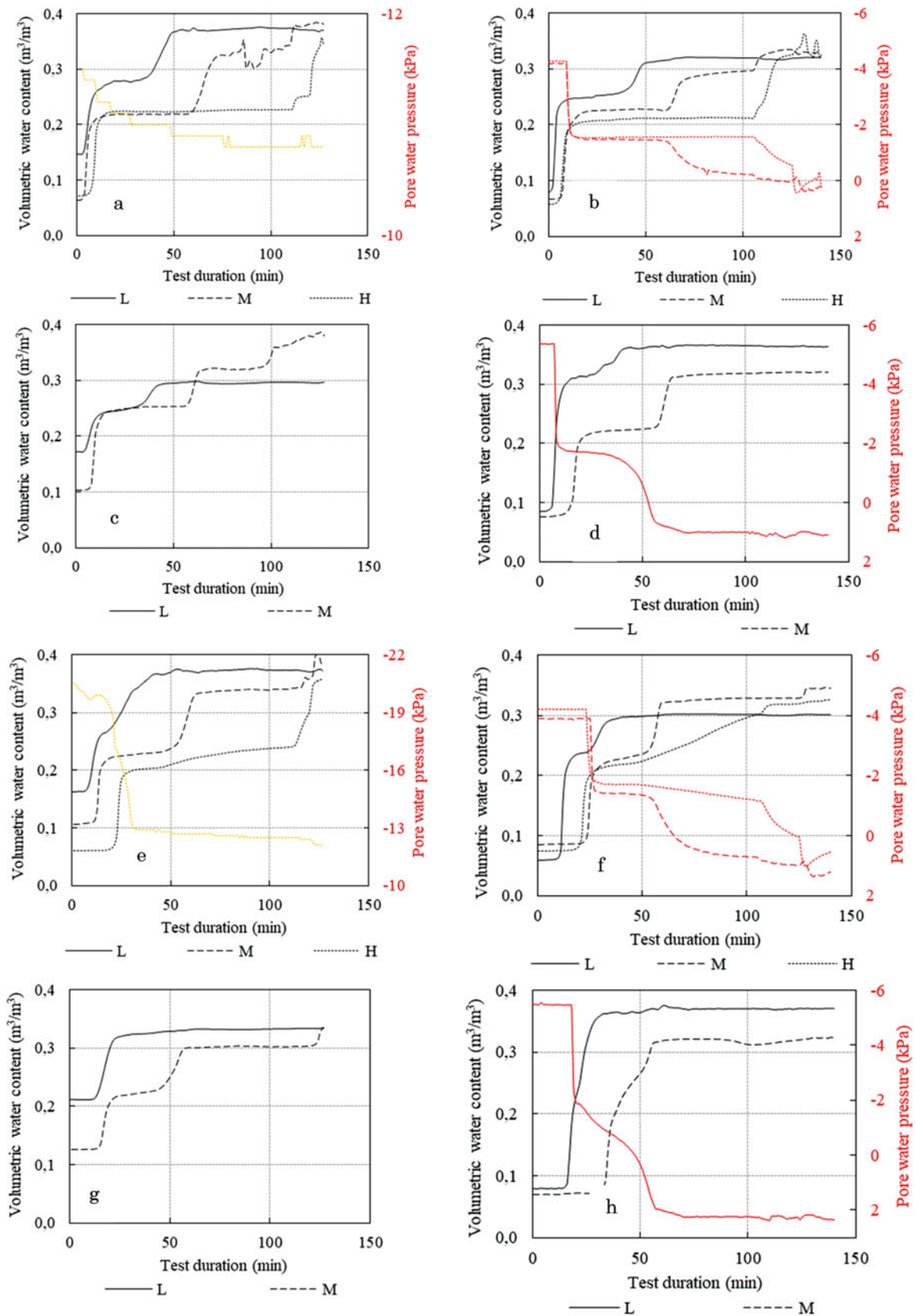


Fig. 13 Volumetric water content and pore water pressure measurements in tests without applied gravity retaining wall (a) at 6 cm below the surface; (c) 12 cm below the surface; (e) 18 cm below the surface; (g) 24 cm below the surface and in the test with applied

gravity retaining wall; (b) at 6 cm below the surface, (d) 12 cm below the surface; (f) 18 cm below the surface; (h) 24 cm below the surface in upper (H), middle (M), and lower (L) part of the slope

slope in both models, no significant deviations in the measurement results were found. Neglecting the differences in water contents at the beginning and during the tests caused by initial differences and heterogeneity in soil density (primarily) and water content (which is also related to density), the plots showing the change in volumetric water content in the model within the tests show similar trends over a similar time period of applied rainfall. This suggests that the main role of the gravity wall and the coarser backfill material behind the wall is to increase soil strength in the slope foot and associated erosion prevention that has occurred on the slope without remedial measures (Arbanas et al. 2022a).

After the rainfall intensity in the upper part of the slope (157.2 mm/h) exceeded the infiltration capacity of the sandy material, there was a sudden development of the erosion process of the sandy material and a global instability of the slope occurred, which resulted in exceeding the bearing capacity of the soil under the foundation of the retaining wall. The retaining wall did not completely collapse and overturn, but the horizontal displacement allowed a global collapse of the slope. The applied rainfall intensities that caused this global collapse are significantly high and, when scaled relative to real slope sizes, represent rare extreme rainfall events. Despite this fact, in the following tests, the applied remedial measures should be improved to avoid this type of collapse even under such extreme circumstances.

4.3 Testing of Slope Model with Gabion Wall

As described earlier, the slope model with a gabion wall applied in the foot of the slope as remedial measure was constructed in a similar way to the slope model with a gravity retaining wall. The results of two tests are presented: models of a silty (SK10) slope with and without a gabion retaining wall applied, exposed to identical intensities of artificial rainfall. The course of the test developments is shown in Fig. 14. In both tests, the slopes were exposed to an initial rainfall intensity of 32.8 mm/h. Again, the selection of rainfall intensity was based on infiltration conditions in a slope and the main requirement was that all rainfall at the point of contact on the model surface infiltrates without forming surface runoff. The intensities applied were at the upper precipitation values that can be infiltrated in a soil.

After the initial establishment of a constant rainfall intensity and a stable infiltration process, the models were exposed to rainfall with constant intensities for both slopes to enable similar rainfall conditions in both models. The intensity of 32.8 mm/h was maintained throughout the tests. The constant groundwater level in the lower (L) part of the model was maintained until the end of the tests and the nozzle above the lower part of the model was closed after the groundwater reached surface in this part of the model.

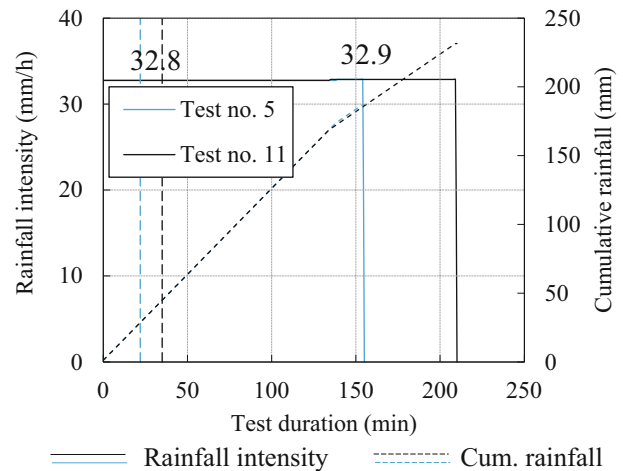


Fig. 14 Simulated rainfall in the test on the silty slope without applied gabion wall (blue) and test on the silty slope with applied gabion wall in the foot of the slope (black). Vertical lines mark times of the first crack evidence

The first crack on the slope without gabion wall applied (Test no. 5) occurred in the 22nd min in the upper part of the slope. Thereafter, the landslide progressively developed to the foot of the slope (Fig. 15a, c). In the 74th min, the ground water level reached the bottom of the slope (Fig. 15a) and started to flow to the surface (Fig. 15a, c). As the test progressed, the ground water in the middle part of the slope (M) was rising, reaching the slope surface (Fig. 16a, c, e, g) in increasingly higher parts of the slope, while the amount of outflow water was gradually increasing (Fig. 15a, c, e). This outflow and the resulting surface runoff as a consequence have two additional processes: washing out of silty (kaolin) particles from the soil in the slope and surface erosion (Fig. 15a, c, e). Surface flow was enhanced by rainfall water that could no longer infiltrate into the slope. Parallel to this process, retrogressive development of the landslide to the top of the slope started (Fig. 15c) and after 135 min the landslide had spread to the top of the slope. A steady state flow conditions were established (Fig. 16a, c, e, g) and no further development of the landslide occurred. Only the erosion process caused by the surface runoff continued and the test was terminated after 155 min.

Under the same rainfall conditions, the behavior of the slope with gabion wall installed differs significantly (Test no. 11). The first crack of the landslide in the slope with the gabion wall applied occurred in the 35th min in the upper part of the slope, but no significant sliding development was observed in the period that followed the landslide initiation. This indicates that the applied remedial measures with gabion wall and coarser backfill material behind the gabion wall confirmed the intended role in retaining the stability of the silty slope (Fig. 15b, d, e). The other differences from the slope without remedial measures are the absence of ground

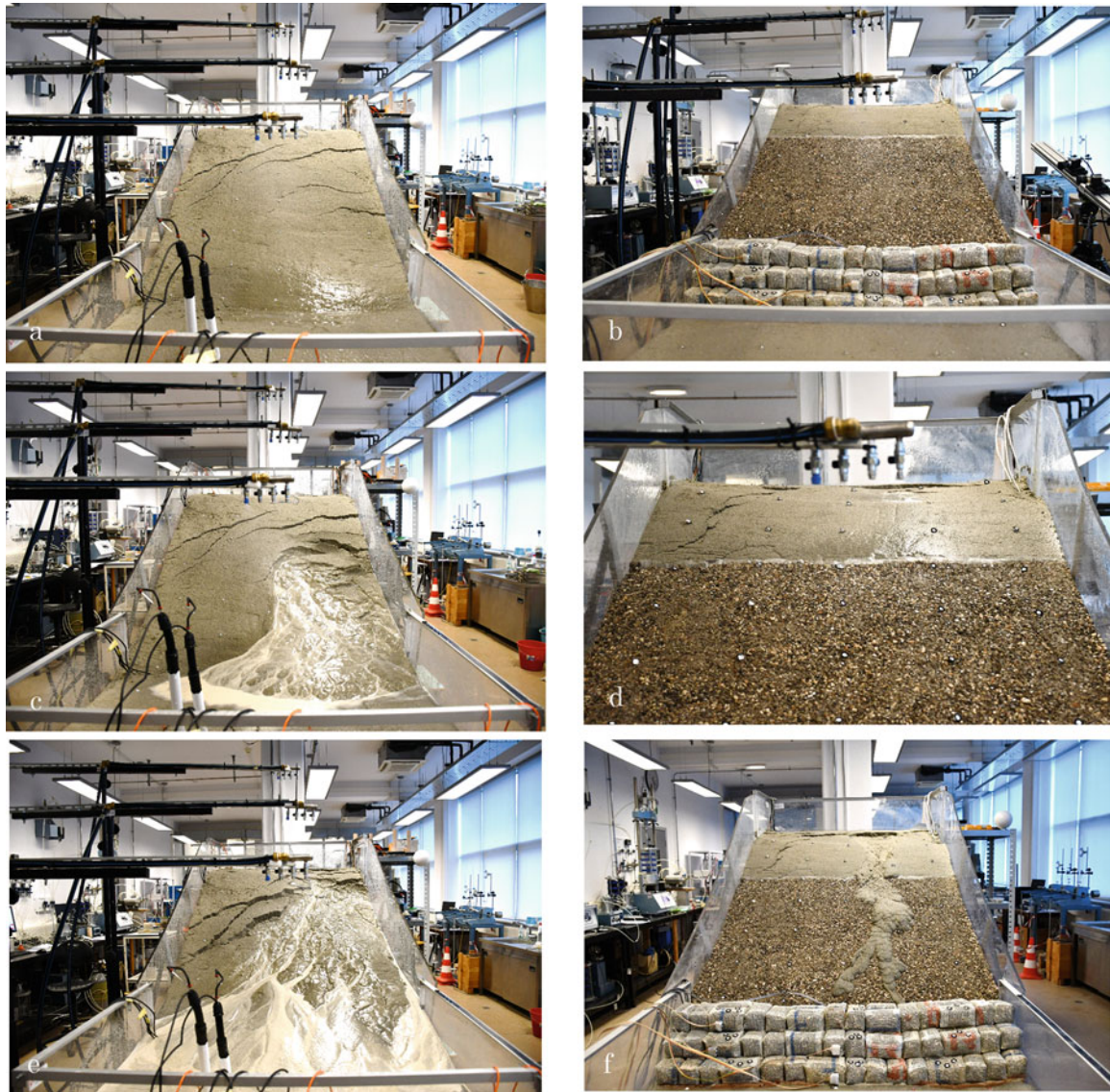


Fig. 15 Development of landslides in small-scale silty slopes without and with installed gabion wall: (a) initial instability in the unsupported slope (79 min), (b) slope before the first cracks in the slope with gabion wall (24 min), (c) progressive development of landslide and flow out of

ground water to the surface (90 min), (d) occurrence of landslide to the top on the slope with gabion wall (135 min), (e) landslide and erosion in the unsupported slope (118 min), (f) a view of the slope with gabion wall at the end of the test (210 min)

water outflow from the slope to the slope surface and, secondarily, washing out of silty particles. It is obvious that the coarser backfill material behind the gabion wall plays an important role in slope surface erosion protection as well as in faster drainage of ground water than the basic silty material in the slope. The test continued with the same rainfall intensity until the 210th min. However, after steady state flow conditions were achieved (Fig. 16b, d, f, h), there was no further landslide development and practically without erosion in the upper part of the slope (Fig. 15f).

Although the stability of overall slope was not completely retained and the main crack at the top of the slope indicated the formation of a sliding surface, the overall displacements

are generally small and no signs of instability in the foot of the slope were visually observed. The displacements measured in the central part of the crown of the gabion wall were less than 2.5 cm, but no visible signs of loss of stability of the gabion wall itself were detected.

The superficial signs of sliding initiation and the causes of their occurrence in the case of the slope with and without applied gabion wall can be explained by analyzing the results of continuous volumetric water content monitoring (Fig. 16a to h). The process of landslide initiation and development was described by the increase in volumetric water content due to infiltration until saturation in the deepest part of the slope, forming the water table. As it becomes established, a

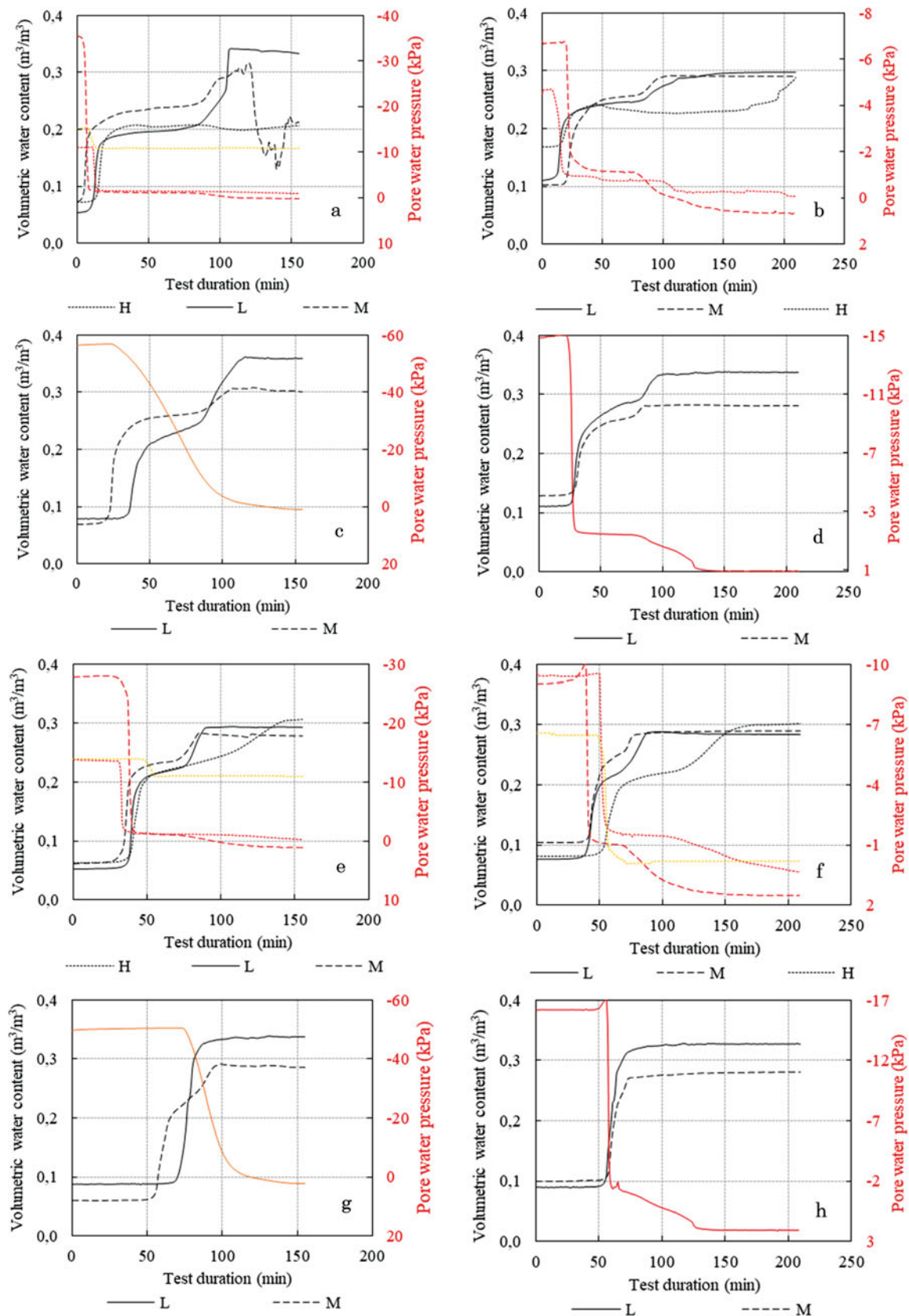


Fig. 16 Volumetric water content and pore water pressure measurements in tests without applied gabion wall (a) at 6 cm below the surface; (c) 12 cm below the surface; (e) 18 cm below the surface; (g) 24 cm below the surface and in the test with applied gravity retaining

wall; (b) at 6 cm below the surface, (d) 12 cm below the surface; (f) 18 cm below the surface; (h) 24 cm below the surface in upper (H), middle (M), and lower (L) part of the slope

flow down the slope begins, causing a rapid rise in the groundwater level in the lower part of the slope. This leads to a decrease in the soil shear strength with complete loss of matric suction, failure, and landslide development to the top of the slope, Fig. 15a to f.

4.4 Testing of Slope Model with Pile Wall

The slope model with installed pile wall as a remedial measure in the foot of the slope was constructed significantly differently from the slope models with gravity retaining wall and gabion wall as described in the previous chapters. The results of two tests are presented here: two models of a clayey (SK15) slope, with and without applied gabion pile wall, which were exposed to identical intensities of artificial rainfall. The course of the test developments is shown in Fig. 17. In both tests, the slopes were exposed to an initial rainfall intensity of 32.8 mm/h. The selection of rainfall intensity was again based on infiltration conditions in a slope and the main requirement was that all rainfall water at the point of contact on the model surface is infiltrated, i.e., no surface runoff is generated. The applied intensities were at the upper precipitation values that can be infiltrated in a soil.

After the initial establishment of a constant rainfall intensity and a stable infiltration process, the models for both slopes were exposed to constant rainfall intensities to enable similar rainfall conditions. The intensity of 32.8 mm/h was maintained throughout the tests. The constant groundwater level in the lower (L) part of the model was maintained until the end of the tests and the nozzle above the lower part of the model was closed after the groundwater reached the surface

in this part of the model. The intensity in the upper parts of the slopes did not change.

The first crack of the landslide in the slope without applied pile wall (Test no. 8) occurred in the middle part of the slope after 35 min. After that, the landslide retrogressively developed to the top of the slope, but without significant displacements. In the 48th min, the ground water level reached the surface in the middle part of the slope (Fig. 18a) and started to flow to the surface (Fig. 15a, c). As the test progressed, the ground water was rising and reached the surface along the slope (Fig. 16a, c, e, g), while the amount of outflow water was gradually increasing (Fig. 18a, c, e). This outflow and the resulting surface runoff as a consequence have two additional processes: the washing out of silty (kaolin) particles from the soil in the slope and surface erosion (Fig. 18a, c, e). Surface runoff was increased by rainfall water that could no longer infiltrate into the slope. During this increasing erosion process, no further landslide development occurred. Once a steady state flow condition was established (Fig. 19a, c, e, g), only the erosion process due to surface runoff continued and the test was terminated after 195 min. Even in the situation when the rainfall intensity was significantly increased (to 82.5 mm/h from the 175th min to the end of the test), no further landslide development occurred.

Under the same rainfall conditions, the behavior of the slope with installed pile wall differs considerably (Test no. 12). The first crack of the landslide in the slope with applied pile wall occurred in the 81st min in the upper part of the slope. Thereafter, no significant sliding displacements occurred in the slope with the pile wall applied, indicating that the applied remedial measures with pile wall and coarser backfill material behind the head beam of the pile wall confirmed the intended role in maintaining the stability of a clayey slope (Fig. 18b, d). The other differences related to the slope without remedial measures are absence of ground water outflow from the slope to the slope surface and washing out of silty particles. The drainage tranches behind the pile wall have an important role in collecting surface water to prevent slope surface erosion. The test was conducted at the same rainfall intensity until the 108th min, when the erosion process started in the upper part of the slope (Fig. 18d). The steady state of the flow (Fig. 19b, d, f, h) was achieved and there was no further development of the landslide until the 230th min of the test. At that moment, the rainfall intensity was significantly increased to 82.5 mm/h (from 230th min to the end of the test), which significantly exceeded the infiltration capacity, intensifying the erosion process in the entire upper part of the slope. Additional displacement of the landslide body was also observed, but the pile wall and buttressing construction in the toe of the slope remained stable (Fig. 18f).

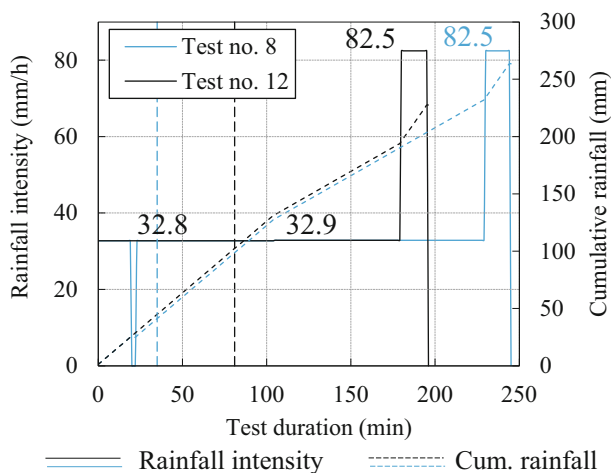


Fig. 17 Simulated rainfall in the test on the clayey slope without applied pile wall (blue) and test on the clayey slope with applied pile wall in the foot of the slope (black). Vertical lines mark times of the first crack evidence

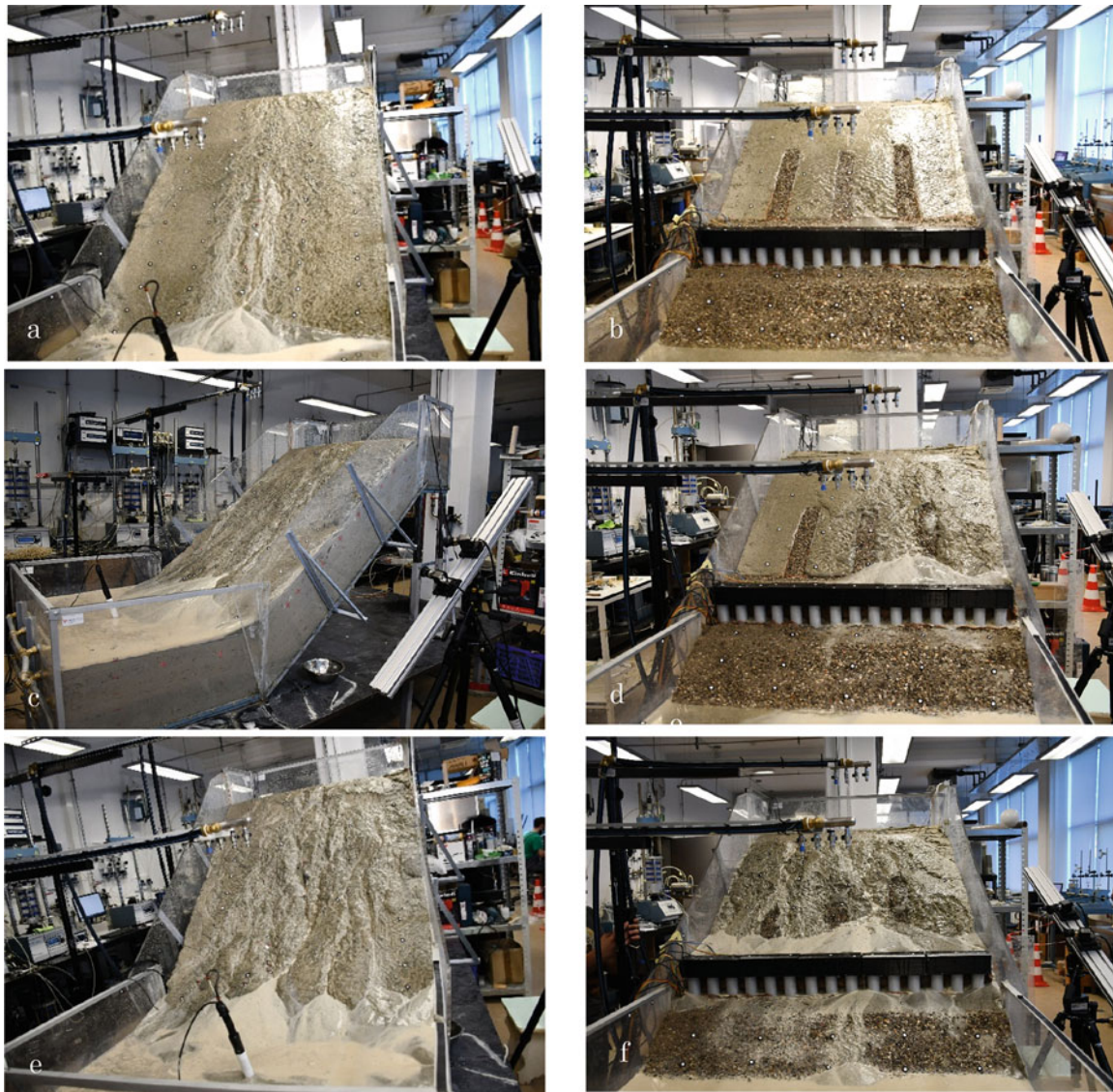


Fig. 18 Development of landslides in small-scale clayey slope without and with installed pile wall: (a) erosion process after initial instability in the unsupported slope (85 min), (b) slope after the first cracks in slope with pile wall (107 min), (c) development of erosion process on

unsupported slope (159 min), (d) start of erosion process in the upper part of the slope with retaining wall (175 min), (e) overall erosion at the unsupported slope (181 min), (f) erosion process in the upper part of the slope with pile wall (194 min)

Although the stability of overall slope with the installed pile wall and buttressing embankment in the toe was not completely retained and the main crack at the top of the slope indicated slip surface formation, the overall displacements were relatively small and there were no visible signs of instability in the foot of the slope. The measured displacements in the central part of the head beam of the pile wall were less than 5 cm, but no visible signs of loss of overall stability of the pile wall structure were observed (Vivoda Prodan et al. 2023b).

The superficial signs of sliding initiations that occurred and the causes for their occurrence on slopes with and without applied pile wall and other remedial elements

(buttressing, drainage tranches) can be explained by the results of continuous volumetric water content monitoring inside the slope (Fig. 19a to h). The process of landslide initiation and development was described by the volumetric water content increase due to infiltration, until the complete saturation in the deepest part of the slope, forming the water table. Once it becomes established, a flow down the slope begins, causing the groundwater level to rise rapidly in the lower part of the slope. This leads to a decrease in the soil shear strength with complete loss of matric suction, an increase in soil weight, failure and landslide development to the top of the slope, Fig. 18a to f.

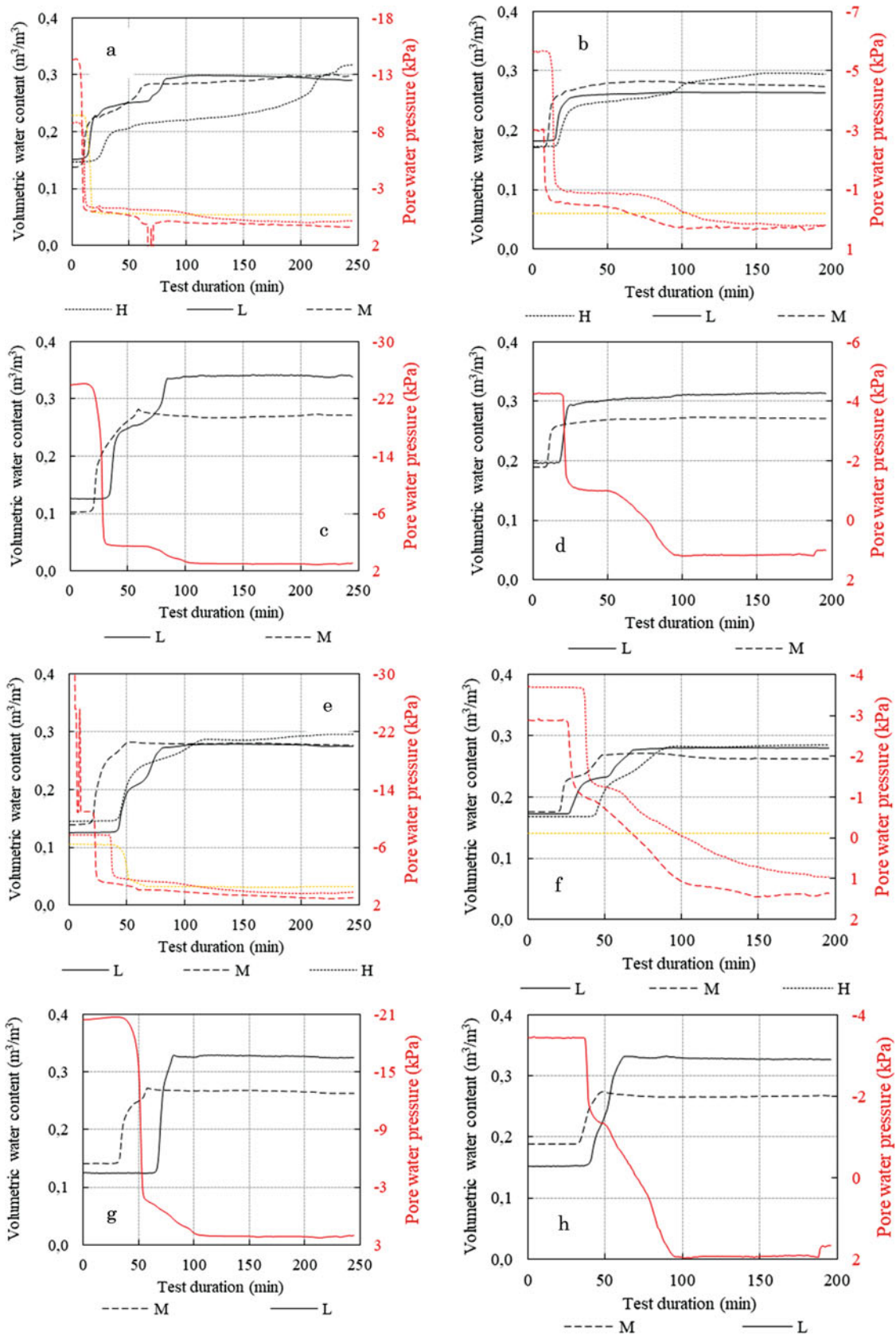


Fig. 19 Volumetric water content and pore water pressure measurements in tests without applied pile wall (a) at 6 cm below the surface; (c) 12 cm below the surface; (e) 18 cm below the surface; (g) 24 cm below the surface and in the test with applied gravity retaining

wall; (b) at 6 cm below the surface, (d) 12 cm below the surface; (f) 18 cm below the surface; (h) 24 cm below the surface in upper (H), middle (M), and lower (L) part of the slope

5 Discussion and Conclusions

Physical modelling of landslides by analyzing small scale landslide models' behavior was started in 1970s and 1980s in Japan on natural slopes exposed to artificial rainfall. Laboratory experiments on landslide behavior in a scaled physical model under 1 g loading conditions started in the 1980s and 1990s in Canada, Japan and Australia.

The small-scale landslide modelling has found a wide application around the world in different aspects of landslide investigations, analyzing different types of landslides (e.g., flows, slides, falls and toppling) as well as different types of materials (rock mass, sandy, silty, and clayey materials) and landslide movements. The main purpose of landslide physical modelling was to study the initiation, motion and accumulation of fast flow-like slides caused by infiltration of surface water into a slope and fluidification, but also to study earthquake-induced landslides. The use of physical modeling in landslide research has been significantly increasing in recent years, as evidenced by the increasing number of articles published in journals and at conferences.

Although the small-scale landslide physical models, modern monitoring techniques and different monitoring equipment enable good insight into initiation and development of modelled landslide, one crucial issue is to establish relationships between small-scale, brief, idealized and by artificial boundary restricted model with the complex natural landslide process. These relationships are known as scaling or scaling laws and play a crucial role in small-scale model designing and interpretation of results. Successful scaling (of material parameters, model dimensions, boundary conditions, rainfall intensity and shaking parameters as triggering factors, measured movements, velocities, accelerations etc.) is a necessary precondition for realization of successful small-scale landslide modelling.

In this paper we presented partial results of the research Project Physical modelling of landslide remediation constructions' behavior under static and seismic actions, funded by the Croatian Science Foundation, started in October 2018 at the Faculty of Civil Engineering, University of Rijeka, Croatia. The main Project aim was modelling and researching the behavior of landslide remedial constructions in physical models of scaled landslides in static and seismic conditions. In this paper, the behavior of small-scale slope models supported by remedial measures under artificial rain in 1 g loading conditions are presented and discussed. Models of slope were built of different soil materials, with and without applied remedial measures (gravity retaining wall, gabion wall, pile wall) and exposed to identical intensities of artificial rainfall. The measurements results collected from the geodetic and geotechnical monitoring systems enabled understanding of overall process of rainfall

infiltration and soil strength reduction to the development of the slip surface in a slope.

In the previous chapter, the results of two series of tests carried out on slope inclinations of 35° degrees built of different soil materials, uniform sand (S) and sand-kaolin mixtures with 10% (SK10) and 15% (SK15) kaolin content, with and without applied remedial measures were presented. The first series of tests was carried out on basic slope models, while in the second series of tests the gravity retaining wall, gabion wall or pile wall were installed as adopted remedial measures and then exposed to artificial rainfall intensities identical to that of the first series of tests. The aforementioned constructions were selected as appropriate remedial measures against instability that occurred on the slope models in the first series of tests without remedial measures. The models, materials and procedures that were applied during the models' construction were presented in detail. Both series of models with and without applied remedial measures were exposed to almost completely identical rainfall scenarios to enable a comparison of the slope behavior results obtained and the effects of the applied remediation measures to slope stability.

As it was described above, in the same time exposed to the same rainfall scenarios, almost no significant sliding processes and displacements in the slope with applied remedial measure occurred that indicate that the applied remedial measures with remedial measure and coarser backfill material behind the wall constructions confirmed the intended role to retain slope stability. However, it should be emphasized that after applying of the rainfall intensity at the upper part of the slopes higher than infiltration capacity of slope materials, sudden development of erosion process of slope materials and occurrence of global instability of slope appeared. The retaining constructions did not collapse but horizontal displacement pointed on global possible global collapse of the slopes in ace of prolonged rainfall of high intensity.

The analyses of the rainfall infiltration and the formation of a ground water level along the slope in both model series with and without remedial measure constructions applied do not reveal any significant deviations in the measurement results, if the differences in water contents at the beginning and during the tests, caused by initial differences and heterogeneity in soil density and water content, are neglected. The graphs representing the development of volumetric water content in the model during the tests show similar trends over similar time periods of applied rainfall in both series of tests, suggesting the conclusion that the main role of the applied remedial constructions and coarser backfill material behind the constructions is in increasing soil strength in the slope foot and the associated erosion prevention in the slopes. As one of the most important findings which came out from this research is that the matric suction in a slope at low

confining stresses, such as those present in slope models, has a governing role in retaining stability of slopes. In almost all cases, the failures, and evidences of sliding process were observed in time period when ground water was formed in a slope causing full saturation and total loss of matric suction. The impact of pore pressure to reduction of effective stresses and strength at the slip surface in small-scale models is too low and has no significant role in instability occurrences in 1 g conditions. This fact can be applied to shallow landslides in general and would be very easy to confirm, despite all the difficulties in applying small-scale model results to real slopes.

The results presented were mostly based on observations from high-speed cameras that enabled to provide stereo image sequences during the sliding process, and on a geotechnical monitoring network of miniature sensors connected to data loggers that provided continuous data collection on soil moisture, positive pore-water pressures and soil suction, electrical conductivity, temperature, and pressures. During the tests, some other equipment was used as part of the slope monitoring, e.g., photogrammetric equipment for multi-temporal landslide analysis of image sequences obtained from a pair of high-speed stereo cameras, terrestrial laser scanning and *SfM* photogrammetry surveys, the results of which were not included in this paper. These data were recorded and collected during the conducted tests, and these results will enable detailed kinematic analyses of the points at the surface of the slope model determined in the pre- and post-slide phases. Although the results currently analyzed already give a relatively good insight into the impact of the applied remedial constructions on increasing the overall stability of the slope in the models, a comprehensive analysis of all collected data will allow a more detailed and precise description of all parts of the models and especially of the remediation structures behavior.

Acknowledgments The research presented in this paper was supported by Croatian Science Foundation under the Project IP-2018-01-1503 Physical modelling of landslide remediation constructions behavior under static and seismic actions (ModLandRemSS). This support is gratefully acknowledged. This research was conducted as part of joint research of Croatian Landslide Group, World Center of Excellence of ICL in Landslide Risk Reduction in the period of 2020-2023.

References

- Arbanas Ž (2013) Photogrammetric monitoring of an artificially generated shallow landslide. *Photogramm Rec* 28:178–195. <https://doi.org/10.1111/phor.12016>
- Arbanas Ž, Jagodnik V, Peranić J et al (2020) Physical model of rainfall induced landslide in flume test: preliminary results. In: Proceedings of European Conference of Physical Modeling in Geotechnics, p 8
- Arbanas Ž, Pajalić S, Jagodnik V et al (2019) Development of physical model of landslide remedial constructions' behaviour. In: Proceedings of the 4th Regional Symposium on Landslides in the Adriatic–Balkan Region. Bosna and Herzegovina Geotechnical Society, pp 103–108
- Arbanas Ž, Peranić J, Jagodnik V, Vivoda Prodan M, Čeh N, Pajalić S, Plazonić D (2022a) Impact of gravity retaining wall on the stability of a sandy slope in small-scale physical model. In: Peranić J, Vivoda Prodan M, Bernat Gazibara S et al (eds) Proceedings of the 5th ReSyLAB 'Landslide Modelling & Applications', Rijeka. Faculty of Civil Eng. University of Rijeka, Croatia, pp 193–200
- Arbanas Ž, Peranić J, Jagodnik V et al (2022b) Behaviour of sandy and clayey slopes exposed to artificial rain in small-scale model. In: Proc of 10th physical modelling in geotechnics. Korean Geotechnical Society (KGS), Daejeon, South Korea, Seoul, Korea, pp 712–715
- Bezak N, Peranić J, Mikoš M, Arbanas Ž (2022) Evaluation of hydrological rainfall loss methods using small-scale physical landslide model. *Water* 14:2726. <https://doi.org/10.3390/w14172726>
- Bitelli G, Dubbini M, Zanutta A (2004) Terrestrial laser scanning and digital photogrammetry techniques to monitor landslide bodies. In: International archives of photogrammetry, remote sensing and spatial information sciences. Istanbul, Turkey, pp. 246–251
- Cignetti M, Godone D, Wrzesniak A, Giordan D (2019) Structure from motion multisource application for landslide characterization and monitoring: the Champlas du col case study, Sestriere, North-Western Italy. *Sensors* 19:2364. <https://doi.org/10.3390/s19102364>
- Cruden DM (1991) A simple definition of a landslide. *Bull Int Assoc Eng Geol* 43:27–29. <https://doi.org/10.1007/BF02590167>
- Čeh N, Peranić J, Jagodnik V, Pajalić S, Vivoda Prodan M, Arbanas Ž (2022) Digital image correlation and the use of high-speed cameras for 3D displacement monitoring in 1g small-scale landslide models. In: Peranić J, Vivoda Prodan M, Bernat Gazibara S et al (eds) Proceedings of the 5th ReSyLAB 'Landslide Modelling & Applications', Rijeka. Faculty of Civil Eng. University of Rijeka, Croatia, pp 181–186
- de Dios R, Enriquez J, Victorino FG et al (2009) A tilt, soil moisture, and pore water pressure sensor system for slope monitoring applications. *Science Diliman* 21:15–27
- Eckersley D (1990) Instrumented laboratory flowslides. *Géotechnique* 40:489–502. <https://doi.org/10.1680/geot.1990.40.3.489>
- Feng T, Mi H, Scaioni M et al (2016) Measurement of surface changes in a scaled-down landslide model using high-speed stereo image sequences. *Photogramm Eng Remote Sens* 82:547–557. [https://doi.org/10.1016/S0099-1112\(16\)82061-3](https://doi.org/10.1016/S0099-1112(16)82061-3)
- Froude MJ, Petley DN (2018) Global fatal landslide occurrence from 2004 to 2016. *Nat Hazards Earth Syst Sci* 18:2161–2181. <https://doi.org/10.5194/nhess-18-2161-2018>
- Hong Y-S, Chen R-H, Wu C-S, Chen J-R (2005) Shaking table tests and stability analysis of steep nailed slopes. *Can Geotech J* 42:1264–1279. <https://doi.org/10.1139/t05-055>
- Hunger O, Morgenstern NR (1984) Experiments on the flow behaviour of granular materials at high velocity in an open channel. *Géotechnique* 34:405–413. <https://doi.org/10.1680/geot.1984.34.3.405>
- Iserloh T, Fister W, Seeger M et al (2012) A small portable rainfall simulator for reproducible experiments on soil erosion. *Soil Tillage Res* 124:131–137. <https://doi.org/10.1016/j.still.2012.05.016>
- Iserloh T, Ries JB, Arnáez J et al (2013) European small portable rainfall simulators: a comparison of rainfall characteristics. *Catena* 110:100–112. <https://doi.org/10.1016/j.catena.2013.05.013>
- Iverson RM (2015) Scaling and design of landslide and debris-flow experiments. *Geomorphology* 244:9–20. <https://doi.org/10.1016/j.geomorph.2015.02.033>
- Jagodnik V, Peranić J, Arbanas Ž (2020) Mechanism of landslide initiation in small-scale Sandy slope triggered by an artificial rain. In: Workshop on world landslide forum. Springer, pp 177–184
- Kimura T (1991) Failure of fills due to rain fall. In: Centrifuge. Balkema, pp. 509–516

- Kutara K, Ishizuka H (1982) Seepage flow in the embankment and stability of slope during rain (in Japanese). Tsuchi-to-kiso, Paper No 1330:
- Ladd (1978) Preparing test specimens using Undercompaction. *Geotech Test J* 8
- Liang T, Knappett JA, Bengough AG, Ke YX (2017) Small-scale modelling of plant root systems using 3D printing, with applications to investigate the role of vegetation on earthquake-induced landslides. *Landslides* 14:1747–1765. <https://doi.org/10.1007/s10346-017-0802-2>
- Lin M-L, Wang K-L (2006) Seismic slope behavior in a large-scale shaking table model test. *Eng Geol* 86:118–133. <https://doi.org/10.1016/j.enggeo.2006.02.011>
- Lora M, Camporese M, Salandin P (2016a) Design and performance of a nozzle-type rainfall simulator for landslide triggering experiments. *Catena* 140:77–89. <https://doi.org/10.1016/j.catena.2016.01.018>
- Lora M, Camporese M, Troch PA, Salandin P (2016b) Rainfall-triggered shallow landslides: infiltration dynamics in a physical hillslope model. *Hydrol Process* 30:3239–3251. <https://doi.org/10.1002/hyp.10829>
- Lu P, Wu H, Qiao G et al (2015) Model test study on monitoring dynamic process of slope failure through spatial sensor network. *Environ Earth Sci* 74:3315–3332. <https://doi.org/10.1007/s12665-015-4369-8>
- Mihalić Arbanas S, Arbanas Ž (2015) Landslides: a guide to researching landslide phenomena and processes. Handbook of research on advancements in environmental engineering 474–510. <https://doi.org/10.4018/978-1-4666-7336-6.ch017>
- Oka H (1972) Impacts by the “artificial landslide”: re-examine the rage of nature (in Japanese). *Kagaku Asahi* 32:152–153
- Ooi GL, Wang Y, Wong T, Wong C (2010) An exploratory study on using miniature sensors to monitor landslide motion. In: *Physical Modelling in Geotechnics, Two Volume Set: Proceedings of the 7th International Conference on Physical Modelling in Geotechnics (ICPMG 2010)*, 28th June-1st July, Zurich, Switzerland. CRC Press, p 367
- Ooi GL, Wang YH (2014) Applying MEMS accelerometers to measure ground vibration and characterize landslide initiation features in laboratory flume test. In: *Geo-congress 2014 technical papers*. American Society of Civil Engineers
- Pajalić S, Peranić J, Maksimović S et al (2021) Monitoring and data analysis in small-scale landslide physical model. *Appl Sci* 11:5040. <https://doi.org/10.3390/app11115040>
- Peranić J, Čeh N, Arbanas Ž (2022a) The use of soil moisture and pore-water pressure sensors for the interpretation of landslide behavior in small-scale physical models. *Sensors* 22:7337. <https://doi.org/10.3390/s22197337>
- Peranić J, Jagodnik V, Čeh N, Pajalić S, Vivoda Prodan M, Arbanas Ž (2022b) Small-scale physical landslide models under 1g infiltration conditions and the role of hydrological monitoring. In Peranić J, Vivoda Prodan M, Bernat Gazibara S et al. (eds) *Proceedings of the 5th ReSyLAB ‘Landslide Modelling & Applications’*, Rijeka, Faculty of Civil Eng. University of Rijeka, Croatia, 171–180
- Peranić J, Jagodnik V, Čeh N et al (2022c) Landslide initiation in small-scale sandy and clayey slopes exposed to artificial rain. In: Rahman J (ed) *Proceedings of the 20th international conference on soil mechanics and geotechnical engineering*. Australian Geomechanics Society, Sydney, Australia, pp 1075–1080
- Popescu M (2001) A suggested method for reporting landslide remedial measures. *Bull Eng Geol Environ* 60:69–74. <https://doi.org/10.1007/s100640000084>
- Scaioni M, Feng T, Barazzetti L et al (2015) Some applications of 2-D and 3-D photogrammetry during laboratory experiments for hydrogeological risk assessment. *Geomat Nat Haz Risk* 6:473–496. <https://doi.org/10.1080/19475705.2014.885090>
- Take WA, Bolton MD, Wong PCP, Yeung FJ (2004) Evaluation of landslide triggering mechanisms in model fill slopes. *Landslides* 1: 173–184. <https://doi.org/10.1007/s10346-004-0025-1>
- Vivoda Prodan M, Peranić J, Pajalić S, Arbanas Ž (2023a) Physical modelling of rainfall-induced Sandy and Clay-like slope failures. *Adv Mater Sci Eng* 2023:1–12. <https://doi.org/10.1155/2023/3234542>
- Vivoda Prodan M, Čeh N, Peranić J, Pajalić S, Jagodnik V, Arbanas Ž (2023b) Influence of pile wall on stability of clay-like slopes during rainfall in a small-scale physical modeling. In: *Proc. of 9th Conference of Croatian Geotechnical Society, Croatian Geotechnical Society, Zagreb*, 293–302
- Wang YH, Ooi GL, Gao Y (2013) New sensing technology and new applications in geotechnical engineering. In: Delage P, Desrues J, Frank R et al (eds) *Proc. of the 18th International Conference on Soil Mechanics and Geotechnical Engineering*, Paris 2013. Balkema. Rotterdam, The Netherlands, Paris
- Wartman J, Seed RB, Bray JD (2005) Shaking table modeling of seismically induced deformations in slopes. *J Geotech Geoenviron Eng* 131:610–622. [https://doi.org/10.1061/\(ASCE\)1090-0241\(2005\)131:5\(610\)](https://doi.org/10.1061/(ASCE)1090-0241(2005)131:5(610))
- Wieczorek GF, Snyder JB (2009) Monitoring slope movements. In: *Geological Monitoring*. Geological Society of America
- Yagi N, Yatabe R, Enoki M (1985) Laboratory and field experiments on prediction method of Occuring time of slope failure due to rainfall. *Journal of Japan Landslide Society* 22:1–7_1. https://doi.org/10.3313/jls1964.22.2_1
- Yamaguchi I, Nishio K, Kawabe H et al (1989) Initiation and fluidization of an artificial landslide: field experiment in Yui Shizuoka prefecture, Japan (in Japanese). *Shinrin Kosoku (Areal Survey)* 158:3–9
- Zanutta A, Baldi P, Bitelli G et al (2006) Qualitative and quantitative photogrammetric techniques for multi-temporal landslide analysis. *Ann Geophys* 14:14

Open Access This chapter is licensed under the terms of the Creative Commons Attribution 4.0 International License (<http://creativecommons.org/licenses/by/4.0/>), which permits use, sharing, adaptation, distribution and reproduction in any medium or format, as long as you give appropriate credit to the original author(s) and the source, provide a link to the Creative Commons license and indicate if changes were made.

The images or other third party material in this chapter are included in the chapter's Creative Commons license, unless indicated otherwise in a credit line to the material. If material is not included in the chapter's Creative Commons license and your intended use is not permitted by statutory regulation or exceeds the permitted use, you will need to obtain permission directly from the copyright holder.





Surficial Geology and Geomorphology of the North Slide, Thompson River Valley, British Columbia, Canada: Application of Fundamental Geoscience Information to Interpretations of Geospatial Monitoring Results

David Huntley, Drew Rotheram-Clarke, Kelvin Sattler, and David Elwood

Abstract

Our study focuses on a slow-moving landslide in the Thompson River valley, south-central British Columbia, Canada, that has posed a hazard to the national railway transportation corridor since 1880. Real-time kinematic global navigation satellite systems, unoccupied aerial vehicles, and satellite synthetic aperture radar interferometry time-series show significant displacement encroaching on railway infrastructure. In this paper, geospatial relationships between landslide distribution and specific terrain features, and the environmental conditions triggering instability are determined from field-based geological observations. We describe how earth material stratigraphy, textures, and penetrative planar structures are important controls on sub-surface drainage, and how these factors influence the style, timing, and rate of slope displacement. West of the railway tracks, slide scarps extend across the toe slope, corresponding to narrow zones of high displacement, presence of perennial springs and seepage, and cutbank erosion along the river channel. Fluvial incision exposes weak, failure-prone units at the base of the fill sequence, and with ongoing channel migration promotes instability by altering landslide toe geometry. Currently, the zone of potential displacement does not extend upslope into the inactive (1880) main slide body, east of the tracks. Seasonal variations in hydrogeological conditions influence the spatial and temporal patterns of surface water and

groundwater flow, in turn controlling the distribution of translational-rotational displacement of slide blocks, and rates of movement on reactivated shear surfaces that extend under Thompson River. Slope failure occurs along weak, sub-horizontal shear zones within poorly drained glaciolacustrine clay and silt units, overlain by rapidly drained glaciofluvial outwash gravel, and imperfectly drained till diamicton. River levels exert a complex control on landslide stability, influencing hydraulic gradients within the basal glaciolacustrine unit, particularly along rupture surfaces within it. Ground displacement occurs while river levels are at their lowest between February and March, before peak flows in June, or after July until December while storm-fed river levels progressively lower to the next winter minimum. Groundwater levels remain elevated in the slide body throughout the year, contained in porous gravel and sand beds, and along brittle fractures and sub-horizontal shear zones in silt-clay varve beds. Geospatial and temporal change-detection monitoring of active landslides and at-risk infrastructure, when benchmarked with terrain and hydrogeological observations, is a cost-effective hazard management practice that provides important geoscience information to help develop appropriate early warning, mitigation, adaptation, and risk reduction measures.

Keywords

National railway infrastructure · Slow-moving landslide change-detection monitoring · Surficial geology · Stratigraphy · Geomorphology · River level · Groundwater · Landslide disaster risk reduction

D. Huntley (✉) · D. Rotheram-Clarke
Geological Survey of Canada, Vancouver, BC, Canada
e-mail: david.huntley@nrcan-mcan.gc.ca; drew.rotheram-clarke@nrcan-mcan.gc.ca

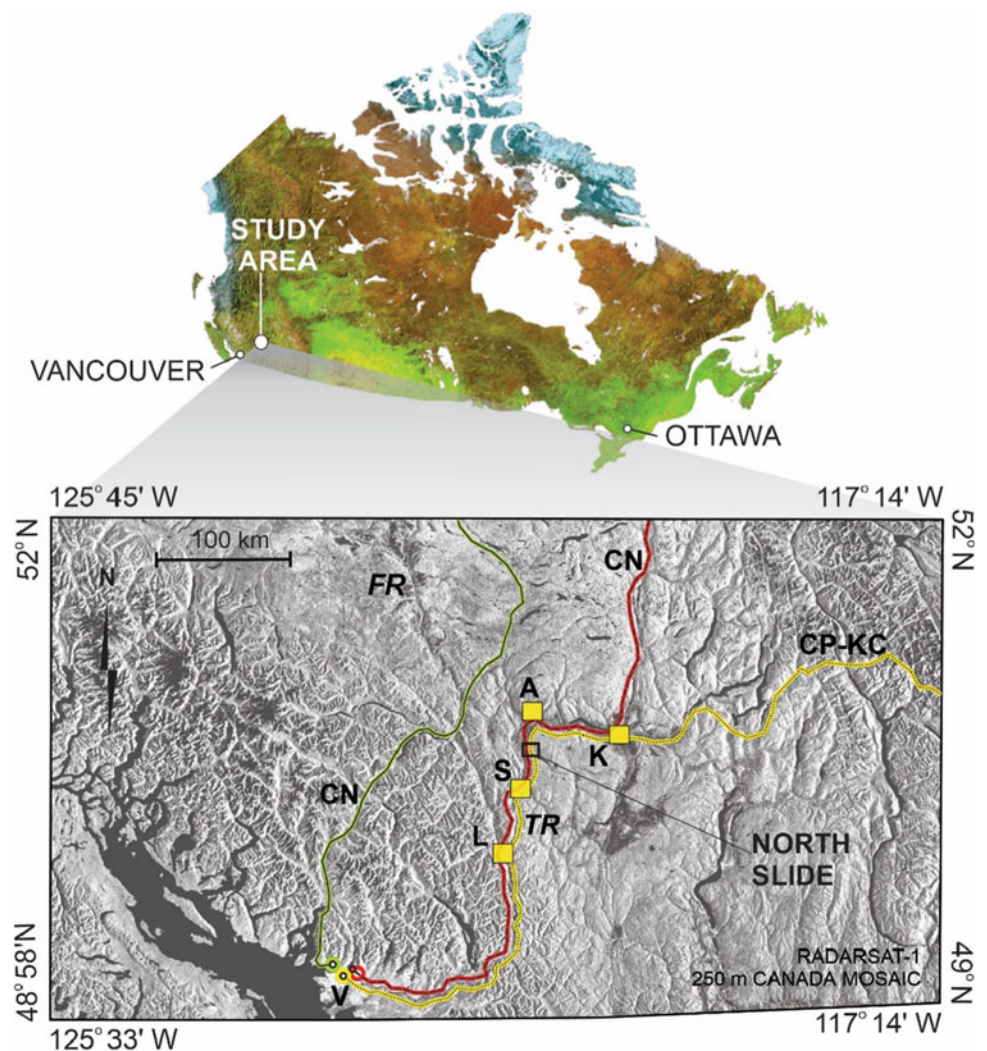
K. Sattler
Clifton Engineering Group, Saskatoon, SK, Canada
e-mail: kelvin_sattler@clifton.ca

D. Elwood
College of Engineering, University of Saskatchewan, Saskatoon, SK, Canada
e-mail: david.elwood@usask.ca

1 Introduction

Safe and secure national railway, highway, pipeline, and power transmission networks are essential for exporting Canada's natural resources (e.g., copper, coal, oil, gas,

Fig. 1 North Slide study area in relation to major national railway transportation corridors in southwestern British Columbia. A Ashcroft; K Kamloops; L Lytton; S Spences Bridge; V Vancouver; CN Canadian National Railways; CP-KC Canadian Pacific Kansas City Railways. TR Thompson River; FR Fraser River



electricity, potash, grains, forest products) to deep-water marine and freshwater terminals, and for transporting goods entering continental North America from global markets. Unfortunately, across much of the country, vital socio-economic infrastructure and operations are confined to transportation corridors where terrain is highly susceptible to landslide activity (Bobrowsky and Dominguez 2012). As part of the International Programme on Landslides (IPL) Project 202, our study contributes to landslide disaster risk reduction along a critical section of the primary national railway corridor (Huntley et al. 2022a).

This paper focuses on the North Slide in south-central British Columbia (Fig. 1), a geomorphically active landslide that has posed a hazard to the national railway transportation corridor traversing the Thompson River valley since 1880 (Fig. 2a). With a surface area of 1 km², the slow-moving translational-rotational landslide is an ideal field laboratory for observing geomorphic processes while testing and evaluating novel slope monitoring and evaluation techniques. Here, we describe the local surficial geology and

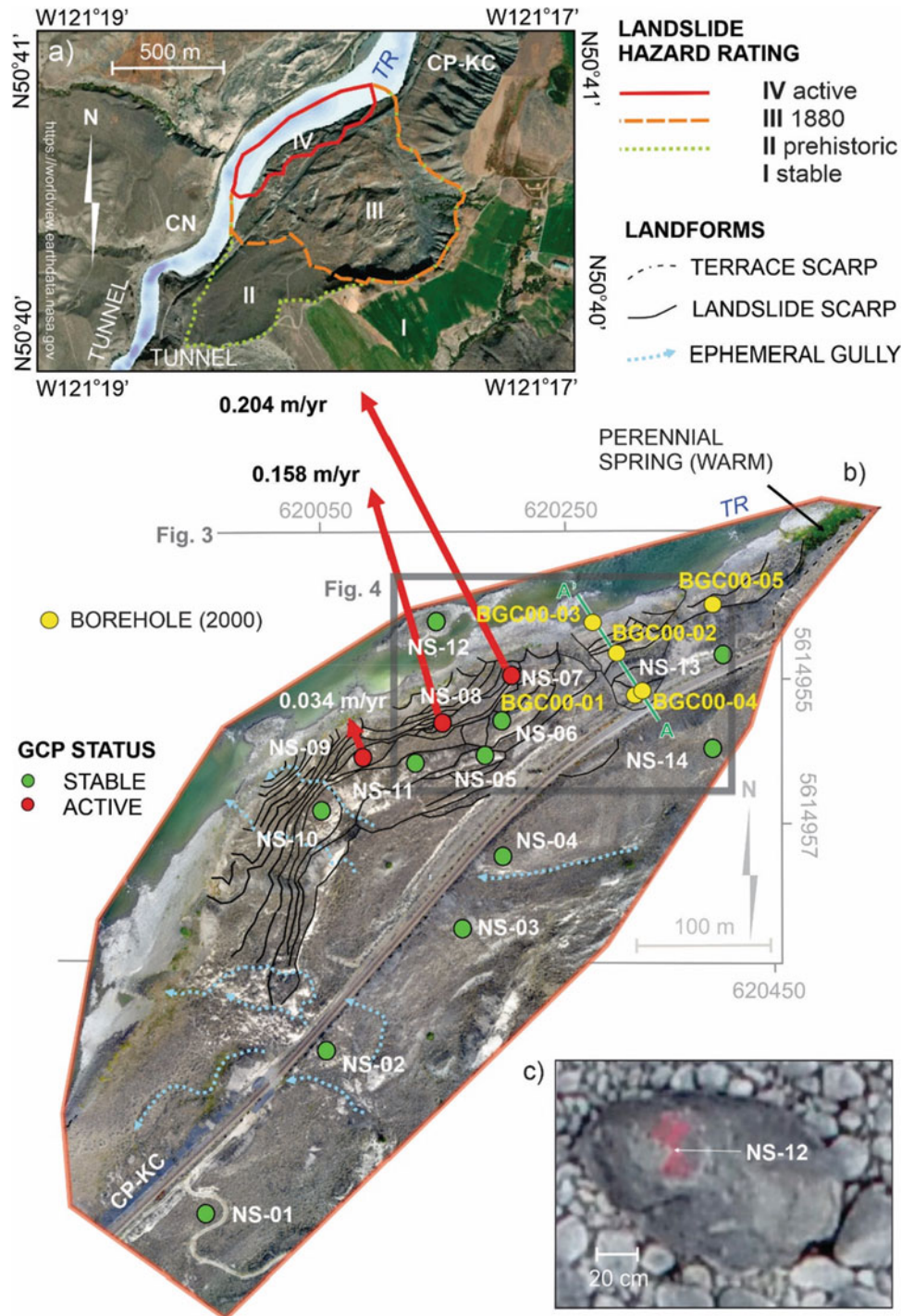
geomorphology, and develop a hydrogeological model to inform the interpretation of results from geospatial monitoring of unstable slopes and at-risk infrastructure (Journault et al. 2018; Huntley et al. 2021; Rotheram-Clarke et al. 2022).

1.1 Generalized Climate and Hydrology at North Slide

The IPL Project 202 study area lies within the drought prone Very Dry Hot subzone of the Bunchgrass biogeoclimatic zone (Nicholson et al. 1991; www.for.gov.bc.ca [2018 URL]). Seasonally variable weather conditions are recorded at Kamloops, 65 km to the east, while river discharge is measured 40 km downstream, near Spences Bridge (Fig. 1).

Precipitation (~250 mm, annual average) is concentrated in May to September (20 mm to 40 mm, monthly) when it falls as rain, and in December and January (20 mm to 30 mm, monthly) when it falls mainly as snow. The driest months are

Fig. 2 WorldView satellite imagery and UAV orthomosaic on the North Slide. (a) Historical activity and landslide hazard rating for the North Slide: IV—Active (0.105 km²); III—1880 landslide (0.753 km²); II—Prehistoric landslide (0.249 km²); I—stable terrain. (b) Orthomosaic image derived from UAV aerial photography, showing location of ground control points, and annual movement (2019–2020). (c) Detail of ground control point NS-12 on a floodplain boulder (2 cm-ground resolution at 70 m above ground surface). A–A'—Cross-section along borehole transect (see Fig. 4); CN Canadian National Railways; CP-KC Canadian Pacific Kansas City Railways; TR Thompson River



February to April (<http://climate.weather.gc.ca/> [2018 URL]) when infiltrating precipitation and snowmelt contributes to shallow groundwater recharge (Holmes et al. 2018; Holmes et al. 2020; Sattler et al. 2020).

Thompson River discharge reflects spring snowmelt and rainfall variation. Baseflow varies annually from $<200 \text{ m}^3 \text{ s}^{-1}$ to $\sim 600 \text{ m}^3 \text{ s}^{-1}$, with a freshet peak in late May or June of $<2000 \text{ m}^3 \text{ s}^{-1}$ to $>4000 \text{ m}^3 \text{ s}^{-1}$ (<http://wateroffice.ec.gc.ca>

[2018 URL]). Across the North Slide toe slope, the river changes in elevation by up to 8 m ($\sim 270 \text{ m}$ to 278 m elevation based on the high-water mark at piping holes observed along the riverbank) in response to spring melt in the surrounding mountains and seasonal precipitation events. River levels are at their minimum between early January and early March; and start to rise in late April to early May, continuing through

until late July. By early August, river levels are starting to decline to the winter minimum beginning in December.

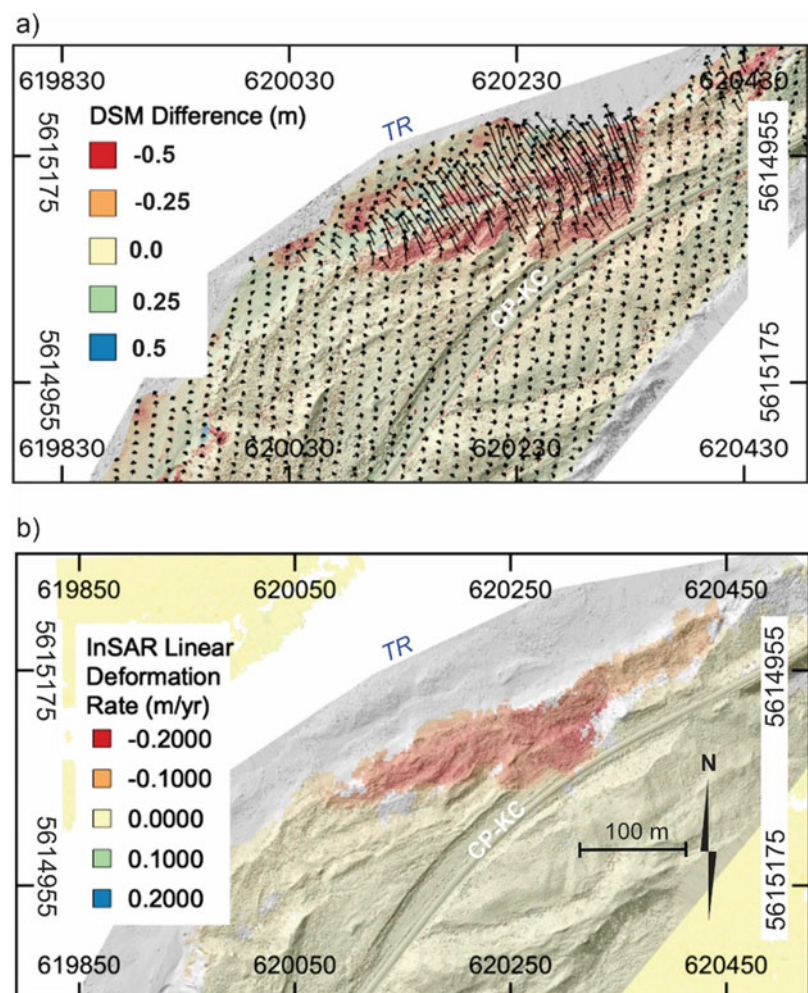
1.2 Historical Change Detection at North Slide

The North Slide is an ancient landslide that reactivated as a sudden onset, rapid retrogressive flow-slide around 9 pm on October 14, 1880 (Stanton 1898; Evans 1984; Clague and Evans 2003; Fig. 2a). In common with other nineteenth Century translational-rotational landslides in the valley, the slope failed during and after the summer months, at a time when terraces were intensively irrigated for agricultural land use, and the toe slope was incised and over-steepened by railway construction. Air photos between 1928 and 1997 showed historical bank erosion rates averaging 70 cm yr^{-1} , with Thompson River eroding the slope below the rail grade (Porter et al. 2002). In October 2000, movement along 150 m of the toe slope resulted in 5 to 15 cm of settlement at the rail grade. Peak observed movement rates were approximately

15 cm yr^{-1} , with an average rate of 3 cm yr^{-1} (Porter et al. 2002).

Recent movement near critical railway infrastructure has been captured by epochal real-time kinematic (RTK) global navigation satellite system (GNSS) monitoring, uninhabited aerial vehicle (UAV) photogrammetry, bathymetric soundings, and ground observations. Ground displacement measurements with these technologies (Fig. 2b) correspond to change-detection results derived from RADARSAT 2 (RS2), SENTINEL 1 (S1) and RADARSAT Constellation Mission (RCM) synthetic aperture radar interferometry (InSAR) datasets (Fig. 3a, b; Huntley et al. 2021; Rotheram-Clarke et al. 2022). From 2019–2020, RTK-GNSS measurements indicated significant NW movement was restricted to ground control points (GCP) NS-7 (NW, 3 cm yr^{-1}), NS-8 (NW, 16 cm yr^{-1}), and NS-9 (NW, 20 cm yr^{-1}). Wide-coverage deformation patterns and vectors (Fig. 3a) were calculated from subpixel offsets between precisely co-registered UAV orthophotos and hill-shaded digital surface models (DSM) (Rotheram-Clarke et al. 2022; Huntley et al. 2023). Digital image correlation and

Fig. 3 Provisional geospatial monitoring results for North Slide (2019–2021). (a) 3D UAV deformation over North Slide between 2019-09-19 and 2021-09-28 (modified from Rotheram-Clarke et al. 2022; Huntley et al. 2022b). Vectors indicate horizontal deformation from digital image correlation and colour scale represents the difference in DSMs. Hill-shade transparency is applied for context. (b) InSAR linear deformation rate map with semi-transparent hill-shade applied for context. Deformation rate is estimated from an InSAR time-series spanning January 5, 2021, to December 3, 2021 (modified from Rotheram-Clarke et al. 2022; Huntley et al. 2022b). *CN* Canadian National Railways; *CP-KC* Canadian Pacific Kansas City Railways; *TR* Thompson River



DSM of differences show significant displacement encroaching on rail infrastructure. West of the tracks toward the river channel, slide scarps extend across the toe slope (Fig. 2b), with corresponding narrow blocks with NW displacement $\geq 50 \text{ cm yr}^{-1}$ (Fig. 3a). RS2, S1, and RCM time-series all reveal similar linear displacement patterns across the landslide toe (Huntley et al. 2021). Between 2016 and 2019, RS2 and S1 peak ground velocities were $< 25 \text{ cm yr}^{-1}$ and $< 15 \text{ cm yr}^{-1}$ respectively, while cumulative displacements were $< 10 \text{ cm yr}^{-1}$ (RS2) and $< 8 \text{ cm yr}^{-1}$ (S1).

The 2020–2021 RCM InSAR results (Fig. 3b) revealed severe deformation from the end of August to middle September, with several fringes indicating movement of approximately 2 cm to 5 cm over 16-day and 28-day periods, and a complex deformation pattern in the most affected zones. Four-day interferograms showed nearly a full fringe cycle, suggesting $\sim 2 \text{ cm}$ of rapid, complex deformation (Huntley et al. 2021; Rotheram-Clarke et al. 2022; Huntley et al. 2023).

Between 2016 and 2021, peak cumulative displacement captured by InSAR analysis, UAV surveys, and RTK-GNSS strongly corresponded to changes in river surface elevation (and water depth) over the submerged toe slope, active floodplain, and along steep channel banks. Peak ground displacement occurred while river levels were at their lowest between February and March (before rising to peak in June), or after July until November as storm-fed river levels progressively lowered to the next winter minimum. Increased displacement rates and peak ground movement velocities toward the river occurred during rapid river drawdown between late summer and early winter, with a $\geq 5.6 \text{ m}$ change in river level between spring and fall and a mean annual discharge above $900 \text{ m}^3 \text{ s}^{-1}$ (Huntley et al. 2021). During these seasons, groundwater levels remained elevated in the slide body, likely contained in porous sand beds and along brittle fractures and sub-horizontal shear zones in silt-clay beds (Porter et al. 2002; Eshraghian et al. 2007; Eshraghian et al. 2008).

1.3 Baseline Geological Conditions at the North Slide

In the vicinity of the North Slide, Thompson River occupies a broad, approximately 1 km-deep, locally steep, bedrock valley. Above $\sim 500 \text{ m}$ elevation, valley slopes are locally mantled by colluvium or drumlinized drift. Valley-bottom benchlands around 350 m elevation have been incised by Thompson River since the last glaciation, forming an inner gorge with steep slopes up to 125 m high (Fig. 2a). Thick (50 m to 150 m) Pleistocene valley-bottom fill is exposed along post-glacial terrace scarps of Thompson River and its tributaries (Ryder 1976; Clague and Evans 2003; Johnsen

and Brennand 2004). These sediments include multiple glaciolacustrine units, separated by till and outwash recording at least three glaciations: the last (Late Wisconsinan) glaciation, the penultimate glaciation (Early Wisconsinan), and an earlier glaciation (Ryder et al. 1991; Clague and Evans 2003). The upper part of the sediment sequence was deposited during deglaciation when repeated glacial lake stages occupied the valley (Fulton 1969; Ryder 1976; Johnsen and Brennand 2004), and shortly after deglaciation when the valley bottom was choked by paraglacial sedimentation (Church and Ryder 1972).

The active toe slope is underlain by silty diamicton that unconformably overlies 8 m of sand and gravel, and a $> 30 \text{ m}$ thick package of sand, silt, and clay (Fig. 4; Porter et al. 2002). Porter et al. (2002) and Huntley et al. (2021) reported that a prominent toe bulge and rhythmically interbedded layers of soft brown clay, stiff, highly plastic dark grey clay and grey silt were exposed on the river floodplain. Borehole piezometer and inclinometer monitoring revealed preferential shearing in similar soft brown clay beds, with rupture zones at 290 m and 270 m elevation, equivalent to 10 and 30 m below the CP-KC rail grade (BGC00–01 and BGC00–04), and 5 to 10 m below the riverbed (BGC00–03) (Porter et al. 2002; Fig. 4). Piezometer data indicated hydrostatic conditions occur locally at depth below the track and an upward groundwater gradient in the landslide toe (Porter et al. 2002).

2 Methods and Observational Results

Landslide research at the North Slide has two aims: (1) to characterize earth material composition, particularly beneath railway infrastructure; and (2) quantify spatial and temporal characteristics of slope displacements. This study relates to the first objective and provides important context for better addressing the second. Landslide form and function in the Thompson River valley are strongly influenced by the stratigraphic ordering of sub-surface earth material textures, porosities, penetrative planar structures, and hydrology (Huntley and Bobrowsky 2014; Huntley et al. 2020).

To help determine the degree to which these controls influence the nature, extent, and activity of the North Slide, we combined terrain mapping ground-truthed by field observations with stratigraphic analysis of legacy borehole logs (Fig. 4) to characterize hydrogeological variability at the test site (cf. Huntley et al. 2022a).

2.1 Terrain and Hydrogeological Mapping

Surficial earth materials and landforms were mapped using Worldview satellite imagery (Fig. 5a), together with a DSM

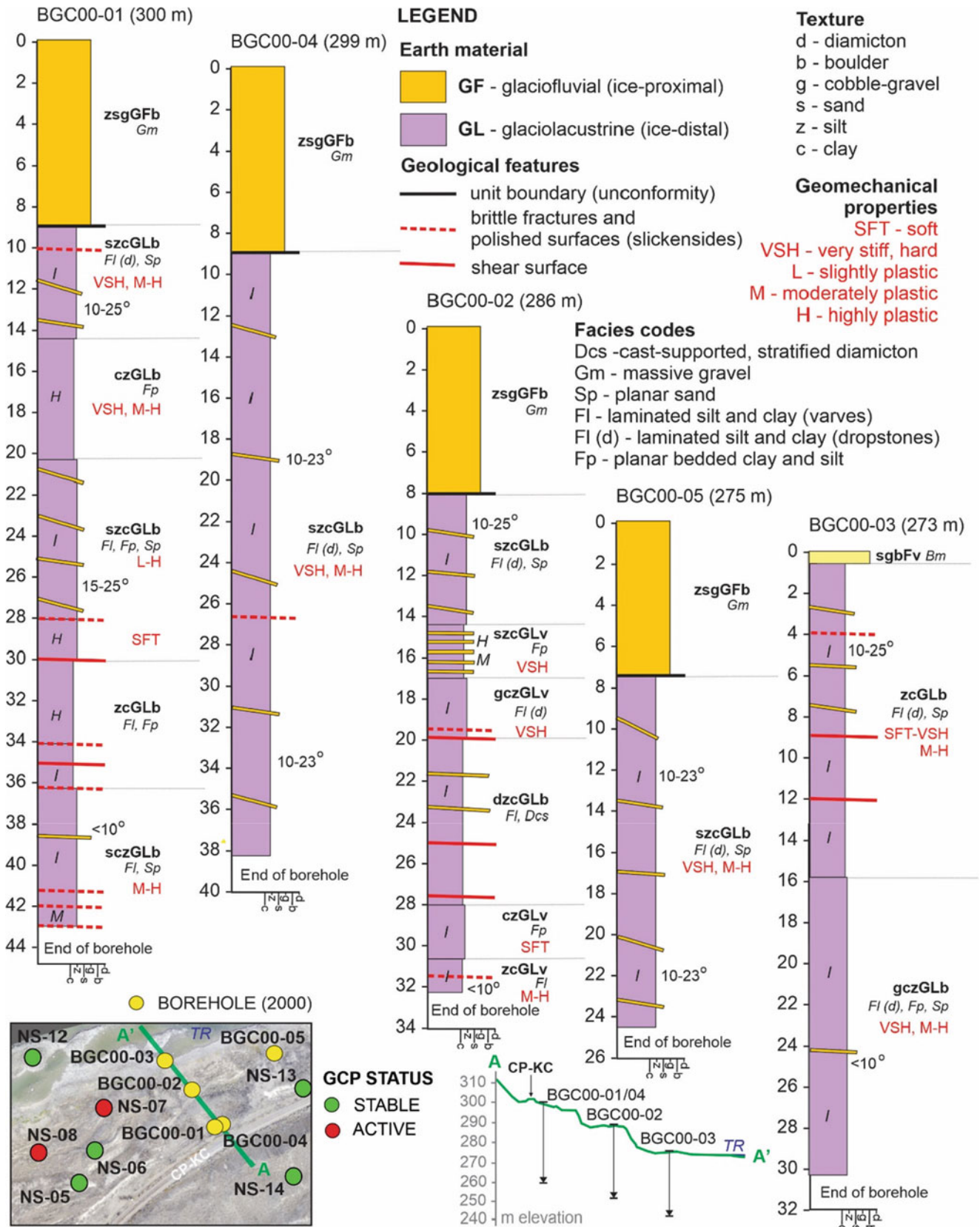


Fig. 4 Boreholes drilled in 2000 by BGC Engineering (Porter et al. 2002). Schematic logged profiles are re-interpreted through correlation with local surficial geology exposed in the Thompson River valley

(Huntley and Bobrowsky 2014). Bedding characteristics: *H* horizontal bedding; *I* inclined or deformed bedding; *M* mottling. *CP-KC* Canadian Pacific–Kansas City Railways; *TR* Thompson River

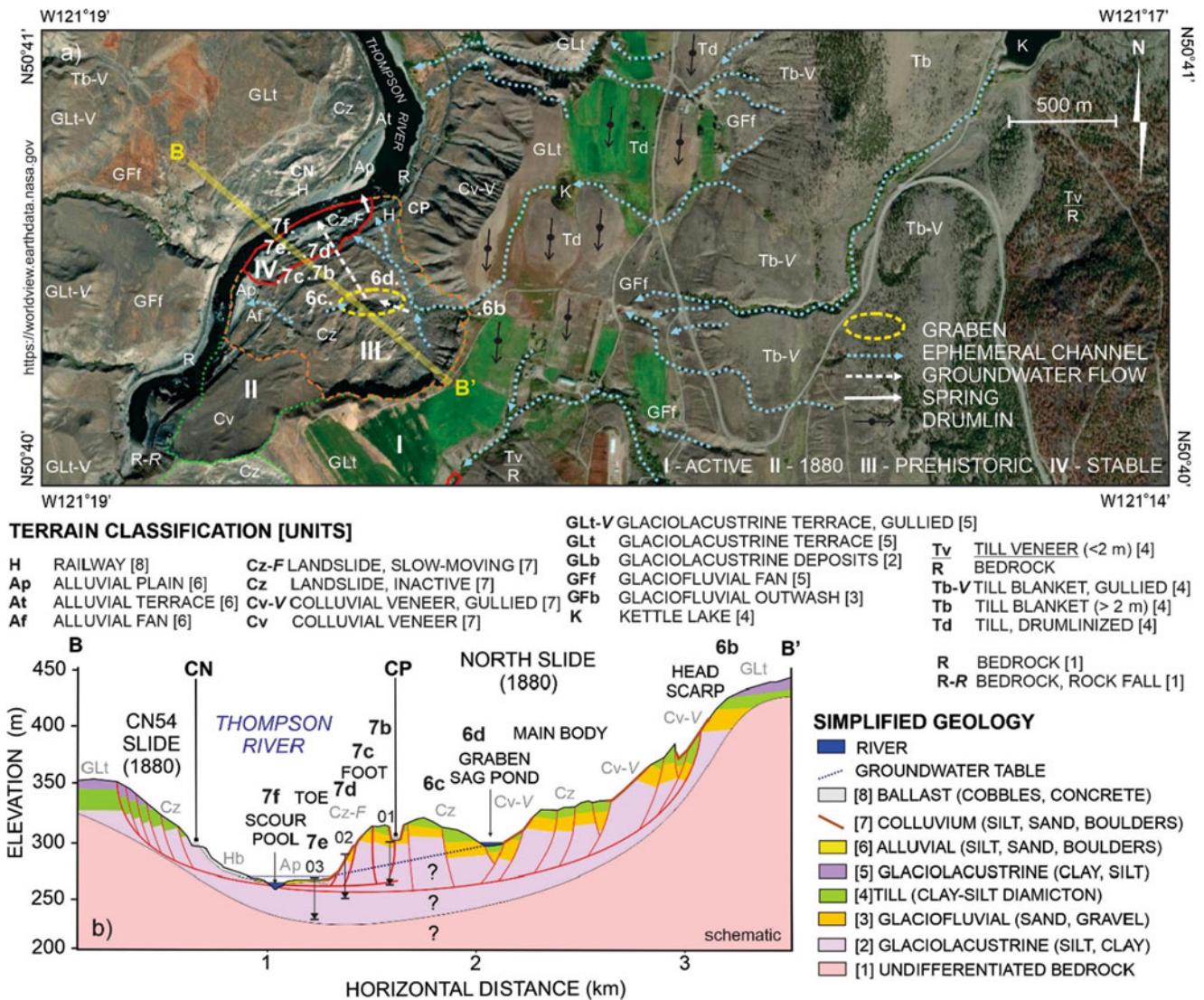


Fig. 5 Generalized surficial geology and geomorphology of the North Slide and adjacent terrain. (a) Distribution of terrain units, landforms, and drainage features. (b) Schematic cross-section along A-A', showing the stratigraphy based on field observations and boreholes. Terrain

coding merges mapping conventions of Howes and Kenk (1997) and Deblonde et al. (2018). Locations of photographs in Figs. 6b-d and 7b-f are also shown

and ortho-rectified and geo-referenced digital natural colour air photographs taken by a Phantom 4 UAV during repeat photogrammetric overflights in September 2019–2022 (Fig. 2b). UAV imagery was sufficient to resolve cobble-sized boulders and anthropogenic features (<5 cm across) at a flight elevation 70 m above ground level (Fig. 2b). During desktop terrain analysis, visual interpretation of imagery relied on the recognition and separation of geological features using colours, tones, surface textures, patterns, shapes, sizes, shadows, and field observations. Hydrogeological interpretations were codified following British Columbia terrain mapping standards and the Geological Survey of Canada (GSC) surficial geology data model (Howes and Kenk 1997; Deblonde et al. 2018).

2.1.1 Benchmarked Satellite Image Interpretation

Worldview satellite imagery (Fig. 5a) and merged orthomosaic air photos (Fig. 2b) capture baseline surface conditions across the active North Slide toe slope, along with the extent of bare earth and vegetation growth (e.g., grasses, shrubs, and trees) on the inactive slide main body and adjacent stable terrain. Larger geomorphic features and terrain units are visible on satellite imagery (Fig. 5a). Forested upper valley slopes, ranging from 16° to 26° to 27° to 35°, are covered by a discontinuous ground moraine veneer (<2 m) overlying glacially streamlined bedrock (Tv/R). Sustained surface drainage to lower slopes is maintained from a moraine-dammed kettle lake confined to a hanging

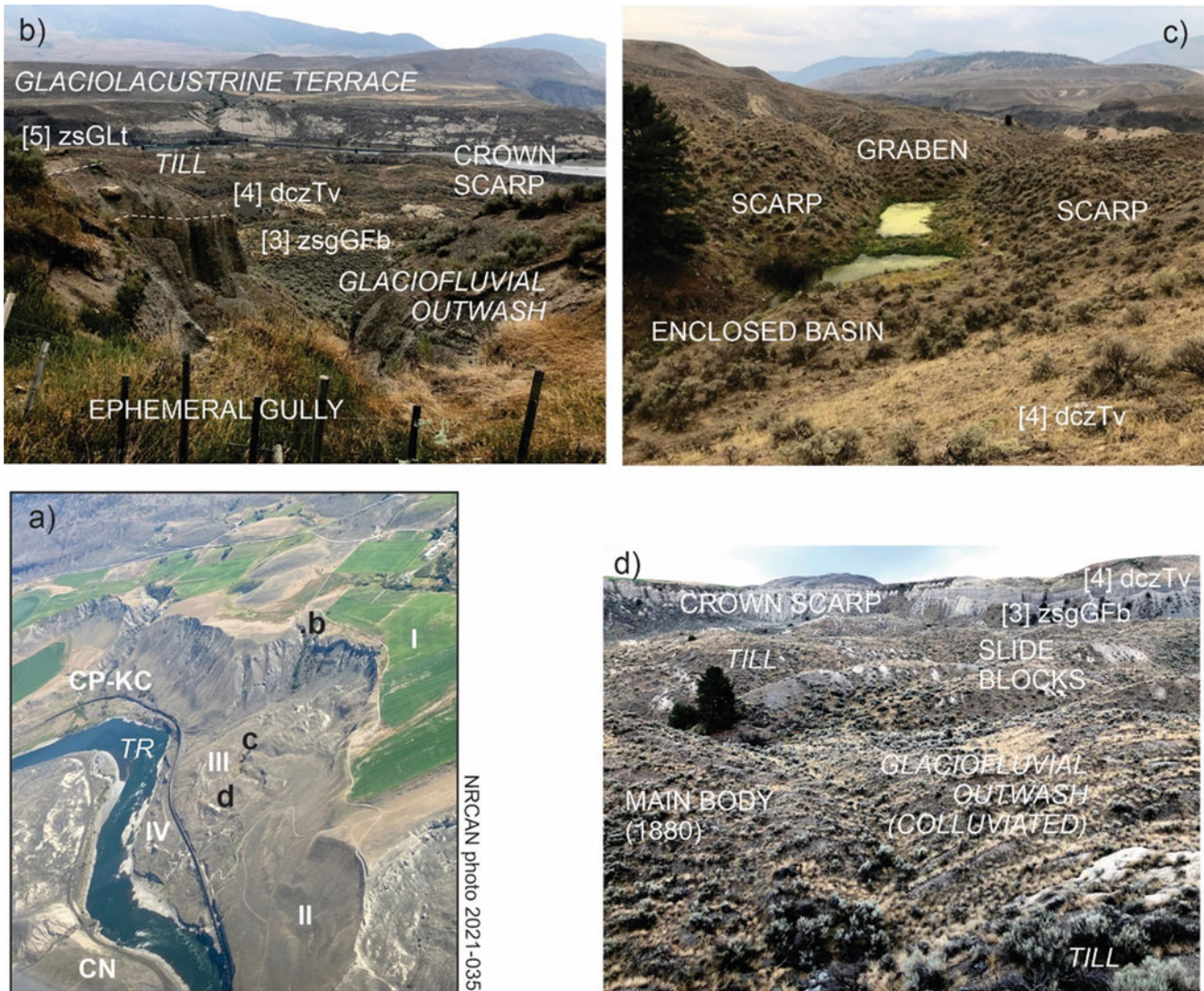


Fig. 6 Field observations of terrain and landforms across the main body and crown scarp of North Slide. (a) Oblique aerial photograph showing location of landslide zones and field photographs. CN Canadian National Railways; CP-KC Canadian Pacific–Kansas City Railways; TR Thompson River. (b) Gullied crown scarp exposing

paleo-valley at 680 m elevation. Sparsely vegetated mid-slopes (16° to 26°) are covered with thicker (>2 m), sometimes gullied ground moraine with surface erratic trains (Tb, Tb-V).

Between 460 m and 440 m elevation, sparsely vegetated and irrigated drumlins (Td) with scattered erratics have slopes from 3° (down-ice) to 16° (up-ice). Drumlin orientation indicates rolling ground moraine was streamlined by SSW-flowing Cordilleran ice in the paleo-Thompson valley. Between approximately 440 m to 360 m elevation, ground moraine is blanketed by gently sloping ($<3^{\circ}$) terraced glaciolacustrine deposits (GLt) and glaciofluvial outwash (GFf). The presence of kettle lakes (K) indicates stagnant

glacial deposits, eroded by ephemeral runoff from irrigated fields upslope. (c) Groundwater-fed enclosed basin in closed extensional basin on the main slide body. (d) Colluviated glacial deposits exposed across the surface of the main slide body

valley ice was partly blanketed by till, outwash, and glacial lake sediments during deglaciation.

Upper and mid-slopes are incised by post-glacial gullies and ungraded streams that channel ephemeral surface runoff from snowmelt, extreme precipitation events, and irrigation to the inner canyon of Thompson River (Fig. 6a, b). Surface runoff is taken up by vigorous vegetation growth in gullies, or percolates into underlying sediment as shallow circulating groundwater (Figs. 2a and 5a). Post-glacial fluvial incision has formed an inner canyon with steep ($>35^{\circ}$) walls and bedrock exposures prone to rock fall (R, R-R). On moderately steep canyon slopes (27° to 35°), thick accumulations of glacial sediments in the canyon (>50 m) are gullied and

colluviated by soil creep (Cv, Cv-V). Inactive landslides (Cz) in the canyon range in extent from $>0.2 \text{ km}^2$ (CN54 Slide) to 1 km^2 (North Slide), and winnowed slopes range from 16° to 26° (Fig. 6c). A key landform on the main slide body is a half-graben, enclosed basin, and sag pond with a (summertime) surface at 305 m elevation, 300 m SE of the railway tracks and ballast (H) at 300 m elevation (Figs. 5a, b and 6d).

West of the railway corridor, high-stage cutbank erosion by Thompson River (ca. 275 m elevation) contributes to unloading, changes in geometry, and reactivated slow-moving failure (Cz-F) of moderately steep foot and toe slopes (27° to 35°) (Fig. 7a-c). Alluvial fans (Af) formed on lower slopes ($<15^\circ$) below gullied glacial terraces, were graded to falling local base levels between 300 m and 280 m elevation. The modern alluvial plain (Ap) comprises stable point bars with gradients $<3^\circ$ confining an active channel with riffle-pool morphology between approximately 275 m and 265 m elevation (Figs. 5a and 7d-f).

2.1.2 Benchmarked UAV Orthomosaic Interpretation

Metre-scale anthropogenic features (e.g., train tracks, signals bungalow, solar panel array) are resolvable in the orthophoto mosaic and DSM (Fig. 2b). Southeast and upslope of the CP-KC tracks, translated back-tilted slide blocks and scarps from the 1880 landslide are now subdued features due to 140 years of wind deflation, soil creep, and surface runoff (Fig. 6b). Hillslopes $\geq 16^\circ$ are underlain by colluviated till, glaciofluvial outwash, and glaciolacustrine sediments. The inactive main body and active toe slope are gullied by ephemeral streams that drain to a coarse alluvial fan prograding over the floodplain along the SW margin of the landslide.

Visible in the UAV orthophoto mosaic are active slide blocks, scarps, tension cracks, and a toe bulge in the floodplain (Figs. 2b and 6e). Landslide scarps follow the arc of relict (1880) back-tilted slide blocks (GCPs NS-05, NS-06, NS-10 and NS-11), and increase in size and activity toward the river (GCPs NS-07, NS-08 and NS-09). Tension cracks are extrapolated beneath railway ballast close to the solar panel array and signals bungalow (between GCPs NS-04, NS-05 and NS-13). Slide scarps, crescentic tension cracks on the slide body and surface relaxation (unloading) fractures along railway embankments are sub-vertical, penetrate deep into the slide body ($>2 \text{ m}$) and cross-cut multiple units (Fig. 6c-d). A perennial nutrient-rich, warm-water spring rising at river level close to the margin of the active slide (Figs. 2b and 5a) indicates permanent artesian groundwater conditions in the toe slope. Groundwater seepage above river level is also indicated by the presence of horsetails (*Equisetum* sp.) growing across the floodplain.

2.2 Field Observations of Earth Material Textures, Porosity Variations, and Slope Failure in Terrain Units

Fieldwork was undertaken periodically between 2019 and 2022 to describe sedimentological characteristics that could not be determined by remote mapping, and to verify desktop air photo interpretations (Figs. 6b-d and 7b-f). At fourteen ground control points (NS-01 to NS-14) and five boreholes (BGC00-01 to BGC00-05) across the most active portion of the landslide (Fig. 2b), hydrogeological units were defined on the basis of lithofacies and landform associations, texture, sorting, colour, sedimentary structures, degrees of consolidation, stratigraphic contact relationships, geological age, and other distinguishing characteristics described in borehole logs and on site (Figs. 4, 5a, b, 6b-d, and 7b-f). Drainage classes were qualitatively determined from field assessments of porosity, unit thicknesses, earth material textures, penetrative planar structures, and slopes driving hydraulic gradients. Hydrogeological units were codified following British Columbia terrain mapping standards and the Geological Survey of Canada (GSC) surficial geology data model (Howes and Kenk 1997; Deblonde et al. 2018).

2.2.1 Bedrock and Undifferentiated Weathered Lag (Unit 1; R, R-R)

Bedrock (R) is not exposed across the historical (1880) slide (Cz), or in the recent (2000-Present) reactivation along the toe slope (Cz-F). To the NE and SW of the landslide, thrust-faulted and folded, weakly consolidated, friable, fine-grained, interbedded shale, and sandstone (unit 1) outcrops at river level (Fig. 5a). Well drained sedimentary bedrock outcrops have low to moderate intergranular and fracture porosities, with weathering rinds and mineral alteration observed along exposed surfaces of open fractures. Unconsolidated glacial deposits in the inner canyon lie above an angular bedrock unconformity interpreted as a paleochannel segment, or part of a depositional basin that extended north to Ashcroft (Fig. 7d).

2.2.2 Glaciolacustrine Sediments (Unit 2; GLb)

A basal lag of cobble-gravels and coarse-grained debris flow diamictons, not encountered in the boreholes, drapes tectonically deformed sedimentary bedrock (Huntley and Bobrowsky 2014; Huntley et al. 2019). The oldest unconsolidated deposit encountered in boreholes BGC00-01 to BGC00-05 was a $> 30 \text{ m}$ thick package comprising cm-thick beds of silt, sand, gravel and diamicton with moderate intergranular porosity, intercalated with silt-clay mm-thick couplets (i.e., varves) containing dropstones with low intergranular porosities, and low to moderate fracture porosities (Fig. 4). Unit 2 is poorly drained, with ice-distal glaciolacustrine sediments deposited during the retreat of the

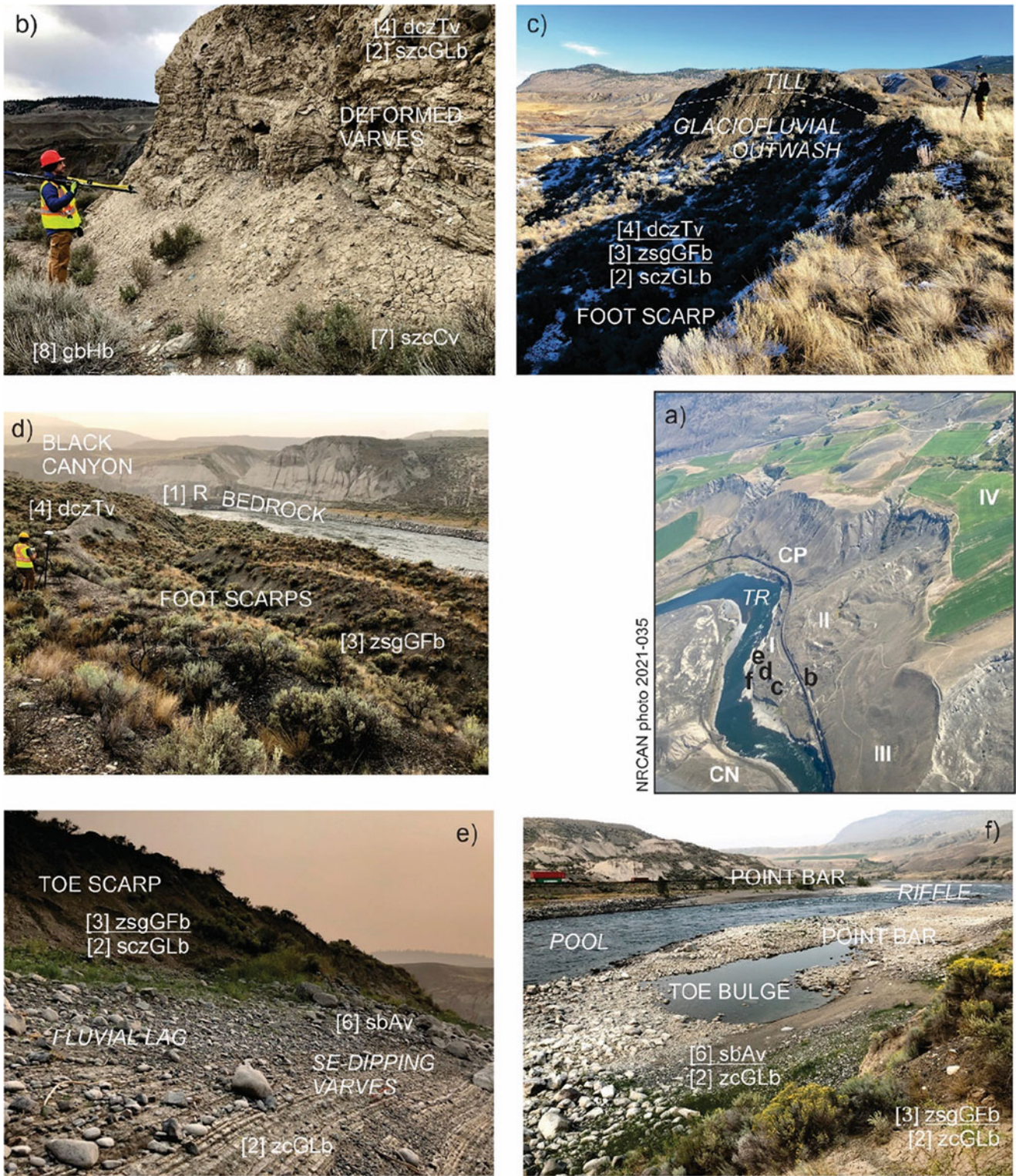


Fig. 7 Field observations of terrain and landforms of foot and toe slopes of the North Slide. (a) Oblique aerial photograph showing location of landslide zones and field photographs. CN Canadian National Railways; CP-KC Canadian Pacific–Kansas City Railways; TR Thompson River. (b) Polyphase deformation in the toe slope, with tills truncating glacially deforming underlying clay-silt-sand varves; both units were further deformed during the 1880 slide event; presently inactive. (c) Glacial sediments exposed in the foot scarp west of the CP-KC rail track. d) Active slide blocks failing toward Thompson

River; note, downstream of landslide, the river is incised into a bedrock paleochannel or basin. (e) Cutbank erosion at the toe scarp exposes back-tilted silt-clay varves, indicating rotational displacement during the 1880 event, and as the toe slope reactivates; gravel lag indicates river levels vary >6 m through the year. (f) Toe bulge expressed in the active floodplain-point bar; attributed to rotational displacement driven by fluvial incision and changing groundwater conditions; note the riffle-pool character of the river

penultimate glaciation and advance phase of the Late Wisconsinan (Late Pleistocene) Cordilleran Ice Sheet. Below the Thompson River floodplain (BGC00–03), unit 2 sediments extend at least 30 m beneath the riverbed. At BGC00–01 and BGC00–04 (Figs. 2b, 4 and 5b), deformed glaciolacustrine sediments extend >40 m below the railway tracks without encountering bedrock. Borehole logs (Fig. 4) and surface exposures (Fig. 7b-e) reveal inclined silt and clay-rich beds are crosscut by multiple discrete zones of translational-rotational shear, fracturing, and polishing (slickensides) between 40 m (BGC00–01) and 5 m (BCG00–03) below ground surface. Soft-sediment deformation structures are attributed to overriding, loading, and erosion by SSW-streaming ice in paleo-Thompson valley, the 1880 landslide event, and recent (post-2000) translational-rotational reactivation along multiple shear surfaces (Figs. 4, 5b and 7b).

2.2.3 Glaciofluvial and Ice-Contact Sediments (Unit 3; GFb)

In boreholes and surface exposures from the crown scarp to the slide toe, unit 2 has an erosional upper contact with an overlying >5–10 m package of massive and crudely stratified open framework, clast-supported diamictons, gravels, cobbles, boulders, and inter-clast silt and sand (Figs. 3 and 5). Unit 3 is interpreted as a Late Wisconsinan ice-proximal or ice-contact coarse-grained glaciofluvial deposit (GFb) with high intergranular porosity and rapid drainage. Across the toe slope, moderate fracture porosity is imparted by surface tension cracks that penetrate >5 m into underlying deformed fine-grained sediments of unit 2 (Figs. 3 and 4). Contorted layering and dewatering structures in outwash are associated with soft-sediment deformation and erosion of saturated outwash by overriding glacier ice, ground displacement during the 1880 landslide, and recent (post-2000) reactivation.

2.2.4 Ground Moraine (Unit 4; Tv, Tb, Tb-V, Td)

Deformed and truncated glaciolacustrine and glaciofluvial units are overlain by up to 5 m of massive, clay-silt matrix-supported diamicton with erratic cobbles and boulders (Figs. 5a and 6b-c). Unit 4 is interpreted as a Late Wisconsinan Cordilleran (subglacial) ground moraine composed of basal lodgement and meltout till. Basal till has a low vugular porosity due to the presence of isolated weathered igneous and sedimentary clasts and sand-filled voids within the fine-grained matrix. Slide scarps, crescentic tension cracks on the slide body, and surface relaxation (unloading) fractures along railway embankments and head scarp are sub-vertical, penetrate deep into the slide body (>2 m depth), and cross-cut multiple units (Fig. 7c-e). These penetrative structures impart the moderate fracture porosity and imperfect drainage of unit 4.

2.2.5 Glaciolacustrine and Glaciofluvial Sediments (Unit 5; GLt, GFt)

Exposures in the slide crown and headscarp reveal that unit 4 till is draped by cm-thick interbeds of clay, silt, pebble-rich sand, and stratified matrix-supported diamicton (Fig. 6b). Unit 5 is generally <10 m thick and interpreted as a Late Wisconsinan retreat phase ice-distal deposit that forms characteristic glaciolacustrine terraces (GLt) and glaciofluvial kame-deltas (GFf) graded to between 440 m and 360 m elevation (Fig. 5a). Penetrative tension cracks and slide scarps impart a moderate fracture porosity and imperfect drainage on diamicton and silt-rich glaciolacustrine beds.

2.2.6 Alluvial Sediments (Unit 6; Ap, at, Af)

On the Thompson River floodplain, ca. 273 m elevation, a boulder veneer drapes back-tilted clay and silt beds (Fig. 2b, NS-12; Fig. 4, BGC00–03; Fig. 7f). Below 275 m elevation, Holocene, and modern alluvial floodplain (Af) and terrace (At) sediments (unit 6) are rapidly drained open framework, clast-supported boulders, and interstitial sand with a high intergranular porosity. Coarse-grained alluvial sediments have no penetrative planar structures, although underlying fine-grained glacial sediments (unit 2) may contain sub-vertical crescentic tension cracks and sub-horizontal unloading fractures. Surface water is quickly removed on the active floodplain during heavy or prolonged rainfall, and boulders and sand are permanently saturated by river water at shallow depth (<2 m). Alluvial fans (Af), fed by ephemeral surface runoff and irrigation drainage (Fig. 5a), prograde across the slide main body and adjacent slopes (<16°) from the lower reaches of tributary channels and gullies, extending into the river at the southern boundary of the slide toe (Fig. 2b). Alluvial fan deposits comprise well drained interbedded stratified debris flow diamictons and open framework, clast-supported cobble-gravels (incised into older units), that fine upward into massive cm-thick sand and silt beds with moderate intergranular porosity.

2.2.7 Colluvial Sediments (Unit 7; Cv, Cz, Cz-F)

Holocene post-glacial colluvium (unit 7) includes discontinuous veneers (<2 m) of stratified massive and clast-supported diamicton containing cobbles, boulders, sand, and silt (Cv, Cv-V) that partly drape older, gullied glacial units exposed in relict and active slide blocks (Cz, Cz-F) (Figs. 2b, 5a and 6d). Hillslope colluvium has high intergranular porosity and is well drained, whereas colluviated slide blocks retain the drainage characteristics of the underlying sediments (e.g., Tb, GFb, GLb). Slide blocks with penetrative sub-vertical crescentic tension cracks and surface relaxation (unloading) fractures have a high fracture porosity. Consequently, on colluvial slopes during heavy or prolonged rainfall, percolating surface water is quickly removed downslope as shallow groundwater flow (Figs. 6d and 7d).

2.2.8 Anthropogenic Deposits (Unit 8; Hb)

Bedrock, glacial, and alluvial sediments (units 1–6) along the railway right-of-way are unconformably overlain by a rapidly drained linear deposit (<5 m thick, ~20 m wide) of open framework, clast-supported cobble-boulder ballast with high intergranular porosity (H, unit 8). Penetrative planar structures are not observed in coarse-grained ballast, although underlying fine-grained glacial sediments (unit 2, 3 and 4) may contain sub-vertical crescentic tension cracks contributing to vertical displacement of ballast (Fig. 2b).

3 Discussion: Fundamental Geoscience Applied to Geospatial Monitoring Results

Slow-moving translational-rotational landslides are perennial natural hazards for the national railway corridor in Thompson River valley between Ashcroft and Spences Bridge, south-central British Columbia (Fig. 1). Ancient (prehistoric, >1000 years before present, yBP), historical (1880), and recent (post-2000) landslide events involved rapid displacement of large areas of the lower valley slope and inner canyon (cumulatively, 1 km²). As a representative landslide in the valley, the North Slide is an ideal field laboratory for testing and evaluating novel slope monitoring and evaluation techniques (cf. Huntley et al. 2017; Holmes et al. 2018, 2020; Sattler et al. 2020).

In this section, we examine how earth material stratigraphy, textures, and penetrative planar structures are important controls on sub-surface drainage, hydrology, and landslide activity. Discussing how these factors influence the style, timing, and rate of slope displacement recorded at the North Slide contributes to landslide disaster risk reduction along a critical section of the primary national railway corridor (Fig. 1). A simple landscape evolution model spanning the interval from the last glacial maximum (ca. 24,000 to 18,000 yBP) to present day provides the framework for this discussion (Fig. 8a-f).

3.1 Hydrogeological Controls on Ancient Landslide Activity

Thick (>150 m) accumulations of unconsolidated Pleistocene glacial deposits and Holocene alluvial fill deposited in a channelized bedrock basin have pre-conditioned the Thompson River valley for colluviation and landslide activity (Fig. 6a). At the close of the penultimate glaciation, and during advance phase of the Late Wisconsinan glaciation, considerable volumes of fine-grained sediment (unit 2, rhythmic varves of sand, silt, and clay) and coarse debris (unit

3, interbeds of stratified diamicton and massive gravel) were deposited in the paleo-Thompson valley. During the last glacial maximum (ca. 24,000 to 18,000 yBP), these sediments were overridden, deeply eroded, truncated, intensively deformed, sheared, then unconformably overlain by drumlinized silt-rich basal tills (unit 4) deposited by the SSW-flowing Cordilleran Ice Sheet (Fig. 8a). As ice retreated (ca. 16,000 to 12,000 yBP), deposits of till formed an extensive ground moraine over middle and lower slopes that was rapidly inundated by shallow retreat-phase proglacial lake system confined to the valley below 460 m elevation (Fulton 1969; Johnsen and Brennand 2004; Fig. 8b). With first-time exposure, poorly consolidated glacial sediments on oversteepened unvegetated slopes were rapidly remobilized (cf. Church and Ryder 1972). Silt-rich outflow and debris flow diamictons from glacial margins contributed to deposition from suspension of fine-grained sediments over moraine deposits, while cobble-rich ice-contact kame-deltas draining emergent proglacial channels and forefields prograded into this lake. Flights of terraces, beach strandlines, and boulder-rich fan deposits (between 460 m and 360 m elevation) indicate falling lake levels, outburst floods, and channel incision continued with ice retreat from the valley, glacioisostatic rebound, and downstream drainage capture by Fraser River during paraglaciation (ca. 12,000 to 10,000 yBP; Fig. 8c).

During the early to middle Holocene (ca. 10,000 to 5000 yBP; Fig. 8d), semi-arid post-glacial conditions fluctuated between warmer and cooler than present. Slopes stabilized with the establishment of vegetation cover, and terraces were rapidly incised by down-cutting tributaries and Thompson River. For much of the Holocene, infiltration of snowmelt, precipitation, and surface runoff into porous silt, sand, gravel, and diamicton was limited on sparsely vegetated alluvial fans (unit 6) and colluvial slopes (unit 7). Generally, winters and springs were dry, and summer heat favoured evapotranspiration of precipitation (Nicholson et al. 1991).

The ancient North Slide failure (Figs. 2a, II and 8d) likely occurred as the Black Canyon was being incised during a wet interval between 6000 and 4000 yBP not much moister than today (Hebda 1982; Mathewes and King 1989; Hebda 1995). Rapid fluvial and colluvial denudation of glacial valley fill altered slope geometry and groundwater conditions, with slope failure triggered by elevated groundwater pressure along glacially pre-sheared discontinuities in unit 2 (Porter et al. 2002; Eshraghian et al. 2008; Bishop et al. 2008).

3.2 Hydrogeological Controls on Historical Landslide Activity

Glacial deformation and prehistoric slope movement created pre-sheared discontinuities in units 2, 3 and 4 at a residual

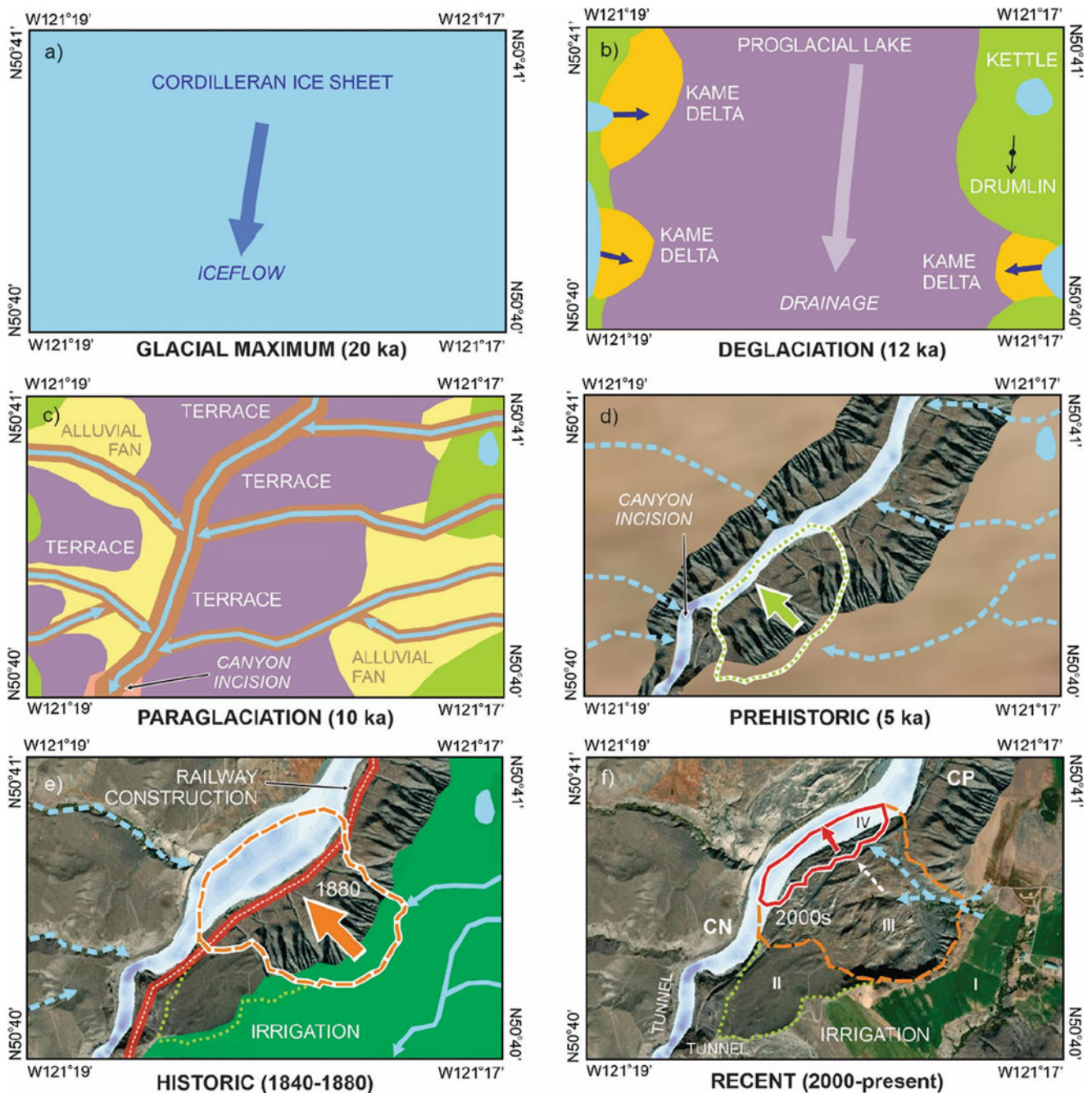


Fig. 8 Paleogeographic reconstruction of the North Slide: (a) last glacial maximum—subglacial erosion and shearing of bedrock and sediments, drumlin formation (ca. 20,000 yBP); (b) deglaciation—glacial lakes, kame deltas, remobilized glacial sediments (ca. 12,000 yBP); (c) paraglaciation—rapid lake drainage, remobilized glacial sediments,

alluvial fan formation, valley incision (ca. 10,000 yBP); (d) prehistoric—valley incision, large landslide (>1000 yBP, II); (e) land use changes—valley incision, irrigation, railway construction (1840s–1880s, III); (f) modern ground conditions—valley incision, irrigation, rail traffic (1900s–2000s, I–IV)

strength that predisposed these sediments to further failure (Porter et al. 2002; Eshraghian et al. 2008; Bishop et al. 2008). It is likely that unconsolidated valley fill was undersaturated through much of the Holocene and remained marginally stable until the 1860s when irrigation, necessary for agriculture on glaciofluvial terraces and alluvial fans above

the river, began (Stanton 1898; Clague and Evans 2003). Pleistocene and Holocene sediments further destabilized after inner canyon toe slopes were excavated in the 1880s to accommodate the national railway corridor (Clague and Evans 2003; Bunce and Chadwick 2012). Artesian

groundwater in unit 2 further contributed to instability (Porter et al. 2002; Eshraghian et al. 2008).

Historical failure of Pleistocene and early Holocene units (Figs. 2a, III, 3a, b and 8e) involved three mechanisms: 1) rapid flow-sliding and slumping, where slide blocks disaggregated and liquefied while moving down slope on translational shear surfaces ($>2 \text{ cm yr}^{-1}$); 2) very slow (2 cm yr^{-1} to 10 cm yr^{-1}) rotational sliding of large, intact blocks of units 2–4 on shear surfaces leading to back-tilted bedding and thrust-faulting of glaciolacustrine unit 2 over glaciofluvial unit 3 in the landslide toe; and 3) very slow (2 cm yr^{-1} to 10 cm yr^{-1}) translational sliding of blocks with little rotation contributing to horst and graben topography on the slide main body. Similar to the ancient landslide, slope failure was triggered by elevated groundwater pressure along pre-sheared discontinuities in unit 2.

3.3 Hydrogeological Controls on Recent Landslide Activity

Intensively irrigated glaciolacustrine terraces and drumlinized ground moraines upslope of the North Slide are currently stable landforms (Figs. 2a, I and 5a). Seasonal ploughing and crop cultivation disturb the upper metre of surficial Pleistocene and Holocene deposits. Deglacial lake and kame-delta deposits with moderate to high intergranular porosity (unit 5), post-glacial alluvial fan diamicton, silt and sand deposits (unit 6), and colluvium (unit 7) are rapidly to well drained. Snowmelt, heavy or prolonged rainfall, and irrigation water readily percolates into underlying glacial sediments (units 2, 3 and 4), or is drained ephemerally by shallow channels incised into the terraces and deep gullies along the crown scarp across the inactive, historical slide main body (Figs. 2a, III, 5a, 6a-d and 7a-f).

On the slide main body (III) upslope of the active toe slope (IV), glacial units 2, 3 and 4 are exposed at surface in back-tilted horst blocks, while graben blocks are generally infilled with coarse colluvium derived from remobilized glacial materials. During heavy or prolonged rainfall and snowmelt, well-drained hillslope colluvium (unit 7) and imperfectly drained till diamicton (unit 4) with tension cracks allow downward infiltration of surface water into underlying units. Exposed glaciofluvial gravels and diamictons (unit 3) with high intergranular porosity rapidly absorb surface runoff and percolating shallow groundwater from overlying unit 4 (Fig. 7d). In contrast, fractured glaciolacustrine varve exposures (unit 2) are poorly drained, so water is slowly removed, saturating surface layers during sustained precipitation and snowmelt, and when inundated by storm runoff from gullied scarp slopes or seasonal irrigation runoff (Fig. 6c).

Unique hydrogeological features on the North Slide are sag ponds in the centre graben of the main body (III), lying 300 m SW of the CP-KC tracks and zone of greatest displacement (I). These perennial bodies of nutrient-rich water are fed by groundwater seepage and ephemeral surface runoff from bounding slide scarps (Figs. 4a and 5). Minimum water levels (around 302 m elevation) are observed during winter months, although needle ice forming in colluvial fill indicates rising groundwater. From summer to fall, the enclosed basin maintains a consistent level around 305 m elevation, suggesting the ponds remain groundwater-fed.

Although the North Slide failed rapidly in the past, currently only the toe slope remains as a reactivated very slow-moving (2 cm yr^{-1} to 30 cm yr^{-1}) translational slide (IV, Figs. 2b, 3a, b, 5b, and 6f). Recent activity, recorded since 2000, has been focused in a 0.1 km^2 portion of the toe slope undercut by Thompson River (Figs. 2b and 3a, b). East of the railway tracks, the zone of potential displacement currently does not extend upslope into the inactive (1880) main slide body. West of the tracks, slide scarps extend across the toe slope, corresponding to narrow zones of high displacement, the presence of perennial springs and seepage, and cutbank erosion along the modern river channel (Figs. 2b and 3a, b). Ground displacement occurs while river levels are at their lowest from February to March, or before peak flows in June, and after July until December as storm-fed river levels progressively fall to the next winter minimum. Groundwater levels remain elevated in the slide body through the year, with shallow contributions from the river, surface runoff on the slide main body, perennial sag ponds, upslope irrigation, and deep flow rising from fracture-faulted bedrock uplands flanking the valley.

The active toe slope is composed of a $> 40 \text{ m}$ package of unconsolidated sediments, with a veneer of post-glacial units 6–7 overlying glacial units 2–4 that unconformably rest on well-drained shale and sandstone (unit 1). Penetrative fault zones, shallow fractures, and folded bedding planes in bedrock allow downward flow of water at exposed surfaces and upwelling of groundwater at river level. Traversing the landslide toe, railway ballast with high intergranular porosity (unit 8) is rapidly drained, and percolating surface water is quickly removed downslope or into the subsurface during heavy or prolonged precipitation. At surface west of the tracks, exposed till diamicton (unit 4) with low vugular porosity and moderate fracture porosity is imperfectly drained, with tension cracks allowing downward infiltration of surface water during heavy or prolonged rainfall and snowmelt. Underlying interbedded glaciofluvial gravels and diamictons (unit 3) have a high intergranular porosity that rapidly absorb surface runoff and percolating shallow groundwater from unit 4, or where exposed across the landslide surface (Fig. 5). Deformed and fractured glaciolacustrine sand, silt, and clay varves (unit 2) underlying

unit 3 are poorly drained with low to moderate intergranular and fracture porosities. Seasonal movement occurs along sub-horizontal translational rupture surfaces corresponding to weak, glacially fractured, and sheared zones ca. 260 m and 270 m elevation (Fig. 3) with high groundwater pressures in glaciolacustrine clay and silt (Porter et al. 2002; Eshraghian et al. 2007, 2008).

On the modern floodplain (Figs. 5a, and 7f), unit 2 is mantled by rapidly drained boulder-rich alluvial floodplain deposits (unit 6) with high intergranular porosity, and well drained coarse-grained hillslope colluvium (unit 7) with moderate intergranular and fracture porosities. At and below river level (ca. 270 m elevation), silt and sand beds in unit 2 and remain saturated for much of the year. Strong river currents have incised two 5 m-deep scour pools into unit 2 and bedrock along the slide toe. Channel scour likely exposes porous bedding planes and slide surfaces below river level, allowing hydraulic connection between the river and landslide mass (cf. Huntley et al. 2020). Scour holes and cutbank erosion are evidence that the river continues to incise the channel floor. Upstream and downstream riffles correspond to sections of the channel where bedrock is closer to surface. Slower movement rates occur during spring run-off when high water levels provide temporary loading support at the landslide toe. Higher ground movement rates occur during autumn and winter when river discharge levels fall, reducing loads on the slide toe, while groundwater pressures in fractured and sheared zones of unit 2 remain elevated (Porter et al. 2002; Eshraghian et al. 2007).

In addition to slow-moving landslide activity, extremely rapid rock falls ($>5 \text{ m s}^{-1}$) and rapid ($>3 \text{ m min}^{-1}$) debris falls (cf. Cruden and Varnes 1996) are initiated on steep bedrock canyon walls upstream and downstream of the North Slide. Water depths in the Black Canyon exceed 50 m (Huntley et al. 2022a), suggesting that rock fall debris is unlikely to block drainage of Thompson River.

3.4 Projecting Future Landslide Activity and Consequences

Future changes in regional climate, extreme weather, landscape conditions, and land use are expected to influence the rate and distribution of slope deformation at North Slide, and by extension other landslides in the Thompson River valley, with consequent detrimental impacts to infrastructure along the railway corridor, the national economy, natural environment, and public safety. Although the average rainfall in the area has increased since the 1920s, there is no direct correlation with landslide activity (Porter et al. 2002; Eshraghian et al. 2007; Tappenden 2016). However, increased duration and magnitude of precipitation, in combination with increased irrigation of terrace benches, loss of vegetation

cover through cattle grazing, or wildfires, and fluctuating river discharge might trigger landslide activity through sustained periods of groundwater recharge, increased groundwater pressures in bedrock and surficial units, higher seasonal river discharges, and greater channel erosion. Higher rates of landslide movement along deep-seated shear planes are anticipated if unit 2 is further exposed during channel incision. Toe slope incision occurs adjacent to where the highest ground motion rates are recorded on the landslide, and where critical railway infrastructures (e.g., tracks, ballast, culverts) are at risk (Huntley et al. 2021; Rotheram-Clarke et al. 2022).

Persisting landslide activity has the potential to cause damage to critical transportation infrastructure and disruption of service. Periodic reactivation and slow displacement rates result in travel orders for reduced speed that create bottlenecks for directional rail traffic that passes through the corridor. As one of the most active landslides in the valley, frequent, costly maintenance involving addition of ballast, track lifting, and ballast tamping will be required until slope mitigation or adaptation measures are designed and implemented for the North Slide. Seasonal addition of ballast, combined with more frequent, longer, and heavier trains crossing the toe slope may contribute to additional subaerial loading and enhanced displacement at, and below the rail grade.

3.5 Geologically Informed Monitoring for Landslide Disaster Risk Reduction

Geotechnical mitigation and adaptation solutions for landslides can carry significant economic costs and environmental consequences, especially if measures fail to stabilize the slopes of concern (Bunce and Chadwick 2012). Knowledge of hydrogeological conditions and displacement characteristics will help the railway industry, governments, and local communities develop robust mitigation, adaptation, and risk reduction measures to accommodate the impacts of changes in landscape conditions related to extreme weather and land use in the Thompson River valley.

Terrain and derivative maps (e.g., landslide susceptibility) that delimit unstable and potentially unstable terrain will be invaluable tools for landslide monitoring and risk management. These GIS products can be applied to calculate spatial relationships between landslide distribution, specific terrain features, and environmental conditions expected to correlate with landslide incidence. Although non-systematic datasets have unequal reliability, accuracy, and precision; they nevertheless provide useful insight into landslide distribution at various scales and help focus attention on areas of interest where rigorous qualitative analyses are warranted.

Table 1 Methods of investigation for landslide disaster risk reduction (after Huntley et al. 2022a)

Method of enquiry	Reconnaissance mapping and fundamental geoscience	Geospatial change detection surveys	In-situ time-series monitoring
On site investigations	Site specific: Slope and drainage; bedrock and structures; geology and landforms; borehole logs and stratigraphy; geophysical investigations (electrical resistivity [ERT], seismic P and S waves)	Site specific: RTK-GNSS monuments, networks, and epochal surveys (daily, monthly, annually)	Borehole logging: Groundwater level (piezometry); shear displacement (inclinometry); shear displacement (acoustic waves) River level: UAV time-series photograms; RTK-GNSS surveys; piezometer-river stage rating curves Bioclimatic variables: Barometric pressure, air temperature; precipitation; snow; relative humidity; wind; ERT and soil moisture
Laboratory testing	Site specific: Stratigraphic units; sedimentology, and structures; geophysical properties; geochemical properties; geotechnical properties	Seasonal sampling: Stratigraphic units; sedimentology and structures; geophysical properties; geochemical properties; geotechnical properties (daily, monthly, annually)	Modelling: Stratigraphic units; sedimentology and structures; geophysical properties; geochemical properties; geotechnical properties (daily, monthly, annually)
Remote sensing	Terrain mapping: Optical satellite imagery; SAR satellite imagery; air photo interpretation; UAV photogrammetry	Change detection: Satellite InSAR interferograms; corner reflectors; UAV time-series photograms (weekly, monthly, annually)	Railway infrastructure: Satellite InSAR interferograms; UAV time-series photograms; fibre optic strain interferometry (weekly, monthly, annually)

Further onsite investigations of slope and drainage characteristics, bedrock and structures, surficial geology and geomorphology, and vegetation and land cover will provide a reliable hydrogeological context for interpreting sedimentary logs of new boreholes, and results from shallow geophysical surveys, petrological and geochemical analyses, and geotechnical studies (Table 1). Monitoring weather variables (e.g., precipitation, air temperature, snow, wind, relative humidity), soil moisture and temperature, river stage measurements, and groundwater pressures in new boreholes will provide quantitative insight into the contributions of precipitation, irrigation runoff from terrace benches, vegetation cover, wildfires, and fluctuating river and groundwater discharge to landslide activity across the toe slope. Additional geospatial and bathymetric monitoring is necessary to establish whether failure and erosion of these blocks contribute to toe slope unloading, and whether rapid movement on rupture surfaces occurs when groundwater levels are elevated relative to lower river elevations.

4 Summary and Conclusion

The overarching goal of our work is the reduction and mitigation of landslide disaster risks to public safety, the environment, transportation infrastructure, and the national economy. Investigation of the North Slide (IPL Project 202) provides important insight into processes and behaviour of large slow-moving landslides along Canada's primary national railway corridor between Ashcroft and Spences Bridge in south-central British Columbia, Canada (Fig. 1),

but is applicable other parts of the world with similar biogeoclimatic conditions.

Here we have applied conventional terrain mapping and borehole logging to address significant knowledge gaps in the nature and distribution of surficial earth materials, their stratigraphic relationships, and the internal structure of the landslide (Figs. 4 and 5b). This new insight helps us understand past change-detection results with an array of instrumentation. Displacement monitoring with borehole inclinometers and piezometers between 2000 and 2002, and epochal surface RTK-GNSS measurements of GCPs, UAV photogrammetry, air photo interpretation, and satellite InSAR time-series since 2016 reveal that active displacement (2 cm yr.^{-1} to 30 cm yr.^{-1}) is confined to the toe slope and related to tension cracks undercutting the CP-KC rail right-of-way (Figs. 2b and 3a, b).

Stratigraphy exerts a first order control on the distribution, geometry, and rate of landslide displacement along the inner gorge (Figs. 4 and 5b). Similar to other slow-moving landslides in the semi-arid Thompson River valley, alluvial and colluvial denudation of glacial valley fill alters slope geometry and groundwater conditions, with failure triggered by elevated groundwater pressure along pre-sheared discontinuities in clay-silt beds that extend below river level. Groundwater conditions are stratigraphically constrained. With evapotranspiration on sparsely vegetated slopes dominating, infiltration of precipitation, snowmelt, and surface runoff into glacial, post-glacial, and anthropogenic deposits (units 2–8) is very limited across the North Slide and adjacent stable terrain. Moderately porous till with deep penetrating tension cracks (unit 4) is underlain by highly

porous glaciofluvial gravel (unit 3), which in turn overlies non-porous, fractured, and sheared glaciolacustrine silt and clay (unit 2). At the landslide toe, artesian conditions in unit 2 are maintained by hydraulic connection between sag ponds confined to a mid-slope graben, scour pools in the river channel along the slide toe, and underlying faulted and folded bedrock. The pool-and-riffle channel morphology is significant because hydraulic conductivity between the river, landslide and groundwater systems likely increases where fractured bedrock and glaciolacustrine units (containing impermeable silt-clay couplets, coarse porous beds, lateral failure planes and vertical tension cracks) are continually exposed by fluvial erosion (cf. Huntley et al. 2019; Huntley et al. 2020).

In closing, our study demonstrates that when informed by knowledge of hydrogeological conditions and displacement characteristics, spatial and temporal change-detection monitoring of active landslides and at-risk infrastructure is an effective geohazard management practice that provides critical information to help the railway industry, governments, and local communities develop appropriate early warning, mitigation, adaptation, and risk reduction measures.

Acknowledgements Research, undertaken as part of the International Consortium on Landslides (ICL) International Programme on Landslides Project 202, is funded by Transport Canada and Natural Resources Canada. Fieldwork would not be possible without the support of Danny Wong (Canadian Pacific—Kansas City Railway, Calgary, Alberta), and Trevor Evans (Canadian National Railway, Kamloops, BC).

References

- Bobrowsky PT, Dominguez, MJ (2012) Landslide susceptibility map of Canada. Geological Survey of Canada, Open File 7228: 1 sheet
- Bishop N, Evans S, Petley D, Unger A (2008) The geotechnics of glaciolacustrine sediments and associated landslides near Ashcroft (British Columbia) and the Grand Coulee Dam (Washington). In: From Causes to Management—Proc 4th Canadian Conference on Geohazards p. 594
- Bunce C, Chadwick I (2012) GPS monitoring of a landslide for railways. In: Eberhardt E et al (eds) Landslides and engineered slopes—protecting society through improved understanding, pp 1373–1379
- Church M, Ryder JM (1972) Paraglacial sedimentation: a consideration of fluvial processes conditioned by glaciation. *Geological Society America Bulletin* 83:3059–3072
- Clague J, Evans S (2003) Geologic framework for large historic landslides in Thompson River valley, British Columbia. *Environ Eng Geosci* 9(3):201–212
- Cruden DM, Varnes DJ (1996) Landslide types and processes. In: Turner AK, Schuster LR (eds) Landslides, investigation and mitigation. Special Report 247. Transportation Research Board, Washington, pp 36–75
- Deblonde C, Cocking RB, Kerr DE, Campbell JE, Eagles S, Everett D, Huntley DH, Inglis E, Parent M, Plouffe A, Robertson L, Smith IR, Weatherston A. (2018) Surficial data model: the science language of the integrated Geological Survey of Canada data model for surficial geology maps. Geological Survey of Canada, Open File 8236, (ed. version 2.3.14), p. 50, (2 sheets)
- Eshraghian A, Martin C, Cruden D (2007) Complex earth slides in the Thompson River valley, Ashcroft, British Columbia. *Environ Eng Geosci* XIII:161–181
- Eshraghian A, Martin C, Morgenstern N (2008) Movement triggers and mechanisms of two earth slides in the Thompson River valley, British Columbia, Canada. *Can Geotech J* 45:1189–1209
- Evans SG (1984) The 1880 landslide dam on Thompson River, near Ashcroft, British Columbia. In: Current Research, Part A: geological survey of Canada Paper 84-1A: pp. 655–658
- Fulton RJ (1969) Glacial Lake history, southern interior plateau, British Columbia. Geological Survey of Canada Paper 69-37, 14
- Hebda RJ (1982) Postglacial history of grasslands of southern British Columbia and adjacent regions. In: Nicholson AC, McLean A, Baker TE (eds) Grassland ecology and classification symposium proceedings. British Columbia Ministry of Forests, Victoria, pp 157–191
- Hebda RJ (1995) British Columbia vegetation and climate history with focus on 6 ka B.P. *Geographic Physique et Quaternaire* 49:55–79
- Holmes J, Chambers J, Donohue S, Huntley D, Bobrowsky P, Meldrum P, Uhlemann S, Wilkinson P, Swift R (2018) The use of near surface geophysical methods for assessing the condition of transport infrastructure. Civil engineering research association, special issue on structural integrity of civil engineering infrastructure, *Journal of Structural Integrity and Maintenance*, p. 6
- Holmes J, Chambers J, Meldrum P, Wilkinson B, Williamson P, Huntley D, Sattler K, Elwood D, Sivakumar V, Reeves H, Donohue S (2020) 4-dimensional electrical resistivity tomography for continuous, near-real time monitoring of a landslide affecting transport infrastructure in British Columbia, Canada. *Near surface Geophysics*, p. 15, <https://doi.org/10.1002/nsg.12102>
- Howes DE, Kenk E (1997) Terrain classification system for British Columbia (revised edition): a system for the classification of surficial materials, landforms, and geological processes of British Columbia. B.C. Ministry of Environment Manual 10, p. 90
- Huntley D, Bobrowsky P (2014) Surficial geology and monitoring of the Ripley slide, near Ashcroft, British Columbia, Canada. Geological Survey of Canada Open File 7531:21
- Huntley D, Bobrowsky P, Zhang Q, Zhang X, Lv Z (2017) Fibre Bragg grating and Brillouin optical time domain reflectometry monitoring manual for the Ripley landslide, near Ashcroft, British Columbia. Geological Survey of Canada Open File 8258:66
- Huntley D, Bobrowsky P, Hendry M, Macciotta R, Elwood D, Sattler K, Chambers J, Meldrum P (2019) Application of multi-dimensional electrical resistivity tomography datasets to investigate a very slow-moving landslide near Ashcroft, British Columbia, Canada. *Landslides* 16:1033–1042. <https://doi.org/10.1007/s10346-019-01147-1>
- Huntley D, Holmes J, Bobrowsky P, Chambers J, Meldrum P, Wilkinson P, Elwood D, Sattler K, Hendry M, Macciotta R (2020) Hydrogeological and geophysical properties of the very slow-moving Ripley landslide, Thompson River valley, British Columbia. *Can J Earth Sci* 57(12):21–1391. <https://doi.org/10.1139/cjes-2019-0187>
- Huntley D, Rotheram-Clarke D, Pon A, Tomaszewicz A, Leighton J, Cocking R, Joseph J (2021) Benchmarked RADARSAT-2, SENTINEL-1 and RADARSAT constellation Mission change detection monitoring at north slide, Thompson River valley, British Columbia: implications for a landslide-resilient national railway network. *Can J Remote Sens* 47(4):635–656. <https://doi.org/10.1080/07038992.2021.1937968>
- Huntley D, Bobrowsky P, MacLeod R, Rotheram-Clarke D, Cocking R, Joseph J, Holmes J, Sattler K, Chambers J, Meldrum P, Wilkinson P, Donohue S, Elwood D (2022a) IPL project 202: landslide monitoring best practices for climate-resilient railway transportation

- corridors in southwestern British Columbia, Canada. *Progress in Landslide Research and Technology* 1(1):18
- Huntley D, Rotheram-Clarke D, MacLeod R, Cocking R, LeSueur P, Lakeland B, Wilson A (2022b) Scalable platform for UAV flight operations, data capture, cloud processing and image rendering of landslide hazards and surface change detection for disaster-risk reduction. *Progress in Landslide Research and Technology* 1(2):15
- Huntley D, Rotheram-Clarke D, MacLeod R, Cocking R, LeSueur P (2023) Landslide monitoring with RADARSAT constellation Mission InSAR, RPAS-derived point-clouds and RTK-GNSS time-series in the Thompson River valley, British Columbia, Canada. *Progress in Landslide Research and Technology* 2(1):10
- Johnsen T, Brennand T (2004) Late-glacial lakes in the Thompson Basin, British Columbia: paleogeography and evolution. *Can J Earth Sci* 41:1367–1383
- Journault J, Macciotta R, Hendry M, Charbonneau F, Huntley D, Bobrowsky P (2018) Measuring displacements of the Thompson River valley landslides, south of Ashcroft, B.C., Canada, using satellite InSAR. *Landslides* 15(4):621–636. <https://doi.org/10.1007/s10346-017-0900-1>
- Mathewes RW, King M (1989) Holocene vegetation, climate, and lake-level changes in the interior Douglas-fir biogeoclimatic zone, British Columbia. *Can J Earth Sci* 26:1811–1825
- Nicholson A, Hamilton E, Harper WL, Wikeen BM (1991) Bunchgrass zone—chapter 8. In: Meidinger D, Pojar J (eds) *Ecosystems of British Columbia*. Ministry of Forests BC Special Report, vol 6, pp 125–137
- Porter M, Savigny K, Keegan T, Bunce C, MacKay C (2002) Controls on stability of the Thompson River landslides. In: *Proceedings of the 55th Canadian Geotechnical Conference: Ground and Water—Theory to Practice*. Canadian Geotechnical Society: pp. 1393–1400
- Rotheram-Clarke D, Huntley D, LeSueur P, Cocking R, Joseph J & MacLeod R (2022) Direct comparison of RADARSAT constellation Mission InSAR, UAV derived point-cloud comparison and RTK-GNSS deformation monitoring at north slide, Thompson River Valley, British Columbia. *GeoCalgary 2022*: p. 9
- Ryder JM (1976) Terrain inventory and quaternary geology, Ashcroft, British Columbia. Geological Survey of Canada, Paper 74-79: 17
- Ryder JM, Fulton RJ, Clague JJ (1991) The cordilleran ice sheet and the glacial geomorphology of southern and Central British Columbia. *Géog Phys Quatern* 45(3):365–377. <https://doi.org/10.7202/032882ar>
- Sattler K, Elwood D, Hendry M, Huntley D, Holmes J, Wilkinson P (2020) Effect of pore-pressure dynamics on progressive failure in clay shale landslides. *Landslides* 17. https://doi.org/10.1007/978-3-030-60706-7_45
- Stanton RB (1898) The great land-slides on the Canadian Pacific railway in British Columbia. *Proceedings Civil Engineers* 132(2):1–48
- Tappenden K (2016) Impact of climate variability on landslide activity in the Thompson River Valley Near Ashcroft, B.C. *Proceedings of the 69th Canadian Geotechnical Conference, October 2–5, 2016, Vancouver, Canada*, p. 10

Open Access This chapter is licensed under the terms of the Creative Commons Attribution 4.0 International License (<http://creativecommons.org/licenses/by/4.0/>), which permits use, sharing, adaptation, distribution and reproduction in any medium or format, as long as you give appropriate credit to the original author(s) and the source, provide a link to the Creative Commons license and indicate if changes were made.

The images or other third party material in this chapter are included in the chapter's Creative Commons license, unless indicated otherwise in a credit line to the material. If material is not included in the chapter's Creative Commons license and your intended use is not permitted by statutory regulation or exceeds the permitted use, you will need to obtain permission directly from the copyright holder.





High Resolution Numerical Weather Simulation for Orographic Precipitation as an Accurate Early Warning Tool for Landslide Vulnerable Terrains

H. A. A. I. S. Bandara and Ryo Onishi

Abstract

Accurate early warning for rain-induced landslides is still challenging due to regional and local variations of rainfall prediction due to low accuracy, and resolution. The “Multi-Scale Simulator for the Geoenvironment (MSSG)” system, developed by the Tokyo Institute of Technology, Japan Agency for Marine-Earth Science and Technology and Waseda University allows for high-resolution simulations and seamless modeling of weather and climate interactions, and employs advanced meteorological aspects.

MSSG simulations compared with rainfall data recorded in the Aranayaka automated rain gauge for past events, including the devastating landslide in 2016. The simulations achieved satisfactory results in reproducing rainfall events. Higher-resolution simulations exhibited higher maximum rainfall intensity and cumulative rainfall accumulation. This study emphasizes the importance of considering finer scales in meteorological simulations to effectively capture the intricate variations associated with extreme rainfall events. This study places significant emphasis on the importance of considering finer scales in meteorological simulations in order to confirm the necessity of high resolutions to capture the temporal and spatial variations of orographic rainfall.

Keywords

Landslide early warning · Multi-scale weather simulation · Orographic precipitation · Turbulence enhancement of

orographic rain · High-resolution simulation · Super-resolution

1 Introduction

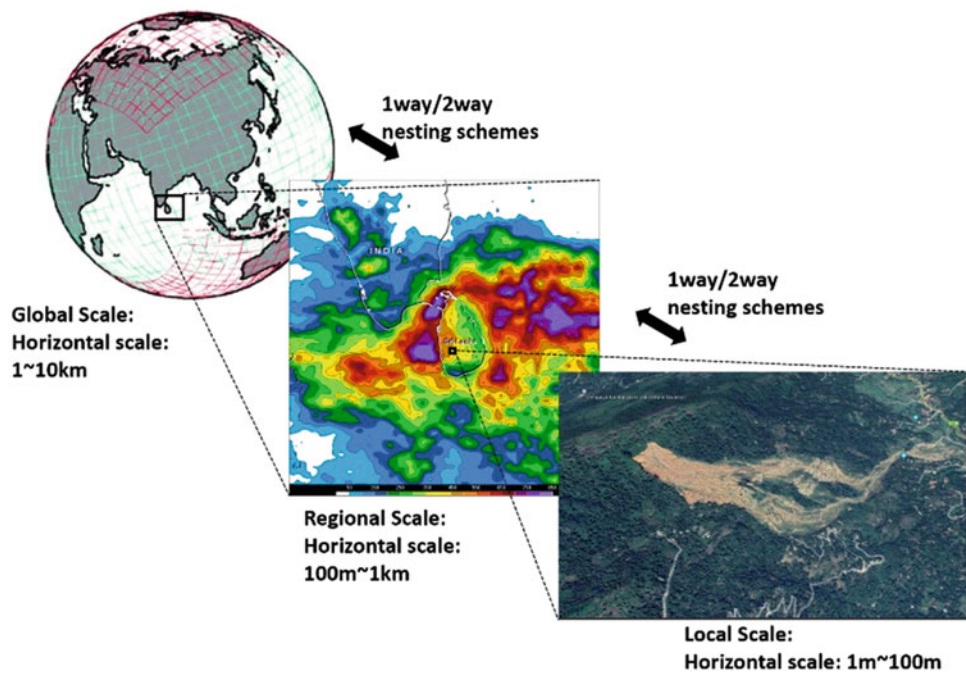
In tropical regions, rainfall is one of the main triggering factors of landslides: Monitoring, early warning, and mitigation; all these three strategies are equally crucial for landslide disaster risk reduction. The current study is a case study from Aranyaka, Sri Lanka, where a devastating landslide occurred in the first monsoon of 2016, May 17th, causing severe human and economic loss. Even though the vulnerable area was already identified as a landslide high hazardous zone, adequate local early warning and evacuation advisories could not be performed timely. Sri Lanka receives high-intensity rainfall as a tropical island during two major monsoons each year: the first monsoon (South and Southwestern region) in May to September and the second monsoon (North and Northeastern region) in December to February. During these seasons, catastrophic landslides have occurred periodically, and records show an increasing tendency of events and losses.

Accurate rainfall prediction is necessary for reliable landslide early warning; therefore, high-resolution numerical weather simulations are important (Kamiya et al. 2019; Onishi et al. 2019). Numerical weather simulation permits mathematical modeling in global, regional, or local scale weather predictions for long-term and short-term forecasts based on current weather. Numerical weather simulation systems which are currently used for rainfall prediction in Sri Lanka, such as ECMWF (European Centre for Medium-Range Weather Forecasts) providing 11 km resolution rainfall data and WRF (Weather Research and Forecasting Model) running with 9 km- and 3 km-resolution simulations, are still not strong enough in providing finer resolution rainfall predictions in landslide early warning perspective. No local weather simulation model is currently operating for

H. A. A. I. S. Bandara (✉)
Department of Mechanical Engineering, Tokyo Institute of Technology,
School of Engineering, Tokyo, Japan
e-mail: bandara.a.aa@m.titech.ac.jp

R. Onishi
Global Scientific Information and Computing Center, Tokyo Institute of
Technology, Tokyo, Japan
e-mail: onishi.ryo@gsic.titech.ac.jp

Fig. 1 Scales of atmospheric simulations. The nesting domain system is used in MSSG multiscale simulations. (a) Global simulations use Yin-Yang grid system, (b) regional simulations use the conventional longitude-latitude orthogonal grid system, (c) local (urban) simulations allow building and residential topography resolved



rainfall forecasting in Sri Lanka. There need to be more local resources to ensure the safety of vulnerable communities on landslides.

Multi-Scale Simulator for the Geoenvironment (MSSG) (Takahashi et al. 2006, 2013), developed by the Tokyo Institute of Technology, Japan Agency for Marine-Earth Science and Technology and Waseda University, is a coupled non-hydrostatic atmosphere-ocean-land global circulation model that permits seamless simulations between weather and climate, serving high-resolution simulations. This MSSG can provide local rainfall predictions that can meet the need for the landslide early warning system in Sri Lanka. MSSG can be run as a multiscale numerical weather simulation model (Fig. 1). It allows to run global simulations with O(1–10 km) horizontal resolutions and regional simulations with O(100 m)–O(1 km) horizontal resolutions. MSSG is also developed to run local scale (urban scale) simulations with O(1 m) horizontal resolution resolving buildings and considering anthropogenic heat releases. In terms of the simulation scales, the high efficiency and reliability of MSSG have been confirmed in all scales using powerful supercomputers (Onishi et al. 2022). In global scale simulations, MSSG uses the Yin-Yang grid system (Kageyama and Sato 2004; Baba et al. 2010), which allows for overcoming the effect of polar singularity and lead to high computational efficiency. In the regional scale simulations, MSSG uses a conventional latitude-longitude system to allow using robust high-order differential schemes.

High-resolution simulations are reliable, but at the same time, they require high computational costs. In case we

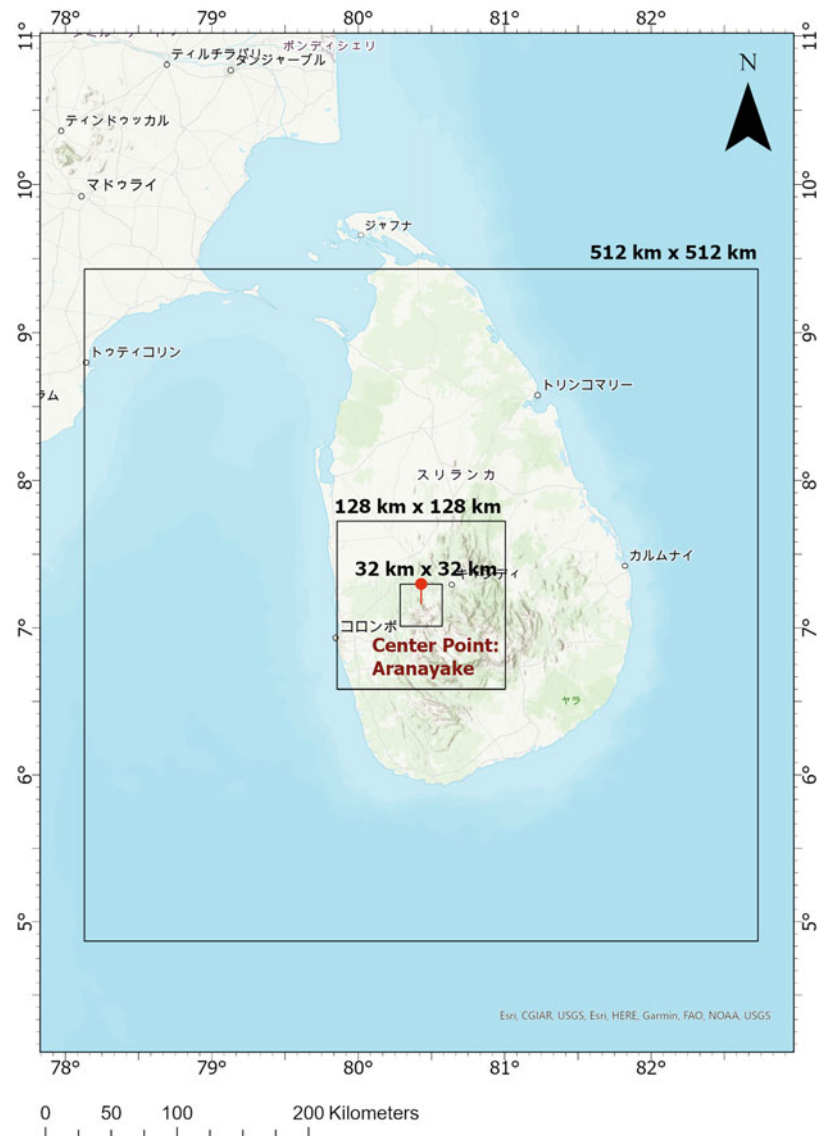
develop an operational rainfall prediction system, the balance between reliability and computational cost. For example, an operational prediction system would be useless if it took 24 h for 24-h prediction. We usually need to compromise on reliability if we use an ordinary computer with limited performance unlike supercomputers. However, the current machine learning technology would relax the compromise in reliability. The deep-learning-based super-resolution technology would help increase the resolution, leading to better reliability at a low computational cost.

We assess the reliability of MSSG high-resolution simulations in comparison with the local observation data in Sri Lanka. We also discuss the potential of using machine-learning-based super-resolution in operational real-time rainfall predictions for landslide early warning systems.

2 Study Area

Figure 2 shows the map of Sri Lanka, centering the focus area of the present study, Aranayaka; more specifically, Samasarakanda in the Aranayaka Divisional Secretariate in the Kegalle District of Sri Lanka, where the devastating landslide occurred in 2016. The area is in the country's central highlands and experiences high yearly rainfall during the southwestern monsoon yearly. An automated rain gauge recorded 426 mm cumulative for 58 h continued rainfall starting from 15th May 2016, which triggered the rapid landslide, which traveled downslope about 2 km air distance causing about 150 human losses.

Fig. 2 The Google Earth picture of Sri Lanka, centering the study point, Aranayaka. The simulation domains utilized in this study are overlaid



3 Methodology

Three computational domains (parent, child and grandchild domains) were selected. The Center of the domains was set at Aranayaka, latitude 7.1541°N, and Longitude 80.4296°E for all the three domains. The parent domain size was selected to cover most of Sri Lanka. The landslide occurred on the slope of a mountain with the half-width of about 2 km. The horizontal resolution of the grandchild domain was set to 500 m considering the reasonable horizontal spacing on the scale of

landslides and limitations due to the performance using a personal computer. Table 1 summarizes the horizontal settings, i.e., longitudinal and latitudinal settings. For the vertical coordinate, 32 grids with irregular intervals were set for all three nesting domains for the height of 30 km. These domain and grid sizes were determined considering the perspective and computer performance.

Numerical weather models compute the advection, i.e., transport of various tracers, including water substances such as water vapor, cloud water, rain, snow, cloud ice, and graupel (Miltenberger et al. 2015). For accurate computation

Table 1 Settings of the computational domains

	Size of horizontal domain	Number of horizontal grids	Horizontal grid spacing
Parent domain	512 × 512 km ²	64 × 64	8 km
Child domain	128 × 128 km ²	64 × 64	2 km
Grandchild domain	32 × 32 km ²	64 × 64	500 m

in advection, the fifth Wicker-Skamarock (W-S) scheme was employed (Wicker and Skamarock 2002).

The six-category bulk cloud microphysics (MSSG-Bulk) (Onishi and Takahashi 2012) was employed to explicitly calculate the cloud dynamics.

4 Results and Discussion

4.1 Five-Day Rainfall Simulation for the Aranayaka Landslide on May 2016

MSSG with the 8 km–2 km–500 m nesting grid system was performed for the rainfall from 00UTC on May 14 to 00UTC on May 19, 2016. Figure 3 shows the rainfall results from the MSSG simulation compared with the observed rainfall recorded in the automated rain gauge of the National Building Research Organization, Sri Lanka, located at Aranayaka. Table 2 summarizes the values of cumulative rainfall and maximum rainfall obtained from observation, GSMAP (the Global Satellite Mapping of Precipitation), and MSSG. As in

the table, cumulative rainfall of 335.7 mm over 5 days was predicted through the simulation, while the observatory recorded 446.3 mm accumulation for the considered period. The maximum hourly average rainfall resulted as 22.7 mm/h through simulation, while the observatory recorded 26.8 mm/h. From the GSMAP data for the above period, cumulative rainfall of 192.0 mm and maximum hourly rainfall of 12.7 mm/h were recorded. When considering this 5-day rainfall event as a whole, the bell-shaped intensity distribution of the long-lasting continuous rainfall is compatible up to a reasonable extent between the observatory record and the MSSG simulation. Compared with the GSMAP, which provides global hourly rainfall at 0.1×0.1 -degree resolution, which roughly corresponds to $10 \text{ km} \times 10 \text{ km}$ horizontal resolution, based on satellite data, the MSSG simulation with 8 km–2 km–500 m resolutions provided closer values to the observatory record. This result confirms that high-resolution simulations are needed for better local rainfall predictions in mountainous areas.

The MSSG simulations conducted for the Aranayaka landslide event, utilizing the 8 km–2 km–500 m resolution, successfully reconstructed a rainfall event that aligned well

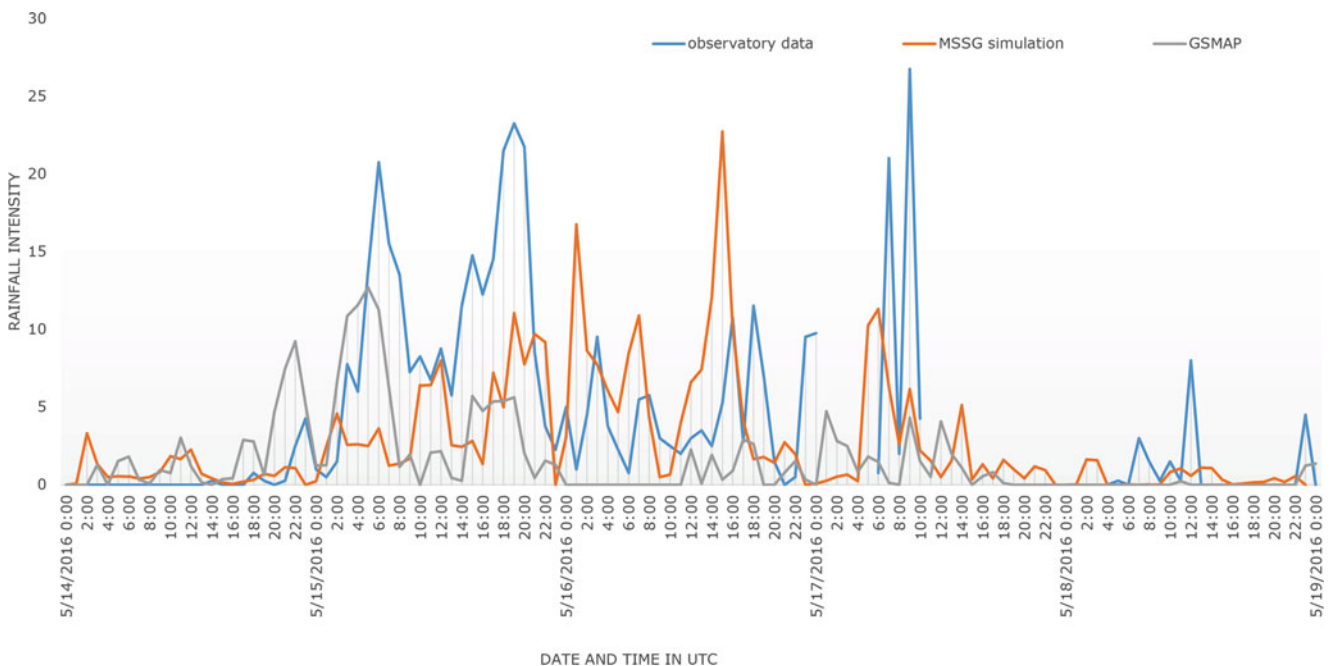


Fig. 3 Rainfall comparison of MSSG 8 km₂ km₅₀₀ m simulation, observatory and Rainfall forecast by GSMAP, for the Aranayaka Landslide event for period of 5 days

Table 2 Rainfall accumulation and maximum rainfall rate at Aranayaka from 2016/5/14 00UTC to 2016/5/19 00UTC

	Rainfall accumulation [mm]	Maximum rainfall [mm/h]
Observation	446.3	26.8
GSMAP	192.0	12.7
MSSG	335.7	22.7

with the observations from the observatory. Although there were variations in the timing and intensity of the rainfall peaks, the overall integration of the event yielded good results. It is worth noting that while comparing point data may have certain limitations, the analysis of the horizontal distribution of rainfall generated by the MSSG simulation indicates highly accurate and reliable predictions. This result suggests that even with the potential drawbacks of point data comparison, the simulation’s ability to depict the spatial distribution of rainfall is remarkably precise and dependable.

4.2 Rainfall Simulations for Past Heavy Rain Events on Aranayaka

Secondly, MSSG simulations were conducted to investigate six previous rainfall events with the high recorded rainfall

accumulation in the Aranayaka rain gauge. Here we performed two sets of MSSG simulations to investigate the impact of increased resolution: One is with 8 km–2 km–500 m nesting grid system and the other with 8 km–2 km nesting grid system.

The results are summarized in Table 3. The findings revealed that the 8 km–2 km–500 m resolution simulation mainly exhibited higher maximum rainfall intensity and more significant overall rainfall accumulation than the 8 km–2 km resolution. In rare instances, the inverse trend is observed, though.

Figure 4 shows the rainfall comparison for event 3 (in Table 3), which resulted in very close values of maximum hourly precipitation and cumulative rainfall during the event. The values of (a) observatory data, (b) MSSG simulation with 8 km–2 km–500 m, (c) MSSG simulation with 8 km–2 km, and (d) GSMAP for maximum hourly average

Table 3 Summary of the simulations performed for high rainfall-accumulation events in the record of Aranayaka automated rain gauge

Event	Date	Rainfall accumulation (mm)			Maximum Rainfall (mm/h)		
		Observed	MSSG (500 m)	MSSG (2 km)	Observed	MSSG (500 m)	MSSG (2 km)
1	2016/05/15 00:00 UTC-2016/05/18 00:00 UTC	417.75	691.4	314.1	26.75	50.0	22.7
2	2018/05/19 18:00 UTC-2018/05/21 18:00 UTC	195.75	0.6	0.8	41.75	0.2	0.3
3	2022/07/31 18:00 UTC-2022/08/01 18:00 UTC	114.50	123.1	41.1	16.00	13.2	4.4
4	2021/05/13 06:00 UTC-2021/05/14 06:00 UTC	111.50	550.4	126.4	19.50	45.1	12.1
5	2022/09/04 12:00 UTC-2022/09/06 12:00 UTC	165.75	123.3	14.3	61.25	8.2	3.7
6	2014/12/25 00:00 UTC-2014/12/26 00:00 UTC	157.00	73.1	77.2	34.50	9.1	10.3

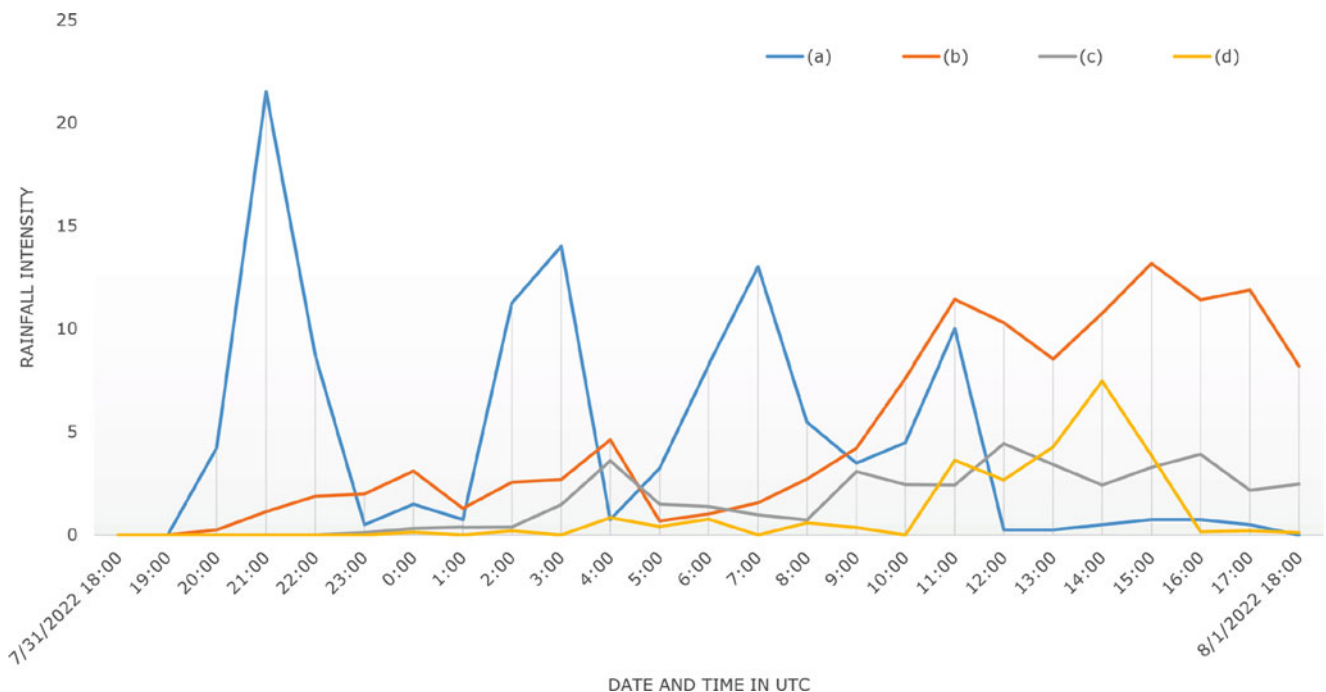


Fig. 4 Rainfall comparison of (a) the observatory, (b) MSSG 8 km–2 km–500 m simulation, (c) MSSG 8 km–2 km simulation and (d) rainfall data by GSMAP for Event 3, from 18UTC on 31 July to 18UTC on 1 August, 2022

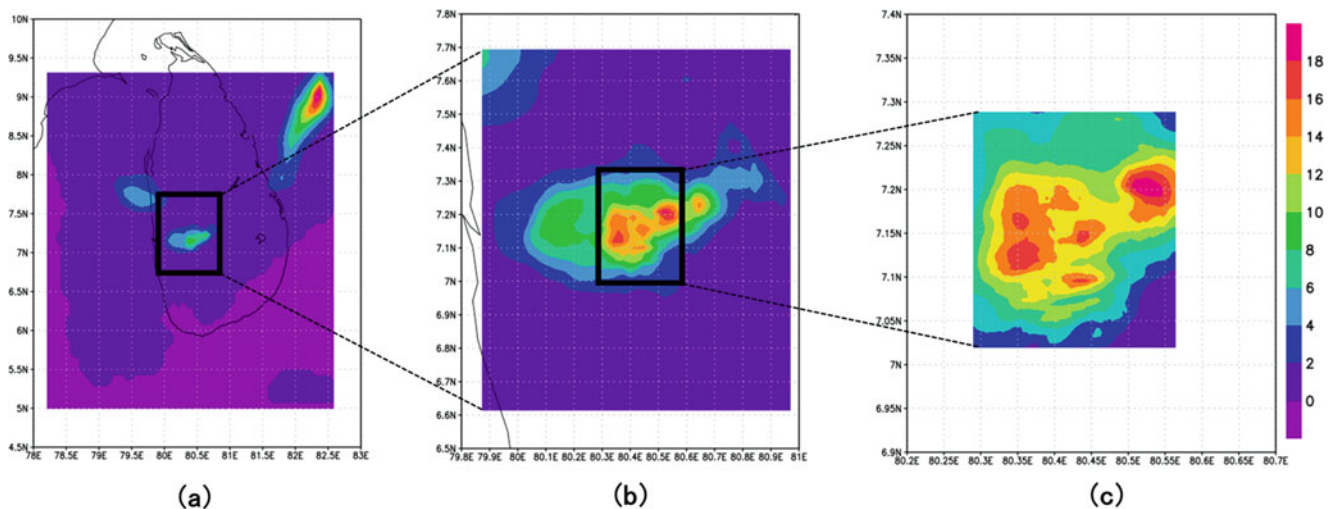


Fig. 5 Regional distribution of rainfall at the time of maximum rainfall through simulation showing the effect of increasing resolution in different domains, (a) 0C_parent domain which the grid size is $8 \text{ km} \times 8 \text{ km}$,

(b) 1C_child domain which the grid size is $2 \text{ km} \times 2 \text{ km}$, (c) 2C_grand child domain which the grid size is $500 \text{ m} \times 500 \text{ m}$

precipitation are, respectively, 16, 13.2, 4.4 and 7.48 mm/h, and for cumulative precipitation, they are, respectively, 114.5, 123.1, 41.1 and 25.81 mm/h. In terms of the timing of major rainfall, MSSG prediction shows the peak at a later time. This time shift can be partly explained by the initial condition of the MSSG simulation. The initial data, created from GSM data by the Japan Meteorological Agency, did not contain cloud substances. This prevents the simulation from producing rainfall in the early time. This initial problem can be solved if we restart the simulation from the previous simulation results. This time, we did not use this solution since we focused on the influence of the simulation resolutions.

The results obtained from the second step of reconstructing high-intensity rainfall events in the past shed light on an important finding: increasing the resolution of the simulations lead to higher values of maximum and cumulative rainfall.

Figure 5 illustrates the increasing accuracy of simulation with increasing resolution. This observation indicates that as the simulation resolution increases, it becomes more capable of capturing the local variations associated with local topography. The relationship between resolution and the ability to accurately represent precipitation patterns highlights the importance of considering finer scales in meteorological simulations to understand better and predict intense rainfall events. Moreover, this study showed that the MSSG simulations were generally successful in simulating the development of isolated or localized cumulonimbus clouds. However, when the size of these cumulonimbus clouds was relatively small or the duration of rainfall was short, reproducing their exact location through the MSSG simulations remained challenging. Nevertheless, from the

current perspective, it is essential to note that landslides are typically not triggered by brief, isolated rainfall events but rather by prolonged periods of continuous rainfall or high-intensity rainfall with a significantly longer duration. The accumulation of water in the soil over time ultimately leads to an increase in mass and loss of cohesion, facilitating downslope movement or rapid erosion. Therefore, the challenges in reproducing the exact location of isolated cumulonimbus clouds do not significantly impact the accuracy of rainfall predictions in the context of landslide early warning systems.

5 Future Work

5.1 Turbulence Enhancement of Orographic Rainfall

This study used the “typical cloud model”, i.e., MSSG-Bulk, installed in MSSG simulation system. Recent research has proven that the turbulence enhancement of collision growth in orographic settings significantly impacts rainfall enhancement (Falkovich and Pumir 2007; Grabowski and Wang 2013; Onishi et al. 2015). The present MSSG have the “turbulence-aware cloud model”, developed by Seifert and Onishi (2016) and Onishi and Seifert (2016), which is capable of considering turbulence enhancement in orographic rainfall.

According to Seifert and Onishi (2016), and as illustrated in Fig. 6, turbulent enhancement in orographic rainfall can impact conversion rates among different categories, i.e., cloud droplet growth.

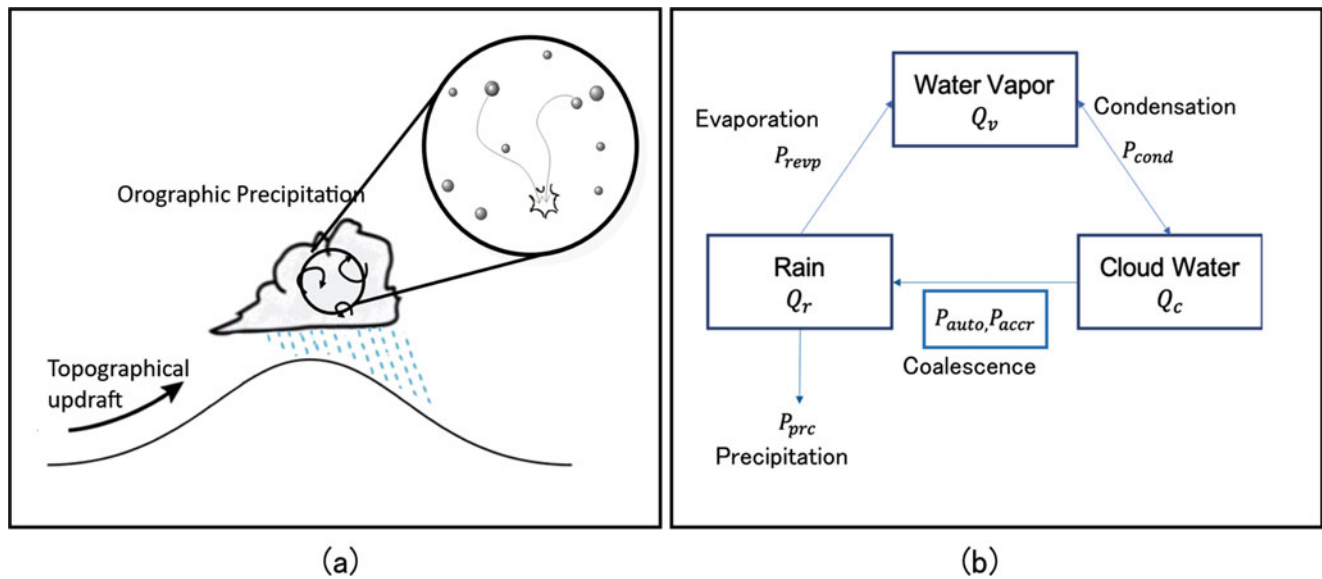


Fig. 6 (a) Schematic illustration of turbulence enhancement of orographic rain, (b) interactions and processes among categories of warm cloud. P_{auto} represent amount of increase in raindrops due to collision of small water droplets and merger into large water droplets, and P_{accr}

Autoconversion, P_{auto} , represents the conversion rate from the cloud-water category to the rain-water category due to collisions among cloud droplets. Accretion, P_{accr} , represents the conversions rate from cloud water to rain-water category due to collections of cloud droplets by rain drop.

The turbulence enhancement in drop collisions enlarges the two conversion rates, P_{auto} and P_{accr} . The present MSSG simulations did not use turbulence-aware cloud models and they are, therefore, not capable of considering turbulence enhancement. The impact of turbulence enhancement in past rainfall events should be assessed as a next step.

5.2 Super-Resolution Simulations

Downscaling techniques, including machine learning models such as artificial neural networks and support vector machines, are employed to enhance the spatial resolution of low-resolution models.

High-resolution (HR) numerical simulations offer superior predictive capabilities to low-resolution (LR) simulations but come at a higher computational cost. The super-resolution (SR) simulation system (Onishi et al. 2019) employs a two-step approach to reduce the computational cost for HR prediction information. Firstly, an LR simulation is conducted, and then the resulting LR prediction images are mapped to HR predictions using an SR method. This combination enables the system to provide HR predictions as reliable as those obtained from HR simulations while at a much smaller computational cost.

implies the amount of increase in raindrops due to large water droplets collecting and merging small water droplets. This two coalescence factors P_{auto} and P_{accr} are enhance due to turbulence

A recently introduced super-resolution (SR) neural network, as proposed by Yasuda et al. (2022), demonstrates its applicability in generating rainfall prediction maps. The SR network can utilize multiple input channels, such as a high-resolution topography map, to enhance the accuracy of the resulting high-resolution (HR) rainfall map and to widen the generality of the network. The SR neural network is trained using HR and low-resolution (LR) simulation results during the training phase. HR simulations, which are computationally intensive and performed on supercomputers, contribute to generating training data sets. In contrast, during operational use, LR simulations require significantly lower computational resources. This SR system holds promise for providing real-time prediction services to local communities needing more computational capabilities.

6 Conclusions

The Multi-Scale Simulator for the Geoenvironment (MSSG) offers a promising tool for enhancing regional simulations with high resolution. The MSSG simulation with an 8 km–2 km–500 m nesting grid system has demonstrated reasonably accurate rainfall predictions, particularly for investigating local orographic rainfall. Occasionally, less accurate rainfall predictions can be attributed to the challenge of reproducing the exact location of short-lived, isolated cumulonimbus clouds.

The MSSG provides more reliable rainfall data as the resolution increases. This study has revealed that by

increasing the resolution from 8 km–2 km to 8 km–2 km–500 m, the cumulative rainfall and maximum hourly-average rainfall for specific events exhibit higher values, which align closer to the observed data. This finding establishes the reliability of the MSSG, paving the way for the confident implementation of fine-resolution simulations.

The real-time operation using the MSSG with an 8 km–2 km–500 m nesting grid system would require expensive computers. The deep-neural-network super-resolution technology would help to reduce the computational cost to produce high-resolution reliable predictions for orographic rainfall. This technology combination positions the MSSG as an effective tool for rainfall forecasting and early warning of landslides.

Acknowledgments This research was partially supported by the Science and Technology Research Partnership for Sustainable Development (SATREPS), the Japan International Cooperation Agency (JICA), the International Consortium on Landslides (ICL), the National Building Research Organization (NBRO), Sri Lanka and the educational development through the Global Scientific Information and Computing Center, Tokyo Institute of Technology.

References

- Baba Y, Takahashi K, Sugimura T, Goto K (2010) Dynamical core of an atmospheric general circulation model on a yin–yang grid. *Monthly Weather Rev* 138:3988–4005
- Falkovich G, Pumir A (2007) Sling effect in collisions of water droplets in turbulent clouds. *J Atmos Sci* 64:4497–4505
- Grabowski WW, Wang L-P (2013) Growth of cloud droplets in a turbulent environment. *Annu Rev Fluid Mech* 45:293–324
- Kageyama A, Sato T (2004) The Yin-Yang grid: an overset grid in spherical geometry. *Geochem Geophys Geosyst* 5:Q09005
- Kamiya T, Onishi R, Kodera S, Hirata A (2019) Estimation of time-course core temperature and water loss in realistic adult and child models with urban micrometeorology prediction. *Int J Environ Res Public Health* 16:5097
- Miltenberger AK, Seifert A, Joos H, Wernli H (2015) A Scaling relation for warm-phase orographic precipitation: a Lagrangian analysis for 2D mountains. *Q J R Meteorol Soc* 141:2185–2198
- Onishi R, Seifert A (2016) Reynolds-number dependence of turbulence enhancement on collision growth. *Atmos Chem Phys* 16:12441–12455
- Onishi R, Takahashi K (2012) A warm-bin-cold-bulk hybrid cloud microphysical model. *J Atmos Sci* 69:1474–1497
- Onishi R, Matsuda K, Takahashi K (2015) Lagrangian tracking simulation of droplet growth in turbulence –turbulence enhancement of autoconversion rate. *J Atmos Sci* 72:2591–2607
- Onishi R, Sugiyama D, Matsuda K (2019) Super-resolution simulation for real-time prediction of urban micrometeorology. *SOLA* 15:178–182
- Onishi R, Hirai J, Kolomenskiy D, Yasuda Y (2022) Realtime high-resolution prediction of orographic rainfall for early warning of landslides. *Book Series Int Consortium Landslides* 1(1):2022
- Seifert A, Onishi R (2016) Turbulence effects on warm-rain formation in precipitating shallow convection revisited. *Atmos Chem Phys* 16:12127–12141
- Takahashi K, Peng X, Onishi R, Ohdaira M, Goto K, Fuchigami H, Sugimura T (2006) Multi-scale weather/climate simulations with multi-scale simulator for the geoenvironment (MSSG) on the Earth Simulator, Annual Report of the Earth Simulator Center, April 2005–March 2006, pp 31–39
- Takahashi K, Onishi R, Baba Y, Kida S, Matsuda K, Goto K, Fuchigami H (2013) Challenge toward the prediction of typhoon behaviour and down pour. *J Phys* 454(012):072
- Wicker LJ, Skamarock WC (2002) Time-split-ting methods for elastic models using forward time schemes. *Monthly Weather Rev* 130:2088–2097
- Yasuda Y, Onishi R, Hirokawa Y, Kolomenskiy D, Sugiyama D (2022) Super-resolution of near-surface temperature utilizing physical quantities for real-time prediction of urban micrometeorology. *Building Environ* 209(108):597

Open Access This chapter is licensed under the terms of the Creative Commons Attribution 4.0 International License (<http://creativecommons.org/licenses/by/4.0/>), which permits use, sharing, adaptation, distribution and reproduction in any medium or format, as long as you give appropriate credit to the original author(s) and the source, provide a link to the Creative Commons license and indicate if changes were made.

The images or other third party material in this chapter are included in the chapter's Creative Commons license, unless indicated otherwise in a credit line to the material. If material is not included in the chapter's Creative Commons license and your intended use is not permitted by statutory regulation or exceeds the permitted use, you will need to obtain permission directly from the copyright holder.





Climate Change as Modifier of Landslide Susceptibility: Case Study in Davao Oriental, Philippines

Mary Antonette A. Beroya-Eitner, May Celine T. M. Vicente, Julie Mae B. Dado, Marion Roel S. Dimain, Joel T. Maquiling, and Faye Abigail T. Cruz

Abstract

Rainfall-induced landslides are widely occurring phenomena that cause billions of US dollars annually in damage, and thousands of deaths globally. The Philippines, due to its climate, geographic location and topography, is among those countries most prone to the hazard. The strong climatic warming trend over the past decades has affected the rainfall pattern in the country, thus affecting the landslide distribution as well. This study aims to determine how the rainfall in our study area, Davao Oriental, is expected to change in the future in response to climate warming and how such a change may affect the landslide susceptibility pattern in the province. Results show that contrary to the general perception of increased landslide susceptibility due to a warming climate, a decreased susceptibility is anticipated in the study area. Despite this decrease, however, there remains high to very high landslide hazard for the northern part of the province well into the future, and risk reduction work is still needed in this area. Moreover, while the projected decrease in rainfall and landslide susceptibility is a positive sign concerning landslide hazard management, such a drying trend may spawn other hazards, including drought and water shortage, underscoring the need for a multi-hazard assessment

that takes into account the complex interrelationships between different hazards. We deem the results of the study to be very important for better prioritization and more efficient allocation of resources for disaster risk management and reduction. The methodology developed for this study can be applied to other parts of the Philippines, and other regions as well.

Keywords

Rainfall-induced landslide · Climate change · Landslide hazard management

1 Introduction

Rainfall-induced landslides are a common occurrence in almost all parts of the world, causing billions of US dollars in damage annually, and thousands of deaths globally. The Philippines is among those countries most prone to this type of hazard, ranking fifth in the world in terms of number of landslide (wet) disaster occurrences from 1970 to 2023 (EMDAT, CRED/UCLouvain 2023) (Fig. 1). The reason for this lies in the climate, geographic location and topography of the country. Climate in the Philippines is generally tropical maritime, characterized by high temperature and high amounts of rainfall. Some regions, particularly those falling within the equatorial climate zone, are hot and wet year-round. Rainfall is governed by the Southwest Monsoon in the boreal summer months, and by the Northeast Monsoon in the boreal winter, with contribution from tropical cyclones (Bagtasa 2017; Matsumoto et al. 2020). The mean annual rainfall varies from about 960 to 4000 mm annually, with the easternmost parts receiving the greatest amount of rain (Olaguera et al. 2022; PAGASA 2023).

Situated in the Northwestern Pacific basin, a great portion of the rain in the Philippines, particularly along the northwestern coast of Luzon, is due to both direct and indirect influence of typhoons (Bagtasa 2017; Cinco et al. 2016). The

M. A. A. Beroya-Eitner (✉)

Department of Civil and Environmental Engineering, Institute of Geotechnics, Technical University of Darmstadt, Darmstadt, Germany

Geohazards International, Pleasanton, CA, USA

e-mail: beroya-eitner@geohaz.org

M. C. T. M. Vicente · J. M. B. Dado · M. R. S. Dimain · F. A. T. Cruz
Manila Observatory, Ateneo de Manila University Campus, Quezon City, Philippines

e-mail: celine@observatory.ph; jmbdado@observatory.ph;

mdimain@observatory.ph; fcruz@observatory.ph

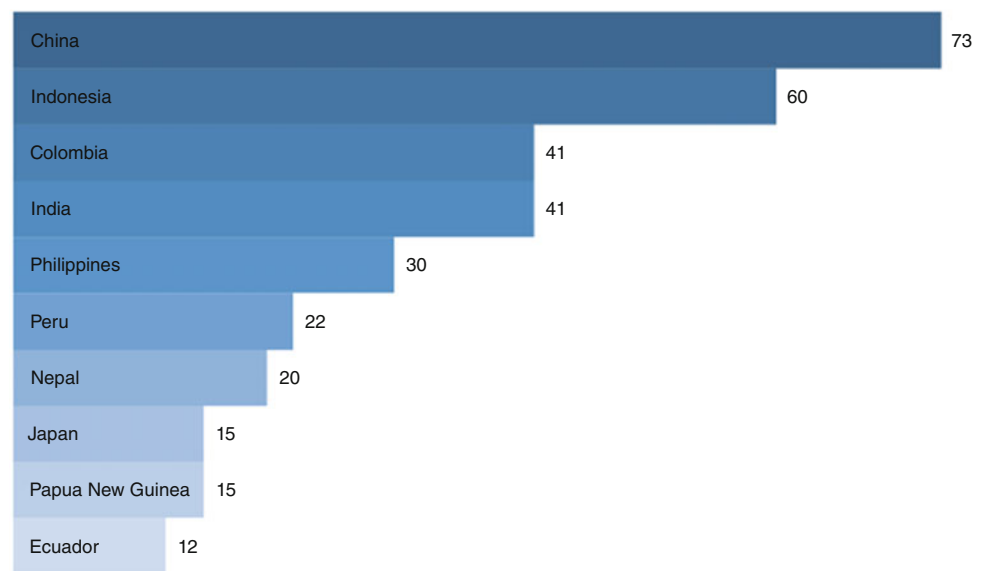
J. T. Maquiling

Ateneo Geophysics Research Laboratory, Department of Physics, School of Science and Engineering, Ateneo de Manila University, Quezon City, Philippines

e-mail: jmaquiling@ateneo.edu

Fig. 1 The Philippines ranks fifth in terms of global occurrences of rainfall-induced landslide disaster from 1970 to 2023 (Data Source: EM-DAT, CRED/UCLouvain 2023)

Global Occurrences of Rainfall-Induced Landslide Disasters, 1970–2023



basin is the most active tropical cyclone (TC) basin on the planet, accounting for about 30% of all TC activities (Fudeyasu et al. 2014). Worldwide, the Philippines ranks second, next only to China, in terms of TC landfalls since 1970 (NOAA's Atlantic Oceanographic and Meteorological Laboratory 2021). About 20 TCs enter the Philippine Area of Responsibility per year, with approximately nine making landfall (Cinco et al. 2016).

Moreover, convective rainfall is also common due to the country's mountainous terrain, interspersed with narrow coastal plains (WBG and ADB 2021; Olaguera et al. 2022). This mountainous terrain is characterized by steep slopes and are, therefore, susceptible to all types of mass movement.

Like in all parts of the world, the strong warming trend over the past few decades has affected the rainfall pattern in the Philippines. For effective disaster management, it is important to determine this change in rainfall pattern and how such a change is, in turn, affecting hydrometeorological hazard patterns. In line with this, the present study was conducted for Davao Oriental as a case study, with the aim of assessing how the rainfall is anticipated to change in the future and how such a change will affect the landslide distribution in this province. Davao Oriental was chosen as the study area due to data availability for validation of results. Nonetheless, the methodology presented in this study can be applied to other parts of the Philippines, and other regions as well.

2 Study Area

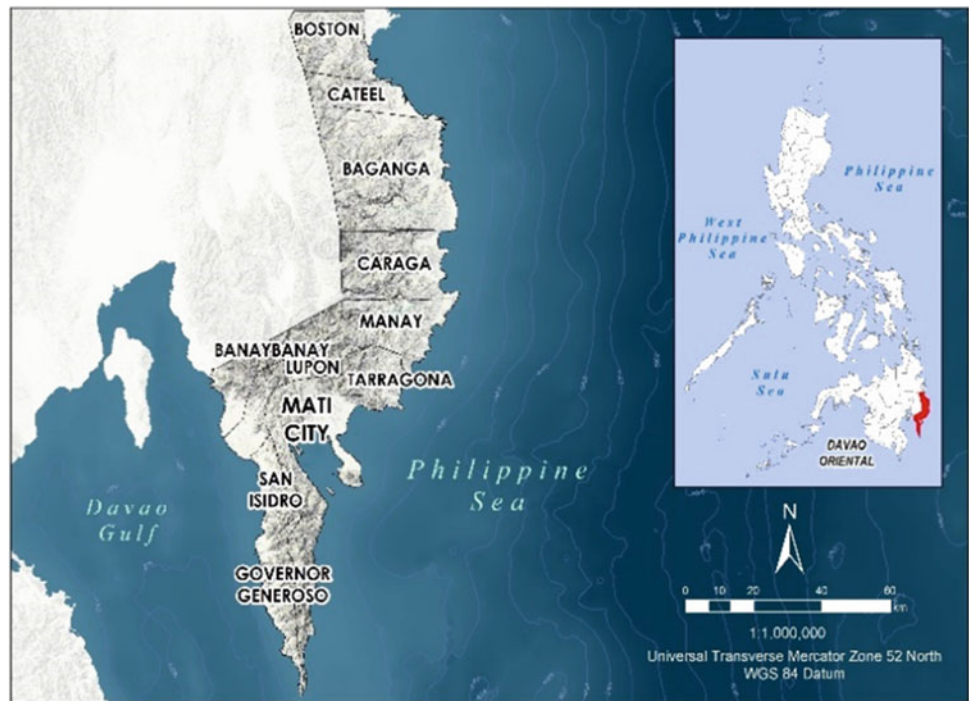
Davao Oriental is located on the island of Mindanao, lying at the southeasternmost tip of the Philippines. It covers a total area of 5680 km², and comprises 10 municipalities and one

city. Mati City serves as the province's capital. Davao Oriental is bounded by the Philippine Sea to the east and Davao Gulf to the west (Fig. 2).

Rainfall in the province is more or less distributed evenly throughout the year, and is influenced by TCs, low pressure systems, cold surges, cold surge shearline, cold surge vortices, and local convective systems (Olaguera et al. 2022). The province also experiences its fair share of TCs. Figure 3a shows the TC tracks from 1971 to 2015 that may have directly or indirectly affected Davao Oriental (i.e., TCs falling within a 250-km buffer zone that is centered in the province). The decade from 1991–2000 has the most numbers of TCs, mostly tropical depressions (Fig. 3b). The decade from 1981–1990 was characterized by three destructive typhoons of Category 4. Figure 3c indicates that most TCs occurred in November and December, which were also the months when two Category 5 TCs passed through this region: Typhoon Mike (Ruping) in November 1990, and Typhoon Bopha (Pablo) in December 2012 (Narisma et al. 2017). A recent analysis of the rainfall associated with TCs (i.e., within a 1100-km radius from the TC center) from 1951–2014 indicates less than 20% contribution of TCs to rainfall over Davao Oriental (Bagtasa 2017); however, this study did not consider the contribution of tropical depressions or low-pressure systems.

Geologically, Davao Oriental is mainly composed of Late Jurassic to Cretaceous basement rocks consisting of meta-greenstones, greenschists and ophiolitic sequences, and Early Miocene clastic rocks (Buena et al. 2019). There are two main tectonic features in the region: (1) the Philippine trench offshore to the east, which marks the subduction of the Philippine Sea Plate beneath the Philippine Mobile Belt, and (2) the southern extension of the Philippine Fault Zone,

Fig. 2 Location of Davao Oriental and the municipalities comprising the province [Sources: Global Administrative Areas (GADM), U.S. Geological Survey and General Bathymetric Chart of the Oceans (GEBCO)]



which is a 1200 km-long strike-slip fault that transects the entire country from north to south, and splits into a number of branches in the study area (Fig. 4). Davao Oriental is therefore prone not only to rainfall-induced landslides but to earthquake-triggered landslides as well.

3 Methodology

3.1 Base Landslide Susceptibility Map

This study used as a base map the official government landslide susceptibility map of Davao Oriental published by the Mines and Geosciences Bureau of the Department of Environment and Natural Resources of the Philippines (DENR-MGB 2022) (Fig. 5). Mainly derived using a field-based, qualitative approach, the map was generated considering the following parameters: slope gradient, weathering/soil characteristics, rock mass strength, ground stability, and human initiated effects (Table 1). The map therefore depicts the likelihood of a landslide occurring in an area based on the local terrain (Soeters and Van Westen 1996; Reichenbach et al. 2018). Ranking into different landslide susceptibility levels (very high, high, moderate and low) was based on the criteria in Table 1. Triggering mechanisms, such as rainfall, were not considered. Thus, in order to get an overview of how the terrain conditions may interact with rainfall at present and in the future, historical and projected rainfall data were incorporated in the present study.

3.2 Historical and Projected Rainfall

As extreme rainfall, from short cloudbursts to prolonged events that last for several days to weeks, is the most significant trigger of landslides (Kirschbaum et al. 2020), extreme rainfall was considered in this study. In particular, the index $R95pTOT$ was used, which is the total amount of annual precipitation that falls on “very wet days”, or when daily rainfall RR exceeds the 95th percentile threshold of the base period (1986–2005), i.e., $RR > 95p$ (Karl et al. 1999; Peterson et al. 2001).

Expressed mathematically,

$$R95p_jTOT = \sum_{w=1}^W RR_{wj} \quad RR_{wj} > RR_{wn95}$$

where RR_{wj} is the precipitation amount on a wet day w (i.e., $RR \geq 1.0$ mm in period j), RR_{wn95} is the 95th percentile of precipitation on wet days in the historical (or projection) period, and W is the number of wet days in the period.

Rainfall data were obtained from a subset of the climate projections from the Southeast Asia Regional Climate Downscaling (SEACLID)/Coordinated Regional Climate Downscaling Experiment Southeast Asia (CORDEX-SEA) project, described in Tangang et al. (2020). Five Coupled Model Intercomparison Project Phase 5 (CMIP5) global climate models (GCM) were used, namely the CNRM-CM5, MPI-ESM-MR, EC-Earth, CSIRO-Mk3.6.0, and HADGEM2-ES. Kamworapan and Surussavadee (2019) provide details on these GCMs. Used for understanding and

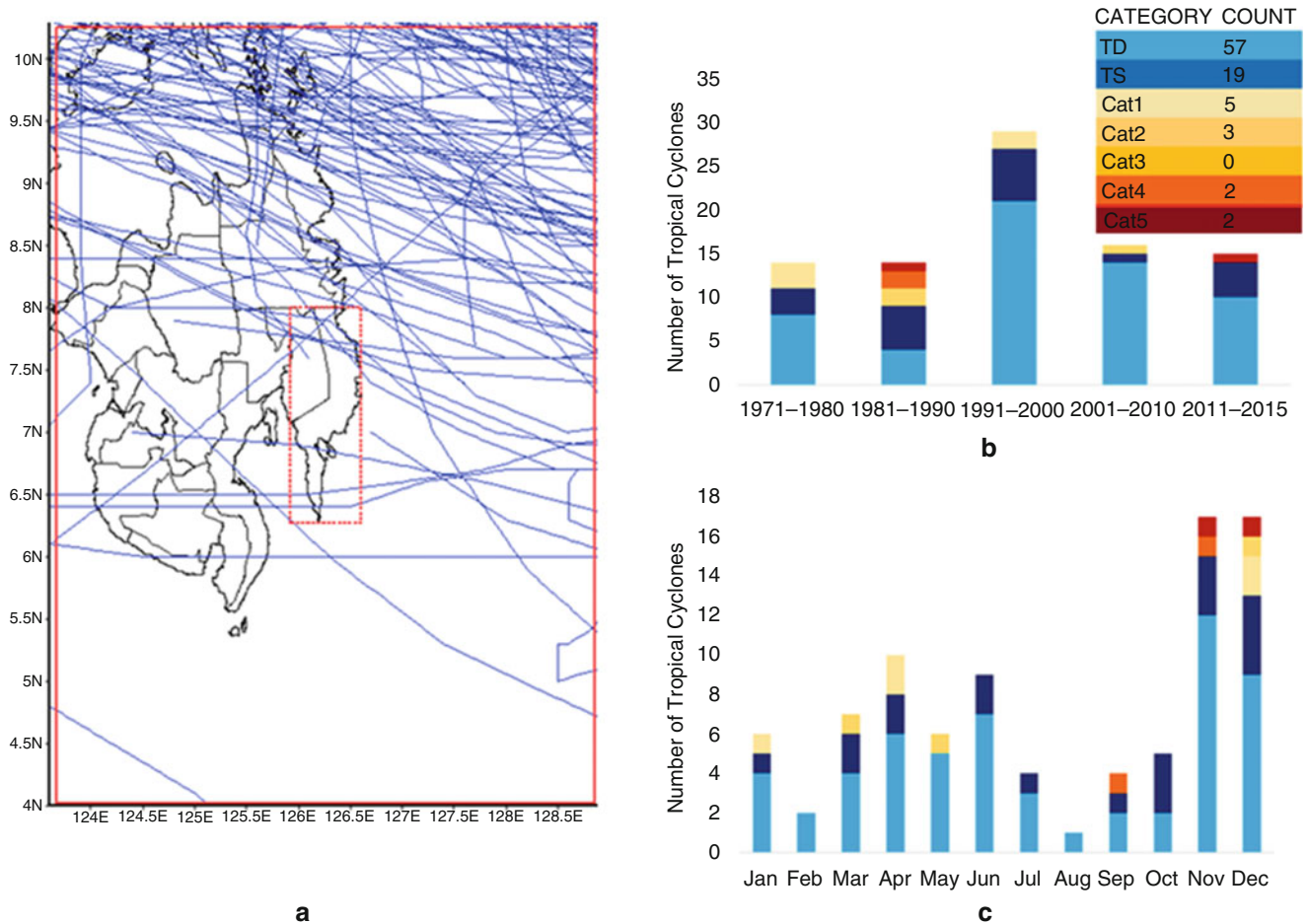


Fig. 3 (a) Tropical cyclone tracks (blue lines) within 250 km of the Davao Oriental boundary (enclosed in dashed box) from 1971 to 2015; (b) Decadal Total Number of Tropical Cyclones for Davao Oriental (1971–2015). Note that there are only five years for 2011 to 2015, (c)

Monthly Total Number of Tropical Cyclones in Davao Oriental (1971–2015) (© 2017 The Oscar M. Lopez Center for Climate Change Adaptation and Disaster Risk Management Foundation, Inc., In: Narisma et al. 2017, used with permission)



Fig. 4 Main tectonic features in the study area (bounded by rectangle); (1) Philippine Trench (2) PFZ—Philippine Fault Zone. Modified from PHIVOLCS (2018)

predicting climate behavior, GCMs are complex mathematical representations of the major climate system components (atmosphere, land surface, ocean, and sea ice) and their interactions. Climate projections from GCMs have coarse resolution and require downscaling at finer scales to be suitable for local analyses. In this study, the GCMs were dynamically downscaled to 25 km resolution using the Abdus Salam International Centre for Theoretical Physics (ICTP) Regional Climate Model version 4.3 (RegCM4.3) (Giorgi and Anyah 2012). The model results have biases when compared to observational datasets. Thus, bias-adjustments were performed against the 0.25-degree resolution Fifth Generation European Centre for Medium-Range Weather Forecast (ECMWF) reanalysis (ERA5) dataset (Hersbach et al. 2018) using a Quantile Delta Mapping technique described in Cannon et al. (2015).

The ensemble mean was taken to prepare the 20-year mean of the annual extreme rainfall total during the historical (1986–2005) and future projection (2046–2065) periods,

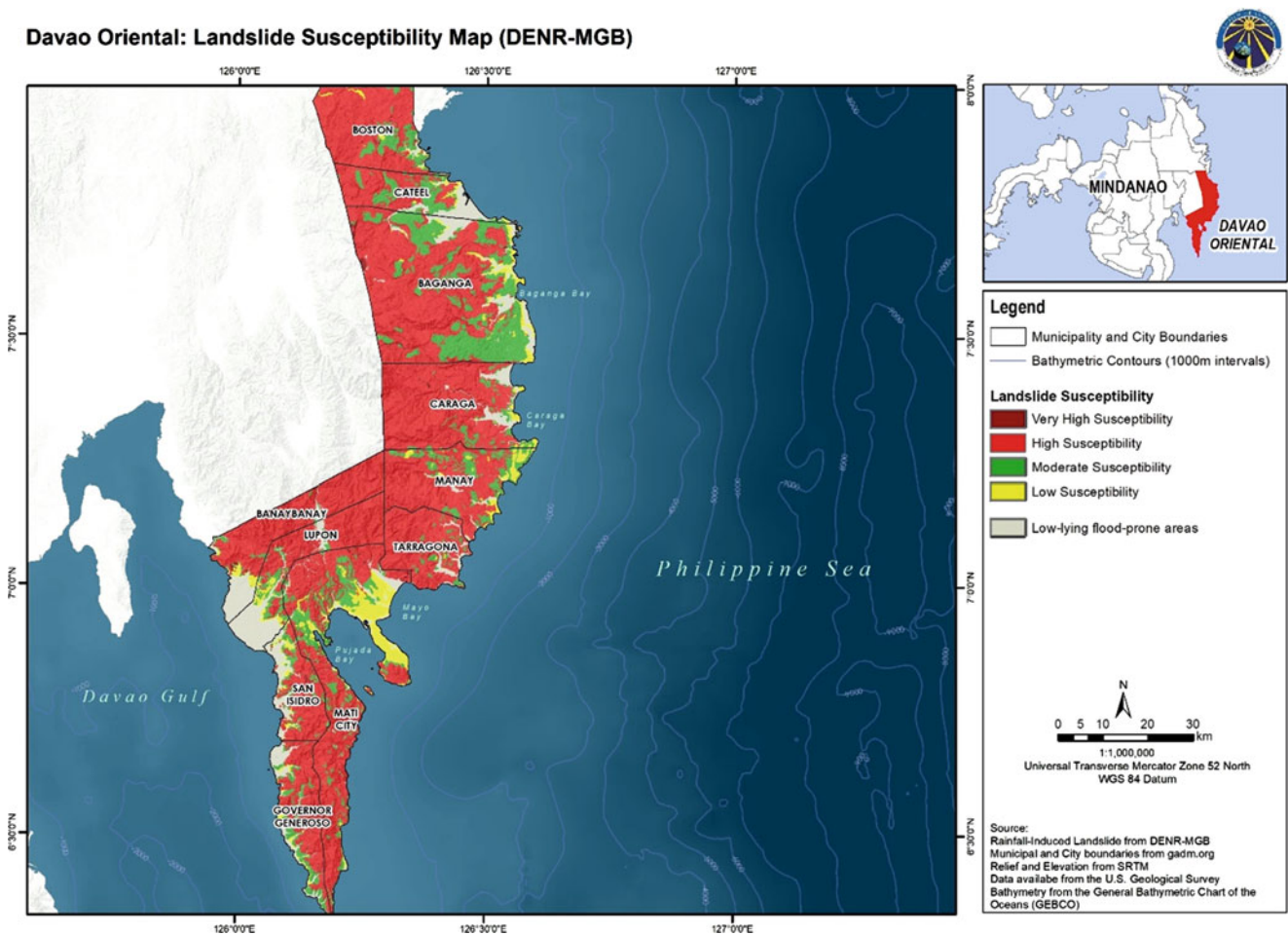


Fig. 5 The landslide susceptibility map of DENR-MGB (2022) used as the base map for this study (used with permission)

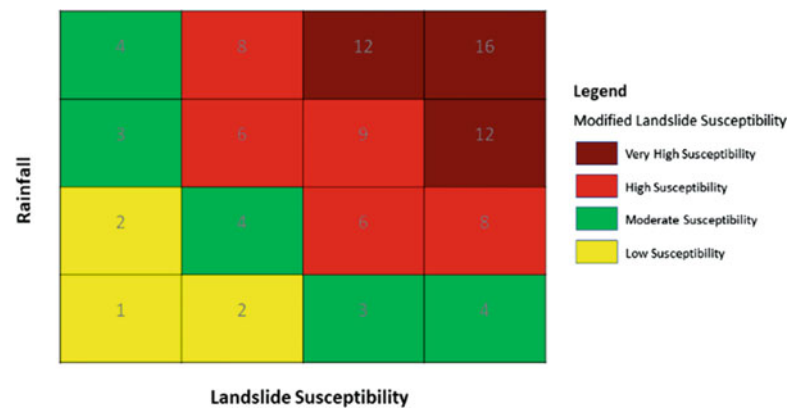
under two scenarios: RCP4.5 and RCP8.5. Used by the Intergovernmental Panel on Climate Change (IPCC) in its fifth assessment report, RCP stands for Representative Concentration Pathways, which predicts the concentration of greenhouse gases (GHG) in the atmosphere as a result of

human activities. The RCP4.5 refers to a moderate scenario in which GHG emissions peak around 2040 and then decline. On the other hand, RCP8.5 is the highest emissions scenario in which emissions continue to rise throughout the twenty-first century (IPCC 2014).

Table 1 DENR-MGB Landslide susceptibility ranking (Garas 2013)

Landslide susceptibility parameters	Low	Moderate	High	Very high
A. Slope gradient	Low to moderate (<18°)	Moderate to steep (18°–35°)	Steep to very steep (>35°)	Steep to very steep (>35°)
B. Weathering/ Soil characteristics	Slight to moderate	Moderate	Intense; soil usually non-cohesive	Intense; soil usually non-cohesive
C. Rock mass strength	Very good to good	Fair	Poor to very poor	Poor to very poor
D. Ground stability	Stable with no identified landslide scars, either old, recent or active	Soil creep and other indications of possible landslide occurrences are present	Inactive landslides evident; tension cracks present	Active landslides evident; tension cracks, bulges, terracets, seepage present
E. Human-initiated effects				May be an aggravating factor

Fig. 6 Scheme for the raster multiplication process and susceptibility level generation



Using the ArcGIS platform, the aggregated rainfall data were then rendered in maps, where areas are categorized into classes based on the relative amount of rainfall received.

3.3 Modified Landslide Susceptibility Map

As a final step, the rainfall maps were combined with the base landslide susceptibility map to generate the modified landslides susceptibility maps. To do this, the values of the rainfall classes and the landslide susceptibility levels in the respective maps were first reclassified into 1 to 4 using the Reclassify tool of ArcGIS, with 1 corresponding to low and 4 corresponding to very high. Then, using the Raster Calculator tool, the reclassified rainfall and landslide susceptibility values were multiplied with each other on a per pixel basis. This step serves as the cross-tabulation of the two variables being combined, which were assumed to have equal weights. Finally, the resulting values from the cross tabulation were classified into different susceptibility levels following the pre-assigned categories in the matrix in Fig. 6.

4 Results and Discussion

Figure 7a–c show the distribution of historical and projected extreme annual rainfall in the study area. Historical total annual extreme rainfall ranges from 244 mm to 477 mm. A clear north-south divide is noticeable where the historical extreme rainfall was higher over the northern than over the southern part of the province. The highest amounts were recorded mainly in Baganga and Cateel, and in parts of Caraga and Boston. This result is consistent with the fact that TCs in the Philippines, with which extreme rainfall is usually associated, generally originate in the Pacific Ocean and follow a northwesterly direction over Mindanao, usually affecting only the northern part of the region, as is also evident from Fig. 3a.

The same general rainfall distribution pattern as in the historical period is observed for the projected period. However, drier conditions are expected by the mid-twenty-first century under both the RCP4.5 and RCP8.5 scenarios, with lesser areas experiencing very high extreme rainfall (Table 2), mainly in Baganga, Cateel and Caraga. Relative to the baseline extreme rainfall total range of 244–477 mm, the decrease in extreme rainfall is greater under RCP4.5, with annual extreme rainfall total range of 221–462 mm, compared to 223–474 mm under RCP8.5.

The resulting modified rainfall-induced landslide susceptibility (RILS) maps are shown in Fig. 8a–c. Comparing the modified historical RILS map (Fig. 8a) with the base RILS map (Fig. 5), it is seen that incorporating rainfall data into the latter map allows further delineation of very highly susceptible areas (Fig. 8a, Table 3). Specifically, the very highly susceptible areas increased by more than 45-fold. For disaster risk management, this modification is deemed very important as it allows better prioritization and more efficient allocation of resources.

The slope failures/movements that were observed during a field survey in the province (Narisma et al. 2017) were plotted in the modified historical RILS map (Fig. 9). As can be seen, they mostly fall on highly to very highly susceptible areas, providing increased confidence in the validity of the modified RILS maps. Note, however, that the field survey was limited only to accessible areas and therefore, by no means an intensive landslide inventory of the study area.

During the inspection, it was observed that when it rains, the rainwater collects and seeps through the fissures in rocks/soils, runs downslope, and oftentimes collects at the foot of the slope. As is generally known, rainwater increases the weight of slope materials, reduces friction along potential failure planes, and increases pore water pressure that then reduces the strength of the slope mass. These may have contributed to the failure of the investigated slopes. The observed slope failures vary in type, including rotational slide, translational slide, debris flow, rock fall and creep.

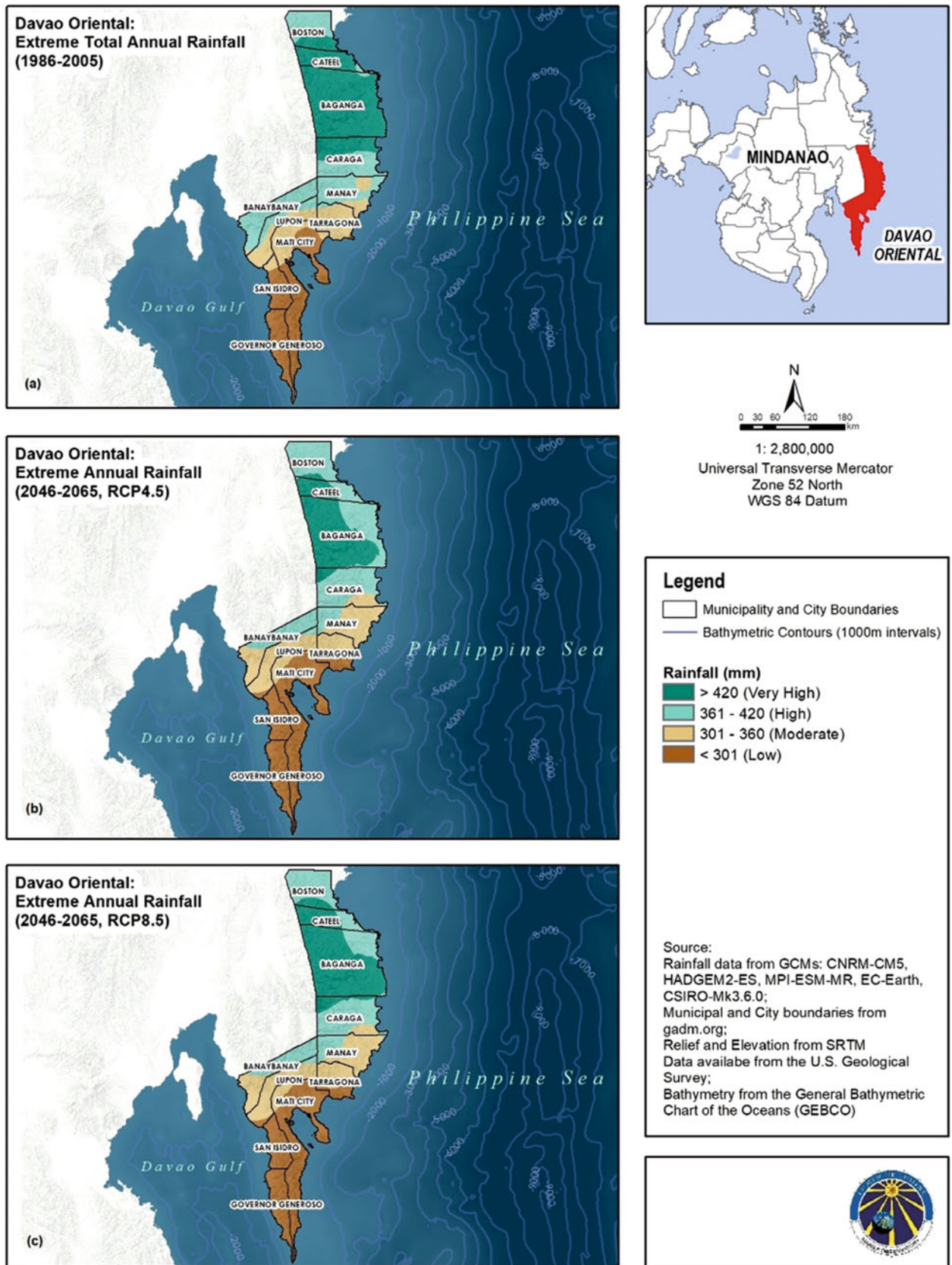


Fig. 7 Annual extreme rainfall in Davao Oriental (a) Historical (1986–2005), (b) Projected under RCP4.5 (2046–2065), and (c) Projected under RCP8.5 (2046–2065). A decrease in areas affected by

very high extreme rainfall is expected by the mid-twenty-first century under both scenarios (see also Table 2), mainly in Baganga, Cateel and Caraga

Table 2 Areas affected by different rainfall classes

Rainfall (mm)	Affected area (sq. km)		
	Historical	RCP4.5	RCP8.5
Very high	1775	1032	1314
High	1445	1637	1368
Moderate	890	1126	1118
Low	1028	1343	1338

It follows from the decreasing future trend of the extreme rainfall intensity that the RILS in the study area would also decrease during the projection period. The expected decrease is stronger under RCP4.5 than under RCP8.5 (Fig. 8; Table 3). Specifically, the very highly susceptible areas are projected to decrease by about 34% and 22% under RCP4.5 and RCP8.5, respectively, while the low susceptible areas are projected to increase by about 31% under both scenarios. Again, the changes are expected to be observed mainly in the municipalities of Baganga, Cateel and Caraga.

The same trend of decreasing landslide susceptibility is actually expected across all of Philippines, as a general drying trend is projected throughout the country, except in some areas in the north, mainly in Luzon Island (DOST-PAGASA, Manila Observatory and Ateneo de Manila University 2021; Narisma et al. 2017). Therefore, contrary to the expectation of future increase in the frequency and magnitude of landslides for most of the world's regions, climate change is positively modifying the landslide hazard susceptibility in Davao Oriental, and the Philippines, in general.

It must be noted, however, that there remains high to very high landslide hazard for northern Davao Oriental well into the future, and that risk reduction work is still needed in this area. Moreover, while the projected decrease in rainfall and landslide susceptibility is a positive sign concerning landslide hazard management, such a drying trend may spawn other hazards, including drought and water shortage, which can have dire consequences on people's health, livelihood and well-being. This underscores the importance of a multi-hazard assessment that takes into account the complex

interactions and interrelationships between the different hazards that an area is subject to.

5 Conclusion and Outlook

One of the greatest concerns about the current warming of the planet is an increase in precipitation and, therefore, the consequent increase in hydro-meteorological hazards such as landslides. In this study, we show that for the study area in Davao Oriental, global warming is causing a general reduction in landslide hazard susceptibility as a consequence of the drying trend expected in the area in the mid-twenty-first century.

Going forward, we deem it necessary that studies like the present be conducted in the other parts of the country, focusing on areas where increased rainfall is expected. Nonetheless, regardless of whether the projection for a given area is of a drying or a wetting trend, it is important to determine the consequent change in the associated patterns of multiple hazards so as to allow better prioritization and more efficient allocation of resources for disaster risk management and reduction.

In this preliminary work, the landslide susceptibility was defined considering the relative amount of extreme rainfall within the study area. In future work, we intend to use empirically-derived rainfall threshold values to define the different susceptibility levels. In addition, the use of other extreme rainfall indices may be explored to better capture the relationship between rainfall and landslide occurrences.

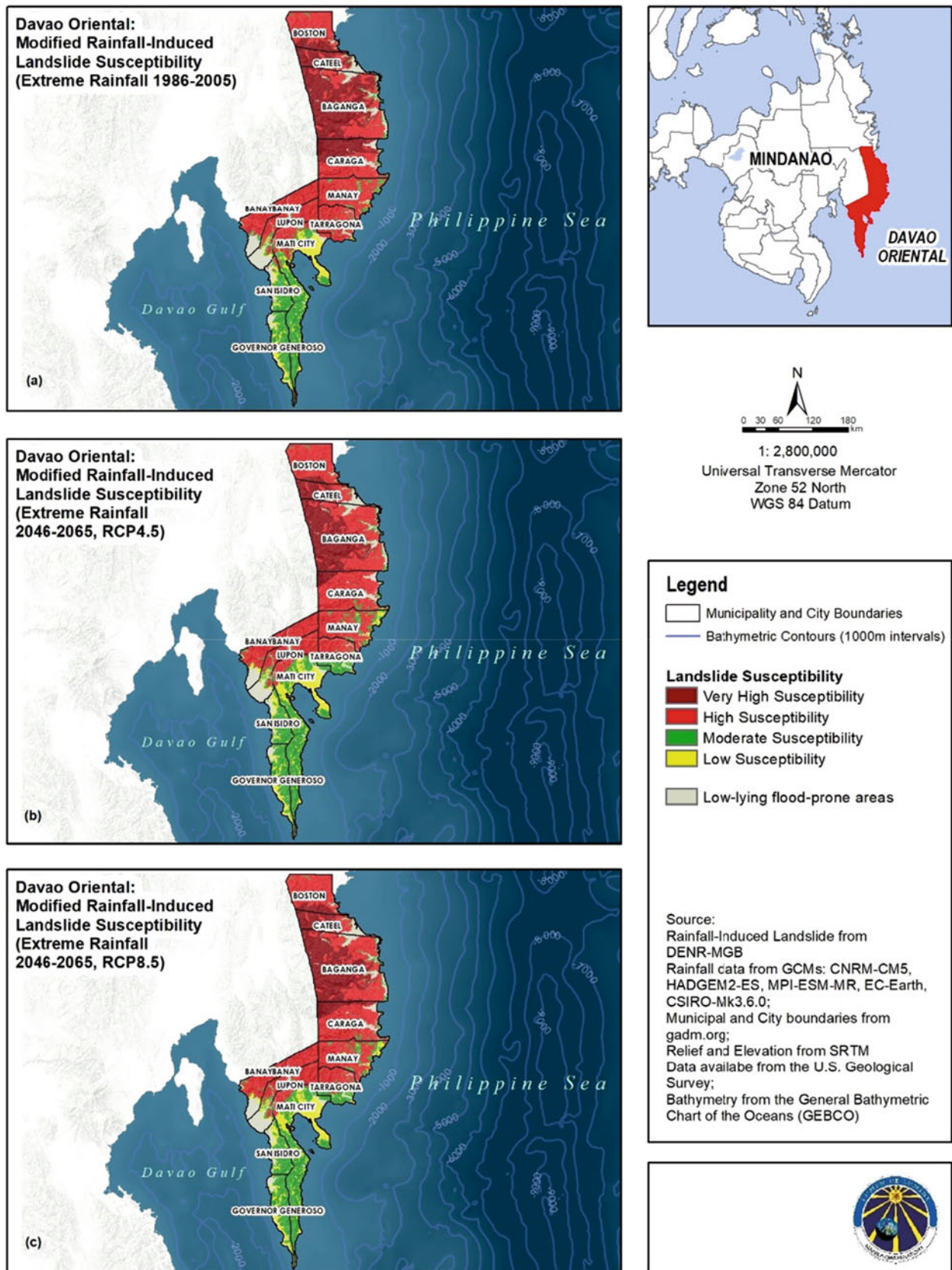


Fig. 8 Modified rainfall-induced landslide susceptibility maps of Davao Oriental (a) Historical (1986–2005), (b) Projected under RCP4.5 (2046–2065), and (c) Projected under RCP8.5 (2046–2065).

A decrease in landslide susceptibility is expected by the mid-twenty-first century (see also Table 3), mainly in Baganga, Cateel and Caraga, following a decrease in extreme rainfall in the area

Table 3 Areas falling on each susceptibility category

Susceptibility level	Affected area (sq.km)			
	Without rainfall	With rainfall		
		Historical	RCP4.5	RCP8.5
Very high	25	1167	774	911
High	3509	2297	2437	2315
Moderate	847	865	1020	1007
Low	257	311	408	406

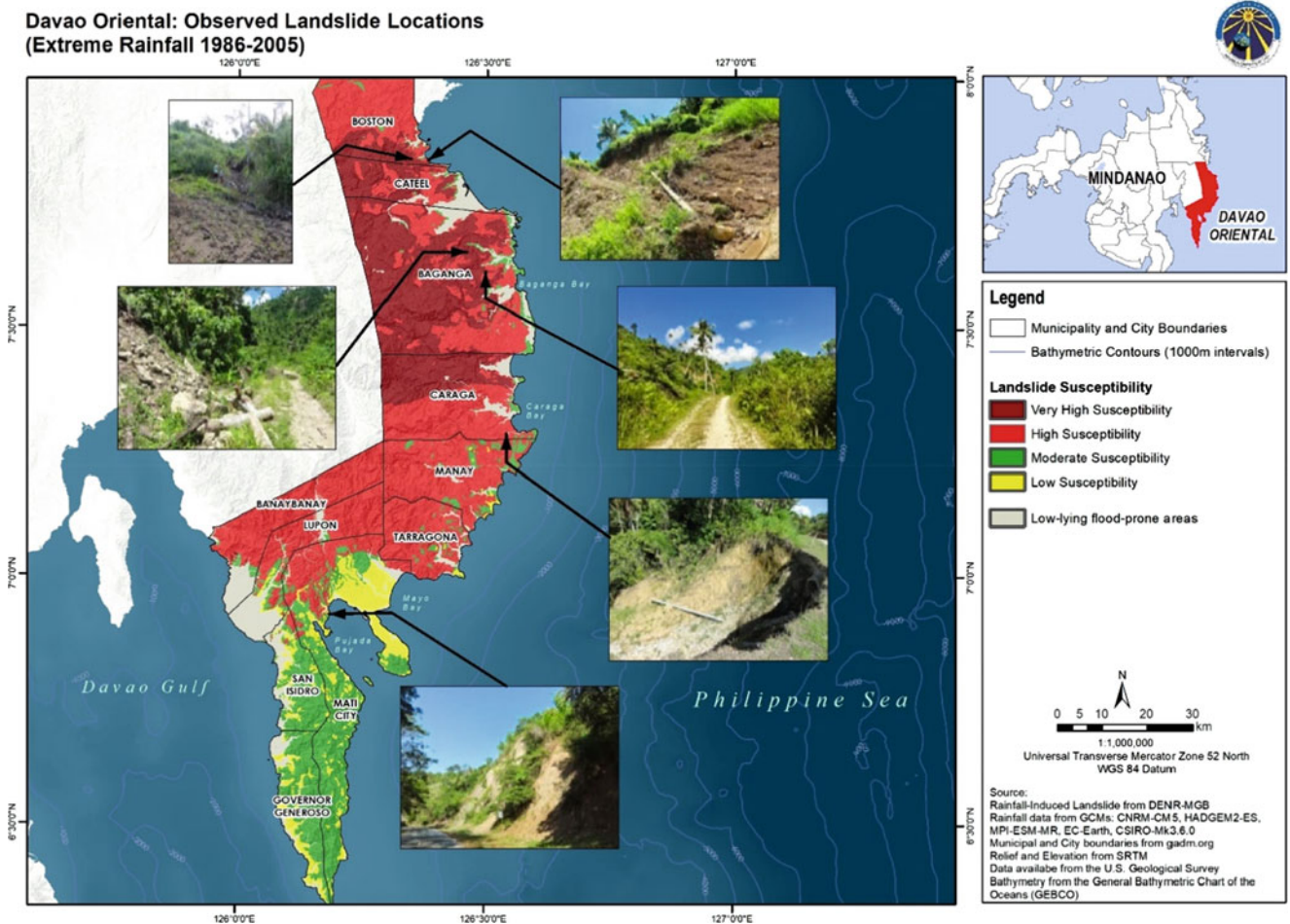


Fig. 9 Observed slope failures/movements in the study area (Landslide photos © 2017 The Oscar M. Lopez Center for Climate Change Adaptation and Disaster Risk Management Foundation, Inc., In: Narisma et al. 2017, used with permission)

Acknowledgments We would like to thank the Mines and Geosciences Bureau (MGB) of the Department of Environment and Natural Resources of the Philippines (DENR-MGB) for providing the base map for this study, and the OML Center for Climate Change Adaptation and Disaster Risk Management Foundation, Inc. for some of the figures in this paper. We also thank Manila Observatory staff Dr. Lyndon Olaguera for his insights on rainfall in Davao Oriental, Mr. Elleesse Pillas for preparing the bias-adjusted climate dataset and Mr. Raul Dayawon for GIS support. Finally, we would like to thank Ms. Heidi Stenner of the Geohazards International for reviewing and proofreading the manuscript, and the anonymous reviewer for the helpful suggestions.

References

Bagtasa G (2017) Contribution of tropical cyclones to rainfall in the Philippines. *J Climate* 30(10):3621–3633. <https://doi.org/10.1175/JCLI-D-16-0150.1>

Buena AE, Villaplaza BR, Payot BD, Gabo-Ratio JA, Ramos NT, Faustino-Eslava DV, Queaño KL, Dimalanta CB, Padrones JT, Tani K, Brown WW, Yumul GP (2019) An evolving subduction-related magmatic system in the Masara Gold District, Eastern Mindanao, Philippines. *J Asian Earth Sci* X 1. <https://doi.org/10.1016/j.jaesx.2019.100007>

- Cannon AJ, Sobie SR, Murdock TQ (2015) Bias correction of GCM precipitation by quantile mapping: how well do methods preserve changes in quantiles and extremes? *J Climate* 28(17):6938–6959. <https://doi.org/10.1175/jcli-d-14-00754.1>
- Cinco TA, de Guzman RG, Ortiz AMD, Delfino RJP, Lasco RD, Hilario FD, Juanillo EL, Barba R, Ares ED (2016) Observed trends and impacts of tropical cyclones in the Philippines. *Int J Climatol* 36(14):4638–4650. <https://doi.org/10.1002/joc.4659>
- DENR-MGB (Department of Environment and Natural Resources-Mines and Geoscience Bureau) (2022) Rainfall-induced landslide susceptibility map of Davao Oriental
- DOST_PAGASA, Manila Observatory and Ateneo de Manila (2021) Philippine climate extremes report in the Philippines to support informed decisions on climate change adaptation and risk management. Philippine Atmospheric, Geophysical and Astronomical Services Administration, Quezon City, Philippines, 145 pp
- EM-DAT, CRED/UCLouvain (2023). Global occurrences from landslide disasters, 1970–2023. <https://public.emdat.be/mapping>
- Fudeyasu H, Hirose S, Yoshioka H, Kumazawa R, Yamasaki S (2014) A global view of the landfall characteristics of tropical cyclones. *Trop Cyclone Res Rev* 3(3):178–192. <https://doi.org/10.6057/2014TCRR03.04>
- Garas KL (2013) Understanding MGB geohazards maps. A presentation during the 'Training on Disaster Risk Reduction: The Role of DOST Regional Offices, December 10–12, 2013, PHIVOLCS Auditorium, Quezon City, Philippines
- Giorg F, Anyah RO (2012) The road towards RegCM4. *Climate Res* 52:3–6. <https://doi.org/10.3354/cr01089>
- Hersbach H, Bell B, Berrisford P, Biavati G, Horányi A, Muñoz Sabater J, Nicolas J, Peubey C, Radu R, Rozum I, Schepers D, Simmons A, Soci C, Dee D, Thépaut J-N (2018) ERA5 hourly data on single levels from 1979 to present. Copernicus Climate Change Service (C3S) Climate Data Store (CDS). Accessed 17 Feb 2020. <https://doi.org/10.24381/cds.adbb2d47>
- IPCC (2014) Synthesis report. Contribution of Working Groups I, II and III to the Fifth Assessment Report of the Intergovernmental Panel on Climate Change [Core Writing Team, R.K. Pachauri and L.A. Meyer (eds.)]. IPCC, Geneva, 151 pp
- Kamworapan S, Surussavadee C (2019) Evaluation of CMIP5 global climate models for simulating climatological temperature and precipitation for Southeast Asia. *Adv Meteorol* 1067365. <https://doi.org/10.1155/2019/1067365>
- Karl TR, Nicholls N, Ghazi A (1999) CLIVAR/GCOS/WMO workshop on indices and indicators for climate extremes: workshop summary. *Climatic Change* 42:3–7
- Kirschbaum D, Kapnick SB, Stanley T, Pascale S (2020) Changes in extreme precipitation and landslides over High Mountain Asia. *Geophys Res Lett* 47:e2019GL085347. <https://doi.org/10.1029/2019GL085347>
- Matsumoto J, Olaguera LMP, Nguyen-Le D, Kubota H, Villafuerte MQ (2020) Climatological seasonal changes of wind and rainfall in the Philippines. *Int J Climatol* 40(11):4843–4857. <https://doi.org/10.1002/joc.6492>
- Narisma GT, Cruz FA, Maquiling JT, Vicente MC (2017) RS-GIS-based integrated analysis on risks to climate change and disasters. OML Project NP 2013–01
- NOAA's Atlantic Oceanographic and Meteorological Laboratory (2021) Hurricane records & ranks. <https://www.aoml.noaa.gov/hrd-faq/#most-hit-countries>. Accessed 1 April 2023
- Olaguera LMP, Cruz FAT, Dado JMB, Villarín JRT (2022) Complexities of extreme rainfall in the Philippines. In: Unnikrishnan A, Tangang F, Durrheim RJ (eds) Extreme natural events. Springer, Singapore. https://doi.org/10.1007/978-981-19-2511-5_5
- PAGASA (Philippine Atmospheric, Geophysical and Astronomical Services Administration) (2023) Climate of the Philippines. <https://www.pagasa.dost.gov.ph/information/climate-philippines>. Accessed 1 April 2023
- Peterson T C, Folland C, Gruza G, Hogg W, Mokssit A, Plummer N (2001) Report on the Activities of the Working Group on Climate Change Detection and Related Rapporteurs 1998–2001. WMO, Rep. WCDMP-47, WMO-TD 1071, Geneva, 143 p
- PHIVOLCS (Philippine Institute of Volcanology and Seismology) (2018) Earthquake Information. <http://www2.phivolcs.dost.gov.ph/index.php/2-uncategorised/1411-019-km-n-27-e-of-digos-city-davao-del-sur-information-no-2>. Accessed 1 April 2023.
- Reichenbach P, Rossi M, Malamud BD, Mihir M, Guzzetti F (2018) A review of statistically-based landslide susceptibility models. *Earth Sci Rev* 180:60–69. <https://doi.org/10.1016/j.earscirev.2018.03.001>
- Soeters R, Van Westen CJ (1996) Slope instability recognition, analysis and zonation. In Turner AK, Schuster RL (eds) Landslides. Investigation and mitigation, transportation research board, special report 247, National Academy Press, Washington DC, pp 129–177
- Tangang F, Chung JX, Juneng L, Supari S, Salimun E, Ngai ST, Jamaluddin AF, Mohd MSF, Cruz F, Narisma G, Santisirisomboon J, Ngo-Duc T, van Tan P, Singhruck P, Gunawan D, Aldrian E, Sopaheluwakan A, Grigory N, Remedio ARC, Sein DV, Hein-Griggs D, McGregor JL, Yang H, Sasaki H, Kumar P (2020) Projected future changes in rainfall in Southeast Asia based on CORDEX–SEA multi-model simulations. *Climate Dyn* 55:1247–1267. <https://doi.org/10.1007/s00382-020-05322-2>
- WBG and ADB (World Bank Group and the Asian Development Bank) (2021) Climate Risk Country Profile: Philippines, 32 p. <https://www.adb.org/sites/default/files/publication/722241/climate-risk-country-profile-philippines.pdf>

Open Access This chapter is licensed under the terms of the Creative Commons Attribution 4.0 International License (<http://creativecommons.org/licenses/by/4.0/>), which permits use, sharing, adaptation, distribution and reproduction in any medium or format, as long as you give appropriate credit to the original author(s) and the source, provide a link to the Creative Commons license and indicate if changes were made.

The images or other third party material in this chapter are included in the chapter's Creative Commons license, unless indicated otherwise in a credit line to the material. If material is not included in the chapter's Creative Commons license and your intended use is not permitted by statutory regulation or exceeds the permitted use, you will need to obtain permission directly from the copyright holder.





Fractal-Based Evaluation of the Spatial Relationship Between Conditioning Factors and the Distribution of Landslides (a Case Study in Tinh Tuc, Cao Bang Province, Vietnam)

Binh Van Duong, Igor K. Fomenko, and Kien Trung Nguyen

Abstract

This paper presents the assessment results of the spatial relationship between past landslides and four landslide factors in Tinh Tuc town, Cao Bang province, Vietnam, including distance to roads, distance to faults, distance to drainage, and distance to geological boundaries. The fractal dimension values were determined using fractal analyses on three sets of raw data, including the number of landslides, landslide density, and landslide relative density. Using a combination of the frequency ratio (FR) method and the fractal method, landslide susceptibility maps were produced to determine which raw data set more properly analyzes the role of factors in the development of the landslide process. Assessment results using the receiver operating characteristic (ROC) method indicate that the fractal analysis of the raw data sets successfully determines the spatial relationship between conditioning factors and landslides in the study area. In addition, relationship analyses using datasets based on landslide density provide more optimal outcomes. The authors also suggest integrating the fractal method with other quantitative assessment methods to improve the accuracy of landslide prediction in Vietnam and worldwide.

Keywords

Fractal method · Landslide · Conditioning factor · Spatial relationship · Frequency ratio method · Tinh Tuc · Vietnam

1 Introduction

The challenge of ensuring the sustainable development of residential communities in the context of rapid urbanization is crucial for developing countries, including Vietnam. With 75% of the territory comprised of mountainous terrain, the frequency of sediment-related natural hazards has increased in recent years (Lan Huong et al. 2022). Consequently, it is necessary to identify hazard zones by producing integrated maps based on the current situation and available materials. These maps include data on the spatial distribution of hazard zones and their temporal evolution. These data are essential for evaluating potential risks, long-term territorial planning, and land use planning.

Compared to other sediment-related disasters, landslides are prevalent in Vietnam, particularly in the northern mountainous regions, and negatively impact the sustainable development of local communities (Thanh Thi Pham et al. 2020). Therefore, numerous studies on landslides have been conducted in these regions (Bien et al. 2022; Hung et al. 2017). According to previous studies, most landslides were triggered by precipitation, and the increase in landslide frequency has been associated with human activities (e.g., road construction) (Do et al. 2022; Tien Bui et al. 2017). When developing models for predicting landslides, determining the relationship between conditioning factors and the distribution of landslides is crucial (Liao et al. 2022). The evaluation results may validate the correctness of the selection of analysis factors and play a significant role in the performance of the prediction models.

This paper presents the results of the fractal-based evaluation of the spatial relationship between conditioning factors

B. Van Duong (✉)

Department of Engineering Geology, Ordzhonikidze Russian State Geological Prospecting University, Moscow, Russia

Department of Engineering Geology, Hanoi University of Mining and Geology, Hanoi, Vietnam

e-mail: duongvanbinh@humg.edu.vn

I. K. Fomenko

Department of Engineering Geology, Ordzhonikidze Russian State Geological Prospecting University, Moscow, Russia

K. T. Nguyen

Department of Hydrogeology and Engineering Geology, Institute of Geological Sciences, Vietnam Academy of Science and Technology, Hanoi, Vietnam

and the distribution of landslides in Tinh Tuc town, Cao Bang province, Vietnam. The spatial relationship was evaluated using three raw data sets, including the number of landslides, relative landslide density, and landslide density. By producing landslide susceptibility zonation maps, this study determined that all three data sets are suitable for assessing the relationship between landslide occurrences and conditioning factors. In addition, this study determined that the prediction model based on relative landslide density and landslide density provided a higher performance in analyzing the relationship between landslides and conditioning factors.

2 Study Area

Cao Bang province (6690 km²; 22° 21' N to 23° 07' N and 105° 16' E to 106° 50' E), which is located in the northeastern mountainous region of Vietnam (Fig. 1), has experienced numerous natural disasters in recent years, especially landslides, due to the influence of various natural, environmental, and social conditions. Nguyen Binh is a mountainous district in the southern portion of Cao Bang province that is

determined to be one of the areas with a very high likelihood of landslides (VIGMR 2017).

Tinh Tuc town is 18 km from the center of Nguyen Binh district and is situated on National Highway 34, which connects Cao Bang province and Ha Giang province (Fig. 1). The study area covers a total of 66.76 km², including Tinh Tuc town and its surroundings. The elevation of the study area ranges from 434 m in the valley to 1876 m in the mountainous terrain, where Phia Oac peak reaches 1932 m (Kien et al. 2021). The studied territory is characterized by geological formations and complexes composed of igneous and sedimentary rocks dated from the Paleozoic to the Quaternary period. The weathering process has contributed to the growth of two main types of weathering crust in the study area: ferosialite (86%) and sialferite (14%). In 2020, a failure volume of 2500 m³ was recorded at Highway 34, Km 192 + 500, on the 3–4 m-thick weathering crust formed from the rocks of the Song Hien formation (Fig. 2a). Another landslide occurred in 2016 at Km 200 + 300 on Highway 34. The weathering crust, with a thickness between 3 and 4 m, formed from the Cao Bang Complex rocks, has produced a sliding mass with a volume of 50,000 m³ (Fig. 2b).

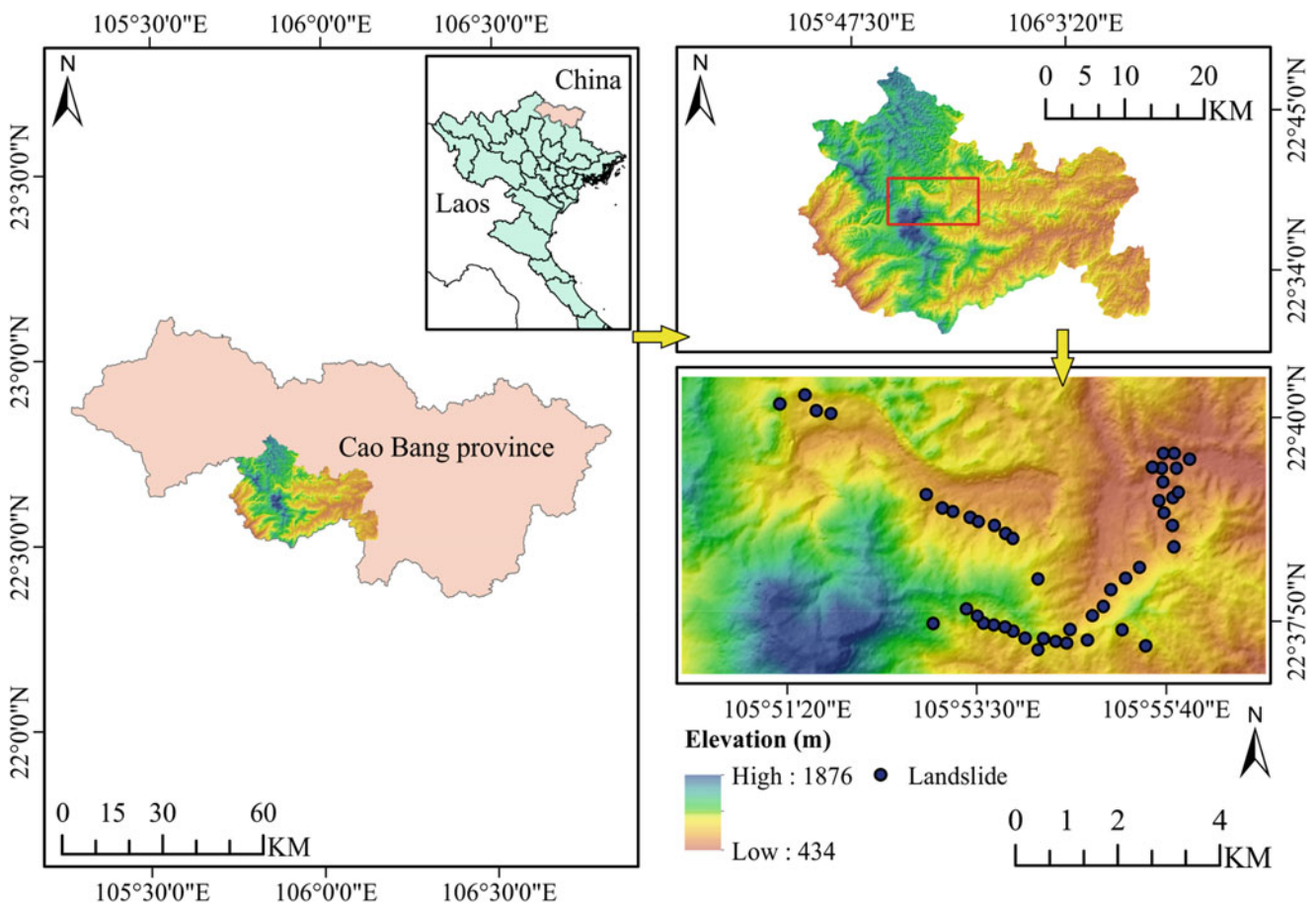


Fig. 1 Location of study area



Fig. 2 Landslides at the national highway 34 km 192 + 500 (a), and at Km 200 + 300 (b). Photo by T. K. Nguyen

Heavy rainfall in a short period of time or prolonged rainfall events have been identified as the trigger of landslides in the study area.

3 Evaluation of the Spatial Relationship Between Conditioning Factors and the Distribution of Landslides

3.1 Methods

Mandelbrot (1967), who initially introduced the fractal theory in his study of the British coastline, determined that the degree of complication of a geographic curve may be characterized by a “dimension” D . Since then, the fractal method has been improved and extensively utilized in numerous fields of research, including medicine (Tanabe et al. 2020), muscle activity patterns during locomotion (Santuz and Akay 2020), materials science (Paun et al. 2022), the characterization of absorption capacity, porosity, and surface area (Elejalde-Cadena and Moreno 2021), natural hazards (Cello and Malamud 2006), etc.

In the landslide susceptibility study, the fractal method is employed to determine the weights of the conditioning factors, therefore indicating the role of each conditioning factor in the occurrence of landslides in the studied territory. The method may be characterized as a power law described by Eq. (1):

$$p(r) \propto C \cdot r^{-D} \quad (1)$$

where r is the feature measured scale, p is the measured value under the corresponding scale r , C is a constant value, and D is the fractal dimension (Hu et al. 2020). Fractal analyses provide a raw data set (P) based on several variables, such as the number of landslides, relative landslide density, and

landslide density. The cumulative sum (S) values are then determined using the formula (2):

$$\{P\} = \{P_1, P_2, \dots, P_n\}$$

$$\{S_1\} = \{P_1, P_1 + P_2, \dots, P_1 + P_2 + \dots + P_n\}$$

$$\{S_2\} = \{S_{11}, S_{11} + S_{12}, \dots, S_{11} + \dots + S_{1n}\} \dots \dots \dots (2)$$

The fractal analysis then constructs the (S , r) graphs and performs a linear fitting to determine the D value for each condition factor. By using the formula (3), the weight of each landslide conditioning factor (W_i) is calculated:

$$W_i = D_i / \sum_{i=1}^n D_i \quad (3)$$

In this study, the Frequency ratio (FR) was integrated with the Fractal method to produce partition landslide susceptibility zonation (LSZ) maps to examine the efficacy of spatial relationship evaluation using different raw data sets. The FR method evaluates the relationship between the distribution of landslides and the subclasses of conditioning factors (Wang et al. 2020) based on the formula (4):

$$FR_i = \%LS_i / \%A_i \quad (4)$$

where FR_i is the FR value of subclass i , $\%LS_i$ is the percentage of landslides in subclass i , and $\%A_i$ is the area percentage of subclass i . The calculated FR value is then normalized to the weight of the factor class (NFR) according to the formula (5):

$$NFR_i = FR_i / \sum_{i=1}^n FR_i \quad (5)$$

Finally, the landslide susceptibility index (LSI) is calculated according to the formula (6):

$$LSI = \sum_{i=1}^n NFR_i \times W_i \tag{6}$$

3.2 Spatial Relationship Between Conditioning Factors and Landslide Distribution

For analyzing the spatial relationship, this study selected four landslide conditioning factors, including distance to roads, distance to faults, distance to drainage, and distance to geological boundaries. Downloaded OpenStreetMap data from Geofabrik was used to produce a map of the distance to roads in the study area (Fig. 3a). Along with a 12.5-m-resolution digital elevation model (DEM), data on geological

units and fault systems were provided by the Institute of Geological Sciences, Vietnam Academy of Science and Technology. Geologically, the study area has six geological units, including the Bac Son formation, Dong Dang formation, Song Hien formation, Quaternary deposits, Cao Bang complex, and Pia Oac complex. Afterward, these data were used to prepare additional factor maps, including distance to faults (Fig. 3b), distance to drainage (Fig. 3c), and distance to geological boundaries (Fig. 3d). Each factor was divided into subclasses for quantifying the relationship between conditioning factors and landslide distribution. Distance to roads, distance to faults, and distance to geological boundaries were subdivided into 11 subclasses, while the distance to drainage was subdivided into seven classes, as shown in Table 1.

Analysis of the spatial relationship between conditioning factors and past landslides revealed that most landslides occurred within 100 m of roads and 200 m of drainage systems. This result demonstrates that the construction of

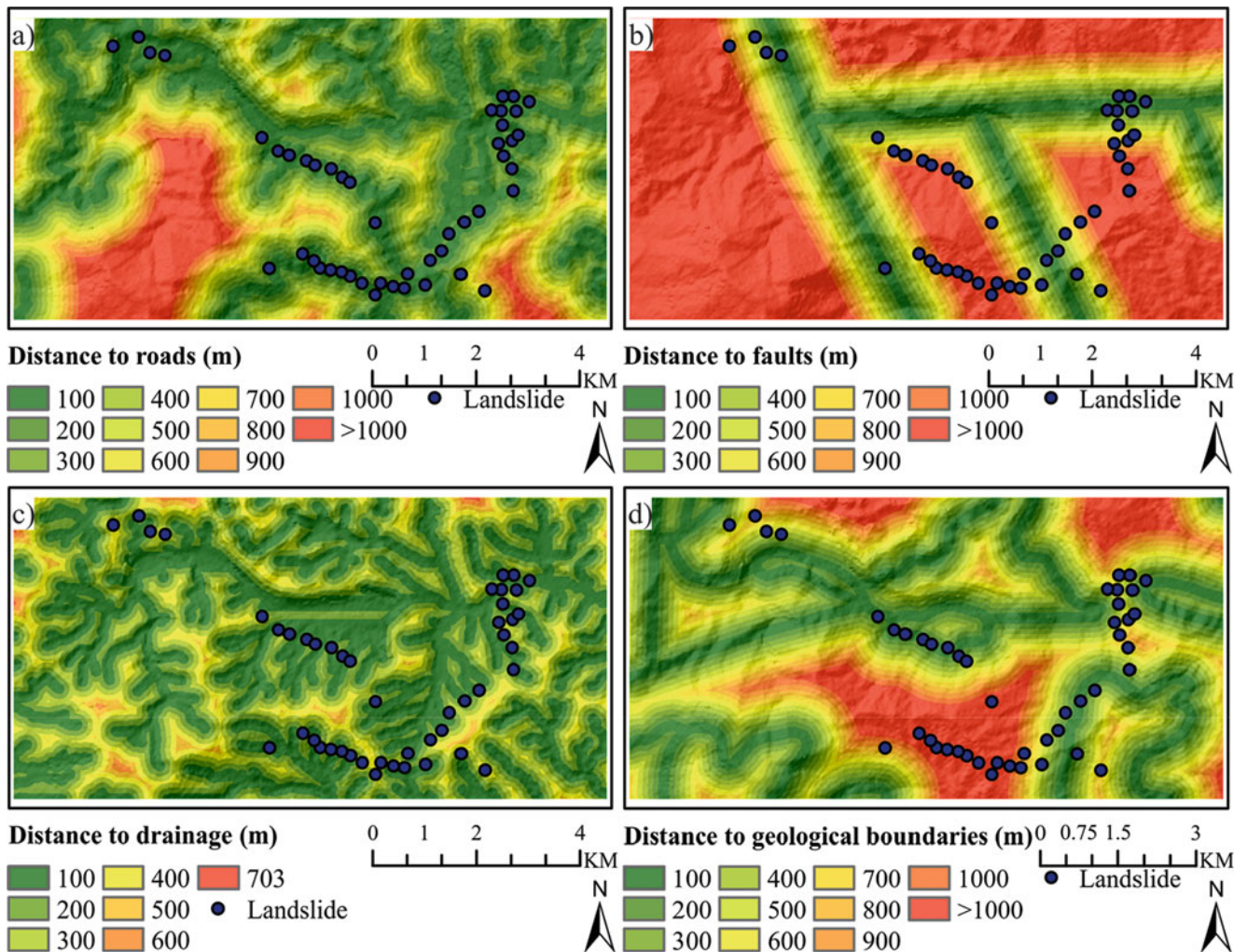


Fig. 3 Maps of distance to roads (a), distance to faults (b), distance to drainage (c), and distance to geological boundaries (d)

Table 1 Spatial distribution analysis of landslides using FR method

Factor	Class	% class area	% landslide	FR	NFR
Distance to roads (m)	0–100	25.802	85.106	3.298	0.724
	100–200	16.806	10.638	0.633	0.139
	200–300	12.734	0	0	0
	300–400	9.935	0	0	0
	400–500	7.93	2.128	0.268	0.059
	500–600	5.966	2.128	0.357	0.078
	600–700	4.554	0	0	0
	700–800	3.193	0	0	0
	800–900	2.42	0	0	0
	900–1000	2.107	0	0	0
	>1000	8.553	0	0	0
Distance to faults (m)	0–100	6.424	8.511	1.325	0.09
	100–200	5.958	12.766	2.143	0.145
	200–300	5.72	2.128	0.372	0.025
	300–400	5.528	6.383	1.155	0.078
	400–500	5.293	6.383	1.206	0.082
	500–600	5.115	4.255	0.832	0.056
	600–700	4.991	2.128	0.426	0.029
	700–800	4.847	17.021	3.512	0.238
	800–900	4.615	10.638	2.305	0.156
	900–1000	4.586	4.255	0.928	0.063
	>1000	46.922	25.532	0.544	0.037
Distance to drainage (m)	0–100	40.8	44.681	1.095	0.309
	100–200	30.05	40.426	1.345	0.38
	200–300	18.829	10.638	0.565	0.16
	300–400	7.954	4.255	0.535	0.151
	400–500	1.814	0	0	0
	500–600	0.495	0	0	0
	600–703	0.058	0	0	0
Distance to geological boundaries (m)	0–100	15.807	17.021	1.077	0.104
	100–200	13.883	4.255	0.306	0.03
	200–300	12.169	10.638	0.874	0.084
	300–400	11.244	12.766	1.135	0.109
	400–500	10.079	12.766	1.267	0.122
	500–600	8.266	6.383	0.772	0.074
	600–700	6.235	4.255	0.682	0.066
	700–800	4.384	4.255	0.971	0.094
	800–900	3.699	4.255	1.15	0.111
	900–1000	3.284	0	0	0
	>1000	10.95	23.404	2.137	0.206

the road system has altered the natural slope, resulting in an imbalance that increases the probability of landslides. Since precipitation is the main trigger of landslides in the study area, landslides frequently occur along drainage systems, where soil and rock are highly saturated because of rainwater infiltration. However, the distribution of landslides within the classes of the remaining two factors is relatively equal.

Figures 4, 5, and 6 represent the outcomes of the fractal-based analysis. The $\ln(S)$ - $\ln(r)$ plots were linearly fitted with a correlation coefficient of $R^2 > 0.995$, as indicated in the figures. Similar to the results of the previous study (Zuo

and Carranza 2017), these graphs demonstrate a non-linear spatial relationship between the number of landslides or landslide density and distance to conditioning factors. By utilizing a data set based on the number of landslides (case study 1), fractal analyses have shown that the distance to drainage is the most influencing factor in the formation of landslides ($D = 2.0088$). However, using datasets based on relative landslide density (case study 2) and landslide density (case study 3), the analysis results indicated that the distance to geological boundaries has the most significant role in the landslide process. The remaining factors (distance to faults,

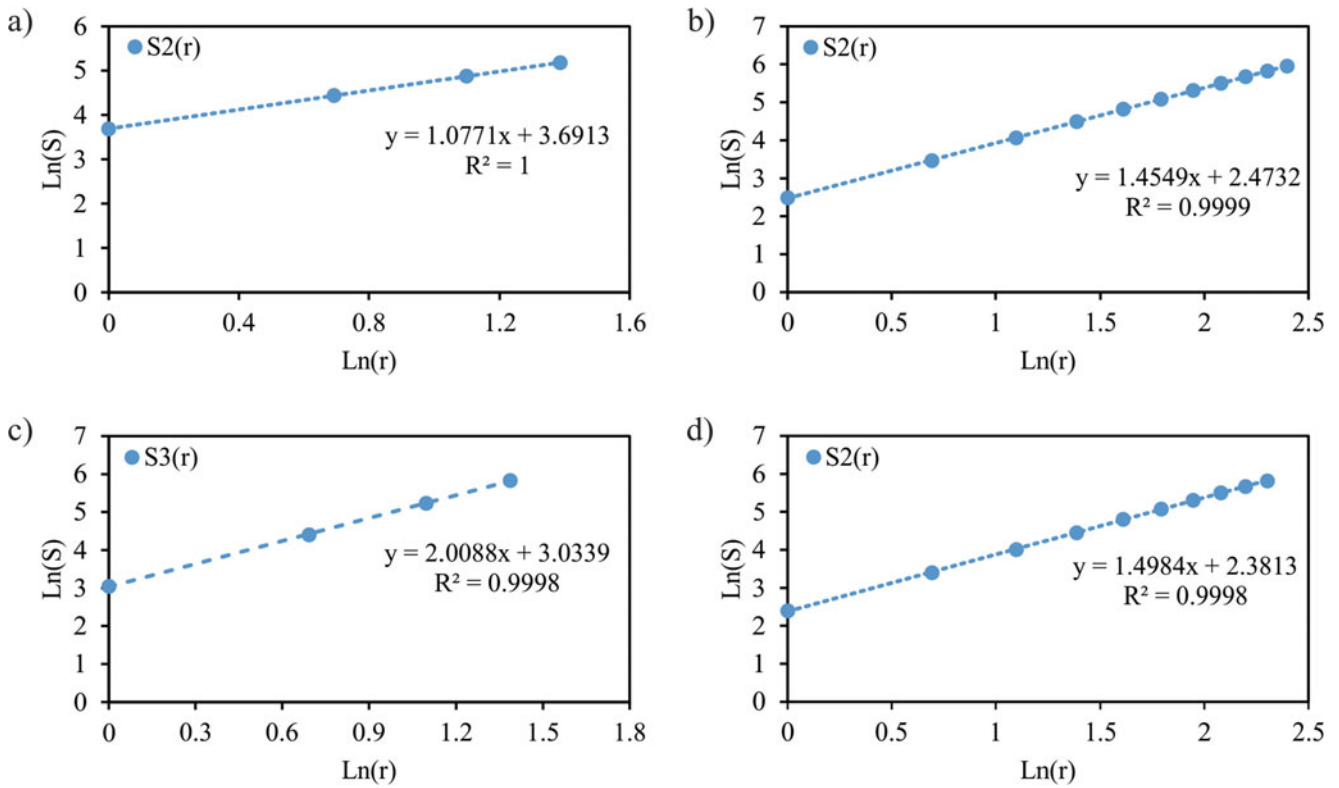


Fig. 4 Fractal analysis using the number of landslides. Graphs of factors: distance to roads (a), distances to faults (b), distance to drainage (c), and distance to geological boundaries (d)

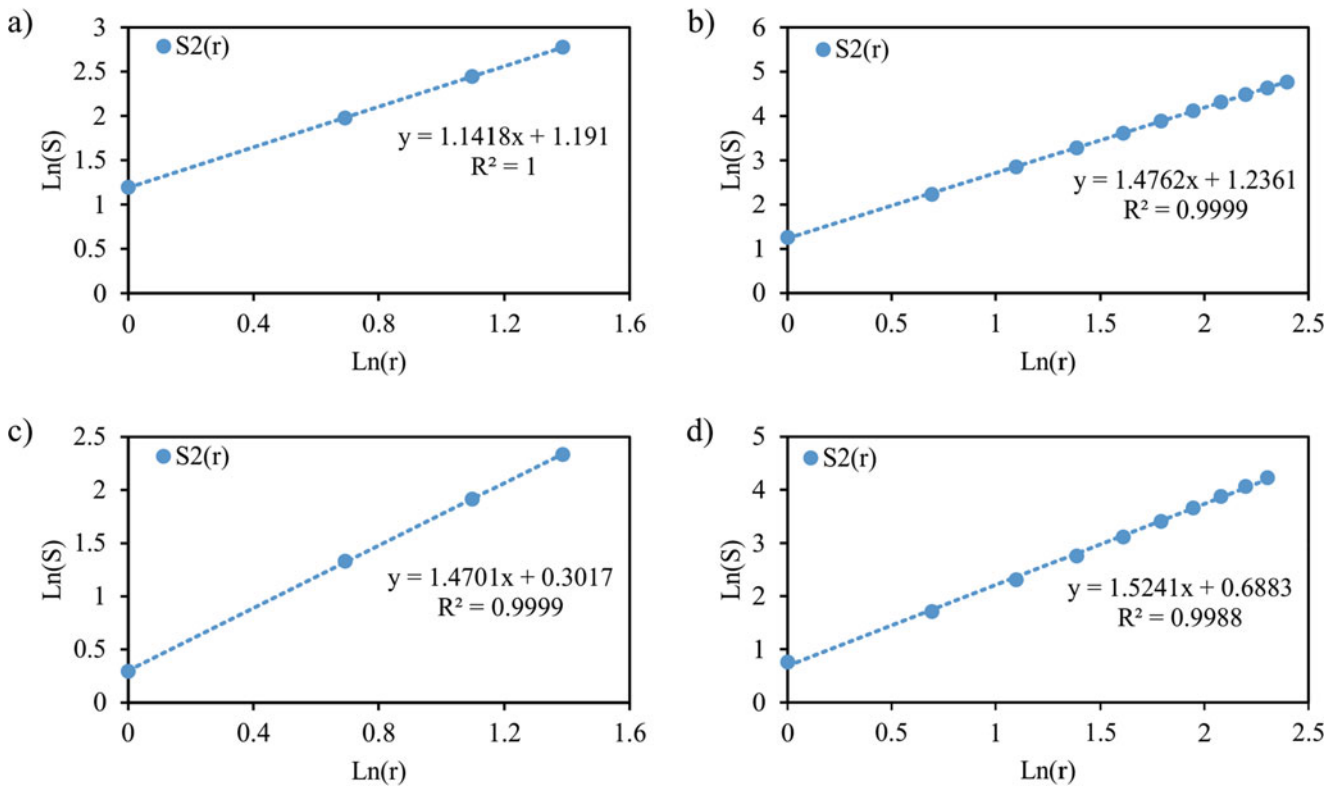


Fig. 5 Fractal analysis using relative landslide density. Graphs of factors: distance to roads (a), distances to faults (b), distance to drainage (c), and distance to geological boundaries (d)

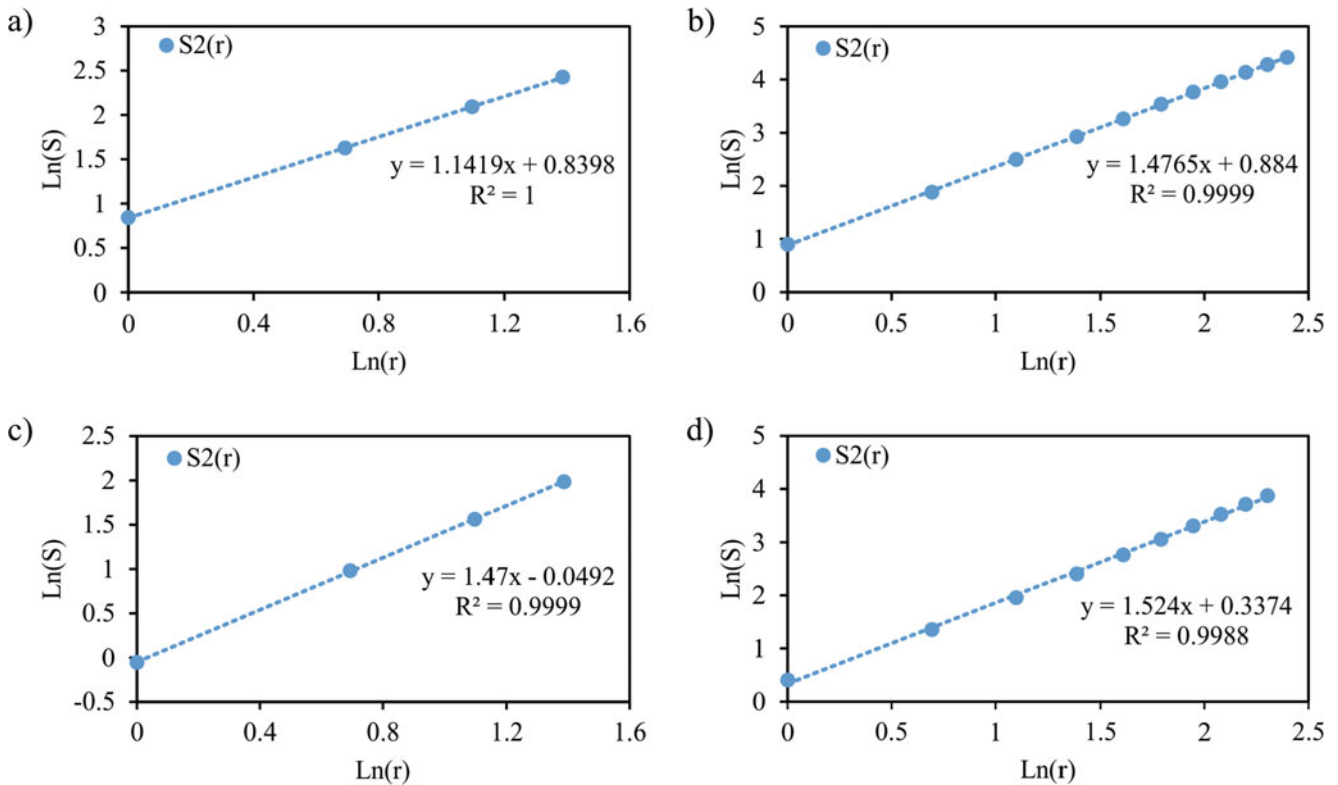


Fig. 6 Fractal analysis using landslide density. Graphs of factors: distance to roads (a), distances to faults (b), distance to drainage (c), and distance to geological boundaries (d)

Table 2 Weights of the factors calculated from fractal analysis

Factor	Case study 1		Case study 2		Case study 3	
	D_i	W_i	D_i	W_i	D_i	W_i
Distance to roads	1.0771	0.178	1.1418	0.203	1.1419	0.203
Distance to faults	1.4549	0.241	1.4762	0.263	1.4765	0.263
Distance to drainage	2.0088	0.333	1.4701	0.262	1.4700	0.262
Distance to geological boundaries	1.4984	0.248	1.5241	0.272	1.5240	0.272

distance to drainage, and distance to roads) have a less significant effect on the landslide process. Based on the formula (3), the D values are then used to calculate the weighted values of the factors (W). The results of the calculations are presented in Table 2.

Using a hybrid fractal-frequency ratio (FFR) model, LSZ maps were produced to compare various data sets for spatial relationship analysis. This model utilizes the results of calculating factor class weights using the frequency ratio method and factor weights using the fractal method. The FFR1 model employs the analysis results of case study 1, while the FFR2 model reflects case studies 2 and 3. A receiver operating characteristic (ROC) analysis was conducted to assess the performance of these models.

3.3 Model Validation

In this study, the well-known ROC method was employed to assess the accuracy of the prediction maps produced by the two models. A ROC curve is a curve in the unit square formed by plotting sensitivity (or True Positive Rate—TPR) versus specificity (1-FPR, FPR—False Positive Rate) at different thresholds (Yu et al. 2021). It is widely accepted that a higher and more leftward-positioned ROC curve in the ROC space indicates better prediction performance (Metz 1978). Based on the landslide inventory map, which included 47 landslides, ROC analyses were conducted to determine the AUC-ROC (area under the ROC curve) value.

3.4 Results of Landslide Susceptibility Using Fractal-Frequency Method (FFR)

The LSI values for the study area were calculated using Eq. (6) to produce landslide susceptibility index maps. The LSI values range from 0.006 to 0.363 (FFR1) and 0.006 to 0.365 (FFR2). Based on the landslide susceptibility index (LSI) maps, we prepared the landslide susceptibility zonation (LSZ) maps in ArcGIS using the Jenks natural breaks classification method. The study area was divided into five landslide susceptibility zones: very low, low, moderate, high, and very high (Figs. 7 and 8). The LSZ maps produced by the two models have similarities when determining the spatial distribution of susceptibility zones. Most high and very high susceptibility zones were identified at low to moderate elevations and are dominated by road and drainage networks. It has also been shown that the fault system and geological boundaries in the study area affect the spatial distribution of these zones.

The proportion of each landslide susceptibility zone predicted by the two models is shown in Fig. 9. As seen in Fig. 9, all susceptibility zones to landslides were assessed similarly by all two models. The very high susceptibility zone predicted by the two models is 24.34 (FFR1) and 25.52% (FFR2). In addition, the very low landslide susceptibility zones assessed by these models are 17.91% and 17.66%, respectively.

By using 47 past landslides in the study area, ROC curves depicting the performance of two models were constructed (Fig. 10). In Fig. 10, the AUC values and ROC curves indicated very good model performance in predicting the spatial distribution of landslides (AUC > 80%) (Swets 1988). All models revealed a relationship between landslide conditioning factors and the distribution of historical landslides in the study area, as shown by an analysis of the

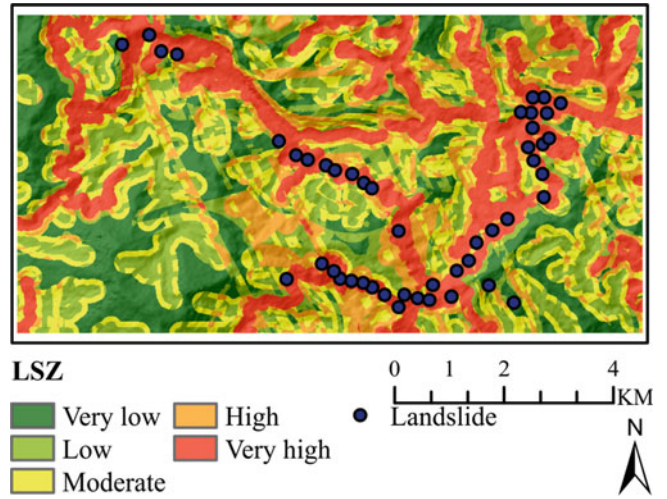


Fig. 8 LSZ map using FFR2 model

success rate curves. Generally, the area under the curve (AUC) values of the success rate curves for the FFR1 and FFR2 models are almost identical. Simultaneously, the analysis outcomes revealed that the FFR2 model performed slightly better than the FFR1 model, indicating strong model performance and prediction accuracy.

According to the study results, all three raw data sets may be utilized to analyze the relationship between landslides and conditioning factors. However, the model using landslide density-based data provides improved prediction performance. This result may be explained by the fact that the landslide density provides a stronger spatial relationship between the distribution of landslides and the area of the factor subclasses. This difference may be defined more clearly if the study is conducted in a region with a significant number of landslides, along with conditioning factors selected depending on data availability, features of landslides, and previous studies in the study area.

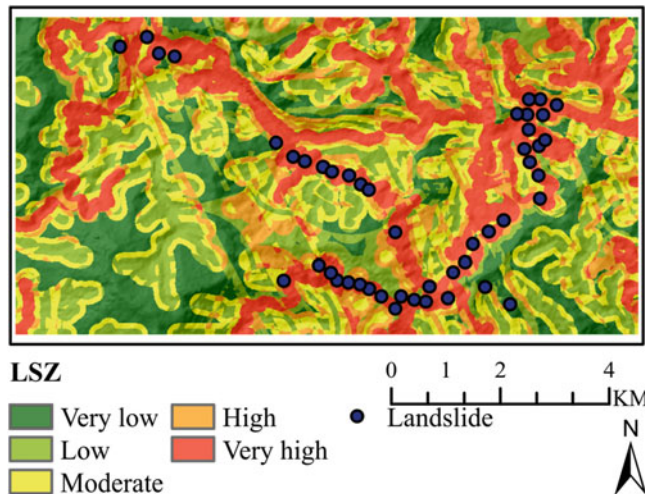


Fig. 7 LSZ map using FFR1 model

4 Conclusions

In landslide hazard and susceptibility studies, the efficacy of assessing the relationship between past landslides and selected factors is crucial to the accuracy of the produced maps. Therefore, this study was conducted to determine the effect of several factors on the distribution of landslides in Tinh Tuc town, Cao Bang province, Vietnam. Three raw data sets were generated using the number of landslides and landslide density. By utilizing the frequency ratio method and the fractal method, the role of subclasses and factors, as expressed by NFR and W values, was evaluated. Afterward, two landslide susceptibility maps were produced based on the selected data sets. The similarity of the susceptibility zone predicted by the two models and the outcomes of the ROC

Fig. 9 Distribution of susceptibility zones for each model

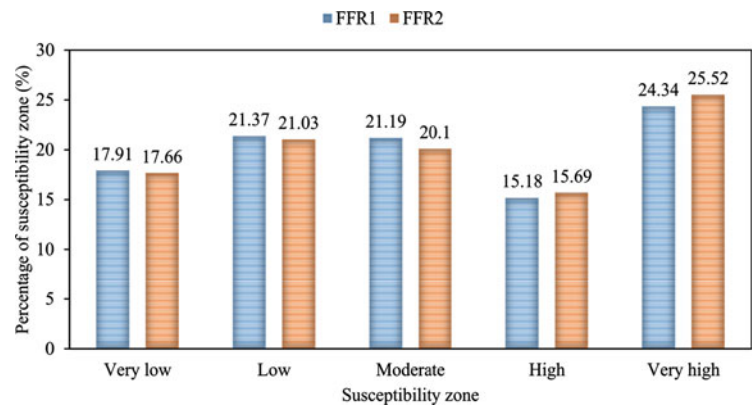
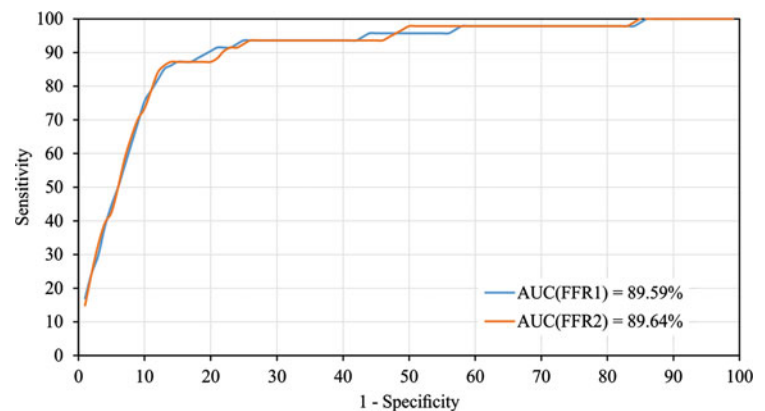


Fig. 10 ROC curves with AUC values of two models



analysis revealed that the data sets are suitable for producing highly accurate landslide susceptibility maps. It is suggested to apply the fractal method in landslide susceptibility studies because it is possible to quantify the influence of conditioning factors, thereby improving the accuracy of landslide prediction.

Acknowledgments We would like to express our gratitude to the Institute of Geological Sciences, Vietnam Academy of Science and Technology, and the national science and technology project under grant number ĐTDL.CN-81/21 for supplying analysis data.

References

- Bien TX, Truyen PT, Phong TV, Nguyen DD, Amiri M, Costache R, Duc DM, Le HV, Nguyen HBT, Prakash I, Pham BT (2022) Landslide susceptibility mapping at sin Ho, Lai Chau province, Vietnam using ensemble models based on fuzzy unordered rules induction algorithm. *Geocarto Int* 1–22. <https://doi.org/10.1080/10106049.2022.2136253>
- Cello G, Malamud BD (2006) Fractal analysis for natural hazards. Geological Society, London. ISBN: 9781862392014. 261 p. <https://doi.org/10.1144/GSL.SP.2006.261>
- Do NH, Goto S, Abe S, Nguyen KT, Miyagi T, Hayashi K, Watanabe O (2022) Torrent rainfall-induced large-scale karst limestone slope collapse at Khanh waterfall, Hoa Binh Province, Vietnam. *Geoenviron Disasters* 9(1). <https://doi.org/10.1186/s40677-022-00206-5>
- Elejalde-Cadena NR, Moreno A (2021) Fractal analysis of the distribution and morphology of pores in dinosaur eggshells collected in Mexico: implications to understand the biomineralization of calcium carbonate. *ACS Omega* 6(11):7887–7895. <https://doi.org/10.1021/acsomega.1c00478>
- Hu Q, Zhou Y, Wang SX, Wang FT, Wang HJ (2020) Fractal-based spatial distribution analysis of geological hazards and measurement of spatial association with hazard-related predisposing factors. *Int Arch Photogramm Remote Sens Spatial Inf Sci XLII-3/W10125–131*. <https://doi.org/10.5194/isprs-archives-XLII-3-W10125-2020>
- Hung LQ, Van NTH, Son PV, Ninh NH, Tam N, Huyen NT (2017) Landslide inventory mapping in the fourteen Northern Provinces of Vietnam: achievements and difficulties. In: Sassa K, Mikoš M, Yin Y (eds) *Advancing culture of living with landslides*. Springer International Publishing, Cham. ISBN: 978-3-319-59,469-9, pp 501–510. https://doi.org/10.1007/978-3-319-59,469-9_44
- Kien NT, Tran TV, Lien VTH, Linh PLH, Thanh NQ (2021) Landslide susceptibility mapping based on the combination of bivariate statistics and modified analytic hierarchy process methods: a case study of Tinh Tuc Town, Nguyen Binh District, Cao Bang Province, Vietnam. *J Disaster Res* 16(4):521–528. <https://doi.org/10.20965/jdr.2021.p0521>
- Lan Huong TT, Van Anh DT, Dat TT, Truong DD, Tam DD (2022) Disaster risk management system in Vietnam: progress and challenges. *Heliyon* 8(10). <https://doi.org/10.1016/j.heliyon.2022.e10701>
- Liao M, Wen H, Yang L (2022) Identifying the essential conditioning factors of landslide susceptibility models under different grid resolutions using hybrid machine learning: a case of Wushan and Wuxi counties, China. *CATENA* 217. <https://doi.org/10.1016/j.catena.2022.106428>

- Mandelbrot B (1967) How long is the coast of Britain? Statistical self-similarity and fractional dimension. *Science* 156(3775):636–638
- Metz CE (1978) Basic principles of ROC analysis. *Semin Nuclear Med* 8(4):283–298. [https://doi.org/10.1016/S0001-2998\(78\)80014-2](https://doi.org/10.1016/S0001-2998(78)80014-2)
- Paun M-A, Paun V-A, Paun V-P (2022) Fractal analysis and time series application in ZY-4 SEM micro fractographies evaluation. *Fractal Fractional* 6(8). <https://doi.org/10.3390/fractalfract6080458>
- Pham TT, Nong ND, Sathyan AR, Garschagen M (2020) Vulnerability assessment of households to flash floods and landslides in the poor upland regions of Vietnam. *Climate Risk Manage* 28. <https://doi.org/10.1016/j.crm.2020.100215>
- Santuz A, Akay T (2020) Fractal analysis of muscle activity patterns during locomotion: pitfalls and how to avoid them. *J Neurophysiol* 124(4):1083–1091. <https://doi.org/10.1152/jn.00360.2020>
- Swets JA (1988) Measuring the accuracy of diagnostic systems. *Science* 240(4857):1285–1293. <https://doi.org/10.1126/science.3287615>
- Tanabe N, Sato S, Suki B, Hirai T (2020) Fractal analysis of lung structure in chronic obstructive pulmonary disease. 11. <https://doi.org/10.3389/fphys.2020.603197>
- Tien Bui D, Tuan TA, Hoang N-D, Thanh NQ, Nguyen DB, Van Liem N, Pradhan B (2017) Spatial prediction of rainfall-induced landslides for the Lao Cai area (Vietnam) using a hybrid intelligent approach of least squares support vector machines inference model and artificial bee colony optimization. *Landslides* 14(2):447–458. <https://doi.org/10.1007/s10346-016-0711-9>
- VIGMR (2017) Report on landslide hazard zonation in Cao Bang province (in Vie). Ministry of Natural Resources and Environment, Hanoi
- Wang Y, Sun D, Wen H, Zhang H, Zhang F (2020) Comparison of random forest model and frequency ratio model for landslide susceptibility mapping (LSM) in Yunyang County (Chongqing, China). *Int J Environ Res Public Health* 17(12). <https://doi.org/10.3390/ijerph17124206>
- Yu X, Zhang K, Song Y, Jiang W, Zhou J (2021) Study on landslide susceptibility mapping based on rock-soil characteristic factors. *Sci Rep* 11(1). <https://doi.org/10.1038/s41598-021-94,936-5>
- Zuo R, Carranza EJM (2017) A fractal measure of spatial association between landslides and conditioning factors. *J Earth Sci* 28(4): 588–594. <https://doi.org/10.1007/s12583-017-0772-2>

Open Access This chapter is licensed under the terms of the Creative Commons Attribution 4.0 International License (<http://creativecommons.org/licenses/by/4.0/>), which permits use, sharing, adaptation, distribution and reproduction in any medium or format, as long as you give appropriate credit to the original author(s) and the source, provide a link to the Creative Commons license and indicate if changes were made.

The images or other third party material in this chapter are included in the chapter's Creative Commons license, unless indicated otherwise in a credit line to the material. If material is not included in the chapter's Creative Commons license and your intended use is not permitted by statutory regulation or exceeds the permitted use, you will need to obtain permission directly from the copyright holder.





Procedure of Data Processing for the Improvement of Failure Time Prediction of a Landslide Based on the Velocity and Acceleration of the Displacement

Imaya Ariyaratna and Katsuo Sasahara

Abstract

Time prediction methods based on monitoring surface displacement (SD) are effective for early warning against shallow landslides. However, failure time prediction by Fukuzono's original inverse-velocity (INV) method is less accurate due to variation in the inverse-velocity ($1/v$) caused by noise in the measured SD, which amplifies the fluctuation in the resultant $1/v$. Therefore, the present study incorporates pre-analysis to acquire better prediction by reducing the effect of noise on the measured SD. The data extraction (DE) and moving average (MA) methods are used to filter the measured SD for better smoothing of $1/v$. The root mean square error (RMSE) and determining factor (f) values are used to select the optimum SD interval (Δx) in the DE method. The RMSE and f values are used to evaluate the reproducibility of the measured data and the scattering in the relationship between velocity and acceleration in an orderly. The data, treated by the DE and MA methods, are utilized to predict the failure time based on the INV method and the relationship between velocity and acceleration on a logarithmic scale (VAA) method. Accordingly, Δx gives the smallest sum of the normalized RMSE and normalized $(1-f)$, which offers a better prediction. When the SD at failure changes, Δx is changed. The best prediction is obtained by DE preprocessing with the VAA method because it minimizes the effect of the individual $1/v$ by reducing the scatter in the relationship between velocity and acceleration. However, the time prediction using data processed by the MA method shows poor prediction due to some scattering of the inverse velocity. In some cases, the prediction by the VAA method using MA data provides better prediction than the results of the INV method.

Keywords

Shallow landslide · Failure time prediction · Model slope · Monitoring surface displacement

1 Introduction

The time prediction of a landslide occurrence is an important task for early warning against landslide disasters, but there is still uncertainty about its precision. However, slope scale prediction is a necessity in the framework of landslide risk reduction. In this regard, prediction based on monitoring displacement data is generally used in practice. Displacement monitoring in indoor model slopes and field experiments using a rainfall simulator have been adopted in recent studies related to shallow landslide failure mechanisms and the forecast time of failure for early warning. For example, Fukuzono (1985) monitored the surface displacement (SD) using extensometers on large-scale indoor model slopes. Furthermore, Moriwaki et al. (2004) conducted the experiments using a full-scale model slope by monitoring the SD with displacement meters. Ochiai et al. (2021) reported the monitoring displacement using extensometers of a field experiment on a natural slope in the city of Futtsu, Chiba Prefecture.

Many researchers have adopted time prediction methods based on monitoring the displacement of slopes (Saito 1965; Fukuzono 1985; Varnes 1982; Voight 1988; Crosta and Agliardi 2003; Rose and Hungr 2007). As mentioned above, the prediction method of the onset of landslide is based on the monitoring of slopes, which is based on the relationship between the time and SD of a slope before the failure occurs, as shown in Fig. 1. Accordingly, the time variation in creep behavior consists of three phases, namely, primary creep, secondary creep and tertiary creep. Among the time prediction methods adopted to date, the method proposed by Fukuzono (1985) has been widely adopted in practice due to its simplicity and convenience of use. He proposed a relationship between the velocity and acceleration of SD

I. Ariyaratna
Life Environment Science, Ehime University, Matsuyama, Japan
K. Sasahara (✉)
Research and Education Faculty, Kochi University, Kochi, Japan
e-mail: sasahara@kochi-u.ac.jp

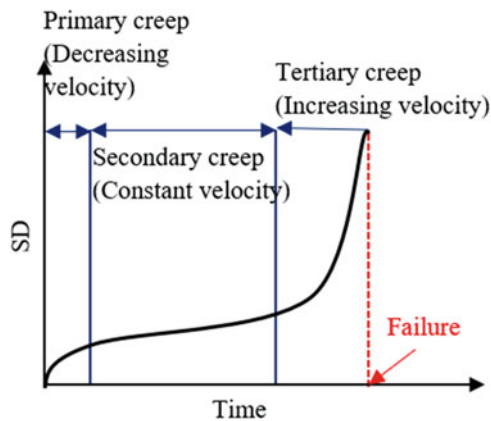


Fig. 1 Relation between time and SD of the soil before failure under constant stress conditions (Saito 1965)

just before failure (for the tertiary creep stage) in a large-scale model slope under sprinkling water, as shown in Eq. 1.

$$\left(\frac{dv}{dt}\right) = a \cdot v^\alpha \quad (1)$$

where v and t are the velocities of the SD and corresponding times, respectively. In addition, a and α are the experimental constants that result from the intercept on the vertical axis and gradient of the relationship line, respectively, when the velocity and acceleration of the SD data are plotted over time (Fig. 2).

Based on the above relationship, he introduced a prediction method called inverse-velocity method (INV), which

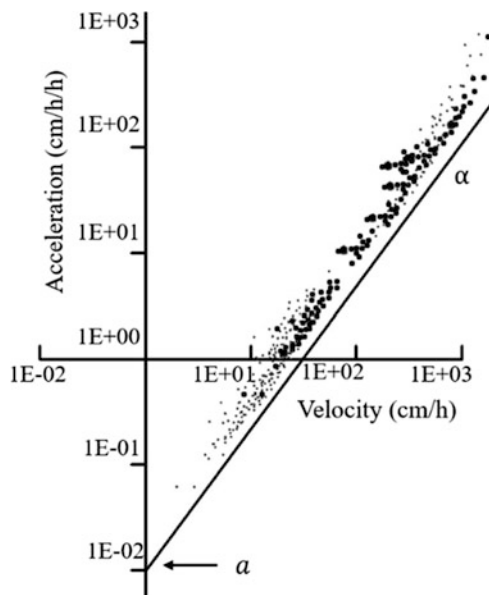


Fig. 2 Relationship between the velocity and acceleration of the SD (Fukuzono 1985)

was created by integrating the relationship between the velocity and acceleration of SD by time just prior to failure (Eq. 2).

$$\frac{1}{v} = \{a(\alpha - 1)\}^{\frac{1}{\alpha-1}}(t_r - t)^{\frac{1}{\alpha-1}} \quad (2)$$

where t_r is the predicted failure time. Fukuzono (1985) noted that the inverse velocity reached zero just before failure. Therefore, the failure time of a slope by the INV method could be determined by extrapolating the resultant curves to cross the time axis.

The past literature reveals that many researchers have adopted the INV method to forecast the failure time of landslides and that some of them achieved precise prediction, while some of them did not succeed completely. For example, Carla et al. (2019) predicted the failure time of a natural rockfall by the GBInSAR method using the INV method, and they conveyed that the INV method gives precise results. Mazzanti et al. (2015) highlighted that an improved version of the INV method called ADF (average data Fukuzono) is necessary to achieve the best results. ADF incorporates the moving average of the displacement data over time and effectively minimizes the prediction error due to scattering of inverse-velocity values. Furthermore, Zhou et al. (2020) emphasized that the time prediction effectiveness using INV is limited for actual landslides and that accuracy can be improved by introducing controllable variables. He proposed the modified INV method, which improves the accuracy of the predicted failure time by avoiding earlier prediction than actual failure time. That report noted that the forecasting effectiveness of the INV methods directly depends on the quality of the measured displacement data. Accordingly, the time prediction by Fukuzono's original INV may succeed in some cases but not in others because the results are widely affected by the quality of the measured data, as the displacement noise amplifies the resultant velocity. If the error in displacement data is not so considerable, the velocity variation, which is calculated using the same displacement data, becomes higher. This results in causes several peak values with up and down variations in velocities over time before failure. Hence, the present study focuses on improving the failure prediction by minimizing the influences of the inverse velocity fluctuation by introducing the preprocessing of displacement data before the prediction.

2 Methodology

2.1 Methods for Raw Data Preprocessing

Data preprocessing is introduced to obtain a better prediction, which reduces the sudden fluctuation of $1/v$ values by decreasing the effect of noise on the measured SD. Two

approaches called the data extraction method (DE) and moving average method (MA) are utilized in the present study.

2.1.1 Data Extraction Method (DE)

The DE method is carried out to determine the optimal displacement interval (Δx) for extracting the data to predict the failure time, which minimizes the scattering of $1/v$ values by avoiding the noise of the measured SD. The root mean square error ($RMSE$) and determining factor (f) values are used as supportive parameters to evaluate the reproducibility of the measured data and scattering in the relationship between velocity and acceleration in order to select Δx for the DE method. The $RMSE$ values are calculated by Eq. 3.

$$RMSE = \sqrt{\frac{1}{N} \sum_{i=1}^N (F_i - A_i)^2} \quad (3)$$

where N is the total number of the data, F_i is the measured SD at time t_i , A_i is the extracted SD at time t_i , and $(F_i - A_i)$ indicates an error between the measured and extracted SD. Suppose there are no data at the time t_i for the extracted data. In that case, data corresponding to t_i are projected by considering the proportional distribution of the extracted data before and after time t_i , as shown in Fig. 3. Generally, when the data extracting SD interval (ΔSD) is increased, the reproducibility of the measured data is decreased, and the calculated $RMSE$ values become larger.

The f values measure how well the regression line fits with the velocity and acceleration data on a logarithmic scale (Fig. 2). The linear regression line was obtained using Microsoft Excel for the relationship between velocity and acceleration on a logarithmic scale utilized to get the f values. It expresses how much percentage of the total variation in acceleration (vertical axis) is described by the velocity variation (horizontal axis) in the relationship between velocity and acceleration on a logarithmic scale which is always between 0.0 to 1.0. A value of 1.0 indicates

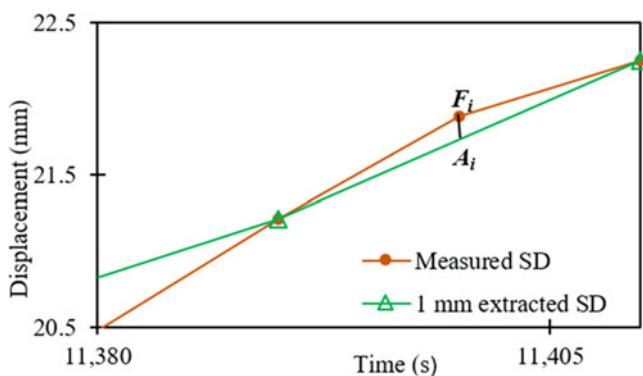


Fig. 3 The comparison of the time variation of displacement for the measured SD and SD extracted in 1 mm intervals

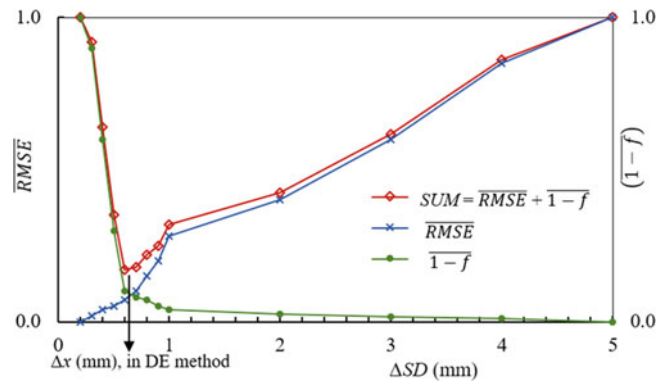


Fig. 4 \overline{RMSE} and $(\overline{1-f})$ value variation with different data extracting SD interval (ΔSD)

a higher relationship strength. It means the lowest value of $(1-f)$ gives the lowest scattering. However, calculated $RMSE$ and $(1-f)$ are not in the same range, which causes the weight ratio between $RMSE$ and $(1-f)$, is changed depending on the ΔSD . So, in the case of $RMSE$, though the minimum value is zero, the maximum value is changed by more than 1.0. In that case, the maximum and minimum value difference is equal to the one and calculate all values within the range of 0.0 to 1.0 as normalized $RMSE$ (\overline{RMSE}). So, both values are normalized into the same range, 0.0 to 1.0, assigning the weight ratio 1:1 between $RMSE$ and $(1-f)$, as shown in Fig. 4. The ΔSD increases, the discrepancy between measured and extracted.

data increases, and scattering in the relationship between the velocity and acceleration decreases. Considering the optimum displacement interval (Δx), it gives at the lowest summation of (\overline{RMSE}) and normalized $(1-f)$, ($\overline{1-f}$).

2.1.2 Moving Average (MA) Method

The moving average inverse velocity ($\overline{1/v}$) values (calculated by considering consecutive $1/v$ values) are used to smooth the time variation of $1/v$ in the MA method. In this regard, we calculate $(\overline{1/v})$ by considering different consecutive values and select the best consecutive value, which gives the best smoothing time variation of $1/v$. The $(\overline{1/v})$ at time step, l , is calculated using Eq. 4.

$$\left(\overline{1/v}\right)_l = \frac{(1/v)_l + (1/v)_{l-1} + \dots + (1/v)_{l-(n-1)}}{n} \quad (4)$$

where n is the number of time steps, l is the present time step, and $1/v$ is the inverse velocity value at the corresponding time step. As an example, when calculating the $(\overline{1/v})$ by considering two ($n = 2$) $1/v$ values, $(\overline{1/v})$ is defined as the summation of the $1/v$ values at present and previous time steps divided by two. As shown in Fig. 5, if the disturbance of SD is not significant, the $1/v$ variation calculated using the same SD

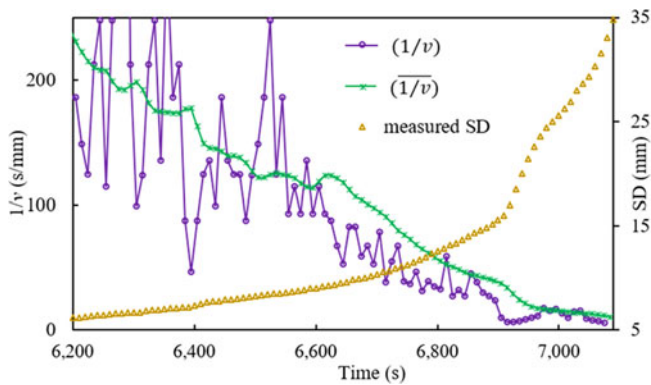


Fig. 5 Time variation of the inverse velocity derived from both the measured $1/v$ and smoothed inverse velocity $(\overline{1/v})$ and the SD

becomes higher. However, the individual fluctuation is lower when considering $(\overline{1/v})$, which gives a smoother curve.

2.2 Prediction of the Failure Time

2.2.1 Calculation of Velocity and Acceleration Values

The calculation of the velocity and acceleration from the measured SD and time data is explained below. First, the velocity is defined as the SD difference between the previous and present time steps divided by the corresponding time step difference. Second, the acceleration is defined as the velocity difference between the previous and present time steps divided by the corresponding time step difference.

2.2.2 Failure Prediction from Fukuzono's Original Inverse-Velocity (INV) Method

The INV method is based on the relationship between $1/v$ and time, which reaches zero just before failure. Therefore, the failure time prediction can be predicted by extrapolating resultant curves to cross the time axis, which is given by the time differentiation $1/v$ in Eq. 2 and some arrangement to produce the ratio of $1/v$ to the increment of the inverse velocity, as shown in Eq. 5.

$$\left(\frac{1}{v}\right) / \left(\frac{d(1/v)}{dt}\right) = -(\alpha - 1)(t_r - t) \quad (5)$$

The failure time can be calculated using the ratio of the $1/v$ to its increment ratio at two different times, as shown in Eq. 6, which is the process of the INV method initially proposed by Fukuzono (1985).

$$t_r = \frac{t_2(1/v)_1 / (d(1/v)/dt)_1 - t_1(1/v)_2 / (d(1/v)/dt)_2}{(1/v)_1 / (d(1/v)/dt)_1 - (1/v)_2 / (d(1/v)/dt)_2} \quad (6)$$

2.2.3 Failure Prediction from the Relationship Between Velocity and Acceleration (VAA) Method

The failure time prediction by the VAA method can be derived from the rearrangement of Eq. 2 to Eq. 7.

$$t_r = t + \frac{1}{a(\alpha - 1)} \left(\frac{1}{v}\right)^{\alpha - 1} \quad (7)$$

The failure time can be derived by substituting the present time (t) and corresponding inverse-velocity values ($1/v$) with a and α values into Eq. 7. The a and α values are derived from the relationship between velocity and acceleration on a logarithmic scale from linear regression analysis as shown in Fig. 2.

2.3 Landslide Field Experiment on a Natural Slope in Futtsu, Chiba Prefecture

2.3.1 Experimental Setups

A landslide field experiment on a natural slope in Futtsu, Chiba Prefecture, was conducted on 12 December 2018 using a rainfall simulator as requested by NHK, Nippon Hoso Kyokai (Japan Broadcast Corporation). The experimental site was sparsely forested with hardwoods with a slope of approximately 40 degrees. The ground surface was a smooth slope surface covered with Simon bamboo and ivy, and part of the lower edge of the slope had previously been quarried for sand. The behavior of the slope was monitored and filmed with multiple cameras during the main experiment.

The grain size distribution of the surface soil layer is shown in Fig. 6. Accordingly, the majority of the soil consists of sand particles (75%), and the rest are silts particles (23%) and clay particles (2%). The mean diameter of the soil particles is 0.1509 mm. The physical properties of the soil are shown in Table 1. Accordingly, soil particle density is 2.574 g/cm³, and the minimum and maximum density of the soil is between 1.082 to 1.361 g/cm³. The thickness of the surface soil layer was approximately 1 m based on the results of a portable penetration test (Japanese Geotechnical Society, 2017) using a number of blows (10 cm penetration) with a 5 kg weight dropped from a height of 50 cm. During the experiment, artificial rainfall was supplied to an area 10 m long and 10 m wide. The pre-experiment with a precipitation intensity of 140 mm/h was conducted for around 1 h on 11 December 2018 to fine-tune the distribution of the

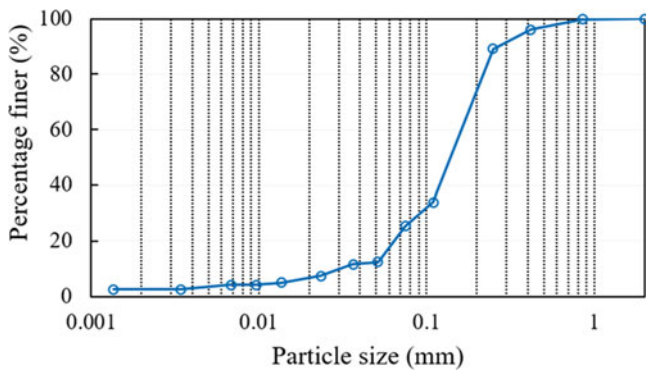


Fig. 6 Grain size distribution of the surface soil at the experimental site

precipitation. A total of six extensometers at three locations along two survey lines were installed (Fig. 7a). Extensometers 1, 2, and 3 were placed on line 1 (Fig. 7b), and the others were placed on line 2. A detailed explanation of the experiment can be found in Ochiai et al. (2021).

2.4 In-door Small-scale Model Slope Experiment

2.4.1 Experimental Setups

The data obtained from the in-door small-scale model slope at Kochi University was utilized in this study. Figure 8a, b show the lateral view and longitudinal section of the small-scale model slope and monitoring device arrangement, respectively, at Kochi University. The model was 110 cm and 55 cm long, respectively, in slope and horizontal sections with a width of 60 cm and depth of 12 cm. The model slope’s base plate consisted of steel blades with a height of 1 cm and length equal to the width of the base plate by every 20 cm from 10 cm to 90 cm from the upper boundary in the slope section and from 7.5 cm to 47 cm from the end of the lower boundary in the horizontal section of the model slope and coarse sand to prevent sliding between the soil and the base plate. The model slope’s dry unit weight, and upper slope inclination were 1.32 g/cm³, and 40 degrees, respectively. The experiment was carried out under sprinkling water with constant discharge from the rainfall simulator, and its intensity was expressed in mm/h. Accordingly, 108 mm/h rainfall

intensity was used for the experiment. Well-graded sand with fine (The Japanese Geotechnical Society, 2015) with a grain size distribution shown in Fig. 9 was used to prepare the model slope and other physical properties are shown in Table 2.

The SD was measured using three displacement gauges fixed at the lateral boundary of the flume from the distance of 25 cm, 55 cm, and 80 cm away from the upper boundary of the flume. The SD data and their corresponding time at the 55 cm (middle) displacement gauge were utilized for the analysis. The displacement gauge’s capacity and resolution are 100 mm and 0.2 mm, respectively and data were logged every 10 s by a data logger. The displacement gauges are the SDP-100CT, strain-generating cantilever type displacement transducer from the Tokyo Sokki Kenkyujo Company, and measure the tension displacement using a hook bolt.

3 Results

This section presents only the results corresponding to extensometer No. 5 (orange colour in Fig. 10) in the natural slope experiment, Futtsu, and the displacement gauge, installed at 55 cm from the upper boundary of the model slope in the small-scale model slope experiment.

3.1 Experimental Results

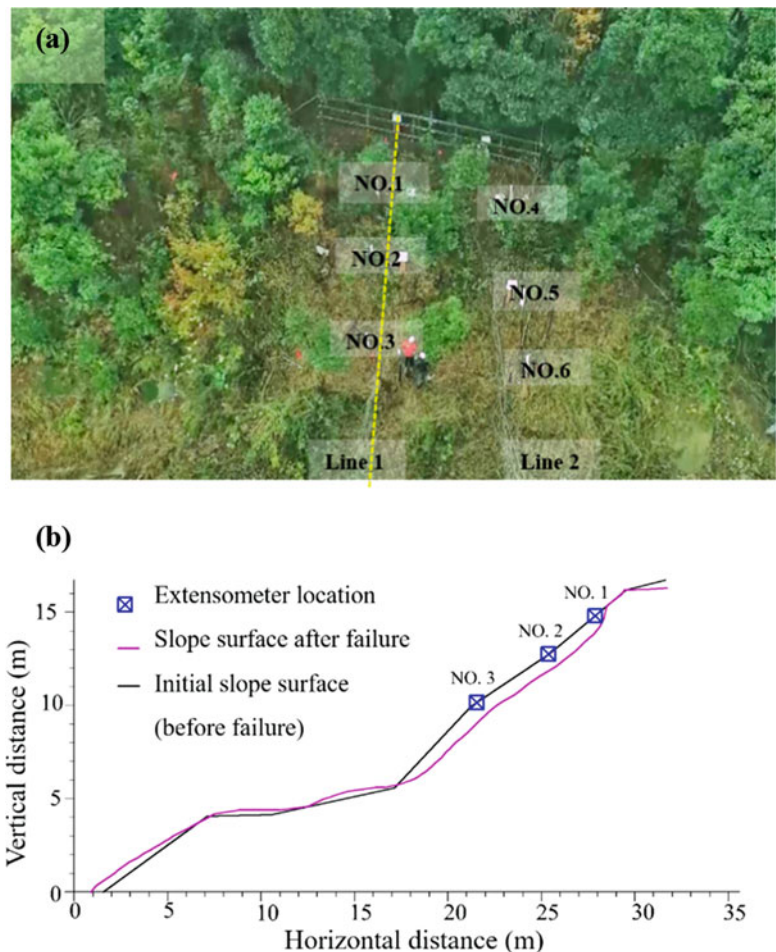
A landslide occurred at field experiment on a natural slope in Futtsu, after 4 h and 25 min of rainfall with an intensity of 140–300 mm/h, and the depth of the landslide was approximately 1 m, according to Ochiai et al. (2021). Furthermore, Fig. 7b shows the cross-section before (black colour line) and after (pink colour line) failure and reveals that the failure was a sliding-type landslide.

Although six extensometers were installed on the experimental slope, only Nos. 1 and 5 were within the landslide mass, and the others were out of the landslide area. Therefore, the SD measured at their corresponding times by extensometers Nos. 1 and 5 was used for the present study. Extensometers No. 1 (blue colour) and No. 5 (orange colour) show the movement along the surface approximately 275 mm

Table 1 Physical properties of the natural slope in Futtsu experiment

Soil particle density (g/cm ³)	2.574
Minimum density (g/cm ³)	1.082
Maximum density (g/cm ³)	1.361
Minimum void ratio of the soil, e_{min}	0.891
Maximum void ratio of the soil, e_{max}	1.379
Coefficient of uniformity	2.3

Fig. 7 (a) Front view of the natural slope in Futtsu and arrangement of displacement gauges, and (b) longitudinal section along line 1 at experimental slope at Futtsu (with the locations of displacement gauges Nos. 1, 2, and 3)



to 204 mm just before the failure (Fig. 10). Figure 11 shows the slope geometry after the failure. The landslide initiation boundary is demarcated using yellow colour dotted line and red color arrows showing the debris moving direction. A closer view of the landslide crest area shows in the upper left corner of Fig. 11. Ochiai et al. (2021) mentioned that the groundwater levels on the upper slope increased again along with the accelerated movements in the middle slope, which led to the landslide initiation. The failure was initiated after the 7,090 s in the in-door small-scale model slope experiment and it was a sliding type failure.

3.2 Data Preprocessing

3.2.1 Data Extraction Method (DE)

Figure 12a, b show \overline{RMSE} and $(1-\overline{f})$ values variation with the different ΔSD intervals (ΔSD) in the DE method for orderly natural slope experiment, Futtsu, and small-scale model slope. In the natural slope experiment and small-scale model slope, recorded ΔSD and time at failure were 204.4 mm and 34.79 mm, and 22,680 s and 7090 s, respectively. According to the results of the DE method, 3.0 mm

and 1.0 mm ΔSD intervals are the optimum displacement interval (Δx) for data extraction corresponding to the natural slope experiment and small-scale model slope orderly to failure time prediction. The analysis is carried out by selecting a ΔSD interval from 0.1 mm to 1.0 mm by a 0.1 mm difference and then a 1.0 mm interval difference until 10.0 mm for the natural slope experiment and a ΔSD interval from 0.2 mm to 1.0 mm by a 0.1 mm difference and then a 1.0 mm interval difference until 5.0 mm for small-scale model slope. Because the accuracy of the displacement gauge used for the in-door small-scale model slope experiment is 0.2 mm, 0.2 mm is used for the minimum ΔSD value in the DE process.

Figure 12a shows that \overline{RMSE} values gradually increase when the ΔSD is increased except at the 0.1 mm interval and 3.0 mm interval. The calculated \overline{RMSE} at the 3.0 mm interval is a similar value, 0.30, with the 2.0 mm interval. The parameter $(1-\overline{f})$ gradually decreases as the ΔSD increases, but a small increase of less than 0.03 can be observed until 0.8 mm from 0.5 mm. Subsequently, the $(1-\overline{f})$ values suddenly drop until reaching 2.0 mm and then decrease smoothly. However, the sum of \overline{RMSE} and $(1-\overline{f})$ shows the lowest value at

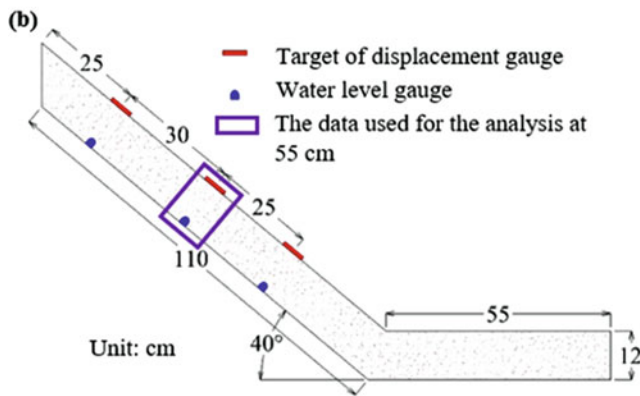


Fig. 8 (a) Lateral view of the model slope, (b) longitudinal section of the model slope and arrangement of measurement devices at Kochi University

3.0 mm as 0.37. The 2.0 mm interval also shows a closer value, 0.38 to 3.0 mm, as the sum of \overline{RMSE} and $(1-f)$.

Figure 12b shows that \overline{RMSE} and $(1-f)$ values increase and decrease in an orderly with increasing the ΔSD , but not gradually, and shows some up and down values. The \overline{RMSE} values increase gradually, with a decreasing value at 0.7 mm and approximately similar at the nearest ΔSD , 0.5 mm and 0.9 mm, with 0.6 mm and 1.0 mm, respectively. $(1-f)$

Fig. 9 Grain size distribution of the model slope's soil

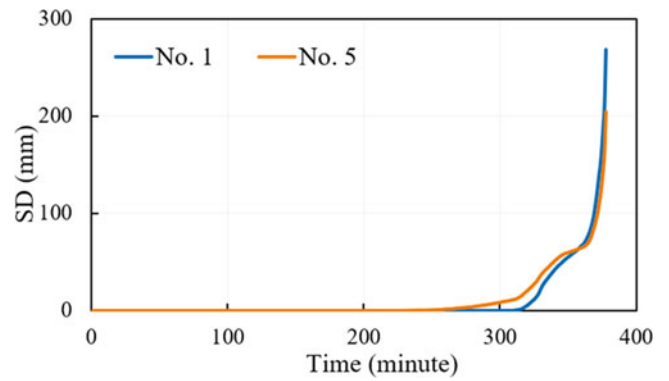
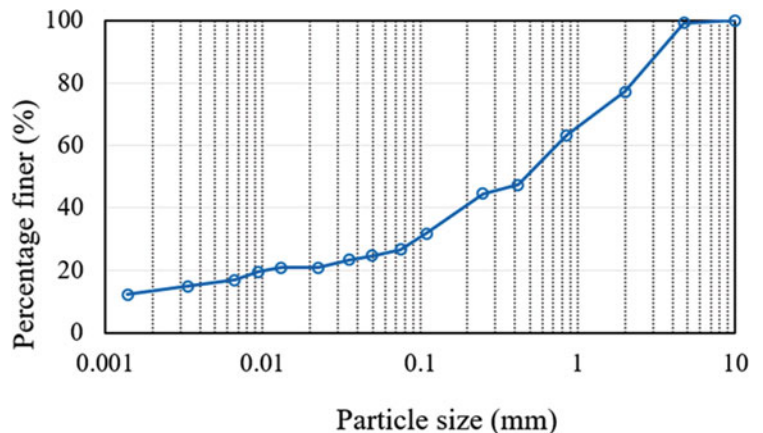


Fig. 10 The time variation of the surface displacement (SD), measured by extensometer Nos. 1 and 5

values suddenly drop from 0.3 mm to 1.0 mm, while showing peak values at 0.6 mm and 0.8 mm. After the 1.0 mm, ΔSD , $(1-f)$ values show some fluctuation within the range of 0.0 to 0.19. However, the sum of \overline{RMSE} and $(1-f)$ values show the lowest value at 1 mm as 0.16. The 0.9 mm interval also shows a closer value, 0.17 to 1.0 mm, as the sum of \overline{RMSE} and $(1-f)$.

3.2.2 Moving Average (MA) Method

Figure 13a, b show the time variation of $1/v$ and $(1/v)$, which is calculated by considering the different number of consecutives $1/v$ to select the best smooth time variation of $(1/v)$ in the MA method for orderly natural slope experiment, Futtzu and in-door small-scale model slope. Accordingly, moving average velocities are calculated using 2, 5, 10, and 20 consecutives (2MA, 5MA, 10MA, and 20MA). The results reveal that when the considered number of consecutives increases, the smoothness of the resultant time variation $(1/v)$ curves is improved, especially just before the failure. Accordingly, the results obtained from the natural slope experiment (Fig. 13a) highlighted that the significant increase of $1/v$ from 19,880 s to 20,990 s and fluctuation until

Fig. 11 A photograph of the experimental slope, Futttsu after landslide occurred



21,540 s, instead of decreasing causes, making a peak in the time variation $(1/v)$ curve.

3.3 Prediction of Failure Time

In the present study, the time remaining to failure (t_r-t) approaching zero just before failure is considered an indicator for failure prediction. Though the time variation of the predicted failure time (t_r) can be used as an indicator, experimental results reveal that it increases and approaches actual failure time with time instead of the constant time variation of predicted failure time. In that scenario, the time just before the failure cannot be easily identified using the time variation of predicted failure time. In contrast, the time variation (t_r-t) leads to a more precise prediction.

3.3.1 Prediction Results by the INV Method

Figure 14a, b show the failure time prediction by the INV method using the data processed by the DE method for the natural slope experiment, Futttsu and small-scale model slope experiments in an orderly. Figure 14a contains the time variation of (t_r-t) by the INV method using the DE processed data by only the data extracting SD intervals (ΔSD), 0.1 mm,

0.6 mm, 3 mm, and 10 mm for the natural slope experiment. It shows that the predicted (t_r-t) by the INV method using DE data for the natural slope experiment tends to lie along the time axis with some up and down fluctuation in the 0.1 mm extracted data. However, upon comparing the results of higher ΔSD , the prediction shows the values away from the time axis, suggesting that when the ΔSD is higher, the method gives a later prediction. However, the prediction using the INV method and DE data for the natural slope experiment shows negative values throughout the prediction in all ΔSD , which means that the prediction results indicate that slope failure has already occurred during the experiment. Figure 14b presents the time variation of (t_r-t) by the INV method using the DE processed data by only ΔSD , 0.2 mm, 0.6 mm, 1 mm, and 5 mm for the small-scale model slope experiment. The predicted (t_r-t) using ΔSD , 0.2 mm, 0.6 mm, and 1 mm shows similar behaviors as the natural slope experiment results. But the predicted (t_r-t) with the 5 mm interval extraction data shows a gradually decreasing trend with time. It used only the five SD values to predict the failure time from 6000 s to collapse, and among them, two values were negative (t_r-t) just before the failure (around 6925 s and 6978 s).

Table 2 Physical properties of the model slope

Soil particle density (g/cm^3)	2.651
Maximum density (g/cm^3)	1.733
Minimum density (g/cm^3)	1.344
Minimum void ratio of the soil, e_{\min}	0.420
Maximum void ratio of the soil, e_{\max}	0.833
Coefficient of uniformity	12.98
Water content of the model slope, w (%)	3.64

Fig. 12 \overline{RMSE} and $(1-f)$ values variation with the different data extracting SD interval (ΔSD) in the DE method for (a) natural slope experiment, Futtsu, and (b) in-door small-scale model slope experiment

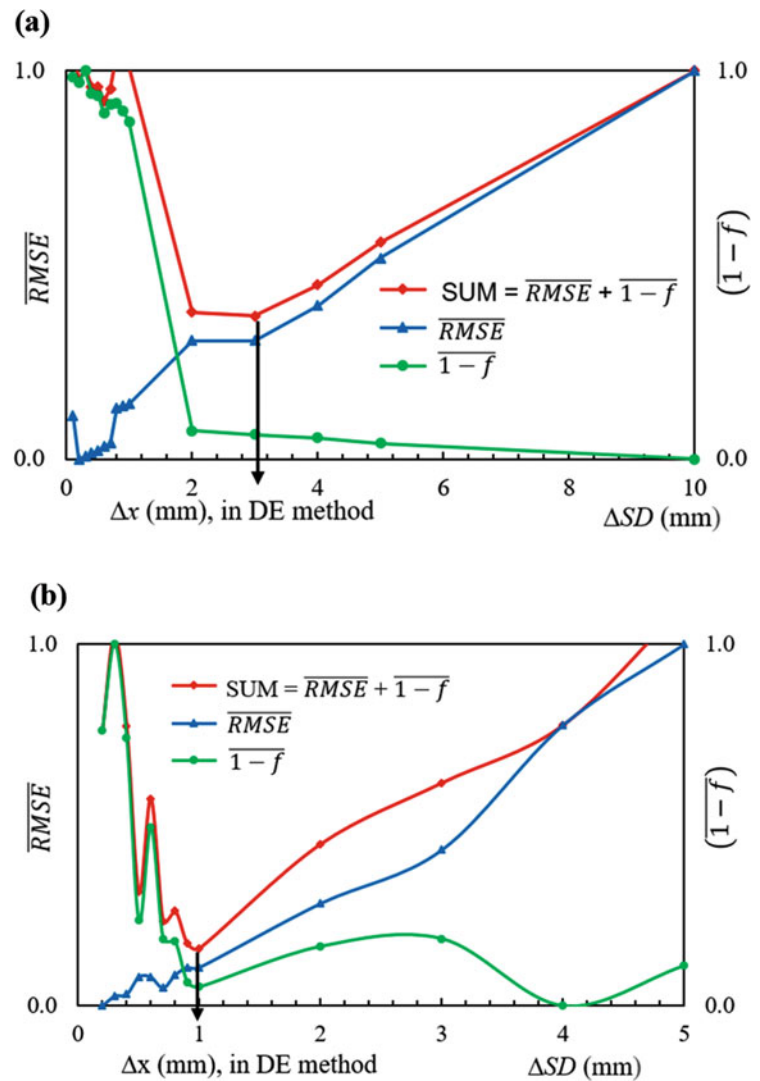
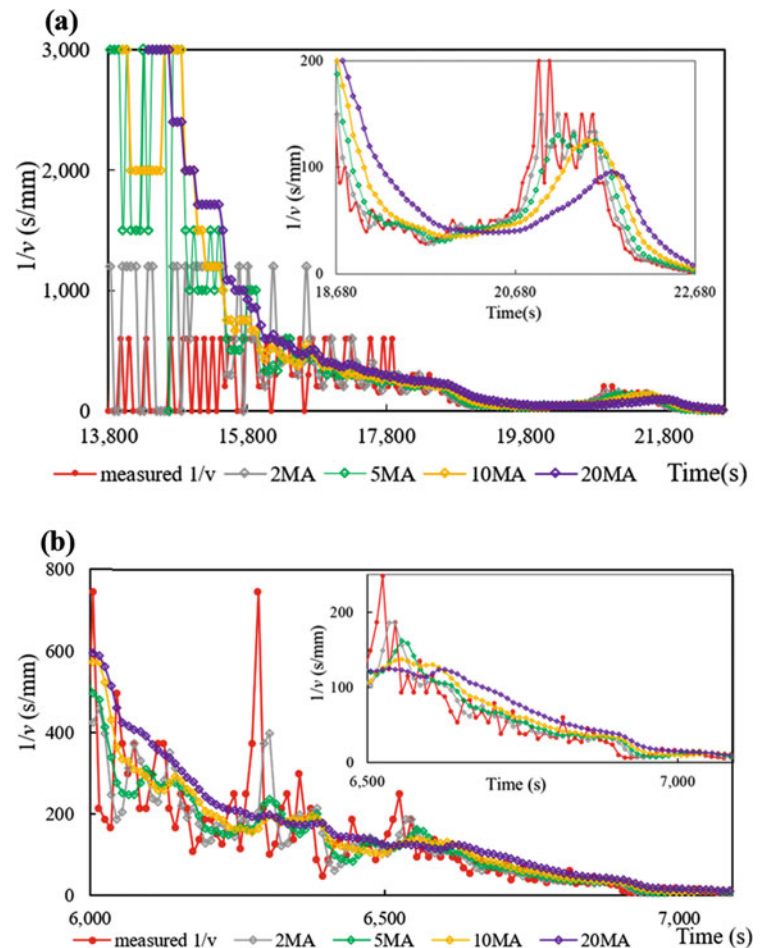


Figure 15a, b show the failure time prediction by the INV method using the data processed by the MA method for the natural slope experiment, Futtsu, and small-scale model slope experiments in an orderly. The predictions were carried out using the MA method by calculating the moving average velocities ($1/v$) using 2, 5, 10, and 20 consecutives, respectively, 2MA, 5MA, 10MA, and 20 MA. In this regard, the variation of (t_r-t) with time is the same pattern in both experiments. The results obtained from the INV method prediction, using MA data, are more scattered than those obtained from the DE data. However, the results from MA data by the INV method prediction show negative values throughout the prediction by the $(1/v)$ using the different number of consecutives. Therefore, the prediction by the INV method, with both DE and MA data, shows less precision because the results still show scattering and negative values just before failure.

3.3.2 Prediction Results by the VAA Method

Figure 16 shows the time variation of (t_r-t) by the VAA method from the data processed by the DE method. In order, Fig. 16a, b refer to the time variation of (t_r-t) for the natural slope experiment, Futtsu, and small-scale model slope experiment just before the failure. The results of the natural slope experiment revealed that the predicted (t_r-t) is generally decreasing and closer to zero just before failure by the data extracted SD interval (ΔSD) of 0.1 mm, 0.6 mm, 3 mm, and 10 mm (Fig. 16a). The prediction using ΔSD , 0.1 mm, and 0.6 mm show some scattering compared with the results obtained from 3 mm and 10 mm. The fluctuation of time remaining to failure (t_r-t) from the ΔSD using 3 mm and 10 mm intervals is minimal compared with the other predictions. When comparing the results from 3 mm and 10 mm intervals, the 3 mm interval gives a better linear decreasing trend than the 10 mm interval. Therefore 3 mm

Fig. 13 Time variation of $1/v$ and $(\overline{1/v})$, for, (a) natural slope experiment, Futtsu, and (b) in-door small-scale model slope experiment (different number of consecutive velocity values, used for calculating $(\overline{1/v})$, considering 2, 5, 10 and 20 adjacent values are referred in orderly 2MA, 5MA, 10MA, and 20MA in the MA method)



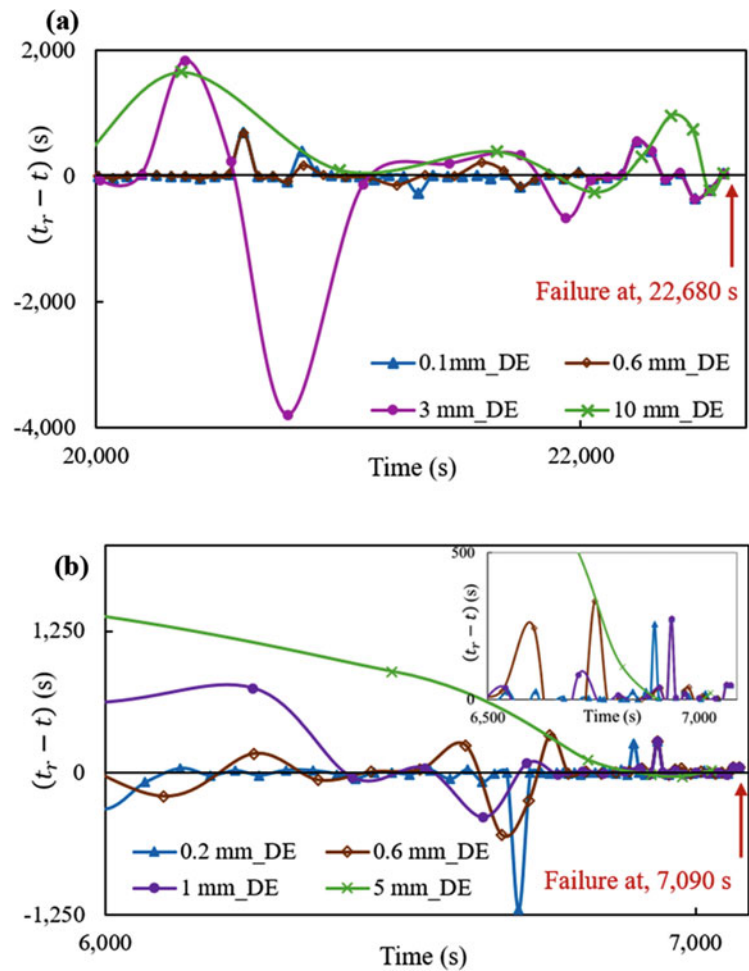
is the optimum displacement interval (Δx) for DE corresponding to the natural slope experiment, as it offers the best results for failure prediction by the VAA method. Figure 16b shows the time variation of $(t_r - t)$ predicted using ΔSD , 0.2 mm, 0.6 mm, 1 mm, and 5 mm, just before the failure. The prediction using 0.2 mm shows some negative predictions, which means that the slope has already collapsed during the experiment monitoring. The ΔSD , 0.6 mm, and 5 mm predictions show relatively higher scattering than the 1 mm. The prediction results by 1 mm show the general trend of decreasing with time and getting closer to zero. Therefore 1 mm is Δx for DE, corresponding to the small-scale model slope experiment, as it offers the best failure prediction by the VAA method.

Figure 17a, b show the time variation of $(t_r - t)$ by the VAA method for the data processed by the MA method in an orderly natural slope experiment, Futtsu, and small-scale model slope experiment, just before the failure. Figure 17a highlights that the VAA method's prediction using the 2MA and 10MA processed data gives the general trend of decreasing $(t_r - t)$ while 5MA and 20MA give the predicted $(t_r - t)$ with negative values and along the time axis, respectively.

However, the results obtained from the 5MA and 20MA show poor prediction. The predicted $(t_r - t)$ obtained from the small-scale model slope experiment (Fig. 17b) highlighted that the VAA method's prediction using the MA method's processed data gives negative predictions, even just before the failure, regardless of the number (n) used for calculating the moving average. The time variation of $(t_r - t)$ by 5MA processed data shows a general decreasing trend just before the failure.

The VAA method's prediction using the MA shows decreasing trends in the latter time before the failure compared with the results of the VAA method using DE data. On the other hand, the results obtained from the VAA method using the MA show a higher scatter just before the failure, while the VAA method using DE gives relatively less scatter. Furthermore, the prediction given by the VAA method using MA data has uncertainty and depends on the conditions, which could not be ensured in every case. In the natural slope experiment, Futtsu revealed that the time variation of $(t_r - t)$ decreases only by 2MA and 10MA processed data, and the small-scale model slope experiment shows a decreasing trend of $(t_r - t)$ with time by only 20MA processed data. For

Fig. 14 Time variation of the time remaining to failure (t_r-t) by the INV method using the data processed by DE method for, (a) natural slope experiment, Futtsu, and (b) in-door small-scale model slope experiment (0.1 mm_DE, 0.2 mm_DE, 0.6 mm_DE, 1 mm_DE, 3 mm_DE, 5 mm_DE, and 10 mm_DE represent the results from the DE by SD intervals of 0.1 mm, 0.2 mm, 0.6 mm, 1 mm, 3 mm, 5 mm, and 10 mm)



example, if the prediction by the VAA method using 2MA and 10MA gives a decreasing trend, then 5MA gives a poor prediction. Based on the present analysis, the prediction given by the VAA method using 10MA gives a linearly decreasing trend compared to 2MA with the above-explained complications. Therefore, the best prediction is obtained from the VAA method using data processed by the DE method.

The failure time prediction made using the VAA method gives better results than the INV method because it utilizes the linear regression analysis in the relationship between velocity and acceleration and causes less influence from the individual variation of the inverse velocity values. But still, some scattering remained, resulting from the noise of the measured SD. Therefore, the data preprocessing method was introduced to acquire better prediction by reducing the effect of noise on the measured SD. The prediction using DE processed data gives better results than MA processed data. So, time prediction based on the VAA method with DE preprocessing data can be used to monitor the real-time data with better precision than others. The prediction results, the VAA method with DE processed data by comparing with other methods, leads to reduce the fluctuation of predicted

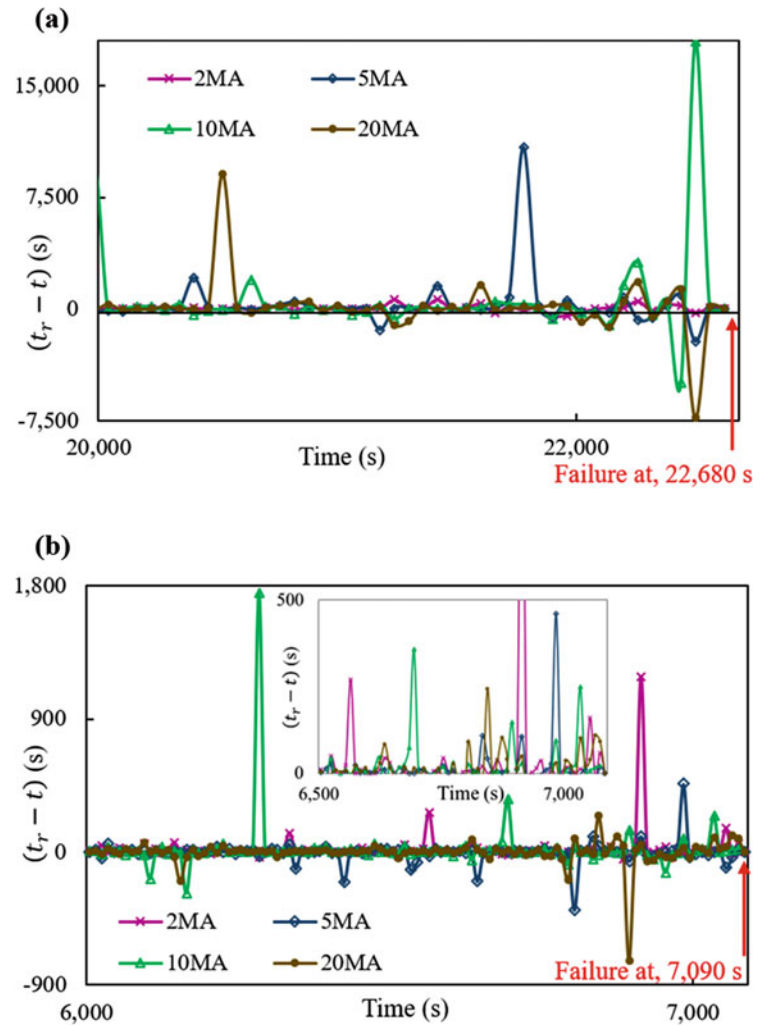
failure time and minimizes the disturbance to decreasing trend. It does not mean all fluctuations can be avoided, but it reduces and improves more than other methods. For example, the prediction by the VAA method using 3 mm extracted data for natural slope experiment, Futtsu, decreasing trend shows two gradients (Fig. 16a pink colour) during its general decreasing trend of predicted time remain to failure (t_r-t) with time. But results are more precise than the others.

4 Conclusions

The present study predicted the failure time using two methods with different preprocessing data methods to evaluate the effectiveness of the preprocessing data methodologies to improve the failure prediction using field experiment data on a natural slope in Futtsu, Chiba Prefecture. During the study, the following conclusions could be drawn.

1. The failure prediction by the VAA method using DE preprocessing gives the best prediction because it minimizes the individual velocity variation. In the process

Fig. 15 Time variation of the time remaining to failure ($t_r - t$) by the INV method using the data processed by MA method, for, (a) natural slope experiment, Futtsu, and (b) in-door small-scale model slope experiment



of DE, not only reproducibility but also equal priority is given to reducing the scatter in the relationship between velocity and acceleration.

2. The optimal displacement interval (Δx) by the DE method corresponds to the smallest sum of \overline{RMSE} and $(\overline{1-f})$, which gives the best prediction using the data extracted by the VAA method. The Δx changes depending on the distance moved by the landslide. Therefore, more studies

on a different scale of landslides are needed to obtain the relationship between Δx and the moved displacement.

3. Best smoothing of the time variation of the inverse velocity curve is obtained from the moving average inverse velocities calculated by a larger number of consecutive inverse velocities than a small number of consecutive inverse velocities. However, the time prediction using data processed by the MA method shows poor prediction due to some scattering of the inverse velocity.

Fig. 16 Time variation of the time remaining to failure ($t_r - t$) by the VAA method using the data processed by the DE method for (a) natural slope experiment, Futtsu, and (b) in-door small-scale model slope experiment

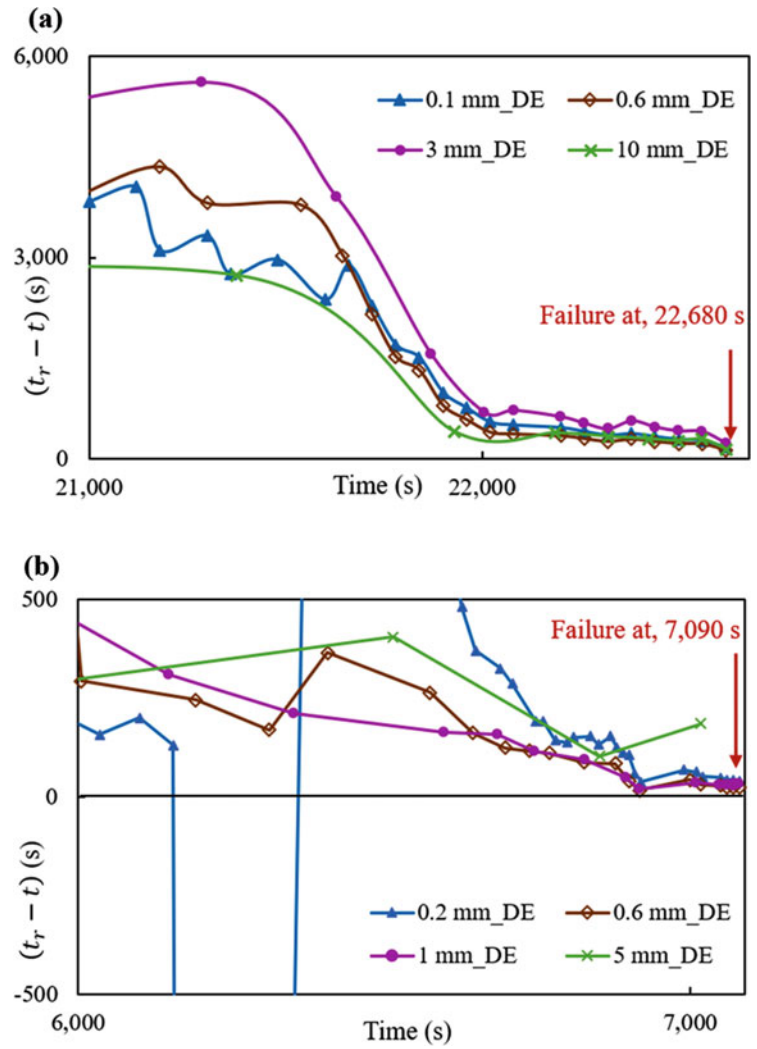
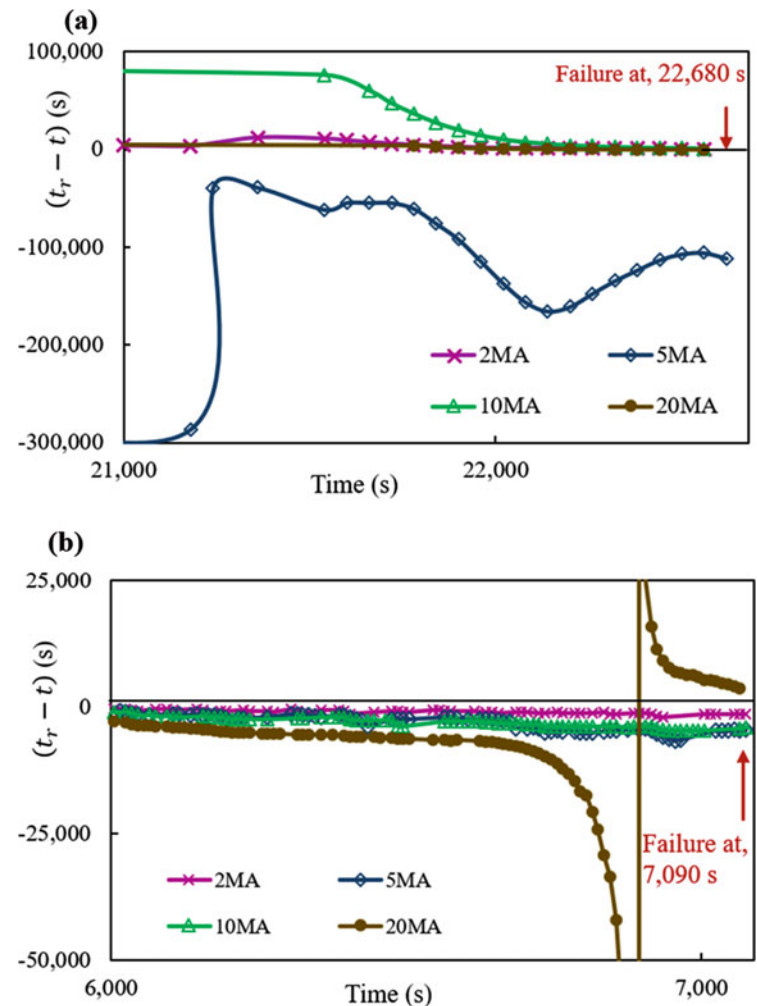


Fig. 17 Time variation of the time remaining to failure ($t_r - t$) by the VAA method using the data processed by the MA method for (a) natural slope experiment, Futtsu, and (b) in-door small-scale model slope experiment



Acknowledgments Part of this research is supported by the Grant-in-Aid for Scientific Research B-KAKENHI-, 18H01674, JSPS, and budget from “Development of early warning technology of Rain-induced Rapid and Long-travelling Landslides (RRLL)” within the framework of “Science and Technology Research Partnership for Sustainable Development (SATREPS)” by the Japanese Government.

References

- Carlà T, Nolesini T, Solari L et al (2019) Rockfall forecasting and risk management along a major transportation corridor in the Alps through ground-based radar interferometry. *Landslides* 16:1425–1435. <https://doi.org/10.1007/s10346-019-01190-y>
- Crosta GB, Agliardi F (2003) Failure forecast for large rock slides by surface displacement measurements. *Can Geotech J* 40:176–119. <https://doi.org/10.1139/t02-085>
- Fukuzono T (1985) A new method for predicting the failure time of a slope. In: *Proceedings of 4th international conference and field workshops on landslides*, Tokyo, Japan, pp 145–150
- Mazzanti P, Bozzano F, Cipriani I, Prestinanzi A (2015) New insights into the temporal prediction of landslides by a terrestrial SAR interferometry monitoring case study. *Landslides* 12:55–58
- Moriwaki H, Inokuchi T, Hattanji T, Sassa K, Ochiai H, Wang G (2004) Failure processes in a full-scale landslide experiment using a rainfall simulator. *Landslides* 1:277–288
- Ochiai H, Sasahara K, Koyama Y (2021) Landslide field experiment on a natural slope in Futtsu city, Chiba prefecture, Understanding and reducing landslide disaster risk, pp 169–175
- Rose ND, Hungr O (2007) Forecasting potential rock slope failure in open pit mines using the inverse-velocity method. *Int J Rock Mech Min* 44:308–320
- Saito M (1965) Forecasting the time of occurrence of a slope failure. In: *Proceedings 6th International Conference on Soil Mechanics and Foundation Eng Montreal, Canada 2*, pp 537–541
- Varnes DJ (1982) Time-deformation relations in creep to failure of earth materials. In: *Proceedings of 7th Southeast Asian Geotechnical Conference 2*, pp 107–130
- Voight B (1988) A relation to describe rate-dependent material failure. *Science* 243:200–203
- Zhou XP, Liu LJ, Xu C (2020) A modified inverse-velocity method of landslides. *Eng Geol* 268. <https://doi.org/10.1016/j.enggeo.2020.105521>

Open Access This chapter is licensed under the terms of the Creative Commons Attribution 4.0 International License (<http://creativecommons.org/licenses/by/4.0/>), which permits use, sharing, adaptation, distribution and reproduction in any medium or format, as long as you give appropriate credit to the original author(s) and the source, provide a link to the Creative Commons license and indicate if changes were made.

The images or other third party material in this chapter are included in the chapter's Creative Commons license, unless indicated otherwise in a credit line to the material. If material is not included in the chapter's Creative Commons license and your intended use is not permitted by statutory regulation or exceeds the permitted use, you will need to obtain permission directly from the copyright holder.





Numerical Analysis of the Effect of Rainfall on the Stability of Sandstone-Covered Mudstone Cutting Slopes

Ying Guo, Yating Du, Wei Shan, and Chengcheng Zhang

Abstract

Landslides caused by rainfall are easily produced when excavating is made in sandstone-covered mudstone strata. The expansion project of the Heishan Village to the Jixi section of the Dan-A Highway is used as an example, this International Consortium on Landslides (ICL) 030 paper studies the formation and damage mechanism of rainfall-induced landslides in sandstone-covered mudstone cutting slopes. The finite element numerical method is used to analyze the stability of the slope for the three different rainfall-influencing factors of rainfall intensity, duration, and rainfall form. The study indicates that the increases in the rainfall time and its intensity will decrease the stability of the cutting slope, and that the effect of rainfall on the slope is lagging behind. When rainfall intensity is 80 mm, rainfall duration is 1 day, and stagnation is 5 h, the slope instability is in the critical state. The front slope toe is the first unstable part in the process of slope instability. Rock and artificial construction are important reasons for this phenomenon.

Keywords

Sandstone mudstone · Rainfall infiltration · Road cutting slope · Numerical analysis

1 Introduction

In Northeast China, sandstone-mudstone interbedding is a typical stratigraphic distribution. Both sandstone and mudstone are sedimentary rocks. Among them, sandstone has great weathering resistance and good permeability, and surface water can easily permeate it. Mudstone, on the other

hand, has low strength and weak permeability and is quickly absorbed and softened by water (Rinaldi and Casagli 1999). It is a slippery stratum in engineering construction. In recent years, the trend of summer rainfall in Northeast China increased (Kong et al. 2017). Due to rain erosion and temperature change, the exposed mudstone interlayer will disintegrate and soften quickly. This process weakens the layer and reduces its strength, which causes a significant drop in the slope safety factor and even destabilization (Pan and Yan 2016; Zhu et al. 2022). Therefore, the sandstone–mudstone interlayer’s slope stability problem has increasingly caught the attention of academics working in the area.

The geotechnical structure and influencing factors are the two main areas of attention for studies on the stability of sandstone and mudstone slopes. According to Tingguo Peng’s (Peng 2013) analysis of the stability of mudstone and muddy siltstone landslides, impermeable siltstone is a necessary element for landslide formation, and surface water infiltration and rainfall both contribute to landslide deformation. However, there is no in-depth analysis of the rainfall factor. By examining the structural characteristics of mudstone rock, Zhenghui Tang (Tang et al. 2009) observed that the rate of rainfall infiltration into the rock affects the rate of expansive argillization, but neglected the intensity of the rainfall infiltration and duration. Based on the instability of siltstone slopes, Q. Li et al. (Li et al. 2020) hypothesized that slope deformation can be divided into a slow creep period caused by excavation and an accelerated sliding period caused by rainfall. Considering the three factors of rainfall intensity, duration, and slope gradient, Zhongming He et al. (He et al. 2012) found that the gradient had a bigger impact on the slope safety coefficient than the rainfall factor. Instead, Xianqi Luo (Luo et al. 2005) simulated infiltration characteristics and deformation damage characteristics of landslides under different rainfall conditions by using an artificial rainfall testbed. However, none of them took into account the impact of stratigraphic lithology on slope stability. Using indoor simulated rainfall experiments, Zhishui

Y. Guo (✉) · Y. Du · W. Shan · C. Zhang
Institute of Cold Regions Science and Engineering, Northeast Forestry University, Harbin, China
e-mail: ying-guo@nefu.edu.cn; yating@nefu.edu.cn; shanwei@nefu.edu.cn; chengcheng@nefu.edu.cn

Liang et al. (Liang et al. 2020) investigated the effects of slope angle, rainfall intensity, and vegetation coverage on sandstone slopes, and concluded that rainfall intensity has the greatest impact on slopes. Researchers, both domestically and internationally, agree that, according to the analysis of the above research, rainfall causes sandstone and mudstone slopes to become unstable. However, there are few studies on landslides caused by rainfall infiltration in sandstone-covered mudstone formations. Determining the crucial range of landslides in intricate rocks under different rainfall conditions is thus necessary.

In order to further deepen the understanding of mudstone softening caused by rainfall infiltration, this paper takes the typical landslide along the Heishan Village to the Jixi section of the Dan-A Highway Expansion Project as an example. Based on extensive fieldwork and laboratory tests, the landslide mechanism and instability state under different rainfall conditions are studied by numerical analysis. Additionally, the influence of different rainfall intensities and duration on the stability of sandstone-covered mudstone slopes is analyzed. Therefore, this case is used to explore the causes of landslides in such slopes so as to prevent landslide disasters better and provide a reference for highway construction in the world's sandstone–mudstone distribution areas.

This article is well aligned with the title and aims of the new ICL book series, and contribute to the KLC 2023 Landslide Commitment activities.

2 Regions and Methods

2.1 Study Area

The research object of this article is the road section of the renovation and expansion project, which is Dan-A highway expansion project from Heishan village to Jixi. The geographical location of the study area is 44°58'8" N and 130°42'8" E, with a height of 438.5 m, as indicated in Fig. 1. The study area is near the permafrost degradation zone, which greatly influences mudstone (Obu et al. 2019; Shan et al. 2022). According to the survey, this road section is excavated by cutting with a maximum slope excavation depth of 18.8 m. As soon as the construction was finished at the end of October 2019, the mudstone of the first-grade slope in the cutting was softened and disintegrated by water due to exposure. The degradation of permafrost causes the pores of mudstone to enlarge, and the mudstone softens faster when rain penetrates the mudstone. This process also led to the collapse of sandstone on the secondary slope. Subsequently, numerous collapses and significant landslides started to

happen. The maximum landslide angle of the slope is 29.81°, and the length is 33.21 m (Fig. 2).

2.2 Meteorology and Hydrology

The research region is in the mid-latitude zone, and belongs to the middle temperate continental monsoon climate zone. Climate change in the seasons is considerable: the spring is drought and windy, the summer is hot and brief with concentrated rain, the fall is chilly and cooling, and the winter is chilly and long. The annual sunshine time is 2565 h, the annual average temperature is 4.2 °C, and the extreme maximum temperature is 38 °C, the extreme minimum temperature is −37 °C. The annual average rainfall is 540 mm, and the period is concentrated from June to August, accounting for more than 60% of annual rainfall. The average frost-free period is 144 days. The ground temperature is lower than 0 °C for 5 months of the year, the permafrost layer is 1.5~2.0 m, the standard freezing depth is 2.0 m, and the maximum freezing depth can reach 2.2 m (Wei et al. 2011; Lu et al. 2012). Strong sunlight and precipitation make it simple for the slope to be in the cycle of water saturation and drying crack. Strong sunlight causes mudstone to weather quickly and lose shear strength completely. In addition, precipitation causes mudstone to relax and soften and changes the structure of it, all of which cause the slope to become unstable.

2.3 Stratigraphic Lithology

The stratum lithologic serves as the foundation for studying landslides. The slope is located in a low hill area with a complicated distribution of geologic rock layers, the terrain is highly undulating with the natural slope of 10~35°, and a relative height difference within 100 m. Based on geological exploration and sampling, geological survey maps were mapped, and the soil was drilled on the site of the study area. The composition of the rocks was determined through indoor tests. The slope is covered with Quaternary residual slope (Q^{del}), which is mainly clay mixed with clastic rock and gravel; the underlying bedrock is weathered sandstone, mudstone, weathered conglomerate, and strongly weathered conglomerate of Lower Cretaceous Muling Formation (K^{lm}). Rainwater can pass through the upper sandstone layer and be blocked by the lower mudstone layer, creating a water-rich layer in the mudstone layer. The mudstone softens, breaks in water, and creeps towards the road, which is insufficient to support the force of the sandstone above. The sandstone is

Fig. 1 Distribution of permafrost in Northeast China and the project location of the study area

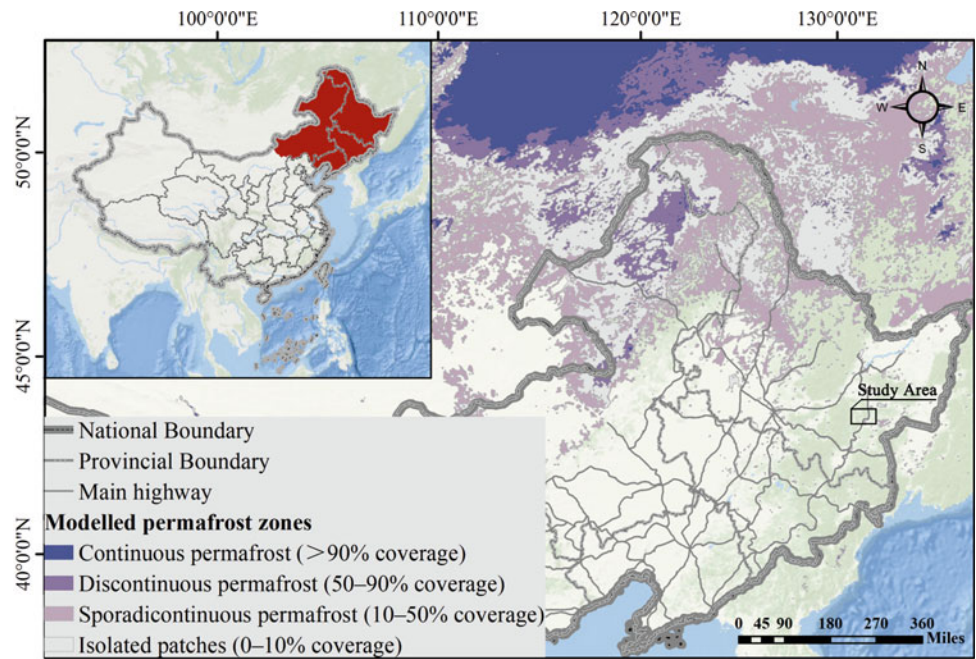


Fig. 2 Landslide of the study area

then broken up into blocks, causing a continual collapse and landslide.

3 Model Building

3.1 Mathematical Model

In the analysis of the seepage flow of the slope under rainfall conditions, the flow of rainwater in unsaturated soil and saturated soil below the groundwater level is a two-dimensional saturated–unsaturated problem. Darcy’s Law is still used to describe the law of saturated and unsaturated seepage. The two-dimensional saturated and

unsaturated seepage control equation has the following form (Bodman and Colman 1944):

$$\frac{\partial}{\partial x} \left(k_x \frac{\partial h_w}{\partial x} \right) + \frac{\partial}{\partial y} \left(k_y \frac{\partial h_w}{\partial y} \right) + Q = m_w \gamma_w \frac{\partial h_w}{\partial t} \quad (1)$$

where k_x and k_y are the hydraulic conductivity of the soil in x and y directions, h_w is hydraulic pressure, Q is the boundary flow of the model, γ_w is the volumetric weight of water, and m_w is the slope of the soil moisture characteristic curve. x is the horizontal direction and y is the vertical direction in two-dimensional space.

The finite element equations are solved in combination with the following boundary conditions.

Head boundary:

$$k \frac{\partial h_w}{\partial n} \Big|_{\Gamma_1} = h(x, y, t) \quad (2)$$

Fluid boundary:

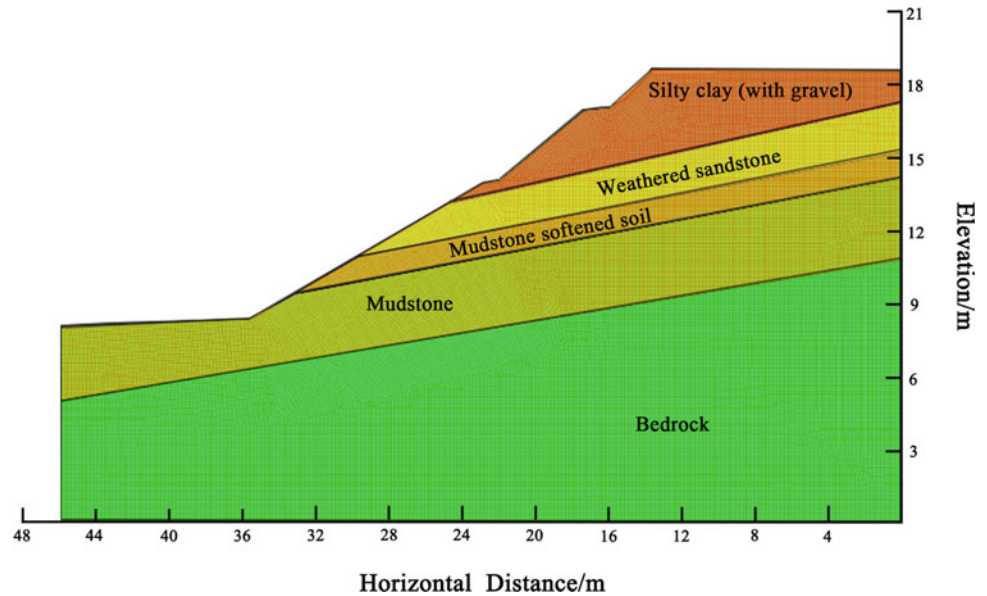
$$k \frac{\partial h_w}{\partial n} \Big|_{\Gamma_2} = q(x, y, t) \quad (3)$$

where n is the external normal direction of the boundary Γ_1 and Γ_2 , h and q are known functions.

The initial conditions for the non-constant seepage:

$$h(x, y, 0) = h_0(x, y) \in \Omega \quad (4)$$

Fig. 3 Finite element mesh schematic diagram of the main slide's cross-section



3.2 Geometric Model and Physical Parameters

According to the geological survey report, the main slide surface was selected as the calculation profile, and a two-dimensional geometric model of 46 m in length and 19 m in height was established (Fig. 3). It can be separated into three sections, including the sliding surface (mudstone softened soil), sliding mass (weathered sandstone, silty clay), and sliding bed (mudstone). The landslide model uses PLANE82 elements from ANSYS Library, with 6379 nodes and 6218 finite elements.

In order to study the failure mechanism of the cutting slope clearly, it is very necessary to conduct indoor tests on the soil properties of undisturbed soil samples in the study area. The laboratory tests include the natural moisture content test, the liquid limit and plastic limit test, the proportion test, the soil-grain size analysis test, the direct shear test, and the variable head permeability test. As a result, the parameters of the sliding zone soil model that were fitted based on engineering geological survey data and laboratory test results are shown in Table 1.

3.3 Boundary Conditions and Initial Conditions of the Model

According to the landslide mechanism of mudstone softening caused by rainfall, the phreatic line is selected on the interface between mudstone and sliding bed in a natural state. According to a detailed geological survey, the groundwater level at the landslide is below the sliding bed, and the study area is a cutting slope, so the problem of the landslide is not related to the groundwater level. Therefore, the model conditions do not consider the groundwater level. In addition, the following boundary conditions are also established.

Infiltration boundary: The upper boundary is the fluid boundary of rainfall infiltration. The pore water pressure is supposed to be numerically equal to the matrix suction, and the slope surface pressure is assumed to be atmospheric pressure. It is assumed that the bottom of the model is an impervious boundary, and the flow rate is set to zero. The vertical boundary of the slope model varies with the rainfall intensity. When the rainfall intensity is greater than the permeability coefficient of the soil, the boundary is the rainfall intensity. Otherwise, it is the soil permeability coefficient.

Table 1 Table of calculation parameters

Name of the soil	Volume content of soil ($\text{m}^3 \cdot \text{m}^{-3}$)	Specific weight of soil ($\text{KN} \cdot \text{m}^{-3}$)	Cohesion (kPa)	Internal friction angle ($^\circ$)	Saturated hydraulic conductivity ($\text{cm} \cdot \text{s}^{-1}$)
Silty clay (with gravel)	0.44	26.3	38.101	26.2	0.35×10^{-5}
Weathered sandstone	0.41	26	20	15.1	0.05×10^{-5}
Mudstone	0.43	23.4	5.2868	37.2	0.98×10^{-4}
Mudstone softened soil	0.72	24.9	52.871	32.3	5.84×10^{-6}

Table 2 Rainfall design table under different working conditions

Working condition	Rainfall intensity (mm/d)	Rainfall duration (d)
Natural working condition	–	–
Working condition I	80	0.5
Working condition II	80	1
Working condition III	40	2
Working condition IV (1d stagnation)	80	1

Stress boundary: The bottom of the model is fixed both horizontally and vertically, whereas the left and right boundaries are fixed horizontally and free vertically.

In order to analyze the influence of rainfall intensity, duration, and stagnation time on the stability of soil slope, the calculation and analysis scheme is established and shown in Table 2.

4 Results

Coupling the fluid and solid stress fields during rainfall infiltration analysis is necessary. Geo-Studio and ANSYS software are combined to conduct a numerical simulation of landslides based on the investigation of the interaction. Geo-Studio is used to analyze the cutting slope stability and obtain the most unfavorable rainfall condition when the slope is damaged. The seepage field of the slope is simulated by using the seepage analysis module (SEEP/W) in Geo-Studio. Then, the pore water pressure results were imported into the slope stability analysis module (SLOPE/W) to calculate the stability coefficients of the slope under various working conditions. In addition, considering the deformation behavior of the solid under the influence of the seepage field, and the influence of the solid deformation on the seepage field, the specific weight of soil, cohesion, and the internal friction angle of landslide soil under different content is assigned in ANSYS. On the basis of the strength reduction method, ANSYS software is used to calculate and analyze the critical state and the development process of slope instability under rainfall infiltration.

4.1 Slope Stability Analysis Under Natural Working Conditions

The geological survey has determined that the groundwater level is within the sliding bed and does not pass through the sliding zone soil; thus, only the unsaturated state is taken into consideration for the slope stability of the cutting slope in its natural state. The Morgenstern–Price method is used to analyze the overall stability of the slope, and the Bishop method is used to automatically search the local stability of the most unstable slip surface. The stability factors obtained by these

two methods are 1.350 and 1.289, respectively, which are stable. The front slope toe of the landslide is the first unstable location in the natural state. This section of the highway is an expansion project; serious excavation was required to meet the road-smoothness requirements. As a result, the location of the foot of the slope was influenced by the construction excavation, creating a local void at the foot and increasing the slope angle of the slide surface here. This process increases the local sliding force and reduces the safety stability coefficient.

4.2 Slope Stability Analysis Under Different Rainfall Conditions

This paper examines the impact on the stability of sandstone-covered mudstone cutting slopes, considering rainfall infiltration from three perspectives: rainfall duration, intensity, and rainfall lag time.

(1) Analysis of pore water pressure variation for different working conditions

Compare the pore water pressure maps of working conditions I and II when the rainfall intensity is the same, but the rainfall duration varied (see Fig. 4). The pore water pressure contours and the phreatic line is basically parallel in the two conditions, and the distribution has a certain regularity. When the rate of precipitation is 80 mm/d, the rising of the saturation line is proportional to the rainfall duration. The pore water pressure change after half a day of rainfall duration in Case I is more than after 1 day in Case II, and the seepage change is more noticeable in Case I than Case II. When rainfall occurs, the soil moisture is low and the permeability is strong. As the rainfall continues, the soil moisture increases continuously and there is a transition from unsaturated to saturated soil in the sliding zone, and the suction of the soil to water decreases, which in turn leads to the permeability of Case II being smaller than that of Case I. The above phenomenon is consistent with the change rule that the unsaturated hydraulic conductivity decreases with the increase in soil moisture. Additionally, by comparing the phreatic line's positions, it can be seen that the phreatic line in Condition II is higher than in Condition I, which is clearly

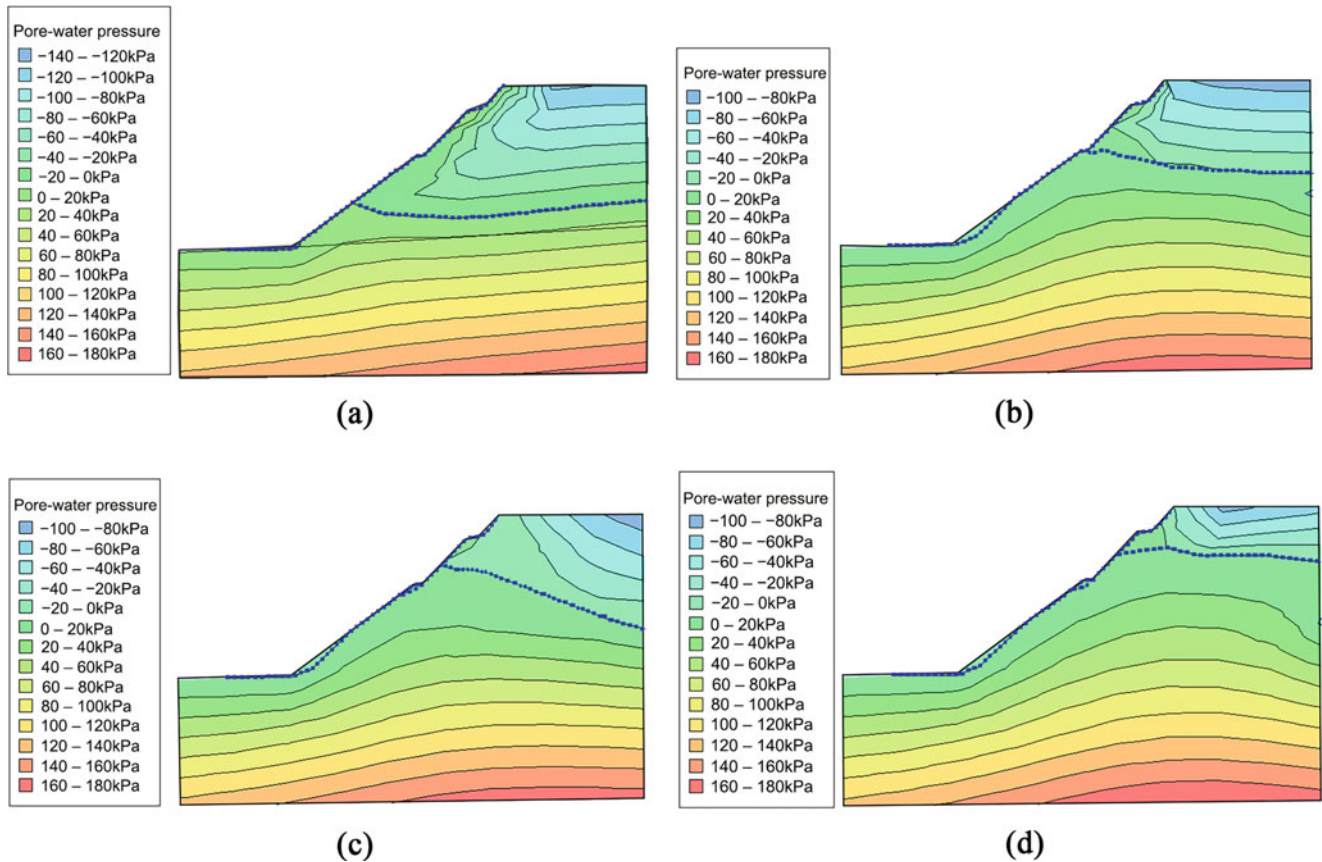


Fig. 4 Pore water pressure distribution for each working condition, where the blue dashed line is the phreatic line. (a) Working condition I; (b) Working condition II; (c) Working condition III; (d) Working condition IV

affected by the total rainfall. In the layer of mudstone and weathered sand, rainfall infiltration makes the sliding zone soil transition from unsaturated to saturated. With continuous rainfall, the unsaturated part of the sliding zone soil decreases, and the negative pore water pressure decreases gradually. A new saturated zone is formed between sandstone and mudstone.

The pore water pressure maps of working conditions II and III were compared, when the total amount of precipitation is the same but the intensity of the precipitation varies. The pore water pressure of rainfall intensity 80 mm/d varies more quickly than that of rainfall intensity 40 mm/d when the rainfall amounts are equal, but the total change value of pore water pressure is the reverse. In the early stage of rainfall, rainwater quickly fills all the voids and cracks and infiltrates the lower layer because the natural moisture of the surface soil is low. However, because of the high intensity of the rainfall, when the intensity exceeds the saturated hydraulic conductivity of the soil itself, rainwater will form runoff along the slope surface and will not infiltrate into the soil. This process corresponds to working Condition II. In Working condition III, the rainfall intensity is low, but the duration is long. The rain will infiltrate the soil as time passes, increasing the saturation zone and the gravity of the slip zone soil

and lifting the phreatic line obviously, which reduces the stability of the landslide in this condition.

Compare the pore water pressure maps of Conditions II and IV, where the stagnation time varies, but the rainfall time and intensity are the same. After 1 day of rain stoppage, the pore water pressure on the surface of the cutting slope decreases significantly. The rise of the saturation line in working condition IV is mainly due to the one-day stagnation, which is correlated with the hydraulic conductivity of the soil layer in the slip zone and the creep of mudstone.

Pore water pressure diagrams were compared under natural and other working conditions (see Fig. 5). The height of the saturation line, moisture content, and soil gravity greatly change under the test conditions. These phenomena indicate that the downslope strength of sliding soil increases, and the anti-sliding force and slope stability decrease. It also accurately reflects the fact that rainfall is a notable consideration in forming the landslide.

(2) Slope stability analysis for each working condition

Different calculation methods obtain the stability coefficient of the cutting slope under different working conditions, and the average value of these slope stability coefficients is used

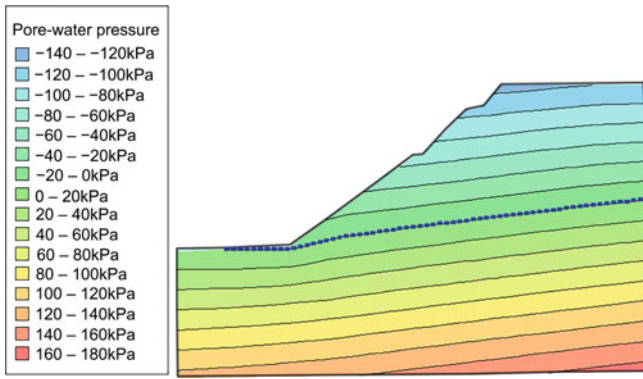


Fig. 5 Pore water pressure distribution in a natural state, where the blue dashed line is the phreatic line

as the final reference index. Figure 6 displays the statistics of the slope stability coefficients.

As shown in Fig. 6, increasing rainfall intensity causes the stability coefficient of slopes in the study area to trend downward for the same rainfall duration. In working condition IV, the stability coefficient is less than 1.05, at which point the slope was damaged. In order to determine the critical state of failure in the study area, it is necessary to analyze the deformation and damage of different time points under working condition IV.

4.3 Analysis of Landslide Deformation and Damage in the Study Area

Numerous researchers at home and abroad have investigated the combination of the strength reduction method and numerical analysis to calculate the stability coefficient of the slope in order to overcome the drawback that the limit equilibrium method cannot give the stability coefficient of slope intuitively (Zienkiewicz et al. 1975; Griffiths and Lane 1999; Zheng et al. 2005; Cheng et al. 2007; Yuan et al. 2016). The strength reduction method is an analytical method developed based on the Mohr Coulomb theory to quantitatively calculate the stability of geotechnical bodies using numerical simulation techniques. It can calculate the stability coefficient of slope based on the shear strength index of soil (Huang and Jia 2009), which is applicable to the research object of this paper. The principle of the strength reduction method is to continually reduce the rock slope’s shear strength parameter

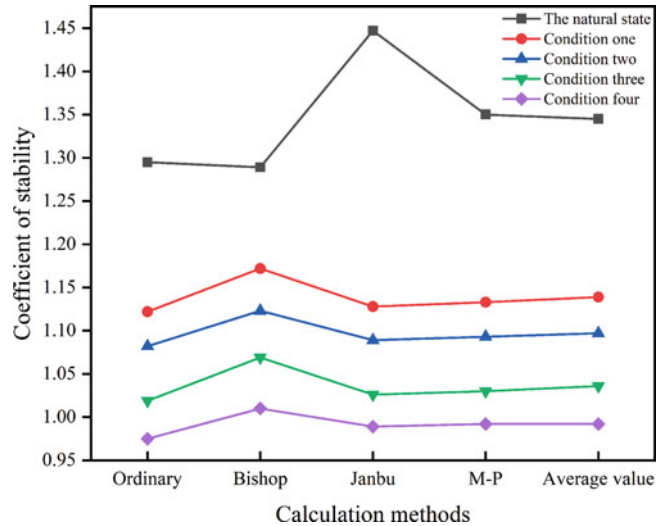


Fig. 6 Statistics of stability coefficients for different working conditions in the study area

and repeat the iterative calculation until the slope reaches the critical failure state. The reduction coefficient at this time represents the stability coefficient of the slope. That is the following:

$$C' = \frac{C}{FS} \tag{5}$$

$$\phi' = \arctan\left(\frac{\tan \phi}{FS}\right) \tag{6}$$

The slope stability coefficient calculated by working condition II is 1.097, while that calculated by working condition IV is 0.992. Rainwater infiltration by rainfall stagnation is the primary cause of slope instability. In order to analyze the critical state when the slope is unstable, the calculation and analysis scheme, as shown in Table 3, is established.

The plastic strain diagrams and X-axis displacement diagrams of the four cases are analyzed (see Figs. 7 and 8).

As indicated in Fig. 7, the foot of the slope experiences the maximal strain, and the maximum strain at the critical state of slope instability is 0.078. The primary cause of the strain at the foot is that rainfall causes the mudstone to soften and the strength to deteriorate. So, the stresses accumulate here. Secondly, the location of the foot of the slope was influenced by the construction excavation, creating a local void at the

Table 3 Rainfall design table under different working conditions of rainfall stagnation

Working condition	Rainfall intensity (mm/d)	Rainfall duration (d)	Rainfall stagnation (d)
Working condition V	80	0.4	—
Working condition VI	80	1	—
Working condition VII	40	1	0.2
Working condition VIII	80	1	0.3

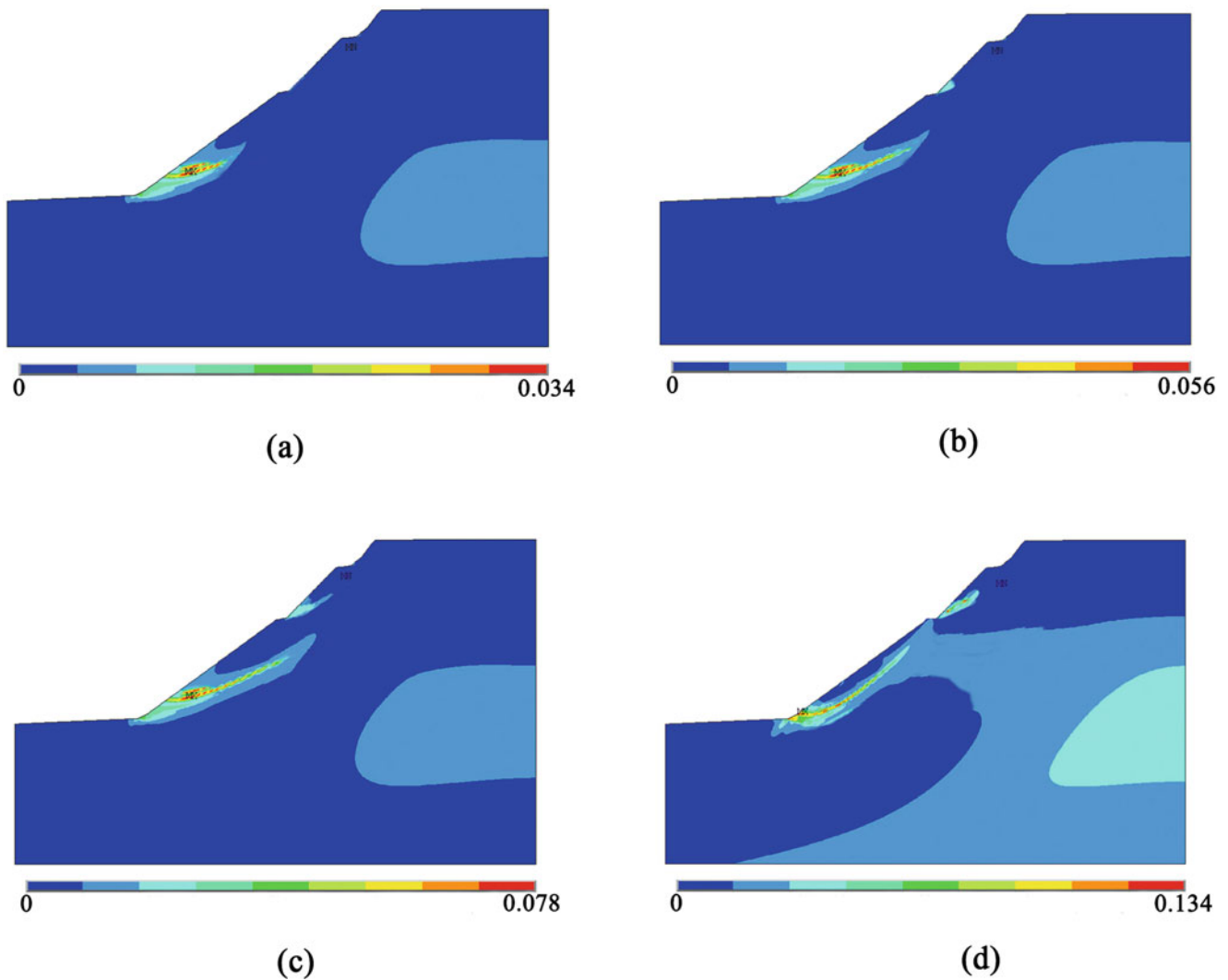


Fig. 7 Plastic strain diagrams. (a) Working condition V; (b) Working condition VI; (c) Working condition VII; (d) Working condition VIII

foot of the slope. The local cavity increases the slope angle of the slide surface here, increases the local sliding force, and reduces the safety stability coefficient. Similarly, it can be seen from Fig. 7 that the critical state of slope failure is that the rainfall intensity of 80 mm lasts for 1 day and stagnates for 5 h. At this time, the plastic strain runs through the entire landslide zone, causing the cutting slope to fail.

Figure 8 displays the maximum displacement of the X-axis of the slope top. Compared with the four plots, it can be seen that the maximum displacement decreases from 466.025 mm to 151.834 mm with the increase in rainfall, indicating that the slope is prone to local instability.

5 Conclusions

In northeast China, the sandstone-covered mudstone layer is a slide-prone stratum, and rainfall infiltration is the primary factor inducing cutting slope landslides.

In this paper, the causes of the landslide as well as the characteristics and process of mudstone softening, are recorded and analyzed in the expansion project of the Heishan village to the Jixi section of the Dan-A highway. The landslide mechanism and instability state of the study area under different working conditions are studied by finite element numerical analysis and the following conclusions are drawn.

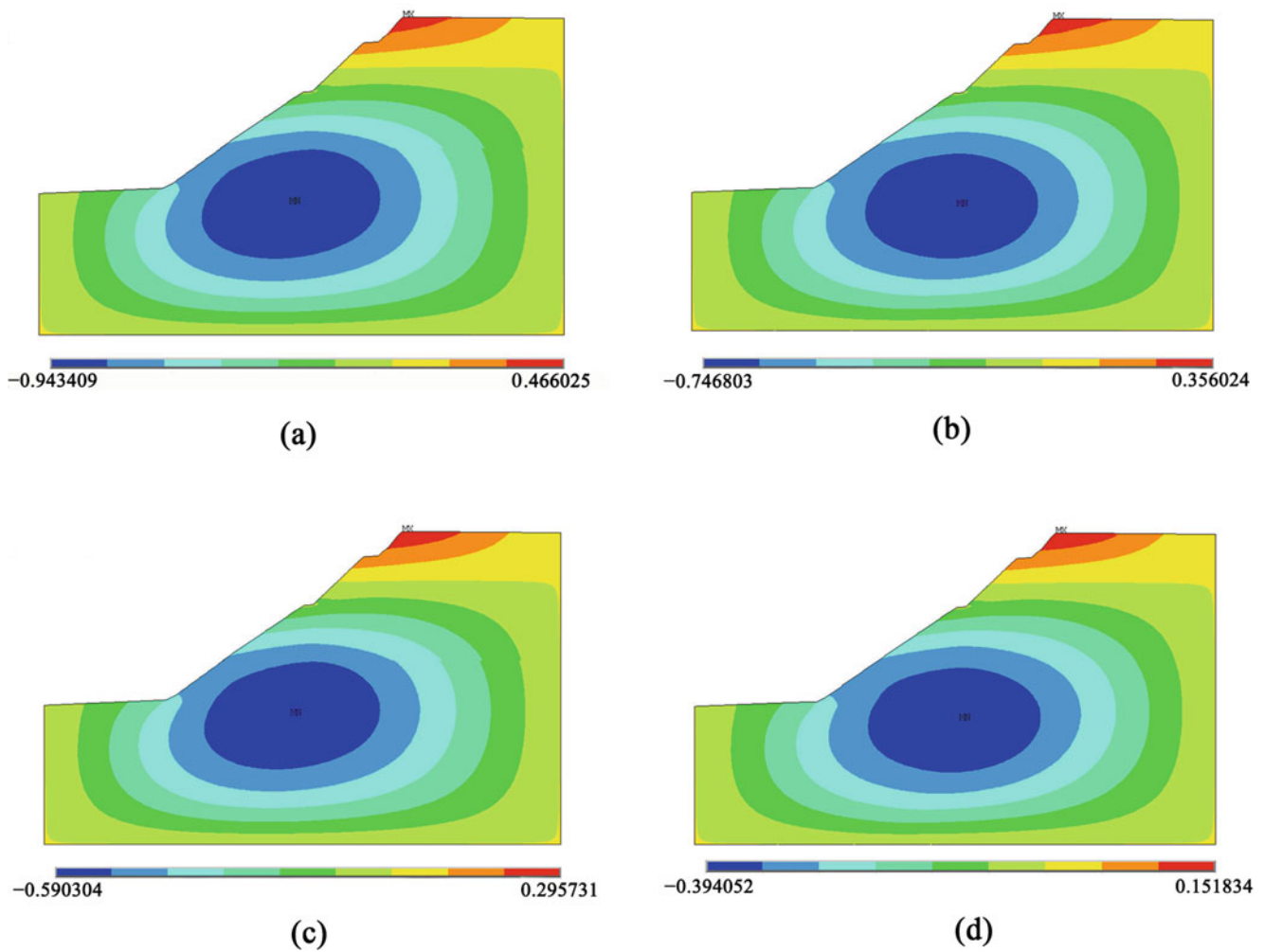


Fig. 8 X-direction displacement diagrams at the top of the slope, where the unit is m. (a) Working condition V; (b) Working condition VI; (c) Working condition VII; (d) Working condition VIII

- (1) Rainfall duration, rainfall intensity, and rainfall lag conditions will decrease the stability of the cutting slope in the study area. When the precipitation is the same, the duration of rainfall is positively correlated with the change of pore water pressure and the rise of phreatic line. However, rainfall intensity is negatively correlated with pore water pressure and phreatic line change. When the rainfall intensity is the same, the change of pore water pressure will increase with the extension of rainfall time, and the maximum change rate of pore water pressure is in the initial rainfall stage. In addition, the influence of rainfall on the slope has a lag effect, which may be related to the hydraulic conductivity of sliding zone soil and mudstone creep.
- (2) It is concluded that the critical state of slope instability in the study area is when the rainfall intensity is 80 mm, the rainfall intensity is 1 day, and the stagnation is 5 h. It is

- primarily caused by rainfall intensity being greater than the infiltration rate and hysteresis effect.
- (3) In the slope stress analysis, the first instability is the front slope toe of the landslide. The maximum strain at the critical state of slope instability is 0.078. The first reason is that rainfall makes mudstone soften and strength attenuate, so the stress gathers here. Second, improper excavation makes the toe of the cutting slope partly free, resulting in a decrease in the stability coefficient. In the X-direction displacement analysis at the top of the slope, the maximum displacement decreases with the increase in rainfall, indicating that the slope is easy to instability. In addition, with the increase in rainfall infiltration time, the plastic strain penetrates from the mudstone softening layer to the whole slip surface, which verifies that the mudstone is extremely easy to soften and disintegrate in water.

- (4) The analysis of the influence of different rainfall factors on slope stability and the critical condition of slope instability in this study can provide an effective basis for landslide early warning work in sandstone–mudstone interbedding areas. Take the rainfall value under the critical condition of slope instability, as the rainfall threshold can effectively prevent the occurrence of such landslide disasters.

The results of this paper contribute to the Kyoto Landslide Commitment 2023 for practical applications and the benefit of society to promote global understanding and reduction of landslide disaster risk.

Acknowledgments We would like to thank all staff members who contributed to this study who are not named here.

We thank the National Natural Science Foundation of China (Grant No. 41641024) and Heilongjiang Province Key R&D projects (GZ20220049) and Carbon Neutrality Fund of Northeast Forestry University (CNF-NEFU) and the Science and Technology Project of Heilongjiang Communications Investment Group (Grant No. JT-100000-ZC-FW-2021-0182) for providing financial support and the Field scientific observation and research station of the Ministry of Education-Geological environment system of permafrost area in Northeast China (MEORS-PGSNEC).

References

- Bodman GB, Colman EA (1944) Moisture and energy conditions during downward entry of water into soils. *Soil Sci Soc Am J* 8:116–122. <https://doi.org/10.2136/sssaj1944.036159950008000C0021x>
- Cheng YM, Lansivaara T, Wei WB (2007) Two-dimensional slope stability analysis by limit equilibrium and strength reduction methods. *Comput Geotech* 34(3):137–150. <https://doi.org/10.1016/j.compgeo.2006.10.011>
- Griffiths DV, Lane PA (1999) Slope stability analysis by finite elements. *Géotechnique* 49(3):387–403. <https://doi.org/10.1680/geot.1999.49.3.387>
- He ZM, Yu T, Cai ZX, Qin YQ (2012) Finite element analysis for soil slope stability considering rainfall infiltration influence. *Min Metall Eng* 32(1):9–11+16. <https://doi.org/10.3969/j.issn.0253-6099.2012.01.003>
- Kong F, Wang YF, Fang J, Lyu LL (2017) Pre-estimation on variations of rainfalls with different intensities and their contributions to total rainfall under emission scenarios in China from 2006 to 2100. *Water Resour Hydropower Eng* 48(12):14–21. +40. <https://doi.org/10.13284/j.cnki.rddl.002962>
- Li Q, Wang YM, Zhang KB, Yu H, Tao ZY (2020) Field investigation and numerical study of a siltstone slope instability induced by excavation and rainfall. *Landslides* 17(6):1485–1499. <https://doi.org/10.1007/s10346-020-01396-5>
- Liang Z, Liu H, Zhao Y, Wang Q, Wu Z, Deng L, Gao H (2020) Effects of rainfall intensity, slope angle, and vegetation coverage on the erosion characteristics of Pisha sandstone slopes under simulated rainfall conditions. *Environ Sci Pollut Res* 27(15):17458–17467. <https://doi.org/10.1007/s11356-019-05348-y>
- Lu YZ, Song GS, Sun L, Yang CG, Zhang JG, Chen YH, Chen MJ, Gao L, Liu Y (2012) The analysis of distribution characteristics of main meteorological factors in the Northeast China. *Chin Agric Sci Bull* 28(14):290–294. <https://doi.org/10.3969/j.issn.1000-6850.2012.14.057>
- Luo XQ, Liu DF, Wu J, Cheng SG, Shen H, Xu KX, Huang XB (2005) Model test study on landslide under rainfall and reservoir water fluctuation. *Chin J Rock Mech Eng* 14:2476–2483. <http://rockmech.whrsm.ac.cn/CN/abstract/abstract21665.shtml>
- Huang MS, Jia CQ (2009) Strength reduction FEM in stability analysis of soil slopes subjected to transient unsaturated seepage. *Comput Geotech* 36:93–101. <https://doi.org/10.1016/j.compgeo.2008.03.006>
- Obu J, Westermann S, Bartsch A, Berdnikov N, Christiansen HH, Dashtseren A, Delaloye R, Elberling B, Etzelmüller B, Kholodov A, Khomutov A, Kääh A, Leibman MO, Lewkowicz AG, Panda SK, Romanovsky V, Way RG, Westergaard-Nielsen A, Wu T, Yamkhin J, Zou D (2019) Northern hemisphere permafrost map based on TTOP modelling for 2000–2016 at 1 km² scale. *Earth Sci Rev* 193:299–316. <https://doi.org/10.1016/j.earscirev.2019.04.023>
- Pan D, Yan M (2016) The summary of research on the softening and disintegration mechanism of mudstone. *Yunnan Water Power* 32(5): 28–30+33. <https://doi.org/10.3969/j.issn.1006-3951.2016.05.00>
- Peng TG (2013) Characteristics of a certain landslide in inter-bedded area of mudstone and argillaceous siltstone in Nanning and its control measures. *Miner Resour Geol* 27(05):421–423. <https://doi.org/10.3969/j.issn.1001-5663.2013.05.013>
- Rinaldi M, Casagli N (1999) Stability of streambanks formed in partially saturated soils and effects of negative pore water pressures: the Sieve River (Italy). *Geomorphology* 26(4):253–277. [https://doi.org/10.1016/S0169-555X\(98\)00069-5](https://doi.org/10.1016/S0169-555X(98)00069-5)
- Shan W, Ma M, Guo Y, Zhang C (2022) Numerical analysis of the influence of foundation replacement materials on the hydrothermal variation and deformation process of highway subgrades in permafrost regions. *Water* 14(17):2642. <https://doi.org/10.3390/w14172642>
- Tang ZH, Chen Z, Nong CS (2009) The distortion principle and protection method of Longlin-Baise highway tertiary side slope. *West China Commun Sci Technol* (9):11–14+19. <https://doi.org/10.13282/j.cnki.wccst.2009.09.003>
- Wei Z, Jin HJ, Zhang JM, Yu SP, Han XJ, Ji YJ, He RX, Chang XL (2011) Prediction of permafrost changes in northeastern China under a changing climate. *Sci China Earth Sci* 41(1):74–84. <https://doi.org/10.1007/s11430-010-4109-6>
- Yuan W, Hu YH, Li XC, Bai B, Wang W, Chen XJ, Ji XL (2016) An approach to determining critical slip surface based on displacement field analysis. *Rock Soil Mech* 37(6):1791–1798. <https://doi.org/10.16285/j.rsm.2016.06.032>
- Zhu SD, Cao XS, Liu Y (2022) Model experimental research on disintegration behaviors of argillaceous rock. *Mod Transp Technol* 19(4): 1–6. <https://doi.org/10.3969/j.issn.1672-9889.2022.04.001>
- Zheng H, Liu DF, Li CG (2005) Slope stability analysis based on elastoplastic finite element method. *Int J Numer Methods Eng* 64(14): 1871–1888. <https://doi.org/10.1002/nme.1406>
- Zienkiewicz OC, Humpheson C, Lewis RW (1975) Associated and non-associated visco-plasticity and plasticity in soil mechanics. *Géotechnique* 25(4):671–689. <https://doi.org/10.1680/geot.1975.25.4.671>

Open Access This chapter is licensed under the terms of the Creative Commons Attribution 4.0 International License (<http://creativecommons.org/licenses/by/4.0/>), which permits use, sharing, adaptation, distribution and reproduction in any medium or format, as long as you give appropriate credit to the original author(s) and the source, provide a link to the Creative Commons license and indicate if changes were made.

The images or other third party material in this chapter are included in the chapter's Creative Commons license, unless indicated otherwise in a credit line to the material. If material is not included in the chapter's Creative Commons license and your intended use is not permitted by statutory regulation or exceeds the permitted use, you will need to obtain permission directly from the copyright holder.



Part III

Review Articles



Post-formation Behavior of Hattian Landslide Dam and Post-breaching Situation

Ahsan Sattar and Kazuo Konagai

Abstract

The Hattian Bala landslide dam, formed by the 8th October 2005 earthquake, provided a rare opportunity to observe and quantify the changes in the body of the debris deposit after its formation. The authors described post-formation behaviors of the debris mass, breaching-inflicted changes of the debris mass, and upstream and downstream reaches in their referred publications. This paper summarizes the findings from the observations of the two referred papers and the comments on the situation of the landmass after almost a decade of post-breaching of landslide mass.

Keywords

Landslide · Breach · Post-breach · Flood · Earthquake

1 Introduction

The October 8, 2005, Kashmir earthquake (epicenter 34°29' 35" N, 73°37'44" E, focal depth 26 km, 7.6 Mw (USGS)) caused widespread destruction in northern areas of Pakistan and Pakistan-administered Kashmir, killing more than 86,000 people. The earthquake also triggered a massive landslide 3.5 km upstream of Hattian-Bala town near the south-eastern end of the activated Balakot-Bagh fault.

The debris deposit resulting from the landslide blocked two tributaries of the Karli branch of the Jhelum River, forming Karli Lake (the large lake) and Tang Lake (the small lake). This landslide dam (called the Hattian Dam) became a significant concern for the people living along the lower reaches of the Karli and the Jhelum Rivers since the failure of such landslide dams usually results in catastrophic

downstream flooding causing loss of lives, houses, and infrastructures.

The Hattian Dam survived the initial overtopping because a spillway was excavated across the Dam's crest as a part of the flood disaster mitigation strategy; however, the danger of catastrophic flood outbursts in the case of the dam breaching was eminent. Sattar et al. (2011) observed deformations/erosions that had been occurring to the debris deposit since the debris dam was formed and estimated the potential outburst flood in case of breaching of the landslide dam. The simulated scenario of the flood water outburst indicated that about 40 buildings along the right bank of the Karli River, bounded by the Karli River on the west side and by the main road on the east side, were potentially in high-risk locations.

The Dam sustained over about 4 years and 4 months, and finally, the water of Karli Lake breached the northwestern part of the Dam on February 9th, 2010, following a continuous 5-day rainfall. As predicted earlier, the flood water engulfed many houses in Hattian Bala along the right bank of the Karli River, swallowing a boy. However, it could have been worse unless residents evacuated quickly.

Later, the water of Tang Lake also breached the northeastern lobe of the Dam during the monsoon rains from July to August 2010.

It was less likely that a flood of the same scale would occur again and cause any hazard for the downstream reach of Karli valley because a bedrock, which appeared on the scoured bottom of the breach channel, was not likely to be eroded any further. However, the remaining mass of the Hattian Bala landslide dam and its vicinity were not entirely out of danger after the breaching of the Dam.

This paper reviews the findings from the authors' observations conducted before and after the dam failure reported by Sattar et al. (2011) and Konagai and Sattar (2011), and the post-breaching behavior of the landslide dam.

A. Sattar (✉)

PARSONS Corp, Riyadh, Saudi Arabia

K. Konagai

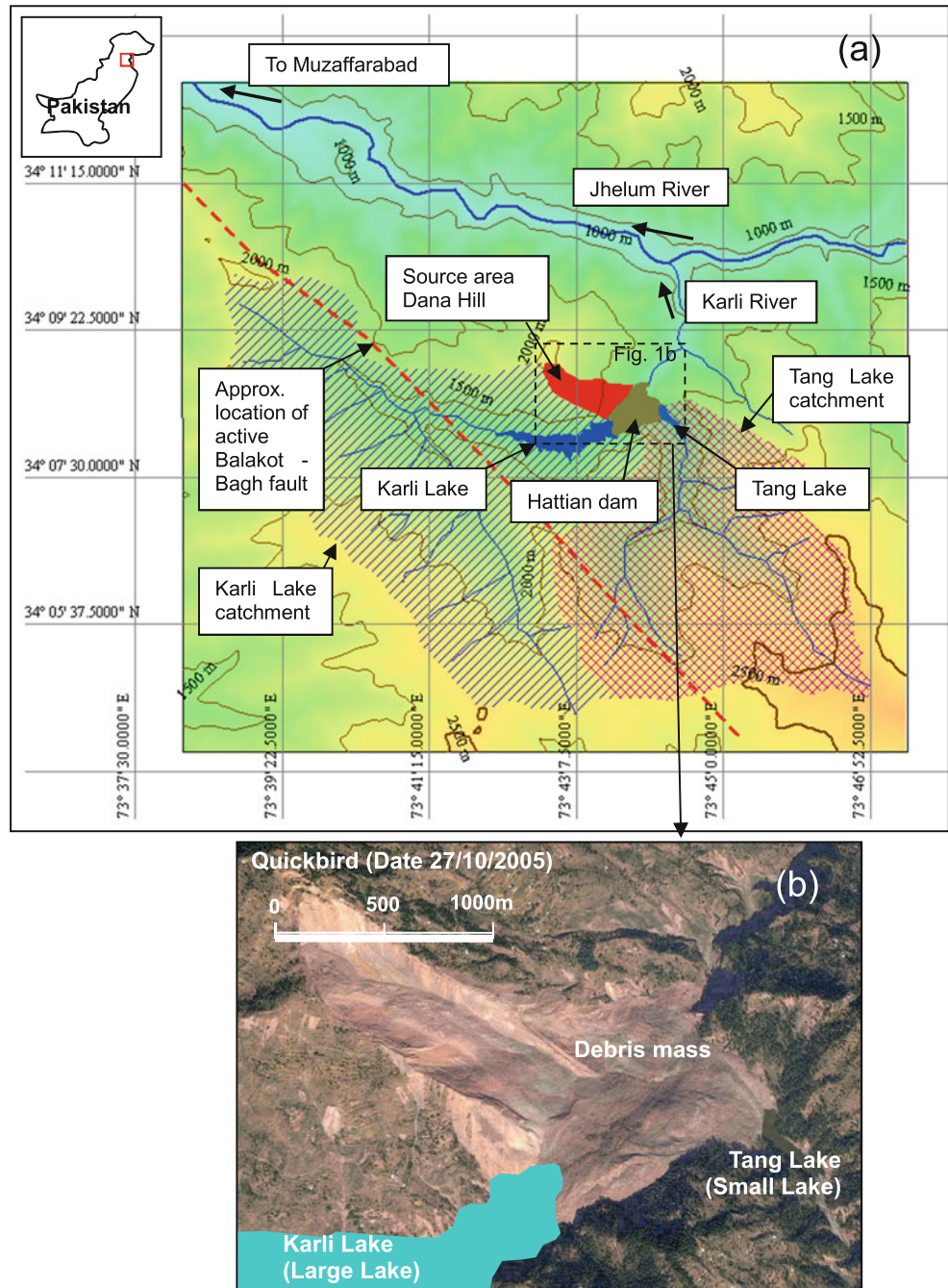
University of Tokyo, Tokyo, Japan

2 Features of Debris Deposit

The surface rupture that caused the 2005 earthquake was along the preexisting active faults or fault segments, collectively called the Balakot-Bagh fault. The Hattian-Bala landslide dam lies near the southern end of the Balakot-Bagh fault at approximately 33 km southeast of Muzaffarabad, the capital and largest city of Azad Kashmir, and 3.4 km from the fault (Fig. 1). Sattar et al. (2011) summarized the seismological and geological aspects of the region.

About 65 million m³ of Hattian landslide mass originating from Dana hill ran down the valley slope and deposited its final volume of 85 million m³ along the Karli River. Immediately after the earthquake, the water levels in the lakes started to rise; therefore, a spillway was constructed across the Dam's crest as a disaster mitigation measure against the potential breaching of the Dam. The water level in Karli Lake reached the maximum invert level (approx. 1354 m elevation above mean sea level, AMSL hereafter) of the artificial spillway in April 2007 and started spilling over. The 18 m deep

Fig. 1 (a) Map of Hattian area showing the source area of Hattian landslide mass, Hattian landslide dam, Karli Lake and Tang Lake with their catchment areas, approximate location of the active Balakot-Bagh fault and the main tributaries of the Karli River and Jhelum River. (b) Quick bird image (27/10/2005) of the Hattian dam Konagai and Sattar (2011)



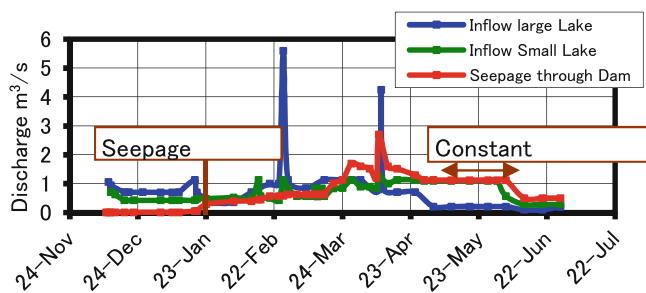


Fig. 2 Discharge data from WAPDA (2006)

excavation of the spillway limited the maximum storage capacity of Karli Lake to 62 million m^3 from its initial 86 million m^3 corresponding to the natural overtopping level, considerably reducing the possible flood magnitude in the case of breaching of the Dam. About 5 million m^3 of water was impounded in Tang Lake.

The Water and Power Development Authority of Pakistan (WAPDA) monitored the landslide dam after its formation. Figure 2 shows the measured inflow of the large lake, the small lake, and seepage through the landslide mass from December 2005 till June 2006, and Fig. 3 shows the water levels in the Small and the large lakes measured during the same time (WAPDA 2006). From the measured water levels and seepage through the landslide mass, Sattar et al. 2011 concluded that the surface part of the dam body was permeable, while the deeper part of the debris deposit was impermeable. It was a distinctive nature of the landslide dam body that larger rocks gathered along shallower and toe parts of the dam body. The small lake reached its maximum capacity of 5 million m^3 at the end of February 2006. The water level in the small lake decreased gradually after April 21st, even though the inflows to the lakes were constant, indicating that the interior of the debris deposit in front of the small lake had developed some piping erosion. The monitoring regime initiated by WAPDA ended after the water levels in the lakes were observed to be stable. The rock/earth wall lining the spillway extended only a short distance over the crest. Nonetheless, monitoring the dam site attracted less attention as the spillway performed well, and no immediate threat was imminent. Beyond the end of the spillway, the water flowed naturally over the body of the landslide mass.

Gradual toe erosion was observed from November 2008 to June 2009 (Fig. 3). A significant retrogressive erosion developed about 300 m through the toe slope at some indeterminate time. Sattar et al. (2011) inferred from the observations that the retrogressive erosion developed because of an extreme rainfall event during the off-monsoonal dry season. Sattar et al. (2011) attributed the accelerated slaking of dried mud rocks of the debris mass to the observed backward erosion.

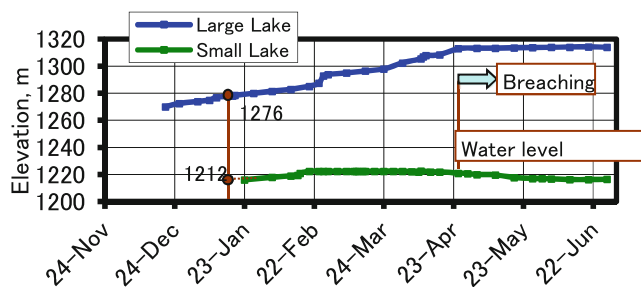


Fig. 3 Water levels of lakes measured from December 2005 till June 2006 (WAPDA 2006)

3 Observation of Changes to the Debris Deposit

Sattar et al. (2011) and Konagai and Sattar (2011) initiated a measurement regime to quantify the changes occurring in the landslide mass after its formation. Differential global positioning system (DGPS) measurements and laser scanning were included in the various techniques for quantifying deformations. The backward erosion mentioned above, which occurred somewhere between November 2008 to June 2009, resulted in the loss of approximately 65,000 m^3 of soil mass from the downstream slope of the landslide dam (Fig. 4). This event raised concerns about the potential risk of breaching. The DGPS measurements conducted over a 6 months interval (June 2009–November 2009) showed that the crest zone of the Dam settled by order of 100 mm and the zone near the head of the eroded gulch was uplifted by a few millimeters (Sattar et al. 2011). Figure 5 shows the settlement observed during the period starting from June 2009 till November 2009. The settlements were observed to be greatest (up to 100 mm) along where the thickness of the debris deposit was greater, i.e. towards the eastern side of the deposit.

Meanwhile, gradual changes were being observed along the northeastern lobe of the debris deposit, where the water from Tang Lake was seeping into the deposit of large segregated boulders and was emerging at some distances downstream. With time, there was a growing suspicion that pipes were being developed in the interior of the debris mass, as indicated by the gradual surface deformations observed over the surface of the deposit (Fig. 6).

4 Dam Break Analysis Prediction by Sattar et al. (2011)

In order to evaluate the inundation level of the flood wave from a breach of the Dam, Sattar et al. (2011) carried out a dam break analysis. The simulation was based on a down-

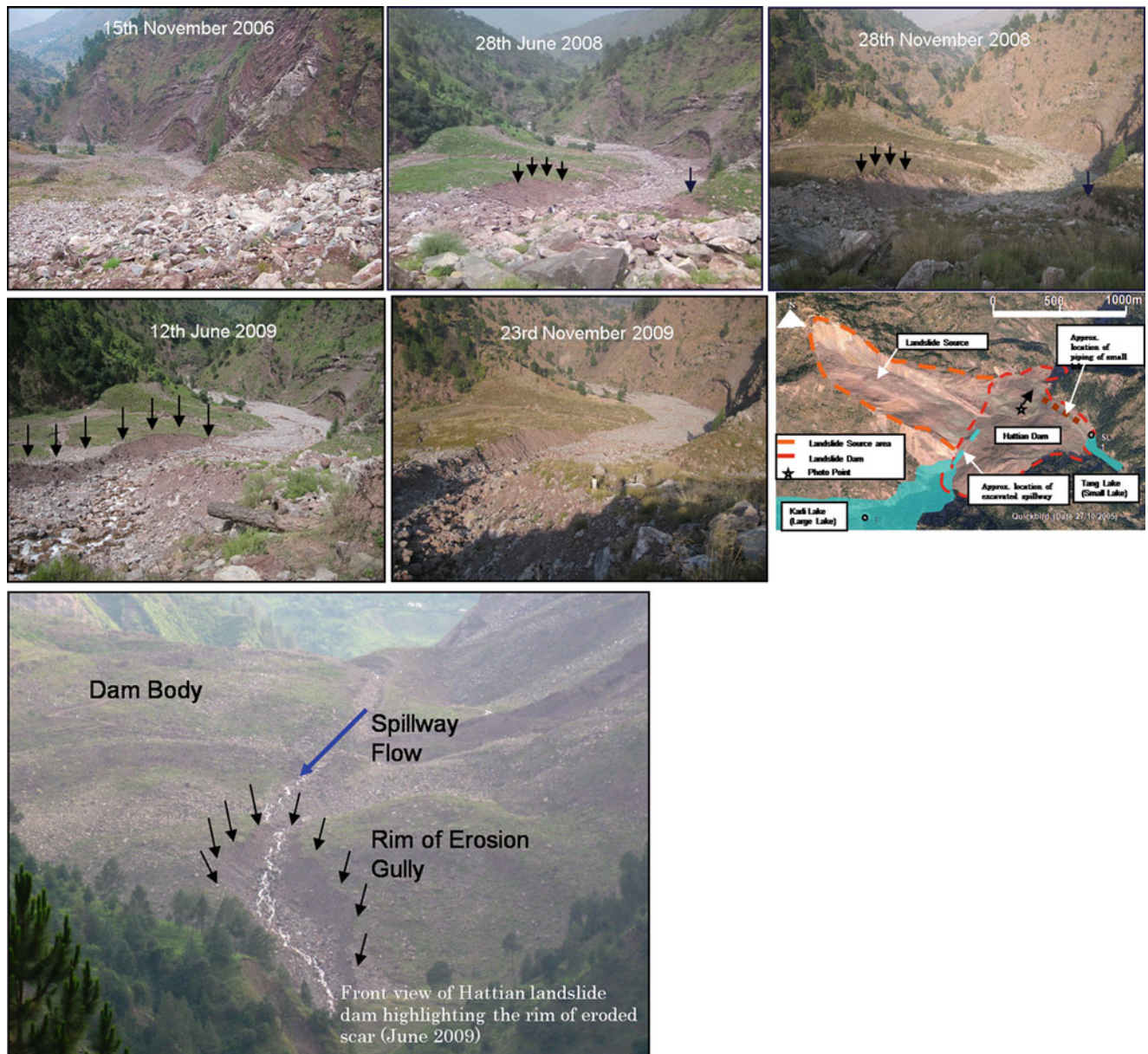


Fig. 4 Retrogressive erosion of debris mass (till Nov 2009) leading to development of erosion gully (June 2009)

cutting rate varying from a minimum of 10 m/h and a maximum of 100 m/h. The digital elevation model (DEM) used for the simulation was extracted from Shuttle Radar Topography Mission SRTM digital data, which covered the region from Hattian to Muzaffarabad city.

A two-dimensional flood routing model by O'Brien et al. (1993), Flo-2D, was used by Sattar et al. (2011) for inundation modeling of the dam breach scenario of the Hattian landslide dam. Flo-2d is a volume conservation model, and its constitutive fluid equations include the continuity equation and dynamic wave momentum equation (Saint Venant equations).

$$\frac{\partial h}{\partial t} + \frac{\partial h V_x}{\partial x} = i \quad (1)$$

$$\frac{1}{g} \frac{\partial V_x}{\partial t} + \frac{V_x}{g} \frac{\partial V_x}{\partial x} + \frac{\partial h}{\partial x} = S_{0x} - S_{fx} \quad (2)$$

where, ' h ' is the flow depth, ' V_x ' is the depth-averaged velocity component and ' i ' is the excess rainfall intensity, ' S_{fx} ' is the friction slope based on Manning's equation, ' S_{0x} ' is the bed slope, and ' g ' is the acceleration due to gravity.

The solution domain is discretized into uniform, square grid elements. The differential form of the continuity and

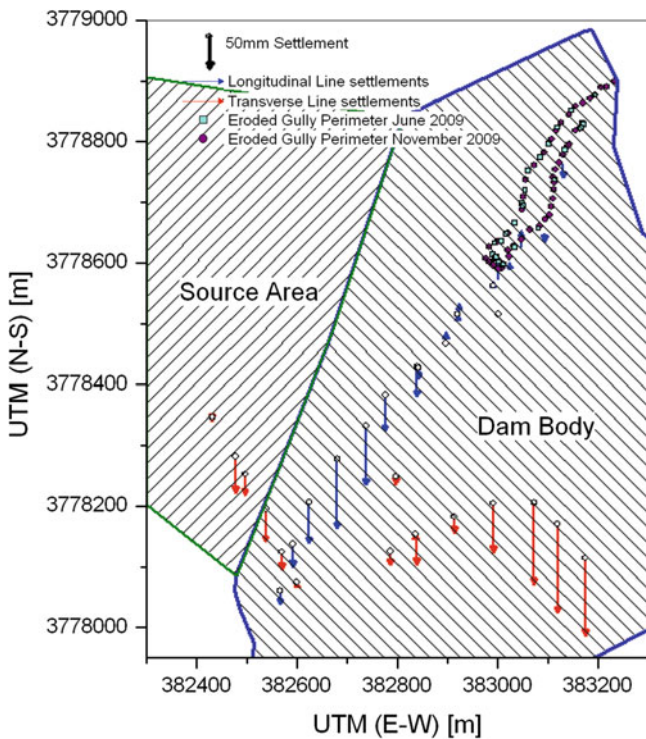


Fig. 5 Settlements obtained by comparing DGPS data for June 2009 and November 2009 surveys. The perimeter of the erosion channel observed in June 2009 and November 2009 is marked near the toe of the debris mass (Sattar et al. 2011)

momentum equations are solved with a central finite difference numerical scheme which solves the momentum equation for the flow velocity across the grid element boundary one element at a time. The incremental discharge for a grid element at a time step and the corresponding increase in flow depth are computed using the velocity components of the grid element.

The breach outflow hydrograph at the toe of Hattian dam for 100 m/h, 50 m/h, and 10 m/h down-cutting rate showed a peak outflow discharge of 13,830 m³/s, 5200 m³/s, and 700 m³/s, respectively.

The maximum flow depth at the confluence of the Karli branch and the Jhelum River (about 3 km downstream of the dam) was estimated to be 22 m (Fig. 7); however, the flow remained confined within the valley. Potentially hazardous low-elevation locations along the Jhelum River possessing a significant number of buildings were identified based on simulation.

The simulation also demonstrates that the flood wave significantly attenuates along the Jhelum River when it reaches the main city of Muzaffarabad, 33 km downstream from the landslide. The simulation result was reported to the State Earthquake Reconstruction and Rehabilitation Agency (SERRA), Azad Government of the State of Jammu & Kashmir, on June 13, 2009, about 8 months before the breaching.

5 Failure of Karli Lake and Tang Lake

After 5 days of continuous rains in early February 2010, the water of Karli Lake breached the debris dam on February 9, 2010. This breaching drained about 36 million m³ of water from the lake, leaving 26 million m³ in the lake. The erosion stopped after the bedrock was exposed at the scoured bottom of the breach channel (Fig. 8). Using the laser scanning technique, we estimated that about 7.78 million m³ of soil was eroded during the breaching event. The flushed debris mass was deposited along the Karli River (Fig. 9). The thickness of the debris deposit was estimated to be up to 80 m close to the toe of the Dam and generally about 15–20 m along the 3.7 km reach of the river till it merges with the Jhelum River at Hattian village.

The TRMM-data-based estimate showed several-day continuous precipitation in early February, immediately before the breaching of Karli Lake. An assessment of the rainfall indicated a peak value of 32 mm/day on February 8th, 1 day before breaching. However, several facts negated the possibility of breaching the Dam solely because of the rainfall.



Fig. 6 View of the path of water flowing from the Tang Lake. The surface change can be observed between November 2006 (left) and June 2008 (middle). While the right most figure shows the breach channel

formed in front of Tang Lake. Photo points are approximately N34.1420°, E73.7347° for the left and middle and N34.1427° E73.7326° for the right

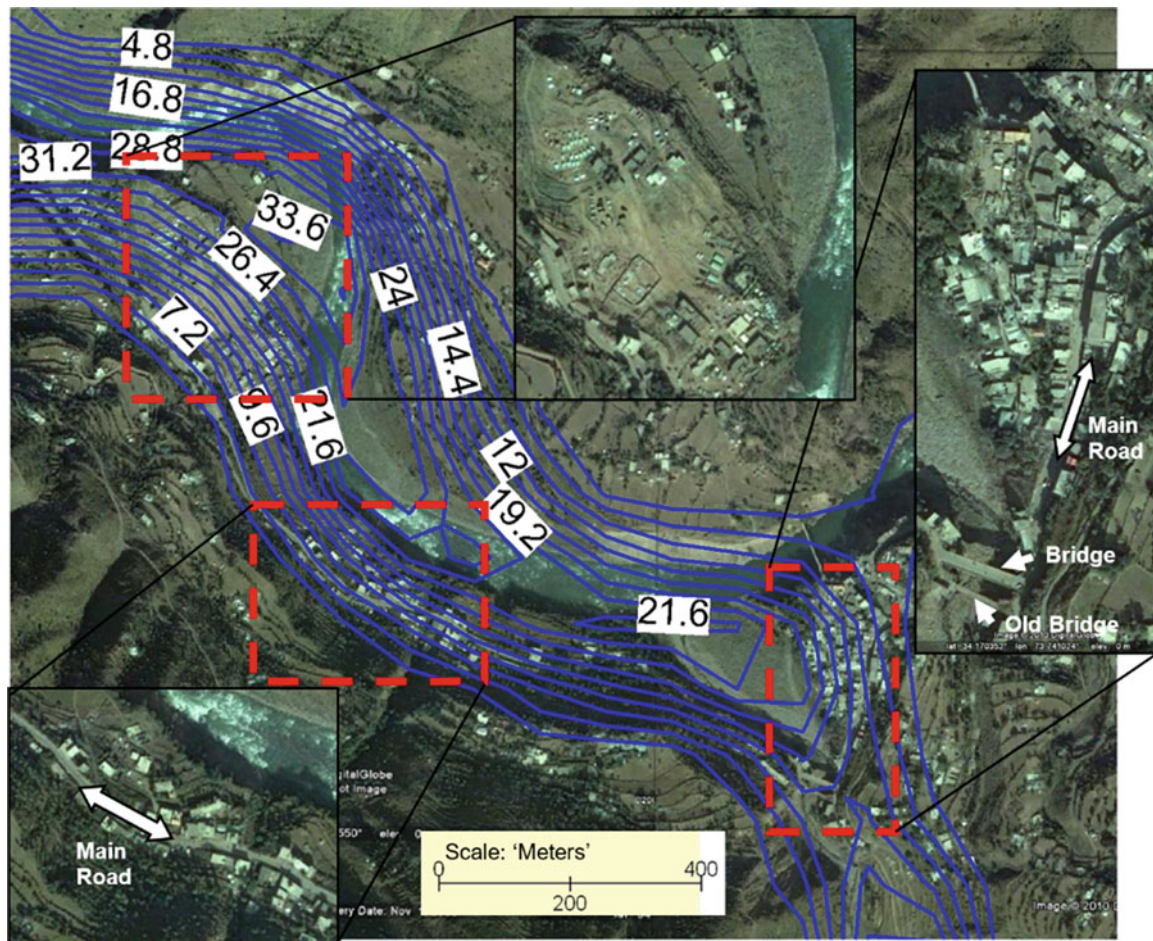


Fig. 7 Google image® of Hattian-Bala district overlain by maximum flow depth contours (in 'meters') of dam breach simulation by Sattar et al. Close-up of potentially hazardous locations along the Jhelum river with significant number of structures are shown

These facts included that the mountain slopes around Hattian Dam were covered with snow when the breaching occurred (Fig. 10), suggesting that only a part of this precipitation may have flowed into the lake. During the authors' survey after the breaching, we saw a landslide mass deposited on the right bank of the emptied large lake. So, among the possible scenarios discussed was the rising lake water level due to the plunging of the unstable landmass into the lake. However, as will be discussed later, such a scenario for the dam breaching was not possible, considering the observations of the eyewitnesses of the event and the post-breaching photographs.

We examined the maximum flood levels during the breaching event by measuring the elevations of the flood marks visible along the downstream reach of the river. It turned out that the peak outflow discharge of $5500 \text{ m}^3/\text{s}$ at a down-cutting rate of 25 m/h best fits the measured flow depths and flow velocities along the Karli River (Fig. 11). As Sattar et al. (2011) predicted earlier, the flood water engulfed many houses in Hattian Bala along the right bank

of the Karli River, swallowing a boy. However, it could have been worse unless residents evacuated quickly.

The monsoon rains in late July 2010 caused a mega-flood in Pakistan, and the flood is considered the worst in the region's record. Intensive rainfall was observed in Muzaffarabad and surrounding areas, including Hattian Bala. Continuous rain reportedly caused extensive landslides along the Neelum valley, and to a lesser extent, along the Jhelum valley. The Tang Lake (smaller lake) breached (Fig. 12) during the days of the most intensive monsoon rains of 2010 (July 27 to August 1); however, the exact day of the breaching remains unknown. The TRMM data indicated a peak rainfall rate of 105 mm/day for July 30 which could have been when Tang Lake breached. In the breaching process, the water from Tang Lake eroded the northeastern end of the landslide lobe, which had been covered with boulders segregated up at the time of deposit. The top 15 m depth of the lake water was drained during the breaching event leaving behind about 1.9 million m^3 of water in the lake. As mentioned earlier, piping is considered to have



Fig. 8 (a) Front view of Hattian landslide dam, before and after failure, (b) Front view of the dam immediately after breaching (Konagai and Sattar 2011)

been developed in the interior of the debris deposit in front of Tang Lake.

It is inferred that the breaching process started as a backward erosion piping. The down-cutting rate of Tang Lake could have been slow because the boulders which were present along the water path were carried downstream without extensive crushing, differing from what we observed in the event of the Karli Lake failure. The slow down-cutting rate of Tang Lake can be attributed to the armoring effect provided by the surface boulder layer. No clear floodwater marks were found for this event, probably because the floodwater discharge was much smaller than Karli Lake's discharge.

6 Discussions

The landslide mass damming Karli Lake failed after a rain/snowfall runoff in early February 2010. It remains to be clarified how the moderate precipitation caused the

breaching, as the debris dam had survived much heavier rainfall before its failure. A possible mechanism that caused the breaching can be explained by considering the weak weathering resistance of the debris material. The debris originated from the Murree formation of Miocene-aged sedimentary rocks composed of reddish mudstones, shales, and greyish sandstones. The effect of weathering on the mudstones had been observed at various locations over the dam body, where mudstone boulders were slaked and reduced to fragments. Reddish watermarks found occasionally along waters seeping out of the dam body indicated that internal seepage flows had washed finer substances out.

The Hattian area experiences extreme weather conditions during summer and winter along with the monsoon season with heavy rainfalls, setting ideal conditions for wetting and drying cycles on the slaking process. Signs of a deteriorating dam body were continuously observed with the gradual surface deformations and later with the sudden detachment of a significant amount of soil from the Dam's downstream face, as discussed above. In February 2010, relatively moderate



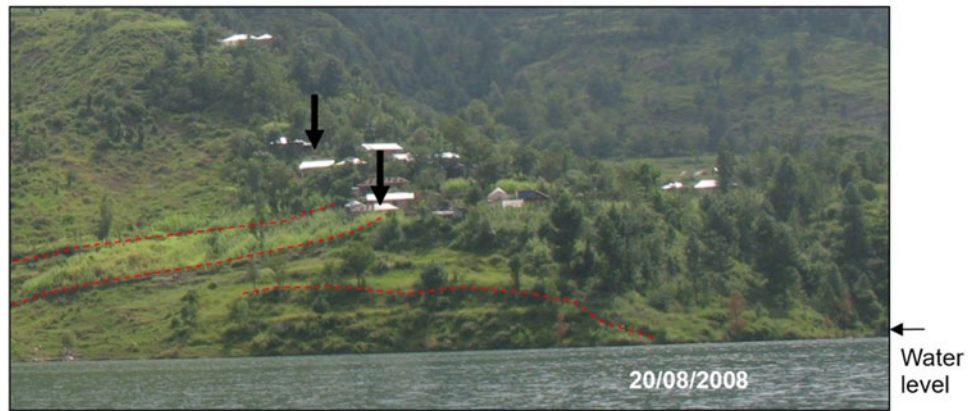
Fig. 9 Partially breached Hattian dam and debris deposit along the Karli River. (Photo taken on sixth June 2010 at N 34.156567°, E 73.744833°)

precipitation extended for 5 days in the Hattian catchment, followed by dry and clear days in February. It thus may have accelerated the slaking process in a way that even moderate waters flowing over and seeping through the debris mass significantly accelerated backward erosion. Kiyota et al. (2011) discussed the slakable nature of the dam material through standard slaking tests and advanced unconventional direct shear tests on prepared soil specimens retrieved from the remaining dam body.

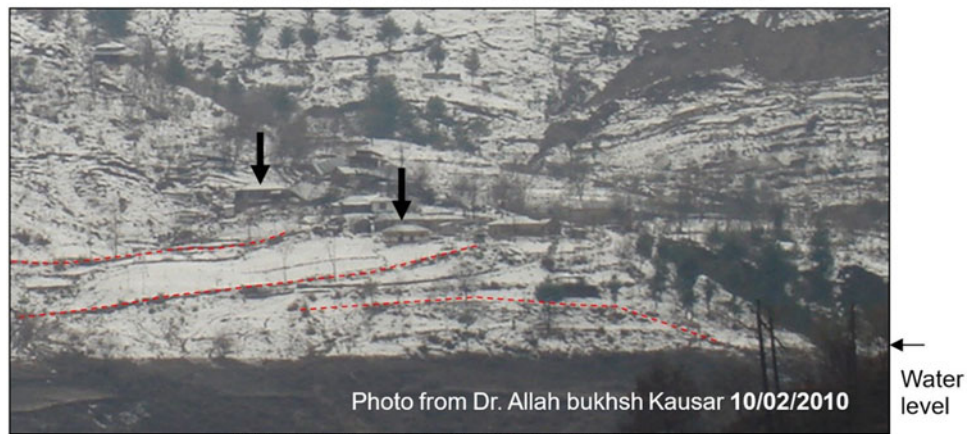
As mentioned earlier, we found a landslide mass deposited on the right bank of the emptied large lake during the post-event survey. According to eyewitness accounts, the breaching of the landslide mass triggered this large landslide, and the mass movement continued for 2 weeks after the breaching event. This coherent landslide mass was about 1000 m long in the runout direction and 800 m wide (as indicated by red arrows on the right bank of Karli Lake in Fig. 13). The landslide destroyed 174 houses and displaced about 1000 residents, making it more extensive damage than the one directly caused by flooding.

As contrasted with the Karli Lake failure, the Tang Lake failure did not produce any significant flood wave; indeed, it was not until the authors reported it that many residents at Hattian Bala knew that Tang Lake had failed. Perhaps, it is

Fig. 10 Right bank slope (a) On 20/08/2008, before the breaching event (b) One day after the breaching event showing snow covered slope and mark of the water level of Karli Lake before breaching event



(a) Toe part of the landslide mass before breaching



(b) Toe part of the landslide mass after breaching

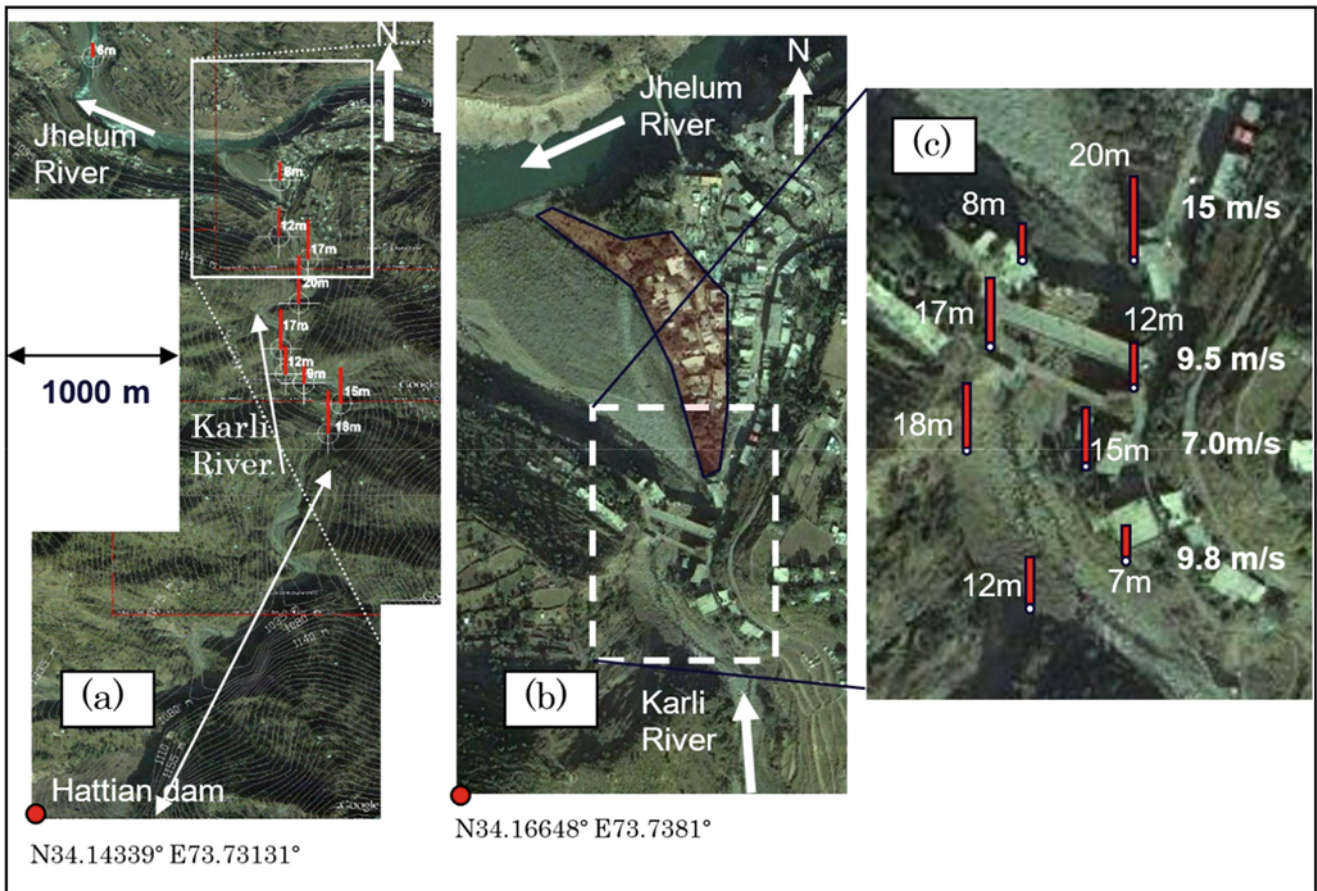


Fig. 11 (a) Flood inundation heights along the Karli River. (b) Houses affected by the debris originating from the Hattian dam. (c) Flow velocities estimated from super-elevations of the measured mud marks near the junction of Karli River and Jhelum River

because the emptied water (1.6 million m³) was much smaller than that from Karli Lake, and the lobe of the debris mass that had been stopping the water of Tang Lake was covered thick with segregated boulders.

It was less likely that a flood of the same scale would occur again and cause any hazard for the downstream reach of Karli Valley because a bedrock, which appeared on the scoured bottom of the breach channel, was not likely to be



Fig. 12 Tang lake after breaching (Photo taken on 6th Dec-2010) GPS coordinates N34.13951° E73.73631°

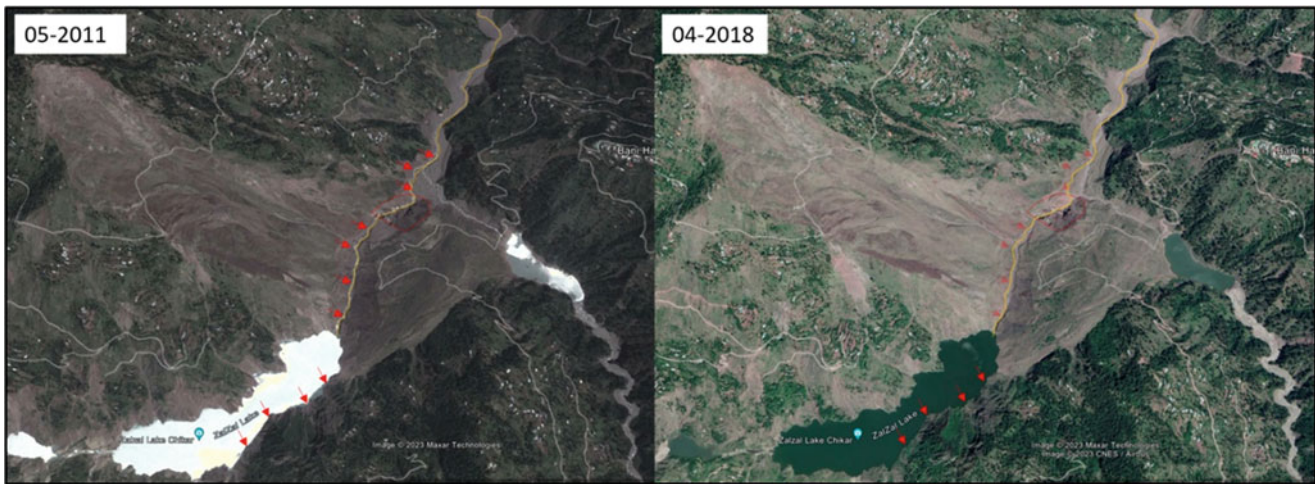


Fig. 13 Google earth® image of the Hattian Bala dam after breaching of the dam and several years post breaching. Red arrows and the yellow line across the dam body indicate the channel's alignment over the dam

eroded any further. However, the exposed bare walls of the remaining Hattian Bala landslide dam were not completely stable. Any collapses of the walls would clog up the breached channel and increase the lake volume at any time (in an earthquake, heavy rainfall, or otherwise). Konagai and Sattar (2011) discussed possible scenarios for these landslides and their impacts. They also reported post-breaching landform changes. These included:

- the erosion of materials from the debris deposit and raising of the river bed level at downstream river reach;
- the hazard posed by the unstable landslide mass at the right bank of Karli Lake;

Figure 13 compares the Google Earth® image of the Hattian Bala landslide dam after the breach (May 2011) and a more recent image of the area (April 2018). The unstable landslide mass at the right bank of Karli Lake showed no clear sign of movement, as apparent from Fig. 13. The gorge formed over the landslide mass body by the overflowing water seems to have slightly changed its course towards the east, as indicated in Fig. 13. Some changes to the landmass near the toe of the landslide mass also appear insignificant. Beyond the toe of the landslide mass, the overflowing water changed its course over time.

The changes observed over seven post-breaching years are relatively insignificant, and the landslide mass appears stable and does not pose an imminent danger.

7 Summary

The October 8, 2005, Mw 7.5 Kashmir earthquake triggered a massive landslide 3.5 km upstream of Hattian-Bala town near the southeastern end of the activated Balakot-Bagh fault. The

body as of May 2011, and the channel alignment as of April 2018 is visible in the figure on the right. Red arrows along the right bank of Karli Lake indicate the coherent landslide mass in both figures

debris deposit resulting from the landslide blocked two tributaries of the Karli branch of the Jhelum River, forming Karli Lake (the large lake) and Tang Lake (the small lake). The Dam sustained over about 4 years and 4 months, and finally, the water of Karli Lake (large lake) of Hattian dam breached the northwestern part of the landslide dam on February 9th, 2010, after 5 days of rains/snowfalls, and the water of Tang Lake (small lake) breached the northeastern lobe of debris deposit during the monsoon rains of July–August, 2010. Until the failure of Karli Lake, the landslide dam had long been a severe threat to people living along the lower reach of the Jhelum River, and the authors had been conducting periodic observations and measurements of changes occurring in the landslide mass since the authors' project started in 2008. The landslide mass started to show more evident signs of gradual deformations/erosions after the overflow started through the spillway, which was excavated to secure the safety of the debris deposit against possible failure of the Karli Lake. Evidence of weathering (slaking) of the mudstones of Murree formation was observed over the boulder-strewn landslide dam. The most significant change observed in the dam body before the failure of Karli Lake was a sudden erosion of an approximately 65,000 m³ soil mass from the downstream slope of the landslide dam during heavy rainfall in 2009. The rainfall estimate over the Hattian catchment area indicates that the precipitation of February 2010 that caused the breaching was less significant than the other heavy rainfalls that the area had experienced since the overflowing from Karli Lake started in April 2007. The breaching was most likely due to the slaking process developed during relatively moderate precipitation in the Hattian catchment, followed by dry and clear days in February, as suggested by Kiyota et al. (2011).

Sattar et al. (2011) estimated that the maximum flow depth at about 3 km downstream of the dam was 22 m and reported

it to the State Earthquake Reconstruction & Rehabilitation Agency (SERRA), Azad Government of the State of Jammu & Kashmir, on June 13th, 2009, about 8 months before the breaching. As predicted, the flood water from the breached dam engulfed many houses in Hattian Bala along the right bank of the Karli River, swallowing a boy. However, it could have been worse unless residents evacuated quickly.

Landslide dams not only pose flood hazards or the associated landmass movements, but these debris deposits can also become an issue for the sustainability of any project on the major rivers if the landmass is relatively large. One example is the Attabad landslide dam blocking the Indus River at its upstream reach. It is to be noted that the Indus cascade, a big project in which the first author is involved, is currently under development in Pakistan. i.e., the cascade of dams, namely the Basha dam, Dasu dam, Patan dam, and Thakot dam; they are all located downstream of the Attabad landslide dam. Safe passage of the flood generated by breaching the landslide dam becomes a critical design consideration for these dams. A breaching scenario of the Attabad Dam thus forms the basis for the safety check floods for these dams. From the perspective of the sustainability of the under-construction hydropower projects, more minor landslides and debris flows associated with monsoon are also an important aspect that requires attention. According to estimates (Roca 2012), about 200 million tons of sediments are transported to the Terbel dam reservoir annually. Apart from the glacial melts, a portion of the source of

sediments is the landslides and debris flow in Nallas during the monsoon, which eventually is transported as bed load and suspended sediments in the Indus River. The Indus cascade development must cope with the transported sediments to sustain the reservoirs.

References

- Konagai K, Sattar A (2011) Partial breaching of Hattian Bala landslide dam formed in the 8th October 2005 Kashmir earthquake. *Pakistan Landslides* 9(1):1–11. <https://doi.org/10.1007/s10346-011-0280-x>
- Kiyota T, Sattar A, Konagai K, Kazmi ZA, Okuno D, Ikeda T (2011) Breaching failure of a huge landslide dam formed by the 2005 Kashmir earthquake. *Soils Found* 51(6):13–19. <https://doi.org/10.3208/sandf.51.1179>
- O'Brien JS, Julien PY, Fullerton WT (1993) Two-dimensional water flood and mudflow simulation. *J Hydr Engrg* 119(2):244–261. [https://doi.org/10.1061/\(ASCE\)0733-9429\(1993\)119:2\(244\)](https://doi.org/10.1061/(ASCE)0733-9429(1993)119:2(244))
- Roca M (2012) Tarbela Dam in Pakistan. Case study of reservoir sedimentation. *Proceedings of River Flow 2012*:5–7. <https://eprints.hrwallingford.com/891/>
- Sattar A, Konagai K, Kiyota T, Ikeda T, Johansson J (2011) Measurement of debris mass changes and assessment of the dam-break flood potential of earthquake-triggered Hattian landslide dam. *Landslides* 8:171–182. <https://doi.org/10.1007/s10346-010-0241-9>
- WAPDA Report (2006) Study of Hattian Ballah landslide, potential hazards of land sliding and mitigation measures at Hattian Ballah and other earthquake hit areas. National Engineering Services Pakistan limited (NESPAK) and Geological Survey of Pakistan (GSP), Water and Power Development Authority (WAPDA), 2006, Government of Pakistan

Open Access This chapter is licensed under the terms of the Creative Commons Attribution 4.0 International License (<http://creativecommons.org/licenses/by/4.0/>), which permits use, sharing, adaptation, distribution and reproduction in any medium or format, as long as you give appropriate credit to the original author(s) and the source, provide a link to the Creative Commons license and indicate if changes were made.

The images or other third party material in this chapter are included in the chapter's Creative Commons license, unless indicated otherwise in a credit line to the material. If material is not included in the chapter's Creative Commons license and your intended use is not permitted by statutory regulation or exceeds the permitted use, you will need to obtain permission directly from the copyright holder.





Investigation of Debris Flow Impact Mechanisms and Designs

Charles W. W. Ng, Sunil Poudyal, Haiming Liu, Aastha Bhatta, W. A. Roanga K. De Silva, and Zhenyang Jia

Abstract

Debris flows are catastrophic landslides increasing in severity in recent decades due to the more frequent and intense rainfall events under climate change. Debris flows pose a serious threat to infrastructure, settlements, and the natural environment in mountainous regions around the world causing considerable economic losses every year. To mitigate debris flows, single and multiple rigid and flexible barriers are constructed along the predicted debris flow paths. Compared with single barriers, multiple barriers are more advantageous in mitigating large debris flow volumes by progressively retaining and decelerating the flow with much smaller barrier sizes. These smaller barriers are not only easier to construct on steep hillslopes but also reduce the carbon footprint compared to large single barriers. However, current understanding of debris flow impact mechanisms on single and multiple barriers is limited due to the complex composition and scale-dependent nature of debris flow. The need of using different barrier configurations further adds to this complexity and the impact mechanisms of debris flow against single and multiple barriers are yet to be elucidated, thereby hindering the development of scientific design guidelines. This paper examines the impact mechanisms of water, dry granular and two-phase debris flows on barriers of varying stiffness, openings and numbers based on physical and numerical results, and provides recommendations for design of debris-resisting single and multiple barriers.

Keywords

Debris flow · Impact mechanisms · Rigid barrier · Basal clearance · Multiple barriers

C. W. W. Ng (✉) · S. Poudyal (✉) · H. Liu · A. Bhatta · W. A. R. K. De Silva · Z. Jia

Department of Civil and Environmental Engineering, The Hong Kong University of Science and Technology, Kowloon, Hong Kong, China
e-mail: charles.ng@ust.hk; spoudyal@connect.ust.hk

1 Introduction

Debris flows are fast-moving mixtures of rock, soil, water, and other debris, classified as flow-like landslides (Hungr et al. 2014), which can cause significant damage to infrastructure and casualties (Froude and Petley 2018). In recent years, changes in rainfall patterns due to climate change have brought more frequent and intense rainfall events with an increase in the number and severity of landslides including debris flows (Guzzetti et al. 2008; Ng et al. 2021d). Urban sprawl in hilly and mountainous areas are expected to face increased risk of landslides due to climate change (Ozturk et al. 2022; Yik et al. 2023). Between 2000 and 2019, landslides have resulted in 11% of all recorded fatalities from natural disasters with more than 70% of these fatalities occurring in Asia (Guha-Sapir 2020). Similarly, average economic losses due to landslides is US\$3.5 billion every year (World Bank 2022) and is expected to increase due to climate change.

Debris-resisting barriers are commonly installed to retard and intercept debris flows from reaching further downstream. Design of these structures requires a reliable estimate of impact load as well as dimensions of openings or clearances (if any) for controlled discharge of debris flows. Current design guidelines only consider the barrier type (rigid or flexible) in their recommendations for estimating design impact force (GEO 2022; Kwan and Cheung 2012; ASI 2013; Volkwein 2014). For simplicity these guidelines prescribe empirical coefficients to consider the effects of flow composition, particle size, size of openings/basal clearances, barrier stiffness and flow-barrier interaction mechanisms on a single barrier impact force. Furthermore, the retention capacity of a single barrier may not be sufficient to arrest large debris flow volumes and require multiple barriers to be installed in a series along a drainage line to progressively impede and arrest debris flow (Huebl and Fiebiger 2005). Existing guidelines (SWCB 2019; VanDine 1996) which focus on volume retention suggest spacing between multiple

barriers without considering flow-barrier interaction mechanisms. As a step forward, recent design recommendations (Ng et al. 2020a; Wendeler et al. 2019) and design guidelines (GEO 2022; Kwan and Cheung 2012) recommend a layer-by-layer filling of the barrier and subsequent overtopping of the barrier in design calculations by simplifying the fundamental impact mechanisms. However, the reliability of these recommendations remains poorly understood. Current understanding of flow-barrier interaction is limited because (1) debris flow impact on barriers are rarely captured in the field with enough resolution to elucidate underlying mechanisms (Takahashi 2014) (2) debris flows are scale-dependent and require unique facilities to correctly model the flow dynamics (Iverson 2015; Zhou and Ng 2010) and (3) impact dynamics of debris flows on barriers strongly depends on flow composition (Choi et al. 2015; Ng et al. 2017, 2022a; Song et al. 2017, 2018) and barrier types (Choi et al. 2016, 2020; Goodwin and Choi 2020; Ng et al. 2020b, 2022b).

In this chapter, the dynamics of debris flows and the interaction mechanisms of debris flow with different types of barriers are presented. The impact mechanisms of water, dry granular and two-phase debris flows on barriers of varying stiffness, openings and numbers are elucidated using results from physical experiments and numerical simulations. Physical experiments were conducted in multi-scale facilities including 5-m long flume and 28-m long flume. Numerical analyses revealed additional insights into the underlying impact mechanisms including evolution of granular shear strains and fluidisation of two-phase debris. Finally, improved understandings of flow-barrier interaction mechanisms from this study are consolidated into recommendations for design impact loads on single and multiple debris-resisting barriers.

2 Understanding Debris Flow-Barrier Interaction Mechanisms

2.1 Preventive Measures Against Debris Flow

Debris flow mitigation measures can be broadly classified into active and passive measures. Active measures focus on the construction of structures for flow energy dissipation, flow retention and reduction of potential risk to communities. Passive measures include risk assessment, risk monitoring and land use zoning to reduce exposure to debris flow hazards. This chapter focuses on the study of active measures, specifically, debris-resisting barriers, which can be broadly categorised as closed and open barriers. Closed barriers intercept the entire flow material preventing downstream discharge until the barrier is overtopped. Closed barriers typically include closed check dams and terminal



Fig. 1 Debris resisting reinforced concrete terminal barrier (modified from Ng et al. 2020a)

barriers made of reinforced concrete that are constructed at the end of debris flow channels to retain the debris materials. These terminal rigid barriers are designed for large forces and for a long service life (Fig. 1).

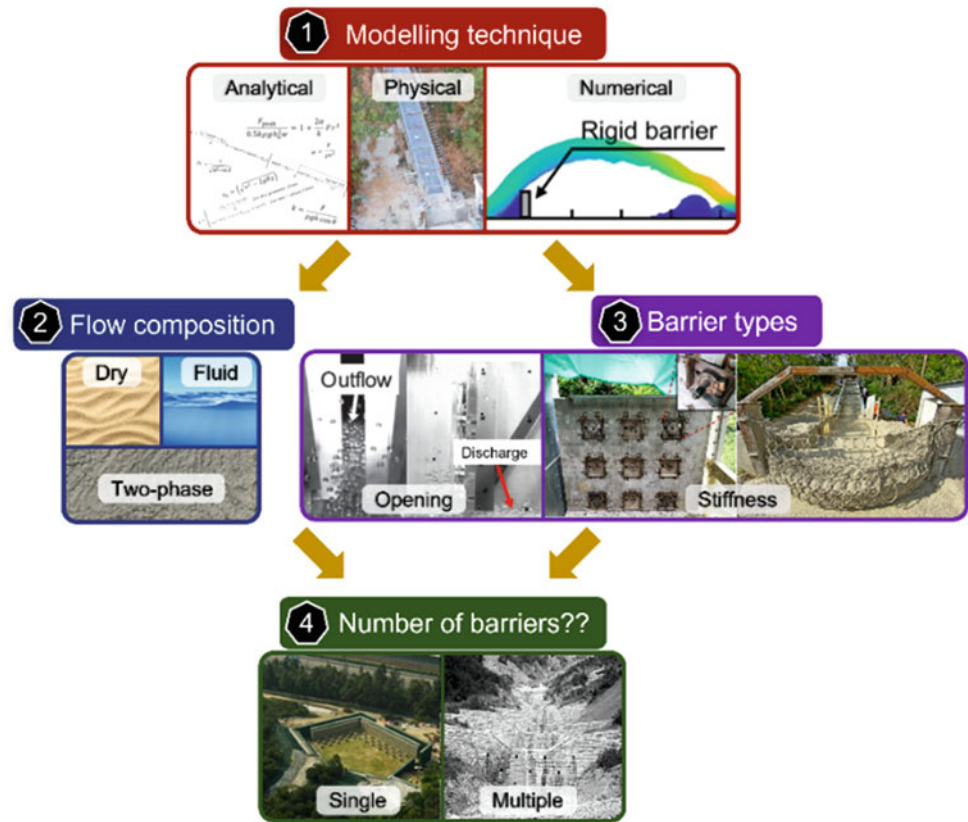
In contrast, open barriers can allow controlled discharge of flow material through openings in the barrier, efficient dissipation of flow energy and partial retention of debris material. Open barriers include open check dams, rigid barriers with basal clearance (Choi et al. 2020), slit dams (Piton and Recking 2016), baffle arrays (Ng et al. 2015) and flexible barriers (Wendeler et al. 2007). Interaction mechanisms between debris flow and different types of barriers vary and need prior understanding for an effective design. The interaction mechanisms of debris flow with closed and open rigid barriers, flexible barriers and multiple barriers are elaborated next.

2.2 Debris Flow Analysis and Modelling

Figure 2 shows a strategy for analysis and modelling of debris flow impact on barriers. Modelling technique refers to tools that can be used to fulfil the specific objective of the study. Flow-barrier interaction can be modelled (1) analytically by defining simplified formulations of debris flow behaviour and its interactions with a barrier, (2) physically by using geotechnical centrifuge, laboratory or field-scale flume tests with well-defined initial and boundary conditions, and (3) numerically by using calibrated numerical models, which can provide insight into underlying physical mechanisms that cannot be observed in physical models/ tests such as evolution of stresses and strains within the debris material.

To successfully derive analytical solutions for flow-barrier interaction problems, many assumptions about debris flow rheology (frictional, viscous, or two-phase mixture), debris

Fig. 2 A research strategy used in analysis and modelling of debris flow impact on barriers



flow regimes (uniform, steady, incompressible) and barrier stiffness (flexible or rigid) are required. While these simplifying assumptions may yield meaningful results for simple flow materials like water or dry granular flow impacting on rigid barriers, the validity of analytical solution (if any) for two-phase debris flow impact on flexible barrier is questionable (Ng et al. 2023b). Numerical modelling relaxes some of the assumptions of analytical models. While numerical modelling of different barrier rigidities may be trivial (Ng et al. 2020b), the same cannot be said about debris flow rheology. Constitutive modelling for capturing debris flow rheology is a challenging task due to the complexities involved in defining the physical interactions between solid and fluid phases (Ng et al. 2023a). Nevertheless, with the help of physical experiments, numerical models can be calibrated to reasonably capture the dynamics of debris flows despite some assumptions in the constitutive models. These calibrated numerical models can be utilised for parametric study to reveal how the stresses and strains evolve inside debris flow during impact against different kinds of barriers giving rise to different impact mechanisms. Ultimately, the results from physical experiments as well as numerical parametric studies are used to produce design guidelines for debris resisting barriers.

Depending on the barrier type (open vs closed), flow material is either completely intercepted or partially

discharged through openings or allowed to overflow once the barrier is filled. If a barrier is designed to allow overflow, then instead of designing a single barrier, multiple barriers can be designed iteratively as a system. Such a multiple barrier system requires consideration of overflow and landing dynamics as well as volume retention by upstream barriers during design. These salient features of flow-barrier impact mechanisms are explored in detail in the next section.

2.3 Preventive Measures Against Debris Flow

2.3.1 Debris Flow Interaction with Single Barriers

2.3.1.1 Influence of Flow Composition

Dry granular and water flows are the two most extreme types of geophysical flows, the former governed primarily by frictional forces and the latter by viscous forces. The influence of these two extreme flow types is firstly discussed to reveal some fundamental impact mechanisms, followed by the effect of two-phase flows in impact mechanism.

Figure 3 shows a comparison of the impact kinematics of dry granular and water flows impacting against a single rigid barrier perpendicular to the ground plane (Choi et al. 2015). The tests were carried out in two different scales: (1) a 5 m-

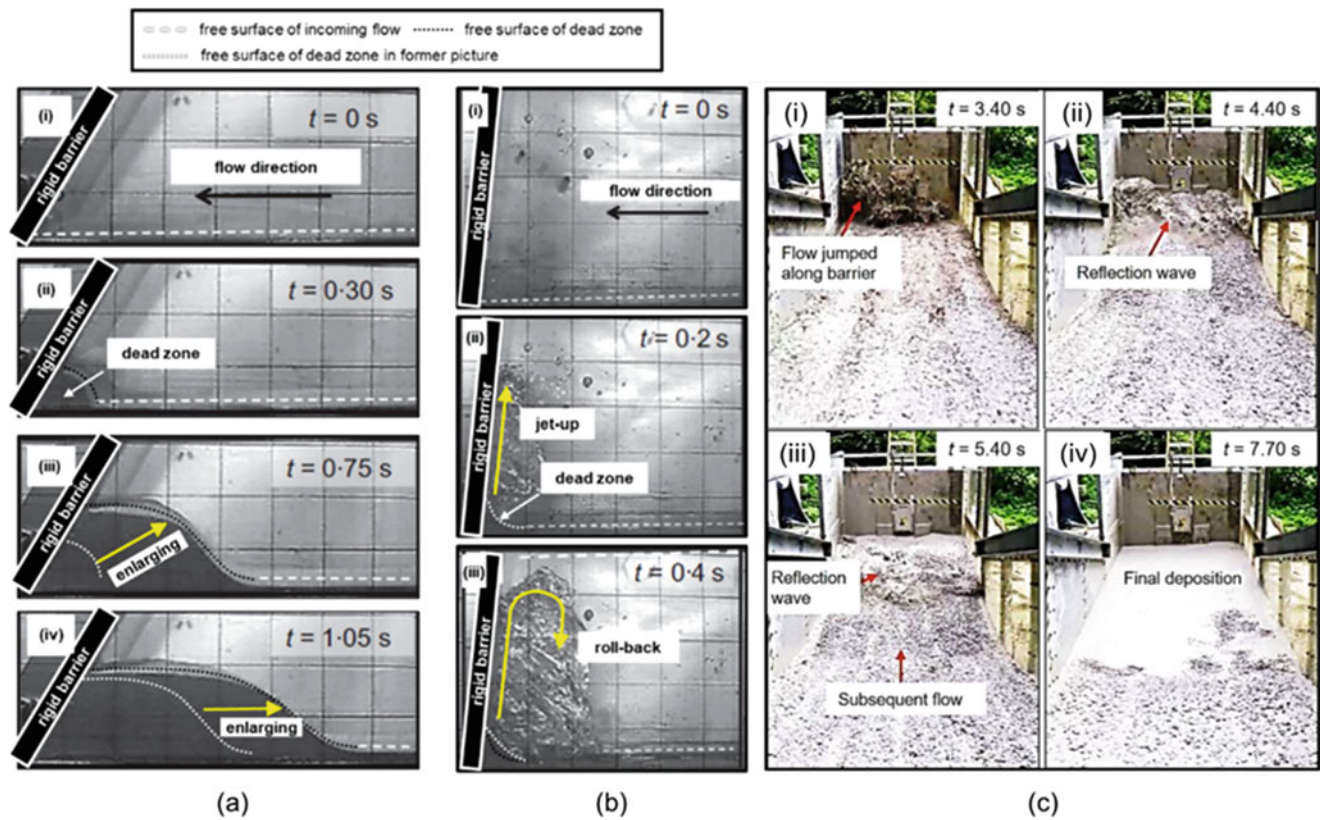


Fig. 3 Comparison of impact mechanisms for a single rigid barrier for: (a) dry granular flow and (b) water in 5 m-long flume (modified from Choi et al. 2015); (c) two-phase flow in 28-m long flume (Ng et al. 2021a)

long flume, inclined at 40° for dry granular (Leighton Buzzard fraction C sand; uniform grain diameters of 0.6 mm) and at 5° for water (Choi et al. 2015), and (2) a 28 m-long flume, inclined at 20° for two-phase flows (Ng et al. 2021a). In Fig. 3a (i), at $t = 0.00$ s, dry granular flow front starts to impact the barrier and gradually piles-up behind the barrier. The wedge-shaped static zone (dead zone) keeps enlarging until $t = 0.75$ s (Fig. 3a (iii)). This pile-up mechanism rapidly attenuates kinetic energy of the dry granular flow with high degree of internal and boundary friction. Furthermore, air in the interstices increases the bulk compressibility of angular sands allowing further dissipation of kinetic energy during impact. This increase in bulk compressibility can be attributed to the changes in void ratio from elastic shearing at contacts without grain crushing (Iverson 2015). As such, the dry granular flow cannot override the deposited material along the free surface and instead, the length of the dead zone keeps increasing when a granular bore propagates (piles-up) upstream at $t = 1.05$ s (Fig. 3a (iv)). For water flow (Fig. 3b), a jet-up like mechanism is observed with supercritical Fr conditions (Choi et al. 2015). Unlike the dry granular flow, the water runs up along the barrier without significant enlargement of the dead zone from $t = 0.2$ s to 0.4 s (as shown in Figs. 3b (ii) and (iii)). When kinetic energy of runup water

completely transfers to gravitational potential energy, it rolls back, falls under gravity and impacts on the flume base.

Tests using dry granular and water flows are valuable in understanding fundamental impact mechanisms in purely frictional stress and viscous stress dominated regimes respectively. However, these two extreme flow types cannot model the solid-fluid interaction intrinsic to debris flows. Pore fluid regulates friction within the solid particles and at boundaries, thereby changing the amount of energy dissipation and consequently the impact mechanism (Song et al. 2017). Figure 3c shows the impact mechanism of debris flow against a single rigid barrier in the 28 m-long flume (Ng et al. 2021a). The debris material was composed of gravel, sand, clay, and water with volumetric fractions of 0.21, 0.36, 0.02, and 0.41, respectively. At $t = 3.40$ s, the flow front jumped along the barrier after impacting and is immediately reflected upstream (Fig. 3c (i)). At $t = 4.40$ s the reflected wave then propagates upstream and interacts with the incoming flow (Fig. 3c (ii)). Although the solid volume fraction of the two-phase flow is 0.59, approximately equal to that of dry granular flow in Fig. 3a, initial jet-like impact mechanism followed by reflected wave occurs rather than pile-up. Similar impact mechanisms have also been observed by Armanini et al. (2020) in 5-m long flume and Song et al. (2017) in

geotechnical centrifuge. The jet-like impact mechanism in two-phase flows can be explained by the fluidisation ratio λ (Ng et al. 2023a), which is the ratio between pore fluid pressure p_f and the total stress (sum of pore fluid pressure p_f and effective stress of solid phase p'):

$$\lambda = \frac{p_f}{p} = \frac{p_f}{p_f + p'} \quad (1)$$

Fluidisation ratio measured in 28 m-long flume tests is approximately equal to one, which implies $p' \approx 0$ and less energy is dissipated due to the low frictional force ($\mu p' \approx 0$, where μ is the friction angle of the solid phase). This can also be inferred from the horizontal free surface of the deposited debris at $t = 7.70$ s (Fig. 3c (iv)).

The distinctly different mechanisms observed for dry granular flow (pile-up) and water (vertical jet) are governed by the difference in energy dissipation in the two flow types during impact. While internal and boundary friction together with bulk compressibility rapidly reduces the flow kinetic energy for dry granular flow (Koo et al. 2017), viscous shearing in water is not as efficient in dissipating energy. These differences in impact mechanisms have a profound effect on the impact force and its distribution on a barrier (Song et al. 2017), which will be discussed in detail later.

2.3.1.2 Effects of Rigid Barrier Opening

The impact mechanisms of different flow compositions against closed rigid barriers, which are usually constructed at the exit of the debris flow channel to resist all the debris, have been discussed in previous section. On the contrary, rigid barriers are also constructed with various types of openings in the field. Piton and Recking (2016) conducted a detailed literature review on the hydraulic and deposition processes of debris flow against open rigid barriers. They summarised unique advantages of open rigid barriers compared to the closed rigid barriers as follows: (1) regulating peak flow rate; (2) increasing energy dissipation; (3) filtering and storing unwanted components, such as separating bed-load sizes or grading wood. Aside from the functioning perspectives of open rigid barriers, the design of these barriers also requires the knowledge of impact force. As such, the discharge of open rigid barriers is discussed in this section and the recommendation of design impact force for open rigid barriers is provided in Sect. 3.

The efficiency of open rigid barriers in dissipating the flow energy can be controlled by designing a basal clearance, which is an opening between the base of the barrier and channel bed, such that the impact force on downstream barriers can be optimised (Choi et al. 2020; Ng et al. 2022b; Liu et al. 2023). By designing a basal clearance, the peak flow discharge rate can be regulated.

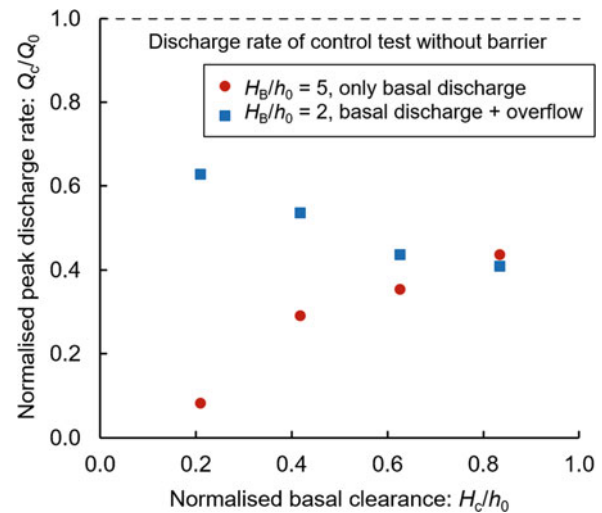


Fig. 4 Influence of basal clearance height on the peak discharge rate

Figure 4 shows the physical test results of peak basal discharge rate Q_c of dry granular flow composed of 3-mm glass beads impacting on rigid barrier with a normalised basal clearance H_c/h_0 ranging from 0.2 to 0.8 (Ng et al. 2022b). In the tests, two barrier heights perpendicular to the channel slope were adopted with five times the flow depth ($H_B/h_0 = 5$) and twice the flow depth ($H_B/h_0 = 2$). The peak discharge rate through the basal clearance is normalised by the peak discharge rate of a control test without barrier. For the tests with $H_B/h_0 = 5$, the large barrier height prevents overflow, and thus the discharge rate is dominated by basal discharge and increases with the increase in basal clearance height. In contrast, when barrier height is lower at $H_B/h_0 = 2$, both overflow and basal discharge occur and influence the downstream discharge rate. With the increase of basal clearance, the peak discharge rate decreases due to the reduced overflow and when H_c/h_0 reaches 0.8, the peak discharge is dominated by basal discharge rather than the overflow. Liu et al. (2023) proposed a new dimensionless number named as overflow number to characterise whether the downstream discharge is dominated by basal discharge or overflow. The overflow number N_{of} is expressed as follows:

$$N_{of} = \frac{h_j}{H_B} \left(1 - \frac{H_c}{h_0} \right) \quad (2)$$

where h_j is the runup height calculated by the momentum-based model (Liu et al. 2023). By comparing the physical and numerical results, the study found that the basal discharge dominates the peak discharge when $N_{of} < 1$, while the overflow dominates when $N_{of} > 1$. A threshold value of $N_{of} = 1$ can be used to optimise the design of the barrier by maximising dissipation of the flow energy.

In addition to discharge, the impact force induced on open barrier by debris flow requires attention and will be discussed later.

2.3.1.3 Role of Barrier Stiffness

After considering the effects of debris flow composition and barrier opening on impact mechanisms, this section discusses the effects of barrier deformation during impact. Ng et al. (2020b) studied the impact of dry granular flows against a deformable cantilever barrier using material point method (MPM). The MPM model was calibrated using flume test results reported in Ng et al. (2017). The calibrated model was then utilised in carrying out a numerical parametric study to investigate how the stiffness of the barrier affects barrier impact force, barrier deformation and energy dissipation during impact. The investigated stiffness (flexural rigidity) ranged from a stiff 1 m-thick concrete barrier ($EI = 4.17 \times 10^8 \text{ N} \cdot \text{m}^2$) to highly flexible 2 mm-thick steel barrier ($EI = 8.33 \text{ N} \cdot \text{m}^2$). To facilitate direct comparison with a 1 m-thick reinforced concrete barrier, the flexural rigidities of all the investigated barriers were normalised by the flexural rigidity of 1 m-thick and 3 m-tall reinforced concrete barrier. The normalised flexural rigidity ratio ($3EI/H_{\text{norm}}^3$) of the 1-m thick and 3 m-tall reinforced concrete barrier is 1.0 while that of the 2 mm-thick steel barrier is 2.5×10^{-6} .

Figure 5 shows the influence of barrier flexural rigidity ratio on the impact force and final barrier deformation. The abscissa shows the normalised flexural rigidity ratio. The ordinate on the left shows peak barrier deformation D_{max} along the impact direction normalised by the barrier height H . The ordinate on the right shows the impact force normalised by computed impact force on a 1 m-thick

reinforced concrete barrier. The computed results reveal that the normalised impact force reduces nonlinearly as the flexural stiffness reduces. Particularly, a 2 mm-thick steel barrier ($3EI/H_{\text{norm}}^3 = 2.5 \times 10^{-6}$) can reduce impact force by 60% while deforming around 40% of the barrier height in the direction of impact compared to a 1 m-thick reinforced concrete barrier that is essentially rigid. This implies, lowering the stiffness of a barrier effectively reduces peak impact force.

Figure 6a, b show how and why the granular flow impact force decreases as the barrier flexural rigidity reduces. These figures compare the accumulated equivalent shear strain of dry sand mass after impacting steel barriers of 2 mm and 5 mm thickness, respectively. The 2 mm-thick steel barrier undergoes (Fig. 6a) more significant deformation upon impact, leading to more distinct shear bands in the sand deposit compared to the 5 mm-thick steel barrier (Fig. 6b). In the 5 mm-thick barrier, the accumulated equivalent shear strain is only noticeable along the boundaries. This suggests that the flow experiences less shearing deformation after impact because of the smaller deflection of the stiffer 5 mm-thick steel barrier.

This section presented the influence of barrier stiffness on reduction of impact force from dry sand flow. A unified approach for estimating the design impact force on rigid and flexible barriers will be discussed later.

2.3.2 Debris Flow Impact on Multiple Barriers

The previous discussions only focused on how debris flows affect a single barrier to reveal the underlying impact mechanisms. To mitigate large volumes of debris flow by retaining debris along its path, however, multiple barriers need to be installed in the flow channel. In addition to impact, multiple barriers require investigation of overflow and landing mechanisms. Downstream barriers should also consider the effects of upstream barriers on debris flow dynamics and

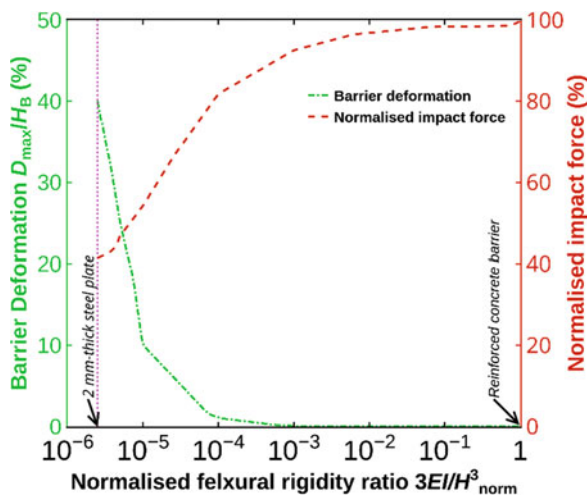


Fig. 5 Normalised barrier impact force and peak barrier deformation against normalised barrier flexural rigidity for dry sand flow impact on deformable barriers (redrawn from Ng et al. 2021c)

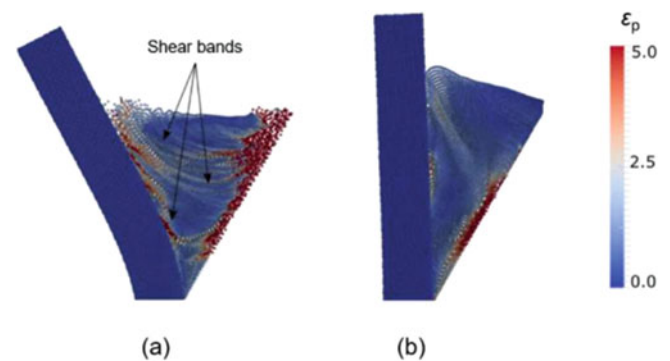


Fig. 6 Equivalent shear strain (ϵ_p) contour and shear bands within dry sands behind (a) 2 mm-thick steel barrier ($3EI/H_{\text{norm}}^3 = 2.5 \times 10^{-6}$) (b) 5 mm-thick steel barrier ($3EI/H_{\text{norm}}^3 = 1.0 \times 10^{-4}$) (redrawn from Ng et al. (2020b))

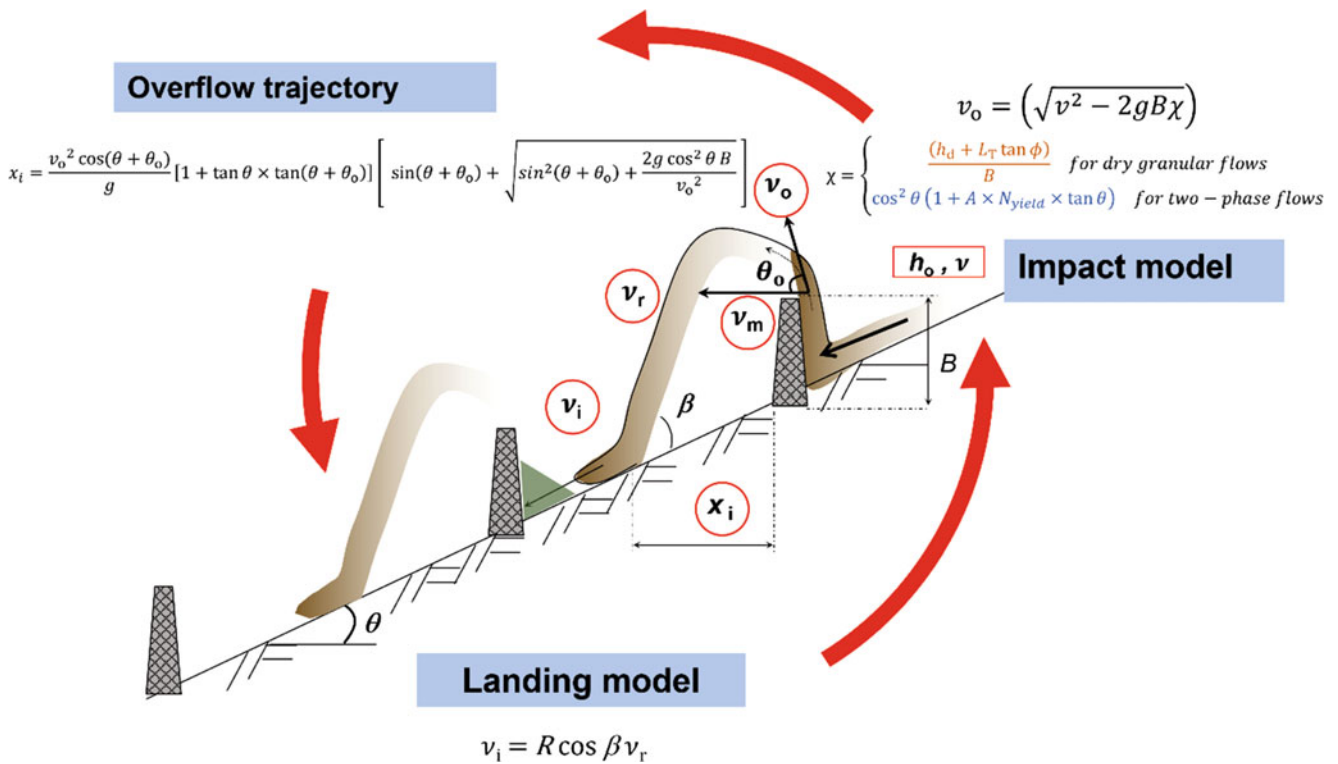


Fig. 7 A schematic diagram of the multiple barrier framework for both dry granular and two-phase flows. The framework includes (1) impact model, (2) overflow and landing kinematics, and (3) subsequent barrier impact

volume retention. Early designs of multiple barriers mainly focused on the volume of debris retained by each barrier, slowing down the flow and stabilising the channel gradient (VanDine 1996). However, this approach neglects the interaction between the flow and barriers (Kwan et al. 2015). An analytical model for a multiple barrier framework has been developed to rationally define barrier spacing, considering velocity attenuation during flow-barrier interaction, defining overflow trajectory, and calculating the velocity after landing that impacts the downstream barrier (Ng et al. 2019). Recently, it was found that contrary to the accretion of flowing grains along the free surface of the deposited material in dry granular flow, debris flow dissipates energy during flow-barrier interaction through internal shearing (Ng et al. 2022a). Debris flow is also found to launch at an angle that results in higher overflow distance requiring larger barrier spacing to prevent overflow from directly impacting or overtopping the subsequent barrier. Furthermore, it was also recently found that the equivalent fluid model may not accurately represent the reduction in friction coefficient between the flow and the bed after landing as it ignores the excess pore pressure generated in fluid phase (Ng et al. 2023a). In light of the new findings the existing multiple barrier framework from Ng et al. (2020a) has been updated to capture salient features of impact and overflow mechanisms for different flow types as shown in a schematic diagram in Fig. 7.

The updated multiple barrier framework in Fig. 7 shows a process-based approach to the design of multiple debris resisting barriers. Analytical equations are used to capture the three key processes of debris flow impact, overflow and landing based on impact mechanisms for different flow types. The framework can be used iteratively to design a series of barriers in the channel to resist a predefined volume of debris flow. Details of the updated multiple barrier framework, primarily the new changes to the existing framework of Ng et al. (2020a) are shown below.

2.3.2.1 Initial Impact Mechanism: Quantifying Energy Dissipation During Pile-Up and Run-Up

The first design step for multiple barriers is to determine energy dissipation at the first barrier and hence define overflow velocity (v_o). As explained earlier, flow can either pile-up, form jump or run-up depending upon the flow composition (Fig. 3). The energy dissipation also differs depending on the mechanism of flow-barrier interaction. For dry granular flows, pile-up mechanism occurs, and energy dissipates due to friction between the deposited and incoming flows. Velocity attenuation model proposed by Koo et al. (2017) can provide energy dissipation in dry granular flows and obtain overflow velocity. Since two-phase flows exhibit a jump or run-up mechanism during flow-barrier interaction, layer by layer frictional dissipation cannot be used. Ng et al. (2022a)

suggests an approach to define energy dissipation for two-phase flows based on yield stress of the interstitial fluid. These two approaches of estimating flow kinetic energy dissipation during barrier interaction can be unified while calculating overflow velocity as follows:

$$v_o = \sqrt{v^2 - 2gB\chi} \quad (3)$$

where,

$$\chi = \begin{cases} \frac{(h_d + L_T \tan \phi)}{B} & \text{for dry granular flows} \\ \cos^2 \theta (1 + A \times N_{\text{yield}} \times \tan \theta) & \text{for two-phase flows} \end{cases} \quad (4)$$

where, v_o is the overflow velocity at the crest of the barrier, g is the acceleration due to gravity, $B = H_B / \cos \theta$ is the vertical height of the barrier, H_B is the height of the barrier perpendicular to the channel inclination, θ is the slope inclination and χ is the flow kinetic energy dissipation, which depends on flow composition. For dry granular flows, h_d is the height of the deposited granular material, L_T is the length of the free surface of arrested granular material and ϕ is the friction angle. For two-phase flows, A is an empirical coefficient that considers the extent of internal shearing in the flow material in proportion to the yield stress of the interstitial fluid (τ_y). $N_{\text{yield}} = \tau_y / \rho g h \sin \theta$ is the dimensionless yield stress of the flow, which is the ratio of yield stress of the interstitial fluid and the driving shear stress component parallel to the slope. $A \times N_{\text{yield}}$ gives the dissipation of kinetic energy within the two-phase flow.

2.3.2.2 Overflow Trajectory and Landing Distance

Ng et al. (2019) assumes that overflow occurs horizontally from the crest of the barrier. This is true for the flow with pile-up mechanism. This assumption provides conservative estimate for the case when the flow overflows at an angle below the horizontal level. However, when the flow launches at an angle (θ_o) with horizontal, overflow distance increases compared to the horizontal launch (Ng et al. 2022a). An overflow trajectory as shown in Fig. 7 can be used to define the landing distance (x_i). Equation (5) provides formulation to calculate the minimum barrier spacing based on this overflow distance.

$$x_i = \frac{v_o^2 \cos(\theta + \theta_o)}{g} [1 + \tan \theta \times \tan(\theta + \theta_o)] \times \left[\sin(\theta + \theta_o) + \sqrt{\sin^2(\theta + \theta_o) + \frac{2g \cos^2 \theta B}{v_o^2}} \right] \quad (5)$$

For dry granular flows or for the cases where overflow occurs horizontally, the above equation transforms into the overflow equation given by Kwan et al. (2015) as:

$$x_i = \frac{v_m^2}{g} \left[\tan \theta + \sqrt{\tan^2 \theta + \frac{2gB}{v_m^2}} \right] \quad (6)$$

Once the overflow lands on the bed, velocity of landed flow can be calculated by using Eq. (7):

$$v_i = R \cos \beta v_r \quad (7)$$

where v_r is calculated by using the overflow trajectory as used in obtaining Eq. (5). This velocity is then used as impact velocity for the downstream barrier.

After landing, landed flow is assumed to flow with a velocity (v_i) and flow depth (h_o) and impact the subsequent barrier. The impact model (Eq. 3) is again applied to obtain overflow velocity and the process continues until the debris flow comes to a stop. Ng et al. (2023a) numerically investigated behaviour of two-phase flow of 500 m³ volume impacting two barriers. The computed results reveal that equivalent fluid models such as 3d-DMM (Koo et al. 2018) and DAN3D (McDougall and Hungr 2004), commonly used for debris flow analysis can underpredict the impact velocity and impact force at the second barrier. This is because when the overflow lands, it induces rapid undrained loading during impact increasing the pore fluid pressure within the landed flow (Ng et al. 2023a). This excess pore fluid pressure cannot be captured by equivalent fluid model. The increase in pore fluid pressure reduces effective basal friction (Eq. 1) resulting in flow acceleration, increased impact velocity at the barrier and hence increased impact force on the downstream barriers.

3 Design Recommendations for Debris Resisting Barriers

3.1 Debris Flow Impact Force on Barriers

Current state of understanding of impact mechanisms of debris flows can be reflected in international design guidelines (ASI 2013; CAGHP 2018; GEO 2022; NILIM 2016; SWCB 2019; Volkwein 2014). These international guidelines assume debris flows behave as continuum fluids. Debris flow impact forces on barriers are estimated using equilibrium of forces in hydrostatic models and conservation of linear momentum in hydrodynamic models. Although these international design guidelines predominantly considered hydrodynamic model only while estimating barrier impact force, multiple researchers have shown that both the

Table 1 Summary of dynamic impact coefficient (α) in international design guidelines

Region	Dynamic impact coefficient (α) (for soil debris impact on rigid barrier)	References
Canada	1.00	Hungr et al. (1984)
Mainland China	1.33 (for rectangular barrier) 1.47 (for square barrier)	CAGHP (2018)
Taipei, China	1.00	SWCB (2019)
HKSAR, China	1.50	GEO (2022)
Japan	1.00	NILIM (2016)
Austria	1.00	ASI (2013)

hydrostatic and hydrodynamic forces should be considered for wide range of impact scenarios (Armanini and Scotton 1992; Ng et al. 2020a; Song et al. 2017). Including both the hydrostatic and hydrodynamic forces, the total impact force exerted by debris flow can be expressed as:

$$F_{\text{peak}} = F_{\text{dynamic}} + F_{\text{static}} = \alpha \rho v^2 h w + 0.5 k \rho g h^2 w \quad (8)$$

where α and k are the dynamic and static impact coefficients, respectively; ρ is the flow density; v is the velocity of the flow; h is the flow depth and w is the channel width. While all the design guidelines assume $k = 1.0$ by neglecting the shear strength of fluidised debris, there is no consensus on the value of dynamic impact coefficient α as shown in Table 1.

Rearranging Eq. (8) gives normalised impact force on the barrier with respect to the hydrostatic force of debris flow as follows:

$$\frac{F_{\text{peak}}}{0.5 k \rho g h^2 w} = 1 + \frac{\alpha v^2}{0.5 k g h} \quad (9)$$

Simplifying the Eq. (9) by expressing the Froude number as $Fr = v/\sqrt{gh}$,

$$\frac{F_{\text{peak}}}{F_{\text{static}}} = 1 + \frac{2\alpha}{k} Fr^2 \quad (10)$$

Equation (10) can be used as a unified approach for estimating the design impact force on debris resisting barriers. In Eq. (10), if α is assumed to be unity, then the impact scenario is inelastic. However, if α is assumed to be two, then the impact scenario is elastic (Ng et al. 2019). Assuming an isotropic stress distribution within the debris material, the hydrostatic impact coefficient becomes $k = 1$ (Ng et al. 2021b). An increase of normalised impact force means the dynamic impact force has a higher contribution towards the peak impact force compared to hydrostatic force.

Figure 8 shows normalised impact force exerted by debris flows for different Froude conditions. In Fig. 8a, the analytical equations with $k = 1.0$; $\alpha = 1.5$ correspond to the design recommendation by Ng et al. (2020a), which was also recently adopted in Hong Kong for debris resisting rigid

barriers (GEO 2022). It is worthwhile to note that $k = 1.0$; $\alpha = 1.5$ provides a theoretical upper-bound for impact force on single rigid barrier for all types of investigated flows: water, two-phase (Liu 2019) and dry granular (Zanuttigh and Lamberti 2006). Another theoretical bounding line using Eq. (10) with $k = 1.0$; $\alpha = 1.0$ provides an upper bound for all data points of flexible barriers impacted by two-phase flow. Given that the existing design guideline in Hong Kong for debris resisting flexible barriers stipulates $k = 1.0$; $\alpha = 2.0$, there are prospects of load optimisation for flexible barrier design. Similarly, normalised peak impact force from dry granular flows on rigid barrier with basal clearance is also shown. The basal clearance H_c is normalised by the maximum flow depth h_0 and reported in the figure alongside the data points. The theoretical bounding line with $k = 1.0$; $\alpha = 1.0$ also provides a conservative estimate of impact force for basal clearances ($H_c/h_0 \leq 1.0$) and can be adopted for designing rigid barriers with a basal clearance.

Figure 8b shows the changes in the normalised peak impact force with flow Froude number (Fr) for the second rigid barrier of a dual barrier system. Measured as well as computed results are used in evaluating the design impact criteria for second barrier in a dual barrier system. Similar to Fig. 8a, the measured peak impact forces (F_{peak}) for dry granular flows and water are normalised by the theoretical static force (F_{static}) $0.5 k \rho g h_0^2 w$. The flow depth before impacting the second barrier is assumed to remain constant and equal to the flow depth at the first barrier for a conservative estimate of impact forces on the second barrier. Measured data from 5 m-long flume experiments using water and dry granular flow and computed results from design case in Hong Kong using two-phase flow are compared. Dry granular flows have lower Froude numbers than water flows because there is more energy dissipation via frictional shearing among the grains (Choi et al. 2015).

Water flows exert higher normalised impact forces compared to dry granular flows because the water overflow lands closer to the first barrier, allowing for sufficient length for flow acceleration (Ng et al. 2020a). The measured impact forces are compared with a theoretical equation for peak impact force (Eq. 10). In comparison with the upper bound for a single rigid barrier (Fig. 8a), $k = 1.0$; $\alpha = 1.5$, an upper bound with $k = 1.0$; $\alpha = 1.0$ provides a conservative estimate

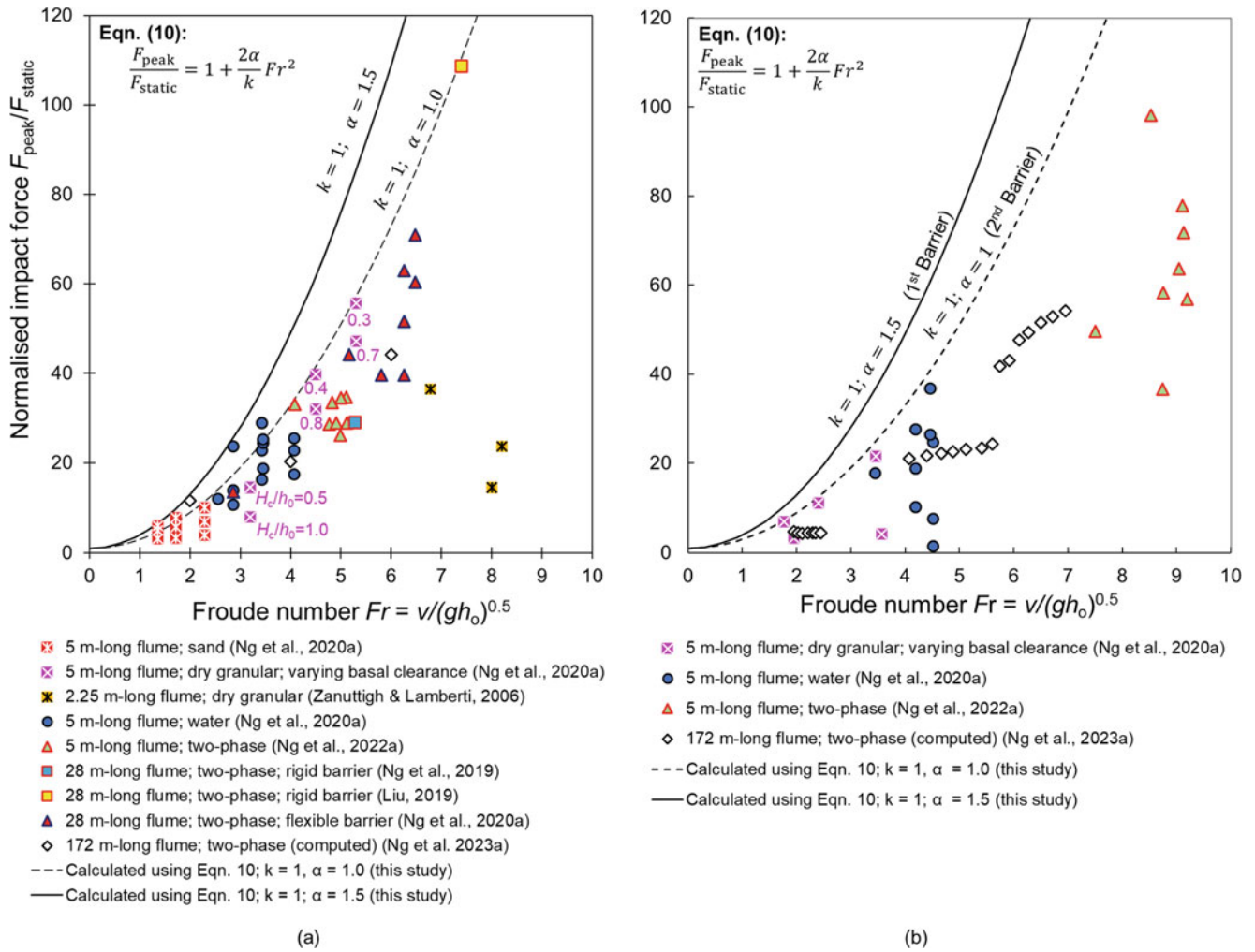


Fig. 8 Design impact force at different Froude numbers for (a) single barrier (rigid closed, rigid with basal clearance and flexible) (b) first and second rigid barrier in dual barrier system (modified from Ng et al. 2020a)

of the impact force exerted on the second barrier. The reduction in normalised peak impact forces for the second barrier is mainly due to energy dissipation during impact on the first barrier and landing between the dual barriers. Design recommendations by Ng et al. (2020a) have been verified with additional experimental and numerical results and are summarised in Table 2.

4 Summary and Conclusions

Current state-of-the-art research on the impact mechanisms of debris flows has been reviewed and discussed in this chapter. This study emphasises how debris flow composition, barrier opening, barrier stiffness and number of barriers govern the debris flow impact dynamics. The following key findings are summarised from this study:

1. Debris flow composition governs the mechanism of impact on barriers. Dry granular flows exhibit a pile-up

mechanism with progressive deposition of material behind the barrier during impact. The flow kinetic energy is dissipated via sustained shearing between grains and large bulk compressibility when the grains are angular. In contrast, water and fluidised two-phase flows show a jet-like runup mechanism. While energy is dissipated solely through viscous shearing in water flows, concentration of solids in two-phase flow dictates whether energy is dissipated by frictional, collisional, and viscous stresses within the flow.

- Newly proposed dimensionless overflow number N_{of} with a threshold value of 1.0 should be used to design rigid barrier with basal clearance ($0.2 \leq H_c/h_0 \leq 0.8$) to regulate discharge of debris material downstream while reducing the impact force.
- Impact force exerted on a barrier reduces nonlinearly with the stiffness of the barrier. Compared to a 1-m thick reinforced concrete barrier, a deformable barrier of 2 mm thick steel plate cantilevered at the base experiences only 40% of the impact force.

Table 2 Design recommendations for estimating the impact loads for different barrier configurations (modified from Ng et al. 2020a)

Design recommendations ^a	Dynamic impact coefficient (α)
Single rigid barrier without basal clearance	1.5
Single rigid barrier with basal clearance ($0.3 \leq H_c/h_0 \leq 1.0$)	1.0
Single flexible barrier	1.0
Second rigid barrier in a dual rigid barrier system	1.0

^a A static impact coefficient $k = 1.0$ is recommended to deduce static load

4. Design loads for a single closed rigid barrier should be estimated using $\alpha = 1.5$ with static load estimated using $k = 1.0$. For a single rigid barrier with basal clearance ($0.3 \leq H_c/h_0 \leq 1.0$), single flexible barrier, and the second barrier in a dual rigid barrier system design load should be estimated using $\alpha = 1.0$ with static load estimated using $k = 1.0$. It is worth noting that these design recommendations are for continuum-like debris material and do not consider discrete impacts from a single boulder or a cluster of boulders. As such, other design guidelines can provide higher α values compared to this study.

Acknowledgments The authors are grateful for financial support from the area of excellence project grant AoE/E-603/18 provided by the Research Grants Council (RGC) of the Government of Hong Kong Special Administrative Region (HKSAR), China. S. Poudyal, A. Bhatta and W.A.R.K. De Silva gratefully acknowledge the support from Hong Kong PhD Fellowship Scheme award provided by RGC of HKSAR.

References

- Armanini A, Scotton P (1992) Experimental analysis on the dynamic impact of a debris flow on structures. In: Proceedings of International Symposium on Interprevent, pp 107–116
- Armanini A, Rossi G, Larcher M (2020) Dynamic impact of a water and sediments surge against a rigid wall. *J Hydraul Res* 58(2):314–325. <https://doi.org/10.1080/00221686.2019.1579113>
- ASI (2013) ONR 24801 protection works for torrent control – static and dynamic actions on structures. Vienna, Austrian Standards Institute, p 32
- CAGHP (2018) Specification of design for debris flow prevention (T/CAGHP 021–2018). China University of Geosciences Press, Wuhan
- Choi CE, Au-Yeung SCH, Ng CWW, Song D (2015) Flume investigation of landslide granular debris and water runoff mechanisms. *Géotechnique Lett* 5(1):28–32. <https://doi.org/10.1680/geolett.14.00080>
- Choi CE, Goodwin SR, Ng CWW, Cheung DKH, Kwan JSH, Pun WK (2016) Coarse granular flow interaction with slit structures. *Géotechnique Lett* 6(4):267–274. <https://doi.org/10.1680/jgele.16.00103>
- Choi CE, Ng CWW, Liu H, Wang Y (2020) Interaction between dry granular flow and rigid barrier with basal clearance: analytical and physical modelling. *Can Geotech J* 57(2):236–245. <https://doi.org/10.1139/cgj-2018-0622>
- Froude MJ, Petley DN (2018) Global fatal landslide occurrence from 2004 to 2016. *Nat Hazards Earth Syst Sci* 18(8):2161–2181. <https://doi.org/10.5194/nhess-18-2161-2018>
- GEO (2022) GEO Technical Guidance Note No. 52 (TGN 52) Enhanced Technical Guidance on Design of Rigid Debris-resisting Barriers. Geotechnical Engineering Office, Civil Engineering and Development Department, The Government of the Hong Kong Special Administrative Region, Hong Kong SAR, 10 p
- Goodwin GR, Choi CE (2020) Slit structures: fundamental mechanisms of mechanical trapping of granular flows. *Comput Geotech* 119: 103376. <https://doi.org/10.1016/j.compgeo.2019.103376>
- Guha-Sapir D (2020) CRED (2020) EM-DAT: the emergency events database. Université catholique de Louvain (UCL), Université catholique de Louvain (UCL)
- Guzzetti F, Peruccacci S, Rossi M, Stark CP (2008) The rainfall intensity–duration control of shallow landslides and debris flows: an update. *Landslides* 5(1):3–17. <https://doi.org/10.1007/s10346-007-0112-1>
- Huebl J, Fiebiger G (2005) Debris-flow mitigation measures. In: Jakob M, Hungr O (eds) *Debris-flow hazards and related phenomena*. Praxis Springer, Berlin, pp 445–487
- Hungr O, Morgan GC, Kellerhals R (1984) Quantitative analysis of debris torrent hazards for design of remedial measures. *Can Geotech J* 21(4):663–677. <https://doi.org/10.1139/t84-073>
- Hungr O, Leroueil S, Picarelli L (2014) The Varnes classification of landslide types, an update. *Landslides* 11(2):167–194. <https://doi.org/10.1007/s10346-013-0436-y>
- Iverson RM (2015) Scaling and design of landslide and debris-flow experiments. *Geomorphology* 244:9–20
- Koo RCH, Kwan JSH, Ng CWW, Lam C, Choi CE, Song D, Pun WK (2017) Velocity attenuation of debris flows and a new momentum-based load model for rigid barriers. *Landslides* 14(2):617–629. <https://doi.org/10.1007/s10346-016-0715-5>
- Koo RCH, Kwan JSH, Lam C, Goodwin SR, Choi CE, Ng CWW, Yiu J, Ho KKS, Pun WK (2018) Back-analysis of geophysical flows using three-dimensional runout model. *Can Geotech J* 55(8):1081–1094. <https://doi.org/10.1139/cgj-2016-0578>
- Kwan JSH, Cheung RWM (2012) Suggestions on design approaches for flexible debris-resisting barriers, Discussion note no. DN 1/2012. Geotechnical Engineering Office HKSAR, Hong Kong, 91 p
- Kwan JSH, Koo RCH, Ng CWW (2015) Landslide mobility analysis for design of multiple debris-resisting barriers. *Can Geotech J* 52(9): 1345–1359. <https://doi.org/10.1139/cgj-2014-0152>
- Liu H (2019) Impact mechanisms of debris flow against multiple rigid barriers with basal clearance. PhD thesis, The Hong Kong University of Science and Technology, HKSAR, China. <https://doi.org/10.14711/thesis-991012752655103412>
- Liu H, Choi CE, Poudyal S, Jia Z, Ng CWW (2023) A new overflow number for analysing and designing dual rigid barriers with basal clearance. *J Geotech Geoenviron* (under-review)
- McDougall S, Hungr O (2004) A model for the analysis of rapid landslide motion across three-dimensional terrain. *Can Geotech J* 41(6):1084–1097. <https://doi.org/10.1139/t04-052>
- Ng CWW, Choi CE, Song D, Kwan JSH, Koo RCH, Shiu H, Ho KKS (2015) Physical modeling of baffles influence on landslide debris mobility. *Landslides* 12(1):1–18. <https://doi.org/10.1007/s10346-014-0476-y>
- Ng CWW, Choi CE, Liu LHD, Wang Y, Song D, Yang N (2017) Influence of particle size on the mechanism of dry granular run-up on a rigid barrier. *Géotechnique Letters* 7(1):79–89. <https://doi.org/10.1680/jgele.16.00159>

- Ng CWW, Choi CE, Majeed U, Poudyal S, De Silva W (2019) Fundamental framework to design multiple rigid barriers for resisting debris flows. In: Proceedings of the 16th Asian regional conference on soil mechanics and geotechnical engineering. Taipei, Taiwan, pp. 1–11
- Ng CWW, Choi CE, Liu H, Poudyal S, Kwan JSH (2020a) Design recommendations for single and dual debris flow barriers with and without basal clearance. In: Sassa K, Mikoš M, Sassa S et al (eds) Understanding and reducing landslide disaster risk. Springer International Publishing, Cham, pp 33–53. https://doi.org/10.1007/978-3-030-60196-6_2
- Ng CWW, Wang C, Choi CE, De Silva WARK, Poudyal S (2020b) Effects of barrier deformability on load reduction and energy dissipation of granular flow impact. *Comput Geotech* 121:103445. <https://doi.org/10.1016/j.compgeo.2020.103445>
- Ng CWW, Liu H, Choi CE, Kwan JSH, Pun WK (2021a) Impact dynamics of boulder-enriched debris flow on a rigid barrier. *J Geotech Geoenviron* 147(3):04021004. [https://doi.org/10.1061/\(ASCE\)GT.1943-5606.0002485](https://doi.org/10.1061/(ASCE)GT.1943-5606.0002485)
- Ng CWW, Majeed U, Choi CE, De Silva WARK (2021b) New impact equation using barrier Froude number for the design of dual rigid barriers against debris flows. *Landslides* 18:2309–2321. <https://doi.org/10.1007/s10346-021-01631-7>
- Ng CWW, Choi CE, Liu H, Wang C, Kwan JSH (2021c) Impact mechanisms of debris flow on barriers: modelling, analysis and design. In: SCG-XIII International Symposium on Landslides. ISSMGE, Cartagena
- Ng CWW, Yang B, Liu ZQ, Kwan JSH, Chen L (2021d) Spatiotemporal modelling of rainfall-induced landslides using machine learning. *Landslides* 18:2499–2514. <https://doi.org/10.1007/s10346-021-01662-0>
- Ng CWW, Bhatta A, Choi CE, Poudyal S, Liu H, Cheung RWM, Kwan JSH (2022a) Effects of debris flow rheology on overflow and impact dynamics against dual-rigid barriers. *Géotechnique* 1–14. <https://doi.org/10.1680/jgeot.21.00226>
- Ng CWW, Liu H, Choi CE, Bhatta A, Zheng M (2022b) Effects of basal clearance on the impact dynamics of dry granular flow against dual rigid barriers. *Can Geotech J* 59(7):1161–1174. <https://doi.org/10.1139/cgj-2020-0682>
- Ng CWW, Jia Z, Poudyal S, Bhatta A, Liu H (2023a) Two-phase MPM modelling of debris flow impact against dual rigid barriers. *Géotechnique* 1–14. <https://doi.org/10.1680/jgeot.22.00199>
- Ng CWW, Choi CE, Liu H, Poudyal S, Bhatta A, De Silva WARK, Cheung RWM (2023b) Class A prediction symposium on debris flow impact forces on single and dual barriers. *HKIE Transactions* (accepted)
- NILIM (2016) Manual of technical standards for establishing Sabo master plan for debris flow and driftwood: Technical note of NILIM, no.905. National Institute for Land and Infrastructure Management Sabo Planning Division Sabo Department, Japan, 84 p
- Ozturk U, Bozzolan E, Holcombe EA, Shukla R, Pianosi F, Wagener T (2022) How climate change and unplanned urban sprawl bring more landslides. *Nature* 608(7922):262–265. <https://doi.org/10.1038/d41586-022-02141-9>
- Piton G, Recking A (2016) Design of sediment traps with open check dams. I: hydraulic and deposition processes. *J Hydraul Eng* 142(2): 04015045. [https://doi.org/10.1061/\(ASCE\)HY.1943-7900.0001048](https://doi.org/10.1061/(ASCE)HY.1943-7900.0001048)
- Song D, Ng CWW, Choi CE, Zhou GGD, Kwan JSH, Koo RCH (2017) Influence of debris flow solid fraction on rigid barrier impact. *Can Geotech J* 54(10):1421–1434. <https://doi.org/10.1139/cgj-2016-0502>
- Song D, Choi CE, Ng CWW, Zhou GGD (2018) Geophysical flows impacting a flexible barrier: effects of solid-fluid interaction. *Landslides* 15(1):99–110. <https://doi.org/10.1007/s10346-017-0856-1>
- SWCB (2019) Soil and water conservation handbook. Soil and Water Conservation Bureau, Taiwan, pp 523
- Takahashi T (2014) Debris flow: mechanics, prediction and countermeasures, 2nd edn. CRC Press. (ISBN 9781138073678). 572 p
- VanDine DF (1996) Debris flow control structures for forest engineering. Res.Br., BC Min.for., Victoria, BC, Work. Pap 8, 1996
- Volkwein A (2014) Flexible debris flow barriers: design and application (WSL reports 18). Swiss Federal Institute for Forest, Snow and Landscape Research WSL, 29 p
- Wendeler C, Volkwein A, Roth A, Denk M, Wartmann S (2007) Field measurements and numerical modelling of flexible debris flow barriers. In: The fourth international conference on debris-flow hazards mitigation: mechanics, prediction and assessment (DFHM-4). Millpress, Chengdu, pp 681–687
- Wendeler C, Volkwein A, McArdell BW, Bartelt P (2019) Load model for designing flexible steel barriers for debris flow mitigation. *Can Geotech J* 56(6):893–910
- World Bank (2022) GFDRR annual report 2022: bringing resilience to scale (English). World Bank Group, Washington, DC
- Yik M, Pun WK, Kwok FH, Pho J, Ng CWW (2023) Perceptions of landslide risks and warnings in Hong Kong. *Landslides* 1–14:1211–1224. <https://doi.org/10.1007/s10346-022-02021-3>
- Zanuttigh B, Lamberti A (2006) Experimental analysis of the impact of dry avalanches on structures and implication for debris flows. *J Hydraul Res* 44(4):522–534. <https://doi.org/10.1080/00221686.2006.9521703>
- Zhou GGD, Ng CWW (2010) Dimensional analysis of natural debris flows. *Can Geotech J* 47(7):719–729. <https://doi.org/10.1139/T09-134>

Open Access This chapter is licensed under the terms of the Creative Commons Attribution 4.0 International License (<http://creativecommons.org/licenses/by/4.0/>), which permits use, sharing, adaptation, distribution and reproduction in any medium or format, as long as you give appropriate credit to the original author(s) and the source, provide a link to the Creative Commons license and indicate if changes were made.

The images or other third party material in this chapter are included in the chapter's Creative Commons license, unless indicated otherwise in a credit line to the material. If material is not included in the chapter's Creative Commons license and your intended use is not permitted by statutory regulation or exceeds the permitted use, you will need to obtain permission directly from the copyright holder.





A Review of the Disaster Risk Assessment Perspectives

Dayan Munasinghe, Terrance Fernando, Kaushal Keraminiyage, and Asiri Karunawardena

Abstract

Researchers have explored different risk assessment approaches from the perspectives of different disciplines to capture urban risks, resulting in many risk assessment frameworks. In these frameworks, the risk environment is analysed using different quantitative and qualitative assessment methods, such as fuzzy set, probability theory, and evidence theory. While each approach has contributed to risk assessment, they suffer from a lack of consensus in defining and measuring the impact of risk in an urban environment.

Therefore, the study aims to conduct a literature survey to consolidate a common set of risk assessment perspectives and approaches for measuring these risks.

A structured review was carried out to achieve the aim of this research. The research question used for conducting the literature review was “What approaches are being used to define and measure the impact of hazard risks in an urban environment?”. The PICO (Population, Intervention, Compression Intervention, and Outcome) method was used to generate the search string for the literature review by considering the keywords in the research question. Initially, 206 research papers were selected through a search strategy, and by applying a screening method, 119 research articles were selected for the detailed review. The Nvivo software was supported for the review purpose; then, a mind map was developed, integrating all the risk assessment perspectives.

Risk assessments were summarised by considering the various researchers’ perspectives. Thirty-four risk perspectives were identified through the literature, and a mind map was developed to understand the connectivity.

This mind map was converted into a network diagram, and future requirements of risk perspectives were identified based on the risk assessment network diagram. According to the analysis, risk communication, risk treatment, critical curve, judgment curve, and risk matrix could be identified as future research areas. The risk reduction measuring strategies were identified by considering the feedback loop of the network diagram. Thus, 14 risk reduction strategies could be identified through the analysis.

The risk assessment frameworks focused on holistic approaches, but most research studies did not adequately follow the risk perspectives. Therefore, research gaps were identified in the risk assessment process, and the areas were highlighted as state-of-the-art to conduct future research studies. The feedback loops of the network diagram emphasised the risk reduction strategies, which could be further researched through application to a case study.

Keywords

Risk assessment · Risk perspective · Risk reduction strategies · Risk communication

1 Introduction

Disaster Risk Assessment (DRA) is a fundamental activity necessary for establishing a clear understanding of local risks to implement appropriate interventions for risk reduction activities and build resilient urban environments. Therefore, there are many international efforts to encourage governments to implement DRA to create sustainable cities and communities through partnerships (Nations U 2015b). For example, many disaster risk reduction action plans such as the International Decade for Natural Disaster Reduction (Nations 1989), the Yokohama Strategy and Plan of Action for a Safer World, the Hyogo Framework for Action (HFA) (2005–2015), Sendai Framework for Disaster Risk Reduction

D. Munasinghe (✉) · A. Karunawardena
National Building Research Organisation, Jaffna, Sri Lanka

T. Fernando · K. Keraminiyage
University of Salford, School of Science, Engineering, and
Environment, Manchester, UK
e-mail: t.fernando@salford.ac.uk; K.P.Keraminiyage@salford.ac.uk

(2015–2030) are calling for governments to focus on disaster risk reduction against climate-induced disasters (Nations U 2015a). In this context, the Sendai Framework calls for strengthening the scientific capacities to develop or apply DRA methodologies and frameworks to assess vulnerabilities, exposure, and disaster risks for various hazards (Nations U 2015b). Such risk assessment frameworks need to take a systemic view of DRA within urban environments by considering the interdependencies of various subsystems and help city governors fully understand the cascading impact of hazards across various subsystems and domains (Hasani 2014).

Due to the complex relationships that exist among the risk assessment variables, researchers have explored different risk assessment approaches, resulting in many risk assessment frameworks (Khazai et al. 2014; Yeganeh and Sabri 2014; Zlatanova et al. 2014; Munasinghe and Wijegunaratne 2015; Torre et al. 2019; Huang et al. 2020). In practice, different institutions and countries have used different risk management frameworks for assessing disaster risks in their local contexts.

A risk management framework is a guided process on risk management principles, policies, and practices developed more systematically by various institutions. Pedro Basabe (2018) has divided these frameworks into four categories: (1) Generic Principles, guidelines, and methods, (2) Applied principles for governmental organisations, (3) Intergovernmental framework, and (4) National Institutionalised Framework. The examples of category one frameworks on “Generic principles” include ISO31000 and IRGC risk frameworks which are purely theoretical frameworks. In contrast, OECD and UNECE risk assessment frameworks are category two frameworks on “Applied principles for governmental organisations”, which are focused on a specific thematic area (OECD 2012). For example, the OECD methodology, developed by G20 countries, focused on assessing the financial risk status of a country (OECD 2012). On the other hand, the Sendai Framework, introduced by UNISDR, is an example of a category three risk framework on “Intergovernmental risk management”, which proposes seven targets and four priorities that are aimed at supporting the reduction of existing and new disaster threats (UNDRR 2015). In contrast, the National Risk Register, prepared by the UK cabinet office, describes the national risk reduction approaches aligned to the National Institutionalised framework type, which comes under category four (Cabinet-Office-UK 2020).

Even though the risk frameworks are different, these frameworks possess common characteristics since they all focus on risk, vulnerabilities, and their causes and consequences. They focus on hazards, existing linkages to development, risk governance and regulations (Pedro Basabe 2018). Therefore, it is essential to understand these frameworks’ common characteristics and terminologies to

establish a holistic risk assessment approach (Hasani et al. 2014).

In these frameworks, the analysis of the risk environment is carried out by using different quantitative and qualitative assessment methods. Some examples of methods used in risk assessment include possibility theory, fuzzy set, probability theory, and evidence theory (Giorgini 2009). Aksha et al. (2020) have identified various limitations in these current multi-hazard risk assessment approaches, which include: a lack of standard definitions for multi-hazard risk, lack of a holistic approach for integrating risks from different hazards, unavailability of intensive data required for risk assessment, confinement of risk assessments within disciplinary boundaries, and the inherent uniqueness of each place generating geographically specific hazard conditions and outcomes.

Therefore, this study aims to understand how the risk assessment characteristics are discussed in various research studies in the urban environment. It aims to answer the question “What approaches are being used to define and measure the impact of hazard risks in an urban environment?”

2 Literature Survey

This section discusses the literature review approach used to gather relevant research papers to explore the research question. The PICO method was used to generate the search string by considering the keywords in the research question for identifying the relevant literature. The PICO represents four groups: Population, Intervention, Comparison intervention, and Outcome. Table 1 presents the initial and extended keywords identified for the literature review.

The keywords were connected with “AND” or “OR” operations. The “OR” connection was used to connect within the group, and the “AND” connection was used to connect between the groups. The following literature searching statement was used to search the research papers that match with keywords, abstract and title of the research papers in the Scopus and the Web of Science databases. Further, eight reports were collected from intergovernmental organisational websites. A total number of 206 research articles were selected for screening.

Literature search statement: (‘Urban’ OR ‘Urban Infrastructure’ OR ‘Urban Development’ OR ‘Urban design*’ OR ‘Urban Plan*’ OR City OR Town) AND (Hazard OR Risk OR ‘Cascading effect’ OR Propagation OR ‘Cascading failure OR ‘Chain Reaction’ Or ‘System thinking’ OR ‘System Dynamics’ OR interdependence*) AND (Resilience OR Impact OR Disaster OR Perturbation OR Damage OR Failure) AND (Model* OR Theory* OR Method* OR Formulas OR Index OR Eq. OR Approach OR Simulation).

Table 1 Keywords selection—PICO method

Population (P)	Intervention/control (I)	Comparison intervention (C)	Outcome (O)
Urban	Hazard risk	Measure impact	Approach
Urban	Hazard	Damage	Method*
Urban infrastructure	Risk	Perturbation	Model*
Urban design*	Propagation	Disaster	Theory*
Urban plan*	Cascading effect	Resilience	Formulas
City	Cascading failure	Failure	Index
Town	Chain reaction	Impact	Simulation
	System thinking		Approach*
	System dynamics		
	Interdependence*		

Figure 1 shows the PRISMA method of screening the literature records for the study. The following inclusion criteria were used to select the most relevant papers for this study, which are most relevant to generate risk propagation modelling: consider only the research papers published after 1999 in English; consider papers only from the key subjects areas Engineering, Environmental science, Physics, Mathematics, and Social Science, which are more relevant with the research scope. This process resulted in 123 papers for further consideration. After reading the abstracts, only 119 research papers were selected for the full paper review process.

2.1 Detailed Review Process

A systematic/ mapping review approach was selected because of mapping the existing characteristics on a network diagram. Accordingly, each research paper was reviewed to identify key risk assessment characteristics and make a network diagram. The Nvivo12 Pro software was used to support the literature review (Sweet 2014), and cases/nodes were created for each risk character. Figure 2 shows different risk management perspectives that were addressed in the chosen research papers in this study.

2.2 DRA Characteristics and Percentage of Research Interests

According to the review, 94% of the research papers discussed the risk analysis approaches, and in there, hazard assessments (97%); vulnerability assessment (82%); exposures (66%); risk propagation (19%); and risk perception (30%) were discussed. Although risk appetite was discussed in 74% of the research papers, this aspect was not discussed in detail. For example, the key elements of risk appetite, such as risk thresholds, risk tolerance, and critical or judgment values, were only found in 1% of research studies. The following section discusses the risk analysis and risk analysis methods in detail.

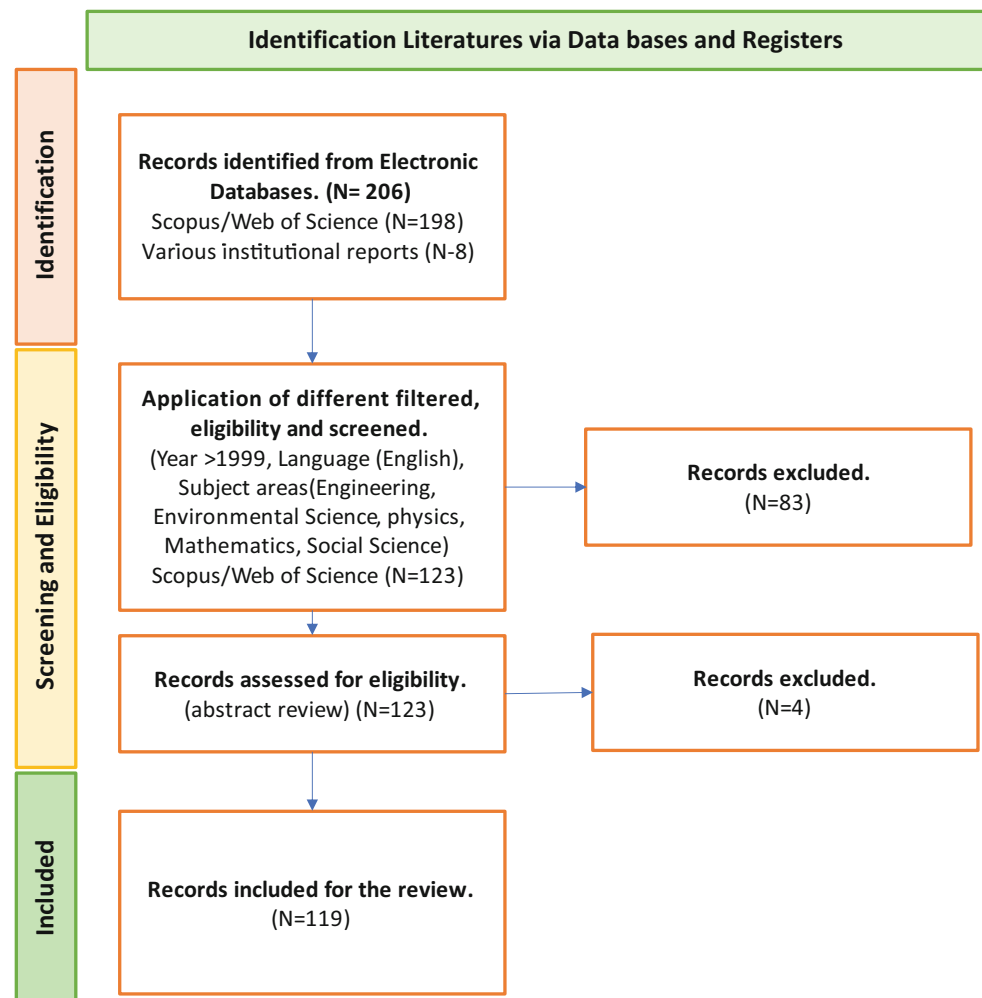
3 Risk Assessment

The risk assessment is an important study in risk management and is conducted to assess the risk status of the community. According to Zlatanova et al. (2014), risk management is comprised of four major phases; (1) risk identification, (2) risk evaluation, (3) choice and implementation of risk reduction measures and instruments, and (4) monitoring and maintenance of acceptable risk. Within this context of risk management, the first two phases (risk identification and risk evaluation) belong to the risk assessment. However, it is evident that there are many ways to define the key risk assessment activities. For example, ISO-Guide73 (2009) has defined risk assessment activities as risk understanding, analysis, and evaluation.

In contrast, Corominas et al. (2013) have proposed risk analysis and risk evaluation as the key phases in risk assessment, where the key activities of risk analysis are hazard identification, hazard assessment, inventory of elements at risk and exposure, vulnerability assessment, and risk estimation. In this phase, hazard identification is the initial step for gaining insights into any threat, uncertainty, vulnerability, and unexpected event that can become a source or trigger for risk to materialise (Tran et al. 2018). Risk evaluation is the stage at which values and judgments enter the decision process, explicitly or implicitly, including considerations of the importance of the estimated risks and the associated social, environmental, and economic consequences to identify a range of alternatives for managing the risks (Corominas et al. 2013).

Risk Evaluation is considered an essential step in the risk assessment process to guide how to improve the current system to face future risks. At this step, values and judgments enter the decision-making process, explicitly or implicitly, to consider the severity of the estimated risks and the associated social, environmental, and economic consequences and to identify a range of alternatives for managing the risks (Corominas et al. 2013).

Fig. 1 Stages in PRISMA review as carried out in the study



3.1 Risk Analysis

There is no exact definition for risk, which varies from discipline to discipline (Stock and Wentworth 2019; Aksha et al. 2020). According to the generic principles, risk analysis is a process of understanding the nature of risk and deciding on the level of risk to provide a basis for risk evaluation and decisions about risk treatment (ISO-Guide73 2009). Typically, risk analysis is conducted by considering three variables: hazard, vulnerability, and exposure (Gallopín 2006; Bibi et al. 2018; Huang et al. 2020; Zhou et al. 2020).

According to the literature, the risk analysis includes parameters such as consequences, probability of occurrence, hazard, exposure, vulnerability, capacity, triggering factors, cycle incubations, perturbation, range of alternatives, uncertainty, unexpected events, threat and perception (Gallopín 2006; Corominas et al. 2013; Zlatanova et al. 2014; Izquierdo-Horna and Kahhat 2018; Tran et al. 2018; Huang et al. 2020; Zhou et al. 2020). The following subsections discuss the connections between the risk analysis variables in detail.

3.2 Risk Analysis Methods

Different risk assessment formulas are used in different assessments, and in general, the risk is considered a function of hazard, vulnerability, and exposure. This section discusses the representation of the risk values to support decision-making. However, Corominas et al. (2013) have developed a formula for landslide risk assessment by subcategorisation of hazard based on its characteristics of magnitude, spatial probability, and temporal probability. His formula and expression can be described as follows.

$$R = P(M_i) \cdot P(X_j | M_i) \cdot P(T | X_j) \cdot V_{ij} \cdot C$$

where R is the risk due to the occurrence of a landslide of magnitude M_i on an element at risk located at a distance X from the landslide source, $P(M_i)$ is the probability of occurrence of a landslide of magnitude M_i , $P(X_j | M_i)$ is the probability of the landslide reaching a point located at a distance X from the landslide source with an intensity j, $P(T | X_j)$ is the

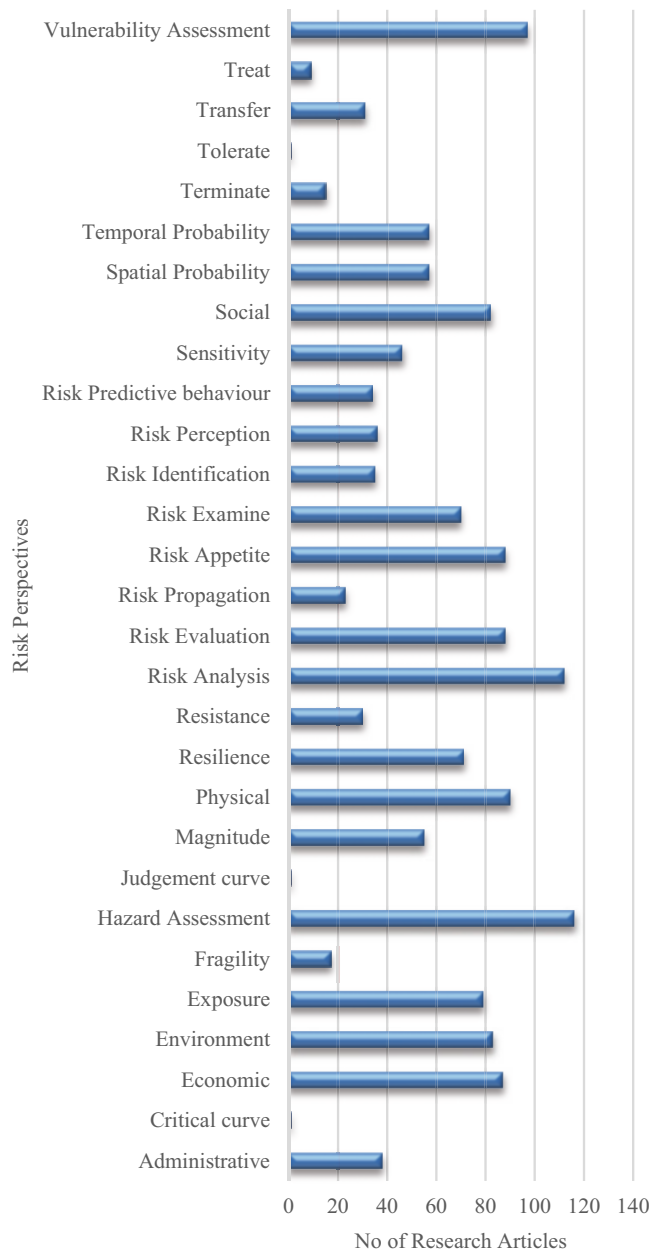


Fig. 2 Number of research papers categorised under each risk characteristic

probability of the element being at the point X at the time of occurrence of the landslide, V_{ij} is the vulnerability of the element to a landslide of magnitude i and intensity j , and C is the monetary value of the element at risk (Corominas et al. 2013). Here, the magnitude defines the event’s size when a risk materialises, sometimes referred to as the ‘severity’ of the event, is compared with the impact or consequences of the risk materialising (Hopkin 2010). Also, the intensity is expressed by considering the propagation mechanism—for example, the landslide intensity coupled with its volume or the kinetic energy (Corominas et al. 2013).

Different theories and approaches are used for different hazard analyses. Mathematical and statistical analysis, quantitative methods, Multi-Criteria Decision Analysis, system dynamic method and uncertainty methods are the most common methodologies to assess disaster risk (Yeganeh and Sabri 2014). These theories and approaches could be categorised into four types; (1) Stochastic programming approach, where variables are considered here as random variables with defined probability distributions; (2) Fuzzy programming approach, which considers variables as fuzzy numbers; (3) Stochastic dynamic programming which considers random variables distributed in all areas of multi-stage decision making; (4) Robust optimisation, which finds the optimum result for a given set of input data to an actual scenario (Yeganeh and Sabri 2014). Yeganeh and Sabri (2014) have identified four common techniques that could be used for developing weights for each variable: ranking method, rating method, pairwise comparison method, and trade-off analysis method & comparing method.

Most of the risk assessment has mainly considered the physical features of settlements. However, some studies address the valuation of human life in risk assessments. For example, Zhou et al. (2020) have considered the ‘Value of Statistical Life (V‘L)’ and calculated risk using the following equation.

$$\text{Risk}(I) = \text{Probability}(I) \times \text{Loss}(I)$$

$$\text{Loss}(I) = \text{LDE}(I) + \text{LVSL}(I)$$

Here, direct loss (Loss(I) is calculated by using direct economic loss (LDE (I)) and the loss of VSL(LVSL(I)). The evaluation method of VSL calculates risk as a human capital approach or willingness-to-pay approach (Zhou et al. 2020).

The presentations of the risk values are also studied in this survey. Lee et al. (2015) described that risk values should be classified into zero (0) to one (1) range for easy classification purposes or assigned unique names for different risk classes according to their probabilities and level of perturbations. For example, based on the risk levels, the following names are assigned: Medusa, Cassandra, Pandora, Pythia, Cyclops, and Damocles (Stock and Wentworth 2019). A risk matrix is a standard method for representing risk values in most risk assessments (Hopkin 2010; Corominas et al. 2013). In this method, a plot is generated by individually considering the expected losses against the probability of occurrence of natural hazards. These individual risk matrices could be integrated into the total risk matrix for a specific area. Figure 3 shows the risk matrix diagram, which is a graph considering two dimensions impact and likelihood.

Trajectory trend curves can be used to monitor risk values with various criteria, and they can be overlaid with the risk

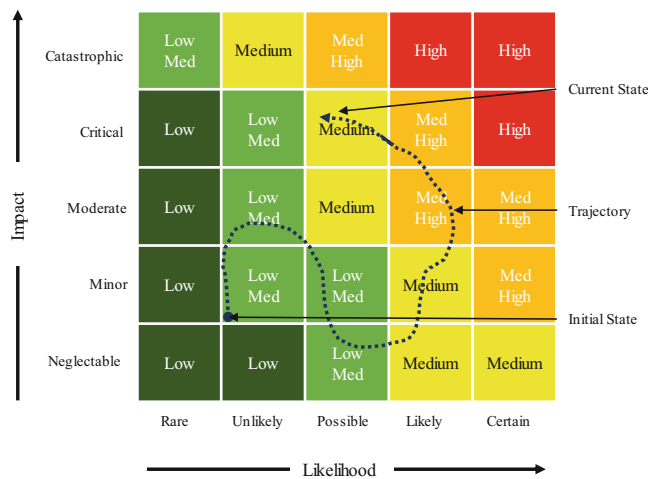


Fig. 3 Risk matrix and trajectory curve

matrix to see the risk value variations with identified variables. This method has been used by Gallopín (2006) to monitor social resilience values as the ability of groups or communities to cope with external stresses and disturbances due to social, political, and environmental change. Figure 3 illustrates the trajectory trends curve with an initial state, trajectories, and current state. This method has linked with a risk matrix.

3.3 Risk Evaluation Methods

Risk evaluation is a significant step in risk assessment and is discussed in the risk management frameworks. The ISO-Guide73 (2009) defines risk evaluation as comparing risk analysis results with risk criteria to determine risk appetite. This risk evaluation assists the risk treatment decisions. For example, gathering the stakeholders' perceptions on risk status can be an evaluation. Kellens et al. (2013) have described risk perception as a subjective risk assessment that can assess the attendees' perception of risk status on an identified perturbation. For example, Xu et al. (2020) have identified that the new communication (media) systems help to increase the community perception level in terms of understanding of risks (magnitude and frequency levels). Therefore, it is required to find literature on risk perception methods that could be used for risk assessments.

3.4 Risk Perception

Risk perception is a complex process that encompasses both cognitive (e.g., likelihood, knowledge) and affective (e.g., feelings, perceived control) aspects (Kellens et al. 2013). Two methods are used for risk perception studies: the

Psychometric Paradigm and the heuristics approaches (Kellens et al. 2011, 2013). The psychometric Paradigm is an influential and popular theoretical framework in risk perception which attempts to quantify personal risk perception and attitudes through a structured questionnaire. Heuristics, or simple and efficient rules of thumb, are often used to simplify complex problems and make decisions without using all of their cognitive capacities. The prominent approaches to examine risk perceptions are Expectancy Valence Approaches (EV) and Applications of Contingent Valuation Methods (CVM).

Expectancy Valence Approaches (EV): This approach focuses on the explanation of people's adaptive behaviour, which can predict by using their valences for different outcomes like a desire to protect oneself, instrumentalities of their performance of actions like installation of flood barriers, and experience of previous successful performances on risk reduction. The concepts are based on psychological theories, and a few other methods are linked with the EV, which could be described as follows.

- **Protection Motivation Theory (PMT):** This tool helps analyse the threat and coping appraisal of a person's perception. Three constructs are defined as a tool to predict the coping appraisal: response efficiency, self-efficiency, and response cost (Kellens et al. 2013). Two constants for predicting the threat appraisal are perceived probability and perceived consequence (Bubeck et al. 2012). Bubeck et al. (2012) have discussed the usability of PMT for flood risk management, emphasising that these aspects should receive greater attention in risk communication policies.
- **RCSA model (Risk, Coping and Social Appraisal):** This model has three appraisals, Risk appraisal (includes a perception of severity and perception of probability), Coping Appraisal (includes self-efficiency and response-efficiency), and Social Appraisal (includes community identification and perceived norms). This tool is used to understand the farmers' drought adaptation practices and concludes that the tool is a better predictor of adaptation intention than a strictly demographic model (Truelove et al. 2015).
- **Protective Action Decision Model (PADM):** This tool is closely like the PMT and is mainly applied for earthquake hazards. Here, efficiency attributes are protecting people, protecting property, and protecting utilities.
- **Motivation Intention Volition Model (MIV):** "Motivation results from perceived risk but may be hampered by a lack of perceived personal responsibility and tendencies to avoid or suppress the perceived threat. A person's intention to adopt hazard adjustments is further influenced by perceived response and self-efficacy. The violation phase

intentions are turned into actions depending on the situational barriers encountered.” (Kellens et al. 2013)

- Risk Information Seeking and Processing Model (RISP): this tool expresses the construct of insufficient information defined as the gap between a person’s current knowledge and his/her knowledge threshold.

Applications of Contingent Valuation Methods (CVM):

This economical approach estimates people’s perceptions. This method is focused on people’s willingness to pay (Kellens et al. 2013). The technique has been used to analyse earthquake disasters in Taiwan by Chen et al. (2020). The study shows that people tend to have greater risk perceptions of future hazard risk and less willingness to pay for retrofitting their houses after a severe disaster. Similarly, people with higher education and a better occupation status may be more willing to pay than others to adopt adaptation behaviour.

In addition, there are non-theoretical approaches to examine the risk perceptions which are based on; (1) awareness (or consciousness, e.g., “Are you aware that you live in a flood-prone area?”); (2) affect (or worry, fear, concern, e.g., “Do you feel personally endangered by a flood?”); (3) likelihood (or probability, e.g., “What do you think about the chances of a flood in your neighbourhood within the next ten years?”); (4) impact (or consequences, vulnerability, e.g., “Rate the following statement: A flood will have fatal consequences for my family and me”); and (5) cause (or origin, e.g., “Can you indicate the cause of the flood risk in your neighbourhood?”) (Kellens et al. 2013). A perception study has been conducted to assess the acceptability of flood risk in Japan’s Toki River basin in Japan. This study identified that public facilities and services perception loss due to floods increases flood risk’s public acceptability (Zhai and Ikeda 2008).

3.5 Risk Predictive Behaviour

Understanding the existing risk and predicting its behaviour are essential to determine the risk reduction approaches (Jemec Auflič et al. 2018). Therefore, understanding the probability of hazard occurrence at the hazard assessment stage is significant, and it involves stakeholder and community engagements to identify the possible hazards (Jemec Auflič et al. 2018). Risk perception techniques are required to capture the existing and possible neighbourhood hazards (Kellens et al. 2013).

The training and knowledge-sharing sessions are required to conduct frequently to upgrade the existing knowledge of

the community and stakeholders to capture the hazard impacts. For example, the Learning-by-doing approach for community awareness of the landslide proved more effective in community awareness programmes (Jemec Auflič et al. 2018). However, the effectiveness of community awareness activities depended on the social classes, impact experience, and affect-length of residence in hazardous areas (Kellens et al. 2013).

Hypothesis or scenarios are required to investigate the community risk by changing various parameters (Xu et al. 2020). Then, the damage assessment (possible) is conducted by considering the hypothesised events and impact on the properties (Xu et al. 2020). Based on the outputs, the risk acceptance is discussed by referring to the cost-benefit or the consequences of the damage assessment (Zhai and Ikeda 2008; Stock and Wentworth 2019). The emergency planning activities are determined based on these risk acceptance priorities (Stock and Wentworth 2019).

The worst-case and the most-probable scenarios play a significant role in emergency planning (Stock and Wentworth 2019). Governments should communicate the most-probable scenario to the public, and community engagement may help validate the scenario outputs by acquiring geographic and physical information (Stock and Wentworth 2019). The reasonable worst-case scenario can represent the challenge to the community but is not necessarily informative for businesses and the public. However, it should be considered in the risk assessment (Stock and Wentworth 2019).

3.6 Risk Appetite

Risk evaluation gives some idea of the risk mitigation options, and risk appetite is for identifying risk capacities related to a settlement. Hopkin (2010) has discussed risk appetite as a technique to identify threshold levels in each risk category; Risk accepts, adopts, adapts, and avoids. The judgement and critical lines could be identified based on the levels of risk management activities (Hopkin 2010). Both lines are plotted on the risk matrix, and the judgement line represents the margin between the comfort and cautious zones. If the risk level belongs to the comfort zone, the dominant response will be Risk Tolerate, and if the risk level belongs to the cautious zone, the dominant response will be either Risk Transfer or Risk Treat (Hopkin 2010). The critical line of risk is the Cautious and Concerned zone’s margin. The dominant response will be risk Terminate if the risk level belongs to the concerned zone (Hopkin 2010).

4 Discussion

4.1 Disaster Risk Assessment Dynamic Connections

Risk assessment characteristics were summarised in the previous sections, and a conceptual diagram was developed for a better presentation. Accordingly, the risk assessment is comprised of three activities: identification, analysis, and evaluation. The risk analysis has three major components: Hazard, Vulnerability, and Exposure assessment. Gallopín (2006) has identified the relationship between each component of hazard, vulnerability, and exposure of the human settlements. Vulnerable elements are the internal processes of human settlements, and hazards or perturbations are the external processes of human settlements.

According to the literature review, hazard assessment has four major elements: spatial probability, temporal probability, magnitude, and resistances. The vulnerability assessment consists of physical, social, economic, environmental, governance, resilience, sensitivity, and fragility. The risk evaluation assessment divides into two: risk perception and risk

appetite (through a risk matrix). Risk perceptions assess people’s perception of known perturbation, and it has two elements: risk examination and risk prediction behaviour. Risk appetite is how people assess the limits and bounds of the risk status. It is a matrix of risk-treating options (Risk tolerance, risk transfer, risk treatment, and risk termination), which is influenced by risk judgment and critical curves. All these concepts were connected as a system in Fig. 4 to illustrate the risk perspectives needed in risk assessment.

4.2 Risk Reduction Strategies

Figure 4 shows the risk perspectives identified through the literature review. Accordingly, a stock-flow diagram was developed to understand the balancing and reinforced loops. The negative (Red) and positive (Blue) connections were also identified in the loops. These loops guide the development of risk-reduction strategies. Consequently, 14 strategies were identified by analysing the balancing loops, connected to the risks, in the network, as shown in Fig. 5.

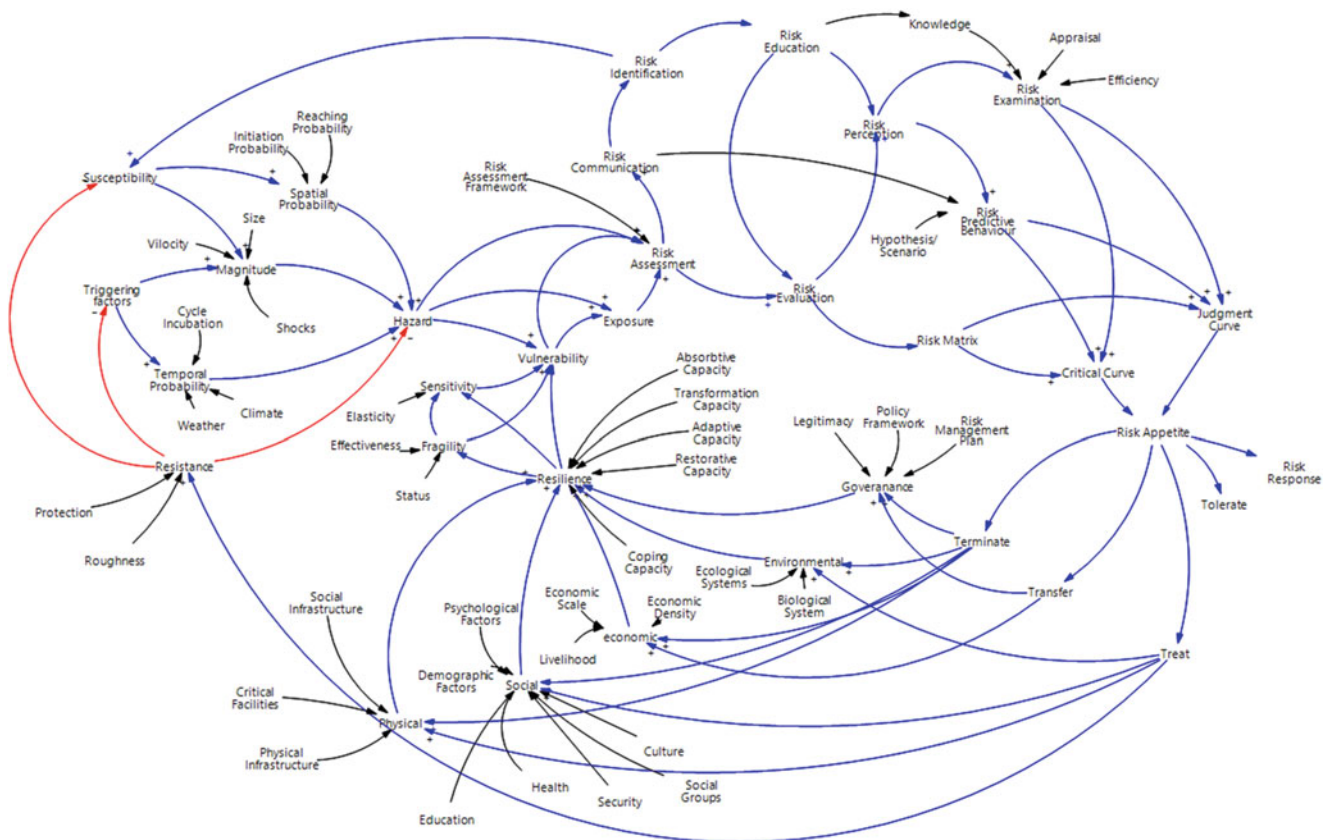


Fig. 4 Risk perspectives connections (a mind map)

Risk Assessment → Risk Education → Risk Perception → Risk Matrix → Risk Appetite → Resilience → Vulnerability → Risk)—Risk perception of the community influences the local risk appetite for choosing appropriate interventions for enhancing community resilience and reducing community vulnerabilities. Therefore, communities' risk knowledge and risk perception can influence their attitude towards investment in various risk reduction activities, such as the implementation of building codes and the construction of retaining walls.

7. **Promote ecosystem management approaches for reducing hazards** (Risk → Risk Assessment → Risk Matrix → Risk Appetite → Resistance → Hazard → Risk)—This balancing loop suggests that risk appetite measures influence resistance to hazards. Therefore, ecosystem management approaches, including structural or non-structural methods, must be introduced for building resistance. As an example, the introduction of appropriate native plants as a nature-based solution can help build resistance to hazards.
8. **Communicate the importance of ecosystem management in mitigating hazards.** (Risk → Risk Assessment → Risk Education → Risk Perception → Risk Matrix → Risk Appetite → Resistance → Hazard → Risk)—The local community should be aware of the importance of ecosystem management for their livelihood through risk education. For example, communities should understand how deforestation in mountainous slopes can lead to potential landslides. The community must practice such risk-reduction approaches to mitigate or reduce hazard occurrences.
9. **Promote ecosystem restoration programs at susceptible locations.** (Risk → Risk Assessment → Risk Matrix → Risk Appetite → Resistance → Susceptibility → Spatial Probability → Hazard → Risk)—The susceptible hazard locations can quickly reach the threshold to trigger a hazard. Therefore, these locations should be thoroughly investigated and introduce nature-based mitigation solutions. For example, SABO dams can be created to control the debris flow and protect the surrounding areas from overflowing water.
10. **Implement a community-led approach to hazard Mitigation at critical locations.** (Risk → Risk Assessment → Risk Education → Risk Perception → Risk Matrix → Risk Appetite → Resistance → Susceptibility → Spatial Probability → Hazard)—The local knowledge of risk perception should be used to identify critical susceptible hazard locations and introduce structural or non-structural mitigation solutions to control the hazard magnitude.
11. **Prioritise ecosystem solutions at locations which can trigger hazards of high magnitude.** (Risk → Risk

Assessment → Risk Matrix → Risk Appetite → Resistance → Susceptibility → Magnitude → Hazard)—It is important to Identify and mitigate the hazard with high magnitudes, by introducing structural or non-structural solutions. Here hazard mitigation is concerned with reducing or eliminating the triggering factors that lead to a high-magnitude hazard. For example, groundwater levels in the landslide-prone area have significantly influenced the triggering of landslides. Therefore, horizontal drains can be applied to remove the excess water on the slope to reduce the magnitude of the triggering factors.

12. **Deploy community-based Hazard Mitigation applications for reducing hazard magnitudes** (Risk → Risk Assessment → Risk Education → Risk Perception → Risk Matrix → Risk Appetite → Resistance → Susceptibility → Magnitude → Hazard)—Some measure leads to reducing the hazard magnitude or slowing down the event. For example, flood weirs and SABO dams were constructed to control the flood water and debris flow speeds. This structural measure leads to reducing the hazard magnitude and reducing impacts.
13. **Communities can understand the hazard triggering factors' temporal variations:** (Risk → Risk Assessment → Risk Matrix → Risk Appetite → Resistance → Triggering Factors → Temporal Probability → Hazard → Risk)—The strategy focuses on understanding the triggering factor's frequencies. Accordingly, the community can take disaster preparedness actions if they know the triggering factors' changes. For example, rainfall is a triggering factor for landslides, and the community should be aware of the frequency of rainfall changes with time.
14. **Implement hazard mitigation applications to reduce hazard frequencies by communities:** (Risk → Risk Assessment → Risk Education → Risk Perception → Risk Matrix → Risk Appetite → Resistance → Triggering Factors → Temporal Probability → Hazard → Risk)—This strategy focuses on reducing hazard frequencies by application of mitigation measures. For example, soil erosions occur due to rapid water flow from mountainous areas. However, the forest areas act as water sponges, gradually releasing the water to the downslope areas. Therefore, it helps to reduce the hazard frequencies in the downslope areas.

Selecting appropriate strategies for risk reduction is challenging in disaster risk assessment. The application of risk reduction strategies is discussed in the risk response stage, which needs to be more focused in the research study.

4.3 Future Research Requirements

The mind map was converted into a risk perspective network diagram by establishing the connections between the variables, and identified literature percentage values could be assigned as the node weight. The edge distance was considered a constant value equal to one. A graph was developed using the Gephi Software, and analysis of the network parameters aligned risk perspectives. The discussion was based on the above analysis.

The graph structure with various risk perspectives presented in Fig. 4 was analysed using the following three tests to identify the key risk perspectives that should be further researched: (1) degree of nodes, (2) closeness centrality, and (3) eigenvector centrality.

Test 1: The degree of a node represents how many connections it has to other nodes in a graph. The higher the degree, a node has more influence on other nodes. Figure 6 shows the degree of nodes of all the risk perspectives. In this figure, the size of the node represents the degree of the node (the larger the circle higher the degree), and the colour variation represents how well it is researched (the darker the colour, the higher the number of research publications). These two variables are illustrated in Fig. 7 as a bar chart,

with blue bars representing the degree of nodes (Degree) and red bars representing the research density(Node_w). This analysis assumes that nodes with a higher degree of nodes but with fewer research publications need further research.

This analysis shows that resilience has the highest degree of node value, and hazard has the highest research publications. It is clear that further research is required in the areas such as Resilience, Risk treatment, risk termination, susceptibility, Risk education, and risk Predictive behaviour.

Test 2: The closeness centrality of the network was assessed to understand the most central risk perspective of the risk assessment. Nodes with the highest closeness centrality are considered as important and significant in a graph. Accordingly, a network graph was developed representing the node size as closeness centrality (the larger the node higher the closeness centrality) and colour density representing research density (the darker the colour, the higher the number of research publications), as shown in Fig. 8. These two variables are illustrated in Fig. 9 as a bar chart, red bars representing the closeness centrality and blue bars representing the research density. This analysis assumes that nodes with higher closeness centrality but with fewer research publications need further research.

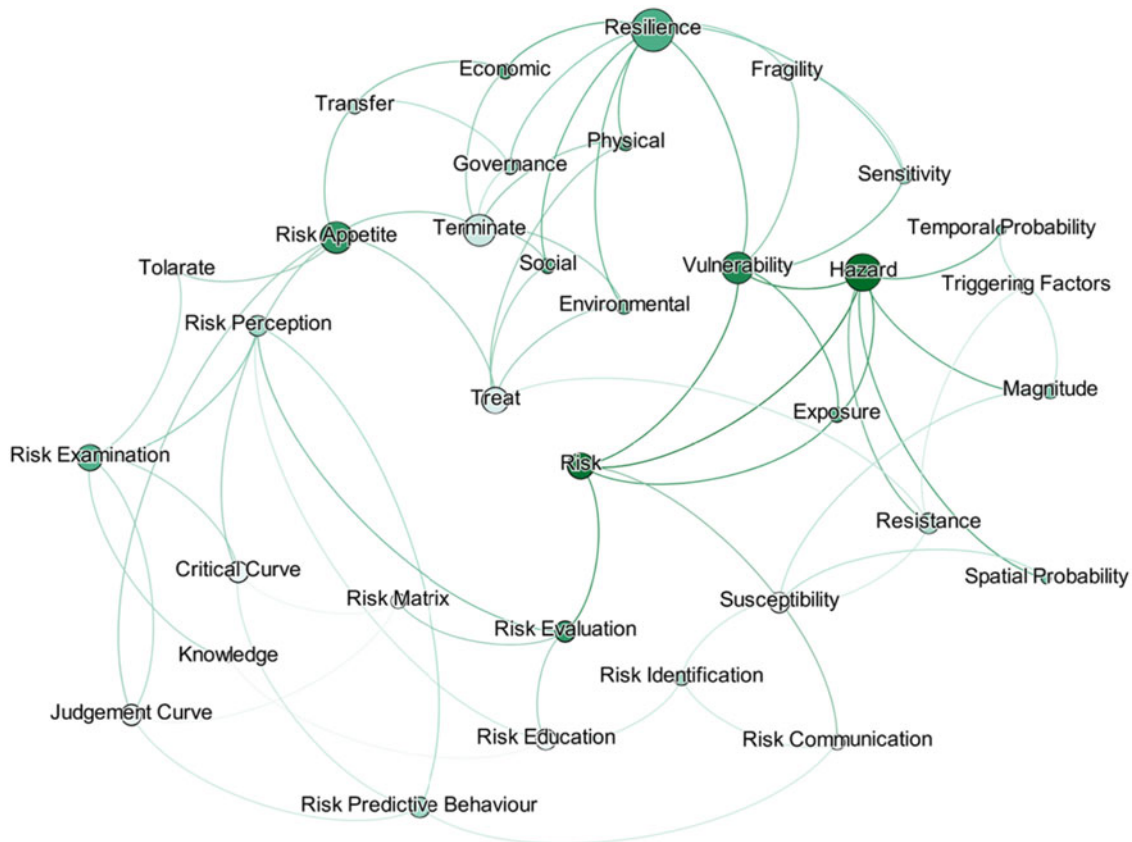


Fig. 6 Test 1 results based on the degree of nodes and research density

Fig. 7 Test 1 a results as a bar chart

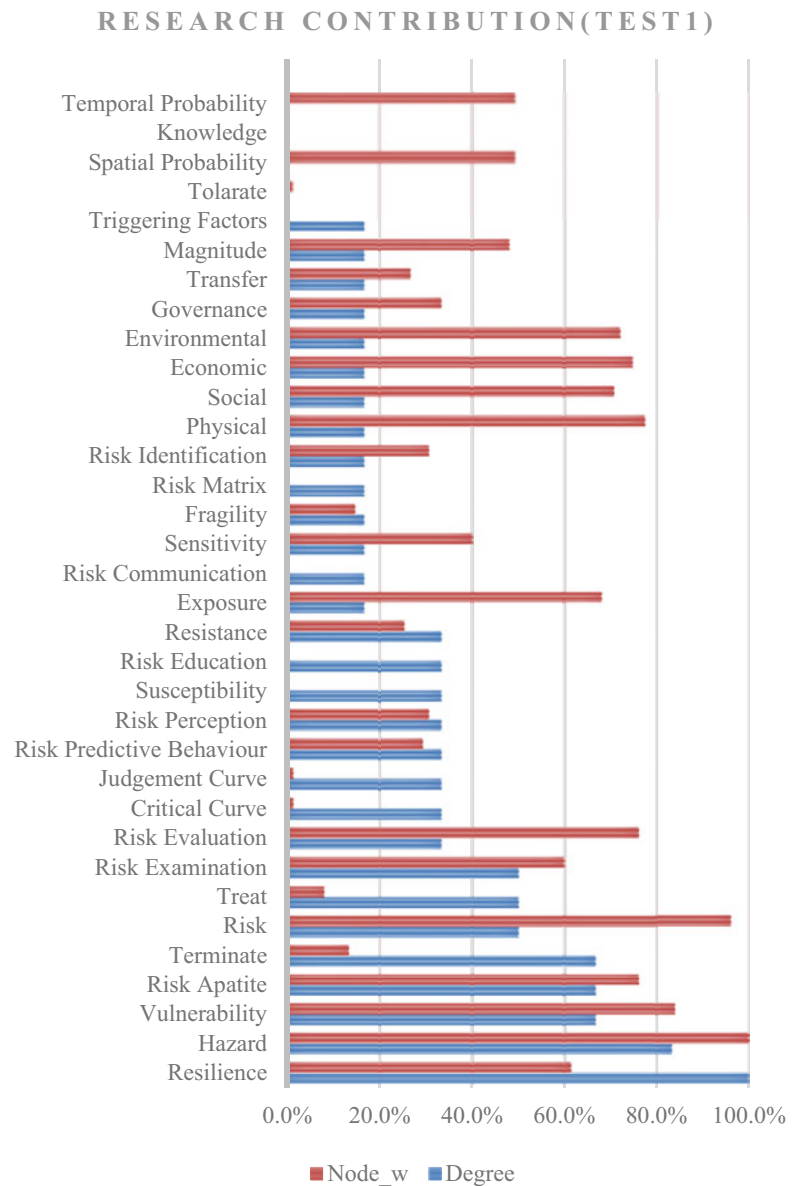


Figure 8 and 9 indicate that the risk appetite has the highest closeness centrality value of the network and highlights the need for further research in risk perspectives such as risk appetite, risk communication, risk treatment, critical curves, judgment curves, and risk identification.

Test 3: Eigenvector centrality was assessed to understand the common nodes in the shortest path that have been adequately researched. Accordingly, a network graph was used to analyse this test.

Figure 10 shows the integrated network diagram of risk perspective density and eigenvector centrality. The significance of eigenvector centrality lies in its ability to capture the idea of “prominence” within a network. Nodes with high eigenvector centrality are not only well-connected but are also connected to other highly central nodes, making them influential within the network. Therefore, the eigenvector

centrality of each node was calculated to identify the most influential risk perspectives. Figure 10 shows eigenvector centrality (the larger the node, the higher the eigenvector centrality) and colour density representing research density (the darker the colour, the higher the number of research publications). These two variables are illustrated in Fig. 11 as a bar chart, the blue bars representing the eigenvector centrality and the red bars representing the research density. This analysis assumes that nodes with higher eigenvector centrality but fewer research publications need further research.

The analysis of Figs. 10 and 11 shows that risk perspectives such as vulnerability, resilience, risk communication, and risk matrix need further research.

The average values of the above three indicators were considered to understand the research by classifying them

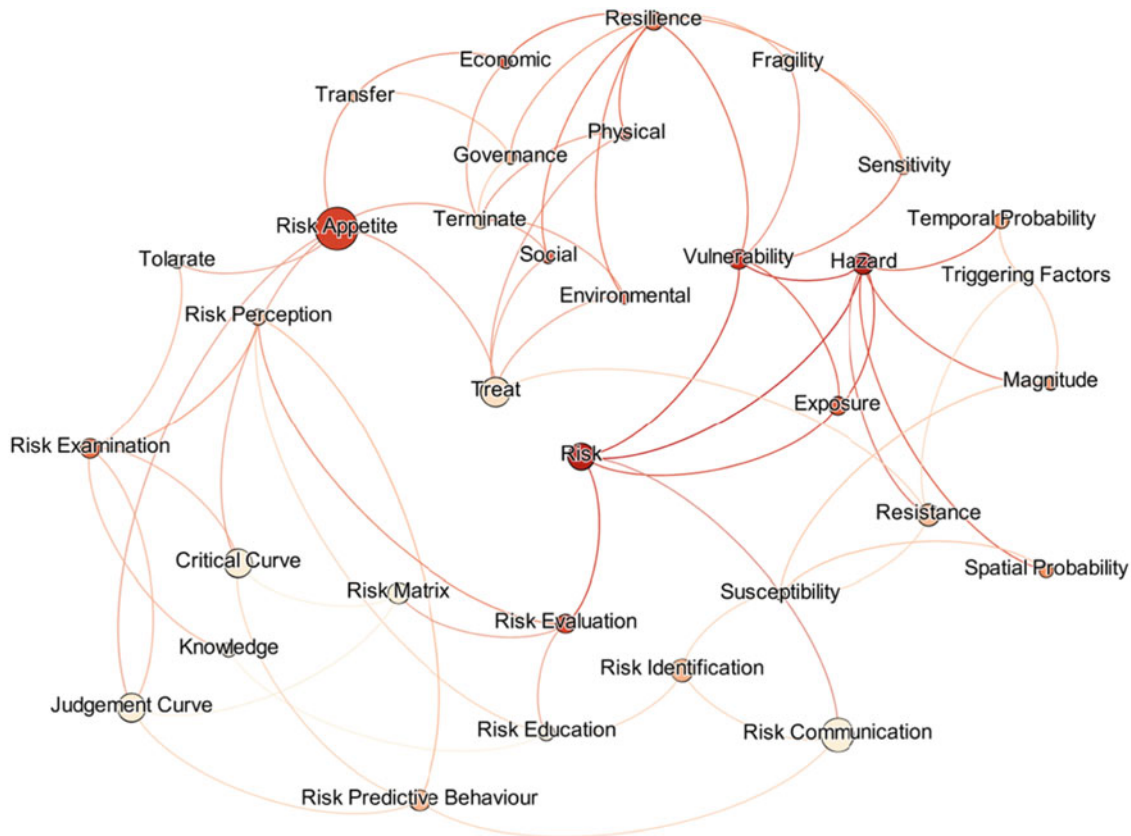


Fig. 8 Test2 results based on closeness centrality and research density

into three groups based on (1) a good amount of research is evident (✓), (2) a moderate amount of research is evident (●), (3) lack of research is evident (✗) (See Fig. 12).

According to this analysis, risk perspectives such as risk communication, risk treatment, critical curve, judgment curve, and risk matrix could be identified as areas requiring future research.

5 Conclusion

This research paper focused on understanding the risk assessment perspectives discussed by various researchers in the disaster risk domain. Accordingly, a systematic literature review was conducted to identify the literature, and a detailed review was conducted with NVIVO software's support. As a result, 34 risk assessment perspectives were identified and plotted as a network diagram for better representation. Accordingly, the identified risk perspectives were discussed in the initial section of the research paper.

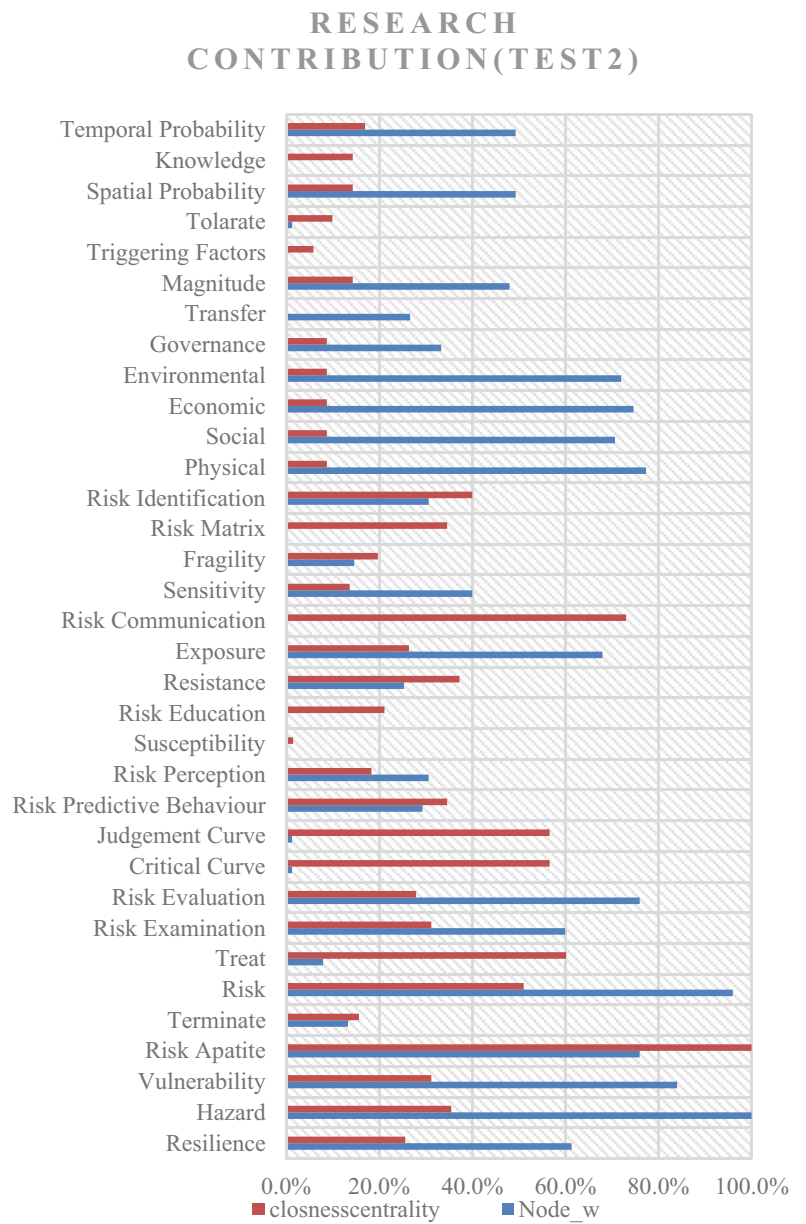
A stock-flow diagram was developed by considering the network diagram, which helps to generate the overall risk

reduction strategies. Here, the stock flow diagram helped to identify the balancing and reinforcing loops to determine the risk reduction measures. Accordingly, 14 balancing loops were identified and analysed to propose risk reduction strategies.

Furthermore, the study analysed future research needs by analysing the importance of each risk perspective and the number of publications against each risk perspective. Consequently, the network diagram was further evaluated by conducting three tests on the network (degree of nodes, closeness centrality and eigenvector centrality). The average results of these three tests show that further research is required in areas such as risk communication, risk matrix, and risk treatment.

The research outputs will be validated in the SATREPS case study locations specified in the landslide risk management in Sri Lanka. A project objective refers to strengthening risk communication to reduce landslide risk. Therefore, the community's and stakeholder's perceptions will be evaluated concerning the stock-flow diagram. The identified actions will be implemented under the purview of the National Building Research Organisation.

Fig. 9 Test 2 result as a bar chart



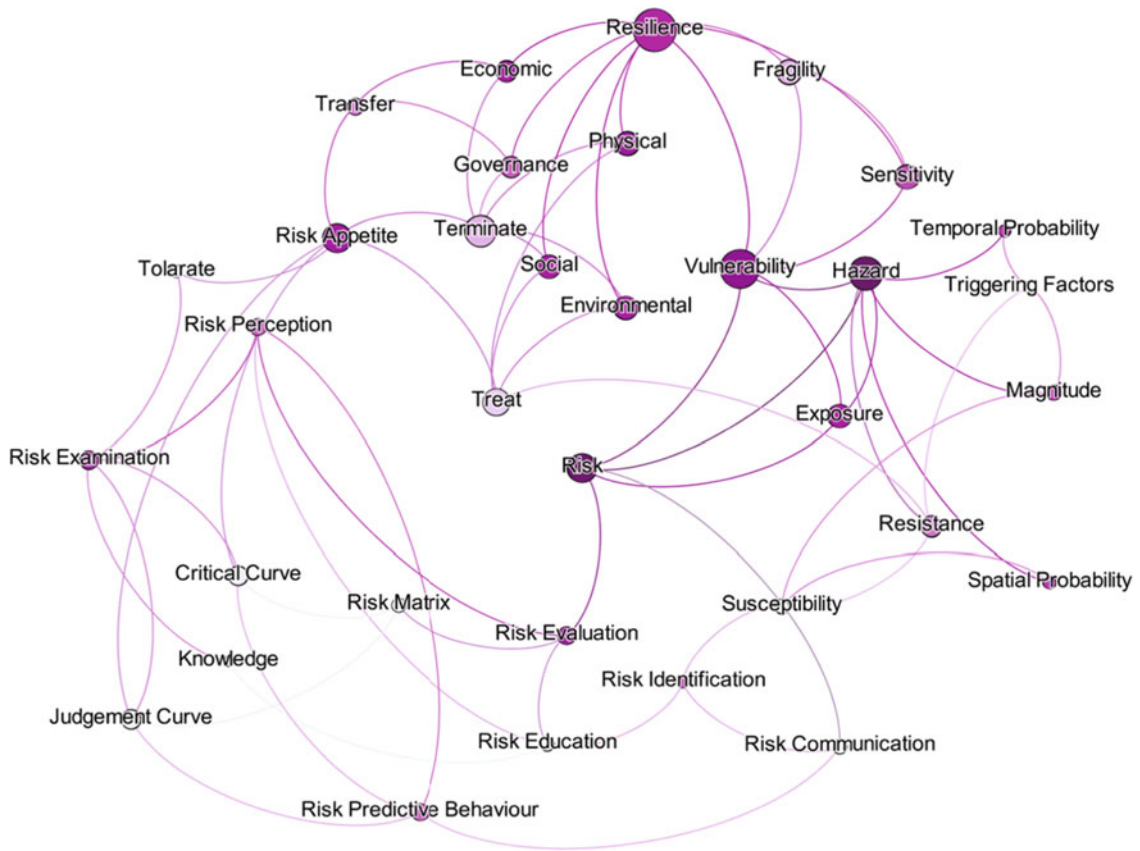
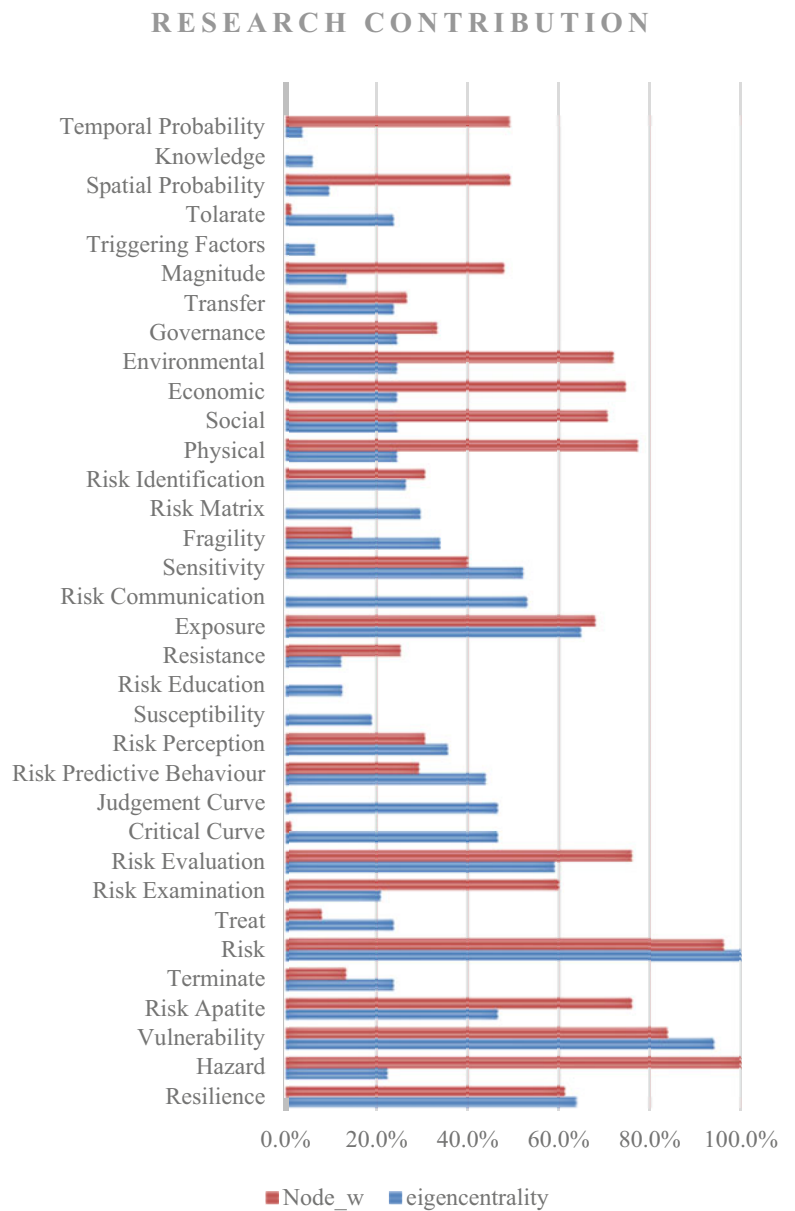


Fig. 10 Test3 results based on eigenvector centrality and research density

Fig. 11 Test 3 results as a bar chart



	Resilience	Hazard	Vulnerability	Risk Appetite	Terminate	Risk	Treat	Risk Examination	Risk Evaluation	Critical Curve	Judgement Curve	Risk Predictive Behaviour	Risk Perception	Susceptibility	Risk Education	Resistance	Exposure	Risk Communication	Sensitivity	Fragility	Risk Matrix	Risk Identification	Physical	Social	Economic	Environmental	Governance	Transfer	Magnitude	Triggering Factors	Tolate	Spatial Probability	Knowledge	Temporal Probability
Test 1(DegreeVsWeight)	⊕	⊕	⊕	⊕	⊕	⊕	⊕	⊕	⊕	⊕	⊕	⊕	⊕	⊕	⊕	⊕	⊕	⊕	⊕	⊕	⊕	⊕	⊕	⊕	⊕	⊕	⊕	⊕	⊕	⊕	⊕	⊕	⊕	⊕
Test 2 (Closeness VsWeight)	⊕	⊕	⊕	⊕	⊕	⊕	⊕	⊕	⊕	⊕	⊕	⊕	⊕	⊕	⊕	⊕	⊕	⊕	⊕	⊕	⊕	⊕	⊕	⊕	⊕	⊕	⊕	⊕	⊕	⊕	⊕	⊕	⊕	⊕
Test 3 (EigenvectorVsWeight)	⊕	⊕	⊕	⊕	⊕	⊕	⊕	⊕	⊕	⊕	⊕	⊕	⊕	⊕	⊕	⊕	⊕	⊕	⊕	⊕	⊕	⊕	⊕	⊕	⊕	⊕	⊕	⊕	⊕	⊕	⊕	⊕	⊕	⊕
Average	⊕	⊕	⊕	⊕	⊕	⊕	⊕	⊕	⊕	⊕	⊕	⊕	⊕	⊕	⊕	⊕	⊕	⊕	⊕	⊕	⊕	⊕	⊕	⊕	⊕	⊕	⊕	⊕	⊕	⊕	⊕	⊕	⊕	⊕

Fig. 12 Research requirement assessment

Acknowledgment This research was conducted as part of a Ph.D. study under the TRANSCEND project at the University of Salford, UK. Also, we would like to extend our appreciation to the SATREPS project team for their constant support, guidance, and encouragement throughout our research journey. Their expertise, timely feedback, and commitment to excellence have been instrumental in shaping the outcomes of our study.

References

- Aksha SK, Resler LM, Juran L, Carstensen LW (2020) A geospatial analysis of multi-hazard risk in Dharan, Nepal. *Geomat Nat Haz Risk* 11(1):88–111
- Bibi T, Nawaz F, Abdul Rahman A, Azahari Razak K, Latif A (2018) Flood risk assessment of river Kabul and SWAT catchment area: district Charsadda, Pakistan. *International archives of the photogrammetry, Remote Sensing and Spatial Information Sciences - ISPRS Archives*
- Bubeck P, Botzen WJ, Aerts JC (2012) A review of risk perceptions and other factors that influence flood mitigation behavior. *Risk Anal* 32(9):1481–1495
- Cabinet-Office-UK (2020) National Risk Register 2020
- Chen T-L, Chao T-Y, Cheng H-T (2020) Exploring the changes in risk perceptions and adaptation behaviors based on various socio-economic characteristics before and after earthquake disasters – a case study in Taiwan. *Nat Hazards Earth Syst Sci* 20(9):2433–2446
- Corominas J, van Westen C, Frattini P, Cascini L, Malet JP, Fotopoulou S, Catani F, Van Den Eeckhaut M, Mavrouli O, Agliardi F, Pitolakis K, Winter MG, Pastor M, Ferlisi S, Tofani V, Hervás J, Smith JT (2013) Recommendations for the quantitative analysis of landslide risk. *Bull Eng Geol Environ* 73(2):209–263
- Gallopín GC (2006) Linkages between vulnerability, resilience, and adaptive capacity. *Glob Environ Chang* 16(3):293–303
- Gorgini P (2009) Tropos: risk analysis
- Hasani S, El-Haddadeh R, Aktas E (2014) A disaster severity assessment decision support tool for reducing the risk of failure in response operations. *WIT Transactions on Information and Communication Technologies*
- Hopkin P (2010) Fundamentals of risk management: understanding evaluating, and implementing effective risk management. The Institute of Risk Management
- Huang X, Li Y, Guo Y, Zheng D, Qi M (2020) Assessing urban risk to extreme heat in China. *Sustainability* 12(7)
- ISO-Guide73 (2009) ISO guide 73–2009 risk management vocabulary. ISO
- Izquierdo-Horna L, Kahhat R (2018) Methodological framework to integrate social and physical vulnerability in the prevention of seismic risk. *WIT Trans Eng Sci*
- Jemec Auflič M, Kumelj Š, Peternel T, Jež J (2018) Understanding of landslide risk through learning by doing: case study of Koroška Bela community, Slovenia. *Landslides* 16(9):1681–1690
- Kellens W, Terpstra T, De Maeyer P (2013) Perception and communication of flood risks: a systematic review of empirical research. *Risk Anal* 33(1):24–49
- Kellens W, Zaalberg R, Neutens T, Vanneuville W, De Maeyer P (2011) An analysis of the public perception of flood risk on the Belgian coast. *Risk Anal* 31(7):1055–1068
- Khazai B, Kunz-Plapp T, Büscher C, Wegner A (2014) VuWiki: an ontology-based semantic wiki for vulnerability assessments. *Int J Disaster Risk Sci* 5(1):55–73
- Lee T-L, Chen C-H, Pai T-Y, Wu R-S (2015) Development of a meteorological risk map for disaster mitigation and management in the Chishan Basin, Taiwan. *Sustainability* 7(1):962–987
- Munasinghe D, Wijegunaratne E (2015) Vulnerability assessment methods for land subsidence prone areas -a case study: Matale municipal council area. NBRO research symposium 2015. Colombo, NBRO
- Nations U (1989) Resolutions adopted on the reports of the second committee, United Nations: 161–162
- Nations U (2015a) Sendai framework for disaster risk reduction 2015–2030
- Nations U (2015b) Transforming our world: the 2030 agenda for sustainable development
- OECD (2012) Disaster risk assessment and risk financing
- Pedro Basabe (2018) Comparing and contrasting approaches to risk governance. IRGC
- Stock M, Wentworth J (2019) Evaluating UK natural hazards: the national risk assessment, Parliamentary Office of Science and Technology (POST)
- Sweet L (2014) Using NVivo and EndNote for literature reviews
- Torre DMG, d Cruz PKA, Jose RP, Gatdula NB, Blanco AC (2019) Geospatial assessment of vulnerabilities of croplands to flooding risks: a case study of philippine river basins. *International archives of the photogrammetry, remote sensing and spatial information sciences, XLII-4/W19*: 173–180
- Tran TH, Dobrovnik M, Kummer S (2018) Supply chain risk assessment: a content analysis-based literature review. *Int J Logistics Syst Manage* 31(4):562–591
- Truelove HB, Carrico AR, Thabrew L (2015) A socio-psychological model for analyzing climate change adaptation: a case study of Sri Lankan paddy farmers. *Glob Environ Chang* 31:85–97
- UNDRR (2015) Sendai Framework for Disaster Risk Reduction 2015–2030 from <https://www.undrr.org/publication/sendai-framework-disaster-risk-reduction-2015-2030>
- Xu D, Zhuang L, Deng X, Qing C, Yong Z (2020) Media exposure, disaster experience, and risk perception of rural households in earthquake-stricken areas: evidence from rural China. *Int J Environ Res Public Health* 17(9)
- Yeganeh N, Sabri S (2014) Flood vulnerability assessment in Iskandar Malaysia using multi-criteria evaluation and fuzzy logic. *Res J Appl Sci Eng Technol* 8(16):1794–1806
- Zhai G, Ikeda S (2008) Empirical analysis of Japanese flood risk acceptability within multi-risk context. *Nat Hazards Earth Syst Sci* 8(5):1049–1066
- Zhou S, Zhai G, Shi Y, Lu Y (2020) Urban seismic risk assessment by integrating direct economic loss and loss of statistical life: an empirical study in Xiamen, China. *Int J Environ Res Public Health* 17(21): 1–21
- Zlatanova S, Ghawana T, Kaur A, Neuvel JMM (2014) Integrated flood disaster management and spatial information: case studies of Netherlands and India. *International Archives of the Photogrammetry, Remote Sensing and Spatial Information Sciences - ISPRS Archives*

Open Access This chapter is licensed under the terms of the Creative Commons Attribution 4.0 International License (<http://creativecommons.org/licenses/by/4.0/>), which permits use, sharing, adaptation, distribution and reproduction in any medium or format, as long as you give appropriate credit to the original author(s) and the source, provide a link to the Creative Commons license and indicate if changes were made.

The images or other third party material in this chapter are included in the chapter's Creative Commons license, unless indicated otherwise in a credit line to the material. If material is not included in the chapter's Creative Commons license and your intended use is not permitted by statutory regulation or exceeds the permitted use, you will need to obtain permission directly from the copyright holder.



Part IV

IPL Projects, World Centres of Excellence on Landslide Risk Reduction, and Kyoto Landslide Commitment 2020



Application of LAND-SUITE for Landslide Susceptibility Modelling Using Different Mapping Units: A Case Study in Croatia

Sanja Bernat Gazibara, Marko Sinčić, Mauro Rossi, Paola Reichenbach, Martin Krkač, Hrvoje Lukačić, Petra Jagodnik, Gabrijela Šarić, and Snježana Mihalić Arbanas

Abstract

LAND-SUITE software was applied to local-scale landslide susceptibility zonation in a study area (20 km²) located in NW Croatia, which is characterised by small and shallow landslides in engineering soils and hard soils-soft rocks. Landslide susceptibility models were prepared using a LiDAR-based landslide inventory, and causal factors derived and/or modified using high-resolution remote sensing data. The landslide susceptibility analysis was carried out using different statistical methods and mapping units. As a result, we obtained ten susceptibility maps, classified into five zones based on modelled landslide probability. The main objective of this paper is to analyse the use of LAND-SUITE for deriving susceptibility zonations, useful to support applications in a spatial planning system on a local scale. One of the most valuable advantage of LAND-SUITE is that the selection of the appropriate causal factor maps can be performed using simple decisions based on multiple analyses, including multicollinearity tables and correlograms. The evaluation of the susceptibility models allowed to conclude that the pixel-based map represents the best option for application in a local-level spatial planning system, although it requires “post-processing” of the susceptibility zones to produce clustered and homogeneous information. LAND-SUITE has proven to be a valuable tool for testing numerous landslide susceptibility hypotheses.

Keywords

Landslide · Susceptibility zonation · LAND-SUITE

1 Introduction

The main problem in the existing landslide risk management practice in Croatia is the lack of analytical landslide maps and the absence of their application in the spatial planning and civil protection system (Mihalić Arbanas et al. 2023). Therefore, the main objective of the project “Methodology development for landslide susceptibility assessment for land-use planning based on LiDAR technology (LandSlidePlan)”, funded by the Croatian Science Foundation (Bernat Gazibara et al. 2022), was the development of landslide susceptibility assessment on a local scale using high-resolution remote sensing data. Within the project, part of the landslide susceptibility modelling (LSM) was carried out with LAND-SUITE, a suite of tools for statistically-based susceptibility zonation developed by Rossi et al. (2021a). As identified by Malamud et al. (2014), the literature often lacks comprehensive assessments of landslide susceptibility modelling and LAND-SUITE provides reliable susceptibility modelling, comprehensive model evaluation and validation tools, and the possibility to prepare high-quality susceptibility maps.

Together with the definition of the most important landslide causal factors, the selection of an appropriate mapping unit and statistical method is a critical phase in LSM (Reichenbach et al. 2018). In this work, the selection of appropriate landslide causal factors was the first step to prepare an LSM. Moreover, we considered 5 m × 5 m regular grid cells and slope units (Alvioli et al. 2016), and investigated the effect of different statistical methods on training LSM using both types of mapping units for application on a local level, i.e. scale 1:5000.

The LSM was conducted for a study area in Hrvatsko Zagorje (NW Croatia), characterised by small and shallow landslides, where most known failures endanger buildings,

S. Bernat Gazibara (✉) · M. Sinčić · M. Krkač · H. Lukačić · G. Šarić · S. Mihalić Arbanas

Faculty of Mining, Geology and Petroleum Engineering, University of Zagreb, Zagreb, Croatia
e-mail: sbernat@rgn.hr

M. Rossi · P. Reichenbach
Research Institute for Geo-Hydrological Protection (IRPI-CNR), Perugia, Italy

P. Jagodnik
Faculty of Civil Engineering, University of Rijeka, Rijeka, Croatia

roads and other infrastructure. For the study area, high-resolution LiDAR DTM was used to prepare a detailed landslide inventory and some causal factors (Sinčić et al. 2022). Furthermore, based on the landslide susceptibility assessment, it was crucial to disseminate location-based disaster risk information to decision-makers and the general public in an appropriate format that can easily be understood and implemented (Mihalić Arbanas et al. 2023).

2 Study Area

The study area of 20.2 km² is located in the Hrvatsko Zagorje region, Croatia (Fig. 1). The area is part of the mega-geomorphological region of the Panonian Basin and the macro-geomorphological region of the Mountain valley area of NW Croatia (Bognar 2001). The area is characterised by a steep morphology, with 71% of its surface having a slope higher than 12°.

According to the Basic Geological Map of Croatia, the area is composed of Miocene (78%), Quaternary (14%) and Triassic sediments (7%) (Aničić and Juriša 1984; Šimunić et al. 1982). The north-eastern part is composed of Triassic sediments: sandstones, shales and dolomites of Lower Triassic, and dolomites, limestones and dolomitised breccias of Middle Triassic. Most of the area is composed of Miocene sediments represented by sandstones; marls; sands; tuffs (Burdigalian); biogenic, sandy, and marly limestones; calcareous marls; and sandstones (Tortonian). The youngest sediments are the Quaternary formations, predominantly composed of sands, silts and gravels, and associated with flat valley terrain around streams and rivers.

The climate is continental with a mild maritime influence, with mean annual precipitation (MAP) value of approx. 830 mm, according to the meteorological station located 30 km east from the area (DHMZ 2022). Rainfall and rapid snow melting are considered the main landslide-triggering factors, as common in NW Croatia (Bernat et al. 2014).

According to the land use information obtained by Sinčić et al. (2022), the area is covered by forest and high vegetation (73%), agricultural zones and low vegetation (24%) and artificial zones (3%). The area is not densely populated, but landslides cause significant damage to buildings, roads and other infrastructures.

3 Methods and Materials

3.1 LAND-SUITE Software

LAND-SUITE is open-source software and consists of three modules: i.e., LAND-SIP (LANDslide Susceptibility Input Preparation), LAND-SVA (LANDslide Susceptibility

Variable Analysis), and LAND-SE (LANDslide Susceptibility Evaluation). The software allows the user to execute different landslide susceptibility applications and zonation using statistically based analyses. In this paper, we briefly summarise the main software characteristics entirely derived from Rossi et al. (2021a), where the software code, a user guide and major functionalities are explained in detail.

LAND-SIP is used to prepare training and validation datasets. Different parameters enable applying numerous scenarios based upon the selection of: (i) balanced or unbalanced random sampling; (ii) subsampling or sampling reducing partitions; and (iii) spatially or temporally-based datasets partition.

LAND-SVA enables the development of multicollinearity tables and correlograms, evaluation the correlation between landslide causal factors. Moreover, outputs such as conditional density analysis, density plots, conditional density plots, histogram plots and mosaic plots enable insight into the causal factors leading to the selection of the most significant thematic data for the analysis.

The main advantage of LAND-SE is the possibility to apply four commonly used statistical methods, i.e., Logistic Regression model (LRM), Linear Discriminant Analysis (LDA), Quadratic discriminant analysis (QDA), Neural network analysis (NNM), and combining them in a model ensemble (CFM) considering different mapping units, i.e., vectors and rasters. LAND-SUITE allows to prepare susceptibility maps of the highest Susceptibility Quality Level, i.e., SQL index, as defined by Guzzetti et al. (2006a, b) and additionally illustrated in Reichenbach et al. (2018). LAND-SUITE or some of its modules have already been used to perform landslide susceptibility assessments in other test areas (e.g., Rossi et al. 2021b; Bornaetxea et al. 2018, 2023; Schlögel et al. 2018).

3.2 Landslide Inventory and Unstable Slope Units

The geomorphological landslide inventory map of the Hrvatsko Zagorje is the result of the visual interpretation of high-resolution LiDAR DTM derivatives (Krkač et al. 2022). The LiDAR DTM for landslide mapping was derived at 0.3 m resolution from a point cloud with a density of 16 pt./m². Considering small and shallow landslides that dominantly occur in NW Croatia, detailed landslide mapping was performed using the highest possible DTM resolution.

Initially, 904 landslides were mapped and dominantly classified as shallow soil slides. From the total number of landslides, 24% were randomly selected and checked in the field. From the 214 checked phenomena, 20 landslides were rejected, and 28 were additionally mapped in the field and added to the inventory. The total number of landslides is

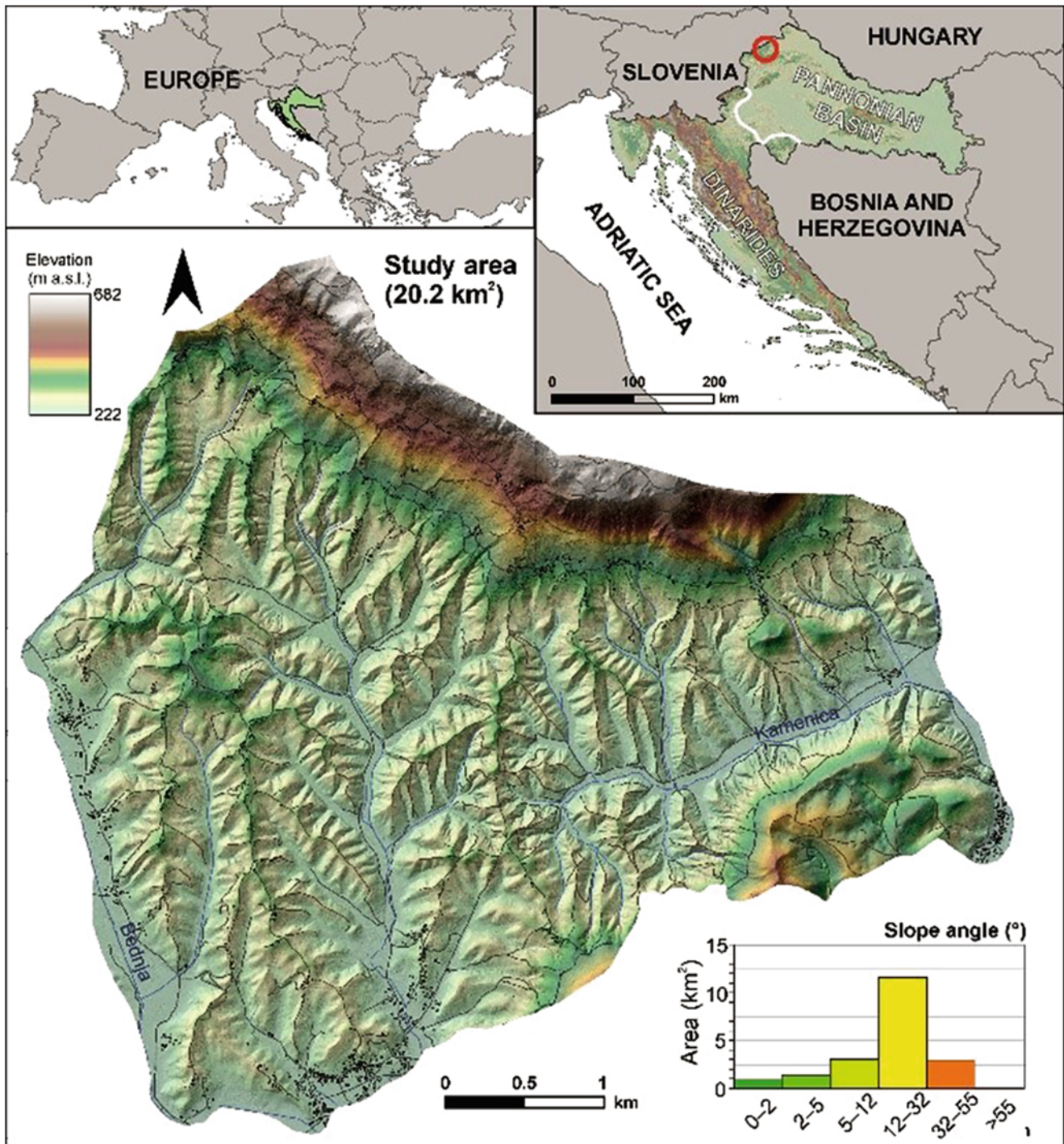


Fig. 1 Location of the Hrvatsko Zagorje study area

912 (Fig. 2). The total area of the mapped landslides is 0.408 km², corresponding to 2.02% of the study area with a mean density of approx. 45 slope failures per square kilometre.

The area of the recorded landslides ranges from a minimum value of 3.3 m² to a maximum of 13,779 m², with an

average of 448 m² (median = 173 m², std. dev. = 880 m²). The most frequent landslide size in the inventory is 200 m² and almost 85% of the landslide bodies showed a size ranging between 40 and 2000 m². The small size of the landslides can probably be explained by the geological (mainly Miocene marls covered with residual soils) and geomorphological

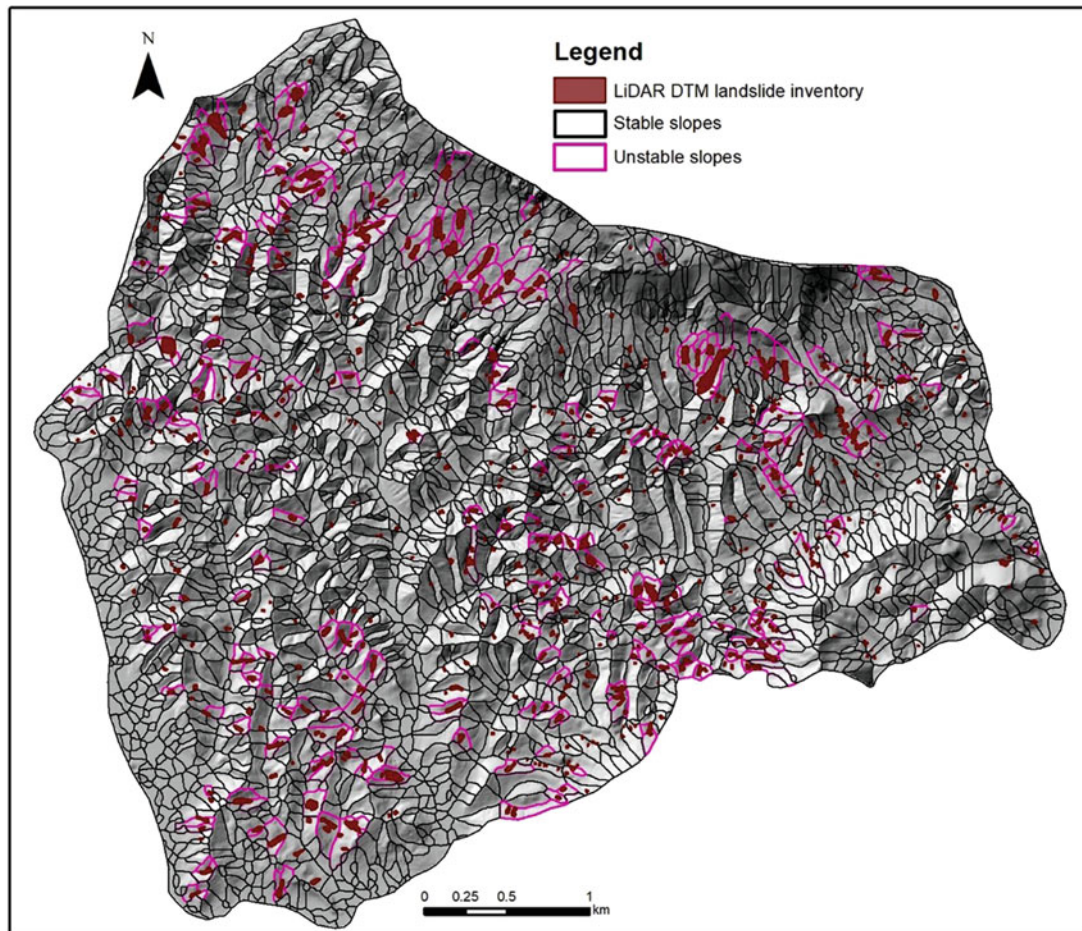


Fig. 2 LiDAR-based landslide inventory, and stable and unstable slope units used for landslide susceptibility modelling for the study area in Hrvatsko Zagorje

conditions, with the differences between the valley bottoms and the top of the hills rarely higher than 100 m (Krkač et al. 2022).

For the slope unit delineation, we used *r.slopeunit* software described in Alvioli et al. (2016). The software is a GRASS GIS module designed for the automatic and adaptive delineation of slope units based on a digital terrain model and a set of user-defined input parameters. In the study area, the most suitable size of the slope units was obtained with the following input parameters: flow accumulation area threshold (t) = 6000 m²; minimum slope planimetric area (a) = 1000 m²; minimum circular variance of terrain aspect within each slope unit (c) = 0.2; reduction factor (r) = 2; threshold value for the cleaning procedure (*clean size*) = 448 m².

The result of *r.slopeunit* is a partition of 2994 slope units ranging from 517 m² to 47,415 m² with an average size of 6747 m². The percentage of landslide area in each slope unit was used to classify stable or unstable units. In particular,

slope units containing >5% of landslide area are classified as unstable. As a result, 342 slope units (11.4%) were classified as unstable.

3.3 Landslide Causal Factors

Landslide causal factor maps used for landslide susceptibility mapping can be divided into four main groups: (1) geomorphological factors; (2) geological factors; (3) hydrological factors; and (4) anthropogenic factors. A list of 22 factor maps, with their minimum and maximum values, class increments and the number of classes, are shown in Table 1.

Maps of the geomorphological factors (elevation, slope gradient, slope orientation, contour density, curvature, roughness and terrain dissection) were derived from the 5 m resolution LiDAR DTM.

Maps of the geological factors were initially derived from the Basic Geological Map of the Republic of Croatia at 1:

Table 1 Landslide causal factor maps prepared for the study area in Hrvatsko Zagorje

Group	Landslide casual factor map	ID	Min. value	Max. value	Class increment	No. of class	Input data for final LSM
Geomorphological factors	Elevation	dem	222	680	50	10	No
	Slope gradient	slp	0	71	5	11	No
	Slope orientation	asp	0	360	45	8	Yes
	Contour density	line_d	0	0.19	0,02	9	No
	Terrain curvature	curv	-125	142	5*	8	Yes
	Terrain roughness	rt	25	79	0.25-1	8	No
	Terrain dissection	sar	0	1	0.1	10	No
Geological factors	Lithology (rock type)	litho	-	-	-	7	No
	Engineering formations (LiDAR-based)	eng_f	-	-	-	5	Yes
	Proximity to geological contact	p_litho	0	650	50	12	No
	Proximity to engineering formation contact	p_eng_f	0	>550	50	10	Yes
	Proximity to faults	p_ft	0	>1200	100	11	No
Hydrological factors	Proximity to drainage network	dn	0	>120	10	13	Yes
	Proximity to springs	spr	0	>1400	100	15	No
	Proximity to permanent streams	str_pr	0	>1900	100	20	No
	Proximity to permanent and temporary streams	str_pr_t	0	>700	100	8	Yes
	Topographic wetness	cti	1	20	2/4	8	No
Anthropogenic factors	Land use	lnd_u	-	-	-	4	No
	Proximity to buildings	d_obj	0	>700	25/50	17	No
	Proximity to roads	p_rod	0	>150	25/50	6	No
	Proximity to buildings and roads	obj_rod	0	>150	25/50	6	No
	Proximity to land use boundary	p_lnd_u	0	>450	25/50	12	Yes

100,000 scale. However, field verifications showed significant deviations between the geological map and actual geological contacts (Sinčić et al. 2022). Therefore, engineering geological formations were additionally mapped by modifying the geological contacts and adding superficial slope-wash and talus sediments using LiDAR DTM derivatives, according to Jagodnik et al. (2020a, b). Combining small-scale geological maps and LiDAR DTM derivatives resulted in significantly reduced deviations from the actual environmental conditions, except for the geological structures, i.e., fault data set (Sinčić et al. 2022).

The hydrological group of causal factors include the drainage network, springs, permanent and temporary streams, and a topographic wetness index. Topographic wetness index and proximity to the drainage network were derived from the LiDAR DTM. In addition, springs, permanent and temporary streams were digitised from the topographic maps of the Republic of Croatia at 1:25,000 scale.

The information related to the anthropogenic factors was derived from: (1) 0.5 m orthophoto of the Republic of Croatia; (2) 0.3 m resolution LiDAR DTM; (3) Open Street Map (OSM); and (4) land-use planning maps. The complex acquisition process of deriving high-resolution land use data, buildings and road inventory, with different processing methods such as image classification and digitisation, is described in detail in Sinčić et al. (2022).

4 Results

The landslide training dataset for pixel and slope-unit landslide susceptibility analysis was defined in LAND-SUITE by a random selection of 50% of the unstable mapping units. Regarding the pixel-based analysis, landslides were pixel-sampled (see case C, Fig. 1 in Rossi et al. 2021a), i.e., 50% of each landslide polygon was used as a training dataset. Then, an equal amount of stable mapping units for the landslide training dataset were randomly selected in the remaining study area.

In this analysis, we first adopted grid cells as mapping units and applied LAND-SVA to ensure that only significant landslide causal factors were used for susceptibility modelling. The continuous variables were classified heuristically based on researchers' previous studies (Sinčić et al. 2022). For categorical variables, we computed frequency ratio (FR) values for each class and used them as relative values for their transformation into continuous variables. Next, the significance of the 22 potential causal factors (Table 1) for the susceptibility modelling was evaluated by observing the loss of model fitting performance in terms of Area Under Curve value and their associated Receiver Operating Characteristic curves (AUC_{ROC}) when removing each single factor from the analysis (i.e.,

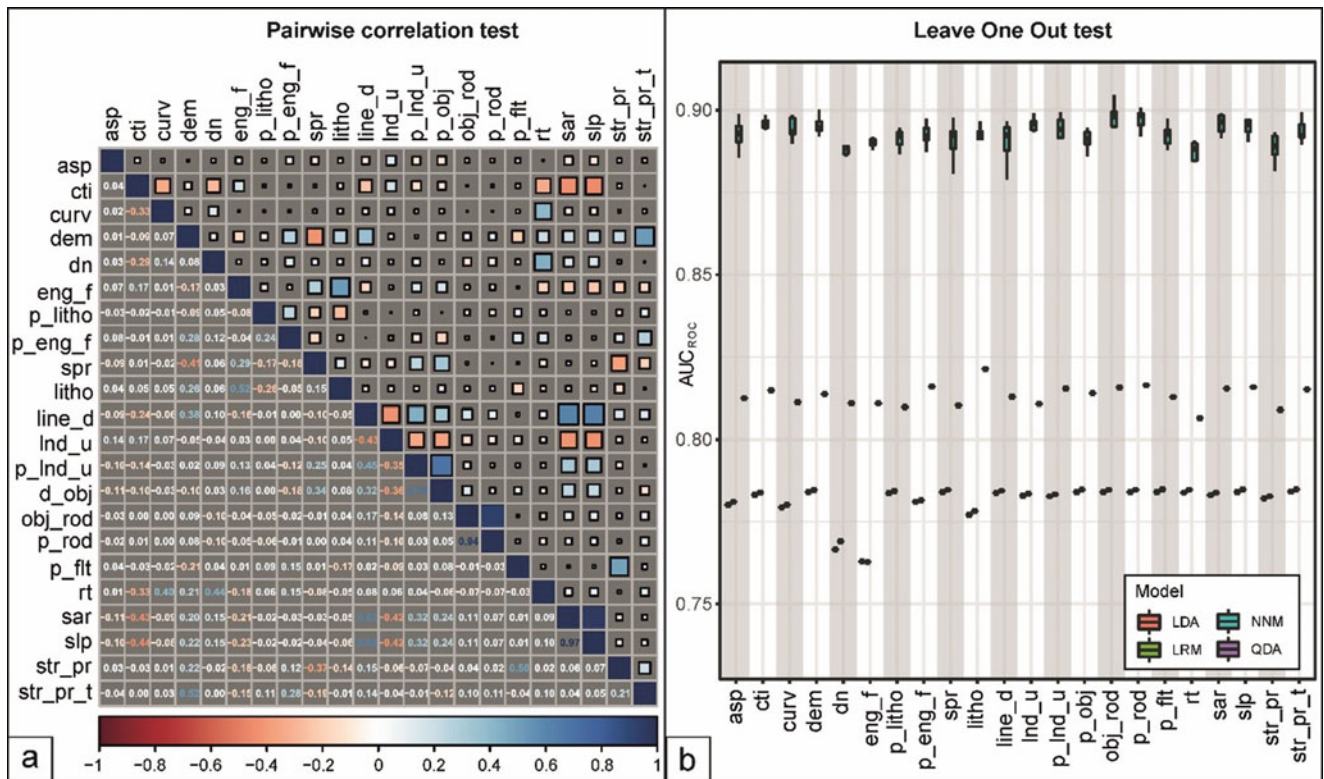


Fig. 3 Results of LAND-SVA evaluations used to define the final set of causal factors for LSM. In the Hrvatsko Zagorje study area were available 22 variables. The figure shows results of: (a) pairwise correlation test; and (b) Leave One Out test

performing a Leave One Out test, see Fig. 3). Variables were considered pairwise correlated when the correlation coefficient was greater than 0.5 with a significance level of 0.01. In such a case, an objective criterion for variable selection was the variable’s lower or irrelevant influence on the overall model fitting performance (AUC_{ROC}). The final set of variables used for grid-based statistical models was also used for the slope unit modelling. The following set of variables was selected to produce pixel and slope-unit based landslide susceptibility maps: slope orientation, terrain curvature, engineering formations, proximity to engineering formation bcontact, proximity to drainage network, proximity to permanent and temporary streams, and proximity to land use boundary (Table 1). Also, LAND-SVA showed that multicollinearity problems between selected variables were not present.

LAND-SE was used to prepare landslide susceptibility maps, i.e., four single statistical models (LRM, LDA, QDA, NNM) and one combined model (CFM) for the two mapping units (5 m × 5 m grid cells and slope units). The fitting performance of the LSM zonations was evaluated quantitatively with the AUC_{ROC} and the Cohen’s Kappa index (Table 2).

Using the training landslide pixel sample, we evaluated the model fitting performance (AUC) for the pixel-based

susceptibility maps. The ROC values indicate similar model fitting performance for the LRM (AUC = 0.775) and the LDA (AUC = 0.773) models with similar results for the Cohen’s Kappa index (Table 2) (k = 0.389 and k = 0.389). The lowest model fitting performance was obtained for the QDA model (AUC = 0.759 and k = 0.350), while the highest was obtained for the NNM model (AUC = 0.793 and k = 0.431). The combined model (CFM) has a similar fitting performance as the NNM (AUC = 0.79 and k = 0.432).

We evaluated the model fitting performance (AUC) for the slope-based susceptibility maps using the slope units training sample. The ROC values indicate similar model fitting performance (Table 2) for the LRM (AUC = 0.764) and the QDA (AUC = 0.745) models and slightly higher performance for the LDA model (AUC = 0.766). The highest model fitting performance was for the NNM model (AUC = 0.854). The Cohen’s Kappa index is similar for all four models (k = 0.314–0.364). The combined model (CFM) has a similar fitting performance as the NNM (AUC = 0.837 and k = 0.383).

The probability of landslide occurrence obtained for each of the ten LSM was classified into five susceptibility classes (Fig. 4): very low (values ranging from 0–0.2), low (0.2–0.45), medium (0.45–0.55), high (0.55–0.8) and very high (0.8–1). Mapping units with a probability value ranging

Table 2 Model evaluation metrics for ten landslide susceptibility models prepared with LAND-SUITE

Method	AUC	Cohen's Kappa index	Area (%) of landslide susceptibility classes based on modelled probability				
			Very low (0–0.2)	Low (0.2–0.45)	Medium (0.45–0.55)	High (0.55–0.8)	Very high (0.8–1)
Pixel-based susceptibility models							
LRM	0.775	0.389	22.94	35.10	14.09	23.65	4.21
LDA	0.773	0.389	21.39	34.09	14.53	26.19	3.79
QDA	0.759	0.350	30.09	12.73	7.20	32.43	17.55
NNM	0.793	0.431	31.48	27.32	11.77	26.22	3.21
CFM	0.791	0.432	34.93	25.71	9.58	26.10	3.69
Slope-unit based susceptibility models							
LRM	0.744	0.314	13.95	25.06	21.17	37.41	2.76
LDA	0.766	0.313	11.50	24.22	22.93	39.18	2.52
QDA	0.745	0.325	8.45	12.04	46.43	13.78	19.66
NNM	0.854	0.364	27.63	1.46	61.39	0.05	9.82
CFM	0.837	0.383	27.59	3.85	23.07	36.22	9.63

from 0.45 to 0.55 correspond to the locations where the model shows the higher classification uncertainty. Considering the pixel-based LSMs, the QDA has the lowest number of mapping units classified in the medium class (7.20%), and the LDA model has the highest value (14.53%). Generally, slope-based LSMs show a higher number of mapping units classified in the medium class, with the LRM, LDA and CFM models having the lower number (from 21.17% to 23.07%) and the NNM model with the higher (61.39%).

Considering only the AUC values, the NNM model and the slope-unit could be considered the best combination, but this zonation shows the largest number of mapping units classified in the medium class, which corresponds to a very large part of the study. In addition, the pixel-based combined susceptibility zonation (CFM) shows the best fitting performance (AUC = 0.793, $k = 0.432$, $u = 9.58\%$) among the ten models obtained with LAND-SUITE.

5 Discussion

The focus of this work was to test LAND-SUITE for landslide susceptibility modelling, including the selection of the appropriate causal factors and the analysis of various statistical models and mapping units. The analysis was conducted for a small study area (20 km²) which can be considered representative to propose a methodology for LSM on a large scale and an example in the Croatian spatial planning system.

In previous work, Sinčić et al. (2022) prepared and analysed high-quality input data derived from high-resolution remote sensing data, i.e., LiDAR data and orthophoto maps, useful for landslide susceptibility assessment in the study area. We have evaluated a large number of geomorphological, geological, hydrological and anthropogenic data as variables, since general criteria or guidelines for the selection

of causal factors for susceptibility modelling are not available.

LAND-SVA multicollinearity analysis and correlograms facilitate the selection of relevant explanatory variables. All explanatory variables with low impact on model fitting performance and/or correlation coefficient higher than 0.5 were omitted from the analysis. From the 22 original factor maps, only 6 were selected, considering the lack of variable relevance on the susceptibility model and following the rule “less is more”, avoiding over-parameterisation issues.

All model evaluation tests indicate that pixel-based models have better model fitting and accuracy than slope-unit based models, regardless of the statistical method. However, the overall performances of the pixel-based susceptibility maps presented are of good-to-fair fitting capacity, with AUC values ranging between 0.759 to 0.793 and Cohen's Kappa index ranging between 0.35 to 0.43 which can be described as moderate (Table 2). Nevertheless, our main interest was not preparing a definitive landslide susceptibility map for the study area, but testing the possibility of using LAND-SUITE for large-scale landslide susceptibility modelling, applying different mapping units and analysing differences on final landslide susceptibility maps. In the future, a more detailed analysis of the input data for LSM will be performed because the availability of new and relevant geo-environmental information can result in better and more reliable susceptibility models and zonations (Reichenbach et al. 2018).

Statistical landslide susceptibility zonations were quantitatively assessed for the entire study area by comparing the total area (Table 2) and the spatial distribution of the susceptibility classes (Fig. 4). The pixel and slope unit-based susceptibility assessment significantly differ for the type of information provided. To emphasise the large-scale application and to highlight the difference between the ten models, detailed views of the derived maps are presented in Fig. 5.

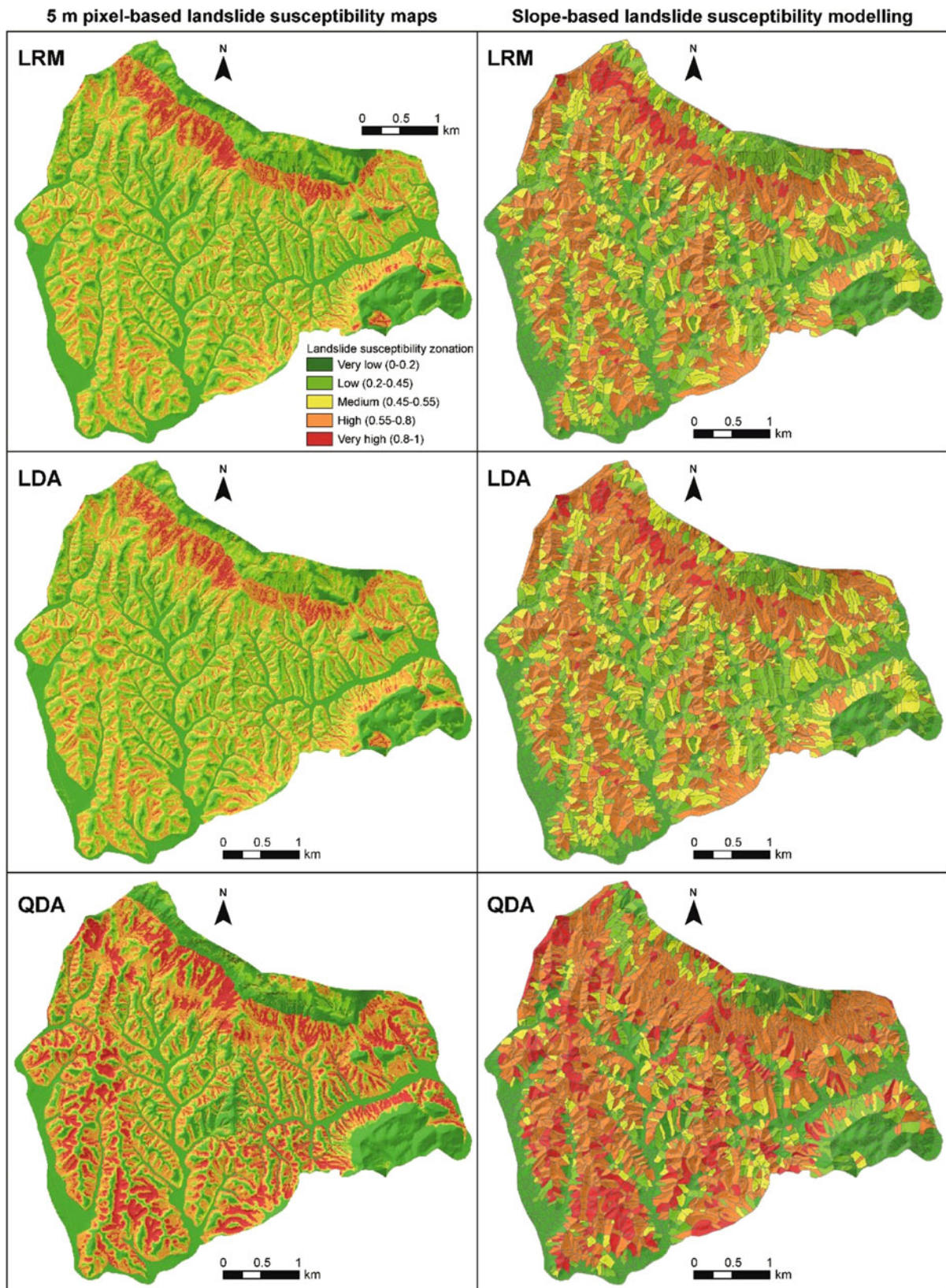


Fig. 4 Pixel and slope unit-based landslide susceptibility maps for the study area located in Hrvatsko Zagorje prepared using LAND-SUITE. Legend: LDA = Linear discriminant analysis; LRM = Logistic regression model; QDA = Quadratic discriminant analysis; NNM = Neural network analysis; CFM = Combined model

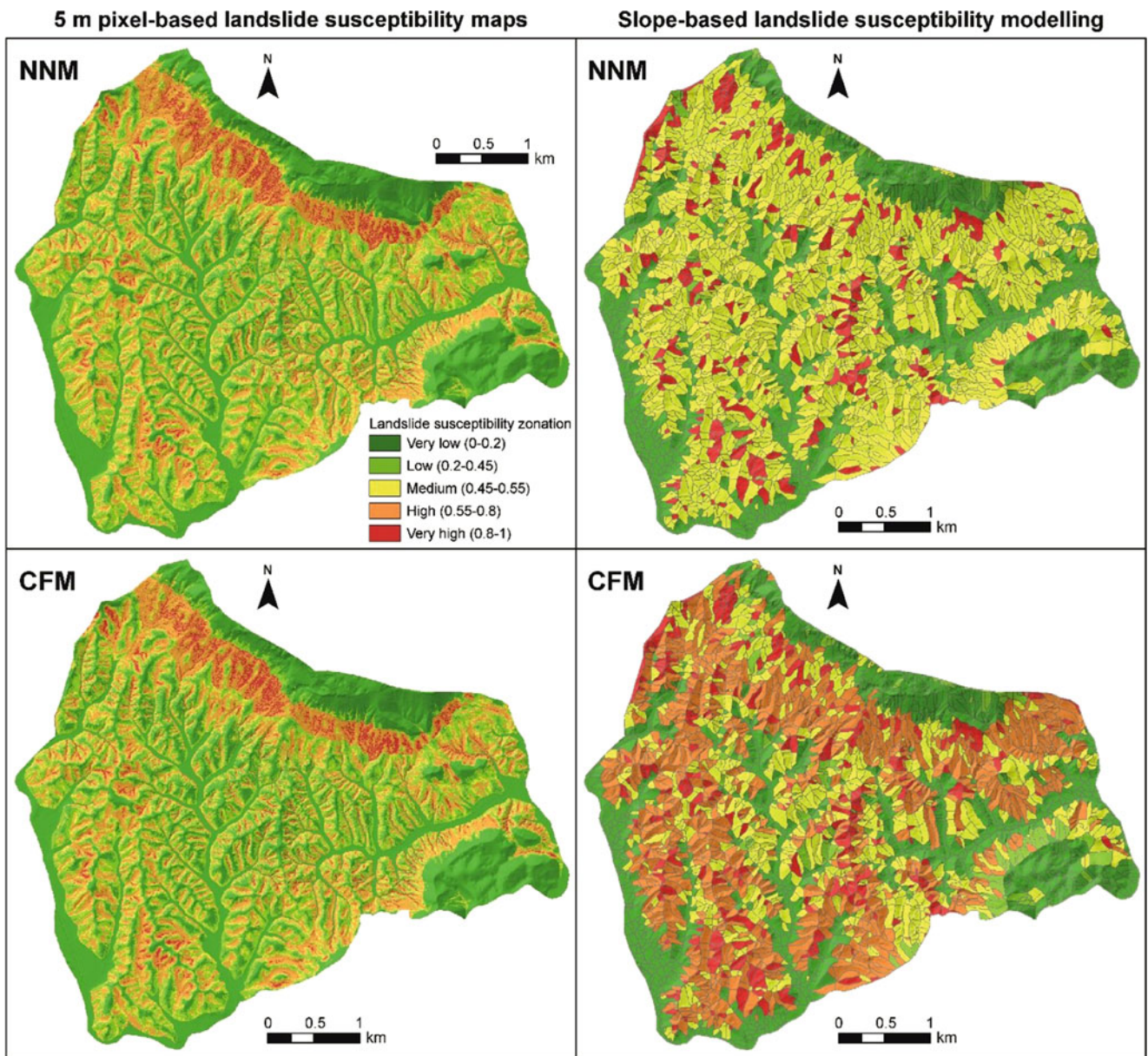


Fig. 4 (continued)

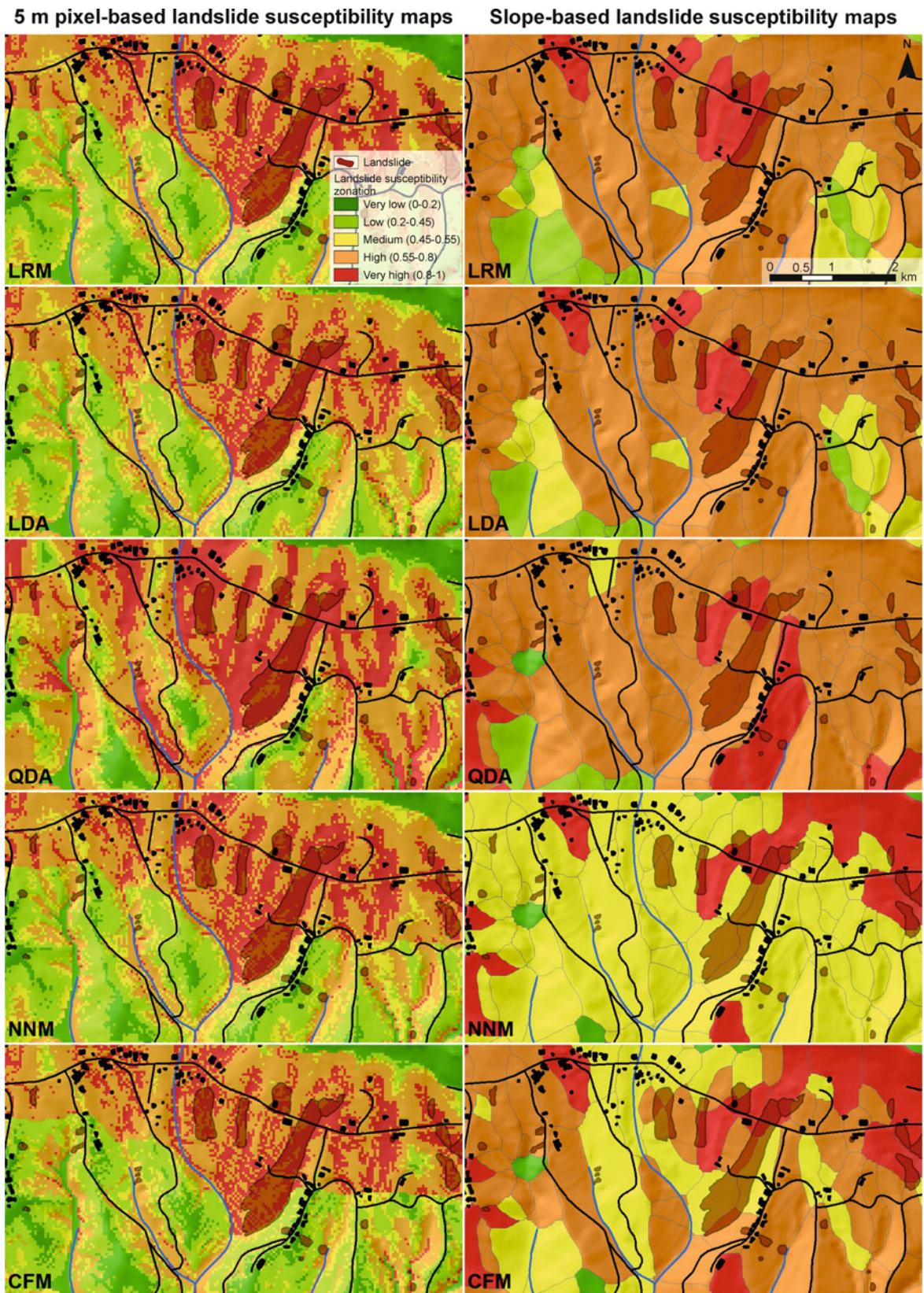


Fig. 5 Close-up views for pixel and slope unit-based landslide susceptibility maps of the study area in Hrvatsko Zagorje prepared using LAND-SUITE. Legend: LDA = Linear discriminant analysis;

LRM = Logistic regression model; QDA = Quadratic discriminant analysis; NNM = Neural network analysis; CFM = Combined model

The close-up extents show the distribution of susceptibility classes together with existing landslides, buildings, roads and water bodies. Moreover, susceptibility zonation on close-up extents can be discussed, considering their further applicability in the spatial planning system. One important conclusion is that a pixel-based map represents a better option due to higher model accuracy and better relation with existing landslides. Although, pixel-based maps require “post-processing” of the susceptibility zones to produce more clustered and homogeneous information for the final purpose, i.e., application in a local-level spatial planning system. Moreover, slope-based maps have a higher relation with the topography, reduced mapping errors and are more appropriate for further applications. The problem is that the size of slope units derived for this analysis does not correspond well with the scale of landslides susceptibility assessment and would be more appropriate at the regional level.

6 Conclusion

The landslide susceptibility analysis for part of the Hrvatsko Zagorje (20 km²) was performed using the LiDAR-based landslide inventory (Krkač et al. 2022) and causal factor maps derived and/or modified with high-resolution remote sensing data (Sinčić et al. 2022). We applied five statistical methods in LAND-SUITE (Rossi et al. 2021a), i.e., four single statistical models (LRM, LDA, QDA, NNM) and one combined model (CFM), for two different types of mapping unit, (i.e., 5 m × 5 m regular grid cells and slope units). In both cases, an equal number of unstable and stable units were randomly selected as training datasets. The original 22 causal factors was checked for mutual collinearity, and only six were classified as significant for LSM (i.e., slope orientation, terrain curvature, engineering formations, proximity to engineering formation contact, proximity to drainage network, and proximity to permanent and temporary streams, and proximity to land use boundary).

Among the pixel training samples, the best model fitting performance was obtained for the NNM (AUC = 0.793 and k = 0.431) and the combined (CFM) models (AUC = 0.79 and k = 0.432). Similarly, the best model fitting performance for the slope-unit was obtained for the NNM (AUC = 0.854 and k = 0.364) and the combined (CFM) models (AUC = 0.837 and k = 0.383).

The probability of landslide occurrence for each of the ten models was classified into five susceptibility classes. The pixel and slope unit-based maps displayed differences in the information detail, indicating that pixel-based models are more appropriate for the local-level spatial planning system.

In this work, LAND-SUITE proved to be a helpful tool for testing landslide susceptibility hypotheses and searching for new insights in landslide applications. Moreover, LAND-SUITE allowed efficient statistically-based modelling and massive code execution, mainly due to the availability of its command line interface (Rossi et al. 2021a).

Acknowledgments This research was fully supported by the Croatian Science Foundation under the project “Methodology development for landslide susceptibility assessment for land-use planning based on LiDAR technology”, LandSlidePlan (HRZZ IP-2019-04-9900, HRZZ DOK-2020-01-2432).

References

- Alvioli M, Marchesini I, Reichenbach P, Rossi M, Ardizzone F, Fiorucci F, Guzzetti F (2016) Automatic delineation of geomorphological slope units with r.slopeunits v1.0 and their optimisation for landslide susceptibility modelling. *Geosci Model Dev* 9:3975–3991. <https://doi.org/10.5194/gmd-9-3975-2016>
- Aničić B, Juriša M (1984) Basic geological map, scale 1:100,000, Rogatec, Sheet 33–68
- Bernat Gazibara S, Mihalić Arbanas S, Sinčić M, Krkač M, Lukačić H, Jagodnik P, Arbanas Ž (2022) LandSlidePlan -scientific research project on landslide susceptibility assessment in large scale. In: 5th Regional Symposium on Landslides in Adriatic-Balkan Region “Landslide Modelling & Applications.” Faculty of Civil Engineering, University of Rijeka and Faculty of Mining, Geology and Petroleum Engineering, University of Zagreb
- Bernat S, Mihalić Arbanas S, Krkač M (2014) Landslides triggered in the continental part of Croatia by extreme precipitation in 2013. In: Lollino G, Giordan D, Crosta GB, Corominas J, Azzam R, Wasowski J, Sciarra N (eds) *Engineering geology for society and territory 2*. Springer International Publishing, Cham, pp. 1599–1603
- Bognar A (2001) Geomorphological regionalisation of Croatia. *Acta Geographica Croatica* 34:27–29. (in Croatian)
- Bornaetxea T, Rossi M, Marchesini I, Alvioli M (2018) Effective surveyed area and its role in statistical landslide susceptibility assessments. *Nat Hazards Earth Syst Sci* 18(9):2455–2469. <https://doi.org/10.5194/nhess-18-2455-2018>
- Bornaetxea T, Blais-Stevens A, Miller B (2023) Landslide Inventory Map of the Valemount Area, British Columbia, Canada. A Detailed Methodological Description. Alcántara-Ayala I, Arbanas Ž, Huntley D, Konagi K, Mikoš M, Sassa K, Sassa S, Tang H, Tiwari B (eds) *Progress in landslide research and technology*, vol 1(2), 2022. Springer International Publishing, Cham, pp. 373–381. https://doi.org/10.1007/978-3-031-18471-0_27
- DHMZ (2022) Climatological data, Varaždin. https://meteo.hr/klima.php?section=klima_podaci¶m=k1&Grad=varazdin. (in Croatian)
- Guzzetti F, Galli M, Reichenbach P, Ardizzone F, Cardinali M (2006a) Landslide hazard assessment in the Collazzone area, Umbria, Central Italy. *Nat Hazards Earth Syst Sci* 6:115–131. <https://doi.org/10.5194/nhess-6-115-2006>
- Guzzetti F, Reichenbach P, Ardizzone F, Cardinali M, Galli M (2006b) Estimating the quality of landslide susceptibility models. *Geomorphology* 81:166–184. <https://doi.org/10.1016/j.geomorph.2006.04.007>
- Jagodnik P, Bernat Gazibara S, Arbanas Ž, Mihalić Arbanas S (2020a) Engineering geological mapping using airborne LiDAR datasets –

- an example from the Vinodol Valley, Croatia. *J Maps* 16:855–866. <https://doi.org/10.1080/17445647.2020.1831980>
- Jagodnik P, Bernat Gazibara S, Jagodnik V (2020b) Types and distribution of quaternary deposits originating from carbonate rock slopes in the Vinodol valley, Croatia – new insight using airborne LiDAR data. *Rudarsko-geološko-naftni zbornik* 35:57–77. <https://doi.org/10.17794/rgn.2020.4.6>
- Krkač M, Bernat Gazibara S, Sinčić M, Lukačić H, Arbanas Mihalić S (2022) Landslide inventory mapping based on LiDAR data: a case study from Hrvatsko Zagorje (Croatia). In: 5th regional symposium on landslides in the Adriatic - Balkan region. Faculty of Civil Engineering, University of Rijeka and Faculty of Mining, Geology and Petroleum Engineering, University of Zagreb, pp 81–86
- Malamud B, Mihir M, Reichenbach P, Rossi M (2014) Report on standards for landslide susceptibility modelling and terrain zonation, LAMPRE FP7 Project deliverables. <https://lampre-project.eu>
- Mihalić Arbanas S, Bernat Gazibara S, Krkač M, Sinčić M, Lukačić H, Jagodnik P, Arbanas Ž (2023) Landslide detection and spatial prediction: application of data and information from landslide maps. In: Alcántara-Ayala I, Arbanas Ž, Huntley D, Konagi K, Mikoš M, Sassa K, Sassa S, Tang H, Tiwari B (eds). *Progress in landslide research and technology*, 1 2. Springer International Publishing, Cham, pp. 195–212. https://doi.org/10.1007/978-3-031-18471-0_16
- Reichenbach P, Rossi M, Malamud BD, Mihir M, Guzzetti F (2018) A review of statistically-based landslide susceptibility models. *Earth Sci Rev* 180:60–91. <https://doi.org/10.1016/j.earscirev.2018.03.001>
- Rossi M, Bornaetxea T, Reichenbach P (2021a) LAND-SUITE V1.0: a suite of tools for statistically-based landslide susceptibility zonation. *Geosci Model Dev* 15:5651–5666. <https://doi.org/10.5194/gmd-15-5651-2022>
- Rossi M, Sarro R, Reichenbach P, Mateos RM (2021b) Probabilistic identification of rockfall source areas at regional scale in El Hierro (Canary Islands, Spain). *Geomorphology* 381:107661
- Schlögel R, Marchesini I, Alvioli M, Reichenbach P, Rossi M, Malet JP (2018) Optimising landslide susceptibility zonation: effects of DEM spatial resolution and slope unit delineation on logistic regression models. *Geomorphology* 301:10–20. <https://doi.org/10.1016/j.geomorph.2017.10.018>
- Šimunić A, Pikija M, Hečimović I (1982) Basic geological map, scale 1: 100,000. Varaždin, Sheet:33–69
- Sinčić M, Bernat Gazibara S, Krkač M, Lukačić H, Mihalić Arbanas S (2022) The use of high-resolution remote sensing data in preparation of input data for large-scale landslide Hazard assessments. *Land* (Basel) 11:1360. <https://doi.org/10.3390/land11081360>

Open Access This chapter is licensed under the terms of the Creative Commons Attribution 4.0 International License (<http://creativecommons.org/licenses/by/4.0/>), which permits use, sharing, adaptation, distribution and reproduction in any medium or format, as long as you give appropriate credit to the original author(s) and the source, provide a link to the Creative Commons license and indicate if changes were made.

The images or other third party material in this chapter are included in the chapter's Creative Commons license, unless indicated otherwise in a credit line to the material. If material is not included in the chapter's Creative Commons license and your intended use is not permitted by statutory regulation or exceeds the permitted use, you will need to obtain permission directly from the copyright holder.





An Integrated Approach to Landslides Risk Management for Local and National Authorities

Biljana Abolmasov, Miloš Marjanović, Uroš Đurić, and Jelka Krušić

Abstract

The University of Belgrade, Faculty of Mining and Geology has been involved in landslide risk reduction activities at the national, regional, and site-specific levels in Serbia for decades. Since 2011 the Faculty has had several activities closely connected with the International Consortium on Landslides, including the International Programme on Landslides Projects 181, 210 and 248, as well as World Centre of Excellency (WCoE) from 2017. In the past decade the Faculty of Mining and Geology was involved in several national, regional and local projects funded by the People of Japan, UNDP and The World Bank on landslide risk reduction in Serbia, Bosnia and Herzegovina and North Macedonia. They all closely involved many stakeholders from national to local authorities including Ministries, Local Self Governments, Public Enterprises, Emergency Offices and Civil Protection units. In this report, the activities of WCoE for national and local authorities on landslide risk reduction will be presented.

Keywords

Landslides · Risk assessment · Risk management · Authorities

1 Introduction

The University of Belgrade, Faculty of Mining and Geology (UBFMG) has been a full member of the International Consortium on Landslides (ICL) since 2011 and has been gradually intensifying its contributions to the ICL worldwide efforts for landslide risk reduction and international promotion of landslide research. UBFMG has been awarded the title of the World Centre of Excellence (WCoE) in Landslide Risk Reduction (2017–2023). UBFMG has contributed to International Programme on Landslides (IPL) with several research projects approved by the IPL Global Promotion Committee, but also by publishing in the Journal of the International Consortium on Landslides and organizing the second and the sixth Regional Symposium on Landslides in the Adriatic-Balkan Region (Arbanas and Arbanas 2022). Finally, it has contributed through active involvement in the ICL regional networks, i.e., ICL Adriatic-Balkan Regional Network from 2012 (Mihalić Arbanas et al. 2013).

UBFMG has contributed to several UNDP and World Bank and Global Facility for Disaster Reduction and Recovery (GFDRR) activities in Serbia and throughout the Balkan region (Bosnia and Herzegovina, North Macedonia), working on landslides risk reduction projects (national, regional and municipality level), with special attention on climate changing conditions. UBFMG is supporting idea of open landslides data and contributes to ICL World Report on Landslides (Abolmasov et al. 2017a), as well as to the National Landslide Database in Serbia. In the last few years, it is an active member of the Serbian National Emergency Bodies for landslide risk reduction. UBFMG has signed KLC2020 and strongly contributes to the Sendai Framework for Disaster Risk Reduction 2015–2030.

B. Abolmasov (✉) · M. Marjanović · J. Krušić
Faculty of Mining and Geology, University of Belgrade, Belgrade, Serbia
e-mail: biljana.abolmasov@rgf.bg.ac.rs; milos.marjanovic@rgf.bg.ac.rs; jelka.krusic@rgf.bg.ac.rs

U. Đurić
Faculty of Civil Engineering, University of Belgrade, Belgrade, Serbia
e-mail: udjuric@grf.bg.ac.rs

2 General Data

The Republic of Serbia is located on the Balkan Peninsula in south-east Europe (Fig. 1), covering an area of 88,499 km² and with a population of 6,647,000, according to the data from the Statistical Office of the Republic of Serbia from 2022 (<http://www.stat.gov.rs/>).

It is a parliamentary republic and has a non-symmetric territorial organization. This administrative organization is inherited from the ex-Yugoslavia period and today, it is slightly changed by the National nomenclature of statistical territorial units (NUTS). The Republic of Serbia is divided into 5 regions (NUTS2), 29 administrative districts (NUTS3), 197 municipalities (LAU1) and 6158 settlements (LAU2).

The territory of Serbia is a hilly to low-mountainous country with many lowlands (around 36% of the Serbian territory is below 200 m), mostly in the northern part of the country around the Pannonia plain. Almost 45% of the territory consists of very gentle slopes (up to 5 degrees), while 15% is rugged mountains with slopes greater than 15 degrees mainly in the central and southern parts of the country. The hydrological system in Serbia consists of several international rivers and significant national rivers, almost all of which drain into the Black Sea, except Pčinja River which drains into the Aegean Sea. Only the Danube (588 km), Sava (206 km) and Tisa (168 km) rivers are navigable all the way through Serbia.

Serbia's climate is influenced by the Eurasian landmass, the Atlantic Ocean, and the Mediterranean Sea. Most of the country has a mid-continental climate with cold winters and hot summers and relatively well-distributed rainfall patterns. The recent report from the Hydrometeorological Service of Serbia provides the spatial distribution of annual averages for temperature and precipitation sum across the territory of the Republic of Serbia for the reference period 1981–2010. Annual mean temperature varies, and most of territory has the temperature between 10.1–12.0 degrees. Annual mean precipitation is from 557 mm in Kikinda (north of Serbia) to 1018 mm in Zlatibor (southwest Serbia) for the same reference period. Annual mean precipitation varies from 500–600 mm in the central to 700–1000 mm in the western part of Serbia.

3 Landslides Risk Reduction on a National Level

The Republic of Serbia is prone to natural disasters such as floods, flash floods, and droughts, but also to geological hazards like landslides, rockfalls and flows, which can cause significant damage to infrastructure and livelihoods. The main geological climate-related hazards in Serbia are landslides in general (the common ones being slides, flows

and falls). Due to complex geological history and terrain composition, in combination with morphological and climate characteristics, 16% of the territory is affected by landslides (Abolmasov et al. 2017c).

In the third week of May 2014, Serbia and Bosnia and Herzegovina experienced its most severe floods in the last 120 years, caused by Cyclone Tamara. Huge amounts of rainfall of 250 to 400 mm for 3 days caused sudden and extreme flooding of several rivers—in particular, the Sava River, but also the Drina River, the Bosna River, the Una River, the Sana River, the Vrbas River, the Kolubara River, the Morava river and their tributaries. In western and central Serbia for instance, daily precipitation on May 15 exceeded the expected average for the entire month (Marjanović et al. 2018b). Urban, industrial and rural areas were completely submerged, cut off without electricity or communications and roads and transport facilities were damaged. As a result, 1.6 million persons (one-fifth of the population) were directly or indirectly affected in Serbia. The floods and landslides caused 51 casualties and around 32,000 people were evacuated (Abolmasov et al. 2021). The Serbian Recovery Needs Assessment (RNA) revealed that the total effects of the disaster in the 24 affected municipalities amount to EUR 1.525 billion (equal to 3% of the Serbian Gross Domestic Product). The Faculty of Mining and Geology participated in RNA in May–June 2014 (Marjanović et al. 2017; Abolmasov et al. 2017c).

In the aftermath of the 2014 floods, Serbia adopted a National Disaster Risk Management Program (NDRMP) aiming to make a critical paradigm shift towards proactive management of disaster risks and increase the country's resilience to natural disasters. NDRMP was structured under six main pillars of action: (i) institutional strengthening; (ii) risk identification and monitoring; (iii) structural and non-structural risk reduction measures; (iv) preparedness and early warning; (v) disaster risk financing and insurance solutions; and (vi) resilient recovery. The main challenge under the NDRMP was to build an appropriate and longstanding system for Disaster Risk Management (DRM) in the country, where different institutions work together to systematically reduce existing risks, avoid the creation of future risks, and respond more efficiently to disasters.

The Emergency Sector under the Ministry of Interior of the Republic of Serbia 2019 assembled a working group that included specialists in the field of corresponding hazards, primarily floods and landslides to develop scenarios and generate corresponding hazard maps at the national level.

Furthermore, "Natural and Technological Risk Assessment of the Republic of Serbia" has been adopted under the Law on Disaster Risk Reduction and Emergency Management. National Disasters Risk Assessment and the landslide susceptibility map at the national level (1:300,000) reached its finalization in 2020 (Fig. 2). The map was prepared by



Fig. 1 Geographical position of the Republic of Serbia

Marjanović et al. (2020),¹ by using the Analytical Hierarchy Process (AHP) and it is published as hazard layer at Disaster Risk Register of the Republic of Serbia.

The map was used further for national road and railway network exposure assessment. Beneficiaries (Public Enterprise Roads of Serbia and Public Enterprise Railway Infrastructure) and end-users are welcome to include results in other application fields.

4 Contribution to Regional Level Landslide Risk Reduction

Landslides, flash floods and floods are the main natural hazards affecting the road network in Serbia. In May 2014, unprecedented rainfall resulted in damage and loss in the transportation sector of 166.5 million euros. The erosion due to flash floods mainly destroyed bridges, embankments and roads, while landslides and debris flows cut off and disrupted the main and local road systems. A rough estimation by Public Enterprise Roads of Serbia (PERS) reported that more than 2000 landslides/flows were activated along state roads of category I and II and more than 3000 along local-municipality roads, during and immediately after May 2014.

By 2017–2021, a comprehensive project funded by the World Bank was conducted and involved the preparation of a more resilient road network design in climate-changing conditions. In short, the project started with localizing the hotspots of landslides, flows, flash floods, and flood hazards

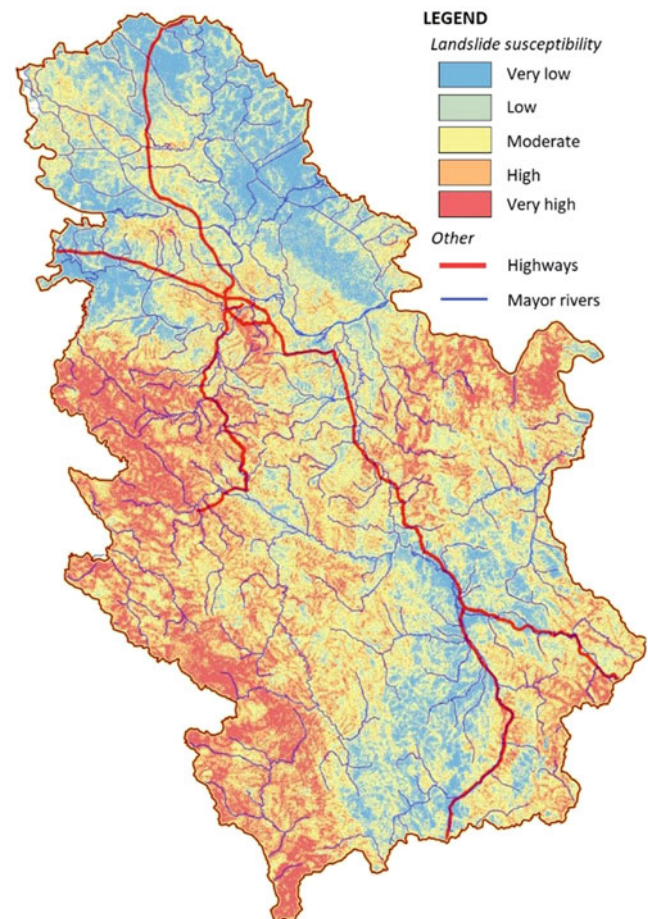


Fig. 2 Landslide hazard map of the Republic of Serbia (<https://drr.geosrbija.rs/drr/map>)

¹ <http://prezentacije.mup.gov.rs/svs/html/licence/Procena%20rizika%20od%20katastrofa%20u%20RS.pdf>

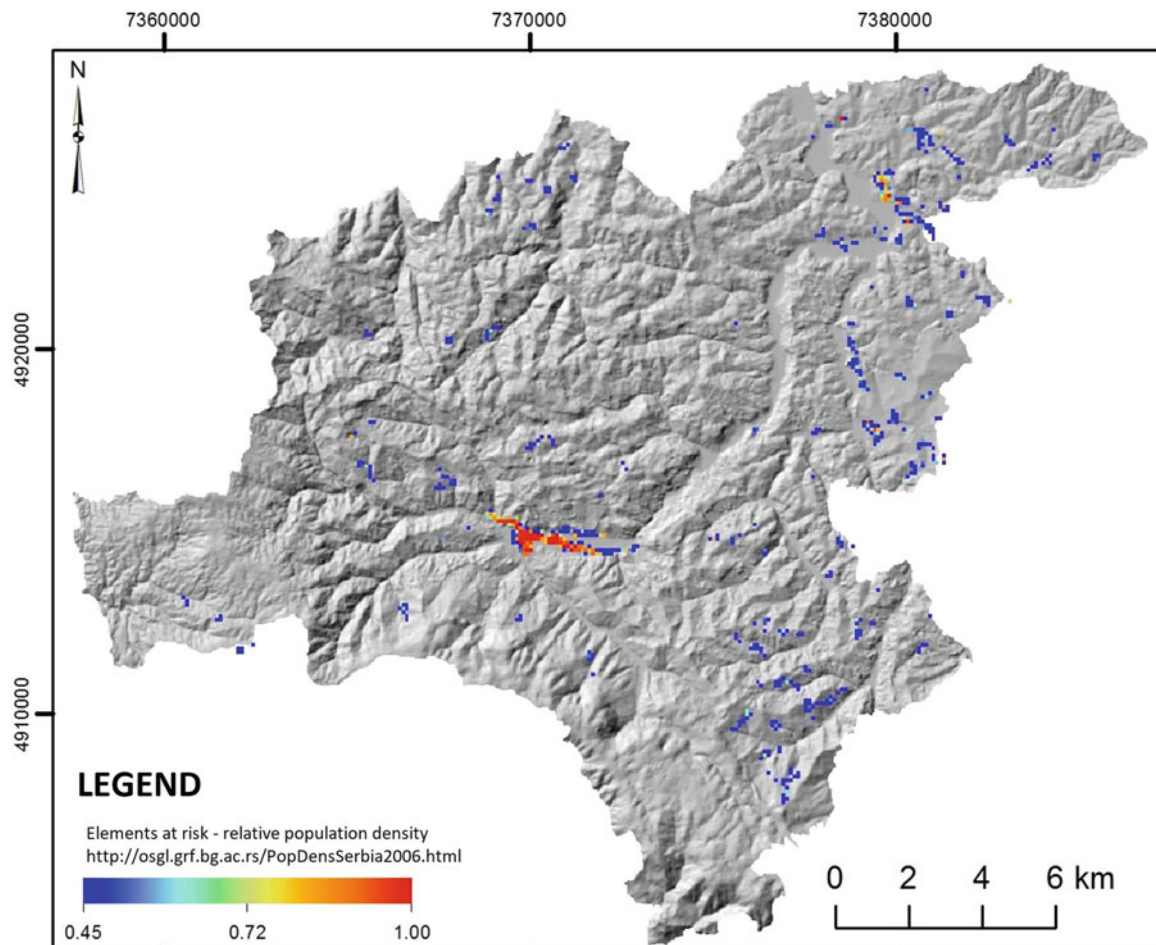


Fig. 3 Elements at risk—relative population density for Krupanj pilot area

and estimating the exposure of the road network over time in two test areas (the Valjevo and Kraljevo region). The main objective of the Project was to support the Government in establishing a foundation for mainstreaming climate resilience considerations in the road transport sector management in Serbia by developing an effective methodology for assessing the vulnerability of the road transport network to climate-related risks, improving capacities of key stakeholders in road network climate resilience planning, and setting the path for the development of structured and systematic response plans. Key beneficiaries from the Project were recognized as PERS and Ministry for Construction, Transport and Infrastructure (MCTI). As a result of Project activities (nicknamed *CliRtheRoads*), 750 km of state regional roads of categories I and II were mapped. Landslides, rockfalls, flash floods and floods hazard were assessed, as well as exposure, vulnerability and risk in climate-changing conditions (Marjanović et al. 2019, 2018a, 2022). Main stakeholders were also provided with a separately developed Android mobile application for

recording of landslides, rockfalls, flows, flash floods, and floods events, with great potential to include it in day-to-day work, and successively and systematically accumulate the data in the Road Asset Management System (RAMS).

5 Improving Landslide Risk Reduction on the Local: Municipality Level

UBFMG was included in several projects related to landslide inventory, susceptibility, hazard and risk assessment on local-municipality level, both in Serbia and Bosnia and Herzegovina, but only activities within the Project BEWARE will be presented.

The project on harmonization of landslide data and training of municipality staff for its monitoring, named BEWARE (BEYond landslide aWAREness) was designed to standardize post-event landslide database and closely involve 27 local communities affected by May 2014 events in Serbia, and prepare them to cope with catastrophic events in the future

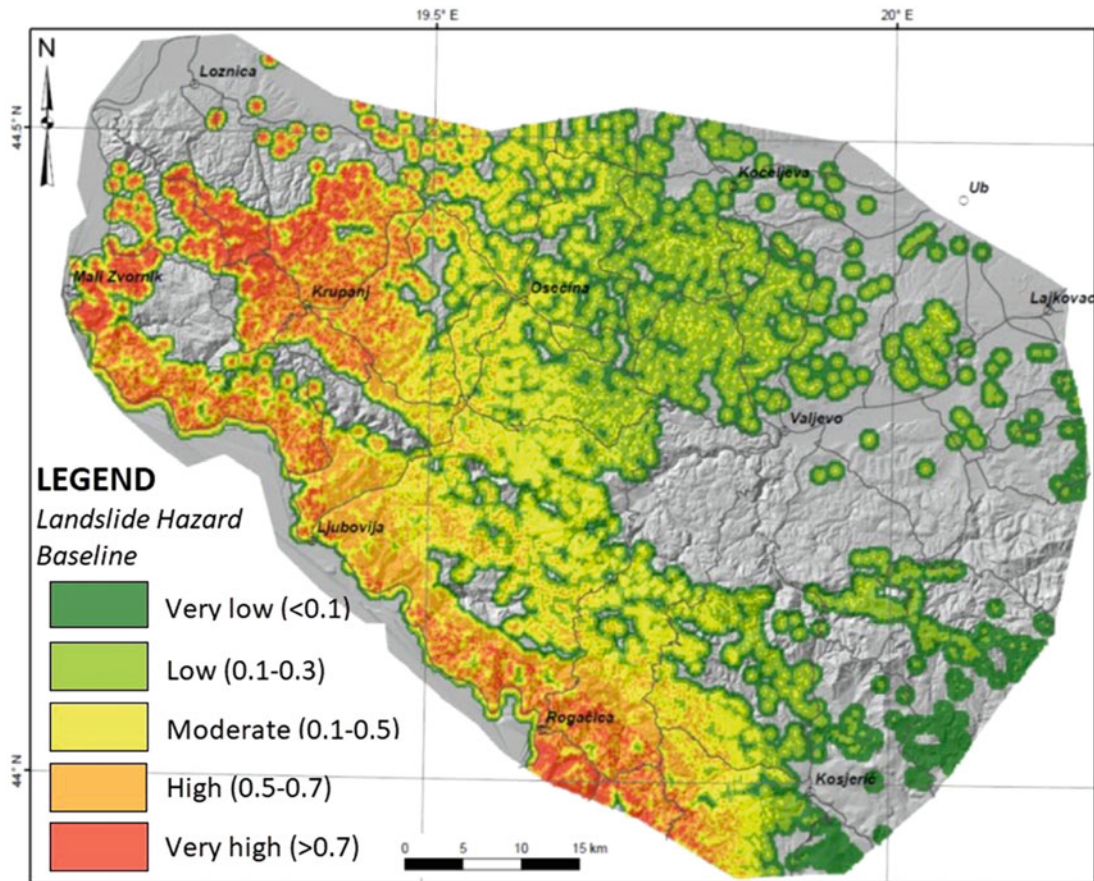


Fig. 4 Landslide susceptibility map for Valjevo pilot area

(Abolmasov et al. 2017b). The project BEWARE was realized from May 2015 to February 2016. Several Work Packages (WP) were posted to realize the project objectives (Đurić et al. 2017), but most important were Landslide Susceptibility Maps for every municipality, Landslide Vulnerability and Risk Assessment Map for population for two municipalities, and open landslide data in WEB GIS Project portal.

Landslide susceptibility maps were prepared in 1:25,000 scale (scale of Municipality Master Plan according to the Law) and provided for each of 27 municipalities as a support for Master Plans documents and as a part of non-structural measures. AHP was used for modeling and assessing landslide susceptibility for selected municipalities. Landslide vulnerability and relative risk assessment to population were prepared for Krupanj (Fig. 3) and Valjevo (Fig. 4) municipalities by using open access Serbian population density data in regional scale (Andrejev et al. 2017). All maps are available to municipal land-use and urban authorities as open access data.

Also, 12 critical sites were chosen for implementation of structural remedial measures, based on affected people and property that have not been already subjected to intervention

in post-event responses. Detailed geotechnical investigations were performed, and remedial measures were proposed and implemented.

Participants of BEWARE project were selected among Faculty of Mining and Geology, University of Belgrade staff/associates and Geological Survey of Serbia staff. Direct beneficiaries are local authorities and Civil Protection/Emergency management units, related governmental institutions, insurance and assessment agencies, municipal enterprises, and general public. Follow up activities are included and supported through the Geological Information System of Serbia <http://geoliss.mre.gov.rs/>.

6 Conclusion

The University of Belgrade, Faculty of Mining and Geology covers technical disciplines of mining and geological engineering, and fundamental geology. The Faculty of Mining and Geology has been involved in landslide risk reduction activities at the national, regional, and site-specific level in Serbia for decades. For more than 40 years, UBFMG has been supporting activities of the national and local authorities

in the field of landslides disaster risk reduction. In the field of capacity building, UBFMG offers courses for graduate and postgraduate students in landslide mechanics, dynamics, monitoring, and landslide risk mitigation, including hazard assessment. In the last ten years, the Faculty has offered courses for PhD students in the field of landslides hazard, vulnerability and risk assessment with special attention to climate changing conditions.

References

- Abolmasov B, Fathani F, Liu K, Sassa K (2017a) Progress of the world report on landslides. In: Sassa K et al (eds) *Advancing culture of living with landslides*, proceedings of 4th world landslide forum, Ljubljana 29 May-02 June 2017, Vol, vol 1. Springer International Publishing, pp 219–226. https://doi.org/10.1007/978-3-319-59469-9_18
- Abolmasov B, Damjanović D, Marjanović M, Stanković R, Nikolić V, Nedeljković S, Petrović Ž (2017b) Project BEWARE—landslide post-disaster relief activities for local communities in Serbia. In: Mikoš M et al (eds) *Advancing culture of living with landslides*, proceedings of 4th world landslide forum, Ljubljana 29 May-02 June 2017, Vol, vol 3. Springer International Publishing, pp 413–422. https://doi.org/10.1007/978-3-319-53487-9_48
- Abolmasov B, Marjanović M, Đurić U, Krušić J, Andrejev K (2017c) Massive landsliding in Serbia following cyclone Tamara in may 2014 (IPL-210). In: Sassa K et al (eds) *Advancing culture of living with landslides*, proceedings of 4th world landslide forum, Ljubljana 29 May-02 June 2017, vol 1, pp 473–484. Springer International Publishing. https://doi.org/10.1007/978-3-319-59469-9_4
- Abolmasov B, Petrović MS, Stanković R, Marjanović M, Krušić J, Đurić U (2021) Extreme rainfall event and its aftermath analysis—IPL 210 project Progress report. In: Sassa K, Mikoš M, Sassa S, Bobrowsky PT, Takara K, Dang K (eds) *Understanding and reducing landslide disaster risk*. WLF 2020. ICL contribution to landslide disaster risk reduction. Springer, Cham, pp 267–273. https://doi.org/10.1007/978-3-030-60196-6_19
- Andrejev K, Krušić J, Đurić U, Marjanović M, Abolmasov B (2017) Relative landslide risk assessment for the City of Valjevo. In: Mikoš M et al (eds) *Advancing culture of living with landslides*, proceedings of 4th world landslide forum, Ljubljana 29 May-02 June 2017, vol 3. Springer International Publishing, pp 525–523. https://doi.org/10.1007/978-3-319-53483-1_62
- Arbanas Ž, Arbanas MS (2022) 10th Anniversary of ICL Adriatic-Balkan Network and 5th Regional Symposium on Landslides. In: Sassa K, Konagai K, Tiwari B, Arbanas Ž, Sassa S (eds) *Progress in Landslide Research and Technology*, vol 1(1), pp 223–234. Springer, Cham. <https://doi.org/10.1007/978-3-031-16898-7>
- Đurić D, Mladenović A, Pešić-Georgiadis M, Marjanović M, Abolmasov B (2017) Using multiresolution and multitemporal satellite data for post disaster landslide inventory in the Republic of Serbia. *Landslides* 14(4):1467–1482. <https://doi.org/10.1007/s10346-017-0847-2>
- <http://geoliss.mre.gov.rs/beware/>
- <https://drr.geosrbija.rs/drr/homef>
- Marjanović M, Abolmasov B, Đurić U, Bogdanović S, Krautblatter M (2017) Landslide events in Serbia in May 2014: an overview. In: Abolmasov B, Marjanović M, Đurić U (eds) *Proceedings of 2nd Regional Symposium on Landslides in the Adriatic-Balkan Region - 2nd ReSyLAB 2015*. University of Belgrade, Faculty of Mining and Geology, Belgrade, Serbia, pp 239–244. ISBN: 978-86-7352-296-8. <http://resylab2015.rgf.rs/>
- Marjanović M, Abolmasov B, Đurić U, Krušić J (2018a) Assessment of landslide-related hazard and risk on the road network of the Valjevo city, Serbia. In: *Proceedings of the 16th Danube-European Conference - Geotechnical hazards and risks: Experiences and practices*, vol 1, Skopje, Macedonia. Wiley, pp 365–370
- Marjanović M, Krautblatter M, Abolmasov B, Đurić U, Sandić C, Nikolić V (2018b) The rainfall-induced landsliding in Western Serbia: a temporal prediction approach using decision tree technique. *Eng Geol* 232:147–159. <https://doi.org/10.1016/j.enggeo.2017.11.021>
- Marjanović M, Abolmasov B, Milenković S, Đurić U, Krušić J, Samardžić Petrović M (2019) Multihazard exposure assessment on the Valjevo City road network. In: Pourghasemi HR, Gokceoglu C (eds) *Spatial modeling in GIS and R for earth and environmental sciences*. Elsevier, pp 671–688. ISBN: 978-0-12-815226-3. <https://doi.org/10.1016/B978-0-12-815226-3.00031-4>
- Marjanović M, Abolmasov B, Đurić U, Krušić J, Bogdanović S (2022) Regional rockfall exposure assessment, experience from Serbia. In: Peranić J, Vivoda Prodan M, Bernat Gazibara S, Krkač M, Mihalić Arbanas S, Arbanas Ž (eds) *Landslide modelling & applications*. Proceedings of the 5th regional symposium on landslides in the Adriatic-Balkan Region. Croatian Landslide Group University of Rijeka, Faculty of Civil Engineering University of Zagreb, Faculty of Mining, Geology and Petroleum Engineering, pp 145–150. https://5resylab.uniri.hr/wp-content/uploads/2022/04/2_Proceedings-of-the-5th-ReSyLAB.pdf
- Mihalić Arbanas S, Arbanas Ž, Abolmasov B, Mikoš M, Komac M (2013) The ICL Adriatic-Balkan network: analysis of current state and planned activities. *Landslides* 10(1):103–109. <https://doi.org/10.1007/s10346-012-0364-2>

Open Access This chapter is licensed under the terms of the Creative Commons Attribution 4.0 International License (<http://creativecommons.org/licenses/by/4.0/>), which permits use, sharing, adaptation, distribution and reproduction in any medium or format, as long as you give appropriate credit to the original author(s) and the source, provide a link to the Creative Commons license and indicate if changes were made.

The images or other third party material in this chapter are included in the chapter's Creative Commons license, unless indicated otherwise in a credit line to the material. If material is not included in the chapter's Creative Commons license and your intended use is not permitted by statutory regulation or exceeds the permitted use, you will need to obtain permission directly from the copyright holder.





Assessing Landslide Hazard in the High City of Antananarivo, Madagascar (UNESCO Tentative Site)

William Frodella, Daniele Spizzichino, Giacomo Lazzeri, Claudio Margottini, Veronica Tofani, and Nicola Casagli

Abstract

Built on the hilltop of a granite ridge rising above the Ikopa River valley (the Analamanga Hill), the High City of Antananarivo (Madagascar) is renowned for its baroque-style palaces the Rova royal complex and gothic cathedrals dating back to the nineteenth Century, and therefore is part of the UNESCO Tentative List. Due to the frequent cyclonic heavy cyclonic rain, geological and geomorphological conditions, and a general lack of urban planning the study area is particularly prone to landslides (as shown by events of the winter of 2015, 2018 and 2019). As a first step towards understanding quantitative landslide risk, the geological, geomorphological, geotechnical features, as well as landslide phenomena were defined in an integrated landslide hazard assessment. Results show that the main factors affecting landslides are slope, lithology, creek-gully erosion and anthropogenic activities, while most of the landslide events are clearly triggered by heavy rainfall events. Thematic maps produced by this study are fundamental land-use management tools to be applied as a first step towards a geo-hydrological risk reduction strategy by the institutions and actors involved in the protection and conservation of the High City.

Keywords

Landslides · Cultural heritage · Landslide hazard · Rainfall

1 Introduction

The risk of natural disasters is often much higher in developing countries, such as Madagascar, where phenomena such as landslides, erosion and floods can lead to catastrophic consequences (Andriamamonjisoa and Hubert-Ferrari 2019). The reason for this lies in the relation between the geographical/climatic setting and the peculiar geological–geomorphological characteristics: heavy rainfall (three to four cyclones affecting the country every year) and a thick lateritic soil cover, resulting from a deep chemical weathering of the crystalline bedrock (Cox et al. 2010). Assessing landslide hazard in Madagascar is both a challenge because of the lack of data and local landslide-knowledge and a fundamental task to provide local authorities and stakeholders with important tools for risk management, building community resilience, protection of the cultural heritage assets, and for increasing the risk perception (especially amongst the poor and less educated citizen, who are the most exposed to landslides). Since 2017, the UNESCO Chair on Prevention and Sustainable Management of Geo-Hydrological Hazards of the University of Florence on behalf of Paris PRX Madagascar, RC-Heritage, and the municipality of Antananarivo, has been carrying out landslide risk research with the aim of enlisting the High City of Antananarivo into the UNESCO World Heritage (ICL 2022). The objective of this work is to describe the research activities to determine the landslide hazard for the Analamanga hill (Fig. 1): to understand the triggering factors and to investigate the impacts on both the historical buildings and the houses of the poorer neighborhoods, contributing towards a quantitative risk analysis. During the field surveys, capacity building was also carried out with local MSc students in geology and engineering from the Polytechnic of Antananarivo. This

W. Frodella (✉) · G. Lazzeri
Department of Earth Sciences, University of Florence, Florence, Italy
e-mail: william.frodella@unifi.it

D. Spizzichino
ISPRA, Higher Institute for Protection and Environmental Research,
Rome, Italy

C. Margottini
UNESCO Chair on Prevention and Sustainable Management of
Geo-Hydrological Hazards, University of Florence, Florence, Italy

V. Tofani · N. Casagli
Department of Earth Sciences, University of Florence, Florence, Italy

UNESCO Chair on Prevention and Sustainable Management of
Geo-Hydrological Hazards, University of Florence, Florence, Italy

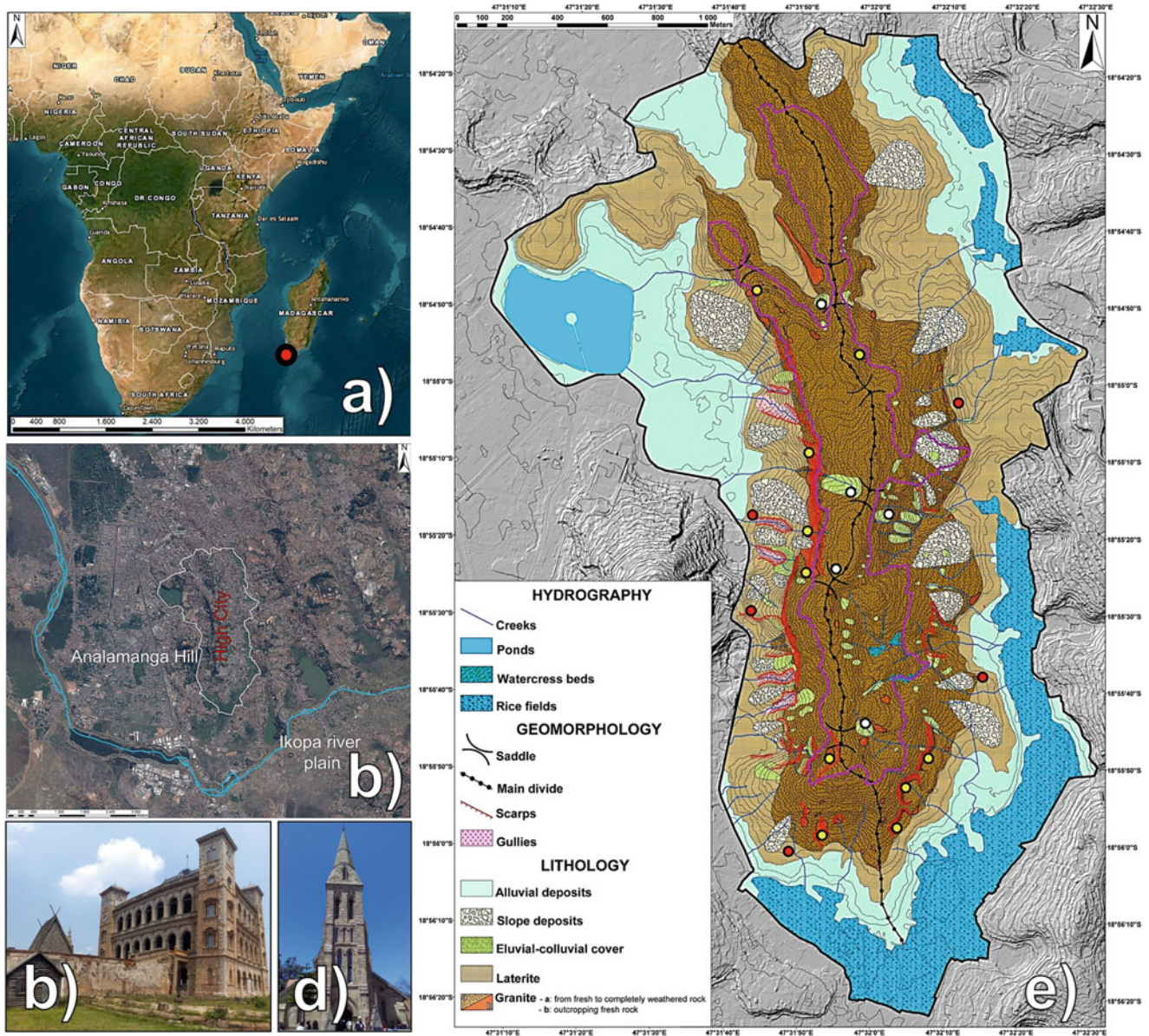


Fig. 1 Geographical location of the study area at a continental (a) and local scale (b) (modified after Ciampalini et al. 2019). Examples of the High City cultural heritage: the Rova (c) and Ambohipotsy Church (d).

Geological setting of the Analamanga Hill: red dots highlight the soil samples while yellow dots locate the rock samples (e) (modified after Frodella et al. 2021a, b)

study represents an important contribution that improves the knowledge on landslide processes in an area with limited landslide data such as Madagascar and can be reproduced in cultural heritage sites characterized by similar geomorphological and urban scenarios.

2 Materials and Methods

As a first step, a multitemporal landslide inventory was compiled involving: (i) geological/geomorphological field surveys (Frodella et al. 2021a); (ii) geotechnical laboratory analyses on collected soil and rock samples (Frodella et al.

2022); (iii) interpretation of remote sensing data, including very high resolution (VHR) multispectral Pleiades images, and two VHR DTMs (Ciampalini et al. 2019); (iv) homogenization in a GIS environment and interpretation to obtain a landslide inventory (Ciampalini et al. 2019); (v) interviews with the local population (Frodella et al. 2022). A rockmass 3D landslide kinematic global analysis (Frodella et al. 2021b) was performed on the rock cliffs to identify the areas more prone to instability. The data obtained were used as input for the landslide hazard assessment (Fell et al. 2008; Reichenbach et al. 2018). Being quite complex, and depending on the geology, erosional features and slope, a shallow landslide susceptibility with the Random Forest

Model (Breiman 2001; Catani et al. 2013) was performed for shallow phenomena (roto-translational slides involving the lateritic soil or the soil cover). For earth-debris flows acting within the large gullies (developed within the lateritic soils on the western footslope) runout simulations were carried out using the GPP code (Wichmann 2017). The trajectories of rockfall phenomena, occurring along the steep granite rock slopes on the top of the western slope and the hill southeastern sector, were modeled using the software ISGeomass (CDM 2019). Finally, global rainfall data from 2015 to 2019 (Climate Engine 2021) and the available landslide temporal occurrence were analysed to identify the rainfall condition associated with the landslide triggering (Abraham et al. 2021).

3 Results

3.1 Multitemporal Landslide Inventory

A multitemporal landslide inventory map (LIM) spanning from 2015 to 2020 (Fig. 2) was compiled in a GIS environment using the outcomes of field surveys, satellite image and DTM interpretation. In particular, two inventories were combined: (i) 78 shapefile points and polygons involving shallow landslide events during the winter 2015 (BNGRC 2015; Ciampalini et al. 2019) and rockfall sources during events in the winters of 2018 and 2019 (BNGRC 2019); (ii) 35 point-type shapefile of rockfalls/slides and debris flow sources mapped in 2020 by integrating field surveys, GPS-RTK, and interviews with local population (Frodella et al. 2022). Four main groups of instability phenomena (Cruden and Varnes 1996) were identified (Frodella et al. 2021a; Fig. 2): (1) unchanneled shallow earth-debris rotational/translational slides (the most diffused phenomena); (2) channeled earth-debris rotational/translational slides; (3) rock falls and slides (planar and wedge); (4) complex rotational/translational slides.

3.2 Shallow Landslide Susceptibility

Once the susceptibility model was successfully trained and tested (AUC = 0.9), it was applied to the whole study area. According to the results, the most important parameters to identify landslide susceptible areas were the NDVI, slope aspect and curvature (both planar and profile curvature), while the less important were the flow accumulation and, as expected, the control parameter made of random values.

The final output is a raster with a 2×2 m cell size, where each pixel has a percentage value expressing the shallow landslide spatial probability of occurrence (Fig. 3). The map shows that most of the Analamanga Hill is affected by

moderate to very high landslide susceptibility. These shallow landslide-prone areas are located along the Middle Town quarters, particularly at the foot of the central sector of the western hillslope (from north to south: Mahamasina, Ankadilalana, Tzimbazaza quarters; Fig. 3).

Here, shallow debris rotational/translational slides involve the eluvial-colluvial and the lateritic deposits, while linear creek erosion of the soft lateritic soils creates large gullies, which are rapidly expanding. Retreating scarps damage the road pavement, while diffuse slope instabilities occur at the headcut of their apex. The eastern slope is less prone to shallow landslides, except for the middle-southern sector, especially in two creek basins: the first is located east of the Rova in the Manjakamiadana quarter, while the second is located east of the Ambohipotsy quarter (Fig. 3). The north hill sector shows a general slope stability due to the widespread urban cover and the lower slope angles. An exception is the area around the tunnel, in the Ambohijatovo quarter. The southern sector shows some potentially unstable areas at the top of the abandoned quarried slope cuts in the Anjahana quarter.

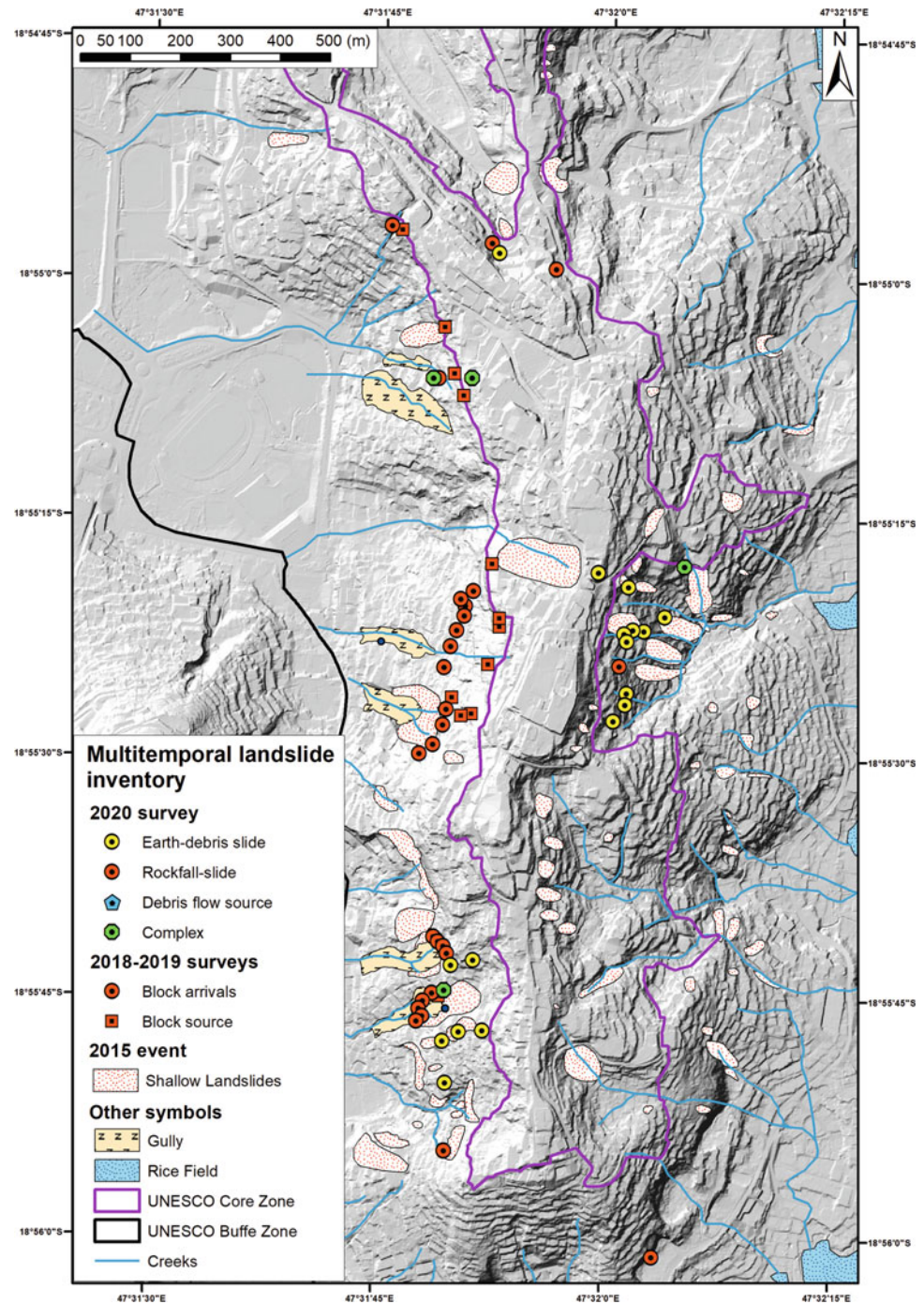
3.3 Earth-Debris Flow Assessment

Following intense rainfall events, shallow earth-debris rotational/translational slides developing from the gully slopes and head-cut apexes can evolve into earth-debris flows that are channel within the hydrographic network (Frodella et al. 2022). These phenomena are more likely to occur in the gullies of the central and southern hill sector, for example the Mahamasina, Ankadilalana and Tzimbazaza quarters (Fig. 4). The earth-debris flow impact probability map shows how these phenomena involve the lateritic soils and anthropogenic waste deposits (since gullies are often used as dumps) that enhances the gully head-cut erosion and the scarp retreat (Fig. 4).

3.4 Preliminary Landslide Frequency Assessment

A preliminary landslide frequency analysis was performed by comparing the landslide frequency obtained by the surveys with the local population and web news, together with rainfall data from 2015 to 2020 (Fig. 5a). The comparison shows clearly that the main landslide events occur after major cyclones, during periods of intense precipitations. In addition, the total rainfall associated with each landslide over different time intervals was analyzed. The total rainfall associated with landslides increases constantly from days 1 to 7, while the rainfall increase from 15 to 30 days is lower than the one from 7 to 15 days, even if it is referred

Fig. 2 LIM of the Analamanga Hill (modified after Frodella et al. 2022)

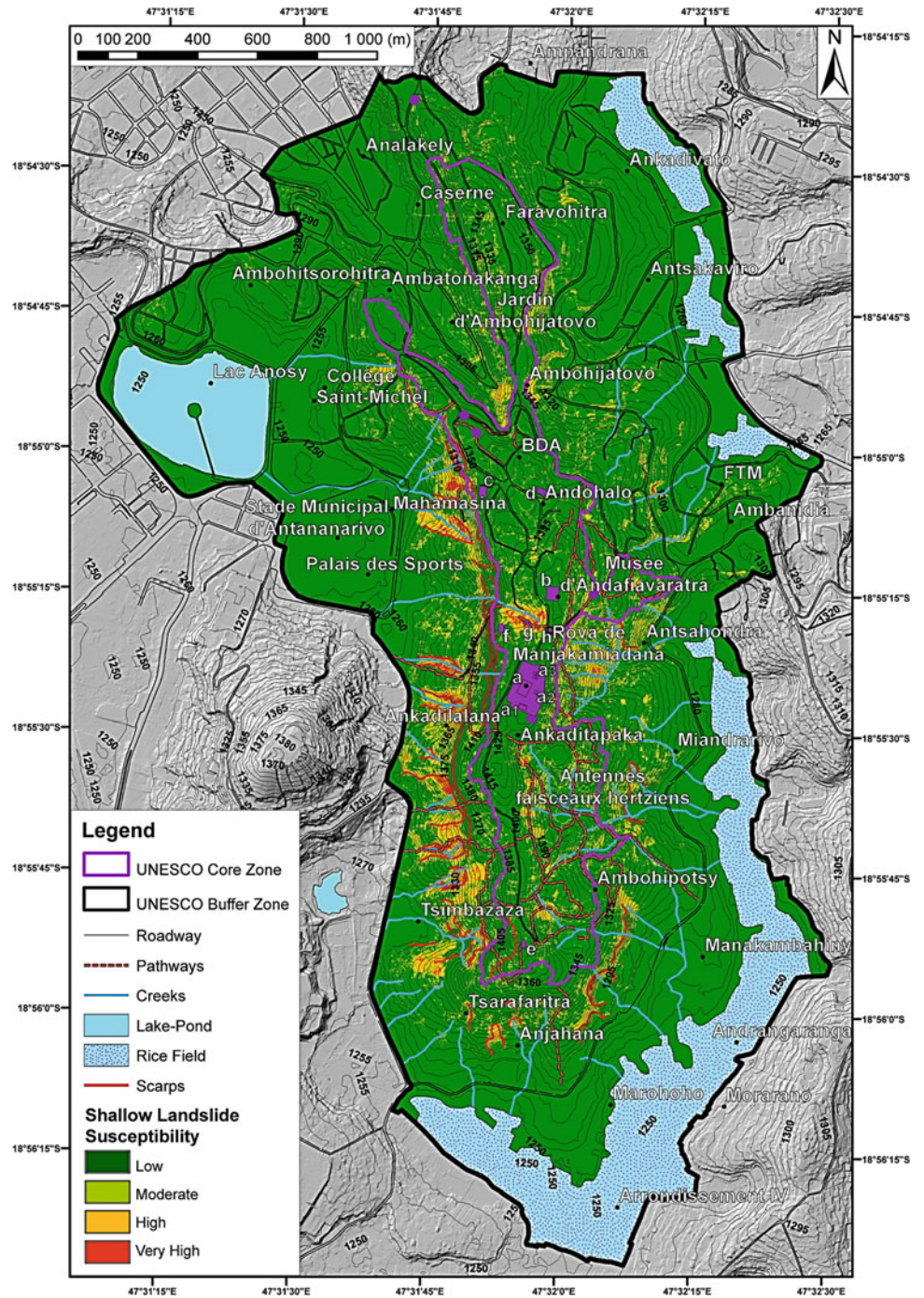


to a longer time interval (Frodella et al. 2022). This suggests that longer rain events have a lesser influence on triggering landslides. A further analysis of mean rainfall intensity helps to highlight that: (i) the intensity referred to 1-day duration shows quite spread values, while the distribution of intensities for longer durations is more constant; (ii) the rainfall intensity of events with 15- or 30-days duration is sensibly lower than that of shorter events (Frodella et al. 2022). On this basis it is possible to hypothesize that the rain events ranging from 2 to 7 days are probably most to be responsible

for the triggering of landslides. The definition of I-D (intensity duration) rainfall thresholds is usually based on hourly rainfall data, but Abraham et al. (2021) explored the possibility of using daily data.

To identify the threshold, the intensity (mm/d) of events with a duration between 2 and 7 days has been considered, based on the outcomes of the previous analyses. For each landslide event, the maximum intensity was extracted, along with its duration and the I-D couples have been plotted as shown in Fig. 5b. Notice in this figure, that some events

Fig. 3 Shallow landslide susceptibility map of the Analamanga Hill (modified after Frodella et al. 2022)



follow a common trend, while other events with a lower intensity, don't show any trend. Due to the paucity of data, a robust statistical analysis was not possible, so the threshold was defined as the lower bound of the most trending events and it is characterized by the equation:

$$I = 121.06D^{-0.3}$$

3.5 Rockmass Instability and Rock Fall Analysis

The 3D kinematic analysis was performed in correspondence of the largest rock outcrops in the study area: the quarry front in the hill south-eastern sector (Manakambahiny-Ankerakely quarter; "Sector 1"), and the rock cliffs along the western slope (from north to south: Mahamasina, Tsimialonjafy, Ambanin'Ampamarinana, Ankadilalana and Tzimbazaza

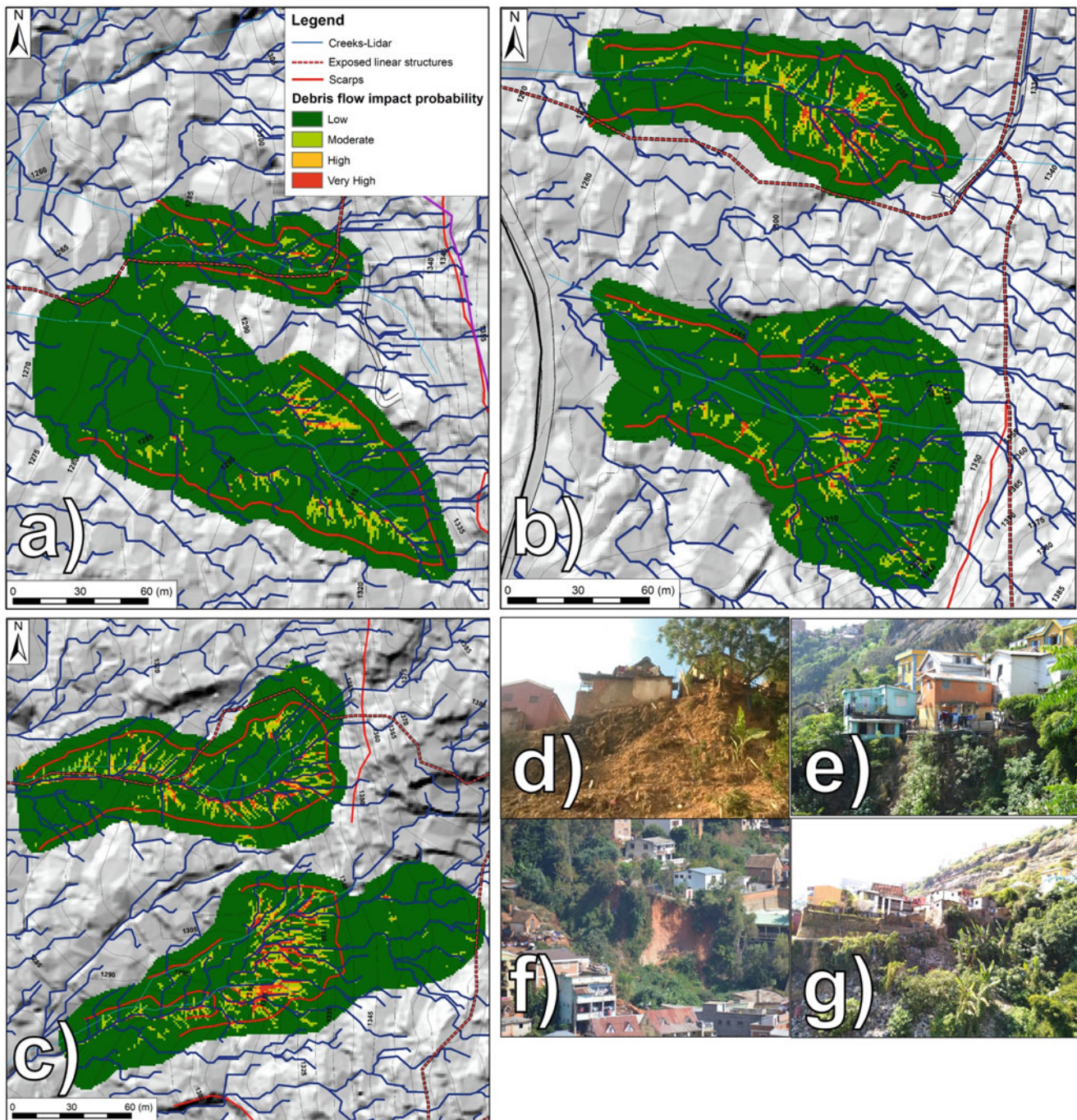


Fig. 4 Debris flow impact assessment map: gullies of Tsimialonjafy (a), Ambanin'Ampamarinana-Ankadilalana (b) and Tsimbazaza (c) quarters. Earth-debris rotational/translational slides involving lateritic

soils and waste-dump deposits causing scarp retreat (a–d) (f), which pose at high risk the housings (modified after Frodella et al. 2022)

quarters; “Sector 2”) (Fig. 6). The maps in Fig. 6a, b show the 3D spatial probability of occurrence (expressed in GKI %; Frodella et al. 2021a, b) for the combined abovementioned instability mechanisms, with colors ranging from green representing stable areas to yellow (low GKI) and red (GKI 26%). The 2D kinematic analysis shows that topples are the most relevant detected instability mechanisms in the field are

(Fig. 6c, d), followed by wedge (Fig. 6e, f) and plane failures (Fig. 6g–h). Quarry fronts in the central-southern area are the most unstable sectors, while in western slope rock cliffs the most unstable sectors are homogeneously distributed (Fig. 5). These unstable areas (selected considering a value of GKI over the 95th percentile of its distribution curve) are used as sources for the rock fall trajectories together with the source

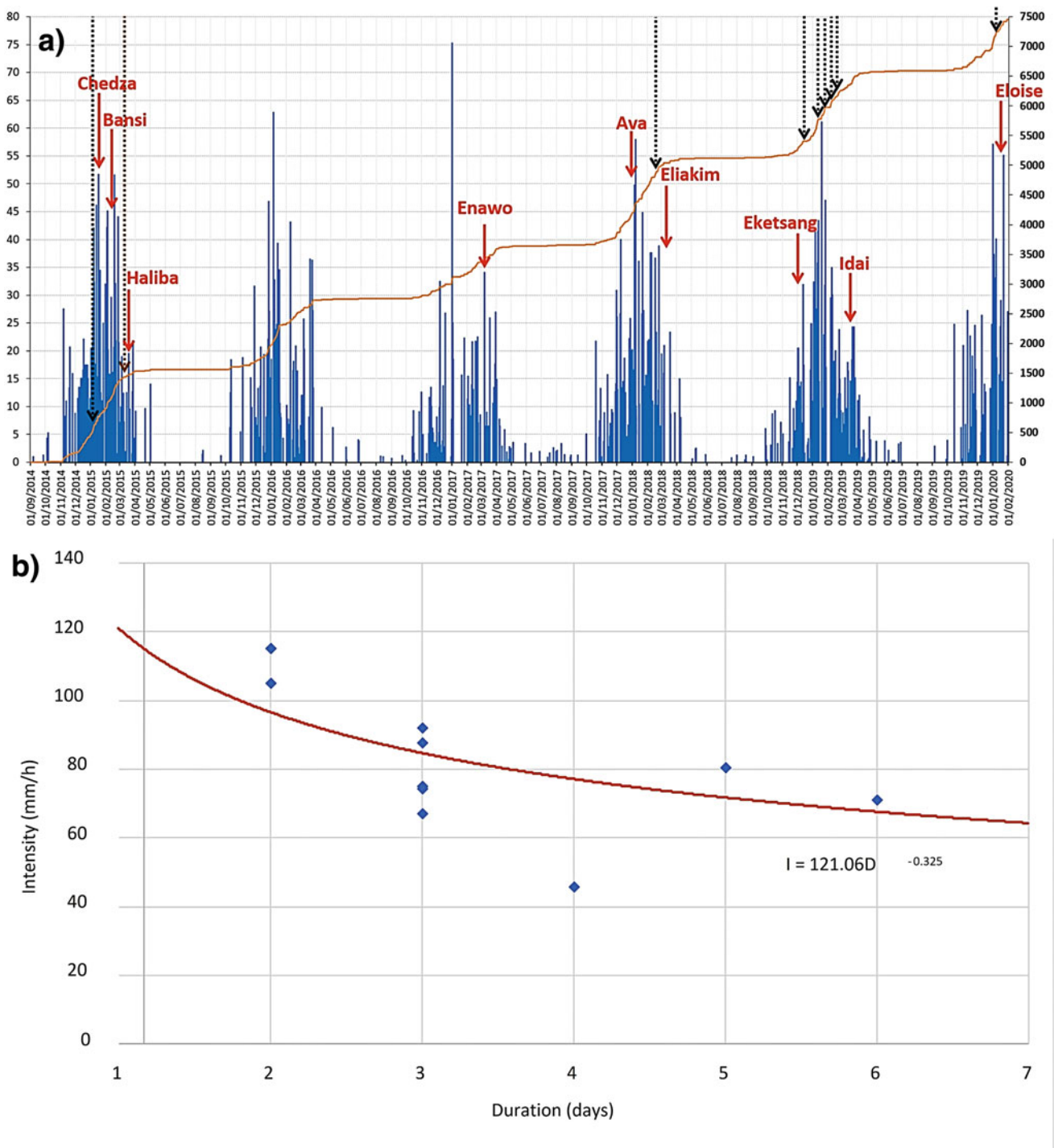


Fig. 5 Comparison between Rainfall data from September 2014 to January 2020 (Daily and cumulated data from Climate Engine, 2015), the recorded landslide events (dashed black arrows), and the recorded Cyclones (red arrows), reported in Frodella et al. 2021a, b (a) (the Dashed brown arrow represents the Winter 2015 landslide event). Intensity—Duration threshold for the study area

areas reported by BNGRC (2015, 2019) and slopes exceeding a steepness of 70°. A new methodology was implemented in a cloud compare (GDM 2015) environment by interpolating on these areas source contour lines at a selected distance based the operator’s judgement; the code selected

the potential block sources along these lines. The trajectories of blocks show that large part of both Sectors 1 and 2 are affected by run-out of rock blocks (Fig. 7a, c, e). The rock fall analysis was calibrated using the outcomes of the field surveys, which allowed the recognition of how the rock cliffs

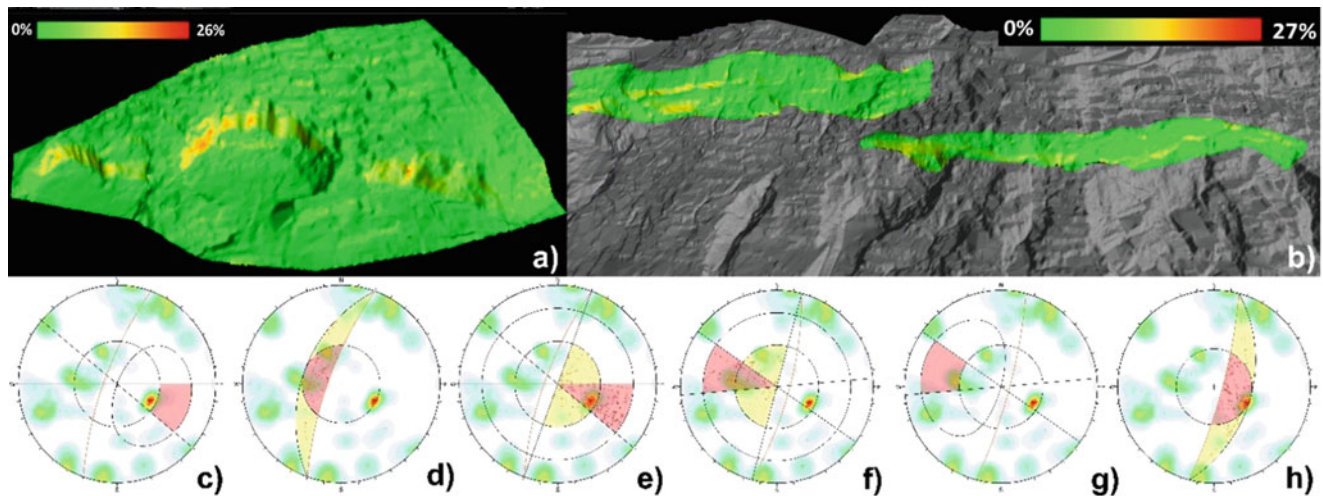


Fig. 6 3D GKI maps of sector 1 (a) and sector 2 (b). 2D kinematic analysis for toppling: sector 1 (c), sector 2 (d); wedge failure: sector 1 (e), sector 2 (f); planar sliding: sector 1 (g); sector 2 (h) (modified after Frodella et al. 2021b)

are frequently affected by blocks of various size, from decametric to plurimetric (Fig. 7d–g).

4 Discussion

Rainfall-induced landslides are a common threat to the communities living on hillslopes in Antananarivo.

The rapid urban development and the lack of a proper urban planning has caused several environmental problems such as intense slash and burn deforestation, illegal quarrying, unauthorized slope cutting and terracing for the construction of hovels, garbage dumping, lacking a proper sewer and drainage systems, narrowing, culverting and the swamping of the creeks (Ciampalini et al. 2019). This anthropogenic pressure does not consider the fragile geological and geomorphological context of the Analamanga Hill. Consequently, the urban area, in particular the slopes and footslopes are prone to landslide phenomena. This instability is especially evident during the frequent heavy cyclonic rainfall, as testified by the winter 2015 and the 2018–2019 landslide events (Frodella et al. 2021a, b). In this framework, the expected future increase of extreme meteorological events can only exacerbate landslide susceptibility.

The shallow landslides connected with the 2015 event slightly affected the UNESCO Core Zone (except for its southern area) along the pathway connecting the Rova palace with Ambohipotsy Cathedral (Figs. 3, 4, and 7). The cultural heritage buildings are not in landslide-prone areas, except for the Trano-Gasy Houses, which are built in an unstable area on the top of the western slope, between the Rova and Andafiavaratra Palace. The most exposed linear structures are the tracks running on both mid-slopes in the central southern sector of the Analamanga Hill. Within the UNESCO

Buffer zone, the most exposed areas are the crude dwellings/hovels of the Middle City area and the mid-slope pathways, particularly the foot of the western hillslope (Tsimialonjafy-Ambanin'Ampamarinana-Ankadilalana-Tzimbazaza quarters) where shallow debris rotational/translational slides develop. Here, earth-debris rotational/translational slides involving residual soil were identified along the slopes of the main creek channels that deeply undercut the slope toe at the foot of the western hillside (Fig. 4). In this area, intense linear creek erosion of the soft lateritic soil cover creates large gullies that are rapidly expanding, damaging road pavement and buildings. The middle southern eastern slope is less prone to shallow landslides, except for an area located in the creek basin east of the Rova. The slope north hill sector shows a general stability due to the widespread urban cover and the low steepness of the gentle slope, while the southern sector shows some prone areas at the top of the abandoned quarry niches. Rock falls severely affect Sector 1 (the western footslope) and Sector 2 (southeastern slope) (Fig. 6). The slope north hill sector shows a general stability due to the widespread urban cover and the lower slope angles, except for the area around the tunnel, in the Ambohijatovo quarter.

Following intense rainfall events, shallow earth-debris rotational/translational slides develop from the slope of gullies and headcut apexes and can evolve into earth debris flows confined to channels within the hydrographic network. These phenomena involve the lateritic soils, as well as the anthropogenic waste deposits (often the gullies are used as dumps), enhancing gully headcut erosion and scarps retreat. Slope instability is more likely to occur in the gullies of the central and southern hill sector (Ankadilalana-Tzimbazaza quarters), and not in the High City's cultural heritage areas. Structures most impacted are the hovels built along the scarps and the pathways connecting with the Low City. An

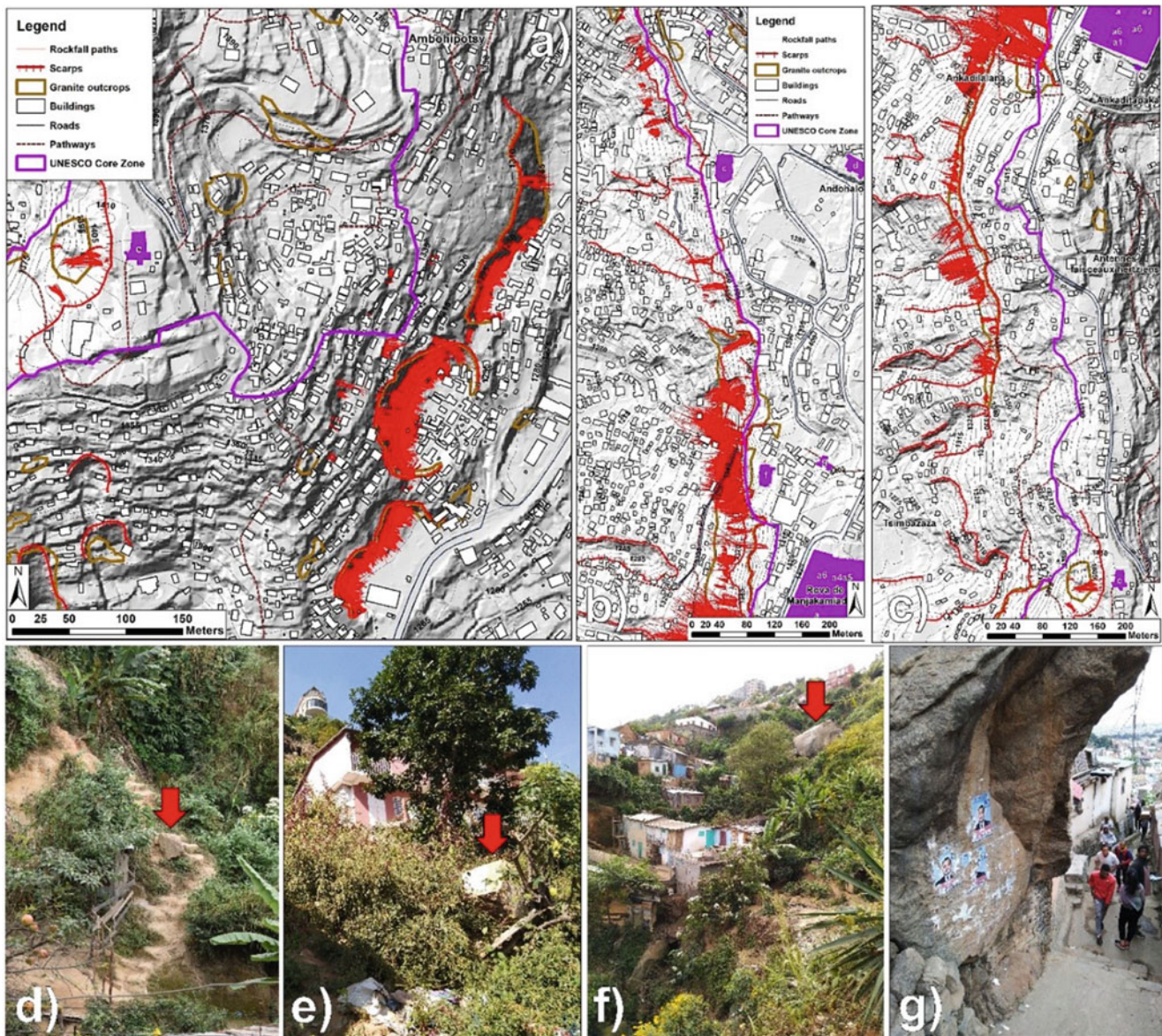


Fig. 7 Rock fall runout simulations. Sector 1: rock blocks trajectories in the analysed area (a); rock fall probability of occurrence (black lines represent the rockfall paths b). Sector 2: rock blocks trajectories in the North (c) and South sectors (e) and corresponding maps of rock fall

probability of occurrence (black lines represent the rockfall paths: North sector (d), South sector (f). Recent and ancient rock block deposits on the western footslopes of decametric (d), metric (e) and plurimetric sizes (f, g)

assessment of rockmass instability associated with the fractured granite cliff corresponding to the abandoned quarries on the western slope and in the south-eastern hill sector. Simulations show that these areas can be sources of rockfall hazardous that may impact on the populated area of the Middle town with poor housings standards.

The landslide maps obtained can be used not only for hazard zoning but also for prioritizing landslide mitigation. Such measures include slope reprofiling, bioengineering methods using local material, wood barriers and check dams, bio-mats and grids to enhance vegetation regrowth in correspondence of the soi bare sectors, creek filtering dams,

nets, and fences for the rockfall/slides. Even if some results are based on very simple approaches and with a certain degree of uncertainty, this work can represent a starting point to create a structured activity aimed to the risk reduction of the area. This activity should start with the creation of a completer and more detailed landslide inventory, where the triggering day, characteristics, dimension of the landslides is defined. The landslide inventory can be used to produce a more accurate and detailed landslide hazard assessment, which, in turn, will result in more precise intervention for landslide risk reduction. For the near future, the Disaster Risk Management activities in Antananarivo should also focus on

the installation of an automated weather station and sensor network to collect accurate rainfall data and implement an Early Warning System. Risk assessment and spatial planning activities should be performed by the municipality of Antananarivo, BNGRDC and technical experts to prevent construction of new buildings in hazardous areas, manage waste materials and avoid the burning of garbage on the hillslopes. To reduce the social vulnerability, these activities should be harmonized with existing on-going projects, while public awareness must be raised to understand the hydrogeological risks. The next phase of activities will focus on sustainable management of the High City within the UNESCO world heritage framework. To this end, our study represents an important contribution for improving the knowledge of landslide processes in Antananarivo, Madagascar, and for other areas with limited data.

5 Conclusions

In this work an integrated landslide hazard assessment was carried out in the High City of Antananarivo, one of the most important cultural heritage sites of Madagascar. As a first step a multitemporal slope scale landslide inventory spanning from 2015 to 2020 was collected by combining field surveys campaigns, interviews with local people and analysing remote sensing data (High-resolution DTM and satellite orthophotos). To assess the hazard of the different identified instability phenomena a shallow landslide susceptibility was carried out using the Random Forest model, while the GPP and IS GeoMassi codes were adopted to perform debris flow-rock fall simulations.

The analysis undertaken shows that most of the mapped areas are affected by moderate to very high landslide susceptibility. Areas characterized by the higher susceptibility are in the Middle Town quarters, particularly at the foot of the central sector of the western hillslope (from north to south: Mahamasina, Ankadilalana, Tzimbazaza quarters). Here shallow debris rotational/translational slides mainly involve eluvial-colluvial and lateritic deposits, while rockfalls originate from the granite cliffs. The densely packed shacks and hovels of the Middle City are particularly prone to rockfalls at the base of steep rocky cliffs. At the western footslope, intense linear creek erosion of the soft lateritic soil cover creates large gullies, which are rapidly expanding. The eastern slope is less prone to shallow landslides, except for the middle-southern sector, especially in two creek basins. The first is located east of the Rova in the Manjakamiadana quarter, while the second is located east of the Ambohipotsy quarter. The southern sector shows unstable areas in proximity to abandoned quarry slope cuts in the Anjahana-Ambohipotsy quarters. Fortunately for the cultural heritage assets of the High City, most of them are not located in

shallow landslide-prone areas. Exceptions are the Trano-Gasy Houses, located on an unstable area at the top of the western slope between the Rova and Andafiavaratra Palace. The most exposed linear structures are tracks running on both mid-slopes in the central-southern sector of the Analamanga Hill.

A preliminary analysis on the rainfall-induced landslide frequency shows that the main landslide events occur after major Cyclones during periods of intense precipitations. Rain events ranging in duration from 2 to 7 days are most probably responsible for the triggering of landslides. Furthermore, we define an intensity (I)-duration (D) rainfall threshold for landslide triggers. Thematic-hazard maps produced as part of our study represent a first step for land-use planning by institutions and actors involved in developing a robust geo-hydrological risk reduction strategy for protection and conservation in the High City.

Acknowledgments This work was carried out in the framework of the activities of the UNESCO Chair on Prevention and Sustainable Management of Geo-Hydrological Hazards of the University of Florence, and, of the IPL-ICL (International Consortium on Landslides) Project n° 260: "Landslide Risk assessment in the High City of Antananarivo". The authors would like to thank Paris Region Expertise Madagascar for giving the logistic support, providing the topographic data, DEMs, and satellite images.

References

- Abraham MT, Satyam N, Rosi A, Pradhan B, Segoni S (2021) Usage of antecedent soil moisture for improving the performance of rainfall thresholds for landslide early warning. *Catena* 200:105147
- Andriamamonjisoa SN, Hubert-Ferrari A (2019) Combining geology, geomorphology and geotechnical data for a safer urban extension: application to the Antananarivo capital city (Madagascar). *J Afr Earth Sci* 151:417–437
- BNGRC - Bureau National de Gestion des Risques et des Catastrophes (2015) Point de situation zone a de glissements de terrains a Antananarivo. February 2015, Technical report
- BNGRC - Bureau National de Gestion des Risques et des Catastrophes (2019) Point de situation zone a risque de glissements de terrains de Manjakamiadana et ses environs. January 2019, Technical Report
- Breiman L (2001) Random forests. *Machine learning* 45(1):5–32
- Catani F, Lagomarsino D, Segoni S, Tofani V (2013) Landslide susceptibility estimation by random forests technique: sensitivity and scaling issues. *Nat Hazards Earth Syst Sci* 13(11):2815–2831
- Ciampalini A, Frodella W, Margottini C, Casagli N (2019) Rapid assessment of geo-hydrological hazards in Antananarivo (Madagascar) historical Centre for damage prevention. *Geomat Nat Haz Risk* 10(1):1102–1124
- Climate Engine (2021). Available online: <https://clim-engine-development.appspot.com>. Accessed 20 Jan 2021
- Cox R, Zentner DB, Rakotondrazafy AFM, Rasoazanamparany CF (2010) Shakedown in Madagascar: occurrence of lavakas (erosional gullies) associated with seismic activity. *Geology* 38(2):179–182
- Cruden DM, Varnes DJ (1996) Landslides: investigation and mitigation. Chapter 3-Landslide types and processes. Transportation research board special report, vol 247, pp 36–75. Transportation Research Board, ISSN: 0360-859X

- Fell R, Corominas J, Bonnard C, Cascini L, Leroi E, Savage WZ (2008) Guidelines for landslide susceptibility, hazard and risk zoning for land-use planning. *Eng Geol* 102(3–4):99–111
- Frodella W, Spizzichino D, Ciampalini A, Margottini C, Casagli N (2021a) Hydrography and geomorphology of Antananarivo High City (Madagascar). *J Maps* 17(4):215–226
- Frodella W, Elashvili M, Spizzichino D, Gigli G, Nadaraia A, Kirkitadze G, Adikashvili L, Margottini C, Antidze N, Casagli N (2021b) Applying close range non-destructive techniques for the detection of conservation problems in rock-carved cultural heritage sites. *Remote Sens* 13:1040
- Frodella W, Rosi A, Spizzichino D, Nocentini M, Lombardi L, Ciampalini A, Vannocci P, Ramboason N, Claudio MC, Tofani V, Casagli N (2022) Integrated approach for landslide hazard assessment in the High City of Antananarivo, Madagascar (UNESCO tentative site). *Landslides* 19(11):2685–2709
- ICL (2022) IPL-ICL Project n°260: Landslide Risk assessment in the High City of Antananarivo (<https://www.landslides.org/projects/ipl-projects/>)
- Reichenbach P, Rossi M, Malamud BD, Mihir M, Guzzetti F (2018) A review of statistically-based landslide susceptibility models. *Earth-Sci Rev* 180:60–91
- Wichmann V (2017) The gravitational process path (GPP) model (v1.0)—a GIS-based simulation framework for gravitational processes. *Geosci Model Dev* 10(9):3309–3327

Open Access This chapter is licensed under the terms of the Creative Commons Attribution 4.0 International License (<http://creativecommons.org/licenses/by/4.0/>), which permits use, sharing, adaptation, distribution and reproduction in any medium or format, as long as you give appropriate credit to the original author(s) and the source, provide a link to the Creative Commons license and indicate if changes were made.

The images or other third party material in this chapter are included in the chapter's Creative Commons license, unless indicated otherwise in a credit line to the material. If material is not included in the chapter's Creative Commons license and your intended use is not permitted by statutory regulation or exceeds the permitted use, you will need to obtain permission directly from the copyright holder.



Part V

ICL Landslide Teaching Tools



Teaching Tool for LS-Tsunami

Khang Dang, Kyoji Sassa, and Doan Huy Loi

Abstract

Landslide-induced tsunamis pose a significant natural hazard with the potential for devastating impacts on coastal communities. This paper discusses the development and application of the LS-Tsunami simulation code, which utilizes landslide motion data from LS-RAPID to model these tsunamis. The program is compatible with Windows PC and features user-friendly visual interfaces and 3D graphical results, making it easy for beginners to conduct integrated landslide and tsunami simulations. The process involves setting the simulation area, editing topographic data, reading landslide results from LS-RAPID, and configuring calculation conditions. In addition to the descriptive steps provided in this paper, a video tutorial is available to guide users through the process of using the LS-Tsunami simulation code. Notably, LS-Tsunami has been successfully applied to various case studies, including a simple coastal landslide-induced tsunami, the 1972 Unzen landslide-induced tsunami in Japan, and a landslide-induced tsunami-like wave in Vietnam.

Keywords

Landslide simulation · Tsunami simulation · LS-RAPID · LS-tsunami

Supplementary Information: The online version contains supplementary material available at https://doi.org/10.1007/978-3-031-44296-4_22.

K. Dang (✉)
International Consortium on Landslides, Kyoto, Japan
VNU University of Science, Hanoi, Vietnam

K. Sassa
International Consortium on Landslides, Kyoto, Japan

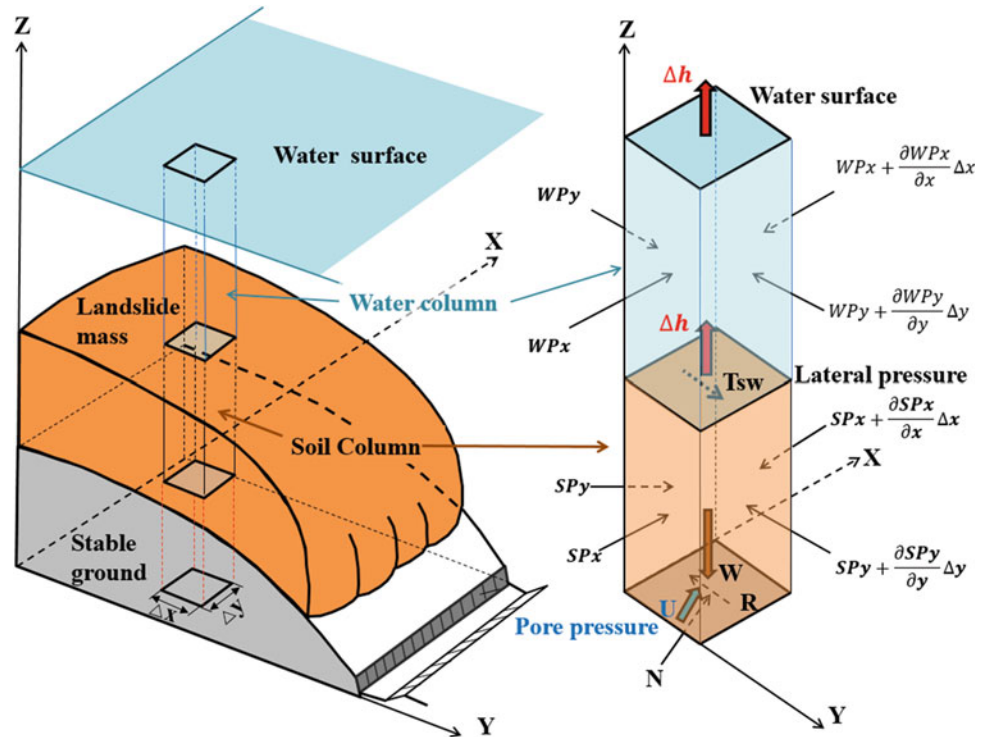
D. H. Loi
International Consortium on Landslides, Kyoto, Japan
Institute of Transport Science and Technology, Hanoi, Vietnam

1 Introduction

Landslide-induced tsunamis are a significant natural hazard caused by different types of landslides. These landslides include coastal and submarine landslides, river landslides, reservoir landslides, lake landslides, and even fjord landslides (Sassa 2023). The 1958 Lituya Bay landslide-induced tsunami in Alaska is a notable example of such events. The massive rockslide created a towering wave exceeding 500 m that devastated the shoreline's trees and buildings. While only two fatalities were reported due to the wave's occurrence in an underpopulated region, the event drew significant attention to the potential catastrophic impact of these tsunamis. Another illustrative example is the 2018 Anak Krakatau landslide-induced tsunami in Indonesia. An underwater landslide caused by the volcanic eruption of Anak Krakatau resulted in a devastating tsunami that caused over 400 fatalities and thousands of injuries in coastal communities. To address such a hazard, LS-Tsunami, a simulation code that uses landslide motion data from LS-RAPID to model landslide-induced tsunamis was developed by Sassa et al. (2016). The model assumes that horizontal forces between the landslide mass and water can be neglected, and the tsunami is triggered solely by the upheaved water mass on the submarine ground due to a moving landslide mass. LS-Tsunami builds on previous studies by Baba et al. (2012), Abe et al. (2008), and Satake (2001) that also used simplified landslide motion to model tsunami generation. The tsunami simulation scheme used in LS-Tsunami is a well-established and widely used model (IOC 1997), ensuring its reliability and accuracy. LS-Tsunami represents a significant advancement in the field of landslide-induced tsunami modeling, offering a valuable tool for predicting and mitigating the impact of these events on coastal communities.

LS-Tsunami model has been applied in many cases of landslide-induced tsunami, such as the world's largest landslide induced-tsunami disaster with 15,153 deaths in Unzen, Nagasaki, Japan in 1972 (Sassa et al. 2016), the hypothetical

Fig. 1 Basic principle of the landslide-induced-tsunami simulation model (Sassa et al. 2016)



Senoumi submarine landslide in Suruga Bay, Japan (Doan et al. 2021), and a case of landslide-induced tsunami-like wave across the Truong river in Quang Nam province, Vietnam (Duc et al. 2020).

2 Basic Principle and Governing Equations

The fundamental concept behind the model for landslide-induced tsunamis utilized in this research is depicted in Fig. 1. The left part of the figure shows the integrated landslide simulation model (LS-RAPID), whereas the right part illustrates the elevated water mass that generates a tsunami wave due to the upward displacement of the interface between the landslide and the water caused by the landslide movement over the sea floor.

When a landslide mass enters or travels across the sea floor, the elevation of the submarine ground surface increases, causing the water mass above the landslide-water interface to rise by an amount, Δh , in a unit time, Δt . The simulation ignored the shear resistance (τ_{sw}) between soil and water at this interface, assuming it to be negligible. The effective stress acting on the surface between the bottom of the soil column and the top of the sea floor was assumed to be unaffected by the increase in water height due to the permeability of the surficial deposit on the sea floor and the fast transmission of water-pressure change from the top to the bottom of the soil column.

The buoyant force by water acts on the soil mass when it enters into water, causing the unit weight of the soil mass (γ_t) to change to the buoyant unit weight, the difference between γ_t and the unit weight of sea water (γ_w). When only a part of the soil mass is submerged, the buoyant force by water only acts on the submerged part. The simulation does not consider any tangential force between soil and water because it is negligible compared to the shear resistance mobilized in the shear surface of large-scale landslides.

In addition to the parameters required for landslide motion simulation using LS-RAPID, the tsunami simulation model LS-Tsunami requires additional parameters, such as the unit weight of sea water and Manning's roughness coefficient for basal resistance between water and ground.

The calculation process for the model of a tsunami caused by a landslide involves two steps. The first step is the simulation of the landslide mass using the "LS-RAPID" integrated landslide simulation model, both on land and on the sea floor. Equations (1)–(4) used in this step are the same as those used in the LS-RAPID model developed by Sassa et al. in 2010. The second step involves simulating the tsunami using the LS-Tsunami model. Equations (5)–(8) used in this step are based on an established tsunami simulation model (IOC 1997). The LS-RAPID model calculates the acceleration (a) of the soil mass (ms) by considering the combined effect of various forces such as self-weight of soil mass, seismic force on the soil column, shear force on the bottom of the soil column, and lateral pressure acting on the sides of the soil

column (Eq. 1). On the other hand, the LS-Tsunami model calculates the acceleration (a) of the water mass (mw) by considering the combined effect of lateral pressure acting on the sides of the water column and Manning's basal shear resistance due to roughness of the ground (Eq. 5). Both sets of Eqs. (1)–(8) are shown below.

2.1 Basic Equations for Motion of Landslide (LS-RAPID)

The explanation for landslide motion equations can be found in the section on Landslide Simulation Model (LS-RAPID) (Sassa and Dang 2018). The fundamental principle behind LS-RAPID involves the relationship between the acceleration (a) of the soil mass (m_s) and the cumulative effect of several forces. These forces include the gravitational force exerted by the soil mass itself, the seismic force acting upon the soil column, the shear force applied to the base of the soil column, and the lateral pressure exerted on the sides of the soil column (Eq. 1).

$$a_{ms} = (W + F_v + F_x + F_y) + \left(\frac{\partial P_x}{\partial x} \Delta x + \frac{\partial P_y}{\partial y} \Delta y \right) + R \quad (1)$$

By expressing Eq. (1) separately in the x and y directions, we derive Eqs. (2) and (3). Additionally, assuming that the total mass of the landslide remains constant during its movement, we obtain Eq. (4).

$$\begin{aligned} & \frac{\partial M}{\partial t} + \frac{\partial}{\partial x}(u_0 M) + \frac{\partial}{\partial y}(v_0 M) \\ & = g h \left\{ \frac{\tan \alpha}{q+1} (1 + K_v) + K_x \cos^2 \alpha \right\} \\ & - (1 + K_v) k g h \frac{\partial h}{\partial x} \\ & - \frac{g}{(q+1)^{1/2}} \cdot \frac{u_0}{(u_0^2 + v_0^2 + w_0^2)^{1/2}} \\ & \times \{h_c(q+1) + (1-r_u) h \tan \varphi_a\} \end{aligned} \quad (2)$$

$$\begin{aligned} & \frac{\partial N}{\partial t} + \frac{\partial}{\partial x}(u_0 N) + \frac{\partial}{\partial y}(v_0 N) \\ & = g h \left\{ \frac{\tan \beta}{q+1} (1 + K_v) + K_y \cos^2 \beta \right\} \\ & - (1 + K_v) k g h \frac{\partial h}{\partial y} \\ & - \frac{g}{(q+1)^{1/2}} \cdot \frac{v_0}{(u_0^2 + v_0^2 + w_0^2)^{1/2}} \\ & \times \{h_c(q+1) + (1-r_u) h \tan \varphi_a\} \end{aligned} \quad (3)$$

$$\frac{\partial h}{\partial t} + \frac{\partial M}{\partial x} + \frac{\partial N}{\partial y} = 0 \quad (4)$$

2.2 Basic Equations for Motion of Water (LS-Tsunami)

$$a_{mw} = \frac{\partial P_x}{\partial x} \Delta x + \frac{\partial P_y}{\partial y} \Delta y + R \text{ (Manning)} \quad (5)$$

where

a: Acceleration of a water column

m_w : Water mass in a column

R(Manning): Manning's basal resistance between water and ground

$\frac{\partial P_x}{\partial x} \Delta x, \frac{\partial P_y}{\partial y} \Delta y$: Lateral pressure acting on the side wall of column in x and y directions

Equation (5) is expressed by Eqs. (6–8).

$$\frac{\partial M}{\partial t} + \frac{\partial}{\partial x}(u_0 M) + \frac{\partial}{\partial y}(v_0 M) = -gh \frac{\partial \eta}{\partial x} - \frac{\tau_x}{\rho} \quad (6)$$

$$\frac{\partial N}{\partial t} + \frac{\partial}{\partial x}(u_0 N) + \frac{\partial}{\partial y}(v_0 N) = -gh \frac{\partial \eta}{\partial y} - \frac{\tau_y}{\rho} \quad (7)$$

$$\frac{\partial h}{\partial t} + \frac{\partial M}{\partial x} + \frac{\partial N}{\partial y} = 0 \quad (8)$$

where

- h : Height of water column within a mesh
 η : Elevation of water surface above sea level datum
 u_0, v_0 : Velocity of a water column in X and Y directions, respectively (velocity distribution in Z direction is neglected, and assumed to be a constant)
 M, N : Discharge of water per unit width in X and Y directions respectively ($M = u_0h, N = v_0h$)
 g : acceleration due to gravity

Manning's basal resistance R (Manning) is expressed as below:

$$\text{X-component: } \frac{\tau_x}{\rho} = \frac{gn^2}{h^{7/3}} M \sqrt{M^2 + N^2}$$

$$\text{Y-component: } \frac{\tau_y}{\rho} = \frac{gn^2}{h^{7/3}} N \sqrt{M^2 + N^2}$$

ρ : Density of sea water,

n : Manning's roughness coefficient.

3 User Manual

The LS-Tsunami software has been created by combining two computational models: LS-RAPID, which simulates landslides, and a tsunami simulation developed by Kyoji Sassa (International Consortium on Landslides) and Hideaki Yanagisawa (Tohoku Gakuin University). This program is designed to work on Windows PCs and includes intuitive visual interfaces and 3D graphical output, making it easy for beginners to run integrated landslide and tsunami simulations. The following steps for conducting a landslide-induced tsunami simulation are provided below and are also demonstrated in the video tutorial entitled "LS-Tsunami Teaching Tool". The starting window of the model is depicted in Fig. 2.

The LS-Tsunami program offers two types of computing simulation (Fig. 3):

- Integrated Landslide and Tsunami Simulation: This involves running a landslide simulation using LS-RAPID, followed by a tsunami simulation using the results from the landslide simulation.
- Tsunami Simulation: This is a regular tsunami computing simulation that uses crust deformation parameters.

The process for simulating a landslide induced tsunami is illustrated in Fig. 4.

3.1 Setting of Simulation Area


To begin a simulation in LS-Tsunami, the first step is to configure the settings for the simulation area as shown in Fig. 5. This can be achieved by clicking on [1:Mesh] - [Simulation area], or by accessing the menu [Edit] - [Setting simulation area and data editing], and inputting the calculation area. The setting procedure for LS-Tsunami is similar to that of LS-RAPID (Ajmera et al. 2023).

3.2 Editing Topographic Data

To input and edit topographic data in LS-Tsunami, users can access the "Editing of mesh" option by clicking on the "Mesh" tab located under the "Flow" menu (Fig. 6). This feature allows users to make necessary modifications to the topographic data and is an essential step in preparing the simulation for accurate and reliable results.

To generate meshed data values for elevation data that is not in mesh format, users can utilize the [Transfer control point data to mesh data] function in LS-Tsunami (Fig. 7). This feature is useful for preparing topographic data for simulation in LS-Tsunami. The process for setting up topographic data in LS-Tsunami is similar to that of LS-RAPID, and interested users can refer to chapter "Landslide Susceptibility Zonation Using GIS-based Frequency Ratio Approach in the Kulon Progo Mountains Area, Indonesia" of the LS-RAPID manual (Ajmera et al. 2023) for further guidance.

3.3 Reading of a Landslide Result (LS-RAPID Data File)

To combine topographic data for landslide and tsunami simulations in LS-Tsunami, users can access the "Select landslide result" option by navigating to the "Calculation condition" tab under the "Flow" menu and selecting [2: Calculation condition]. Clicking on the symbol  in the dialogue box to display how to merge the two data sets (Fig. 8).

After clicking on the folder icon to open the LS-RAPID data file, users can access a window that displays the landslide simulation area superimposed onto the tsunami simulation area (Fig. 9). This feature allows users to visualize the potential impact of a landslide on tsunami propagation and assess the accuracy of their simulations.

The next window shows the landslide simulation area on the tsunami simulation area (Fig. 10). There are two methods

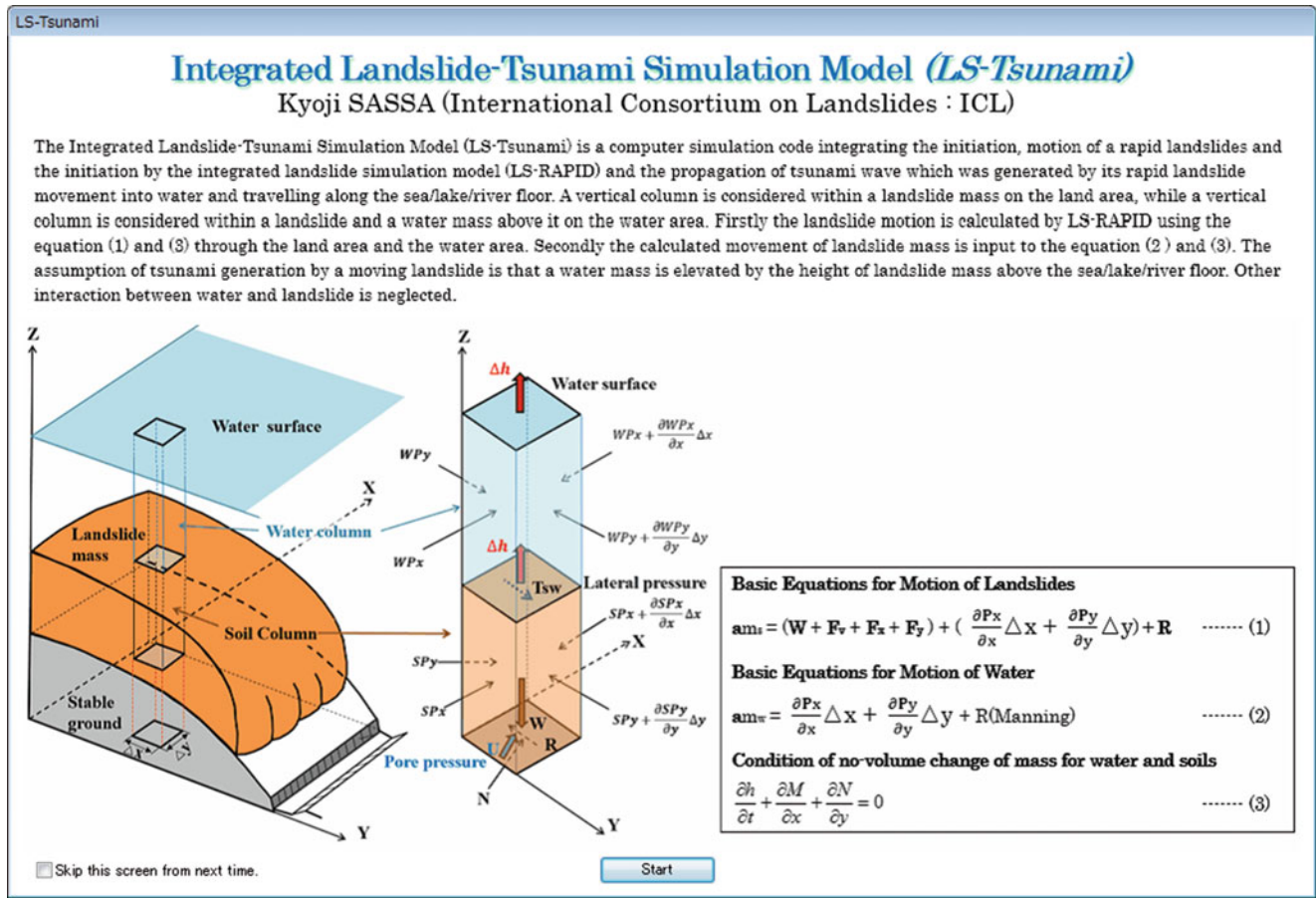



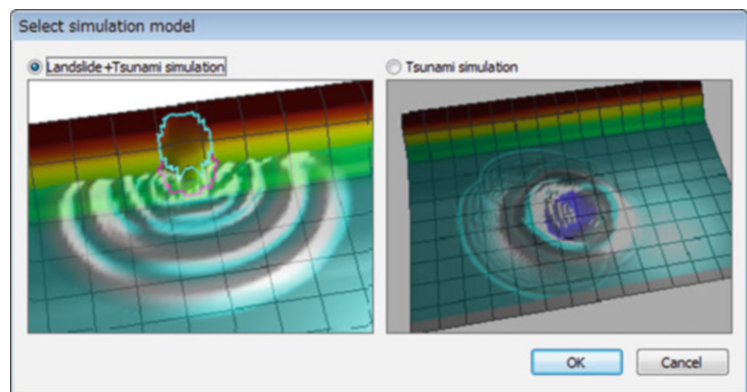
Fig. 2 Starting window of the LS-Tsunami model

to accurately overlap topography in LS-RAPID and LS-TSUNAMI; refer to Fig. 11. Input the X-min and Y-min coordinates of the landslide simulation area’s bottom-left corner into the “Position X” and “Position Y” fields in the tsunami simulation area (Fig. 11a). Emplace the landslide simulation area on the tsunami simulation area by mouse operation (Fig. 11b). Click  to show how to operate this command.

Once the landslide simulation data has been loaded into LS-Tsunami, users can click on the [OK] button to proceed (Fig. 12). This action will open a new dialogue box that displays additional information and options related to the simulation results.

Important note: It is imperative to conduct a landslide simulation using LS-RAPID prior to proceeding with the LS-Tsunami simulation. Therefore, the following three settings must be completed:

Fig. 3 Two types of computer simulation in LS-Tsunami



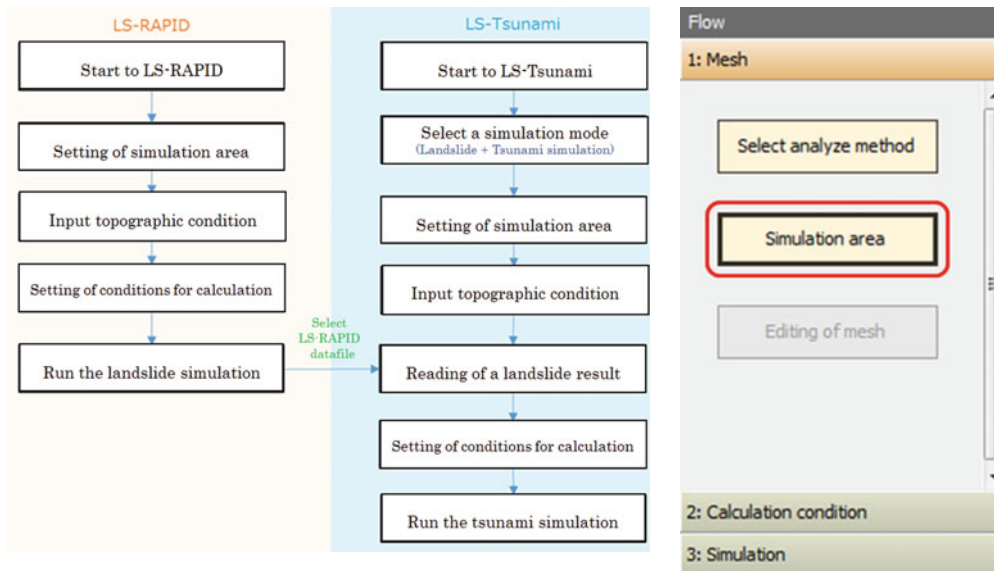


Fig. 4 Flowchart containing steps for integrated landslide and tsunami simulation

1. Enable the [Calculate submergence] option and configure its parameters (Fig. 13).
2. Adjust the [Level of the water surface] to match the conditions of the tsunami simulation (Fig. 14).
3. Enable the [Output the altitude calculation result data] option by checking the corresponding box (Fig. 15).

3.4 Setting of Conditions for Calculation

In order to facilitate calculations, certain conditions must be established. These conditions can be accessed through two avenues: by selecting the “Conditions for calculation” option in the Section “Calculation condition” within the “Flow” panel located on the left side of the program (Fig. 16), or by navigating to the “Conditions for calculation” section within the “Parameters” menu.

To properly set the conditions for calculation in LS-Tsunami, users must consider the following parameters:

- Number of CPU threads: This should be set to match the number of CPU cores available on the user’s PC. It is important to note that using all cores for the simulation can impact the performance of other tasks, so users should set this number based on their experience.
- Calculation time: This should be set based on the area of the simulation. Users need to determine the appropriate duration for their specific simulation.

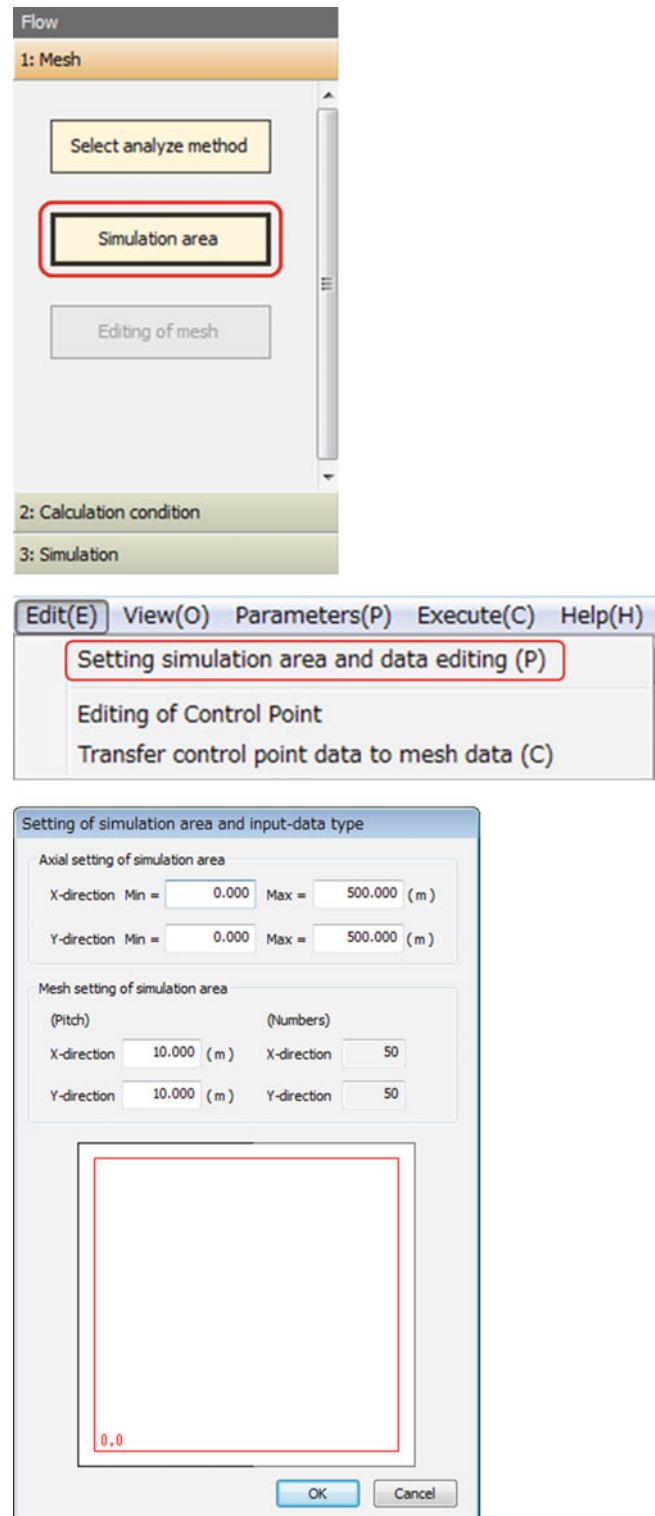


Fig. 5 Screenshots of the Setting of Simulation Area and Input - Data Type Window

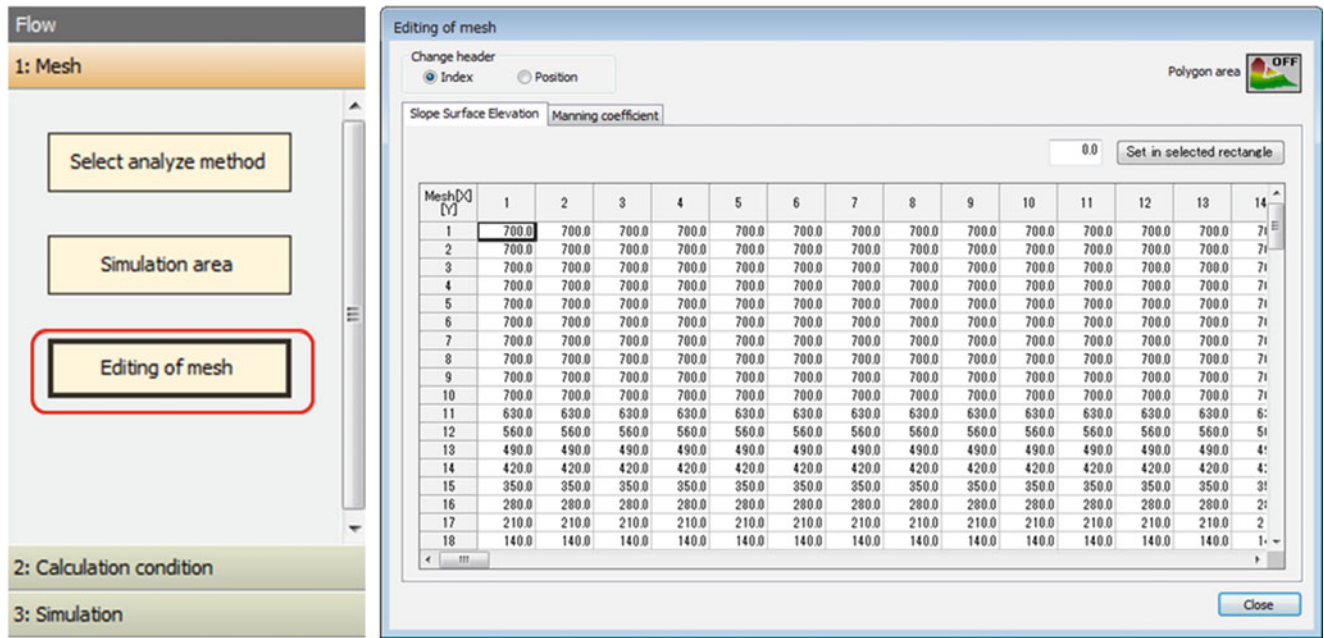
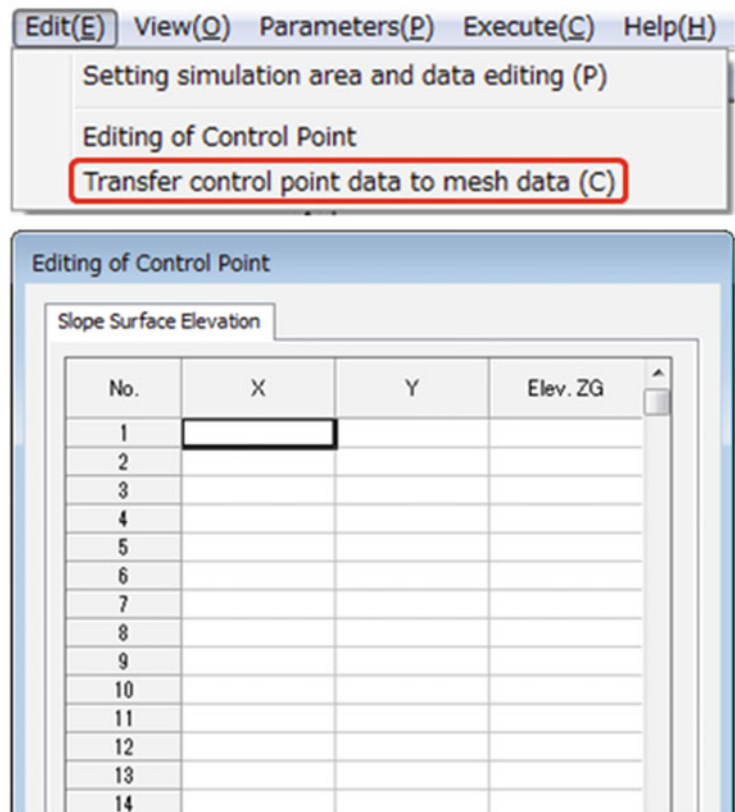


Fig. 6 Screenshots of the Editing of mesh

- Calculation time (per step): This should be set to the time interval for the calculation of LS-RAPID. The number of calculation steps is calculated by dividing the calculation

time by the time for each step. To conduct a stable numerical simulation of a tsunami, it is necessary to satisfy the Courant-Friedrichs-Lewy (CFL) condition.

Fig. 7 Screenshots of the Transfer control point data to mesh data



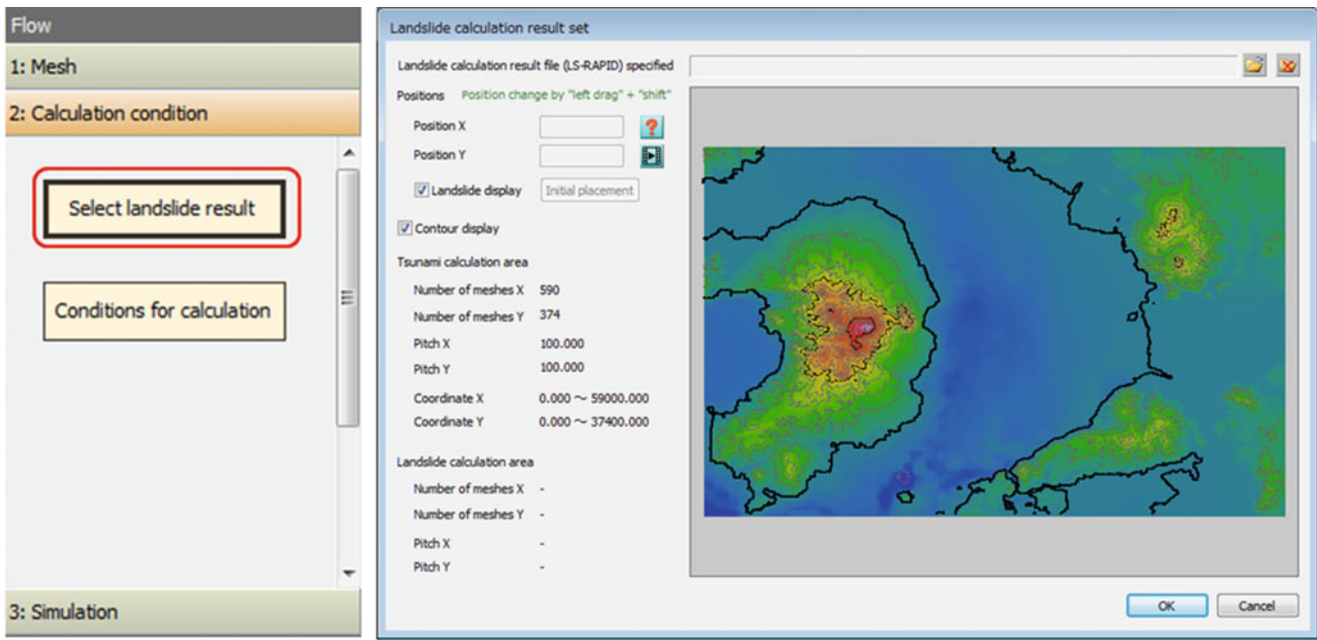


Fig. 8 Screenshots of the “Select landslide result”

$$\frac{\Delta x}{\Delta t} \geq \sqrt{2gh_{max}}$$

where Δt , Δx are temporal and spatial grid sizes, h_{max} is the maximum still water depth in the simulation area.

- Output snapshots: This should be set to the output data interval for each step. Users should adjust this number depending on the duration of their simulation. A value of around 100 is often used.
- Manning coefficient: This should be set to Manning's roughness coefficient. Users can choose to set this number

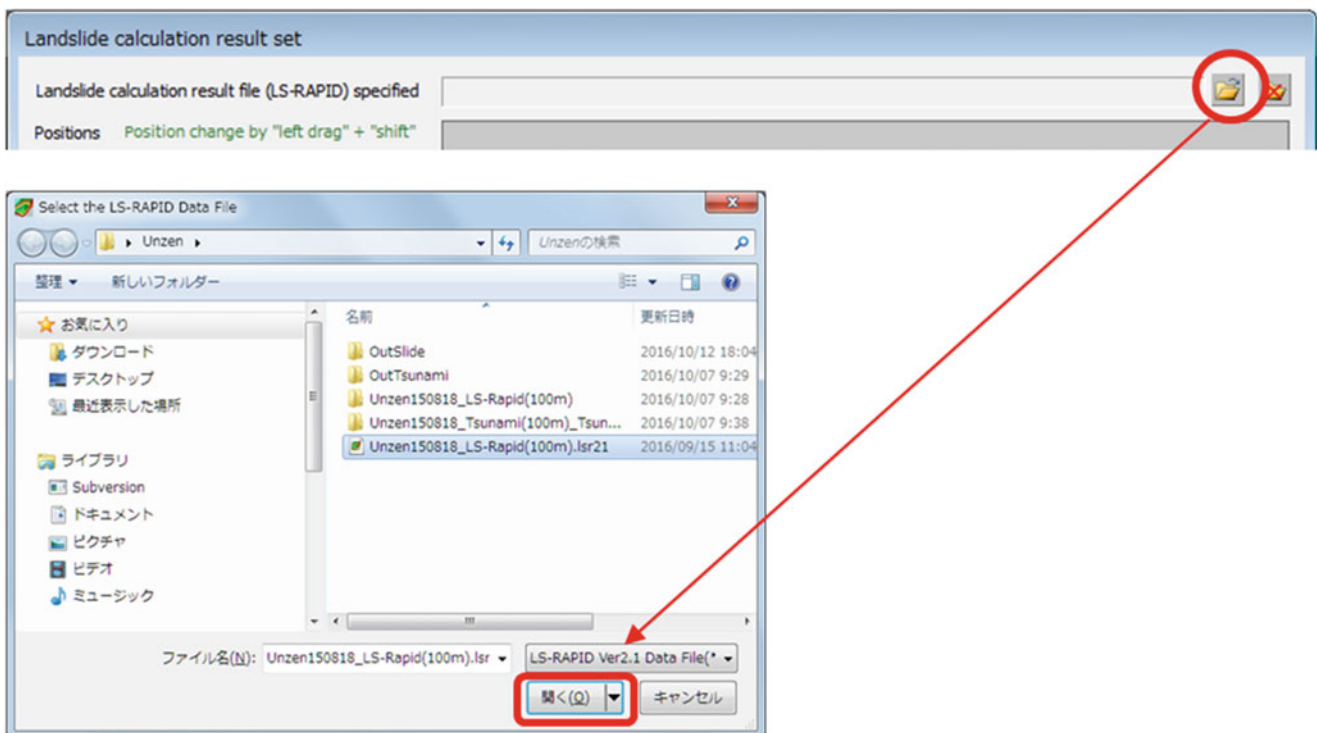


Fig. 9 Screenshots showing the step to open the data file of LS-RAPID

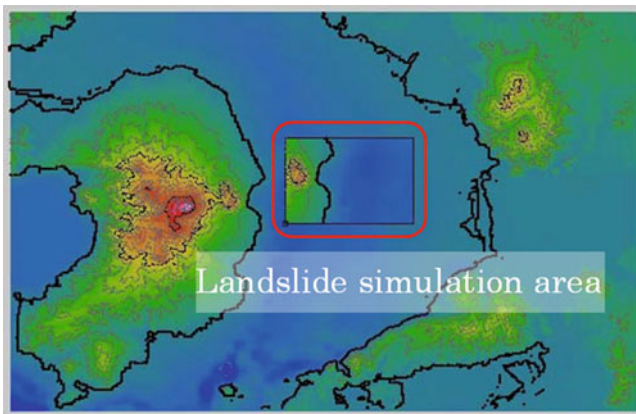


Fig. 10 Screenshots showing the landslide simulation area on the tsunami simulation area

for each mesh datum by selecting the “Use parameters on each mesh datum” option and clicking “Manning coefficient mesh editing” to input the number for each mesh datum in a manner similar to inputting an elevation datum.

- Folder for output tsunami result files: Users should designate a folder for saving the output of the tsunami computing simulation. It is not necessary to change the default folder, but users should ensure that they do not designate a folder in which they have stored important files.
- Boundary conditions: Users should select either “Wide area condition” or “Narrow area condition” based on the characteristics of the simulation area. The wide area mode is effective for areas including deep water and uses the conditions for linear progressive waves. The narrow area mode is effective for areas including shallow and coastal areas and uses the boundary condition of Sommerfeld type. Users should also set “Reflection” or “Open” to the squares based on the boundary position, with Bottom being Y (-) of the coordinate, Top being Y (+), Left being X (-), and Right being X (+).

3.5 Settings for Output and Visualization

To configure the output and visualization settings for simulations, the user can navigate to the “Set calculation output” option either through the “Simulation” drop-down menu or the “Execute” menu (Fig. 17). Once selected, a dialog box of “Output setting” will appear, allowing the user to customize the desired output and visualization settings.

3.6 Start the Simulation

To begin the simulation, click on [3: Simulation] - [Start simulation], or select [Execute] from the menu and then choose [Start simulation] (Fig. 18).

This will bring up the next window and the simulation will start to run (Fig. 19).

If the simulation has finished running properly, you will see a notification that says “Computation Terminated”. At this point, you can close the simulation window.

3.7 Display the Results

To view the visualized results of the simulation, click on the [3: Simulation] - [Result of simulation] flow or go to the menu and select [Execute] - [Display the simulation results]. This will open a window where you can see the results of the simulation (Fig. 20).

4 Application Examples

4.1 Application of the Model to a Simple Coastal Landslide

The initial instance of the landslide-induced tsunami simulation was introduced through a hypothetical scenario involving a fictitious slope, as documented by Sassa et al. (2016). This case study entailed specific dimensions and characteristics for the slope (Fig. 21). The maximum depth reached 313 m, with a maximum length of 1230 m and a maximum width of 1000 m. The total volume of the landslide was calculated to be 170×10^6 cubic meters. The slope configuration encompassed a level crest, inclined at an angle of 35° , with a flat seabed at its base. The peak friction angle (φ_p) was set to be 42° , while the friction angle during motion (φ_m) was set to be 40° . The starting point of the landslide corresponded to the summit of the slope, while the toe of the landslide extended to the water surface. In Fig. 20, the left extremity was positioned 2000 m away from the coastline, while the horizontal distance from the coast to the bottom of the figure spanned 10,000 m.

Figure 22 illustrates the profiles of both the landslide and the ensuing tsunami during their motion, with a water depth of 200 m. Approximately 21 s after the initiation of the simulation, the top of the landslide mass made contact with the sea floor, leading to the generation of the tsunami. By the 26.5-s mark, the landslide mass had started to move along the sea floor, resulting in the formation of a distinct and significant tsunami wave. Notably, the positions of the tsunami head and the landslide head were nearly identical. Around 57.5 s into the simulation, the head of the tsunami began to outpace the head of the landslide. At 139 s, the landslide mass completely moved away from the source area. Subsequently, at 180 s, the tsunami head reached a distance of 10 km from the coastline. The movement of the tsunami wave on the water surface is depicted in the top-left corner of the figure, where the red region represents a tsunami wave higher than

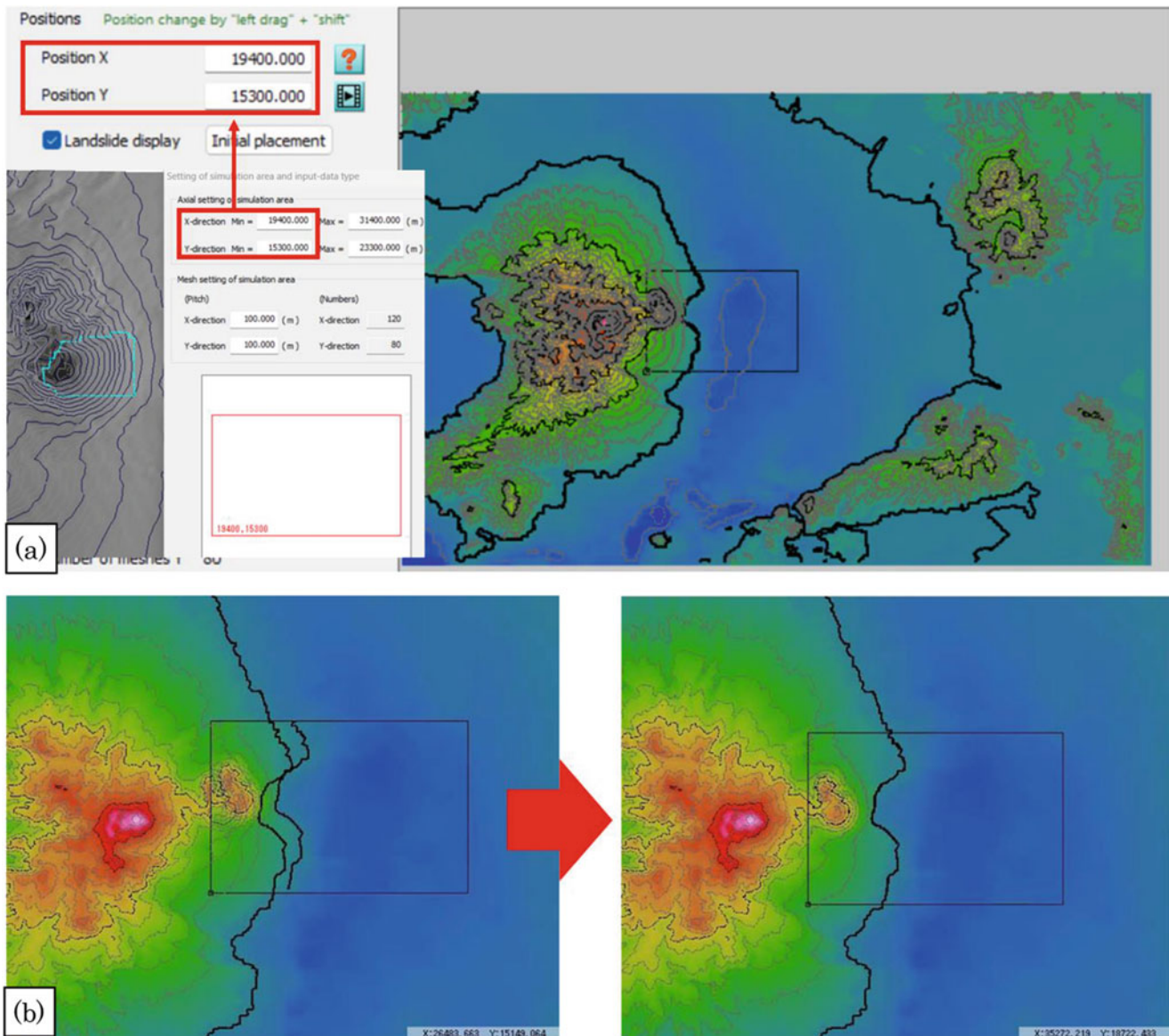


Fig. 11 Screenshots illustrating the process of placing the landslide simulation area onto the tsunami simulation area through (a) inputting the coordinates and (b) mouse operation

the sea level, while the blue region represents a tsunami wave lower than the sea level.

4.2 Application of the Model to a Landslide-Induced Tsunami-Like Wave Across a River

The second application example of the LS-Tsunami software entailed simulating a tsunami-like wave induced by a landslide along a river in Vietnam. Detailed findings and analysis of this study can be found in Duc et al. (2020). On November 5th, 2017, around 4 pm, a heavy rainfall triggered a landslide

on the right bank of Truong River, situated in Tra Giang commune, Bac Tra My District, Quang Nam province, Vietnam (Fig. 23). The landslide rapidly moved and unleashed a tsunami-like wave that resulted in the complete destruction of three houses, partial damage to three other houses, one fatality, and three injuries on the opposite bank. Testimonies from witnesses and on-site evidence indicated that the maximum wave height reached approximately 8.5 m. This unprecedented disaster event captured significant public attention within the region.

Site surveys were conducted to examine the characteristics of the landslide. The slope area prior to the sliding was covered by a forest of *Acacia mangium* Willd. The landslide,

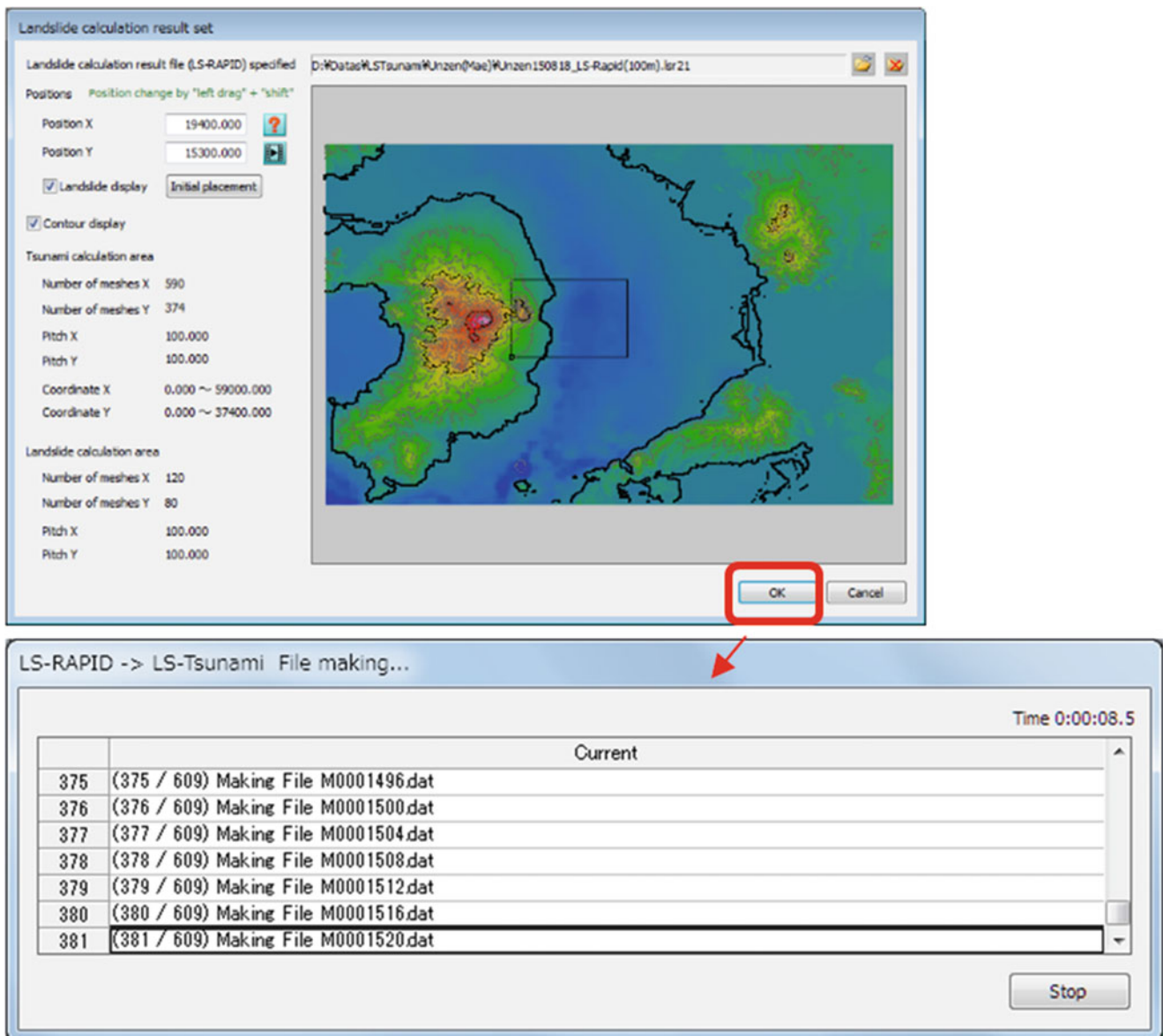


Fig. 12 Screenshots illustrating the process of loading simulation data into LS-Tsunami

with a length of approximately 154.8 m and a width of 64 m, occurred on a slope with a gradient of 35° . The total volume of the landslide was estimated to be about $31,600 \text{ m}^3$ with a maximum depth of around 11 m. The sliding mass failed at an elevation of 140 m a.s.l., traveled down the river course at an elevation of 76 m a.s.l., and continued to move across the river, ultimately depositing at the opposite bank at Km 90 + 000 m on National Highway No. 24C. The landslide occurred on a slope of weathered granite bedrock and was characterized by a rotational type with an observable sliding surface in the head scarp and body. The deposits consisted of weathered and loose materials of granite, granodiorite mixed by conglomerate. The rocks were strongly weathered and

fractured due to the influence of the Truong River tectonic fault. Elevation images after the event derived from UAV photos and geological profiles of the landslide generated from DEM data are presented in Fig. 24.

4.2.1 Landslide Simulation with LS-RAPID Model

To simulate the motion of the Tra Giang landslide and the resulting surge wave, two computer models, LS-RAPID and LS-Tsunami, were used. These models require input of three topography components: ground surface topography before the landslide, topography of sliding surface, and depth distribution of the landslide mass or unstable soil layer. A Digital

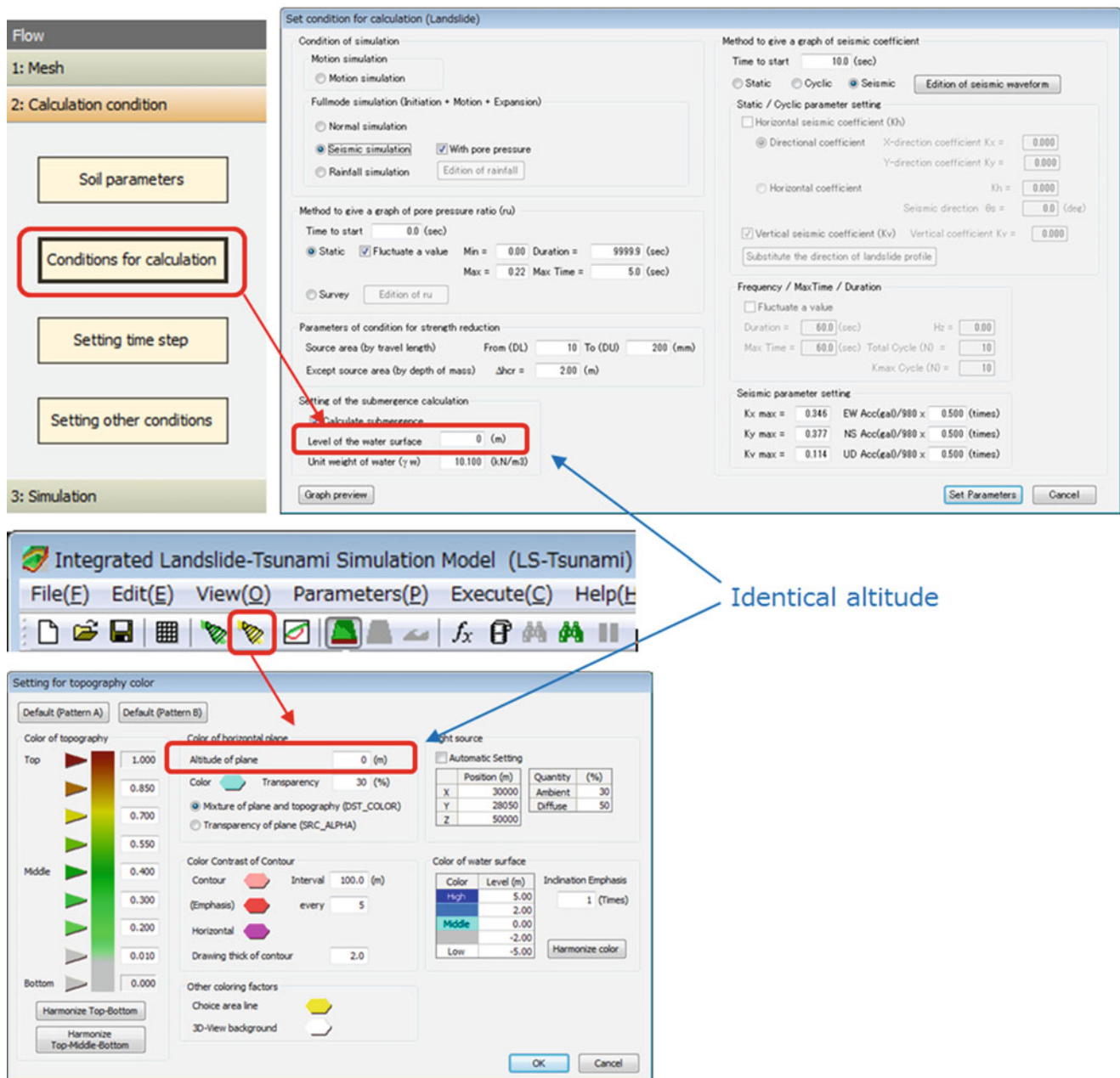


Fig. 14 Screenshots illustrate the steps to adjust the [Level of the water surface]

second figure (Fig. 27b) shows the wave reaching the opposite side at 53.5 s, with a maximum wave height of 3.2 m. The third figure (Fig. 27c) shows the wave moving up to the land, with a maximum height of 5 m at 61.5 s. In this figure, the dark blue color represents waves higher than 5 m above the riverwater level, blue represents waves from 2 m to 5 m, and cyan represents waves from 0 to 2 m. The last figure (Fig. 27d) shows the simulation at 100 s when the wave returned to the river.

4.3 Application to the 1792 Unzen-Mayuyama Megalide-and-Tsunami Disaster

The LS-Tsunami software was employed in the third case study, as documented in the publication by Sassa et al. (2016). The study focused on simulating the 1792 Unzen Mayuyama megalide and the resulting tsunami, which represents the largest landslide-tsunami disaster and the

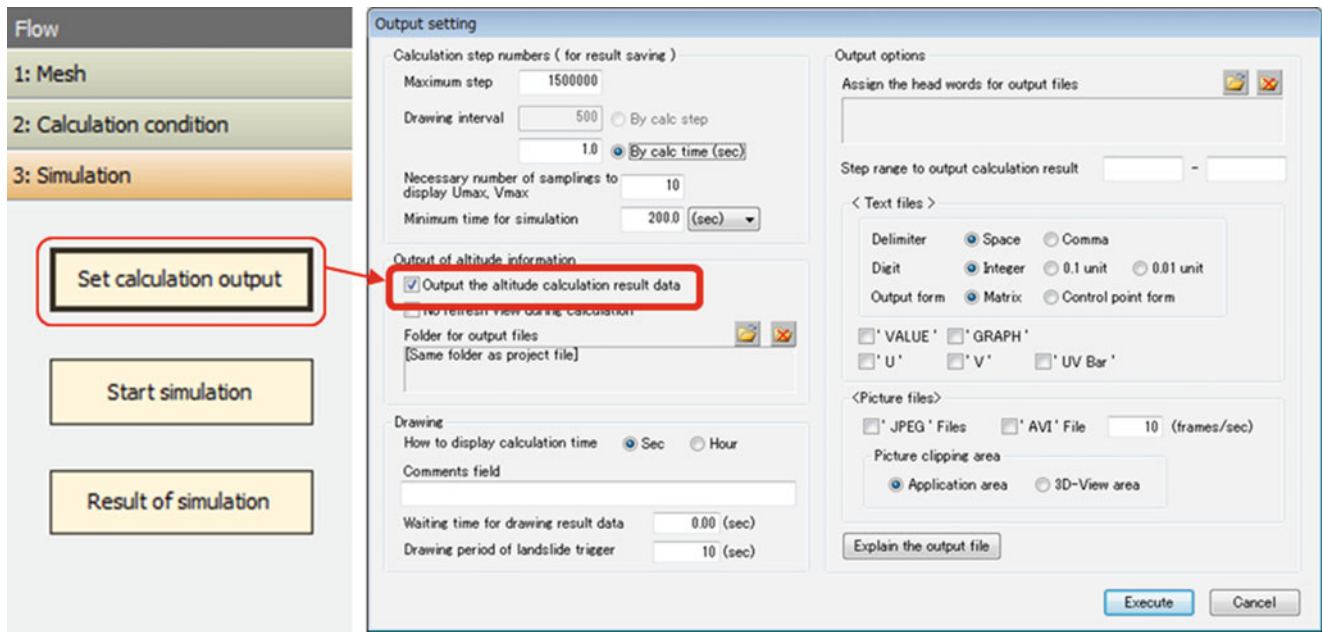


Fig. 15 Screenshots illustrate the steps to enable the [Output the altitude calculation result data] option

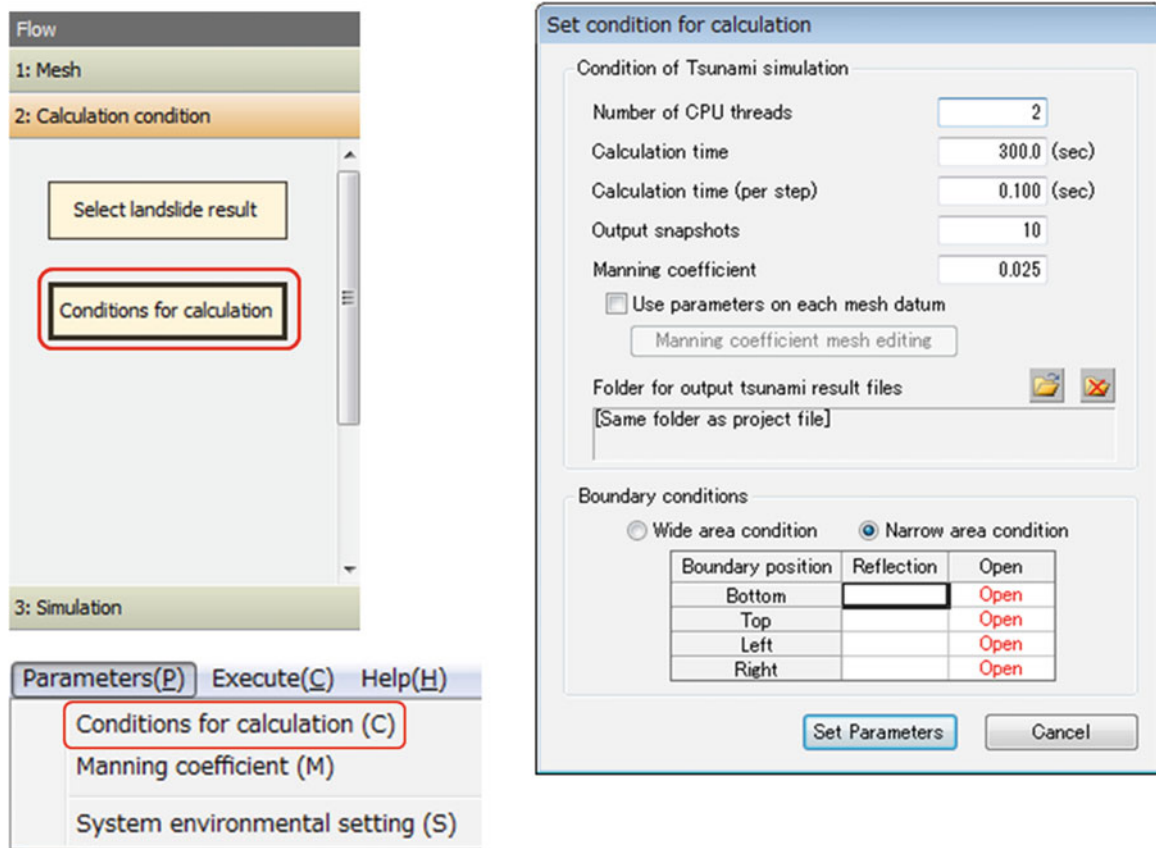


Fig. 16 Screenshots of Setting of conditions for calculation

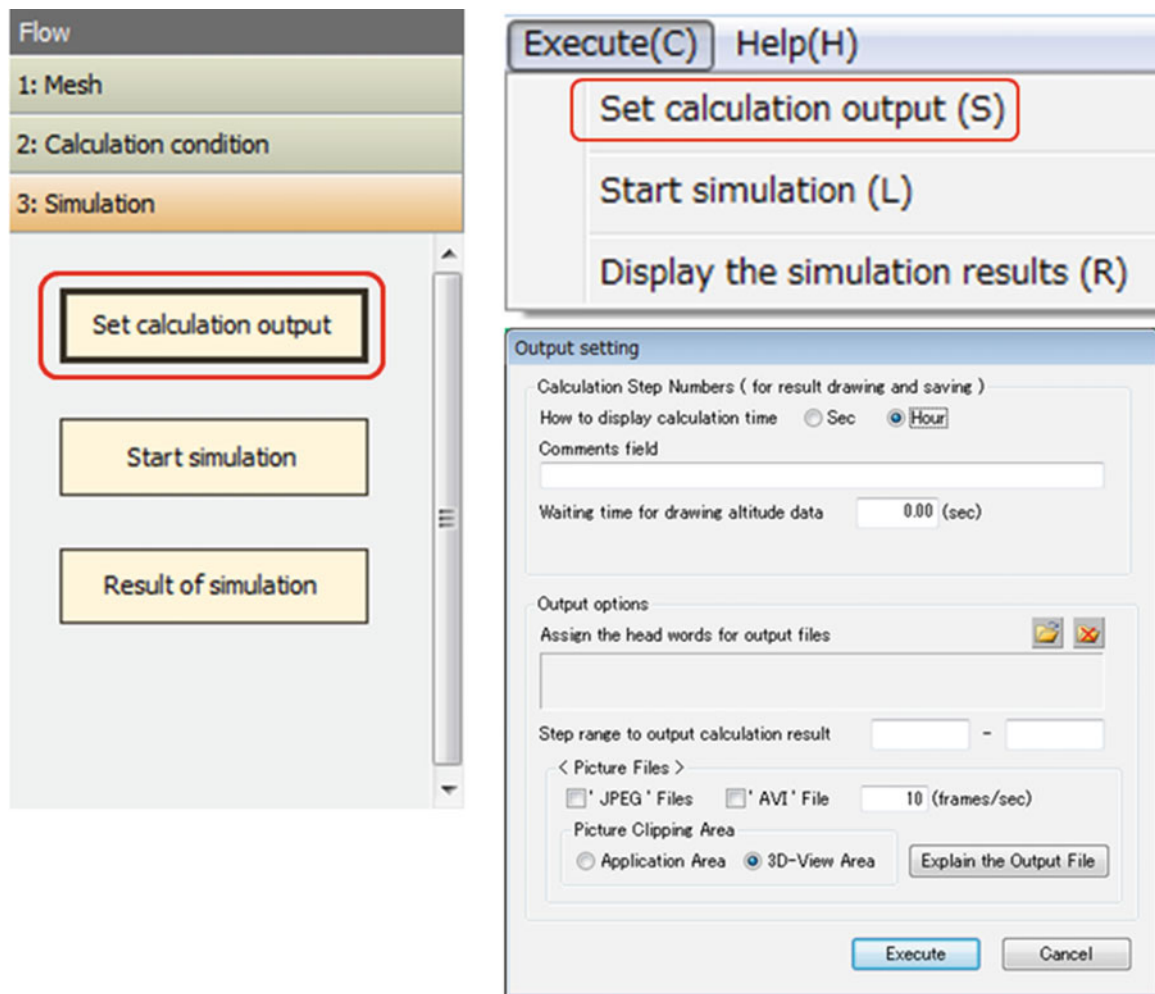


Fig. 17 Screenshots of Settings for output

most significant volcanic calamity in Japan's history. This catastrophic event resulted in the tragic loss of human lives, with a total of 15,153 individuals perishing. The geographical extent of the landslide is illustrated in Fig. 28, showcasing the location of the head scarp, the direction of landslide movement, and the inclusion of several islands formed as a result of the landslide in the sea.

A previous researcher conducted an estimation of the topography prior to the landslide and identified the potential sliding surface based on the current digital map (Unzen Restoration Office of the Ministry of Land, Infrastructure and Transport, Japan 2002, 2003). Figure 29 illustrates the pre-landslide ground surface topography (left) and the sliding surface of the landslide (right) depicted using LS-RAPID.

Various tests on the two samples collected from the site using the undrained loading ring-shear apparatus were conducted to measure and estimate the necessary landslide dynamic parameters (Sassa et al. 2014). For further analysis, landslide dynamic parameters and a seismic earthquake record were input into LS-RAPID to conduct the landslide simulation. The landslide dynamics parameters used in this simulation are presented in Table 2.

The dataset of landslide motion, obtained from LS-RAPID calculations at a temporal resolution of 0.1 s, served as input for LS-Tsunami to initiate the corresponding tsunami event. LS-Tsunami incorporated additional parameters such as the unit weight of seawater and the Manning's roughness

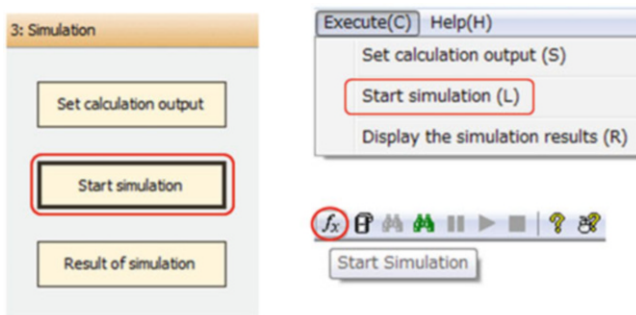


Fig. 18 Screenshots of Start simulation

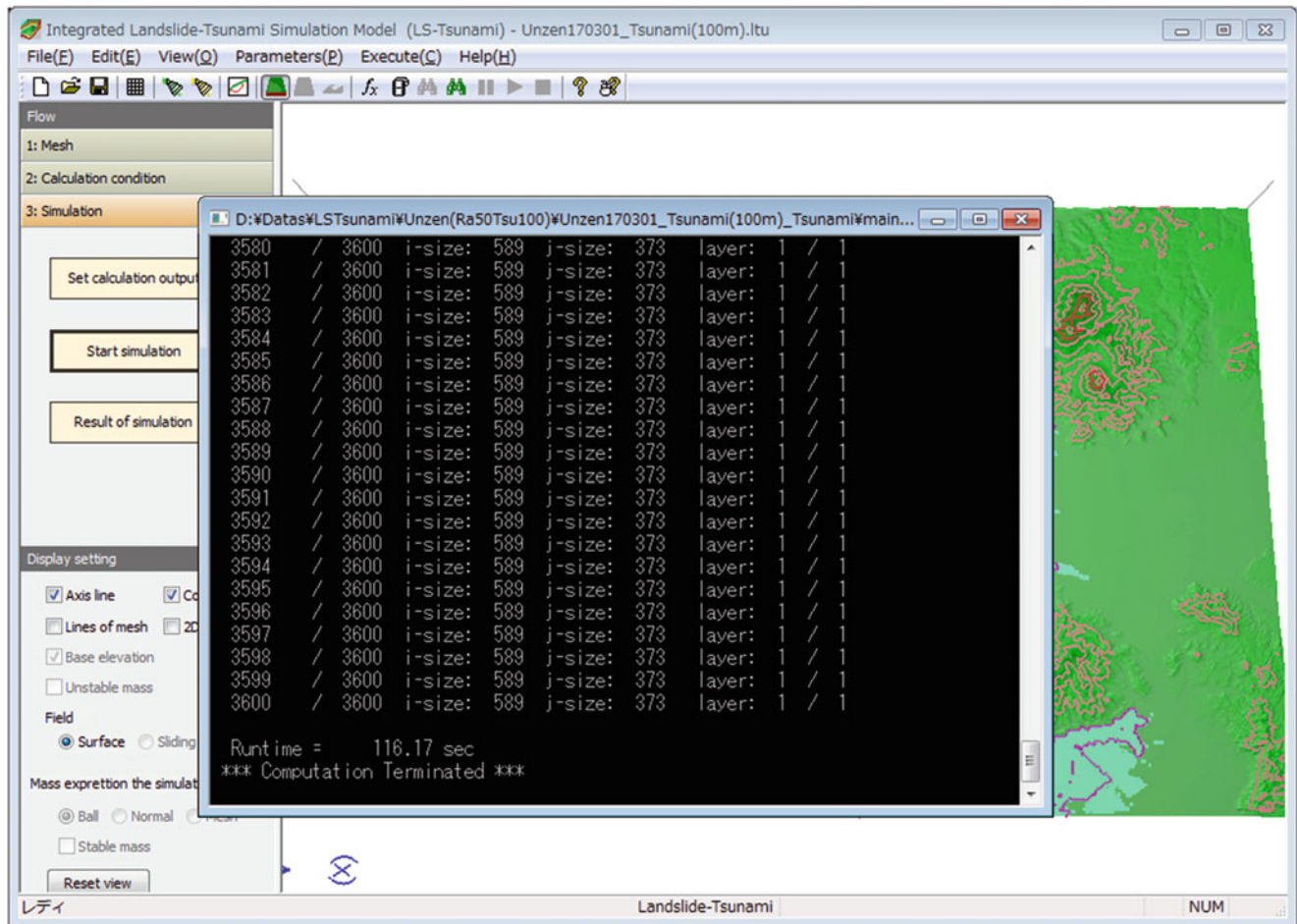


Fig. 19 Screenshots demonstrate the execution of the simulation

coefficient to account for basal resistance within the ocean. Utilizing the input from LS-RAPID, LS-Tsunami conducted calculations to simulate the motion of the resulting tsunami. The simulated tsunami heights were recorded and stored at each mesh point, with intervals of 0.05 s. The findings of the simulated tsunami are depicted in Fig. 30.

5 Conclusions

In conclusion, LS-Tsunami is a powerful software program that combines landslide simulation and tsunami simulation models to provide an integrated approach for predicting and

mitigating the impact of landslide-induced tsunamis. The program offers user-friendly interfaces and 3D graphical output, making it accessible to beginners in the field. By utilizing the LS-RAPID landslide simulation model and incorporating additional parameters for tsunami simulation, LS-Tsunami enables accurate and reliable predictions of tsunami generation and propagation from landslides. It has been successfully applied to various cases, including a simple coastal landslide, a landslide-induced tsunami-like wave across a river in Vietnam, and a major landslide-induced tsunami disaster in Japan. The step-by-step user manual and the video tutorial provided in this paper outline the process of using LS-Tsunami, from configuring the simulation area to

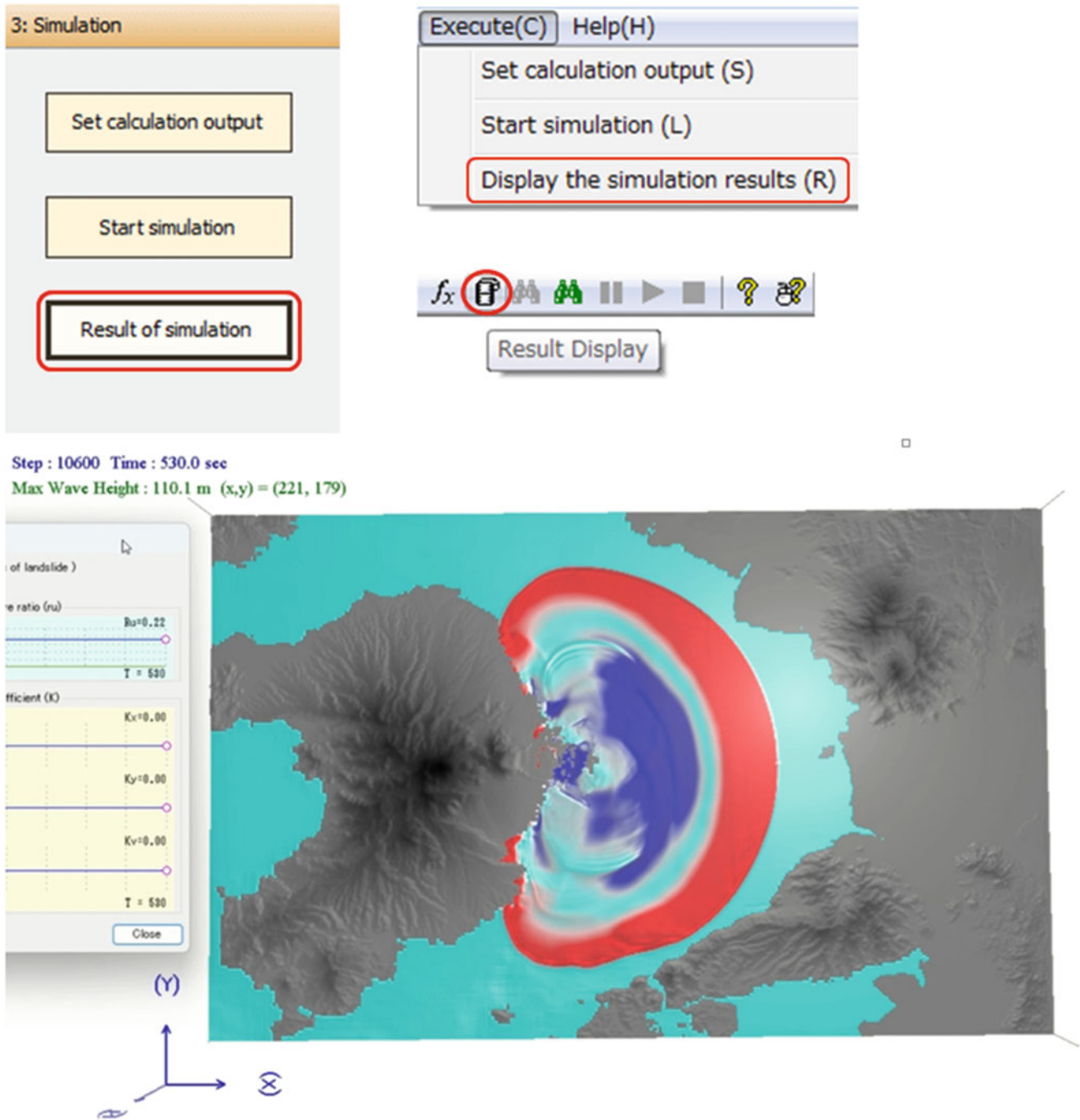


Fig. 20 Screenshot of the simulation results display

setting calculation conditions. With its capabilities and potentials for hazard assessment, disaster mitigation, and risk management in coastal areas, LS-Tsunami serves as a

valuable tool for researchers, engineers, and decision-makers involved in mitigating the impact of landslide-induced tsunamis.

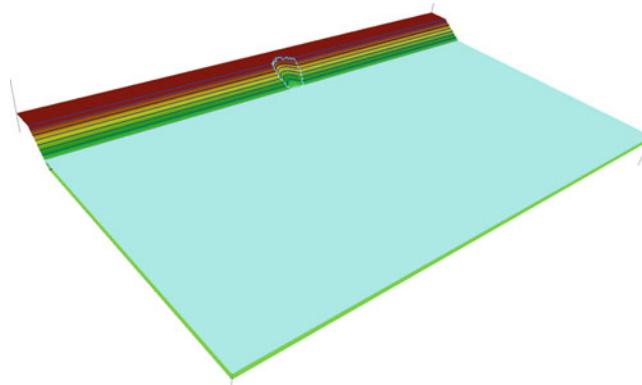
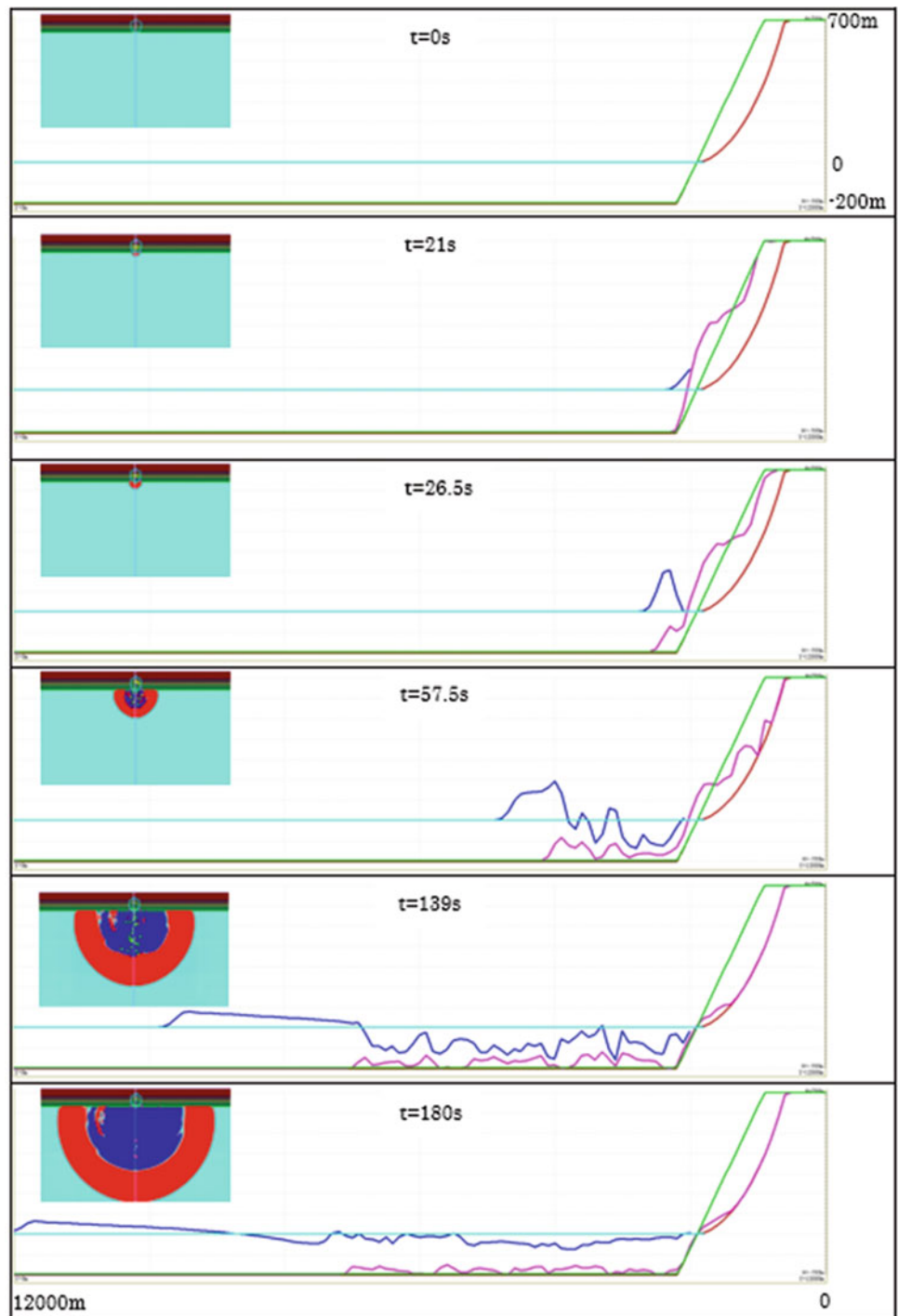


Fig. 21 Design of the simple coastal landslide

Fig. 22 Tsunami and landslide profiles during motion (Sassa et al. 2016)



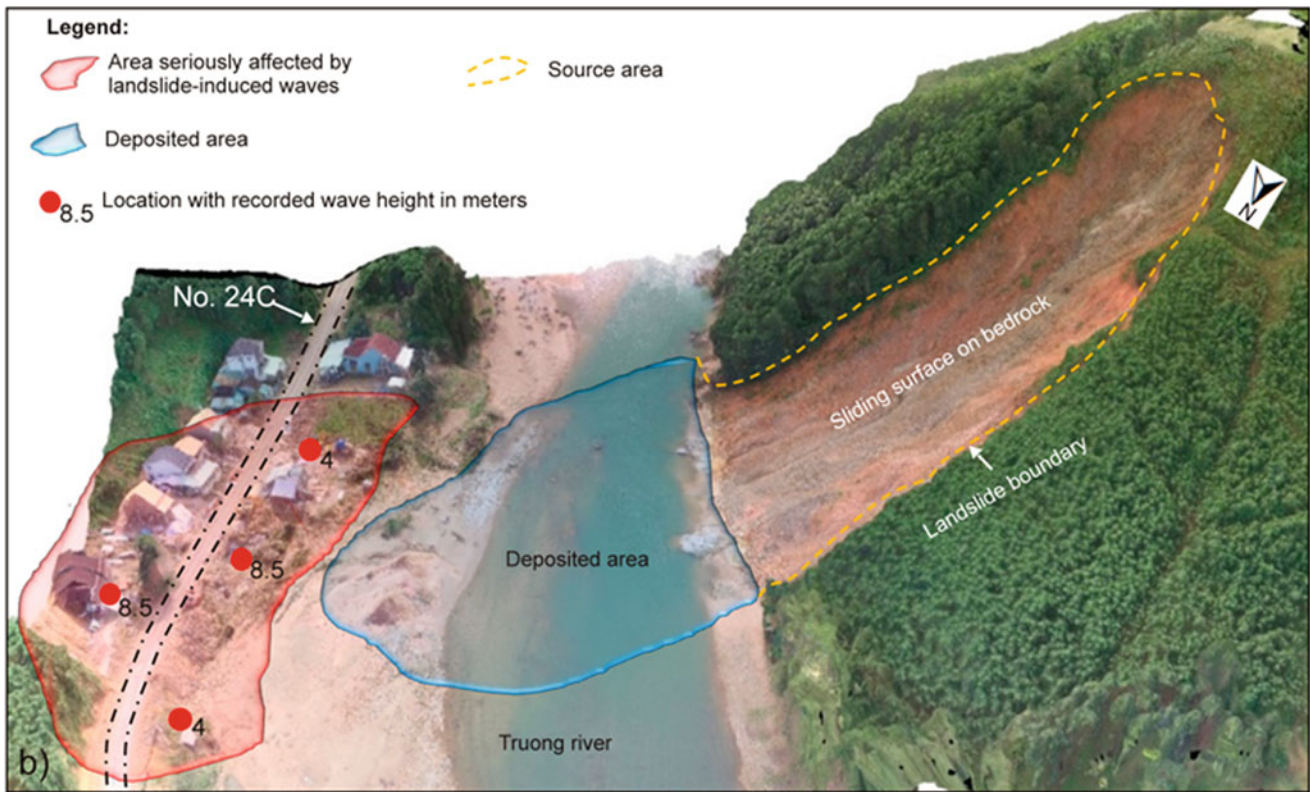
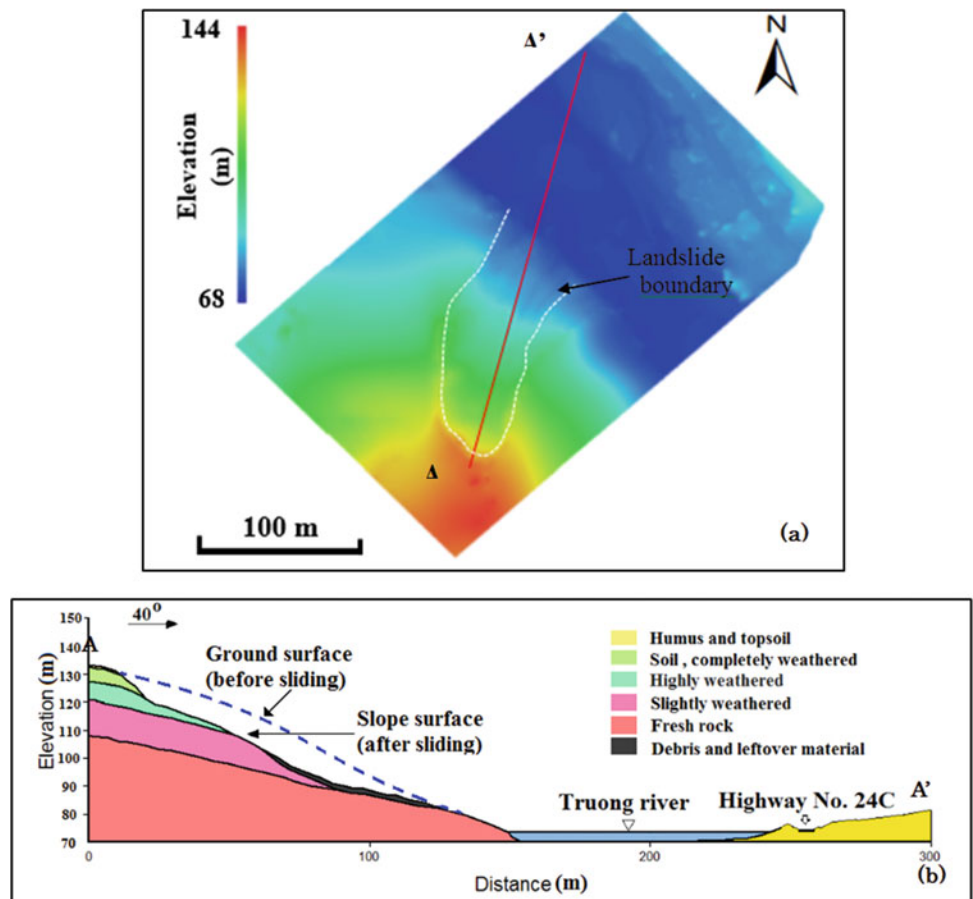


Fig. 23 3D view of the Tra Giang landslide (from Duc et al. 2020)

Fig. 24 Elevation image after the event (a) and geological profile of the landslide (b) (from Duc et al. 2020)



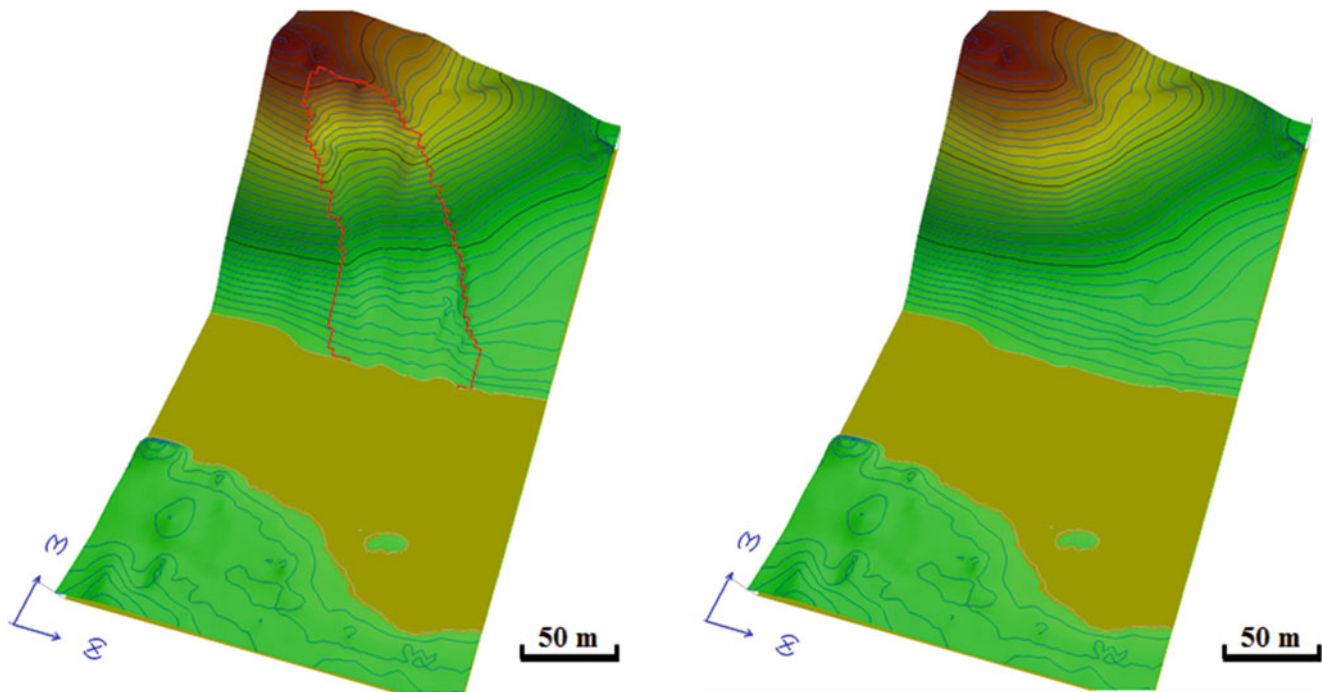


Fig. 25 DEMs of the landslide area saved in LS-RAPID for simulation. Left figure is the topography of the sliding surface; red line is the border of initial landslide source area. Right figure is the topography of the estimated ground surface before the landslide (from Duc et al. 2020)

Table 1 Parameters used in LS-RAPID and LS-Tsunami computer simulation models (from Duc et al. 2020)

Parameters	Normal values	Values used for Tra Giang landslide	Source
Lateral pressure ratio ($k = \sigma_h/\sigma_v$)	0.3–0.6	0.3–0.6	Assumed
Steady state shear resistance (τ_{ss} , kPa)	5–50	10–15	Ref. to Quang et al. (2017)
Shear displacement at the start of strength reduction (D_L , mm)	5–100	5	Ref. to Quang et al. (2017)
Shear displacement at the end of strength reduction (D_U , mm)	100–5000	1000	Ref. to Quang et al. (2017)
Peak friction coefficient at sliding surface ($\tan \phi_p$)	0.65–0.78	0.78	Ref. to Quang et al. (2017)
Peak cohesion at sliding surface (c_p , kPa)	10–100	10–20	Ref. to Quang et al. (2017)
Friction coefficient during motion at sliding surface ($\tan \phi_m$)	0.46–0.70	0.68	Ref. to Sassa et al. (2010), and Quang et al. (2017)
Friction coefficient inside landslide mass ($\tan \phi_i$)	0.36–0.58	0.57	Ref. to Sassa et al. (2010)
Pore pressure ratio ($r_u = \Delta u/\Delta \sigma$)	0.0–1.0	0–0.5	Assumed
Pore pressure generation rate (B_{ss})	0.0–1.0	0.6–0.99	Assumed
Coefficient for non-frictional energy consumption (α)	–	1.0	Ref. to Sassa et al. (2010)
Threshold value of velocity (m/s)	–	50	Record data
Threshold value of soil height (m)	–	50	Record data
Manning coefficient	–	0.025	Ref. to Sassa et al. (2016)
Total unit weight of the mass (γ_t , kN/m ³)	–	18.2	Test data
Unit weight of water (γ_w , kN/m ³)	–	9.81	Normal value

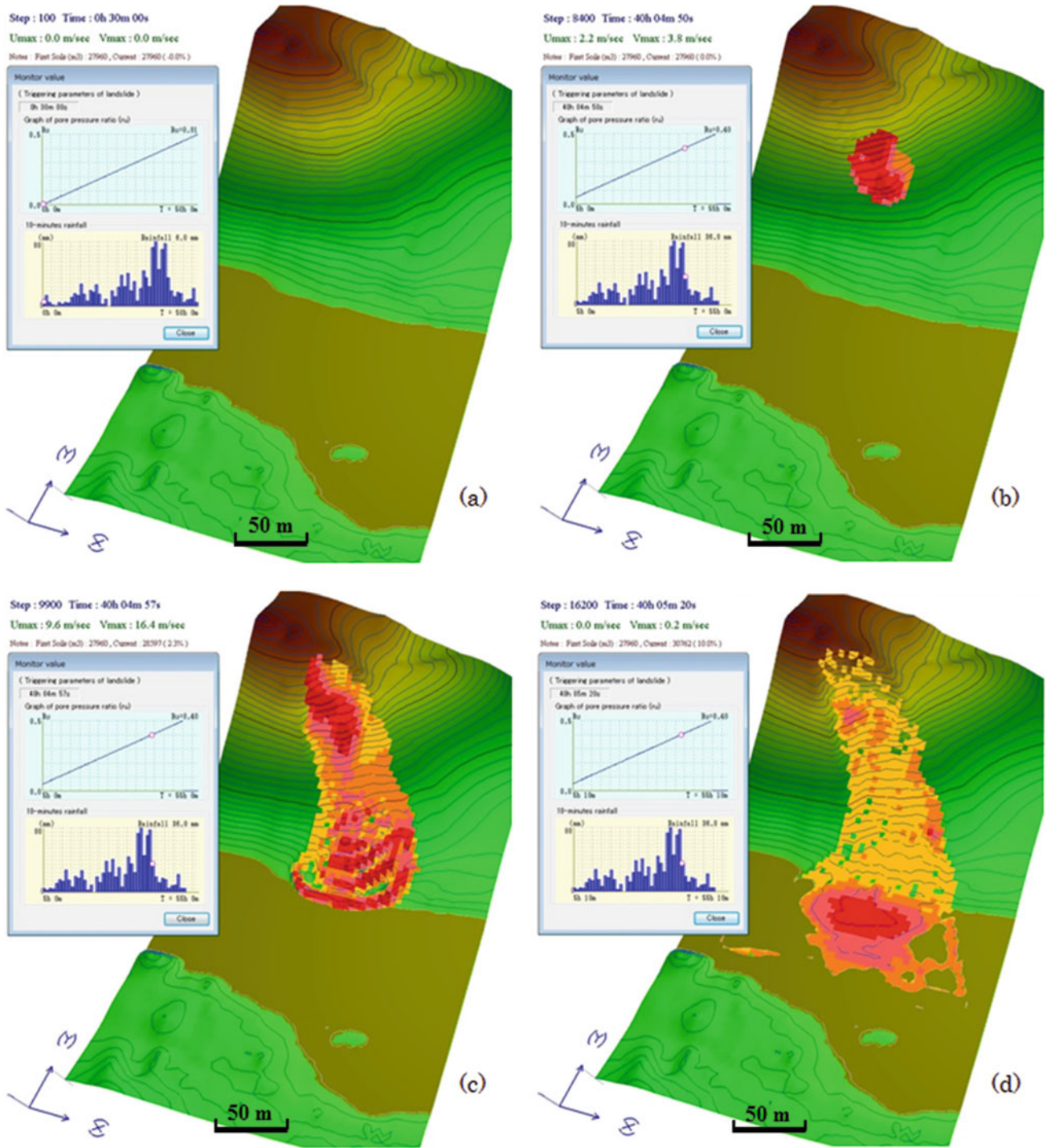


Fig. 26 Simulation of rainfall-induced landslide by LS-RAPID model (from Duc et al. 2020)

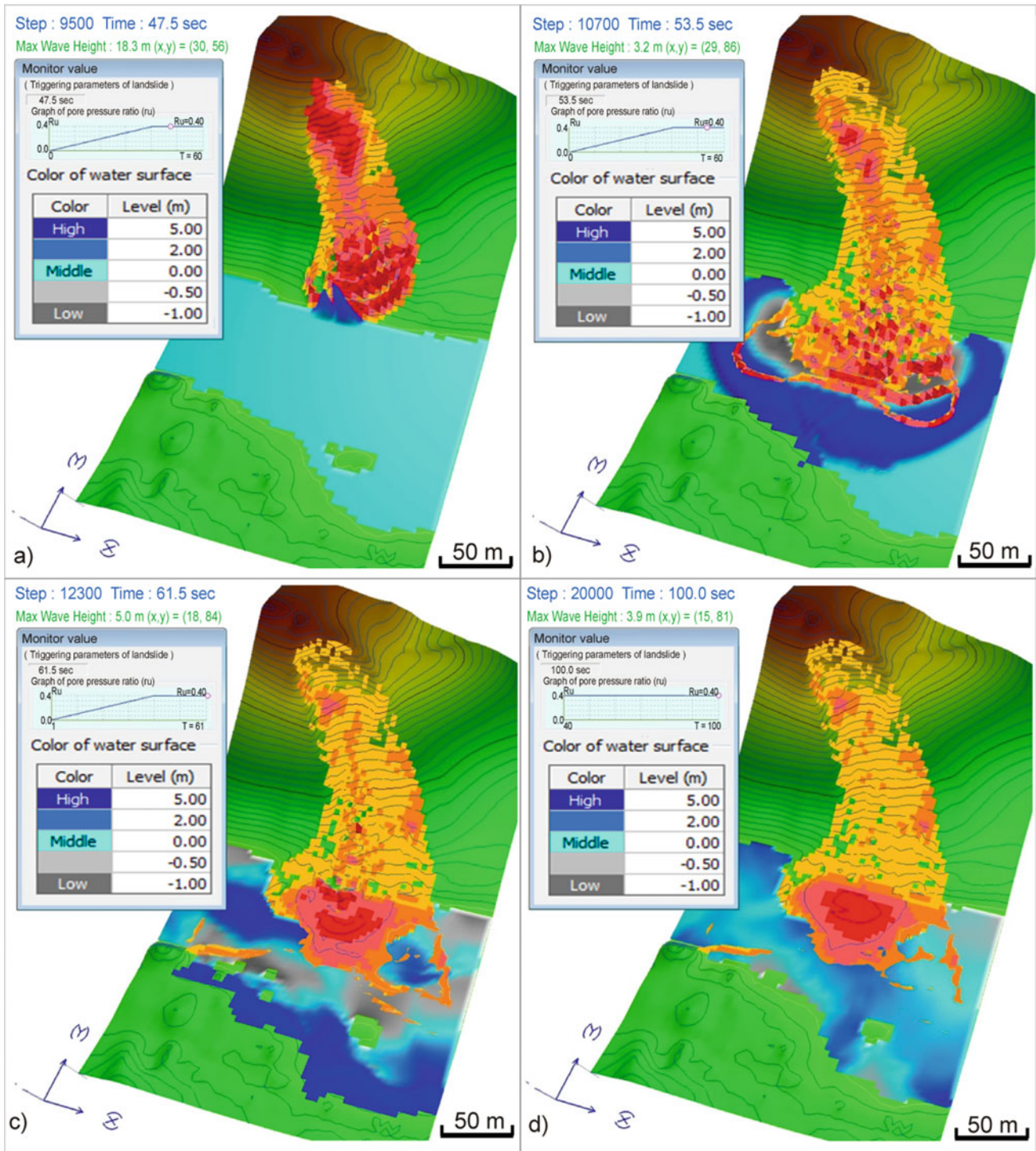


Fig. 27 Simulation of tsunami-like wave across the Truong River propagating from the landslide (from Duc et al. 2020)

Fig. 28 Google Earth image depicting the Mayuyama landslide and the islands formed as a result of the landslide (modified from Sassa and Dang 2018)

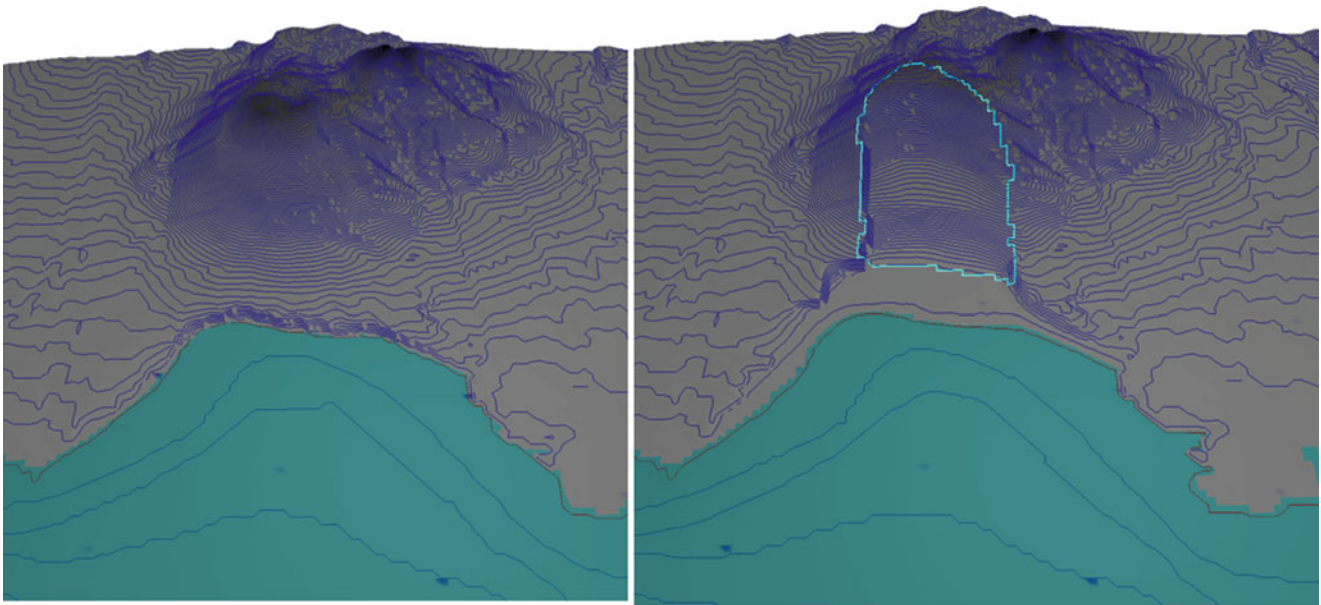


Fig. 29 Ground surface topography before the Unzen-Mayuyama landslide (left) and topography of the sliding surface (right) (Sassa and Dang 2018)

Table 2 Parameters used in the computer simulation LS-RAPID for Unzen-Mayuyama landslide-and-tsunami disaster (from Sassa and Dang 2018)

Parameters used in simulation	Value
<i>Parameters of soils in the source area (deeper area)</i>	
Steady-state shear resistance (τ_{ss})	120 kPa
Lateral pressure ratio ($k = \sigma_h / \sigma_v$)	0.7–0.8
Friction angle at peak (ϕ_p)	42.0°
Cohesion at peak (c)	10 kPa
Friction angle during motion (ϕ_m)	40.0°
Shear displacement at the start of strength reduction (D_L)	6 mm
Shear displacement at the start of steady state (D_U)	90 mm
Pore pressure generation rate (B_{ss})	0.7–0.9
Total unit weight of the mass (γ_t)	19.5 kN/m ³
Unit weight of sea water (γ_w)	10.1 kN/m ³
<i>Parameters of soils in the moving area (shallower area)</i>	
Steady-state shear resistance (τ_{ss})	30–80 kPa
Lateral pressure ratio ($k = \sigma_h / \sigma_v$)	0.8–0.9
Friction angle at peak (ϕ_p)	40.0°
Cohesion at peak (c)	10 kPa
Friction angle during motion (ϕ_m)	40.0°
Shear displacement at the start of strength reduction (D_L)	6 mm
Shear displacement at the end of strength reduction (D_U)	90 mm
Pore pressure generation rate (B_{ss})	0.7–0.9
Total unit weight of the mass (γ_t)	19.5 kN/m ³
<i>Triggering factor</i>	
Excess pore pressure ratio in the fractured zone (r_u)	0.21
0.5 times of the 2008 Iwate-Miyagi earthquake	Max: 370 cm/s ²
<i>Parameters of the function for non-frictional energy consumption</i>	
Coefficient for non-frictional energy consumption	1.0
Threshold value of velocity	100 m/s
Threshold value of soil height	400 m
<i>Other factors</i>	
Steady-state shear resistance under sea	10 KPa
Unit weight of sea water	10.1 kN/m ³
Manning's roughness coefficient	0.025

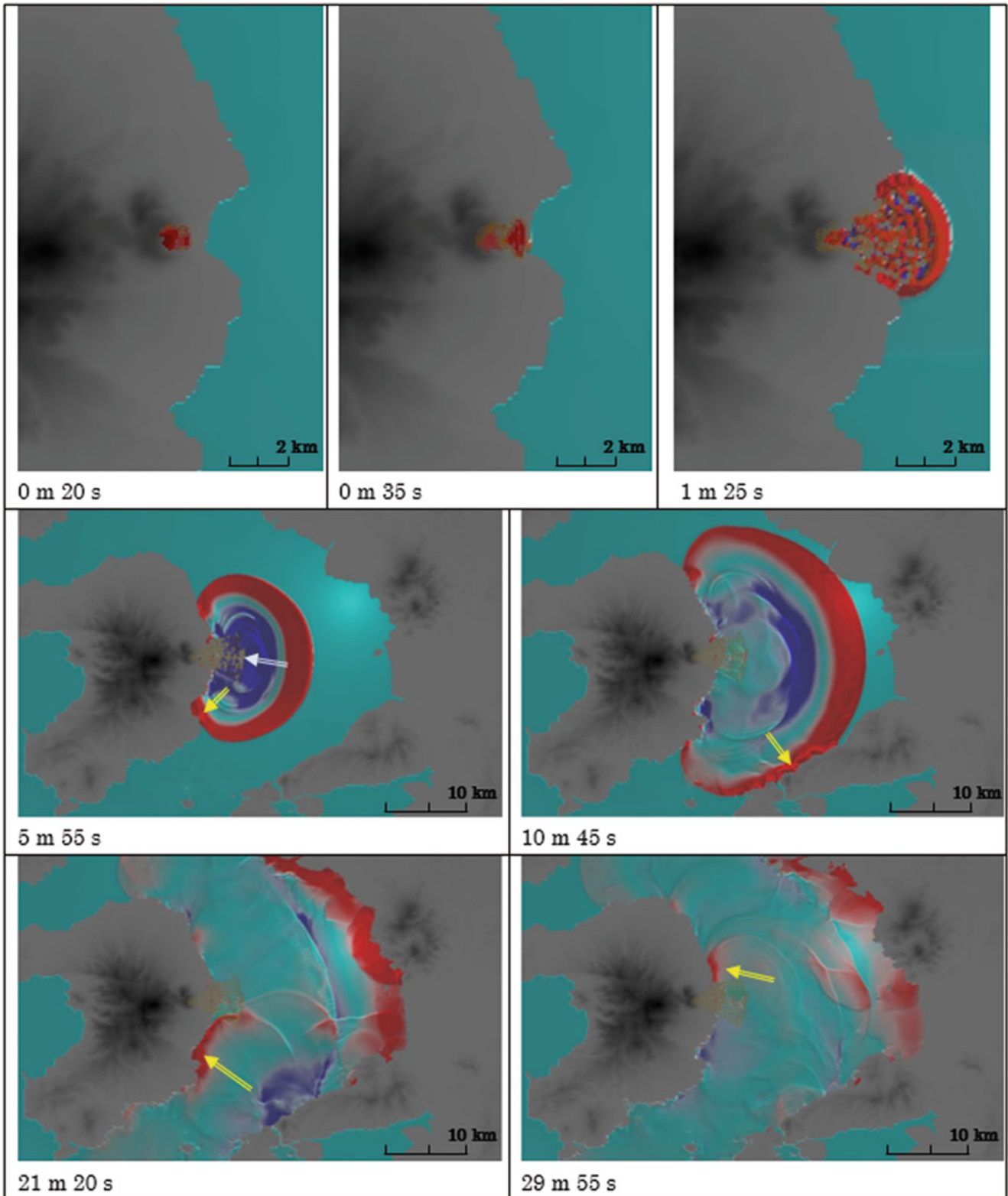


Fig. 30 LS-Tsunami simulation outcome depicting the tsunami disaster triggered by the Unzen-Mayuyama landslide in 1792 (from Sassa et al. 2016)

Acknowledgments We would like to express our sincere gratitude to Prof. Hideaki Yanagisawa for his pioneering work in tsunami simulation, which served as the foundation for the LS-Tsunami model. We would like to acknowledge the technical team from Godai Kaihatsu Co., Ltd. involved in the development of the LS-Tsunami software. Their expertise in software engineering and computational modeling has been instrumental in creating a user-friendly tool that enables integrated landslide and tsunami simulations. Additionally, we express our gratitude to the efforts of the reviewers and editor, whose constructive suggestions have significantly improved the quality and clarity of this paper.

References

- Abe I, Goto K, Imamura F, Shimizu K (2008) Numerical simulation of the tsunami generated by the 2007 Noto Hanto earthquake and implications for unusual tidal surges observed in Toyama Bay. *Earth Planets Space* 60:133–138
- Ajmera B, Ahari HE, Loi DH, Setiawan H, Dang K, Sassa K (2023) LS-RAPID manual with video tutorials. In: Sassa K, Konagai K, Tiwari B, Arbanas Ž, Sassa S (eds) *Progress in landslide research and technology*, vol 1 Issue 1, 2022
- Baba T, Matsumoto H, Kashiwase K, Hyakudome T, Kaneda Y, Sano M (2012) Microbathymetric evidence for the effect of submarine mass movement on tsunami generation during the 2009 Suruga bay earthquake, Japan. In: Yamada et al (eds) *Submarine mass movements and their consequences*. *Advances in natural and technological hazards research* 31. Springer, pp 485–494
- Doan H L, Sassa K, Dang K, Miyagi T (2021) Simulation of Tsunami waves induced by coastal and submarine landslides in Japan. In: Kyoji Sassa, Matjaž Mikoš, Shinji Sassa, Peter T. Bobrowsky, Kaoru Takara, Khang Dang (eds) *Understanding and reducing landslide disaster risk*. Springer, Cham, vol 1. Sendai landslide partnerships and Kyoto landslide commitment, pp 295–327
- Duc DM, Khang DQ, Duc DM, Ngoc DM, Quynh DT, Thuy DT, Giang NKH, Tien PV, Ha NH (2020) Analysis and modeling of a landslide-induced tsunami-like wave across the Truong river in Quang Nam province. *Vietnam Landslides* 17:2329–2341
- Intergovernmental Oceanographic Commission (IOC) (1997) Numerical method of tsunami simulation with the leap-frog scheme. IUGG/IOC time project IOC manuals and guides, No. 3, UNESCO, 126 p
- Sassa S (2023) Landslides and Tsunamis: multi-geohazards. *Landslides* 20(7):1335–1341
- Sassa K, Dang K (2018) TXT-tool 0.081-1.1: landslide dynamics for risk assessment. In: Kyoji Sassa, Fausto Guzzetti, Hiromitsu Yamagishi, Zeljko Arbanas, Nicola Casagli, Mauri McSaveney, Khang Dang (eds) *Landslide dynamics: ISDR-ICL landslide interactive teaching tools*. Springer, vol 1 Fundamental, mapping and monitoring, pp 1–79
- Sassa K, Nagai O, Solidum R et al (2010) An integrated model simulating the initiation and motion of earthquake and rain induced rapid landslides and its application to the 2006 Leyte landslide. *Landslides* 7:219–236
- Sassa K, Dang K, He B et al (2014) A new high-stress undrained ring-shear apparatus and its application to the 1792 Unzen–Mayuyama megaslide in Japan. *Landslides* 11:827–842
- Sassa K, Dang K, Yanagisawa H, Bin H (2016) A new landslide-induced tsunami simulation model and its application to the 1792 Unzen–Mayuyama landslide-and-tsunami disaster. *Landslides* 13(6): 1405–1419
- Satake K (2001) Tsunami modeling from submarine landslides. In: *Proceedings of the international tsunami symposium*, pp 665–674
- Unzen Restoration Office of the Ministry of Land, Infrastructure and Transport of Japan (2002) *The catastrophe in Shimabara: 1791–92 eruption of Unzen-Fugendake and the sector collapse of Mayuyama*. An English leaflet (23 p)
- Unzen Restoration Office of the Ministry of Land, Infrastructure and Transport of Japan (2003) *The catastrophe in Shimabara: 1791–92 eruption of Unzen-Fugendake and the sector collapse of Mayuyama*. A Japanese leaflet (44 p)

Open Access This chapter is licensed under the terms of the Creative Commons Attribution 4.0 International License (<http://creativecommons.org/licenses/by/4.0/>), which permits use, sharing, adaptation, distribution and reproduction in any medium or format, as long as you give appropriate credit to the original author(s) and the source, provide a link to the Creative Commons license and indicate if changes were made.

The images or other third party material in this chapter are included in the chapter's Creative Commons license, unless indicated otherwise in a credit line to the material. If material is not included in the chapter's Creative Commons license and your intended use is not permitted by statutory regulation or exceeds the permitted use, you will need to obtain permission directly from the copyright holder.



Part VI

Technical Notes and Case Studies



CliRtheRoads: An Integrated Approach to Landslide Risk Management on Roads in Serbia

Biljana Abolmasov, Ranka Stanković, Miloš Marjanović, Nikola Vulović, and Uroš Đurić

Abstract

In the framework of the project “Mainstreaming Climate Resilience in the Road Transportation Management in Serbia (CliRtheRoads)”, a complex mapping tool was developed to support the Government of Serbia and Public Enterprise Roads of Serbia in climate change adaptation planning and management. The software solution comprises of: a web portal for data entry and management for authorised users; a publicly available web-GIS application; a mobile GIS application; and a back-end database. This paper briefly overviews the system, focusing on the landslide data model. Therein, the main system and software solution breakthrough is automatizing the estimation of investment costs of engineering and non-engineering measures recommended at affected locations along the road network. A retrospective on its applicability and user feedback is also included. The objective was to facilitate seamless road management by providing necessary data in a simple, understandable fashion, indicating which locations on the road network have higher priority. The introduced level of automation allows easier decision-making and investment planning.

Keywords

Landslides database · Mobile app · Road management · Climate change

B. Abolmasov (✉) · R. Stanković · M. Marjanović
Faculty of Mining and Geology, University of Belgrade, Belgrade, Serbia
e-mail: biljana.abolmasov@rgf.bg.ac.rs; ranka.stankovic@rgf.bg.ac.rs; milos.marjanovic@rgf.bg.ac.rs

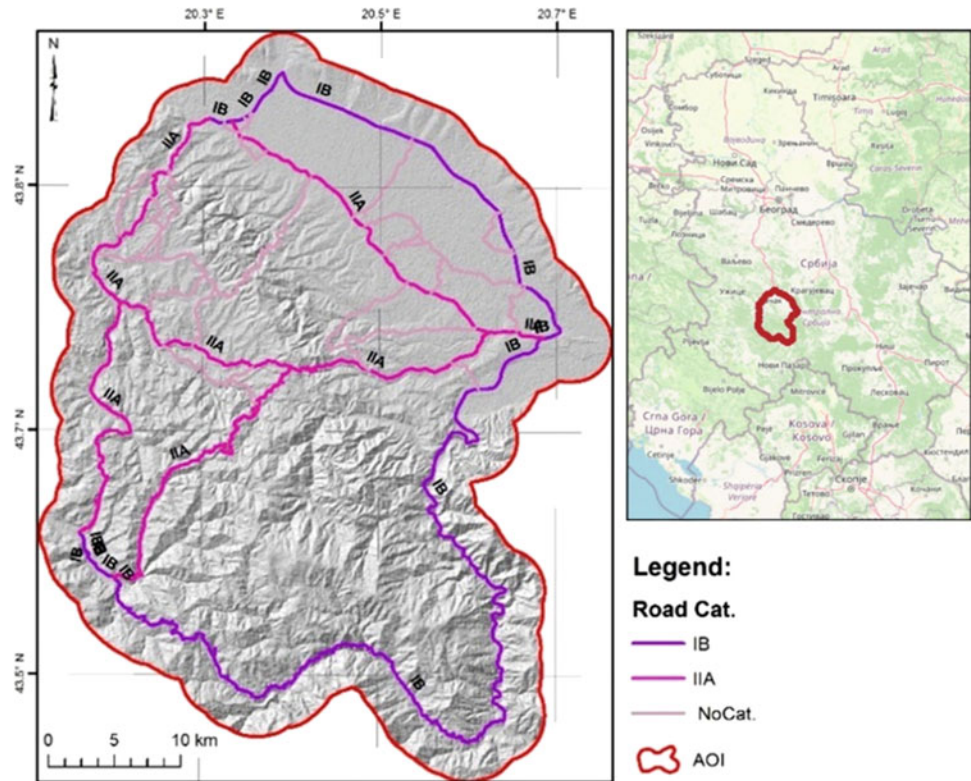
N. Vulović
ENVI Software Solutions, Belgrade, Serbia

U. Đurić
Faculty of Civil Engineering, University of Belgrade, Belgrade, Serbia
e-mail: udjuric@grf.bg.ac.rs

1 Introduction

Since 2016, The World Bank Transport Team has supported the Government of Serbia to mainstream climate resilience in the road transportation sector. The general idea was to connect transportation and natural disaster management after devastating floods and landslides in 2014 (Abolmasov 2019; Đurić et al. 2017; Marjanović et al. 2018a, 2018b). The total negative effect on the transport sector was EUR 166.5 million (RNA Report 2014). Jotić et al. (2015) estimated that approximately more than 2000 landslides were activated on the state roads and more than 3000 on the local roads. Several activities and projects were conducted under the support of The World Bank in recent years, including a project titled “Mainstreaming Climate Resilience in Road Transport Management in Serbia” (CliRtheRoads). The project’s main objectives were to support the Serbian government to mainstream climate resilience in the road transport sector management in Serbia, by enforcing public agencies in charge of roads to follow the climate proofing agenda and include it in day-to-day practice. To that end, the primary step was to develop a practical methodology for assessing the road transport network’s climate-related hazards, vulnerability and risks. It was necessary to improve the capacities of key stakeholders in road network climate resilience planning and set the path for the development of structured and systematic response plans. The agenda included two parts, split into many different tasks, wherein one of them was to test the proposed methodology. The City of Valjevo was selected as a pilot region, followed by other regions. A crucial sub-task was the development of corresponding geographic information systems (GIS) maps for hazard, vulnerability, and risks; and mapping tools to collect the data in the first place. The project was led by IMC Worldwide Ltd. (UK) in partnership with the University of Belgrade, Faculty of Mining and Geology (SER), the Highway Institute Belgrade (SER) and the Acclimatise (UK) in 2017–2018.

Fig. 1 The study area location and the road network



The second phase of the project was led by the ARUP d.o.o. (SER) as a branch office of the Ove Arup and Partners International Limited (UK) and the University of Belgrade, Faculty of Mining and Geology as a partner. The second phase was finalized in 2020–2021. The testing area was changed to the Kraljevo-Čačak-Ivanjica region (Fig. 1) with an additional task to improve data acquisition by designing an Android application for mobile devices.

The previous research and system development that influenced CliRtheRoads software solution was the project BEWARE, which developed an interactive web-GIS portal (Abolmasov et al. 2021; Abolmasov et al. 2017, 2018). The BEWARE mobile application, as a part of the integrated system, was built for the fieldwork and adapted for quick entry of field data, considering users' experience in local self-governments (LSGs) (Vulović et al. 2017). Similar functionality was envisaged for CliRtheRoads with an additional focus on road management issues, such as cost estimation, automation in staff shortage circumstances, and so on.

The mission of this project and other initiatives was to raise awareness of the natural hazards and climate change within the public enterprise (PE) sector and LSGs and to motivate the legislative authorities to improve design standards in future and take these effects into account. Once the entire decision-making pyramid is updated with climate changing hazard approach, the management of the road network will become more sustainable. In this particular case, public enterprise staff and relevant decision-makers were

supplied with equipment and software, and then trained to use it, thereby allowing to digitize their day-to-day practice, with an emphasis of hazardous events along the road and forward thinking on their mitigation.

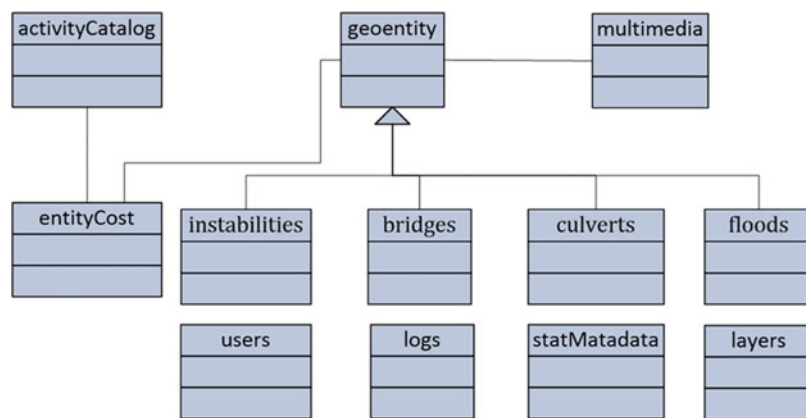
2 Data Model

The data model (Fig. 2) behind the CliRtheRoads system includes: (1) main concepts (entity types for instabilities, with detailed data comprising of common and specific attributes); (2) storage of multimedia (photographs from fieldwork); (3) knowledge base with the cost of activities, including catalogue per each entity type with job type and description, unit and total price, maintenance type (regular maintenance, rehabilitation, urgent maintenance), including recommending activities (the system allows users to add specific activities, description and cost of recommended works that is further calculated and aggregated with other data); and (4) secondary data from other sources (other projects, archived data and external resources), or from interpreted data (primarily from existing hazard models).

2.1 Main Concepts

Data acquisition was first conceived using analogue data forms to inventory affected road assets. The forms were

Fig. 2 The data model used for data entry, data editing, and storage of photographs



retrieved from various sources and experiences and simplified to the level of checkboxes and short inputs. Based on the adopted paper form, a digital version was developed with all related data definitions and specifications.

Data fields used for all datatypes included general identification data like: ID, project name, road mark, location (descriptive and geolocation), registration date, responsible researcher, and some metadata related to the user and data status (submitted for verification, pending, verified). Geolocations were recorded as longitude/latitude and chainage (start/end). Additional data may vary depending on the natural hazard at hand.

For instabilities/slope failures (slides, falls, topples, and flows), additional data included: the date of activation or/and reactivation, type of movement, the material involved, water content, the velocity of movement, state of activity, geometry (dimensions), lithological composition, soil thickness, watercourses (permanent or intermittent), hydrogeological causes/triggers of instability, the position of the phenomenon in relation to the road, the threat of the road by the instability, traffic interruption, previous investigation and recommendations of various mitigation activities.

According to recommended activity group (e.g., maintenance, investigation, design, and monitoring), the system allows the users to add specific activities within that group, with their further description and cost that is automatically calculated (in particular, for all maintenance activities, which are calculated per the legislative price list, while for others the cost is estimated by the expert) and aggregated with other data.

2.2 Data Storage

The Android mobile application of the CliRtheRoads facilitates the input of all these relevant data interactively in online or offline mode (in remote areas with no internet coverage). The data is locally stored and subsequently

uploaded to the server once the Android device is back on the grid.

A web application of the CliRtheRoads (<http://clirtheroads.rgf.rs/>) was developed in parallel (using PHP) to facilitate data input (by downloading data from the mobile app or by direct web app input). All web forms were standardized, with specified required and optional fields and logical constraints, to help speed up the data digitalization phase and to ensure unified inputs. Data editing and validation were also included. Data filtering and keyword-based searches provided easy access to the data stored in the database.

Once all data was collected, it was stored in the PostgreSQL database using a model adapted to the input data forms. The database developed in the first phase of the project (for the Valjevo area) was modified to include new datasets and to store new data categories (such as floods, culverts, and bridges) and new modules (activity type and cost). Each data entry was assigned a code for the corresponding project: CliRtheRoadS1 (the Valjevo region) or CliRtheRoadS2 (the Kraljevo-Čačak-Ivanjica region).

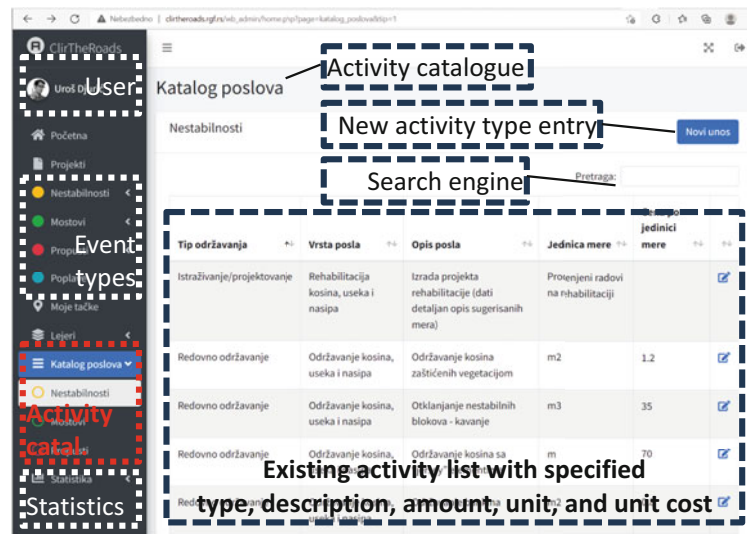
3 Data Management

A screenshot from the web application with an overview of the catalogue for mitigation activities is presented in Fig. 3. In contrast, Fig. 4 shows the data entry form for this catalogue.

Once defined in the catalogue, the interventions can be assigned to each observation entry (instabilities, culverts, bridges, floods), wherein all generic intervention costs (such as maintenance and urgent maintenance costs) are automatically calculated, while rehabilitation and design costs have to be additionally estimated by the expert user (as it is a site-specific matter).

Thus, apart from entering instabilities (landslides), culverts, bridges, and floods that users encounter on the field (along the road) and reporting through the mobile or

Fig. 3 The preview of the main panel with activated (red) Activities catalogue, wherein a list of recommended activities can be defined (<http://clirtheroads.rgf.rs/>)



web app, a completely new cost module was developed, allowing direct estimation of the site mitigation cost. Generic recommended activities (e.g., maintenance) can be entirely customized regarding cost calculation. The catalogues based on data templates for different levels of predefined interventions include: the type of intervention, intervention description, unit, unit price, total price, and maintenance type (regular maintenance, rehabilitation, and urgent maintenance) per each entity type (instabilities, culverts, bridges, floods). They can be edited and changed if, for example, the unit price for specific activity becomes more expensive. A screenshot from the web application with part of the data entry form of recommended activities is presented in Fig. 5.

In the first and the second phase of the project, ten users (field specialists), two application administrators (senior experts) and two database administrators (IT specialists) populated the database using either a web form or a mobile app. However, the tool is intended to be used by field workers from the PE or LSG after being adequately trained to report the event on a road network, recommend its impact

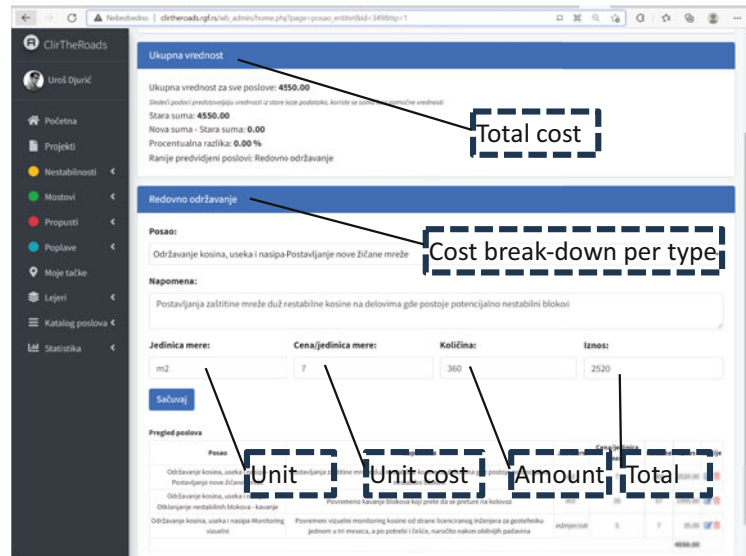
mitigation and estimate the cost of undertaken measures. It is a challenging task and could require a multidisciplinary team comprising different engineering fields, preferably geological, civil engineering, etc. On the other hand, PE, or even more so LSG is expected to cope with the shortage of such staff profiles, another stimulus to improve the staff capacity in this respect.

Various statistical analysis with graphical representation has been included in the CliRTheRoads application. An example is given in Fig. 6. Apart from the previous 187 records (CliRTheRoads1), there are 264 new records (CliRTheRoads2) with fully described instabilities, supplemented by numerous photographs from the field. For culverts, 145 records from the first phase were appended, with 190 new records illustrated by several photographs per culvert. For bridges, there were 123 records, while the new dataset included 71 records supported with 3–6 photographs per entry. The flood module is introduced within this project, and it contains ten unique records.

Fig. 4 An example of recommended activities editing/creating new (from the available list of activities), with the specified group, type of work/intervention, its description, amount (defined by dimension), and unit



Fig. 5 An example of a completed data entry form for maintenance activity subgroup



A statistical module enabled a comprehensive overview of the data against different classification parameters. This was supported with a graphical preview of charts and tables, with links to appropriate data collections. Data classification can be represented and structured by various attributes, supplemented by basic statistics for road section, hazard process, geologic composition, length, depth, activity, traffic impact, etc. Almost any data category from the web form can be used as a classification parameter, with classes deduced from the database.

4 GIS Component

PostGIS Extension to PostgreSQL Database for hosting GeoServer was used to implement a website with mapping capabilities to provide the demanded geospatial data. To host GeoServer, the PostgreSQL database was extended with PostGIS. With the PostGIS extension, PostgreSQL can be used as a backend spatial database for GIS. GeoServer

provides a set of required functions, such as spatial data entry, management, analysis, and visualization, by sharing and publishing GIS resources on the web as web services. GeoServer is an open-source Java software server. It is used for generating, sharing, and managing geospatial data. Using open standards, GeoServer publishes data from any major spatial data source.

This system consists of the database and the web application. It is also supported by a flexible web-GIS application containing selected data for public and internal use with maps produced by the field acquisition or external GIS processing, as seen in Fig. 7. It provides insight into the current, present, and future zones exposed to target hazards along the road network. A web-GIS application was developed on an open-source spatial database using the PostgreSQL database management system. This is currently one of the most popular open-source spatial databases.

Mobile applications in offline mode manage data in local data storage. In contrast, in connected mode (when the connection via the Internet can be established with the central

Fig. 6 The example of statistical overview: the landslide data group (in particular, landslides in respect to road alignment: road below the landslide (orange bar); road crossing the landslide middle (blue bar), etc.)

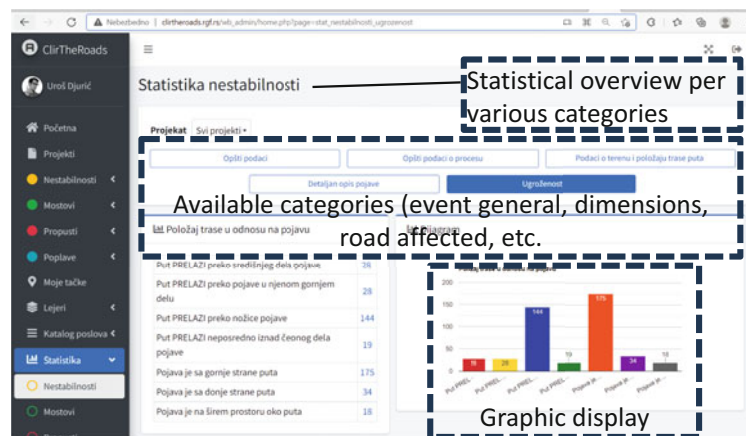
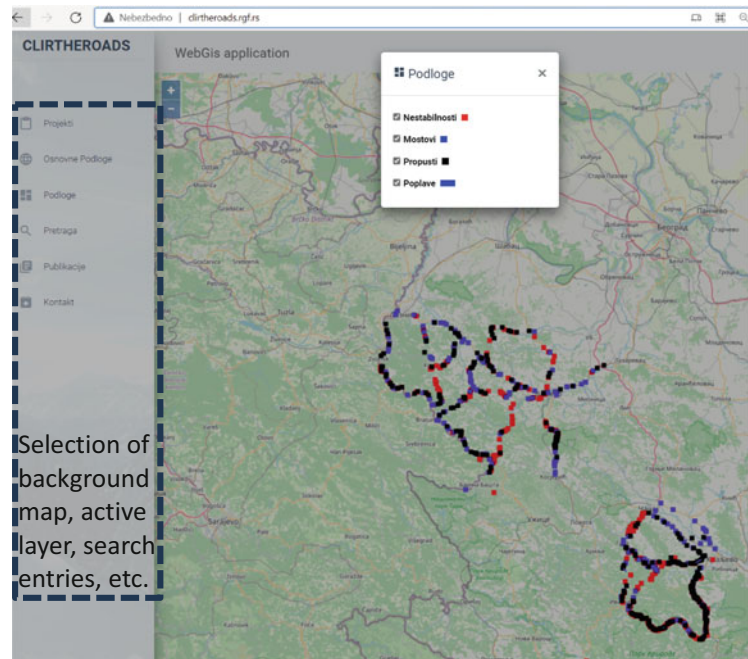


Fig. 7 Screenshot of the Web-GIS output (entry points with different colours for different types: red—instabilities; blue—bridges; black—culverts; blue section—flood)



server), the data are sent to a central repository. The mobile application supports shorter data sets (e.g., entries completed by filling in only required fields) that can be further complemented (additional photographs can be uploaded, and other comments typed), edited and verified via the web application. The web application can be accessed from mobile phones since the interface is responsive and adaptable to the screen size (phone, tablet, laptop, desktop). The entry can be entirely on the field if there is appropriate internet coverage.

Due to the risk of hazards recurring in the exact location, this inventory will provide planners with a screening tool showing the geographic distribution of known and potentially new occurrences and serving as a helpful decision-making tool that relates directly to road maintenance or remediation requirements.

The main project outputs can be downloaded as open data in various machine-readable formats to enable the reuse of data for other related projects and research.

The following raster outputs are included: hazard maps, the exposure to the hazard of the road network per link, and the hazard of the road network per segment (links split into 500 m intervals). In addition, there are maps representing vulnerability and risk. The GIS maps are available in a raster (.tiff) format with: associated colour maps (to keep the visual appearance of the maps constant regardless of the user system and software preferences), a vector (.shp) format with associated (.lyr) files (compatible with ESRI software only, and also intended for preserving the visualization standards), and in Map Exchange Document (.mxd) files to preserve the symbology, order of appearance, background and layout

settings of the maps, legends, grids, scale bars, etc. (compatible with ESRI software only). There are also map package (.mpk) files available for ESRI software users, prepared in the same fashion (as .mxd format) but more suitable for transfer and sharing.

5 Conclusion

In the CliRtheRoads system, thematic road-related data were managed and stored in a PostgreSQL database. At the same time, mobile and web application developed using PHP programming was used to facilitate data input. Potential users can benefit from the CliRtheRoads application as the interaction is simplified to the level of advanced field users. The user should be a PE or LSG staff member familiar with the hazard processes (primarily floods, flash floods, rockfalls and slides) and the affected road asset. Ideally, the team for data collection should comprise engineering geologists and civil engineers trained to use the app. The system allows decision-makers to use primary outputs directly per affected location or road link/segment. The system enables decision-makers to act more confidently without knowing in-depth hazard analysis, structural remediation or other components because they are scaled down to estimated risk and cost. Although available for all Android devices, it is recommended to use the app on a tablet of 10" or similar size for better perspective and power autonomy (an Android phone can be used for other purposes during the day and drain the battery). It is also advisable to make entries in paper form in parallel, especially in long field campaigns and if the

field team is large enough (three or more members). In this project, two regions were used to test all functionalities: the Valjevo and the Kraljevo-Čačak-Ivanjica regions. A total of 461 records were collected with fully described instabilities (slides, falls, topples, flows), documented by many photographs from the field. Additionally, every record is supplemented by engineering solutions to support field engineers or decision-makers for better road management in climate changing conditions.

Acknowledgments The presented research was financially supported by the project “Road Rehabilitation and Safety Project Consulting Services for Technical Assistance to the Project Implementation Team” supported by PE Roads of Serbia under agreement with World Bank Group where partners were JV ARUP d.o.o. (SER) and Ove Arup & Partners International Limited (UK) and the University of Belgrade, Faculty of Mining and Geology.

References

- Abolmasov B (2019) Hazard od klizišta u 21.veku. Ciklus predavanja 5: Geohazard u Srbiji u 21. veku – znanje je najbolji bedem protiv stihije. In: Cvetković V (ed) Srpska Akademija nauka i umetnosti. Beograd. pp. 65–88. ISBN: 978-86-7025-844-0. (In Serbian)
- Abolmasov B, Damjanović D, Marjanović M, Stanković R, Nikolić V, Nedeljković S, Petrović Ž (2017) Project BEWARE - landslides post-disaster relief activities for local communities in Serbia. In: Mikoš et al (eds) Advancing culture of living with landslides, proceedings of 4th world landslide forum, Ljubljana 29 May-02 June 2017, vol 3, pp 413–422. Springer International Publishing. https://doi.org/10.1007/978-3-319-53487-9_48
- Abolmasov B, Damjanović D, Marjanović M, Todorović S, Stanković R, Đurić U, Nikolić V (2018) Project BEWARE - approaching to open landslides data. 17th Serbian geological congress, May 17-20. Vrnjačka Banja Abstract Book 2:605–609
- Abolmasov B, Marjanović M, Đurić U, Krušić J (2021) From post-disaster landslides inventory to open landslides data. In: Proceedings of 3rd European regional conference of IAEG, Athens, Greece, 6-10 October 2021. Book of abstracts, pp 263–264
- Đurić D, Mladenović A, Pešić-Georgiadis M, Marjanović M, Abolmasov B (2017) Using multiresolution and multitemporal satellite data for post-disaster landslide inventory in the Republic of Serbia. *Landslides* 14:1467–1482
- Jotić M, Vujanić V, Jelisavac B, Zlatković M, Milenković S (2015) Klizišta i štete na saobraćajnoj infrastrukturi u Srbiji. *IZGRADNJA* 69(5–6):215–224. (In Serbian)
- Marjanović M, Krautblatter M, Abolmasov B, Đurić U, Sandić C, Nikolić V (2018a) The rainfall-induced landsliding in Western Serbia: a temporal prediction approach using decision tree technique. *Eng Geol* 232:147–159
- Marjanović M, Vulović N, Đurić U, Božanić B (2018b) Coupling field and satellite data for an event-based landslide inventory. In: *Landslides and engineered slopes. Experience, theory and practice*. CRC Press, pp 1361–1366
- Recovery Need Assessment 104714 (2014). <http://www.obnova.gov.rs/uploads/useruploads/Documents/RNA-REPORT-140714.pdf>
- Vulović N, Kitanović O, Stanković R, Vorkapić D, Vulović A (2017) BEWARE multi-device web GIS application for landslides. Advancing culture of living with landslides. In: Mikoš M, Arbanas Ž, Yin Y, Sassa K (eds) *Proceeding of 4th world landslides forum*, Ljubljana, Slovenia, 29 May-02 June 2017, vol 3 *Advances in landslides technology*. Springer International Publishing, pp 423–430. <https://doi.org/10.1007/978-3-319-53487-9>

Open Access This chapter is licensed under the terms of the Creative Commons Attribution 4.0 International License (<http://creativecommons.org/licenses/by/4.0/>), which permits use, sharing, adaptation, distribution and reproduction in any medium or format, as long as you give appropriate credit to the original author(s) and the source, provide a link to the Creative Commons license and indicate if changes were made.

The images or other third party material in this chapter are included in the chapter's Creative Commons license, unless indicated otherwise in a credit line to the material. If material is not included in the chapter's Creative Commons license and your intended use is not permitted by statutory regulation or exceeds the permitted use, you will need to obtain permission directly from the copyright holder.



Part VII

World Landslide Reports



Rock Slope Instabilities Affecting the AIUla Archaeological Sites (KSA)

José Ignacio Gallego, Claudio Margottini, Ingrid Perissé Valero, Daniele Spizzichino, Tommaso Beni, Daniela Boldini, Francesca Bonometti, Nicola Casagli, Riccardo Castellanza, Giovanni Battista Crosta, Paolo Frattini, William Frodella, Giovanni Gigli, Edoardo Lusini, Serena Rigamonti, Giulia Rusconi, and Lorenzo Vitrano

Abstract

The paper focuses on the geomorphological processes and potential geo-hazards affecting the cultural heritage rock-cut sites of AIUla region. Its best-known site is Hegra, with more than 110 monumental tombs with elaborated façades carved directly into the sandstone rock. In addition, AIUla hosts a number of fascinating historical and archaeological sites such as its Old Town, surrounded by an ancient oasis, and Dadan, the capital of the Dadan and Lihyan kingdoms. The study is mainly aimed at investigating the local rock material, evaluating

characteristics of rock masses, understanding rock degradation processes and characterizing the potential impact of slope instabilities on the conservation of cultural heritage.

Keywords

Geomorphological processes · Rock slope instabilities · Cultural heritage

J. I. Gallego

RCU Royal Commission for AIUla, AIUla, Saudi Arabia
e-mail: j.revilla@rcu.gov.sa

C. Margottini (✉)

UNESCO Chair on the Prevention and Sustainable Management of Geo-Hydrological Hazards, University of Florence, Florence, Italy

I. Perissé Valero

AFALULA French Agency for the Development of AIUla, Paris, France
e-mail: ingrid.perisse@afalula.com

D. Spizzichino

ISPRA Geological Survey of Italy, Rome, Italy
e-mail: daniele.spizzichino@isprambiente.it

T. Beni · N. Casagli · W. Frodella · G. Gigli

Department of Earth Sciences, UNESCO Chair on the Prevention and Sustainable Management of Geo-Hydrological Hazards, University of Florence, Florence, Italy
e-mail: tommaso.beni@unifi.it; nicola.casagli@unifi.it; william.frodella@unifi.it; giovanni.gigli@unifi.it

D. Boldini

Sapienza University of Rome, Rome, Italy
e-mail: daniela.boldini@uniroma1.it

F. Bonometti · R. Castellanza · G. B. Crosta · P. Frattini · S. Rigamonti · G. Rusconi · L. Vitrano

University of Milano Bicocca, Milan, Italy
e-mail: riccardo.castellanza@unimib.it; giovannibattista.crosta@unimib.it; paolo.frattini@unimib.it

E. Lusini

University of Bologna, Bologna, Italy
e-mail: edoardo.lusini@unibo.it

1 Introduction

The present paper focuses on the preliminary assessment of the ongoing and potential geo-hazards affecting the AIUla archaeological sites. Located at 1100 km West from Riyadh, AIUla covers an archaeological area (e.g., necropolis, quarries and settlements) of more than 22,000 m² (Fig. 1), where it is possible to walk in a luxury oasis through ancient world heritage sites in a rock cut landscape shaped over million years (Margottini and Spizzichino 2021). Its best-known site is Hegra, the main southern city of the Nabataean kingdom, before becoming a Roman outpost, and the first UNESCO world heritage site in Saudi Arabia. It is conserving over 110 monumental tombs with elaborated façades carved into the sandstone rock. In addition to Hegra, AIUla hosts a number of fascinating historical and archaeological sites such as its Old Town, surrounded by an ancient oasis; Dadan, the capital of the Dadan and Lihyan kingdoms, considered one of the most developed cities of the first millennium BC in the Arabian Peninsula; and thousands of ancient rock-art sites (e.g. Abu Ud, Jabal Ikma).

Many rock-cut monuments are affected by different natural threats such as surface weathering and erosion, rising dampness, rock surface detachment and large-volume slope instabilities. To ensure the long-term conservation of sites affected by such natural threats, detailed investigations, monitoring and consolidation measures are required, specifically developed for rupestrian cultural heritage sites (Spizzichino et al. 2016; Boldini et al. 2017; Margottini and Spizzichino

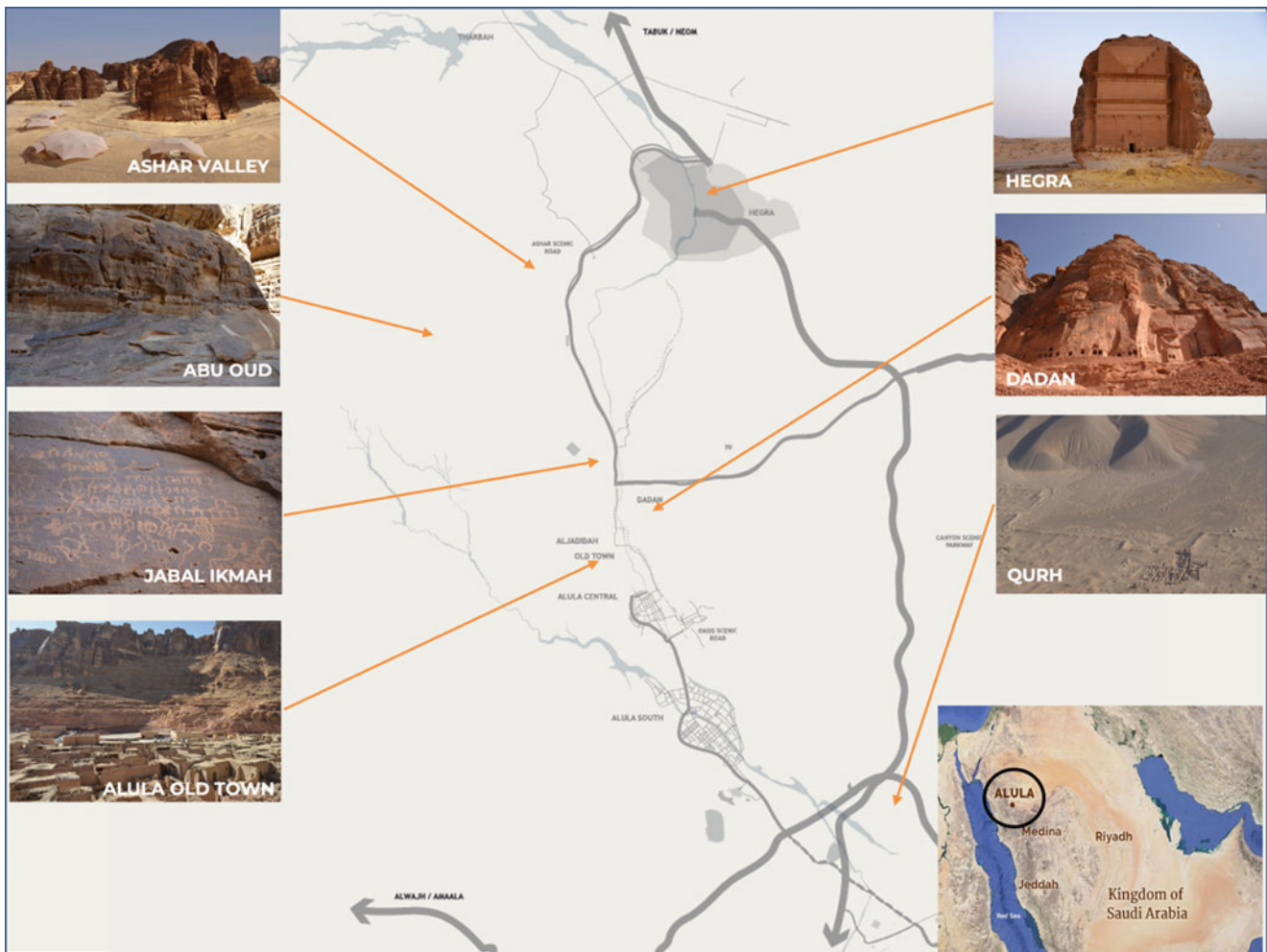


Fig. 1 Map of AlUla oasis and investigated archaeological and natural sites

2022). The activities are characterized by a thorough multi-disciplinary approach including competencies in archaeology, engineering geology, rock mechanics, landslide risk assessment and management as well as in conservation, protection and mitigation measures.

To define the main physical and mechanical properties of the rock materials, two laboratory test campaigns were carried out, in 2020 and 2021. The structural setting of the rock-mass (bedding planes, joints, faults), related to the stratigraphical genesis, the tectonic activity of the Red sea, and the geomorphological evolution of the slope, was identified and classified. Local rock-mass conditions were found to promote slope instabilities (e.g., rockfall, sliding, toppling) that may affect both the heritage itself and visitors.

This preliminary assessment of prevailing kinematics and potential geo-hazards will allow the implementation of a general master plan, to be considered as a first step for the following detailed design stage. The master plan will contain a first selection of the most appropriated mitigation and

consolidation measures, characterized by a low environmental impact and employing, as much as possible, traditional knowledge to site preservation.

2 The AlUla Archaeological Section

The province of AlUla keeps and shows extraordinary human and natural heritage. Its homonym capital is in the center of Wadi Al-Qura, an impressive valley carved out of sandstone, in which there is evidence of human presence, at least, since 200,000 BP. The AlUla *wadis* were a meeting point and a natural route for millennia, crossed by important trade routes used since prehistory, and with special intensity since the first millennium BC. With the flourishing of the cultures of Dadan—Lihyan, and Nabatean one later, the Incense Route, which from the south of the Arabian Peninsula crossed the AlUla region, reached the main eastern ports of the Mediterranean Sea. In this sense, the discussion on the introduction



Fig. 2 Nabatean tombs in the Hegra archaeological site

and spreading of the Neolithic phenomenon in the peninsula is also particularly interesting. These traditional communication routes are punctuated by an astonishing dispersion of rock art and monumental rock structures that provide us with a wealth of information. Regarding the latter, the research projects promoted by the Kingdoms Institute of the Royal Commission for AIUla (Thomas et al. 2021) detected close to 1400 Mustatils. It was possible to obtain the absolute dating of them with 14C, that takes us to the late Neolithic, around 6000 BC (Ramsey 2020; Reimer et al. 2020). AIUla is home to some of the main archaeological landmarks of Arabia, such as the site of Al-Khuraybah, ancient Dadan, capital city of the Dadanite and Lihyanite kingdoms. Dadan was likely one of the most developed cities of the first millennium BC. of the region. As an indisputable heritage legacy, the sandstone valleys also protect thousands of inscriptions in several different languages and alphabets, from Dadanite to modern Arabic. Jabal Ikmah, Abu Ud or Al-Aqra'a are an undoubted and powerful human testimony in the area. Without a doubt, the most recognized archaeological site is Hegra. Extending over 52 hectares, Hegra was the most important Nabatean city and royal cemetery in the south of their kingdom, since at least the first century BC (Fig. 2). UNESCO world heritage site since 2008, Hegra protects more than a hundred monumental tombs from this period, and had

continuity during the Roman period, probably as one of the southernmost places in the province of Arabia Petrea. After the transition to Islam in the seventh century, the cities of Q'uhr and AIUla appeared in written sources as important places for pilgrimage routes. Testimony of this is reflected both in the archaeological remains of the first, next to the town of Mughaira, and in the Old Town of AIUla, whose streets, squares, and farms seem frozen in time.

The latest reflection of this evolution is made up of the characteristic elements of the Ottoman presence, both in the form of various fortifications and military equipment, as well as that of the Hijaz railway. Its construction, which was intended to complete the connection of Damascus with Madinah, was suspended by the First World War. Figure 3 summarizes the chronology for AIUla civilization.

3 Geological Setting

From the geological point of view, the area of AIUla is located at the border between the basement complex and the Arabian foreland, constituted by coarse clastic sediments (mainly sandstone). The detailed distribution of the various geological formations is reported in Fig. 3 (modified after Donald and Hadley 1987).

Outcropping succession in the AIUla archaeological region includes the Siq Sandstone and Quweira Sandstone and the upper Quaternary alluvial deposits. The sandstone layers are sub-horizontal, gently dipping about 5° in N-NE (330°N). From the geological profile reconstructed by Buro Happold Engineering (2019) it is possible to notice that, due to this gentle dipping and due to topography, the Siq Red Sandstone is mainly outcropping in AIUla and surrounding (Dadan, Old Town, etc.) while, in the Hegra area, the Quweira Sandstone is dominant. The Quweira occurs in cross-bedded stratifications with bed thicknesses of 2 to 5 m (Table 1).

The Siq Sandstone, dark red to brownish-red and medium-grained, is divided into three sub-units, namely the Lower (sandstone conglomerate of white quartz cobbles), Middle (fine, fractured strata) and Upper Siq (massive and very compact) Sandstones (Fig. 4).

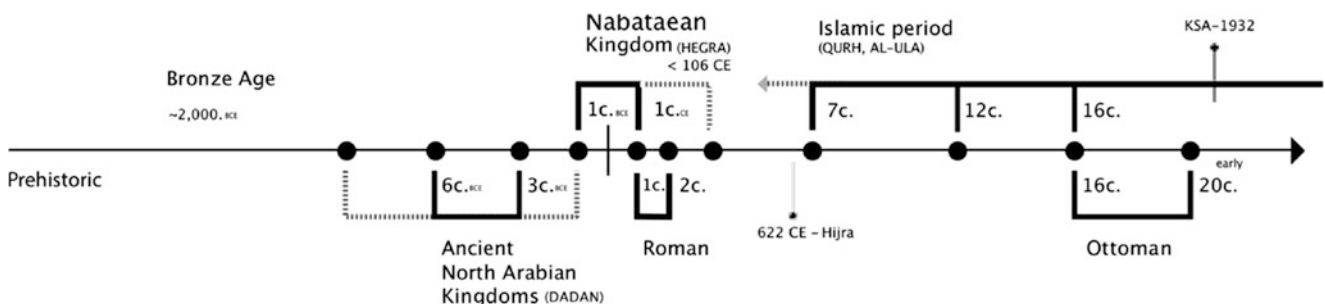


Fig. 3 The AIUla chronology (source <https://www.rcu.gov.sa>)

Table 1 Litho-stratigraphic units and sub-units in the region of AIUla

Age (period)	Geological unit	Sub unit
Early Ordovician	Saq Sandstone	
Late Cambrian	Quweira Sandstone	
Middle Cambrian		
Early Cambrian	Siq Sandstone	Upper Middle Lower
Proterozoic basement (pre-Cambrian Arabian shield)	Jibalah Group and basement	

The panoramic photograph in Fig. 5, taken on 2014 from the “highpoint” on top of Harrat (lava plain or volcanic field of Al Uwayrid west of AIUla - Wahbi), displays most of the lytho-stratigraphic succession in the area. This division is evident from the erosion profile of the outcrops in the area (Fig. 5).

4 Physical and Mechanic Characterization of Rock Mass and Rock Material

4.1 Field Survey and Rock-Mass Characterization

Geo-mechanical characteristics of the AIUla rock formations were investigated through geomechanical field surveys and laboratory tests, these latter executed directly in Italy



SYMBOL	ID	AGE	UNIT	MATERIAL
	Qal	Quaternary		Alluvium
	Qu			Alluvium
	Tb	Quaternary	Harrat	Flood basalt
	Qeqr	Ordovician	Saq Sandstone,	Sandstone
		–	Sandstone,	
		Cambrian	Quweira group,	
	Es		Siq group	Sandstone
	Ju	Proterozoic
	dq	
	aju		Lower Jiddah pyroclastic group	Lava and pyroclastic rock

Fig. 4 Geological map of AIUla region (modified after Donald and Hadley 1987)

(Gallego et al., in printing). The surveys were carried out following the recommendation of the International Society for Rock Mechanics (ISRM 1978a, b, 1981). The following activities were carried out directly during field surveys in Hegra and Dadan (Table 2):

1. geo-structural analysis of the slope façades (orientation and main characteristics of discontinuities);
2. Barton’s profilometer tests for reconstructing the joint roughness (JRC);
3. sampling of blocks to be used for laboratory testing;
4. Schmidt-hammer tests on joint surfaces and intact rock blocks for in-situ assessment of the uniaxial compressive strength (JCS);
5. tilt tests for base friction angle assessment (ϕ_b).

The rock mass classification index GSI was also assessed (Table 2).

4.2 Laboratory Tests

During the December 2020 campaign (Gallego et al. 2022), five rock samples were collected near the cities of Mada’in Salih (better known as Hegra) and Dadan (Fig. 5). They consist of two Yellowish Sandstone blocks, belonging to the Quweira Group, and three Red Sandstone blocks of the Siq Group (Fig. 6). A total of 40 specimens were prepared for the mechanical tests, of which 22 for the uniaxial compression test (Fig. 7a), with a diameter of about 25 mm, and 18 for the Brazilian test (Fig. 7b), with a diameter of about 50 mm. Uniaxial compression tests and Brazilian tests were performed using a 10 and 50 kN load cells, applying respectively a load rate of 0.5 MPa/s and 200 N/s (ISRM 1978c). Before the mechanical tests, the P wave velocity was also measured on all the specimens. The average values of the physical and mechanical properties for each sample are summarized in Table 3.

The increase in porosity reduces significantly V_P values for both rock formations, with differentiated trends for the Yellowish and Red Sandstone samples (Fig. 7).

The uniaxial compressive strength σ_c ranges from less than 10 MPa for a specimen of the sample 2 to over 50 MPa for a specimen of the sample 1, both belonging to

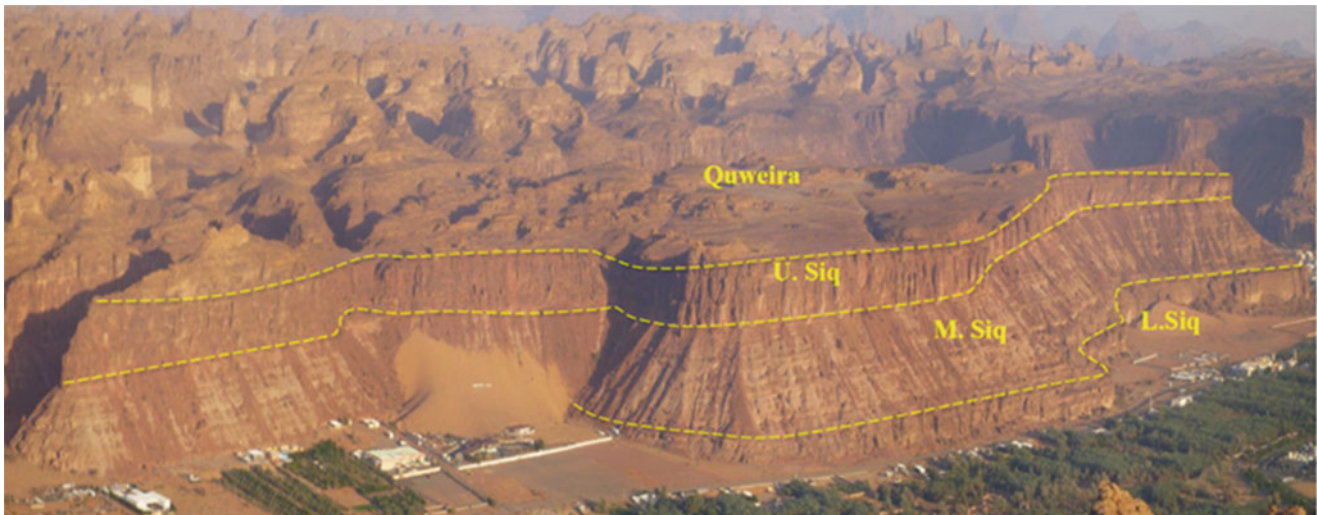


Fig. 5 Panoramic view (slightly vertically-exaggerated) of the lithostratigraphic succession in the AIUla area, taken from the highpoint of Harrat Al Uwayrid, west of the town of AIUla. Sandstone units are

recognized in this section, except for the Saq Sandstone, which outcrops out further north of this area (Wahbi 2014)

the Yellowish Sandstone lithotype. Specimens prepared from the Red Sandstone blocks are characterized by σ_c values in the range 18–42 MPa.

Consistently, specimens from samples 1 and 2 display respectively the highest and lowest values of the tensile strength σ_t , from almost 8 MPa in the case of the first block down to about 0.5 MPa in the second one. Values of σ_t similar to those obtained for the sample 1 were identified for specimens obtained from samples 3 and 4, while significantly lower values were attained by the two specimens cored from sample 5. In general, inspection of the two figures highlights the substantial influence of porosity on the rock material strength (Fig. 8).

5 Geo-hazards and Morphological Processes Threatening the Sites

The term geo-hazards includes very different types of morphological processes and involve both long-term and short-term geological processes. In the following, the main instability and weathering problems affecting the sites at different scales are briefly described.

The different archaeological sites of AIUla region are completely carved and realized into the Quweira and Siq

Sandstones. The local quality of the rock-mass is directly depending on:

1. lithology and rock material of depositional layers (e.g. minerals, texture and composition);
2. level and typology of weathering and erosion;
3. structural setting (e.g. joints, fractures, faults).

The slope angle for most of the rock faces is prevalently higher than 80° , with frequent overhanging surfaces consequent to erosive processes or block collapses at their base. Slope kinematics, and thus potential failure modes, is mainly ruled by high and medium dip angle of the main discontinuities versus local slope orientation. Also the presence of horizontal discontinuities (bedding planes) is conditioning failure modes and volumes of potential instability (see Fig. 10).

Following is a description for each investigated site.

5.1 Hegra

The archaeological area of Hegra occupies a flood plain in the orographic left area of the northern part of the AIUla oasis. It is characterized by the outcrop of small hills formed by sandstone blocks (QEqr) completely immersed in a real small desert of gravel deposits (Qu).

Table 2 Average discontinuity and rock mass parameters for Hegra and Dadan sites from the first campaign in 2020 (Gallego et al. 2022)

	JCS	JRC	Φ_b	GSI
	MPa	–	($^\circ$)	–
Hegra	32–42	2–6	37–43	67
Dadan	28–41	4–8	40–45	65

Fig. 6 Location of rock blocks collection



The characteristic formations that host the Nabatean necropolis are the final and cumulative result of two different and combined (mutually interdependent) morphological processes. The first, with very slow evolution, concerns the effects of wind erosion and precipitation. The second, in rapid evolution, concerns the diffused collapse phenomena

that develop along the edges of the façades for structural and geo-mechanical factors.

The first process leads to the creation of spectacular weathering and erosive forms typical of these geological formations which in their final stage produce the so-called rock mushroom (Fig. 9).

In the second case widespread processes of morphological instability or geo-hazards (mainly rockfall) occur, which characterize both the external and internal portion of the tombs and also the rock masses in which they were built.

The erosional phenomena promote also the thinning of different support structures (pillar, eaves, rock wall, architraves and gates) inside and outside the tomb as well along and on the top of natural slope.

The main instability processes affecting the whole Hegra archaeological area are:

1. Rockfall, rock sliding, wedge failure, toppling, free fall (from small to medium to large dimensions) affecting both the rock façade and the slope in which the tombs are carved;
2. Collapse (from very small to medium dimensions) involving directly the carved architectonic structure of the Tombs;
3. Weathering and erosion processes (from small to large scale) affecting both the slope facade and Tombs.

Some examples of the three typologies above mentioned are reported in the following Fig. 10.

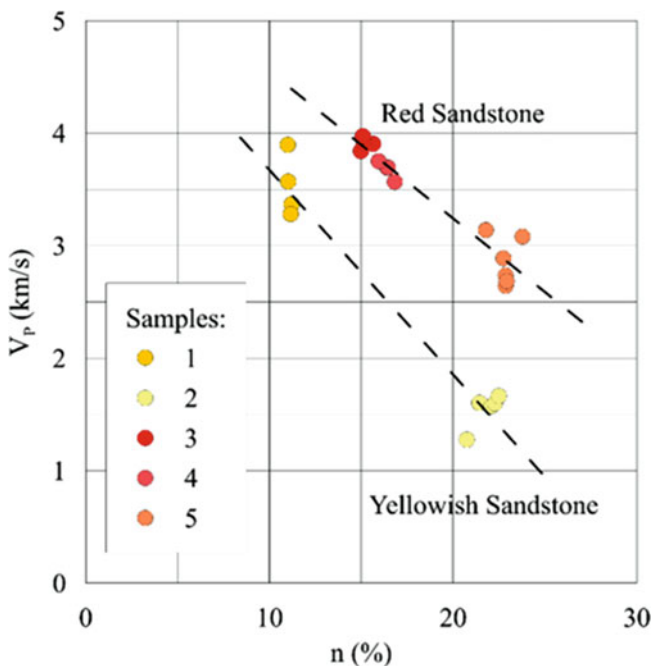


Fig. 7 P wave velocity against total porosity (Gallego et al. 2022)

Table 3 Summary of the physical and mechanical properties of the rock materials (Gallego et al. 2022)

Sample	ρ_{dry} (Mg/m ³)	ρ_s (Mg/m ³)	n (%)	V_p (km/s)	σ_c (MPa)	σ_t (MPa)
1	2.390	2.688	11.1	3.5	50.24	6.83
2	2.087	2.669	21.8	1.5	9.93	0.50
3	2.265	2.679	15.8	3.9	38.51	7.68
4	2.238	2.678	16.4	3.7	41.18	6.46
5	2.060	2.694	23.6	2.9	24.85	2.74

All the 138 tombs were investigated, collecting parameters that are synthesized in the following Table 4. Geometrical data were provided by a laser scanning survey TLS (Fig. 11).

All the information were managed within a GIS software, providing detail information about the state of conservation for each tomb. A global rank about the state of conservation among all tombs was also provided, giving an outcome as showed for some examples in Fig. 12.

5.2 Dadan

The site of Dadan is landscaped composed by an alluvial plane with archaeological remains only partially excavated, a gentle slope with few tombs, a vertical cliff that in the lower part was used as a quarry to collect stones for the construction of nearby village and where, at later stage, many tombs belonging to people with high social status were digged, the upper part of the mountain where ritual installations, rock art and defensive installation are located (Fig. 13).

From the previous landscape zoning it is quite evident that the highest energy of relief, a quantitative parameter

representing the maximum difference in elevation between the highest point and the lowest point measured in a given area, is concentrated on the vertical cliff were the quarry and the tombs are located. High energy of relief means high susceptibility of cliff instabilities, potentially involving both archaeological remains and visitors.

From a mechanical point of view, the area of Dadan (Fig. 14) is characterized by a 20 to 25 m thick massive sandstone layer in the upper Siq (SU), laying directly over the transition from the Middle Siq to the Upper Siq unit (characterized also by a small thickness silty to clayey beds, such as SM). The SU layer was quarried because of the position and of the physical and mechanical characteristics that made the rock material suitable for construction. Excavation was carried out with different techniques that can be identified by the presence of natural and induced fractures or linear pick marks. Extraction was performed both parallel and perpendicular to the slope face. Some evidence of the quarrying activities is the presence of holes for placing scaffolding-like structures or for moving along the slope or for anchoring ropes. Quarrying was performed by taking advantage of weak bedding or lamination planes, and open or latent discontinuities. Chisels, points, hammers, picks,

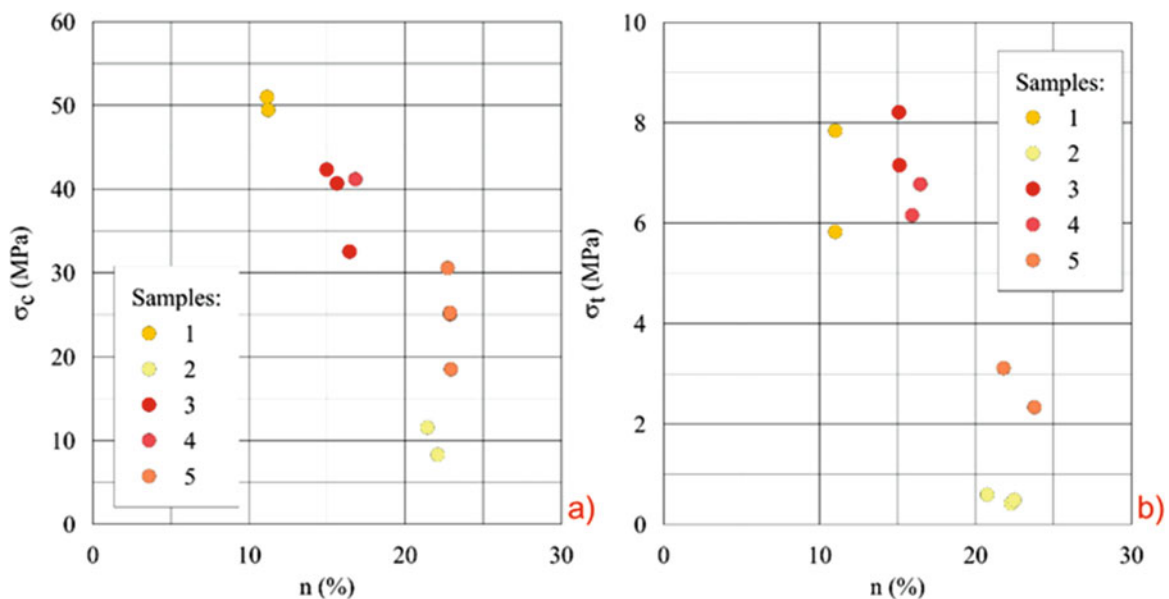


Fig. 8 Uniaxial compressive strength (a) and tensile strength (b) against total porosity (Gallego et al. 2022)



Fig. 9 Typical weathering and erosional patterns in the Hegra site

saws, and wedges were used to cut, excavate and open artificial fractures or for removal of large blocks by a progressive lowering of the upper rock face surface.

In the upper part, the Quweira sandstone (Q) is outcropping.

As a matter of fact, the area of Dadan is highly affected by rockfalls in general. Some relevant examples of potentially unstable blocks affecting the rocky cliff were surveyed during field investigations and are summarized in the following. The slopes are prevalently sub vertical to vertical ($>80^\circ$), especially along the quarry area, and gentler along the talus and quarry waste deposits. The outcropping sandstone



Fig. 10 Example of the main instability processes affecting the different tombs in Hegra: upper sequence of photos stands for rock slide and free fall; middle sequence is reporting small cracks, fractures and

detachment affecting the tomb façade; lower sequence is showing weathering and erosive processes present in the area

Table 4 Information provided for each tomb

	Parameters	Description
P1	Generalities	Group, Name of the tomb (if any); Number; coordinates
P2	Map	Topography or Google Earth image
P3	Photo	Number
P4	TLS	
P5	Archeology	Brief description of the tomb and relevant index
P6	State of conservation from visual inspection	Describe surface erosion, weathering, small falls etc.; excellent; very good; good; low; very low—endangered;
P6–1	Numerical ranking	(Ranking: 100–75–50–25–0)
P7	Geomorphological phenomena	Describe occurred or potential rockfall, wedge, planar, toppling instabilities and their possible volume (cm ³)
P8	Geology	
P9	Groundwater	
P10	Rock/soil materials	Density, UCS (Hammer), JCS, Tilt test, GSI
P11	Kinematic analysis	Stereo plot
P11–1	Slope face	Dip direction and dip angles (α and β)
P12	Possible monitoring	Proposal
P13	Potential evolution or risk	Hypothesis
P14	Notes	

presents a few prominent sub vertical discontinuity sets (N-S, E-W, ENE-WSW) whose origin, especially the joint system parallel to the slope face, can be associated to main regional tectonic trends. Unstable blocks, kinematics and the potential failure modes are mainly ruled by steeply dipping discontinuities sub parallel to the local slope orientation (see Fig. 14) and the sub horizontal bedding. These generate detachments with overhanging elements and only very minor sliding components.

In addition, it can be noted that the main joint sets have been used as weak planes along which quarrying activities were carried. The presence, spacing and continuity of bedding are conditioning factors controlling both the failure modes and unstable block volumes (Fig. 15).

According to the geomorphological survey of the area, the main typologies of instability processes are rockfalls (planar slide, wedge failure, toppling and free fall) in the vertical cliff with Upper Siq sandstone and Quweira on top of the area and

rill erosion in the gentle slope where the Middle siq is outcropping. More in detail it is possible to recognize the following processes and related dangerous situations:

1. potential planar slide, wedge failure, toppling and free fall (from small to medium to large dimensions), affecting the whole rocky cliffs, both in the vertical Upper Siq sandstone and in the topmost Quweira sandstone;
2. runout of blocks collapsing from the cliff, falling, bouncing and rolling in the lower part of the cliff, mainly concentrated along the gorges of the slope but also along the talus;
3. fall of loose small blocks and debris, standing on the various morphological terraces above the quarry. This category can be considered a subset of item 1;
4. in the intermediate Siq formation, represented by the inclined deposit at the bottom of the cliff, also partially covered by collapsed blocks and debris from the quarry, in occasion of heavy rainfall some important rill erosion may occur.

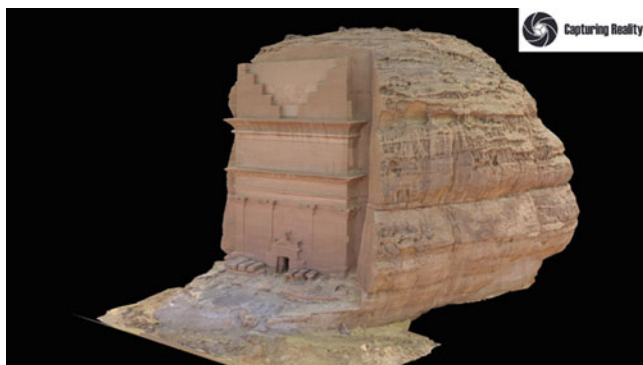


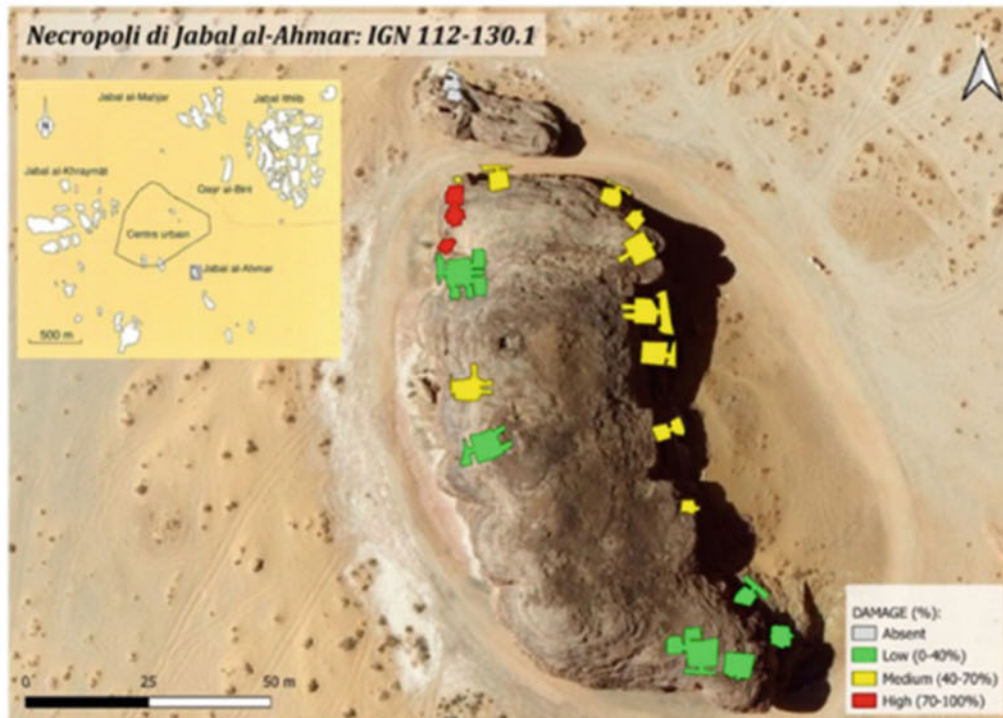
Fig. 11 Example of laser scanner survey (TLS) in Hegra: the tomb of Al Farid (courtesy of Factum Foundation)

Figures 16, 17, 18 and 19 show the above four typologies of geomorphological instability processes.

When looking at the impact of previous processes (hazard) on exposed elements, it is important to notice the following (Fig. 20):

1. the collapse of small/medium blocks from the quarried part of the cliff may damage the archaeological remains, i.e. the tombs carved on the cliff, either directly impacting on them or having the carved tomb as part of the collapsing block (Fig. 18);

Necropolis of Jabal al-Ahmar



ID tomb	State of conservation	Geom. Phenomena	Damage	Geology	Groundwater	Kinematic analysis	Slope face	Possible monitoring	Potential evolution or risk	notes	estimated tomb height (m)
112	75%	E(b), I	L	Q	N	2	190/87	VI	Ev(l,u)	Cl(u), Di	10
113	75%	E(b), K	L	Q	N	1	185/85	VI	EvK(i)	NR	10
114	75%	S(u)	L	Q	N	1	78/85	VI	EvK(e,u)	Cl(u), Di	7
115	75%	S(u)	L	Q	N	1	40/88	VI	EvI, Co	NR, Co(e,l)	7
116	50%	O(u)	M	Q	N	2	92/70	VI	EvI(u)	Im(a)	2
116,1	50%	S(u)	M	Ab	Ab	0	65/89	VI	Ev(u)	Im(a)	4
117	50%	S(u)	M	Q	N	2	102/90	VI	Ex(i), Ck(fa)	NR	5
118	50%	S(u), K(fa), De(j)	M	Q	N	0	260/90	VI	EvI(i), K(c)	Pr	8
119	50%	E(b), In(fa)	M	Q	N	0	66/90	VI	C(u)	Di	8
120	50%	E(b), In (fa)	M	Q	N	0	56/90	VI	In	Di	7
121	50%	E(b)	M	Q	N	0	30/85	VI	EvI(i), Rf(u)	Im(a)	6
122	50%	E(b)	M	Q	N	0	175/85	VI	EvI(i), Rf(u)	NR	7
123	25-50%	C	M	Q	N	0	284/90	VI	EvC(l,u)	Ua	2
124	20%	C, I(u)	H	Q	N	1	285/90	VI	C(r)	Su, Co	3
125	20%	I, O(f)	H	Q	N	0	285/90	VI	C(f)	Di	2
126	20%	E(fa), C(r)	H	Q	N	0	285/90	VI	C(r)	Su	3
127	75%	K, In	L	Q	N	0	276/90	VI	K	Ks, Im(a)	6
128	25-50%	C, E(b), K(a)	M	Q	N	3	265/90	VI	C(a), I(i), Rs, Rf(u)	Su, Di	7
129	75%	E(b), I(i), O(u), De(ev)	L	Q	N	2	253/90	VI	F	Di	7
130	Ab	Ab	Ab	Q	N	Ab	Ab	Ab	Ab	Ab	Ab

Fig. 12 Global ranking for the state of conservation of Hegra tombs. Example from Necropolis of Jabal al-Ahmar. The color is indicating the degree of damage

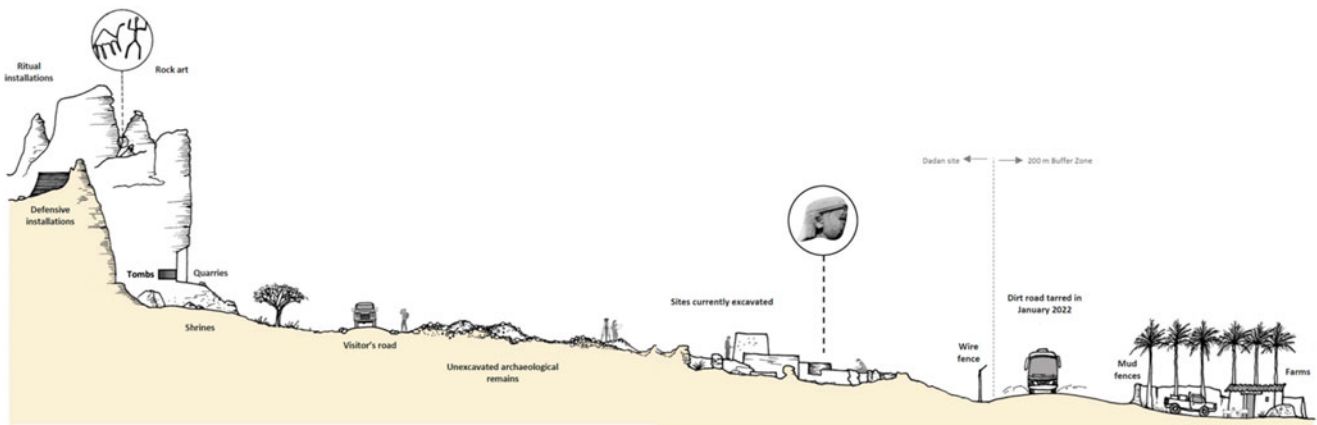


Fig. 13 The landscape zoning with major archaeological settlements in Dadan area (After Moriset and Gandreau 2022)

2. fallen blocks from the upper part of the cliff, during the runoff, may potentially impact on visitors at the toe of the slope (Fig. 21) and on cars driving on the earth road inside the archaeological park; such block can also damage the tombs located in the intermediate Siq formation (Fig. 22);
3. the already detached small blocks and debris standing on the various morphological terraces above the quarry may potentially impact on visitors at the toe of the slope;
4. the occasional rill erosion in the medium Siq formation may also damage the tombs located in this part of the slope.

In the present situation is becoming essential to understand the potential impact on people and buildings of falling blocks coming from the Western cliff, investigating their possible trajectory and runoff.

According to Varnes (1978), rockfall events involve the detachment (sliding, wedge, toppling and free fall) of rock mass fragments, which are then transported by gravity (runout) through free fall, bouncing, rolling, sliding, and are ultimately deposited on a talus cone or as individual debris deposits. Thus, rockfalls can be damaging events, and assessing rockfall potential and past rockfall events are important to analyse potential risks and discuss mitigation strategies. Review works on rockfall hazard assessments are provided by Ferrari et al. (2016), Gerber (2019), Loew et al. (2021) and Marija et al. (2022).

5.3 AIUla Old Town

AIUla Old Town is currently exhibiting an important development. Buildings are under restoration and the main road is showing new shops and commercial activities (Fig. 23).

The measurement of size and shape for a large number of boulders (rock blocks) in the field is cumbersome and very time-consuming. Nevertheless, the size (volume) and shape of the boulders belonging to a rockfall are expected to provide helpful information for the understanding of transport

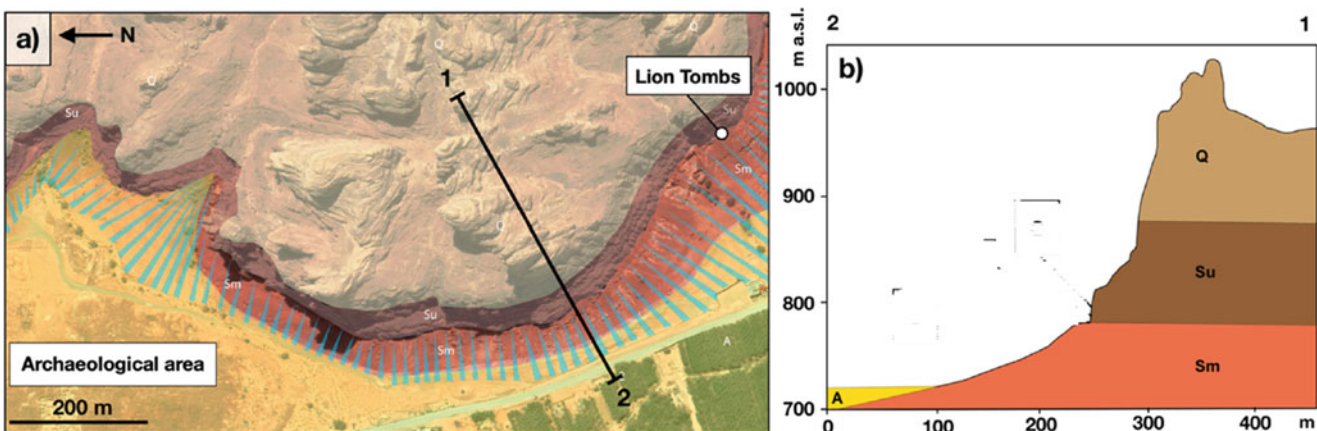


Fig. 14 Geological insights of the Dadan archaeological area: (a) the geologic chart projected on the satellite image (from Google Earth©), the blue lines represent the debris from the old quarry, as well as the

debris cones and the talus accumulation, “Sm” stands for Middle Siq sandstone, “Su” for Upper Siq sandstone, “Q” for Quweira sandstone and “A” for alluvial deposits



Fig. 15 Examples of rock façade at Dadan site. Type, spacing and fracturing of the joints are clearly evident. The lower strata are interested by the quarry excavated during the Dadanite time. In the latter joints and discontinuities were used to facilitate the carving of the quarry, as well as of the ancient tombs

and run-out dynamics of rock particles as well as calibration for modelling. Therefore, lidar point cloud and satellite images were used to measure the size (volume), the shape and the run-out length of most boulders.

Such approach provided a landslide inventory map, in terms of surface block distribution, as relevant input data for a 3D rockfall simulation model, coupled with topographic and geotechnical data. The map in Fig. 24 represents the accumulation area where the boulders runout after the detachment from the cliff. Figure 24 provides also a detail of the general rockfall inventory map and the related frequency/distance chart.



Fig. 16 Example of rockfall affecting the rocky cliff of Dadan



Fig. 17 Rock boulders freely running on the slope after the collapse, until resting at the toe of the cliff

Considering the difficulties in the direct identification of source areas in the field, due to the elevated morphology, a relevant support was provided by the use of a semi-automatic kinematic analysis (Gigli and Casagli 2011). From this tool, the identification of susceptible areas was developed and coupled with field survey. Figure 25 shows the global kinematic index, summing up the hazard for the various typologies of instabilities (Gigli and Casagli 2011).

The rockfall runout simulation was performed by using the 3D model Hy-STONE (Agliardi and Crosta 2003; Crosta and Agliardi 2003).

The 3D models are able to simulate block motion along a slope by including lateral dispersion of trajectories due to large and small scale morphological complexity (Descœudres and Zimmermann 1987; Guzzetti et al., 2002; Agliardi and Crosta 2003; Crosta and Agliardi 2003; Dorren et al. 2006). The obtained results are spatially distributed over the entire study area, without need for any interpolation of



Fig. 18 Already detached small blocks and debris on the cliff terraces, potentially falling on visitors

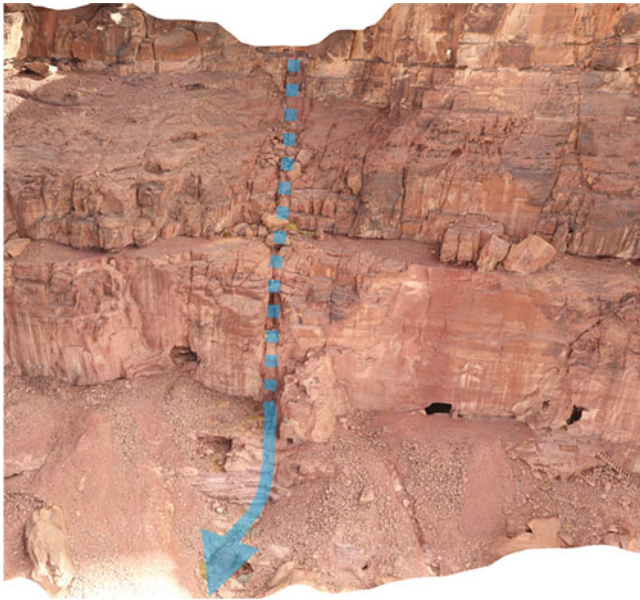


Fig. 19 Rill erosion (dashed line) occurring at the medium Siq formation (inclined strata) in occasion of heavy rainfall, damaging the archaeological remains

data computing along specific trajectories or imposing predetermined fall direction.

Hy-STONE incorporates both kinematic (lumped mass) and hybrid (mixed kinematic-dynamic) algorithms, allowing to model free fall, impact and rolling. Different damping relationships are available to simulate energy loss at impact or by rolling. The topography is described by a raster DEM, which is converted in a vector topographic model (Triangulate Regular Network, Guzzetti et al. 2002) for the solution of impact and rolling.

The stochastic nature of rockfall processes is introduced as a function of model spatial resolution and by random sampling most parameters from different PDFs (e.g. uniform,



Fig. 20 Potential collapse in the quarried part of the slope and involving archaeological remains



Fig. 21 Collapsed blocks at the toe of the cliff with the pedestrian pathway passing through. This is a clear example of a pathway standing too close to the cliff and exposing visitors to a potential risk of being involved in a rockfall



Fig. 22 Tombs located in the intermediate Siq formation and damaged by the runoff of collapsed blocks



Fig. 23 General view of AIUla Old Town and the dangerous Western cliff

Fig. 24 Rock block inventory along the Western cliff and frequency/distance distribution from origin source

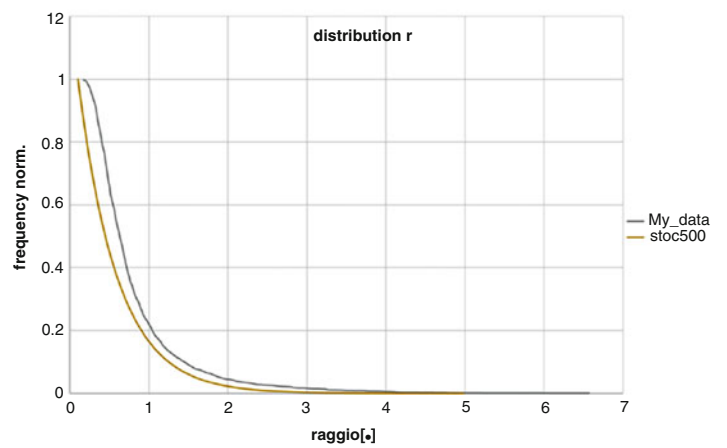
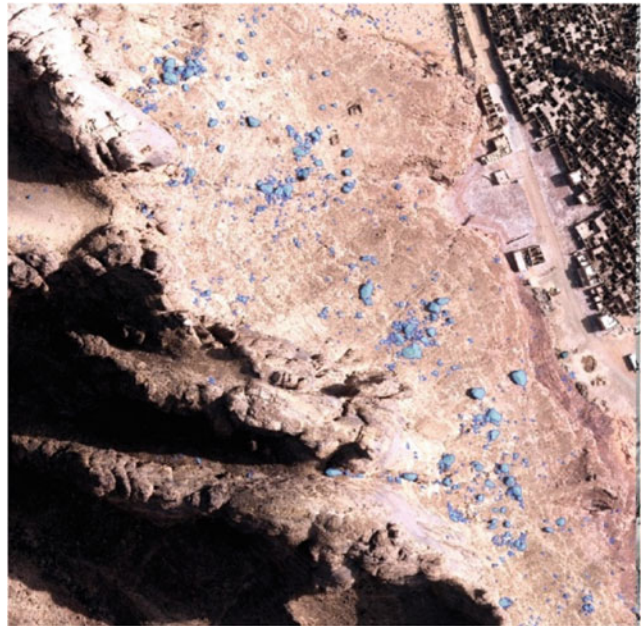
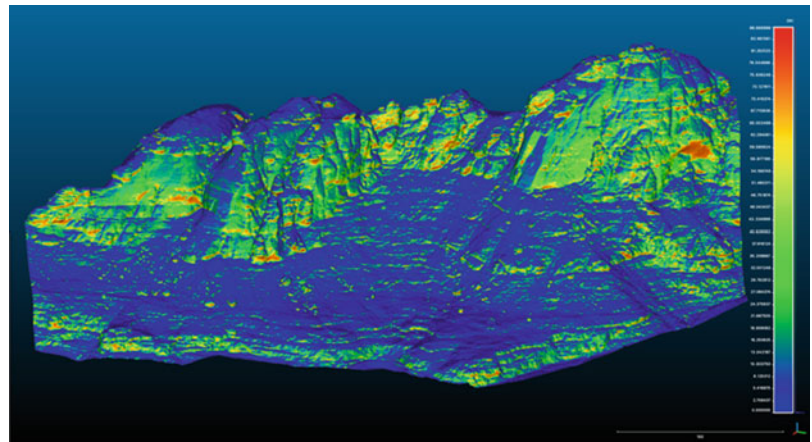


Fig. 25 Global kinematic index for the Western cliff of AIUla



normal, lognormal, exponential). The capability to simulate the effect of passive countermeasures, dynamics of “flying rocks” and the effect of vegetation were implemented and tested against real events (Frattoni et al. 2012). A special elasto-viscoplastic strain hardening model for impact on soft ground (Di Prisco and Vecchiotti 2006) was also implemented. Model results are provided in both raster and vector formats and these include rockfall frequency, density of arrest points, critical sources area, fly height, rotational and translational velocity and kinetic energy, as well as information about motion type, and impact locations.

The following Fig. 26 shows the result of the 3D modelling, highlighting that the possibility that some

trajectories of falling boulders are arriving till the border of Old Town is not negligible.

6 Conclusion

The AIUla oasis covers a wide archaeological area where it is possible to visit ancient heritage sites in a rock cut landscape shaped over thousand years. In addition to its best-known World Heritage site of Hegra, the region hosts a number of fascinating historical and archaeological sites such as its Old Town; Dadan and many ancient rock-art sites.

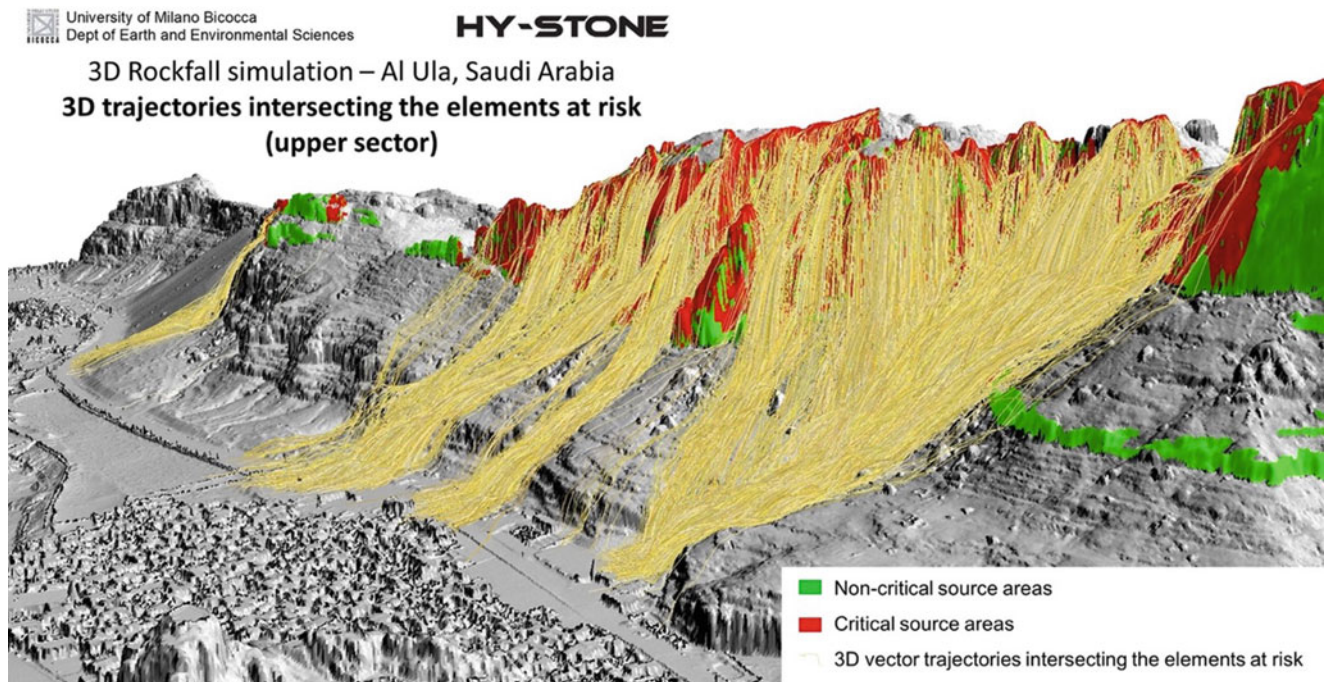


Fig. 26 3D trajectories intersecting the elements at risk in AIUla Old Town. In this simulation the source for falling boulders is the upper part of the Western cliff

The entire area is characterized by the presence of low to medium strength sandstone formations. More in detail, the north area shows the outcropping of the Quweira Yellowish sandstone unit while in the central and Southern area (Old Town and Dadan) and further south the Siq Red Sandstone appears, divided into three main sub-units (Lower, Middle and Upper). The poor geological and geomechanical characteristics of these two formations affect the potential instability and weathering of the cultural heritage sites carved into them.

The geological formations are characterized by a significant internal variability, both vertical and lateral. The Quweira Yellowish Sandstone, of interest for the site of Hegra, is mainly interested by diffused weathering and erosional phenomena as well as rockfall connected to internal structural asset. The archaeological areas in the Siq Red Sandstone, i.e. Dadan and Old Town, are mainly affected by rockfall and slides as a consequence of the local discontinuities pattern.

Acknowledgments The reported activities were carried out thanks to the collaboration between the UNESCO Chair on Prevention and Sustainable Management of Geo-Hydrological Hazards of the University of Florence, the Italian Institute for Environmental Protection and Research (ISPRA), the Sapienza University of Rome and the University of Milano Bicocca, coordinated by the Royal commission for AIUla (RCU) and the French Agency for AIUla Development (AFALULA), in the framework of the International Programme on Landslides IPL-259 project “Landslide Risk assessment in AIUla Archaeological sites—Kingdom of Saudi Arabia”. LAGIRN laboratory of the University of Bologna, in the person of Dr. Fausto Peddis and Dr. Barbara Ravaglia, is highly acknowledged for the activity of laboratory testing. Jhaed Kamuzaman Abul provided also his help in this stage of the research.

References

- Agliardi F, Crosta G (2003) High resolution three-dimensional numerical modelling of rockfalls. *Int J Rock Mech Min Sci* 40:455–471
- Boldini D, Guido GL, Margottini C, Spizzichino D (2017) Stability analysis of a large-volume block in the historical rock-Cut City of Vardzia (Georgia). *Rock Mech Rock Eng* 51:341–349. <https://doi.org/10.1007/s00603-017-1299-7>
- Crosta GB, Agliardi F (2003) A methodology for physically based rockfall hazard assessment. *Nat Hazards Earth Syst Sci* 3:407–422
- Descoedres F, Zimmermann TH (1987) Three dimensional dynamic calculation of rockfalls. In: *Proceedings 5th international congress on rock mechanics, Montreal (Canada), vol I*, pp 337–342
- Di Prisco C, Vecchiotti M (2006) A rheological model for the description of boulder impacts on granular strata. *Geotechnique* 56(7): 469–482
- Donald G, Hadly G (1987) Explanatory notes to the geological map of the Sahl Al Matran Quadrangle, sheet 26 C, Kingdom of Saudi Arabia, pp 1–24
- Dorren LKA, Berger F, Putters US (2006) Real-size experiments and 3-D simulation of rockfall on forested and non-forested slopes. *Nat Hazards Earth Syst Sci* 6:145–153. <https://doi.org/10.5194/nhess-6-145>
- Ferrari F, Giacomini A, Thoeni K (2016) Qualitative rockfall hazard assessment: a comprehensive review of current practices. *Rock Mech Rock Eng* 49:2865–2922. <https://doi.org/10.1007/s00603-016-0918-z>
- Fratini P, Crosta GB, Lari S, Agliardi F (2012) Probabilistic rockfall hazard analysis (Prha). *Landslides and engineered slopes: protecting society through improved understanding - proceedings of the 11th international and 2nd north American symposium on landslides and engineered slopes, 2012, 2*, pp 1145–1151
- Gallego JI, Margottini C, Spizzichino D, Boldini D, Abul JK (2022) Geomorphological processes and rock slope instabilities affecting the AIUla archaeological region. In: Lancellotta R, Viggiani C, Flora A, de Silva F, Mele L (eds) *Geotechnical engineering for the preservation of monuments and historic sites III. Proceedings of the third international ISSMGE TC301 symposium, Napoli, 22–24 June 2022*
- Gerber W (2019) *Naturgefahr Steinschlag – Erfahrungen und Erkenntnisse*. Eidg. Forschungsanstalt für Wald, Schnee und Landschaft WSL, Birmensdorf. WSL Berichte 74:149
- Gigli G, Casagli N (2011) Semiautomatic extraction of rock mass structural data from high resolution LIDAR point clouds. *Int J Rock Mech Min Sci* 48(2):187–198
- Guzzetti F, Crosta GB, Detti R, Agliardi F (2002) STONE: a computer program for the three-dimensional simulation of rockfalls. *Comput Geosci* 28(9):1081–1095
- ISRM (1978a) Suggested methods for the quantitative description of discontinuities in rock masses. *Int J Rock Mech Min Sci Geomech*
- ISRM (1978b) Suggested methods for determining hardness and abrasiveness of rocks. *Int Rock Mech Min Sci Geomech*
- ISRM (1978c) International society for rock mechanics commission on standardization of laboratory and field tests. *Int J Rock Mech Min Sci Geomech Abstr* 15:319–368. [https://doi.org/10.1016/0148-9062\(78\)91472-9](https://doi.org/10.1016/0148-9062(78)91472-9)
- ISRM (1981) Suggested methods for determining tensile strength of rock materials. In: Brown ET (ed) *Suggested method: rock characterization, testing and monitoring*. Pergamon Press, Oxford, p 211
- Loew S, Hantz D, Gerber W (2021) Rockfall causes and transport mechanisms: a review. In: *Treatise of geomorphology, 2nd edn*. Elsevier. <https://doi.org/10.1016/B978-0-12-818234-5.00066-3>
- Margottini C, Spizzichino D (2021) Traditional knowledge and local expertise in landslide risk mitigation of world heritages sites. In: Sassa K, Mikoš M, Sassa S, Bobrowsky PT, Takara K, Dang K (eds) *Understanding and reducing landslide disaster risk*. WLF 2020. ICL contribution to landslide disaster risk reduction. Springer, Cham. https://doi.org/10.1007/978-3-030-60196-6_34
- Margottini C, Spizzichino D (2022) Weak rocks in the Mediterranean region and surroundings: threats and mitigation strategies for selected rock-cut heritage sites. *Eng Geol* 297:106511. ISSN 0013-7952. <https://doi.org/10.1016/j.enggeo.2021.106511>
- Marija L, Martin Z, Jordan A et al (2022) Rockfall susceptibility and runoff in the valley of the kings. *Nat Hazards* 110:451–485. <https://doi.org/10.1007/s11069-021-04954-9>
- Moriset S, Gandreau D (2022) Dadan 2022–2030. *Conservation Management Plan*. AFALULA and RCU
- Ramsey BC (2020) OxCal. Available at: <https://c14.arch.ox.ac.uk/oxcal.html>. Accessed 29 Mar 2021
- Reimer P, Austin W, Bard E, Bayliss A, Blackwell P, Bronk Ramsey C, Talamo S (2020) The IntCal20 northern hemisphere radiocarbon age calibration curve (0–55 cal kBP). *Radiocarbon* 62(4):725–757. <https://doi.org/10.1017/RDC.2020.41>
- Spizzichino D, Margottini C, Chiessi V, Boldini D (2016) Assessment of the stability conditions of a large-volume sandstone block in the northern sector of the Siq of Petra. *Landslides and engineered slopes. Experience, theory and practice*, pp 1851–1858
- Thomas H, Kennedy M, Dalton M, McMahon J, Boyer D, Repper R (2021) The mustatils: cult and monumentality in Neolithic North-Western Arabia. *Antiquity* 95(381):605–626. <https://doi.org/10.15184/aqy.2021.51>

- Varnes DJ (1978) Slope movement types and processes. In: Schuster RL, Krizek RJ (eds) Landslide analysis and control. Transportation Research Board, Special report 176. National Academy Sciences, Washington, DC, pp 11–33
- Wahbi AM (2014) Sedimentological and stratigraphic studies of the cambro-ordovician succession in Northwest Saudi Arabia. Master Thesis of King Fahd University of Petroleum & Minerals. Dhahran

Open Access This chapter is licensed under the terms of the Creative Commons Attribution 4.0 International License (<http://creativecommons.org/licenses/by/4.0/>), which permits use, sharing, adaptation, distribution and reproduction in any medium or format, as long as you give appropriate credit to the original author(s) and the source, provide a link to the Creative Commons license and indicate if changes were made.

The images or other third party material in this chapter are included in the chapter's Creative Commons license, unless indicated otherwise in a credit line to the material. If material is not included in the chapter's Creative Commons license and your intended use is not permitted by statutory regulation or exceeds the permitted use, you will need to obtain permission directly from the copyright holder.





Refugees' Perception of Landslide Disasters: Insights from the Rohingya Camps in Cox's Bazar, Bangladesh

A. S. M. Maksud Kamal, Anika Samm-A, Bayes Ahmed, and Peter Sammonds

Abstract

The Kutupalong-Balukhali expansion Rohingya camp provides shelter to nearly one million refugees in a landslide-prone area. The Rohingyas seeking refuge in the camps deal with annual landslide events. This study looks into the existing risk perception of landslides in this shelter-seeking refugee community. Using a structured questionnaire, we conducted a face-to-face survey of 400 Rohingya people from six selected camps in March 2022. We collected information about refugees' perceptions towards landslide disasters, exposure to hazardous events, mitigation measures, preparedness knowledge, and risk communication. Descriptive statistical analysis was carried out to find out the existing condition of the camps. A regression analysis (Proportional Odds Model) was applied to determine the perception of people at risk. We found that exposure to previous landslides, mitigation measure quality, and emergency managers' roles were crucial in defining people's risk perception compared to the demographic characteristics of the Rohingya population. A combination of integrated mitigation, preparedness, and inclusion of laypeople in the overall management process would reduce landslide disaster risk inside the camps.

Keywords

Landslides · Proportional odds model · Rohingya · Bangladesh · Disaster risk reduction

A. S. M. M. Kamal · A. Samm-A
Department of Disaster Science and Climate Resilience, University of Dhaka, Dhaka, Bangladesh
e-mail: maksudkamal@du.ac.bd

B. Ahmed (✉) · P. Sammonds
Institute for Risk and Disaster Reduction (IRDR), University College London (UCL), London, UK
e-mail: bayes.ahmed@ucl.ac.uk; p.sammonds@ucl.ac.uk

1 Introduction

Landslide hazards have become an annual event for the hill tracts of Bangladesh in the monsoon. Kutupalong Rohingya camp lies in this hill tract regime (seismically active zone), providing shelter to conflict-fled Rohingya (Kamal 2013; Rahman et al. 2020). Despite being located in a landslide-prone site, an extensive area of the camp's terrain has been flattened to accommodate the enormous influx of these people. Rohingya cut the slopes and construct their bamboo-based makeshift shelters as they are allocated designated sites in the fixed camp. Unfortunately, these folks are contributing to more hazards. After the arrival of the Rohingyas in 2017, the camp repeatedly dealt with landslide events. There have been reports of landslide occurrence for four consecutive years (2018, 2019, 2020, and 2021) with casualties in the camp (Ahmed et al. 2018, 2020; ISCG 2018; Reliefweb 2018, 2019; Aziz 2021; Marie Giespie 2021). The camp population, already living in a humanitarian assistance area, is trying its best to face these monsoon monsters. During any hazard, lay people's perceptions or thoughts towards the hazard play a significant role in managing that disaster. Risk perception is considered one of the predominant factors that govern the response and coordination behavior of the affected community towards risk management authority (Tulloch and Lupton 2003). The perception is often regulated by the decisions taken by the policymakers, such as non-structural measures, zoning guidelines, and directives. Therefore, for the management to be effective, the managerial authority must also acknowledge the locals' feedback. However, perception analysis is a challenging task. It demands information on social bonding, socio-cultural identities, and socio-economic status as prerequisites. Some researchers believe that risk is associated with uncertainty in understanding and managing the risk (Kasperson et al. 1988; Beck 1992; Lash et al. 1996; Lash 2000).

2 Theoretical Framework

Risk perception is quite different from actual risk. While risk measurement involves quantitative (probability) or qualitative assessment, but risk perception ultimately depends on people's judgment. The judgment can vary from person to person (Sjöberg 2000). For example, lay people evaluate risk in a very different way than the experts. While it is common for experts to define risk in terms of the probability of hazard occurrence and the likelihood of its impact, the commoners mainly attribute this risk to their exposure history. While assessing the risk, experts remain very careful of the hazard, elements at risk, the vulnerability of the exposed community, and the assets; non-experts can choose to characterize the risk based on their appraisal of the hazard. This perception is often structured by the existing pattern of risk acceptance in society (Lichtenstein et al. 1978; Slovic and Fischhoff 1980; Siegrist and Gutscher 2006).

Understanding risk perception has become crucial because it can affect risk management efforts. Owing to the perceived risk, lay people can carry out self-evacuation or may shape their decision to cooperate with the responding agencies or emergency managers. Several researchers report that along with the hazard characteristic, Perceiver's particular characteristics define their reaction towards the risk (Renn and Levine 1991; Boholm 1998; Wachinger et al. 2013).

Social vulnerabilities are reported to direct risk perception, eventually reflecting lay people's capacity or willingness to practice adaptation strategies. People in direct exposure often perceive themselves in danger (Bickerstaff 2004). Demographic features of a community can be a mediating factor in risk perception. Age, gender, occupation, and education play a significant role in depicting risk perception. For example, people of different age groups (children, adolescents, and older adults) do not perceive the risk of a hazard similarly. Children and older adults may perceive a greater risk of hazards due to difficulties of mobilization. Unemployed and uneducated people perceive higher risk than employed and educated ones. Minority, cultural entity, and ethnicity can also affect risk perception (Flynn et al. 1994; Boholm 1998; Sjöberg 2000; Soori 2000; Greening et al. 2005; Burningham et al. 2008; Cutter and Finch 2008; Gyekye and Salminen 2009; Payne et al. 2017; Bhuiya et al. 2021).

Another determinant commonly found in several studies is the experience of previous hazards. The timeframe, recurrence, and severity of impact let the Perceivers rank their risk. People often rank their future risk as low of any dangerous hazard if they have experienced any negligible hazard, referred to as normalization bias (Mileti and O'Brien 1992).

Sometimes, Lay people who trust their preparedness, adaptation measures, and knowledge tend to perceive risk at lower levels. People's trust in emergency managers' efficacy

also plays the role of a significant component in shaping risk perception. Emergency managers' efforts, activeness, honesty, and willingness to help build the trust of non-experts in the experts (Bostrom 1997; Lazo et al. 2000).

The number of studies investigating risk perception for natural hazards is limited. Researchers are recently shifting their focus to risk perception-related studies for hydro-meteorological hazards. These studies assess how people perceive their risk towards the hazards and how much they are willing to act accordingly to combat that hazard (Damm et al. 2013; Hernández-Moreno and Alcántara-Ayala 2017; Oliveira et al. 2017; Qasim et al. 2018; Antronico et al. 2020). The affected population is reported to be concerned and attentive to landslide hazard information, yet they are less likely to consider mitigation measures despite perceiving a higher risk. A population that repeatedly encounters landslide hazards is found to be more risk-informed than others. Additionally, the influence of risk mitigation measures on perceived risk is evaluated (Calvello et al. 2016). However, people willingly living on the hill slopes miscalculate their risk due to the lack of awareness. Negligence or underestimation of the risk can be detrimental to risk management efforts.

However, previous studies have only conducted risk perception assessments focusing on these parameters. There should be an investigation into how risk perception for a specific hazard is influenced in an environment where the residents are already distressed about their day-to-day living. Risk perception in a shelter camp for forcibly displaced people can vary dynamically due to the different restricted lifestyle patterns (housing, education, food, nutrition, exposure to hazards, mitigation measures, etc.) Therefore, there is a scope for exploring how people perceive their risk for a hydro-meteorological hazard attributed to them due to the restricted shelter space, how they respond to that hazard and their attitude towards the emergency management authority.

3 Methodology

3.1 Study Area

The shelter camp situated in Bangladesh for the violence fled stateless Rohingya (Muslim minority) of Myanmar is our study area. Kutupalong-Balukhali expansion camp, Jamtoli camp, and Hakimpura camps are closely situated in Ukhiya, Cox's Bazar. These camps shelter over 958,000 Rohingya people (as of January 2023) (UNHCR 2023). Camps 9, 10, 17, and 20 of the Kutupalong Balukhali expansion area, camp no 14 of Hakimpura, and camp no 15 of Jamtoli are shortlisted for the investigation due to high to moderate landslide susceptibility (UNHCR 2019). These camps are located in the hilly areas of Bangladesh, where the slopes

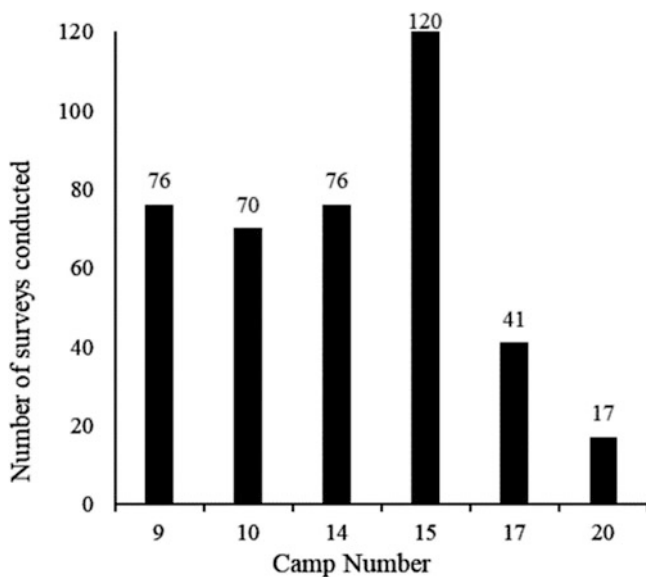


Fig. 1 Number of samples collected from different camps

become unstable during the monsoon. The camp population, repeatedly being affected by the landslide events, is trying its best to deal with the situation along with the emergency management authority. The area is already under the humanitarian response; therefore, the mitigation and response measures to landslide hazard is explicitly not similar to those of the regular residential area. Perception of the population and the determinants behind this perception should be identified to support better the management efforts required during the chaotic monsoon situation. Hence, the study aims to investigate this dimension.

3.2 Sample Size and Data Collection

The study conducted the face-to-face interview in March 2022 using a structured questionnaire among the Rohingya population (total of 400 surveys using random sampling technique) Fig. 1, where the population size of the six selective camps played a significant role. These six camps are selected because these camps have high to moderate landslide susceptibility, according to OCHA 2022. The questions and variables were developed through an extensive literature review. The study was also adjusted, modified, and adopted based on the local context. Since the study area is a specialized humanitarian support center, the investigation parameters are customized according to the requirement of the study. A pilot test of the questionnaire was carried out to establish the credibility of the variables. The questionnaire included dichotomous, multiple-choice, and statement-based questions with the response on the Likert Scale. An extensive literature review was employed to construct and support the questionnaire. The questions were amended, improved, and

adapted following the local context (forcibly displaced Myanmar nationals' shelter camp perspective). The questionnaire comprised dichotomous response questions, multiple-choice questions, Likert scale-based responses, and open-ended questions.

3.3 Data Analysis

IBM SPSS Statistics 23 was used for digitizing and analyzing the field records. Frequency analysis, Pearson's Chi-squared test, and ordinal regression analysis were run on the response records. Descriptive statistical analyses were mainly run to obtain a comprehensive idea of the existing situation in the camp area. Regression analysis was run to identify determinants that shape the risk perception of the camp area and finally quantify their significance.

Research ethics The respondents were fully aware of the purpose of the data collection. We collected verbal consent from them, and the survey was anonymous. No respondents' personal information will be disclosed from the researcher's end. Formal high-risk ethical approval, fieldwork permissions and risk assessments were conducted following the institutional procedures.

4 Results and Discussion

4.1 Demographic and Socio-economic Context

The study findings differ from any other risk perception study as the study area differs from any other ordinary place in Bangladesh. The camp administration regulates the demographic scenario in the camp area. All the respondents reside in makeshift houses made of bamboo and thatched roofs. However, there lies a difference in the house's location on the slope (Top, Middle, and bottom). There is negligible diversification in the occupational status as all the respondents depend on the relief activities allowed by the camp administration. All the respondents belong to the same ethnic group, as the camp provides shelter to a common group. The comprehensive demographic and socio-economic variables are present in Table 1.

4.2 Landslide Exposure and Emergency Management Scenario

The existing hazard scenario must first be characterized to comprehend the respondents' perceptions. Exposure to landslides, their intensity, and emergency management

Table 1 Demographic profile of the respondents

Variables	Class/Group	Percent	Mean	SD
Gender	Male (1)	57	1.42	0.49
	Female (2)	43		
	Others (3)	0		
Occupation	Unemployed (1)	85.3	1.27	0.74
	Seasonal day laborer (2)	7.5		
	Shopkeeper (3)	2		
	Others (4)	5.3		
Age	16–20 years (1)	5.8	3.05	1.33
	21–30 years (2)	36.8		
	31–40 years (3)	28.2		
	41–50 years (4)	11.5		
	51–60 years (5)	12		
	61–70 years (6)	4.8		
	71 and above (7)	1		
Location at slope	Top (1)	33	1.84	0.69
	Middle (2)	50		
	Bottom (3)	17		
Years of education	No Education (0)	85.8	0.22	0.58
	1–5 years (1)	7.2		
	6–10 years (2)	6.3		
	11–15 years (3)	0.8		

condition are presented in Table 2. The respondents identified multiple adverse consequences of the last landslide (Damage to home 92.7%, self-injury 0.5%, household member injury 6.3%). The respondents were asked to rate their pre-landslide preparedness knowledge and post-landslide response measure's effectiveness. They identify shelter and slope strengthening as their preparedness measure. In the during and post-landslide response activities, they are found to adopt multiple measures:

- removing the debris that entered their shelter (61.4%)
- relocating or shifting household materials (32.8%)
- informing about the damage in the CIC office (94%)
- self-restoration of slope (74.9%)

Each camp has a separate CIC office designated with the management activity of the camp. Upon reporting to the CIC office, the members visit the site and propose slope mitigation measures if necessary. Respondents identify CIC, IOM, SMEP, and different NGOs as emergency managers who work in collaboration.

4.3 Mitigation Measure Scenario

Several infrastructural mitigation measures have been taken throughout the camp to prevent landslides. Respondents identified the mitigation measures available on the slopes they live at. In some cases, the slopes were not fully protected

or given partial protection. Structural mitigation measures are Terrace of geotextile tubes, Terrace of geotextile tubes supported by bamboo fences, terrace of tin sheets supported by bamboo fences, layers of tarpaulin, plantation, terrace of bamboo fence sheets only, terrace of sandbags and concrete walls (Fig. 2).

4.4 Determinants of Risk Perception in the Proportional Odds Model

The dependent variable, respondents' perceived risk (response taken in ordinal format), was regressed against independent variables. The independent variables include age, years of education, gender, location of the shelter, the severity of the last landslide event, evacuation during the previous event, slope stabilization measure's coverage, mitigation measure material, structural measure building quality, activeness of emergency managers, adequacy of slope stabilization and shelter reinforcing material, trust in early warning) using Proportional Odds Model (POM). The independent variables were inspected for multi-collinearity. Only the "trust in early warning" variable showed this relation. The rest of the variables were used in POM. The results are exhibited in Table 3. The test result shows that variables like age, gender, years of education, occupation, location of the shelter, structural mitigation measure material (except terrace of sandbags), and sufficiency of shelter building materials are insignificant ($\text{sig } p > 0.05$). The severity of

Table 2 Landslide exposure and emergency management scenario

Variables	Class/Group	Percent	Mean	SD
Frequency of landslide hazard	Never (1)	0.5	3.15	0.58
	Once in the living period (2)	9.3		
	Once in every year (3)	64.8		
	Twice or more in every year (4)	25.5		
Severity of last event	Very low (1)	2	3.41	0.88
	Low (2)	12.5		
	Moderate (3)	36		
	High (4)	41		
	Very High (5)	8.3		
Accuracy of early warning during last landslide event	Very low (1)	0.3	3.38	0.61
	Low (2)	4.9		
	Moderate (3)	52.3		
	High (4)	41.5		
	Very High (5)	1		
Left house during landslide	Yes (1)	29.8	1.7	0.45
	No (2)	70.3		
Type of shelter facility	Authorized, mainly in learning centers and mosques (1)	8.8	1.9	0.28
	Self-managed in relative's house or secondary houses (2)	91.2		
Precautionary measure knowledge	Very low (1)	14.1	2.6	0.88
	Low (2)	24.4		
	Moderate (3)	49.5		
	High (4)	11.6		
	Very High (5)	0.5		
Effectiveness of post-landslide measures	Very low (1)	7.3	1.9	0.24
	Low (2)	19.5		
	Moderate (3)	54.9		
	High (4)	16.3		
	Very High (5)	2.0		
Precautionary measure taken	None	22	2.6	1.0
	Shelter strengthening	16.8		
	Slope strengthening	38.3		
	Both strengthening	23		
Activeness of emergency managers	Excellent (1)	1.5	3.72	1.14
	Very good (2)	18.4		
	Good (3)	18.4		
	Fair (4)	29		
	Poor (5)	32		
Adequacy of received slope building material	Excellent (1)	3.3	3.89	3.63
	Very good (2)	15.5		
	Good (3)	17.8		
	Fair (4)	15.3		
	Poor (5)	48.3		
Adequacy of received shelter building material	Excellent (1)	1.6	3.63	1.08
	Very good (2)	12.6		
	Good (3)	36.6		
	Fair (4)	18.9		
	Poor (5)	30.3		

the last event, evacuation during the previous event, slope stabilization measure's coverage, structural measure building quality, activeness of emergency managers, and adequacy of

slope stabilization material play an influential role in determining the risk perception of the Rohingya population of the camp.



Fig. 2 Different types of structural mitigation measures exist on the slopes of the camp area (a) terrace of geotextile tubes, (b) Terrace of geotextile tubes supported by bamboo fences, (c) terrace of tin sheets

supported by bamboo fences, (d) layers of tarpaulin, (e) plantation, (f) terrace of bamboo fence sheets only, (g) terrace of sandbags, and (h) concrete walls (double column width)

5 Conclusion

This study looked into how a group that already lives in a camp for people who had been forcibly displaced perceives the risk of landslides. The camp area is a landslide-prone region, so the displaced population knows this hazard. They are almost the annual victim of these slides in the monsoon time. Due to their residence in a restricted area, different demographic characteristics (occupation, years of education) are uniform for the entire population. Therefore, demographic characteristics are not playing the role of significant variables for defining risk perception. Although the camp is already run under some authorized monitoring, managerial

skills significantly impact how much risk people perceive for the landslides. People living on slopes with total coverage slope protection mitigation measures perceive risk at a lower level than the others. The residents are found to believe that the emergency managers are providing them with quite an accurate early warning. They are more likely to trust the authority responsible for emergency management. Besides this, the severity of the exposure to previous landslide events affects the population's perceived risk. People who had to leave their own makeshift houses during the landslide perceived the risk as higher than those who did not have to go. Living here with recurrent landslide events, people have started to adopt some adaptive strategies and response measures along with the initiatives taken by the managerial

Table 3 Determinants of risk perception in proportional odds model

Variables	Categories	Estimate	SE	Wald	Sig.	95% confidence interval		
						Lower bound	Upper bound	
Age		0.003	0.010	0.086	0.770	-0.016	0.022	
Gender (Female as reference)	Male	0.160	0.261	0.379	0.538	-0.350	0.671	
Years of Education		0.144	0.058	6.207	0.013	0.031	0.257	
Occupation (Others as reference)	Unemployed	0.806	0.599	1.811	0.178	-0.368	1.980	
	Seasonal Day laborer	0.254	0.693	0.134	0.714	-1.105	1.613	
	Shopkeeper	-0.371	1.037	0.128	0.720	-2.403	1.660	
Location of shelter (Bottom as reference)	Top	0.567	0.352	2.601	0.107	-0.122	1.257	
	Middle	0.254	0.338	0.566	0.452	-0.408	0.916	
Severity of last event (Very high as reference)	Very low	-4.550	1.189	14.639	0.000	-6.881	-2.219	
	Low	-5.306	0.723	53.888	0.000	-6.723	-3.889	
	Moderate	-3.296	0.577	32.644	0.000	-4.427	-2.165	
	High	-1.938	0.525	13.603	0.000	-2.968	-0.908	
Evacuation during last event	Yes	0.410	0.265	2.394	0.122	-0.109	1.246	
Slope mitigation measure coverage extent (Partial coverage as reference)	Full coverage	-1.011	0.442	5.229	0.022	-1.877	-0.831	
Mitigation measure material	Terrace of geo-textile tubes (No as reference)	Yes	-0.214	0.507	0.178	0.673	-1.207	0.779
	Terrace of geo-textile tubes supported by bamboo fences (No as reference)	Yes	-0.688	0.437	2.476	0.116	-1.545	0.169
	Terrace of tin sheets supported by bamboo fences (No as reference)	Yes	0.010	0.758	0.000	0.989	-1.475	1.495
	Layers of tarpaulin (No as reference)	Yes	-0.012	0.257	0.002	0.964	-0.516	0.493
	Plantation (No as reference)	Yes	-0.082	0.388	0.045	0.832	-0.843	0.678
	Terrace of bamboo fence sheets (No as reference)	Yes	-0.046	0.281	0.027	0.870	-0.597	0.505
	Terrace of sandbags (No as reference)	Yes	-0.534	0.260	4.218	0.040	-1.044	-0.024
	Concrete walls (No as reference)	Yes	0.022	0.471	0.002	0.963	-0.901	0.944
Structural measure building quality (Poor as reference)	Excellent	1.149	1.042	1.214	0.270	-0.894	3.192	
	Very good	0.225	0.793	0.081	0.777	-1.330	1.780	
	Good	0.106	0.678	0.025	0.875	-1.222	1.435	
	Fair	0.501	0.500	1.005	0.316	-0.479	1.481	
Activeness of emergency managers (Poor as reference)	Excellent	-6.701	1.629	16.921	0.000	-9.893	-3.508	
	Very good	-4.613	0.894	26.642	0.000	-6.364	-2.861	
	Good	0.415	0.556	0.557	0.456	-0.675	1.505	
	Fair	-0.407	0.414	0.967	0.325	-1.218	0.404	
Adequacy of slope stabilization (Poor as reference)	Excellent	-2.699	0.956	7.971	0.004	-4.573	-0.825	
	Very good	-1.873	0.656	8.156	0.004	-3.159	-0.588	
	Good	-1.433	0.519	7.621	0.006	-2.451	-0.416	
	Fair	0.668	0.383	3.045	0.081	-0.082	1.418	
Adequacy of shelter strengthening material (Poor as reference)	Excellent	-1.189	1.130	1.107	0.293	-3.404	1.026	
	Very good	-0.776	0.550	1.992	0.158	-1.853	0.301	
	Good	0.297	0.410	0.523	0.469	-0.507	1.101	
	Fair	0.083	0.393	0.045	0.833	-0.687	0.852	

Parallel line test: 0.0001, goodness-of-fit test of overall model: Deviance, p value = 1.00, Nagelkerke's R = 0.705, S.E: Standard error

authority. Based on the findings, the study would like to present some recommendations. These recommendations reflect the response from this study's respondents and the authors' observations. The camp residents are willing to participate in mitigation activities which can reduce the severity of their exposure to the hazard. These people should be actively integrated into the landslide risk management activities (mitigation-response-recovery) in a more organized way. Active community engagement in a more standardized way may add value to the response efforts of the camp's managerial authority, and these can eventually help this large, distressed population.

Acknowledgments The authors thank the Office of the Refugee Relief and Repatriation Commissioner (RRRC), Cox's Bazar, Bangladesh, for allowing fieldwork inside the Camp area.

Funding The Royal Society funded this study as part of the project, 'Resilient Futures for the Rohingya Refugees' (Award Reference: CHL\R1\180288), supported under the UK Government's Global Challenges Research Fund (GCRF).

References

- Ahmed B, Rahman MS, Islam R et al (2018) Developing a dynamic web-GIS based landslide early warning system for the Chittagong metropolitan area, Bangladesh. *Int J Geo-Inf* 7
- Ahmed B, Rahman MS, Sammonds P et al (2020) Application of geospatial technologies in developing a dynamic landslide early warning system in a humanitarian context: the Rohingya refugee crisis in Cox's Bazar, Bangladesh. *Geomat Nat Haz Risk* 11:446–468. <https://doi.org/10.1080/19475705.2020.1730988>
- Antronico L, De Pascale F, Coscarelli R, Gullà G (2020) Landslide risk perception, social vulnerability and community resilience: the case study of Maierato (Calabria, southern Italy). *Int J Disaster Risk Reduction* 46:101529. <https://doi.org/10.1016/j.IJDRR.2020.101529>
- Aziz A (2021) 4 children among 8 killed in Cox's Bazar landslides. Dhaka tribune
- Beck U (1992) Risk society: towards a new modernity
- Bhuiya T, Klares R, Conte MA, Cervia JS (2021) Predictors of misperceptions, risk perceptions, and personal risk perceptions about COVID-19 by country, education and income. *J Investig Med* 69:1473–1478. <https://doi.org/10.1136/jim-2021-001835>
- Bickerstaff K (2004) Risk perception research: socio-cultural perspectives on the public experience of air pollution. *Environ Int* 30:827–840. <https://doi.org/10.1016/j.envint.2003.12.001>
- Boholm Å (1998) Comparative studies of risk perception: a review of twenty years of research. *J Risk Res* 1:135–163. <https://doi.org/10.1080/136698798377231>
- Bostrom A (1997) Risk perceptions: "Experts" vs. "lay people". *Duke Environ Law Policy Forum* 8:101–113
- Burningham K, Fielding J, Thrush D (2008) "It'll never happen to me": understanding public awareness of local flood risk. *Disasters* 32: 216–238. <https://doi.org/10.1111/j.1467-7717.2007.01036.x>
- Calvillo M, Papa MN, Pratschke J, Nacchia Crescenzo M (2016) Landslide risk perception: a case study in southern Italy. *Landslides* 13:349–360. <https://doi.org/10.1007/s10346-015-0572-7>
- Cutter SL, Finch C (2008) Temporal and spatial changes in social vulnerability to natural hazards. *Proc Natl Acad Sci U S A* 105: 2301–2306. <https://doi.org/10.1073/pnas.0710375105>
- Damm A, Eberhard K, Sendzimir J, Patt A (2013) Perception of landslides risk and responsibility: a case study in eastern Styria, Austria. *Nat Hazards* 69:165–183. <https://doi.org/10.1007/s11069-013-0694-y>
- Flynn J, Slovic P, Mertz CK (1994) Gender, race, and perception of environmental health risks. *Risk Anal* 14:1101–1108. <https://doi.org/10.1111/j.1539-6924.1994.tb00082.x>
- Greening L, Stoppelbein L, Chandler CC, Elkin TD (2005) Predictors of children's and adolescents' risk perception. *J Pediatr Psychol* 30: 425–435. <https://doi.org/10.1093/jpepsy/jsi066>
- Gyekye SA, Salminen S (2009) Educational status and organizational safety climate: does educational attainment influence workers' perceptions of workplace safety? *Saf Sci* 47:20–28. <https://doi.org/10.1016/j.ssci.2007.12.007>
- Hernández-Moreno G, Alcántara-Ayala I (2017) Landslide risk perception in Mexico: a research gate into public awareness and knowledge. *Landslides* 14:351–371. <https://doi.org/10.1007/s10346-016-0683-9>
- ISCG (2018) Risk on flood and landslide for Kutupalong RC I HumanitarianResponse. In: Humanitarian Services, OCHA. <https://www.humanitarianresponse.info/ru/operations/bangladesh/infographic/risk-flood-and-landslide-kutupalong-rc>. Accessed 25 Dec 2021
- Kamal ASMM (2013) Earthquake risk and reduction approaches in Bangladesh. In: R. Shaw et al (eds) *Disaster risk reduction approaches in Bangladesh*, pp 103–130
- Kasperson RE, Renn O, Slovic P et al (1988) The social implications of risk: a conceptual framework. *Risk Anal* 8:177–187
- Lash S (2000) Risk culture. In: Adam B, Beck U, Van Loon J (eds) *The risk society and beyond: critical issues for social theory*. Sage, pp 47–62
- Lash S, Szerszynski B, Wynne B (eds) (1996) *Risk, environment & modernity*. Sage
- Lazo JK, Kinnell JC, Fisher A (2000) Expert and layperson perceptions of ecosystem risk. *Risk Anal* 20:179–194. <https://doi.org/10.1111/0272-4332.202019>
- Lichtenstein S, Slovic P, Fischhoff B et al (1978) Judged frequency of lethal events. *J Exp Psychol Hum Learn* 4:551–578. <https://doi.org/10.1037/0278-7393.4.6.551>
- Marie Giiespie (2021) Kutupalong chronicles: floods and landslides. In: *Chronicles from the Margins*. <https://cov19chronicles.com/kutupalong-chronicles-floods-and-landslides-kill-6-rohingya-refugees-and-leave-5-million-homeless-in-coxs-bazaar-bangladesh/>. Accessed 25 Dec 2021
- Mileti DS, O'Brien PW (1992) Warnings during disaster: normalizing communicated risk. *Soc Probl* 39:40–57. <https://doi.org/10.2307/3096912>
- Oliveira SC, Zêzere JL, Guillard-Gonçalves C, et al (2017) Surveying perception of landslide risk management performance, a case study in Norway. *Advancing Culture of Living with Landslides* 543–553. https://doi.org/10.1007/978-3-319-59469-9_47
- Payne BK, Brown-Iannuzzi JL, Hannay JW (2017) Economic inequality increases risk taking. *Proc Natl Acad Sci U S A* 114:4643–4648. <https://doi.org/10.1073/pnas.1616453114>
- Qasim S, Qasim M, Shrestha R, Nawaz Khan A (2018) Socio-economic determinants of landslide risk perception in Murree hills of Pakistan. *AIMS Environ Sci* 5:305–314. <https://doi.org/10.3934/ENVIRONSCI.2018.5.305>
- Rahman MZ, Siddiqua S, Kamal ASMM (2020) Seismic source modeling and probabilistic seismic hazard analysis for Bangladesh. *Nat Hazards* 103:2489–2532. <https://doi.org/10.1007/s11069-020-04094-6>

- Reliefweb (2018) Rohingya influx overview: key changes during 2018 monsoon season - Bangladesh | ReliefWeb. Cox's Bazar
- Reliefweb (2019) Bangladesh: Rohingya face monsoon floods, landslides - Bangladesh | ReliefWeb. In: OCHA Services. <https://reliefweb.int/report/bangladesh/bangladesh-rohingya-face-monsoon-floods-landslides>. Accessed 25 Dec 2021
- Renn O, Levine D (1991) Credibility and trust in risk communication. *Communicating Risks to the Public* 175–217. https://doi.org/10.1007/978-94-009-1952-5_10
- Siegrist M, Gutscher H (2006) Flooding risks: a comparison of lay people's perceptions and expert's assessments in Switzerland. *Risk Anal* 26:971–979. <https://doi.org/10.1111/j.1539-6924.2006.00792.x>
- Sjöberg L (2000) Factors in risk perception. *Risk Anal* 20:1–12. <https://doi.org/10.1111/0272-4332.00001>
- Slovic P, Fischhoff B (1980) Facts and fears: understanding perceived risk. In: Schwing RC, Albers WA (eds) *Societal risk assessment: how safe is safe enough?* Plenum Press, New York, pp 181–214
- Soori H (2000) Children's risk perception and parents' views on levels of risk that children attach to outdoor activities. *Saudi Med J* 21:455–460
- Tulloch J, Lupton D (2003) *Risk and everyday life*. Sage
- UNHCR (2019) Bangladesh: Cox's Bazar: Rohingya Refugee Crisis - Cox's Bazaar District: Landslide Hazard - Susceptibility Model Version 2.0 (17 June 2019), Bangladesh, ReliefWeb. <https://reliefweb.int/map/bangladesh/bangladesh-coxs-bazar-rohingya-refugee-crisis-coxs-bazaar-district-landslide-hazard>. Accessed 25 Oct 2022
- UNHCR (2023) Joint Government of Bangladesh - UNHCR Population map as of January 2023. <https://data.unhcr.org/en/documents/details/98700>. Accessed 24 Mar 2023
- Wachinger G, Renn O, Begg C, Kuhlicke C (2013) The risk perception paradox-implications for governance and communication of natural hazards. *Risk Anal* 33:1049–1065. <https://doi.org/10.1111/j.1539-6924.2012.01942.x>

Open Access This chapter is licensed under the terms of the Creative Commons Attribution 4.0 International License (<http://creativecommons.org/licenses/by/4.0/>), which permits use, sharing, adaptation, distribution and reproduction in any medium or format, as long as you give appropriate credit to the original author(s) and the source, provide a link to the Creative Commons license and indicate if changes were made.

The images or other third party material in this chapter are included in the chapter's Creative Commons license, unless indicated otherwise in a credit line to the material. If material is not included in the chapter's Creative Commons license and your intended use is not permitted by statutory regulation or exceeds the permitted use, you will need to obtain permission directly from the copyright holder.



KLC2020 Official Promoters

The Kyoto Landslide Commitment 2020 (KLC2020)

Kyoto 2020 Commitment for Global Promotion of Understanding and Reducing Landslide Disaster Risk

A Commitment to the Sendai Landslide Partnerships 2015–2025, the Sendai Framework for Disaster Risk Reduction 2015–2030, the 2030 Agenda Sustainable Development Goals, the New Urban Agenda and the Paris Climate Agreement-

KLC2020 Official promoters are public and private organizations who promote the Kyoto Landslide Commitment 2020 and provide financial support for the implementation of the KLC2020 activities including the Open Access Book Series “Progress in Landslide Research and Technology.”

Host organization

International Consortium on Landslides (ICL)/Nicola Casagli.

Public sectors: KLC2020 Official Promoters-public

International Unions/Associations, Governmental organizations, Universities and Research institutes

- The International Union of Geological Sciences (IUGS)/John Ludden

- The International Union of Geodesy and Geophysics (IUGG)/Kathy Whaler
- The International Association for the Engineering Geology and the Environment/Rafiq Azzam
- International Geosynthetics Society (IGS)/John Kraus
- Geological Survey of Canada, Natural Resources Canada, Canada/Daniel Lebel
- Faculty of Civil and Geodetic Engineering, University of Ljubljana, Slovenia/Matjaž Mikoš
- China University of Geosciences, Wuhan, China/Huiming Tang
- Department of Civil Engineering, National Taiwan University, Chinese Taipei/Shang-Hsien Hsien
- Institute of Rock Structure and Mechanics, the Czech Academy of Sciences/Josef Stemberk
- Institute of Cold Regions Science and Engineering, Northeast Forestry University/Wei Shan.

Private sectors: KLC2020 Official Promoters-private

Companies and corporation.

- Marui & Co. Ltd., Japan
- Nippon Koei Co., Ltd., Japan
- Ellegi srl, Italy
- Chuo Kaihatsu Corporation, Japan
- Godai Kaihatsu Corporation, Japan
- Kiso-Jiban Consultants Co., Ltd., Japan
- Kokusai Kogyo Co., Ltd., Japan
- OSASI Technos, Inc., Japan.



Geological Survey of Canada, Natural Resources Canada

GSC-Pacific Division

Geological Survey of Canada: Who We Are

The Geological Survey of Canada (GSC) is part of the Earth Sciences Sector of Natural Resources Canada. The GSC is Canada's oldest scientific agency and one of its first government organizations. It was founded in 1842 to help develop a viable Canadian mineral industry by establishing the general geological base on which the industry could plan detailed investigations. Throughout its long and colourful history, the GSC has played a leading role in exploring the nation.

Today, the GSC is Canada's national organization for geoscientific information and research. Its world-class expertise focuses on the sustainable development of Canada's mineral, energy and water resources; stewardship of Canada's environment; management of natural geological and related hazards; and technology innovation (Fig. A.1).

The GSC celebrated its 175th anniversary in 2017 which coincided with Canada's 150th anniversary of Confederation. The GSC co-leads the Canada-Nunavut Geoscience Office and works with dozens of universities and research institutes, industry organizations, other federal departments, provinces, territories and municipalities in Canada and across the world. In particular, we work closely with other geological survey organizations in Canada through the unique Intergovernmental Geoscience Accord.

Every year, we publish hundreds of maps, Open Files, peer-reviewed papers and other reports. Our scientists are recognized worldwide and sought after for their expert advice on locating mineral, energy and groundwater resources, reducing risk from natural hazards and reviewing environmental assessments.

GSC-Pacific Division
Vancouver, BC, Canada
e-mail: David.Huntley@nrcan-mcan.gc.ca

Strategic Priorities

The GSC has attempted to plot a course through this changing, uncertain world.

First, we identify three core areas of persistent scientific endeavour, which reflect stable, long-term needs of society:

- **Geological knowledge for Canada's onshore and offshore lands**
- **Geoscience for sustainable development**
- **Geoscience for keeping Canada safe.**

Next, we outline a new, fourth area of endeavour, Geoscience for society, which is the need to address the uncertainties of the changing world by expanding the reach and impact of geoscience knowledge in land-use decision making and in efforts to reduce the risk of disasters.

Finally, we recognize that our strength lies in a fifth area of endeavour, Our people, Our science, which we need to nurture to maintain a high-performing workforce capable of world leading innovative geoscience for the benefit of Canada.

(a) **Geological knowledge for Canada's onshore and offshore lands**

Geoscientific knowledge is fundamental to managing our onshore and offshore lands and their abundant resources. With its 10 million km² of onshore land and an additional 7 million km² of ocean estate, Canada is a vast country and a core mission of the GSC is to map and understand the land and its resources. Our Geo-mapping for Energy and Minerals (GEM) program continues to advance our knowledge of the North and by 2020 will complete a first mapping of surface geology at a coarse scale.

In the offshore lands, our geoscience knowledge also serves to confirm the farthest extents of the Canadian territory. Our joint program with Global Affairs Canada and Fisheries and Oceans Canada to delineate the outer limits of the continental shelf in the Atlantic and Arctic



Fig. A.1 Paleotsunami investigations in order to understand regional earthquake cycles and submarine landslide hazards

Oceans will reach a critical milestone in 2019. The program will file its Arctic submission under the United Nations Convention on the Law of the Sea (UNCLOS) (Fig. A.2).

(b) **Geoscience for sustainable development**

Finding new resources remains a major challenge. Many near-surface deposits have been discovered in Canada, but significant mineral resources remain to be found in less accessible regions and at depths below the surface. Finding new resources requires systematic, intensive and innovative methods to assess the mineral potential in remote locations.

It requires searching beneath overburden cover, imaging the 3-D structure of the earth and understanding the geological processes that lead to concentration of minerals in certain locations (Fig. A.3).



Fig. A.2 The GSC studies the sea floor of the Arctic to understand its geology and geohazards. Here a small craft surveys the bottom of Southwind Fjord (Baffin Island, N Nunavut)



Fig. A.3 GSC geologists near the Heiberg Formation in northern Ellesmere Island (NU) as part of the geo-mapping for energy and minerals program. This formation is the primary host of major gas accumulations in the Canadian High Arctic

For the Energy sector, the greatest challenge is in the transition to a low-carbon economy. Although global fossil fuel use is likely to continue to grow over the foreseeable future, the trend will likely be at a decreasing rate. Canada has an abundant supply of conventional and unconventional (oil sands and shale) oil and gas, so development in frontier areas is likely to be slow. In addition, the government has placed a moratorium on exploration activity in the Arctic offshore lands.

(c) **Geoscience for keeping Canada safe**

The GSC will continue to work on understanding how landscapes will change, how infrastructure will be affected and how resilience to climate change can be built into new infrastructure. Climate change will likely have a significant impact on the water cycle. GSC research will shed light on the risk to potable water supplies, hydroelectric power generation, and hazards from floods and drought (Fig. A.4).

(d) **Geoscience for society**

The scientific knowledge required to assess cumulative effects is broad. The complex interactions between land use, water management and waste management require an integrated approach at a landscape scale. The GSC is a national provider of information on both land (surficial and solid geology) and water, including the integration of surface water and groundwater into the complete water cycle (Fig. A.5).

The GSC recognizes that this area of endeavour involves inherent complexities and that our goals in this area will be to some degree aspirational. However, we will investigate new ways of planning our programs, undertaking our fieldwork, interacting with key stakeholders, and communicating our expert knowledge in ways that contribute positively to decision making about resource development.



Fig. A.4 The GSC conducts climate change studies, here documenting the effects of fast melting permafrost leading to extreme coastal erosion on Pelly Island, NT

(e) **Our people, Our science**

As a science organization within the federal government, the GSC's mandate is to conduct world-class science to inform public decision making. The Canadian government has articulated and adopted the principle of evidence-based decision making and reaffirmed the need for government science to be objective and non-partisan.

To remain at the leading edge, our scientists need to work with a variety of partners. We need to reinforce the central role that the GSC plays in the Canadian geoscience community by building networks of collaboration, fully participating in national geoscience initiatives, and advocating for Canadian geoscience at the international level (Fig. A.6).



Fig. A.5 The GSC conducts geohazard studies to reduce risks to people and infrastructure, here installing equipment to monitor landslide activity above a critical railway corridor in central BC



Fig. A.6 Among many celebratory activities for the GSC's 175th anniversary in 2017, the GSC held a Rock and Fossil Exhibit, at its site at the Bedford Institute of Oceanography (Dartmouth, NS), as part of a two-day open-house event, where more than 20,000 visitors participated

Moving Forward

Some of the objectives and goals that the GSC has set represent familiar territory for a national geoscience organization, but many others will pull us out of our comfort zone. We will take the time to better understand the challenges of delivering objective, nonpartisan science to support evidence-based decision making in Canada at a time of great technological and social change.

We will not be able to do this alone, so we look forward to strengthening our ties to other federal departments, provinces and territories, universities, Indigenous organizations, the private sector and civil society as a whole.

We ask all our stakeholders to contact us, to challenge us and, most importantly, to join with us to assure the future of Canada through thoughtful, respectful dialogue about the land we live on, its resources and its future (Fig. A.7).

Exploring Canada

Through its history, the GSC has been responsible for mapping the land mass of Canada, which supported the integration of the western provinces and northern territories into the country that we have today. The limit of Canada's offshore territory is still being extended today through surveys conducted by the GSC and the Canadian Hydrographic Service.

In more recent years, the GSC helped find the first economic diamond deposit in the Northwest Territories, leading

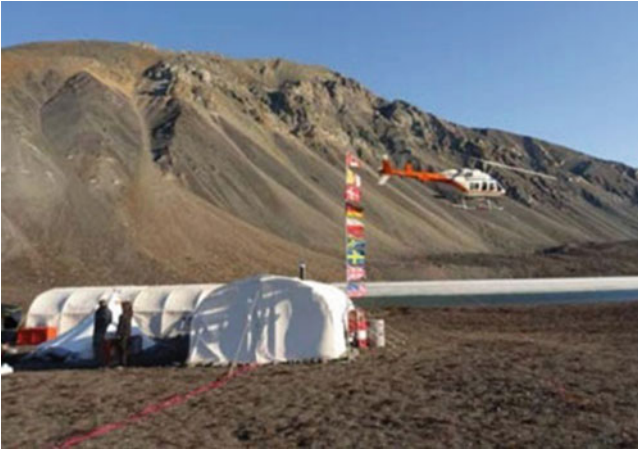


Fig. A.7 Joint Canadian/German (GSC/BGR) field mapping camp on northern Ellesmere Island, looking west as the fog covered sea ice of Yelverton Inlet, 2017

to the expansion of diamond mining in Canada. These are only a few of the key GSC achievements that have built our knowledge of Canada's lands and provided the building blocks of its natural resource economy.

Today, exploration of this vast land is still reaping its natural resource rewards. The search for natural resources is difficult, akin to looking for a needle in a haystack.

The GSC's GEM program is exploring vast tracts of Canada's North, a land mass roughly equivalent to the combined areas of Quebec, Ontario and Manitoba, to find the

"haystacks" with resource potential. This information is shared with the provinces and territories, as well as the private sector, so that the search for the "needles" can continue. The information is also critical to inform land-use planning.



In November 2016, the Royal Canadian Geographical Society (RCGS) awarded its prestigious Gold Medal to the GSC in recognition of the Survey's outstanding contribution to the development of Canada on the occasion of its 175th anniversary.



Faculty of Civil and Geodetic Engineering, University of Ljubljana

Matjaž Mikoš

Summary

The Faculty of Civil and Geodetic Engineering of the University of Ljubljana (UL FGG) covering engineering disciplines, including water science and technology, has been involved in landslide risk reduction activities at the national level in Slovenia (former Yugoslavia, until 1991) for decades. In 2008, UL FGG became an ICL Full Member and has gradually developed its ICL engagement. UL FGG has been awarded the title of the World Centre of Excellence (WCoE) in Landslide Risk Reduction for 5 consecutive periods (2008–2011, 2011–2014, 2014–2017, 2017–2020, 2020–2023). Together with the Geological Survey of Slovenia, UL FGG hosted in 2017 the 4th World Landslide Forum in Ljubljana, Slovenia.

UL FGG strongly supports diverse activities of the International Consortium on Landslides, Kyoto, Japan, and thus contributes to the 2030 Agenda for Sustainable Development, as well as to the Sendai Framework for Disaster Risk Reduction 2015–2030 (SF DRR). UL FGG was a signatory of the Sendai Landslide Partnerships 2015–2030, and is a dedicated official promoter of the Kyoto Landslide Commitment 2020, a SF DRR voluntary commitment by ICL.

In 2016, UL FGG started to host the University of Ljubljana UNESCO Chair on Water-related Disaster Risk Reduction (WRDRR), being still the only UNESCO Chair at this university, and one of a few in Slovenia. Among different activities, in 2022 the WRDRR Chair supported

the launching of the regional platform called Resili-Enhance for enhancing the resilience to disasters for sustainable development. UL FGG also supports activities of the Slovenian National Committee for UNESCO Intergovernmental Hydrological Programme (IHP), now working on the IHP-IX programme (2022–2029).

UL FGG is actively involved in numerous international (bilateral) and national research projects in the field of hydrology and hydraulic engineering, including topics such as landslide research, landslide risk mitigation, natural risk dialogue, and capacity building for society resilience.

In the field of capacity building, UL FGG offers several courses for graduate and postgraduate students in landslide mechanics and dynamics, landslide stabilization and landslide risk mitigation. In this article, a short overview of the past and current activities of UL FGG as ICL Full Member and KLC2020 Official Promoter is shown.

World Centre of Excellence on Landslide Risk Reduction and IPL Projects

WCoE Activities

The title of World Centre of Excellence (WCoE) on Landslide Risk Reduction is given to a governmental or non-governmental entity, which contributes to the landslide disaster risk reduction at a regional and/or global level in a specific unique field of expertise, as well as helps promoting International Programme on Landslides (IPL) and landslide research intellectually, practically and financially (<https://www.landslides.org/ipl-info/world-centre-of-excellence/>).

M. Mikoš
Faculty of Civil and Geodetic Engineering, University of Ljubljana,
Jamova c. 2, Ljubljana, Slovenia
e-mail: matjaz.mikos@fgg.uni-lj.si

UL FGG was granted the title of WCoE five consecutive times:

- WCoE 2008–2011 and 2011–2014: Mechanisms of landslides in over-consolidated clays and flysch.
- WCoE 2014–2017: Mechanisms of landslides and creep in over-consolidated clays and flysch.
- WCoE 2017–2020: Landslides in Weathered Flysch: from activation to deposition.
- WCoE 2020–2023: Landslides in Weathered Heterogeneous Sedimentary Rock Masses such as Flysch.

The research efforts at UL FGG were focused on:

- Mechanisms of triggering such landslides (mud flows), estimation of debris-flow magnitudes triggered as shallow or deep-seated landslides (debris slides), and triggering of shallow rainfall-induced landslides using advanced statistical methods.
- Field and laboratory investigations of suction in over-consolidated clays and flysch, such as to improve the understanding of softening in stiff over-consolidated clays and marls, using soil matrix suction as an indicator

for mudflow occurrence, and executing suction long-term monitoring of the Slano Blato landslide.

- Laboratory investigations of coarse debris-flow rheological parameters and soil–water characteristic curve of residual soil from a flysch rock mass.
- Mathematical modelling of debris flows (hazard assessment in deposition areas), using different numerical models and different digital terrain models.

The WCoE activities were financially supported by the Slovenian Research Agency through the Research Programme P2-0180 “Water Science and Technology, and Geotechnical Engineering: Tools and Methods for Process Analyses and Simulations, and Development of Technologies,” as well as by several national (Fig. A.8) and international (bilateral) research projects.

UL FGG and the Geological Survey of Slovenia jointly organized 4th World Landslide Forum (WLF4), in Ljubljana between May 29 and June 2, 2017. With over 600 participants from 49 countries and 5 international organizations, WLF4 was promoting the culture of living with natural hazards.

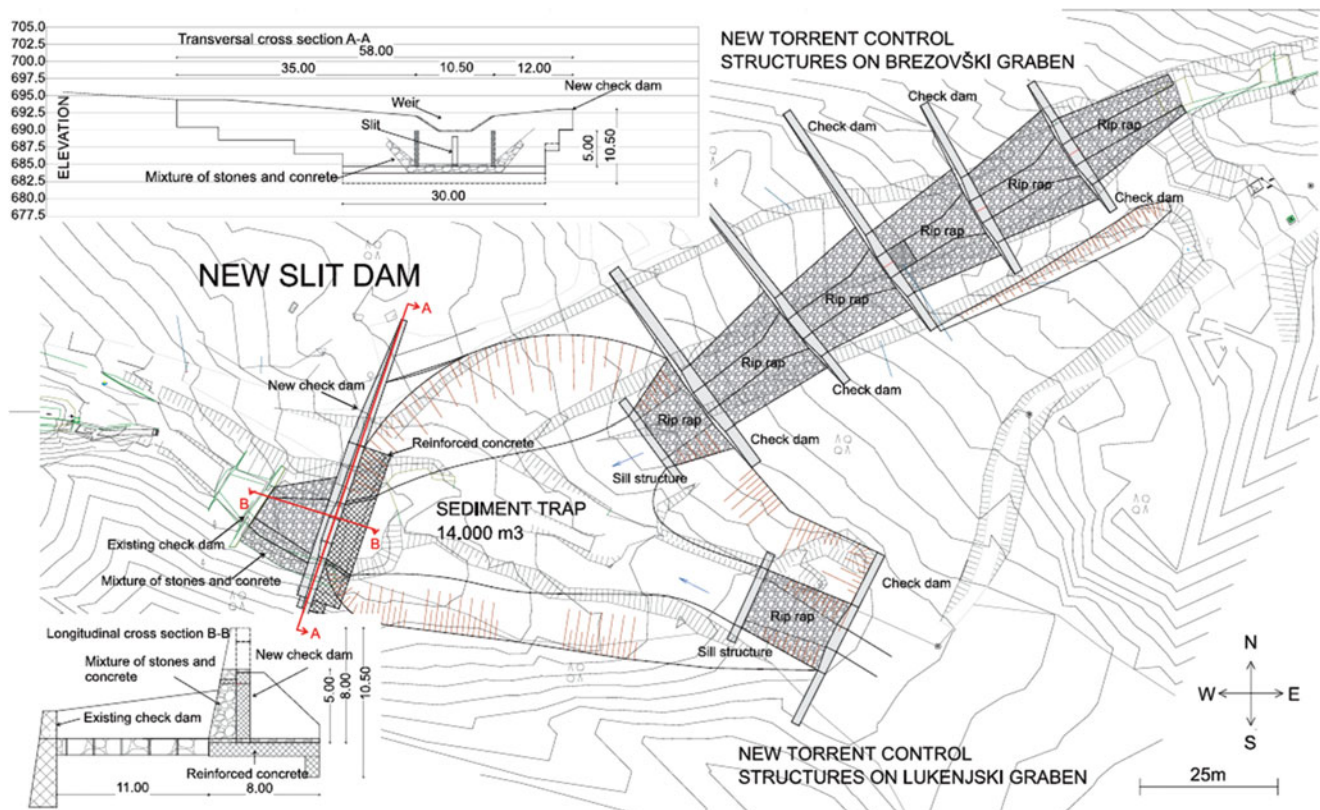


Fig. A.8 Technical countermeasures for future debris floods threatening the cabin station of the Kravvec ski area in N Slovenia (Fig. 7 in Bezak et al. (2019): An extreme May 2018 debris flood case study in

northern Slovenia: analysis, modelling, and mitigation. Landslides 17: 2373–2383, DOI 10.1007/s10346-019-01325-1)

IPL projects

An important ICL activity is IPL projects (<https://www.landslides.org/projects/ipl-projects/>). The IPL Evaluation Committee examines the submitted proposals of ICL members by carefully reading the written proposals and by listening to their presentations at annual ICL conferences. The initially accepted proposals by the IPL Evaluation Committee are discussed and then approved at the annual Board of Representatives meeting of ICL members (Annual Assembly). Finally, the IPL projects are approved annually by the Global Promotion Committee IPL-KLC. UL FGG has successfully submitted several proposals for IPL projects and has been so far actively involved in the following ones:

- IPL-151 Soil matrix suction in active landslides in flysch—the Slano Blato landslide case (2010–2012).
- IPL-225 Recognition of potentially hazardous torrential fans using geomorphometric methods and simulating fan formation (2017–2020).
- IPL-226 Studying landslide movements from source areas to the zone of deposition using a deterministic approach (2017–2020)—coordinated by the Geological Survey of Slovenia.
- IPL-261 World-wide-web-based Landslide Observatory (W3bLO) (2022–2024)

ICL Thematic and Regional Networks

Following the ICL Strategic Plan 2012–2021, several thematic networks and regional networks have been established (for an overview, see <https://www.landslides.org/projects/icl-networks/>).

Landslide Monitoring and Warning Thematic Network: LaMaWaTheN

In 2012, UL FGG proposed the ICL landslide monitoring and warning thematic network—almost 10 ICL members joined the initiative. The general objective of the proposed network was to compare experiences in the field of landslide monitoring and installed early warning systems for active landslides in various regions of the world. Lately, we contributed to the network activities by preparing practice guidelines on monitoring and warning technology for debris flows.

The idea of the network was partially taken over by the web database ICL World Report on Landslides (<https://www.landslides.org/projects/world-report-on-landslides/>), created to be a platform to share landslide case studies among the global landslide community, with monitoring and warning systems being a part of the platform.

ICL Adriatic-Balkan Network: ICL ABN

Jointly with other ICL members from Croatia and Serbia, in 2013, UL FGG proposed to establish an ICL Adriatic-Balkan Regional Network. Various network activities were proposed, the most active being the organization of biennial regional symposia on landslide risk reduction in the Adriatic-Balkan Region (called ReSyLAB). UL FGG supported the 1st Symposium in Zagreb (Croatia, 2013), 2nd in Belgrade (Serbia, 2015), 3rd in Ljubljana (Slovenia, 2017), 4th (Sarajevo, 2019), and 5th in Rijeka (Croatia, 2022).

In the last decade, UL FGG has signed bilateral research projects with the ICL members in the region: “Adriatic-Balkan Regional Network: Landslide Risk Mitigation for Society and Environment” (2012–13 with University of Belgrade, Serbia), “Study of landslides in flysch deposits: sliding mechanisms and geotechnical properties for landslide modelling and landslide mitigation SoLiFlyD” (2014–15 with University of Rijeka, Croatia), and “Laboratory investigations and numerical modelling of landslides in flysch deposits in Croatia and Slovenia” (2016–17 with the University of Rijeka, Croatia). This joint research has helped strengthen regional cooperation within the ICL ABN regional network.

Other ICL-Related International Activities

UL FGG served the ICL by taking different leading roles in the Consortium, i.e. UL FGG member served as Chair of IPL Evaluation Committee, twice as ICL Vice President, and was elected to Co-Chair and in 2021 to Chair of the IPL-KLC (<https://www.landslides.org/ipl-info/ipl-klc-globalpromotion-committee/>).

UL FGG has been strongly supporting the journal *Landslides: Journal of the International Consortium on Landslides*, published by Springer Nature (<https://link.springer.com/journal/10346>) since its launch in 2004. UL FGG works for the journal in the roles of reviewers and an associate editor, and regularly publishes its top research results in the journal, as well as disseminates information important for capacity building in landslide risk reduction—such as results of bibliometric studies on the journal *Landslides* and ICL books.

UL FGG also contributed to the two-volume set of *Landslide Dynamics: ISDR-ICL Landslide Interactive Teaching Tools (LITT)*, namely to Vol. 1: Fundamentals, Mapping and Monitoring by practice guidelines on monitoring and warning technology for debris flows (<https://www.springer.com/gp/book/9783319577739>), and to Vol. 2: Testing, Risk Management and Country Practices (<https://www.springer.com/gp/book/9783319577760>) by a state-of-the-art overview on

landslide disaster risk reduction in Slovenia, a study on two-dimensional debris-flow modelling and topographic data, and by study on intensity duration frequency curves for rainfall-induced shallow landslides and debris flows using copula functions.

UL FGG also contributed to the open-access book series “Progress in Landslide Research and Technology” Vol. 1 by a review article on the history of the International Programme on Landslides (IPL) (https://doi.org/10.1007/978-3-031-16898-7_3), an original article on the natural-hazard-related web observatory as a sustainable development tool (https://doi.org/10.1007/978-3-031-16898-7_5), and an original article on landslide research and technology in patent documents (https://doi.org/10.1007/978-3-031-18471-0_3).

University of Ljubljana UNESCO Chair on Water-related Disaster Risk Reduction (2016–2020 and 2020–2024)

Experiences and knowledge accumulated in the past decades at the Chair on Hydrology and Hydraulic Engineering at UL FGG in the field of (applied) hydrology in experimental basins, hydraulic engineering, landslide research, landslide risk reduction, and flood risk management, culminated in 2016 in the establishment of the UNESCO Chair on Water-related Disaster Risk Reduction (WRDRR Chair; www.unesco-floods.eu) at the University of Ljubljana. The UNESCO WRDRR Chair was positively evaluated by UNESCO in 2020 and prolonged for another 4 years (2020–2024). The Chair is associated to the university twinning and networking UNITWIN UNESCO—Kyoto University—ICL on “Landslide and Water-Related Disaster Risk Management”.

The UNESCO WRDRR Chair is involved into numerous international (bilateral) and national research projects. Their results are timely reported in scientific literature (<https://www.unesco-floods.eu/category/publications/>).

In 2022, the UNESCO Chair supported launching of the ResiliEnhance Program for enhancing the resilience to disasters for sustainable development (<https://unescochair-sprint.uniud.it/en/resilience-program/>). The program is at

the moment focused to Central and Eastern Europe, and supported by the Central Europe Initiative (CEI).

In 2022, the UNESCO Chair started to lead the University of Ljubljana project on Sustainable Development (2022–2025; www.unesco-floods.eu/ultra-pilot-projects/) to modernize university professional study programmes, especially in civil engineering, to increase students’ competences for sustainable development, including disaster risk reduction and resilience building.

UL FGG supports activities of the Slovenian National Committee for UNESCO Intergovernmental Hydrological Programme (www.ncihp.si)—focus of the activities is the development of the IHP-IX Programme (2022–2029).

Conclusions

UL FGG as one of World Centres of Excellence in Landslide Risk Reduction, hosts the UNESCO Chair on Water-related Disaster Risk Reduction. UL FGG strongly supports ISDR-ICL Sendai Partnerships 2015–2025 for global promotion of understanding and reducing landslide disaster risk, and its extension to 2030 and beyond: the Kyoto 2020 Commitment for Global Promotion of Understanding and Reducing Landslide Disaster Risk that that was signed in November 2020. UL FGG is proud to be its Official Promoter, and will specifically work for its Actions 2, 5, 6, 9 and 10.

This review article is intentionally written without a list of references to described activities. For this purpose, listed websites and links may be used.

The author wants to thank colleagues from UL FGG and University of Ljubljana, and from the ICL community for the past and long-lasting excellent cooperation with a joint vision to reduce landslide disaster risk.



China University of Geosciences, Wuhan

Huiming Tang, Changdong Li, and Qinwen Tan

Introduction

China University of Geosciences, Wuhan (CUG), founded in 1952, is a key national university affiliated with the Ministry of Education. It is also listed in the National “211 Project”, the “985 Innovation Platform for Advantageous Disciplines,” and the “Double First-class Plan”. CUG, featuring geosciences, is a comprehensive university that also offers a variety of degree programs in science, engineering, literature, management, economics, law, education, and arts. Its Geology and Geological Resources & Engineering have both been ranked as the national number one disciplines.

CUG has two campuses in Wuhan. The main campus is the Nanwang Mountain Campus, located in the heart of the Wuhan East Lake National Innovation Demonstration Zone, which is popularly known as China Optics Valley. The Future City Campus is located in the east of Wuhan and is 27 km from the main campus. These two picturesque campuses cover a combined area of 1,474,353 m². They are ideal places to study, work, and enjoy life. CUG owns a 4A-Level tourist attraction—the Yifu Museum. CUG also boasts four field training centers: Zhoukoudian in Beijing, Beidaihe in Hebei Province, Zigui in Hubei Province, and Badong in Hubei Province.

CUG has established a complete education system. As of December 2020, 30,239 full-time students, including 18,080 undergraduate students, 9302 master’s students, 1916 doc-

toral students, and 941 international students, have enrolled in its subsidiary 23 schools and 86 research institutes. CUG currently has a faculty of 1858 full-time teachers, among which there are 539 professors (11 of which are members of the Chinese Academy of Sciences) and 984 associate professors.

CUG is focused on fostering high-quality talent. Among its over 300,000 graduates, many have gone on to become scientific and technological elites, statesmen, business leaders and athletes. And they have made great contributions to the nation and society, represented by former Premier WEN Jiabao and 39 members of the Chinese Academy of Sciences and Chinese Academy of Engineering.

CUG has strengthened exchanges and cooperation with international universities. It has signed friendly cooperation agreements with more than 100 universities from the United States, France, Australia, Russia, and other countries. CUG has actively carried out academic, scientific, and cultural exchanges with universities around the world. There are about 1000 international students from more than 100 countries studying at CUG. It also sponsors more than 900 teachers and students to study abroad or conduct international exchanges and invites more than 400 international experts to visit, lecture, and teach at CUG every year. In 2012, CUG initiated and co-established the International University Consortium in Earth Science (IUCES) with 11 other world-renowned universities. IUCES is committed to promoting the common development of geosciences education and scientific research through resource sharing, exchange, and cooperation among its member institutions. In addition, CUG has partnered with Bryant University from the USA, Alfred University from the USA, and Veliko

H. Tang · C. Li · Q. Tan
China University of Geosciences, Wuhan, P.R. China
e-mail: tanghm@cug.edu.cn

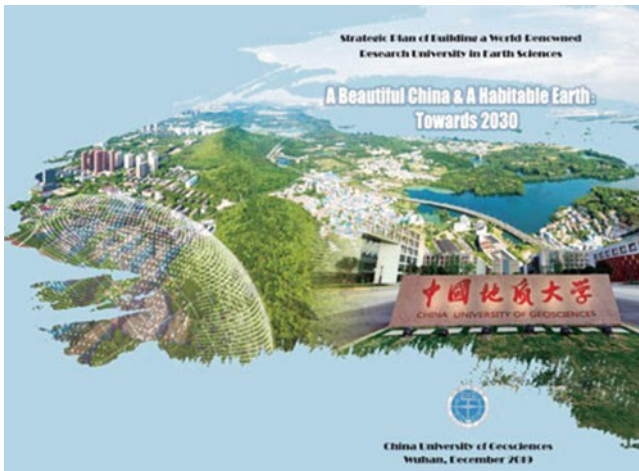


Fig. A.9 Strategic plan of building a world-renowned research university in earth science

Turnovo University from Bulgaria in establishing three Confucius institutes on their campuses (Fig. A.9).

Strategic Plan of Building a World-Renowned Research University in Earth Sciences: A Beautiful China and a Habitable Earth: Towards 2030

CUG reviewed and approved Strategic Plan of Building a World-Renowned Research University in Earth Sciences on December 25 of 2019.

Themed “A Beautiful China & A Habitable Earth”, the Plan depicts the blueprint of the second goal of the “three-step strategic goals”, which is to build a world-renowned research university in Earth Sciences by 2030 based on the attained goal of developing CUG into a “high-level university with first-class Earth Sciences and coordinated development of multi-disciplines”.

According to the Plan, our education missions are: Remaining true to CUG’s core value of “seeking harmonious development between man and nature” we are committed to cultivating innovative talents who have lofty morality, solid foundation, and profound expertise and who pursue the unity of knowing and doing. We should provide personnel support and endeavor to innovate, apply and spread knowledge in order to provide theories, technologies, and approaches for the construction of a Beautiful China and a Habitable Earth. We should strive to optimize governance, reform culture, and fully invigorate the vitality of running a university. We should provide our service to the construction of an innovative country and to the promotion of a harmonious co-existence between man and nature. We should provide our service to the people and the governance of China. We should provide our service to the consolidation and

development of the system of socialism with Chinese characteristics. We should provide our service to the reform and opening up and to the construction of socialist modernization.

According to the Plan, our endeavoring goals are: By 2030, we will have built a world-renowned research university in Earth Sciences, whose main indexes will have reached or nearly reached the level of other world-class universities. To upgrade CUG into a world-class university, we will endeavor to make the discipline of Earth Sciences rank top in the world and forge boldly ahead in competition to improve the quality of other disciplines of CUG. We will assemble a contingent of teachers and researchers with international competitiveness and influences to build a university with Chinese characteristics and superiority. We will build a world-class university that will be fully engaged in international exchange and cooperation and that will achieve educational, academic, cultural, and administrative excellence.

Outstanding Recent Achievements

In recent years, CUG has achieved significant progress in the research fields of geohazards, water resource, geochemistry, paleontology, geodetic surveying and lunar exploration program, etc. To keep to the theme of KLC2020, recent achievements on geohazards researches of CUG are focused and introduced.

(a) Approval of National Observation and Research Station for Geohazards in the Three Gorges Reservoir Area, Hubei

CUG was newly approved **National Observation and Research Station for Geohazards in the Three Gorges Reservoir Area, Hubei**. This station, founded and administrated by Prof. Huiming Tang, is responsible to carry out field observations and scientific research on geohazards in condition of reservoir operation.

The central site of the station is located in Badong County of the Three Gorges Reservoir area (hereinafter abbreviated as the TGR area), and a larger monitoring network of multiple sites has been established, including the geohazard field test site for the Majiagou landslide, Zigui County, and systematic geophysical monitoring station for the whole TGR area, etc.

The Badong field site (also named Badong in-situ large-scale experimental station) is located in the Huangtupo landslide area, which has been recognized the largest reservoir landslide by volume in the TGR area. The field site consists of a tunnel complex and a series of monitoring systems (Fig. A.10). The tunnel complex, built in the Huangtupo riverside sliding mass #1, consists of a main tunnel with a length of 908 m and a width of 5 m,

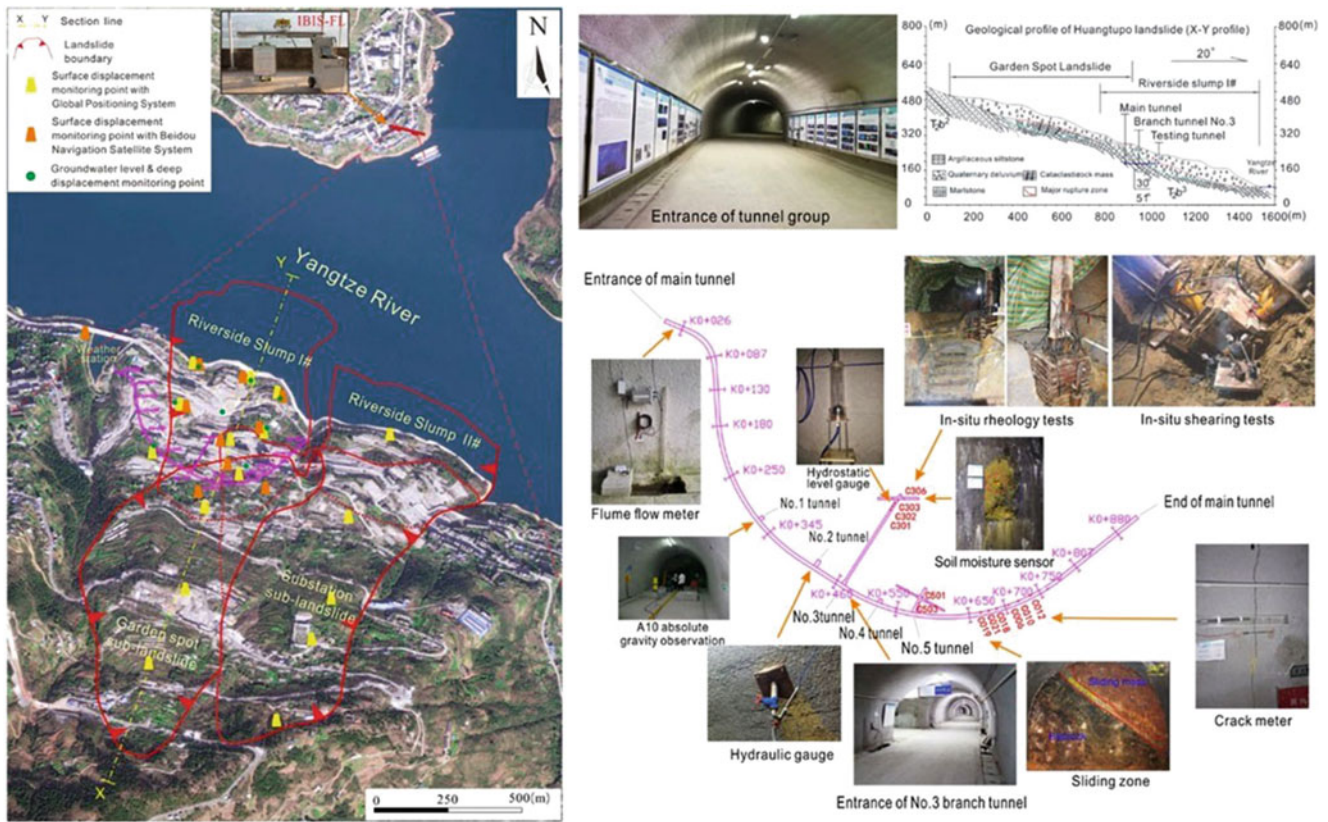


Fig. A.10 Badong in-situ large-scale experimental station of the National Observation and Research Station for Geohazards in the Three Gorges Reservoir Area, Hubei

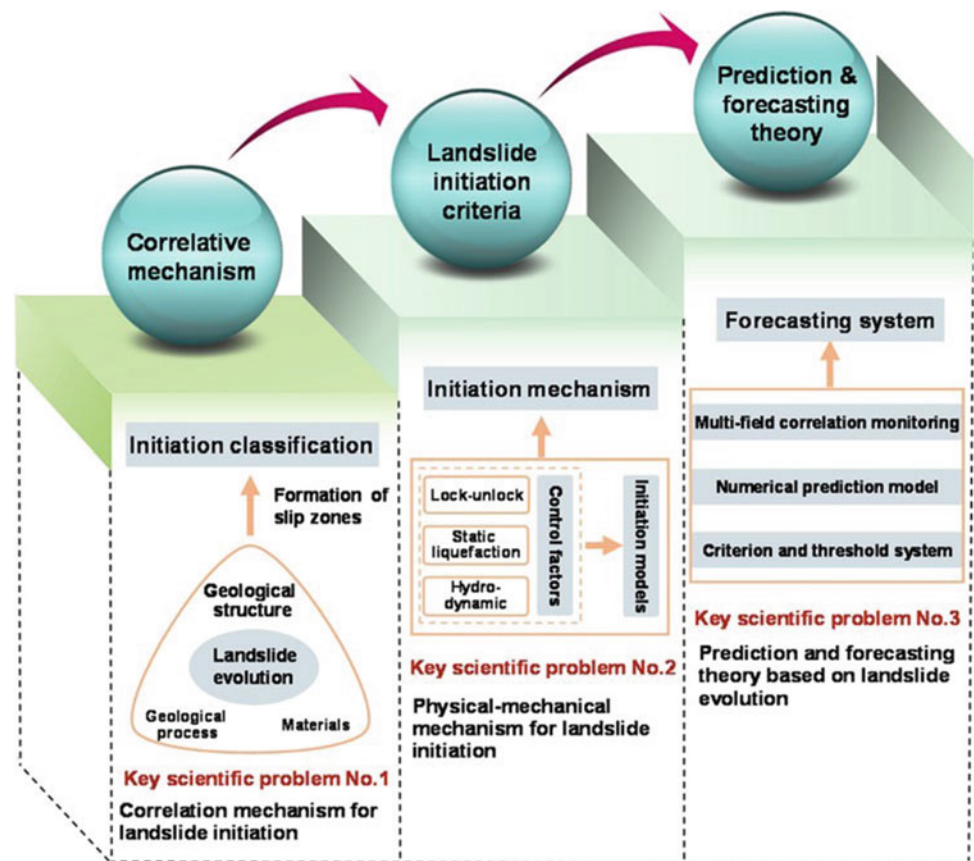
five branch tunnels (5 m to 145 m long, 3.5 m wide), two test tunnels, and 35 observation windows. The test tunnels exposed the sliding zones of the landslide, facilitating their direct observation and the execution of scientific experiments, such as large-scale in-situ mechanical tests and deep deformation monitoring. The monitoring systems measure deformation as well as hydrologic, meteorological and hydro-chemical variables. The deformation system is composed of a slope surface displacement measurement unit and an underground displacement measurement unit. The slope surface displacement unit includes a number of GPS (Global Positioning System) and BDS (BeiDou Navigation Satellite System) measurement points, as well as an IBIS-FL (Interferometric Radar) monitoring system (Fig. A.12). The underground displacement unit includes nine deep inclinometer boreholes, a number of crack meters installed on the ground and the walls of tunnels, and many hydrostatic level gauges that measure the settlement of the tunnels in the sliding mass. The hydrologic system includes a number of devices that allow for observation of the water level of the Yangtze River, the ground water level and water discharge of the tunnels (Fig. A.12). A small meteorological station is

located on the landslide and provides rainfall data. So far, multiple and massive data have been collected for the landslide area since the year 2012, when the field site was constructed; over 10,000 people with a variety of geology-related backgrounds from >20 countries have visited this experimental station.

(b) **Approval of the Basic research on the prediction and forecasting of major landslides program supported by the Major Program of NSFC**

CUG was approved the **Basic research on the prediction and forecasting of major landslides program** (2021–2025), supported by the Major Program of the National Natural Science Foundation of China. The program was designed for the prediction and forecasting of major landslides, with the concentration on the core scientific problems of landslide evolution process and physical-mechanical mechanism. Three key scientific problems, including correlation mechanism for landslide initiation, physical-mechanical mechanism for landslide initiation, and prediction and forecasting theory based on landslide evolution were proposed. Five topics were set up to achieving those objectives. Topic 1 was proposing the initiation classification of major landslides based on large field test platform,

Fig. A.11 Scientific thought for the implement of research



with the adoption of field prototype test and other technical means. Topics 2-4 aimed to reveal the physical and mechanical mechanism of locked-segment dominated landslide, static liquefaction loess landslide and hydrodynamic pressure-driven landslide, and to establish the corresponding landslide initiation criteria, respectively. Topic 5 was responsible to established the prediction mode and real-time forecasting system. Ultimately, the landslide prediction and forecasting theory based on the evolution process and physical-mechanical mechanism would be put forward. The scientific thought for the implement of research is exhibited in Fig. A.11.

The implementation of the research is respected to lay the geological, mechanical and physical foundation for the above three types of landslide prediction, and to substantially promote the research on landslide prediction.

Figure A.12 shows the old Badong county, situated in the Huangtupo landslide area, and the exposures of the main rupture zones are now more than 50 m below the water surface of the Three Gorges Reservoir (Tang et al. 2015a). During the second relocation from 1982 to 2003, the county moved from Xinling town to the Huangtupo landslide area (Gong et al. 2021). A series of investigations were conducted during that period, and the new county area was further

confirmed to be on the site of an ancient landslide then (Gong et al. 2021). Huangtupo landslide is developed in the Middle Triassic Badong Formation strata, within which interbedded strata structures are often observed, and many geohazards developed. The material composition of the Huangtupo landslide includes mudstone, pelitic siltstone, and argillaceous limestone (Tang et al. 2015b). Multiple slumps formed the complex mass at least 4000 years ago (Tang et al. 2015b). The elevation of the crown of the landslide is about 600 m asl., while its toe varies from 50 to 90 m, submerged in the Yangtze River. The composite landslide covers an area of 1.35 km², and its volume of nearly 70 million m³ makes it the largest reservoir landslide in China (Tang et al. 2015b). Considering the risk of landslide reactivation by long-term reservoir operation and human activities, the drainage system and the anchored defense structures along its leading edge were constructed to control the landslide. Huangtupo demonstration base was designed and constructed in 2012, during the third relocation period from 2007 to 2017 (Gong et al. 2021). At that time, some Badong county residents still lived in the Huangtupo area, facing the unsure threat. The old giant landslide is in need of further research to ensure its safety as well as provide access for landslide hazard study. The demonstration base was in great request. With the building and development of the



Fig. A.12 Photo of old Badong County, showing the populated area built on the Huangtupo landslide (Tang et al. 2015a)

demonstration base, Over 10,000 people with various geology-related backgrounds from more than 20 countries have visited. A national observation station was also settled rely on the base in 2020.

Gong W, Juang CH, Wasowski J (2021) Geohazards and human settlements: Lessons learned from multiple relocation events in Badong, China – Engineering geologist's perspective. *Eng Geol* 285:106051

References

- Tang H, Li C, Hu X, Wang L, Criss, R, Su A, Wu Y, Xiong C (2015a) Deformation response of the Huangtupo landslide to rainfall and the changing levels of the Three Gorges Reservoir. *Bull Eng Geol Environ* 74 (3):933–942
- Tang H, Li C, Hu X, Su A, Wang L, Wu Y, Criss R, Xiong C, Li Y (2015b) Evolution characteristics of the Huangtupo landslide based on in situ tunneling and monitoring. *Landslides* 12(3):511–521



Department of Civil Engineering, National Taiwan University

Department of Civil Engineering, National Taiwan University

Introduction

National Taiwan University (NTU) was originally established in 1928, when Taiwan was under Japanese rule, as Taihoku Imperial University. The current name dates back to 1945. As Taiwan's oldest and most prestigious university, we are also the largest comprehensive higher education institution (HEI) in the country. The academic freedom that we cherish and our excellent faculties attract both domestic and international students. Throughout our 90-year history, we have nurtured many talents, including leading academics and leaders in the public and private sectors. Our campus is vast, and spans across multiple locations, including Taipei, Yilan, Hsinchu, Yunlin, and mountainous areas in central Taiwan—accounting for nearly 1% of Taiwan's total land area. This provides teachers and students with an environment rich in biological and ecological diversity.

As the leading university in Taiwan, we are strongly committed to social responsibility as we strive to drive sustainable development and influence positive change in society. This was also reflected in the first University Impact Rankings launched in 2019 by Times Higher Education (THE), which measure the contributions of HEIs to the United Nations' Sustainable Development Goals (SDGs). We were ranked 70th in the world overall, and 1st in the world for SDG16: Peace, Justice, and Strong Institutions. Starting from creating a sustainable culture on campus, we

aim awareness about sustainability throughout the university, through innovative teaching and research, environmental protection and recycling efforts, and a school administration that supports equality and wellbeing. Our sustainability efforts extend beyond our campus through industry-academia collaborations and service teams deployed to remote areas. In the near future, we will continue to reinforce the spirit of innovation and sustainability thinking among all faculty members and students. We will also continue our efforts to address economic, environmental, and social challenges through interdisciplinary collaboration, as we create connections between the local and the international community. The Department of Civil Engineering (Fig. A.13) can be regarded as the root of The College of Engineering. The early civil engineering education covers a wide range of professions. With the development and differentiation of various social industries, some fields have gradually separated and established specialized departments. We have also moved on, combining different fields and top-notch technology to remain as the leader of the tide.

Civil engineering is inseparable from the development of human civilization. From the beginning of civilization, all man-made structures have enmeshed and highlighted the value of civil engineering. NTU Civil Engineering is no exception. From the Department of Civil Engineering of the Imperial College of Taipei to the National Taiwan University Department of Civil Engineering today, the majority of Taiwan's significant constructions is and will always be our finest gallery.

In National Taiwan University, you will obtain high-quality guidance in and out of the classroom. Academic resources in the classroom and sports culture clubs, various student activities throughout the year, will bind you together

Department of Civil Engineering, National Taiwan University
Department of Civil Engineering, National Taiwan University, Taipei,
Taiwan
e-mail: louisge@ntu.edu.tw

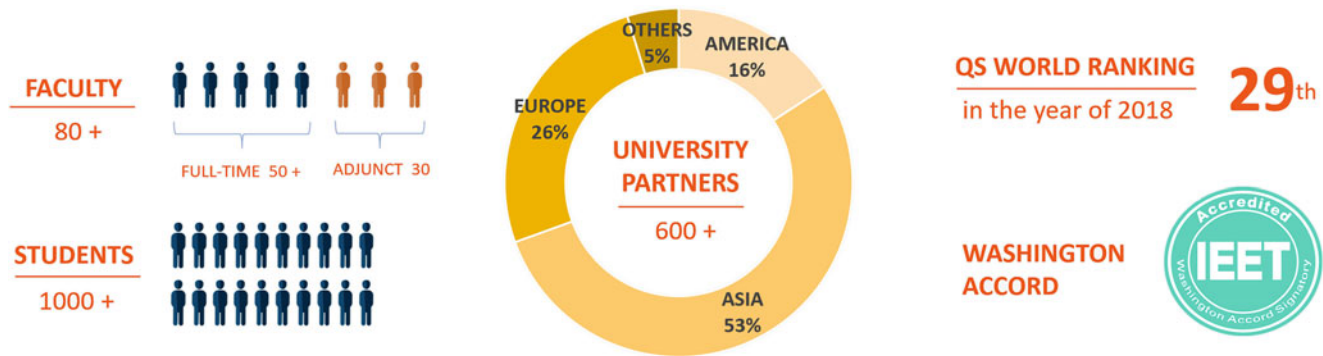


Fig. A.13 Quick facts of the Department of Civil Engineering

with peers of the same dream. These friends may also be partners that can help you in future careers. If you are willing to take civil engineering as a career and take on the challenges and step forward as a team, then listen to your inner call, join us, and let us stride ahead hand in hand (Fig. A.14).

Outstanding Recent Achievements

Mitigating the Impacts of Natural Disasters via Cutting Edge Technology

Taiwan is located in the Circum-Pacific seismic belt, with many active faults and frequent typhoons. Due to the effects of climate change, extreme rainfall events that used to occur once in a century are now becoming more frequent, exacerbating the threat of landslides and debris flows. The prevention and mitigation of natural disasters such as earthquakes and flooding have therefore become a priority for the twenty-first century.

- (a) **Earthquake Early Warning Systems: gain valuable response time**



Fig. A.14 Life beyond Classroom

For most natural disasters, potential losses to life and property can be mitigated through early warning and prevention. After the earthquake disaster of September 21st, 1999, building safety inspections needed to be conducted all across Taiwan. Our faculty and students with expertise in civil engineering and geology were quick to respond to this urgency, working closely with the National Center for Research on Earthquake Engineering to help the government improve the earthquake resistance standards and test specifications. Moreover, they proposed a more elaborate system for earthquake damage and liquefaction assessment, and conducted a complete review and classification of the earthquake risk tolerance for all areas in Taiwan. The team also developed new disaster prevention technologies. One of the most significant contributions was to assist the public high (vocational) schools around Taiwan with assessments of the earthquake resistance and reinforcement needs of old buildings. In the numerous earthquakes that have since occurred, the effect of these reinforcements has become apparent. The stronger earthquake resistance of these buildings has improved safety for 2.65 million teachers and students around Taiwan (Fig. A.15).

Our school has also developed technology to monitor the status of bridges with high traffic volumes. This optical fiber monitoring system will emit a warning whenever poor conditions are recorded, prompting an early response from management that can prevent a disaster from happening. When bridges in remote areas are damaged, a lightweight bridge developed by NTU out of composite materials can be assembled by residents in short time. In this way, access to affected areas can be quickly restored, and disaster relief provided more efficiently. In the event of an earthquake, Taiwan's citizens will immediately receive an emergency alert by text message. This warning system, which was developed by Professor Wu, Yih-Min at our Department of Geosciences, analyzes the properties

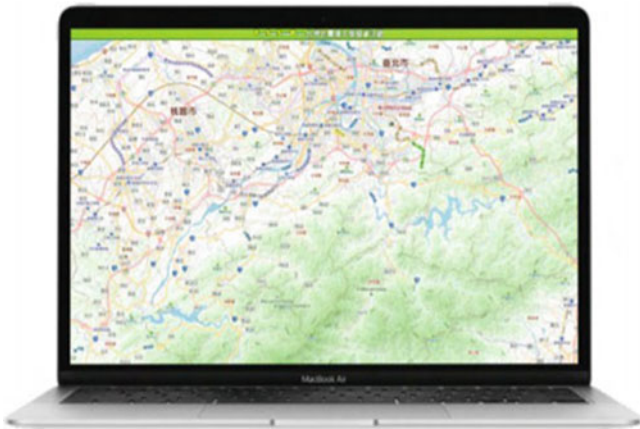


Fig. A.15 Taiwan Earthquake Loss Estimation System (TELES)

of a P-wave within three seconds after detecting the wave so that it can issue an alert to citizens more than 10 s before the S-wave, which is most likely to cause damage arrives. This early warning system is accurate and fast, giving people valuable seconds to escape to safety. Because it is also much cheaper to manufacture network of multiple sites has been established, including the geohazard field test site for the Majiagou landslide, Zigui County, and systematic geophysical monitoring station for the whole TGR area, etc. than previous seismographs, it could be rapidly rolled out to several hundred elementary and junior high schools, ensuring better protection of our country's younger generation. Moreover, this system has been successfully introduced in other earthquake-threatened countries, such as Indonesia, India, Vietnam, Nepal, and Mexico.

(b) **After the Flood: Rapid Mobilization and Improved Ability to Provide Relief**

Another critical area is flood disaster prevention. Also here, our faculty and students are actively involved in key activities ranging from early warning and response during the disaster, to raising the awareness of, and capability for, disaster prevention among citizens more generally. Our Center for Weather Climate and Disaster Research comprises experts in meteorology, hydrology, bioenvironmental engineering, and geology etc. This

center helped New Taipei City and Keelung City establish an extreme weather and flood monitoring and warning system. Other projects include combining advanced deep learning with the analysis of radar data, which allows for closer monitoring of rainfall data in hydrologically sensitive areas. The improvement of flood models increases the accuracy of flood warnings and provides disaster prevention units with valuable information for them to rapidly formulate response strategies. From past experiences outside of Taiwan, we know that self-help and mutual support account for the largest share of the relief effort (90%) in the event of a disaster. In other words, even if flood warnings are effective, people in the affected area still need to be able to take own measures to protect themselves. At NTU, we actively participate in the community-level disaster relief preparations around the country, as well as in the training of disaster relief officers. Our experts provide citizens with the most up-to-date knowledge in disaster prevention, operate independent disaster relief systems, and evaluate the safety of shelters. These efforts contribute to the resilience and ability of local communities to mitigate impact, helping them recover more quickly. A plan for how to improve the disaster relief ability in the country proposed by our experts is another example of how we help make sure that the best disaster response capacity is in place. After improving the ability to respond to disasters, NTU's team also contributed to disaster prevention infrastructure around Taiwan, such as seismic isolation technology for buildings and equipment, or detention ponds in communities at risk. Our work and efforts in these areas help protect lives and property. As climate change continues to impact the world, we hope to leverage our technologies and expertise in these domains even further, and help strengthen the capacity to prevent and withstand natural disasters throughout the world.



Institute of Cold Regions Science and Engineering, Northeast Forestry University

Wei Shan and Ying Guo

Introduction

Institute of Cold Regions Science and Engineering of Northeast Forestry University (ICRSE-NEFU) is committed to the environmental geology and engineering geology of high latitude permafrost region and deep seasonal frozen area under the background of climate change, and attaches importance to the combination of basic research and applied research. With undergraduate, master, doctor, postdoctoral professional training system and standards, ICRSE-NEFU initiated “Geological environment risk research plan for permafrost degraded areas in Northeast China (GERRP)”. With the support of the Chinese government, “Field scientific observation and research station of the Ministry of Education—Geological environment system of permafrost area in Northeast China (FSSE-PFNEC)” was established. Its observation stations cover all kinds of permafrost areas in Northeast China. At the same time, in order to develop and transfer technologies related to environmental governance and infrastructure construction in permafrost regions, “Provincial Collaborative Innovation Centre, Environment and road construction & maintenance in permafrost area of Northeast China (PCIC-PFER)” was established. Over the years, ICRSE-NEFU have continuously established cooperation with academic institutions and organizations at home and abroad, held various academic exchanges and regularly held “Academic Seminar on Engineering Geology and Environmental Geology in the Permafrost Along the Sino-Russian-Mongolian Economic Corridor”, edited and published research cases of geoenvironmental disasters in

permafrost regions in Northeast China, and shared the research results of GERRP. At present, the research results of GERRP are gradually enriched, some of them have highly academic value, and have been put into engineering practice. ICRSE-NEFU has gradually shown its unique research charm since it became an ICL member in 2003 2002. In 2012, ICRSE-NEFU established a landslide research network in cold regions (ICL-CRLN), and then Research Center of Cold Regions Landslide was built.

Permafrost as one of the elements of the cryosphere, the change of thermodynamic stability of permafrost will directly affect the changes of hydrosphere, biosphere and lithosphere. Under the trend of global warming, the frequency and intensity of environmental and engineering geological disasters caused by permafrost degradation are getting higher and higher (Figs. A.16 and A.17). Taking the cold area in the southern boundary of the permafrost zone in Northeast China as study area, disasters such as ground subsidence, slope icing, landslides and other disasters caused by permafrost melting were studied. At the same time, we found melting permafrost also leads to seasonally high concentrations of greenhouse gases, triggering wildfires that may further accelerate permafrost degradation and environmental changes of terrestrial ecosystems and roads.

W. Shan · Y. Guo
Institute of Cold Regions Science and Engineering Northeast Forestry
University, Harbin, China
e-mail: shanwei456@163.com

Fig. A.16 Permafrost distribution in NE of China (2014–2019)

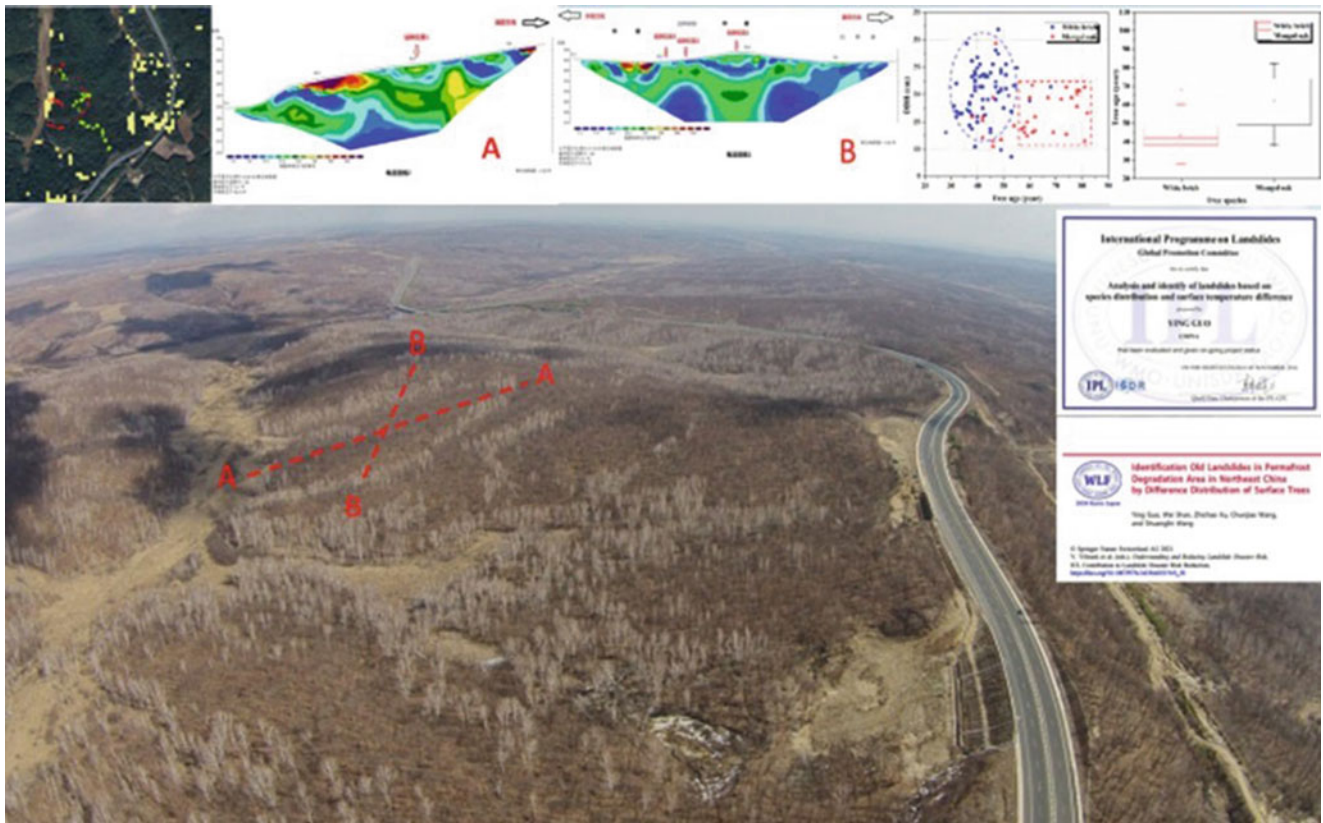
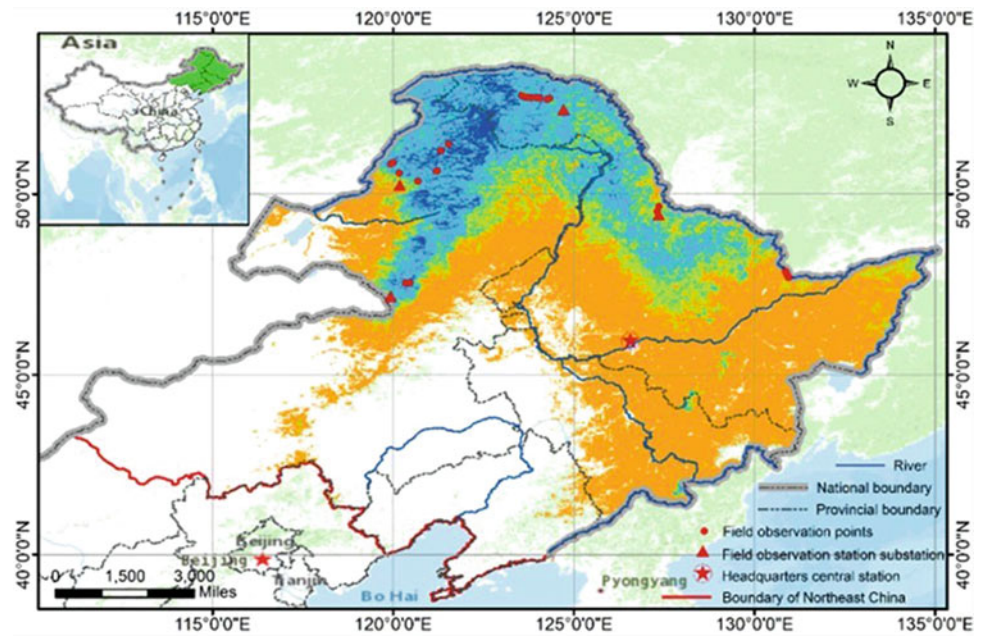


Fig. A.17 Different tree species and ages in the landslide area caused by permafrost degradation



Marui & Co. Ltd.

Taketoshi Marui and Yuji Ikari

Introduction

Marui & Co. Ltd. celebrated its 100th anniversary in 2020. Marui, as one of the leading manufacturers of testing apparatuses in Japan, has constantly been striving further to improve its service since its foundation in 1920, thus contributing to the sustainable development of our nation and society. Our main products cover various destructive and non-destructive testing apparatuses in geotechnical engineering, concrete engineering (mortar, aggregates, etc.), and ceramic engineering (Fig. A.18). Of particular note is that Marui has been helping manufacture ring-shear apparatuses (Fig. A.19) for the past half-century based on the leading-edge idea of Dr. Kyoji Sassa, Professor Emeritus at Kyoto University. Marui has delivered seven ring-shear apparatuses to the Disaster Prevention Research Institute, Kyoto University, and two to the International Consortium on Landslides. Also, the apparatuses were exported to the United States of America, China, Croatia, and Vietnam.

Since 2002, Marui has been a supporter of the International Consortium on Landslides (ICL) and has gradually been intensifying its contribution to the ICL's worldwide efforts for landslide risk reduction and international promotion of landslide research. According to NASA, more frequent and intense rainfall events due to climate change have been causing frequent landslides, particularly in mountains of Asian regions, including Japan, where waters can be stored in various ways. Summer monsoon rains, snow and glacier melt waters can destabilize steep mountainsides, triggering landslides, which are down-slope movements of rocks, soils, water, trees, etc. Marui, as an engineering supporter,

commits deeply to various activities of research, particularly on triggering mechanisms of landslides.

In addition to the ring-shear apparatuses mentioned above, our company develops and sells soil and ground testing equipment. For example, our standard cyclic triaxial testing machine (Fig. A.20) is used by geological consultants, research laboratories, and educational institutions such as universities and technical colleges. Ground destruction phenomena, which often occur concurrently with earthquakes, significantly affect the seismic resistance of superstructures. Cyclic triaxial tests are used to determine the constants required to judge the liquefaction potential and to determine the cyclic deformation characteristics of the ground required for seismic response analysis.

This equipment can perform not only liquefaction and deformation tests, but also static triaxial tests, isotropic consolidation tests, and anisotropic consolidation tests.

In addition, control and data recording can be processed entirely on a personal computer.

Marui & Co. Ltd. takes great pleasure in developing, manufacturing, and providing new products of high value, sharing the sense of achievement with our customers and thus contributing to social development. The entire staff of Marui is determined to devote ceaseless effort to keep its organization optimized for its speedy and high-quality services, by the motto "Creativity and Revolution," and strive hard to take a step further as a leading manufacturer of testing apparatuses, to answer our customer's expectations for the twenty-second century to come.

Marui continuously contributes to the 2030 Agenda for Sustainable Development and the Sendai Framework for

T. Marui · Y. Ikari
Marui & Co. Ltd, Osaka, Japan
e-mail: hp-mail@marui-group.co.jp; <http://marui-group.co.jp/en/index.html>

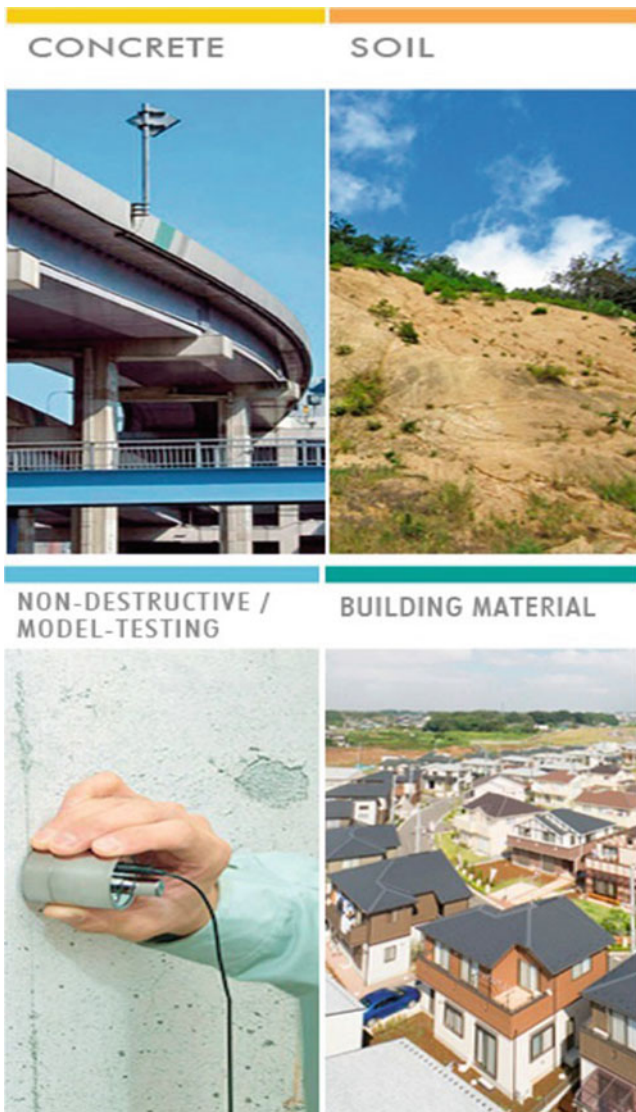
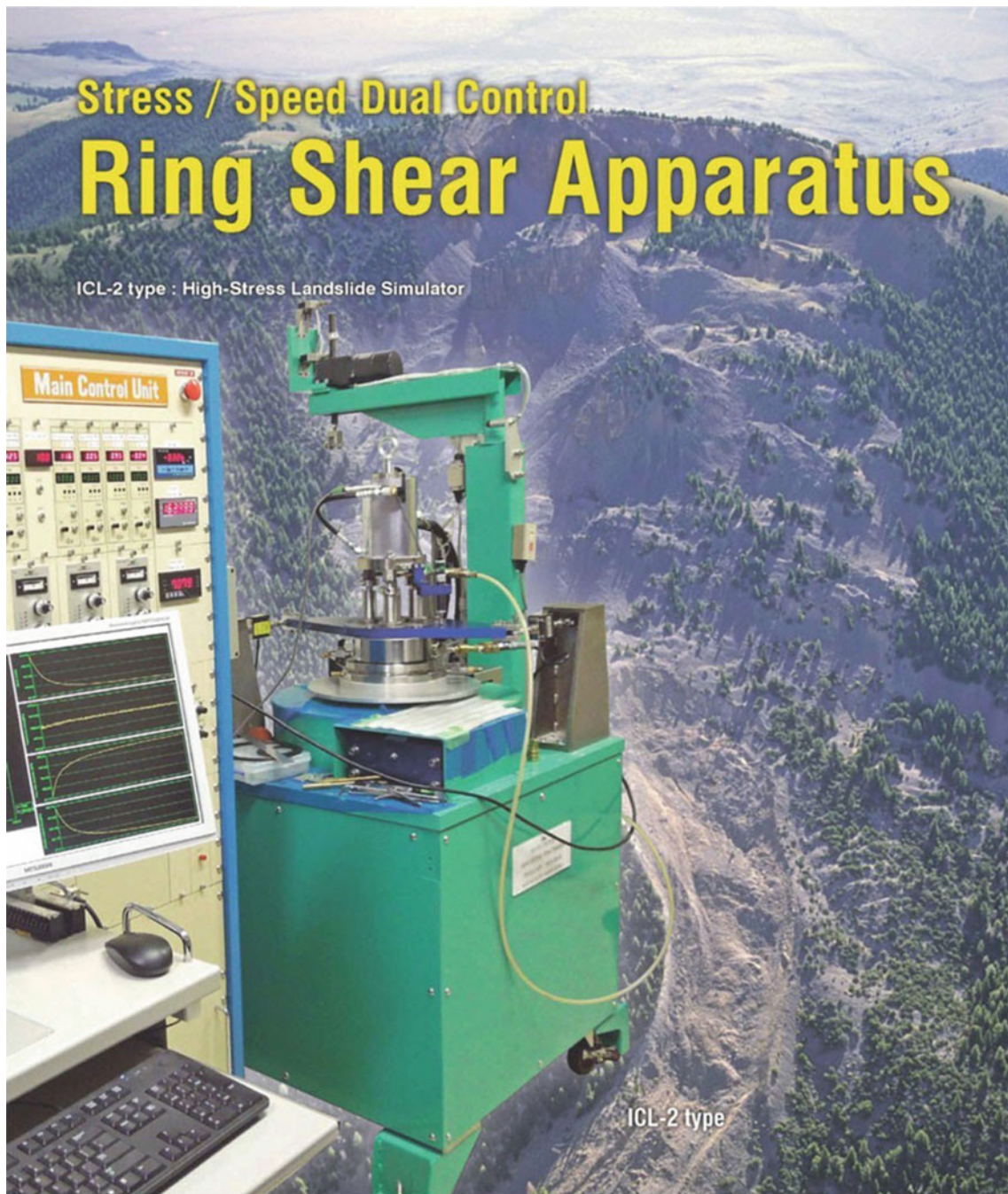


Fig. A.18 Products of testing apparatus such as non-destructive/model-testing for measuring intensity, physical property, durability, etc. for concrete, soil, building material, etc.

Disaster Risk Reduction 2015–2030. In line with this, Marui signed KLC2020 in 2019 and will strongly support its actions, especially KCL2020 Actions 3, 4, 5, and 9.



Web site : <https://www.marui-group.co.jp/en/>
E-mail : hp-mail@marui-group.co.jp
Address : 1-9-17 Goryo, Daito City,
Osaka Prefecture,
574-0064, Japan
Phone : 81-72-869-3201
F a x : 81-72-869-3205

Fig. A.19 High-stress landslide simulator



Compliant standards	JGS 0541 / JGS 0542
Dynamic vertical load	Pneumatic servo system: 1 kN
Static vertical load	Servo motor method: 5 kN
Side pressure load	Air regulator method: 1 MPa
Back pressure load	Air regulator method: 0.5 MPa
Dynamic control method	Load/displacement control: 0.05 to 1.0 Hz
Static control method	Displacement control: 0.005 to 5.0 mm/min
Three-axis room	<ul style="list-style-type: none"> • Three-pillar fixed system • Specimen size: $\phi 50 \times H 100$ mm
Measurement	<ul style="list-style-type: none"> • Axial pressure (external): 5 kN • Axial pressure (internal): 1 kN • External displacement: 25 mm • Internal displacement: ± 2 mm x 2 • Side pressure: 1 MPa • Pore pressure: 1 MPa • Volume change: 50 cc

Fig. A.20 Cyclic triaxial testing machine

Hiroaki Tauchi

Introduction

The Nippon Koei Group (NK) has been a leading international consultant providing engineering consulting services to over 5500 multi-disciplinary infrastructure and development projects in 160 countries worldwide. The landslide prevention specialist team (now called Geohazard Management Division) was established in 1966 to provide countermeasures against sediment disasters. Over the last 50 years, we have significantly improved the capacity of countries to respond and reduce risk from debris flows, slope instabilities, landslides, avalanches, and rock falls due to torrential rains, large-scale earthquakes, and volcanic eruptions that threaten a country's vital economic infrastructure lifelines, especially the road networks. At present, approximately 160 engineers provide a variety of technical consulting services to protect communities from disasters, as shown in Fig. A.21.

During disasters, we utilize remote sensing technologies such as 3D point clouds and interferometric SAR to create 3D models and gather surface and damage information to conduct a broad area survey, as shown in Fig. A.22. Based on this information, we provide experienced professional engineers to assess risk quickly and promptly respond with engineering design analyses and emergency and permanent measures based on our extensive experience and know-how. In order to efficiently plan and design disaster countermeasure works, we have implemented the automated design using visual programming. This automated design enables us to perform the 3D design of countermeasures quickly and calculate project costs, streamlining the overall process. Organizing design and construction information in 3D facilitates the construction process and allows for permanent maintenance by passing it on to the maintenance management phase as BIM (Building Information Modeling). As a result, the information necessary for effective maintenance is

readily available and can be utilized throughout the project's lifespan.

To maximize the effectiveness of infrastructures, we address efficient countermeasure plans, design, and research regarding cost reduction and cost-effectiveness using various numerical analyses such as the finite element method (FEM) and discrete element method (DEM), etc.

With climate change, the scale of disasters is enlarged and the frequency of disasters is increasing. This has resulted in more severe damage in more widespread and more urbanized areas, and more diverse and higher risks of disasters. In addition, in response to the SDG concept of "leaving no one behind," developing countries are lagging behind in hazard zoning and other efforts, which must be resolved. For this reason, NKG believes that it is important to assume that multiple types of disasters, such as floods, landslides and tsunamis, occur at the same time and in the same place. NKG provides risk mapping services using multi-hazard analysis as shown in Fig. A. 23.

In Japan, we have worked hard to restore and recover from sediment-related disasters caused by earthquakes and heavy rainfalls that have frequently occurred in recent years (the 2011 Great East Japan Earthquake, the Northern Kyushu Flood in 2017, etc.). We have received letters of appreciation from national and local governments for our efforts.

Our major international projects include "The Project for Countermeasure Construction Against the Landslides on Sindhuli Road Section II, Nepal," "The project for the rehabilitation of Sindhuli road affected by the 2015 Gorkha Earthquake, Nepal," and "The project for landslide prevention for National Road 6 in Honduras"; all funded by the Japan International Cooperation Agency (JICA) grants-in-aid. Through these projects, we are contributing to the socioeconomic development of each country by improving vulnerable locations in road networks against sediment disasters, promoting traffic safety, and providing logistics assistance for road users. In particular, the 1st of the three NK's projects mentioned above won the "3rd JAPAN Construction International Award" from the Ministry of Land, Infrastructure, Transport and Tourism as the project that has realized "high-

H. Tauchi
Geohazard Management Division, Tokyo, Japan

Fig. A.21 Our service for geohazard management

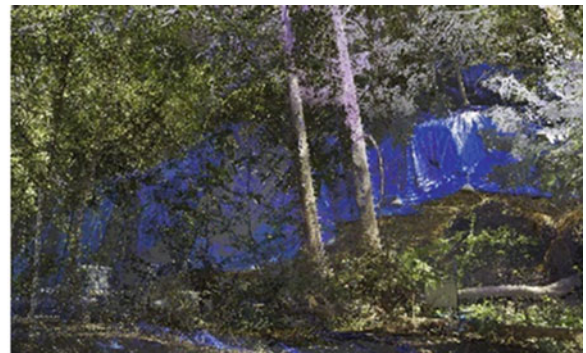
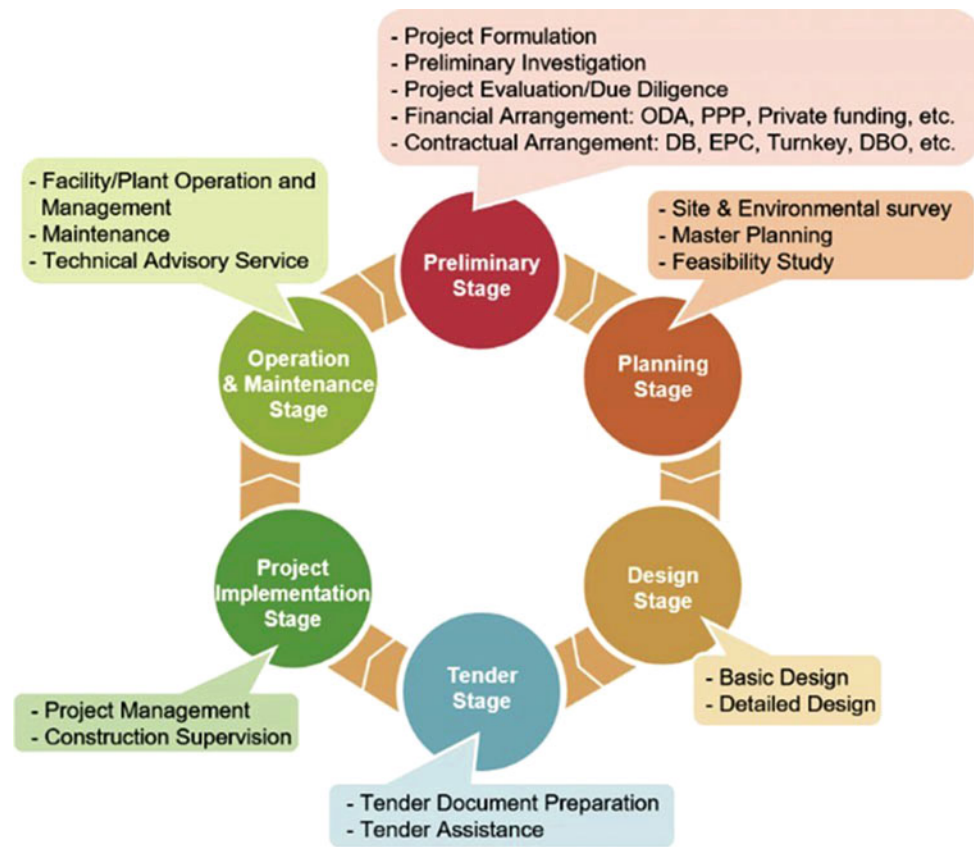


Fig. A.22 (left) a Landslide site, (right) 3D Point Clouds

quality infrastructures” through its excellent know-how, technical capabilities, and project management capabilities.

NK is an ICL supporter as well as a KLC official promoter and has been using its technology to reduce geohazard risk. Through various projects, NK continuously contributes to the 2030 Agenda for Sustainable Development and the Sendai Framework for Disaster Reduction

2015–2030. Using our full capability with abundant experiences in Japan and Asia prone to natural disasters, we hope to contribute much more to reducing global sediment disasters, including landslides (Fig. A.24). In line with this, NK has signed the KLC 2020 and will strongly support its actions.

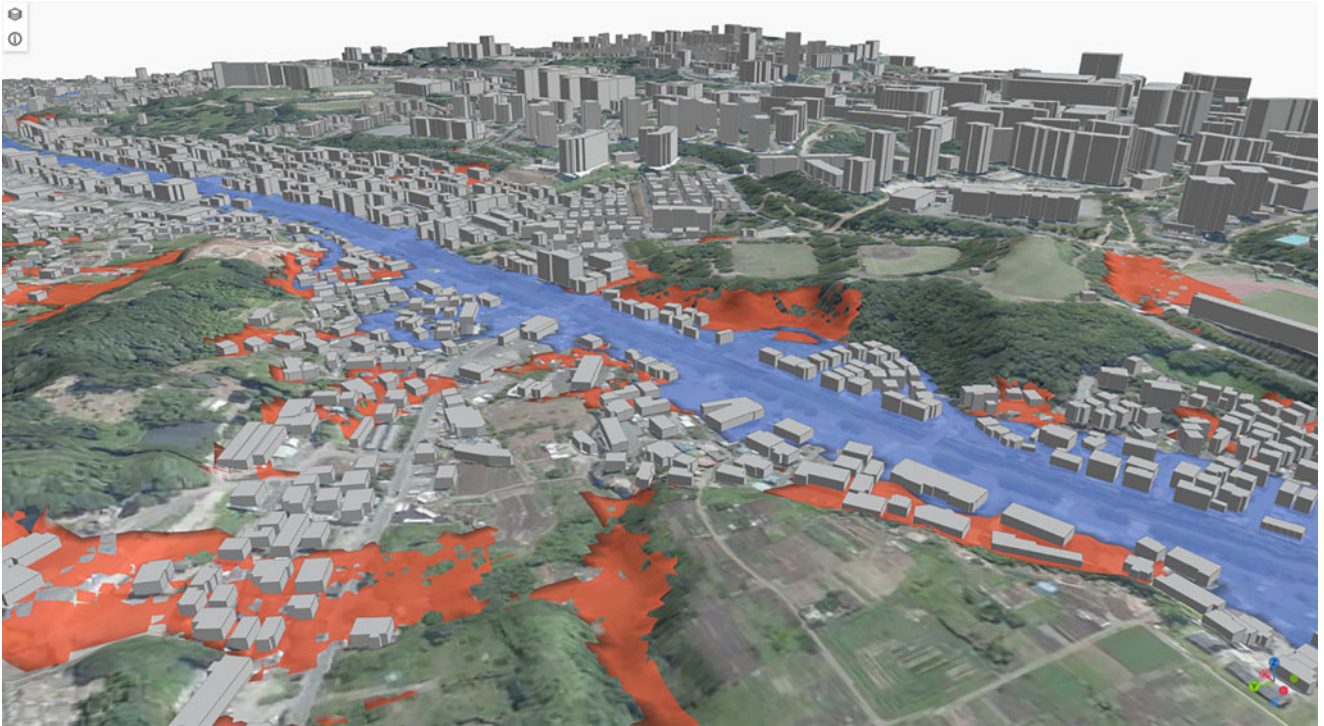


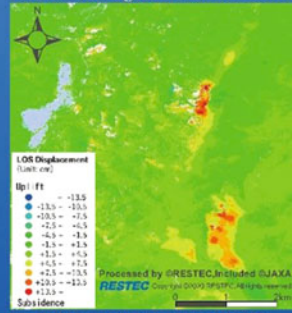
Fig. A.23 Visual programming and Automated design

Geohazard Management

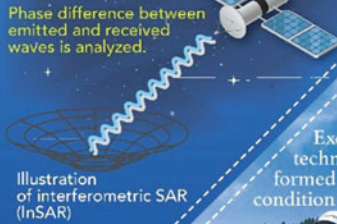
Response to natural disasters with various technologies from space to the surface

Remote Sensing Technology

Potential hazards around the globe are assessed by optical remote sensing and InSAR which can detect land-resources, topographic features, and ground deformation. Example of InSAR, shown below, is a new effective way to detect deformation of slopes along infrastructures such as roads and railways.



Landslide monitoring using InSAR



Phase difference between emitted and received waves is analyzed.

Illustration of interferometric SAR (InSAR)

Integrated technologies and engineers' Application of spaceborne, airborne, and ground-based technologies for disaster risk reduction.

A team of 5,497 multidisciplinary experts

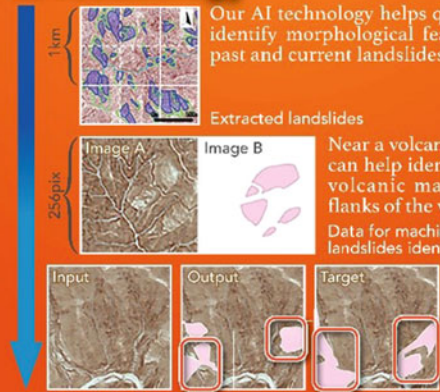
Excellent teams, covering advanced and wide range of technologies based on long-standing experiences, are formed to provide optimum solutions customized for each condition and needs.



Field survey by experienced engineers

AI Technology

Our AI technology helps quickly identify morphological features of past and current landslides.



Extraction of landslide topography using AI technology

Extracted landslides

Near a volcano, our AI technology can help identify unstable masses of volcanic matters perching on the flanks of the volcano.

Data for machine learning: DEM and landslides identified by an expert

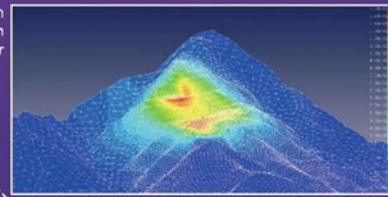
Numerical simulation

We can predict the extent of damage in the event of a disaster and the effectiveness of countermeasure works by numerical analysis.



Three-dimensional rockfall simulation by R&D center

Numerical simulation for slope excavation by R&D center



R&D center

State-of-the-Art Nippon Koei's R&D Center



NIPPON KOEI
Global Consulting Engineering Firm

Head Office 5-4 Kojimachi, Chiyoda-ku, Tokyo 102-8539, Japan

TEL +81-3-3238-8030

Website www.n-koei.co.jp/english



Fig. A.24 Introduction of our survey analysis technology for geohazard



Ellegi Srl

Ellegi Srl

Introduction

Ellegi srl provides worldwide monitoring services and produces Ground Based synthetic aperture radar (GBInSAR) for remote measurement of displacements and deformations on natural hazards and manmade buildings using its own designed and patented LiSALab system.

Its activities started in 2003 as a spin off project to exploit commercially the Ground Based Linear Synthetic Aperture Radars technology developed by European Commission's Ispra Joint Research Centre and based on the results of more than 10 years of research. Since then, Ellegi has industrialized and developed the core technology of the LiSALab system and latest LiSAMobile system represents the 5th generation of development.

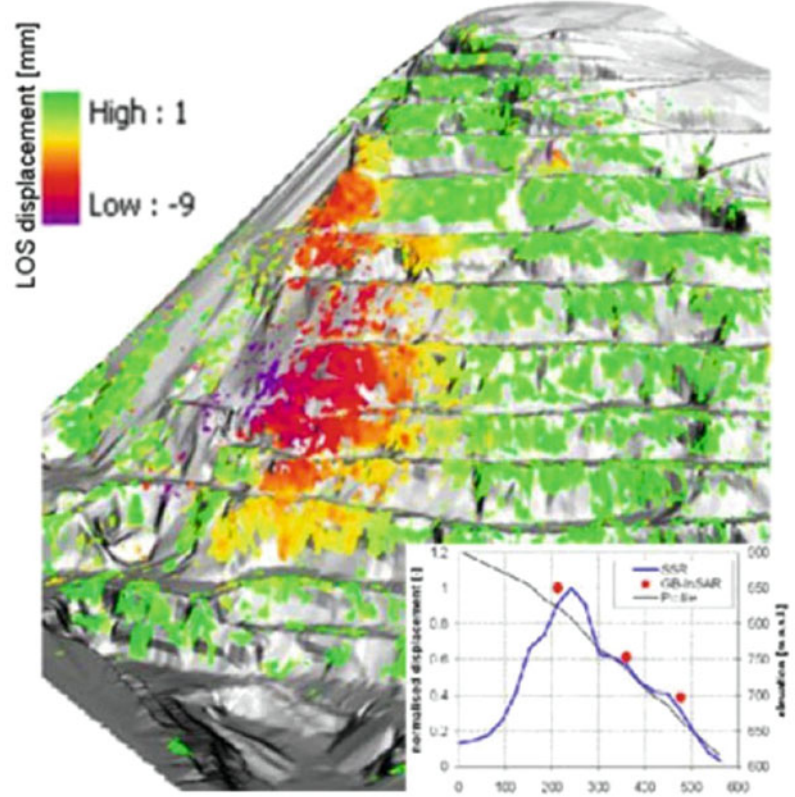
In 2003 it was the first commercial company in the world to provide GBInSAR measurements of natural hazards and structure (Figs. A.25 and A.26).

Ellegi srl offers:

- Displacement fields measurement, control and monitoring of the deformation caused by natural hazards, like landslides, rockslides, sinkhole, volcanic deformation in every operative condition, including emergencies,
- Structural strain fields measurement, control, monitoring and diagnosis of the deformation affecting buildings, bridges, viaducts, dams.
- GBInSAR monitoring systems, installation, management and maintenance in order to provide information about natural hazards or anthropic activity, that can generate or cause slopes failures or buildings instabilities.

In all the above-mentioned activities Ellegi srl uses the GBInSAR LiSALab technology that represents a real “break-through”.

Fig. A.25 GBInSAR LiSALab technology quarry monitoring example and displacements' field comparison between the GBInSAR measurement and FEM model results



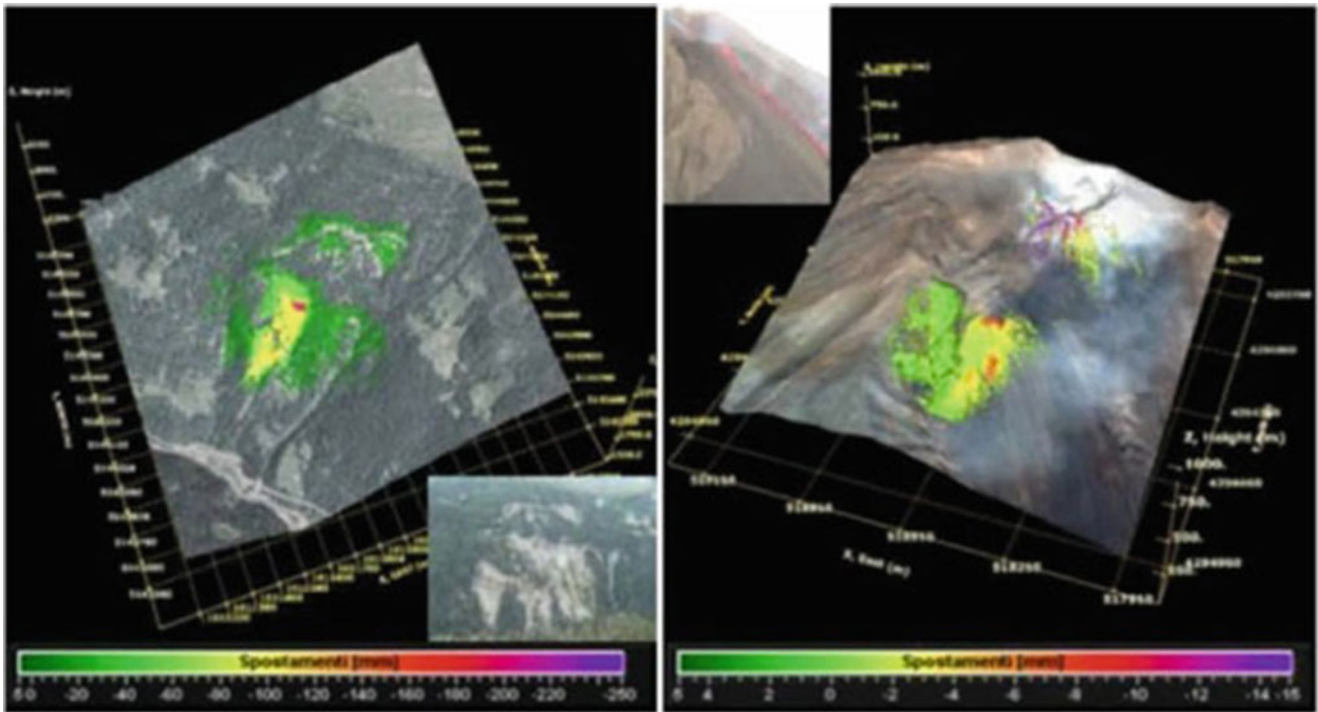


Fig. A.26 GBInSAR LiSALab technology result in monitoring a slope affected by a landslide (left) and a volcanic slope affected by deformation (right). Landslide or moving area mapping and boundaries identification is made easy by GBInSAR LiSALab technology



Chuo Kaihatsu Corporation

Lin Wang

Introduction

Chuo Kaihatsu Corporation (CKC) was founded in 1946, and has been aiming to become the “Only One” consultant for our customers. We engage in the hands-on work that will “Remain with the earth, Remain in people’s hearts, and Lead to a prosperous future”. We focus on road, river and dam engineering to flesh out industrial infrastructures specifically by means of geophysical/geotechnical/geological investigations, civil engineering surveys and project implementations. In recent years, we make significant efforts on earthquake disaster mitigation, sediment disaster prevention/mitigation and ICT information services. Many achievements of ours have already contributed to the mitigation of natural disasters such as landslides, earthquakes and slope failures in Japan, Asia and the Pacific Region. We aim to provide technological contributions so that a sustainable society will continue to develop in the future (Figs. A.27, A.28, A.29 and A.30).



Fig. A.27 Design for various structures

L. Wang
Chuo Kaihatsu Corporation, Tokyo, Japan
e-mail: wang@ckcnet.co.jp; <https://www.ckcnet.co.jp/global/https://www.ckcnet.co.jp/contactus/>

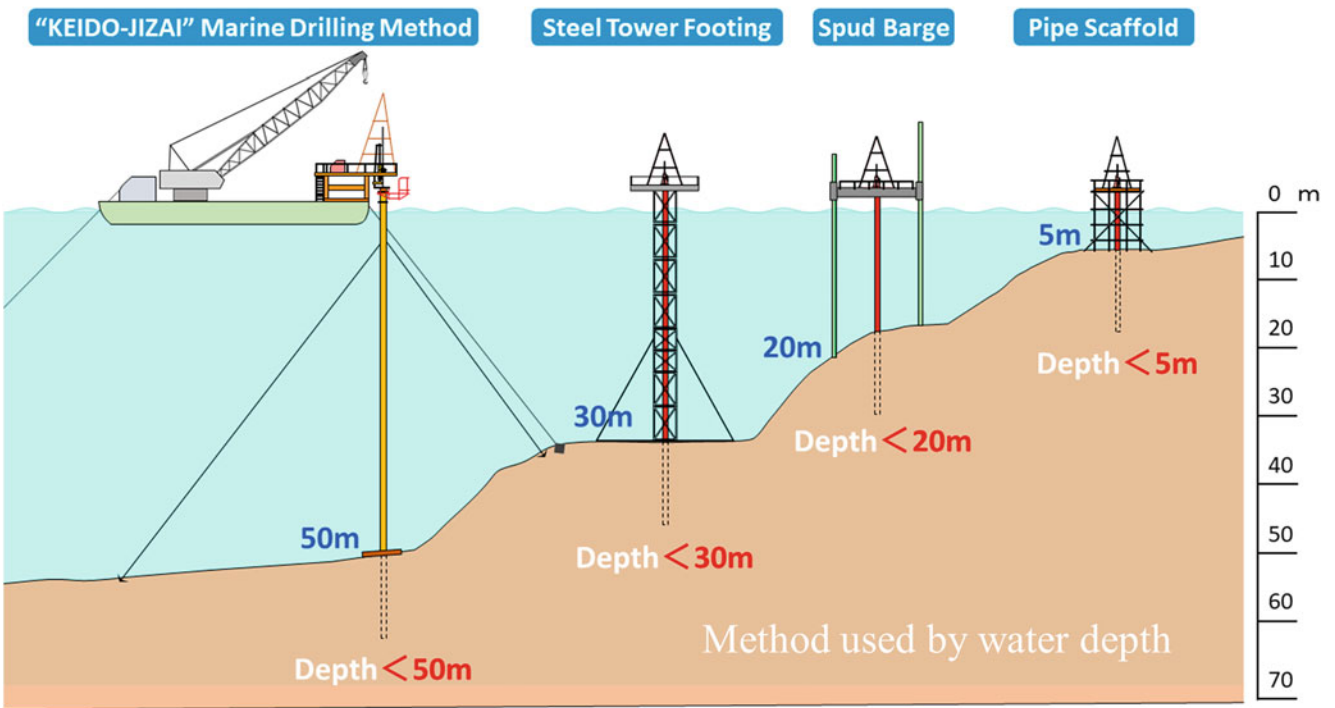


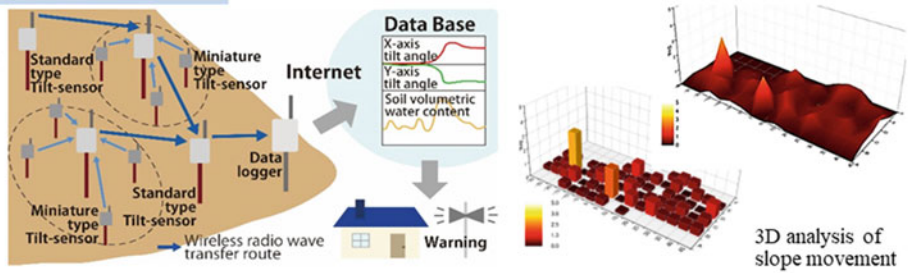
Fig. A.28 Deepwater drilling surveys

Objectives and Subjects

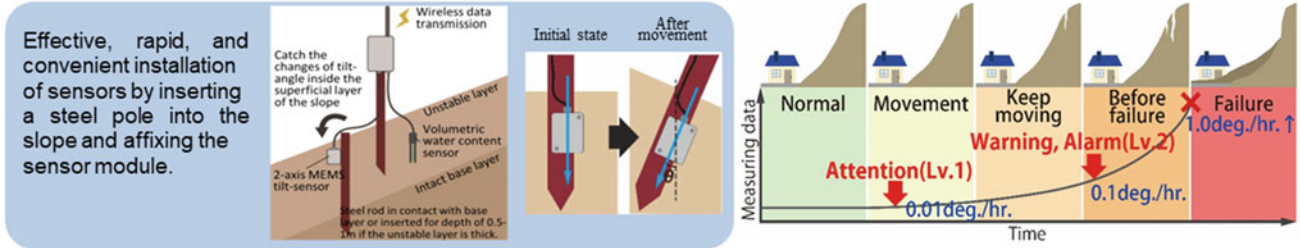
NETIS (MLIT) : KT-130093-A
 Japanese Geotechnical Society Award for Technology Development 2014
 The Society of Instrument and Control Engineers Award for Technology Development 2015
 NETIS (MLIT) Evaluation Promotion Technology from 2016

Research and develop a highly accurate, multi-point early-warning system for slope failure using low-cost tilt sensors

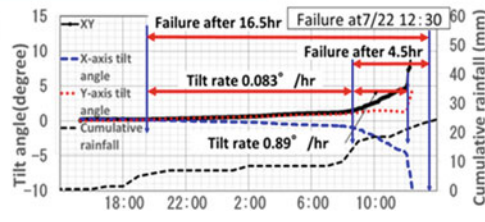
- Low-cost, easily-installed tilt sensors.
 ⇒ **Realized low cost multi-point measurement.**
- Prediction of slope deformation by multi-point measurements.
 ⇒ **Realized high-precision, stable, early warning slope failure system.**



Accomplishments



Utilization example
 At other field sites, the tilt rate increased toward failure within a relatively short time before slope failure. Tilt rate is thus inversely proportional to the remaining time until failure.



Early warning can be issued based on the relationship between tilt rate and remaining time to failure.

Fig. A.29 The early warning monitoring system of slope failure using multi-point tilt change and volumetric water content



Godai Kaihatsu Corporation

Godai Kaihatsu Corporation

Introduction

Ever since its foundation in 1965, Godai Kaihatsu Co. Ltd. a civil engineering consulting firm, has long been providing a variety of software and measures particularly for natural disaster mitigation. With its rich expertise in both civil engineering and information technology (IT), the company has its primary goal to address real-world needs of disaster mitigation. All the staff of Godai Kaihatsu Co. Ltd. feels it more than happy that their cutting-edge technologies help mitigate natural disasters (Figs. [A.31](#), [A.32](#), [A.33](#) and [A.34](#)).

Godai Kaihatsu Corporation
Godai Kaihatsu Corporation, Kanazawa City, Ishikawa, Japan
e-mail: pp-sales@godai.co.jp; <https://soft.godai.co.jp/soft/>

© The Author(s) 2023
I. Alcántara-Ayala et al. (eds.), *Progress in Landslide Research and Technology, Volume 2 Issue 2, 2023*, Progress in Landslide Research and Technology, <https://doi.org/10.1007/978-3-031-44296-4>

Fig. A.31 Integrated model simulating of earthquake & rain induced rapid landslides (LS-RAPID)

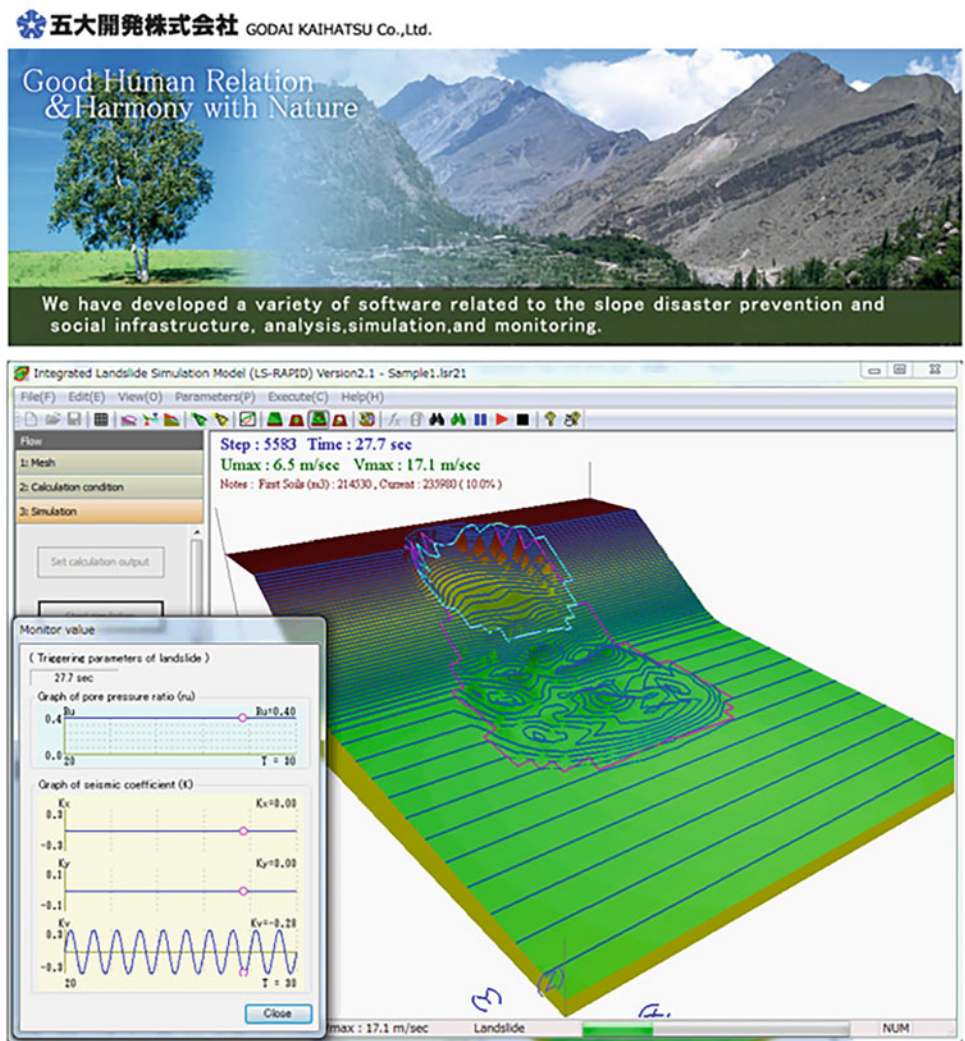
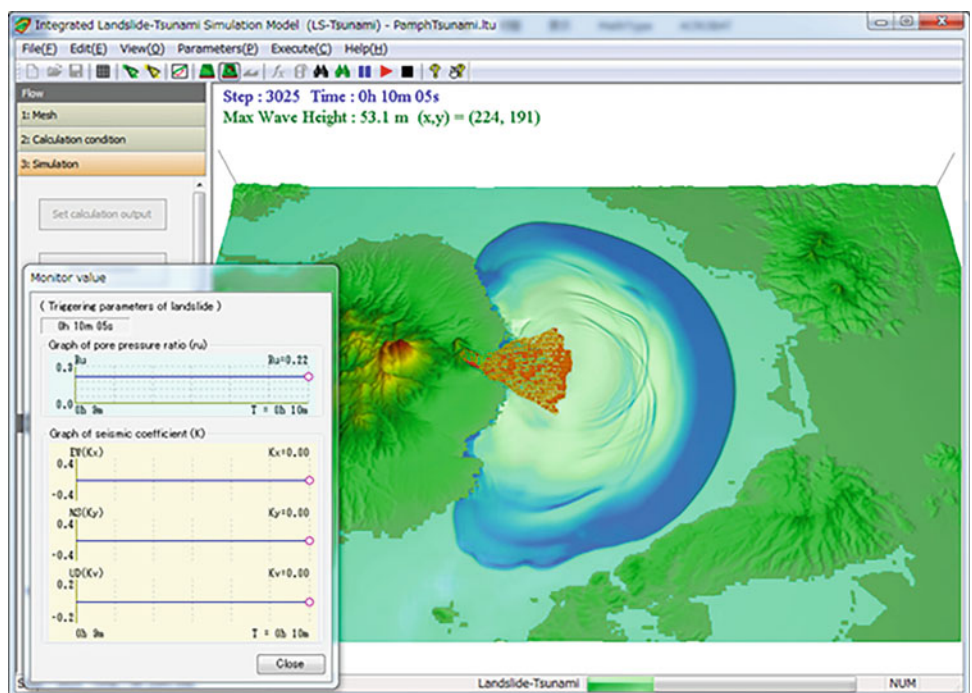
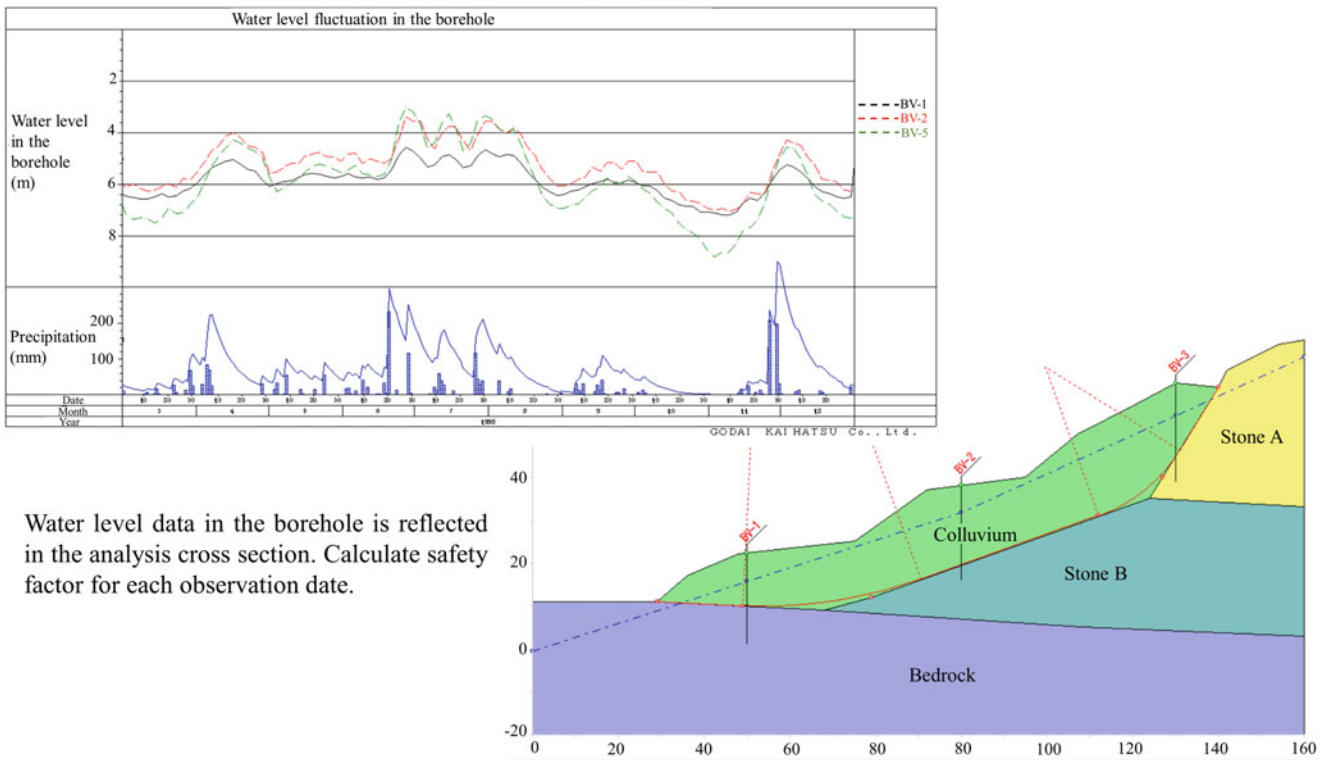


Fig. A.32 Tsunami model (LS-Tsunami)





Water level data in the borehole is reflected in the analysis cross section. Calculate safety factor for each observation date.

Fig. A.33 Power SSA PRO-Two-dimensional slope stability calculation of earthquake and rain induced landslide

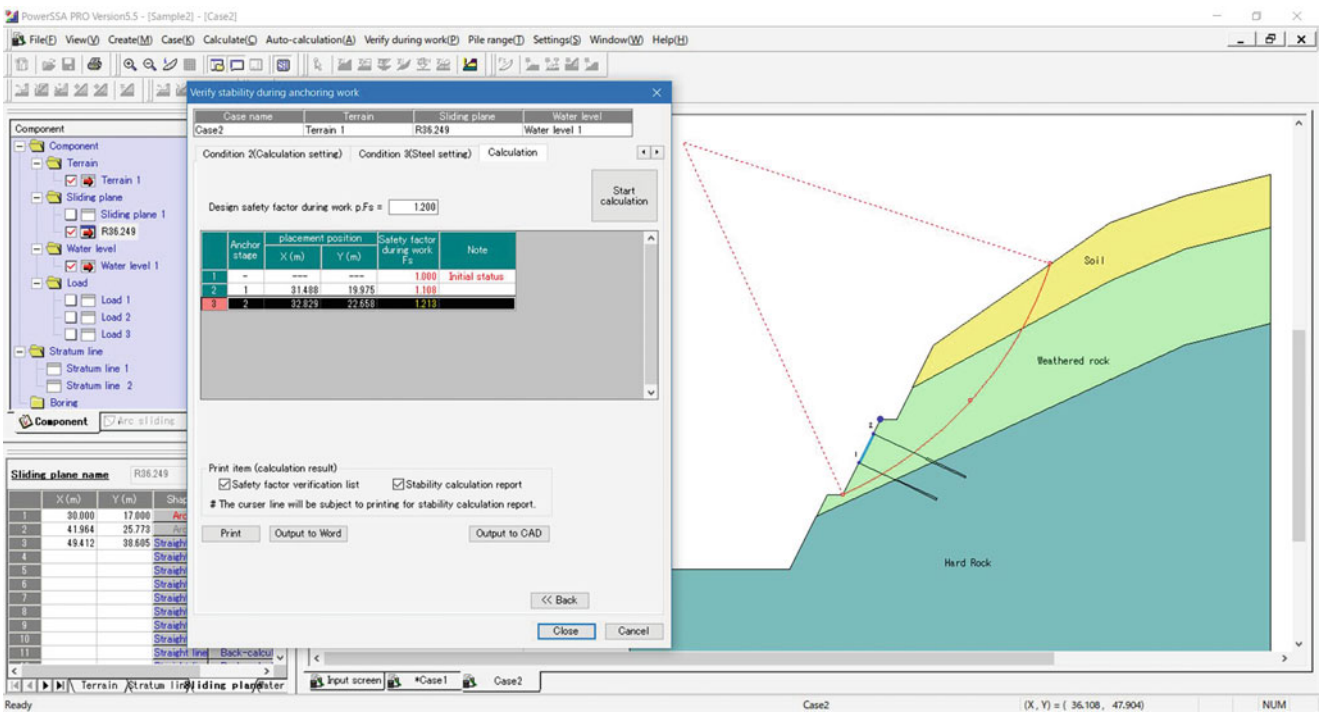


Fig. A.34 Anchor software-slope stability analysis for ground anchor

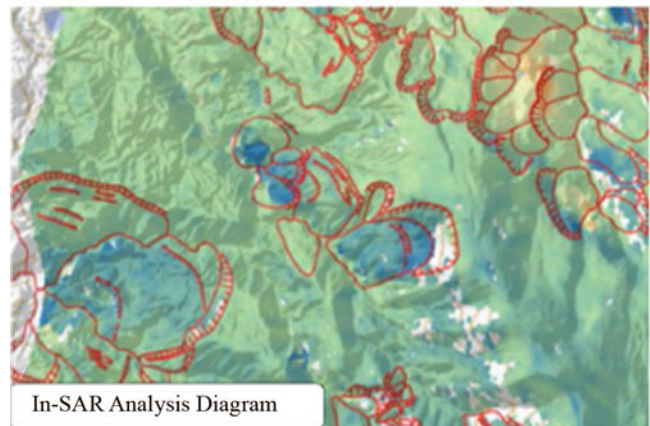
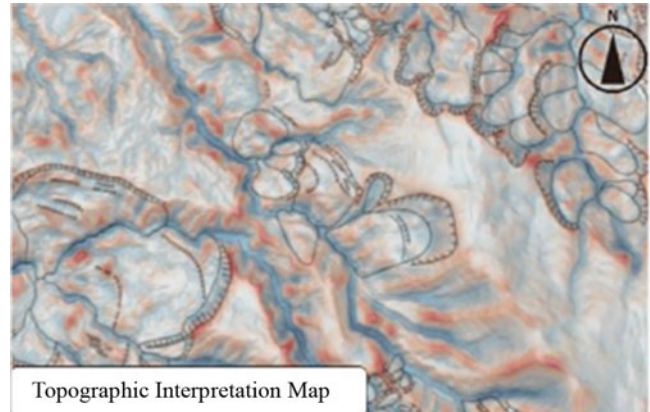
Kaoru Hanai and Junichiro Odaka

Introduction

Since its establishment in 1953, Kiso-Jiban has been contributing on the development of social infrastructure as a “comprehensive construction consultant with strong geotechnical capabilities” in various situations, such as ground investigation, laboratory testing, analysis, civil structure design, etc. Kiso-Jiban has been working on the technological development for disaster prevention and mitigation against the recent exacerbation of natural disasters.

InSAR (Interferometric Synthetic Aperture Radar)

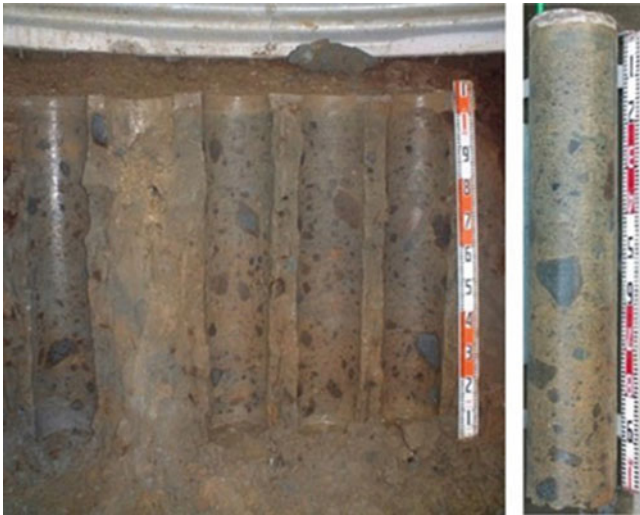
SAR is a technique that utilizes interference of radio waves for precise determination of distance. Kiso-Jiban has succeeded in estimation of both extent and rate of landslide movements by combining the topography interpretation and InSAR analysis.



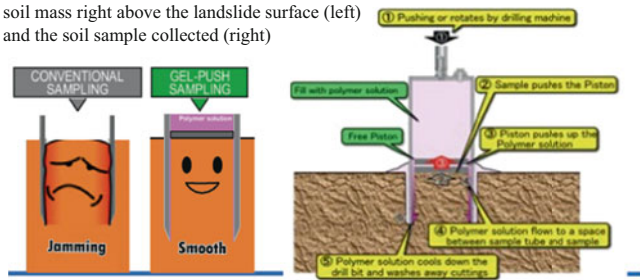
GP (Gel-Push) Sampling

GP Sampling can collect gravelly soil, etc., which is difficult to be collected by conventional samplers, by using a highly-concentrated water-soluble polymeric gel. GP Sampling was introduced in ISO 22475-1: 2021 revised in October 2021 as Category A, which provides the highest quality soil samples.

K. Hanai · J. Odaka
Kiso-Jiban Consultants Co. Ltd., Tokyo, Japan
e-mail: kisojiban-contactus@kiso.co.jp; <https://www.kisojiban.com/>



GP Sampling was performed in the disturbed soil mass right above the landslide surface (left) and the soil sample collected (right)



Inspection Technique for Disaster Danger Spots Using Mixed Reality (MR) Technology

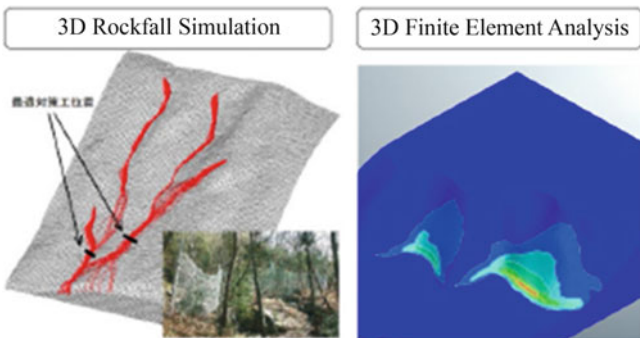
MR (Mixed reality) is a technology that blends physical and digital worlds by superimposing 3D data and digital information on the real world as computer graphics.

Dangerous slopes with rockfall sources are spots where many unstable bedrocks and floating rocks exist. In many cases, approaching the inspection point on an outcrop is a difficult and dangerous task for investigators. Using MR technology makes it possible to realistically reproduce the outcrop situation at the site as a hologram. The outcrop situation can be safely inspected and confirmed without going to the site.



Slope Stability Analysis and Evaluation

Kiso-Jiban provides a wide range of numerical analyses related to slope stability evaluation. We have a wide range of analysis methods, from general two-dimensional limit equilibrium analysis to finite element analysis and analysis of rock masses with discontinuities, and we are challenging on the analysis that considers variability of ground and modelling uncertainty.



One example of the Mixed Reality



Kokusai Kogyo Co. Ltd

Kokusai Kogyo Co. Ltd.

Introduction

Kokusai Kogyo Co. Ltd. as a leading company of geospatial information technologies has long been providing public services with its comprehensive expertise to address real-world needs and cutting-edge measurement technologies. Kokusai Kogyo Co. Ltd. helps rebuild “Green Communities,” which has been of our great concern in terms of “environment and energy,” “disaster risk reduction” and “asset management”. Kokusai Kogyo Co. Ltd. offers advanced and comprehensive analyses of geospatial information for developing new government policies, maintaining and operating social infrastructures safe and secure, and implementing low-carbon measures in cities. Influenced by the recent global climate change, extreme rainfall events have become more frequent worldwide and resultant hydro-meteorological hazards are creating more deaths and devastations particularly in many developing countries where effective advanced countermeasures are not readily available. Kokusai Kogyo Co. Ltd. is proud of its achievements in establishing resilient infrastructure systems and implementing effective monitoring/early warning systems in developing countries, which have long been helping reduce the risks from natural hazards (Figs. [A.35](#), [A.36](#), [A.37](#) and [A.38](#)).

Kokusai Kogyo Co. Ltd.

© The Author(s) 2023

I. Alcántara-Ayala et al. (eds.), *Progress in Landslide Research and Technology, Volume 2 Issue 2, 2023*, Progress in Landslide Research and Technology, <https://doi.org/10.1007/978-3-031-44296-4>

485

Fig. A.35 Our realtime hazard map reflects up-to-date information of soil natures and precipitations at landslide hazard sites, etc. that can constantly be changing, and evaluates area-wide hazard risk in real-time



Fig. A.36 ELSAMAP is our cutting-edge 3D terrain visualization method allowing great geomorphological details to be visualized in one glance with gray-scaled slope inclinations and colored altitudes. ELSAMAP has been used to interpret micro-topographies, landslides and some other things

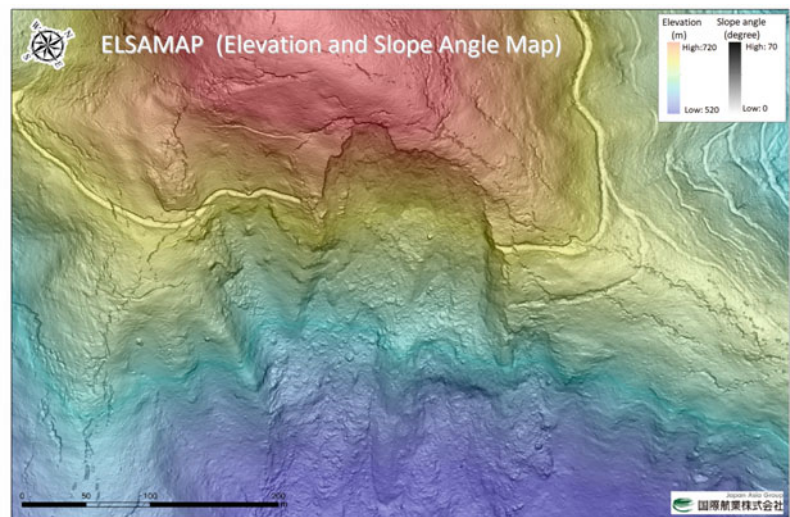


Fig. A.37 3D-GIV can help grasp the ground surface displacement caused by natural phenomena such as landslide by analyzing differences between digital geomorphic images obtained through ad hoc Airborne Laser Surveys

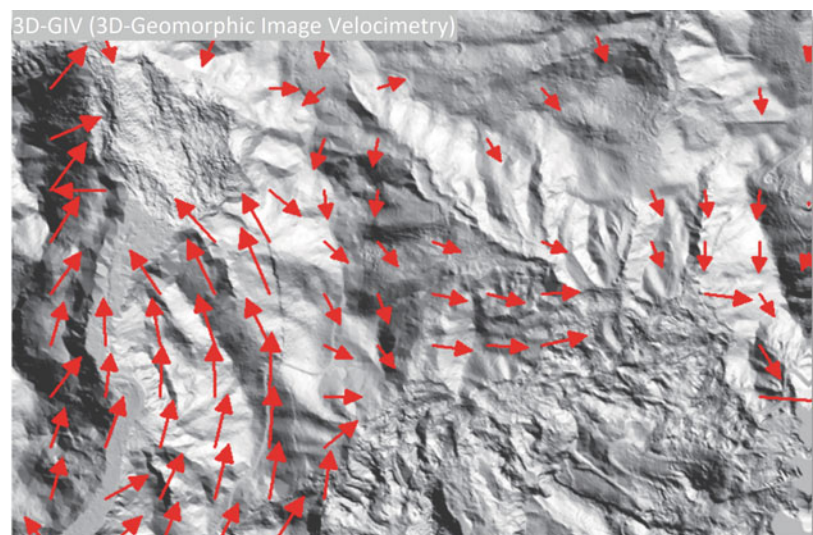


Fig. A.38 “Shamen-net” is a total monitoring system integrating GNSS and other monitoring device (Measurement precision: \pm mm, on a real time basis)





OSASI Technos, Inc.

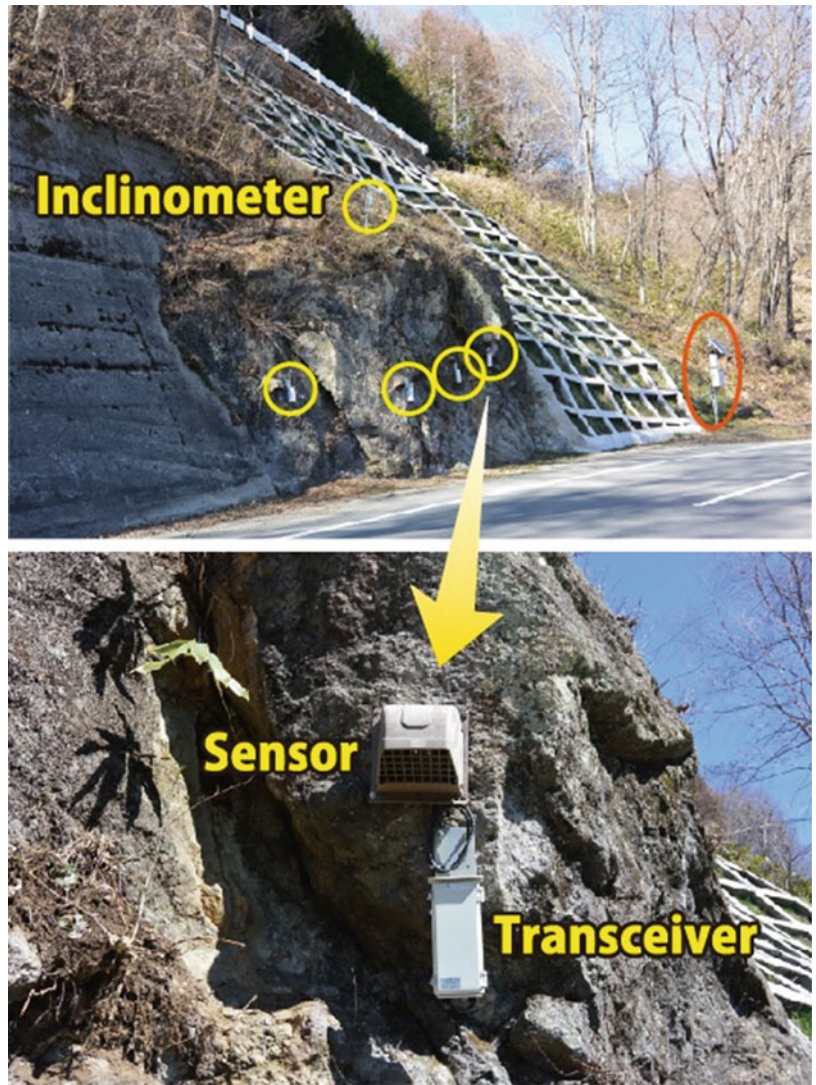
OSASI Technos, Inc.

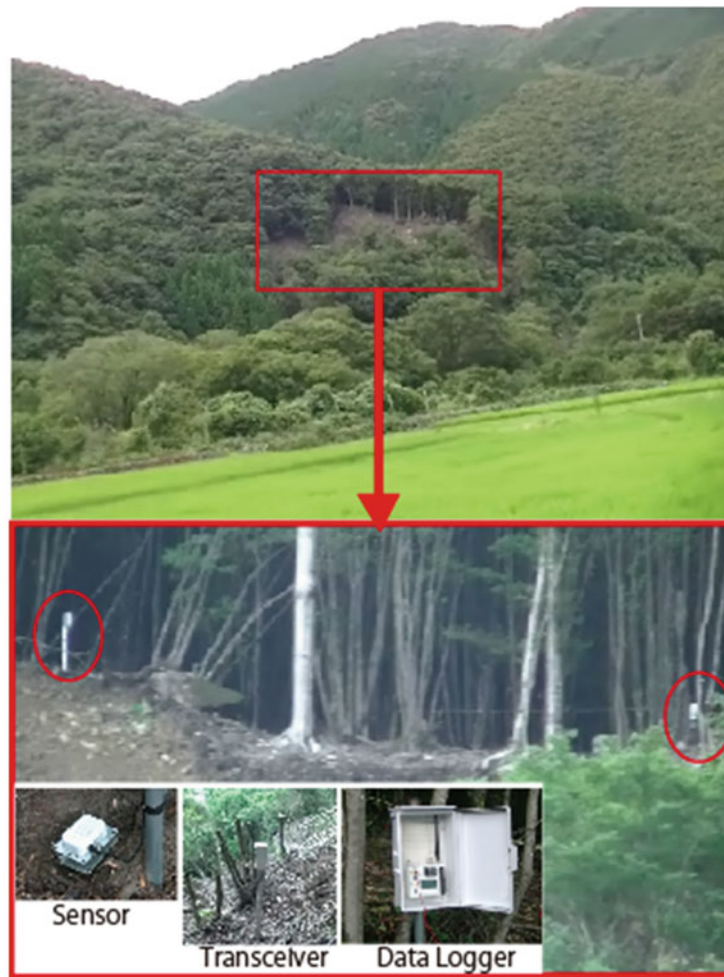
Introduction

OSASI Technos, Inc. has been making its best efforts to develop its cutting-edge technologies for landslide early warning. Its unique compact and lightweight sensors making up the Landslide Early Warning System enable long-term monitoring of unstable landslide mass movements, precipitations, porewater pressure buildups, etc. in a remote mountainous area where commercial power is often unavailable. OSASI Technos, Inc. is also proud of its advanced technology to transfer observed data even in areas with poor telecom environments as proven in the successful implementations in South Asia. All staff members of OSASI Technos work together for mitigation of landslide disasters worldwide (Figs. [A.39](#), [A.40](#), [A.41](#) and [A.42](#)).

OSASI Technos, Inc.
OSASI Technos, Inc., Kochi City, Kochi, Japan

Fig. A.39 Bedrock slope monitoring (maintenance control)





【Inclination and Precipitation】

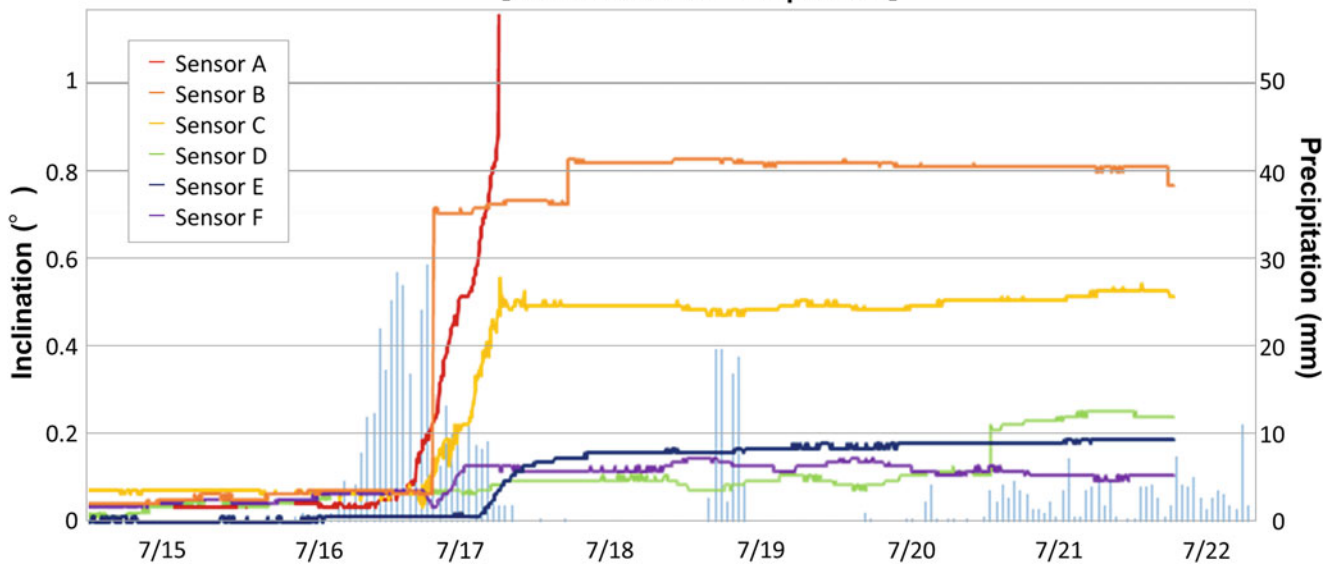


Fig. A.40 Measurement of the dynamic state of landslide using inclinometers with a wireless function

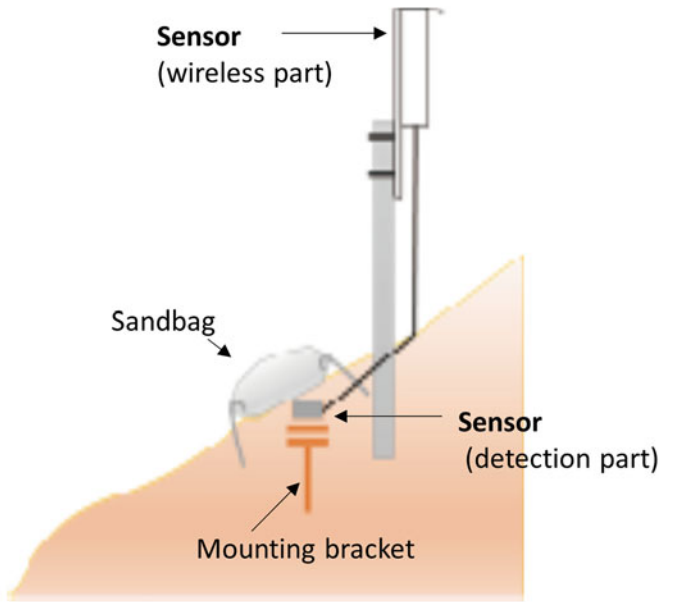


Fig. A.41 Cut slope monitoring Example of sensor installation



Fig. A.42 Compact alarm device to alert local people to landslide risk

List of ICL Members

International Consortium on Landslides

An international non-government and non-profit scientific organization promoting landslide research and capacity building for the benefit of society and the environment.

President: Nicola Casagi (University Florence, Italy)

Vice Presidents: Peter Bobrowsky (Geological Survey of Canada, Canada), Zeljko Arbanas (University of Rijeka, Croatia), Binod Tiwari (California State University, USA), Faisal Fathani (University of Gadjah Mada, Indonesia), Veronica Tofani (University of Florence, Italy), Vit Vilimek (Charles University, Czech Republic) Executive Director: Kaoru Takara (National Research Institute for Earth Science and Disaster Resilience, Japan), Treasurer: Kyoji Sassa (Prof. Emeritus, Kyoto University, Japan)

Country/Region	ICL Full member
Bosnia and Herzegovina	The Geotechnical Society of Bosnia and Herzegovina
Brazil	Center for Scientific Support in Disasters – Federal University of Parana
Canada	Geological Survey of Canada University of Alberta
China	Northeast Forestry University, Institute of Cold Regions Science and Engineering China University of Geosciences Chinese Academy of Sciences, Institute of Mountain Hazards and Environment Tongji University Shanghai Jiao Tong University Tsinghua University Civil Engineering and Development Department, Geotechnical Engineering Office, Hong Kong The Hong Kong University of Science and Technology The University of Hong Kong
Colombia	Universidad Nacional de Colombia
Croatia	Croatian Landslide Group from Faculty of Civil Engineering University of Rijeka and Faculty of Mining, Geology and Petroleum University of Zagreb
Czech Republic	Charles University, Faculty of Science
Egypt	The American University in Cairo
Germany	Technische Universität Darmstadt, Institute and Laboratory of Geotechnics
Georgia	Department of Geology of National Environmental Agency of Georgia
India	Amrita Vishwa Vidyapeetham, Amrita University National Institute of Disaster Management, New Delhi
Indonesia	Gadjah Mada University, Center for Disaster Mitigation and Technological Innovation (GAMA-InaTEK) Parahyangan Catholic University Agency for Meteorology, Climatology, and Geophysics of the Republic of Indonesia (BMKG Indonesia)
Italy	UNESCO Chair for the prevention and the sustainable management of geo-hydrological hazards—University of Florence ISPRA-Italian Institute for Environmental Protection and Research University of Calabria, DIMES, CAMILAB Istituto di Ricerca per la Protezione Idrogeologica (IRPI), of the Italian National Research Council (CNR) Centro di Ricerca CERi—Sapienza Università di Roma National Institute of Oceanography and Applied Geophysics—OGS, Italy

(continued)

Japan	Kyoto University, Disaster Prevention Research Institute Japan Landslide Society International Consortium on Geo-disaster Reduction
Korea	Korean Society of Forest Engineering National Institute of Forest Science Korea Authority of Land & Infrastructure Safety Korea Institute of Civil Engineering and Building Technology
Mexico	Institute of Geography, National Autonomous University of Mexico (UNAM)
Russia	Moscow State University, Department of Engineering and Ecological Geology JSC “Hydroproject Institute”
Serbia	University of Belgrade, Faculty of Mining and Geology
Slovakia	Comenius University, Faculty of Natural Sciences, Department of Engineering Geology
Slovenia	University of Ljubljana, Faculty of Civil and Geodetic Engineering (ULFGG) Geological Survey of Slovenia
Sri Lanka	Central Engineering Consultancy Bureau (CECB) National Building Research Organization Engineering Geology Research Group (EGRG), Department of Geology, University of Peradeniya
Chinese Taipei	Landslide group in National Central University from Graduate Institute of Applied Geology, Department of Civil Engineering, Center for Environmental Studies National Taiwan University, Department of Civil Engineering
Thailand	Ministry of Agriculture and Cooperatives, Land Development Department Asian Disaster Preparedness Center (ADPC)
Ukraine	Institute of Telecommunication and Global Information Space
United Kingdom	British Geological Survey
USA & Nepal	California State University, Fullerton & Tribhuvan University, Institute of Engineering
Viet Nam	Institute of Transport Science and Technology Vietnam Institute of Geosciences and Mineral Resources (VIGMR)
Country/Region	ICL Associate member
Belgium	Liege University, Georisk and Environment (G&E) group
China	State Key Laboratory of Geohazard Prevention and Geoenvironment Protection (Chengdu University of Technology) State Key Laboratory of Plateau Ecology and Agriculture (Qinghai University)
Czech Republic	Czech Geological Survey Institute of Rock Structure and Mechanics, Department of Engineering Geology Brown Coal Research Institute
Italy	Department of Earth and Environmental Sciences, University Aldo Moro, Bari University of Sannio, Department of Sciences and Technologies Geotechnical Engineering Group (GEG), University of Salerno Department of Earth and Environmental Sciences – University of Pavia University of Chieti-Pescara, Department of Engineering and Geology Federico II University of Naples, Department of Earth, Environmental and Resource Sciences DIA—Università degli Studi di Parma University of Urbino “Carlo Bo”, Department of Pure and Applied Sciences University of Turin
Japan	Ehime University, Center for Disaster Management Informatics Research Kochi University National Institute of Maritime, Port and Aviation Technology
North Macedonia	Macedonian Association for Geotechnics
Russia	Russian State Geological Prospecting University n.a. Sergo Ordzhonikidze (MGRI-RSGPU)
Slovenia	University of Ljubljana, Faculty of Natural Sciences and Engineering (UL NTF)
Switzerland	Institute of Earth Sciences, Faculty of Geoscience and Environment/University of Lausanne
USA	Iowa State University

(continued)

Country/Region	ICL Supporter	
Italy	IDS GeoRadar s.r.l.	
Japan	Marui & Co., Ltd., Osaka	Okuyama Boring Co., Ltd., Yokote
	Ohta Geo-Research Co., Ltd., Nishinomiya	Japan Conservation Engineers Co., Ltd., Tokyo
	Sabo Technical Center, Tokyo	GODAI Kaihatsu Corp., Kanazawa
	OYO Corporation, Tokyo	Kokusai Kogyo Co., Ltd., Tokyo
	OSASI Technos Inc., Kochi	NIPPON KOEI CO., LTD.
Chinese Taipei	Sinotech Engineering Consultants, Inc.	
ICL Secretariat		
Secretary General: Kyoji Sassa		
International Consortium on Landslides, 138-1 Tanaka Asukai-cho, Sakyo-ku, Kyoto, 606-8226, Japan		
Web: https://www.landslides.org /E-mail: secretariat@landslides.org		
Tel:+81 (75) 723 0640, Fax:+81(75) 950 0910		

Index

A

Aaron, J., 56
Abdel-Ghaffar, M.E.M., 29
Abdrakhmatov, K., 55, 89, 175
Abe, I., 375
Abolmasov, B., 176, 355–360, 403–409
Abraham, M.T., 363, 364
Achu, A.L., 5
Adler, C., 161
Agliardi, F., 269, 424
Ahmed, B., 431–438
Airey, D.W., 22
Ajmera, B., 3–51, 176, 378
Akay, T., 261
Akca, D., 200
Akgün, A., 121
Aksha, S.K., 324, 326
Alcántara-Ayala, I., 155–164, 432
Ale, B., 137, 139, 140, 143
Aleotti, P., 127
Alvioli, M., 343, 346
Anayi, J.T., 23
Andersen, K.H., 27
Anderson, M.G., 183
Andrade, S.D., 106
Andrejev, K., 359
Andriamamonjisoa, S.N., 361
Aničić, B., 344
Antronico, L., 432
Anyah, R.O., 250
Arbanas, M.S., 355
Arbanas, S.M., 343–353
Arbanas, Ž., 197–219, 355
Ariyaratna, I., 269–282
Armanini, A., 314, 319
Arnone, E., 127
Arrowsmith, J.R., 81, 89
Aucote, H.M., 156
Aziz, A., 431

B

Baba, T., 375
Baba, Y., 240
Bæverfjord, M.G., 169
Bagtasa, G., 247, 248
Bandara, H.A.A.I.S., 239–246
Barden, L., 18, 19
Barnett, J., 156
Barrett, G., 184
Barth, N.C., 55

Baruah, S., 5
Basharat, M., 84
Baum, R.L., 127
Beck, U., 431
Beni, T., 413–428
Bernat Gazibara, S., 343–353
Bernat, S., 344
Beroya-Eitner, M.A.A., 247–256
Berrill, J.B., 43
Bezak, N., 209, 448
Bhatta, A., 311–321
Bhuiya, T., 432
Bibi, T., 326
Bickerstaff, K., 432
Bicocchi, G., 129
Bien, T.X., 259
Bishop, A.W., 18, 19, 23
Bishop, N., 232, 233
Bitelli, G., 200
Bjerrum, L., 22
Blisniuk, P.M., 56
Bobrowsky, P., 225
Bobrowsky, P.T., 222
Bodman, G.B., 287
Bognar, A., 344
Boholm, Å., 432
Boldini, D., 413–428
Bonometti, F., 413–428
Borden, R.H., 33
Bornaetxea, T., 344
Bostrom, A., 432
Boucek, B., 23
Brandon, T.L., 29
Bray, J.D., 27
Breakwell, G.M., 156
Breiman, L., 363
Brennand, T., 225
Bromhead, E.N., 23, 25, 26
Brown, S.F., 27
Bubeck, P., 328
Buena, A.E., 248
Bufe, A., 81
Bulut, F., 117
Bunce, C., 233, 235
Birmingham, K., 432

C

Cagnoli, B., 56
Calvello, M., 432
Can, R., 184

Cancelli, A., 33
 Cannon, A.J., 250
 Capobianco, V., 178
 Carlà, T., 270
 Carranza, E.J.M., 263
 Casagli, N., 285, 361–370, 413–428
 Cascini, L., 175
 Castellanos, B.A., 29
 Castellanza, R., 413–428
 Catane, S.G., 55
 Catani, F., 363
 Čeh, N., 197–219
 Cello, G., 261
 Cepeda-Diaz, A.F., 33
 Chadwick, I., 233
 Chandler, R.J., 18, 19
 Charrière, M., 84, 106
 Chen, T.-L., 329
 Cheng, D., 5
 Cheng, Q., 55–108
 Cheng, Y.M., 291
 Cheung, R.W.M., 311, 312
 Chevalier, M.L., 89
 Choi, C.E., 312–315, 319
 Chung, S.L., 72
 Church, M., 225, 232
 Ciampalini, A., 362, 363, 368
 Cieslik, K., 184
 Cignetti, M., 200
 Cinco, T.A., 247, 248
 Cirak, N.S., 169
 Clague, J., 224, 225, 233
 Coe, J.A., 5
 Collotta, T., 34
 Colman, E.A., 287
 Conforti, M., 115
 Corominas, J., 138, 325–327
 Coulomb, C.B., 10
 Cowgill, E., 81
 Cowles, B., 144
 Cox, L.A. Jr., 142
 Cox, R., 361
 Cripps, J.C., 23
 Cross, T.C., 169
 Crosta, G., 424
 Crosta, G.B., 269, 413–428
 Cruden, D.M., 62, 73, 83, 197, 235, 363
 Cruz, F.A.T., 247–256
 Cuomo, S., 128
 Cutter, S.L., 432

D

Dado, J.M.B., 247–256
 Dai, F.C., 61, 137
 Damm, A., 432
 Dang, K., 375–400
 Davies, T.R., 56, 60, 65
 Davis, R.O., 43
 de Dios, R., 200
 De Silva, W.A.R.K., 311–321
 Deblonde, C., 227, 229
 Dekens, J., 184
 Delaney, K.B., 55
 Descoeurdes, F., 424
 Dewhurst, D.N., 23

Dewi, R.P., 169
 Di Prisco, C., 427
 Dimain, M.R.S., 247–256
 Do, N.H., 259
 Doan, H.L., 376
 Dominguez, M.J., 222
 Donald, G., 415
 Dorren, L.K.A., 424
 Du, Y., 285–294
 Duc, D.M., 376, 384, 393–396
 Dufresne, A., 56, 59–61, 65, 84, 89, 106
 Duncan, J.M., 11
 Dunning, S.A., 55, 60
 Đurić, U., 355–360, 403
 Dyvik, R., 22

E

Eckersley, D., 198
 Eid, H.T., 23, 29, 33, 34
 Ekkirala, H.C., 183–195
 Elejalde-Cadena, N.R., 261
 Elliott, J.R., 56
 Elwood, D., 221–237
 Ericksen, G.E., 55
 Ering, P., 5
 Erzagian, E., 115–125
 Eshraghian, A., 225, 232–235
 Evans, S.G., 55, 56, 84, 224

F

Falkovich, G., 244
 Fan, C., 5
 Fan, G., 55, 89
 Farmer, F.R., 139, 143
 Farvacque, M., 144
 Fathani, T.F., 115–125, 183
 Fell, R., 138–140, 156, 362
 Feng, T., 200
 Feng, Z., 55–108
 Fernandez, R., 29
 Fernando, T., 323–338
 Ferrari, F., 423
 Fiebigger, G., 311
 Finch, C., 432
 Finlay, P.J., 156
 Finn, W.D.L., 26
 Fischhoff, B., 432
 Flynn, J., 432
 Fomenko, I.K., 259–267
 Fookes, P.G., 115, 118
 Foott, R., 36
 Franceschinis, C., 184
 Frattini, P., 413–428
 Friele, P., 55
 Frodella, W., 361–370, 413–428
 Froude, M.J., 197, 311
 Frydman, S., 128
 Fu, B., 89
 Fudeyasu, H., 248
 Fukuoka, H., 5
 Fukuzono, T., 269, 270, 272
 Fulton, R.J., 225, 232

G

Gallego, J.I., 413–428
 Gallopín, G.C., 326, 328, 330
 Gandreau, D., 423
 Garnica-Peña, R.J., 155–164
 Gauthier, D., 5
 Gaventa, J., 184
 Geertsema, I.M., 56
 Gerber, W., 423
 Giadrossich, F., 128
 Gibo, S., 33
 Gigli, G., 413–428
 Gill, J.C., 144
 Gillet, J.E., 137, 141, 143, 144
 Giorgi, F., 250
 Giorgini, P., 324
 Girgin, S., 144
 Giusti, I., 169
 Godt, J., 127
 Gokceoglu, C., 184
 Gong, W., 454
 Goodchild, M., 184
 Goodwin, G.R., 312
 Grabowski, W.W., 244
 Greening, L., 432
 Greiving, S., 137
 Griffiths, D.V., 291
 Grimaz, S., 178
 Gu, J., 184
 Guha-Sapir, D., 311
 Guntha, R., 183–195
 Guo, C.B., 62
 Guo, Y., 169, 285–294, 461–462
 Gustafson, P.E., 156
 Guthrie, R.H., 55
 Gutscher, H., 432
 Guzzetti, F., 311, 344, 424, 425
 Gyekye, S.A., 432

H

Habib, P., 56
 Hadley, G., 415
 Haimes, Y.Y., 137, 138, 141, 147
 Haklay, M.M., 184
 Han, W.B., 61
 Hanai, K., 483–484
 Haque, U., 121
 Harris, A.J., 23, 25
 Harrison, T.M., 56, 61, 72
 Hartford, D., 139
 Hasani, S., 324
 Hatibe, A., 169
 Hawkins, A.B., 23, 33
 He, B., 176
 He, S.M., 56
 He, Z.M., 285
 Hebda, R.J., 232
 Heim, A., 62, 83
 Henkel, D.J., 18, 19
 Hernández-Moreno, G., 156, 432
 Hersbach, H., 250
 Hewitt, K., 55
 Hilbert, G., 5
 Hirota, K., 176
 Hiwasaki, L., 184

Holcombe, E., 183
 Holmes, J., 223, 232
 Hong, Y.-S., 198
 Hopkin, P., 327, 329
 Howes, D.E., 227, 229
 Hu, Q., 261
 Hu, W., 56
 Huang, M.S., 291
 Huang, R.Q., 55
 Huang, X., 324, 326
 Hubert-Ferrari, A., 361
 Huebl, J., 311
 Hung, L.Q., 259
 Hunger, O., 198
 Hungr, O., 56, 143, 269, 311, 318, 319
 Huntley, D., 221–237
 Hussain, M., 29
 Hutchinson, J.N., 33
 Hutter, K., 56
 Hvorselv, M.J., 23, 36

I

Itto, F., 115
 Ikari, Y., 463–466
 Ikeda, S., 329
 Ilia, I., 118
 Ischuk, A., 89
 Iserloh, T., 201
 Ishihara, K., 37
 Ishizuka, H., 198
 Iverson, R.M., 56, 128, 198, 312, 314
 Izquierdo-Horna, L., 326

J

Jaboyedoff, M., 56, 137–151
 Jagodnik, P., 343–353
 Jagodnik, V., 197–219
 Jemec Auflič, M., 329
 Jia, C.Q., 291
 Jia, Z., 311–321
 Joffe, H., 156
 Joffé, H., 156
 Johnsen, T., 225, 232
 Johnson, B.C., 56
 Johnson, C.G., 106
 Jonkman, S.N., 139
 Jotić, M., 403
 Journault, J., 222
 Juang, C.S., 184
 Juriša, M., 344

K

Kageyama, A., 240
 Kahhat, R., 326
 Kaklamanos, J., 169
 Kalsnes, B., 178
 Kamal, A.S.M.M., 431–438
 Kamiya, T., 239
 Kamworapan, S., 249
 Kanji, M.A., 33
 Kanungo, D.P., 118
 Karl, T.R., 249
 Karnawati, D., 175

Karunawardena, A., 323–338
 Kasperson, R.E., 431
 Kellens, W., 328, 329
 Kenk, E., 227
 Keraminiyage, K., 323–338
 Khazai, B., 324
 Kien, N.T., 260
 Kilburn, C.R.J., 156
 Kimura, T., 198
 King, M., 232
 Kirschbaum, D., 249
 Kiyota, T., 306, 308
 Kocaman, S., 184
 Konagai, K., 299–309
 Kong, F., 285
 Koo, R.C.H., 315, 317, 318
 Kotz, S., 147
 Krause, J.-P., 138
 Krkač, M., 343–353
 Kropáček, J., 56
 Krušić, J., 355–360
 Kutara, K., 198
 Kwan, J.S.H., 311, 312, 317, 318

L

Labibah, U.N., 169
 Labiouse, V., 56
 Lacasse, S., 137, 141, 142
 Ladd, C.C., 29, 36
 Lade, P.V., 23
 LaGatta, D.P., 23
 Lamberti, A., 319
 Lan Huong, T.T., 259
 Landeros-Mugica, K., 161
 Landva, A., 22
 Lane, P.A., 291
 Larsen, I.J., 57
 Larson, K.M., 56
 Lash, S., 431
 Lateltin, O., 149
 Lazo, J.K., 432
 Lazzeri, G., 361–370
 Lee, S., 117
 Lee, T.-L., 327
 Legros, F., 55
 Leroueil, S., 141
 Levine, D., 432
 Li, C., 451–455
 Li, Q., 285
 Liang, T., 198
 Liang, Z., 286
 Liao, M., 259
 Lichtenstein, S., 432
 Limousin, P., 150
 Lin, A., 56
 Lin, M.L., 198
 Lin, Q., 55–108
 Lin, Y.N., 5
 Liu, H., 311–321
 Liu, X., 89
 Lo Presti, D., 169
 Locat, J., 141
 Loew, S., 423
 Loi, D.H., 176, 375–400
 Løken, T., 33

Longchamp, C., 78, 106
 Lora, M., 201
 Lu, N., 127
 Lu, P., 200
 Lu, Y.Z., 286
 Lucas, A., 55, 62, 73, 83
 Lukačić, H., 343–353
 Luo, X.Q., 285
 Lupini, J.F., 23, 33
 Lupton, D., 431
 Lusini, E., 413–428

M

Macciotta, R., 138
 Mainsant, G., 148
 Malamud, B., 343
 Malamud, B.D., 144, 261
 Malisan, P., 178
 Mandelbrot, B., 261
 Manzella, I., 56
 Maquiling, J.T., 247–256
 Margottini, C., 361–370, 413–428
 Marija, L., 423
 Marjanović, M., 355–360, 403–409
 Martelloni, G., 127
 Martinez-Marquez, D., 144
 Marui, H., 25, 26, 33–37, 42, 50, 51
 Marui, T., 463–466
 Masi, E.B., 127–134
 Mathewes, R.W., 232
 Matsumoto, J., 247
 Mazzanti, P., 270
 McColl, S.T., 60
 McDermott, R.J.W., 18, 19
 McDougall, S., 56, 318
 McSaveney, M.J., 56
 Meehan, C.L., 14, 18–21
 Melosh, H.J., 56
 Mereu, A., 143
 Mergili, M., 56
 Mersha, T., 115, 117, 118
 Mesri, G., 29, 33
 Meten, M., 115
 Metz, C.E., 265
 Mihalić Arbanas, S., 200–202, 344, 355
 Mikoš, M., 167–178, 447–450
 Miller, S.A., 55
 Miltenberger, A.K., 241
 Ming, J., 55–108
 Mitchell, A., 59
 Mohanan, N.K., 183–195
 Mohr, O., 10
 Moon, A.T., 29
 Moreno, A., 261
 Moreno, A.R., 156, 157
 Morgenstern, N., 139
 Morgenstern, N.R., 198
 Moriset, S., 423
 Moriwaki, H., 269
 Müller-Vonmoss, M., 33, 34
 Munasinghe, D., 323–338
 Munoz, V.A., 169
 Murillo-García, F., 159
 Murillo-García, F.G., 156

N

Nadim, F., 137
Nakagawa, H., 5
Narisma, G.T., 248, 250, 252, 253, 256
Ng, C.W.W., 311–321
Nguyen, K.T., 259–267
Nicholson, A., 222
Nicoletti, P.G., 106
North, M.A., 121

O

O'Brien, J.S., 302
Obu, J., 286
Ochiai, H., 269, 273, 274
Odaka, J., 483–484
Oka, H., 198
Olaguera, L.M.P., 247, 248
Oliveira, S.C., 432
Onishi, R., 239–246
Ooi, G.L., 200
Operstein, V., 128
Ostermann, M., 55, 106
Ouyang, C.J., 56
Ozkazanc, S., 169
Ozturk, U., 311

P

Pack, R., 127
Paguican, E.M.R., 78, 106
Pajalić, S., 201, 206
Pan, D., 285
Pando, M.A., 169
Parajuli, B.P., 184
Parise, M., 106
Park, H.J., 127
Pasman, H.J., 137, 140, 143
Paun, M.-A., 261
Payne, B.K., 432
Peacock, W.H., 26
Peng, T.G., 285
Peranić, J., 197–219
Perdomo, J.L., 169
Perissé Valero, I., 413–428
Peterson, T.C., 249
Petley, D.J., 18, 19
Petley, D.N., 197, 311
Petrella, E., 174
Pham, T.T., 259
Pidgeon, N., 156
Piersanti, A., 56
Piton, G., 312, 315
Plafker, G., 55
Popescu, M., 202
Porter, M., 139, 141, 143, 224–226, 232–235
Poudyal, S., 311–321
Prakasam, C., 172
Privett, K.D., 23, 33
Psomiadis, E., 118, 121
Pudasaini, S.P., 56
Pumir, A., 244
Putrich, S.F., 33

Q

Qasim, S., 432

R

Rabie, K.H., 29
Raetz, H., 145
Rahardjo, W., 116, 118
Ramesh, M.V., 183–195
Ramsey, B.C., 415
Ranglund, O.J., 169
Rasyid, A.R., 117
Raydugin, Y., 140
Recking, A., 312, 315
Reichenbach, P., 249, 343–353, 362
Reimer, P., 415
Renn, O., 432
Reznichenko, N.V., 57
Rhymsburger, D., 130
Rigamonti, S., 413–428
Rinaldi, M., 285
Ritchie, H., 4, 6
Robbins, J.C., 5
Robinson, A.C., 81
Roca, M., 309
Rohan, T.J., 184, 185
Rose, N.D., 269
Rossi, G., 127–134
Rossi, M., 343–353
Rotheram-Clarke, D., 221–237
Rusconi, G., 413–428
Rutzinger, M., 171
Ryder, J.M., 225

S

Sabri, S., 324, 327
Saito, M., 269, 270
Salciarini, D., 127
Saleh, A.A., 29
Salminen, S., 432
Salvatici, T., 127–130
Samm-A, A., 431–438
Sammonds, P., 431–438
Sancio, R.B., 27
Sanders, D., 55
Santuz, A., 261
Šarić, G., 343–353
Sarkar, S., 118
Sasahara, K., 269–282
Sassa, K., 155, 156, 164, 168, 176, 375–400, 463
Satake, K., 375
Sato, T., 240
Sattar, A., 299–309
Sattler, K., 221–237
Scaioni, M., 200
Schlögel, R., 344
Schmocker, L., 144
Schwanghart, W., 57
Scotton, P., 319
See, L., 184
Seed, H.B., 26
Seifert, A., 244
Seong, Y.B., 81, 82
Sezgin, S., 169
Shakya, P., 184

Shan, W., 285–294, 461–462
 Shea, T., 56, 78, 106
 Shi, A., 55–108
 Shi, A.W., 81, 89, 91, 93
 Shrestha, B.B., 5
 Shreve, R.L., 56
 Siegrist, M., 432
 Silver, M.L., 26
 Silvertown, J., 184
 Simoni, S., 127
 Šimunić, A., 344
 Sinčić, M., 343–353
 Singh, B., 183–195
 Sivakumar Babu, G.L., 5
 Sjöberg, L., 432
 Skamarock, W.C., 242
 Skempton, A.W., 11, 18, 19, 33
 Skilodimou, H.D., 115
 Slovic, P., 156, 432
 Snyder, J.B., 200
 Soeters, R., 249
 Solana, M.C., 156
 Solheim, A., 144
 Song, B., 26
 Song, D., 312, 314, 315, 319
 Song, Z., 55–108
 Soori, H., 432
 Soret, M., 57
 Spizzichino, D., 361–370, 413–428
 Srl, E., 471–473
 Stanković, R., 403–409
 Stanton, R.B., 224, 233
 Stark, T.D., 23, 29, 30, 33–35, 42
 Steward, H.E., 23
 Stock, M., 326, 327, 329
 Strecker, M.R., 81, 89
 Strom, A., 55, 57, 59, 60, 81, 89, 106, 175
 Sujatha, E.R., 183
 Sun, B.G., 82
 Sun, P., 55
 Surussavadee, C., 249
 Sweet, L., 325
 Swets, J.A., 266

T

Takahashi, K., 240, 242
 Takahashi, T., 312
 Take, W.A., 198
 Talib, J.A., 117
 Tan, Q., 5, 451–455
 Tanabe, N., 261
 Tang, H., 451–455
 Tang, R.C., 61
 Tang, Z.H., 285
 Tangang, F., 249
 Tappenden, K., 235
 Tapponnier, P., 56
 Tauchi, H., 467–470
 Tazik, E., 117
 Thakur, V., 169
 Thirugnanam, H., 183–195
 Thomas, H., 415
 Thompson, N., 106
 Tien Bui, D., 259
 Tika, T.E., 33

Tiwari, B., 3–51
 Tofani, V., 127–134, 361–370
 Torre, D.M.G., 324
 Toyota, H., 33
 Tran, T.H., 325, 326
 Truelove, H.B., 328
 Tsangaratos, P., 118
 Tulloch, J., 431
 Türk, N., 121
 Turner, A.K., 183

U

Uzielli, M., 177

V

Valderrama, P., 106
 Valentino, R., 172
 van Drop, J.R., 147
 Van Duong, B., 259–267
 Van Westen, C.J., 137, 249
 van Wyk de Vries, B., 56, 78, 106
 VanDine, D.F., 311, 317
 Varnes, D.J., 62, 235, 269, 363, 423
 Vecchiotti, M., 427
 Vengeon, J.M., 142, 147
 Vicente, M.C.T.M., 247–256
 Vinodini Ramesh, M., 189
 Vitrano, L., 413–428
 Vivoda Prodan, M., 197–219
 Voight, B., 33, 269
 Volkwein, A., 311, 318
 Vose, D., 147
 Vrijling, J.K., 137
 Vucetic, M., 26
 Vulović, N., 403–409

W

Wachinger, G., 432
 Wadhawan, S.K., 185
 Wahbi, A.M., 417
 Wang, K.-L., 198
 Wang, L., 475–477
 Wang, L.-P., 244
 Wang, X., 138
 Wang, Y., 55–108, 261
 Wang, Y.F., 68, 73, 83, 84, 106
 Wang, Y.H., 200
 Wartman, J., 5, 198
 Watry, S.M., 23
 Watson, P.D.J., 23
 Wei, Z., 286
 Weidinger, J.T., 56, 57, 61
 Wendeler, C., 312
 Wentworth, J., 326, 327, 329
 Whipple, K., 56, 57
 Wichmann, V., 363
 Wicker, L.J., 242
 Widagdo, A., 115, 116
 Wiczorek, G.F., 200
 Wijegunaratne, E., 324
 Wilopo, W., 115–125
 Wong, H.N., 143
 Wood, D.M., 22

Wright, S.G., 29, 30
Wu, Y.-M., 458
Wu, Z.H., 73

X

Xu, D., 328, 329
Xu, X.W., 61

Y

Yagi, N., 198
Yalcin, A., 117, 121
Yamaguchi, I., 198
Yan, M., 285
Yang, H., 5
Yasuda, Y., 245
Yeganeh, N., 324, 327
Yik, M., 311
Yin, A., 56, 61
Yin, Y., 175
Yoshida, H., 106, 107
Yu, X., 265
Yuan, W., 291
Yuan, Z.D., 57, 83, 91
Yuksel, U.D., 169

Z

Zadeh, L.A., 146
Zanutta, A., 200
Zanuttigh, B., 319
Zeng, Q.L., 68
Zhai, G., 329
Zhang, C., 285–294
Zhang, D., 144
Zhang, J., 5
Zhang, P.Z., 56
Zhang, S., 5
Zhang, Y., 5
Zhang, Y.B., 55
Zhang, Z., 72
Zheng, H., 291
Zhou, G.G.D., 312
Zhou, S., 326, 327
Zhou, X.P., 270
Zhu, S.D., 285
Zhu, Y.X., 55, 83
Zienkiewicz, O.C., 291
Zimmermann, T.H., 424
Zlatanova, S., 324–326
Zubovich, A.V., 89